

Vol. 20, No. 1, March, 2021

ISSN (Print): 0972-6268; ISSN (Online) : 2395-3454

NATURE ENVIRONMENT & POLLUTION TECHNOLOGY

*A Multidisciplinary, International Journal
on Diverse Aspects of Environment*



Technoscience Publications

website: www.neptjournal.com



Technoscience Publications

A-504, Bliss Avenue, Balewadi,
Opp. SKP Campus, Pune-411 045
Maharashtra, India

www.neptjournal.com

Nature Environment and Pollution Technology

(An International Quarterly Scientific Research Journal)

EDITORS

Dr. P. K. Goel

Former Head, Deptt. of Pollution Studies
Y. C. College of Science, Vidyanagar
Karad-415 124, Maharashtra, India

Dr. K. P. Sharma

Former Professor, Deptt. of Botany
University of Rajasthan
Jaipur-302 004, India

Published by : Mrs. T. P. Goel, B-34, Dev Nagar, Tonk Road, Jaipur-302 018
Rajasthan, India

Managing Office : Technoscience Publications, A-504, Bliss Avenue, Balewadi,
Pune-411 045, Maharashtra, India

E-mail : contact@neptjournal.com; journalnept@gmail.com

INSTRUCTIONS TO AUTHORS

Scope of the Journal

The Journal publishes original research/review papers covering almost all aspects of environment like monitoring, control and management of air, water, soil and noise pollution; solid waste management; industrial hygiene and occupational health hazards; biomedical aspects of pollution; conservation and management of resources; environmental laws and legal aspects of pollution; toxicology; radiation and recycling etc. Reports of important events, environmental news, environmental highlights and book reviews are also published in the journal.

Format of Manuscript

- The manuscript (*mss*) should be typed in double space leaving wide margins on both the sides.
- First page of *mss* should contain only the title of the paper, name(s) of author(s) and name and address of Organization(s) where the work has been carried out along with the affiliation of the authors.

Continued on back inner cover...

Nature Environment and Pollution Technology

Vol. 20, No. (1), March 2021

CONTENTS

1. **Feifei Wang, Huan Zhang, Mingming Du, Jinling Li, Penghui Yang, Tao Yu, Yijun Wang and Chengtun Qu**, Effects of TiO_2 /Bentonite on the Pyrolysis Process of Oily Sludge 1-12
2. **M. Pal, M. Gope, A. Basu, T. Laha, R. E. Masto, R. Labar, T. K. Kundu, R. R. Hoque, P. S. Khillare and S. Balachandran**, Indoor Quality of Residential Homes and Schools of an Industrial Area in Asansol: Characterization, Bioaccessibility and Health Risk Assessment of Potentially Toxic Elements 13-28
3. **Kai Su and Chienming Lee**, Spatial Dependence Pattern of Energy-Related Carbon Emissions and Spatial Heterogeneity of Influencing Factors in China: Based on ESDA-GTWR Model 29-38
4. **Weidong Ma, Dacheng Sun, Yongsheng Deng, Xianyun Meng and Mi Li**, Analysis of Carbon Emissions of Prefabricated Buildings from the Views of Energy Conservation and Emission Reduction 39-44
5. **S. Herat**, E-Waste Management in Asia Pacific Region: Review of Issues, Challenges and Solutions 45-53
6. **Haibo Kang, Jiahui Gu, Gang Liu, Ben li and Wei Wang**, Performance and Mechanism of Layered Double Hydroxide to Remove Graphene Oxide in Aqueous Solution 55-62
7. **F. Ahmed, A. N. M. Fakhruddin, Z. Fardous, M. A. Z. Chowdhury, M. M. Rahman and M. M. Kabir**, Accumulation and Translocation of Chromium (Cr) and Lead (Pb) in Chilli Plants (*Capsicum annum L.*) Grown on Artificially Contaminated Soil 63-70
8. **H. Joga Rao**, Modelling and Optimization of Energy-Efficient Procedures for Removing Lead from Aqueous Solutions Using Activated Carbons Prepared from Waste Tyres and *Bauhinia purpurea* Leaves 71-83
9. **Sura Taha Al-Harabsheh**, Swimming Pool Water in Mafraq City in Northern Jordan: Quality Evaluation 85-92
10. **Vivek Chopra and Jai Gopal Sharma**, SEM-EDAX analysis of the Soil Samples of River Yamuna in Delhi Region 93-103
11. **B. Tengjaroenkul, S. Boonmee and L. Neeratanaphan**, Analysis of the Genetic Effects to Frogs (*Fejervarya limnocharis*) After Acute Lead Exposure *In Vivo* 105-112
12. **Priya Gaur, Mohnish Pichhode, Jatan Dudwe, C.S. Shrivastava and S. Gaherwal**, Residential, IUCN and WPA Status of the Avian Fauna Observed in Indore city (M.P.), India 113-121
13. **Quan Yuan, Kefeng Li, Ruifeng Liang, Yuanming Wang, Jingjie Feng, Qianfeng Ji and Yaodan Zhang**, Physiological Response of Juvenile *Schizothorax prenanti* under Supersaturated Stress 123-132
14. **Manish Ranjan, Prabhat Kumar Singh and Arun Lal Srivastav**, Application of Hydrous Bismuth Oxide for Arsenic Removal from Aqueous Solutions 133-145
15. **Wenfang Zhou**, Carbon Emission Estimation of Prefabricated Buildings Based on Life Cycle Assessment Model 147-152
16. **Y. X. Fang, G. J. Liu and R. J. Liu**, Fish Community Structure and Ecological Health Assessment of the Shuaishui River Basin, China 153-161
17. **Bibhabasu Mohanty, Anirban Das, Reema Mandal, Upasana Banerji and Sukanya Acharyya**, Heavy Metals in Soils and Vegetation from Wastewater Irrigated Croplands Near Ahmedabad, Gujarat: Risk to Human Health 163-175
18. **Xianqi Zhang, Yang Yang and Zhiwen Zheng**, Analysis of Temporal Evolution Characteristics of Annual Precipitation in the Yellow River Delta 177-184
19. **B. W. Zhao, X. J. Nan, Y. Q. Li, H. Liu and K. X. Duan**, Modelling Sorption and Leaching Behaviour of Sulphate in Light Sierozem (Calcids) Columns with Rape Straw Biochar Amendments with Steady Flow 185-192
20. **Brototi Biswas and Abinada Azyu**, Water Resources and Management System of the Himalayan Region: Case Study of Mizoram, India 193-201
21. **Q. Wang, L.P. Liang, F.F. Xi, Q. Wu, Y.Y. Xue, L.B. Cheng, Y.T. Zhang and X. Meng**, Kinetics Studies on Toxic Hexavalent Chromium Removal from Aqueous Solutions by Magnetic Nano-Magnetite 203-209
22. **D. Tamilmathi and M. R. Rajan**, Genotoxic Effect of Iron Oxide Nanoparticles Treated Tannery Effluent on Zebrafish *Danio rerio* 211-219
23. **Yushan Wan, Juan Zhai and Anwei Wang**, Comparative Study on Electrode Arrangement in Electrokinetic Remediation of Contaminated Soil 221-227
24. **Linsheng Wang and Wei Yang**, Electronic Waste Recycling Mode and Control Measures in China Based on PEST and SWOT 229-235
25. **Ramdiana Muis, Nani Anggraini, Fitri Ariani, Sattar Yunus and Zulkifli**, Survey of Environmental Baseline in the Nunukan Agriculture Area, Indonesia 237-242
26. **M. P. Choudhary, H. D. Charan and B. Acharya**, A Novel Approach for Disposing Agriculture Waste, Minimizing Air Pollution and Amending Soil Through Biochar Production and Application 243-249
27. **G. V. Satyanarayana, T. Byragi Reddy, R. S. S. Srikanth Vemuri, K. Suryanarayana Rao and Manoj Kumar Karnena**, A Study on Development of Pollution Index Models and Multivariate Statistical Analysis for Heavy Metals in the Soils of APIIC, Visakhapatnam 251-257

28. **M. Maheshwari and P. Vijayarengan**, Phytochemical Evaluation, FT-IR and GC-MS Analysis of Leaf Extracts of *Pergularia daemia* 259-265
29. **I. Sharma, P. Tongkumchum and A. Ueranantasun**, Regression Analysis of Normalized Difference Vegetation Index (NDVI) to Compare Seasonal Patterns and 15 Year Trend of Vegetation from East to West of Nepal 267-273
30. **R. S. Ahmed and M. D. Swargiary**, Plastic and Petroleum Hydrocarbon Degrading Potentials of Single and Mixed Bacterial Cultures Isolated from Garbage Areas of Darrang, Assam 275-280
31. **Hasan Fadhil Al Rubai, Ahmed Khudhair Hassan, Muntadhar Salih Sultan and Waleed Mohammed Abood**, Kinetics of Adsorption of Reactive Red 120 Using Bentonite Modified by CTAB and Study the Effect of Salts 281-289
32. **Jing Dai, Ruolin Xu, Wangying Li, Yulin Li, Yang Yang, Yang Xiao, Huan Mao, Muqing Qiu, Hai Wang, Ningcan Yang and Li Han**, Effect of Pyrolysis Temperature on Adsorption Characteristics of Biochar Derived from Corn Straw 291-296
33. **Muhamad Saffih Lola and Anton Abdulbasah Kamil**, Estimating Discharge of Nitrogen in Zero Water Exchange at I-Sharp Setiu, Terengganu, Malaysia, Based on System Dynamic Approach 297-303
34. **A. Rajini and K. Revathy**, Effect of Chlorpyrifos 50% + Cypermethrin 5% EC on *Eisenia fetida* Exposed in Coco Peat and Sphagnum Peat 305-309
35. **Y. Wang, M.C. Wei, Q.C. Yu and M.T. Zhu**, Temperature-Sensitive Ionic Liquid-Based Dispersive Microextraction for Removal of Industrial Dyes in Water 311-316
36. **Jia Jia, Jingjing Yang, Yawen Song, Huimin Chen and Xi Zhang**, Development of Emissions Inventory and Pollution Classification for Energy-Intensive Heavy Metal Industries in A Densely Distributed Area 317-328
37. **M. Bouzid, A. Djadi and B. Bezzazi**, Study and Physicochemical Characterization of the Diesel Particles Inducing Bronchopulmonary Obstructions and Inflammation 329-334
38. **Xiuli Li and Xu Wu**, Study on the Effects of Sewage Irrigation on Soil 335-340
39. **Shihu Liu, Ziyuan Lin, Jiong Zhou, Yongsheng Zhang, Jiale Wang and Jian Zhou**, Effect of Temperature Downshifts on Performance and Microbial Community Structure on Pilot-Scale Sequencing Batch Biofilm Reactors Treating Hypersaline Wastewater 341-347
40. **A. Geethakarathi**, Novel Approaches Towards Sustainable Management of an Agricultural Residue - The Rice Husk 349-355
41. **L.H. Sun and S.B. Feng**, Pollution Assessment of Trace Elements in the Soil Planting Chinese Herbaceous Peony in Suzhou, China 357-362
42. **Mingwei Li and Huijuan Zhao**, Contribution of Low-carbon Transport Policy to the Improvement of Urban Traffic Ecological Environment 363-370
43. **G. Sahu and V. Kumar**, The Toxic Effect of Fluoride and Arsenic on Behaviour and Morphology of Catfish (*Clarias batrachus*) 371-375
44. **Yuan Yuan Li and Ting Ting Zhang**, Stability Properties of Chromium in Cr(VI)-Contaminated Soil Stabilized by Calcium Polysulfide (CaS_3) 377-383
45. **Kai Wang**, Impact of Corporate Governance on Environmental Protection Investment of China's Listed Enterprises in High-polluting Industry 385-390
46. **P. H. Patil, V. R. Parate, J. J. Jankar, A. S. Deshpande and B. N. Annapurve**, Development of Activated Carbon from Agricultural Waste: Sapota Peels 391-396
47. **Wenju Zhao, Junhong Hu, Zongli Li, Ping Yu and Changquan Zhou**, Numerical Simulation of Effect of Sand Thickness on Soil Evaporation 397-403
48. **R. Q. Gao, Y. R. Huang, D. Liu and G. T. Li**, Effect of Heat Treatment Process on the Structure and Properties of Nano- TiO_2 405-410
49. **Yuan Yuan Li and Ting Ting Zhang**, Studies on Engineering and Microstructure Properties of Chromium(VI)-Contaminated Soil 411-416
50. **Aifang Gao, Yiyun An, Liuliu Ma, Yingying Lian and Aiguo Li**, Fenton Oxidation Kinetics of Azo Dye Acid Light Yellow 2G Wastewater by Online Spectrophotometry 417-423
51. **Ananto Aji, Sigit Bayhu Iryanthony, Wahid Akhsin Budi Nur Sidiq and Edy Trihatmoko**, Relationship Between NDVI and the Microbial Content of Soil in Detecting Fertility Level at Semarang Regency, Jawa Tengah, Indonesia 425-432
52. **Xitong Zheng, Long Fu, Hao Deng, Keyuan Huang, Tianqi Liu, Yulin Deng, Jiaming Luo, Miao Xiang, Anjie Wang, Muqing Qiu, Li Han and Hai Wang**, Adsorption of U(VI) in Solution by Biochar and FeS Nanoparticles 433-437
53. **Yanchun Hao**, Study on Hazards of Chemical Fibre Wastewater and Evaluation of Uncertainty in Environmental Monitoring 439-445

The Journal
is
Currently
Abstracted
and
Indexed
in:

International Scientific Indexing (UAE) with Impact Factor 2.236 (2018)

NAAS Rating of the Journal (2019) = 3.85

Scopus®, SJR (0.127) 2019

Index Copernicus (2018) = 135.97

EI Compendex of Elsevier

Indian Science Abstracts,
New Delhi, India

Chemical Abstracts, U.S.A.

Elsevier Bibliographic
Databases

Pollution Abstracts, U.S.A.

Zoological Records

Paryavaran Abstract,
New Delhi, India

Indian Citation Index (ICI)

Scopus CiteScore (2019) = 0.5

Electronic Social and Science
Citation Index (ESSCI)

EBSCO: Environment Index™

Ulrich's (Refereed) database

CrossRef (DOI)

DOAJ

Zetoc

Google Scholar

ProQuest, U.K.

J-Gate

Environment Abstract, U.S.A.

British Library

Centre for Research Libraries

WorldCat (OCLC)

JournalSeek

Connect Journals (India)

CSA: Environmental Sciences and Pollution Management

Research Bible (Japan)

Indian Science

Geobase

Elektronische
Zeitschriftenbibliothek (EZB)

SHERPA/RoMEO

Directory of Science

CNKI Scholar (China National
Knowledge Infrastructure)

Access to Global Online Research in Agriculture (AGORA)

AGRIS (UN-FAO)

Present in UGC-CARE List (Group II)

UDL-EDGE (Malaysia) Products like *i*-Journals, *i*-Focus and *i*-Future

www.neptjournal.com

Nature Environment and Pollution Technology

EDITORS

Dr. P. K. Goel

Former Head, Deptt. of Pollution Studies
Yashwantrao Chavan College of Science
Vidyanagar, Karad-415 124
Maharashtra, India

Dr. K. P. Sharma

Former Professor, Ecology Lab, Deptt. of Botany
University of Rajasthan
Jaipur-302 004, India
Rajasthan, India

Manager Operations: Mrs. Apurva Goel Garg, C-102, Building No. 12, Swarna CGHS, Beverly Park, Kanakia, Mira Road (E) (Thane) Mumbai-401107, Maharashtra, India (**E-mail: operations@neptjournal.com**)

Business Manager: Mrs. Tara P. Goel, Technoscience Publications, A-504, Bliss Avenue, Balewadi, Pune-411 045, Maharashtra, India (**E-mail: contact@neptjournal.com**)

EDITORIAL ADVISORY BOARD

1. **Dr. Prof. Malay Chaudhury**, Department of Civil Engineering, Universiti Teknologi PETRONAS, Malaysia
2. **Dr. Saikat Kumar Basu**, University of Lethbridge, Lethbridge AB, Canada
3. **Dr. Sudip Datta Banik**, Department of Human Ecology Cinvestav-IPN Merida, Yucatan, Mexico
4. **Dr. Elsayed Elsayed Hafez**, Deptt. of of Molecular Plant Pathology, Arid Land Institute, Egypt
5. **Dr. Dilip Nandwani**, College of Agriculture, Human & Natural Sciences, Tennessee State Univ., Nashville, TN, USA
6. **Dr. Ibrahim Umaru**, Department of Economics, Nasarawa State University, Keffi, Nigeria
7. **Dr. Tri Nguyen-Quang**, Department of Engineering Agricultural Campus, Dalhousie University, Canada
8. **Dr. Hoang Anh Tuan**, Deptt. of Science and Technology Ho Chi Minh City University of Transport, Vietnam
9. **Mr. Shun-Chung Lee**, Deptt. of Resources Engineering, National Cheng Kung University, Tainan City, Taiwan
10. **Samir Kumar Khanal**, Deptt. of Molecular Biosciences & Bioengineering, University of Hawaii, Honolulu, Hawaii
11. **Dr. Sang-Bing Tsai**, Zhongshan Institute, University of Electronic Science and Technology, China
12. **Dr. Zawawi Bin Daud**, Faculty of Civil and Environmental Engg., Universiti Tun Hussein Onn Malaysia, Johor, Malaysia
13. **Dr. Srijan Aggarwal**, Civil and Environmental Engg. University of Alaska, Fairbanks, USA
14. **Dr. M. I. Zuberi**, Department of Environmental Science, Ambo University, Ambo, Ethiopia
15. **Dr. Prof. A.B. Gupta**, Dept. of Civil Engineering, MREC, Jaipur, India
16. **Dr. B. Akbar John**, Kulliyyah of Science, International Islamic University, Kuantan, Pahang, Malaysia
17. **Dr. Bing Jie Ni**, Advanced Water Management Centre, The University of Queensland, Australia
18. **Dr. Prof. S. Krishnamoorthy**, National Institute of Technology, Tiruchirapally, India
19. **Dr. Prof. (Mrs.) Madhoolika Agarwal**, Dept. of Botany, B.H.U., Varanasi, India
20. **Dr. Anthony Horton**, Envirocarb Pty Ltd., Australia
21. **Dr. C. Stella**, School of Marine Sciences, Alagappa University, Thondi -623409, Tamil Nadu, India
22. **Dr. Ahmed Jalal Khan Chowdhury**, International Islamic University, Kuantan, Pahang Darul Makmur, Malaysia
23. **Dr. Prof. M.P. Sinha**, Dumka University, Dumka, India
24. **Dr. G.R. Pathade**, H.V. Desai College, Pune, India
25. **Dr. Hossam Adel Zaqoot**, Ministry of Environmental Affairs, Ramallah, Palestine
26. **Prof. Riccardo Buccolieri**, Deptt. of Atmospheric Physics, University of Salento-Dipartimento di Scienze e Tecnologie Biologiche ed Ambientali Complesso Ecotekne-Palazzina M S.P. 6 Lecce-Monteroni, Lecce, Italy
27. **Dr. James J. Newton**, Environmental Program Manager 701 S. Walnut St. Milford, DE 19963, USA
28. **Prof. Subhashini Sharma**, Dept. of Zoology, University of Rajasthan, Jaipur, India
29. **Dr. Murat Eyvaz**, Department of Environmental Engg. Gebze Inst. of Technology, Gebze-Kocaeli, Turkey
30. **Dr. Zhihui Liu**, School of Resources and Environment Science, Xinjiang University, Urumqi, China
31. **Claudio M. Amescua García**, Department of Publications Centro de Ciencias de la Atmósfera, Universidad Nacional Autónoma de México
32. **Dr. D. R. Khanna**, Gurukul Kangri Vishwavidyalaya, Haridwar, India
33. **Dr. S. Dawood Sharief**, Dept. of Zoology, The New College, Chennai, T. N., India
34. **Dr. Amit Arora**, Department of Chemical Engineering Shaheed Bhagat Singh State Technical Campus Ferozepur -152004, Punjab, India
35. **Dr. Xianyong Meng**, Xinjiang Inst. of Ecology and Geography, Chinese Academy of Sciences, Urumqi, China
36. **Dr. Sandra Gómez-Arroyo**, Centre of Atmospheric Sciences National Autonomous University, Mexico
37. **Dr. Manish Sharma**, Deptt. of Physics, Sharda University, Greater Noida, India
38. **Dr. Wen Zhang**, Deptt. of Civil and Environmental Engineering, New Jersey Institute of Technology, USA



Effects of TiO₂/Bentonite on the Pyrolysis Process of Oily Sludge

Feifei Wang^(**), Huan Zhang^{***}, Mingming Du^{*}, Jinling Li^{*}, Penghui Yang^{*}, Tao Yu^{*}, Yijun Wang^{****}
and Chengtun Qu^(**)†

^{*}College of Chemistry and Chemical Engineering, Xi'an Shiyou University, Xi'an 710065, P. R. China

^{**}State Key Laboratory of Petrochemical Pollution Control and Treatment, Beijing 102206, P. R.China

^{***}School of Chemistry and Chemical Engineering, Southwest Petroleum University, Chengdu 610500, P. R.China

^{****}Karamay City Sanda Testing and Analysis Co., Ltd, 834000, P.R.China

†Corresponding author: Chengtun Qu; xianquct@163.comm

Nat. Env. & Poll. Tech.
Website: www.neptjournal.com

Received: 21-02-2020

Revised: 13-03-2020

Accepted: 02-05-2020

Key Words:

Oily sludge

Catalyst

TiO₂/bentonite

Catalytic pyrolysis

ABSTRACT

Oil sludge is one of the major industrial solid wastes from petroleum production and refining. Implementing the harmless and resource treatment of oily sludge is an urgent problem to be solved. In this paper, TiO₂/bentonite was prepared by sol-gel method, which was characterized by scanning electron microscope (SEM), transmission electron microscope (TEM), X-ray diffraction (XRD), X-ray photoelectron spectroscopy (XPS) and infrared spectroscopy (FT-IR), and then used in the pyrolysis process of oily sludge. The addition of TiO₂/bentonite give the best quality of pyrolysis oil; maximum oil recovery was achieved when setting the pyrolysis condition at 420°C for final pyrolysis temperature, 3 h for reaction time, 10°C/min for heating rate, 100 mL/min for nitrogen flow rate and 1% for catalyst dosage. Compared with the non-catalyst, oil recovery rate can be increased from 76.06% to 84.16%, the oil content of the residue decreased from 2.23% to 1.36%. The pyrolysis recovery oil was analysed by GC-MC, and the fractions of pyrolysis oil C₆-C₁₅ were increased by 27.84%. This shows that the addition of TiO₂/bentonite decreased the carbon residue, increased oil recovery and improved product quality.

INTRODUCTION

Oil sludge is one of the major industrial solid wastes from petroleum production and refining process (Mrayyan & Battikhi 2005, Agar et al. 2018), which is increasing quickly (Zhao et al. 2019, Wang et al. 2019) with the rapid development of economy, and it have been listed to the *Directory of National Hazardous Waste* as one of the most hazardous solid wastes. If oily sludge is discharged into the environment directly without reasonable treatment, it is not only harmful to the surrounding environment, animal and plant health, but also is a waste of resources because the containing of some content oil (Gong et al. 2018). Many countries are paying more attention to sewage sludge effective treatment and recycling, while the low-temperature pyrolysis of sludge is a new sludge treatment technology which developed in the recent years (Folgueras et al. 2013, Botella et al. 2015). The pyrolysis of the sludge is an emerging process technology, which is a promising alternative for sludge treatment in terms of treatment efficiency pollution reduction (Wang et al. 2018, Wang et al. 2017, Tang et al. 2018) and energy and resource recovery. But the quality of the oil obtained from the pyrolysis of sewage sludge cannot be used directly, the upgrading of sludge oil is indispensable.

To improve the quality of oil and enhance oil recovery, a series of studies on the addition of catalysts or additives during the pyrolysis of sludge were carried out. The addition of catalyst in the pyrolysis process of oily sludge can reduce the pyrolysis temperature, shorten the reaction time, improve the pyrolysis efficiency and decrease the amount of solid residue (Yang et al. 2018, Lin et al. 2017, Lin et al. 2019, Liu et al. 2015). Many scholars (Wang et al. 2015, Wang et al. 2008, Shie et al. 2004) found that the addition of catalyst can improve the yield and quality of oil products from oil sludge during the pyrolysis process. In recent years, an intense effort has been focused on the preparation of metal-oxide nanocrystals owing to their markedly different physical and chemical properties with respect to bulk materials. Particularly, titanium dioxide has been studied extensively as a photocatalyst to deal with environmental pollution, water purification, wastewater treatment, hazardous waste control, and air purification, due to its good characteristics of chemical stability, endurance, thin-film transparency and lower production costs. However, there are certain shortcomings associated with conventional TiO₂ powders catalysts, including TiO₂ is difficult to recover in the catalytic process, easy to lose, easy to agglomerate, and its application is limited. So the TiO₂ exhibits a poor catalytic

activity to non-polar organic compounds, resulting in limited catalytic efficiency. To enhance the catalytic activity onto the catalyst surface, various porous solid supports such as zeolite, silica and clay are utilized to support TiO_2 . For this reason, TiO_2 can be supported on some inexpensive and readily available catalyst supports with good adsorption and large specific surface area to make the supported catalysts. On the one hand, TiO_2 can be immobilized, and on the other hand, the layered molecular structure of bentonite can be modified to increase the contact area between the catalyst and the oily sludge, and play a role of synergistic catalysis, so as to improve the catalytic performance. Xiao et al. (2012) studied the pyrolysis characteristics and pyrolysis kinetics of paper sludge before and after the addition of MnO_2 , Al_2O_3 , MgO , Fe_2O_3 , CuO or CaO by thermogravimetric analysis. The results showed that the influence of these metal oxides on the pyrolysis of sludge was mainly in the middle and high temperature stage. Shao et al. (2010) studied the catalytic effect of Fe_2O_3 , ZnO , Al_2O_3 , CaO and TiO_2 on sludge pyrolysis, and found that these metal oxides could promote the decomposition of volatilization in sludge at the initial stage of the reaction. Since the bentonite has a significant effect on the pyrolysis of the low temperature zone during the pyrolysis of the oily sludge, the catalytic effect on the pyrolysis of the medium and high temperature zone is poor. Therefore, the bentonite is combined with the TiO_2 that plays a catalytic role in the middle and high temperature areas to play a synergistic catalytic role. The main objectives of this study were: (1) To evaluate the influence of TiO_2 /bentonite on the quality of oil products; (2) To evaluate the effect of TiO_2 /bentonite on the oil recovery rate of the pyrolysis process.

MATERIALS AND METHODS

Materials

The oily sludge sample used in this study was derived from the bottom sludge of an oil-separating tank in the Shanbei oil field Branch Company, China. The oily sludge sample appears black and possesses poor settling ability. The composition (including oil content and water content of sludge) of the oily sludge has been analysed and listed in Table 1. The water content was determined by ASTM-D95-13 (Lin et al. 2019) and oil content of sludge was determined by Soxhlet extraction using petroleum ether as a solvent. Tetrabutyl titanate, anhydrous ethanol, distilled water, acetic acid, bentonite and petroleum ether were all analytically pure reagents. The experimental water used was deionized water. All chemicals have been used as received without further purification.

Preparation of Catalysts

In this study, the supported catalyst was prepared by Sol-Gel method based on bentonite as matrix material (Yao et al. 2012, Cao et al. 2010, Li et al. 2007, Chen et al. 2009). The preparation process is shown in Fig. 1. The precursor was tetrabutyl titanate ($\text{Ti}(\text{OC}_4\text{H}_9)_4$, 97%). $\text{Ti}(\text{OC}_4\text{H}_9)_4$ was dissolved in anhydrous ethanol, and then mixed with acetic acid and deionized water under stirring. To avoid rapid precipitation during polycondensation and formation of unstable colloidal sols, the hydrolysing water was homogeneously released by the esterification of ethanol and acetic acid (Zhao et al. 2009). The clear solution was stabilized by stirring at ambient temperature for 1 h, then placed and

Table 1: Chemical characteristics of oily sludge.

Element composition (%)						Oil content/%	Water content/%	Calorific value (kJ/kg)
C(%)	N(%)	H(%)	S(%)	C/N	C/H			
21.63	1.45	4.25	2.36	14.949	5.086	18.67	11.20	12813.69

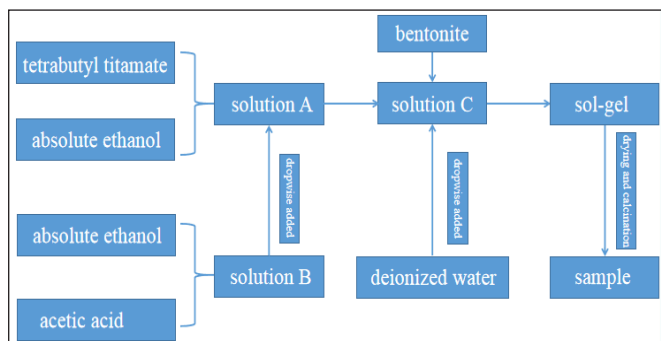


Fig. 1: The flow chart to prepare TiO_2 /bentonite catalysts.

aged for 24 h. Subsequently, the transparent sol was dried at 150°C, and then calcined to burn off hydrocarbons. The sample was crushed into powder in a mortar at last. Liu et al. (2009) studied the effect of calcination temperature on the structure of titanium dioxide photocatalyst. When the calcination temperature is 500-550°C, the development of TiO₂ crystal is gradually complete, and the lattice structure tends to be perfect, which is an anatase crystal phase with a catalytic effect. Therefore, it is selected to calcine at 500°C for 3 hours. The white powder obtained is TiO₂/bentonite, which is recorded as TiO₂/bentonite (1) (*n*Si:*n*Ti = 8:1). TiO₂/bentonite (2) (*n*Si:*n*Ti = 4:1) and TiO₂/bentonite (3) (*n*Si:*n*Ti = 1:1) was synthesized by changing the ratio of butyl titanate to bentonite in the same way.

Characterization of Catalysts

The surface morphology was investigated by scanning electron microscopy (SEM) using a JEOL JSM 6400 electronic microscope equipped with an energy-dispersive X-ray (EDX) detector (eXL10 from Link Analytical). X-ray diffraction (XRD) patterns were recorded by an Empyrean X-ray diffractometer with Cu K α radiation. X-ray photoelectron spectroscopy (XPS) measurements were performed using a Thermo ESCALAB 250 spectrometer with Al K α radiation as an excitation source. In order to analyze the surface chemical state of the obtained samples, the publicly available XPSPEAK v4.1 software package was used to perform a curve fitting of the raw data corresponding to the Ti2p high-resolution spectra. Fourier transform infrared (FTIR) spectra were obtained in a Bruker Vertex 70 spectrometer, with KBr pellets and a resolution of 2 cm⁻¹. Nitrogen adsorption isotherms were measured using a Micromeritics ASAP 2020 analyser. Samples were degassed at 300°C and 5×10⁻³ torr vacuum. The surface area was obtained by the BET method, and t-plot external area, micropore area, and micropore volume were also calculated.

Thermogravimetric Analysis

The thermogravimetric analysis (TG/DTG) was performed with a DSC/DTA-TG STA449F3 (Germany) thermogravimetric analyser. The initial mass of the samples was kept between 5 and 10 mg to avoid any possible effect on mass and heat transfer during the decomposition process. The samples were heated from 25 to 900°C at a heating rate of 10°C/min for solving the compensation effect under a nitrogen atmosphere with a flow rate of 20 mL min⁻¹ to investigate the effect of adding different catalysts on pyrolysis.

Catalytic Cracking Tests

Experimental method for pyrolysis of oily sludge: the catalyst was mixed with oily sludge in a certain proportion and

then placed in a pyrolysis furnace for pyrolysis. The performance of the catalyst was studied according to the analysis of pyrolysis products and the recovery rate of pyrolysis oil.

Products Analysis

The study examined the liquid products and solid products obtained by catalytic pyrolysis. The analysis of liquid phase pyrolysis products: composition of the liquid phase of pyrolysis products was explored by GC-MS (Yang et al. 2014) and four components of pyrolysis liquid phase products were determined by NB/SH/T0509-2010 oil bitumen four-component determination method (Zhang et al. 2009). The analysis of pyrolysis solid products: elemental analysis, oil content and calorific value of pyrolysis residue.

RESULTS AND DISCUSSION

Catalysts Characterization

Morphological feature: The SEM images are typical of the catalyst materials synthesized during this study. The SEM analysis of bentonite, TiO₂/bentonite(1), TiO₂/bentonite(2) and TiO₂/bentonite(3) are shown in Fig. 2. The surface of bentonite (a) was tight and the porosity was small, while the surfaces of TiO₂/bentonite(1) (b) was loose with more pores, the surface of TiO₂/bentonite(2) (c) was loose with more pores and small granules, the surface of TiO₂/bentonite(3) (d) was tight with small granules. The reason for this phenomenon is that the bentonite after loading titanium dioxide changes its morphology, increases the porosity and increases the specific surface area.

The EDS analysis of bentonite, TiO₂/bentonite(1), TiO₂/bentonite(2) and TiO₂/bentonite(3) are shown in Fig. 3. It can be seen that the content of Ti appeared compared with bentonite, which indicates that Ti was loaded onto bentonite. In addition, titanium content of TiO₂/bentonite(2) is greater than that of TiO₂/bentonite(1) and titanium content of TiO₂/bentonite(3) is greater than that of TiO₂/bentonite(2). From Fig. 3, the bentonite contains other elements, such as Al, Si and so on. The presence of these elements can promote the pyrolysis of sludge, thus actively promoting the research and development of pyrolysis catalysts for oily sludge.

Infrared Spectral Analysis

It also can be seen the O-H stretching vibration of adsorbed water in the interlayer of montmorillonite structure nearby 3439 cm⁻¹ (Zhu et al. 2012). It had stretching vibration band of O-H near 1642 cm⁻¹, and the peak near 1035 cm⁻¹ attributed to the asymmetry bending stretching of Si-O-Si. The bending vibration absorption peak of Si-O-Al near 519

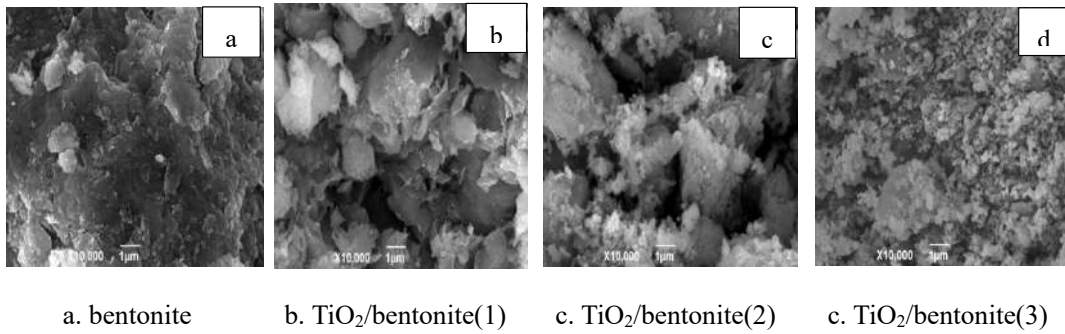


Fig. 2: SEM analysis of bentonite, *TiO₂/bentonite(1)*, *TiO₂/bentonite(2)* and *TiO₂/bentonite(3)*.

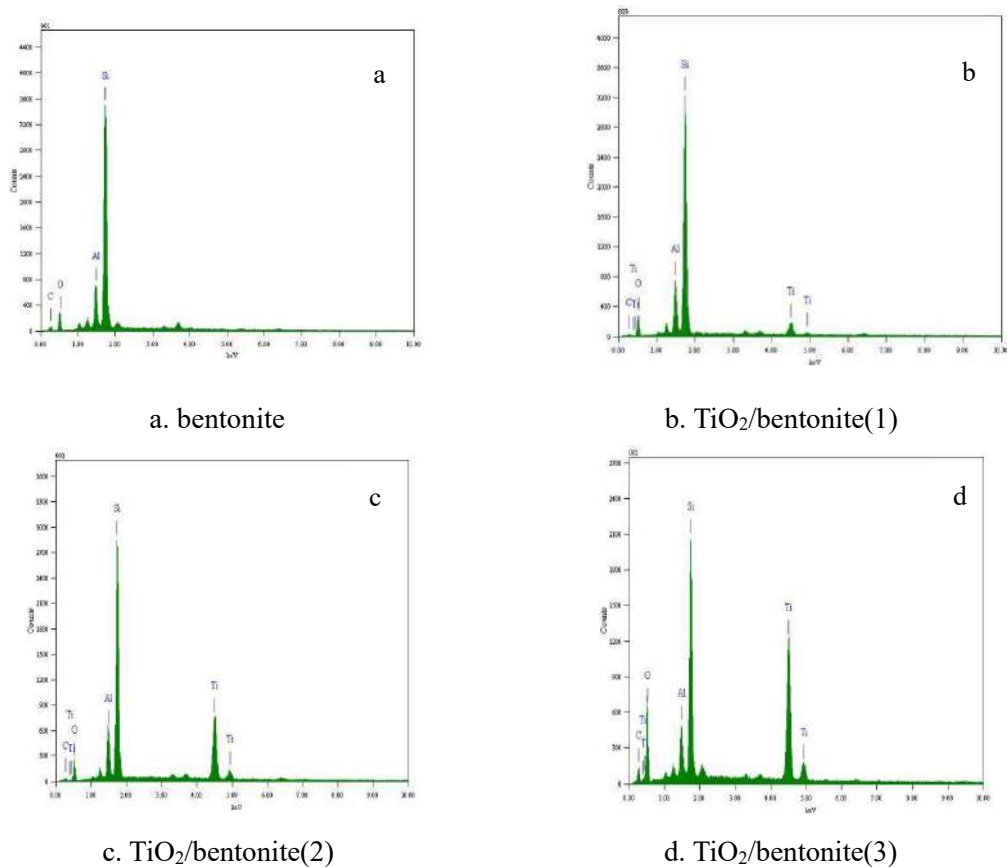


Fig. 3: EDS analysis of bentonite, *TiO₂/bentonite(1)*, *TiO₂/bentonite(2)* and *TiO₂/bentonite(3)*.

cm^{-1} , the peak near 1407 cm^{-1} is attributable to the bending stretching of Si-O-Si. The peak near 1035 cm^{-1} is attributed to the asymmetry bending stretching of Si-O-Si. It can be seen that *TiO₂/bentonite(1)* composite (Fig. 4b), *TiO₂/bentonite(2)* composite (Fig. 4c) and *TiO₂/bentonite(3)* (Fig. 4d) the peak near $600\text{--}900 \text{ cm}^{-1}$ has obvious absorption peak. This is the absorption peak of Ti-O bond of TiO₂ (Liu et al. 2011). The results revealed that TiO₂ was inserted into bentonite's layers.

X-ray Diffraction Pattern Characteristics

XRD patterns of the bentonite, *TiO₂/bentonite(1)*, *TiO₂/bentonite(2)* and *TiO₂/bentonite(3)* were obtained as shown in Fig. 5. The anatase phase of the corresponding diffraction peaks appeared at $2\theta = 25.2^\circ$, 37.8° , 48.1° , and 55.2° in both the *TiO₂/bentonite(1)*, *TiO₂/bentonite(2)* and *TiO₂/bentonite(3)* samples (Yu et al. 2017). The d (001) plane diffraction peaks of *TiO₂/bentonite(1)*, *TiO₂/bentonite(2)* and

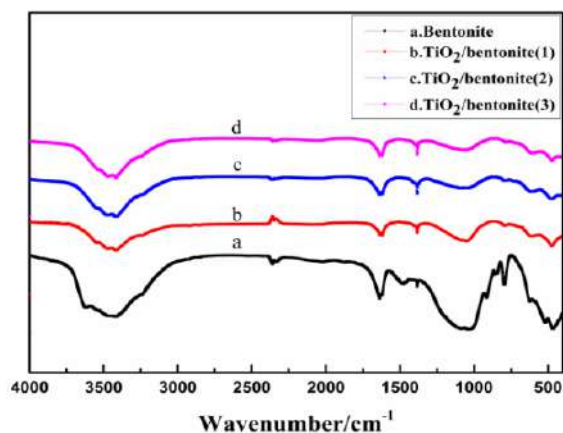


Fig. 4: FTIR of the bentonite, TiO₂/bentonite(1), TiO₂/bentonite(2) and TiO₂/bentonite(3).

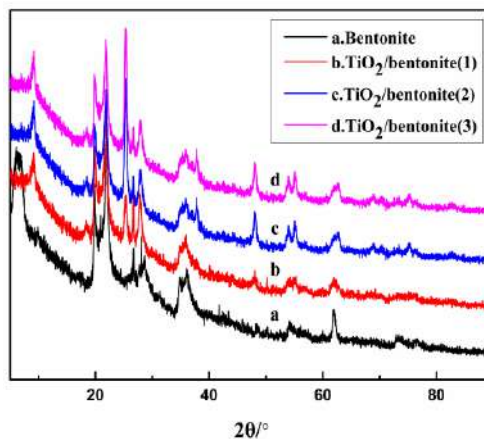


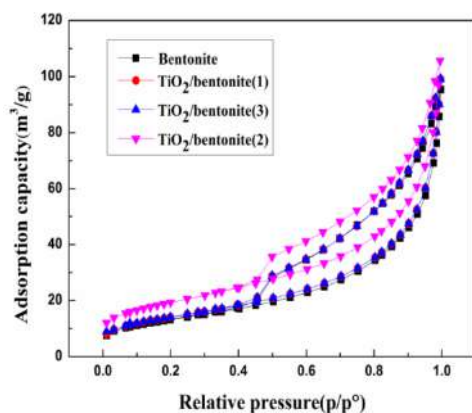
Fig. 5: XRD of the bentonite, TiO₂/bentonite(1), TiO₂/bentonite(2) and TiO₂/bentonite(3).

TiO₂/bentonite(3), i.e. the position and intensity of the first peak have changed obviously. The intensity of the diffraction peak is weaker than that of bentonite. At the same time, compared with the bentonite, the d(001) diffraction angles of TiO₂/bentonite(1), TiO₂/bentonite(2) and TiO₂/bentonite(3) increased. It can be seen from the Bragg equation $n\lambda = 2d\sin\theta$ that the layer spacing d (001) of catalyst is smaller than that of bentonite (Yang 2012). This phenomenon is caused by the replacement of calcium hydrate between bentonite layers by titanium ions. The results revealed that TiO₂ were inserted into bentonite's layers.

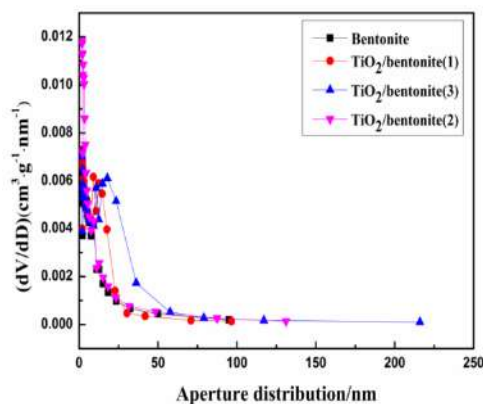
Specific Surface Area and Aperture Determination

The specific surface area is one of the important parameters in catalysts. This characteristic must be taken into account

especially in the case of supported catalysts (Cecílio et al. 2004, Yahya & Ngadi 2016). The N₂ adsorption/desorption isotherms for the TiO₂/bentonite(1), TiO₂/bentonite(2) and TiO₂/bentonite(3) are shown in Fig. 6(a). It should, however, be noted that in all the isotherms hysteresis is present in the low relative pressure range at $p/p^0 > 0.4$, due to the phenomenon of capillary condensation in the adsorption process, the adsorption isotherm and the desorption isotherm do not coincide, resulting in a hysteresis lag, and the desorption isotherm is above the adsorption isotherm, resulting in a retention ring; and also well-developed hysteresis loops which testify to the development of the mesopore structure. It can be seen from Table 2 that the specific surface area of the bentonite increased after loading, the specific surface area increased from 47.69 m²/g to 67.76



a. Isothermal adsorption curve.



b. Aperture distribution curve.

Fig. 6: Isothermal adsorption curve and aperture distribution curve of the bentonite, TiO₂/bentonite(1), TiO₂/bentonite(2) and TiO₂/bentonite(3).

Table 2: Mesopore surface area and pore volume results of catalysts.

	S_{mes} (m^2/g)	V_{mes} (cm^3/g)	BJH average aperture (\AA)
Bentonite	47.69	0.13	125
TiO ₂ /bentonite (1)	50.01	0.14	115.78
TiO ₂ /bentonite (2)	67.76	0.18	95.60
TiO ₂ /bentonite (3)	55.17	0.16	110.14

m^2/g , and the specific surface area of TiO₂/bentonite(2) was larger than that of TiO₂/bentonite (1), TiO₂/bentonite(2) and TiO₂/bentonite(3). What is more, TiO₂/modified residue has higher V_{mes} (0.18 cm^3/g) and S_{mes} (67.76 m^2/g) according to Table 2, this is the reason why TiO₂/bentonite(2) possesses superior catalytic activity towards other kinds of catalysts. The V_{mes} and S_{mes} of catalysts prepared are also consistent with their catalytic activity. Because the surface morphology of bentonite changes greatly after loading, from a smooth and compact structure to an increase in porosity and a loose layer structure, the specific surface area increases. At the same time, the bentonite support could disperse the catalyst, increase the surface-active area of the catalyst. The increase of specific surface area will increase the contact area between the catalyst and oily sludge, thus improving its catalytic performance.

Analysis of X-ray Photoelectron Spectroscopy (XPS)

XPS analysis was carried out to investigate the surface/interface chemical states of the samples. In this paper, the valence

of titanium in TiO₂/bentonite supported catalyst is judged by XPS analysis. Full spectra of X-ray photoelectron spectroscopy of (a) TiO₂/bentonite(2) is shown in Fig. 7. Besides, a Ti2p peak located at 458.9 eV is observed in Fig. 7. This result provides further evidence that TiO₂ was successfully coated on the residue surface. The high-resolution XPS spectra of the Ti2p region is shown in Fig. 7(b). The peaks located at 458.9 eV and 464.9 eV correspond to the Ti2p_{3/2} and Ti2p_{1/2} binding energy regions, respectively (An et al. 2018, Wu et al. 2013). The results show that titanium exists in the catalyst with Ti⁴⁺, and titanium exists in the form of TiO₂ in the composite catalyst.

Effect of Catalyst on Pyrolysis Performance of Oily Sludge

Effect of catalyst species on pyrolysis treatment: When the pyrolysis time was 4 h, the pyrolysis temperature was 450°C, the heating rate was 10°C/min, the nitrogen flow rate was 100 mL/min. Pyrolysis experiments were carried out with the addition of 1% of the two catalysts. Experimental results are given in Table 3.

It can be seen from Table 3 that the oil recovery rate of the bentonite and loaded bentonite is higher than that without the catalyst. And the catalytic effect of TiO₂/bentonite(2) is better than that of TiO₂/bentonite(1) and TiO₂/bentonite(1). Because the specific surface area of TiO₂/bentonite(2) was larger than that of TiO₂/bentonite(1) and TiO₂/bentonite(3), its catalytic effect is better. The prepared supported catalyst

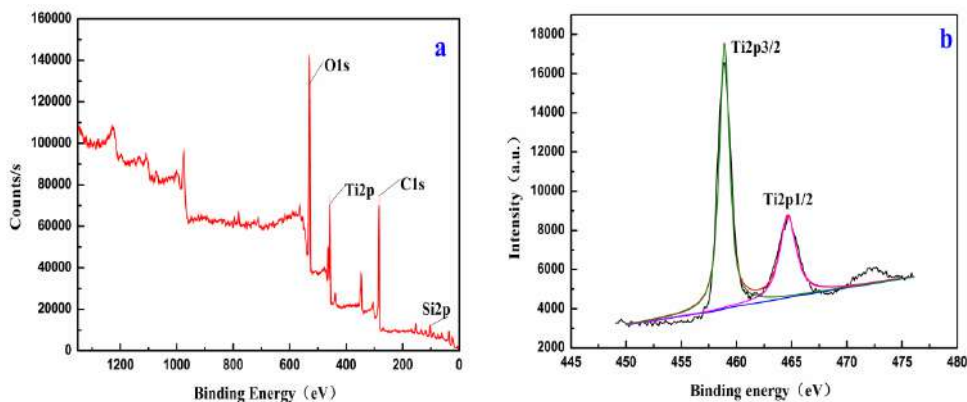
Fig. 7: XPS survey spectra of (a)TiO₂/bentonite(2); High-resolution Ti2p spectra of (b)TiO₂/bentonite(2).

Table 3: Effect of catalyst species on the recovery of pyrolysis oil.

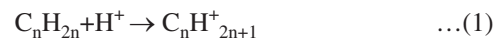
Catalyst species	Non- catalyst	Bentonite	TiO ₂ /bentonite(1)	TiO ₂ /bentonite(2)	TiO ₂ /bentonite(3)
Oily sludge quantity (g)	20.07	20.04	20.03	20.05	20.07
Oil recovery quantity (g)	2.85	2.94	3.08	3.15	3.10
Oil recovery rate (%)	76.06	78.61	82.35	84.16	82.73

(TiO₂/bentonite) can increase the number of the active sites of catalyst and enhance the catalytic activity. The specific surface area of catalyst increases, which increases the contact area between the catalyst and oily sludge and promotes the pyrolysis of oily sludge. This is consistent with the mesopore surface area and pore volume results of catalysts.

Thermogravimetric Analysis

To detect the catalytic effect of the catalyst on the pyrolysis of oily sludge, the catalyst was added to the oily sludge in a certain proportion for thermal weight analysis. Thermogravimetric analysis has been an interesting and useful analytical technique for the characterization of different organic products such as pitches, sewage sludges and other waste materials (Méndez et al. 2005). Thermogravimetric analysis is an important method to study the characteristics of sludge weight loss, which is of great significance to explore the reasonable reaction mechanism and kinetic parameters. The thermogravimetric data (TG) curves and first derivative data curves (DTG) of raw sludge and TiO₂/bentonite(2) at 10°C/min are shown in Fig. 8. As illustrated in Fig. 8(b), three peaks were identified in the DTG curves, leading to the partition of these thermogravimetric curves. The corresponding DTG curves were derived from the first derivative of the TG curves. It can be found that three peaks appeared in the DTG curve of oily sludge, the temperature ranges of which were region I(25-150°C), region II(150-450°C), region III(450-700°C), respectively. The weight loss of oily sludge in the first region was attributed to the evaporation of adsorbed water from the surface of the sludge particles, while the decomposition of sludge components was responsible for the weight loss in the other

two regions (Tang et al. 2018, Hayhurst 2013). More than 70% of the overall weight loss, as depicted in Fig. 8(a) occurred when the temperature was heated up from 25°C to 700°C, which is generally the highest temperature applied for sludge pyrolysis in practice (Tang et al. 2017). It can be seen from the Fig. 8(a), that the total weightlessness is affected by the added catalyst, and the addition of the catalyst increases the weightlessness. When the temperature was increased further, the weight loss of TiO₂/bentonite(2)-blended sludge was appreciably larger when compared to that of the oily sludge and TiO₂/bentonite(1)-blended sludge. The results show that the addition of catalyst promotes the pyrolysis of oily sludge. This result is consistent with the previous characterization. The theory of carbonium ion explains the reaction mechanism of TiO₂/bentonite(2) catalytic cracking. A carbonium ion is a hydrocarbon ion formed by carbon lacking a pair of valence electrons. The carbonium ion is generated by obtaining a hydrogen ion H⁺ from an olefin molecule, as shown in formula (1). The carbonium ion theory illustrates the role of the catalyst, which provides H⁺ on the catalyst surface. The hydrocarbon can react by the way of forming carbonium ion so that the activation energy of the reaction can be reduced and the reaction rate can be increased.



Effect of Catalyst on Pyrolysis Conditions of Oily Sludge

The effect of the amount of catalyst on the oil recovery rate of pyrolysis process: When the pyrolysis time was 4 h, the pyrolysis temperature 450°C, the heating rate 10°C/min and the nitrogen flow rate 100 mL/min, the effect

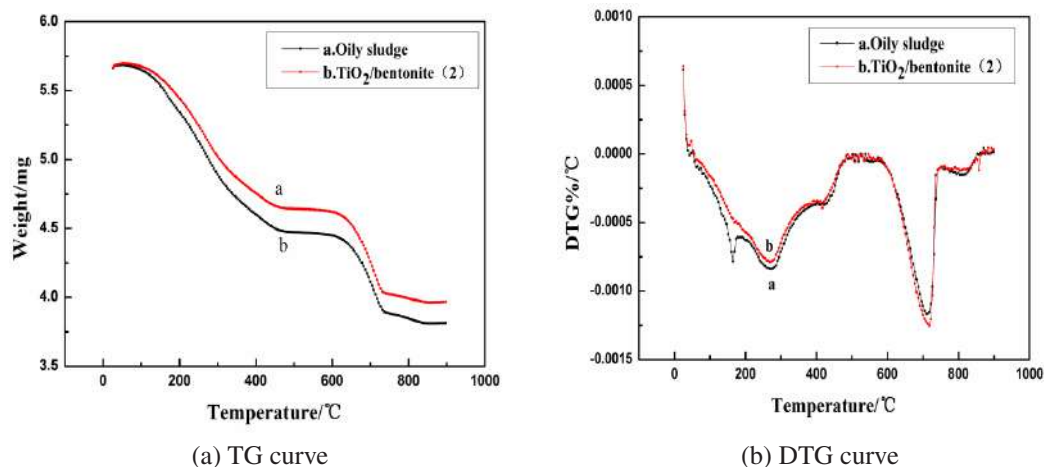


Fig. 8: Thermogravimetric analysis of the oily sludge and TiO₂/bentonite(2).

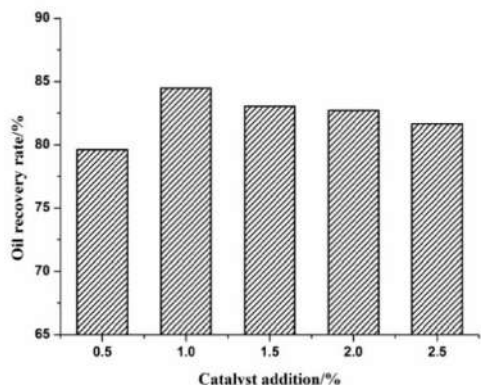


Fig. 9: The effect of the amount of catalyst on the oil recovery rate of the pyrolysis process.

of the amount of catalyst on the oil recovery rate of pyrolysis process was investigated.

From Fig. 9, the oil recovery rate increases with the increase of catalyst addition amount when the catalyst addition is between 0.5-1%. When the amounts of catalysts are more than 1%, the oil recovery rate has decreased. Considering the cost of the catalyst, when the amount of catalyst added was 1%, the oil recovery rate is the highest.

Effect of catalyst on pyrolysis temperature of oily sludge:

When the pyrolysis time was 4 h, the heating rate was 10°C/min, the nitrogen flow rate was 100 mL/min and catalyst quantity was 1%, the effect of the pyrolysis temperature on the oil recovery rate of pyrolysis process was investigated.

It can be seen from Fig. 10 that in the process of sludge pyrolysis, the oil recovery rate without the catalyst and the optimum catalyst is different from the change of temperature. The pyrolysis process without catalyst added the maximum oil recovery at 450°C, which was 76.06%. With

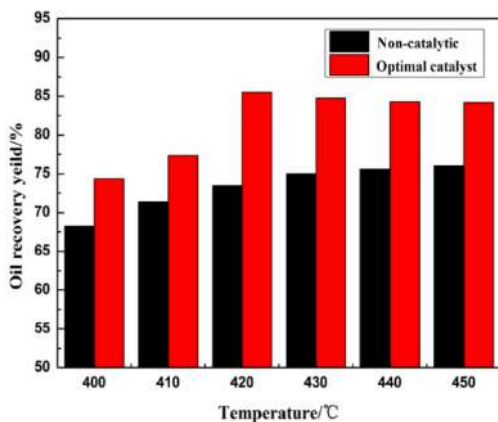


Fig. 10: The effect of pyrolysis temperature on the oil recovery rate of the pyrolysis process.

the addition of a catalyst, the maximum oil recovery can reach 85.49% at 420°C. The recovery rate of pyrolysis oil is significantly higher than that without catalyst and compared with non-catalyst, it can be reduced by 30°C when the maximum oil recovery rate is reached. When the temperature gradually increased, macromolecular organic compounds began to pyrolyse into some small molecules, oil recovery rate gradually increased as the temperature continues to rise, macromolecular pyrolysis reaction process with many intermediate products will occur secondary pyrolysis (Zheng 2013, Yang et al. 2014). This will lead to lower oil recovery rates. It is indicated that the catalyst has an obvious effect on the pyrolysis process.

Effect of catalyst on pyrolysis time of oily sludge: When the pyrolysis temperature was 420°C, the heating rate 10°C/min, the nitrogen flow rate 100 mL/min and catalyst quantity 1%, the effect of the pyrolysis time on the oil recovery rate of pyrolysis process was investigated.

From Fig. 11 it can see that the pyrolysis time is a balance factor of the pyrolysis of oily sludge, which also has a direct impact on the pyrolysis process. It can be seen from the figure that the recovery rate of pyrolysis oil increases first and then decreases with the extension of residence time. Without a catalyst, the oil recovery rate was 76.07% at 4 h pyrolysis time. After adding a catalyst, the oil recovery rate reached 85.82% at 3 h pyrolysis time. During the reaction, when the reaction stays for a short time, some of the sludge has not reached the current temperature of the full state of pyrolysis, and when the reaction time is too long, the oil occurred the secondary pyrolysis (Zhang 2016). Compared with the non-catalyst, it can be reduced by 1 h when the maximum oil recovery rate is reached. Catalyst has the obvious promoting effect on the pyrolysis reaction and increased the recovery rate of oil. The activation energy required for pyrolysis reaction

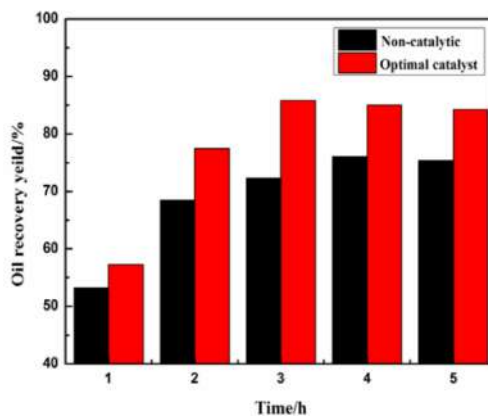


Fig. 11: The effect of pyrolysis time on the oil recovery rate of the pyrolysis process.

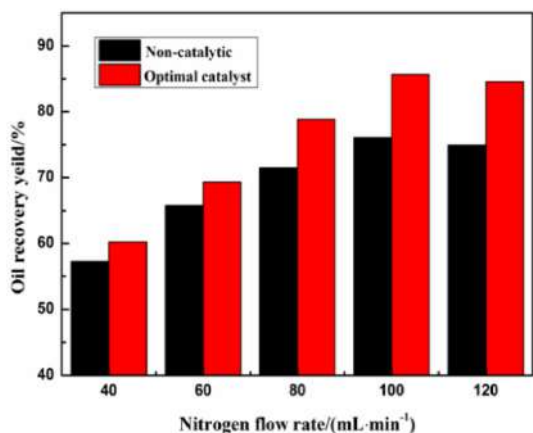


Fig. 12: The effect of nitrogen flow rate on catalytic pyrolysis of oily sludge.

is reduced, and the pyrolysis reaction time is shortened. It provides technical support for catalytic pyrolysis technology.

Effect of catalyst on the nitrogen flow rate of oily sludge:

When the pyrolysis temperature was 420°C, the pyrolysis time 3 h, the heating rate 10°C/min and catalyst quantity 1%, the effect of nitrogen flow rate on the oil recovery rate of oily sludge was studied. The result is shown in Fig. 12.

It can be concluded that the oil recovery rate increases first, and then decreases with the increase of nitrogen flow rate. When the nitrogen flow rate under 100 mL·min⁻¹, the oil recovery rate shows an increasing trend. Because part of the oil-water mixture produced in the pyrolysis cannot be taken out to the condensation system in time, and secondary cracking occurs. However, when the nitrogen flow rate is greater than 100 mL·min⁻¹, the oil recovery rate is reduced. This is due to the excessive nitrogen flow rate causes the oil-water mixture generated during the pyrolysis process

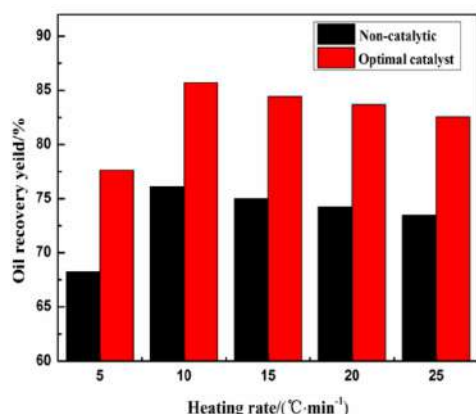


Fig. 13: The effect of the heating rate on the oil recovery rate of the pyrolysis process.

to be carried to the tail gas emission system with nitrogen (Liu 2016). Compared with the non-catalyst, the addition of TiO₂/bentonite(2) in the process of pyrolysis of oily sludge has an obvious effect in promoting the recovery rate of oil.

Effect of catalyst on the heating rate on of oily sludge:

When the pyrolysis temperature was 420°C, the pyrolysis time 3 h, the nitrogen flow rate 100 mL/min and catalyst quantity 1%, the effect of the heating rate on the oil recovery rate of pyrolysis process was studied. The result is shown in Fig. 13.

The Fig. 13 shows that when the heating rate is 10°C·min⁻¹, the oil recovery rate reaches the maximum. At the low heating rate, it means that the pyrolysis time of oily sludge is prolonged under low temperature conditions so that the cracking rate of light components and heavy components in the sludge is slowed down. At the high heating rate, the light component evaporates quickly without sufficient pyrolysis and only the cracking of the heavy components occurs, so that the pyrolysis of oily sludge cannot be fully carried out (Yang et al. 2015). Compared with the non-catalyst, the addition of TiO₂/bentonite(2) in the process of pyrolysis of oily sludge has an obvious effect in promoting the recovery rate of oil.

Analysis of Pyrolysis Products

Composition Analysis of the Liquid Phase of Pyrolysis Products

It can be seen from Fig. 14 that after the addition of the catalyst, the content of heavy components in the pyrolysis oil decreases, and the content of light components increases, among them C₁₆-C₂₀ are the master components. In the process of pyrolysis of oily sludge, the catalyst was added to promote the cracking of heavy components in oily sludge,

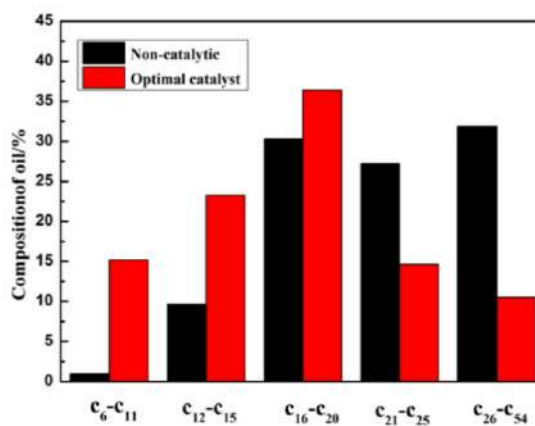


Fig. 14: Composition analysis of the liquid phase of pyrolysis products.

which increased the content of light components in the recovered oil. It not only improves the recovery rate of pyrolytic oil but also improves the quality of the oil. Among the three catalysts: bentonite, $\text{TiO}_2/\text{bentonite}(1)$ and $\text{TiO}_2/\text{bentonite}(2)$, the catalytic effect of $\text{TiO}_2/\text{bentonite}(2)$ is the best.

Determination of Four Components of Pyrolysis Liquid Phase Products

As can be seen from Table 4, compared with the non-catalyst, the content of aromatic hydrocarbons, colloids and bitumen in the four components of the pyrolysis liquid phase product with the catalyst is reduced, and the content of saturated hydrocarbons is significantly increased. It is indicated that the addition of catalyst promotes the further pyrolysis of oily sludge, especially the decomposition of heavy oil so that the heavy oil of pyrolysis oil is light.

Table 4: Analysis of four components of pyrolysis liquid phase products.

Samples	Component/%			
	Saturated hydrocarbon	Aromatic hydrocarbons	Glial	Asphaltene
Non-catalyst	18.65	32.61	1.95	9.73
Optimum catalyst	30.43	15.52	1.12	1.32

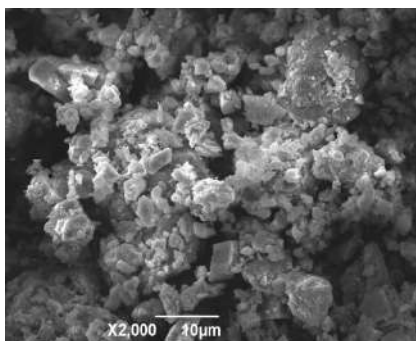


Fig. 15: SEM image of optimal catalyst.

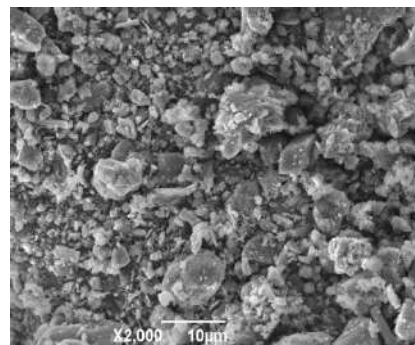


Fig. 16: SEM image of raw mud.

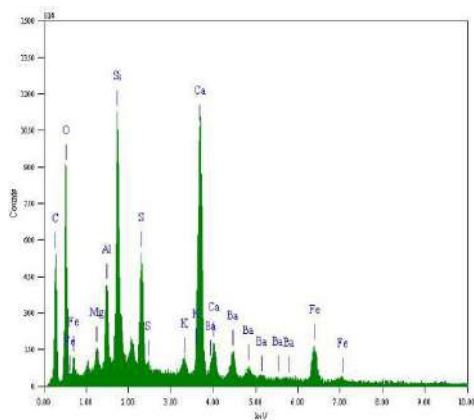


Fig. 17: EDS spectra of optimal catalyst.

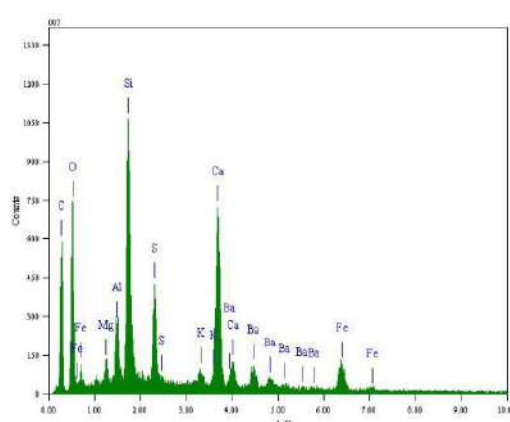


Fig. 18: EDS image of raw mud

Morphology Analysis of Pyrolysis Residue

The SEM analysis of optimum catalyst pyrolysis residue and raw mud pyrolysis residue are shown in Fig. 15 and Fig. 16. The EDS analysis of pyrolysis residue and raw mud pyrolysis residue are shown in Fig. 17 and Fig. 18. Compared with the raw mud pyrolysis residue, the optimal catalyst pyrolysis residue is porous, the porosity is increased, the particle accumulation is loose, the particles become smaller, and the particles are not found to be coked (Li et al. 2018). This provides a condition for the residue to act as a catalyst (Li et al. 2018, Yang et al. 2018, Cheng et al. 2015).

Specific Surface Area and Aperture Determination of Pyrolysis Residue

It can be seen from Table 5 that the specific surface area of

Table 5: Mesopore surface area and pore volume results of pyrolysis residue.

	S _{mes} (m ² /g)	V _{mes} (cm ³ /g)	BJH average aperture (Å)
Non- catalyst	3.49	0.014	205.2
Optimum catalyst	4.24	0.02	167.5

Table 6: Elemental analysis, oil content and heating value of pyrolysis residue.

Samples	Element composition (%)							
	N (%)	C (%)	H (%)	S (%)	C/N	C/H	Oil content/%	Calorific value/(kJ/kg)
Non- catalyst	0.04	6.89	0.485	2.835	179.95	14.21	2.23	3176.55
TiO ₂ /bentonite (2)	0.19	8.34	0.49	2.67	56.97	14.51	2.02	2897.45

the optimum catalyst pyrolysis residue is higher than that of raw mud pyrolysis residue, the specific surface area increased from 3.49 m²/g to 4.24 m²/g. This provides a condition for the residue to act as a catalyst.

Elemental Analysis, Oil Content and Calorific Value of Pyrolysis Residue

According to Table 6, the content of N element in residue increases obviously after adding a catalyst, the content of H element decreases, the C/N decreases, and the C/H increases, which indicates that the catalyst can fix nitrogen and dehydrogenate during pyrolysis. The oil content of the residue without catalyst was 2.23%, while the oil content of the residue was reduced to less than 2% after adding the catalyst, indicating that after adding the catalyst, more oil components were converted into the liquid phase and gas phase, thus oil content of the residue has reduced. The lower the oil content in the residue, the smaller the corresponding calorific value.

CONCLUSIONS

1. A TiO₂/bentonite system with well-dispersed TiO₂ particles in the bentonite was prepared by the sol-gel method. It was characterized that TiO₂ was successfully loaded onto bentonite.
2. The effects of catalysts on different pyrolysis temperature, pyrolysis time, heating rate and nitrogen flow rate were obtained. The recovery rate of pyrolysis oil is significantly higher than that without catalyst and compared with non-catalyst, it can be reduced by 30°C when the maximum oil recovery rate is reached. Compared with the non-catalyst, it can be reduced by 1 h when the maximum oil recovery rate is reached.
3. This work shows the feasibility of introducing TiO₂/bentonite catalysts to sewage sludge for regulating pyrolysis and consequently both the yield of pyrolysis oil and the quality of pyrolysis oil were enhanced. The recovery rate was 8.1% higher than that without a catalyst.

ACKNOWLEDGMENTS

This work was supported by the Open Project Program of State Key Laboratory of Petroleum Pollution Control; and Shaanxi Youth Science and technology new star project (2017KJXX-49); and Scientific Research Program Funded by Shaanxi Provincial Education Department (Program No.18JS088); and Natural Science Basic Research Plan in Shaanxi Province of China (Program 2019JM-506)

REFERENCES

- Agar, D. A., Kwapinska, M. and Leahy, J. J. 2018. Pyrolysis of wastewater sludge and composted organic fines from municipal solid waste: laboratory reactor characterisation and product distribution. *Environmental Science and Pollution Research*, 25(12): 1-9.
- An, N., Ma, Y., Liu, J., Ma, H., Yang, J. and Zhang, Q. 2018. Enhanced visible-light photocatalytic oxidation capability of carbon-doped TiO₂ via coupling with fly ash. *Chinese Journal of Catalysis*, 39(12): 1890-1900.
- Botella, L., Sierra, M., Bimbela, F., Gea, G., Sánchez, J. L. and Gonzalo, A. 2016. Enhancement of biodiesel oxidation stability using additives obtained from sewage sludge fast-pyrolysis liquids. *Energy & Fuels*, 30(1): 302-310.
- Cao, L., Qu, Y., Xie, D. and Jing, C. 2011. Preparation and characterization of porous TiO₂ with La₂O₃ load. *Rare Metals*, 30(1): 221-224.
- Chen, J., Yao, N., Wang, R. and Zhang, J. 2009. Hydrogenation of chloronitrobenzene to chloroaniline over Ni/TiO₂ catalysts prepared by sol-gel method. *Chemical Engineering Journal*, 148(1): 164-172.
- Cecilio, A. A., Pulcinelli, S. H., Santilli, C. V., Maniette, Y. and Silva, V. T. D. 2004. Improvement of the Mo/TiO₂-Al₂O₃ catalyst by the control of the sol-gel synthesis. *Journal of Sol-Gel Science and Technology*, 31(1-3): 87-93.
- Cheng, S., Li, A. and Yoshikawa, K. 2015. High quality oil recovery from oil sludge employing a pyrolysis process with oil sludge ash catalyst. *Int. J. Waste. Resour.*, 5(2): 176.
- Folgueras, M. B., Alonso, M. and Díaz, R.M. 2013. Influence of sewage sludge treatment on pyrolysis and combustion of dry sludge. *Energy*, 55(1): 426-435.
- Gong, Z., Wang, Z., Wang, Z., Du, A., Fang, P., Sun, Z. and Li, X. 2018. Study on pyrolysis of oil sludge with microalgae residue additive. *The Canadian Journal of Chemical Engineering*, 96(9): 1919-1925.
- Hayhurst, A. N. 2013. The kinetics of the pyrolysis or devolatilisation of sewage sludge and other solid fuels. *Combustion and Flame*, 160(1): 138-144.

- Lin, B., Wang, J., Huang, Q. and Chi, Y. 2017. Effects of potassium hydroxide on the catalytic pyrolysis of oily sludge for high-quality oil product. *Fuel*, 200: 124-133.
- Lin, B., Huang, Q., Ali, M., Wang, F., Chi, Y. and Yan, J. 2019. Continuous catalytic pyrolysis of oily sludge using U-shape reactor for producing saturates-enriched light oil. *Proceedings of the Combustion Institute*, 37(3): 3101-3108.
- Liu, P., Zhang, Z., Jia, M., Gao, X. and Yu, J. 2015. ZSM-5 zeolites with different SiO₂/Al₂O₃ ratios as fluid catalytic cracking catalyst additives for residue cracking. *Chinese Journal of Catalysis*, 36(6): 806-812.
- Li, Y., Zhang, S., Yu, Q. and Yin, W. 2007. The effects of activated carbon support on the structure and properties of TiO₂ nanoparticles prepared by a sol-gel method. *Applied Surface Science*, 253(23): 9254-9258.
- Liu, J. P., Zhao, H., Song, X. L. and Li, X. L. 2009. Effects of calcination temperature on structure of titanium oxide photocatalyst. *Inorganic Chemicals Industry*.
- Liu, X. Y., Yang, Y. Q. and Chen, H. J. 2011. Organic bentonite load ZnO/TiO₂ photodegradation catalyst development and performance. *Chinese Journal of Spectroscopy Laboratory*, 28(03): 1154-1157.
- Liu, L. Z. 2016. Study on low temperature catalytic pyrolysis of oil sludge catalyst synthesis and application technology. Xi'an Shiyou University.
- Li, J. L., Qu, C. T., Zhu, S. D., Fan, X. Y. and Zhu, Z. H. 2018. Characteristics and reutilization of pyrolytic residues of oily sludge: An overview. *Materials review A: review papers*, 32(17): 3023-3032.
- Li, Y., Hu, H. J., Qu, C. T. and Yu, T. 2018. Influencing factors for catalytic pyrolysis of oily sludge and analysis of pyrolysis products. *Modern Chemical Industry*, (1): 15.
- Mrayyan, B. and Battikhi, M. N. 2005. Biodegradation of total organic carbons (TOC) in Jordanian petroleum sludge. *Journal of Hazardous Materials*, 120(1-3): 127-134.
- Méndez, A., Gascó, G., Freitas, M. M. A., Siebielec, G., Stuczynski, T. and Figueiredo, J. L. 2005. Preparation of carbon-based adsorbents from pyrolysis and air activation of sewage sludges. *Chemical Engineering Journal*, 108(1-2): 169-177.
- Naqvi, S. R., Tariq, R., Hameed, Z., Ali, I., Naqvi, M., Chen, W. H. and Shahbaz, M. 2019. Pyrolysis of high ash sewage sludge: Kinetics and thermodynamic analysis using Coats-Redfern method. *Renewable energy*, 131: 854-860.
- Shie, J. L., Lin, J. P., Chang, C. Y., Shih, S. M., Lee, D. J. and Wu, C. H. 2004. Pyrolysis of oil sludge with additives of catalytic solid wastes. *Journal of Analytical and Applied Pyrolysis*, 71(2): 695-707.
- Shao, J., Yan, R., Chen, H., Yang, H. and Lee, D. H. 2010. Catalytic effect of metal oxides on pyrolysis of sewage sludge. *Fuel Processing Technology*, 91(9): 1113-1118.
- Tang, S., Zheng, C., Yan, F., Shao, N., Tang, Y. and Zhang, Z. 2018. Product characteristics and kinetics of sewage sludge pyrolysis driven by alkaline earth metals. *Energy*, 153: 921-932.
- Tang, S., Tian, S., Zheng, C. and Zhang, Z. 2017. Effect of calcium hydroxide on the pyrolysis behavior of sewage sludge: reaction characteristics and kinetics. *Energy & Fuels*, 31(5): 5079-5087.
- Wang, Z., Wang, J., Xie, L., Zhu, H. and Shu, X. 2019. Influence of the addition of cotton stalk during co-pyrolysis with sewage sludge on the properties, surface characteristics, and ecological risks of biochars. *Journal of Thermal Science*, 28(4): 755-762.
- Wang, J., Sun, C., Lin, B. C., Huang, Q. X., Ma, Z. Y., Chi, Y. and Yan, J. H. 2018. Micro- and mesoporous-enriched carbon materials prepared from a mixture of petroleum-derived oily sludge and biomass. *Fuel Processing Technology*, 171: 140-147.
- Wang, J., Liu, T. L., Huang, Q. X., Ma, Z. Y., Chi, Y. and Yan, J. H. 2017. Production and characterization of high quality activated carbon from oily sludge. *Fuel Processing Technology*, 162: 13-19.
- Wang, H., Jia, H., Wang, L. and Chen, H. 2015. The catalytic effect of modified bentonite on the pyrolysis of oily sludge. *Petroleum Science and Technology*, 33(13-14): 1388-1394.
- Wang, W. L., Liu, B. J. and Zeng, X. J. 2008. Catalytic cracking of C₄ hydrocarbons on ZSM-5 molecular sieves with low SiO₂/Al₂O₃ molar ratio. *Acta Physico-Chimica Sinica*, 24(11): 2102-2107.
- Wu, X., Yin, S., Dong, Q., Guo, C., Li, H., Kimura, T. and Sato, T. 2013. Synthesis of high visible light active carbon doped TiO₂ photocatalyst by a facile calcination assisted solvothermal method. *Applied Catalysis B: Environmental*, 142: 450-457.
- Xiao, H. M. 2012. Study on catalytic pyrolysis characteristics and kinetics of paper making sludge. *Journal of Zhaoqing University*, 33(02): 28-32.
- Yang, J., Xu, X., Liang, S., Guan, R., Li, H., Chen, Y. and Hou, H. 2018. Enhanced hydrogen production in catalytic pyrolysis of sewage sludge by red mud: thermogravimetric kinetic analysis and pyrolysis characteristics. *International Journal of Hydrogen Energy*, 43(16): 7795-7807.
- Yao, K. S., Hsu, J. J. and Chang, C. Y. 2012. Study on the photocatalytic degradation of wastewater under the optimal preparation of the activated carbon supported TiO₂ thin film. In: *Advanced Materials Research*, 356: 313-317, Trans Tech Publications Ltd.
- Yang, X., Wang, X., Zhao, B. and Li, Y. 2014. Simulation model of pyrolysis biofuel yield based on algal components and pyrolysis kinetics. *Bioenergy Research*, 7(4): 1293-1304.
- Yu, X. D., Zhou, Y. J. and Yang, S. C. 2017. Preparation and adsorption capacity of oxytetracycline hydrochloride by nano titania loaded organic bentonite. *Chinese Journal of Environmental Engineering*.
- Yang Z. L. 2012. Study on preparation and catalytic organic reaction of modified bentonite catalyst. Qufu Normal University.
- Yahya, N. Y. and Ngadi, N. 2016. Effect of calcination temperature on catalyst surface area of Ca supported TiO₂ by sol-gel method for biodiesel production. In: *Applied Mechanics and Materials*, 818: 219-222, Trans Tech Publications Ltd.
- Yang, P. H., Wei, J. and Qu, C. T. 2015. Vacuum pyrolysis of oil sludge from Yancheng oilfield. *Environmental Engineering*, 10: 22.
- Yang, J., Xu, X., Liang, S., Guan, R., Li, H., Chen, Y. and Hou, H. 2018. Enhanced hydrogen production in catalytic pyrolysis of sewage sludge by red mud: Thermogravimetric kinetic analysis and pyrolysis characteristics. *International Journal of Hydrogen Energy*, 43(16): 7795-7807.
- Zhao, B., Jin, J., Li, S., Liu, D. and Yang, H. 2019. Co-pyrolysis characteristics of sludge mixed with Zhundong coal and sulphur contaminant release regularity. *Journal of Thermal Analysis and Calorimetry*, 1.
- Zhao, Z., Fan, J., Liu, S. and Wang, Z. 2009. Optimal design and preparation of titania-supported CoPc using sol-gel for the photo-reduction of CO₂. *Chemical Engineering Journal*, 151(1-3): 134-14.
- Zhang, M., Huang, G. H., Hu, G. Y. and Zhao, H. J. 2009. Geochemical study on oil-cracked gases and kerogen-cracked gases (i)-experimental simulation and products analysis. *Science in China*, 52(1 Supplement), 1-9.
- Zhu, P. F., Liu, M., Zhu, T. J. and Song, C. 2012. Preparation and characterization of iron-doped TiO₂/bentonite photocatalyst. *Chinese Journal of Spectroscopy Laboratory*.
- Zheng, Y. Y. 2013. Research on composition of gases and liquids obtained from different pyrolysis conditions of sewage sludge. *Harbin Institute of Technology*.
- Zhang, J. D. 2016. Research on three phase products in sludge pyrolysis process. *Harbin Institute of Technology*.



Indoor Quality of Residential Homes and Schools of an Industrial Area in Asansol: Characterization, Bioaccessibility and Health Risk Assessment of Potentially Toxic Elements

M. Pal*, M. Gope**, A. Basu*, T. Laha*, R. E. Mastro***, R. Labar****, T. K. Kundu****, R. R. Hoque*****, P. S. Khillare***** and S. Balachandran*†

*Department of Environmental Studies, Siksha-Bhavana, Visva-Bharati, Santiniketan-731235, West Bengal, India

**Department of Chemistry, National Institute of Technology, Durgapur (NIT Durgapur), Durgapur-713209, West Bengal, India

***Environmental Management Division, CSIR-Central Institute of Mining and Fuel Research, Digwadih Campus, CFRI, Dhanbad-826015, Jharkhand, India

****Department of Physics, Siksha-Bhavana, Visva-Bharati, Santiniketan-731235, West Bengal, India

*****Department of Environmental Sciences, Tezpur University, Tezpur-784028, Assam, India

*****School of Environmental Sciences, Jawaharlal Nehru University, New Delhi-100 067, India

†Corresponding author: S. Balachandran; s.balachandran@visva-bharati.ac.in

Nat. Env. & Poll. Tech.
Website: www.neptjournal.com

Received: 30-07-2020

Revised: 08-10-2020

Accepted: 15-10-2020

Key Words:

Indoor dust

PTEs

SBET

Health risk assessment

Monte Carlo analysis

ABSTRACT

Bioaccessibility of eight potentially toxic elements (PTEs), their human exposure and health risk assessments were determined in the indoor dust of residence and schools from the Asansol Industrial area, India. The PTEs concentrations were maximum during the winter both at houses and schools. The average PTEs concentrations throughout the year in Asansol were 3.16, 120, 156, 41708, 2354, 61.3, 115 and 345 mg.kg⁻¹ for Cd, Cr, Cu, Fe, Mn, Ni, Pb and Zn respectively. X-ray powder diffraction indicated an abundance of quartz in the indoor dust. Principal component analysis (PCA) indicated multiple sources such as traffic, industries, and lithogenic sources for PTEs in indoor dust. Percentage of bioaccessibility was maximum for Cd (55.3% throughout the year). Total PTEs concentration and a bioaccessible fraction of PTEs both were used for health risk assessment, and non-carcinogenic health risk was <1 for total PTEs and the bioaccessible fraction of PTEs. Health risk of total PTEs' (HI_{total}) for Mn was high for both children and adult (6.76E-01 and 1.3E-01, respectively). Monte Carlo simulation model indicated that all the cumulative probability of Hazard Quotient (HQ) for collectively eight metals was below 1.

INTRODUCTION

Indoor settled dust is an important environmental media, which needs serious attention due to increased levels of toxicants to which human are daily exposed. The primary sources of PTE's into the indoor environment are indoor activities and infiltration of the outdoor aerosols into indoors. Indoor activities like cooking, vacuum cleaning, smoking and resuspension of dust particles also contribute to indoor dust pollution (Ali et al. 2019). PTEs can enter into indoor through the suspended particles from the outdoor air (Rasmussen et al. 2018), high vehicular traffic (Rohra et al. 2018) and the dirt that adheres to footwear (Ali et al. 2019, Kelepertzis et al. 2019, Cheng et al. 2018). Various researches indicate that outdoor aerosols are a significant contributor to indoor pollutants, of which street dust can contribute to 20-95% to household dust (Rasmussen et al. 2001, Torres-Sanchez et al. 2017).

PTEs causes various health effects like decreased bone density, renal disorder, nervous system damage, disturb natural brain development etc. (Chen et al. 2015). Moreover, it interferes with the child's neural development which is highest during their growth period and is more risk-prone to PTEs (Muhamad-Darus et al. 2017). PTEs tend to accumulate into the tissue and results in biological magnification through time.

To accurately assess the ingested oral risk of PTEs exposure, it is essential to know the PTEs oral bioaccessibility. Although there are a lot of *in vitro* models developed to assess the bioavailability of PTEs among which SBET is a very simple process and also cost very low. Various studies were conducted to estimate the in-vitro bioaccessibility of PTEs in indoor settled dust (Bot et al. 2010, Turner 2011, Wang et al. 2016). However, in urban industrial areas like

Asansol, India, which has various anthropogenic activities which release various PTEs (Gope et al. 2017); however, the oral bioaccessibility of various PTEs in indoor dust has not been investigated.

The overarching aim of this study was to analyse (i) the seasonal variation of PTE's level in indoor settled dust of houses and schools (ii) mineralogical study (iii) sources identification of PTEs (iv) oral bioaccessibility, (v) health risk assessment, and (vi) Monte Carlo simulation.

MATERIAL AND METHODS

Study Area

Asansol is a metropolitan city located in the western part of West Bengal, India, with medium industrial activities and a part of Chhotanagpur Plateau (Fig. 1). The population of this city was 5,64,491 as per the census of 2011 (Govt of India 2011). It is situated beside NH-2 'The Grant Trunk Road' one of the oldest and busiest roads in India. IISCO (Indian Iron and Steel Corporation), Eastern Coalfield, Burnpur Cement etc. are the primary industries located at Asansol industrial area. Very high traffic density was observed throughout 24 hrs. at Asansol, >7000 h in peak hour and >2000 h in the lean hour (Gope et al. 2017).

Sample Collection

Sites were selected randomly, and samples were collected from three residential areas, viz. Sarada Pally, Puranhhat and Santinagar. Four houses from each residential area and four primary schools were selected for sample collection. Total 48 dust samples were collected throughout the study period, March 2014 to February 2015. A 0.5 square meter glass plate was kept on the top of the almirah and bunker. Settled dust was collected from the glass plate in a plastic zipper pack through a nylon brush and brought to the laboratory for analysis (Pitawala et al. 2013). Dust samples were collected in four months interval at schools and houses.

Ground floor was selected for sampling in case of houses, but in case of schools, the 1st floor was used. Sarada Pally is very close to steel plant and NH. The houses are east facing and well ventilated with 2 windows and two doors in the room where the plate was kept. In Puranhhat area, houses are old; these are housing complex of steel industries. Houses are not well ventilated with the presence of one door plus one window at one side and one window on the other side. Santinagar is a very congested area and rooms are very small (8×8 ft). Only one door and one window are present on one side. All the schools are well ventilated with windows on three sides and door present on one side.

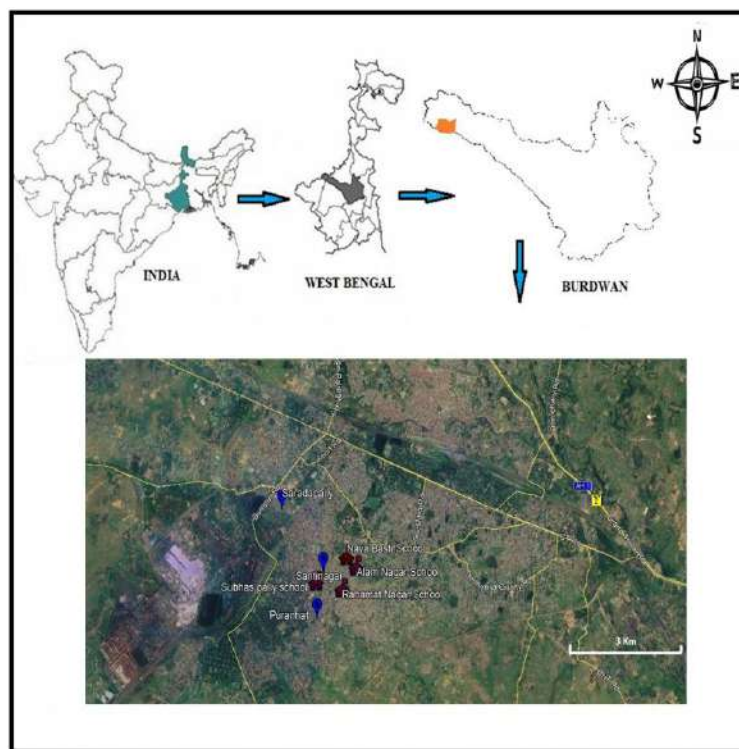


Fig. 1: The study area.

Verandah is present in every school. Three schools (Naya Basti primary school, Allamnagar primary school and Rahamat Nagar primary school) are east facing and playground present in the east side just after verandah. Subhas Pally primary school is north facing, and they do not have any playground.

Sample Preparation for Pseudo Total PTEs Concentration

Dust samples of 0.2 g were weighed and transferred into a Teflon vessel. HNO_3 , HF and HCl were mixed with the dust samples in a ratio of 2:1:1 (v/v) and the mixture was digested for 35 minutes at 210°C temperature in a microwave digester (Jupiter-A, Sr. No. JP127A) and the digestion procedure was adopted from Hussain et al. (2015) with some modification as per our requirement. The digested solution was filtered using Whatman No. 42 filter paper and made up to 25 mL using 12N HCl. PTEs concentration was measured by Inductively Coupled Plasma-Optical Emission Spectrometry (ICP-OES, iCAP 6300, Thermo Fisher Scientific, UK). Quality control and quality assurance are provided in our earlier paper (Gope et al. 2018).

Sample Preparation for SBET

During SBET extraction, 0.1 g dust was weighed out from each sample and transferred into a test tube, and 10 mL 0.4 M Glycine (pH 1.5) was added to the sample, and the test tube was centrifuged at 30 rpm at 37°C for one hour. After digestion, the aliquot was filtered through a 0.45 µm cellulose acetate disk filter (Ruby et al. 1996, Oomen et al. 2002). Filtrates were stored at 4°C and analysed using Inductively Coupled Plasma-Optical Emission Spectrometry (ICP-OES) for detection of PTEs.

Bioaccessibility

Bioaccessibility was calculated using the following formula (Oomen et al. 2002).

Bioaccessibility percentage (%) =

$$\frac{\text{Metal concentration } \left(\frac{\text{mg}}{\text{kg}}\right) \text{ determined in gastric phase}}{\text{Total metal content } \left(\frac{\text{mg}}{\text{kg}}\right) \text{ in environmental media}} \times 100 \quad \dots(1)$$

XRD Analysis

At room temperature, Rigaku Ultima IV with CuK_α ($k = 1.514 \text{ \AA}$, over the range, 2θ 4-84°) was used to study X-ray Powder diffraction patterns of dust samples. To identify the phase, the obtained diffraction designs were studied using X'Pert High Score software and ICDD database (Labar & Kundu 2018).

Human Exposure Risk Assessment

Ingestion, inhalation and dermal absorption are the three main exposure routes through which PTEs can enter into the body. The exposure risk assessment was calculated for children and adult. To assess the potential health risk, chronic daily intake (CDI) was calculated for each PTEs through individual exposure pathways.

$$CDI_{ing} = C \times \frac{R_{ing} \times F_{exp} \times T_{exp}}{ABW \times T_{avg}} \times 10^{-6} \quad \dots(2)$$

$$CDI_{inh} = C \times \frac{R_{inh} \times F_{exp} \times T_{exp}}{PEF \times ABW \times T_{avg}} \quad \dots(3)$$

$$CDI_{dermal} = C \times \frac{SAF \times A_{skin} \times DAF \times F_{exp} \times T_{exp}}{ABW \times T_{avg}} \times 10^{-6} \dots(4)$$

Where, CDI = Chronic Daily Intake ($\text{mg} \cdot \text{kg}^{-1} \cdot \text{day}^{-1}$); C = Concentration of PTE; R_{ing} = Ingestion rate [$200 \text{ mg dust day}^{-1}$ for children (1-6 years), $100 \text{ mg} \cdot \text{day}^{-1}$ for adults]; R_{inh} = Inhalation rate ($20 \text{ m}^3 \cdot \text{day}^{-1}$ for adults, $7.6 \text{ m}^3 \cdot \text{day}^{-1}$ for child); F_{exp} = Exposure frequency [$365 \text{ day} \cdot \text{year}^{-1}$]; T_{exp} = Exposure duration [6 years for child and 24 years for adults]; A_{skin} = Skin area [2800 cm^2 for child and 5700 cm^2 for adults]; SAF = Skin adherence factor [$0.2 \text{ mg} \cdot \text{cm}^{-2} \cdot \text{h}^{-1}$ for child and $0.07 \text{ mg} \cdot \text{cm}^{-2} \cdot \text{h}^{-1}$ for adults]; DAF = Dermal absorption factor (unit less), [0.001 for both child and adults]; PEF = Particle Emission Factor [$1.36 \times 10^9 \text{ m}^3 \cdot \text{kg}^{-1}$ for both cases]; ABW = Average Body Weight (18 kg for child and 60 kg for adults); T_{avg} = Averaging Time (for non-carcinogens, $T_{avg} = T_{exp} \times 365$) (Gope et al. 2018).

Hazard Quotient (HQ) was calculated for individual PTE in each exposure pathway. The calculated CDI values were subtracted with the corresponding reference dose (RfD) of PTEs. Reference doses were listed in Table 3.

$$HQ = \sum \frac{CDI}{RfD} \quad \dots(5)$$

Hazard index (HI) was calculated for each PTE. HI is the summation of three HQ for each PTE.

$$HI = \sum HQ \quad \dots(6)$$

Statistical Analysis

Principal Component Analysis (PCA), and Tukey test of PTEs were done by SPSS statistical software version 21.

Monte Carlo simulation was performed by using Crystal Ball (v11.1.1.1.00).

RESULTS AND DISCUSSION

Total PTEs Content

The concentration of all PTEs in the indoor dust of houses

and schools varied significantly by season (Fig. 2). Studied eight PTEs had maximum concentration (Cd, Cr, Cu, Fe, Mn, Ni, Pb and Zn) during the winter followed by summer and monsoon (Fig. 2). In summer, for ventilation, windows and doors are kept open, leading to accumulation of dust in the indoor environment and due to windy (maximum 3.6km/hr) and dry condition (maximum 48°C). In monsoon due to heavy rain, pollutants could have washed-out from atmosphere leading to a low concentration of aerosols in the outdoor and ultimately leading to less PTEs concentration during monsoon (Kulshrestha et al. 2009). Low atmospheric temperature, low mixing height and temperature inversion during winter would have led to the movement of fine dust through the window and doorsill and get accumulated into the

indoor environment from an outdoor source could be responsible for higher PTEs concentration in winter when compared to monsoon and summer (Khillare et al. 2004, Kulshrestha et al. 2009). A similar variation of PTEs concentration in street dust was also reported by Gope (2016) in Asansol.

A maximum Cd concentration of 4.94 ± 1.6 and $3.85 \pm 1.9 \text{ mg.kg}^{-1}$ was observed in houses and schools respectively during winter. The major source of Cd in indoor dust could be from other outdoor sources like coal combustion, petroleum combustion and fossil fuel burning (Li et al. 2016, Soleimani et al. 2018). The high concentration of Cd in indoor dust at Asansol is due to the influence of outdoor aerosols into the indoor environment, originating from industrial activities like ceramic industries, steel plant (Liang et al. 2017, Soleimani

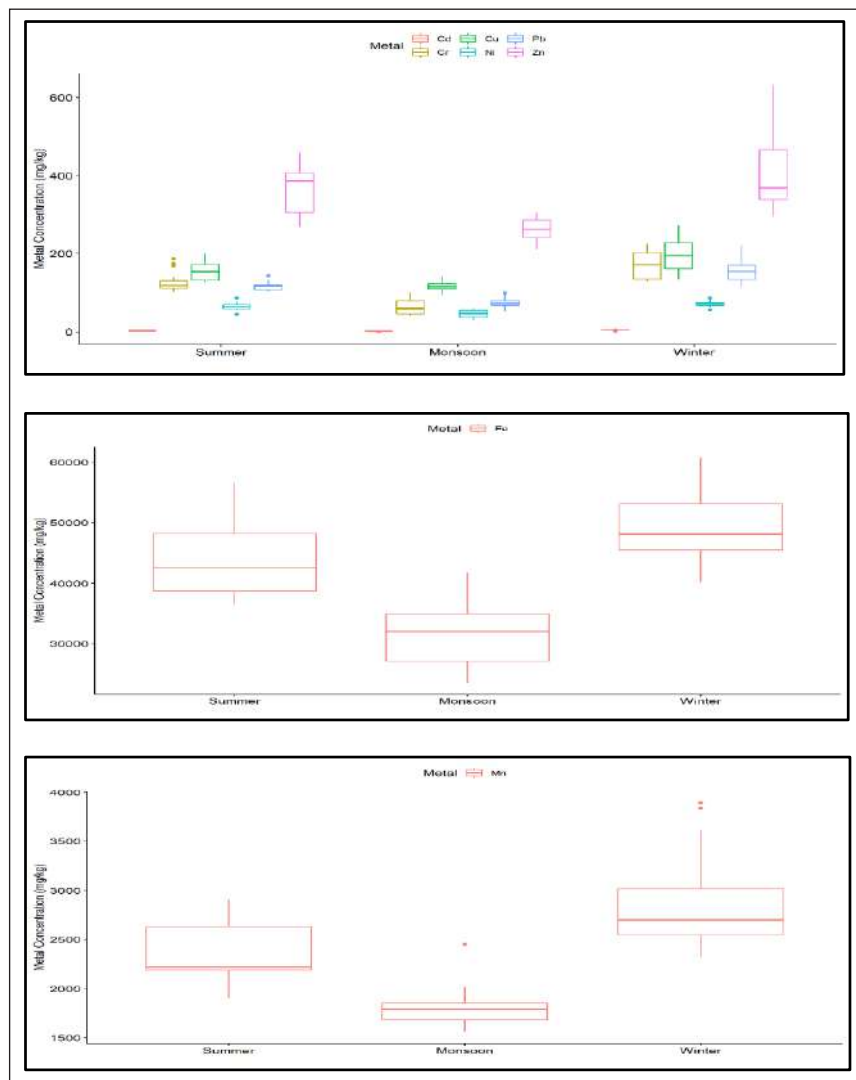


Fig. 2: Seasonal variation of total PTEs (Cd, Cr, Cu, Fe, Mn, Ni, Pb and Zn) concentration in settled indoor dust of Asansol.

et al. 2018), cement industries (Shen et al. 2017, Hua et al. 2016), fossil fuel burning, engine oil, and tires wear (Novo et al. 2017, Gope et al. 2018).

During winter maximum average Cr concentration in Asansol was $169 \pm 33 \text{ mg.kg}^{-1}$ while the maximum average concentration at schools was $135 \pm 2.5 \text{ mg.kg}^{-1}$. The high concentration of Cr in the indoor could be sourced to infiltration of outdoor aerosols into indoor which might be due to their release from the vehicles traffic (Muhamad-Darus et al. 2017, Soleimani et al. 2018), weathering of Cr-Ni plated automobile parts, yellow road paint (Iwegbue et al. 2017) and some indoor sources of Cr are mosquito coil and incense stick burning (Lin & Shen 2003, 2005), Cr coated household items (Iwegbue et al. 2017, Al-madanat et al. 2017, Muhamad-Darus et al. 2017).

Average Cu concentrations at schools were 164 ± 29 , 6.0 ± 116 and $33 \pm 179 \text{ mg.kg}^{-1}$ during summer, monsoon and winter respectively. Cu concentration was highest ($196 \pm 42 \text{ mg.kg}^{-1}$) during winter and was lowest during monsoon ($117 \pm 11 \text{ mg.kg}^{-1}$). Uses of Cu based biocides in home gardens and Cu containing wood preservatives (copper arsenate, copper sulphate, etc.) are the sources of indoor Cu contamination (Iwegbue et al. 2017). Vehicular emission is a very common source of Cu (Muhamad-Darus et al. 2017, Al-madanat et al. 2017) as well as coal combustion (Gope et al. 2018) which could be transported from outdoor to indoor environment. Besides, vehicular emission, industries at Asansol use coal as a fuel and which could increase Cu concentration in outdoor as well as indoor.

The average Fe concentration was highest during the winter ($49538 \pm 6004 \text{ mg.kg}^{-1}$) followed by summer ($44044 \pm 6045 \text{ mg.kg}^{-1}$) and monsoon ($31544 \pm 5697 \text{ mg.kg}^{-1}$), while maximum Fe concentration at schools was $53863 \pm 6656 \text{ mg.kg}^{-1}$ during winter followed by summer ($44523 \pm 4576 \text{ mg.kg}^{-1}$) and monsoon ($27782 \pm 4066 \text{ mg.kg}^{-1}$). Fe concentration is high in lateritic soil (Goldberg 1989, Emeh et al. 2019), and this Fe containing dust enter into houses from the playground, roadside dust, and different barren places. Steel industries and various ferroalloy industries are also major sources of Fe pollution, which could enter into indoor through outdoor aerosol. During monsoon, heavy rain decreases the dust levels leading to decreased Fe concentration in indoor dust.

The highest average Mn concentration was observed at houses during winter ($2881 \pm 499 \text{ mg.kg}^{-1}$) at Asansol. Maximum average Mn concentration at schools was $3115 \pm 755 \text{ mg.kg}^{-1}$ during winter. Major sources of Mn in household dust could be the use of household washing agents, and outdoor sources for automobile emissions (Iwegbue et al. 2017). Mn is the main raw material used in steel plant

and is the main source of Mn contamination in an outdoor environment (Gope et al. 2018), and Mn contaminated aerosol enter into indoor from the outdoor environment.

Average highest Ni concentration at Asansol was $72.6 \pm 7.93 \text{ mg.kg}^{-1}$ during winter, while the highest average Ni concentration in schools was $65.5 \pm 7.6 \text{ mg.kg}^{-1}$ during winter. Some of the major indoor sources of Ni in the indoor environment are mosquito coil and incense burning (Lin & Shen 2005, Li et al. 2016). Ni is mainly released into the outdoor environment from vehicular emission, iron-steel plant, thermal power plant (mainly combustion of coal) (Muhamad-Darus et al. 2017, Li et al. 2016, Wan et al. 2016, Soleimani et al. 2018) which is entered into houses and schools through outdoor aerosol.

The average Pb concentrations were 117 ± 10.9 , 75.4 ± 13.5 and $154 \pm 27.9 \text{ mg.kg}^{-1}$ during summer, monsoon and winter respectively, while in schools, the maximum Pb concentration was $136 \pm 16 \text{ mg.kg}^{-1}$ during winter. The major indoor sources of Pb are Pb-based paint, lead solder, lead pipes, cigarette smoke (Iwegbue et al. 2017). The sources of Pb in indoor could be traced the dust emitted from industries, which could penetrate the indoor environment like vehicular exhausts (Iwegbue et al. 2017, Nawazish et al. 2017), coal combustion (Pacyna et al. 2009, Sen et al. 2016), fly ash from fly ash brick manufacturing plant (Gope et al. 2018), cement industries (Bermudez et al. 2010), etc.

The average Zn concentration was 363 ± 58.8 , 263 ± 30.1 and $410 \pm 94.7 \text{ mg.kg}^{-1}$ respectively during summer, monsoon and winter in Asansol. Zn concentration was higher during winter than summer and monsoon. Maximum Zn concentration in schools was $345 \pm 32 \text{ mg.kg}^{-1}$ during winter. Zn can be sourced into indoor dust from rubber underlay, galvanized iron roofing, and carpets (Iwegbue et al. 2017). Depreciation of vulcanized rubber tires, decomposition of galvanized vehicular parts, and lubricating oils also release Zn in the outdoor environment which could be traced into the indoor environment by outdoor aerosols (Muhamad-Darus et al. 2017, Sulaiman et al. 2017). Moreover, brass and bronze, dry cell batteries, paints, rubber, ceramic are responsible for Zn contamination in indoor dust (Gope et al. 2018).

Comparison of total PTEs concentration in indoor dust reported from other countries along with this study is presented in Table 1.

Mineral Composition

X-ray diffraction study was performed to identify the various minerals present in the indoor dust samples (Fig. 3a, 3b). Quartz and magnetite was the most abundant mineral present in the analysed indoor dust. The identified quartz minerals

Table 1: Comparison of Total PTEs concentrations (mg/kg dry weight) in house dust of Asansol (n = 48) with other studies.

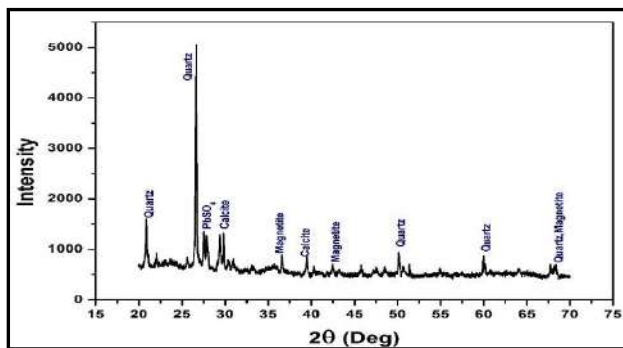
S. No	Type of Indoor dust	Location	Cd	Cr	Cu	Fe	Mn	Ni	Pb	Zn	References
2	Household dust	Istanbul, Turkey	0.80	55.0	156	n.a	136	263	28.0	832	Kurt-Karakus (2012)
3	Indoor dust	Canada	6	117	279	n.a	n.a	102	210	833	Rasmussen et al. (2013)
4	Indoor dust	Katmandu, Nepal	8.2	29.9		n.a	n.a	23.9	40	76.2	Shakya (2013)
5	Indoor dust	Pretoria, South Africa	1.47	109	186	11000	n.a	59.5	110	669	Kefeni and Okonkwo (2013)
7	Preschools	Malaysia	0.23	11.9	n.a	4801		n.a	253.5	144.9	Latif et al. (2014)
8	Indoor	Tokyo, Japan	1.02	67.8	304	10000	226	59.6	57.9	920	Yoshinaga et al. (2014)
9	Nursery schools	Xi'an, China	n.a	159.7	74.20	n.a	397.5	36.2	176.2	462.6	Lu et al. (2014)
11	Primary schools	Sri Serdang, Malaysia	1.73	n.a	54.71	n.a	n.a	n.a	34.17	n.a	Praveena et al. (2015)
14	Indoor dust	Huainan city, China	n.a	76.5	114.5	n.a	n.a	41.8	116.9	602.8	Lin et al. (2016)
15	Indoor dust	Xi'an, Central China	n.a	94.6	100.7	n.a	452.9	157.5	148.4	621.1	Wan et a. (2016)
16	Indoor dust	Hunan Province, China	2.15	130.1	34.3	n.a	445	119.3	72.07	250.2	Cao et al. (2016)
17	Indoor dust	Chengdu, China	8.31	315	419	n.a	879	495	366	2630	Li et al. (2016)
18	Indoor dust	Tianjin, China	2.98	127	171	n.a	604	68.9	181	1370	Li et al. (2016)
19	Indoor dust	Delta State, Nigeria	BDL-21.2	BDL-117	3.37 – 2310	219 – 37,700	4.25 – 365	BDL-471	BDL-182	6.18-61,600	Iwegbue et al. (2017)
20	Indoor dust	Huelva (Spain)	2	69	965	20000	n.a	55	152	882	Torres-Sánchez et al. (2017)
21	Indoor dust	Al-Karak city, Jordan	n.a	72.5	90.5	n.a	38.8	90.5	51.39	n.a	Al-Madanat et al. (2017)
22	Indoor dust	Cawangan Pahang, Malaysia	n.a	n.a	97.42-193.7	10809-51312	n.a	n.a	8.72-27.36	2879-30776	Sulaiman et al. (2017)
23	Indoor dust	Chengdu, China	2.37	82.7	190	n.a	n.a	52.6	123	675	Cheng et al. (2018)
25	Indoor dust	Estarreja, Portugal	1.4	63	311	n.a	188	73	380	2090	Plumejeaud et al. (2018)
26	Indoor dust	Asansol	3.16	120	156	41708	2354	61.3	115	345	Present study

were preiswerkite, clintonite, fayalite with clay forming minerals such as calcite, gypsum, dolomite, microcline, muscovite, prasoichrome, zincian. Pb containing mineral such as anglesite (PbSO_4) was observed which could be due to traffic and fly ash released from fossil fuel burning. Wulfenite (PbMoO_4), a secondary mineral, was detected in one sample, but the intensity was low. ZnMoO_8 is a zinc-containing mineral found in the Asansol industrial area. Magnetite and hematite were detected in both the samples. Siderite (FeCO_3) and pyrite (FeS_2), iron-containing minerals were

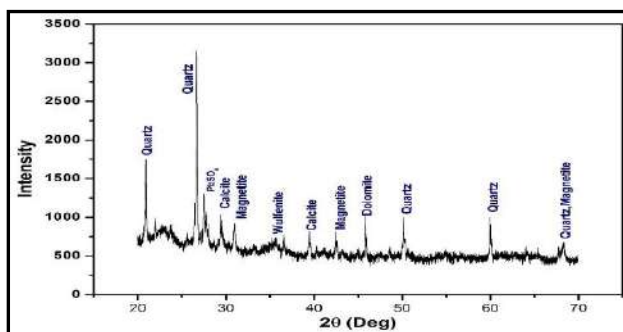
found in the indoor dust samples. Iron-containing minerals are introduced in the indoor dust due to fossil-fuel burning, traffic emissions, steel plant and other industries (Ram et al. 2014, Lu et al. 2007). Presence of clay forming mineral-like dolomite [$\text{CaMg}(\text{CO}_3)_2$] could be due to cement industries present in the Asansol industrial area.

Source Identification

Principal component analysis (PCA): PCA was used to identify the PTEs sources in the indoor settled dust of Asansol



(a)



(b)

Fig. 3: XRD of dust samples (a and b) collected from Asansol.

industrial area (Table 2a). In this study, two components were extracted with 81.55% of the total variance. Cd, Cr, Cu, Ni, Pb, and Zn occupied the same component with respective loading of 0.809, 0.700, 0.709, 0.695, 0.745, 0.885 might be indicating traffic emission. Kelepertzis et al. (2019) supported the traffic source of Pb, Zn, and Cu. Traffic source of Cd, Cr, and Ni was also supported by Deghani et al. (2017). On the other hand, Fe and Mn were in PC2 component indicating the industrial source and lithogenic source of Fe and Mn. Lithogenic source of Fe and Mn also reported in a study in Athens (Kelepertzis et al. 2019) in a study in Athens, Greece, moreover Fe and Mn might also be released from steel industries (Gope et al. 2018).

Tukey analysis: Season wise significant difference of PTEs can be explained by Post-Hoc (Tukey) analysis (Table 2b). Tukey analysis showed that Cd, Cr, Cu, Mn, and Pb concentrations were significantly different during summer, monsoon, and winter at 95% significant level but Fe, Ni, and Zn concentration was not significantly different during

Table 2: a) Principal Component Analysis (PCA), and b) Tukey analysis results of studied PTEs (Cd, Cr, Cu, Fe, Mn, Ni, Pb and Zn) in the deposited indoor dust of Asansol.

(a) Principal component analysis (PCA).

Rotated Component Matrix

PTEs	Component	
	1	2
Cd	.809	.429
Cr	.700	.574
Cu	.709	.567
Fe	.330	.885
Mn	.415	.758
Ni	.695	.502
Pb	.745	.516
Zn	.885	.255
% of variance	46.86	34.70
Cumulative %	46.86	81.55

(b) Tukey analysis.

PTEs	Season	Season	Significance	95% confidence interval	
				Lower boundary	Upper boundary
Cd	Summer	Monsoon	0.001	0.59	2.48
	Summer	Winter	0	-2.85	-0.96
	Monsoon	Winter	0	4.38	-2.49
Cr	Summer	Monsoon	0	40.7	86.8
	Summer	Winter	0	-64.3	-18.2
	Monsoon	Winter	0	-128	-82.0
Cu	Summer	Monsoon	0.001	14.4	63.3
	Summer	Winter	0.001	-65.1	-16.1
	Monsoon	Winter	0	-104	-54.9
Fe	Summer	Monsoon	0	7430	17571
	Summer	Winter	0.031	-10564	-423
	Monsoon	Winter	0	-23065	-12923
Mn	Summer	Monsoon	0	255	873
	Summer	Winter	0.001	-816	-198
	Monsoon	Winter	0	-1381	-762
Ni	Summer	Monsoon	0	10.9	27.1
	Summer	Winter	0.076	-15.5	0.62
	Monsoon	Winter	0	-34.5	-18.4
Pb	Summer	Monsoon	0	25.0	57.6
	Summer	Winter	0	-53.8	-21.3
	Monsoon	Winter	0	-95.1	-62.6
Zn	Summer	Monsoon	0	43.0	157
	Summer	Winter	0.132	-103	10.8
	Monsoon	Winter	0	-204	-89.4

* The mean difference is significant at the 0.05 level.

summer and winter. Fe, Ni, and Zn concentration were not significantly different during summer and winter, which might be due to the influences of some local sources of these PTEs. Cement industries at Asansol industrial area situated at the north-east region of the area and as in summer the wind at that area blow from the North-East direction, the Zn concentration in that area is not significantly different during winter with summer. During summer and winter, the dispersion of pollutants is different, which could be responsible for Fe, Zn, and Ni concentration not significant during these two seasons.

Bioaccessibility

Seasonal variation of PTEs bioaccessibility in indoor settled dust was observed and represented as the percentage of bioaccessibility (Fig. 4a). Cd and Zn bioaccessibility was higher during the summer, followed by winter. Bioaccessibility of Cr, Cu, Ni, and Pb was higher during the winter followed

by the monsoon. Fe and Mn bioaccessibility was maximum during monsoon followed by summer. Seasonal variation of bioaccessibility was observed in the indoor settled dust at Asansol industrial area might be due to different soil parameters, and this theory was supported in a study reported from China (Wang et al. 2016). The bioaccessible fraction of Cd was higher when compared to other PTEs, and the bioaccessible fraction of Fe was lower in the present study. The main controlling factors of bioaccessibility of PTEs are speciation of PTEs, pH, presence of organic matter and mineral composition of matter (Roussel et al. 2010, Hu et al. 2012, Pelfrene et al. 2012, 2013). Mineralogy is one of the important controlling factors of bioaccessibility (Ettler et al. 2019). PTEs might occur as exchangeable form, reducible form, oxidizable form and residual form, which plays an important role in Bioaccessibility. SBET estimate the amount of PTEs that is dissolved from ingested dust in the gastric juice and available for transport through the intestinal membrane

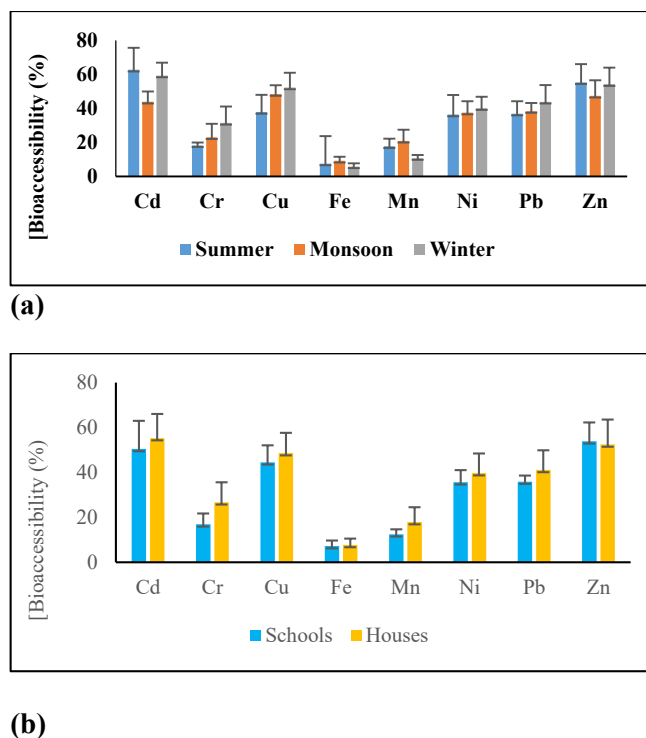


Fig. 4: (a) Bioaccessible fraction (%) of PTEs in indoor dust of Asansol (b) comparison of bioaccessible fraction (%) between schools and houses.

(Cao et al. 2009, Hu et al. 2012, Wang et al. 2016). Low pH of gastric juice is responsible for the bioaccessibility of PTEs. The decreasing order of bioaccessible fraction was $Cd > Zn > Cu > Pb > Ni > Cr > Mn > Fe$ during summer and winter, but during monsoon the order was $Cu > Zn > Cd > Pb > Ni > Cr > Mn > Fe$.

In this study, the bioaccessibility fraction between schools and houses (Fig. 4b) was compared. Only Zn bioaccessibility was higher in schools than houses, while bioaccessibility of other 7 PTEs was higher in house dust. Mainly outdoor aerosol particulates vehicular exhausts are responsible for high Zn bioaccessibility in schools' dust.

Human Health Risk Assessment

The health risk of PTEs was calculated for children and adult in the indoor settled dust samples of Asansol industrial area (Table 3). Ingestion, inhalation, and dermal contacts are the three main pathways and were considered for health risk assessment. Hazard Quotient (HQ) and Hazard Index (HI) were separately calculated for each PTE. In this study, total PTEs concentration and SBET-extracted PTEs concentration were used separately for health risk assessment. During use of total PTEs (Cd, Cr, Cu, Mn, Ni, Pb and Zn) concentration for health risk assessment, ingestion was the main exposure

route both in child and adults followed by dermal contact (Li et al. 2013, Wang et al. 2016) but in case of Fe, maximum risk observed for dermal contact. During use of SBET-extracted PTEs concentration for health risk assessment, the result was similar like total PTEs concentration. Here, ingestion was the main exposure followed by dermal contact for all observed PTEs except Fe. Decreasing order of non-carcinogenic health risk for total PTEs concentration was $Mn > Fe > Cr > Pb > Cd > Cu > Ni > Zn$ and $Fe > Mn > Cr > Pb > Zn > Cd > Cu > Ni > Zn$ in children and adults respectively, whereas risk for SBET-extracted PTEs concentration was $Fe > Mn > Cr > Pb > Cu > Cd > Ni > Zn$ and $Fe > Mn > Cr > Pb > Cd > Cu > Ni > Zn$ in children and adults respectively. In all cases, health risk due to Zn was lower when compared to other observed PTEs. The health risk assessment of the actual concentration of ingested and absorbed PTEs measured by SBET is more reliable and accurate (Oomen et al. 2002, Wang et al. 2016). Calculated health risk both for total PTEs concentration and SBET-extracted concentration of PTEs were < 1 , indicating non-carcinogenic health risk was observed in the indoor settled dust of residence and schools at Asansol industrial area. Calculated health risk also indicated that children were more vulnerable group than adult (Gu et al. 2018, Gope et al. 2018). The HI values of Fe, Mn and Cr were close to 1, which indicates that these PTEs can cause health risk in future.

Monte Carlo simulation was performed only for ingested PTEs, and the distribution of the parameters are given in Table 4a and 4b. Cumulative hazard index of PTEs ingestion was calculated for the Monte Carlo simulation. From the sim-

ulation, it is clear that 95% of the values of HQ (collectively for eight metals) was below 1. We can see that the cumulative HI was maximum during winter and was minimum during monsoon for both child and adult. From the cumulative

Table 3: Human Health risk assessment using total metal and SBET-extracted concentration of studied PTEs (Cd, Cr, Cu, Mn, Ni, Pb and Zn) in the settled indoor dust of Asansol.

PTEs	Type of Exposure	RfD	Summer		Monsoon		Winter	
			Child	Adult	Child	Adult	Child	Adult
Cd	Ingestion	1.00E-03	2.89E-03	1.73E-03	1.43E-03	8.57E-04	4.70E-03	2.82E-03
	Ingestion _{bioaccessible}	1.00E-03	1.80E-03	1.08E-03	6.50E-04	3.90E-04	2.74E-03	1.64E-03
	Inhalation	5.70E-06	1.86E-05	4.47E-05	9.21E-06	2.21E-05	3.03E-05	7.28E-05
	Dermal	1.00E-05	8.09E-04	6.91E-04	4.00E-04	3.42E-04	1.32E-03	1.13E-03
	HI _{total metal}		3.72E-03	2.47E-03	1.84E-03	1.22E-03	6.05E-03	4.02E-03
	HI _{bioaccessible}		2.63E-03	1.81E-03	1.06E-03	7.54E-04	4.08E-03	2.84E-03
Cr	Ingestion	3.00E-03	4.06E-02	2.43E-02	2.03E-02	1.22E-02	5.37E-02	3.22E-02
	Ingestion _{bioaccessible}	3.00E-03	7.39E-03	4.43E-03	4.63E-03	2.78E-03	1.75E-02	1.05E-02
	Inhalation	2.80E-05	1.60E-04	3.84E-04	8.01E-05	1.92E-04	2.11E-04	5.07E-04
	Dermal	7.50E-05	4.55E-03	3.89E-03	2.28E-03	1.95E-03	6.01E-03	5.14E-03
	HI _{total metal}		4.53E-02	2.86E-02	2.27E-02	1.43E-02	5.99E-02	3.79E-02
	HI _{bioaccessible}		1.21E-02	8.70E-03	6.98E-03	4.92E-03	2.37E-02	1.61E-02
Cu	Ingestion	4.00E-02	3.70E-03	2.22E-03	2.78E-03	1.67E-03	4.67E-03	2.80E-03
	Ingestion _{bioaccessible}	4.00E-02	1.39E-03	8.32E-04	1.34E-03	8.06E-04	2.44E-03	1.47E-03
	Inhalation	4.02E-02	1.35E-07	3.25E-07	1.02E-07	2.44E-07	1.71E-07	4.10E-07
	Dermal	1.20E-02	3.45E-05	2.95E-05	2.59E-05	2.22E-05	4.36E-05	3.72E-05
	HI _{total metal}		3.74E-03	2.25E-03	2.80E-03	1.69E-03	4.71E-03	2.84E-03
	HI _{bioaccessible}		1.42E-03	8.62E-04	1.37E-03	8.28E-04	2.49E-03	1.50E-03
Fe	Ingestion	8.40	4.99E-03	3.00E-03	3.58E-03	2.15E-03	5.62E-03	3.37E-03
	Ingestion _{bioaccessible}	8.40	3.82E-04	2.29E-04	3.33E-04	2.00E-04	3.28E-04	1.97E-04
	Inhalation	7.0E-02	2.20E-05	5.29E-05	1.58E-05	3.79E-05	2.48E-05	5.95E-05
	Dermal	2.2E-03	5.34E-02	4.56E-02	3.82E-02	3.27E-02	6.00E-02	5.13E-02
	HI _{total metal}		5.84E-02	4.87E-02	4.18E-02	3.49E-02	6.57E-02	5.48E-02
	HI _{bioaccessible}		5.38E-02	4.59E-02	3.86E-02	3.29E-02	6.04E-02	5.16E-02
Mn	Ingestion	4.60E-02	4.91E-02	2.95E-02	3.75E-02	2.25E-02	5.96E-02	3.58E-02
	Ingestion _{bioaccessible}	4.60E-02	8.69E-03	5.21E-03	7.80E-03	4.68E-03	6.44E-03	3.87E-03
	Inhalation	1.43E-05	5.81E-03	1.39E-02	4.43E-03	1.06E-02	7.05E-03	1.69E-02
	Dermal	1.84E-03	3.44E-03	2.94E-03	2.62E-03	2.24E-03	4.17E-03	3.57E-03
	HI _{total metal}		5.84E-02	4.64E-02	4.45E-02	3.53E-02	7.09E-02	5.63E-02
	HI _{bioaccessible}		1.79E-02	2.21E-02	1.49E-02	1.76E-02	1.77E-02	2.44E-02
Ni	Ingestion	2.00E-02	3.10E-03	1.86E-03	2.20E-03	1.32E-03	3.46E-03	2.07E-03
	Ingestion _{bioaccessible}	2.00E-02	1.16E-03	6.79E-04	8.27E-04	4.96E-04	1.40E-03	8.39E-04
	Inhalation	2.06E-02	1.11E-07	2.66E-07	7.84E-08	1.88E-07	1.23E-07	2.96E-07
	Dermal	5.40E-03	3.22E-05	2.75E-05	2.28E-05	1.95E-05	3.58E-05	3.06E-05
	HI _{total metal}		3.13E-03	1.89E-03	2.22E-03	1.34E-03	3.49E-03	2.10E-03
	HI _{bioaccessible}		1.16E-03	7.07E-04	8.50E-04	5.16E-04	1.44E-03	8.70E-04

PTEs	Type of Exposure	RfD	Summer		Monsoon		Winter	
			Child	Adult	Child	Adult	Child	Adult
Pb	Ingestion	3.50E-03	3.17E-02	1.90E-02	2.05E-02	1.23E-02	4.20E-02	2.52E-02
	Ingestion _{bioaccessible}	3.50E-03	1.17E-02	7.01E-03	7.95E-03	4.77E-03	1.86E-02	1.12E-02
	Inhalation	3.52E-03	1.16E-06	2.79E-06	7.50E-07	1.80E-06	1.53E-06	3.68E-06
	Dermal	5.25E-04	5.93E-04	5.07E-04	3.83E-04	3.27E-04	7.83E-04	6.70E-04
	HI _{total metal}		3.23E-02	1.96E-02	2.09E-02	1.26E-02	4.27E-02	2.58E-02
	HI _{bioaccessible}		1.23E-02	7.52E-03	8.33E-03	5.10E-03	1.94E-02	1.18E-02
Zn	Ingestion	3.00E-01	1.15E-03	6.92E-04	8.36E-04	5.01E-04	1.30E-03	7.80E-04
	Ingestion _{bioaccessible}	3.00E-01	6.41E-04	3.85E-04	3.96E-04	2.38E-04	7.13E-04	4.28E-04
	Inhalation	3.00E-01	4.24E-08	1.02E-07	3.07E-08	7.37E-08	4.78E-08	1.15E-07
	Dermal	6.00E-02	1.62E-05	1.38E-05	1.17E-05	1.00E-05	1.82E-05	1.56E-05
	HI _{total metal}		1.17E-03	7.06E-04	8.47E-04	5.11E-04	1.32E-03	7.96E-04
	HI _{bioaccessible}		6.57E-04	3.99E-04	4.08E-04	2.48E-04	7.31E-04	4.43E-04

Ingestion + Inhalation + Dermal = HI_{total metal}

Ingestion_{bioaccessible} + Inhalation + Dermal = HI_{bioaccessible}

Table 4: Distribution of parameter for Monte Carlo simulation: (a) Parameters for different population group (b) distribution for PTEs.

(a) Parameters for the different population groups.

Parameters	Symbols	Units	Distribution	Adult	Child	References
Metal Concentration	C		Log-normal	Changes according to seasons and metals		Present Study
Ingestion rate	IR	mg/day	Triangular	25 (0.1-50)	X	LaGoy (1987)
			Log-normal	X	24 (±4)	Stanek et al. (2001)
Exposure Frequency	EF	Days/year	Triangular	345 (180-365)	345 (180-365)	Smith (1994)
Exposure duration	ED	Years	Point	24	6	USEPA1991, USEPA (2011)
Body weight	BW	Kg	Log-Normal	58.7 (±12)	X	Yang et al. (2005)
			Normal	X	16.5 (±2.4)	ICMR (2009)
Reference doses	RfD	µg/kg/day	Point	Changes according to metals		USEPA (2011)

(b) Distribution for PTEs

Metal	Summer (mg/kg)	Monsoon (mg/kg)	Winter (mg/kg)
Cd	0.95 (±2.28)	0.94 (±6.47)	8,598.70 (±1.00)
Cr	19.94 (±2.57)	19.39 (±2.46)	166.01 (±1.22)
Cu	153.86 (±1.16)	152.04 (±1.08)	191.76 (±1.24)
Fe	43,665.29 (±1.14)	31,071.17 (±1.20)	49,201.84 (±1.13)
Mn	734.14(±1.49)	1,798.71 (±1.11)	2,843.43 (±1.18)
Ni	64.40 (±1.17)	34,201.06 (±1.00)	72.18 (±1.12)
Pb	116.21 (±1.10)	46.32 (±1.32)	151.91 (±1.19)
Zn	269,731.99 (±1.00)	123,786.26 (±1.00)	400.18 (±1.25)

*Values are given in geometric mean and standard deviation.

probabilistic simulation, it can be concluded that children are more susceptible than an adult during all three seasons. During the three seasons, the cumulative HQ of 8 metals indicated that risk was persistently higher for children than adult (Fig. 5a and b). Calculated cumulative hazard index of all 8 PTEs are given in Table 5 were the distributions were considered as point distribution. It is found out that baseline

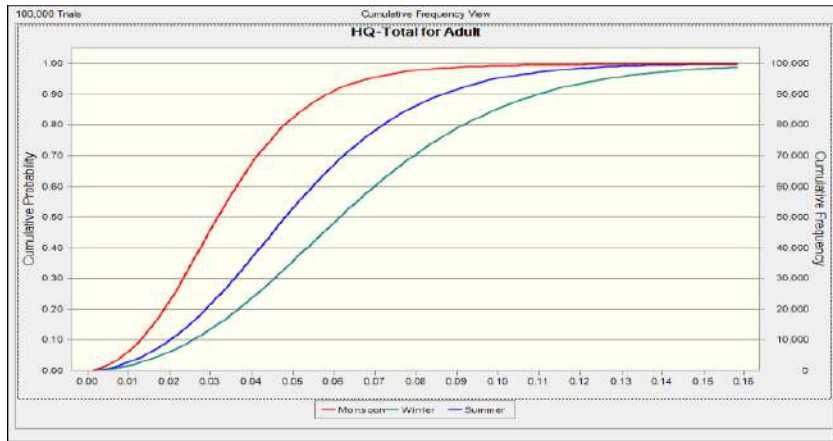
case falls within 1. Predicted probability density functions of non-carcinogenic risk for summer, monsoon, and winter for adult and child are given in Fig. 6.

CONCLUSION

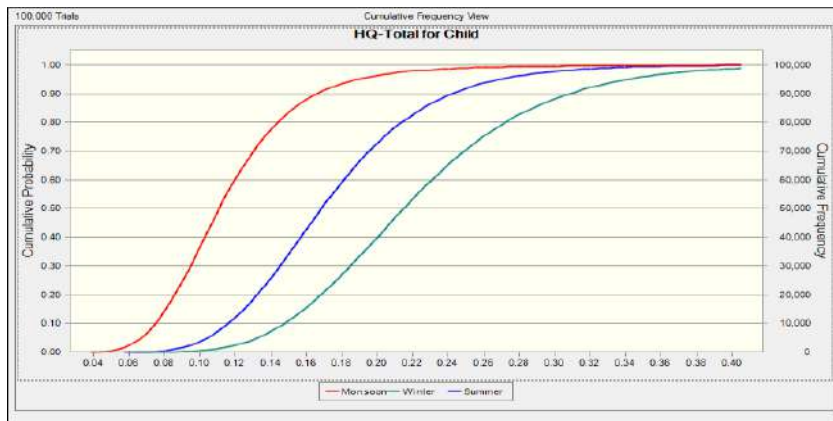
PTEs concentration in most of the cases is high in the

Table 5: HI value due to ingestion of different PTEs through Monte Carlo simulation.

PTEs	Type of Exposure	RfD	Summer		Monsoon		Winter	
			Child	Adult	Child	Adult	Child	Adult
Cd	Ingestion _{bioaccessible}	1.00E-03	1.80E-03	1.08E-03	6.50E-04	3.90E-04	2.74E-03	1.64E-03
Cr	Ingestion _{bioaccessible}	3.00E-03	7.39E-03	4.43E-03	4.63E-03	2.78E-03	1.75E-02	1.05E-02
Cu	Ingestion _{bioaccessible}	4.00E-02	1.39E-03	8.32E-04	1.34E-03	8.06E-04	2.44E-03	1.47E-03
Fe	Ingestion _{bioaccessible}	8.40E+00	3.82E-04	2.29E-04	3.33E-04	2.00E-04	3.28E-04	1.97E-04
Mn	Ingestion _{bioaccessible}	4.60E-02	8.69E-03	5.21E-03	7.80E-03	4.68E-03	6.44E-03	3.87E-03
Ni	Ingestion _{bioaccessible}	2.00E-02	1.16E-03	6.79E-04	8.27E-04	4.96E-04	1.40E-03	8.39E-04
Pb	Ingestion _{bioaccessible}	3.50E-03	1.17E-02	7.01E-03	7.95E-03	4.77E-03	1.86E-02	1.12E-02
Zn	Ingestion _{bioaccessible}	3.00E-01	6.41E-04	3.85E-04	3.96E-04	2.38E-04	7.13E-04	4.28E-04
Cumulative HQ (HI)			3.32E-02	1.99E-02	2.39E-02	1.44E-02	5.02E-02	3.01E-02



(a)



(b)

Fig. 5: Cumulative probability of hazard quotient (HQ) for (a) adult and (b) child during summer, monsoon and winter for bioaccessible metal content through Monte Carlo simulation.

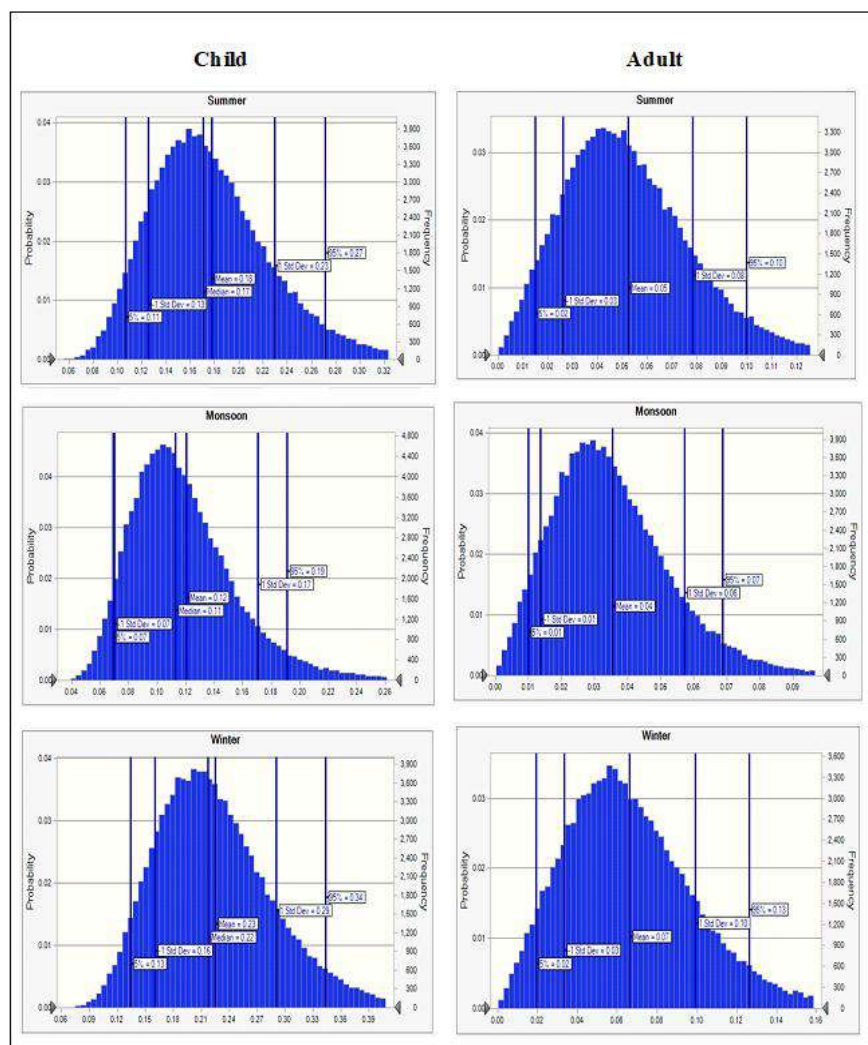


Fig. 6: Predicted probability density functions of non-carcinogenic risk for bioaccessible metal content in summer, monsoon, and winter for adult and child through Monte Carlo simulation.

house dust than school dust, which is highly influenced by the outdoor environment. During summer and winter, Fe and Mn concentrations were higher at schools. At schools, Cu concentration was higher during summer and Cr concentration during monsoon. It was observed that the major sources of PTE's in the indoor environment of schools and houses are from the outdoor environment, particularly from industries and vehicular exhaust. High Cd enrichment was noted at all four sampling sites of the Asansol industrial area. PCA indicated industrial emission, lithogenic and traffic-related materials as major sources. The health risk was <1 for total concentration and SBET-extracted PTEs concentration. Risk assessment with the average values for PTEs concentration indicated that Cr, Cu, Fe and Pb could cause health risk in future. Monte Carlo simulation depicted

that chances of children getting affected by the PTEs are prominently higher than adults. Harmful effects of PTEs in different seasonal conditions vary differently, and the study concluded that in summer, monsoon, and winter scenario, monsoon, in general, is relatively less risky. Further studies are required encompassing a broader spectrum of the season and different social categories for a comprehensive understanding of risks associated with the PTEs. Studies enquiring further into identifying the particular sources, PTEs emission rate, chemical speciation and mobility of PTEs in indoor dust is required.

ACKNOWLEDGEMENT

The first author received fund from UGC Non-NET

Fellowship through Visva-Bharati, Santiniketan, India during the work period. CSIR-Central Institute of Mining and Fuel Research (Digwadih Campus), Dhanbad (India) and Department of Environmental Sciences, Tezpur University, Assam are greatly acknowledged for their instrumental support during this work.

REFERENCES

- Ali, M. U., Liu, G., Yousaf, B., Ullah, H., Irshad, S., Ahmed, R., Hussain, M. and Rashid, A. 2019. Evaluation of floor-wise pollution status and deposition behaviour of potentially toxic elements and nanoparticles in air conditioner dust during urbanistic development. *Journal of Hazardous Materials*, 365: 186-195.
- Al-Madanat, O., Jiries, A., Batarseh, M. and Al-Nasir, F. 2017. Indoor and outdoor pollution with heavy metals in Al-Karak City, Jordan. *J. Int. Environmental Application and Science*, 12: 131-139.
- Bermudez, G. M., Moreno, M., Invernizzi, R., Plá, R. and Pignata, M. L. 2010. Heavy metal pollution in topsoils near a cement plant: the role of organic matter and distance to the source to predict total and HCl-extracted heavy metal concentrations. *Chemosphere*, 78: 375-381.
- Bot, B., Gilles, E., Durand, S. and Glorennec, P. 2010. Bioaccessible and quasi-total metals in soil and indoor dust. *European Journal of Mineralogy*, 22: 651-657.
- Cao, S., Duan, X., Zhao, X., Chen, Y., Wang, B., Sun, C., Zheng, B. and Wei, F. 2016. Health risks of children's cumulative and aggregative exposure to metals and metalloids in a typical urban environment in China. *Chemosphere*, 147: 404-411.
- Cao, X., Wahbi, A., Ma, L., Li, B. and Yang, Y. 2009. Immobilization of Zn, Cu, and Pb in contaminated soils using phosphate rock and phosphoric acid. *Journal of Hazardous Materials*, 164: 555-564.
- Census, 2011. Population Census of India is collection of census data reports by Govt of India. (www.census2011.co.in).
- Chen, H., Teng, Y., Lu, S., Wang, Y. and Wang, J. 2015. Contamination features and health risk of soil heavy metals in China. *Science of the Total Environment*, 512: 143-153.
- Cheng, Z., Chen, L. J., Li, H. H., Lin, J. Q., Yang, Z. B., Yang, Y. X., Xu, X. X., Xian, J. R., Shao, J. R. and Zhu, X. M. 2018. Characteristics and health risk assessment of heavy metals exposure via household dust from urban area in Chengdu, China. *Science of The Total Environment*, 619: 621-629.
- Dehghani, S., Moore, F., Keshavarzi, B. and Beverley, A. H. 2017. Health risk implications of potentially toxic metals in street dust and surface soil of Tehran, Iran. *Ecotoxicology and Environmental Safety*, 136: 92-103.
- Emeh, C., Igwe, O. and Onwo, E. S. 2019. Potential effect of environmental pollution on the degree of dissolution of iron and aluminium oxides in lateritic soils. *Environmental Earth Sciences*, 78: 256.
- Ettler, V., Cihlová, M., Jarošíková, A., Mihaljevi, M., Drahot, P., K íbek, B., Van k, A., Penížek, V., Sracek, O., Klementová, M., Engel, Z., Kamona, F. and Mapani, B. 2019. Oral bioaccessibility of metal(loid)s in dust materials from mining areas of northern Namibia. *Environment International*, 124: 205-215.
- Goldberg, S. 1989. Interaction of aluminium and iron oxides and clay mineral and their effect on soil physical properties: A review. *Commun. Soil Sci. Plant. Anal.*, 20: 1181-1207.
- Gope, M. 2016. Risk assessment of potentially toxic elements and polycyclic aromatic hydrocarbons in the street dust (<53µm) of Asansol and Durgapur, West Bengal, India. Thesis submitted to the Department of Environmental Studies, Siksha-Bhavana, Visva-Bharati, Santiniketan.
- Gope, M., Masto, R. E., George, J. and Balachandran, S. 2018. Tracing source, distribution and health risk of potentially harmful elements (PHEs) in street dust of Durgapur, India. *Ecotoxicology and Environmental Safety*, 154: 280-293.
- Gope, M., Masto, R. E., George, J., Hoque, R. R. and Balachandran, S. 2017. Bioavailability and health risk of some potentially toxic elements (Cd, Cu, Pb and Zn) in street dust of Asansol, India. *Ecotoxicology and Environmental Safety*, 138: 231-241.
- Gu, Y. G. and Gao, Y. P. 2018. Bioaccessibilities and health implications of heavy metals in exposed-lawn soils from 28 urban parks in the megacity Guangzhou inferred from an in vitro physiologically-based extraction test. *Ecotoxicology and Environmental Safety*, 148: 747-753.
- Hu, X., Zhang, Y., Ding, Z., Wang, T., Lian, H., Sun, Y. and Wu, J. 2012. Bioaccessibility and health risk of arsenic and heavy metals (Cd, Co, Cr, Cu, Ni, Pb, Zn and Mn) in TSP and PM_{2.5} in Nanjing, China. *Atmospheric Environment*, 57: 146-152.
- Hua, S., Tian, H., Wang, K., Zhu, C., Gao, J., Ma, Y., Xue, Y., Wang, Y., Duan, S. and Zhou, J. 2016. Atmospheric emission inventory of hazardous air pollutants from China's cement plants: Temporal trends, spatial variation characteristics and scenario projections. *Atmospheric Environment*, 128: 1-9.
- Hussain, K., Rahman, M., Prakash, A. and Hoque, R. R. 2015. Street dust bound PAHs, carbon and heavy metals in Guwahati city-Seasonality, toxicity and sources. *Sustainable Cities and Society*, 19: 17-25.
- ICMR. 2009. Nutrient requirements and recommended dietary allowances for Indians, Hyderabad (India). National Institute of Nutrition, Indian Council of Medical Research.
- Iwegbue, C. M., Oliseyenum, E. C. and Martincigh, B. S. 2017. Spatio-temporal distribution of metals in household dust from rural, semi-urban and urban environments in the Niger Delta, Nigeria. *Environmental Science and Pollution Research*, 24: 14040-14059.
- Kefeni, K. K. and Okonkwo, J. O. 2013. Trace metals, anions and polybromodiphenyl ethers in settled indoor dust and their association. *Environmental Science and Pollution Research*, 20: 4895-4905.
- Kelepertzis, E., Argyraki, A., Botsou, F., Aidona, E., Szabó, Á. and Szabó, C. 2019. Tracking the occurrence of anthropogenic magnetic particles and potentially toxic elements (PTEs) in house dust using magnetic and geochemical analyses. *Environmental Pollution*, 245: 909-920.
- Khillare, P. S., Balachandran, S. and Meena, B. R. 2004. Spatial and temporal variation of heavy metals in atmospheric aerosol of Delhi. *Environmental Monitoring and Assessment*, 90: 1-21.
- Kulshrestha, A., Satsangi, P. G., Masih, J. and Taneja, A. 2009. Metal concentration of PM_{2.5} and PM₁₀ particles and seasonal variations in urban and rural environment of Agra, India. *Science of the Total Environment*, 407: 6196-6204.
- Kurt-Karakus, P. B. 2012. Determination of heavy metals in indoor dust from Istanbul, Turkey: Estimation of the health risk. *Environment International*, 50: 47-55.
- Labar, R. and Kundu, T. K. 2018. Barrier inhomogeneities in n-ZnO/p-Si heterojunctions fabricated with ZnO nanorods. *Journal of Electronic Materials*, 47: 3628-3633.
- LaGoy, P. K. 1987. Estimated soil ingestion rates for use in risk assessment. *Risk Analysis*, 7: 355-359.
- Latif, M. T., Yong, S. M., Saad, A., Mohamad, N., Baharudin, N. H., Mokhtar, M. B. and Tahir, N. M. 2014. Composition of heavy metals in indoor dust and their possible exposure: A case study of preschool children in Malaysia. *Air Quality, Atmosphere and Health*, 7: 181-193.
- Li, H., Qian, X., Hu, W., Wang, Y. and Gao, H. 2013. Chemical speciation and human health risk of trace metals in urban street dusts from a metropolitan city, Nanjing, SE China. *Science of the Total Environment*, 456: 212-221.
- Li, Y., Pi, L., Hu, W., Chen, M., Luo, Y., Li, Z., Su, S., Gan, Z. and Ding, S. 2016. Concentrations and health risk assessment of metal(loid)s in indoor dust from two typical cities of China. *Environmental Science and Pollution Research*, 23: 9082-9092.
- Liang, J., Feng, C., Zeng, G., Gao, X., Zhong, M., Li, X., Li, X., He, X.

- and Fang, Y. 2017. Spatial distribution and source identification of heavy metals in surface soils in a typical coal mine city, Lianyuan, China. *Environmental Pollution*, 225: 681-690.
- Lin, T. S. and Shen, F. M. 2003. Trace metals in Chinese joss stick smoke. *Bulletin of Environmental Contamination and Toxicology*, 7: 135-141.
- Lin, T. S. and Shen, F. M. 2005. Trace metals in mosquito coil smoke. *Bulletin of Environmental Contamination and Toxicology*, 74: 184-189.
- Lin, Y. S., Fang, F. M., Wu, J. Y., Zhu, Z., Zhang, D. and Xu, M. 2016. Heavy metal in indoor dust of Huainan, China: Concentrations, affecting factors and risk assessment. *Fresenius Environ. Bull.*, 25: 4651-4659.
- Lu, S. G., Bai, S. Q. and Xue, Q. F. 2007. Magnetic properties as indicators of heavy metals pollution in urban topsoils: a case study from the city of Luoyang, China. *Geophysical Journal International*, 17: 568-580.
- Lu, X., Zhang, X., Li, L. Y. and Chen, H. 2014. Assessment of metals pollution and health risk in dust from nursery schools in Xi'an, China. *Environmental Research*, 128: 27-34.
- Muhamad-Darus, F., Nasir, R. A., Sumari, S. M., Ismail, Z. S. and Omar, N. A. 2017. Nursery schools: Characterization of heavy metal content in indoor dust. *Asian Journal of Environment-Behaviour Studies*, 2: 63-70.
- Nawazish, S., Bukhari, S. M., Muhammad, A., Khan, I. U., Alhassan, A. J., Hussain, M. and Zaidi, A. 2017. Correlation analysis of toxic metals on motorway and national highway. *Kuwait Journal of Science*, 44(2): 121-128.
- Novo, L. A., Onishi, V. C., Bernardino, C. A. and Da Silva, E. F. 2017. Metal bioaccumulation by plants in roadside soils: Perspectives for bioindication and phytoremediation. In: *Enhancing Cleanup of Environmental Pollutants*, pp. 215-230.
- Oomen, A. G., Hack, A., Minekus, M., Zeijdner, E., Cornelis, C., Schoeters, G., Verstraete, W., Wiele, T. V. De, Wragg, J., Rempelberg, C. J. M., Sips, A. J. A. M. and Wijnen, J. H. V. 2002. Comparison of five in vitro digestion models to study the bioaccessibility of soil contaminants. *Environmental Science and Technology*, 3: 3326-3334.
- Pacyna, J. M., Pacyna, E. G. and Aas, W. 2009. Changes of emissions and atmospheric deposition of mercury, lead, and cadmium. *Atmospheric Environment*, 43: 117-127.
- Pelfrene, A., Waterlot, C. and Douay, F. 2013. Influence of land use on human bioaccessibility of metals in smelter-impacted soils. *Environmental Pollution*, 178: 80-88.
- Pelfrene, A., Waterlot, C., Mazzuca, M., Nisse, C., Cuny, D., Richard, A., Denys, S., Heyman, C., Roussel, H., Bidar, G. and Douay, F. 2012. Bioaccessibility of trace elements as affected by soil parameters in smelter-contaminated agricultural soils: A statistical modeling approach. *Environmental Pollution*, 160: 130-138.
- Pitawala, A., Herath, D. and Piyatunga, N. 2013. Chemical characterization of household dust in two major cities: Colombo, the capital and Kandy, the hill capital, Sri Lanka. *Carpathian Journal of Earth and Environmental Sciences*, 8: 89-95.
- Plumejeaud, S., Reis, A. P., Tassistro, V., Patinha, C., Noack, Y. and Orsière, T. 2018. Potentially harmful elements in house dust from Estarreja, Portugal: characterization and genotoxicity of the bioaccessible fraction. *Environmental Geochemistry and Health*, 40: 127-144.
- Praveena, S. M., Abdul Mutalib, N. S. and Aris, A. Z. 2015. Determination of heavy metals in indoor dust from primary school (Sri Serdang, Malaysia): Estimation of the health risks. *Environmental Forensics*, 16: 257-263.
- Ram, S. S., Majumder, S., Chaudhuri, P., Chanda, S., Santra, S. C., Maiti, P. K., Sudarshan, M. and Chakraborty, A. 2014. Plant canopies: Bio-monitor and trap for re-suspended dust particulates contaminated with heavy metals. *Mitigation and Adaptation Strategies for Global Change*, 19: 499-508.
- Rasmussen, P. E., Levesque, C., Chénier, M., Gardner, H. D., Jones-Otazo, H. and Petrovic, S. 2013. Canadian House Dust Study: Population-based concentrations, loads and loading rates of arsenic, cadmium, chromium, copper, nickel, lead, and zinc inside urban homes. *Science of the Total Environment*, 443: 520-529.
- Rasmussen, P. E., Subramanian, K. S. and Jessiman, B. J. 2001. A multi-element profile of house dust in relation to exterior dust and soils in the city of Ottawa, Canada. *Science of the Total Environment*, 267: 125-140.
- Rasmussen, P.E., Levesque, C., Chenier, M. and Gardner, H.D. 2018. Contribution of metals in resuspended dust to indoor and personal inhalation exposures: Relationships between PM10 and settled dust. *Building and Environment*, 143: 513-522.
- Rohra, H., Tiwari, R., Khare, P. and Taneja, A. 2018. Indoor-outdoor association of particulate matter and bounded elemental composition within coarse, quasi-accumulation and quasi-ultrafine ranges in residential areas of northern India. *Science of the Total Environment*, 631-632: 1383-1397.
- Roussel, H., Waterlot, C., Pelfrène, A., Pruvot, C., Mazzuca, M. and Douay, F. 2010. Cd, Pb and Zn oral bioaccessibility of urban soils contaminated in the past by atmospheric emissions from two lead and zinc smelters. *Archives of Environmental Contamination and Toxicology*, 58: 945-954.
- Ruby, M. V., Davis, A., Schoof, R., Eberle, S. and Sellstone, C. M. 1996. Estimation of lead and arsenic bioavailability using a physiologically based extraction test. *Environmental Science and Technology*, 30: 422-430.
- Sen, I. S., Bizimis, M., Tripathi, S. N. and Paul, D. 2016. Lead isotopic fingerprinting of aerosols to characterize the sources of atmospheric lead in an industrial city of India. *Atmospheric Environment*, 129: 27-33.
- Shakya, P. R. 2013. Chemical associations of lead, cadmium, chromium, nickel and zinc in household dust of Kathmandu metropolitan area. *Pakistan Journal of Analytical & Environmental Chemistry*, 14: 7.
- Shen, W., Liu L., Yan B., Wang J., He P., Zhou C., Huo X., Zhang W., Xu G. and Ding, Q. 2017. Cement industry of China: Driving force, environment impact and sustainable development. *Renewable and Sustainable Energy Reviews*, 75: 618-628.
- Smith, R. L. 1994. Use of Monte Carlo simulation for human exposure assessment at a superfund site. *Risk Analysis*, 14: 433-439.
- Soleimani, M., Amini, N., Sadeghian, B., Wang, D. and Fang, L. 2018. Heavy metals and their source identification in particulate matter (PM2.5) in Isfahan City, Iran. *Journal of Environmental Sciences*, 72: 166-175.
- Staneek, E. J., Calabrese, E. J. and Zorn, M. 2001. Soil ingestion distributions for Monte Carlo risk assessment in children. *Human and Ecological Risk Assessment*, 7: 357-368.
- Sulaiman, F. R., Bakri, N. I. F., Nazmi, N. and Latif, M. T. 2017. Assessment of heavy metals in indoor dust of a university in a tropical environment. *Environmental Forensics*, 18: 74-82.
- Torres-Sánchez, R., de la Campa, A. M. S., Beltrán, M., Sánchez-Rodas, D. and Jesús, D. 2017. Geochemical anomalies of household dust in an industrialized city (Huelva, SW Spain). *Science of the Total Environment*, 587: 473-481.
- Turner, A. 2011. Oral bioaccessibility of trace metals in household dust: A review. *Environmental Geochemistry and Health*, 33: 331-341.
- USEP 2011. A Exposure Factors Handbook (ed.), <http://cfpub.epa.gov/ncea/risk/recordisplay.cfm?deidD236252>, US Environmental Protection Agency, Washington DC, USA.
- USEPA 1991. Risk Assessment Guidance for Superfund: Volume 1, Human Health Evaluation Manual, Washington, DC, USA.
- Wan, D., Han, Z., Liu, D. and Yang, J. 2016. Pollution levels and spatial distribution of heavy metals in house dust from an industrial area in Xi'an, Central China. *Fresenius Environ. Bull.*, 25: 839-851.

- Wang, K., Tian H., Hua S., Zhu C., Gao J., Xue Y., Hao J., Wang Y. and Zhou, J. 2016. A comprehensive emission inventory of multiple air pollutants from iron and steel industry in China: Temporal trends and spatial variation characteristics. *Science of The Total Environment*, 559:7-14.
- Yang, X.G., Li, Y.P., Ma, G.S., Hu, X.Q., Wang, J.Z., Cui, Z.H., Wang, Z.H., Yu, W.T., Yang, Z.X. and Zhai, F.Y. 2005. Study on weight and height of the Chinese people and the differences between 1992 and 2002. *Chinese J. Epidemiology*, 26: 489-93.
- Yoshinaga, J., Yamasaki, K., Yonemura, A., Ishibashi, Y., Kaido, T., Mizuno, K., Takagi, M. and Tanaka, A. 2014. Lead and other elements in house dust of Japanese residences-Source of lead and health risks due to metal exposure. *Environmental Pollution*, 189: 223-228.



Spatial Dependence Pattern of Energy-Related Carbon Emissions and Spatial Heterogeneity of Influencing Factors in China: Based on ESDA-GTWR Model

Kai Su^(**) and Chienming Lee^{*†}

*Natural Resource Management Institute, National Taipei University, Taipei 23741, China

**Anxi College of Tea Science, Fujian Agriculture and Forestry University, Fuzhou 350002, China

†Corresponding author: Chienming Lee; 2150525002@fafu.edu.cn

Nat. Env. & Poll. Tech.

Website: www.neptjournal.com

Received: 05-02-2020

Revised: 21-02-2020

Accepted: 02-05-2020

Key Words:

Carbon emissions

Spatial heterogeneity

GTWR

ESDA

Spatial differentiation

ABSTRACT

To find out the spatial dependence of carbon emissions and its evolution characteristics is the key to achieving regional differential emission reduction strategy. In this study, 30 provinces with different population sizes and in different stages of development in China, were selected to explore the spatial heterogeneity of carbon emissions by exploratory spatial data analysis (ESDA), combined with geographically and temporally weighted regression (GTWR). The findings revealed that (1) energy-related carbon emissions at the province-level in China increased from 1997 to 2016, with an increment of 8,893 million tons; (2) there is a significant positive spatial correlation between provincial carbon emissions, which showed the characteristics of rising first and then falling; this indicated that provincial carbon emissions have obvious spatial dependent characteristics; (3) the tertiary industry ratio had a restraining effect on carbon emissions, whereas the other three variables, namely GDP, urbanization rate, and energy intensity had a positive effect on carbon emissions of provinces in China; and (4) province-scale spatial differences in and distribution patterns of carbon emissions within the same countrywide, which will help decision making in terms of carbon trading and ecological compensation mechanisms. Therefore, we suggested that in the formulation of reduction policies for carbon emissions, policymakers need to adapt to local conditions which accord to the characteristics of the province.

INTRODUCTION

Global warming largely caused by carbon emissions is a serious problem threatening ecosystems and human development globally (Villoria-Sáez et al. 2016). In its 'Intended Nationally Determined Contributions', China, the top carbon emitter globally (Guan et al. 2009), has committed to reducing carbon dioxide emissions per gross domestic product (GDP) by 60%-65% from the 2005 level by 2030 (Mi et al. 2016). As the world's largest developing country, China is in a period of rapid industrialization and urbanization. However, the continuous improvement in living standards has inevitably led to continuous increasing carbon emissions (Shan et al. 2018, Wang & Zhao 2018). To accomplish the above goal, the Chinese government will face enormous pressure for the next 10-15 years. Due to China's vast territory, there are significant differences in resource endowments, economic development, industrial structure and energy consumption structure between regions, and there are spatial linkages. Thus, it is necessary to find out spatial dependence of provincial energy-related carbon emissions in China, and spatial heterogeneity of its influencing factors, to formulate emission reduction measures in a targeted manner.

Study on carbon emissions in the existing literature mainly focuses on four aspects. (1) Applying the inverted U-curve to explore the carbon emission pathways, the calculation of inflexion points and the applicability of carbon emissions to EKC. For instance, Chen et al. (2019) found that no matter in the eastern, central and western regions in China, the curve relation between carbon emissions and economic development does not meet to EKC hypothesis of inverted U-curve, but there are different inflexion points. Zaidi et al. (2019) took APEC countries as an example, and it is found that there is an inverted "U" type relationship between carbon emissions and economic globalization, and the EKC curve is valid. (2) Using factor decomposition model to explore the driving factors and mechanism of carbon emissions. For instance, the LMDI method was applied to decompose China's household carbon emissions, and the results show that the household consumption structure has the characteristics of high carbonization (Cao et al. 2019). On the other hand, based on the approaches of LMDI and Tapio, the findings of Liang et al. (2019) indicated that the decoupling of carbon intensity from per capita income in the residential building sector of China's four megalopoles, namely Beijing, Tianjin, Shanghai and Chongqing have

been implemented. (3) Taking carbon emissions per capita and carbon emission intensity as indicators, the studies analyze the spatial difference, pattern evolution and emission reduction path of carbon emissions. For example, Dong et al. (2018) analysed the curve relationship between land urbanization (LU) and carbon emission intensity (CEI) by using the methods of Diff-GMM and Sys-GMM. (4) The spatial distribution pattern and difference of carbon emission were studied from the perspective of spatial correlation. Yan et al. (2017) analysed the regional difference and spatial correlation of inter-provincial carbon emission efficiency in China, and there is a significant spatial autocorrelation and obvious cluster trend of inter-provincial carbon emission efficiency. Moreover, by analysing the impact of spatial correlation on the geographical and economic matrix, Wang & He (2019) verifies that the spatial neighbourhood described in the bilateral economic relationship is much superior in trapping the spatial dependence of carbon emissions. In general, the existing literature has made a lot of discussions on carbon emissions and achieved important results, which can be used as a reference for energy-related carbon emissions research. However, most previous studies had seldom considered the spatial dependence of regional carbon emissions, but regard regions as independent and homogeneous individuals. Energy-related carbon emissions are not only influenced by factors such as the industrial structure, economic development level, urbanization and population size of the region, but also the potential correlation between carbon emissions in the surrounding areas. There may be obvious spatial dependence on carbon emissions between regions, and there is spatial heterogeneity of factors affecting carbon emissions. Due to the vast territory and uneven distribution of resources in China, there are great differences in development among provinces. Thus, it is clear that we cannot adopt the policy of cutting at one stroke in dealing with carbon emissions problems.

Furthermore, in the existing academic literature, most researchers used GWR (Geographically Weighted Regression) method to analyze spatial heterogeneity. Although the GWR model considers spatial effects and spatial heterogeneity, it still has some shortcomings. For instance, the GWR model can only consider regression the cross-section data and does not take into account the influence of time effect. GTWR (Geographically and Temporally Weighted Regression) can overcome the above problems effectively. It introduces the

time dimension into the model to make the estimation more effective, which provides a new method for the test of spatial heterogeneity. However, the existing literature rarely studies the spatial heterogeneity of the factors affecting carbon emissions based on this method. To address this gap, taking 30 provinces in China as the research object, this study used exploratory spatial data analysis (ESDA) and GTWR model to analyze the spatial heterogeneity of factors affecting energy-related carbon emissions in China. The results can be used as data support for the formulation and implementation of energy-related carbon emission reduction policies in China and provide a reference for other countries/regions, particularly a developing country, to carry out relevant research at the provincial scale.

MATERIALS AND METHODS

Calculation of Carbon Emissions

The baseline method provided in the 2006 IPCC Guidelines National Greenhouse Gas Inventories (Eggleston et al. 2006), was used to calculate energy-related provincial carbon emissions in China:

$$C = \sum_{i=1}^n e_i \times f_i \times k_i \times 44/12 \quad \dots(1)$$

Where, C represents carbon emissions generated by the consumption of various types of fossil energy; n is fossil energy types; e_i is the consumption of certain fossil fuels; f_i indicates the standard coal conversion factor, which is used to convert different types of energy into standard coal equivalent; k_i is the carbon emission coefficient for different fossil fuels (taken from IPCC reference values), and 44/12 indicates the molecular weight ratio of carbon dioxide to carbon. The calculated parameters for carbon emissions from different types of fossil fuels are given in Table 1.

ESDA

ESDA mainly uses the methods of statistics, image and chart to analyze the spatial data and explore the spatial relationship of the object of study. Spatial autocorrelation analysis is the main content of ESDA. It aims to study the spatial distribution and correlation of sample objects and reveal the visual phenomenon of spatial dependence and spatial heterogeneity of sample data. Spatial autocorrelation mainly includes global spatial autocorrelation and local spatial autocorrelation.

Table 1: Calculation parameters of carbon emissions for different types of fossil energy.

Energy types	Raw Coal	Coke	Crude Oil	Gasoline	Kerosene	Diesel	Natural Gas	Fuel Oil
Coefficient of standard coal ($10^4\text{tce}/10^4\text{t}$)	0.7143	0.9714	1.4286	1.4714	1.4714	1.4571	1.3300	1.4286
Carbon emission coefficient ($10^4\text{t}/10^4\text{tce}$)	0.7559	0.8550	0.5857	0.5538	0.5714	0.5921	0.4483	0.6185

1. Global spatial autocorrelation. It mainly reveals the spatial relevance and difference degree of the whole region. Global Moran's I_g is an estimation of global spatial autocorrelation statistics, which is expressed as follows:

$$I_g = \frac{\sum_{i=1}^N \sum_{j=1}^N w_{ij} (x_i - \bar{x})(x_j - \bar{x})}{\sum_{i=1}^N \sum_{j=1}^N w_{ij} (x_i - \bar{x})^2} \dots(2)$$

Where, I_g is the coefficient of global spatial autocorrelation, its value range is [-1,1]; the positive value indicates that the areas with higher (or lower) carbon emissions are spatially significantly agglomerated, and negative values indicate significant spatial differences in carbon emissions levels between the region and its surrounding areas. n is the number of samples, that is, the total evaluation area. x_i and x_j are observations of spatial positions i and j , respectively; \bar{x} is the average value of x . w_{ij} stands for weight, reflecting the degree of influence between the spatial unit of region i and j .

2. Local spatial autocorrelation. Global spatial autocorrelation can reveal the spatial dependence of provincial carbon emissions, but it cannot measure the local spatial differences. Thus, the local spatial autocorrelation to measure the degree and significance of the spatial difference between a certain area and its surroundings, and combined with LISA (Local Indicators of Spatial Association) clustering map to analyze the local spatial distribution law. It is expressed as follows:

$$I_l = \frac{(x_i - \bar{x}) \sum_{j=1}^N w_{ij} (x_j - \bar{x})}{\sum_{i=1}^N (x_i - \bar{x})^2} \dots(3)$$

At a given significant level, $I_l > 0$ indicates that carbon emissions of the observed provinces are similar to those of neighbouring provinces, that is, high-high or low-low; and $I_l < 0$ indicates that carbon emissions of the observed provinces are different from those of neighbouring provinces (low-high or high-low).

GTWR

Factors affecting carbon emissions (such as population size, urbanization rate, GDP, energy structure, energy intensity, and industrial structure, etc.) are both unstable and heterogeneous, as well as spatially related. If the traditional regression model is still used to estimate its parameters, it is difficult to reflect the spatial heterogeneity between regions. The GWR (geographically weighted

regression) model, initially developed by Brunson et al. (1996), which considers the spatial characteristics of the observed variables into the model, revealing the spatial non-stationarity and spatial dependence of the studied variables from a local perspective. Consequently, it is widely used to solve the spatial heterogeneity between units. However, the GWR model can only regress the cross-section data without considering the influence of time factors (Li et al. 2019). Thus, it is necessary to embed the time effect into the regression model and construct the geographical and temporally weighted regression (GTWR), which can capture the parameter variation of different spatial units in two dimensions of time and space, so as to make up for the deficiency of GWR model effectively (Huang et al. 2010, Fotheringham et al. 2015). The general formula of GTWR model is as follows:

$$y_i = \beta_0(u_i, v_i, t_i) + \sum_{k=1}^d \beta_k(u_i, v_i, t_i) x_{ik} + \varepsilon_i, i=1, 2, \dots, n; k=1, 2, \dots, d \dots(4)$$

Where, y_i is the interpreted variable of the i -th sample point; u_i, v_i and t_i represent the longitude coordinates, latitude coordinates, and time coordinates of the i -th sample point, respectively. (u_i, v_i, t_i) represents the space-time dimension coordinates of the i -th sample point; $B_0(u_i, v_i, t_i)$ is the constant term of the i -th sample point; $\beta_k(u_i, v_i, t_i)$ denotes the regression coefficient of the k -th explanatory variable at the i -th sample point. x_{ik} is the k -th explanatory variable of the i -th sample point; ε_i indicates a random error.

Data Source and Variables Selection

Based on referring to the above-related research results, this study selects four indicators GDP(G), Urbanization rate (U), Tertiary industry ratio (S) and Energy consumption per unit of GDP(E) to measure the provincial energy-related carbon emissions from the four aspects of economic development level, population composition, industrial structure and energy intensity, respectively. To reduce the heteroscedasticity of spatial data in the model, the data of each variable were processed by natural logarithm at first, which were identified as lnG, lnU, lnS and lnE, respectively.

Energy-related carbon emissions of each province in 1997-2016 were calculated by equation (1). The data of socio-economic and energy consumption in 30 provinces (Tibet, Hong Kong, Taiwan and Macao are not included due to the lack of data) were all from National Bureau of Statistics of China (<http://data.stats.gov.cn/english/>). Besides, this paper set 1997 as the benchmark year, so GDP and energy intensity were converted to constant prices to avoid the impact of inflation. Additionally, the base map comes from Data Centre for Resources and Environmental Sciences of the Chinese Academy of Sciences (www.resdc.cn).

RESULTS AND ANALYSIS

Energy-Related Carbon Emissions of Provinces

According to equation (1), cumulative carbon emissions of each province in China from 1997 to 2016 were listed in Table 2.

From 1997 to 2016, the three provinces in China with the highest cumulative carbon emissions (Table 2) were Shandong (16061 M_t), Hebei (12730 M_t) and Shanxi (11972 M_t), accounting for 23.80% of the cumulative carbon emissions in China, which has significantly contributed to national carbon emissions. The three cities with the lowest cumulative carbon emissions were Ningxia (2115 M_t), Hainan (716 M_t) and Qinghai (696 M_t). Their total accumulated carbon emissions were 3527 M_t, accounting for only 2.06% of the nation's cumulative carbon emissions over the study period. Each province's carbon emissions tend to be closely related to the region's economy and industrial structure. For example, by the end of 2016, the comprehensive energy consumption of Shandong, Hebei and Shanxi reached 62356.44×10^4 , 39912.13×10^4 and 39146.06×10^4 t, respectively, accounting for 10.76, 6.89, and 6.75% of the total energy consumption above the designated size in China.

To reveal the spatial characteristics of energy-related carbon emissions at the province scale in China, the calculated data of carbon emissions were classified and

archived. The Natural Breaks Method was used to cluster the carbon emissions of each province by ArcGIS10.7, and the corresponding spatial distribution is shown in Fig. 1.

From 1997 to 2016, the medium-high and high emission areas moved to coastal provinces from inland areas, which were related to the urbanization and industrialization of coastal provinces. For instance, due to urban infrastructure construction, coupled with urbanization and industrialization, the socio-economic development in Jiangsu province has further accelerated in recently; this has led to an increase in fossil energy consumption, which in turn has boosted its carbon emissions. In contrast, Liaoning, Jilin and Heilongjiang, which are located in northeast China, have a lower level with respect to economic development in recent years; therefore, there was a downward trend of its carbon emissions. Additionally, it is worth pointing out that Beijing, as the capital of China, its carbon emissions peaked in 2010, reaching 138.61 M_t; then declined by 29.2% in 2016, at 107.34 M_t. The primary cause for the reductions is due to its technological progress, developed tertiary industry (e.g. modern service industry and financial industry) and emissions reduction policies. Data indicated that in 2018, Beijing's primary industry, secondary industry and tertiary industry accounted for 0.4%, 18.6% and 81.0%, respectively; among them, the financial industry has become the first pillar industry, effectively reducing its consumption of fossil energy.

Table 2: Cumulative carbon emissions at the province scale in China during 1997-2016 (Million tons, M_t).

Beijing	Tianjin	Hebei	Shanxi	Inner Mongolia	Liaoning	Jilin	Heilongjiang	Shanghai	Jiangsu
2349	2872	12730	11972	8992	10925	4042	5685	4627	10722
Zhejiang	Anhui	Fujian	Jiangxi	Shandong	Henan	Hubei	Hunan	Guangdong	Guangxi
6481	5188	3316	2790	16061	9114	5613	4587	8816	2714
Hainan	Chongqing	Sichuan	Guizhou	Yunan	Shaanxi	Gansu	Qinghai	Ningxia	Xijiang
716	2329	5213	4104	3529	5239	2962	696	2115	4811

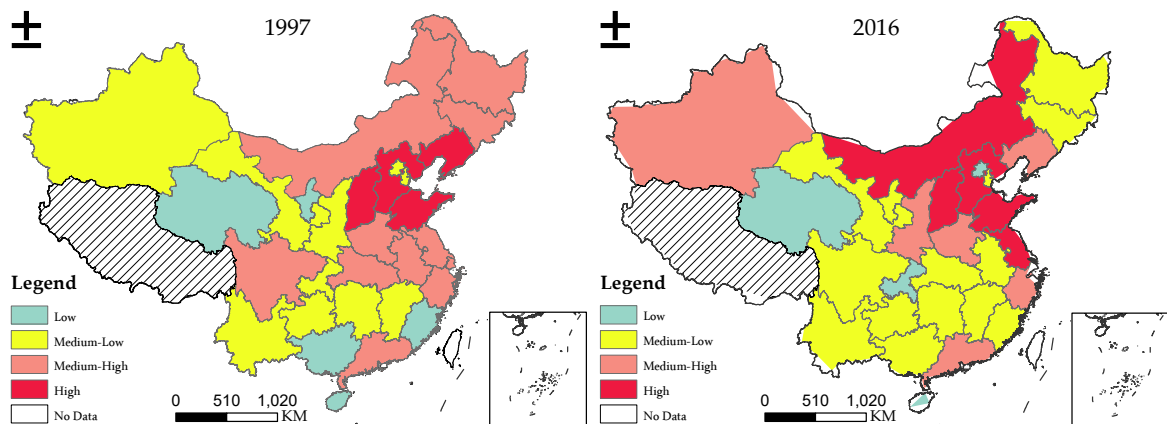


Fig. 1: The spatial layout of carbon emissions at the province scale in China.

Global Spatial Dependence Pattern of Provincial Energy-Related Carbon Emissions

This study used ArcGIS10.7 to conduct spatial autocorrelation analysis on carbon emissions data of 30 provinces in China from 1997 to 2016. The variation curves of Moran's I index and P-value for each year were shown in Fig. 2.

As can be seen from Fig. 2, the Moran's I_g index from 1997 to 2016 is positive and all passed the significance test at the level of 5%, indicating that the spatial distribution of provincial carbon emissions in China is not completely random, but has significant spatial dependence characteristics. In other words, provinces with relatively high carbon emissions tend to be adjacent to other provinces with high carbon emissions, while provinces with relatively low carbon emissions tend to be adjacent to other provinces with low carbon emissions. From the perspective of the change process, the spatial correlation trend of provincial carbon emissions showed a pattern of rising and then decreasing. From 1997 to 2008, the Moran's I_g index showed an upward trend, indicating that the spatial dependence of provincial-scale carbon emissions was increasing, reaching the highest value of 0.27 in 2008. Since 2008, Moran's I_g index has shown a fluctuating downward trend, indicating that the spatial concentration effect of provincial carbon emissions in China is weakening as a whole.

The above changes in the Moran's I_g index showed that the spatial dependence of provincial-scale carbon emissions in China mainly occurs at four-time nodes, namely 1997, 2008, 2009 and 2016. Therefore, the following contents mainly focus on these four-time nodes for further analysis.

Local Spatial Dependence Pattern of Provincial Energy-Related Carbon Emissions

The global Moran's I_g index can only explain the overall

spatial dependence of carbon emissions at the provincial scale in China, however, it cannot represent the specific structure and spatial correlation of spatial dependence of provincial carbon emission. Hence, according to the spatial and temporal distribution characteristics of different provinces, representative years (1997, 2008, 2009, 2016) were selected for comparative study, and LISA clustering map of four years were drawn by using ArcGIS 10.7 (Fig. 3).

As shown in Fig. 3, at a significant level of 5%, the local spatial dependence of carbon emissions at the provincial scale in China is relatively obvious. There are two significant regions in the northwest and central China, suggesting that there is a positive spatial effect between provinces, which makes the provinces and the surrounding areas show the development trend of mutual connection and interaction. It is mainly reflected in the small spatial difference, the region with high carbon emissions in the region itself and surrounding provinces (High-High), mainly concentrated in Hebei, Shandong, Henan and Anhui. The reason is that these provinces have a good industrial foundation, a developed heavy chemical industry and abundant energy resources. The rapid progress of industrialization consumes a large amount of fossil energy, resulting in strong regional spatial correlation and interactive spillover. Moreover, Hebei, Shandong, Henan and Anhui have reached significant levels in four periods. The spatial difference is large, and the regional carbon emissions are higher, but the lower average areas (High-Low) are mainly distributed in Xinjiang. Although the spatial difference is small, the region itself and the surrounding average lower region (Low-Low), all provinces have not passed significant tests. In terms of the overall number, the number of High-High types of provinces has been increasing since 1997, which is consistent with the upward trend of global Moran's I_g values

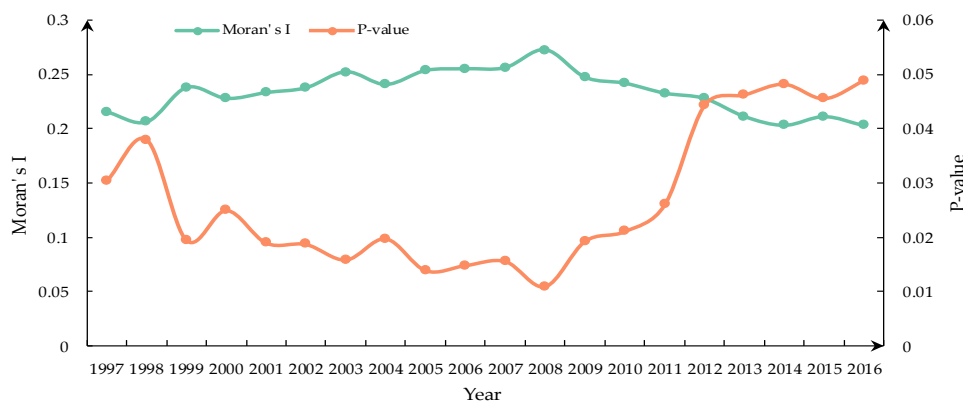


Fig.2: Global Moran's I index of provincial carbon emissions in China from 1997 to 2016.

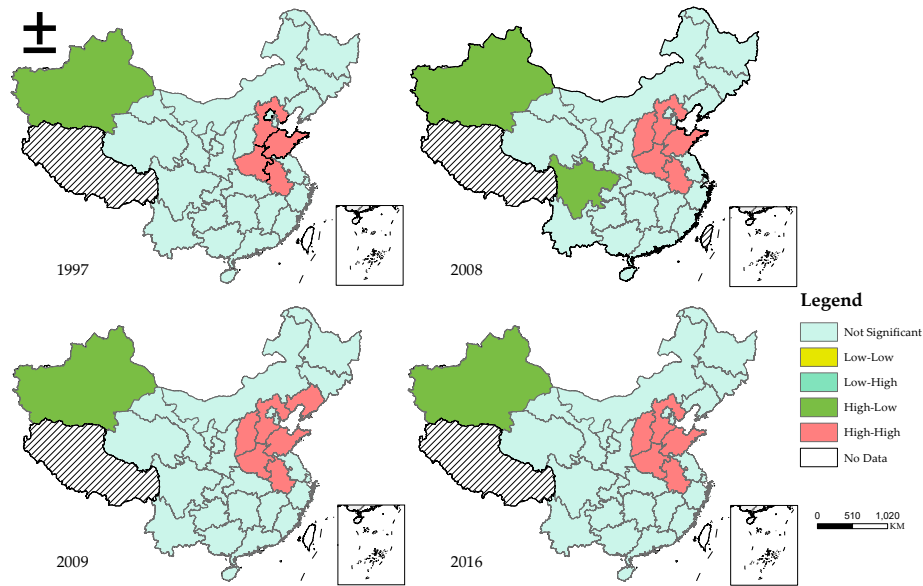


Fig. 3: LISA clustering map of provincial carbon emission in China.

from 1997 to 2008. Thus, the diffusion effect of carbon emissions reduction is gradually increasing.

Spatial Heterogeneity of Influencing Factors of Provincial Carbon Emissions

The above ESDA analysis showed that the spatial distribution of carbon emissions in China is significantly spatially dependent. To analyze the distribution of each influencing factor more clearly, it is necessary to apply the GTWR model for measurement. This study mainly used ArcGIS 10.7 to realize the coefficient estimation of GTWR model based on the attributes of time and space. The estimation results of the regression coefficient calculated by GTWR were listed in Table 3, while the coefficient distribution of each influencing factor in 1997 and 2016 are shown in Fig. 4.

As can be seen from Table 3, the value of R^2 and adjusted R^2 of GTWR were 0.995981 and 995956, respectively, indicating that the GTWR model can better explain the influence of independent variables (influencing factors) on dependent variables (carbon emissions), and better explain the data with spatio-temporal characteristics. This means the GTWR's coefficients are more in line with real-world interpretations. Accordingly, the distribution characteristics

of each influencing factor in different temporal and spatial dimensions are shown in Fig. 4.

Spatio-Temporal Variation of Economic Development (Lng) on Carbon Emissions

It can be seen from Fig. 4 that GDP has an obvious influence on carbon emissions and is positively correlated with carbon emissions, indicating that GDP growth is a key factor in increasing carbon emissions. The regression coefficients of Xinjiang, Qinghai and Liaoning are larger, while the provinces with smaller coefficients are Sichuan, Fujian and Zhejiang. This showed that the differences in economic development between different provinces in China are quite prominent. Therefore, when determining the countermeasures for carbon emissions reduction in each province, the implementation of policies should be determined according to the specific economic development stage of each province. Moreover, carbon emissions have increased rapidly in the process of economic growth in areas with low economic development level in the western areas of China, such as provinces of Qinghai and Xinjiang. Therefore, at this stage, the government should focus on transforming the economic structure and introducing low-energy industries from the developed eastern regions to reduce the growth of carbon emissions.

Table 3: Estimation results of regression coefficient calculated by GTWR.

Bandwidth	Residual Squares	Sigma	AICc	R^2	adjusted R^2	Spatio-temporal Distance Ratio	Trace of SMatrix
0.114996	6.25916	0.098894	-991.525	0.995981	0.995956	0.273068	67.1389

Additionally, carbon emissions growth rate in Sichuan, Hainan and Guangdong has slowed down in the process of economic growth, which requires the government to take policy measures to bring it to an inflexion point in terms of technological upgrading of energy efficiency and low carbonation of the industrial structure. Overall, China's provincial GDP growth will exacerbate carbon emissions during the study period, while other conditions remain unchanged.

Spatio-Temporal Variation of Population Composition (Lnu) on Carbon Emissions

The lnU estimation coefficient reflects the contribution of different regional urbanization rates to the carbon emissions growth, and the spatial spillover effect of urbanization rates in neighbouring provinces.

As can be seen from Fig. 4, the high-value areas of regression coefficient of urbanization rate are concentrated in Xinjiang, Qinghai, Gansu, showing a certain gradient distribution. This indicated that in these western regions where industrial-oriented industries are being promoted, most of the employed labour force is transferred to the industrial industry in the context of increasing urbanization rate, causing an increase in the scale of carbon emissions. The low values of the regression coefficient of the urbanization rate are concentrated in the central region, which has a relatively high degree of urbanization. However, due to its advanced economy and technology, the improvement of the urbanization rate is not the most important reason affecting the carbon emission of these regions. However, it should be noted that the increase in urbanization rate does not mean that it always promotes carbon emission growth. Some scholars believe that there is an inverted "U-shaped" relationship between urbanization level and carbon emissions (Ehrhardt-Martinez et al. 2002, York et al. 2003). This means that the overall development of urbanization still plays a role in promoting carbon emissions when the inflexion point of urbanization inverted "U" curve is not reached; however, when it reaches the inflexion point, the urbanization level has a slowing effect on carbon emissions.

Spatio-Temporal Variation of Industrial Structure (Lns) on Carbon Emissions

The industrial structure is an important factor that influencing carbon emissions. The results indicated that the tertiary/service industry had a reduced effect on carbon emissions in most China's provinces, and there are regional differences in the influence of industrial structure on carbon emissions (Fig. 4). Judging from the regression coefficients, the regression coefficient between the tertiary industry ratio and carbon emissions showed an increasing trend from west to east of China. Among them, the provinces with greater impact on

carbon emissions from the industrial structure are Hubei, Henan, Zhejiang and Fujian in central and eastern China, while the provinces with relatively smaller impact are Gansu, Qinghai, Xinjiang and Guizhou in northwest China. This means that carbon emissions from provinces, located in the eastern coastal area, are more vulnerable to the industrial structure than in the inland western regions. The reason may be related to the differences in the original economic structure and the different ideas of industrial development in different provinces, which may lead to the more regional characteristics of the local industrial structure.

In general, except that tertiary industry ratio (S) had an inhibitory effect on carbon emissions in Fujian's cities, the other three variables (GDP, urbanization rate, and energy consumption per unit of GDP) had a promoting effect on carbon emissions. This means that with accelerating urbanization and industrialization, the energy consumption of China's provincial areas is continuously increasing. If the principle of 'business as usual' is followed, the carbon emissions in China's provincial areas has an increasing trend; in contrast, if the proportion of low-carbon industries, such as the service industry, is further increased, energy efficiency will be further improved through technology, thereby reducing energy intensity. The growth of carbon emissions in various provinces of China therefore had a certain inhibitory effect. In short, the development of the tertiary industry should be encouraged, as it can reduce carbon emissions and environmental pollution and save the land.

Spatial-Temporal Variation of Energy Intensity (Lne) on Carbon Emissions

Energy intensity reflects the contribution of technological progress in different regions to their own carbon emissions growth. According to the results, the coefficients of energy intensity's impact on provincial carbon emissions in China are positively correlated, and there are significant spatial differences. This suggested that energy intensity can promote carbon emissions, and there is a significantly promote carbon emissions in different provinces. Compared with other factors, energy intensity has the least effect on carbon emissions, which is mainly concentrated in the western regions of China such as Xinjiang, Gansu and Qinghai, and is gradually increasing to the southeast, according to the data. This is mainly because the eastern region of China is rich in resources and in a period of rapid industrialization, which will inevitably increase its energy intensity, thus increasing the pressure on carbon emissions reduction.

In a word, the provinces with higher technical level and better economic conditions in eastern China, energy intensity has a relatively large impact on the distribution

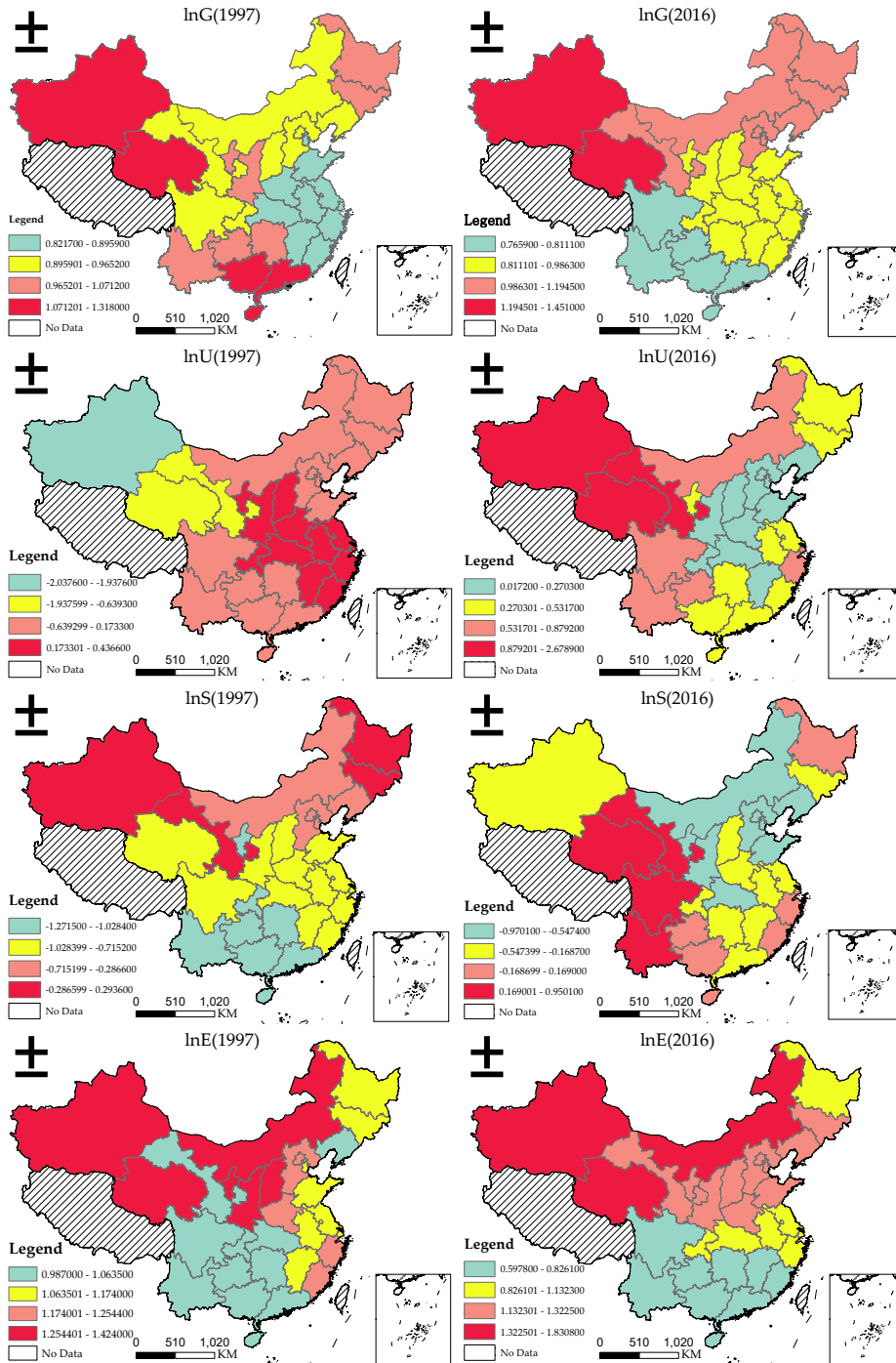


Fig. 4: Spatial distribution of regression coefficients calculated by GTWR model in 1997 and 2016.

of provincial carbon emissions. On the other hand, in the western provinces of China with lower technical level and relatively poor economic conditions, energy intensity has a relatively small impact on carbon emissions. Hence, to

achieve carbon emissions reduction targets, the government needs to improve energy efficiency by introducing energy conservation and emission reduction technologies, according to the low carbon development model in different regions.

These measures can achieve the dual objectives of controlling carbon emissions and reducing carbon intensity.

DISCUSSION AND CONCLUSIONS

Considering the deficiency of past literature study on spatial heterogeneity of factors affecting carbon emissions, this study introduced geographically and temporally weighted regression (GTWR) into the spatial analysis of carbon emissions, which provides a new approach to spatial heterogeneity testing. Based on the provincial panel data of China from 1997 to 2016, 30 provinces with different population sizes and in different stages of development in China, were selected to analyze the influencing factors of carbon emissions by exploratory spatial data analysis (ESDA) combined with GTWR method. Thus, the major conclusions are summarized herein and put forward targeted policy recommendations accordingly.

Energy-related carbon emissions at the province level in China had increased by 215.08 % from 1997 to 2016, with an increment of 8893 M_t . Provinces such as Anhui, Jiangsu, and Hebei have high-level carbon emissions, while Guizhou, Qinghai and Hainan on the contrary. These results suggest that the government formulate corresponding incentive measures or economic incentives to encourage enterprises to accelerate the energy-saving technological transformation and improve energy efficiency. Therefore, it is necessary to unswervingly promote the existing energy conservation and emission reduction policies and measures to achieve China's further emission reduction targets, including financial incentives for energy conservation technology transformation, as well as the mandatory target of provincial energy intensity (Du et al. 2018).

From 1997 to 2016, the global Moran's I index has a positive value and showed a trend of rising first and then falling, and all passed the 5% significance test. This indicated that provincial carbon emissions in China have a significant positive spatial correlation, that is, provinces with higher or lower carbon emissions tend to be spatially adjacent. Moreover, there is a positive spatial effect between provinces, which makes the development trend of mutual relationship and interaction between provinces and surrounding areas; therefore, carbon emissions are affected by different geographical locations, according to LISA clustering map of local autocorrelation. Also, the regression results of the GTWR model indicated that the influencing factors of carbon emissions have obvious spatial heterogeneity. The findings revealed that tertiary industry ratio had a restraining effect on the carbon emissions, whereas the other three variables, namely, GDP, urbanization rate and energy intensity had a positive effect on carbon emissions of provinces in China.

These results suggest that in the formulation of reduction policies for energy-related carbon emissions, policymakers need to adapt to local condition according to the characteristics of the province. Specifically, for the north-western provinces of China with low economic development (e.g. Guizhou, Gansu, Qinghai, etc.), the government should focus on improving energy efficiency and improving energy consumption structure; meanwhile, the government should further readjust and optimize industrial structures and develop low-carbon industries such as high-tech and service industries. On the other hand, for the economically developed eastern and southern coastal provinces (e.g. Shanghai, Zhejiang, Guangdong, and Jiangsu, etc.), the government should focus on new technologies, green energy, and modern services; meanwhile, it will build an economic structure transformation and upgrading that promotes low-carbon development across provinces, thereby forming a reduction path for coordinated economic and environmental development. Furthermore, the government should strengthen the guidance of low-carbon policy in energy-rich areas such as Hebei, Shanxi, etc. The dual reduction targets of carbon emissions and energy intensity will be incorporated into the local government assessment system, and policymakers need to implement the accountability system for carbon emissions reduction.

Additionally, this study revealed a province-scale spatial difference in and distribution pattern of carbon emissions within the same countrywide, which will aid decision making in terms of carbon trading and ecological compensation mechanisms. The results may provide policymakers with insight into spatial patterns of carbon emissions among provinces when macro-control policies are formulated. Our study suggested that inland provinces' overall carbon emissions levels were lower than those of coastal provinces in China. Apart from different provinces being stages of economic development, this is likely mainly due to their various natural environments and resource. The coastal areas of China are economically developed and highly dependent on resources from inland areas. Further development in such areas is often constrained by carbon emission quotas. Therefore, they have the option to buy additional carbon emission credits from other regions, since it is more expensive for them to cut emissions than it is for inland regions. Some inland areas of China, such as Yunnan, Guangxi and Sichuan, etc., are mostly located in mountainous areas with rich ecological resources, especially in terms of the forest. Forestry ecosystem has carbon storage and sequestration functions making these regions large carbon sinks and provide surplus carbon emissions quotas for carbon trading if needed. Our results can thus provide helpful information and accurate data for formulating policies to promote the formation of a beneficial interactive spatial pattern of countrywide carbon emissions.

Targets can be realized by establishing carbon emission trading system as ecological compensation for implementing green development strategies to increase ecosystem service in inland areas, from which the coastal areas in China can purchase carbon emission quotas.

It is worth mentioning here that our studies aimed to address a gap in relevant research. To a certain extent, this study revealed the spatial heterogeneity of driving factors affecting energy-related carbon emissions, which can provide data support for the formulation of carbon emission reduction strategies. However, the spatial interaction effect between driving factors can also affect the spatial differentiation pattern of carbon emissions. Hence, efforts to explore the correlation between factors by using Geodetector method should be seriously considered in future research.

ACKNOWLEDGMENTS

The authors gratefully acknowledge the financial support from the Natural Science Foundation of Fujian Province, China (Grant No. 2018J01652).

REFERENCES

- Brunsdon, C., Fotheringham, A.S. and Charlton, M.E. 1996. Geographically weighted regression: a method for exploring spatial nonstationarity. *Geogr. Anal.*, 28: 281-298.
- Cao, Q., Kang, W., Xu, S., Sajid, M. J. and Cao, M. 2019. Estimation and decomposition analysis of carbon emissions from the entire production cycle for Chinese household consumption. *Journal of Environmental Management*, 247: 525-537.
- Chen, Yu., Zhao, J.C., Lai, Z.Z., Wang, Z. and Xia, H.B. 2019. Exploring the effects of economic growth, and renewable and non-renewable energy consumption on China's CO₂ emissions: Evidence from a regional panel analysis. *Renew. Energ.*, 140(2): 341-353.
- Du, Q., Lu, X., Li, Y., Wu, M., Bai, L. and Yu, M. 2018. Carbon emissions in China's construction industry: calculations, factors and regions. *Int. J. Environ. Res. Public Health.*, 15(6): 1220.
- Dong, F., Bian, Z., Yu, B., Wang, Y., Zhang, S., Li, J., Su, B. and Long, R. 2018. Can land urbanization help to achieve CO₂ intensity reduction target or hinder it? Evidence from China. *Resour. Conserv. Recy.*, 134: 206-215.
- Eggleston, H.S., Buendia, L., Miwa, K., Ngara, T. and Tanabe, K. 2006. 2006 IPCC Guidelines for National Greenhouse Gas Inventories. Institute for Global Environmental Strategies, Kanagawa, Japan, Intergovernmental Panel on Climate Change.
- Ehrhardt-Martinez, K., Crenshaw, EM. and Jenkins, J.C. 2002. Deforestation and the environmental Kuznets curve: A cross-national investigation of intervening mechanisms. *Soc. Sci. Q.*, 83(1): 226-243.
- Fotheringham, A.S., Crespo, R. and Yao, J. 2015. Geographical and temporal weighted regression (GTWR). *Geogr. Anal.*, 47(4): 431-452.
- Guan, D., Peters, G.P., Weber, C.L. and Hubacek, K. 2009. Journey to world top emitter: An of the driving forces of China's recent CO₂ emissions surge. *Geophys. Res. Lett.*, 36 (4): 1-5.
- Huang, B. Wu, B. and Barry, M. 2010. Geographically and temporally weighted regression for modeling spatio-temporal variation in house prices. *Int. J. Geogr. Inf. Sci.*, 24: 383D401.
- Li, M.J., Wang, J. and Chen. Y.H. 2019. Evaluation and influencing factors of sustainable development capability of agriculture in countries along the Belt and Road Route. *Sustainability*, 11: 2004.
- Liang, Y., Cai, W. and Ma, M. 2019. Carbon dioxide intensity and income level in the Chinese megacities' residential building sector: Decomposition and decoupling analyses. *Sci. Total. Environ.*, 677: 315-327.
- Mi, Z., Zhang, Y., Guan, D., Shan, Y., Liu, Z., Cong, R., Yuan, X.C. and Wei, Y.M. 2016. Consumption-based emission accounting for Chinese cities. *Appl. Energy.*, 184: 1073-1081.
- Shan, Y., Guan, D., Zheng, H., Ou, J., Li, Y., Meng, J., Mi, Z., Liu, Z. and Zhang, Q. 2018. China CO₂ emission accounts 1997-2015. *Scientific Data*, 5(1): 1-14.
- Villoria-Sáez, P., Tam, V.W.Y., Merino, M.D.R., Arrebola, C.V. and Wang, X. 2016. Effectiveness of greenhouse-gas Emission Trading Schemes implementation: A review on legislations. *J. Clean. Prod.*, 127: 49-58.
- Wang, Y. and Zhao, T. 2018. Impacts of urbanization-related factors on CO₂ emissions: evidence from China's three regions with varied urbanization levels. *Atmos. Pollut. Res.*, 9(1): 15-26.
- Wang, Y.Y. and He, X.B. 2019. Spatial economic dependency in the environmental Kuznets curve of carbon dioxide: The case of China. *J. Clean. Prod.*, 218: 498-510.
- Zaidi, S.A.H., Zafar, M.W., Shahbaz, M. and Hou, F. 2019. Dynamic linkages between globalization, financial development and carbon emissions: Evidence from Asia Pacific economic cooperation countries. *J. Clean. Prod.*, 228: 533-543.
- York, R., Rosa, E.A. and Dietz, T. 2003. STIRPAT, IPAT and ImPACT: Analytic tools for unpacking the driving forces of environmental impacts. *Ecol. Econ.*, 46: 351-365.
- Yan, D., Lei, Y., Li, L. and Song, W. 2017. Carbon emission efficiency and spatial clustering analyses in China's thermal power industry: Evidence from the provincial level. *J. Clean. Prod.*, 156: 518-527.



Analysis of Carbon Emissions of Prefabricated Buildings from the Views of Energy Conservation and Emission Reduction

Weidong Ma*, Dacheng Sun†, Yongsheng Deng**, Xianyun Meng** and Mi Li**

*Henan Huaxia Construction Management Co. Ltd., Zhengzhou 450053, China

**Zhumadian Cigarette Factory of China Tobacco Henna Industrial Co, Ltd., Zhumadian 463000, China

†Corresponding author: Dacheng Sun; zszdz1977@outlook.com

Nat. Env. & Poll. Tech.
Website: www.neptjournal.com

Received: 23-07-2020

Revised: 15-11-2020

Accepted: 14-12-2020

Key Words:

Prefabricated buildings

Carbon emission

Comprehensive evaluation

Emission reduction measures

ABSTRACT

As a pillar industry with high energy consumption and low efficiency, the building industry of China has produced consistently high carbon emission levels in recent years. The important goals in the coordinated development of this industry include the large-scale development of green buildings, the use of energy technologies to reduce carbon emissions, and an effective reduction of carbon intensity. Prefabricated buildings have become popular in this industry due to their low energy consumption, emission, and pollution and environment-friendly nature. This paper examines those factors that influence the carbon emissions from the construction of prefabricated buildings across three phases, namely, production in plants, logistics transportation, and assembly construction, builds an evaluation index system for studying the carbon emissions in the materialization phase of prefabricated buildings, and employs the hierarchical fuzzy comprehensive evaluation method to construct an evaluation model. Results show that the overall energy consumption of prefabricated buildings is lower than that of traditional concrete pouring-type buildings. The hierarchical fuzzy comprehensive evaluation model is scientific and reasonable when used to measure the comprehensive benefits of carbon emissions from prefabricated buildings. By taking a project in Zhengzhou City, Henan Province as an example, the comprehensive evaluation results show that the carbon emissions of this project are at moderate levels. The carbon emissions from prefabricated buildings can be reduced by expanding the market scale of the building industry, adjusting its use of building materials, and setting up special funds for these buildings. The findings of this work provide a certain reference value for analysing the differences between prefabricated and traditional buildings in terms of their carbon emissions in the materialization phase, for evaluating how the carbon emissions of the former can be reduced, and for formulating and executing building emission reduction plans.

INTRODUCTION

As a pillar industry in China, the building industry is related to the raw production of steel and cement at the upper end of the industrial chain and the sale of real estate at the tail end. This industry plays a critical role in promoting economic development, maintaining social stability, and driving the development of other industries. While the building industry only ranks second to the power, transportation, and manufacturing industries in terms of carbon emissions, due to its high energy consumption and low efficiency, the carbon emissions of this industry have remained at high levels in recent years. As shown in Fig. 1, the proportion of energy consumed by the building industry is continuously rising, and the total carbon emissions in China will inevitably increase along with the growth of built areas in the country. In response to these issues, the “13th Five-Year Plan of the Building Industry” issued in 2017 highlighted the importance of energy conservation, emission reduction,

and low-carbon development of buildings. Along with the gradual deterioration of the environment, many issues, such as environmental pollution and energy consumption, have become important problems in all walks of life. The European Architects Association claimed that the building industry is the main contributor to global greenhouse gas (GHG) emissions, thereby highlighting the importance of studying the green and low-carbon orientations of this industry. To achieve a coordinated development, the building industry of China needs to realize a large-scale production of green buildings on the precondition of steady development, strive for low-carbon development by using energy technologies, and effectively reduce its carbon intensity.

To achieve its goal of developing a low-carbon, sustainable economy, the building industry is aiming toward low energy consumption, low emission, low pollution, and environment-friendly directions to satisfy the ever-increasing demand of humans. Low-carbon buildings are known for their low utilization of fossil energy resources, high ener-

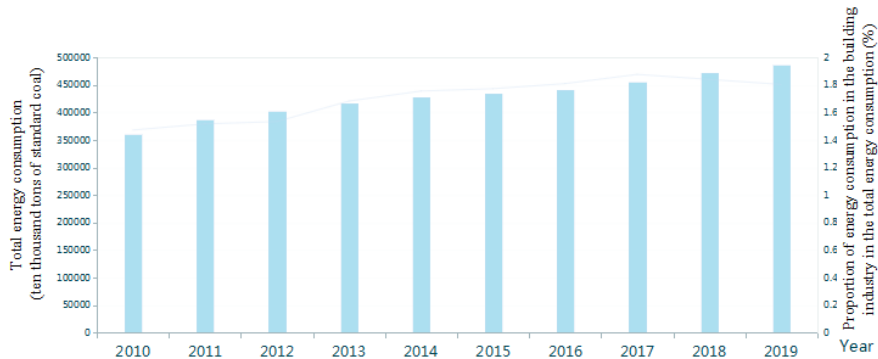


Fig. 1: Total energy consumption in China and the proportion of energy consumption of the building industry from 2010 to 2019.

gy efficiency, and zero carbon emissions throughout their whole life cycle. All or some components of prefabricated buildings are produced in a plant in advance, transported to the construction site, and assembled by using suitable installation machinery and methods. Under the industrialized production mode, prefabricated buildings have numerous advantages over traditional cast-in-place buildings, including their convenient construction, fast construction progress, negligible impacts on the environment, and low carbon emission. Therefore, these buildings play an important role in realizing a low-carbon, sustainable development of the building industry. The construction mode of these buildings also satisfies the development requirements for low-carbon buildings.

PAST STUDIES

The building industry is continuously moving toward low energy consumption, low emission, low pollution, and environment-friendly directions to satisfy the ever-increasing demand of humans. Carbon emission reduction plays an essential role in curbing GHG emissions. As prefabricated buildings produce limited carbon emissions during their materialization phase, they have become an important development trend in the building industry. Accordingly, these buildings have been subject to critical examinations in the literature. For instance, Seongwon et al. evaluated the carbon emission in the full lifecycle, materialization phase, and operation and maintenance phase of residential buildings by using the mixed evaluation, input-output, and process evaluation methods, respectively (Seongwon et al. 2001). Hens H. et al. established a carbon emission model by using the checklist method to statistically analyze the carbon emissions of five building types and found that the envelope structure of buildings has the greatest influence on carbon emissions during the building construction and operation phase (Hens et al. 2010). Blengini & Di Carlo et al. analysed the carbon

emission and energy consumption of Japanese buildings throughout their lifecycle and calculated the resource supply for office buildings (Blengini & Di Carlo 2010). Hu et al. constructed an overall evaluation system for low-carbon buildings that analyses the virtual energy, energy utilization efficiency, and equipment performance of buildings and argued that evaluating the carbon emissions of buildings throughout their lifecycle should cover the material production, building construction, material replacement, equipment operation, and demolition phases of these structures (Hu et al. 2011). Sivaraman constructed a refined evaluation model for studying the performance of low-carbon buildings throughout their lifecycle and identified two major factors that influence the carbon emissions of these buildings, namely, building materials and maintenance during use (Sivaraman 2011). After calculating the carbon emissions and energy consumption throughout the lifecycle of the Engineering Building of the Curtin University of Technology, Biswas. et al. found that the carbon emissions generated by this building throughout its use phase were 63% lower than that generated by other buildings (Biswas et al. 2014). Hong et al. examined the processes in the building construction phase and calculated the carbon emissions in the manufacturing, transportation, and construction phases of construction engineering materials by using the input-output and process-based methods (Hong et al. 2014). After calculating the carbon emissions of three types of buildings, Fenglai et al. analysed the limitations of the process-based and input-output methods and proposed a mixed method that integrates the characteristics of these two methods (Fenglai et al. 2016). Ciutina et al. found that the collective apartment buildings constructed in Romania by using large-scale precast concrete planks have low energy efficiency (Ciutina et al. 2016). Hong et al. found that prefabricated construction, which can effectively improve the production efficiency of the building industry, has attracted the attention of many countries and, by taking a practical building project as an example, discussed the

energy use of prefabricated parts throughout their lifecycle. Their case results show that the recovery of prefabricated parts can save 16% to 24% of energy (Hong et al. 2016). Li et al. measured the GHG and non-GHG emissions during the building construction phase by using the process-based method (Li et al. 2017). Kou et al. established a dynamic full-life-cycle simulation model and analysed the available measures for reducing the energy consumption of residential buildings (Kou et al. 2019). Boutouil et al. eliminated the environmental impacts caused by heat treatment and concrete and further reduced the carbon footprints generated in the cement industry by using ground granulated blast furnace slag and ultrafine Portland cement (Boutouil et al. 2020). Gao et al. found that the GHG emissions in the building industry increase at an annual rate of 1.5% and used the mixed model to evaluate the environmental impacts of prefabricated and traditional cast-in-place buildings throughout their lifecycle. Their results show that prefabricated buildings have total energy consumption and carbon emission of 7.54% and 7.17% throughout their lifecycle, respectively, both of which are lower than those of traditional cast-in-place buildings (Gao et al. 2020). Kuusk et al. introduced methods and results that can facilitate the selection of thermal insulation components that are prefabricated by using complete sets of wooden frames in major house renovations and found that such schemes satisfy the energy performance requirements specified by the New Zealand Energy Bureau and reduce carbon emissions (Kuusk et al. 2020).

These studies all show that the global building industry is continuously developing toward low energy consumption, low emission, low pollution, and environment-friendly directions to satisfy the ever-increasing needs of humans. Given their ability to effectively reduce the consumption of

resources and energy sources and produce minimal waste on construction sites, prefabricated buildings have become the mainstream development trend in the building industry. However, China lags behind developed countries in terms of developing prefabricated buildings due to a series of difficulties related to costs, technologies, evaluation standards, and management. Therefore, an evaluation index system was constructed in this paper to analyze those factors that influence the carbon emissions of prefabricated buildings across three phases, namely, production in plants, logistics transportation, and assembly construction. An evaluation model was also constructed by using the hierarchical fuzzy comprehensive evaluation method, the differences between prefabricated and traditional buildings were analysed, and the emission reduction of the former was evaluated. The findings of this work are expected to provide a basis for formulating effective building emission reduction plans.

BRIEF INTRODUCTION TO THE MODEL

Evaluation Indexes

Carbon emission indexes should be set in consideration of various carbon sources and factors that influence carbon emissions. These indexes should also be able to reflect the utilized resources and energy sources and the waste generated during the construction of prefabricated buildings. The setting of these indexes should also follow the principles of pollution prevention, easy quantification and measurement, scientificity, and dynamics. From the perspectives of energy conservation, emission reduction, environmental protection, and resource-saving and in reference to the assessment standards for green and prefabricated buildings, an evaluation index system was formulated in this paper as summarized in Table 1.

Table 1: Evaluation of the index system for the carbon emissions of prefabricated buildings.

Level I index	Level II index	Level III index
Utilization of resources and energy sources (B ₁)	Investment amount (C ₁)	Investment amount (D ₁)
	Resource consumption (C ₂)	Material utilization amount (D ₂)
	Energy consumption (C ₃)	Coal (D ₃)
		Diesel oil (D ₄)
		Gasoline (D ₅)
Construction and ecological environment (B ₂)	Environmental protection degree of construction organization (C ₄)	Personnel organization (D ₆)
		Utilization of new technologies and new processes (D ₇)
		Utilization of advanced construction machinery (D ₈)
	Waste (C ₅)	Design and management of construction organization (D ₉)
		Amount of construction wastes (D ₁₀)
		Construction waste recycling (D ₁₁)
Implementation degree of environmental policies (C ₆)	Implementation of national construction standard (D ₁₂)	

Model Profile

Establishment of a fuzzy factor set: First, the influence factor set, namely, the comprehensive evaluation factor set U , was constructed as

$$U = \{u_1, u_2, u_3 \dots u_n\} \dots(1)$$

Where $u_i = (i = 2, \dots, n)$ represents the influence factors. The 12 factors in Tab. 1 were chosen to form an evaluation factor set for the carbon emissions of prefabricated buildings.

Establishment of a comprehensive evaluation set: The single-factor fuzzy evaluation, that is, the problem analysis of a specific factor serves as the basis of a comprehensive evaluation. Single-factor fuzzy evaluation is generally realized through investigation followed by the construction of a comprehensive evaluation set and a combination of possible evaluation results given by the evaluator for the evaluation objects.

Weight determination: The analytic hierarchy process (AHP) was used to calculate the weight of each index as W_i .

$$W = (w_1, w_2, \dots, w_i), 0 \leq w_i \leq 1, \sum_{i=1}^n w_i = 1 \dots(2)$$

where w_i denotes the index weight calculated *via* AHP.

Fuzzy comprehensive evaluation based on AHP: By using the fuzzy comprehensive evaluation method based on AHP, the first-grade judgment matrix was formed as:

$$C_i = W_{ci} \times R_{ci} \dots(3)$$

Where C_i is the first-grade comprehensive membership. Afterwards, the second-grade judgment matrix was constructed as:

$$B_i = W_{Bi} \times R_{Bi} \dots(4)$$

Where $R_{B1} = [C_1 \ C_2 \ C_3]^T, R_{B2} = [C_4 \ C_5 \ C_6]^T$. In the end, the third-grade judgment matrix was formed as:

$$A = W \times R, R = [B_1 \ B_2]^T, \dots(5)$$

Where A is the fuzzy comprehensive evaluation result for the carbon emission of prefabricated buildings.

Case analysis: The project case was located in Zhengzhou City, Henan Province. The project site was featured by an overall open terrain and convenient transportation that facilitated the transportation of building materials and mechanical equipment. The prefabricated construction was integrated with the traditional cast-in-place construction in this project. Specifically, the related components were produced in a plant in advance followed by their field installation. The investment amount was calculated by the construction cost per square meter of the building. According to the Settlement Document and Material List from the factory for prefabrication, the material consumption was calculated by using related data obtained from the investigation, whereas the mechanical energy consumption was derived from the energy consumed during the processing of components in the plant, the energy consumed during transportation, and the energy consumed during site construction. The components in this project were produced in the plant by means of standard and information-based management, which not only improved the standard and quality of the components but also effectively enhanced their production efficiency. As for their installation, the components and construction machinery were reasonably arranged to avoid unnecessary rehandling within the construction site and block carbon emissions during the transportation process. The wastes of

Table 2: Weight table of the evaluation index.

Level I index	Weight	Level II index	Weight	Level III index	Weight
B ₁	0.65	C ₁	0.28	D ₁	1
		C ₂	0.13	D ₂	1
		C ₃	0.59	D ₃	0.33
				D ₄	0.14
				D ₅	0.53
B ₂	0.35	C ₄	0.31	D ₆	0.17
				D ₇	0.33
				D ₈	0.33
		C ₅	0.11	D ₉	0.17
				D ₁₀	0.75
				D ₁₁	0.25
C ₆	0.58	D ₁₂	1		

the prefabricated buildings in this project mainly included concrete, insulation boards, mortars, steels, and timbers. The timbers, which were mainly timber formworks, were uniformly classified and were not stacked together with other solid wastes. The wastes generated by the prefabricated building construction were reduced, the steel materials were recycled on the site, and other materials, such as concrete, insulation boards, and mortars, were almost not reused.

Nine experts in profound studies of prefabricated buildings were invited to score the index system, and the weight table (Table 2) was obtained through the calculation.

The scores of level I indexes were calculated according to formulas (2) to (5).

$$B_1 = [0.28 \ 0.13 \ 0.59] \cdot \begin{bmatrix} 1 & 0 & 0 \\ 0 & 0 & 1 \\ 0 & 0.53 & 0.47 \end{bmatrix} = [0.28 \ 0.31 \ 0.41]$$

$$B_2 = [0.28 \ 0.31 \ 0.41] \cdot \begin{bmatrix} 0.33 & 0.34 & 0.33 \\ 0.25 & 0.75 & 0 \\ 1 & 0 & 0 \end{bmatrix} = [0.58 \ 0.33 \ 0.09]$$

Through a second-grade judgment, the comprehensive scores of resource and energy utilization, construction organization, and ecological environment were obtained. According to the maximum membership principle, the comprehensive score of carbon emission from resources and energy sources was 0.41, whereas that from construction and the ecological environment was 0.58. The third-grade judgment, which refers to the highest index level and layer, was used to obtain the comprehensive evaluation result for the carbon emissions of prefabricated buildings.

$$A = W \cdot R \cdot [B_1 \ B_2]^T = [0.41 \ 0.58] \cdot \begin{bmatrix} 0.28 & 0.31 & 0.41 \\ 0.58 & 0.33 & 0.09 \end{bmatrix} = [0.45 \ 0.32 \ 0.22]$$

According to the maximum membership principle, the evaluation score for the carbon emission of prefabricated buildings was 0.45. Based on its evaluation result, the project case in Zhengzhou City, Henan Province had a moderate level of carbon emissions.

POLICY SUGGESTIONS

Expand the Market Scale of the Building Industry and Boost Market Competition

Increasingly fierce market competition can be observed in the building industry. To survive and seek long-term development amid this competition, the related industries should engage in low-carbon technological innovation. Therefore, construction enterprises should be guided to expand their market scale and

enhance market competition, which will encourage them to carry out low-carbon technological innovation activities to improve their competitiveness. The market demand should also be increased, enterprise innovation should be guided, and construction enterprises should develop low-carbon products by increasing the consumer demand for these products. Certain subsidies can be provided to consumers who purchase low-carbon products, the related product purchase taxes should be reduced, and incidental services of low-carbon products can be reinforced.

Adjust the Utilization of Building Materials and Strengthen the Technological Innovation

Among the total carbon emissions of the building industry, those generated by the consumption of building materials, particularly cement and steel, account for a large proportion. Moreover, the high energy consumption and carbon emissions of building materials are direct causes of extremely high levels of carbon emission intensity. Therefore, the technological innovation level in the production of building materials should be increased, and construction enterprises should be encouraged to promote new types of energy-saving and renewable building materials and increase the proportion of high-intensity and high-performance building materials that they use. Their construction processes should also be optimized, their building materials should be recycled, and the amount of building materials they use should be reduced. The construction and utilization of prefabricated buildings should also be strengthened, and the development of intelligent and integrated buildings should be promoted.

Set up Special Funds for Prefabricated Buildings and Provide Tax Preferences

Setting up special funds for the development of prefabricated buildings can increase the development and construction area of these buildings. In the initial development phase of these buildings, high costs are among the primary factors that restrict related R&D works. Setting up special funds can also promote the development of human resources, energy sources, and equipment, encourage innovations in production and construction technologies, and effectively monitor and manage information-based projects. In view of the current development status of prefabricated buildings in China, tax preferences should be continuously improved. Preferential policies in income and value-added taxes should be provided to component manufacturers and enterprises specializing in the development and construction of prefabricated buildings. The corresponding directory and detailed preferences for the production and use of building materials should be refined to motivate initiatives in the building industry.

Strengthen the Monitoring of Prefabricated Construction and Reduce the Discharge of Pollutants

Several factors should be considered when optimizing a logistics transportation plan, including transportation time, transportation mode, transportation route, and component loading plan. Logistics transportation can be optimized only based on a comprehensive analysis of the aforementioned influencing factors. Unnecessary secondary logistics transportation should be avoided as much as possible, and the usage of clean energy vehicles should be promoted. Resources and energy sources, such as water, electricity, and other materials, can be conserved by using advanced construction machinery. Turnover can be increased by saving materials on construction sites. To realize scientific management, the building materials should be saved as much as possible, and their waste should be reduced to the maximum extent. A scientific and reasonable arrangement of work implementation and operations should be formulated prior to the construction and early-stage prevention works to reduce the generation of construction waste and to increase material recycling efficiency. Land should be conserved to the highest degree, the stacking of building materials should be well controlled, and stacking and transportation schemes should be optimized to reduce unnecessary secondary transportation.

CONCLUSION

Aiming toward a low-carbon, sustainable economy, the building industry has shifted its development direction toward low energy consumption, low emission, low pollution, and environment-friendly directions to satisfy the ever-increasing demands of humans. Under the industrialized production mode, prefabricated buildings demonstrate various advantages over traditional cast-in-place buildings, such as their convenient and fast construction, negligible effects on the environment, and low carbon emissions. Accordingly, prefabricated construction has become an important path to realize the low-carbon and sustainable development of the building industry. Prefabricated construction also conforms to the development requirements for low-carbon buildings. Those factors that influence prefabricated buildings across three phases, namely, production in plants, logistics transportation, and assembly construction, were analysed in this paper. An evaluation index system for evaluating the carbon emissions of prefabricated buildings during their materialization phase was constructed, and an evaluation model was built by using the hierarchical fuzzy comprehensive evaluation method. Results show that the hierarchical fuzzy comprehensive evaluation model is scientific and reasonable for measuring the comprehensive carbon emission benefits of prefabricated buildings. A comprehensive evaluation of

a project in Zhengzhou City, Henan Province reveals that this project had a moderate level of carbon emissions. Several emission reduction measures were also proposed, including expanding the market scale of the building industry, adjusting the use of building materials, setting up special funds for prefabricated buildings, and strengthening the monitoring of prefabricated construction. The differences between prefabricated and traditional buildings in terms of their social comprehensive benefits can be explored in depth in future studies, and a carbon emission factor database and carbon emission standard for prefabricated buildings should also be established.

REFERENCES

- Blengini, G.A. and Di Carlo, T. 2010. The changing role of life cycle phases, subsystems and materials in the LCA of low energy buildings. *Energy and Buildings*, 42(6): 869-880.
- Boutouil, M. and Sebaibi N. 2020. Reducing energy consumption of prefabricated building elements and lowering the environmental impact of concrete. *Engineering Structures*, 213: 110594.
- Biswas, Wahidul K. 2014. Carbon footprint and embodied energy consumption assessment of building construction works in Western Australia. *International Journal of Sustainable Built Environment*, 3(2): 179-186.
- Ciutina, A., Floricel, A., Ungureanu, V. and Zagari, G. 2016. Structural solutions based on intensive use of steel for over-roofing of existing precast concrete panel buildings. *Advances in Structural Engineering*, 19(12): 1940-1948.
- Fenglai, Xiaocun, Wang, Zhang. 2016. Assessment of embodied carbon emissions for building construction in China: Comparative case studies using alternative methods. *Energy & Buildings*, 130: 330-340.
- Gao, W., Kuroki, S., Wang, H. and Zhang, Y. 2020. Life cycle environmental and cost performance of prefabricated buildings. *Sustainability*, 12.
- Hong, T., Ji, C. Y., Jang, M. H. and Park, H.S. 2014. Assessment model for energy consumption and greenhouse gas emissions during building construction. *Journal of Management in Engineering*, 30(2): 226-235.
- Hong, J., Li, K., Li, Z., Mao, C. and Shen, G. Q. 2016. Life-cycle energy analysis of prefabricated building components: An input-output-based hybrid model. *Journal of Cleaner Production*, 112: 2198-2207.
- Hens, H. and Verbeeck, G. 2010. Life cycle inventory of buildings: A calculation method. *Building & Environment*, 45(4): 1037-1041.
- Hu, D., Wang, B., You, F., Ye, Y., Zhang, G., Zhen, H. and Zhao, Y. 2011. Carbon emissions in the life cycle of urban building system in China-A case study of residential buildings. *Ecological Complexity*, 8(2): 201-212.
- Kuusk, K., Kalamees, T. and Pihelo, P. 2020. Development and performance assessment of prefabricated insulation elements for deep energy renovation of apartment buildings. *Energies*, 13.
- Kou, C., Li, G. and Wang H. 2019. Estimating city-level energy consumption of residential buildings: A life-cycle dynamic simulation model. *Journal of Environmental Management*, 240(15): 451-462.
- Li, C., Luo, W., Sandanayake, M., Setunge, S. and Zhang, G. 2017. Estimation and comparison of environmental emissions and impacts at foundation and structure construction stages of a building-A case study. *Journal of Cleaner Production*, 151(May 10): 319-329.
- Sivaraman, D. 2011. An integrated life cycle assessment model: Energy and greenhouse gas performance of residential heritage buildings, and the influence of retrofit strategies in the state of Victoria in Australia. *Energy & Buildings*, (5): 29-35.
- Seongwon, S. and Yongwoo, H. 2001. Estimation of CO₂ Emissions in life cycle of residential buildings. *Journal of Construction Engineering & Management*, 127(5): 414-418.



E-Waste Management in Asia Pacific Region: Review of Issues, Challenges and Solutions

S. Herat†

School of Engineering and Built Environment, Griffith University, Queensland 4111, Australia

†Corresponding author: S. Herat; s.herat@griffith.edu.au

Nat. Env. & Poll. Tech.
Website: www.neptjournal.com

Received: 17-07-2020

Revised: 06-10-2020

Accepted: 09-10-2020

Key Words:

E-waste
Extended producer responsibility
Informal recycling
Regulations

ABSTRACT

Proper management of used electrical and electronic equipment (EEE), known as e-waste, is causing a significant challenge for many countries around the world. United Nations estimate that the world generated 53 million metric tonnes (Mt) of e-waste in 2019, mostly from the Asian region. Poor handling of e-waste can cause severe environmental and human health issues due to the toxic compounds in e-waste. E-waste also contains valuable metals worth recovering. Environmentally sound management (ESM) of e-waste is either absent or limited in developing countries due to the informal recycling sector's dominance. Many countries are in the process of developing regulations based on extended producer responsibility (EPR) concepts. This paper aims to review the current status, issues, and challenges faced by Asia Pacific countries and suggest a way forward for the ESM of e-waste.

INTRODUCTION

The waste from used electrical and electronic equipment (EEE), commonly known as electronic waste or e-waste, is growing at an alarming rate in many countries. The rapid advancement of high technology equipment has helped to drive the economy in many countries. However, the knowledge of detrimental impacts on the environment and human health due to poor management of e-waste has only come up in recent years. The availability and affordability of many EEE with newer features have motivated the consumers to retire EEE well before their end-of-life (EOL), requiring a significant amount of e-waste to be handled and processed safely. The average life span of many essential EEE, such as computers and mobile phones, has fallen dramatically, causing the early obsolescence of these items. The United Nations (UN) has estimated that the world generated around 53 million tonnes (Mt) of e-waste in 2019 with a projection to reach 74 Mt by the year 2030 (Forti et al. 2020). The UN has also predicted that e-waste generation will be doubled from current levels to 111 Mt by the year 2050, effectively increasing by 2 Mt every year (Parajuly et al. 2019).

The transboundary movement of e-waste from industrialised countries to emerging and developing economies has caused significant challenges in countries in the Asia Pacific region due to a lack of infrastructure and financial resources

to deal with the issue. To compound the problems, the domestic consumption of EEE has also risen significantly in the region, further adding to the e-waste quantities. Due to the limited availability of formal e-waste recycling sector in countries in the Asia Pacific region, e-waste is predominantly handled by the informal e-waste recycling sector that utilises rudimentary recycling methods to extract the valuable metals while disposing the toxic compounds into the open environment. Such practices have caused severe environmental and health impacts. The industrialised countries have successfully developed regulations to deal with the issue based mainly on the extended producer responsibility (EPR) concepts where the manufacturers are required to finance the e-waste recycling operations. The Asia Pacific countries have been the target by many industrialised countries to dispose of their e-waste stream due to weak regulatory frameworks in those countries and cheap labour for recycling e-waste. To mitigate the adverse impacts on the environment and human health due to the transboundary movement of e-waste and the significant increase in domestic EEE consumption, the Asia Pacific countries are now developing stringent regulations mainly based on EPR concepts.

This paper aims to review the current status, issues, and challenges faced by Asia Pacific countries and suggest a way forward for environmentally sound management (ESM) of e-waste.

Table 1: Classification of e-waste.

Category	Items
Temperature equipment	Refrigerators, air conditioners, freezers
Monitors and Screens	Televisions, laptops, notebooks, monitors, tablets
Lamps	Light bulbs, fluorescent bulbs,
Large items	Washing machines, dryers, dishwashing machines, PV panels, photocopiers, electric stoves
Small items	Microwaves, vacuum cleaners, electric kettles, video cameras, calculators, toys, electrical tools, small medical devices, toasters, shavers, hairdryers, scales, many small EEE used in the kitchen
Small high tech items	Mobile phones, personal computers, printers, telephones, routers

Source: Forti et al. (2020)

GLOBAL GENERATION OF E-WASTE

The United Nations (UN) defines EEE a wide range of products with electronic circuits or electrical components that requires power supply from electric power supply or batteries. EEE comprises several household and business items and equipment used in services such as health, transport, and security systems. With the invention of the Internet of Things (IoT), EEE is widely used in developing smart cities. Table 1 summarises some of the EEE used in our society once discarded become part of the e-waste stream.

The generation of reliable data to determine the e-waste generation has been a challenge as many countries have not developed proper inventories. Most of the estimates are based on either sales data or predictions based on the estimated life span of EEE. The problem is compounded by many consumers deciding to store their used EEE hence not reaching the collection and recycling channels. The most reliable and recent statistics related to global e-waste generation can be found in 'The Global E-waste Monitor 2020' published by the United Nations University (Forti et al. 2020). Tables 2 and 3 summarise the regional and selected country data on e-waste generation in the year 2019.

According to Table 2, the Asia Pacific region (Asia and Oceania combined) generated nearly half the global e-waste quantities in 2019. Among the Asian nations, China (10.1Mt), India (3.2Mt), Japan (2.5 Mt), and Indonesia (1.6 Mt) are the highest e-waste generators in the region (Forti et al. 2020).

Table 2: E-waste generation in regions.

Region	Annual e-waste generation (Mt)	% of world e-waste generation	E-waste (kg/person)
Asia	24.9	46.5	5.6
Americas	13.1	24.4	13.3
Europe	12	22.4	16.2
Africa	2.9	5.4	2.5
Oceania	0.7	1.3	16.1

Source: Forti et al. (2020)

Table 3: E-waste generation in selected countries.

Country	E-waste (tonnes/year)	E-waste (kg/person)
Argentina	465,000	10.3
Australia	554,000	21.7
Austria	168,000	18.8
Bangladesh	199,000	1.2
Belgium	234,000	20.4
Brazil	2,143,000	10.2
Cambodia	19,000	1.1
Canada	757,000	20.2
China	10,129,000	7.2
Columbia	318,000	6.3
Hong Kong	153,000	20.2
France	1,362,000	21.0
Germany	1,607,000	19.4
India	3,230,000	2.4
Indonesia	1,618,000	6.1
Italy	1,063,000	17.5
Japan	2,569,000	20.4
Malaysia	364,000	11.1
Nigeria	461,000	2.3
Pakistan	433,000	2.1
Philippines	425,000	3.9
Republic of Korea	818,000	15.8
Russian Federation	1,631,000	11.3
Saudi Arabia	595,000	17.6
Singapore	113,000	19.9
Sri Lanka	138,000	6.3
Thailand	621,000	9.2
United Kingdom	1,598,000	23.9
United States of America	6,918,000	21.0
Vietnam	257,000	2.7

Source: Forti et al. (2020)

PROBLEMS AND OPPORTUNITIES ASSOCIATED WITH E-WASTE

Description of Problems

The problems associated with poor e-waste management are readily described in the scientific literature. In general, EEE contains a significant number of materials, a mixture of highly toxic compounds and valuable substances. The production of semiconductors and printed circuit boards are associated with several heavy metals such as antimony, silver, chromium, zinc, lead, tin, and copper. Although the regulations in certain countries have prohibited the use of toxic metals such as lead, mercury, cadmium, hexavalent chromium, current e-waste streams contain these metals due to previously used EEEs. In addition to the heavy metals, EEE also contains chemical compounds such as polybrominated biphenyls (PBBs) and polybrominated diphenyl ethers (PBDEs), which are also known as brominated flame retardants (BFRs).

Due to the complex nature of compounds, proper recycling and resource recovery of e-waste require advanced technologies and skilled operations, which can be costly in industrialised countries due to stringent environmental regulations. For this reason, there is a tendency for industrialised countries to move their e-waste to emerging and developing nations where weak regulatory structures and cheap labour are common. Unfortunately, many recycling and resource recovery facilities in these countries operate in an environmentally unsound manner using rudimentary technologies. It is common to observe e-waste being disposed of in open-land and waterways. The informal sector that dominates e-waste recycling in emerging and developing economies extracts the valuable metals and eliminates toxic residues into an open environment causing significant impacts on human health. The open burning of e-waste to recover precious metals has caused significant environmental pollution and the generation of persistent organic pollutants (POPs).

Description of Opportunities

E-waste is widely considered as a problem due to the adverse environmental and health impacts that occur due to rudimentary methods adopted during the recycling process. However, if adequately recycled using safe and advanced formal technologies, e-waste also presents an opportunity to extract valuable and precious metals. The extraction of metals contained in e-waste, known as above-ground mining, requires only a fraction of energy compared to mining them from natural ores.

E-waste contains up to 69 elements in the periodic table. These include precious metals such as gold, silver, copper,

platinum, palladium, and critical raw materials such as cobalt, indium, and germanium bismuth, and antimony which are considered to be diminishing from natural ores. The UN estimates that the value of selected raw materials in e-waste amounts to USD 57 billion during 2019. Iron (24 billion USD), copper (11 billion USD), gold (9 billion USD), Aluminium (6 billion USD) are considered to be the highest value materials contained in e-waste (Forti et al. 2020).

INTERNATIONAL POLICIES, REGULATIONS, AND INITIATIVES RELATED TO E-WASTE

To overcome the adverse impacts on the environment and human health, many countries in the world have developed or in the process of developing regulations and policies related to e-waste management. Initially pioneered by the European Union (EU), the concept of EPR has become the central theme of many of these regulations. EPR is regarded as a policy approach where the producer's responsibility is extended beyond the sales stage. Such responsibility shifts the physical and financial responsibility of managing e-waste from governments or local authorities to the producers. EPR also incentivises producers to take environmental considerations during design and manufacturing phases (design for the environment) to reduce environmental impacts during the whole life cycle of a product from raw material extraction to the final disposal. The product take-back scheme is one of the most common EPR applications where producers are required to organise facilities for consumers to deposit their used EEE (free of charge) at designated outlets and finance the cost of safe recycling. Such schemes are generally administered by government-appointed producer responsibility organisations (PROs) who act on behalf of the Government to achieve the set recycling targets. This section of the paper will describe the regulations developed by major e-waste generating countries.

E-Waste Regulations in the European Union

The EU has developed the following Directives to manage used EEE in the region:

- Waste Electrical and Electronic Equipment (WEEE) Directive
- Restriction of Hazardous Substances (RoHS) Directive

The WEEE Directive aims to minimise the adverse effects of used EEE by enhancing the reuse and recycling rates and reducing the waste from reaching landfills. To achieve the objectives, the WEEE Directive requires producers to take full financial and physical responsibility of their products by financing the collection, treatment, and recovery of e-waste without any cost to the consumers. The original

Directive 2002/96/EC was passed in European Parliament in February 2003 and came into force in August 2005 (European Commission 2003b). The Directive required the producers to set up collection outlets for consumers to return their used EEE free of charge and achieve a rate of 4kg of e-waste per person/year from December 2006. The Directive was revised in 2008 with the new Directive 2012/19/EU entering into force in August 2012 and valid from February 2014 (European Commission 2012). The new Directive moved away from the fixed weight requirement to a collection target of 45% of the average weight of EEE sold in the market from 2016, increasing to 65% from 2019. The WEEE Directive has been instrumental in reducing a significant amount of e-waste moving from the EU to developing countries. Further, many other countries in the world have taken the lead from the Directive to establish their regulations.

The RoHS Directive aims to restrict the use of certain hazardous substances during the manufacture of EEE. The RoHS 1, which came into effect in July 2006, required EEE manufacturers to avoid six hazardous substances: lead, mercury, hexavalent chromium, cadmium, PBDEs, and PBBs (European Commission 2003a). The RoHS 1 was recast in 2011 to accommodate the challenges of growing volumes of e-waste in the EU. The revised Directive 2011/65/EU on the restriction of the use of certain hazardous substances in EEE referred to as RoHS 2, came into force in January 2013 (European Commission 2011). The revised Directive did not add more substances but recommended to remove hexabromocyclododecane (HBCDD), bis (2- ethylhexyl phthalate (DEHP), butyl benzyl phthalate (BBP), and dibutyl phthalate (DBP) from EEE. The Directive is recast regularly to accommodate new scientific knowledge about the toxicity of materials used in EEE manufacture. As with the WEEE Directive, many countries around the world have taken the lead from EU Directive to develop their own RoHS regulations.

E-Waste Regulations in Japan

Japan is the 3rd highest generator of e-waste in the world, producing 2.5 Mt in 2019 and 10% of e-waste generated in the Asian region. Japan has a long history of waste reuse and recycling due to the shortage of natural resources. The first Japanese law on recycling (Law for Promotion of Utilisation of Recyclable Resources) or LPUR came into force in 1991 to promote recycling and design for resource recovery. This law was amended in 2000 to accommodate waste prevention, eco-design, and design for recycling (Law for Promotion of Effective Utilisation of Resources). Japan's regulations related to e-waste are:

- Law for Recycling of Specific Kinds of Home Appliances, commonly known as the 'Home Appliance Recycling Law.'

- Law for Recycling of Small Electronic Appliances, commonly known as 'Small WEEE Law.'

The 'Home Appliance Recycling Law' came in to effect April 2001, covering air conditioners, refrigerators/freezers, televisions, and washing machines/clothes dryers. Consumers cover the cost of recycling. The consumers pay a collection fee when they drop off their used product to finance the collection, transport, and recycling costs. The retailers are responsible for collecting used home appliances, and the manufacturers are responsible for the recycling of them. The consumers are required to return their above-used appliances to retailers or municipalities and pay the required fees.

The 'Small WEEE Law' came into force in 2013 to cover all household appliances such as personal computers, cameras, video game consoles, and mobile phones that are not covered by the 'Home Appliances Recycling Law.' Funded by the Government, the law requires consumers to deliver the used small appliances to the retailer of the designated collector. Manufacturers are required to reduce the recycling costs by improving design and using recyclable materials in their production.

E-Waste Regulations in China

China is the largest producer of EEE in the world. In 2019, China produced 10.1 Mt of e-waste to become the top e-waste generator in the Asian region. During this period, China produced 40% of the total e-waste generated in the Asian region (Forti et al. 2020). Given the significant quantities of e-waste to deal with, China has developed quite several environmental laws and regulations. The key regulations related to e-waste are:

- Law on the Promotion of Cleaner Production (2002) promotes the concepts of waste prevention during the design and production of EEE and their treatment at the end of life
- Law on the Promotion of Circular Economy (2008) specifies concepts of 3R (Reduce, Reuse, Recycle) during the production, consumption, and other stages of the life span of EEE
- Law on the Prevention of Environmental Pollution from Solid Waste (2004) requires e-waste treatment plants to safely obtain permits from local environmental protection agencies to handle hazardous components of e-waste.

China has also developed several Administrative Measures to deal with the e-waste problem. The 'Administrative measures on the prevention and control of environmental pollution by WEEE' (2007) deals with the prevention and control of environmental impacts resulting from the disas-

sembly, recycling, and disposal of e-waste. The 'Administrative measures on the qualification of WEEE treatment' (2010) requires the licencing procedure and qualification of e-waste treatment facilities, including supervision activities. The 'Administrative measures on the distribution of used electrical and electronic products' (2013) deals with the procedures related to the purchase or sale of used EEE.

China also passed the following two laws to strengthen e-waste management further:

- Ordinance on Management of Prevention and Control of Pollution from Electronic and Information Products (2006) - referred to as China's RoHS Directive.
- Administrative Regulation for the Collection and Treatment of Waste Electronic and Electrical Equipment (2009) – referred to as China's WEEE Directive, came into force in 2011 with emphasise on EPR, centralised disassembly of e-waste, and qualification of recycling plants.

E-Waste Regulations in India

India is the 2nd highest generator of e-waste in the Asian region producing 3.2 Mt of e-waste during 2019 (Forti et al. 2020). The informal sector dominates India's e-waste recycling industry. India's Central Pollution Control Board (CPCB) published the 'Guidelines for Environmentally Sound Management of E-waste in India' in 2005. The guidelines provided directions for the identification of various sources of e-waste with recommended procedures for handling e-waste. India's Ministry of Environment and Forest (MoEF) enacted the 'E-waste (Management and Handling) Rule of 2011, ' which came into force in May 2012. The Rule requires manufacturers to take responsibility for collecting and financing the e-waste management system through the EPR concept. In 2016, the Government of India developed the new 'E-waste (Management) Rules, 2016' (the EWM Rules, 2016), which superseded the 2011 rule and came into effect from October 2016. The revised Rule improved the EPR concept. In 2018, the Ministry of Environment, Forest and Climate Change (MoEF&CC) amended the 2016 Rules introducing e-waste collection targets to be met according to a graduating scale from 10% in 2018 to 70% in 2023. The amended Rule 'E-waste (Management) Amendment Rules, 2018' has the provision of registering a PRO for managing the EPR system.

SPECIFIC CHALLENGES, ISSUES, AND OPPORTUNITIES RELATED TO E-WASTE MANAGEMENT IN ASIAN COUNTRIES

Issues and Challenges for Environmentally Sound Management (ESM) of E-Waste

The issues and challenges of ESM of e-waste in the Asia Pacific region have compounded due to the transboundary movement of e-waste from industrialised countries to the region. A large amount of used EEE is currently being exported to Asian countries, particularly India, China, Indonesia, Cambodia, Vietnam, Sri Lanka, Pakistan, Philippines, and Bangladesh, for reuse. With the recent China ban on the waste import, most e-waste is now ending up in neighbouring countries like Thailand and Vietnam. However, most of these used EEEs are in the final stages of their life span and end up as e-waste in Asian countries quickly. There are also reports that e-waste is illegally transported to Asian countries in containers that contain used EEE. According to the Basel Convention, used EEE can be exported for reuse, whereas toxic compounds contained in e-waste are not allowed.

The e-waste recycling sector in Asian countries is dominated by the informal sector, which works in smaller groups employing mainly women and children with minimum safeguards to their health and safety of handling e-waste. The informal sector workers have limited knowledge about the health impacts of poor handling of toxic components in e-waste. Using basic recycling processes, the informal sector concentrates on extracting valuable metals components in e-waste while disposing of the poisonous residues to open the environment and waterways. Examples of environmental and health impacts of poor e-waste management in Asian countries are discussed in the next section.

The existence of the informal e-waste recycling sector also present challenges to the formal e-waste recycling sector whose operations have minimum environmental and health impacts. The formal e-waste recycling operations require investment in advanced technologies to ensure efficient recovery of valuable metals while any toxic residues are treated and managed correctly. Unfortunately, in Asian countries, used EEE is collected by the informal sector by providing financial incentives to the customers, thereby denying the necessary inputs for the formal sector to operate.

As observed in a later section of the paper, many Asian countries have a weak regulatory framework to deal with the e-waste issue. Many Asian countries have developed regulations to deal with hazardous waste streams but lack specific regulations on e-waste. Also, many Asian countries have no official inventory of e-waste generation. Besides, financing the infrastructure required for proper collection, storage, transportation, and processing of e-waste, educating the public on the toxicity of e-waste components, and implementing mandatory or useful product take schemes through EPR are additional challenges facing Asian countries to manage e-waste properly.

Environmental and Health Impacts of E-Waste Management in Asian Countries

The recent past has seen an increasing number of research publications related to human health and environmental impacts due to poor e-waste processing in developing countries. These studies, mainly conducted in countries like China, India, and Ghana, where the informal e-waste sector is thriving, have studied the adverse impacts on soils and sediments, impacts on human health, and impacts on general biota.

Huo et al. (2020) conducted a study to investigate the relationship between chronic exposure of Pb and oral anti-inflammatory potential of preschool children living near an informal e-waste recycling site in China. They found a strong correlation between excessive Pb exposure and lower oral anti-inflammatory ability of oral sialic acids. Liu et al. (2018) evaluated the association of e-waste exposure in children with paediatric hearing ability. The study concluded that early childhood exposure to Pb maybe is a risk factor for hearing loss in children living near e-waste sites. The adverse impacts of poor e-waste recycling are not only limited to direct human health. They extend to indirect health impacts as a result of consuming food grown inland contaminated with e-waste recycling. Wu et al. (2019) found a serious health risk associated with paddy cultivation near informal e-waste recycling sites. Tables 4: Summaries some studies undertaken to measure the impact of e-waste recycling in soils, sediments, and human health.

CURRENT PRACTICES IN ASIA PACIFIC REGION ON E-WASTE MANAGEMENT

Australia

The Australian Government introduced the National Tele-

vision and Computer Recycling Scheme (NTCRS) in 2011 under the Product Stewardship Act 2011 to provide households and small businesses free access to an industry-funded e-waste recycling scheme to dispose of their used televisions, computers, and printers. The 'Product Stewardship Act 2011' provides the regulatory framework for NTCRS under the 'Product Stewardship (Televisions and Computers) Regulations 2011'. Under NTCRS, companies who import or manufacture computer and television products over a certain threshold are required to pay a fee based on the proportion of recycling by becoming a member of the co-regulatory arrangement (PRO). The television and computer industries are needed to fund the collection and recycling of the proportion of televisions and computers disposed of in Australia each year to achieve an 80% recycling rate in 2026-27. Currently, the Australian Government approved the following PROs:

- Australian & New Zealand Recycling Platform Ltd (TechCollect)
- Electronics Product Stewardship Australasia
- E-Cycle Solutions Pty Ltd
- MRI PSO Pty Ltd (Drop Zone)

The approved PROs are required to provide annual reports to ensure the annual government targets are met. PROs are also needed to engage recycling services providers certified to AS5377: The Australian Standard for collection, storage, transport, and treatment of end-of-life electrical and electronic equipment (<https://www.environment.gov.au/protection/waste-resource-recovery/television-and-computer-recycling-scheme>)

The co-regulatory arrangement appointed by the Government is responsible for the day-to-day operations of the scheme by organising the collection and recycling of e-waste on behalf of their members. The households and small businesses can dispose of their used televisions and

Table 4: Impacts on soils, sediments and human health near e-waste recycling sites in Asia.

Study details	Reference
Effects of PBDEs and heavy metals generated from e-waste recycling on microbial species in soil	Wu et al. 2019
Investigation of heavy metal contamination in soils from an abandoned e-waste recycling site in Moradabad, India	Singh et al. 2018a
Genotoxicity of e-waste and heavy metal exposure from e-waste recycling site in Manila, Philippines	Alam et al. 2019
Assessment of decrease in serum cortisol levels and an increase in sensory integration difficulties among preschool children living near e-waste recycling site	Cai et al. 2019
Blood Pb and Cd levels in hospitalised patients living close to an e-waste recycling site in Guiyu, China	Chen et al. 2019
High exposure to PAHs generated from informal e-waste recycling sites in China on pregnant women.	Huo et al. 2019
Cancer risk of e-waste dismantling workers in Thailand due to airborne exposure of Cd, Cu, Ni, and Pb from e-waste operations	Puangprasert 2019
Health risk assessment of households in a Vietnamese village due to exposure of heavy metals from e-waste processing	Oguri et al. 2018
Health risks associated with heavy metals generated in e-waste recycling sites in Punjab, India	Singh et al. 2018b
Contamination of PBDEs in sediments and plant issues adjacent to an e-waste recycling site in China	Zhou et al. 2019

computers at designated collection points. Under the Product Stewardship (Televisions and Computers) Regulations 2011, the PROs are required to provide independently verified annual reports to the department outlining the achievements in the given period. The department has the authority to cancel the co-regulatory arrangement if the PRO is found to be unsatisfactory. Currently, Ecycle Solutions (Ecycle), Australian and New Zealand Recycling Platform (ANZRP), Electronics Product Stewardship Australasia (EPSA), and MRI PSO (MRI) manage the day-to-day operation of the scheme.

Bangladesh

As with many developing countries, there are several estimates related to e-waste generation in Bangladesh. According to Masud et al. 2019, Bangladesh generates around 2.81 Mt of e-waste annually, with most of it ending up in an open environment. The shipbreaking is a major industry in Bangladesh. According to Islam (2016), e-waste generated ship breaking yards alone is around 2.5 Mt annually. More recent studies on e-waste conducted by Mahmud et al. (2020) found e-waste generation to be approximately 400,000 metric tonnes annually, which more in agreement with Forti et al. (2020) estimate of 199,000 metric tonnes annually. As observed above, data on e-waste generation varies significantly, justifying the need for a formal national inventory of e-waste generation. This is vital as Bangladesh aims to achieve a fully digital country status by 2021. Hence, it will develop many IT-related projects, which will ultimately generate a significant amount of e-waste.

Bangladesh currently has no specific regulations or guidelines directly related to managing e-waste. The Bangladesh Environment Conservation Act of 1995, the Environmental Court Act of 2000, and The Environmental Conservation Rules of 1997 provide a necessary framework for developing the e-waste regulation. Recently, the Bangladesh Department of Environment (DoE) has announced the draft e-waste management rules referred to as 'Hazardous Waste (E-Waste) Management Rules, 2019'. The Rule restricts the use of as many as 15 substances or group of substances in certain EEE. The products under Rule include household appliances, monitoring, and control equipment, medical equipment, automatic machines, and IT & telecommunication equipment. The manufacturers are required to register with the DoE and present a detailed plan as to how they intend to treat the EOL EEE. Also, they must provide a list of hazardous substances contained in the product.

Cambodia

Cambodia currently has no specific regulations related

to e-waste management, although some regulations exist on activities related to impacts on human health and the environment. The existing laws lack the strength to enforce e-waste activities. The informal e-waste recycling sector is highly active in the country resulting in significant environmental and health impacts. There is no formal inventory of e-waste generation in Cambodia. The Ministry of Environment, Cambodia, in collaboration with the Ministry of Environment, Korea has recently developed the 'Guideline on Environmental Sound Management of Waste Electrical and Electronic Equipment (Xavier et al. 2020).

Malaysia

The data related to e-waste generation in Malaysia vary significantly. According to Azad et al. (2017), e-waste generation in Malaysia in 2006 was estimated to be 652,909 tonnes, increasing to 706,000 tonnes by 2010 and finally reaching 1.2 Mt in 2020. More recent estimates by Yong et al. (2019) have stated that Malaysia will generate 1.1 Mt of e-waste with an annual increase of 14%. Forti et al. 2020 have estimated the e-waste generation to be 364,000 tonnes in 2019.

E-waste management in Malaysia is governed by the Department of Environment (DOE) within the Ministry of Natural Resources and the Environment. Currently, there are no specific rules or regulations directly related to e-waste management. The Environmental Quality (Scheduled Waste) Regulations 2005 and the Environmental Quality (Prescribed Premises) (Treatment, Disposal Facilities for Scheduled Waste) Regulations, 1989 (control on the collection, treatment, recycling, and disposal of scheduled waste including e-waste). The 'Guidelines for Classification of Used Electrical and Electronic Equipment in Malaysia' was issued by DOE in January 2008 (Azad et al. 2017)

Pakistan

Pakistan lacks reliable data on e-waste generation and research studies related to environmental and health impacts due to improper e-waste management. A survey conducted by Iqbal et al. (2015) has estimated e-waste generation to be 315,000 tonnes in 2015. A more recent study by Shaikh et al. (2020) estimates Pakistan's e-waste generation during 2018-2019 to be 1.79 Mt. The informal e-waste recycling sector is very active in Pakistan with open burning of e-waste becoming an everyday activity.

Currently, there are no laws or regulations to deal with the e-waste problem. The Pakistan Environmental Protection Act (1997), the National Waste Policy (2005), and Import Policy Order (2016) have provisions to prohibit e-waste imports to Pakistan. However, several used EEE is still being imported as second-hand EEE.

Philippines

The high growth of domestic consumption of EEE has created a significant e-waste issue in the Philippines. In the absence of formal recycling facilities, most of the e-waste is handled by the informal sector, which consists of more than 2300 registered and unregistered junkshops with the Metropolitan Manila Development Authority. There are several waste pickers, women, and children engaged in e-waste recycling (Alam et al. 2019). There is no formal inventory of e-waste generation in the Philippines. The Department of Environment and Natural Resources has published the 'Guidelines on the Environmentally Sound Management (ESM) of Waste Electrical and Electronic Equipment (WEEE) 'under the Republic Act (RA) 6969.

Vietnam

Vietnam lacks an official inventory of e-waste generated in the country. However, few studies have managed to estimate the e-waste generation using sales information and modelling. Hai et al. (2017) report on estimates by 2020, Vietnam will generate 10.6 million Units of e-waste which will include 4.85 million TV's, 2.27 million refrigerators, 2.6 million washing machines as 873 thousand air conditioners, Another estimate reports that by 2020 Vietnam will generate 12.1 million Units of e-waste by 2020 which will include 6.5 million TVs, 3.4 million refrigerators, 1.9 million washing machines, 284 thousand air conditioners.

In August 2013, the Prime Minister of Vietnam signed the Decision No. 50/2013/QD-TTg, which requires the enterprises manufacturing or importing electrical and electronic products to be responsible for the collection, transport, and processing of e-waste. This decision has now been replaced by the Prime Minister's Decision No. 16/2015/QD-TTg that came into effect from 1 July 2016. Currently, the Vietnamese Government is revising the e-waste regulations to improve the efficiency of EPR implementation.

CONCLUSIONS

E-waste generation in the world is currently much higher than most other waste streams. Although Asia Pacific countries have developed several initiatives to achieve ESM of e-waste, success and effectiveness are challenged by many issues. Identifying the key stakeholders and promoting cooperation among them is the key to tackling these issues. Asia Pacific countries are experiencing significant challenges due to a lack of policies, infrastructure, and financial resources. Although e-waste is a problem due to its hazardous components, it is also a solution to the depletion of scarce materials that the manufacture of EEE depends on. If undertaken correctly, re-

cycling of e-waste can provide an excellent business opportunity by harvesting these resources. The e-waste recycling step consists of three stages: collection, sorting and dismantling, and end-processing. In Asia Pacific countries, these steps are all undertaken by the informal waste recycling sector that lacks skilled operations. The formal e-waste recycling sector is very limited in these countries. The informal sector could conduct the first two stages of the e-waste recycling without much environmental and health impacts. However, the last step, if undertaken by the informal sector, could result in severe environmental pollution.

The transfer of formal technology to Asia Pacific countries should be undertaken considering the social, environmental, and economic boundaries. Direct technology transfer without any consideration given to inter-linked non-technical aspects of waste management could lead to unsustainable systems. In particular, the transfer of technology to Asia Pacific countries needs to consider the informal sector's dominance and success. Innovative models that allow the informal sector to be involved in the process by adopting safe recycling practices while hazardous operations are transferred to formal recycling recyclers are the key to a successful e-waste management program. Such business models would require consideration given to improved collection and pre-processing of e-waste by the informal sector through training and technology transfer to ultimately benefit the operations of state-of-art e-waste processing facilities towards the end of recycling chain.

Many Asia Pacific countries favour EPR for developing regulations to deal with the e-waste. Most industrialised countries have had much success in implementing EPR successfully. The proper implementation of EPR requires several pre-conditions to be met, including the correct indemnification of the producer/importer and managing the producers' funds. Due to the informal sector operations, implementation of EPR in Asia Pacific countries has become very challenging. Hence, Asia Pacific countries should avoid directly adopting EPR procedures adopted in industrialised countries and develop their EPR schemes based upon their capacity to implement them.

As a way forward, Asia Pacific countries need to develop well defined national e-waste management strategy based upon circular economic concepts. Such an approach should not only look at solving the existing environmental and health impacts of e-waste but also reduce e-waste through design for environment practices. The strategy should also create enabling conditions for the private sector to develop business and economic opportunities to recover the materials from e-waste. The strategy should take into account the financial, institutional, political, and social aspects of the

country, focusing on how to synergise the informal e-waste recycling sector with the formal sector.

REFERENCES

- Azad, A.K., Islam, MohdAminul and Hossin, M.M. 2017. Generation of electronic-waste and its impact on environment and public health in Malaysia. *Annals of Tropical Medicine and Public Health*, 10(5): 1123-1127.
- Alam, Z.F., Riego, A.J.V., Samson, J.H.R.P. and Valdez, S.A.V. 2019. The assessment of the genotoxicity of e-waste leachates from e-waste dumpsites in Metro Manila, Philippines. *International Journal of Environmental Science and Technology*, 16(2): 737-754.
- Cai, H., Xu, X., Zhang, Y., Cong, X., Lu, X. and Huo, X. 2019. Elevated lead levels from e-waste exposure are linked to sensory integration difficulties in preschool children. *Neuro Toxicology*, 71: 150-158
- Chen, Y., Xu, X., Zeng, Z., Lin, A., Qin, Q. and Huo, X. 2019. Blood lead and cadmium levels associated with hematological and hepatic functions in patients from an e-waste-polluted area. *Chemosphere*, 220: 531-538.
- European Commission 2017. Directive (EU) 2017/2102 of the European Parliament and of the Council of 15 November 2017 amending Directive 2011/65/EU on the restriction of the use of certain hazardous substances in electrical and electronic equipment. *Official Journal of the European Union*, 305: 8-10.
- European Commission 2011. Directive 2011/65/EU of the European Parliament and of the Council of 8 June 2011 on the restriction of the use of certain hazardous substances in electrical and electronic equipment. *Official Journal of the European Union*, 174: 88-110.
- European Commission 2012. Directive 2012/19/EU of the European Parliament and of the Council of 4 July 2012 on waste electrical and electronic equipment (WEEE). *Official Journal of the European Union*, 197: 38-71.
- European Commission 2005. Commission decision of 18 August 2005 amending Directive 2002/95/EC of the European Parliament and of the Council for the purpose of establishing the maximum concentration values for certain hazardous substances in electrical and electronic equipment. *Official Journal of the European Union*, 48: 65.
- European Union 2003a. Directive 2002/95/EC of the European Parliament and of the Council of 27 January 2003 on the restriction of the use of certain hazardous substances in electrical and electronic equipment. *Official Journal of the European Union*, 46: 9-23.
- European Commission 2003b. Directive 2002/96/EC of the European Parliament and the Council of 27 January 2003 on waste electrical and electronic equipment (WEEE). *Official Journal of the European Union*, 46: 24-39.
- Forti, V., Balde, C.P., Kuehr, R. and Bel, G. 2020. The Global E-waste Monitor 2020: Quantities, flows and the circular economy potential. United Nations University (UNU)/United Nations Institute for Training and Research (UNITAR) – co-hosted SCYCLE Programme, International Telecommunication Union (ITU) & International Solid Waste Association (ISWA), Bonn/Geneva/Rotterdam
- Hai, H.T., Hung, H.V. and Quang, N.D. 2017. An overview of electronic waste recycling in Vietnam. *Journal of Material Cycles and Waste Management*, 19(1): 536-544.
- Huo, X., Wu, Y., Xu, L., Zeng, X., Qin, Q. and Xu, X. 2019. Maternal urinary metabolites of PAHs and its association with adverse birth outcomes in an intensive e-waste recycling area. *Environmental Pollution*, 245: 453-461.
- Iqbal, M., Breivik, K., Syed, J.H., Malik, R.N., Li, J., Zhang, G. and Jones, K.C. 2015. Emerging issue of e-waste in Pakistan: A review of status, research needs and data gaps. *Environmental Pollution*, 207: 308-318.
- Islam, M. N. 2016. E-waste management of Bangladesh. *International Journal of Innovative Human Ecology and Nature Studies*, 4(2): 1-12.
- Liu, Y., Huo, X., Xu, L., Wei, X., Wu, W., Wu, X. and Xu, X. 2018. Hearing loss in children with e-waste lead and cadmium exposure. *Science of the Total Environment*, 624: 621-627.
- Mahmud, I., Sultana, S., Rahman, A., Ramayah, T. and Cheng Ling, T. 2020. E-waste recycling intention paradigm of small and medium electronics store managers in Bangladesh: An S-O-R perspective. *Waste Management and Research*, DOI: 10.1177/0734242X20914753.
- Masud, M.H., Akram, W., Ahmed, A., Ananno, A.A., Mourshed, M., Hasan, M. and Joardder, M.U.H. 2019. Towards the effective e-waste management in Bangladesh: a review. *Environmental Science and Pollution Research*, 26(2): 1250-1276.
- Oguri, T., Suzuki, G., Matsukami, H., Uchida, N., Tue, N.M., Tuyen, L.H., Viet, P.H., Takahashi, S., Tanabe, S. and Takigami, H. 2018. Exposure assessment of heavy metals in an e-waste processing area in northern Vietnam. *Science of the Total Environment*, 621: 1115-1123.
- Parajuly, K., Kuehr, R., Awasthi, A. K., Fitzpatrick, C., Lepawsky, J., Smith E., Widmer, R. and Zeng, X. 2019. Future E-waste Scenarios, StEP (Bonn), UNU VIE-SCYCLE (Bonn) & UNEP IETC (Osaka).
- Puangprasert, S. and Prueksasit, T. 2019. Health risk assessment of airborne Cd, Cu, Ni and Pb for electronic waste dismantling workers in Buriram Province, Thailand. *Journal of Environmental Management*, 252: 109601
- Shaikh, S., Thomas, K. and Zuhair, S. 2020. An exploratory study of e-waste creation and disposal: Upstream considerations. *Resources, Conservation and Recycling*, 155: 104662.
- Singh, A., Dwivedi, S.P. and Tripathi, A. 2018a. Study of the toxicity of metal contamination in soil samples collected from abandoned e-waste burning sites in Moradabad, India. *Nature Environment and Pollution Technology*, 17 (3): 973-979.
- Singh, M., Thind, P.S. and John, S. 2018b. Health risk assessment of the workers exposed to the heavy metals in e-waste recycling sites of Chandigarh and Ludhiana, Punjab, India. *Chemosphere*, 203: 426-433.
- Wu, Z., Gao, G. and Wang, Y. 2019. Effects of soil properties, heavy metals, and PBDEs on microbial community of e-waste contaminated soil. *Ecotoxicology and Environmental Safety*, 180: 705-714.
- Xavier, L.H., Giese, E.C., Ribeiro-Duthie, A.C. and Lins, F.A.F. 2019. Sustainability and the circular economy: A theoretical approach focused on e-waste urban mining. *Resources Policy*, 101467.
- Yong, Y.S., Lim, Y.A. and Ilankoon, I.M.S.K. 2019. An analysis of electronic waste management strategies and recycling operations in Malaysia: Challenges and future prospects. *Journal of Cleaner Production*, 224: 151-166.
- Zhou, H., Tam, N.F.Y., Cheung, S.G., Wei, P., Li, S. and Wu, Q. 2019. Contamination of polybrominated diphenyl ethers (PBDEs) in watershed sediments and plants adjacent to e-waste sites. *Journal of Hazardous Materials*, 379: 120788.



Performance and Mechanism of Layered Double Hydroxide to Remove Graphene Oxide in Aqueous Solution

Haibo Kang*, Jiahui Gu*, Gang Liu**, Ben li* and Wei Wang*†

*School of Civil Engineering, Shaoxing University, Shaoxing, Zhejiang, P. R. China

**School of Architecture and Civil Engineering, Jiangsu University of Science and Technology, Zhenjiang, P. R. China

†Corresponding author: Wei Wang; wellswang@usx.edu.cn

Nat. Env. & Poll. Tech.

Website: www.neptjournal.com

Received: 09-07-2020

Revised: 09-09-2020

Accepted: 16-09-2020

Key Words:

Graphene oxide

Layered double hydroxide

Wastewater

Adsorption

ABSTRACT

Intending to remove toxic graphene oxide (GO) from wastewater, LDH (layered double hydroxide) was employed to recover GO by adsorption method. The adsorption performance and the mechanism of LDH for GO have been systematically studied by diverse characterization technologies and methods. The relevant effects of solution pH (2-9), adsorbent dosage (5-25mg) and the concentration of GO (20-160mg/L) were investigated in detail. The main driving force of GO condensation on LDH may be electrostatic interaction and hydrogen bonding, SEM, TEM, AFM, FT-IR and XRD analysis further confirmed this. XPS test shows that the adsorption process is carried out through C-O and O-C=O. We have got a high removal rate of 92% and an adsorption capacity of 1472 mg/g under an optimized conditions (pH = 3.0, equilibrium time = 6.0 h, dosage = 10mg, C₀ = 160 mg/L). The analyses implied that LDH will be a very promising candidate for recovery of GO from wastewater.

INTRODUCTION

Graphene oxide (GO) is synthesized by the oxidation of two-dimensional carbon allotrope graphene, known for its extraordinary specific surface area and abundant O-containing functional groups (such as -COOH and -OH). GO shows great potential in multi-disciplinary fields such as medical, energy, environmental pollution (Azadian et al. 2020, Baragaño et al. 2020, Wu et al. 2020). Particularly, these characteristics provide graphene oxide with many adsorption sites for various heavy metal ions and organic pollutants (Awad et al. 2020, Duru et al. 2016, Xing et al. 2020). For example, magnetic GO composite materials have been synthesized and used to remove Cd(II) and Pb(II) from aqueous solutions (Bao et al. 2020). A graphene oxide/bentonite-loaded nano-iron synthesized by liquid-phase redox method was used to treat lead-contaminated water (Yu et al. 2020). Continuously photocatalytic removal of chromium (VI) reduced graphene oxide microspheres (Liu et al. 2020) by using structured porous Ag/Ag₃PO₄.

Although GO and GO-based nanomaterials have been widely used as adsorbents for clean environmental pollution, GO will inevitably be released into the environment and ecosystems, including surface water and groundwater (Zhang et al. 2020). Once in natural and drinking water, GO may undergo physical and chemical changes due to exposure to sunlight and chlorination disinfection, respectively. Besides,

the transformation of GO under light leads to the increase of toxicity of GO to biological cells (Gao et al. 2019). Because of these potential negative risks associated with GO, it is important to remove GO during drinking and wastewater treatment. Besides, in mammals, GO exposure may lead to lung or reproductive toxicity (Liang et al. 2015, Yang et al. 2013a), exposure to GO may have adverse effects on organisms, such as fish and shrimp (Batista de Melo et al. 2019, Paital et al. 2019).

Generally, layered double hydroxide (LDH) adopts an anionic layered structure like hydrotalcite, which is assembled through a non-covalent bond interaction between the cationic host layer and the anion guest intermediate layer (Pang et al. 2019). LDH materials can be expressed according to the general formula $[M_{1-p}^{2+}M_p^{3+}(\text{OH})_2]^{p+}[(A^{q-})_{p/q}]^{p-} \cdot y \text{H}_2\text{O}$, in which M²⁺ and M³⁺ represent bi-/trivalent metal cations (Mg²⁺, Ca²⁺, Ni²⁺, Al³⁺ and Fe³⁺), A^{q-} represents non-framework (in)organic q-valent interlayer anions (NO₃⁻, ClO₄⁻, and SO₄²⁻), p denotes the molar ratio of M²⁺/(M²⁺+M³⁺), and y denotes the molar amount of intercalated water. Due to its special structural advantages, such as larger interlayer spacing, wider chemical composition, and ion exchange capacity, LDH materials are widely used as catalysts or adsorbents in the field of water remediation (Song et al. 2018, Wang et al. 2016, Wang et al. 2018, Yang et al. 2017, Yu et al. 2017). Compared with conventional flocculants, LDHs can be produced from the natural

environment and can aggregate with nanomaterials, which can form target stable complexes in aqueous solutions and form new minerals (secondary minerals). However, as far as we know, there are few studies on the interaction between GO and LDH in aqueous solution. This knowledge is very important to improve the surface condensation/precipitation model and to better assess the environmental fate of toxic GO nanomaterials.

In this work, LDH was used as an adsorbent to remove GO from aqueous solutions. Environmental conditions such as pH, LDH content, and initial GO concentration were studied to evaluate the removal performance in detail. X-ray diffraction (XRD), Fourier transform infrared spectroscopy (FT-IR), scanning electron microscope (SEM), transmission electron microscope (TEM), atomic Force Microscope (AFM), and X-ray photoelectron spectroscopy (XPS) were used for characterization of the interactive mechanism. The results may contribute to new insights into the transportation and environmental fate of GO in the aquatic environment.

MATERIALS AND METHODS

Adsorption of GO

At room temperature, macro-batch experiments were carried out on the adsorption and co-adsorption of GO on the LDH surface in 100mL glass bottles. Simply put, add LDH suspension and GO stock solution to a glass bottle to obtain different components with specified concentrations. By adding a negligible 0.1 mol/L HCl and/or NaOH solution, the pH value of these interaction systems is adjusted in the range of 1.0-8.0. Similarly, a slight increase in the total volume of the interaction system has almost no obvious effect on the solid/liquid ratio. The interacting suspension is gently shaken for 6 hours to achieve adsorption equilibrium. The bottle is then left on a flat surface for 1.0 days to completely settle the large GO aggregate. Finally, LDH was separated from the solution by centrifugation at 18,000 RPM for 30 minutes.

The concentration of GO remaining in the supernatant was analysed with an ultraviolet-visible spectrophotometer (UV1800, chemical) at a wavelength of 210 nm. To calculate the GO removal rate R and distribution coefficient K_d , the equations (1), (2) and (3) were used.

$$R = \frac{C_0 - C_e}{C_0} \times 100\% \quad \dots(1)$$

$$Q_e = \frac{(C_0 - C_e) \times V}{m} \quad \dots(2)$$

$$K_d = \frac{Q_e}{C_e} \quad \dots(3)$$

Where C_0 (mg/L) and C_e (mg/L) are the initial and equilibrium concentrations of GO, Q_e is the amount of adsorption. Considering GO loss required for LDH adsorption (GO adsorption on glass bottle wall), calibration curves were obtained under the same conditions as the adsorption process, but without LDH. According to the calibration curve, the adsorption capacity of GO was calculated by subtracting the mass in solution from the added mass. To confirm the accuracy of data repeatability, experiments were carried out in duplicate, and each data were measured in triplicate. The relative error is less than 5% (Wang et al. 2016, Zou et al. 2016).

Materials

All the chemicals used in the experiment were purchased from China Petroleum & Chemical Corporation (Beijing, China). Mg/Al layered double hydroxide (LDH) was prepared by the co-precipitation method (Chang et al. 2017, Hu et al. 2017). The graphene oxide aqueous solution was purchased from Suzhou Tanfeng Graphene Technology Co., Ltd. (Jiangsu, China).

Characterization

The crystal structure of the absorber was examined with X-ray diffractometer (XRD, Empyrean) using Cu K α radiation. The functional groups were identified by Fourier transform infrared spectroscopy (FTIR, NEXUS) with a scanning range of 400-4000 cm^{-1} . Scanning electron microscope (SEM, JSM-6360LV), atomic force microscopy (AFM, SPA 400), and high-resolution transmission electron microscope (HRTEM, JEM-2100F) were used to study morphology and elemental composition of the synthetic materials. Thermo ESCALAB 250 performs X-ray photoelectron spectroscopy (XPS) spectroscopic analysis using a focused monochromatic Al K α X-ray source ($h\nu = 1486.6$ eV).

RESULTS AND DISCUSSION

Characterization

The surface morphology of the material can be observed from the scanning electron microscope (SEM) and transmission electron microscope (TEM) images. The results show that the LDH of hexagonal overlapping crystals is smooth and well-shaped (Fig. 1A and B). The GO agglomerates are multi-layered, with lateral dimensions ranging from a few nanometres to tens of nanometres (C and D). Besides, The LDH/GO-pH < 7 presents uneven morphology (Fig. 1E). Compared with LDH/GO-pH < 7, the LDH/GO-pH > 7 shows the characteristic of smooth surface and relative homogeneous flaky structure (Fig. 1 G). Besides, TEM images revealed

the sheet-like structure of LDH/GO more clearly (Fig. 1 F). On the other hand, compared with GO and LDH before adsorption, after adsorption, TEM of LDH/GO adhered to black substance, with irregular shape and uneven thickness, indicating that GO adsorbed on LDH surface.

To reveal the adsorption mechanism, XRD technology was used to characterize the composite material. From the X-ray diffraction (XRD) pattern of GO (Fig. 2 a), a characteristic peak can be observed at $2\theta=10.32$, indicating GO's (001) reflection. As shown in Fig. 2 compared with

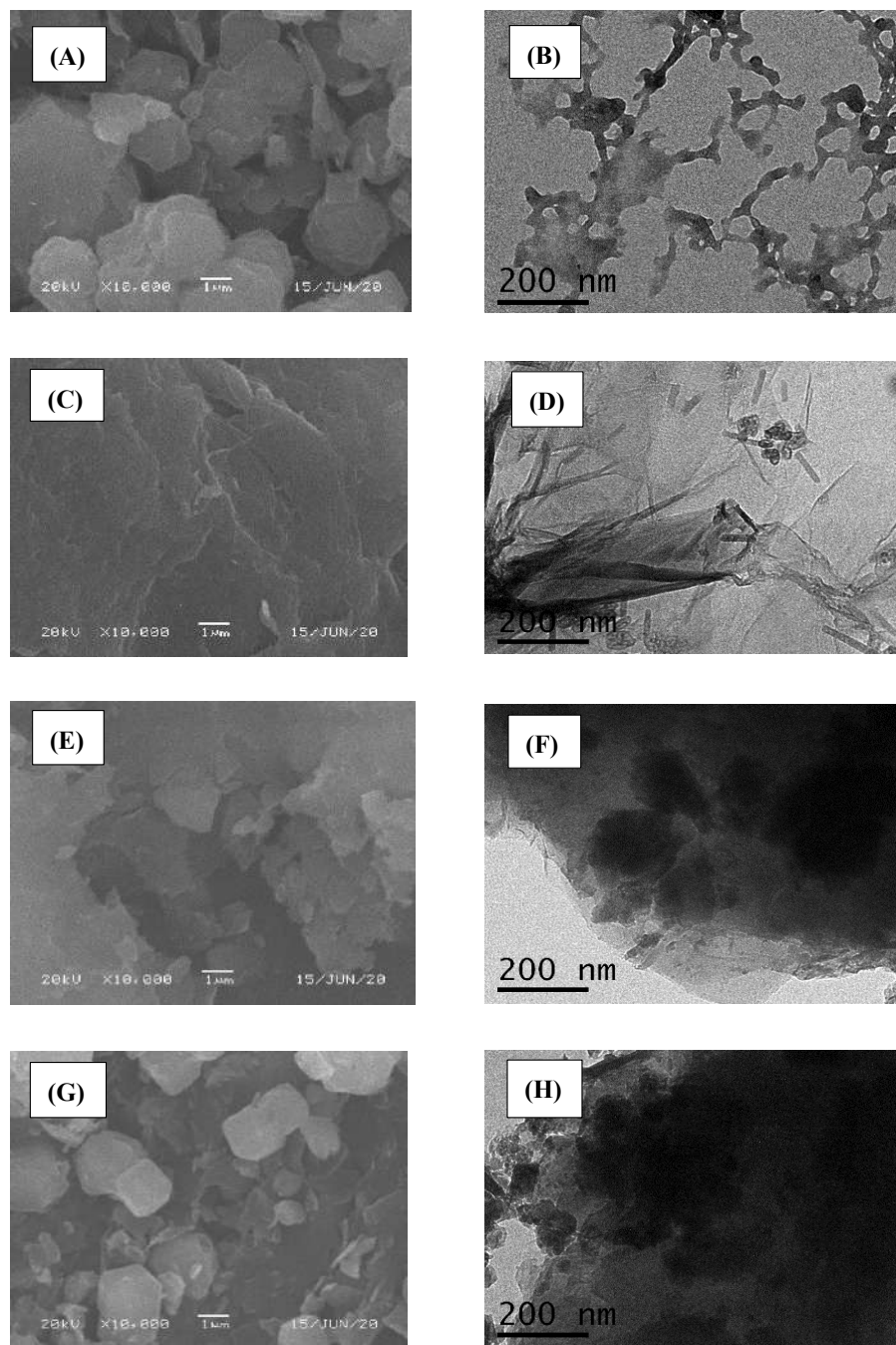


Fig. 1: SEM (A) and TEM (B) of LDH, SEM (C) and TEM (D) of GO, SEM (E) and TEM (F) of LDH-pH < 7, SEM (G) and TEM (H) of LDH/GO-pH > 7.

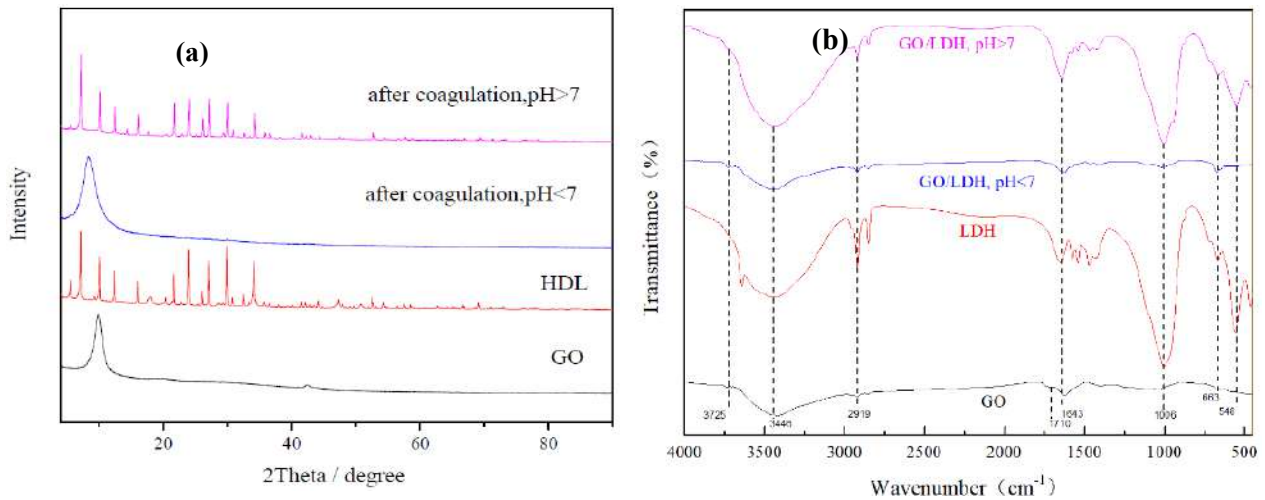


Fig. 2: XRD patterns (a) of GO, LDH, LDH-pH < 7, LDH/GO-pH > 7, FT-IR spectra (b) of GO, LDH, LDH-pH < 7, LDH/GO-pH > 7.

the characteristic diffraction peaks of GO and LDH before adsorption, the characteristic diffraction peaks under acidic conditions are similar to GO, indicating that GO adsorption under acidic conditions occurs on the surface of LDH. However, the characteristic diffraction peak under alkaline conditions is almost unchanged from that of LDH, which shows that there is no-GO aggregation on the surface of LDH under alkaline conditions.

FT-IR spectroscopy is very helpful for characterizing surface functional groups. As shown in Fig. 2 b, the band at 3500 cm⁻¹ indicates the O-H stretching mode, which involves hydrogen bonding or interlayer water molecules, the band at ~1006 cm⁻¹ is attributed to C-O group, the band at ~1643 cm⁻¹ is attributed to C=C group, the band at ~1710 cm⁻¹ is attributed to C=O group, indicating the presence of an amount of oxygen-containing functional groups on GO. The broadband at 3446 cm⁻¹ is attributed to the hydrogen bonding or the stretching mode of the OH group with the interlayer water molecules involved. The C=C stretching vibration of GO shows the energy band in the energy range of ~1643cm⁻¹ (Goh & Lim 2010, Rao et al. 2005), which also appeared in the spectra of LDH/GO-pH < 7 and LDH/GO-pH > 7, indicating that GO was successfully adsorbed on the surface of LDH.

Effect of pH

The adsorption of GO on non-specific and specific adsorbents depends on pH. pH significantly affects the surface chemistry and adsorption chemistry of LDH-containing mixtures (González et al. 2014). The removal rate, removal efficiency, and distribution coefficient of GO on LDH as a function of pH are shown in Fig. 3. The removal of GO on

LDH was studied with a different pH value of 2, 3, 4, 5, 6, 7, 8 and 9 respectively shows that the removal capabilities are influenced by pH values. It can be seen from Fig. 3 that when pH < 5, as the pH increases, the removal rate and distribution coefficient of GO decreases rapidly, while when pH > 5, as the pH increases, the removal rate and distribution coefficient remains unchanged, 17.9% and 0.43 respectively. The maximum removal rate of GO by LDH is 93%, which is due to the electrostatic action between the negative charge of GO and the positive charge of LDH. At pH < 5, the main interaction is controlled by chemical adsorption, electrostatic attraction and hydrogen bonding. Because of electrostatic attraction, the negatively charged graphene oxide is easy to agglomerate and adsorb on positively charged LDH. However, at a pH above 5.0, by increasing the pH value, the carboxyl group on the GO group is deprotonated and inhibits the bonding and accumulation of cations and graphene oxide,

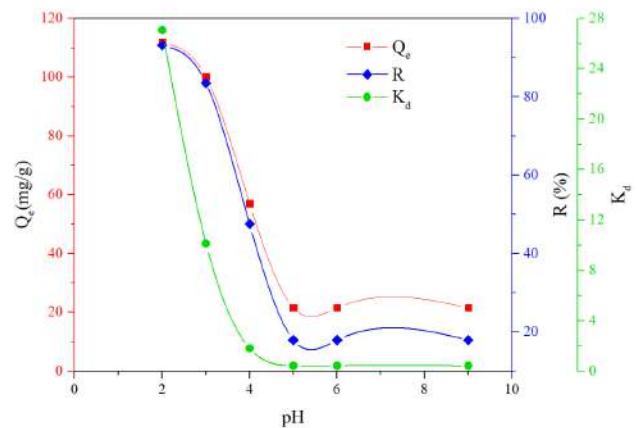


Fig. 3: Removal of GO on LDH as a function of pH value.

thereby weakening the electron acceptor ability of these substances (Yang et al. 2013b). On the other hand, the GO carried when the pH value changes from 5 to 9 will cause the electrostatic repulsion between GO and LDH to increase, so the adsorption capacity decreases (Tang et al. 2020), and the main interaction is controlled by physical adsorption.

Therefore, it can be concluded that low pH facilitates the adsorption of GO by LDH and alkaline conditions will inhibit the adsorption of GO by the LDH, which is the adsorption of LDH to GO is pH-dependent, it is recommended to carry out the adsorption process at a pH close to strong acidity.

Effect of Adsorbent Dosage

Adsorption dosage is also one of the parameters which directly affects the removal of pollutants from aqueous solutions. The removal of GO on LDH was studied with different LDH content of 5, 10, 15, 20 and 25 mg, respectively shows the removal capabilities are influenced by LDH content. Fig. 4 shows the effect of LDH content on adsorption capacity, efficiency and distribution coefficient. In the solution with pH 3.0 and GO=100mg/L, the LDH content was changed to 5-25mg, the equilibrium time was 6h, and the corresponding tests were carried out. It can be seen from the figure that as the LDH content increases, the removal rate gradually decreases and tends to 0%. Similarly, the adsorption amount and distribution coefficient are also oriented to 0. This shows that, while maintaining GO concentration to a certain extent, adding LDH can greatly decrease the adsorption capacity of LDH. It shows that LDH has high coagulation ability at low concentration, which is crucial for the application of LDH in the coagulation treatment of GO in aqueous solution.

When the content of LDH increased from 5mg to 15mg, the adsorption ability decreased, although the removal rate

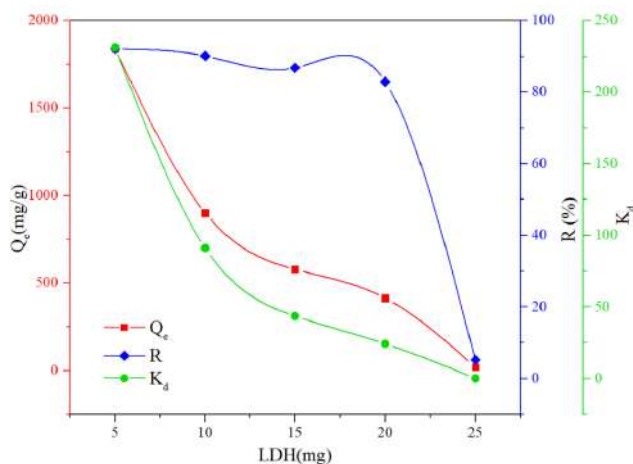


Fig. 4: Removal of GO on LDH as a function of LDH contents.

of GO was maintained. This was because the adsorption sites in aqueous solution increased with the increase of the LDH, the concentration of adsorption sites with higher energy may lead to the reduction of active sites with lower energy, resulting in the reduction of adsorption (Zubair et al. 2017). Therefore, reducing the amount of LDH can not only improve the removal rate of GO in the aqueous solution but also save costs.

Effect of GO Initial Concentration

The removal of GO on LDH were studied with different GO initial concentrations of 20, 40, 60, 80, 100, 120, 140 and 160 mg/L, respectively. The result demonstrates the removal capabilities are influenced by GO initial concentrations. Fig. 5 shows the effect of GO concentration on adsorption capacity, efficiency, and distribution coefficient. In the solution with pH 3.0 and LDH = 10mg, the GO concentration was changed to 20-160mg/L, the equilibrium time was 6h, and the corresponding tests were carried out. There is little difference at GO initial concentration less than 60 mg/L, maintain at 60%. However, it can be seen from the Fig. 5 that as the GO concentration increases, the removal rate gradually increases and tends to 92%, the fastest rising stage is within the range of 60-100 mg/L, there is a similar trend in adsorption amount and distribution coefficient. This shows that, while maintaining LDH to a certain extent, adding GO can greatly improve the adsorption capacity of LDH, this may be due to the increased GO concentration increasing the electrostatic interaction with LDH.

Therefore, between the above description, LDH has great potential for the adsorption of GO in aqueous solution. Due to the limitation of the experimental conditions, the maximum adsorption amount of GO for further research is still needed.

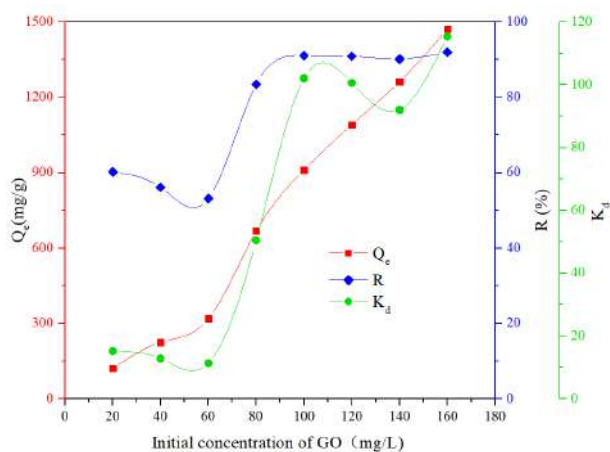


Fig. 5: Removal of GO on LDH as a function of GO contents.

Adsorption Mechanism

To further explore the adsorption mechanism of LDH to GO, the LDH/GO solution of pH=3 was analysed by XPS and AFM, and the results are shown in Fig. 6 and Fig. 7. As shown in Fig. 6 (a), various strong peaks can be observed, such as Al 2p, Mg 1s, Ca 2p, S 2p, O 1s, C 1s. From the C 1s high-resolution spectra before and after the adsorption of GO, the C1 spectral deconvolution can be divided into three components, which are about 284.7 eV, 285.8 eV, and 289.3 eV, respectively. However, after the adsorption and condensation of GO, the strength and position of the C 1s component of LDH/GO changed obviously. Compared with

that before the adsorption of GO, the relative area of C-O and O-C=O assigned to LDH/GO after GO adsorption increased significantly, and the peak position of O-C=O changed from 289.3 eV to 287.8 eV. The interaction between GO and LDH is carried out by C-O and O-C=O during the coagulation process. From the height of the AFM image and its corresponding morphology, the thickness of GO is 2.78 nm, and the thickness of LDH/GO is 3.89 nm, which indicates that GO is adsorbed on the surface of LDH, which is consistent with the TEM results. Based on the above analysis, it is shown that through the condensation of GO on the surface of LDH, LDH can effectively remove GO.

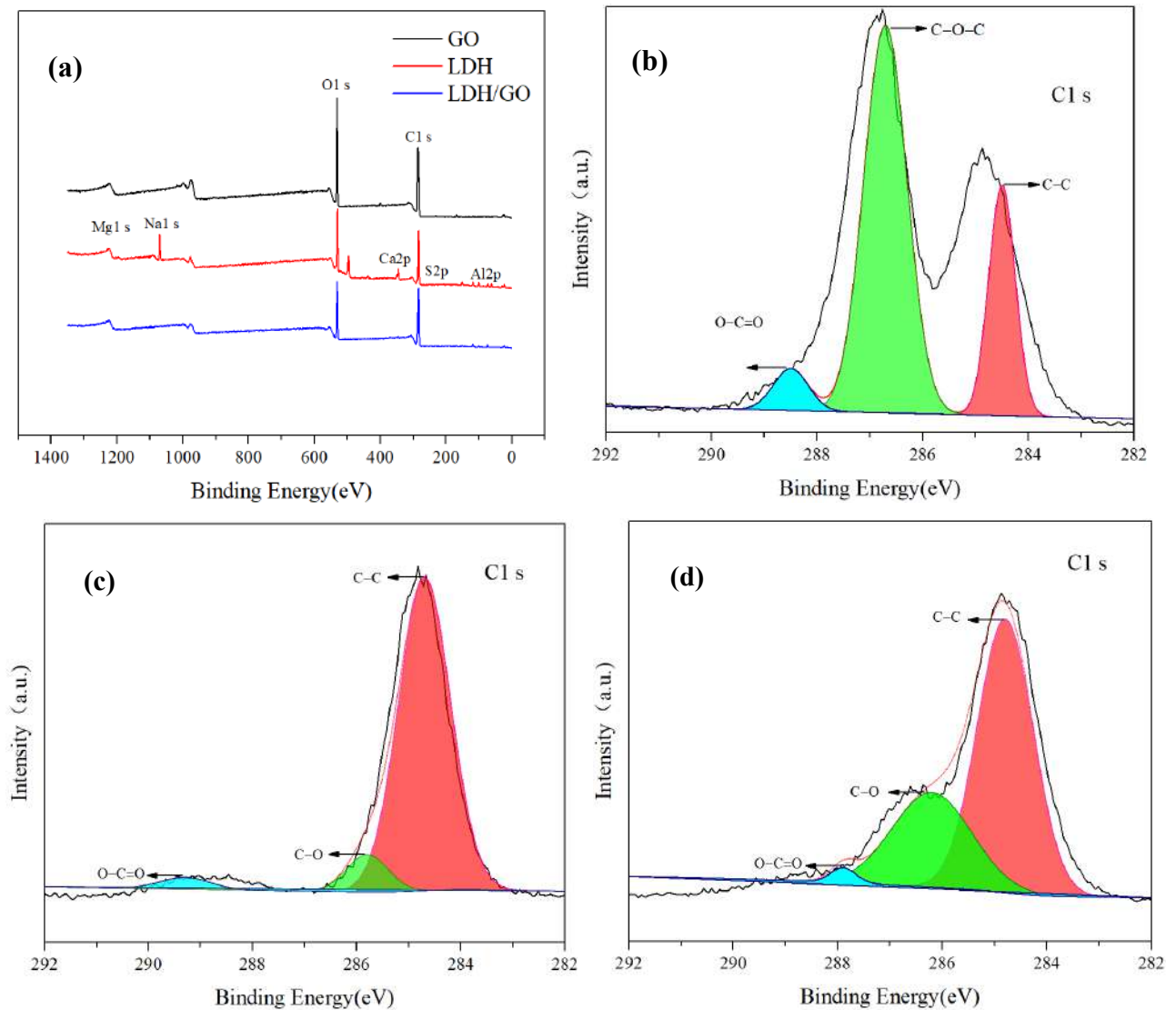


Fig. 6: XPS spectra of LDH/GO before and after GO removal (a), the high C 1s deconvolution of GO (b), before (c), and after (d) GO coagulation on LDH/GO.

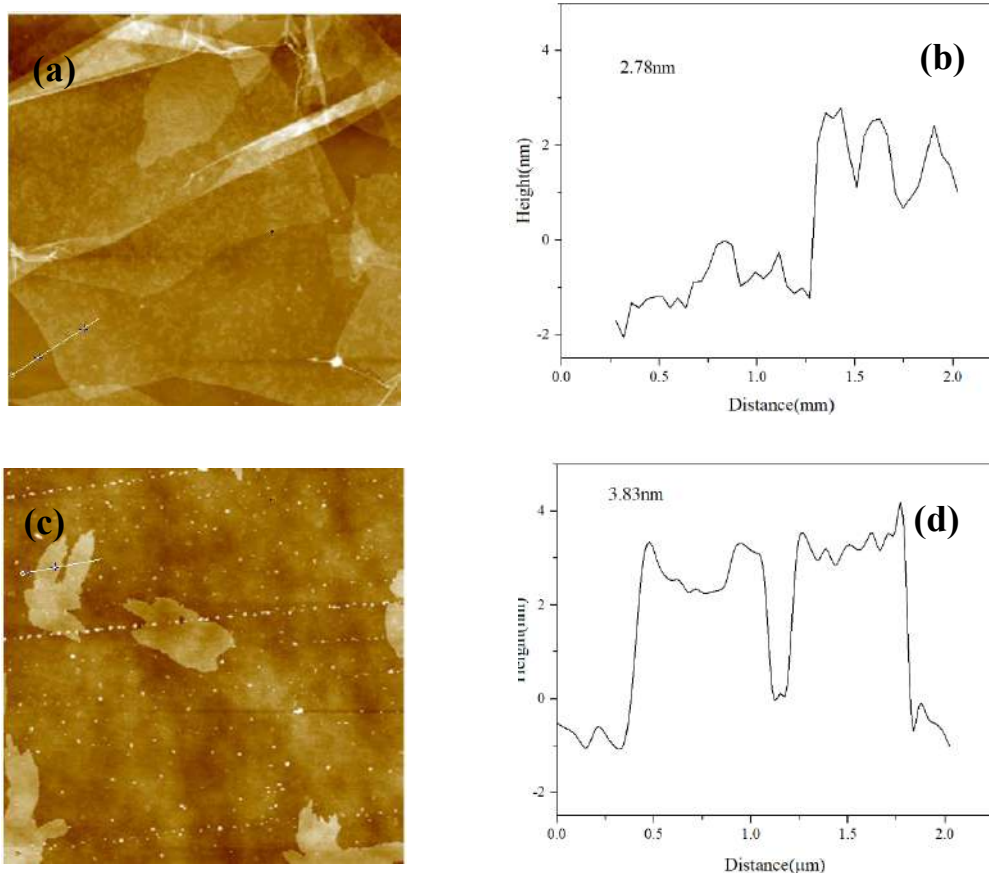


Fig. 7: AFM image and the corresponding height profiles of GO (a) (b) and LDH/GO (c) (d).

CONCLUSION

With the rapid development and wide application of GO products, it is inevitable to release them into the natural environment. Therefore, the rapid coagulation of GO is particularly important and urgent due to its high activity and toxicity in the environment. Here, we found that LDH can effectively remove GO from the aqueous solution and came to some meaningful conclusions: The significant change in GO removal indicates that the coagulation behaviour is pH dependent. Its adsorption capacity depends largely on the pH of the solution, LDH content, and GO content, the maximum removal rate of GO by LDH can reach 92%, the adsorption capacity can reach 1472 mg/g. On the other hand, XPS spectroscopy has been fully studied, the interaction between GO and LDH is carried out by C-O and O-C=O during the coagulation process.

In a word, LDH material has high condensation ability to GO in aqueous solution, which indicates that LDH material can be a promising material to effectively remove GO from

aqueous solution by simple and rapid chemical condensation. Therefore, the results of this work may contribute to a better understanding of the condensation behaviour of GO and other carbon-based materials in natural and engineering aqueous solutions, which is essential for eliminating GO in aqueous solutions and reducing the environmental toxicity of GO in natural environments.

REFERENCES

- Awad, F. S., Abou Zied, K. M., Abou El-Maaty, W. M., El-Wakil, A. M. and Samy El-Shall, M. 2020. Effective removal of mercury (II) from aqueous solutions by chemically modified graphene oxide nanosheets. *Arabian Journal of Chemistry*. 13(1): 2659-2670.
- Azadian, E., Arjmand, B., Ardeshiryajimi, A., Hosseinzadeh, S., Omidi, M. and Khojasteh, A. 2020. Polyvinyl alcohol modified polyvinylidene fluoride-graphene oxide scaffold promotes osteogenic differentiation potential of human induced pluripotent stem cells. *J. Cell. Biochem.*, 121(5-6): 3185-3196.
- Bao, S., Yang, W., Wang, Y., Yu, Y. and Sun, Y. 2020. One-pot synthesis of magnetic graphene oxide composites as an efficient and recoverable adsorbent for Cd(II) and Pb(II) removal from aqueous solution. *J. Hazard Mater.*, 381: 120914.

- Baragaño, D., Forján, R., Welte, L. and Gallego, J.L.R. 2020. Nanoremediation of As and metals polluted soils by means of graphene oxide nanoparticles. *Scientific Reports*, 10(1).
- Batista de Melo, C., Coa, F., Alves, O. L., Martinez, D. S. T. and Barbieri, E. 2019. Co-exposure of graphene oxide with trace elements: Effects on acute ecotoxicity and routine metabolism in *Palaemon pandaliformis* (shrimp). *Chemosphere*, 223: 157-164.
- Chang, K., Sun, Y., Ye, F., Li, X., Sheng, G., Zhao, D., Linghu, W., Li, H. and Liu J. 2017. Macroscopic and molecular study of the sorption and co-sorption of graphene oxide and Eu(III) onto layered double hydroxides. *Chemical Engineering Journal*, 325: 665-671.
- Duru, ., Ege, D. and Kamali, A. R. 2016. Graphene oxides for removal of heavy and precious metals from wastewater. *Journal of Materials Science*, 51(13): 6097-6116.
- Gao, Y., Ren, X., Zhang, X. and Chen, C. 2019. Environmental fate and risk of ultraviolet- and visible-light-transformed graphene oxide: A comparative study. *Environ. Pollut.*, 251: 821-829.
- Goh, K. H. and Lim, T. T. 2010. Influences of co-existing species on the sorption of toxic oxyanions from aqueous solution by nanocrystalline Mg/Al layered double hydroxide. *J. Hazard. Mater.*, 180(1-3): 401-408.
- González, M. A., Pavlovic, I., Rojas-Delgado, R. and Barriga C. 2014. Removal of Cu²⁺, Pb²⁺, and Cd²⁺ by layered double hydroxide-humate hybrid. Sorbate and sorbent comparative studies. *Chemical Engineering Journal*, 254: 605-611.
- Hu, B., Huang, C., Li, X., Sheng, G., Li, H., Ren, X., Ma, J., Wang, J. and Huang, Y. 2017. Macroscopic and spectroscopic insights into the mutual interaction of graphene oxide, Cu(II), and Mg/Al layered double hydroxides. *Chemical Engineering Journal*, 313: 527-534.
- Liang, S., Xu, S., Zhang, D., He, J. and Chu, M. 2015. Reproductive toxicity of nanoscale graphene oxide in male mice. *Nanotoxicology*, 9(1): 92-105.
- Liu, Y., Yang, D., Xu, T., Shi, Y., Song, L. and Yu, Z.Z. 2020. Continuous photocatalytic removal of chromium (VI) with structurally stable and porous Ag/Ag₃PO₄/reduced graphene oxide microspheres. *Chemical Engineering Journal*, 379: 122200.
- Paital, B., Guru, D., Mohapatra, P., Panda, B., Parida, N., Rath, S., Kumar, V., Saxena, P. S. and Srivastava A. 2019. Ecotoxic impact assessment of graphene oxide on lipid peroxidation at mitochondrial level and redox modulation in freshwater fish *Anabas testudineus*. *Chemosphere*, 224: 796-804.
- Pang, H., Wu, Y., Wang, X., Hu, B. and Wang, X. 2019. Recent advances in composites of graphene and layered double hydroxides for water remediation: a review. *Chemistry-An Asian Journal*, 14(15): 2542-2552.
- Rao, M. M., Reddy, B. R., Jayalakshmi, M., Jaya, V. S. and Sridhar, B. 2005. Hydrothermal synthesis of Mg-Al hydroxalicates by urea hydrolysis. *Materials Research Bulletin*, 40(2): 347-359.
- Song, S., Yin, L., Wang, X., Liu, L., Huang, S., Zhang, R., Wen, T., Yu, S., Fu, D., Hayat, T. and Wang, X. 2018. Interaction of U(VI) with ternary layered double hydroxides by combined batch experiments and spectroscopy study. *Chemical Engineering Journal*, 338: 579-590.
- Tang, H., Zhang, S., Huang, T., Cui, F. and Xing, B. 2020. pH-dependent adsorption of aromatic compounds on graphene oxide: An experimental, molecular dynamics simulation and density functional theory investigation. *Journal of Hazardous Materials*, 395: 122680.
- Wang, J., Wang, X., Tan, L., Chen, Y., Hayat, T., Hu, J., Alsaedi, A., Ahmad, B., Guo, W. and Wang, X. 2016. Performances and mechanisms of Mg/Al and Ca/Al layered double hydroxides for graphene oxide removal from aqueous solution. *Chemical Engineering Journal*, 297: 106-115.
- Wang, X., Yu, S., Wu, Y., Pang, H., Yu, S., Chen, Z., Hou, J., Alsaedi, A., Hayat, T. and Wang, S. 2018. The synergistic elimination of uranium (VI) species from aqueous solution using bi-functional nanocomposite of carbon sphere and layered double hydroxide. *Chemical Engineering Journal*, 342: 321-330.
- Wu H.Y., Li, S.T., Shao, Y.W., Jin, X.Z., Qi, X.D., Yang, J.H., Zhou, Z.W. and Wang, Y. 2020. Melamine foam/reduced graphene oxide supported form-stable phase change materials with simultaneous shape memory property and light-to-thermal energy storage capability. *Chemical Engineering Journal*, 379: 122373.
- Xing, M., Zhuang, S. and Wang, J. 2020. Efficient removal of Cs(I) from aqueous solution using graphene oxide. *Progress in Nuclear Energy*, 119: 103167.
- Yang, D., Song, S., Zou, Y., Wang, X., Yu, S., Wen, T., Wang, H., Hayat, T., Alsaedi, A. and Wang, X. 2017. Rational design and synthesis of monodispersed hierarchical SiO₂@layered double hydroxide nanocomposites for efficient removal of pollutants from aqueous solution. *Chemical Engineering Journal*, 323: 143-152.
- Yang, K., Li, Y., Tan, X., Peng, R. and Liu, Z. 2013a. Behavior and toxicity of graphene and its functionalized derivatives in biological systems. *Small*, 9(9-10): 1492-1503.
- Yang, Z., Yan, H., Yang, H., Li, H., Li, A. and Cheng, R. 2013b. Flocculation performance and mechanism of graphene oxide for removal of various contaminants from water. *Water Res.*, 47(9): 3037-3046.
- Yu, C., Shao, J., Sun, W. and Yu, X. 2020. Treatment of lead contaminated water using synthesized nano-iron supported with bentonite/graphene oxide. *Arabian Journal of Chemistry*, 13(1): 3474-3483.
- Yu, S., Wang, X., Chen, Z., Wang, J., Wang, S., Hayat, T. and Wang X. 2017. Layered double hydroxide intercalated with aromatic acid anions for the efficient capture of aniline from aqueous solution. *Journal of Hazardous Materials*, 321: 111-120.
- Zhang, Z., Liu, X., Wu, J., Ren, X. and Li, J. 2020. Insight into the removal of graphene oxide by nanoscale zero-valent iron. *Journal of Molecular Liquids*, 314: 113553.
- Zou, Y., Wang, X., Ai, Y., Liu, Y., Li, J., Ji, Y. and Wang, X. 2016. Coagulation behavior of graphene oxide on nanocrystalline Mg/Al layered double hydroxides: Batch experimental and theoretical calculation study. *Environ. Sci. Technol.*, 50(7): 3658-3667.
- Zubair, M., Daud, M., McKay, G., Shehzad, F. and Al-Harhi, M. A. 2017. Recent progress in layered double hydroxides (LDH)-containing hybrids as adsorbents for water remediation. *Applied Clay Science*, 143: 279-292.



Accumulation and Translocation of Chromium (Cr) and Lead (Pb) in Chilli Plants (*Capsicum annuum* L.) Grown on Artificially Contaminated Soil

F. Ahmed*†, A. N. M. Fakhruddin**, Z. Fardous***, M. A. Z. Chowdhury***, M. M. Rahman*** and M. M. Kabir****

*Department of Environmental Science, Bangladesh University of Professionals, Mirpur Cantonment, Dhaka, Bangladesh

**Department of Environmental Sciences, Jahangirnagar University, Savar, Dhaka 1342, Bangladesh

***Agro-chemical and Environmental Research Division, Institute of Food and Radiation Biology, Atomic Energy Research Establishment, Savar, Dhaka 1349, Bangladesh

****Department of Environmental Science and Disaster Management, Noakhali Science and Technology University, Noakhali-3814, Bangladesh

†Corresponding author: F. Ahmed; fowzia.ahmed@bup.edu.bd

Nat. Env. & Poll. Tech.
Website: www.neptjournal.com

Received: 15-06-2020

Revised: 18-09-2020

Accepted: 09-10-2020

Key Words:

Chromium

Lead

Health risk index

Carcinogenic risks

Capsicum annuum L.

ABSTRACT

The current study is an endeavour to measure the bioaccumulation potentials of heavy metals in different parts of chilli plants (*Capsicum annuum* L.) grown in artificially contaminated soil with various concentrations of Cr and Pb. The concentrations of heavy metals were estimated by Atomic Absorption Spectroscopy (AAS) technique. The mean concentration of Cr and Pb accumulated in different parts of plants in high, medium, and low levels of contamination was in the following order: roots > leaves > shoots > fruits. Cr concentration in fruits was lower than that of the WHO standard. However, fruits grown on medium contaminated soil contained 0.695 mg/kg Cr which did not follow the safe guideline by SEPA. A significant amount of Pb was traced in fruits grown in highly contaminated soil that exceeded the standard limit set by FAO/WHO. Accumulation of Pb was higher than Cr at different levels of contamination in every part of the chilli plants. The transfer factor for Cr and Pb was found in the following order, leaves > shoots > fruits > roots and leaves > shoots > roots > fruits, correspondingly at every level of contamination. The bioconcentration factors were higher in Pb than Cr. The daily intake of metals in combination with health and carcinogenic risk indexes indicated that the edible parts of chilli plants are safe to consume as recommended by SEPA/WHO/FAO. The present study can be considered a reference for assessment and monitoring of heavy metals associated with human health risks in chilli plants at different industrially contaminated sites.

INTRODUCTION

Since the enhancement of industrialization, heavy metal pollution in soil and water has become a widespread phenomenon that can pose a threat to human and biotic life. Because of low biodegradability, heavy metals accumulate in the soil adjacent to industrial areas. Crops grown in contaminated soil can accumulate heavy metals in their edible parts and cause serious health issues to both human and animal consumers (Sarma et al. 2011). Not only human health but also plants are affected by heavy metal contamination in many ways. Plant growth, seed germination, metabolism, chlorophyll content, etc. are affected by heavy metal pollution in the soil (Pandey & Sharma 2002, Aydinalp & Marinova 2009). Contamination of toxic heavy metals has been rapidly spreading in the crop fields of Bangladesh. Due to industrial development, some of the regions of Bangladesh such as Gazipur,

Savar, Narayanganj (Hossain et al. 2015), Tangail (Proshad et al. 2019), etc. are getting highly polluted by the contamination of heavy metals. Buriganga, Sitalakhya and Turag are some of the polluted rivers around Dhaka city. Heavy metals dissolved in industrial water are severely polluting the sediments of these rivers. A high concentration of heavy metals has been found in different crops of Bangladesh, for example, paddy (Halim et al. 2014), vegetables (Naser et al. 2012), spices (Gleason et al. 2014), etc. Heavy metals enter into the human body through the consumption of the edible parts of these plants. Although some metals are necessary for biochemical and physiological functions, a good number of them cause numerous complications in human health. The nervous system, kidney, liver and other organs of the human body suffer from cancer and other complicated diseases as a result of heavy metal consumption (Karbassi et al. 2018).

Chilli (*Capsicum annum* L.) is one of the most popular spices in Bangladesh. The use of chilli is found indispensable in the preparation of dishes ranging from green salad to red curries. Chillies have been a part of the regular human diet in Bangladesh (BBS 2015). The chilli belongs to the Solanaceae family, having a variety of names depending on its production location and type. Chillies are small in size and widely used as spices for their sharp, acidic flavour and colour (BBS 2015). A significant amount of vitamins A and C are found in chillies which are essential for human health. Chillies also contain a wide variety of minerals such as potassium, magnesium and iron. Like other vegetables of Solanaceae family, the chilli plant accumulates and translocates heavy metals from soil to its fruits (Guertin 2004). Heavy metals can accumulate in the root, shoot, and fruits of chilli at its different growth stages. Among the heavy metals, Cr and Pb and their compounds are widely used in the industrial sectors. Chromium (VI) consumption may cause adverse gastrointestinal effects, including abdominal pain, vomiting, gastrointestinal ulceration, haemorrhage and necrosis, and bloody diarrhoea (Guertin 2004, Kabir et al. 2017, Kabir et al. 2018). Consumption of lead is also lethal for human health; it is six-times toxic than absorbed by the skin. Repetitive consumption of lead and chromium through food like chilli may cause a serious health impact on human (Akintan et al. 2019).

This study aims to determine the accumulation and translocation of Cr and Pb in different parts of chilli plants (roots, shoots, leaves, and fruits) grown in artificially contaminated soil with various concentrations of Cr and Pb which is the first of its kind, so far, reporting bioaccumulation potentials of chilli plants. This study will be a baseline for future environmental contaminant's human health risk identification in chilli plants at the field level of Bangladesh.

MATERIALS AND METHODS

Soil Preparation

The soil sample was collected from the arable horizon (0-30 cm depth) of the Botanical garden of Jahangirnagar University, Dhaka. The soil was mixed with cow dung as an amendment. Under room temperature, the soil was air-dried, cleansed to remove grass and dirt, and ground. Every 4 L of plastic pot was filled with 3 kg of soil, which was sprayed with different concentrations of chromium (Cr) and lead (Pb). The stock solutions of varying levels of Cr and Pb were prepared by $K_2Cr_2O_7$ and $Pb(NO_3)_2$, respectively, and sprayed onto the soil samples with continuous mixing to homogenize the distribution of the applied heavy metals. Four levels (0, 100, 200 and 400 mg/kg soil) of Cr and Pb

such as unadulterated, low, medium and high levels respectively were sprayed distinctly in soil with three replicates. The spiked soils were allowed to be air-dried for one hour.

Soil Sample Preparation and Digestion

With the addition of concentrated HNO_3 acid and concentrated $HClO_4$ acid, soil samples were digested for heavy metal determination (Allen et al. 1986). One g of homogenized composite soil sample was taken into the clean beaker, and 10 mL of 65% concentrated HNO_3 acid and 5 mL of 70% concentrated $HClO_4$ acid were added to it. Then the mixture was heated in a hot plate at different temperatures up to dryness in a fume chamber. After cooling it down, the beaker was washed with distilled water, and the mixture was transferred into a volumetric flask to make the volume to 50 mL. Then the solution was filtered into a plastic bottle through Whatman No. 1 and finally taken for heavy metals determination by Atomic Absorption Spectroscopy (AAS).

Quality Control and Quality Assurance

Quality control and quality assurance have been integrated into this study. Representative standards of the heavy metals (Cr and Pb) at four different levels (0, 100, 200 and 400 ppm) were spiked into the soil free of heavy metals. The mixed soil was allowed to be air-dried for one hour. After that, it was analysed according to the following procedure (Chowdhury et al. 2013). By using the following equation, the percentage of recovery was calculated.

$$\text{Percentage recovery} = (\text{CE}/\text{CM} \times 100) \quad \dots(1)$$

Where, CE is the experimental concentration and CM is the spiked concentration.

Percentage recoveries of the tested metals in soil samples were 77.5% to 91.84% (Table 1). According to the European Commission, the data between 70%-110% indicate that the method is accurate and precise.

Table 1: The percentage of recoveries of tested metals from soil samples.

Heavy Metals	Concentration (mg/kg)	Concentration (mg/kg)		
		Spiked	Measured	Recovery %
Chromium (Cr)	Control	0.00	1.148	-
	Sample-1	400	310.275	77.5%
	Sample-2	200	169.274	84.64%
	Sample-3	100	87.512	87.50%
Lead (Pd)	Control	0.00	0.186	-
	Sample-1	400	318.657	79.66%
	Sample-2	200	168.978	84.49%
	Sample-3	100	91.847	91.84%

Growth of Chilli (*Capsicum annuum*) Plants in Artificially Contaminated Soil

Chilli (black cobra peepers) plant saplings were collected from a nursery nearby Jahangirnagar University. They were about 4-5 inches in height and planted in the artificially contaminated soil. Plants were irrigated with tap water and allowed to grow until fruits came out. For the blank sample, four levels of Cr and Pb (0, 100, 200 and 400 mg/kg soil) contaminated soil with three replicates remain kept without any plant.

Plant Material Digestion

Different parts of chilli plants were collected and washed in distilled water. All the parts of the plants were oven-dried. Then they were crushed with a mortar and stored in a plastic container. The powdered samples were placed into the crucible, to which 10 mL of 65% concentrated HNO₃ acid and 5 mL of 70% concentrated HClO₄ acid were added. Then the mixture was heated in a hotplate at different temperatures up to dryness in a fume chamber. Then, samples were cooled and filtered through Whatman No. 1 filter paper. The volume of the residues was made up to 50 mL. Finally, the solution was ready for analysis.

Determination of Heavy Metal Concentrations of Soil and Plant Samples

Atomic Absorption Spectroscopy (AAS) (Model: AA-6300, Atomic Absorption Flame Spectrophotometer, SHIMADZU, Japan) was used for the determination of heavy metals as described by Allen et al. (1986).

Transfer Factor (TF)

The transfer factor was calculated to determine the translocation of heavy metals from soil to different parts of the plants (Lawrence & Borkowsky 1983). To determine the transfer factor, the concentration of heavy metals in the root of *Capsicum annuum* was divided by the total heavy metal concentrations in soil. Transfer of heavy metals from root to shoot, shoot to leaves, and leaves to fruit was also determined by using the following equation.

$$TF = \frac{\text{Concentration of metal in root}}{\text{Concentration of metal in soil}} \quad \dots(2)$$

Bioconcentration Factor (BCF)

The BCF of metal is an index that determines a plant's capacity to accumulate a specific metal regarding its concentration in the soil. It is a valuable indicator of the bioaccumulation potential of a substance. BCF was calculated by determining the ratio of the concentration of a metal in a plant to the concentration in the soil. The equation is given below.

$$BCF = \frac{\text{Metal concentration in plant tissue (whole plant)}}{\text{Initial concentration of metal in substrate (soil)}} \quad \dots(3)$$

The high BCF value indicates the more suitability of plant for phytoextraction (Mackay 1982).

Daily Intake of Heavy Metals (DIM)

The daily intake of heavy metals was calculated by the multiplication of the concentration of heavy metals in vegetables with conversion factors and daily intake of vegetables. Then, this value was divided by the average body weight. The determination of DIM value was calculated according to the following equation (Khan et al. 2009).

$$DIM = C_{\text{metal}} \times C_{\text{factor}} \times F_{\text{ood intake}} / B_{\text{average weigh}} \quad \dots(4)$$

Where, M_{etal} = heavy metals concentration in vegetables (mg/kg), C_{factor} = conversion factor of 0.085, $F_{\text{ood intake}}$ = daily intake of vegetables (kg/day) and $B_{\text{average weight}}$ = average body weight, kg. An estimated value of the daily intake of chilli is 15 g per day per person, and the average weight is 60 kg.

Health Risk Index (HRI)

The health risk index of Cr and Pb by consumption of contaminated chilli was estimated by dividing the DIM to oral reference dose RfD values.

$$HRI = DIM/RfD \quad \dots(5)$$

R_{fD} is the USEPA's highest tolerable oral dose of a lethal substance.

In this study, the oral reference dose values for Cr (0.003 mg kg⁻¹ per day) and Pb (0.0035 mg kg⁻¹ per day) were considered as described by WHO (1993). The safe health risk index for the exposed population is not more than 1 (Tsafe et al. 2012).

Carcinogenic Risk (CR)

Carcinogenic risk (CR) is an index which determines the risk of cancer. It can be calculated by using the following equation, which was modified from Shaheen et al. (2016).

$$CR = DIM/CSFo \quad \dots(6)$$

Here, CSFo is the oral carcinogenic slope factor, which was 0.0085 mg/kg/day for Pb and 0.041 mg/kg/day for As (USEPA 2017).

RESULTS AND DISCUSSION

Effects on Chilli Plants Grown in Artificially Contaminated Soil by Cr and Pb

Consumption and distribution of total chromium and lead (mg/kg) in different parts of chilli (*Capsicum annuum* L.) plants have been illustrated in Table 2. By evaluating the similarities

with control, all parts of the chilli plant accumulated Cr and Pb. Roots exhibit the highest concentration of both Cr and Pb at high, medium and low levels of contamination. Leaves accumulated a significant amount of chromium and lead than shoot, and translocation from shoot to leaves was higher than any other parts of the plants. Moreover, in the case of both metals, translocation from soil to fruit was not so high. The average concentration of chromium and lead in different parts of chilli plants in high, medium, and low levels of contaminations were found to decrease in the order of roots > leaves > shoots > fruits.

Table 3 represents the safe limit of heavy metal concentration in vegetables (mg/kg) which indicated that the Cr concentrations in fruits were found much lower compared to the WHO standard. However, fruits of medium contamination (0.695 ± 0.151 mg/kg) slightly exceeded the safe limit of 0.5 mg/kg given by USEPA 2005. At a low contamination level, the chilli plant accumulated only 0.248 ± 0.156 mg/kg of Cr. In this study, Cr did not yield any fruits at a high level of contamination. The plant growth was considerably hampered because of the high concentration of Cr. Growth reduction and biomass accumulation had been caused due to the high toxicity of Cr (Iqbal et al. 2001). Photosynthesis, respiration, water and minerals intake mechanisms are significantly disturbed by Cr accumulation (Dube et al. 2003). Accumulation of Cr is responsible for the reduction of starch and nitrogen metabolism. It can directly influence the enzyme activity or production of reactive oxygen species (Singh et al. 2013). Mellem et al. (2009) examined a similar study on translocation and accumulation of Cr in *Amaranthus dubius* and reported that Cr is stored in the roots of plants, and a few of them translocate to the aerial parts too. Similar results have been observed in the current study suggesting the roots of

the chilli plant accumulated more Cr than other parts. Fruits did not exceed the safe limit of Pb accumulation, according to both FAO/WHO (1985) and USEPA (2005) (Table 3).

However, fruits of high contamination exceeded the safe limit of 0.3 mg/kg given by FAO/WHO (2001). Lead (Pb) accumulation in the medium and low level of contamination was found 0.881 ± 0.410 mg/kg and 0.530 ± 0.139 mg/kg, respectively. According to Lima et al. (2009), Pb accumulation in different parts of vegetable plants was found in the following order, root > stems > leaves > edible parts where the plants were grown on the soil contaminated by battery recycling waste. However, the current study shows the order of leaves > shoots > fruits for Pb accumulation. Pb and Ni accumulation were found in the greatest concentration in Cauliflower and cabbage (Singh et al. 2012). Gupta et al. (2007) reported a diverse variety of vegetables grown on exaggeratedly contaminated soil and all the vegetables accumulated heavy metals (Pb, Zn, Cd, Cr and Ni) which concentrations exceeded the safe limits. Hung et al. (2014), investigated a similar study and found that roots of the okra plant (*Abelmoschus esculentus*) accumulated more lead than the leaves and fruits, which is similar to the current study.

Comparison Between Accumulation of Cr and Pb in Different Parts of Chilli Plants

In the body of the plants, accumulation varies from metal to metal. There are both similarities and differences in the accumulation of Cr and Pb in the plants. The similarity between elemental distribution appeared in both metals and was found in the decreasing order: roots > leaves > shoot > fruits. At every level of contamination, the accumulation of Pb was higher than Cr in every part of the chilli plants. At high concentration, accumulations of Pb in roots were two

Table 2: Uptake and distribution of total chromium (mg/kg) and lead (mg/kg) in different parts of chilli plant.

Level of contamination	Average Concentration of Cr (mg/kg)				
	Soil	Roots	Shoots	Leaves	Fruits
Control	1.489 ± 0.441	0.165 ± 0.035	0.087 ± 0.022	0.094 ± 0.018	0.048 ± 0.013
High	65.448 ± 6.136	7.932 ± 1.40	2.780 ± 0.303	3.013 ± 0.749	NA
Medium	31.088 ± 2.093	5.906 ± 0.653	1.978 ± 0.996	2.641 ± 0.657	0.695 ± 0.151
Low	10.302 ± 1.172	1.904 ± 0.934	0.905 ± 0.233	1.257 ± 0.41	0.248 ± 0.156
Level of contamination	Average Concentration of Pb (mg/kg)				
	Soil	Roots	Shoots	Leaves	Fruits
Control	0.161 ± 0.091	0.303 ± 0.137	0.09 ± 0.019	0.283 ± 0.054	0.161 ± 0.031
High	71.054 ± 6.698	17.035 ± 8.33	6.362 ± 2.138	9.925 ± 2.568	1.986 ± 0.694
Medium	28.088 ± 6.297	7.008 ± 2.283	2.522 ± 0.511	3.708 ± 0.319	0.881 ± 0.410
Low	14.302 ± 5.216	4.087 ± 2.018	1.681 ± 0.444	2.566 ± 0.370	0.530 ± 0.139

NA=Not Available

Table 3: Safe limit of heavy metal concentration in vegetable (mg/kg).

Metal	Safe limit ^a	Safe limit ^b	Safe limit ^c
Cr	2.3	5	0.5
Pb	0.3	5	9
Cd	0.2	0.3	0.2
Cu	73.5	40	20

^aFAO/WHO standard (Codex Alimentarius Commission, 2001); ^bFAO/WHO standard (Codex Alimentarius Commission, 1985); ^cSEPA (2005)

times higher than the accumulation of Cr. Pb concentration in shoots and leaves were approximately three times higher than Cr at a high level of contamination. At this level, no plants grown in Cr contaminated soil yielded fruits. At the medium level of contamination, the difference between the accumulation of Cr and Pb was not so high. In comparison with high levels, accumulations in roots, shoots, leaves, and fruits were close to each other. Roots accumulated two times higher Pb than Cr at a low level of contamination. Pb accumulation in fruits was significantly higher than Cr. Moreover, Pb exceeded the safe level of 0.3 mg/kg suggested by FAO/WHO (2001). The accumulation trend of Pb was root > leaves > shoots, which is completely similar to this study and the order of Cr accumulation was slightly dissimilar (root > shoots > leaves).

Transfer of Heavy Metals from Contaminated Soil to Different Parts of Chilli Plants

The transfer factor (TF) of chromium and lead from soil to root, root to shoot, shoot to leaves, and leaves to fruits of chilli plants have been illustrated in Table 4. TF of both Cr and Pb for soil to root was the lowest at three levels of contamination. The highest TF values were found in the shoot to leaves because shoots accumulated less concentration of metals than leaves. At a low level of contamination, the

transfer factor was higher among different organs of the plants. The TF values of Cr maintained the order: leaves > shoots > fruits > roots at every level of contamination. Zayed et al. (1998) reported Cr accumulation in roots and shoots of vegetable plants in various chemical forms such as Cr³⁺ and CrO₄²⁻ and recommended that roots accumulation was 100 times higher than shoots, which indicates that the translocation from root to shoot is very limited.

The TF values of Pb were found in the following order: leaves > shoots > roots > fruits at every level of contamination. Transfer factors for leaves to fruits were 0.20, 0.23, and 0.21 for high, medium, and low levels of contamination, respectively. Several studies were conducted to determine the transfer factor (TF) of Cr and Pb in various types of plants, especially vegetables. Table 5 illustrates the comparison of TF values of Cr and Pb of previous studies and present one. The plants grown on heavy metal contaminated soil, accumulate and transfer Cr and Pb from the soil such as metal-scrap dumpsite (Yashim et al. 2014), ferro-alloy manufactory site (Liao et al. 2011), domestic sewage sludge (Jamali et al. 2009) etc. It is evident from the earlier investigations that the TF value of most plants was <1, which is analogous to the present study. Leafy vegetables like Red spinach (*Basella alba*) can translocate a high amount of metals than other plants (Akhtaruzzaman et al. 2013).

Bio-Concentration Factor (BCF)

The Bioconcentration Factor (BCF) Index symbolizes the capability of the chilli plant to extract heavy metals from the soil. Table 6 illustrates the BCF of Cr and Pb from the soil to the whole chilli plant. However, the highest BCF value was found on a medium level of contamination, which was 0.07 and 0.04 was the lowest value found on a high level of contamination. In every level of contamination, Pb was higher

Table 4: Transfer factor of Cr and Pb from soil to different parts (roots, shoots, leaves, and fruits) of chilli plant.

Transfer factor (TF) for Cr				
Level of contamination	TF for soil to roots	TF for root to shoots	TF for the shoot to leaves	TF for leaves to fruits
High	0.12	0.27	1.08	NA
Medium	0.11	0.33	1.33	0.26
Low	0.18	0.47	1.39	0.20
Mean	0.14	0.36	1.27	0.23
Transfer factor (TF) for Pb				
Level of contamination	TF for soil to roots	TF for root to shoots	TF for the shoot to leaves	TF for leaves to fruit
High	0.24	0.37	1.56	0.20
Medium	0.25	0.36	1.47	0.23
Low	0.29	0.41	1.52	0.21
Mean	0.26	0.38	1.52	0.21

Table 5: Comparison of transfer factors of Cr and Pb of different plant species with the present study.

Name of the studied plants	Transfer factor (TF): Soil to plants		References
	Cr	Pb	
Paddy (<i>Oryza sativa</i>)	1.97	0.29	Payus et al. (2015)
Red spinach (<i>Basella alba</i>)	1.173-3.83	0.695-3.155	Akhtaruzzaman et al. (2013)
Spinach (<i>Spinacia oleracea</i> L)	0.91	0.50	Tiwari et al. (2010)
Tomato (<i>Lycopersicon esculentum</i>)	0.009	0.008	Jolly et al. (2013)
	0.39	0.70	Tiwari et al. (2010)
Cauliflower (<i>Brassica oleracea</i>)	0.008	0.015	Jolly et al. (2013)
Celery (<i>Apium graveolens</i>)	0.002	-	Liao et al. (2011)
Lettuce (<i>Lactuca sativa</i>)	0.03	-	Liao et al. (2011)
Cabbage (<i>Brassica oleracea</i>)	0.04	-	Liao et al. (2011)
	-	0.339	Radulescu et al. (2013)
	0.58	0.50	Tiwari et al. (2010)
Orange (<i>Citrus reticulata</i>)	0.59	0.33	Mbong et al. (2014)
Radish (<i>Raphanus sativus</i>)	0.029	0.034	Jolly et al. (2013)
	0.58	0.70	Tiwari et al. (2010)
Maize (<i>Zea mays</i>)	-	0.166	Lato et al. (2012)
Eggplant (<i>Solanum melongena</i>)	-	1.93	Yashim et al. (2014)
	0.63	0.60	Tiwari et al. (2010)
Chilli (<i>Capsicum annum</i>)	0.83	0.40	Tiwari et al. (2010)
Chilli (<i>Capsicum annum</i>)	High contamination	0.21	Present study
	Medium contamination	0.36	
	Low contamination	0.42	

than Cr. BCF values for Pb are 0.11, 0.09 and 0.10 for high, medium and low levels of contamination, respectively. BCF values > 2 were considered as high (Blaylock et al. 1997). However, the BCF values were below this limit in the current study. Therefore, it can be concluded that the chilli plant has the lowest capacity to accumulate heavy metals. Mellem et al. (2009) studied on *Amaranthus dubius*, where they found that BCF value was higher in Pb than Cr, which is similar to this study. Both studies show BCF values Cr<Pb, although *Amaranthus dubius* has more phytoextraction capability than *Capsicum annum*. The BCF values of Pb and Cr in a variety of vegetables were found within the range of 0.0001-0.0648 and 0.0002-0.027, respectively (Chang et al. 2013).

Daily Intake of Metals (DIM), Health Risk Index and Carcinogenic Risks

The daily intake of Cr and Pb, health risk index and carcinogenic risks were estimated for the chilli plants grown in artificially contaminated soils and presented in Table 7. DIM value for Cr and Pb was the smallest in all levels of contamination, although chilli is needed in the daily diet in

Bangladesh, usually used as a spice and condiment, thus taken in low quantity. That may be the reason for the lower DIM values for the Chilli plant in this study. Accumulation ability and DIM values of Pb in the Chilli plant were higher than Cr.

The DIM values for Cr and Pb did not exceed the standard value set by WHO/FAO. Therefore, chilli grown on this soil can be considered completely safe to eat. However, chilli plants grown on highly contaminated soil exceeded the DIM value of WHO/FAO (Likuku & Obuseng 2015). Cr, Pb and Zn accumulations were considerably high in green peppers

Table 6: Bioconcentration factor (BCF) of Cr and Pb from the soil to the whole chilli plant.

Level of contamination	Bioconcentration factor (BCF)	
	Cr	Pb
High	0.04	0.11
Medium	0.07	0.09
Low	0.05	0.10

Table 7: Daily intake of metals (DIM) and Health risk index of Cr and Pb from chilli plant grown on artificially contaminated soil.

Level of contamination	Daily Intake of Metals (mg/day)		Health risk index		Cancer Risk (CR)	
	Cr	Pb	Cr	Pb	Cr	Pb
High	NA	4.22×10^{-5}	NA	0.012	NA	3.587×10^{-7}
Medium	1.47×10^{-5}	1.87×10^{-5}	0.005	0.005	6.027×10^{-7}	1.59×10^{-7}
Low	0.5×10^{-5}	1.12×10^{-5}	0.017	0.003	2.05×10^{-7}	9.52×10^{-8}
WHO/FAO*	0.05-0.2	0.214				

NA=Not Available; *WHO/FAO values in mg/day are based on a 60 kg body weight adult.

(*Capsicum annum* L.) as compared to the safe limit of the joint WHO/FAO Food Standards Program Code Alimentarius Commission. The health risk index (HRI) values of Cr and Pb were 0.005 and 0.017 for the medium and low levels of contamination, respectively. HRI value was higher in high (0.012) Pb treatment than medium (0.005) and low (0.003) treatment. In this study, the HRI value was less than 1, which indicates the consumers were safe. Based on the results of Carcinogenic risks (CR) values in the present study (Table 7), contamination by Cr and Pb in Chilli plant can be said safe in terms of carcinogenic risks. According to USEPA (2015), CR values exceeding 1×10^{-4} cause significant cancer risks. However, the CR values in this study ranged 2.05×10^{-7} to 6.027×10^{-7} and 1.59×10^{-7} to 9.52×10^{-8} for Cr and Pd, respectively although the elevated level of carcinogenic risks posed by Cr and Pb were recorded in *Centella asiatica* and other several varieties of vegetable plants (Ruchuwarak et al. 2018).

CONCLUSIONS

Heavy metals are considered dreadful pollutants that cause damage to plants as well as human health. The soils adjacent to the industrial area accumulate metals and transfer these to the edible parts of plants. In this study, at a high level of contamination, plants did not yield any fruits. Cr concentration (0.695 ± 0.151 mg/kg) in fruits grown on medium contaminated soil slightly exceeded the safe limit of 0.5 mg/kg. Fruits grown on high Pb contaminated soil (1.986 ± 0.694 mg/kg) exceeded the safe limit of 0.3 mg/kg. Accumulation of Pb was higher than Cr in every part of the chilli plants at three levels of contamination. The Transfer Factor (TF) for Cr has been found in the order of leaves > shoots > fruits > roots, and for Pb transfer, the order was leaves > shoots > roots > fruits at every level of contamination. Daily Intake of Metals (DIM) for Cr and Pb was deficient in all levels of contamination, and it was higher for Pb than Cr. Therefore, industrial waste containing heavy metals needs treatment before discharging into the environment. Consumption of plants grown in the contaminated area also requires proper pre-treatment.

REFERENCES

- Aktaruzzaman, M., Fakhruddin, A.N.M., Chowdhury, M.A.Z., Fardous, Z. and Alam, M.K. 2013. Accumulation of heavy metals in soil and their transfer to leafy vegetables in the region of Dhaka Aricha highway, Savar, Bangladesh. Pak. J. Biol. Sci., 16: 332-338.
- Akintan, O., Olusola, J. and Azeez, A. 2019. Heavy metals loads in soil, farmlands and plant crop at open dumpsite. Global J. Environ. Sci. Manage., 5(4): 449-460.
- Allen, S.E., Grimshaw, H.M. and Rowland, A.P. 1986. Chemical analysis. In: Methods in Plant Ecology, Moore PD and SB Chapman (Eds). Blackwell scientific publication, Oxford, London, 285-337.
- Aydinalp, C. and Marinova, S. 2009. The effects of heavy metals on seed germination and plant growth on Alfalfa Plant (*Medicago sativa*). Bulg. J. Agric. Sci., 15(4): 347-350.
- BBS 2015. Statistical Yearbook of Bangladesh. Bangladesh Bureau of Statistics, Planning Division, Ministry of Planning, Dhaka, Bangladesh, 1-393.
- Blaylock, M.J., Salt, D.E., Dushenkov, S., Zakharova, O., Gussman, C., Kapulnik, Y., Ensley, B.D. and Raskin, I. 1997. Enhanced accumulation of Pb in Indian mustard by soil-applied chelating agents. Environ. Sci. Technol., 31(3): 860- 865.
- Chang, C.Y., Yu, H.Y., Chen, J.J., Li, F., Zhang, H. and Liu, C. 2014. Accumulation of heavy metals in leaf vegetables from agricultural soils and associated potential health risks in the Pearl River Delta, South China. Environ. Monit. Assess., 186: 1547-1560.
- Chowdhury, M.A.Z., Fakhruddin, A.N.M., Islam, M.N., Moniruzzaman, M., Gan, S.H. and Alam, M.D. 2013. Detection of the residues of nineteen pesticides in fresh vegetable samples using gas chromatography mass-spectrometry. Food Control, 34: 457-465.
- Dube, B.K., Tewari, K., Chatterjee, J. and Chatterjee, C. 2003. Excess chromium alters uptake and translocation of certain nutrients in *Citrullus*. Chemosphere, 53: 1147-1153.
- FAO/WHO standards. 1985. Codex Alimentarius Commission (FAO/WHO): Food Additives and Contaminants, ALINORM 85/15, 1-100.
- FAO/WHO standards. 2001. Codex Alimentarius Commission (FAO/WHO): Food Additives and Contaminants, ALINORM 01/12, 1-197.
- Gleason, K., Shine, J.P., Shobnam, N., Rokoff, L.B., Suchanda, H.F., Ibne Hasan, M.O.S., Mostofa, G., Amarasiriwardena, C., Quamruzzaman, Q., Rahman, M., Kile, M.L., Bellinger, D.C., Christiani, D.C., Wright, R.O. and Mazumdar, M. 2014. Contaminated turmeric is a potential source of lead exposure for children in rural Bangladesh. J. Environ. Public Health, Article ID 730636: 1-5
- Guertin, J. 2004. Toxicity and health effects of chromium (All Oxidation States). Chromium VI Handbook. CRC Press LLC. 216-230.
- Gupta, N., Khan, D.K. and Santra, S.C. 2007. An assessment of heavy metal contamination in vegetables grown in wastewater irrigated areas of Titagarh, West Bengal, India. Bull. Environ. Contam. Toxicol., 80(2): 115-118.
- Halim, M.A., Majumder, R.K. and Zaman, M.N. 2014. Paddy soil heavy metal contamination and uptake in rice plants from the adjacent area

- of Barapukuria coal mine, Northwest Bangladesh. *Arabian J. Geosci.*, 8(6): 3391-3401.
- Hossain, M.S., Fakhruddin, A.N.M., Chowdhury, M.A.Z., Rahman, M.A. and Khorshed, A. 2015. Health risk assessment of selected pesticide residues in locally produced vegetables of Bangladesh. *Int. Food Res J.*, 22(1): 110-115.
- Hung, N.M., Hiep, N.V., Dung, B.N. and Hai, N.X. 2014. Lead accumulation in different parts of okra plant (*Abelmoschus esculentus*). *ARPN. J. Agri. Biol. Sci.*, 9(6): 190-194.
- Iqbal, M.Z., Saeeda, S. and Muhammad, S. 2001. Effects of chromium on an important arid tree (*Caesalpinia pulcherrima*) of Karachi city, Pakistan. *Ekologia Bratislava*, 20: 414-422.
- Jamali, M.K., Kazi, T.G., Arain, M.B., Afridi, H.I., Jalbani, N., Kandhro, G.A. and Baig, J.A. 2009. Heavy metal accumulation in different varieties of wheat (*Triticum aestivum L.*) grown in soil amended with domestic sewage sludge. *J. Hazard. Mater.*, 164: 1386-1391.
- Jolly, Y.N., Islam, A. and Akbar, S. 2013. Transfer of metals from soil to vegetables and possible health risk assessment. *Springerplus*, 2: 385.
- Kabir, M.M., Fakhruddin, A.N.M., Chowdhury, M.A.Z., Fardous, Z. and Islam, R. 2017. Characterization of tannery effluents of Hazaribagh area, Dhaka, Bangladesh. *Pollution*, 3: 395-406.
- Kabir, M.M., Fakhruddin, A.N.M., Chowdhury, M.A.Z., Pramanik, M.K. and Fardous, Z. 2018. Isolation and characterization of chromium (VI)-reducing bacteria from tannery effluents and solid wastes. *World J. Microbiol. Biotechnol.*, 34: 126.
- Khan, S., Farooq, R., Shahbaz, S., Khan, M.A. and Sadique, M. 2009. Health risk assessment of heavy metals for population via consumption of vegetables. *World Applied Sci. J.*, 6(12): 1602-1606.
- Karbassi, A., Tajziehchi, S. and Khoshgalb, H. 2018. Speciation of heavy metals in coastal water of Qeshm Island in the Persian Gulf. *Global J. Environ. Sci. Manage.*, 4(1): 91-98.
- Lato, A., Radulov, I., Berbecea, A., Lato, K. and Crista, F. 2012. The transfer factor of metals in soil-plant system. *Res. J. Agri Sci.*, 44(3): 67-72.
- Lawrence, H.S. and Borkowsky, W. 1983. A new basis for the immunoregulatory activities of transfer factor--an arcane dialect in the language of cells. *Cell. Immunol.*, 82 (1): 102-116.
- Liao, Y., Wang, Z., Yang, Z., Chai, L., Chen, J. and Yuan, P. 2011. Migration and transfer of chromium in soil-vegetable system and associated health risks in vicinity of ferro-alloy manufactory. *T. Nonferr. Metal Soc. Chin.*, 21(11): 2520-2527.
- Likuku, A.S. and Obuseng, G. 2015. Health risk assessment of heavy metals via dietary intake of vegetables irrigated with treated wastewater around Gaborone, Botswana. *International Conference on Plant, Marine and Environmental Sciences*, 1(2): 32-37.
- Lima, F.S., Nascimento, C.W., Silva, F.B., Carvalho, V.G. and Filho, M.R. 2009. Lead concentration and allocation in vegetable crops grown in a soil contaminated by battery residues. *Hortic. Bras.*, 27: 362-365.
- Mackay, D. 1982. Correlation of bioconcentration factors. *Environ. Sci. Technol.*, 16: 274-278.
- Mbong, E.O., Akpan, E.E. and Osu, S.R. 2014. Soil-plant heavy metal relations and transfer factor index of habitats densely distributed with *Citrus reticulata* (tangerine). *J. Res. Environ. Sci. Toxicol.*, 3(4): 61-65.
- Mellem, J.J., Bajinath, H. and Odhav, B. 2009. Translocation and accumulation of Cr, Hg, As, Pb, Cu, and Ni by *Amaranthus dubius* (Amaranthaceae) from contaminated Sites. *J. Environ. Sci. Health Part A*, 44: 568-575.
- Naser, H.M., Sultana, S., Gomes, R. and Noor, S. 2012. Heavy metal pollution of soil and vegetable grown near roadside at Gazipur, Bangladesh. *J. Agri. Res.*, 37(1): 9-17.
- Pandey, N. and Sharma, C.P. 2002. Effect of heavy metals CO²⁺, Ni²⁺, and Cd²⁺ on growth and metabolism of cabbage. *Plant Sci.*, 163: 753-758.
- Ruchuwarak, P., Intama, S., Tengjaroenkul, B. and Neeratanaphan, L. 2018. Bioaccumulation of heavy metals in local edible plants near a municipal landfill and the related human health risk assessment. *Hum. Ecol. Risk Assess.*, 25(7): 1760-1772.
- Payus, C., Talip, A.F.A. and Hsiang, T.W. 2015. Heavy metals accumulation in paddy cultivation area of Kompipinan, Papar district, Sabah. *J. Sust. Sci. Manag.*, 10(1): 76-86.
- Proshad, R., Kormoker, T., Islam, M.S. and Chandra, K. 2019. Potential health risk of heavy metals via consumption of rice and vegetables grown in the industrial areas of Bangladesh. *Hum. Ecol. Risk Assess.*, 26(4): 921-943.
- Radulescu, C., Stihl, C., Popescu, IV., Dulama, I.D., Chelarescu, E.D. and Chilian, A. 2013. Heavy metal accumulation and translocation in different parts of *Brassica oleracea L.* *Rom. Journ. Phys.*, 58(9-10): 1337-1354.
- Sarma, H., Deka, S., Deka, H. and Saikia, R.R. 2011. Accumulation of heavy metals in selected medicinal plants. *Rev. Environ. Contam. T.*, 214: 63-86.
- Shaheen, N., Irfan, N. and Khan, I.N. 2016. Presence of heavy metals in fruits and vegetables: health risk implications in Bangladesh. *Chemosphere*, 152: 431-438.
- SEPA, 2005. The limits of Pollutants in Food. China: State Environmental Protection Administration, GB2762-2005.
- Singh, H.P., Mahajan, P., Kaur, S. and Kohli, R. 2013. Chromium toxicity and tolerance in plants. *Environ. Chem. Letters.*, 11(3): 229-254.
- Singh, S., Zacharias, M., Kalpana, S. and Mishra, S. 2012. Heavy metals accumulation and distribution pattern in different vegetable crops. *J. Environ. Chem. Ecotoxicology*, 4(10): 170-177.
- Tiwari, K.K., Singh, N.K., Patel, M.P., Tiwari, M.R. and Rai, U.N. 2011. Metal contamination of soil and translocation in vegetables growing under industrial wastewater irrigated agricultural field of Vadodara, Gujarat, India. *Ecotoxicol. Environ. Safe.*, 74: 1670-1677.
- Tsafe, A.I., Hassan, L.G., Sahabi, D.M., Alhassan, Y. and Bala, B.M. 2012. Evaluation of heavy metals uptake and risk assessment of vegetables grown in Yargalma of Northern Nigeria. *J. Basic Appl. Sci. Res.*, 2(7): 6708-6714.
- USEPA (US Environmental Protection Agency). 2015. Risk based screening table. Composite Table: Summary Tab 0615.
- USEPA (US Environmental Protection Agency) 2017. Regional Screening Level (RSL) Summary Table (TR=1E-06, HQ=1).
- World Health Organization (WHO) 1993. Evaluation of Certain Food Additives and Contaminants. In: Forty-First Report of the Joint FAO/WHO Expert Committee on food additives. 1-223.
- Yashim, Z.I., Israel, O.K. and Hannatu, M. 2014. A study of the uptake of heavy metals by plants near metal-scrap dumpsite in Zaria, Nigeria. *J. Appl. Chem.*, Article ID 394650.
- Zayed, A., Mel Lytle, C. Qian, J. and Terry, N. 1998. Chromium accumulation, translocation, and chemical speciation in vegetable crops. *Planta*, 206: 293-299.



Modelling and Optimization of Energy-Efficient Procedures for Removing Lead from Aqueous Solutions Using Activated Carbons Prepared from Waste Tyres and *Bauhinia purpurea* Leaves

H. Joga Rao

Department of Chemical Engineering, GMR Institute of Technology, Rajam-532127, Andhra Pradesh, India

†Corresponding author: H. Joga Rao; hjrgmrit@gmail.com

Nat. Env. & Poll. Tech.
Website: www.neptjournal.com

Received: 29-08-2020

Revised: 28-09-2020

Accepted: 16-10-2020

Key Words:

Activated carbon
Bauhinia purpurea
Lead removal
Waste tyres

ABSTRACT

The present study provides two naturally available sources for making adsorbents, waste tyres and *Bauhinia purpurea* leaves, for the removal of lead from effluents. Equilibrium isotherms, kinetic models and thermodynamic studies were applied to observe the suitability of these adsorbents. Response surface methodology was adopted to investigate the influence of different process variables in lead adsorption process using both the adsorbents. For all the process parameters, the square and linear model terms were having significant effect than interactive model terms of lead adsorption process for both the adsorbents. The interaction effects of the process variables of X_1X_2 , X_1X_3 , X_2X_3 and X_2X_4 were highly influenced by the percentage removal of lead by using activated carbons prepared from waste tyres. To study the interaction effects of the process variables of X_1X_2 , X_2X_3 and X_2X_4 were highly influenced by the adsorption efficiency of lead by using activated carbons prepared from *Bauhinia purpurea* leaves. All the squared terms, X_1 , X_2 , X_3 and X_4 show a negative influence on the adsorption of lead on the two adsorbents. The interaction effect between process variables of X_1X_2 ($p: 0.000$, $t: 9.243$), X_1X_3 ($p: 0.03$, $t: 2.36$), X_2X_3 ($p: 0.000$, $t: 4.75$) and X_2X_4 ($p: 0.02$, $t: 2.71$), were found to be statistically significant and have positive effect on adsorption efficiency using ACWT as an adsorbent. The interaction effect between process variables of X_1X_2 ($p: 0.000$, $t: 8.1049$), X_2X_3 ($t: 5.9657$, $p: 0.000$) and X_2X_4 ($t: 5.9657$, $p: 0.000$) was found to be statistically significant and positive effect on adsorption efficiency of lead, whereas other interactions were insignificant and did not influence the adsorption efficiency of lead using activated carbons of *Bauhinia purpurea* leaves adsorbent. Based on the statistical approach, the experimental results were analysed by using ACWT and ACBPL adsorbents for the removal of lead and the optimum process conditions were as follows: pH: 4.98 and 4.77, C_i : 140.01 mg/L and 105.7 mg/L, w : 0.12 g and 0.123 g, T : 314.46 K and 305.31 K and maximum adsorption efficiency of 95.64% and 95.55%, respectively.

INTRODUCTION

For a sustainable human society clean technology and green chemistry is needed for preserving and/or reducing the adverse effects of pollutants on the environment. To provide comforts and necessities to the unceasing global population, rapid industrialization is inevitable, but the environment is severely affected by this large scale industrialization and human activities in the name of development (Mishra et al. 2009). The environmental contamination of heavy metals has become an issue of great concern worldwide (Chung-Hsin et al. 2016). It is often the result of uncontrolled and unlimited discharges from manufacturing, processing and purifying industries (Fu & Wang 2011) (Table 1). Lead, zinc, cadmium, mercury, arsenic, chromium, copper and nickel are the common trace elements found in the aqueous solutions which are non-biodegradable and high toxic (Akunwa et al. 2014). Once the toxic elements are released

into the environment, they are difficult to be treated by natural processes and continue to bio-accumulate in the human body and the food chain (Gercel et al. 2007). Therefore, the government environmental protection agencies have set acceptable limits for the heavy metals in drinking water as well as wastewaters (Momcilovic et al. 2011). These strict regulations and standards encouraged researchers to search for new technologies which are environmentally friendly and can reduce heavy metal concentrations in the discharged wastewaters to be within the maximum allowable limits (Corda & Kini 2020). Sources of heavy metals and their impacts are given in Table 1.

Among all the heavy metals, lead is considered as one of the toxic pollutants is generated from a majority of industrial operations (Table 1) (Karnib et al. 2014). A major use of lead is the production of anti-knock compounds for addition to petrol, particularly tetraethyl lead, $Pb(C_2H_5)_4$. The impacts

Table 1: Heavy metals sources, impacts on the health of mankind and acceptable limits in drinking water (Salam et al. 2011).

Heavy metal	Sources	Impacts on humans	Acceptable limits in drinking water (mg/L) IS 10500:2012
Cd	Mining of metals, Smelting and fossil fuel combustion	Affects renal functions, bone, Pulmonary and cardiovascular tissues, lung cancer, etc.	0.003
Pb	Batteries, Cable Sheathing, Sheets and pipes, Chloro-alkali, Petroleum refinery, Paints and dyes, Fertilizers and Motor vehicles	Damage to nervous system, brain and kidney, loss of appetite, High blood pressure, Digestive issues, Muscle and joint pain.	0.01
Hg	Metal Finishing, Metallurgical Industries	Tremors and Incoordination, manic behaviour, anaemia	0.001
Zn	Car and Aeronautic industries, galvanizing plants, textile, etc.	Nausea, Vomiting, dizziness, diarrhoea, fever	5.0
Cu	Alloys, Catalyst, Anti-fouling Paints, Wood Preservative	Convulsions, Cramps, death	0.05
Ni	Electroplating, Catalyst materials, Arc welding, Batteries, etc.	Sensitization of immune system, pulmonary fibrosis and skin dermatitis	0.02

of lead on humans are given in Table 1. Generally, the current trend of research is focused on the usage of naturally available and waste material for the treatment of wastewater. This area is getting importance throughout the world since it minimizes the cost of operation as naturally available materials can obtain cheaply and it also curtails the waste disposal problems (Chowdhury et al. 2012). Especially in developing countries like India, this technique becomes most attractive since most of the industries discharge effluents directly into water bodies because of their high treatment cost (Gaya et al. 2015). The best choice to mitigate heavy metal contamination in wastewater is to eliminate it at the origin, i.e. before the dispersion of metal contaminant to multifarious ecosystems (Bohli et al. 2013, Caccin et al. 2016). Conventional methods are either less effective or more expensive in treating high volumes; require the use of expensive chemicals and low metal concentration in the aqueous form (Juanqin et al. 2016). Most of these processes suffer from high operating cost and recurring expenses such as chemicals, which are not suitable for the small-scale industries (Salam et al. 2011, Jia & Li 2015). Low cost activated carbons are prepared by thermo-chemical methods of various unused materials and plant biomass used for the removal of heavy metals and dyes, recovery of valuable materials (Juan et al. 2013). The literature also reviewed that the plant biomass as waste materials such as leaves, pods, peel, bark, activated carbon cloth (ACC), etc., had been extensively used as adsorbents for the removal of heavy metals from effluents (Gupta et al. 2014, Ming-sheng et al. 2016). The present study aims to investigate the feasibility of alternative, low cost and novel adsorbents for efficient removal of lead and from an aqueous solution. The two adsorbents chosen for the present study are available plenty in nature. Hence, the present investigation is carried out to remove lead onto activated carbon of waste tyres and *Bauhinia purpurea* leaves using adsorption tech-

nique (Joga Rao et al. 2019). The present work is focused to test the equilibrium data using different isotherm models and to estimate kinetic parameters using different kinetic models available in the literature. Thermodynamic studies are used to evaluate the thermodynamic energy parameters and compare the adsorption capacities of different adsorbents used in the literature with activated carbon of waste tyres and *Bauhinia purpurea* leaves (Joga Rao et al. 2018). The literature survey also includes the optimization of process variables by using response surface methodology (Jain et al. 2011).

MATERIALS AND METHODS

Chemicals and Instrumentation

The chemicals and instruments used for the experimentation are given in Table 2.

Preparation of Adsorbents

The raw adsorbents, waste tyres and *Bauhinia purpurea* leaves used in the present study were collected in Rajam and Srikakulam. Low cost activated carbons are prepared by carbonization and activation of carbonaceous materials by either physical or chemical activation methods (Joga Rao

Table 2: Chemicals and instrumentation.

Chemicals	Instruments
Pb(NO ₃) ₂ (99%)	Orbital shaker (REMI-CIS-24plus model)
NaOH (98%)	pH Meter
HCl (35%)	Filter paper (Whatman-42)
ZnCl ₂ (70%)	Analytical Balance (Shimadzu, AUX220)
H ₂ O ₂ (30%)	Atomic Absorption Spectrometer (AAS) (Perkin Elmer model 400A)

et al. 2016). The dried products of both the adsorbents were sieved to the desired particle size range of 74-177 μm .

Preparation of Metal Solutions

Adsorbate solution of lead with a concentration of 1000 mg/L was prepared separately by dissolving 1.598 g of 100% $\text{Pb}(\text{NO}_3)_2$ in 1000 mL of double-distilled water. From the standard stock solutions, working solutions of lower concentrations of lead were prepared (100, 125, 150, 175 and 200 mg/L) for use in batch experiments. After adsorption, the final effluent solution was analysed by atomic absorption spectrophotometer of Perkin Elmer model-3100, a flame type AAS.

Batch Adsorption Experimental Studies

The adsorption studies were conducted for both the adsorbents in the exploratory conditions of various effective process parameters of pH 2-8, contact time 2-120 min, metal ion concentration ranges from 100-200 mg/L, the dosage of the adsorbent 0.025-0.15 g and the particle size of the adsorbent vary from 74 (200 mesh)-177 (85 mesh) μm . Agitation speed of 250 rpm was kept constant in the orbital shaker with a suitable time interval of 2 -120 min. The mixed adsorbent solutions were taken out and filtered by Whatman filter paper and analysed for lead ion concentration. Batch experiments were conducted at various temperatures of the metal solution using orbital shaker from 303-323 K with an optimum contact time of 60 min for the lead at pH value of 5. Samples were analysed by AAS to assess the thermodynamic parameters and study the feasibility of the process with temperature. The amount of lead deposited on the adsorbent surface was determined by using the following equation.

$$q_t = \frac{V(C_o - C_f)}{1000w}$$

Where, q_t is the amount of lead deposited on the adsorbent surface (mg/g), C_o is the initial solute concentration in the solution before adsorption (mg/L), C_f is the final concentration of solute in the solution after adsorption (mg/L), V is the volume of the metal solution (L) and w is the dosage of the adsorbent (g).

Adsorption Isotherms, Thermodynamic and Kinetic Models

The adsorption isotherms indicate the distribution of adsorbed molecules between the liquid phase and solid phase when the adsorption process reaches an equilibrium state. Linear isotherm models, Langmuir, Freundlich, and Dubinin-Radushkevich (D-R) were tested for the equilibrium studies of lead metal ion using both the adsorbents. The fitness of

equilibrium data for the pseudo-first-order and pseudo-second-order models were investigated and compared for the two adsorbents. Thermodynamic studies provide information about the feasibility of the adsorption process. It also plays an important role in the study of the nature of the adsorption process. The thermodynamic energy parameters like Enthalpy change (ΔH°), Entropy change (ΔS°), and Gibb's free energy (ΔG°) are used to determine the spontaneity, heat change and affinity of the adsorption process. For isotherm and kinetic analysis, adsorption experiments were conducted by varying the isothermal temperatures of lead solution from 303-323 K with different initial concentrations (100-200 mg/L). 0.1 g of activated carbon of optimum particle size was added to flasks containing 25 mL of lead solution with optimum solution pH. Flasks were shaken at constant mixing speed (250 rpm) at a predetermined temperature in a defined time intervals (equilibrium time constant for isotherm modelling). Then the samples were withdrawn from the shaker, filtered and analysed for metal concentration. The isotherms, kinetic and thermodynamic feasibility modelling equations used for the fitness of the adsorbents of the lead adsorption process are listed in Tables 3 and 4.

The central composite design (CCD) was used to optimize lead removal by activated carbons prepared from waste tyres and *Bauhinia purpurea* leaves in a batch system (Joga Rao et al. 2016). Initial metal ion concentration, pH, temperature and adsorbent dosage are the input variables considered for the optimization of heavy metal removal.

RESULTS AND DISCUSSION

The effect of various process parameters on the removal of lead from aqueous solutions prepared in the laboratory by using activated carbon of waste tyres and *Bauhinia purpurea* leaves were presented. The parameters studied and the range of parameters covered is compiled in Table 5. The experimental data were first analysed graphically and then theoretically to justify the observations made from the graphical analysis. The equilibrium calculations, kinetic models developed, thermodynamic data and optimization of selected variables using response surface methodology are presented here.

Suitability of Two Parameter Adsorption Isotherms

The equilibrium isothermal results were analysed using three of the most commonly used isotherm equations, Langmuir, Freundlich and Dubinin-Radushkevich (D-R). The experimental data were tested for the fitness of Freundlich isotherm model of lead adsorption process by using activated carbons prepared from waste tyres (ACWT) and *Bauhinia purpurea*

Table 3: Linear isotherm model equations.

Isotherm	Modelling equation	Specifications
Freundlich	$\ln q_{eq} = \ln K_f + \frac{1}{n_f} \ln c_{eq}$	q_{eq} is the metal uptake at equilibrium (mg/g); C_{eq} is the equilibrium concentration (mg/L); K_f is the Freundlich constant [(mg/g)/(L/g) ⁿ]; n_f is the adsorption intensity constant.
Langmuir	$\frac{1}{q_{eq}} = \frac{1}{q_{max}K_L C_{eq}} + \frac{1}{q_{max}}$ $R_L = \frac{1}{1 + K_L C_i}$	q_{max} is the adsorption binding capacity (mg/g) K_L is an affinity of adsorbent (L/g); R_L is the separation factor ($0 < R_L < 1$; Favourable).
D-R	$\ln q_{eq} = \ln q_o - K_d \varepsilon^2$ $\varepsilon = RT \ln(1 + \frac{1}{C_e})$ $E = \frac{1}{\sqrt{2K_d}}$	ε is Polanyi potential; K_d (Mol ² /J ²) is the free energy of adsorption per mole of the adsorbate; q_o (mg/g) is the Dubinin-Radushkevich isotherm constant; E (kJ/mol) is the mean adsorption energy (≤ 8 kJ/mol, physical adsorption; > 8 kJ/mol, chemisorption).

Table 4: Linear kinetic and thermodynamic feasibility model equations.

Model	Modeling equation	Specifications
First order kinetic	$\ln(q_{eq} - q_t) = \ln q_{eq} - k_f t$	q_t (mg/g) is the adsorption intensity at time t; q_{eq} (mg/g) is the adsorption intensity at equilibrium; k_f (1/min) is the rate constant of the first-order adsorption.
Second order kinetic	$\frac{t}{q_t} = \frac{1}{k_s q_{eq}^2} + \frac{1}{q_{eq}}(t)$	k_s is the rate constant of pseudo-second order sorption, (g/mg/min).
Thermodynamic feasibility	$\ln K_e = \frac{\Delta S^\circ}{R} - \frac{\Delta H^\circ}{RT}$ $\Delta G^\circ = -RT \ln K_e$	K_e is the adsorption equilibrium constant

leaves (ACBPL) and analysed by plotting $\ln q_e$ versus $\ln C_e$ as shown in Figs.1 (a) and 1(b). The Freundlich isotherm model, gives the straight line relationship with correlation coefficients (0.972 for ACWT and 0.996 for ACBPL at 303K) decreasing with increasing temperature and described that at lower temperatures and concentrations this model was fitted for both the adsorbents as given in Table 6. The values of $1/n_f < 1$ (0.221 for ACWT and 0.223 for ACBPL), and K_f (19.10 for ACWT and 22.03 for ACBPL) obtained

indicated the fast uptake capacity of the adsorbent. The K_f value of lead adsorption was decreased with an increase in temperature (303-323 K). At a low isothermal temperature, the adsorption capacity is more than at higher temperatures.

Based on the equilibrium experimental data, the Figs. 2(a) and 2(b) show the Langmuir plot ($1/q_e$ versus C_e) for the adsorption of lead at different isothermal temperatures, yielding multiple straight lines of different Langmuir isothermal parameters as tabulated in Table 6. The values of

Table 5: Range of process parameters covered in the present study for the adsorption of lead.

Process parameter	ACWT		ACBPL	
	Min	Max	Min	Max
Time of contact, t (min)	1	90	5	60
Initial metal ion concentration of the solution, C_i (mg/L)	100	200	100	200
pH of the solution	2	8	2	8
Average particle size of the adsorbent, d (μ m)	74	177	74	177
Adsorbent dosage, w (g)	0.025	0.15	0.025	0.15
Temperature, T (K)	303	323	303	323

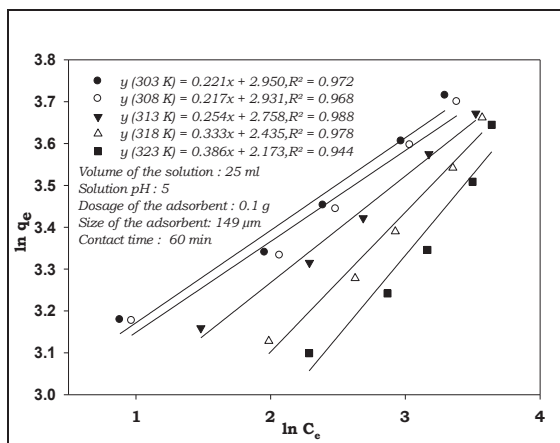
correlation coefficient (R^2) of lead adsorption decreased (0.901 to 0.888) with increasing temperature using activated carbon of waste tyres adsorbent, indicating that the Langmuir model is favourable at lower temperatures. Fig. 2(b) shows the R^2 values (0.9005 to 0.9915) of lead adsorption process increased with increasing temperature using *Bauhinia purpurea* leaves adsorbent, indicating that the Langmuir model is favourable at moderate temperatures. At temperature 303 K, the maximum value of lead adsorption capacity Q_{\max} and K_L values (Table 3) were found to be 41.66 mg/g and 0.923 L/mg for ACWT and 40.81 mg/g and 0.935 L/mg, respectively.

The linear plots of D-R isotherm for both the adsorbents of lead adsorption process are shown in Figs 3(a) and 3(b). The values of D-R isotherm parameters were calculated by using equations (Table 3) and given in Table 6. From the

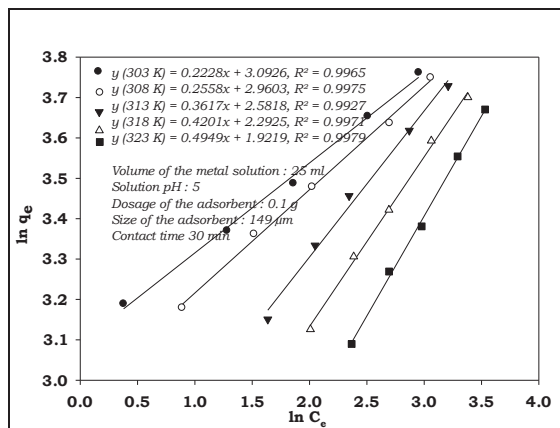
plots, at 303 K, the maximum adsorption capacity, q_0 value found to be 35.12 mg/g and 37.18 mg/g for ACWT and ACBPL adsorbents respectively. The magnitude of E can be decided by the chemical or physical adsorption by using suitable adsorbents. The mean adsorption energy E values of lead adsorption process were decreased with increasing isothermal temperature (303-323 K) from 1-0.267 KJ/mole and 1.29-0.223 KJ/mole for ACWT and ACBPL adsorbents respectively. These results revealed that the adsorption process of lead on both the adsorbents could be taken place by physisorption mechanism.

Isothermal Models

The equations given in Table 7 were correlated for the removal of lead by using activated carbon prepared from waste tyres and *Bauhinia purpurea* leaves.

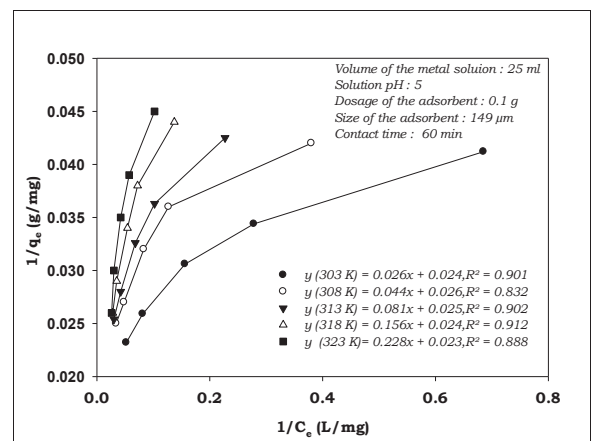


(a)

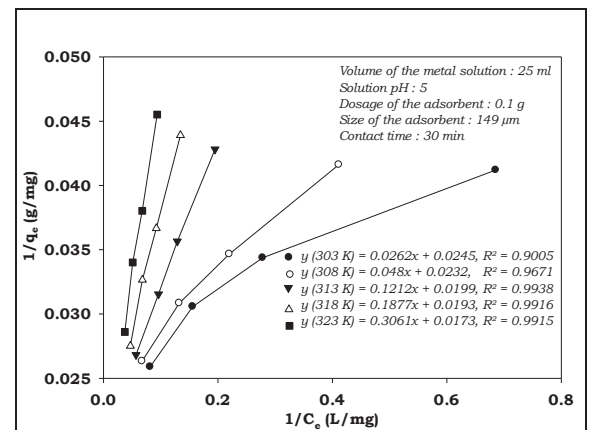


(b)

Fig.1: Freundlich isotherm model for adsorption of lead using ACWT (a) and ACBPL (b) adsorbents.



(a)



(b)

Fig. 2: Langmuir isotherm model for adsorption of lead using ACWT (a) and ACBPL (b) adsorbents.

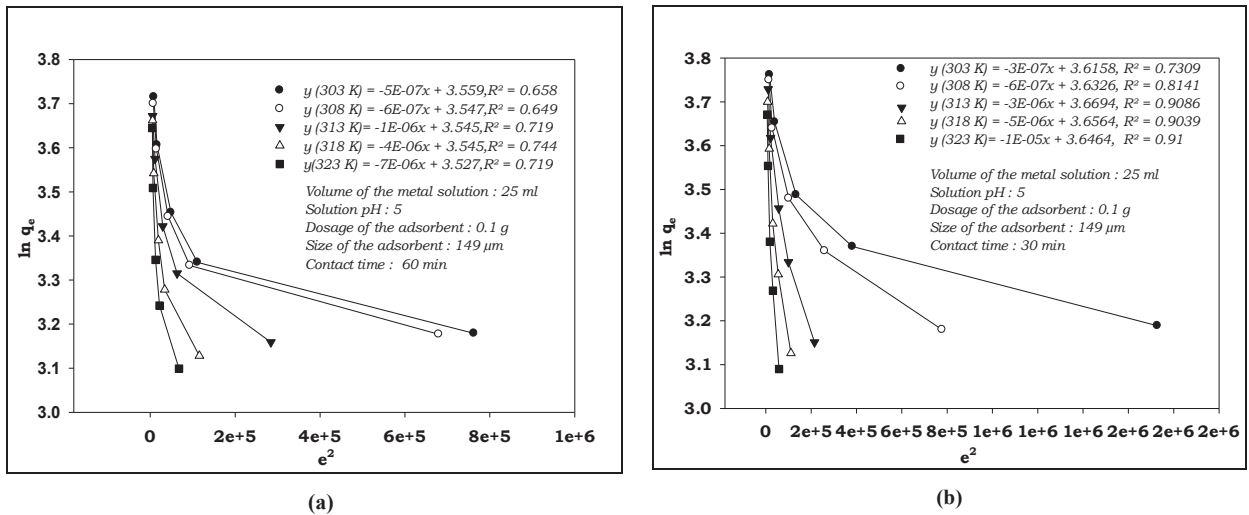


Fig. 3: Dubinin-Radushkevich isotherm model for adsorption of using ACWT (a) and ACBPL (b) adsorbents.

Table 6: Isotherm constants for lead adsorption onto activated carbon of waste tyres (t: 60 min) and *Bauhinia purpurea* leaves (t: 30 min).

Activated carbon of waste tyres		<i>Bauhinia purpurea</i> leaves									
Temperature (K)		303	308	313	318	323	303	308	313	318	323
Freundlich	K_f	19.1	18.7	15.7	11.4	8.78	22.0	19.3	13.22	9.89	6.83
	n_f	4.52	4.60	3.93	3.0	2.59	4.48	3.90	2.76	2.38	2.02
	R^2	0.97	0.96	0.99	0.97	0.94	0.99	0.99	0.992	0.99	0.99
Langmuir	q_{max}	41.6	38.4	40.0	41.6	43.4	40.8	43.1	50.25	51.8	57.8
	K_L	0.92	0.59	0.30	0.1	0.1	0.93	0.48	0.164	0.10	0.05
	R^2	0.90	0.83	0.90	0.91	0.88	0.90	0.96	0.993	0.99	0.99
	R_L	0.01	0.01	0.03	0.06	0.09	0.00	0.02	0.057	0.08	0.15
D-R	q_0	35.1	34.7	34.6	4.63	34.0	37.1	37.8	39.22	38.7	38.3
	E	1	0.91	0.70	0.35	0.26	1.29	0.91	0.408	0.31	0.22
	R^2	0.65	0.64	0.64	0.90	0.71	0.73	0.81	0.908	0.90	0.91

Kinetic Modelling

The kinetics of adsorption studies describes the metal deposition rate and residence time of sorption reaction. The kinetic data provide the necessary information required for optimizing the operating conditions in full scale batch or continuous adsorption process. The kinetic data also help in determining the rate limiting step involved in the adsorption process. The experimental results were analysed to test the kinetic model and the linear plots of $\ln(q_{eq} - q_t)$ versus t (Table 4) are shown in Figs. 4 (a) and 4(b) for ACWT and ACBPL adsorbents, respectively. The calculated first-order rate constants (k_f) and their corresponding linear regression correlation coefficient values are compiled in Table 8. The linear regression correlation coefficient values R^2 were

found in the range of 0.949 to 0.974 and 0.966 to 0.891 for ACWT and ACBPL adsorbents respectively. The results show that the correlation coefficients were very high, the experimental q_{eq} values did not agree with the calculated q_{eq} values. This implies that the adsorption of the lead for both the adsorbents did not follow the first-order kinetics. The validity of the pseudo-second-order kinetic model for the adsorption of lead using activated carbons prepared from waste tyres and *Bauhinia purpurea* leaves adsorbents were evaluated separately with the help of the linear plots of t/q_t versus t (Table 4). The value of the constant k_s and q_{eq} can be calculated from the slope and intercept of Figs.5 (a) and 5(b). The pseudo-second-order rate constant k_s , the calculated q_{eq} value and the corresponding linear regression correlation coefficient values R^2 are given in

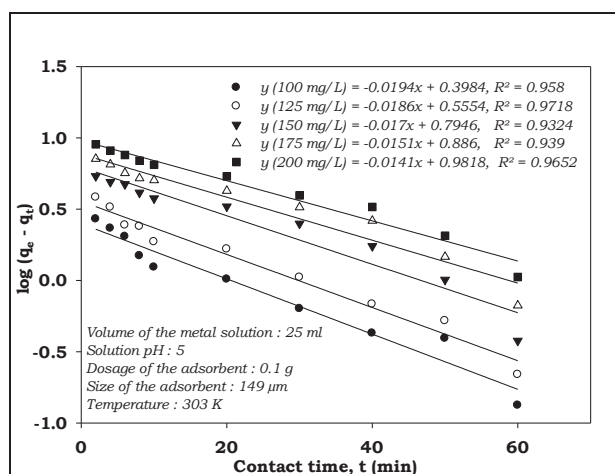
Table 9. The results indicate that the experimental q_e , and calculated q_e values are very close to each other and also R^2 value is closer to unity for both the adsorbents. The high R^2 values indicate that the experimental data are well correlated to the second-order kinetic equation.

Kinetic Models

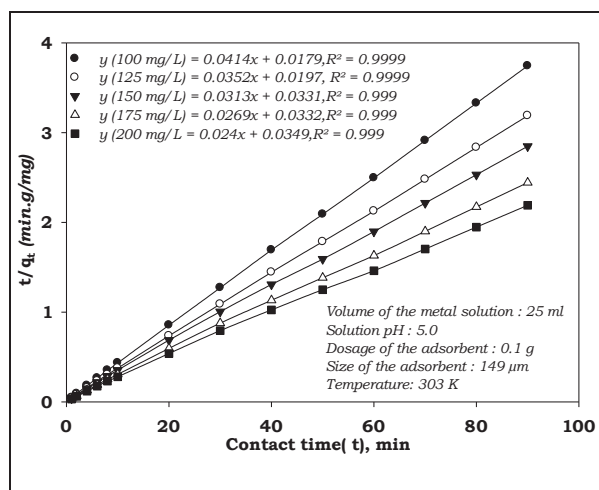
The following equations in Table 10 were correlated for the removal of lead by using activated carbon prepared from waste tyres and *Bauhinia purpurea* leaves.

Table 7: Isothermal Modeling for the removal of lead using activated carbons.

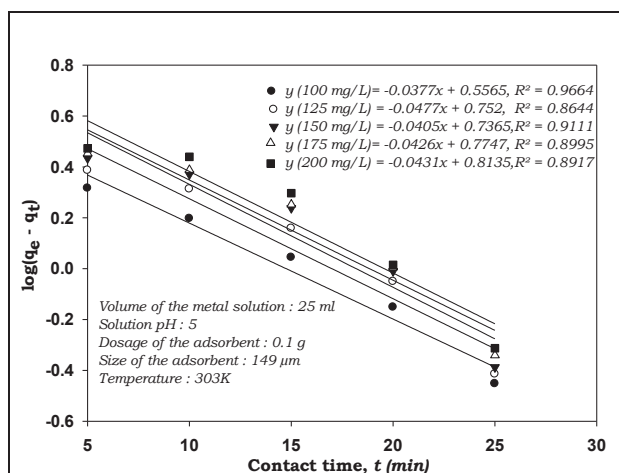
Isotherm	ACWT		ACBPL	
	Modelling	R^2	Modelling	R^2
Langmuir	$q_e = \frac{38.45C_e}{1 + 0.923C_e}$	0.901	$q_e = \frac{38.15C_e}{1 + 0.935C_e}$	0.900
Freundlich	$q_e = 19.1C_e^{0.22}$	0.972	$q_e = 22.03C_e^{0.22}$	0.996
R-D	$q_e = 35.12e^{(-5 \cdot 10^{-7})\epsilon^2}$	0.659	$q_e = 37.18e^{(-3 \cdot 10^{-7})\epsilon^2}$	0.731



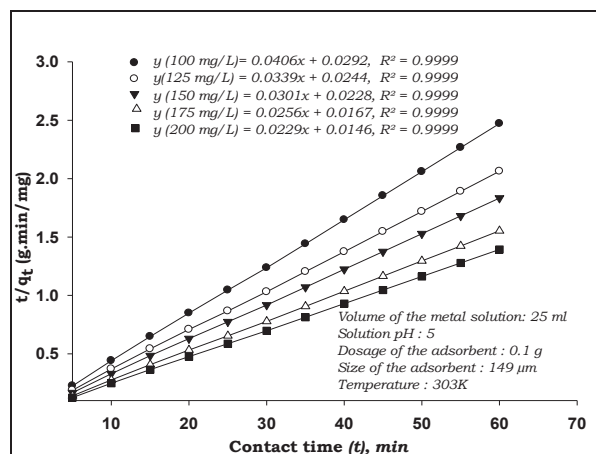
(a)



(a)



(b)



(b)

Fig. 4: First-order Kinetic model for adsorption of lead using ACWT (a) and ACBPL (b) adsorbents.

Fig. 5: Second-order kinetic model for adsorption of lead using ACWT (a) and ACBPL (b) adsorbents.

Table 8: First-order kinetic constants for the adsorption of lead using ACWT and ACBPL adsorbents.

C _i	q _{e, exp}	ACWT			q _{e, exp}	ACBPL		
		k _f	q _{eq cal}	R ²		k _f	q _{eq cal}	R ²
100	24.034	0.023	1.42	0.949	24.27	0.037	1.74	0.966
125	28.221	0.022	1.66	0.974	29.09	0.047	2.12	0.864
150	31.59	0.025	2.22	0.895	32.71	0.040	2.08	0.911
175	36.81	0.018	2.34	0.966	38.62	0.042	2.16	0.899
200	41.06	0.017	2.58	0.974	43.03	0.0431	2.25	0.891

Table 9: Second-order kinetic constants for the adsorption of lead using ACWT and ACBPL adsorbents.

C _i	q _{e, exp}	ACWT			q _{e, exp}	ACBPL		
		k _s	q _{eq cal}	R ²		k _s	q _{eq cal}	R ²
100	24.03	0.098	24.3	0.999	0.419	0.180	0.489	0.996
125	28.22	0.064	28.57	0.999	0.694	0.055	0.870	0.990
150	31.59	0.029	32.25	0.999	1.033	0.052	0.990	0.991
175	36.81	0.021	37.17	0.999	1.299	0.050	1.142	0.992
200	41.06	0.016	41.67	0.999	1.507	0.041	1.306	0.991

Thermodynamic Modeling

Thermodynamic energy parameters (ΔH° , ΔS° , and ΔG°) give evidence of the direction of the adsorption process. The experiments were conducted for lead using activated carbon prepared from waste tyres and *Bauhinia purpurea* leaves at different initial concentrations (100-200 mg/L) of metal solutions with the solution temperature varied in the range of 303 to 323 K. The equilibrium constants (K_e) obtained from the equation given in Table 4 were used to evaluate the thermodynamic energy parameters. The values of ΔH° , ΔS° and ΔG° were calculated from the slope and intercept of the linear Vant-Hoff's plot, i.e. $\ln K_e$ vs $\left(\frac{1}{T}\right)$. These plots are

shown in Figs. 6(a) and 6(b) for ACWT and ACBPL adsorbents, respectively. The estimated thermodynamic energy parameter values of ΔH° , ΔS° and ΔG° are given in Table 11. The variation of thermodynamic energy parameters (ΔG° , ΔH° and ΔS°) with solution temperature of the adsorbents were described that the adsorption process

is exothermic, increased the adsorption efficiency and lead deposition on both the adsorbent surfaces and spontaneous at lower temperatures. The negative value of ΔS° indicates the decreased randomness at the solid-solute interface during the adsorption process.

Optimization of Adsorption Process Parameters Using RSM

In the present study, response surface methodology was adopted to investigate the influence of different process variables in the adsorption process using activated carbons prepared from waste tyres and *Bauhinia purpurea* leaves. The effect of various parameters such as pH (X_1), initial metal concentration (X_2), dosage of the adsorbent (X_3) and temperature (X_4) of lead onto activated carbon of waste tyres and *Bauhinia purpurea* leaves were studied using full factorial central composite design (CCD). The response was expressed as the adsorption efficiency (%) of lead on both the adsorbents. The levels of independent process variables used in a CCD are shown in Table 12.

Table 10: Kinetic models for the removal of lead using activated carbons.

Model	ACWT		ACBPL	
	Kinetic model	R ²	Kinetic model	R ²
1 st First order	$q_t = 24.034 (1 - e^{-0.023t})$	0.949	$q_t = 24.27 (1 - e^{-0.037t})$	0.966
2 nd order	$\frac{dq_t}{dt} = 0.098(24.03 - q_t)^2$	0.999	$\frac{dq_t}{dt} = 0.056(24.27 - q_t)^2$	0.999

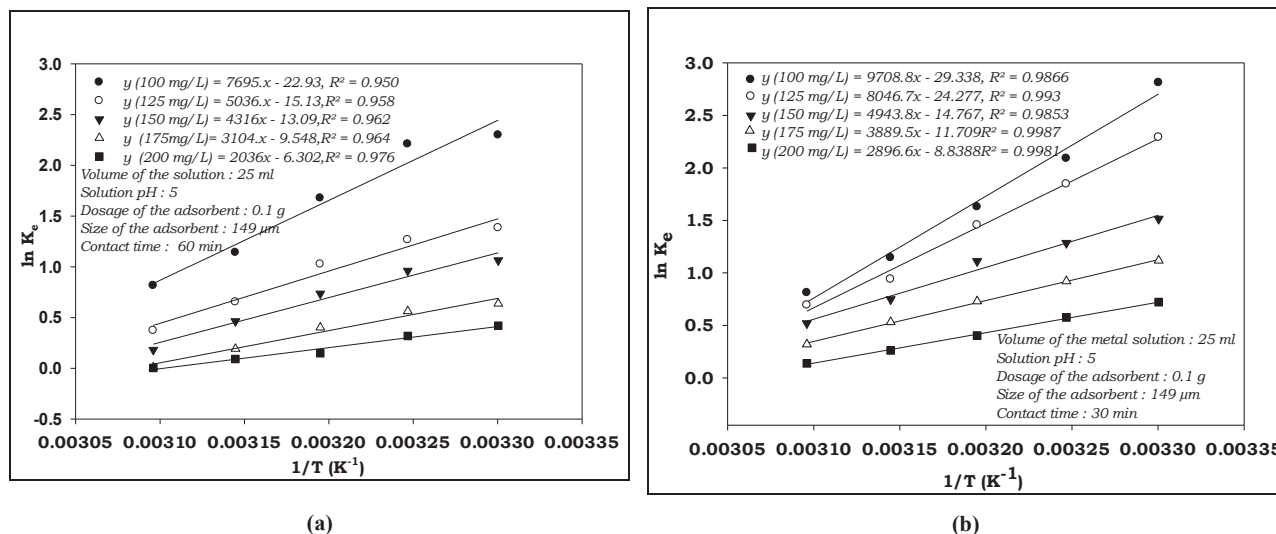


Fig. 6: Van't-Hoff relation for the determination of thermodynamic properties.

Table 11: Variation of thermodynamic parameters for the adsorption of lead using ACWT and ACBPL adsorbents.

C_i (mg/L)	ACWT		ACBPL		T (K)	$-\Delta G^\circ$ (kJ/mol)	
	$-\Delta H^\circ$ (kJ/mol)	$-\Delta S^\circ$ (kJ/mol.K)	$-\Delta H^\circ$ (kJ/mol)	$-\Delta S^\circ$ (kJ/mol.K)		ACWT	ACBPL
100	63.976	0.196	80.78	0.243	303	5.78	7.08
125	41.869	0.125	66.9	0.201	308	5.65	5.87
150	35.883	0.108	41.10	0.122	313	4.36	4.68
175	25.806	0.079	32.33	0.097	318	3.01	3.44
200	16.927	0.052	24.08	0.073	323	2.18	2.22

RSM was used to develop a mathematical model to represent all the correlations among independent variables and responses of interest, i.e. adsorption efficiency of metals. The experimental data with multiple regression analysis were obtained from the following second-order polynomial equations found to represent the adsorption efficiencies of lead ($Y_1\%$) for ACWT and ($Y_2\%$) for ACBPL adsorbents, respectively.

$$\begin{aligned}
 (Y_1\%) &= -7779.95 + 86.38 X_1 - 1.71 X_2 - 375.23 X_3 + 49.62 X_4 \\
 &\quad - 9.35X_1^2 - 653X_3^2 - 0.08X_4^2 + 0.18 X_1X_2 + 45.40 X_1X_3 \\
 &\quad - 0.07X_1X_4 + 1.83X_2X_3 + 0.01X_2X_4 + 2.4X_3X_4 \\
 (Y_2\%) &= -1729.67 + 39.37X_1 - 0.6X_2 + 258.18X_3 + 11.45X_4
 \end{aligned}$$

$$\begin{aligned}
 &- 4.49X_1^2 - 1333.33X_3^2 - 0.02 X_4^2 + 0.03X_1X_2 + 2.90X_1X_3 \\
 &+ 0.4X_2X_3 + 0.05X_3X_4
 \end{aligned}$$

The influence of linear, square and interaction effects of process variables on the adsorption efficiency of lead by using activated carbons prepared from waste tyres and *Bauhinia purpurea* leaves are given in Tables 14, 15, 16 and 17. These results were demonstrated by means of Fisher's F -test and Student t -test and p -value. For all the parameters (Tables 14 and 15), the square ($F = 378.03$ and $P = 0.000006$ for ACWT; $F = 420.223$ and $P = 0.00$ for ACBPL) and linear ($F = 4032.26$ and $P = 0.000006$ for ACWT; $F = 6248.36$ and $P = 0.000$ for ACBPL) model terms were having significant effect than interactive ($F = 122.54$ and $P = 1.248$ for ACWT;

Table 12: Experimental variables and levels investigated by central composite design for the adsorption of lead.

Variable	Process parameter	Level of Process parameters				
		-2	-1	0	1	2
X_1	Solution pH	3	3.5	4	4.5	5
X_2	Initial metal concentration, C_i (mg/L)	100	125	150	175	200
X_3	Dosage of the adsorbent, w (g)	0.05	0.075	0.1	0.125	0.15
X_4	Temperature (K)	303	308	313	318	323

Table 13: The optimal values of the process variables and responses (adsorption efficiency) by using RSM.

Process Variable	ACWT		ACBPL	
	Opt.	Expt.	Opt.	Expt.
pH	4.98	5	4.77	5
C_i (mg/L)	140.01	150	105.7	125
w (g)	0.12	0.125	0.123	0.125
T (K)	314.46	313	305.31	303
(% Y)	95.64	94.26	95.55	98.14

$F = 28.804$ and $P = 0.447$ for ACBPL) model terms of lead adsorption process for both the adsorbents. Because of their p-values being less than 0.05; the interaction effects of the process variables of X_1X_2 , X_1X_3 , X_2X_3 and X_2X_4 were highly influenced on the percentage removal of lead, whereas combinations of X_1X_4 and X_3X_4 were insignificant effect on the percentage removal of lead by using activated carbons prepared from waste tyres (Table 14). To study the interaction effects of the process variables of X_1X_2 , X_2X_3 and X_2X_4 were highly influenced on the percentage removal of lead, whereas combinations of X_1X_3 , X_1X_4 and X_3X_4 were insignificant effect on the percentage removal of lead by using activated carbons prepared from *Bauhinia purpurea* leaves (Table 15). The magnitude of t -value gives the positive or

negative influence of the independent or process variables on % removal, whereas p-value indicates the significant or insignificant effect of process variables on % removal of metals. The coefficients of X_1 and X_4 showed the greatest significant negative effect and the positive effect by the other variable X_4 (Table 16) on the lead adsorption process by using ACWT adsorbent. Whereas, the coefficients of X_1 , X_3 and X_4 showed the greatest linear positive effect and the negative effect by the other variable X_2 (Table 17) on lead removal by using ACBPL adsorbent. All the squared terms, X_1 , X_2 , X_3 and X_4 shows a negative influence on the adsorption of lead on both the adsorbents. The interaction effect between process variables of X_1X_2 ($p = 0.000$, $t = 9.243$), X_1X_3 ($p = 0.03$, $t = 2.36$), X_2X_3 ($p = 0.000$, $t = 4.75$) and X_2X_4 ($p = 0.02$, $t = 2.71$), were found to be statistically significant and having positive effect on % removal using ACWT as an adsorbent, whereas the combination of X_1X_4 were insignificant effect on the adsorption efficiency of lead. The interaction effect between process variables of X_1X_2 ($p = 0.000$, $t = 8.1049$), X_2X_3 ($t = 5.9657$, $p = 0.000$) and X_2X_4 ($t = 5.9657$, $p = 0.000$) was found to be statistically significant and positive effect on adsorption efficiency of lead, whereas other interactions are insignificant and not influenced on the adsorption efficiency of lead using activated carbon of *Bauhinia purpurea* leaves

Table 14: Analysis of variance (ANOVA) for response surface quadratic model for the adsorption of lead using ACWT as an adsorbent.

Source	SS	DF	MS	F	P (Prob>F)
Linear	3721.305	4	3721.305	4032.266	0.000006
X_1	2263.207	1	2263.207	2452.326	0.000000
X_2	1245.889	1	1245.889	1349.998	0.000000
X_3	152.611	1	152.611	165.364	0.000000
X_4	59.598	1	59.598	64.578	0.000006
Square	348.88	4	348.88	378.033	0.000006
X_1^2	95.421	1	95.421	103.395	0.000001
X_2^2	92.787	1	92.787	100.540	0.000001
X_3^2	90.985	1	90.985	98.587	0.000001
X_4^2	69.687	1	69.687	75.511	0.000003
Interaction	113.0981	5	113.0981	122.549	1.248837
X_1X_2	78.854	1	78.854	85.444	0.000002
X_1X_3	5.153	1	5.153	5.583	0.037618
X_1X_4	0.0001	1	0.0001	0.00	0.953030
X_2X_3	20.839	1	20.839	22.581	0.000598
X_2X_4	6.812	1	6.812	7.381	0.020044
X_3X_4	1.440	1	1.440	1.560	0.237545
Error	10.152	11	0.923		
Total SS	3994.534	25	$R^2 = .9974$	R^2 (Adj) = .9942	

DF: degree of freedom; SS: sum of squares; F: factor; P: probability.

Table 15: Analysis of variance (ANOVA) for response surface quadratic model for removal of lead using ACBPL as an adsorbent.

Source	SS	DF	MS	F	P (Prob>F)
Linear	688.303	4	172.075	6248.36	0.000000
X ₁	389.7816	1	389.7816	14153.60	0.000000
X ₂	182.7120	1	182.7120	6634.57	0.000000
X ₃	91.6504	1	91.6504	3327.98	0.000000
X ₄	24.1603	1	24.1603	877.30	0.000000
Square	46.291	1	11.573	420.223	0.000000
X ₁ ²	22.0255	1	22.0255	799.78	0.000000
X ₂ ²	8.1503	1	8.1503	295.95	0.000000
X ₃ ²	12.1212	1	12.1212	440.14	0.000000
X ₄ ²	3.9936	1	3.9936	145.02	0.000000
Interaction	3.966	1	0.793	28.804	0.447000
X ₁ X ₂	1.8090	1	1.8090	65.69	0.000006
X ₁ X ₃	0.0210	1	0.0210	0.76	0.400924
X ₁ X ₄	0.0001	1	0.0001	0.00	0.953030
X ₂ X ₃	0.9801	1	0.9801	35.59	0.000094
X ₂ X ₄	1.1556	1	1.1556	41.96	0.000046
X ₃ X ₄	0.0006	1	0.0006	0.02	0.882981
Error	0.3029	11	0.0275		
Total SS	717.5999	25	R ² =.9995	R ² (Adj) = .99904	

DF: degree of freedom; SS: sum of squares; F: factor F; P: probability.

Table 16: Estimated regression coefficients and corresponding *t* and *p* values for the adsorption of lead using activated carbon of waste tyres.

Adsorption process Parameter (Mean value)	Regression Coefficient	Standard Error	<i>t</i> -Value	<i>p</i> -Value
Constant	-7779.95	927.3439	-8.3895	0.000004
X ₁	86.38	31.1518	2.7729	0.018133
X ₂	-1.71	0.6175	-2.7667	0.018336
X ₃	-375.23	613.4817	-0.6116	0.553203**
X ₄	49.62	5.7811	8.5837	0.000003
X ₁ ²	-9.35	0.9198	-10.1683	0.000001
X ₂ ²	-0.00	0.0004	-10.0270	0.000001
X ₃ ²	-3653.00	367.9076	-9.9291	0.000001
X ₄ ²	-0.08	0.0092	-8.6897	0.000003
X ₁ X ₂	0.18	0.0192	9.2436	0.000002
X ₁ X ₃	45.40	19.2133	2.3629	0.037618
X ₁ X ₄	-0.07	0.0961	-0.7755	0.454392**
X ₂ X ₃	1.83	0.3843	4.7519	0.000598
X ₂ X ₄	0.01	0.0019	2.7169	0.020044
X ₃ X ₄	2.40	1.9213	1.2491	0.237545**

**insignificant ($p \geq 0.05$)

adsorbent. To maximize the adsorption efficiency of lead, regression model equations developed by using response surface methodology for the prediction of the effect of process variables % removal of lead were optimized separately

with ACWT and ACBPL adsorbents. The optimal values of the process variables and responses (adsorption efficiency) are provided in Table 13.

The data indicated that the adsorption capacity of the

Table 17: Estimated regression coefficients and corresponding *t* and *p*-values for the adsorption lead (ACBPL).

Adsorption parameter (Mean value)	Regression Coefficient	Standard Error	<i>t</i> -Value	<i>p</i> -Value
Constant	-1729.67	160.1935	-10.7974	0.000000
X ₁	39.37	5.3813	7.3158	0.000015
X ₂	-0.60	0.1067	-5.6486	0.000149
X ₃	258.18	105.9756	2.4363	0.033041
X ₄	11.45	0.9986	11.4608	0.000000
X ₁ ²	-4.49	0.1589	-28.2804	0.000000
X ₂ ²	-0.00	0.0001	-17.2032	0.000000
X ₃ ²	-1333.33	63.5540	-20.9795	0.000000
X ₄ ²	-0.02	0.0016	-12.0423	0.000000
X ₁ X ₂	0.03	0.0033	8.1049	0.000006
X ₁ X ₃	2.90	3.3190	0.8738	0.400924**
X ₁ X ₄	0.00	0.0166	0.0603	0.953030**
X ₂ X ₃	0.40	0.0664	5.9657	0.000094
X ₂ X ₄	0.00	0.0003	6.4779	0.000046
X ₃ X ₄	0.05	0.3319	0.1506	0.882981**

**insignificant ($P \geq 0.05$)

activated carbons prepared from waste tyres and *Bauhinia purpurea* leaves adsorbents were higher than most of the adsorbents/biosorbents reported in the literature for the removal of lead from effluents. The results also showed that the adsorption capacity of activated carbon of *Bauhinia purpurea* leaves is high when compared with activated carbon of waste tyres adsorbent for the removal of lead under similar experimental conditions studied.

CONCLUSIONS

The following conclusions could be drawn from the present study on the removal of lead from aqueous solutions using adsorption technique:

- The equilibrium contact time for the adsorption of lead onto activated carbons prepared from waste tyres and *Bauhinia purpurea* leaves were 60 and 30 min, respectively. The maximum rate adsorption was obtained at pH of 5 for both the adsorbents.
- It was found that the experimental data were fitted very well with the Freundlich and Langmuir isothermal models for both the adsorbents, suggesting the involvement of both physisorption and chemisorption.
- Kinetic studies indicated that the adsorption process followed well with the pseudo-second-order kinetic model for the adsorption of lead using activated carbons of waste tyres and *Bauhinia purpurea* leaves for

the range of initial metal concentrations studied for the entire adsorption period.

- The thermodynamic feasibility of lead adsorption process with both the adsorbents were described the negative significance values of ΔG° , ΔH° and ΔS° revealed that the adsorption process is exothermic, feasible and spontaneous, and increased the adsorption efficiency and lead deposition on the adsorbent surfaces at lower temperatures.
- For all the process parameters, the square (F: 378.03 and P: 0.000006 for ACWT; F: 420.223 and P: 0.00 for ACBPL) and linear (F: 4032.26 and P: 0.000006 for ACWT; F: 6248.36 and P: 0.000 for ACBPL) model terms were having significant effect than interactive (F: 122.54 and P: 1.248 for ACWT; F: 28.804 and P: 0.447 for ACBPL) model terms of lead adsorption process for both the adsorbents.
- The interaction effects of the process variables of X_1X_2 , X_1X_3 , X_2X_3 and X_2X_4 were highly influenced on the percentage removal of lead, whereas combinations of X_1X_4 and X_3X_4 were insignificant effect on the percentage removal of lead by using activated carbons prepared from waste tyres.
- To study the interaction effects of the process variables of X_1X_2 , X_2X_3 and X_2X_4 were highly influenced on the percentage removal of lead, whereas combinations of

X_1X_3 , X_1X_4 and X_3X_4 were insignificant effects on the percentage removal of lead by using activated carbons prepared from *Bauhinia purpurea* leaves.

- The coefficients of X_1 , and X_4 showed the greatest significant negative effect and the positive effect by the other variable X_4 on the lead adsorption process by using ACWT adsorbent, whereas, the coefficients of X_1 , X_3 and X_4 showed the greatest linear positive effect and the negative effect by the other variable X_2 on lead removal by using ACBPL adsorbent.
- Based on the statistical approach the experimental results were analysed by using ACWT and ACBPL adsorbents for the removal of lead and the optimum process conditions were identified as pH: 4.98 and 4.77, Ci: 140.01 mg/L and 105.7 mg/L, w: 0.12 g and 0.123 g, T: 314.46 K and 305.31 K and maximum adsorption efficiency of 95.64% and 95.55%, respectively.

REFERENCES

- Akunwa, N. K., Muhammad, M. N. and Akunna, J. C. 2014. Treatment of metal-contaminated wastewater: A comparison of low-cost biosorbents. *J. Environ. Mang.*, 146: 517-523.
- Bohli, T., Ouederni, A., Fiol, N. and Villaescusa, I. 2013. Single and binary adsorption of some heavy metal ions from aqueous solutions by activated carbon derived from olive stones. *Desalin. Water Treat.*, 70: 1082-1088.
- Caccin, M., Giorgi, M., Giacobbo, F., Da Ros, M., Besozzi, L. and Mariani, M. 2016. Removal of lead (II) from aqueous solutions by adsorption onto activated carbons prepared from coconut shell. *Desalin. Water Treat.*, 57: 10.
- Chowdhury, Z. Z., Zain, S. M., Khan, R. A., Rafique, R. F. and Khalid, K. 2012. Batch and fixed-bed adsorption studies of lead (II) cations from aqueous solutions onto granular activated carbon derived from *Mangostana garcinia* shell. *Bioresources*, 7: 2895-2915.
- Chung-Hsin, Wu., Chao-Yin, Kuo and Shu-Shian, Guan 2016. Adsorption of heavy metals from aqueous solutions by waste coffee residues: Kinetics, equilibrium, and thermodynamics. *Desalin. Water Treat.*, 57: 11.
- Cordeiro, N. and Kini, M.S. 2020. Recent studies in adsorption of Pb(II), Zn(II) and Co(II) using conventional and modified materials: A review. *Sep. Sci. Technol.*, 55: 15.
- Fu, F. and Wang, Q. 2011. Removal of heavy metal ions from wastewaters: A review. *J. Environ. Mang.*, 92: 407-418.
- Gaya, U.I., Otene, E. and Abdullah, A.H. 2015. Adsorption of aqueous Cd (II) and Pb (II) on activated carbon nanopores prepared by chemical activation of doum palm shell. *SpringerPlus*, 4(1): 458.
- Gercel, O. and Gercel, H. F. 2007. Adsorption of lead (II) ions from aqueous solutions by activated carbon prepared from the biomass plant material of *Euphorbia rigida*. *Chem. Eng. J.*, 132: 289-297.
- Gupta, V.K., Nayak, A., Agarwal, S. and Tyagi, I. 2014. Potential of activated carbon from waste rubber tire for the adsorption of phenolics: Effects of pretreatment conditions. *J. Colloid Interface Sci.*, 417: 420-430.
- Jain, M., Garg, V.K. and Kadirvelu, K. 2011. Investigation of Cr (VI) adsorption onto chemically treated *Helianthus annuus*: Optimization using response surface methodology. *Bioresour. Technol.*, 102: 600-605.
- Jia, D. and Li, C. 2015. Adsorption of Pb(II) from aqueous solutions using corn straw. *Desalin. Water Treat.*, 56: 1.
- Joga Rao, H., King, P. and Prasanna Kumar, Y. 2016. Experimental investigation and statistical modeling of the cadmium adsorption in aqueous solution using activated carbon from waste rubber tire. *Indian J. Sci. Technol.*, 9(45): 1-13.
- Joga Rao, H., King, P. and Prasanna Kumar, Y. 2018. Application of response surface methodology for optimization of cadmium adsorption in an aqueous solution by activated carbon prepared from *Bauhinia purpurea* leaves. *Rasayan J. Chem.*, 11 (4): 1577-1586.
- Joga Rao, H., King, P. and Prasanna Kumar, Y. 2018. Equilibrium isotherm, kinetic modeling, and characterization studies of cadmium adsorption in an aqueous solution by activated carbon prepared from *Bauhinia purpurea* leaves. *Rasayan J. Chem.*, 11(3): 1376-1392.
- Joga Rao, H., King, P. and Prasanna Kumar, Y. 2019. Effect of process parameters on adsorption of cadmium from aqueous solutions by activated carbon prepared from *Bauhinia purpurea* leaves. *Nat. Environ. Pollut. Technol.*, 18(1): 141-148.
- Juanqin, Xue, Xiande, Jing, Shudi, Hu, Yuhong, Tian, Yonghui Song and Xinzhe, Lan 2019. Process optimization for the preparation of activated coke from industrial waste using response surface methodology. *Nat. Environ. Pollut. Technol.*, 18(4): 1415-1421.
- Juan Daniel Martinez, Neus Puy, Ramon Murillo Tomas Garcia, Maria Victoria Navarro, Ana Maria Mastral 2013. Waste tyre pyrolysis – A review. *Renew. Sustain. Energy Rev.*, 23: 179-213.
- Karnib, M., Kabbani, A., Holail, H. and Olama, Z. 2014. Heavy metals removal using activated carbon, silica and silica activated carbon composite. *Energy Procedia*, 50: 113-120.
- Ming-sheng, Miao, Yan-na, Wang, Qiang, Kong and Li, Shu 2016. Adsorption kinetics and optimum conditions for Cr(VI) removal by activated carbon prepared from luffa sponge. *Desalin. Water Treat.*, 57: 17.
- Momcilovic, M., Purenovic, M., Bojic, A., Zarubica, A. and Randelovid, M. 2011. Removal of lead(II) ions from aqueous solutions by adsorption onto pinecone activated carbon. *Desalin. Water Treat.*, 276: 53-59.
- Mishra, P.C. and Patel, R.K. 2009. Removal of lead and zinc ions from water by low cost adsorbents. *J. Hazard. Mater.*, 168 (1): 319-325.
- Salam, O. E. A., Reiad, N. A. and ElShafei, M. M. 2011. A study of the removal characteristics of heavy metals from wastewater by low-cost adsorbents. *J. Adv. Res.*, 2(4): 297-303.



Swimming Pool Water in Mafraq City in Northern Jordan: Quality Evaluation

Sura Taha Al-Harashsheh

Al al-Bayt University, Institute of Earth and Environmental Sciences, Mafraq, Jordan

†Corresponding author: Sura Taha Al-Harashsheh; sura@aabu.edu.jo

Nat. Env. & Poll. Tech.
Website: www.neptjournal.com

Received: 26-01-2020

Revised: 17-02-2020

Accepted: 16-04-2020

Key Words:

Swimming pools
Water quality
Residual chlorine
Total organic carbon
Trihalomethane
Total coliforms

ABSTRACT

The objective of this study is to examine the physical, chemical and biological characteristics of swimming pool water in Mafraq city, north of Jordan and the overall quality of the used water. Three public swimming pools were selected from Mafraq city [Areef Pool (SW1), Teachers Club Pool (SW2) and Anakeel Pool (SW3)] to analyze the physical, chemical and biological properties of their water as well as determine their compliance with the Jordanian Standards for Swimming Pools Water. Sampling was carried out weekly for eight successive weeks between July and August 2019 before bathing (after disinfection) and after bathing and analysed in Al al-Bayt University and Ministry of Environment laboratories. The parameters used to evaluate the quality of water in swimming pools were temperature, pH, electrical conductivity (EC), dissolved oxygen (DO), residual chlorine (Cl_2), total organic carbon (TOC), trihalomethanes (THM), major cations and anions, selected heavy metals, and total coliform bacteria, *E. coli* and *Pseudomonas*. Most of the physical and chemical parameters analysed were within the recommended limit except for pH and EC. Residual chlorine exceeded the permissible limits in SW3 before and after bathing, recording mean values of pH, EC (4.3 ± 0.25 - 4.33 ± 0.44), (2314 ± 343 - 2453 ± 460), respectively. The dissolved oxygen was less than the recommended limit. Total coliforms, *E. coli* and *Pseudomonas* counts were < 1 before and after bathing in all the samples.

INTRODUCTION

Swimming is one of the best sports that people of all ages can practice in their lives to maintain good health, especially for children with asthma. This is because inhaling moist air is less conducive to triggering exercise-induced asthma (Nemery et al. 2002).

Swimming pools are used by a wide range of people of various ages, health statuses and standards of hygiene (Public and Environment Health 1998). The water in swimming pools contains many microorganisms and undesirable dissolved chemical substances from several sources, including swimmers, animals, and debris like leaves, grass and dust (Popadopoulou et al. 2008). It contains many undesirable pollutants, such as skin cells, urine, sweat, saliva, ammonia, nose and throat secretions, and cosmetics. Urine and sweat are the most important components of swimming pools, and their presence spreads diseases and infections linked to the faecal contamination of water.

The increased concentration of some ions originating from pollutants, such as nitrates and phosphates, leads to algal growth. As the algae die, it decomposes and consume the dissolved oxygen in the water. This creates an anaerobic reaction that forms substances like acid, methane gas, and some harmful organic compounds.

These pollutants in swimming-pool water are removed via several physical and chemical methods, such as filtration, algaecides, disinfection, coagulants, acids and alkalis, and balancing the water pH.

One mechanical method for cleaning swimming-pool water is filtration, in which a filter removes virtually all particulate matter, so the water remains clear enough for continued use in the pool. Algaecide ($C_5H_{12}NOCl$), which is cationic, polymeric, and non-foaming, is used in swimming pools to control the growth of algal bloom and slime. After the use of algaecide, the pool water is filtered quickly to prevent the algae from depositing (www.ikingnod.com) (<https://www.okchem.com/product/nndimethyl2hydroxypropylammonium-chloride-polymer-25988970-201811051257620.html>)

Disinfection is the most important way to remove pathogens from swimming pools and minimize the risk to pool users from microbial contaminants. It involves adding chlorine gas or its derivatives, such as sodium hypochlorite, calcium hypochlorite, chloroisocyanurate, or trichloroisocyanuric acids (Yan et al. 2018).

One problem associated with the disinfection of water using a chlorine product is the accumulation of potentially toxic and disinfection by-products (DBPs) that result from the reaction of chlorine with organic matter, such as humic

and fulvic acids, which include chloramines, trihalomethanes (THMs), and haloacetic acids (HAAs) (Lempart et al. 2018, Chowdhury et al. 2014). Coagulants may be added as part of the water treatment process to enhance the removal of dissolved, colloidal, or suspended material. Acids and alkalis may also be added to the water to maintain an appropriate pH for optimal water treatment and the comfort of swimmers (WHO 2006).

Many studies have been conducted on swimming-water quality in different parts of the world. In Nigeria, Omoni et al. (2019) found that most of the physiochemical parameters analysed were within the recommended limits, except for residual chlorine, turbidity, dissolved oxygen, and total dissolved solids, which exceeded the permissible limit in swimming pools both before and after swimming, while two of the swimming pools studied increased in total coliforms (150% and 86%) and faecal coliform (105% and 22%) after swimming. In Ghana, Addo et al. (2018) found that the mean residual chlorine was significantly higher in the VH pool (1.357 ± 1.09) than the SH (0.353 ± 0.45) and RS (0.95 ± 0.93) pools, while the total coliforms, total dissolved solids (TDSs), and pH were within acceptable limits.

Ferres et al. (2016) found the mean values of residual chlorine and pH to be outside the recommended ranges, while the other physiochemical parameters, such as dissolved solids, turbidity, and electrical conductivity, were within established sanitary standards. The microbiological test showed that 30% of the pools tested had an average value

for heterotrophic organisms of 107 CFU/mL, higher than the limits set by Venezuelan law. Of the pools studied, 75% and 60% presented at least one positive test tube for total and faecal coliforms, respectively.

Fadaei et al. (2013) found that the values of biological parameters for the swimming pools they tested, such as total faecal coliform, *Escherichia coli*, *Legionella*, *Pseudomonas* and heterotrophic organisms, exceeded the guidelines, except for *Staphylococcus aureus*. While the correlation coefficient between the swimmer's load and the total faecal coliforms and heterotrophic bacteria was (0.949), the turbidity, free residual chlorine, and hardness of all the swimming pools were out of compliance with the standard guidelines.

Bilahac et al. (2012) analysed the free chlorine, pH, and some microbiological parameters in indoor pool waters in hotels. According to the results, 82.8% of their samples were microbiologically unacceptable, with free chlorine levels below 0.2 mg/L. They suggested that to reduce microbial risks to an acceptable level, the level of free chlorine above 0.2 mg/L.

Sagarat et al. (2012) investigated the water quality of swimming pools in Amman, Jordan. They found that the major inorganic chemical composition (HCO_3^- , Cl^- , NO_3^- , SO_4^{2-} , Ca^{2+} , Na^+ , and PO_4^{3-}), BOD and COD was acceptable according to both Jordanian and WHO standards.

The present study was performed to determine the microbiology quality as well as some physical and chemical quality parameters of the water of swimming pools of Mafraq City, Jordan. The objective was to identify whether the

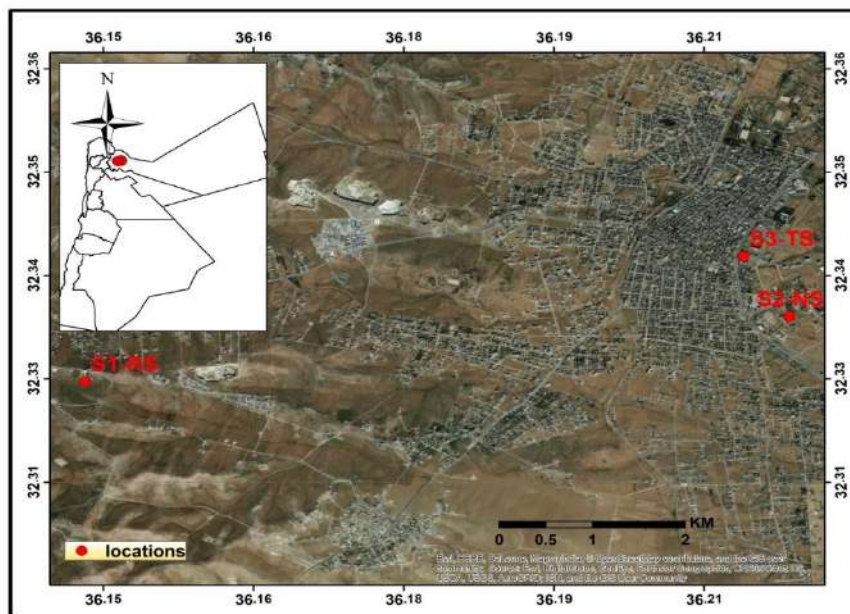


Fig. 1: Location of the study area.

swimming pools complied with WHO and Jordanian water standards (JS1526/2004). This study will provide an initial collection of data about the quality of public swimming pools in Mafraq and examine the risk factors associated with using these pools. This study is an attempt to recommend reformatory measures to safeguard swimmers from the health risks associated with swimming in unsterilized pools.

MATERIALS AND METHODS

Study Area

The study area is located in the city of Mafraq in northern Jordan (Fig. 1). Sampling was done of the three pools most used by swimmers of different ages: Areef (SW1), Teachers' Club (SW2), and Anakeel (SW3). These pools are supplied with high quality potable groundwater from the Amman-Zarqa Basin. The swimming pools are supplied with water at the beginning of the summer once without change, with more water added if the water level in the pools is reduced due to evaporation resulting from high temperatures in the study area, which during summer sometimes exceed 40°C.

Samples of pool water were collected twice a day after disinfection, once at 7 AM, before swimming activities begin, and once at 7 PM, when swimming activities end. Water sampling was done using two types of container: a 250 mL glass container for the microbiological test and a 1 L polyethylene container for the physical and chemical tests. The samples were collected below the water surface and placed in cold storage (4-10°C) immediately after collection. The samples were transported to the Institute of Earth and Environment Sciences Laboratories at Al al-Bayt University and analysed within 24 hours.

Physical and Chemical Analyses

Tables 1 and 2 show the physical and chemical characteristics of the studied swimming pools before and after swimming.

The analyses included temperature (°C), dissolved oxygen (DO, mg/L), electrical conductivity (EC, $\mu\text{S}/\text{cm}$), and pH and salinity, which were measured on-site using a WTW conductivity meter (Multi3320). Residual chlorine and total organic carbon (TOC) were determined by a spectrophotometer 7600 (DIN EN ISO 7393-2 and DIN38402A51), respectively. Trihalomethane (THM) samples were analysed using Gas Chromatography (Trace-GC). The major cations, such as total hardness (TH) and Ca^{2+} , were measured using the EDTA titrimetric method, and Mg^{2+} by calculation. Na^+ and K^+ were determined using a flame photometer. Cl^- and HCO_3^- were measured with silver nitrate and sulfuric acid titrimetric method, respectively. NO_3^- , SO_4^{2-} and PO_4^{3-} were analysed using an ultraviolet spectrometric method. Heavy metals, such as Mn, Zn, Cu, Cr and Pb, were measured using an Inductivity Coupled Plasma ICP-OES (Perkin Elmer). Preparation and measurements were performed according to standard methods (APHA 2005).

Biological Analysis

Microbiological contamination using defined substrate technology detected the presence of total coliforms, *Escherichia*, and *Pseudomonas* per 100 mL. Total coliforms, *Escherichia coli* and *Pseudomonas* were determined using the Coliler-18 (Quanti-Tray/2000) and Pseudalert® (Quanti-Tray/2000) methods, respectively, according to the manufacturer's instructions.

RESULTS AND DISCUSSION

Physical and Chemical Parameters of the Swimming Pools

From Table 1 and Fig. 2, it can be seen that the mean temperature of the swimming pools' water samples was within the acceptable limits set by JS and WHO of 21-32°C; it ranged from 24.4°C to 26.3°C before swimming and 26.3°C to 26.7°C after swimming.

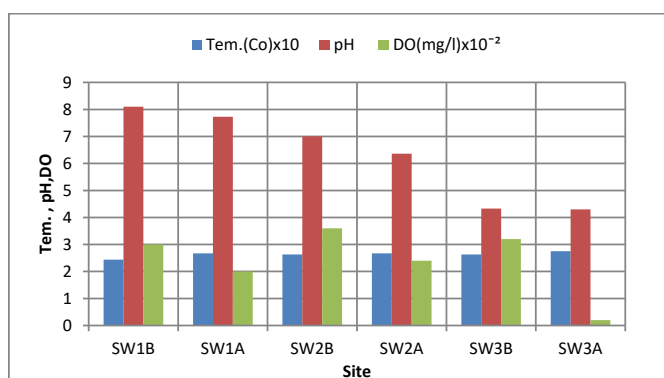


Fig. 2: Temperature (°C), pH, and DO (mg/L).

Table 1: Mean values and standard deviations of physical and chemical characteristics of the studied swimming pools before and after swimming.

Parameters		SW1B	SW1A	SW2B	SW2A	SW3B	SW3A	JS and WHO
Temperature (°C)	Max.	25	27.3	26.7	28.8	27.3	28.3	22–29
	Min.	24	25.9	25.6	25.9	25	27	
	Mean ± SD	24.4±0.42	26.7±0.62	26.3±0.46	26.7±1.21	26.3±1.08	27.5±0.52	
pH	Max.	8.71	8.06	7.82	7.81	4.95	4.6	7.2–7.8
	Min.	7.76	7.74	4.22	3.48	4.14	4.0	
	Mean ± SD	8.1±.37	7.73±0.13	7.01±1.57	6.36±1.60	4.33±0.44	4.3±0.25	
Dissolved O ₂ (mg/L)	Max.	2.04	1.03	3.07	1.03	2.06	0.03	5
	Min.	0.02	0.02	0.02	0.02	0.03	0.02	
	Mean ± SD	2.03±0.007	1.02±0.006	3.036±0.02	1.024±0.006	2.032±0.005	0.0023±0.005	
EC (µS/cm)	Max.	1179	1635	1421	1710	2900	3190	
	Min.	1025	1038	1087	1086	2030	2050	
	Mean ± SD	1075±64	1217±259	1189±138	1312±260	2314±343	2453±460	
Salinity (mg/L)	Max.	358.6	576.4	473.9	589.2	813.3	1056.6	
	Min.	268.97	301	320.21	326.6	525.2	595.6	
	Mean ± SD	310.6±40	376.5±114	389.1±70	431.6±113	658±118	765.9±182	
Residual Chlorine (mg/L)	Max.	2.59	2.21	3.8	3.13	0.5	0.16	1–3
	Min.	0.15	0.09	0.11	0.05	0.12	0.05	
	Mean ± SD	0.998±1.16	0.873±1.04	1.26±3.4	1±1.3	0.26±0.13	0.117±0.03	
TOC (mg/L)	Max.	85.3	47.1	83.5	83.1	80.1	50.5	
	Min.	30.2	19.6	27.7	18.8	20.2	30.2	
	Mean ± SD	45.82±22.7	28.76±10.9	54.86±26.2	41.26±25.3	42.26±23.8	39.2±7.3	
THM (mg/L)	Max.	0.07	0.054	0.054	0.052	0.047	0.038	0.15
	Min.	0.053	0.052	0.053	0.049	0.042	0.034	
	Mean ± SD	0.062±0.012	0.053±0.001	0.054±0.001	0.051±0.002	0.045±0.004	0.036±0.003	
Na ⁺ (mg/L)	Max.	187.8	249.9	148.6	143.6	313.1	315.1	200–300
	Min.	131.8	139.6	129.6	136.6	249.9	251.9	
	Mean ± SD	152.3±21.1	171.9±52.2	138.7±8.6	139.3±3.4	277.3±27.8	284.8±32.5	
K ⁺ (mg/L)	Max.	18.2	18.4	9.9	15.3	17.7	21.7	12
	Min.	14.8	15.5	6.5	5.8	14.0	14.3	
	Mean ± SD	16.3±3	17.3±1.2	7.9±1.5	9.1±3.9	15.7±1.8	17.5±3.3	
Ca ²⁺ (mg/L)	Max.	155.0	148.9	138.7	130.6	142.8	163.2	250
	Min.	93.8	53.0	57.1	69.4	106.1	110.2	
	Mean ± SD	108.5±27.9	115.8±43.2	103.6±34.6	111.2±28.1	126.5±15.3	137.9±21.5	
Mg ²⁺ (mg/L)	Max.	31.6	36.5	46.2	38.9	51.03	60.75	250
	Min.	2.4	4.9	12.2	2.4	24.3	24.3	
	Mean ± SD	13.6±11.6	14.9±14.5	23.7±16.0	25.8±24.9	36.5±11.0	42.5±14.8	
Cl ⁻ (mg/L)	Max.	198.5	319.1	262.3	326.1	450.2	584.9	500
	Min.	148.9	166.6	177.3	180.8	290.7	329.7	
	Mean ± SD	171.9±22.1	214.5±71.0	215.4±38.5	238.9±62.7	364.2±65.6	424±100.5	
HCO ₃ ⁻ (mg/L)	Max.	171.0	158.8	183.21	158.8	Not found	Not found	
	Min.	97.6	73.2	109.9	146.6			
	Mean ± SD	128.2±30.8	129.4±38.2	150.6±37.3	154.7±7.1			
NO ₃ ⁻ (mg/L)	Max.	35.6	24.6	27.37	27.8	39.6	37.9	50
	Min.	20.6	3.7	24.2	5.6	34.9	5.97	
	Mean ± SD	26.0±6.6	18.3±8.5	25.7±1.32	22.2±9.3	37.0±2.2	30.5±13.8	
SO ₄ ²⁻ (mg/L)	Max.	24.8	24.8	16.8	17.16	29.5	31.14	500
	Min.	12.7	14.9	10.1	10.31	10.8	10.87	
	Mean ± SD	16.9±6.8	18.2±5.7	13.4±3.4	13.6±3.4	21.8±9.8	22.7±10.5	
PO ₄ ³⁻ (mg/L)	Max.	0.092	0.391	0.194	0.671	0.403	0.342	0.03
	Min.	0.009	0.049	0.076	0.082	0.112	0.086	
	Mean ± SD	0.044±0.038	0.12±0.149	0.011±0.056	0.275±0.236	0.219±0.14	0.209±0.113	

One of the most important items to test in swimming water is pH. The mean values of the swimming pools' water ranged between 4.33 in SW3 and 8.1 in SW1 before swimming and from 4.3 in SW3 to 7.73 in SW1 after swimming (Fig. 2). The pH for SW1B, SW2A, and SW3 was not within the recommended standard of 7.2-7.8. All pH values for SW3 were less than 5, due to excessive chlorination resulting from using trichloroisocyanuric acid ($C_3Cl_3N_3O_3$) in the disinfection process; the trichloroisocyanuric acid raised the acidity of the water. It was found that the soda ash (Na_2CO_3) used to neutralize the pH was insufficient, causing burns on the skin of some children who used this pool (Fig. 3). It was noted during sample collection that the managers of SW3 evacuated the pool and disinfected the water every 3 hours, which in turn affected the health of the pool users.

Dissolved oxygen is probably the most critical quality parameter in swimming-pool water. The DO level can indicate how polluted the water is and how well it can support aquatic plant and animal life (Omoni et al. 2019). The DO content was significantly lower than the acceptable standard (7.5 mg/L); it ranged between 2.03 mg/L and 3.036 mg/L before swimming and between 0.0023 mg/L and 1.024

mg/L after swimming (Fig. 2). This reduction is due to its consumption by bacteria, which decompose the organic pollutants in swimming pools. Generally, a higher DO level indicates better water quality and healthier sampled pools. The depletion of DO in water could facilitate the microbial conversion of nitrates (WHO 2008), and a low level of DO in pool water is not healthy for humans.

Fig. 4 shows the mean values of EC and salinity. The mean value of EC ranged between 1075 $\mu S/cm$ and 2314 $\mu S/cm$ before swimming and between 1217 $\mu S/cm$ and 2453 $\mu S/cm$ after swimming. The mean value of the salinity ranged between 310.6 mg/L and 658.12 mg/L before swimming and between 376.5 mg/L and 765.9 mg/L after swimming. These values are within the permissible limits set by JS and WHO, except for SW3, which exceeded the recommended standards due to the high percentage of dissolved salt in the water and the addition of pollutants from swimmers.

Table 1 and Fig. 5 show the residual level of chlorine concentration before swimming, which is higher than the level after swimming. The mean values of the residual chlorine ranged between 0.26 and 2.26 mg/L before swimming and



Fig. 3: Burns on the bodies of some children attending SW3.

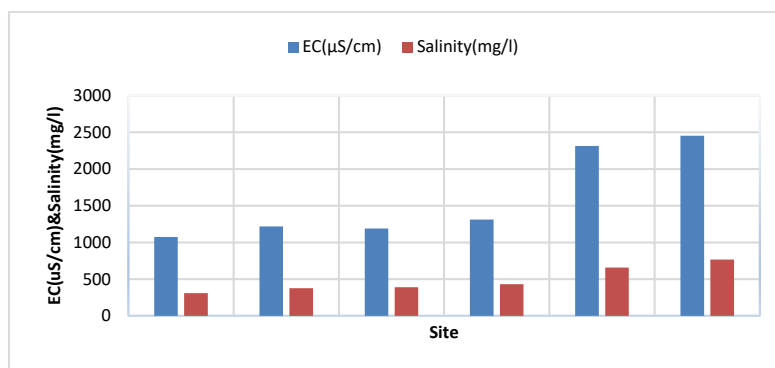


Fig. 4: EC ($\mu S/cm$) and salinity (mg/L).

between 0.117 and 1 mg/L after swimming. The results show that the mean residual chlorine was significantly higher in SW2 than in the other pools (SW1 and SW3). The obtained results were within the standards set by WHO and JS. In this study, the main reason for low residual chlorine is the consumption of chlorine in killing microbes in the water and its interaction with organic substances, forming undesirable compounds, such as THMs and HAAs.

Swimming pools must be disinfected to prevent the spread of disease among swimmers and the unwanted growth of bacteria and algae. When chlorine comes into contact with organic matter, it may result in the production of undesirable and dangerous substances for human health and the environment, such as THMs (chloroform, bromodichloromethane, dibromochloromethane and bromoform) and HAAs. In this study, the mean concentration of TOC before swimming ranged between 39.2 mg/L and 54.86 mg/L, and of THMs between 0.045 mg/L and 0.062 mg/L, and after swimming ranged between 28.7 mg/L and

41.26 mg/L and between 0.036 mg/L and 0.053 mg/L, respectively (Fig. 5). Because it is an indoor pool, SW1 showed a higher concentration of THMs than did other pools, but no pool exceeded permissible limits, as most of the chlorine was used to remove pathogens and react with TOC to form THM and HAA compounds. THMs are naturally volatile and can evaporate from the water, a process that depends on several factors, including their concentration in the water, the temperature, the amount of splashing, and surface disturbance (WHO 2006). As shown in Fig. 5, THMs increased with acidity, due to a longer reaction time and higher chlorination dosage (Wang et al. 2015). Potential THM formation increases with the concentration of TOC. The yield of THMs increased with pH, which ranged from 5 to 10 (Wang et al. 2015). This was inconsistent with the observations of other researchers (Zhang et al. 2010).

TH, Ca^{2+} , Mg^{2+} , K^+ , Na^+ , Cl^- , HCO_3^- , NO_3^- , and SO_4^{2-} in all pools were within the recommended standards; HCO_3^- was

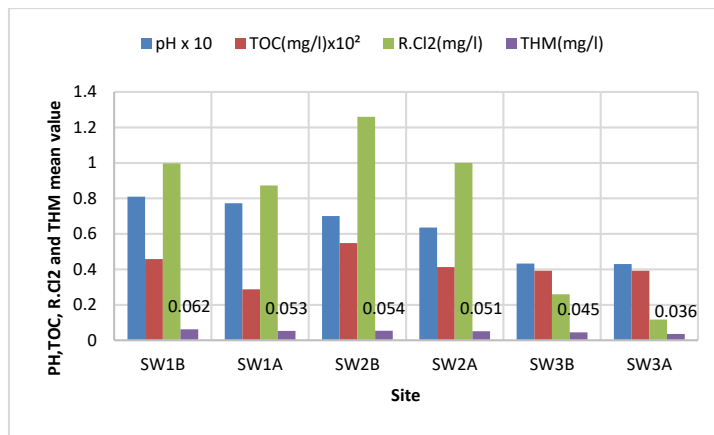


Fig. 5: Mean pH and mean concentrations of TOC, Residual chlorine and THM (mg/L).

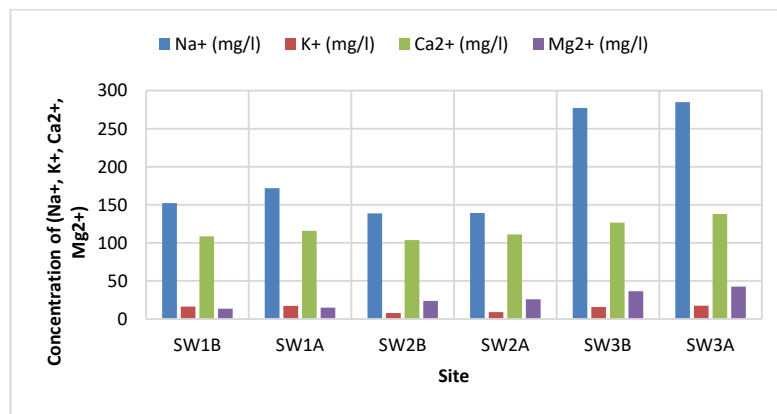


Fig. 6: Concentration of Na⁺, K⁺, Ca²⁺ and Mg²⁺ (mg/L).

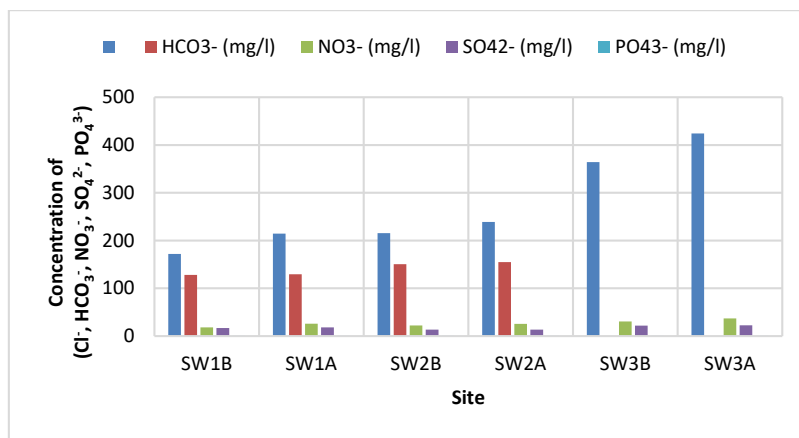


Fig. 7: Concentration of Cl⁻, HCO₃⁻, NO₃⁻, SO₄²⁻, and PO₄³⁻ (mg/L).

Table 2: Mean concentrations of the measured heavy metals (DL: Detection limit).

Parameter	SW1B	SW1A	SW2B	SW2A	SW3B	SW3A	JS&WHO
B (mg/L)	<DL	<DL	<DL	0.127	0.098	0.177	1
Mn (mg/L)	0.033	0.015	<DL	<DL	0.019	0.018	0.1
Zn (mg/L)	<DL	<DL	0.036	0.061	1.018	0.665	4
Cu (mg/L)	0.0227	0.027	0.038	0.103	0.031	0.034	0.2
Cr (mg/L)	0.01	0.009	0.033	0.004	<DL	0.032	0.05
Pb (mg/L)	<DL	<DL	<DL	<DL	<DL	<DL	0.01

not. The concentration of HCO₃⁻ was zero in SW3 because the mean value of its pH was less than 5 both before and after swimming. This study shows that the concentration of PO₄³⁻ was higher than the recommended standards (<0.03 mg/L) in both SW1 and SW3 both before and after swimming (Table 1 and Figs. 6 and 7).

Table 2 shows the concentration of heavy metals B, Mn, Zn, Cu, Cr and Pb. All mean values measured were lower than the recommended standards for water used for drinking and recreation.

Microbiological Parameters

The results of the study indicate that the swimming water improved in total coliform, *Escherichia* and *Pseudomonas* before and after swimming due to the effectiveness of the disinfection process and compliance with JS and WHO <1/100mL.

CONCLUSIONS

Our study has provided information on the quality of the swimming water in some selected swimming pools in Mafraq City in Northern Jordan. Most parameters tested in SW3 did not meet the Jordanian or WHO standards for the physical

and chemical quality of swimming pools, but most physical and chemical parameters in SW1 and SW2 were found to be within the permissible limits of both sets of standards. The microbiological loads of all the swimming pools, however, were acceptable according to both Jordanian and WHO standards. The THMs increase when the pH increases due to the longer reaction time and higher chlorination dosage.

REFERENCES

- Addo, M., Tee, J. and Larbi, J. 2018. Recreational water quality assessment of some selected swimming pool in Asuogyaman district, Ghana. *Microbiology Research Journal International*, 26(5): 1-8.
- APHA 2005. *Standard Methods for the Examination of Water and Wastewater*, 20^{ed}. American Public Health Association, American Water Works Association and Water Environment Federation. Washington DC.
- Bilahac, L., Lusic, D., Jelinic, J. and Rukavina, T. 2012. Microbiological and chemical indicators of water quality in indoor hotel swimming pools before and after training of swimming pool operators. *Journal of Water and Health*, 10(1): 108-115.
- Chowdhury, S., Alhooshanik, K. and Karanfil, T. 2014. Disinfections byproducts in swimming pools: Occurrences, implications and future needs, a review. *Water Research*, 53: 68-109.
- Fadaei, A. and Amiri, M. 2013. Comparison of chemical, biological and physical quality assessment of indoor swimming pools in Shahrekord city, Iran in 2013. *Global Journal of Health Science*, 7(3): 240-248.
- Ferres, S., Colina, C., Morales, P., Torres, R., Castellano, C. and Leal, J. 2016. Physicochemical and microbiological quality of swimming

- pool water of two recreational complexes in Zulia State. *Boletín de Malariología y Salud Ambiental*, 2: 202-210.
- Hong, H., Yujing, X., Mengyong, R., Fanglei, L., Hongjun, L. and Yan, L. 2012. Factors affecting THMs, HAAs and HNMs formation of Jin Lan reservoir water exposed to chlorine and monochloramine. *Science of the Total Environment*, 444: 196-204.
<https://www.okchem.com/product/nndimethyl2hydroxypropylammonium-chloride-polymer-25988970-201811051257620.html>
- Lempart, A., Kudlek, E. and Dudziak, M. 2018. Determination of micropollutants in water samples from swimming pool systems. *Water*, 10: 1083.
- Nemery, B. Hoet, P.M. and Nowak, D. 2002. Indoor swimming pools, water chlorination and respiratory health. *Eur. Respir.*, 19: 790-793.
- Nowack, R. and Views, C. 2016. *The Chemistry of Pools*, copyright: Wiley-VCH Verlag GmbH & CO. kGaA Weinheim.
- Omoni, V., Torjir, D. and Okeporo, S. 2019. Studies on the physicochemical and bacteriological properties on the semi-public swimming pools in Makurdia, Nigeria, *African Journal of Microbiology Research*, 13(4): 264-272.
- Popadopoulou, C., Economou, V., Sokkas, H., Gousia, P., Giannakopoulos, X. and Dontorou, C. 2008. Microbiological quality of indoor and outdoor (1998-2019). Swimming pools in Greece: Investigation of the antibiotic resistance of the bacterial isolates. *Int. J. Hyg. Environ. Health*, 211(3-4): 385-97.
- Public and Environmental Health Act of Government of Australia 1998. Standard for the Operation of Swimming Pools and Spa Pools in South Australia. Public and Environmental Health Act of Government of Australia.
- Sagarat, B., Harahsheh, S. and Jiries, A. 2012. Inorganic chemical composition of swimming pools in Amman-Jordan. *Research Journal of Environmental and Earth Sciences*, 4(10): 890-849.
- Wang, F., Baoyu, G., Defang, M., Ruihua, L., Shenglei, S., Qinyan, Y., Yan, W. and Qian, L. 2016. Effects of operating conditions on trihalomethanes formation and speciation during chloramination in reclaimed water. *Environ. Sci. Pollut. Res.*, 23(2): 1576-1583.
- WHO 2006. *Guidelines for Safe Recreational Water Environments*, Vol. 2, Swimming Pools and Similar Environments. World Health Organization.
- Yan, M., Roccaro, P., Fabbicino, M. and Korshin, G. 2018. Comparison of the effects of chloramine and chlorine on the aromaticity of dissolved organic matter and yields of disinfection by-products. *Chemosphere*, 191: 477-484.
- Yang, L., Chene, X., Shef, Q., Cao, G., Liua, Y., Chang, V. and Tangh, C. 2018. Regulation, formation, exposure, and treatment of disinfection by-products (DBPs) in swimming pool waters: A critical review. *Environment International*, 121(1039-1057).
- Zhang, Y.J., Zhou, L.L., Zeng, G., Song, Z.G. and Li, G.B. 2010. Factors affecting the formation of trihalomethanes in the presence of bromide during chloramination. *J. Zhejiang Univ. Sci. A*, 11(8): 606-612.



SEM-EDAX analysis of the Soil Samples of River Yamuna in Delhi Region

Vivek Chopra* and Jai Gopal Sharma**†

*Department of Botany, Hindu College, University of Delhi, Delhi-110007 India

**Department of Biotechnology, Delhi Technological University, Delhi-110042, India

†Corresponding author: Jai Gopal Sharma; sharmajai@gmail.com

Nat. Env. & Poll. Tech.
Website: www.neptjournal.com

Received: 24-03-2020

Revised: 27-04-2020

Accepted: 27-05-2020

Key Words:

SEM-EDAX
River Yamuna
Soil analysis
Niobium
Aluminium

ABSTRACT

A total of 18 samples were collected from two different sites at different depths of Yamuna river bed in Delhi. Nine samples were collected at Site A (Palla Village) from three different locations at different depths of the river bed. A similar set of 9 samples were collected from Site B (Okhla barrage). All samples were analysed for atomic and weight percentage of elements using SEM-EDAX. The major elements found in the study were Si, O, Al and Nb. Si and O are found in a maximum amount in all the samples with a varying range of atomic percentage 25.3-89.27 and 55.09-95.78 respectively. The recorded atomic percentage of Nb was 0.32 while Al was 16.7-25.51. Site A, Palla is least affected by pollution while at Site B the presence of Al revealed contamination from pollutants. The weight percentage of the elements has also been calculated. SEM images of soil samples revealed the platy flakes, irregular and spongy structure of soil particles.

INTRODUCTION

The River Yamuna is the longest and second largest tributary of river Ganga. Originating from the Yamunotri glaciers at a height of 6,387 M on the uppermost region of the lower Himalayas in Uttarakhand. Its 48 km stretch which passes from Delhi is a major source of drinking and potable water for the 70% population of Delhi (CPCB 2006). It shows the importance of river Yamuna as a major source of water and an indispensable part of the ecosystem. Many studies explain about the water quality of the river but hardly any are available about soil elemental composition. The present study reveals the atomic and weight percentage of different elements as well as some physical properties of soil samples collected from different depths of the river bed. The important elements observed in the following study are Silica (Si), Oxygen (O), Aluminium (Al) and Niobium (Nb). The aim of the study is to reveal the concentration of the elements at different depths of the river bed using SEM-EDAX techniques to enhance our knowledge about the physicochemical nature of the alluvial deposits in the river bed.

MATERIALS AND METHODS

A total of 18 samples were collected from two different sites (Fig. 1) of river Yamuna in March 2019. Site A (28°85'61.7"N; 77°20'80.2"E) was located at Palla village which is the point where River Yamuna enters in Delhi. Site

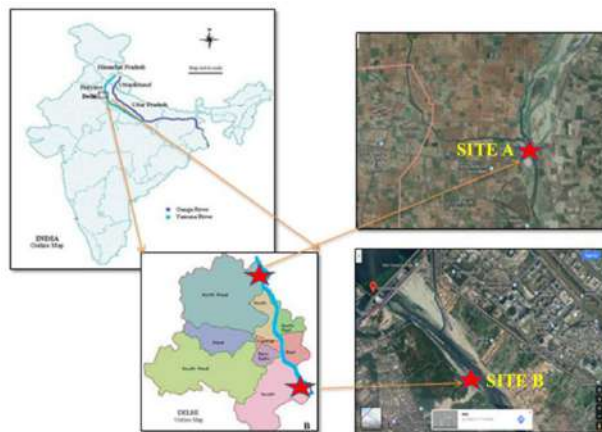


Fig. 1: Location of Site A (Palla village) and Site B (Okhla barrage) in Delhi.

A is comparatively free from pollutants and other anthropogenic activities beside agriculture in the vicinity. Multiple samples were collected to yield a better and authentic interpretation of results. Nine samples were collected from 3 different locations of Site A.

At location 1, the samples were taken from the surface (0-2 cm) and at the depth of 30-32 cm and 78-80 cm of the river bed. From location 2 and location 3, samples were taken from the surface (0-2 cm), 30-32 cm and 74-76 cm and 0-2 cm, 26-28 cm and 59-61 cm respectively. The

same set of sampling was done at Site B, i.e. Okhla barrage (28°32'10.5"N, 77°19'29.6"E) with 9 samples in total from three different locations at the surface (0-2 cm) and at various depths of 30-32 cm and 96-98 cm from location 4 and from location 5 and 6 at the surface (0-2 cm), 30-32 cm and 62-64 cm and 0-2 cm, 30-32 cm and 62-64 cm respectively. Site B is one of the most polluted stretches of river Yamuna where it receives a heavy load of industrial effluents and household sewage discharge from many major drains. Geographical locations were taken by Garmin GPSMAP 76 CSX global positioning system. Five-10 mg subsamples were homogenized, sun-dried and sieved out to remove excess

unwanted debris, later the samples were dried in an oven at 60°C for three days to remove moisture completely (Das & Mondal 2011, Tan 2005). Dried samples were mounted and microstructure was analysed using Scanning Electron Microscope model Zeiss EVO 18 research. The elemental composition was determined by an Energy Dispersive X-ray Spectroscopy (EDAX) attached to SEM.

RESULTS AND DISCUSSION

In all the 18 samples, EDAX analysis was performed to study the elements present in the soil. Si, O, Nb, and Al

Table 1: Elements Atomic % of three locations at Site A (Palla Village).

Elements	Depths at Location 1			Depths at Location 2			Depths at Location 3		
	0-2 cm	30-32 cm	78-80 cm	0-2 cm	30-32 cm	74-76 cm	0-2 cm	26-28 cm	59-61 cm
Atomic %									
Oxygen (O)	57.78	0	55.09	0	58.92	95.35	0	0	91.84
Silicon (Si)	36.78	83.85	38.69	89.27	35.49	0	79.82	81.94	0
Niobium (Nb)	0.32	0	0	0	0	0	0	0	0
Aluminium (Al)	0	0	0	0	0	0	0	0	0

Table 2: Elements Weight % of three locations at Site A (Palla Village).

Elements	Depths at Location 1			Depths at Location 2			Depths at Location 3		
	0-2 cm	30-32 cm	78-80 cm	0-2 cm	30-32 cm	74-76 cm	0-2 cm	26-28 cm	59-61 cm
Weight %									
Oxygen (O)	30.86	27.6	0	0	31.01	62.51	0	0	47.76
Silicon (Si)	34.48	34.03	42.54	54.26	32.79	0	36.06	39.28	0
Niobium (Nb)	0.98	0	0	0	0	0	0	0	0
Aluminium (Al)	0	0	0	0	0	0	0	0	0

Table 3: Elements Atomic % of three locations at Site B (Okhla barrage).

Elements	Depths at Location 4			Depths at Location 5			Depths at Location 6		
	0-2 cm	30-32 cm	76-98 cm	0-2 cm	30-32 cm	67-69 cm	0-2 cm	26-28 cm	62-64 cm
Atomic %									
Oxygen (O)	86.66	92.36	0	62.31	0	92.2	95.78	94.43	56.2
Silicon (Si)	0	0	81.67	31.75	60.17	0	0	0	25.3
Niobium (Nb)	0	0	0	0	0	0	0	0	0
Aluminium (Al)	0	0	0	0	25.51	0	0	0	16.7

Table 4: Elements Weight % of three locations at Site B (Okhla barrage).

Elements	Depths at Location 4			Depths at Location 5			Depths at Location 6		
	0-2 cm	30-32 cm	76-98 cm	0-2 cm	30-32 cm	67-69 cm	0-2 cm	26-28 cm	62-64 cm
Weight %									
Oxygen (O)	34.54	49.54	0	32.6	0	48.98	64.86	57.94	37.24
Silicon (Si)	0	0	38.85	29.16	32.5	0	0	0	29.43
Niobium (Nb)	0	0	0	0	0	0	0	0	0
Aluminium (Al)	0	0	0	0	13.24	0	0	0	18.67

were the main elements found in the analysis. Si and O were present in major quantities in almost all the samples while Nb was recorded in very less amount in the sample taken from the surface (0-2 cm) of location 1 of Site A (Palla). Al was recorded from location 5 and 6 of Site B at the depth of 30-32 cm and 62-64 cm. Elemental weight percentage

and atomic percentage distribution in all the soil samples and the various depths on which samples were taken have been elucidated in Tables 1-4, while SEM images showing soil particles and EDAX spectrum representing all observed elements are shown in Figs. 2-7 and Figs. 8-25 respectively [Gold (Au) was also shown in graphs because soil samples

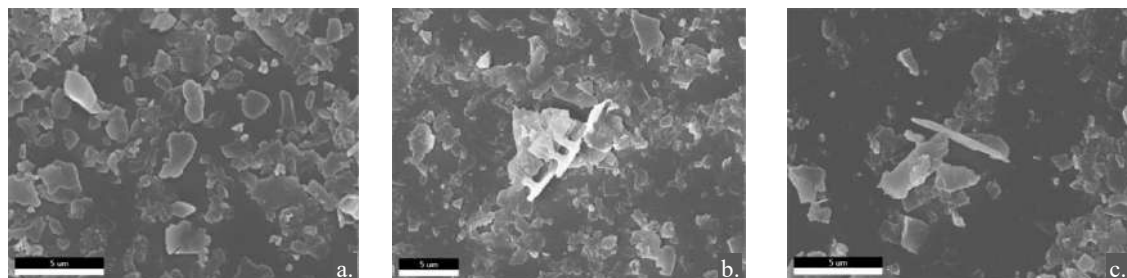


Fig. 2: a,b,c. SEM images showing soil particles of different depths 0-2 cm(a), 30-32 cm(b), 78-80 cm(c) at Location 1 at Site A (Palla Village).

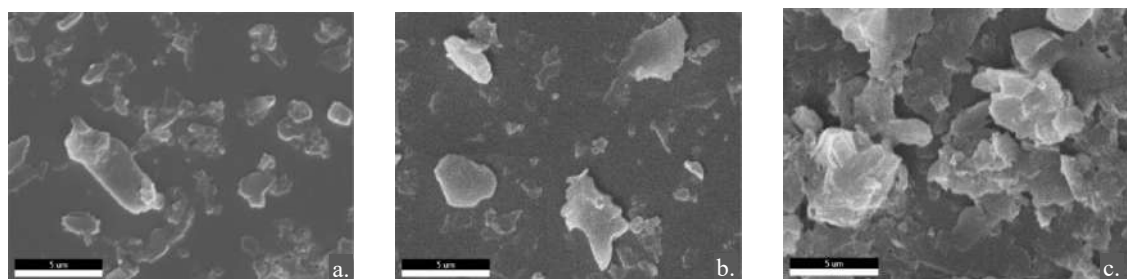


Fig. 3: a,b,c. SEM images showing soil particles of different depths 0-2 cm (a), 30-32 cm (b), 74-76 cm (c) of Location 2 at Site A (Palla Village).

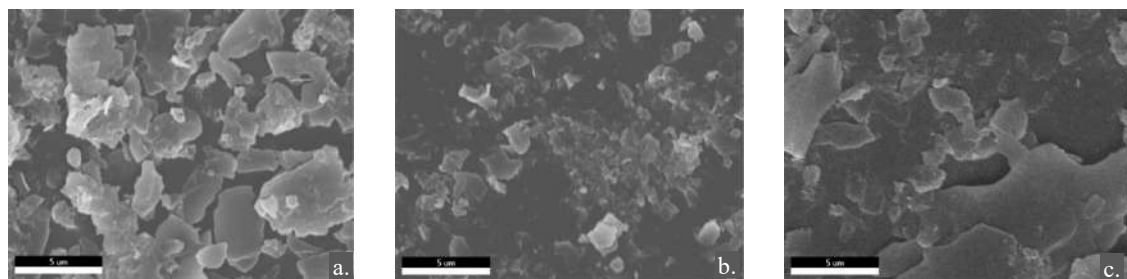


Fig. 4: a,b,c. SEM images showing soil particles of different depths 0-2 cm (a), 26-28 cm (b), 59-61 cm(c) of Location 3 at Site A (Palla Village).

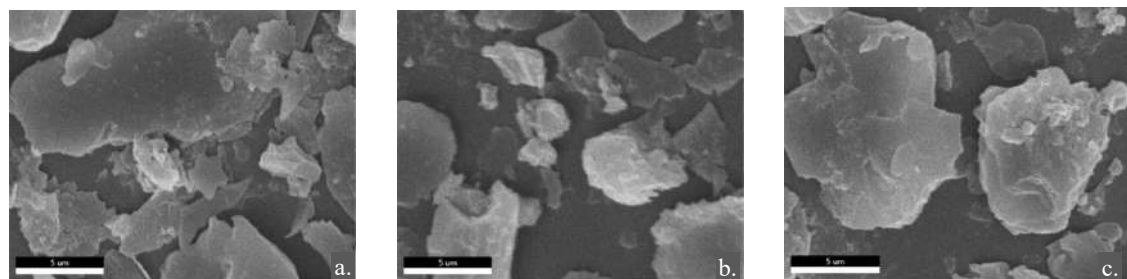


Fig. 5: a,b,c. SEM images showing soil particles of different depths 0-2 cm (a), 30-32 cm (b) and 76-98 cm (c) at Location 1 at Site B (Okhla barrage).

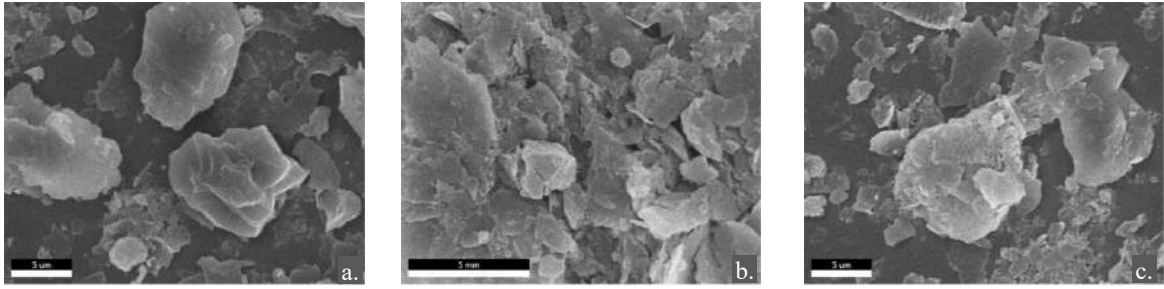


Fig. 6: a,b,c. SEM images showing soil particles of different depths 0-2 cm (a), 30-32 cm (b) and 67-69 cm (c) at Location 2 at Site B (Okhla barrage).

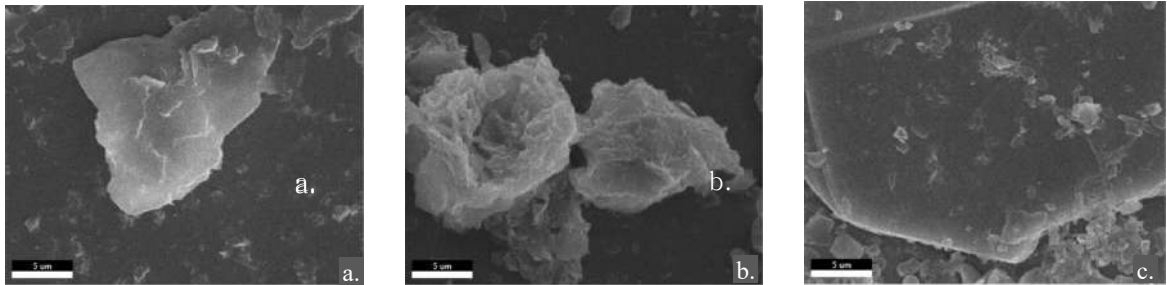


Fig. 7: a,b,c. SEM images showing soil particles of different depths 0-2 cm (a), 26-28 cm (b) and 62-64 cm (c) at Location 3 at Site B (Okhla barrage).

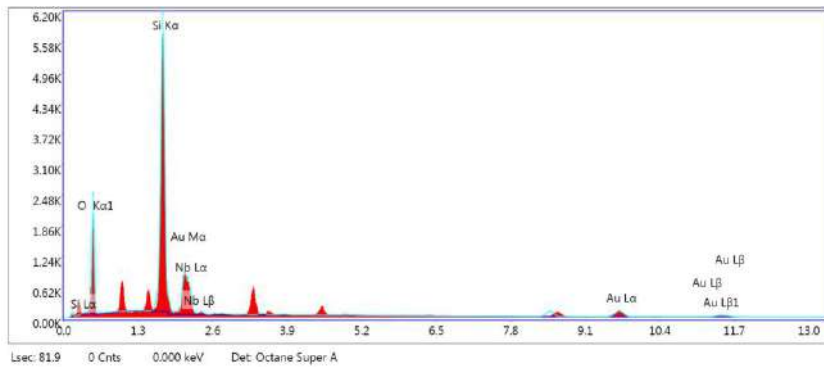


Fig. 8: EDAX spectrum of Location 1 (Depth 0-2 cm) at Site A (Palla Village).

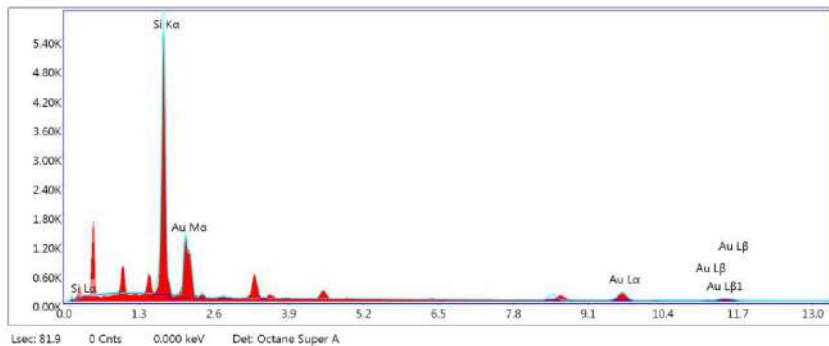


Fig. 9: EDAX spectrum of Location 1 (Depth 30-32 cm) at Site A (Palla Village).

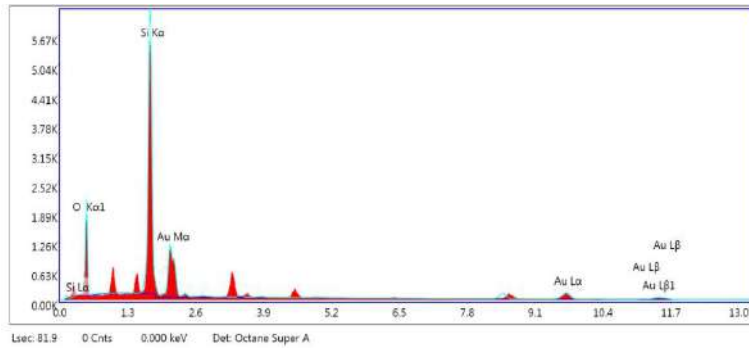


Fig. 10: EDAX spectrum of Location 1 (Depth 80-82 cm) at Site A (Palla Village).

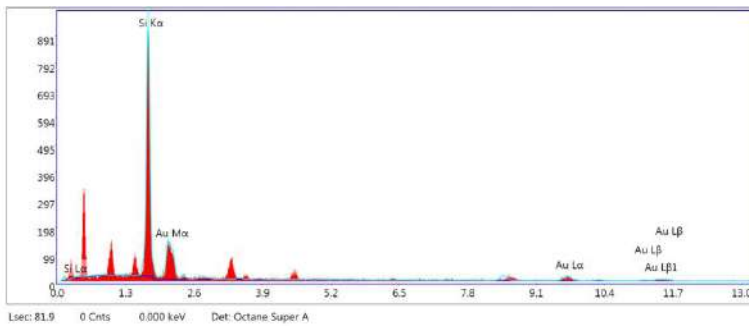


Fig. 11: EDAX spectrum of Location 2 (Depth 0-2 cm) at Site A (Palla Village).

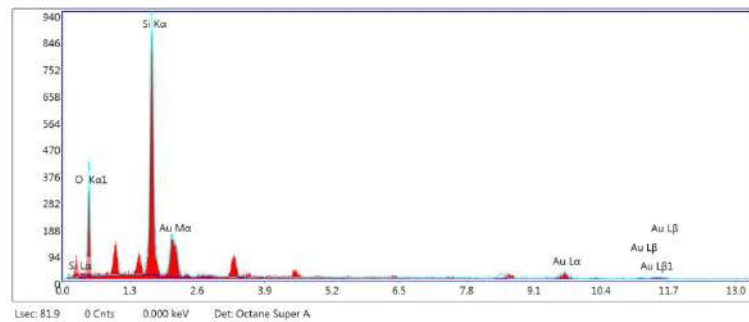


Fig. 12: EDAX spectrum of Location 2 (Depth 30-32 cm) at Site A (Palla Village).

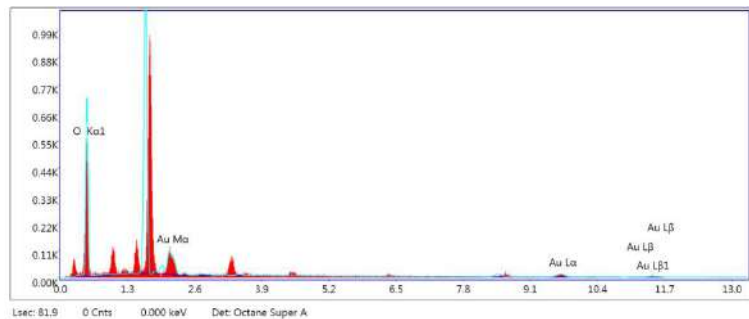


Fig. 13: EDAX spectrum of Location 2 (Depth 74-76 cm) at Site A (Palla Village).

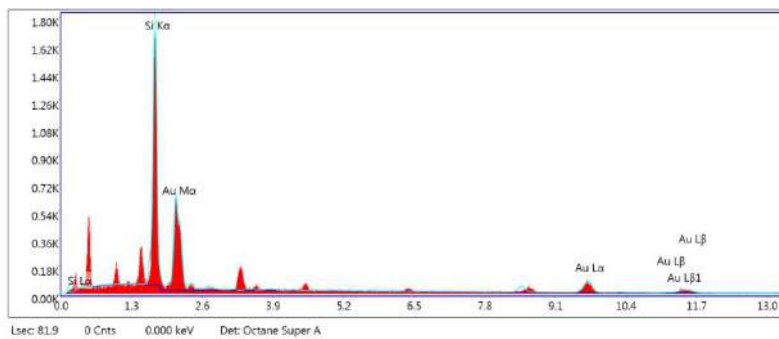


Fig. 14: EDAX spectrum of Location 3 (Depth 0-2 cm) at Site A (Palla Village).

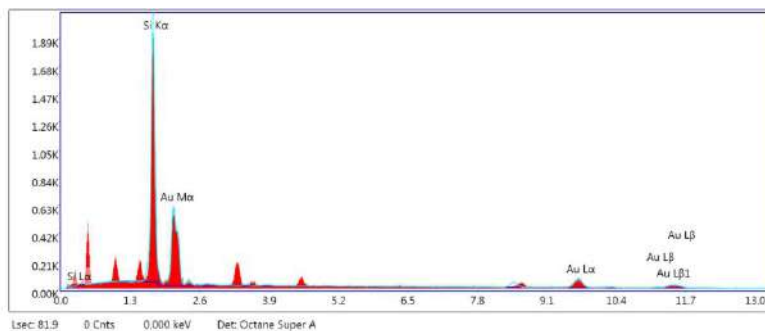


Fig. 15: EDAX spectrum of Location 3 (Depth 26-28 cm) at Site A (Palla Village).

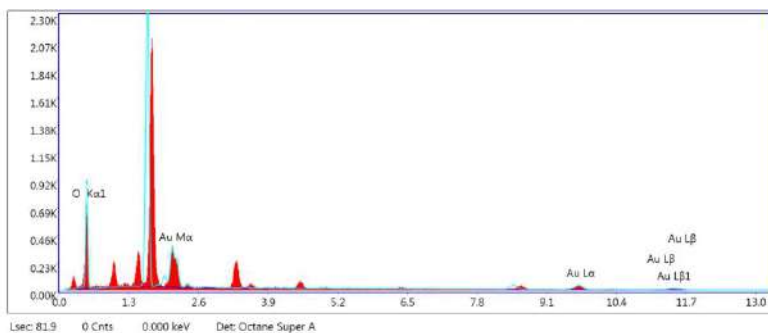


Fig. 16: EDAX spectrum of Location 3 (Depth 59-61 cm) at Site A (Palla Village).

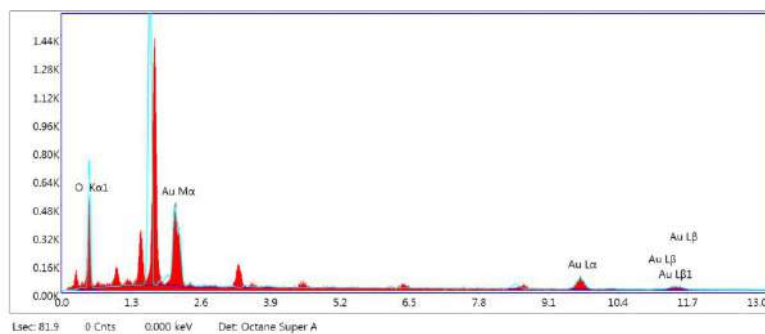


Fig. 17: EDAX spectrum of Location 1 (Depth 0-2 cm) at Site B (Okhla barrage).

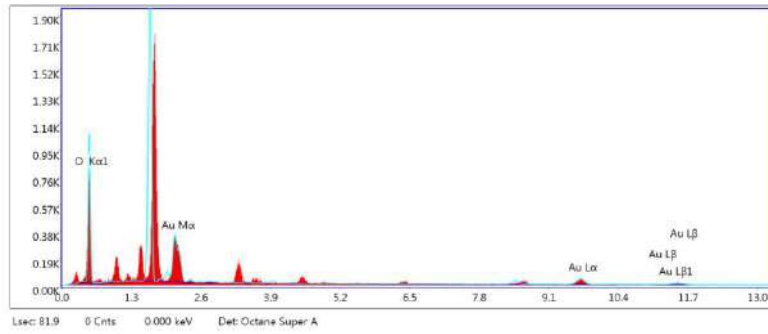


Fig. 18: EDAX spectrum of Location 1 (Depth 30-32 cm) at Site B (Okhla barrage).

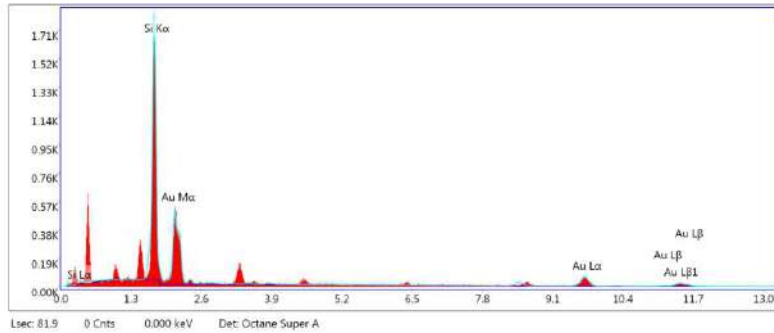


Fig. 19: EDAX spectrum of Location 1 (Depth 76-98 cm) at Site B (Okhla barrage).

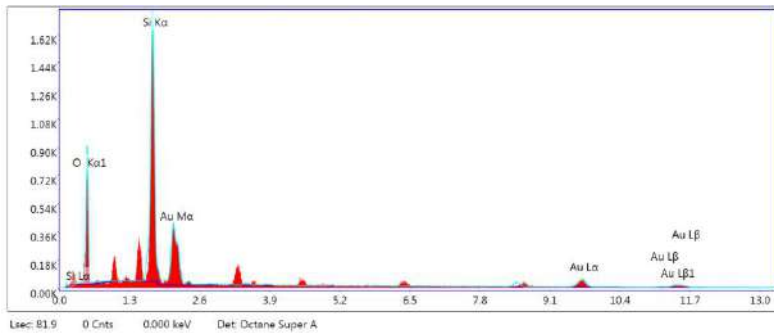


Fig. 20: EDAX spectrum of Location 2 (Depth 0-2 cm) at Site B (Okhla barrage).

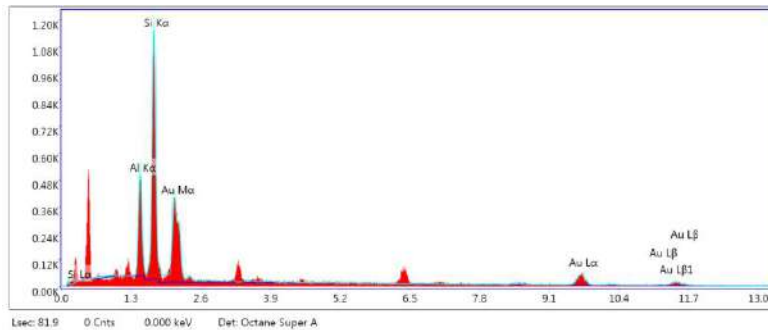


Fig. 21: EDAX spectrum of Location 2 (Depth 30-32 cm) at Site B (Okhla barrage).

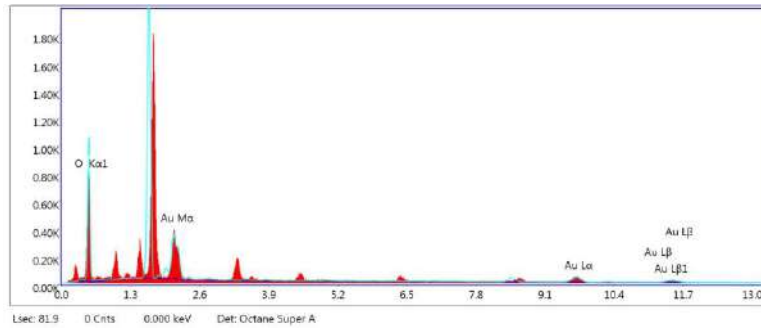


Fig. 22: EDAX spectrum of Location 2 (Depth 67-69 cm) at Site B (Okhla barrage).

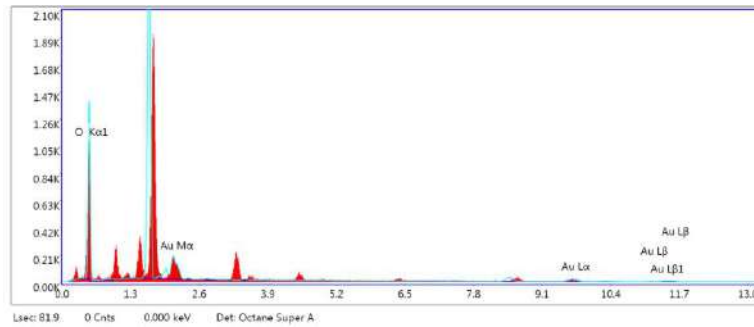


Fig. 23: EDAX spectrum of Location 3 (Depth 0-2 cm) at Site B (Okhla barrage).

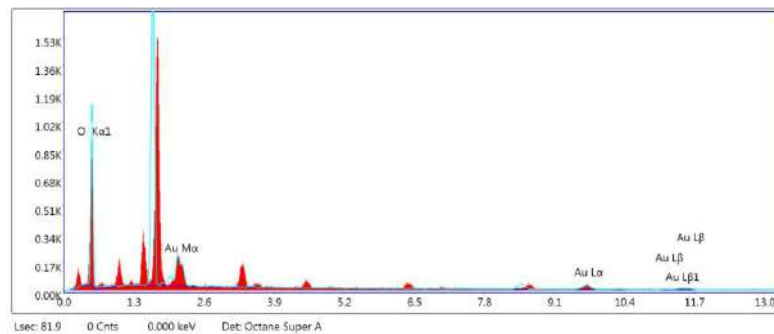


Fig. 24: EDAX spectrum of Location 3 (Depth 26-28 cm) at Site B (Okhla barrage).

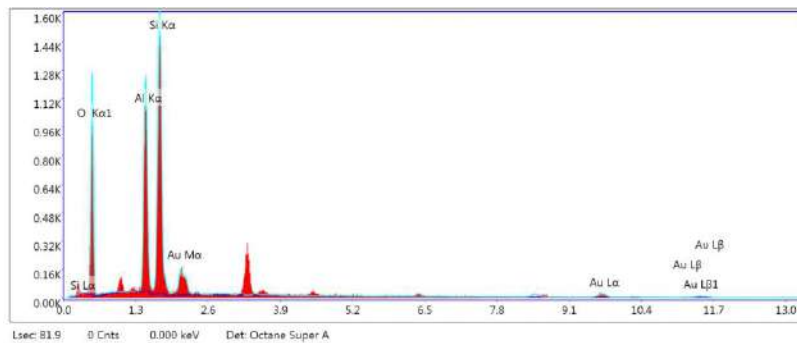


Fig. 25: EDAX spectrum of Location 3 (Depth 62-64 cm) at Site B (Okhla barrage).

were plated with gold to observe diatoms, therefore, Au value has been discarded in the present study].

Isotopic composition of silicon in river sediments and its relation to climate was explained by Bayon et al. (2018). Distribution and retention of silicon in river beds and its effects on biogeochemical nature and aquatic food webs in coastal environments were discussed by Humborg et al. (2000), while the distribution of biogenic silica in sediments of the Yellow River was discussed by Yang et al. (2016). Mil-Homens et al. (2013) has talked about the occurrence of silicon as aluminosilicates in the sediments of Minho River, Spain. In the present study, the spatial distribution pattern of Si in different soil samples does not show any specific trend. Silicon affects the uptake and accumulation of different plant nutrients and most of the silicon is locked up in intractable silicate minerals and only a much smaller fraction is available for plants (Struyf et al. 2010). Silicon forms solid-phase phytoliths after absorbed in plants and with the deterioration of dead plant material these are recycled to the soil solution which may again be taken up by plants (Carey & Fulweiler 2012). Hydrogen bound Si-organic complexes are often found in plant tissues (Carlisle et al. 1977) which permeates the walls of vessels and epidermis and reduces fungal infections and water transpiration by strengthening the plant tissues (Kaufman et al. 1969). It also associates with cell wall components like lignins, polysaccharides, and proteins (Perry & Lu 1992). Silicon affects the uptake, distribution and functionality of several mineral nutrients like nitrogen (N), phosphorus (P), potassium (K), magnesium (Mg) and calcium (Ca) (Wallace 1989, Miyake 1993, Brackhage et al. 2013, Neu et al. 2016, Sattar et al. 2016, Kostic et al. 2017) and strongly influence the uptake of boron (B), iron (Fe), zinc (Zn) and manganese (Mn) (Nable et al. 1990, Bityutskii et al. 2014). Soil concentrations of oxygen in solution are comparatively lesser than in the soil atmosphere which is used by aerobic microorganisms as a terminal electron acceptor for the period of degradation of organic compounds and xenobiotics and percentage volume basis of oxygen varies in the atmosphere, well-aerated soil surface and fine clay or saturated soil (Pepper & Gerba 2019). Yamada et al. (2012) explained Dissolved Oxygen concentration in sediments of downstream of rivers in Lake Biwa in Japan. Similar studies on Dissolved Oxygen and Nutrient Fluxes across the Sediment-Water Interface of the Neckar River in Germany was performed by Haag et al. (2006). Concept of sediment oxygen demand (SOD) and the importance of oxygen was discussed by Belo (2008) in Pasing River.

Rock-forming minerals such as sphene, cassiterite rutile and biotite contain trace levels of Niobium and it shows a strong correlation with Ti, Ta, Th, U, Zr, Rb, Ga, Fe, V, Y

and with some heavy Rare Earth Elements like Dy, Ho, Er, Tm and Yb while has a good negative correlation with CaO and forms some relatively rare, but economically significant minerals (Forges Geochemical Atlas of Europe). Production of steel, nuclear fuel and welding practice are some main human activities which lead Niobium in the environment (Reimann & De Caritat 1998). It also has some industrial significance like manufacture cutting tools, pipelines and super magnets. It is considered non-essential and very less is known about its toxicity but its existence is not denied in living organisms and stream sediment. Astrom et al. (2008) did extensive studies on 807 streams spread over 26 countries in Europe for necessary statistics on the abundance, movement and transportation of Niobium in sediments of boreal stream water. Borghesi et al. (2015) studied the geochemical classification of surface sediments from wetlands around the Po river delta in Italy and suggested that organic matter in these wetlands can influence Niobium sediments. Periodic variations occurring in water quality in streams and rivers were demonstrated by Henriksen et al. (1984). In water bodies, Al can be added by industrial sources which are lethal for aquatic fauna (Hunter et al. 1980). The acidification caused by Al in water streams has generally been a reason for declining numbers of benthic and planktonic invertebrates (Okland & Okland 1986, Haines 1981). The biological significance of Al toxicity on freshwater invertebrates was revealed by Herrmann (1987) and on fish by Driscoll et al. (1982). Horst et al. (1982) found aluminium traces in the mucilage layer on the root tips and the cell wall pectins while only a small extent is translocated to shoots. Physiological and biochemical implications of Al studies have been reported on humans as well as animals (Siegel 1985, Trapp 1986).

The shape, size and chemical constituents of soil reserves are vastly variable (Takahashi et al. 2001). SEM images revealed the irregular, elliptical, platy and spongy structures of soil particles in almost all the samples. Similar results and such inhomogeneous nature of the soil was reported by Sharma et al. (2016) in Hasdeo river basin in Chhattisgarh and by Thambavani & Kavitha (2014) in Suruli river, Karnataka in India. Soils were sandy as all the samples were taken from the river bed which is mainly constituted of alluvial deposits. Sajitha et al. (2017) also used SEM EDAX to analyze Mineralogical and Morphological Characterization of Coastal Soil Samples of Kanyakumari District. The colour of the soil was light greyish at the Site A while it was darker and blackish at Site B because of the accumulation of sewage pollutants from nearby drains.

Studies revealed that the type and concentration of elements vary at different depths of the river bed and there

is no unique pattern of occurrence of elements along the gradients of the river bed. It can be explained by the fact that the river ecosystem is a very dynamic one and the alluvial deposition can be easily disturbed by the flow of water or floods. Though the percentage of Si and O was significantly distributed in all the sites, the occurrence of Al at Site B proves the heavy load of pollution in the area and the potential source of the Al contamination might be from industrial effluents. The occurrence of Nb at Site A could be because of depositions from weathered rocks as Nb is an important part of many forms of rocks.

CONCLUSION

The extent of pollution faced by the Yamuna is a severe threat to its identity as a river. The study reveals that Site A lacks any type of heavy pollutant while the occurrence of Al at Site B confirms the presence of pollutants. The concentration of elements keeps varying from the surface to the bottom of the river bed and they do not follow any particular pattern of concentration. The present study helps us to understand the elemental composition and morphology of soil grains in the river bed. This further enhances our knowledge about the complex nature of elements distribution along the depths of the river bed which can be used for conservation studies and protection of such a fragile wetland ecosystem of our rivers.

ACKNOWLEDGEMENTS

We would like to thank Dr Neel Ratan, Mr Jogender Singh, Mr Virender Kumar and Mr Lalit Yadav for their kind help in the collection of soil samples. A kind thanks are also due to Mr. Madan Mohan Sharma for his assistance during SEM-EDAX analysis at SAIF, AIIMS, Delhi.

REFERENCES

- Astrom, M., Peltola P., Virtasalo, J., Kotilainen, A. and Salminen, R. 2008. Niobium in boreal stream waters and brackish-water sediments. *Geochemistry Exploration Environment Analysis*, 8: 139-148. 10.1144/1467-7873/07-155.
- Bayon, G., Delvigne, C., Ponzevera, E., Borges, A. V., Darchambeau, F., De Deckker, P. and André, L. 2018. The silicon isotopic composition of fine-grained river sediments and its relation to climate and lithology. *Geochimica et Cosmochimica Acta*, 229: 147-161. 10.1016/j.gca.2018.03.015.
- Belo, Lawrence 2008. Measurement of the Sediment Oxygen Demand in Selected Stations of the Pasig River Using a Bench-scale Benthic Respirometer. 10.13140/2.1.3159.1369.
- Bitvutskii, N., Pavlovic, J., Yakkonen, K., Maksimovi, V. and Nikolic, M. 2014. Contrasting effect of silicon on iron, zinc and manganese status and accumulation of metal-mobilizing compounds in micronutrient-deficient cucumber. *Plant Physiology and Biochemistry*, 74: 205-211.
- Borghesi, F., Migani, F. and Dinelli, E. 2015. Geochemical characterization of surface sediments from the northern Adriatic wetlands around the Po river delta. Part I: Bulk composition and relation to local background. *Journal of Geochemical Exploration*, 156. 10.1016/j.gexplo.2015.05.003.
- Brackhage, C., Schaller, J., Bäucker, E. and Dudel, E.G. 2013. Silicon availability affects the stoichiometry and content of calcium and micro nutrients in the leaves of common reed. *Silicon*, 5(3): 199-204.
- Carey, J.C. and Fulweiler, R.W. 2012. The terrestrial silica pump. *PLoS One*, 7(12): e52932.
- Carlisle, E.M., McKeague, J.A., Siever, R. Van and Soest, P.J. 1977. *Silicon. In: Geochemistry and the Environment*, Elsevier, Washington, DC, USA, Volume 2.
- CPCB, 2006. Assessment and development of the river basin series, water quality status of Yamuna River 1999-2005. Eds Sengupta, B. Central Pollution Control Board, Delhi, India
- Das, B. and Mondal, N. K. 2011. Calcareous soil as a new adsorbent to remove lead from aqueous solution: equilibrium, kinetic and thermodynamic study. *Universal Journal of Environmental Health and Biology*, 1(4): 515-530.
- Driscoll, C.T., Baker, J.P., Bisogni, J.J.Jr. and Schofield, C.L. 1982. Effects of aluminum speciation on fish in dilute acidified waters. *Nature*, 284: 161-164.
- Forges Geochemical Atlas of Europe. Website address: weppi.gtk.fi>publ>foregsatlas>text>Nb
- Haag, I., Schmid, G. and Westrich, B. 2006. Dissolved oxygen and nutrient fluxes across the sediment-water interface of the Neckar river, Germany: in situ measurements and simulations. *Water, Air & Soil Pollution, Focus*, 6(5-6): 413-422.
- Haines, T. 1981. Acidic precipitation and its consequences for aquatic ecosystems: A review. *Trans. Am. Fish. Soc.*, 110: 669-707.
- Henriksen, A., Skogheim, O.K. and Rosseland, B.O. 1984. Episodic changes in pH and aluminium-speciation kill fish in a Norwegian salmon river. *Vatten*, 40: 255-260.
- Herrmann, J. 1987. Aluminium impact on freshwater invertebrates at low pH: A review. In: *Speciation of Metals in Water, Sediment and Soil Systems*, 157-175. Springer, Berlin, Heidelberg.
- Horst, W.J., Wagner, A. and Marschner, H. 1982. Mucilage protects root meristems from aluminium injury. *Zeitschrift für Pflanzenphysiologie*, 105(5): 435-444.
- Humborg, C., Conley, D.J., Rahm, L., Wulff, F., Cociasu, A. and Ittekkot, V. 2000. Silicon retention in river basins: Far-reaching effects on biogeochemistry and aquatic food webs in coastal marine environments. *AMBIO: A Journal of the Human Environment*, 29(1): 45-50.
- Hunter, J.B., Ross, S.L. and Tarmahill, J. 1980. Aluminium pollution and fish toxicity. *Water Pollut. Contr.*, 79: 413-420.
- Kaufman, P.B., Bigelow, W.C., Petering, L.B. and Drogoz, F.B. 1969. Silica in developing epidermal cells of *Avena internodes*. *Science*, 166: 1015-1017.
- Kostic, L., Nikolic, N., Bosnic, D., Samardzic, J. and Nikolic, M. 2017. Silicon increases phosphorus (P) uptake by wheat under low P acid soil conditions. *Plant Soil*, 419: 447-455.
- Miyake, Y. 1993. Silica in soil and plants. *Sci. Rep. Fac. Agric.*, 81: 61-79.
- Mil-Homens, M., Costa, A.M., Fonseca, S., Trancoso, M.A., Lopes, C., Serrano, R. and Sousa, R. 2013. Characterization of heavy-metal contamination in surface sediments of the Minho River Estuary by way of factor analysis. *Archives of Environmental Contamination and Toxicology*, 64(4): 617-631.
- Nable, R.O., Lance, R.C.M. and Cartwright, B. 1990. Uptake of boron and silicon by barley genotypes with differing susceptibilities to boron toxicity. *Ann. Bot. Rev.*, 66: 83-90.
- Neu, S., Schaller, J. and Dudel, G.D. 2016. Silicon availability modifies nutrient use efficiency and content, C:N:P stoichiometry, and productivity of winter wheat (*Triticum aestivum* L.). *Sci. Rep.*, 7: 1-8.
- Okland, J. and Okland, K.A. 1986. The effects of acid deposition on benthic animals in lakes and streams. *Experientia*, 42: 471- 486.

- Pepper, I.L. and Gerba, C.P. 2019. Environmental and Pollution Science. Elsevier.
- Perry, C.C. and Lu, Y. 1992. Preparation of silica from silicon complexes: Role of cellulose in polymerisation and aggregation control. *J. Chem. Soc. Faraday Trans.*, 88: 2915-2921.
- Reimann, C. and De Caritat, P. 1998. Chemical elements in the environment: Factsheets for the geochemist and environmental scientist. Springer Science & Business Media. 398 pp. Berlin, Heidelberg, New York, London, Paris, Tokyo, Hong Kong, Springer-Verlag.
- Sajitha, S.S., Metilda, P. and Jenin, G.A. 2017. Morphological and mineralogical characterization of coastal soil samples of Kanyakumari District by FT-IR, XRD, SEM/EDAX. *International Journal of Scientific Research and Management (IJSRM)*, 5(10): 7163-7171. 10.18535/ijsrcm/v5i10.01.
- Sattar, A., Cheema, M.A., Ali, H., Sher, A., Ijaz, M., Hussain, M., Hassan, W. and Abbas, T. 2016. Silicon mediates the changes in water relations, photosynthetic pigments, enzymatic antioxidants activity and nutrient uptake in maize seedling under salt stress. *Grassl. Sci.*, 62: 262-269.
- Sharma, R., Patel, K.S., Lata, L. and Milosh, H. 2016. Characterization of urban soil with SEM-EDX. *American Journal of Analytical Chemistry*, 7(10): 724-735. 10.4236/ajac.2016.710065.
- Siegel, N. 1985. Aluminum interaction with biomolecules: The molecular basis for aluminium toxicity. *Am. J. Kidney Dis.*, 6: 353-357.
- Struyf, E., Smis, A., Van Damme, S., Garnier, J., Govers, G., Van Wesemael, B., Conley, D.J., Batelaan, O., Frot, E., Clymans, W. and Vandevenne, F. 2010. Historical land use change has lowered terrestrial silica mobilization. *Nat. Commun.*, 1: 129.
- Takahashi, T., Dahlgren, R.A., Theng, B.K.G., Whitton, J.S. and Soma, M. 2001. Potassium-selective, halloysite-rich soils formed in volcanic materials from Northern California. *Soil Science Society of America Journal*, 65: 516. <http://dx.doi.org/10.2136/sssaj2001.652516x>.
- Tan, K.H. 2005. Soil Sampling, Preparation and Analysis. 2nd Edition, CRC Press, Boca Raton.
- Thambavani, S. and Kavitha, B. 2014. Mineralogical characterization of river bed soil from Tamilnadu by FT-IR, XRD and SEM/EDAX. *International Journal of Advanced Research*, 2: 656-659.
- Trapp, G.A. 1986. Interactions of aluminum with co-factors, enzymes, and other proteins. *Kidney Int.*, 29, Suppl., 18: S12-S16.
- Wallace, A. 1989. Relationships among nitrogen, silicon, and heavy metal uptake. *Soil Sci.*, 147: 457-460.
- Yamada, Y., Mito, Y., Igeta, A. and Wada, E. 2012. Dissolved oxygen concentration in river sediment of the Lake Biwa tributaries, Japan. *Limnology*, 13: 149-154. <https://doi.org/10.1007/s10201-011-0348-2>.
- Yang, X.H., Yang, H.W., Li, W.J. and Li, P. 2016. Distribution of biogenic silica in sediments of the Yellow River (Upper and Middle Reaches). *Chemical Engineering Transactions*, 55: 361-366.



Analysis of the Genetic Effects to Frogs (*Fejervarya limnocharis*) After Acute Lead Exposure *In Vivo*

B. Tengjaroenkul*, S. Boonmee** and L. Neeratanaphan***†

*Research Group on Toxic Substances in Livestock and Aquatic Animals, Khon Kaen University, Khon Kaen 40002, Thailand

**Department of Environmental Science, Faculty of Science, Khon Kaen University, Khon Kaen 40002, Thailand

†Corresponding author: L. Neeratanaphan; hlanya@kku.ac.th

Nat. Env. & Poll. Tech.
Website: www.neptjournal.com

Received: 14-01-2020
Revised: 24-02-2020
Accepted: 16-04-2020

Key Words:

Genotoxicity
Genetic differentiation
Lead; Frog
Fejervarya limnocharis

ABSTRACT

This study aimed to investigate the bioaccumulation and elimination of lead (Pb) in *Fejervarya limnocharis* frogs as well as to determine the genotoxic effects of direct Pb exposure at different concentrations and lengths of time. Four varying concentrations (0, 5, 10 and 20 mg.L⁻¹) of lead acetate (Pb(CH₃COO)₂) solutions were injected intraperitoneally into *F. limnocharis*. The concentration of Pb in the water samples used to house the frogs and the concentration of lead in frog muscle tissues were analysed at 24, 48 and 72 hours after injection by inductively coupled plasma optical emission spectrometry. Pb was detected at a level that exceeded the standard (0.03 mg.kg⁻¹) in all samples of frogs injected with Pb. The water samples indicated that the Pb concentrations were significantly different from the control ($p < 0.05$), except for the 5 and 10 mg.L⁻¹ concentrations after 24 hours groups and 5 mg.L⁻¹ concentration after 48 hours group. Only the concentration of the water in the 20 mg.L⁻¹ for 72 hours group exceeded the standard (0.05 mg.L⁻¹). Genetic differentiation was studied by inter simple sequence repeats (ISSR) with dendrogram construction and analysis of genetic similarity (S) for each duration of exposure. A total of 1158, 1205 and 1277 bands were generated by ISSR for the 24, 48 and 72 hours groups, respectively. In each dendrogram, individual injections with the same Pb concentration clustered together, and it appeared that higher concentrations resulted in greater genotoxicity. Genotoxicity was concentration- and time-dependent, with a correlation between the concentration and S-value for the 72 hours group ($R^2 = 0.77$, $p < 0.05$). In addition, this study could provide a basic application to develop *F. limnocharis* as a biomarker for Pb contamination by measuring genotoxic consequences.

INTRODUCTION

Lead (Pb) contamination is an important environmental problem that affects water, soil and air quality worldwide (Mitchell et al. 2011, Jaishankar & Mathew 2014). Pb contamination is especially problematic near mines, at sites of industrial wastewater discharge and from leachate from polluted areas. Pb is detrimental to various animals, and its toxicity can harm human health as the accumulation of Pb reaches excessive levels (IARC 2004, Martin & Griswold 2009, Olafisoye et al. 2013). Pb can enter creatures through many routes, including skin contact, consumption of contaminated foods and water and breathing contaminated air (Kakker & Jaffery 2004, Yan et al. 2018). Low-level Pb toxicity is often nonspecific and may cause fatigue and intellectual impairment (Méndez-Gómez et al. 2008). Severe Pb toxicity affects multiple organ systems and can result in renal, haematological, neurological and cardiovascular

diseases (Correia et al. 2000, Kalia & Flora 2005, Navas et al. 2007, ATSDR 2007). Pb toxicity can occur in kidney, spleen, heart, liver, lung, bone, brain and skeletal muscle (Patra et al. 2001, Vargas et al. 2003, ATSDR 2007, Sharma et al. 2011). Acute and chronic Pb toxicity in organisms depends on the concentration and duration of exposure (Needleman 2004, ATSDR 2007, Cleveland et al. 2008).

Furthermore, several published reports have revealed that Pb causes genotoxicity and cytotoxicity through oxidative stress and DNA damage (Kasuba et al. 2004, Zhang & Li 2013). The genotoxicity of Pb is related to the oxidative stress that occurs when there is a lack of proportion between the formation and removal of reactive oxygen species (ROS). During oxidative stress, ROS impair cells by oxidizing membrane lipids and proteins as well as DNA. DNA damage is a process with a facilitative role for Pb in carcinogenesis and cell death (Kosnett 2006, Beyersmann & Hartwig 2008).

Polymerase chain reaction with inter simple sequence repeats (PCR-ISSR) is a technique that can be used to analyze genetic relationships using molecular markers and has high resolving power at the population level without prior molecular knowledge of the organism (Zietkiewicz et al. 1994, Wu et al. 1994). This technique can be used to detect various types of genetic differentiation or DNA damage and mutations, such as point mutations, rearrangements and small deletions or insertions of DNA in plants and animals (Neeratanaphan et al. 2014, Mahfouz & Rayan 2016, Al-Qurainy et al. 2017). The ISSR method represents one of the most promising tools for the detection of genetic alterations in response to heavy metal toxicity by looking directly at the DNA sequence and structure (Behura 2006, Héry et al. 2008).

Amphibians are sensitive and important indicators to exposure to environmental pollutants because of their extremely permeable skin (Huang et al. 2007, Falfushinska et al. 2008, Kerby et al. 2010, Burlibasa et al. 2011). The rice field frog (*Fejervarya limnocharis*) is a native species found in Southeast Asia, including Thailand, Laos and Cambodia (Liu et al. 2011), and this creature is an important animal in the food chain, particularly on agricultural land in Southeast Asia. The toxicity of Pb has been studied widely in fish, but evidence relating to amphibians is relatively sparse (Linder & Grillitsch 2000). Some studies have related the concentration of Pb in amphibians to that in their surrounding environment; however, these field studies cannot establish causes and effects. Therefore, laboratory-based studies are required to reveal the effects of Pb accumulation in *F. limnocharis* by simulation of environmental exposure. A frog (*F. limnocharis*) model was chosen for this study because this frog species is abundant in aquatic ecosystems. The objectives of the study were to investigate the concentrations of Pb in *F. limnocharis* and water after *in vivo* injection with different concentrations of lead acetate for different exposure times and to determine the relationship to genomic changes using the PCR-ISSR technique.

MATERIALS AND METHODS

Experimental design: Frogs of the species *Fejervarya limnocharis*, weighing approximately 15 grams, were collected from a private culture farm located in Khon Kaen Province, Thailand. Healthy *F. limnocharis* were randomly selected for the experiment. The frogs were allowed to acclimate to the laboratory conditions for 5 days and then randomly divided into 12 experimental groups: 3 control groups and 9 treatment groups. The experiments were performed in triplicate with 5 frogs in each group. Each plastic bucket as the experimental unit had a 15 L capacity and contained 1 L of dechlorinated tap water.

Lead acetate exposure concentration: For the lead acetate exposure study, 100 μL of deionized water (control groups 1-3) or solutions of $\text{Pb}(\text{CH}_3\text{COO})_2$ (experimental groups 4-12) of varying concentrations (5, 10 and 20 $\text{mg}\cdot\text{L}^{-1}$) were prepared and applied to the frogs. At each concentration, the frogs were exposed to the injected solution for 24, 48 or 72 hours before being analysed. The water in the buckets was not changed during the experimental period.

Lead acetate analysis in frogs (*F. limnocharis*): Frogs of the species *F. limnocharis* were anaesthetized with ice, and the muscle samples were cut into small pieces. Exactly 1 g of muscle tissue was placed into a beaker and digested with 7 mL of concentrated nitric acid (HNO_3) and 1 mL of concentrated hydrogen peroxide (H_2O_2), placed in a water bath at $90 \pm 5^\circ\text{C}$ for 2 hours, and then allowed to cool to room temperature. The digested muscle samples were adjusted to a final volume of 25 mL with deionized water and then filtered.

Inductively coupled plasma optical emission spectrometry (ICP-OES) analysis: The digested samples of water and frog muscle were analysed for their Pb concentrations using ICP-OES. The ICP-OES wavelength for Pb analysis was set at 220.353 nm. The detection limit of Pb was 0.005 $\text{mg}\cdot\text{L}^{-1}$. The precision of the metal concentrations was evaluated with a certified reference material (CRM) via the 3111C method (APHA 2005, Chand & Prasad 2013).

Genotoxicity analysis: Total genomic DNA was extracted from *F. limnocharis* livers using a Genomic DNA Extraction Kit (Tissue) (RBC Bioscience) following the kit protocol. Extracted DNA was inspected by 0.8% agarose gel electrophoresis and ViSafe Green gel staining.

Later, a polymerase chain reaction was performed with a reaction mixture (10 μL) consisting of BlueMix DNA polymerase MasterMix (RBC Bioscience), 1.25 μM primers and 20 ng of genomic DNA extracted from *F. limnocharis* liver tissue. Twenty-four ISSR primers were screened with DNA from the representative frogs at the different concentrations and at each duration length, and the experimental primers were selected based on their amplification profile. The 14 primers that amplified favourably for the 24, 48 and 72 hours experiments are shown in Table 1.

The PCR profile was demonstrated by predenaturation at 94°C for 5 minutes, 35 cycles of denaturation at 94°C for 1 minute, annealing at 52°C for 1 minute and 30 seconds, and extension at 72°C for 2 minutes, and a final extension at 72°C for 7 minutes using a thermal cycler (Analytik Jena). After amplification, the PCR products were resolved by electrophoresis on 2% agarose gels and ViSafe Green gel staining.

Data analyses: The Pb concentrations in the water and frog samples were analysed using ANOVA followed by Tukey's

Table 1: List of ISSR primers according to the duration of exposure.

14 ISSR primers amplified	
5'-CTCTCTCTCTCTCTGC-3'	5'-GAGGAGGAGGC-3'
5'-CACACACACACAAC-3'	5'-CTCCTCCTCGC-3'
5'-CACACACACACAGT-3'	5'-GTGGTGGTGGC-3'
5'-CACACACACACAAG-3'	5'-ACTGACTGACTGACTG-3'
5'-CACACACACACAGG-3'	5'-GACAGACAGACAGACA-3'
5'-GAGAGAGAGAGACC-3'	5'-ACACACACACACACAGC-3'
5'-CACACCACGC-3'	5'-CCCTCCCTCCCTCCCT-3'

post hoc test. The results are expressed as the mean \pm SD. All statistical data were carried out with SPSS for Windows (version 19), and the significance level was set at $p < 0.05$.

Polymorphic bands amplified by the ISSR markers were scored as present =1 or absent = 0 compared to a standard DNA ladder. The data were entered into NTSYS-pc version 2.10p (Rohlf 2009) to construct the dendrogram and perform statistical analysis. Regression analysis was performed using SPSS.

RESULTS AND DISCUSSION

Pb concentrations in the water and *F. limnocharis* samples: The Pb concentrations in the water after *F. limnocharis* were injected with Pb concentrations of 0, 5, 10 and 20 mg.L⁻¹ for exposure times of 24, 48 and 72 hours are given in Table 2. The Pb concentrations of the water samples did not exceed the standard of the Pollution Control Department of Thailand of water quality standards (0.05 mg.L⁻¹) (TPCD 1986), except for the highest Pb concentration of the 20 mg.L⁻¹ for 72 hours (0.05 \pm 0.01 mg.L⁻¹). The Pb concentrations of the water samples between the experimental and control groups were significantly different ($p < 0.05$) for all experimental groups except for the 5 and 10 mg.L⁻¹ groups for 24 hours and 5 mg.L⁻¹ group for 48 hours.

The Pb concentrations in *F. limnocharis* muscle after injection with different Pb concentrations and durations of exposure are given in Table 3. Pb was not detected in the *F. limnocharis* muscles of the control group. The Pb concentrations of *F. limnocharis* muscles in all experimental groups exceeded the standard of the Pollution Control Department of Thailand (0.03 mg.kg⁻¹) (TPCD 2001). The highest Pb concentration was found in the 20 mg.L⁻¹ 72 hours group (0.78 \pm 0.04 mg.kg⁻¹). The statistical analysis results indicated that the Pb concentrations in all experimental *F. limnocharis* muscle samples were significantly different from the controls ($p < 0.05$).

These results suggest that the Pb found in the water samples originated from *F. limnocharis* frogs. It appeared

that higher concentrations of injected Pb and longer exposure times resulted in increased Pb concentrations in the water. Pb accumulates mainly in the liver and kidney of *F. limnocharis* (Hopkins 1989, Jan ová et al. 2002, Zhang et al. 2007) and is excreted through the urine, faeces and skin (Akerstrom et al. 2013). Consequently, *F. limnocharis* may not eliminate all of the Pb from their bodies, and some Pb remains in the muscles and other organs.

Several studies are confirming that the Pb concentrations absorbed in frog bodies can be transported to various target organs, such as the liver and kidney, compared with transportation to the muscles (Jarup et al. 1988, Grosicki & Kowalski 2002, Formicki & Stawarz 2004). The intracellular movement of Pb across cellular membranes occurs via active transport, which is facilitated by P-type ATPase ionic pumps (Zelikoff et al. 1988, Gatti et al. 2000, Patric 2006). Among heavy metals, Pb has a higher propensity to bioaccumulate in frog organs involved in the detoxification process.

Genotoxic effects in *F. limnocharis*: Fourteen clear and reproducible ISSR primers generated ISSR bands for the 24, 48 and 72 hours groups as 1158, 1205 and 1277, respectively, ranging in size from 100 bp to 3000 bp. Examples of these ISSR bands for different primers are shown in Fig. 1. These bands were used for dendrogram construction for each duration of exposure (Figs. 2-4). For each dendrogram, the closest individuals from the same Pb concentration clusters demonstrate that they are genetically similar. These clusters were grouped at varying distances between the other Pb concentration groups with a trend towards greater distances as greater Pb concentrations.

The genetic differentiation values between individuals of each Pb concentration and duration of exposure groups were almost identical (0.98-1.00). The minimum and maximum ranges of genetic differentiation values were 0.51-0.96, 0.44-0.81 and 0.49-0.74 for the 24, 48 and 72 hours of exposure dendrograms, respectively. At 24 hours of exposure, the differentiation values of the experimental groups compared to the control group were 0.54-0.55, 0.51-0.52 and 0.53-0.54 for 5, 10 and 20 mg.L⁻¹, respectively. At 48 hours of exposure, the

Table 2: The Pb acetate concentrations in water samples ($\bar{X} \pm SD$).

Lead acetate concentration (mg.L ⁻¹)	Pb concentration in the water (mg.L ⁻¹)			Thailand standard* (mg.L ⁻¹)
	24 h	48 h	72 h	
0	ND	ND	ND	0.05
5	0.01 ± 0.00 ^a	0.01 ± 0.00 ^a	0.03 ± 0.00 ^b	
10	0.02 ± 0.00 ^a	0.03 ± 0.00 ^b	0.03 ± 0.01 ^b	
20	0.03 ± 0.01 ^b	0.03 ± 80.01 ^b	0.05 ± 0.01 ^b	

Remarks: ND=Not detected (less than the detection limit of Pb); a= nonsignificant difference compared to the control; b=significant difference compared to the control (p 0.05).

*Water quality standards for surface water sources, Pollution Control Department, Ministry of Natural Resources and Environment, Thailand (PCD 2014).

Table 3: The Pb concentrations in *F. limnocharis* muscles ($\bar{X} \pm SD$).

Lead acetate concentration (mg.kg ⁻¹)	Pb concentration in <i>F. limnocharis</i> muscles (mg.kg ⁻¹)			Thailand standard* (mg.kg ⁻¹)
	24 hours	48 hours	72 hours	
0	ND	ND	ND	
5	0.28 ± 0.03 ^a	0.44 ± 0.02 ^a	0.32 ± 0.06 ^b	≤ 0.03
10	0.27 ± 0.09 ^a	0.34 ± 0.03 ^b	0.30 ± 0.02 ^b	
20	0.35 ± 0.03 ^b	0.63 ± 0.04 ^b	0.78 ± 0.04 ^b	

Remarks: ND=Not detected (less than the detection limit of Pb); a = nonsignificant compared to the control; b = significant compared to the control (p 0.05).

*Standard for contaminants in the food according to the Notification of the Ministry of Public Health No. 273/2 (Ministry of Public Health 2003).

differentiation values of the experimental groups compared with the controls were 0.55, 0.44-0.45 and 0.48 for 5, 10 and 20 mg.L⁻¹, respectively. At 72 hours of exposure, the differentiation values of the samples from each experimental

group compared to the control group were 0.69, 0.59-0.60 and 0.49 for 5, 10 and 20 mg.L⁻¹, respectively. As Pb was detected in all *F. limnocharis* samples except for the control group, this suggests that the injected Pb was responsible

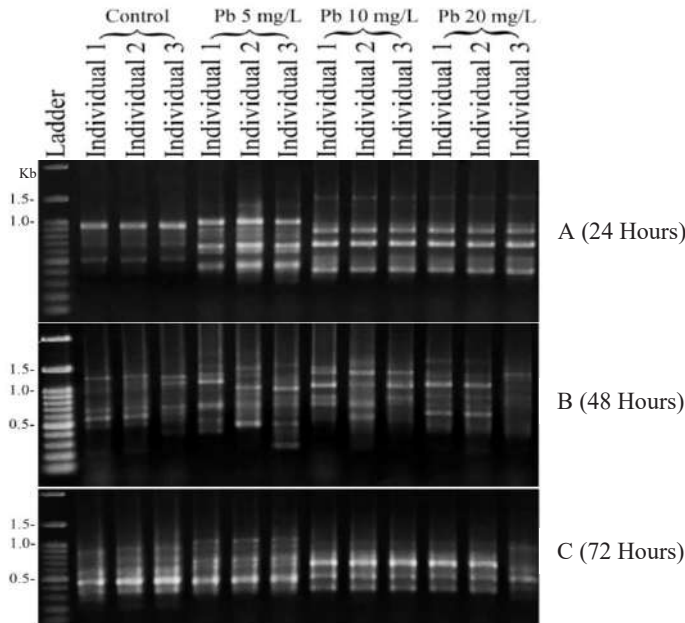


Fig. 1: Examples of the ISSR fingerprints from *F. Limnocharis* samples in the three experimental groups and the control groups for durations of 24, 48 and 72 hours generated using the primers ACACACACACACACG (A), CACACACACACAGG (B) and CACCACCACGC (C).

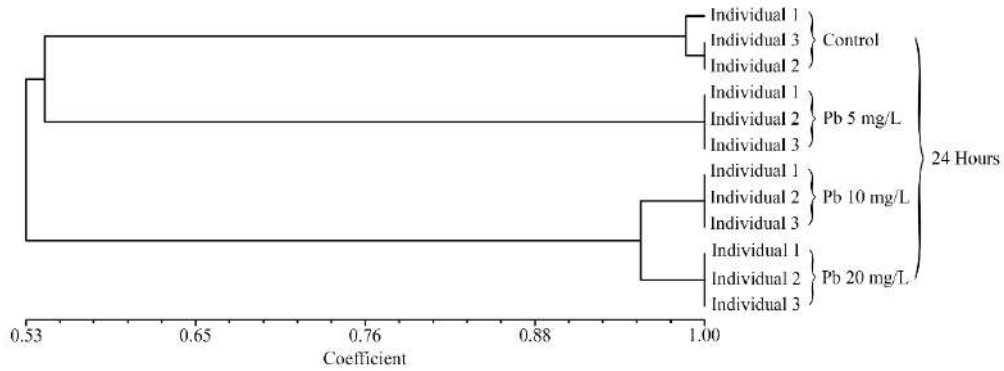


Fig. 2: The dendrogram constructed using 13 ISSR primers and the NTSYSpc 2.10p program showing the genetic relationships among the individual samples in the three experimental groups and the control group for 24 hours.

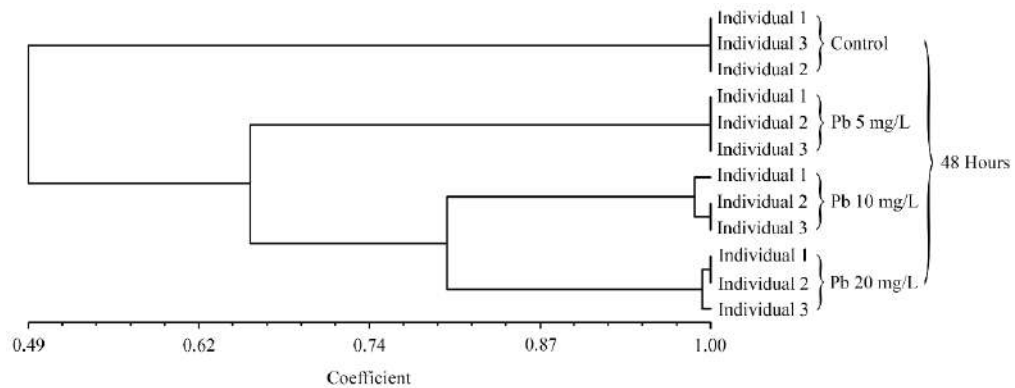


Fig. 3: The dendrogram constructed using 12 ISSR primers and the NTSYSpc 2.10p program showing the genetic relationships among the individual samples in the three experimental groups and the control group for 48 hours.

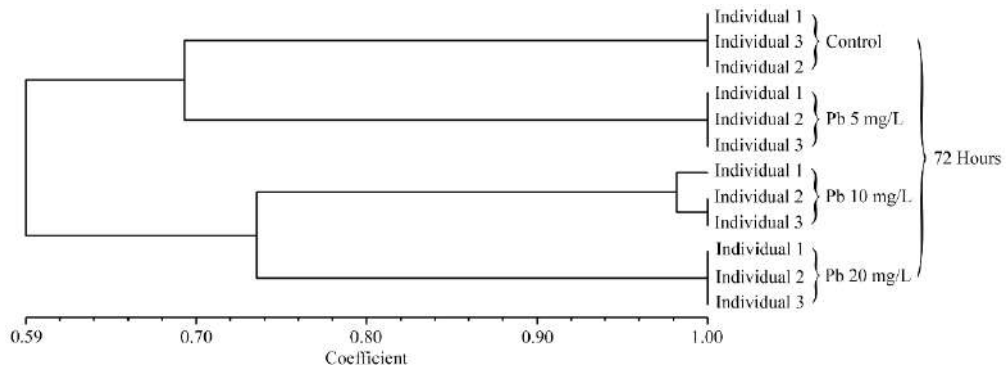


Fig. 4: The dendrogram constructed using 14 ISSR primers and the NTSYSpc 2.10p program showing the genetic relationships among the individual samples in the three experimental groups and the control group for 72 hours.

for the genotoxic effects, as evidenced by the genetic differentiation values of the experimental groups compared with the control group. Differences in Pb concentrations were calculated between the groups and correlated against the genetic differentiation values with linear regression analysis. There was no significant correlation between the

concentration differences and genetic differentiation values for 24 hours ($R^2 = 0.05$, $p = 0.89$) (Fig. 5) and 48 hours ($R^2 = 0.086$, $p = 0.57$) of exposure (Fig. 6). For 72 hours of exposure, there was a significant correlation between the differences in Pb concentration and genetic similarity values ($R^2 = 0.77$, $p < 0.05$) (Fig. 7). These results suggest that the

genotoxic effects of Pb depend on both the exposure time and concentration.

The results of this study indicate that intraperitoneal injection of Pb solutions leads to contamination of the water in the frog's environment by excretion via urine and faeces. This study also showed that Pb induced genotoxicity in a time and concentration-dependent manner. These results have also been observed in many other studies; however, the vast majority of previous studies relating to the genotoxic effects of Pb have been undertaken in fish, rats, mice and rabbits, with a clear gap in the literature regarding frogs (García-Lestón et al. 2010). There are various mechanisms of genotoxicity that have been discussed in previous literature, including oxidative stress from the generation of reactive oxygen species and by DNA repair enzymes (Hwang & Kim 2007, Gueranger et al. 2011, Krisko & Radman 2013, McAdam et al. 2016). The reported mechanisms may be responsible for the genotoxic effects of Pb observed in the frogs in this study.

Frogs were selected for this study because they have the potential to be useful biomarkers for environmental contamination of Pb due to their highly permeable skin (Othman 2009; Thammachot et al. 2012). The disadvantage

of this study in exploring the application of frogs as biomarkers of the genotoxic effects of the environment is that *in vivo* intraperitoneal injections do not completely simulate exposure to Pb in the natural environment. Therefore, this study provides basic knowledge for future research, particularly for the use of frogs as biomarkers of heavy metal contamination in relation to genotoxicity consequences.

CONCLUSION

Intraperitoneal injection of a Pb solution into *F. limnocharis* frogs was responsible for the contamination of lead into water and its accumulation in muscles. Genotoxicity effects after Pb exposure, as evidenced by dendrograms and genetic differentiation values, are concentration-dependent and additive. This study revealed that *F. limnocharis* frogs can potentially be used as biomarkers for Pb contamination through measurement of the genotoxic effects.

ACKNOWLEDGMENTS

This research was supported by the Research Group on Toxic Substances in Livestock and Aquatic Animals and the Graduate School of Khon Kaen University, Thailand.

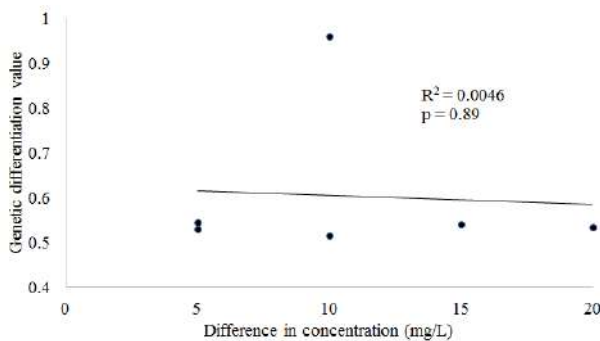


Fig. 5: Genetic differentiation values according to differences in the concentration for 24 hours of exposure.

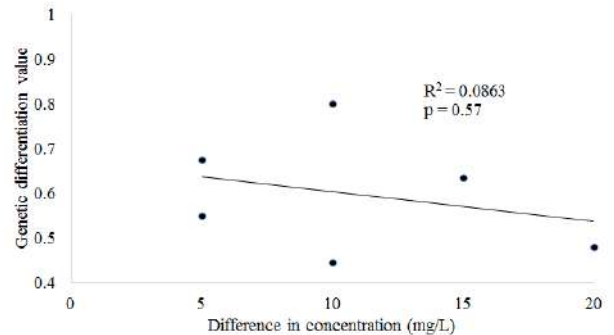


Fig. 6: Genetic differentiation values according to differences in the concentration for 48 hours of exposure.

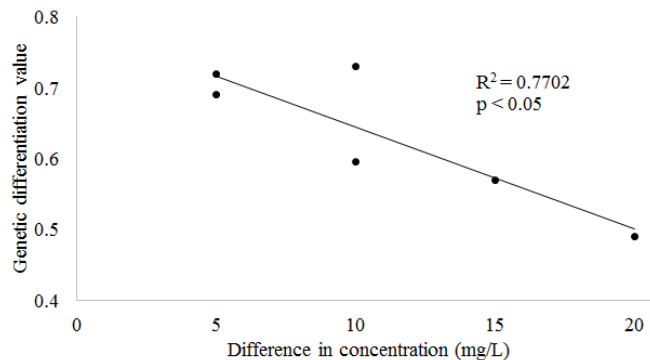


Fig. 7: Genetic differentiation values according to differences in the concentration for 72 hours of exposure.

REFERENCES

- Agency for Toxic Substances and Disease Registry (ATSDR) 2007. Toxicological Profile for Lead. Agency for Toxic Substances and Disease Registry, Washington DC, USA.
- Akerstrom, M., Barregard, L., Lundh, T. and Sallsten, G. 2013. The relationship between cadmium in kidney and cadmium in urine and blood in an environmentally exposed population. *Toxicol. Appl. Pharmacol.*, 268(3): 286-93.
- Al-Qurainy, F., Khan, S., Tarroum, M., Nadeem, M., Alansi, S. and Alshameri, A. 2017. Biochemical and genetical responses of *Phoenix dactylifera* L. to cadmium stress. *Biomed. Res. Int.*, 4: 1-9.
- American Public Health Association (APHA) 2005. Standard Methods for the Examination of Water and Wastewater. American Public Health Association, 21st edition. Washington DC, USA.
- Behura, S.K. 2006. Molecular marker systems in insects: current trends and future avenues. *Mol. Ecol.*, 15(11): 3087-3113.
- Beyersmann, D. and Hartwig, A. 2008. Carcinogenic metal compounds: Recent insight into molecular and cellular mechanisms. *Arch. Toxicol.*, 82: 493-512.
- Burlibasa, L. and Gavrilu, L. 2011. Amphibians as model organisms for study environmental genotoxicity. *Appl. Ecol. Env. Res.*, 9(1): 1-15.
- Chand, V. and Prasad, S. 2013. ICP-OES assessment of heavy metal contamination in tropical marine sediments: A comparative study of two digestion techniques. *Microchemical*, 111: 53-56.
- Cleveland, L.M., Minter, M.L., Cobb, K.A., Scott, A.A. and German, V.F. 2008. Lead hazards for pregnant women and children: Part 1: immigrants and the poor shoulder most of the burden of lead exposure in this country. Part I of a two-part article details how exposure happens, whom it affects, and the harm it can do. *Nursing American Nurses Association*, 108: 40-49.
- Correia, P.R.M., Oliveira, E. and Oliveira, P.V. 2000. Simultaneous determination of Cd and Pb in foodstuffs by electro-thermal atomic absorption spectrometry. *Anal. Chim. Acta.*, 405(1-2): 205-211.
- Falfushinska, H., Loumbourdis, N., Romanchuk, L. and Stoliar, O. 2008. Validation of oxidative stress responses in two populations of frogs from Western Ukraine. *Chemosphere*, 73(7): 1096-1101.
- Formicki, G. and Stawarz, R. 2004. Cadmium accumulation and depuration in common frog (*Rana temporaria* L.) larvae exposed to ultraviolet radiation. *Risk Factors of Food Chain, Slovak University of Agriculture, Slovakia*.
- Garcia-Leston, J., Méndez, J., Pásaro, E. and Laffon, B. 2010. Genotoxic effects of lead: An updated review. *Environ. Int.*, 36: 623-636.
- Gatti, D., Mitra, B. and Rosen, B.P. 2000. Escherichia coli soft metal ion-translocating ATPases. *J. Biol. Chem.*, 275(44): 34009-34012.
- Grosicki, A. and Kowalski, B. 2002. Whole-body and organ retention of cadmium after repeated administration to rats. *Bull. Vet. Inst. Pulawy.*, 46: 143-147.
- Gueranger, Q., Kia, A., Frith, D. and Karran, P. 2011. Crosslinking of DNA repair and replication proteins to DNA in cells treated with 6-thioguanine and UVA. *Nucleic. Acids. Res.*, 39: 5057-5066.
- Héry, M., Gault, A.G., Rowland, H.A., Lear, G., Polya, D.A. and Lloyd, J.R. 2008. Molecular and cultivation dependent analysis of metal-reducing bacteria implicated in arsenic mobilization in south-east Asian aquifers. *Appl. Geochem.*, 23: 3215-3223.
- Hopkins, S.P. 1989. *Ecophysiology of Metals in Terrestrial Invertebrates*, Barking (UK), Elsevier Applied Science.
- Huang, Y. and Li, L. 2013. DNA crosslinking damage and cancer a tale of friend and foe. *Transl. Cancer. Res.*, 2(3): 144-54.
- Hwang, E.S. and Kim, G.H. 2007. Biomarkers for oxidative stress status of DNA, lipids, and proteins *in vitro* and *in vivo* cancer research. *Toxicology*, 229: 1-10.
- International Agency for the Research on Cancer (IARC) 2004. *Inorganic and Organic Lead Compounds*. IARC Monographs on the Evaluation of Carcinogenic Risks to Human. Lyon.
- Jaishankar, M., Mathew, B.B., Shah, M.S. and Gowda, K.R.S. 2014. Biosorption of few heavy metal ions using agricultural wastes. *J. Environ. Poll. Hum. Health*, 2(1): 1-6.
- Janová, A., Massányi, P. and Gálová, J. 2002. The concentration of cadmium and lead in liver and kidneys in *Apodemus flavicollis* and *Clethrionomys glareolus*. *NIH*, 46: 65-67.
- Jarup, L., Berglund, M., Elinder, C.G., Nordberg, G. and Vahter, M. 1988. Health effects of cadmium exposure - A review of the literature and a risk estimate. *Scand. J. Work. Environ. Health*, 24(1): 1-51.
- Kakker, P. and Jaffery, F.N. 2004. Biological markers for metals toxicity. *Environ. Toxicol. Pharmacol.*, 19: 335-49.
- Kalia, K. and Flora, S.J. 2005. Strategies for safe and effective therapeutic measures for chronic arsenic and lead poisoning. *J. Occup. Health*, 47: 1-21.
- Kasuba, V., Rozgaj, R., Fuic, A., Varnai, V.M. and Piasek, M. 2004. Lead acetate genotoxicity in suckling rats. *Biologia.*, 59(6): 779-785.
- Kerby, J.L., Richards, K.L., Storfer, A. and Skelly, D.K. 2010. An examination of amphibian sensitivity to environmental contaminants: Are amphibians poor canaries? *Ecol. Lett.*, 13: 60-67.
- Kosnett, M.J. 2006. *Lead*. In: Olson K.R, Editor. *Poisoning and Drug Overdose*. 5th ed., McGraw Hill Professional.
- Krisko, A. and Radman, M. 2013. Phenotypic and genetic consequences of protein damage. *Plos. Genet.*, 9: e1003801.
- Linder, G. and Grillitsch, B. 2000. *Ecotoxicology of metals*. In: Sparling DW, Linder G, Bishop CA, Editors. *Ecotoxicology of Amphibians and Reptiles*. Pensacola, FL. Society of Environmental Toxicology and Chemistry (SETAC).
- Liu, W.Y., Wang, C.Y., Wang, T.S., Fellers, M.G., Lai, B.C. and Kam, Y.C. 2011. Impacts of the herbicide butachlor on the larvae of a paddy field breeding frog (*Fejervarya limnocharis*) in subtropical Taiwan. *Ecotoxicology*, 20(2): 377-384.
- Mahfouz, H. and Rayan, W.A. 2016. Assessment of lead stress using genome template stability in *Hordeum vulgare*. *Egypt. J. Genet. Cytol.*, 45: 297-321.
- Martin, S. and Griswold, W. 2009. Human health effects of heavy metals. *Environ. Sci. Technol. Briefs Citizens*, 15: 1-6.
- McAdam, E., Brem, R. and Karran, P. 2016. Oxidative stress-induced protein damage inhibits DNA repair and determines mutation risk and anticancer drug effectiveness. *Mol. Cancer. Res.*, 14: 612-622.
- Méndez-Gómez, J., García-Vargas, G.G., López-Carrillo, L., Calderón-Aranda, E.S., Gómez, A., Vera, E., Valverde, M., Cebrián, M.E. and Rojas, E. 2008. Genotoxic effects of environmental exposure to arsenic and lead on children in region Lagunera, Mexico. *Ann. NY. Acad. Sci.*, 1140: 358-367.
- Ministry of Public Health. 2003. *Standard of Contaminants in Food*. Notification of the Ministry of Public Health No. 273/2, Bangkok, Thailand.
- Mitchell, E., Frisbie, S. and Sarkar, B. 2011. Exposure to multiple metals from groundwater a global crisis: geology, climate change, health effects, testing, and mitigation. *Metallomics*, 3: 874-908.
- Navas, A.A., Guallar, E., Silbergeld, E.K. and Rothenberg, S.J. 2007. Lead exposure and cardiovascular disease a systematic review. *Environ. Health. Perspect.*, 115(3): 472-82.
- Needleman, H. 2004. Lead poisoning. *Annu. Rev. Med.*, 55: 209-222.
- Neeratanaphan, L., Sudmoon, R. and Chaveerach, A. 2014. Assessment of genotoxicity through ISSR marker in *Pistia stratiotes* induced by lead. *Environment Asia*, 7(2): 99-107.
- Olafisoye, B.O., Adefisoye, T. and Osibote, O.A. 2013. Heavy metals contamination of water, soil, and plants around an electronic waste dumpsite. *Pol. J. Environ. Stud.*, 22(5): 1431-1439.
- Othman, M.S. 2009. *Using the Rice Frog (Fejervarya limnocharis) as A sentinel Species for Cadmium Contamination in Tak Province, Thailand*. Doctoral dissertation, Program in Environmental

- Management, Graduate School, Chulalongkorn University, Thailand.
- Patra, R.C., Swarup, D. and Dwivedi, S.K. 2001. Antioxidant effects of α -tocopherol, ascorbic acid and L-methionine on lead-induced oxidative stress of the liver, kidney and brain in rats. *Toxicology*, 162: 81-88.
- Patric, L. 2006. Lead toxicity part II: the role of free radical damage and the use of antioxidants in pathology and treatment of lead toxicity. *Altern. Med. Rev.*, 11(2): 114-127.
- Pollution Control Department (PCD) 2014. Thailand State of Pollution Report. Ministry of Natural Resources, Bangkok, Thailand.
- Rohlf, F.J. 2009. NTSYS_pc: Numerical Taxonomy and Multivariate Analysis System, Version 2.2. Applied Biostatistics Inc., New York.
- Sharma, S., Sharma, V., Paliwal, R. and Pracheta. 2011. Lead toxicity, oxidative damage and health implications, a review. *Int. J. Biotechnol. Mol. Biol. Res.*, 2(13): 215-221.
- Thailand Pollution Control Department (TPCD) 1986. The Standard Levels of Heavy Metals in Tissues of Aquatic Animals. Notification in Ministry of Public Health, No. 98. Bangkok, Thailand.
- Thailand Pollution Control Department (TPCD) 2001. Water Quality Standards. Notification in Ministry of Public Health, No. 98, Bangkok, Thailand.
- Thammachoti, P., Khonsue, W., Kitana, J., Varanusupakul, P. and Kitana, N. 2012. Morphometric and gravimetric parameters of the rice frog *Fejervarya limnocharis* living in areas with different agricultural activity. *Environ. Prot.*, 3: 1403-1408.
- Vargas, I., Castillo, C. and Posadas, F. 2003. Acute lead exposure induces renal heme oxygenase-1 and decreases urinary Na^+ excretion. *Hum. Exp. Toxicol.*, 22: 237-244.
- Wu, K., Jones, R., Dannaerberger, L. and Scolnik, P.A. 1994. Detection of microsatellite polymorphisms without cloning. *Nucleic. Acids. Res.*, 22: 3257-3258.
- Yan, X., Liu, M., Zhong, I., Guo, J. and Wu, W. 2018. How human activities affect heavy metal contamination of soil and sediment in a long-term reclaimed area of the Liaohe river delta, North China. *Sustainability*, 10: 338.
- Zelikoff, J.T., Li, J.H., Hartwig, A., Wang, X.W., Costa, M. and Rossman, T.G. 1988. Genetic toxicology of lead compounds. *Journal of Carcinogenesis*, 9: 1727-1732.
- Zhang, Y., Huang, D., Zhao, D., Long, J., Song, G. and Li, A. 2007. Long-term toxicity effects of cadmium and lead on *Bufo raddei* tadpoles. *Bull. Environ. Contam. Toxicol.*, 79(4): 178-183.
- Zietkiewicz, E., Rafalski, A. and Labuda, D. 1994. Genome fingerprinting by simple sequence repeat (SSR) anchored polymerase chain reaction amplification. *Genomics*, 20: 176-183.



Residential, IUCN and WPA Status of the Avian Fauna Observed in Indore city (M.P.), India

Priya Gaur*, Mohnish Pichhode*, Jatan Dudwe*, C.S. Shrivastava** and S. Gaherwal*†

*Department of Zoology, Government Holkar (Model, Autonomous) Science College, Indore, M.P., India

**Department of Zoology, Government College, Mundi, Khandwa, M.P., India

†Corresponding author: S. Gaherwal; psgaherwal@yahoo.com

Nat. Env. & Poll. Tech.

Website: www.neptjournal.com

Received: 17-03-2020

Revised: 16-05-2020

Accepted: 27-05-2020

Key Words:

WPA

Avian fauna

Migratory birds

Biodiversity

ABSTRACT

The objective of the present study was to prepare a record of the Residential, IUCN and WPA status of the birds recorded in four sites of Indore city. The study was of one-year duration (2018). The results showed that there were five species as winter migrants, one as summer migrant, six as local migrants, and 46 as resident species. Only one species, i.e. *Psittacula eupatria* was found to be in the near threatened category. According to WPA status, 5 species were Schedule I species, 1 schedule V, and 52 species as schedule IV species. These sites have a potential of augmentation of avian fauna shortly and these spaces abide by many species with a larger diversity than estimated. The present study is the first-ever record of avian species in the three sites of Indore city. The results of this study support the scope of conservation of these spaces for increasing the number of species shortly.

INTRODUCTION

Due to rich vegetation and well-protected areas, recreational man-made parks have succeeded in attracting good avifauna. These areas with its rich flora supported a rich and varied avifauna. Adaptation of birds depends upon their body mass and feeding habits, because of which they have followed human colonization. Although not all birds can thrive in urbanized habitat, some have been able to adapt and survive in artificial habitats. Some of the most common and familiar birds seen in our cities or villages are Red-vented Bulbul, House Crow, Blue-rock Pigeon, Common Myna, Rose-ringed Parakeet and House Sparrow (Seress & Liker 2015). Green spaces in cities have been formally identified as areas with notable avian biodiversity. However, the urban environment is not appraised areas with conservation importance (Vallejo et al. 2009). Due to the increase in population, the interaction between human and ecosystem is expanding. Due to alarming interference, avian diversity is in danger because of a few more reasons; for example, development of the residential area and urbanized colonies. Factors like green space dimension and the number of trees are responsible for the number of avian species present in an area. The structural heterogeneity of trees inside the study area is a crucial aspect supporting high levels of species abundance (Sharma & Shukla 2015).

Birds due to their sensitivity to the environmental perturbations, relevance to ecosystem functioning; example seed

dispersal and pollination; and their relative ease in sampling, they are well known as Indicator taxa. Similarly, bird diversity and abundance are different in different vegetation types and dependent primarily on plant community diversity and vegetation structure (Sharma & Shukla 2015). Because of this reason, they are used to monitor the quality of any habitat or niche and hence they are the key elements of any ecosystem (Mariappan et al. 2013). They play an important role in any ecosystem as they are potential bio-indicators, pollinators, seed dispersers and scavengers, and beneficial to humans in agriculture by checking the population of harmful pests (Dhindsa & Saini 1994). The numbers of migratory birds visiting any area also indicate the health of that particular environment (Panwar & Salunkhe 2014). Hence, the present study aimed to estimate the residential, IUCN and WPA status of the avian fauna in the selected sites of Indore city.

MATERIALS AND METHODS

Study area: Four sites were selected from Indore city according to their construction and maintenance. Site 1: Meghdoot Garden; Site 2: Nehru Park; Site 3: Lalbagh; Site 4: Pipliyapala Regional Park.

Study period: One year, i.e. January to December 2018.

After preparing a checklist of avian fauna at all the sites, these birds were categorized according to Table 1 (Datta 2016).

Table 1: Resident and migratory status of the birds.

S. No.	Category	Residential Status	Abbreviation
1	Breeding in the same place and are non-migratory.	Resident	R
2	Winter migratory birds	Winter Migrant	WM
3	Summer visitors	Summer Migrant	SM
4	Species found irregularly but are resident in the State (M.P.).	Local Migrant	LM

Initially, a checklist of the avian fauna was prepared (Gaur et al. 2019); then all the species were categorised according to the Birdlife international (mentioned in Data zones). Their IUCN status was mentioned along with their Wildlife Protection Act (1972) categories.

RESULTS

In Site 1, out of 39 species recorded 35 species were resident species (90%); two species were winter migratory birds (5%) (*Hirundo rustica* and *Phylloscopus trochiloides*) and two were local migrating species (5%) (*Rhipidura albicollis* and *Terpsiphone paradisi*), which were resident to the state of Madhya Pradesh. Similarly, in Site 2, total 34 species were observed in all the four seasons collectively, out of which 30 resident species were noted; two were winter migratory species (6%) (*Ficedula parva* and *Saxicola maurus*) and two were local migrating species (6%) (*Rhipidura albicollis* and *Leptocoma zeylonica*) belonging to resident species. In Site 3, we recorded 41 species of avian fauna; there were two winter migratory species (5%) (*Hirundo rustica* and *Ficedula parva*) and two local

migratory species (5%) (*Prinia socialis* and *Oenanthe fusca*) in this study site, there were 37 resident species (90%) of avian fauna. Interestingly, there were 58 species of birds in Site 4 which is highest in this study. Out of these, 46 species were resident species (79%); five species were winter migratory (9%) (*Ficedula parva*, *Saxicola maurus*, *Phylloscopus trochiloides*, *Hirundo rustica* and *Motacilla alba*); one species was summer migratory (2%) (*Clamator jacobinus*) and the six were local migratory avian species (10%) (*Oenanthe fusca*, *Pavo cristatus*, *Rhipidura albicollis*, *Terpsiphone paradisi*, *Leptocoma zeylonica* and *Prinia socialis*).

From Tables 2-5 and Figs. 1-4, we can conclude that the highest number (46) of resident birds were recorded in Site 4 and the lowest count (30) was observed in Site 2. The highest number of winter migratory species (5) was recorded in Site 4. Similarly, local migratory species were highest (6) in Site 4.

The data (Tables 2-5) depicts the species recorded at Site 1, Site 2, Site 3 and Site 4 in 2018. Their IUCN status and WPA Schedule have been mentioned. In Site 1, 38

Table 2: IUCN status and WPA schedule of the recorded avian fauna at Site 1 in 2018.

Order	Species	R/WM/SM/LM	IUCN Status	WPA
Columbiformes	<i>Columba livia</i>	R	LC	Schedule-IV
	<i>Streptopelia chinensis</i>	R	LC	Schedule-IV
	<i>Streptopelia senegalensis</i>	R	LC	Schedule-IV
Cuculiformes	<i>Centropus sinensis</i>	R	LC	Schedule-IV
	<i>Eudynamis scolopaceus</i>	R	LC	Schedule-IV
Pelecaniformes	<i>Bubulcus ibis</i>	R	LC	Schedule-IV
Charadriiformes	<i>Vanellus indicus</i>	R	LC	Schedule-IV
Accipitriformes	<i>Accipiter badius</i>	R	LC	Schedule-I
	<i>Milvus migrans</i>	R	LC	Schedule-I
Strigiformes	<i>Athene brama</i>	R	LC	Schedule-IV
Bucerotiformes	<i>Ocyrceros birostris</i>	R	LC	Schedule-IV
Piciformes	<i>Psilopogon haemacephalus</i>	R	LC	Schedule-IV
Coraciiformes	<i>Merops orientalis</i>	R	LC	Schedule-IV
	<i>Halcyon smyrnensis</i>	R	LC	Schedule-IV
Psittaciformes	<i>Psittacula eupatria</i>	R	NT	Schedule-IV
	<i>Psittacula krameri</i>	R	LC	Schedule-IV

Table Cont....

Order	Species	R/W/M/SM/LM	IUCN Status	WPA
Passeriformes	<i>Pericocotus cinnamomeus</i>	R	LC	Schedule-IV
	<i>Aegithina tiphia</i>	R	LC	Schedule-IV
	<i>Dicrurus macrocercus</i>	R	LC	Schedule-IV
	<i>Rhipidura albicollis</i>	R/LM	LC	Schedule-IV
	<i>Dendrocitta vagabunda</i>	R	LC	Schedule-IV
	<i>Corvus splendens</i>	R	LC	Schedule-V
	<i>Terpsiphone paradisi</i>	R/LM	LC	Schedule-IV
	<i>Dicaeum agile</i>	R	LC	Schedule-IV
	<i>Cimyrus asiaticus</i>	R	LC	Schedule-IV
Passeriformes	<i>Euodice malabarica</i>	R	LC	Schedule-IV
	<i>Passer domesticus</i>	R	LC	Schedule-IV
	<i>Machlolophus xanthogenys</i>	R	LC	Schedule-IV
	<i>Orthotomus sutorius</i>	R	LC	Schedule-IV
	<i>Hirundo rustica</i>	WM	LC	Schedule-IV
	<i>Ptyonoprogne concolor</i>	R	LC	Schedule-IV
	<i>Pycnonotus cafer</i>	R	LC	Schedule-IV
	<i>Phylloscopus trochiloides</i>	WM	LC	Schedule-IV
	<i>Zosterops palpebrosus</i>	R	LC	Schedule-IV
	<i>Turdoides striata</i>	R	LC	Schedule-IV
	<i>Gracupica contra</i>	R	LC	Schedule-IV
	<i>Acridotheres tristis</i>	R	LC	Schedule-IV
	<i>Saxicoloides fulicatus</i>	R	LC	Schedule-IV
	<i>Copsychus saularis</i>	R	LC	Schedule-IV

(R = Resident; WM = Winter Migrant; SM = Summer Migrant; LM = Local Migrant; LC = Least Concern & NT = Near Threatened)

Table 3: IUCN status and WPA schedule of the recorded avian fauna at Site 2 in 2018.

Order	Species	R/W/M/SM/LM	IUCN STATUS	WPA Schedule
Columbiformes	<i>Columba livia</i>	R	LC	Schedule-IV
	<i>Streptopelia chinensis</i>	R	LC	Schedule-IV
	<i>Streptopelia senegalensis</i>	R	LC	Schedule-IV
Caprimulgiformes	<i>Apus affinis</i>	R	LC	Schedule-IV
Cuculiformes	<i>Eudynamys scolopaceus</i>	R	LC	Schedule-IV
Pelecaniformes	<i>Bubulcus ibis</i>	R	LC	Schedule-IV
Charadriiformes	<i>Vanellus indicus</i>	R	LC	Schedule-IV
Accipitriformes	<i>Accipiter badius</i>	R	LC	Schedule-I
	<i>Milvus migrans</i>	R	LC	Schedule-I
Strigiformes	<i>Athene brama</i>	R	LC	Schedule-IV
Bucerotiformes	<i>Ocyrceros birostris</i>	R	LC	Schedule-IV
Piciformes	<i>Psilopogon haemacephalus</i>	R	LC	Schedule-IV
Coraciiformes	<i>Merops orientalis</i>	R	LC	Schedule-IV
	<i>Halcyon smyrnensis</i>	R	LC	Schedule-IV
Psittaciformes	<i>Psittacula krameri</i>	R	LC	Schedule-IV

Table Cont....

Order	Species	R/W/M/SM/LM	IUCN STATUS	WPA Schedule
Passeriformes	<i>Oriolus kundoo</i>	R	LC	Schedule-IV
	<i>Aegithina tiphia</i>	R	LC	Schedule-IV
	<i>Dicrurus macrocercus</i>	R	LC	Schedule-IV
	<i>Rhipidura albicollis</i>	R/LM	LC	Schedule-IV
	<i>Dendrocitta vagabunda</i>	R	LC	Schedule-IV
	<i>Corvus splendens</i>	R	LC	Schedule-V
	<i>Corvus macrorhynchos</i>	R	LC	Schedule-IV
	<i>Dicaeum agile</i>	R	LC	Schedule-IV
	<i>Leptocoma zeylonica</i>	R/LM	LC	Schedule-IV
	<i>Passer domesticus</i>	R	LC	Schedule-IV
	<i>Orthotomus sutorius</i>	R	LC	Schedule-IV
	<i>Ptyonoprogne concolor</i>	R	LC	Schedule-IV
	<i>Pycnonotus cafer</i>	R	LC	Schedule-IV
	<i>Turdoides striata</i>	R	LC	Schedule-IV
	<i>Acridotheres tristis</i>	R	LC	Schedule-IV
	<i>Saxicoloides fulicatus</i>	R	LC	Schedule-IV
	<i>Copsychus saularis</i>	R	LC	Schedule-IV
	<i>Ficedula parva</i>	WM	LC	Schedule-IV
<i>Saxicola maurus</i>	WM	LC	Schedule-IV	

(R = Resident; WM = Winter Migrant; SM = Summer Migrant; LM = Local Migrant; LC = Least Concern & NT = Near Threatened)

Table 4: IUCN status and WPA schedule of the recorded avian fauna at Site 3 in 2018.

Order	Species	R/W/M/SM/LM	IUCN STATUS	WPA Schedule
Columbiformes	<i>Columba livia</i>	R	LC	Schedule-IV
	<i>Streptopelia chinensis</i>	R	LC	Schedule-IV
	<i>Streptopelia senegalensis</i>	R	LC	Schedule-IV
Caprimulgiformes	<i>Apus affinis</i>	R	LC	Schedule-IV
Cuculiformes	<i>Centropus sinensis</i>	R	LC	Schedule-IV
	<i>Eudynamys scolopaceus</i>	R	LC	Schedule-IV
Charadriiformes	<i>Vanellus indicus</i>	R	LC	Schedule-IV
Accipitriformes	<i>Elanus caeruleus</i>	R	LC	Schedule-I
	<i>Milvus migrans</i>	R	LC	Schedule-I
Strigiformes	<i>Athene brama</i>	R	LC	Schedule-IV
Bucerotiformes	<i>Ocyrceros birostris</i>	R	LC	Schedule-IV
Piciformes	<i>Psilopogon haemacephalus</i>	R	LC	Schedule-IV
Coraciiformes	<i>Merops orientalis</i>	R	LC	Schedule-IV
	<i>Halcyon smyrnensis</i>	R	LC	Schedule-IV
Psittaciformes	<i>Psittacula krameri</i>	R	LC	Schedule-IV
Passeriformes	<i>Pericrocotus cinnamomeus</i>	R	LC	Schedule-IV
	<i>Coracina javensis</i>	R	LC	Schedule-IV
	<i>Oriolus kundoo</i>	R	LC	Schedule-IV
	<i>Aegithina tiphia</i>	R	LC	Schedule-IV
	<i>Dicrurus macrocercus</i>	R	LC	Schedule-IV
	<i>Dendrocitta vagabunda</i>	R	LC	Schedule-IV

Table Cont....

Order	Species	R/W/M/SM/LM	IUCN STATUS	WPA Schedule
	<i>Corvus splendens</i>	R	LC	Schedule-V
	<i>Corvus macrorhynchos</i>	R	LC	Schedule-IV
	<i>Cinnyris asiaticus</i>	R	LC	Schedule-IV
	<i>Euodice malabarica</i>	R	LC	Schedule-IV
	<i>Passer domesticus</i>	R	LC	Schedule-IV
	<i>Motacilla maderaspatensis</i>	R	LC	Schedule-IV
	<i>Prinia socialis</i>	R/LM	LC	Schedule-IV
	<i>Orthotomus sutorius</i>	R	LC	Schedule-IV
	<i>Hirundo smithii</i>	R	LC	Schedule-IV
	<i>Hirundo rustica</i>	WM	LC	Schedule-IV
	<i>Pycnonotus cafer</i>	R	LC	Schedule-IV
	<i>Zosterops palpebrosus</i>	R	LC	Schedule-IV
	<i>Turdoides striata</i>	R	LC	Schedule-IV
	<i>Gracupica contra</i>	R	LC	Schedule-IV
	<i>Acridotheres tristis</i>	R	LC	Schedule-IV
	<i>Saxicoloides fulicatus</i>	R	LC	Schedule-IV
	<i>Copsychus saularis</i>	R	LC	Schedule-IV
	<i>Cyornis tickelliae</i>	R	LC	Schedule-IV
	<i>Ficedula parva</i>	WM	LC	Schedule-IV
	<i>Oenanthe fusca</i>	R/LM	LC	Schedule-IV

(R = Resident; WM = Winter Migrant; SM = Summer Migrant; LM = Local Migrant; LC = Least Concern & NT = Near Threatened)

Table 5: IUCN status and WPA schedule of the recorded avian fauna at Site 4 in 2018.

Order	Species	R/W/M/SM/LM	IUCN STATUS	WPA Schedule
Galliformes	<i>Pavo cristatus</i>	LM	LC	Schedule-I
Columbiformes	<i>Columba livia</i>	R	LC	Schedule-IV
	<i>Streptopelia chinensis</i>	R	LC	Schedule-IV
	<i>Streptopelia senegalensis</i>	R	LC	Schedule-IV
Caprimulgiformes	<i>Apus affinis</i>	R	LC	Schedule-IV
Cuculiformes	<i>Centropus sinensis</i>	R	LC	Schedule-IV
	<i>Clamator jacobinus</i>	SM	LC	Schedule-IV
	<i>Eudynamis scolopaceus</i>	R	LC	Schedule-IV
Pelecaniformes	<i>Ardeola grayii</i>	R	LC	Schedule-IV
	<i>Bulbulcus ibis</i>	R	LC	Schedule-IV
Charadriiformes	<i>Vanellus indicus</i>	R	LC	Schedule-IV
Accipitriformes	<i>Elanus caeruleus</i>	R	LC	Schedule-I
	<i>Pernis ptilorhynchus</i>	R	LC	Schedule-I
	<i>Accipiter badius</i>	R	LC	Schedule-I
	<i>Milvus migrans</i>	R	LC	Schedule-I
Strigiformes	<i>Athene brama</i>	R	LC	Schedule-IV
Bucerotiformes	<i>Ocyrceros birostris</i>	R	LC	Schedule-IV
Piciformes	<i>Psilopogon haemacephalus</i>	R	LC	Schedule-IV

Table Cont....

Order	Species	R/W/M/SM/LM	IUCN STATUS	WPA Schedule
Coraciiformes	<i>Merops orientalis</i>	R	LC	Schedule-IV
	<i>Halcyon smyrnensis</i>	R	LC	Schedule-IV
Psittaciformes	<i>Psittacula cyanocephala</i>	R	LC	Schedule-IV
	<i>Psittacula eupatria</i>	R	NT	Schedule-IV
	<i>Psittacula krameri</i>	R	LC	Schedule-IV
Passeriformes	<i>Pericrocotus cinnamomeus</i>	R	LC	Schedule-IV
	<i>Coracina javensis</i>	R	LC	Schedule-IV
	<i>Oriolus kundoo</i>	R	LC	Schedule-IV
	<i>Aegithina tiphia</i>	R	LC	Schedule-IV
	<i>Dicrurus macrocercus</i>	R	LC	Schedule-IV
	<i>Rhipidura albicollis</i>	R/LM	LC	Schedule-IV
	<i>Dendrocitta vagabunda</i>	R	LC	Schedule-IV
	<i>Corvus splendens</i>	R	LC	Schedule-V
	<i>Corvus macrorhynchos</i>	R	LC	Schedule-IV
	<i>Terpsiphone paradisi</i>	R/LM	LC	Schedule-IV
	<i>Dicaeum agile</i>	R	LC	Schedule-IV
	<i>Leptocoma zeylonica</i>	R/LM	LC	Schedule-IV
	<i>Cinnyris asiaticus</i>	R	LC	Schedule-IV
	<i>Eurydice malabarica</i>	R	LC	Schedule-IV
	<i>Passer domesticus</i>	R	LC	Schedule-IV
	<i>Motacilla maderaspatensis</i>	R	LC	Schedule-IV
	<i>Motacilla alba</i>	WM	LC	Schedule-IV
	<i>Machlolophus xanthogenys</i>	R	LC	Schedule-IV
	<i>Prinia socialis</i>	R/LM	LC	Schedule-IV
	<i>Orthotomus sutorius</i>	R	LC	Schedule-IV
	<i>Hirundo smithii</i>	R	LC	Schedule-IV
	<i>Hirundo rustica</i>	WM	LC	Schedule-IV
	<i>Ptyonoprogne concolor</i>	R	LC	Schedule-IV
	<i>Pycnonotus cafer</i>	R	LC	Schedule-IV
	<i>Phylloscopus trochiloides</i>	WM	LC	Schedule-IV
	<i>Zosterops palpebrosus</i>	R	LC	Schedule-IV
	<i>Turdoides striata</i>	R	LC	Schedule-IV
	<i>Gracupica contra</i>	R	LC	Schedule-IV
	<i>Acridotheres tristis</i>	R	LC	Schedule-IV
	<i>Saxicoloides fulicatus</i>	R	LC	Schedule-IV
<i>Copsychus saularis</i>	R	LC	Schedule-IV	
<i>Cyornis tickelliae</i>	R	LC	Schedule-IV	
<i>Ficedula parva</i>	WM	LC	Schedule-IV	
<i>Saxicola maurus</i>	WM	LC	Schedule-IV	
<i>Oenanthe fusca</i>	R/LM	LC	Schedule-IV	

(R = Resident; WM = Winter Migrant; SM = Summer Migrant; LM = Local Migrant; LC = Least Concern & NT = Near Threatened)

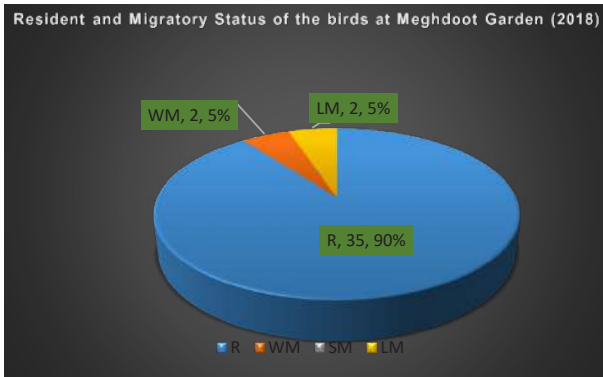


Fig. 1: Percentage composition of R/SM/WM/LM avian fauna at Site 1.

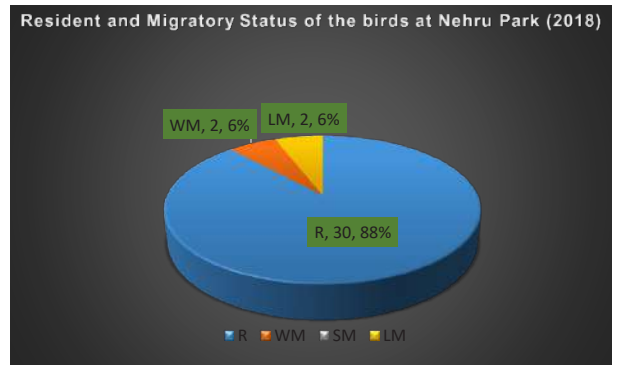


Fig. 2: Percentage composition of R/SM/WM/LM avian fauna at Site-2.

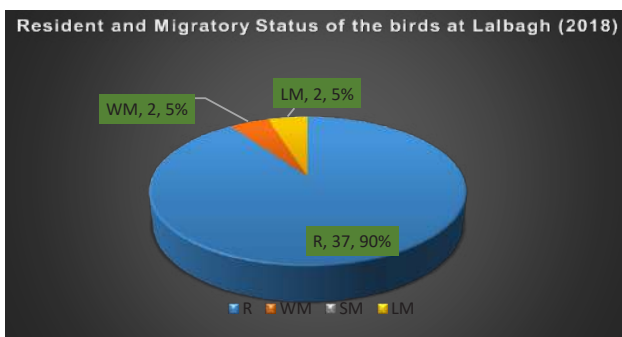
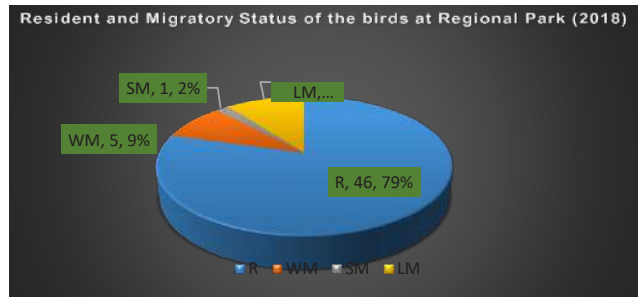


Fig. 3: Percentage composition of R/SM/WM/LM avian fauna at Site-3.



(Legends - R = Resident; WM = Winter Migrant; SM = Summer Migrant; LM = Local Migrant)

Fig. 4: Percentage composition of R/SM/WM/LM avian fauna at Site-4.

species belonged to the Least Concern category and only one species (*Psittacula eupatria*) is in the Near Threatened category (*Psittacula eupatria*). Similarly, in Site2, all the 34 species belonged to the Least Concern category. In Site 3, 41 species were recorded and interestingly, all belonged to the Least Concern category. Lastly, there is only one species (*Psittacula eupatria*) in the Near Threatened category in Site 4 and the remaining 57 species belonged to the Least Concern category.

According to Wildlife Protection Act, 1972, the results (Figs. 5-8) showed that in Site-1 there are two species (*Accipiter badius* and *Milvus migrans*) in schedule I; one species (*Corvus splendens*) in Schedule V and 36 species in Schedule IV. Moreover, in Site-2, there are two species (*Accipiter badius* and *Milvus migrans*) in schedule I, one species (*Corvus splendens*) in Schedule V, and 31 species in Schedule IV. Furthermore, in Site-3, there are two species (*Accipiter badius* and *Milvus migrans*) in schedule

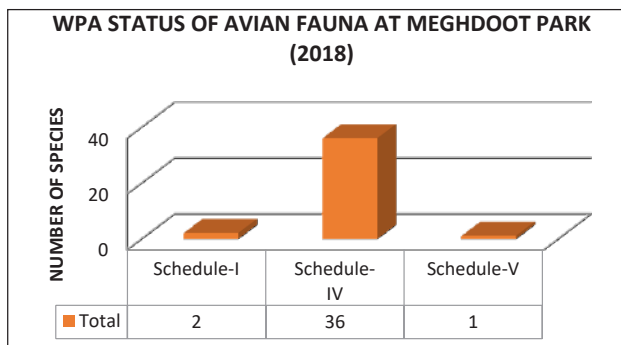


Fig. 5: WPA schedule of the recorded avian fauna at Site-1 in 2018.

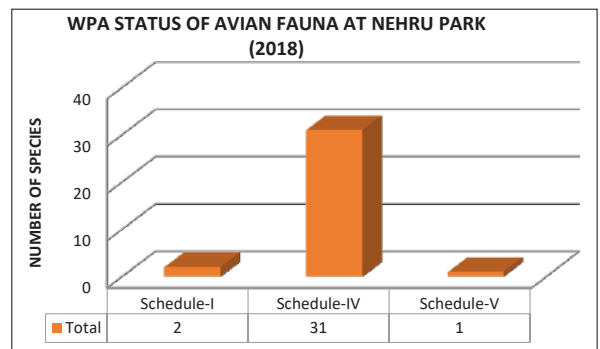


Fig. 6: WPA schedule of the recorded avian fauna at Site-2 in 2018.

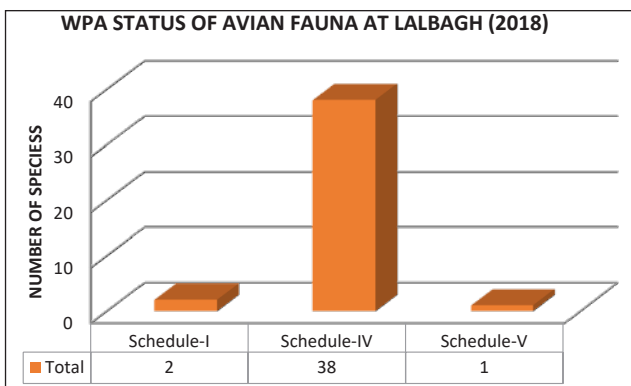


Fig. 7: WPA schedule of the recorded avian fauna at Site-3in 2018.

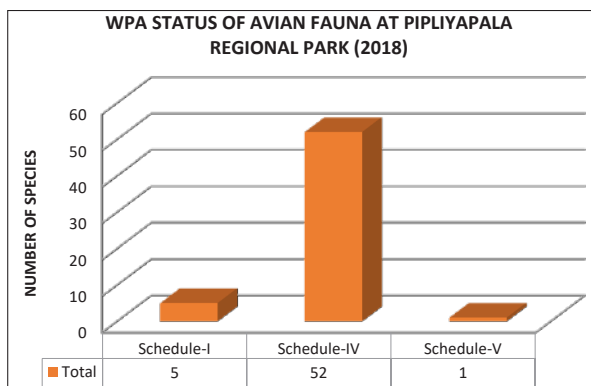


Fig. 8: WPA schedule of the recorded avian fauna at Site-4 in 2018.



Fig. 9: Some photographs of the recorded species.

I; one species (*Corvus splendens*) in Schedule V and 38 species in Schedule IV. In addition to this, at Site-4 there are five species (*Pavo cristatus*, *Elanus caeruleus*, *Pernis ptilorhynchus*, *Accipiter badius* and *Milvus migrans*) are in Schedule I; one species (*Corvus splendens*) in Schedule V, and 52 species in Schedule IV. Fig. 9 shows some photographs of the recorded species.

DISCUSSION

We have reported the IUCN status for various greenspaces of Indore city. This is the first-ever record for such parameters. Interestingly, Khah & Wani (2012) used a similar methodology and concluded that several species were breeding residents in their area; which is quite similar in our study. These species include Jungle crow and Stone chat. Ramesh et al. (2011) reported 129 species in Kuno wildlife

sanctuary and found that 97 species were residents; 25 winter migrants; 4 summer migrants; and 6 local migrating species of Central India. 73 species were observed by Arya et al. (2013) in Shivpuri district. Out of which 25 species were residential; 29 resident migrants and 38 winter migrating species. This study is quite corroborating with our study.

Similarly, analyses of residential status of avian species (Central India) done by Kumar & Kanaujia (2015), revealed that 32 species were winter visitors; 24 species residential, 16 were residential/local migratory and three local migratory. Similar observations were recorded by Kumar et al. (2015) in their preliminary study at Nawabganj Bird Sanctuary. They reported six species of Near Threatened category in their study period, in which Alexandrine parakeet was also mentioned. Parveen & Llyas (2019) also conducted a preliminary survey of birds in Pench Tiger reserve and found

seven species in Near Threatened category and 208 species belonged to Least Concern Category. Adhikari et al. (2019) studied the factors affecting diversity and distribution of birds of IUCN Red List. They also have marked seven species of Near Threatened category including Alexandrine parakeet which resembles our study results.

ACKNOWLEDGEMENT

The authors are highly grateful to The Head, Dr. M.M.P. Shrivastava and Principal, Dr. Suresh T. Silawat, Govt. Holkar Science College, Indore for their immense help and support for conducting this study.

REFERENCES

- Adhikari, J.N., Bhattaraj, B.P. and Thapa, T.B. 2019. Factors affecting diversity and distribution of threatened birds in Chitwan National Park, Nepal. *Journal of Threatened Taxa*, 11(5): 13511-13522.
- Arya, M., Rao, R.J. and Mishra, A.K. 2014. Avifaunal occurrence and distribution of wetland birds in Sakhya Sagar and Madhav lakes in Madhav National Park, Shivpuri, India. *Journal of Environmental Biology*, 35(4): 703-708.
- Datta, M. 2016. Status, guild and diversity of avian fauna from a wetland site and surroundings, in Krishnagar, a city beside tropic of cancer, West Bengal, India. *Int. J. of Fauna and Biological Studies*, 3(4): 68-75.
- Dhindsa, M.S. and Saini, H.K. 1994. Agricultural ornithology: An Indian perspective. *J. Biosciences*, 19: 391-402.
- Gaur, P., Shrivastava, C. S. and Gaherwal, S. 2019. Spatial variation in avifaunal diversity from various green spaces of Indore city, Madhya Pradesh. *International Journal of Current Research and Reviews*, 11(14): 06-15.
- Khah, S., Rao, R. and Wani, K. 2012. Studies on bird diversity of Overa-Aru Wildlife Sanctuary of Jammu and Kashmir, India. *Journal of Threatened Taxa*, 4(13): 3228-3232. <https://doi.org/10.11609/JoTT.o2899.3228-32>.
- Kumar, A. and Kanaujia, A. 2015. Waterbird diversity of Samaspur Bird Sanctuary, Rae Bareli, District, Uttar Pradesh. *Discovery Nature*, 9(23): 48-57.
- Kumar, A., Kanaujia, A., Kushwaha, S. and Kumar, A. 2015. A Preliminary assessment of avifaunal diversity of Nawabganj Bird Sanctuary, Unnao, Uttar Pradesh. *IOSR Journal of Environmental Science, Toxicology and Food Technology (IOSR-JESTFT)*, 9(4): 81-91.
- Mariappan, N., Ahmed Khalfan, B.K. and Krishnakumar, S. 2013. Assessment of bird population in different habitats of agricultural ecosystem. *International Journal of Scientific Research in Environmental Sciences (IJSRES)*, 1(11): 306-316.
- Panwar, S.K. and Salunkhe, P.S. 2014. Study of migratory birds in and around Pandharpur city with special reference to Takali (Padmavati) lake, Pandharpur, Dist. Solapur (M.S.). *Avishkar-Solapur University Journal*, 3: 38-44.
- Parveen, T. and Llyas, O. 2019. A preliminary survey of birds in Pench Tiger Reserve, Madhya Pradesh, India. *Asian Journal of Environment & Ecology*, 9(1): 1-20.
- Ramesh, T., Sridharan, N. and Kalle, R. 2011. Birds of Kuno Wildlife Sanctuary, Central India. *Zoos print.*, XXVI (12): 25-29.
- Seress, G. and Liker, A. 2015. Habitat urbanization and its effects on birds. *Acta Zoologica Academiae Scientiarum Hungaricae*, 61(4): 373-408.
- Sharma, S. and Shukla, A. 2015. Preliminary study on avian faunal diversity of Polipathar area in Jabalpur (M.P.). *International Journal of Current Advanced Research*, 4(9): 364-367.
- Vallejo, B.M., Aloy, A.B. and Ong, P.S. 2009. The distribution, abundance and diversity of birds in Manila's last greenspaces. *Landscape and Urban Planning*, 89(3-4): 75-85.



Physiological Response of Juvenile *Schizothorax prenanti* under Supersaturated Stress

Quan Yuan, Kefeng Li, Ruifeng Liang†, Yuanming Wang, Jingjie Feng, Qianfeng Ji and Yaodan Zhang

State Key Laboratory of Hydraulics and Mountain River Engineering, Sichuan University, Chengdu 610065, China

†Corresponding author: Ruifeng Liang;

Nat. Env. & Poll. Tech.
Website: www.neptjournal.com

Received: 04-01-2020

Revised: 17-02-2020

Accepted: 16-04-2020

Key Words:

Supersaturated water
Schizothorax prenanti
Antioxidant enzyme
Net-cage experiment
Bubble disease

ABSTRACT

Supersaturated water can adversely affect many species of fish and can sometimes lead to death. In the present study, we established an experimental platform on the downstream section of the Dagangshan Hydropower Station on the Dadu River. During flood discharge at the Dagangshan Hydropower Station, the river water supersaturation concentration at the experimental site was monitored, and a unique fish in the river section was selected for a cage experiment. Juvenile fish die under the 110% gas supersaturation conditions in the river, accompanied by symptoms of bubble disease. After the end of flood discharge, the remaining experimental fish were placed in clean water for approximately 180 days, and all the fish died. Exposing the experimental fish to a 127% concentration test tank in the laboratory revealed that the onset of death, semi-lethal time and total death time were 6.7 hours, 12 hours, 31.5 hours, respectively. The test fish that were exposed to supersaturated water for 6 hours were placed in clean water and tested every hour, and the change was minimal. Six-hour exposure may cause irreversible damage to the experimental fish.

INTRODUCTION

Supersaturated water has negative impacts on fish and widely studied for a long time. Abnormal behaviour was observed after fish were exposed to supersaturated water for short time (Gray et al. 1983, Shrimpton et al. 1990). When fish are exposed to supersaturated water for long periods, the formation of bubbles in fish tissues gradually damages the physiological functions of fish (Ebel & Raymond 1976, Krise & Herman 1989, Mesa et al. 2000, Mesa & Warren 1997, Smiley et al. 2011) and may also hinder growth (Krise 1993, Liu et al. 2011). High concentrations of supersaturation may lead to acute death in fish (Backman & Evans 2002, Ebel & Raymond 1976, Weitkamp & Katz 1980). Low concentrations of supersaturation lead to gas bubble disease and chronic death in fish. Specifically, some types of fish cannot avoid supersaturated water in low-saturated water (Stevens et al. 1980). Previous studies have shown that bubble disease can have irreversible negative effects on eggs, juveniles and adult fish (Backman & Evans 2002, Jensen 1988, Smiley et al. 2011).

An important cause of supersaturation in water bodies is the supersaturation of downstream gas caused by flood discharge from dams. In the 1960s, the US Army Corps of Engineers observed supersaturated water bodies downstream of several dams along the Columbia River and its tributary,

the Snake River, with total dissolved gas (TDG) saturation levels of 120-140%; as a result, 18.1% of the fish downstream of the dam suffered from air bubble disease (Nakasone 1987). Colt et al. (1991) found that water oversaturation downstream of the Folsom Dam in the United States was 126-130%. To test the effects of supersaturation on downstream fish during dam flood discharge, a series of field surveys were conducted. A large number of fish with bubble disease were found in Lake Wisconsin (Ryan & Dawley 1998). During flood discharge, a large number of wild fishes with bubble disease were detected in an ice port reservoir and the area downstream of the ice port and Bonneville Dam (Bouck 1980).

In recent years, a large number of water conservancy projects have been built in China. During flood discharge from the water conservancy projects, the total dissolved gas supersaturated concentration ranges from 120% to 143%. Rivers that are hundreds of kilometres downstream of the Manwan and Dachaoshan Dams are supersaturated (Qu et al. 2011). Such supersaturated concentrations lead to a higher risk of bubble disease in downstream river fish, but studies on the effects of supersaturation on the endemic fish in these rivers are still lacking (Cao et al. 2016, Huang et al. 2010, Yuan et al. 2018). Juveniles are more sensitive to supersaturation than adult fish, which is particularly worthy of attention (Weitkamp & Katz 1980).

The extent of the effects of supersaturation on fish depends on the concentration and time. The degree of the negative impact of supersaturation on fish can be determined by their physiological response before the lethal time is reached. On the one hand, TDG saturation can be regarded as a kind of water pollutant. Fish tissue enzyme activity is sensitive to environmental toxic reactions (Livingstone 2001). On the other hand, blood is a relatively stable indicator. Fish blood indicators are widely used to evaluate the health status of fish and their adaptation to the environment. Fish blood is an important physiological, pathological and toxicological indicator. The organic components of blood in fish also change when fish are sick (Bálint et al. 1997, Ceron et al. 1996). The functional changes in organisms that are indicated by changes in blood indexes provide a powerful basis for elucidating the mechanism of environmentally toxic substances.

This study aimed to assess the damage caused by flood discharge at the Dagangshan Dam to the endangered rivers. During flood discharge at the dam, we selected juvenile Prenant's schizothoracin (*Schizothorax prenanti*) as the research subjects to carry out a cage experiment in the downstream channel and assess the death characteristics and presence of bubble disease. The fish that survived the flood were then placed in clear water. Observations were subsequently made for half a year. We then analysed the death characteristics of the experimental fish in supersaturated water in the laboratory. At the same time, the physiological responses of the experimental fish to supersaturated water before the lethal time in supersaturation and the physiological changes in the experimental fish suffering from bubble disease after saturation stress during recovery in clear water were studied. The results of this study can serve as a reference for protecting this species.

MATERIALS AND METHODS

Ethics Statement

The experimental proposal was approved by the Ethics Committee for Animal Experiments of the College of Life Sciences of Sichuan University. All experiments were exe-

cuted in accordance with the animal management regulations of Sichuan Province in China.

Experiment Fish

This study was conducted using six-month-old juvenile Prenant's schizothoracin that were obtained from the Sichuan Fisheries Research Institute. Healthy and active individuals were selected. Two days before the start of the field experiment, the experimental fish were transported to the experimental site for temporary maintenance (Fig. 1) to eliminate the stress response of the experimental fish during transportation. A plastic water tank (length: 0.4 m; width: 0.3 m; and height: 0.3 m) was filled with water and used for temporarily raising the larvae. The clear water in the holding tank was taken from the Dagangshan Reservoir, and the water temperature was close to the water temperature of the river where the experimental point was located. The water in the tank was continuously oxygenated, and feeding was prohibited during the holding process. Other juvenile Prenant's schizothoracin were sent to the laboratory of Sichuan University. The fish were kept in 4 tanks (length: 0.6 m; width: 0.6 m; and water depth: 0.45 m) for acclimatization. The fish were kept in freshwater for 2 days to eliminate the stress reaction in the transportation process. At that time, the oxygen saturation was increased by $100 \pm 2\%$ with an oxygen pump, and the water was cleaned every 12 hours.

Net-Cage Experiment

We established an experimental platform in the downstream channel of Dagangshan Dam (Fig. 1 shows the experimental point). During flood discharge of the upstream dam, the experimental fish were placed in cages with different depths (0~1 m, 1~2 m, 2~3 m, and 0~3 m) that were fixed on the experimental platform. The experimental cages were checked every morning. To assess the survival of the fish, dead fish were removed from the various cages with nets. The weight and length of each dead experimental fish were measured on the experimental platform, symptoms of bubble disease on the body surface were observed, and typical symptoms were photographed. During the lethal flooding and supersaturation stress killing experiments, the TDG concentration

Table 1: Numbers, lengths and weights of the experimental fish.

		Sample size	Fork length (cm)	Weight (g)
Field experiments	0~1m	60	10.38 ± 2.19	10.63 ± 4.82
	1~2m	60	9.57 ± 1.58	8.92 ± 3.63
	2~3m	60	10.68 ± 2.13	9.98 ± 4.37
	0~3m	60	10.35 ± 1.42	9.71 ± 4.03
Laboratory experiment	Lethal experiments	40	9.41 ± 1.32	7.92 ± 2.41
	Physiological experiment	72	11.27 ± 1.80	12.30 ± 3.4

at the experimental point was determined with a TGP meter (Point Four, Canada).

After flood discharge, the surviving experimental fish were removed from the cages and immediately transported approximately 120 kilometres to Heimao Extension Station of the Pubugou Hydropower Station. The experimental fish were grouped according to exposure death and kept in different water tanks; the group and death date of each dead fish were recorded. The water quality was tested once a month, and recovery from air bubble disease in the fish that were subjected to saturation stress was observed. During recovery in clean water, the water quality of each set of water tanks was monitored once a month. The TDG concentration was monitored using a Point Four TGP meter, and the DO concentration was monitored using an Oxyguard TGP meter (Oxyguard, Denmark).

Lethality Experiment in the Laboratory

The laboratory experiments were conducted at the State Key Laboratory of Hydraulics and Mountain River Development and Protection, Sichuan University. The experimental setup is shown in Fig. 2. TDG supersaturated water was produced by increasing the pressure of the water supply, and the required TDG saturation was achieved by adjusting the volume of freshwater. The volume of TDG supersaturated water was adjusted to the concentration level of 125%. Oxygen supersaturation exposure was performed in a tank (width: 0.6 m; depth: 0.45 m) when the supersaturated concentration was completely stable. The experimental water depth was approximately 0.35 m. The water tank was divided into two

parts with a plexiglass orifice plate, and each part was filled with 20 experimental fish. The behaviours of the fish were observed and recorded in the experiment, and the death time of each experimental fish was recorded. During the experiment, portable oxygen meters (Point Four trackers) were placed near the bottoms of the respective tanks, where TDG oversaturation was measured. The temperature was $11.4 \pm 0.3^\circ\text{C}$, and the pH was 7.1 ± 0.2 .

Sample Treatment

The experimental device for assessing the physiological responses of the juvenile fish to supersaturation was the same as the lethal experimental device. The first group was used to test the biochemical reactions of oversaturation stress within 6 hours, and the second group was used to test the biochemical reactions during the restoration in freshwater after six hours of exposure.

Six Prenant's schizothoracin were randomly selected every hour during the exposure period. After being anaesthetized with 0.3 mg/L of MC 222, blood was collected from the caudal arteries of the fish with a syringe. Each of the three was considered a sample. The sampling process in the recovery experiment was consistent with that in the exposure experiment. The blood samples were centrifuged for 20 minutes with a TGL-M high speed and low temperature centrifuge at 10000 r/s. The serum biochemical indexes were detected with a Cobas c311 automatic biochemical analyser. During exposure to TDG supersaturation, six fish were taken at random each hour. Parallel samples were taken for each tissue sample. The gills and muscles were excised

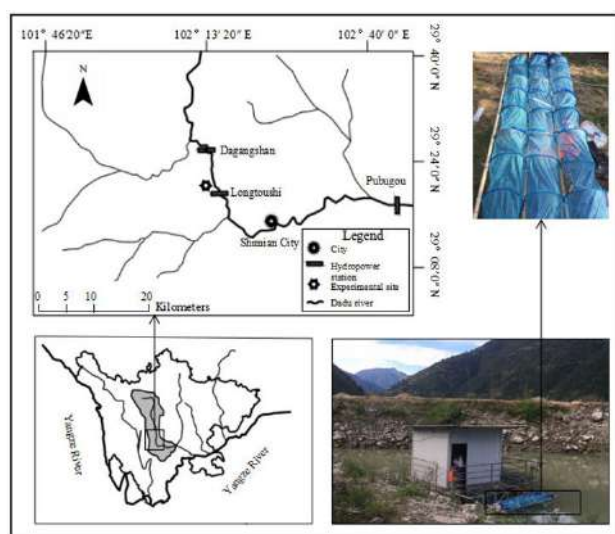


Fig. 1: Location of the study sites on the mainstem of the Dadu River in Sichuan Province, China.

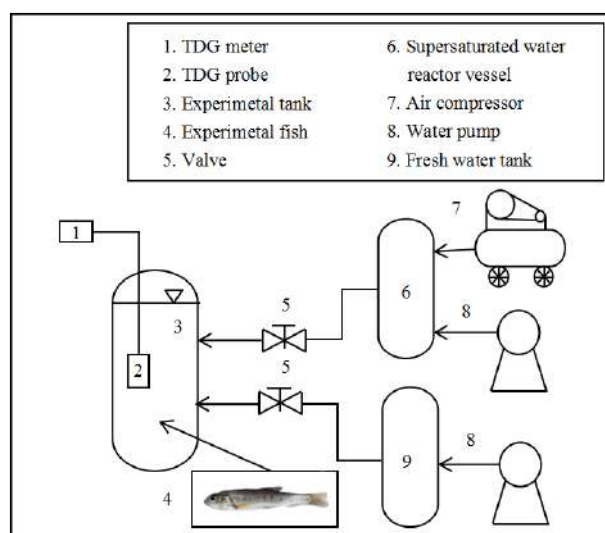


Fig. 2: Sketch of the experimental setup in the laboratory.

and weighed. A total of 0.2 g of tissue was removed from the muscles and gills and placed into a 1 mL centrifuge tube for the detection of superoxide dismutase (SOD) and CAT. A total of 0.3 g of muscle was placed into a 1 mL centrifuge tube to measure the MDA content.

Biochemical Assays

Then, 1.6 mL of 0.05 mol/L sodium phosphate buffer (pH 7.8) was added to the centrifuge tube containing 0.2 g of the tissue sample, soaked in liquid nitrogen and ground in a multi-sample tissue grinder. Then, the crude extract was obtained at 12000 r/min for 20 minutes at 4°C. The supernatant was obtained and used for assaying the SOD and CAT enzyme activities. Based on the experimental scheme of (Liu et al. 2011), the SOD and CAT assay was carried out.

The samples were prepared and tested within 24 hours. The sampling and preparation methods of enzymatic activity in the recovery process were consistent with the exposure process.

Statistical Analysis

The data were presented as the mean \pm standard deviation (SD). For the physiological indicators, the difference between groups was determined by one-way analysis of variance (ANOVA), and Duncan's test was applied. The two groups were considered to be statistically different at $P < 0.05$. The computer programme SPSS for Win 8.0 was used. This paper uses original display pictures.

RESULTS

Net-Cage Experiment

The flood discharge lasted approximately 5 days. The flood

discharge began at 9:00 every morning and lasted until 5 pm. During the period, the water in the river was always saturated, and the values of TDG and DO fluctuated little. The maximum TDG was 117.6%, the minimum was 105.8%, and the average was 110.5%; the maximum DO was 10.21 mg/L, the minimum was 7.65 mg/L, and the average was 9.20 mg/L [Fig. 3(a)]. In the cages with different depths, the number of dead fish in the surface water (0~1 m) was significantly higher than those in the other cages [Fig. 3(b)]. Some obvious symptoms of bubble disease were found on the dead experimental fish. The experimental fish in each cage showed differences in their death characteristics and symptoms and the probability of bubble disease were shown in [Fig. 3 (c)]. The experimental fish suffering from air bubble disease after the end of flood discharge was placed in clear water and observed. After approximately 180 days, all the experimental fish died, and there were no significant differences in the death characteristics of the different groups.

Lethality Experiment in the Laboratory

The water depth of the laboratory water tank was approximately 0.35 m, and the TDG fluctuated in the range of 118.0~131.0%, with an average of 127.8%. The average value of DO in the 117.9~129.0% range was 123.4% [Fig. 4(a)]. The juvenile larvae had more obvious death characteristics in the supersaturated water, and no death occurred in the first stage. The experimental fish began to die after approximately 6.7 hours. The second stage was the start of death to the semi-lethal time (12 hours), and death occurs faster. The third stage was from the semi-lethal time to total death (31.5 hours), and death was slower Fig. 4(b).

Biochemical Responses

Under supersaturation stress, the enzymes in the blood of

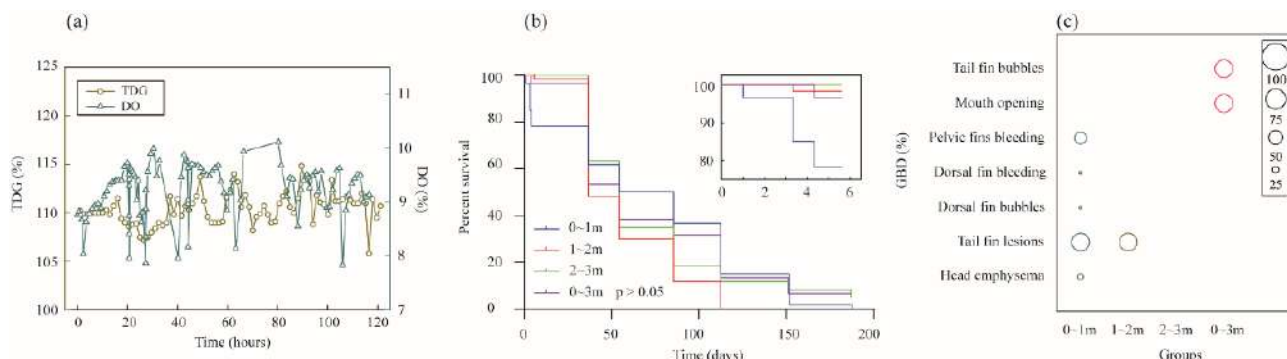


Fig. 3: During flood discharge, the performances of the experimental fish that were subjected to supersaturation stress were assessed. (a) TDG changes in the flood discharge processes; (b) survival curve of the experimental fish with bubble disease at varying water depth and survival curve of the control group (the small image is part of the survival curve of the flood discharge process); (c) probability of bubble disease in the experimental fish at different water depths during the flood discharge.

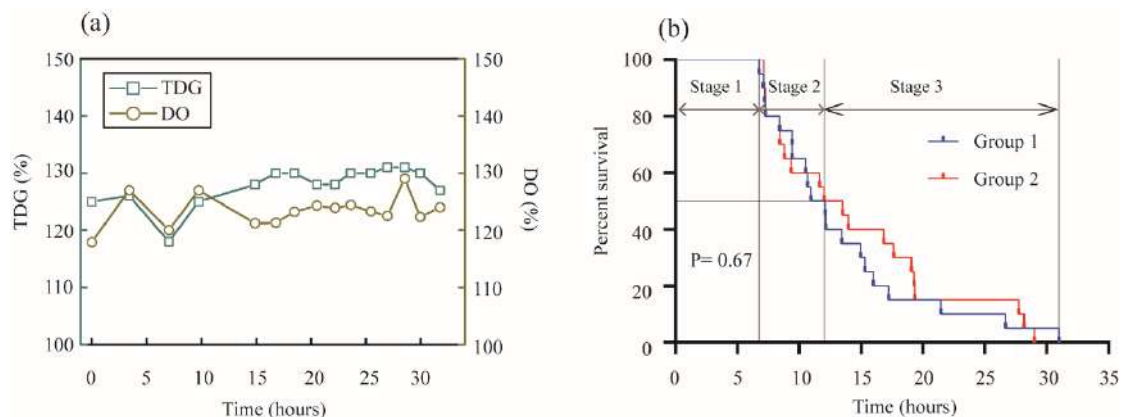


Fig. 4: The performances of the experimental fish that were subjected to supersaturation stress were assessed in laboratory. (a) TDG changes during the processes; (b) survival curve of the experimental fish with bubble disease.

the experimental fish showed obvious changes. Aspartate aminotransferase activity increased first and then began to decline a small amount. At the third hour, the activity level decreased to a value that was close to the control value, which was 1.2 times that of the control group. The regularity of creatine kinase activity was consistent with the trend in aspartate aminotransferase, i.e. increasing first, and after the first hour, continuing to increase from 2 to 6 hours, and the value was 2.3 times that of the exposed group at 6 hours [Fig. 5(a₁)]. The amount of A enzyme in the blood decreased from 1.9 times to 1.3 times in the control group. There was an upward trend between 3 and 5 hours. The maximum value at 5 hours was 2.4 times that of the control group and 2.1 times that of the control group by the 6th hour of recovery. The variation trend in the C enzyme was consistent with that of the A enzyme. From 0~3 hours, a downward trend was observed, from 2.3 times that of the control group to 1.35 times that of the control group. From 3-5 hours, an upward trend was observed, with the highest value at 5 hours being 3.2 times that of the control group and 2 times that of the control group at 6 hours [Fig. 5(a₂)].

When the experimental fish were exposed to 125% supersaturated water, the supersaturated environment activated the antioxidant system of the fish. The activities of SOD, CAT, and MDA changed significantly within 6 hours.

The MDA value declined first and then increased within 6 hours, and the changed trend was consistent with that of SOD. After the first 2 hours, the MDA value decreased significantly, remained at a low value until the fourth hour, and increased at the fifth hour. There was no increase at the 6th hour and the value was 0.87 times that of the control group. The experimental fish that were exposed to 125% supersaturated water did not die [Fig. 5(b₁)]. The supersaturation valve was closed, and the saturation level was reduced to 100% at

the same temperature and water level of the water tank. The enzyme indices were tested for 6 hours to observe the law of self-recovery of the antioxidant system of the experimental fish. The MDA values showed an upward trend between 4 and 6 hours of exposure but continued to decline within 6 hours of recovery, from 0.86 times that of the control group to 0.39 times [Fig. 5(b₂)]. The CAT value began to increase rapidly during the first hour and reached a maximum value of 8.4 times that of the unexposed group. When the high value was maintained at the second hour, the value slowly decreased from the second hour to the sixth hour, and there was no significant difference between the CAT value and the control group value [Fig. 5(b₃)]. CAT activity decreased significantly during the exposure period from 2 to 6 hours and increased significantly during the recovery period from 0 to 3 hours, from 0.73 times to 1.6 times that of the control group; the value remained relatively high from 3 to 6 hours, at 1.58 times the value of the control group at 6 hours [Fig. 5(b₄)]. SOD activity showed a trend of first decreasing and then increasing. SOD activity decreased significantly in the first two hours and remained at a low level from the second hour to the fifth hour. SOD activity was significantly inhibited by oversaturation [Fig. 5(b₅)]. For enzyme activity in the muscles, the value of SOD increased at 5-6 hours of exposure but decreased slowly from 0-6 hours during recovery, from 0.89 times to 0.7 times that of the control group [Fig. 5(b₆)].

The changes in SOD and CAT in the gills under highly saturated stress were significant, but the supersaturation change trends observed in the fish differed. CAT continued to increase after the first hour, and at 6 hours, the value was 6.8 times that of the control group, which was significantly higher than the value without exposure. The relative enzyme activity in the fish gills was higher than that in the muscles, indicating that the enzymes in the fish gills were more sensi-

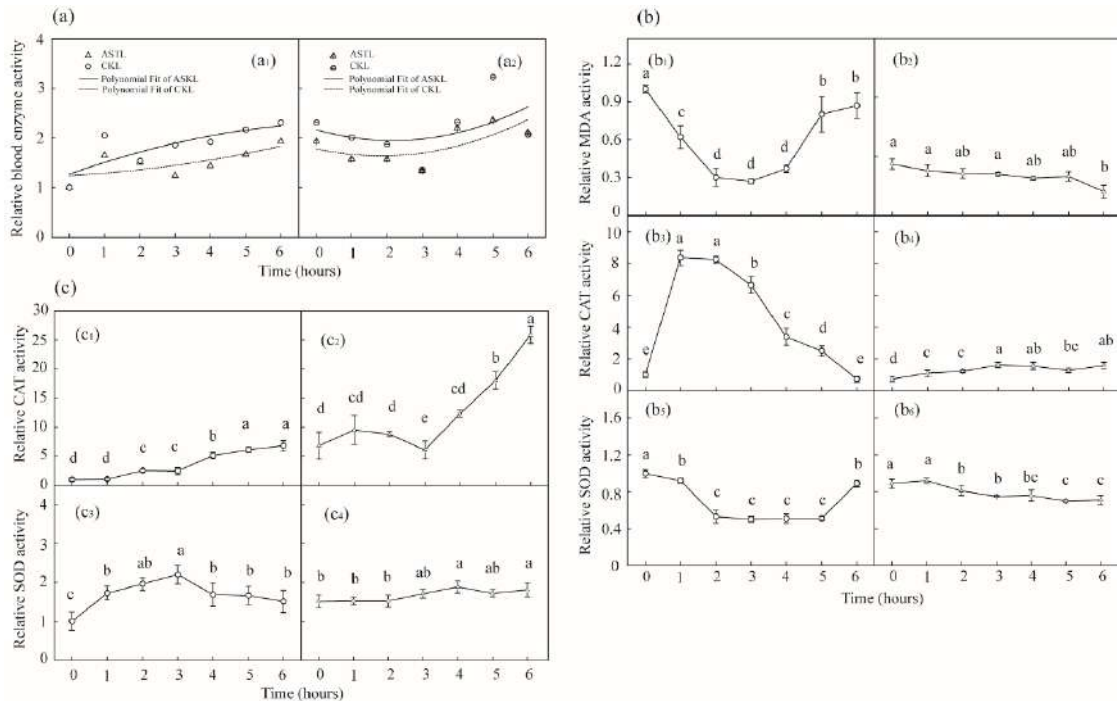


Fig. 5 (a) Changes in enzymatic activity in the blood of Prenant's schizothoracin [(a₁) aspartate aminotransferase and creatine kinase activities after exposure to TDG, and (a₂) aspartate aminotransferase and creatine kinase activities in freshwater]; (b) changes in enzymatic activity in the muscle of Prenant's schizothoracin [(b₁) relative MDA activity after exposure to TDG, (b₂) relative MDA activity in freshwater, (b₃) relative CAT activity after exposure to TDG, (b₄) relative CAT activity in freshwater, (b₅) relative SOD activity after exposure to TDG, and (b₆) relative SOD activity in freshwater]; (c) changes in enzymatic activity in the gills of Prenant's schizothoracin [(c₁) relative CAT activity after exposure to TDG, (c₂) relative CAT activity in freshwater, (c₃) relative SOD activity after exposure to TDG, and (c₄) relative SOD activity in freshwater].

tive to the stress of oversaturation [Fig. 5(c₁)]. CAT increased continuously during the exposure period, and the value was 6.8 times that of the relative control group at 6 hours; the value continued to increase during the recovery period, and the value was 25.8 times that of the relative control group at the recovery time of 6 hours [Fig. 5(c₂)]. SOD rose sharply in the first three hours, with a maximum exposure of 3 hours at 2.2 times the control value, and then began to decline after 4 hours. There was no significant change from 4 to 6 hours, and the value was approximately 1.6 times that of the control group [Fig. 5(c₃)]. For SOD, after fish were exposed to supersaturation for 3~6 hours, a downward trend was observed; the level continued to increase during recovery, and the value increased from 1.5 times to 1.8 times that of the relative control group [Fig. 5(c₄)].

DISCUSSION

Net-Cage Experiment

The concentration of supersaturated water in the river at our field site during this experiment averaged 110%, and juvenile Prenant's schizothoracin with bubble disease were

found in the cages (Fig. 3). The symptoms observed were similar to those observed in previous field studies of fish in supersaturated water (Renfro 1963). Another obvious phenomenon was that the death rate of young fish in the 0~1 m surface cage was highest in the saturated water under stress. Juvenile Chinook salmon and steelhead in the Columbia and Snake River Basins were existing at a water depth with TDG oversaturation most of the time, between 2 and 4 m, and the level was rarely above 2 m (Beeman & Maule 2006, Johnson et al. 2005). The avoidance ability of Chinese suckers in the vertical direction was observed when the fish were exposed to water with high TDG levels. The fish in clear water remained at a depth of 2~3 m and kept diving below 4 m when the oversaturated water concentration was 150% (Cao et al. 2016).

Fish caught in supersaturated river water had different stress levels and different symptoms of bubble disease (Weitkamp et al. 2003). Bubble disease is also more difficult to detect in young fish than in adults (Smiley et al. 2011). However, in addition to bubble disease symptoms that can be observed with the naked eye, supersaturation stress can also cause internal damage (Bouck 1980, Newcomb 1974).

Just because bubble disease is observed to be mild, it does not mean that the damage to the fish was minor. Symptoms of GBT could be observed in sockeye salmon and steelhead when the TDG concentration level exceeded 126%, while symptoms of bubble disease in Chinook salmon were still rarely observed when the TDG level exceeded 130% (Backman & Evans 2002). At the end of the field experiment, the surviving fish were placed in clear water and observed. No obvious symptoms of bubble disease were observed in the surviving juvenile fish, but they continued to die in the clear water. This result indicates that irreversible damage was caused by low supersaturation concentrations and long-term stress. In addition, the death rate of fish at different water depths showed no significant difference. For juvenile schizostoma, compensating for the water depth in the channel could not significantly alleviate the negative harm of supersaturation to the experimental fish.

Acute Lethal Experiments

At the start of the experiment, fish swam freely around the tank. Abnormal behaviour began to be observed approximately 7 hours later, and the fish began to gather at the bottom and corners of the tanks. Some fish were very active, and some fish started to swim quickly and suddenly; side swimming was observed. Bubble disease began to unbalance the fish, and they sometimes jumped in the air and then fell slowly to the bottom of the tank. At approximately hour 12, the fish began to die. Dead experimental fish floated on the water, and their mouths were wide open. Bubble disease could be observed on some of the dead experimental fish, such as bubbles on fins, the protrusion of eyes and protrusions of the abdomen. In oversaturated water, the behaviours of white bass include loss of buoyancy control, lethargy, crashing into the walls and bottoms of aquariums, occasional darting, violent shaking, the rapid opening of the mouth, opening of the gills, and swimming at the bottom of the tank (Smiley et al. 2011). Chinese suckers show signs of spinning, and in some cases, they float to the surface of the water and go back to the bottom, where they lie (Cao et al. 2016). Fish held in supersaturated water show an increase in swim bladder pressure, and gas is expelled through the pneumatic duct, which may explain the abnormal behaviour of the experimental fish when exposed to supersaturation to some extent (Shrimpton et al. 1990).

The processes of fish exposure to supersaturated water, suffering from bubble disease and eventually dying could be divided into three distinct periods. We found that there were three stages of supersaturated death of the juvenile fish under laboratory conditions, which is consistent with previous studies. During the first phase, bubbles begin to form in the

blood vessels. The second stage is the time when the mortality rate is gradually increasing. The third stage of death is slow and lasts relatively longer (Bouck 1980).

The tolerances of different fish to TDG oversaturated water often differ. The lethal exposure times to 50% mortality for Chinook and steelhead at 125% nitrogen saturation were 13.6 hours and 14.2 hours, respectively. The median lethal time (LT_{50}) was determined to evaluate the acute lethal effects on several species of endemic fish to the upper reaches of the Yangtze River at a level of 125% supersaturation. The shortest time was observed for juvenile rock carp, 15.4 hours (Huang et al. 2010), followed by Chinese suckers (*Myxocyprinus asiaticus* Bleeker), with an LC_{50} value of 43.4 h (Chen et al. 2012). Silver carp tolerated supersaturation best, with a lethal time of approximately 67.71 h (Cao et al. 2016). Compared with the half-lethal times of several species that are endemic to the middle and upper reaches of the Yangtze River under the same laboratory conditions, the half-lethal time of juvenile *Schizothorax chinensis* was 12 hours, which showed poor tolerance to supersaturation.

Biochemical Indicator of Blood Serum

Fish may experience physiological and blood composition changes in response to the level of oxygen in the water. Under the condition of water hypoxia, the blood pressure in the abdominal aorta and dorsal aorta of fish slightly decreases, and the amount of haemoglobin also decreases (Holeton 1972). The serum potassium, phosphate and serum albumin, calcium, cholesterol, total protein and alkaline phosphatase levels in steelhead increased after 35 days of exposure to 110% total atmospheric gas saturation (Newcomb 1974). Long-term supersaturation stress changes the blood gas exchange, pH, plasma ion, respiratory rate and cardiovascular function of fish (Wilkes et al. 1981). In freshwater rainbow trout, respiratory acidosis that was induced by 70 h of exposure to a high oxygen environment was also associated with the reduction in the gill chlorine cell surface area (CCFA). After 72 hours of exposure to high oxygen levels, metabolic alkalosis was observed in normal water for 6 hours (Gilmour & Perry 1994). The content of AST is low in fish with normal physiological states. When the body is under stress, AST is released into the blood from liver cells. AST is also often used as the detection index of environmental stress, especially toxicity tests. We found liver cell damage in the juvenile fish that experienced supersaturated water stress. The increasing concentration in the CK was consistent with the observed abnormal activity [Fig. 5 (a)].

Blood markers can also describe a fish's recovery from bubble disease. In *Clarias batrachus* and *Heteropneustes fossilis* with severe bubble disease, bubble collapse led

to liver, kidney, tubule and glomerular degeneration and haematopoietic necrosis. At the same time, the erythrocyte count and haemoglobin content decreased significantly. After a period of recovery, normal swimming was restored, and the red blood cell counts and haemoglobin levels also recovered from the disease (Kulshrestha & Mandal 1982). In hyper-aerobic processes, the ultimate recovery of both pHe and pH_i must occur in the kidneys or gills (Wood et al. 1984). However, in our observations, the blood indicators showed no signs of recovery after 6 hours of stress [Fig. 5 (b)].

Activities of Antioxidant Enzymes

The enzyme activities in the gills of fish tend to be more sensitive than those in the muscles (Fig. 5). Liu indicated that CAT activities in gills were higher than those in muscles (Liu et al. 2011). Severe damage to fish gills caused by high oxygen and high pressure in supersaturated water is a major cause of death (Barthelemy et al. 1981, Sebert et al. 1984). One possible reason is that hyperoxia induces respiratory acidosis in rainbow trout, and 90% of the net acid is excreted through fish gills (Wood 1991).

Previous studies have shown that antioxidant enzyme activity can be used to evaluate the degree of stress of TDG oversaturated water on fish. Chen found that changes in the CAT activities in the muscles and gills of Chinese suckers that were exposed to a gas saturation level of 140% exhibited a regular decrease after an increase. The CAT activities in the muscles could return to the normal level at LT₅₀. However, the CAT activities in the gills were significantly lower than those in the control group (TDG level of 100%) after 3/5 LT₅₀ (Chen et al. 2012). Qing Liu demonstrated that CAT activity in the muscles and gills of juvenile rock carp increased after long-term exposure at low TDG levels. CAT activity in the muscles increased 1.7-fold at 112%, and the activity in gills that were exposed to a 108% level of TDG was 1.5-fold higher than that in the control group at 21 days (Qing Liu et al. 2015). Asian carp were exposed to a 140% concentration of supersaturated water. The CAT activity increased significantly within 2 hours. Over time, the CAT activity gradually decreased, and the CAT activity in the oversaturated fish was lower than that in the fish in fresh water at 5 hours (Cao et al. 2016). The variation trend in SOD activity in oversaturated fish was consistent with that in CAT activity (Qing Liu et al. 2015). The content of MDA can be used as an index to investigate the severity of cell stress. Research on variation trends in MDA is lacking.

In our study, the variation trend in enzyme activity over time in Prenant's schizothoracin under saturated stress showed that CAT activity first increased and then decreased over time, which was consistent with previous studies (Cao

et al. 2016, Chen et al. 2012). SOD and MDA decreased first and then increased over time. The SOD activity results were inconsistent with the findings of previous studies (Liu et al. 2011, Qing Liu et al. 2015), mainly because those studies assessed long-term changes in fish exposure, while our study assessed short time changes. The activities of the three enzymes in our study, SOD, CAT and MDA, in the muscles of the fish showed relatively obvious recovery phenomena within 6 hours, indicating that the fish had a certain adaptability and self-regulation ability in response to supersaturation stress within the recovery time range.

Previous studies found that fish suffering from bubble disease in oversaturated water can recover to some extent (Knittel et al. 1980, Meekin & Turner 1974). Signs of recovery were observed in fizzy trout (Rukavina & Varenika 1956). After being exposed to oversaturated water for 96 hours, fish recovery was observed. There was no significant difference between the red blood cells and haemoglobin, and the swimming performance returned to normal (Kulshrestha & Mandal 1982). Some species of fish are highly adapted to supersaturated environments. Sea bass can recover quickly when exposed to normal conditions after being exposed to a TDG level greater than 220% (Lemarié et al. 2011).

CONCLUSION

In this study, the physiological and biochemical reactions of Prenant's schizothoracin were determined during recovery in water after exposure to a supersaturation concentration of 125% after 6 hours of stress. The results showed that the SOD enzyme activity and MDA activity in the muscles of fish continued to decline within 6 hours, and the CAT activity in the muscles and SOD activity and CAT activity in the gills of fish continued to decline. These findings indicate that the antioxidant enzyme activity of fish cannot effectively recover in clear water after 6 hours. The changes in AST enzyme activity and CK enzyme activity in the fish serums were consistent, and the recovery trend was obvious within 6 hours.

ACKNOWLEDGMENTS

This work was supported by the National Natural Science Foundation of China (Grants 51379136 and 51509213) and the National Key Project for Research and Development Plan (2016YFC0401710).

REFERENCES

- Backman, T.W. and Evans, A.F. 2002. Gas bubble trauma incidence in adult salmonids in the Columbia River Basin. *North American Journal of Fisheries Management*, 22: 579-584.

- Bálint, T., Ferenczy, J., Kátai, F., Kiss, I., Kráczér, L., Kufcsák, O., Láng, G., Polyhos, C., Szabó, I. and Szegletes, T. 1997. Similarities and differences between the massive eel (*Anguilla anguilla* L.) devastations that occurred in Lake Balaton in 1991 and 1995. *Ecotoxicology and Environmental Safety*, 37: 17-23.
- Barthelemy, L., Belaud, A. and Chastel, C. 1981. A comparative study of oxygen toxicity in vertebrates. *Respiration Physiology*, 44: 261-268.
- Beeman, J.W. and Maule, A.G. 2006. Migration depths of juvenile Chinook salmon and steelhead relative to total dissolved gas supersaturation in a Columbia River reservoir. *Transactions of the American Fisheries Society*, 135: 584-594.
- Bouck, G.R. 1980. Etiology of gas bubble disease. *Transactions of the American Fisheries Society*, 109: 703-707.
- Cao, L., Li, K., Liang, R., Chen, S., Jiang, W. and Li, R. 2016. The tolerance threshold of Chinese sucker to total dissolved gas supersaturation. *Aquaculture Research*, 47: 2804-2813.
- Cao, L., Liang, R., Tuo, Y., Li, Y. and Li, K. 2016. Influence of total dissolved gas-supersaturated water on silver carp (*Hypophthalmichthys molitrix*). *Water Science and Engineering*, 9: 324-328.
- Ceron, J. J., Sancho, E., Ferrando, M.D., Gutierrez, C. and Andreu, E. 1996. Metabolic effects of diaziron on the European eel: *Anguilla anguilla*. *Journal of Environmental Science and Health Part B*, 31: 1029-1040.
- Chen, S., Liu, X., Jiang, W., Li, K., Du, J., Shen, D. and Gong, Q. 2012. Effects of total dissolved gas supersaturated water on lethality and catalase activity of Chinese sucker (*Myxocyprinus asiaticus* Bleeker). *Journal of Zhejiang University Science B*, 13: 791-796.
- Colt, J.E., Orwicz, K. and Brooks, D. 1991. Gas supersaturation in the American River. *California Fish and Game*, 77: 41-50.
- Ebel, W.J. and Raymond, H.L. 1976. Effect of atmospheric gas supersaturation on salmon and steelhead trout of the Snake and Columbia rivers. *Marine Fisheries Review*, 38: 1-14.
- Gilmour, K. and Perry, S. 1994. The effects of hypoxia, hyperoxia or hypercapnia on the acid-base disequilibrium in the arterial blood of rainbow trout. *Journal of Experimental Biology*, 192: 269-284.
- Gray, R.H., Page, T.L. and Saroglia, M.G. 1983. Behavioral response of carp, *Cyprinus carpio*, and black bullhead, *Ictalurus melas*, from Italy to gas supersaturated water. *Environmental Biology of Fishes*, 8: 163-167.
- Holeton, G.F. 1972. Gas exchange in fish with and without hemoglobin. *Respiration Physiology*, 14: 142-150.
- Huang, X., Li, K., Du, J. and Li, R. 2010. Effects of gas supersaturation on lethality and avoidance responses in juvenile rock carp (*Procypris rabaudi* Tchang). *Journal of Zhejiang University Science B*, 11: 806-811.
- Jensen, J. 1988. Combined effects of gas supersaturation and dissolved oxygen levels on steelhead trout (*Salmo gairdneri*) eggs, larvae, and fry. *Aquaculture*, 68: 131-139.
- Johnson, E.L., Clabough, T.S., Bennett, D.H., Bjornn, T.C., Peery, C.A., Caudill, C.C. and Stuehrenberg, L.C. 2005. Migration depths of adult spring and summer Chinook salmon in the lower Columbia and Snake rivers in relation to dissolved gas supersaturation. *Transactions of the American Fisheries Society*, 134: 1213-1227.
- Knittel, M.D., Chapman, G.A. and Garton, R.R. 1980. Effects of hydrostatic pressure on steelhead survival in air-supersaturated water. *Transactions of the American Fisheries Society*, 109: 755-759.
- Krise, W.F. 1993. Effects of one-year exposures to gas supersaturation on lake trout. *The Progressive Fish Culturist*, 55: 169-176.
- Krise, W.F. and Herman, R.L. 1989. Tolerance of lake trout, *Salvelinus namaycush* (Walbaum), sac fry to dissolved gas supersaturation. *Journal of Fish Diseases*, 12: 269-273.
- Kulshrestha, A.K. and Mandal, P.K. 1982. Pathology of gas bubble disease in two air-breathing catfishes (*Clarias batrachus* Linn. and *Heteropneustes fossilis* Bloch.). *Aquaculture*, 27: 13-17.
- Lemarié, G., Hosfeld, C.D., Breuil, G. and Fivelstad, S. 2011. Effects of hyperoxic water conditions under different total gas pressures in European sea bass (*Dicentrarchus labrax*). *Aquaculture*, 318: 191-198.
- Liu, X., Li, K., Du, J., Li, J. and Li, R. 2011. Growth rate, catalase and superoxide dismutase activities in rock carp (*Procypris rabaudi* Tchang) exposed to supersaturated total dissolved gas. *Journal of Zhejiang University Science B*, 12: 909.
- Livingstone, D.R. 2001. Contaminant-stimulated reactive oxygen species production and oxidative damage in aquatic organisms. *Marine Pollution Bulletin*, 42: 656-666.
- Meekin, T.K. and Turner, B.K. 1974. Tolerance of salmonid eggs, juveniles and squawfish to supersaturated nitrogen. *Nitrogen Supersaturation Investigations in the Mid-Columbia River*, Washington Department of Fisheries Technical Report, p. 75-126.
- Mesa, M.G., Weiland, L.K. and Maule, A.G. 2000. Progression and severity of gas bubble trauma in juvenile salmonids. *Transactions of the American Fisheries Society*, 129: 174-185.
- Mesa, M.G. and Warren, J.J. 1997. Predator avoidance ability of juvenile chinook salmon (*Oncorhynchus tshawytscha*) subjected to sublethal exposures of gas-supersaturated water. *Canadian Journal of Fisheries and Aquatic Sciences*, 54: 757-764.
- Nakasono, H. 1987. Study of aeration at weirs and cascades. *Journal of Environmental Engineering*, 113: 64-81.
- Newcomb, T.W. 1974. Changes in blood chemistry of juvenile steelhead trout, *Salmo gairdneri*, following sublethal exposure to nitrogen supersaturation. *Journal of the Fisheries Board of Canada*, 31: 1953-1957.
- Qing Liu, X., K. Feng Li, Jiang, W. and Wu, S. 2015. Biochemical responses and survival of rock carp (*Procypris rabaudi*) to total dissolved gas supersaturated water. *Ichthyological Research*, 62: 171-176.
- Qu, L., Li, R., Li, J., Li, K. and Deng, Y. 2011. Field observation of total dissolved gas supersaturation of high-dams. *Science China Technological Sciences*, 54: 156-162.
- Renfro, W.C. 1963. Gas-bubble mortality of fishes in Galveston Bay, Texas. *Transactions of the American Fisheries Society*, 92: 320-322.
- Rukavina, J. and Varenika, D. 1956. Air bubble disease of trout at the source of the river Bosna. *Sport Fishery Abstr.*, 4147.
- Ryan, B.A. and Dawley, E.M. 1998. Effects of dissolved gas supersaturation on fish residing in the Snake and Columbia rivers, 1997, Bonneville Power Administration.
- Sebert, P., Barthelemy, L. and Peyraud, C. 1984. Oxygen toxicity in trout at two seasons. *Comparative Biochemistry and Physiology Part A: Physiology*, 78: 719-722.
- Shrimpton, J.M., Randall, D.J. and Fidler, L.E. 1990. Factors affecting swim bladder volume in rainbow trout (*Oncorhynchus mykiss*) held in gas supersaturated water. *Canadian Journal of Zoology*, 68: 962-968.
- Smiley, J.E., Drawbridge, M.A., Okihiro, M.S. and Kaufmann, R.S. 2011. Acute effects of gas supersaturation on juvenile cultured White Seabass. *Transactions of the American Fisheries Society*, 140: 1269-1276.
- Stevens, D.G., Nebeker, A.V. and Baker, R.J. 1980. Avoidance responses of salmon and trout to air-supersaturated water. *Transactions of the American Fisheries Society*, 109: 751-754.
- Weitkamp, D.E., Sullivan, R.D., Swant, T. and DosSantos, J. 2003. Gas bubble disease in resident fish of the lower Clark Fork River. *Transactions of the American Fisheries Society*, 132: 865-876.
- Weitkamp, D.E. and Katz, M. 1980. A review of dissolved gas supersaturation literature. *Transactions of the American Fisheries Society*, 109: 659-702.
- Wilkes, P., Walker, R.L., McDonald, D.G. and Wood, C.M. 1981. Respiratory, ventilatory, acid-base and ionoregulatory physiology of the white sucker *Catostomus commersoni*: The influence of hyperoxia.

- Journal of Experimental Biology, 91: 239-254.
- Wood, C.M. 1991. Branchial ion and acid-base transfer in freshwater teleost fish: Environmental hyperoxia as a probe. *Physiological Zoology*, 64: 68-102.
- Wood, C.M., Wheatly, M.G. and H be, H. 1984. The mechanisms of acid-base and ion regulation in the freshwater rainbow trout during environmental hyperoxia and subsequent normoxia. III. Branchial exchanges. *Respiration physiology*, 55: 175-192.
- Yuan, Y., Wang, Y., Zhou, C., An, R. and Li, K. 2018. Tolerance of Prenant's schizothoracin *Schizothorax prenanti* to total dissolved gas supersaturated water at varying temperature. *North American Journal of Aquaculture*, 80: 107-115.



Application of Hydrous Bismuth Oxide for Arsenic Removal from Aqueous Solutions

Manish Ranjan*†, Prabhat Kumar Singh* and Arun Lal Srivastav**

*Department of Civil Engineering, Indian Institute of Technology (BHU), Varanasi, India

**Chitkara University School of Engineering and Technology, Chitkara University, Himachal Pradesh, India

†Corresponding author: Manish Ranjan; manish040533@gmail.com

Nat. Env. & Poll. Tech.
Website: www.neptjournal.com

Received: 10-04-2020

Revised: 02-06-2020

Accepted: 04-06-2020

Key Words:

Arsenic removal
Metal pollution
Hydrous bismuth oxide
Langmuir isotherm
XRD; SEM

ABSTRACT

The present study is devoted to arsenic sorption on hydrous bismuth oxide (HBO) through batch and column studies. Advantage of the adsorbent includes arsenic removal in addition to the simultaneous removal of nitrate and fluoride from aqueous solution. Both the forms of arsenic tested by adsorbent in which affinity for arsenic (V) was found better than arsenic (III). Langmuir isotherm and pseudo-second-order kinetic models were found a fit with the experimental data. Calculation of adsorption energy and increased level of chloride in treated water indicated the possible role of physical adsorption and ion exchange phenomenon in arsenic(V) sorption. A fixed bed column study gave 615 mL of treated water [As (V) \leq 0.01mg/L] from 0.085 mg/L arsenic (V) spiked influent with a sorption potential of 13.1-19.6 μ g/g. XRD and EDS analyses confirmed the adsorption of arsenic (V) and the presence of chloride in the exhausted bed of adsorbent. The thermodynamic parameter has shown the endothermic and spontaneous process of adsorption.

INTRODUCTION

Groundwater is a major source of drinking water and its per capita availability is getting reduced over the last decades because of chemical contamination, hence its quality needs to be protected. Arsenic is one of the major groundwater contaminants widely found in the eastern regions of Indian sub-continent (Nath et al. 2008). Due to the adverse health effects including carcinogenic nature (Sarkar & Paul 2016), the maximum allowable concentration of arsenic in drinking water set by United States Environmental Protection Agency (USEPA) is 0.01 mg/L (Iesan et al. 2008). World Health Organization also recommended the maximum permissible limit of arsenic as 0.01 mg/L in drinking water (Vaclavikova et al. 2008). Hence, excess of arsenic in ground water used for drinking is toxic to humans and could be taken as serious threat for human health (Srivastav & Ranjan 2020). The removal of arsenic by adsorption process was studied in the present paper.

Arsenic is a semi-metal and commonly found in four oxidation states of +5, +3, 0, -3. Inorganic arsenic acids or arsenates (H_3AsO_4 , H_2AsO_4^- , HAsO_4^{2-} and AsO_4^{3-}) are found in the oxidation state of +5 and collectively referred as As(V), whereas arsenous acids or arsenites (H_3AsO_3 , H_2AsO_3^- , HASO_3^{2-} and AsO_3^{3-}) are found in the oxidation state of +3 and collectively referred as As(III) (Zhou et al. 2017). The

solubility of arsenic is greatly affected by pH of the solution (Mudhoo et al. 2011). Arsenic (V) predominates as H_3AsO_4 in aerobic waters (high redox potential) with lower pH (<2) whereas arsenic species H_2AsO_4^- and HASO_4^{2-} are found in pH range of 2-11 as shown in Fig. 1 (Khan et al. 2004). Similarly, arsenic (III) exists as H_3AsO_3 at low pH (<3) but gets easily replaced by H_2AsO_3^- as the pH increases beyond 9.2 and further at high pH (>12), only HASO_3^{2-} can be observed in water as shown in Fig. 1 (Mudhoo et al. 2011). Hence, pH is one of the prime factors for redox equilibrium (Fig. 1) between arsenic (V) and arsenic (III) thus, arsenic speciation and its mobility is greatly affected by pH as well as the redox potential (Doušova et al. 2003). But, oxygen present in air leads to an increase in the redox potential of the groundwater when it is exposed to the open atmosphere. Consequently, arsenic (III) immediately changes into arsenic (V) (Ngai et al. 2006). Hence, arsenic (V) is a dominant species over arsenic (III) in an oxidative environment (Sarkar & Paul 2016). The major component of arsenic (V) in aqueous environment are anionic species (H_2AsO_4^- , HASO_4^{2-} and AsO_4^{3-}) and mostly found in the pH range of 6-8 as reported by Ngai (2002).

Adsorption process is one of the widely applied methods to remove arsenic from water due to its simplicity (Bhatnagar & Sillanpaa 2011). Many inorganic adsorbents are investigated for water treatment because organic

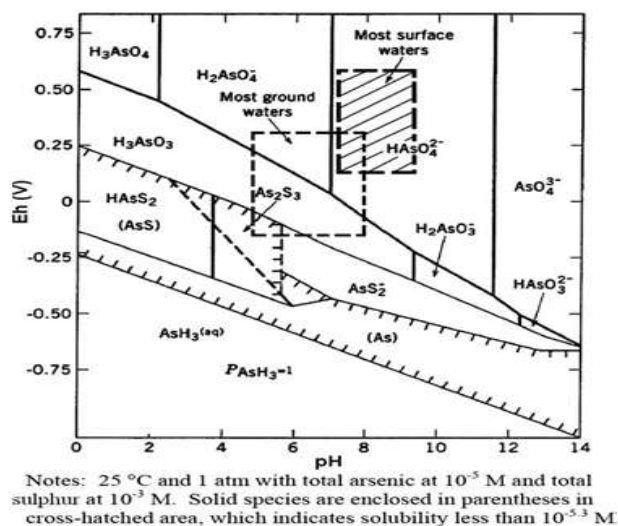


Fig. 1: Eh-pH diagram for arsenic (Mudhoo et al. 2011)

adsorbents reported to have fouling problems (Ustun et al. 2007). In the water, it is observed that metal oxide has a high affinity towards negatively contaminates (Yao et al. 2011). Several researchers have examined the application of hydrous metal oxide (HMO) as adsorbents for arsenic remediation from aqueous solutions. Hydrous metal oxides (HMOs) are amongst the largest group of studied inorganic materials because of having advantages like suitability for sorptive filtration and ease in regeneration and reuse. Among various metal oxides the oxide of titanium (Wagle & Shipley 2016), iron (Puente-Urbina & Montero-Campos 2017), activated alumina (Sinha et al. 2011), zinc (Li et al. 2011), aluminium (Park et al. 2012) and zirconium (Chaudhry et al. 2017) have been reported with good arsenic sorption capacity from water. Researchers have also used mixed oxides like Fe-Ti (Gupta & Ghosh 2009), Ce-Ti (Li et al. 2010), Fe-Zr (Ren et al. 2011), Fe-Cr (Basu & Ghosh 2011), Fe-Al (Basu et al. 2012), Fe-Cu (Zhang et al. 2013), Fe-Mn (Kong et al. 2014), Mn-Al (Wu et al. 2017), Zr-Ti (Anđelković et al. 2017), Fe-Ti-Mn composite oxide (Zhang et al. 2018), Fe/Al composite (Inchaurrondo et al. 2019) and Fe_3O_4 @ TiO_2 sheets nanocomposite (Deng et al. 2019) for the same.

A thorough literature review reveals that hydrous metal oxide has been used by many researchers for the removal of arsenic from water. Recently, hydrous bismuth oxide (HBO) is reported to have excellent and promising adsorptive properties of nitrate and fluoride sorption from aqueous solution. Initially, Fritsche (1993) found sorptive property of yellow bismuth hydroxide for nitrate removal. Further, Singh (1999) investigated the potentials of various bismuth compounds for nitrate removal from aqueous solution due to the ion exchange of nitrate with embedded chloride of

HBO. Hydrous Bismuth Oxide (HBO) is the precipitated product of bismuth trioxide in the presence of strong acid with a strong base. A ratio of 1:1 is used to make precipitate, which is designated as HBO1, similarly 1:2 and 1:3 named as HBO2 and HBO3 respectively. Excess of strong base results in polymerizations of HBO as reported by Ranjan et al. (2019). HBO2 and HBO3 are the final polymeric products of hydrous bismuth oxides which have excellent nitrate removal efficiency (82%) at the initial nitrate concentration of 62 mg NO_3^-/L (Singh et al. 2012). Further, Srivastav et al. (2014) reported a maximum sorption potential of 0.992 mg NO_3^-/g by HBO2 with 62 mg NO_3^-/L initial concentration in batch experiments. In another study, Singh et al. (2015) reported 0.974 mg NO_3^-/g nitrate sorption using HBO3 at neutral pH. Srivastav et al. (2013) observed that HBO1 has 0.196 mg F/g sorption potential at 20 mg F/L initial concentration. However, HBO2 could remove only 51% fluoride at 10 mg F/L of initial concentration with 100 g/L adsorbents Srivastav et al. (2015). To increase the anionic sorptive potential of HBO powders, Ranjan et al. (2015); (2019) prepared HBO2 adsorbent in the presence of varying concentrations of cations like Fe, Ca, Mg and Cu. This leads to increase the fluoride removal efficiency by 31% when HBO2 prepared in presence of 0.1M MgCl_2 with respect to unamended HBO2, whereas, HBO2 in presence of 0.07 M FeCl_3 found gainful to increase the nitrate sorption potential. Characterization of prepared materials has confirmed the presence of cationic ligands in the matrix of HBO2 material. Hence, the material exhibited high adsorption capacities towards nitrate (NO_3^-) and fluoride (F^-).

Based on the affinity exhibited by hydrous bismuth oxide towards major anionic contaminants (i.e., nitrate and fluoride) the possibility of arsenic removal from aqueous solution was tested and discussed in the present study. Adsorption behaviour of arsenic (V) and arsenic (III) by hydrous bismuth oxide (HBO1) was compared by keeping them under the same condition (Fig. 2).

Of both, arsenic (III) and arsenic (V) removals were examined by HBO1 under similar condition. But, removal efficiency for arsenic (V) was found to be 16.5% greater than arsenic (III). Lower adsorption of arsenic (III) can be better correlated to the uncharged (Fig. 2) form of arsenic species in environment relevant pH (Zhu et al. 2016). Hence, arsenic (V) removal using HBO1 was chosen for further experiments during the present study.

MATERIALS AND METHODS

Arsenic Solutions

4.1601 g of sodium arsenate ($\text{Na}_2\text{HAsO}_4 \cdot 7\text{H}_2\text{O}$, E. Mark,

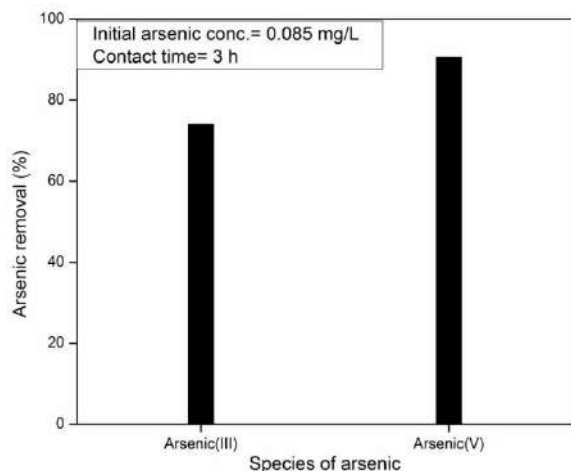


Fig. 2: Percentage removal of arsenic.

Germany) was dissolved in one litre of double distilled water in order to make 100 mg/L stock solution of arsenic (V). Further dilution methods were used for making the working solutions of arsenic.

Preparation of Hydrous Bismuth Oxide (HBO)

Hydrous Bismuth Oxide (HBO) was prepared by using bismuth trioxide powder of commercial AR grade. 0.1 M Bi_2O_3 was prepared by dissolving bismuth trioxide in 2N HCl solutions and precipitated hydrous bismuth oxide was obtained as per the method reported by Singh et al. (2012). Three forms of HBOs designated as HBO1, HBO2 and HBO3 were prepared using 0.1 M Bi_2O_3 solution in 2N HCl with successively increasing volumetric proportions of 2N NaOH in the ratio of 1:1, 1:2 and 1:3 respectively. The obtained precipitates were washed with distilled water till pH and chloride reduce to a minimum level. It is then kept in the oven drying at $103 \pm 2^\circ\text{C}$ for 24 h (Srivastav et al. 2015). HBO1 was visibly white in colour but yellow precipitate has been shown by HBO2 and HBO3. All three forms of Hydrous Bismuth Oxide (HBOs) was found better in the arsenate removal from water hence, HBO1 was selected for further study due to less cost of synthesis.

Measurement of Arsenic Concentration

Arsenator (Model No: Wag-WE10500 made by Wag-Tech, England) was used for determination of arsenic concentration in aqueous solutions.

The performance of adsorbent for arsenic removal was calculated by using equation (1):

$$\text{Arsenic removal (\%)} = \frac{(C_0 - C_e)}{C_0} \times 100 \quad (1)$$

Where, C_0 and C_e are the initial and final concentrations of arsenic in mg/L.

Experiments with triplicate samples were carried out in at a controlled temperature of $25 \pm 2^\circ\text{C}$ and an average value is reported. Digital pH meter was used for the determination of pH. Sulphate, chloride and alkalinity (bicarbonate) were determined by titration method as given in Standard Method (Clesceri et al. 2005). Bismuth ion in treated water was determined by Atomic Absorption Spectrophotometer (Model AAS4141, ECIL, India).

Batch Experiment

A standard solution of 0.10 mg/L of arsenic (V) concentration was prepared from stock solution. Powder dosage of 6 g/L was taken with continuous stirring for 180 minutes. Finally, the powder was removed by using Whatman 42 filter paper and determination of pH, remaining arsenic, and chloride concentrations were carried out for filtrate. For kinetic studies, 100 mL of 0.05, 0.10, 0.15, 0.20 and 0.25 mg/L arsenic solution was taken for varying contact time from 60 to 360 minutes with 6 g/L adsorbent dosage at 298K. After 60 minutes of time interval, the filtrate was collected through Whatman 42 and pH, remaining arsenic and chloride was determined. Equilibrium studies were carried out on varying initial arsenate concentration from 0.05 to 0.25 mg/L. 100 mL of 0.05, 0.10, 0.15, 0.20 and 0.25 mg/L arsenic solution, with an initial neutral pH condition at temperatures of 298, 308 and 318 K were mixed with an adsorbent dose of 6 g/L with contact period of 180 minutes in agitating condition.

Column Experiment

The particle size of HBO1 powder is very fine and to use in column adsorption study, HBO1 powder and sand was mixed in the ratio of 1:4 (w/w). The sand was initially soaked in 0.1 N HCl for 24 h and then washed with sufficient distilled water. A glass column was filled up to the height of around 12 cm with the mixed media ($d_{10} = 0.18$, $C_u = D_{60}/D_{10} = 2.4$, $\text{pH} \sim 7.0$). A simulated solution of 0.085 mg/L arsenic (V) was taken for column study which resembles with the level of arsenate present in groundwater of our country. The arsenic contaminated water was passed with a flow rate of 1.23 mL/min, (EBC = 30.65 minutes). The samples of effluents were collected at a scheduled time interval and used for the determination of pH, chloride and arsenic concentration.

Characterization

To diagnose chemical species and structural arrangement of adsorbent (HBO1), the characterization was carried out using X-ray diffraction (XRD), Scanning electron microscopy (SEM) and energy-dispersive X-ray spectroscopy (EDS). The information about possible structural compound formed could be obtained from the X-ray diffraction pattern by X-ray

diffraction (Philips, Netherlands, 1710). Surface morphology and elemental analysis have been done by SEM and EDS (ZEISS EVO 18 Model-2045, Industrial Measurements and Medical Devices, Germany).

RESULTS AND DISCUSSION

Batch Experiment for Arsenic (V) Removal

The results of As (V) removal using hydrous bismuth oxide (HBO1) from aqueous solutions with 0.10 mg/L initial arsenic (V) concentration are given in Table 1.

Excellent removal efficiency (> 90%) of arsenic was observed using HBO1 powder is a significant finding of the present observations with 0.10 mg/L initial concentration in groundwater. The obtained pH water quality after treated water was in the range 8.3-8.5 indicating hydroxide ions were not eluted during As(V) adsorption. Hence hydroxide ions are not competing for anions for arsenic sorption on

HBO1. Chloride could be caustic agent for As(V) removal. Chloride seems to attach with the bismuth as loose bond and could be able to go for transitional exchange with As(V) under suitable condition, whereas hydroxide strongly bonded with bismuth and couldn't avail changes. Similar results were demonstrated by Ruixia et al. (2002) and Singh et al. (2012) with highlighting an elevated level of chloride in the effluent. Park et al. (2008) concluded the fluoride and nitrate sorption by cement paste column as the result of ion exchange mechanism.

Effect of Adsorbent Dosage

The effects of adsorbent dosage on As(V) removal and final pH were also studied and it ranges from 1 to 10 g/L with 180 minutes of contact time and 0.10 mg/L of initial As(V) concentration.

From Fig. 3a, it is observed that 6 g/L dosage was optimum for As(V) removal using HBO1 adsorbent.

Table 1: arsenic (V) sorption at different adsorbent dosage.

S No.	Dosage of HBO1 (g/L)	Water quality before treatment		Water quality after Treatment			Removal efficiency (%)	Chloride Exchange Ratio = Chloride eluted/ Arsenic sorbed
		pH	Cl ⁻ (mg/L)	pH	As(V) (mg/L)	Cl ⁻ (mg/L)		
1.	1	7.3	6.6	8.38	0.034	27	66	0.56
2.	2	7.2	6.6	8.40	0.023	22	77	0.56
3.	3	7.3	6.6	8.43	0.019	30	81	0.61
4.	4	7.4	6.6	8.40	0.012	31	88	0.59
5.	5	7.3	6.6	8.46	0.007	33	93	0.60
6.	6	7.4	6.6	8.52	0.006	37	94	0.62
7.	7	7.5	6.6	8.34	0.006	32	94	0.64
8.	8	7.3	6.6	8.46	0.006	31	94	0.62
9.	9	7.6	6.6	8.44	0.006	33	94	0.64
10.	10	7.5	6.6	8.47	0.006	28	94	0.62

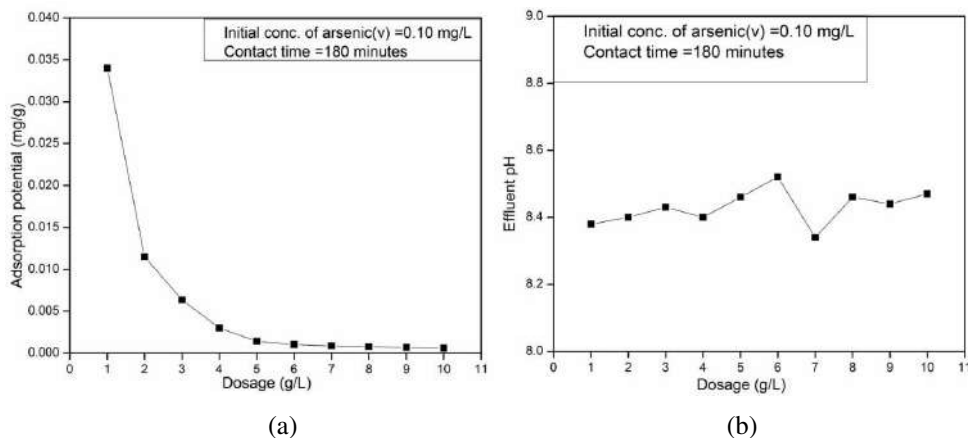


Fig. 3(a): Variation of adsorbent dosage on As(V) sorption. 3(b): Variation of adsorbent dosage on effluent pH.

Abundant numbers of adsorption sites are available at low dosages, but at higher dosages overlapping of active sites may reduce the effective surface area of adsorbent (Luther et al. 2012). Hence, further experiments were done by considering 6 g/L as optimum dosage for As(V) sorption.

Fig. 3b shows the treated water pH on As(V) removal with different dosages of HBO1 powder. It is observed that the solution pH did not get affected significantly due to As(V) removal by HBO1 in aqueous solution. Similar observations have been reported by Srivastav et al. (2014) and Singh et al. (2015) in his study for nitrate sorption by HBO2 adsorbent.

Effect of Contact Time

The variation of contact time on the adsorption of As(V) from the water was studied by taking five initial concentrations (0.05, 0.10, 0.15, 0.20 and 0.25 mg/L) of As(V) by hydrous bismuth oxide (HBO1). The contact time ranged from 60 to 360 minutes (Fig. 4a) and a time interval of 60 minutes was selected for samples collection.

Initially, 70-80 % of removal was reported in the initial contact time of 180 minutes and further, the rate of removal became slow or insignificant. During the initial stage, large numbers of active sites are available for adsorption but as the reaction progresses, the active sites are no longer available to occupy because of saturation (Swain et al. 2012). Hence, 180 minutes considered to be the optimum contact time for arsenic removal from aqueous solution for further studies. It was confirmed by Singh et al. (2015) with experimental data showing the maximum adsorption took place in the first 180 minutes of contact time.

Chloride Exchange Ratio (CER)

The effluents were found to have elevated levels of chloride with respect to the influent. Hence, HBO1 may contain some

amount of chloride sorbed in its material matrix, which could be exchanged with arsenic during sorption process. During equilibria study, apart from As(V) concentration, chloride level of treated water was also determined. Chloride Exchange Ratio (CER) may be defined as:

$$\text{CER} = \text{Chloride eluted (meq/g)} / \text{arsenic (V) taken up (meq/g)}$$

An analysis of total As(V) sorbed and chloride eluted in the water at a different dose of hydrous bismuth oxide (HBO1) was carried out. It is observed that CER of hydrous bismuth oxide (HBO1) is found in the range of 0.59 - 0.64. It indicates that possibly partial As(V) removal is through ion exchange mechanism with embedded chloride in HBO1 matrix. The nitrate removal experiment using yellow bismuth hydroxide and yellow hydrous bismuth oxide had been carried out by Fritsche (1993) and Singh et al. (2012) respectively. The authors emphasized the ion exchange mechanism responsible for nitrate sorption. No leaching of bismuth ion and increased concentration of chloride in treated water may be indicative of partial exchange of chloride with sorbed As(V) ions.

Effect of Competitive Anions

The presence of competitive ions bicarbonate (as alkalinity) and sulphate may hinder the adsorption of As(V) and because of this reason their effect has been also studied in the range from 1 to 5 meq/L (Fig. 4b) with 0.10mg/L initial As(V) concentration level.

It can be noted that As(V) removal efficiency of HBO1 decreased in order as given below:



The lower hydration energy of bicarbonate ion could be the reason for fast competing anions among bicarbonate ($\Delta G^\circ = 380$ KJ/mol) and sulphate ($\Delta G^\circ = -1,103$ KJ/mol).

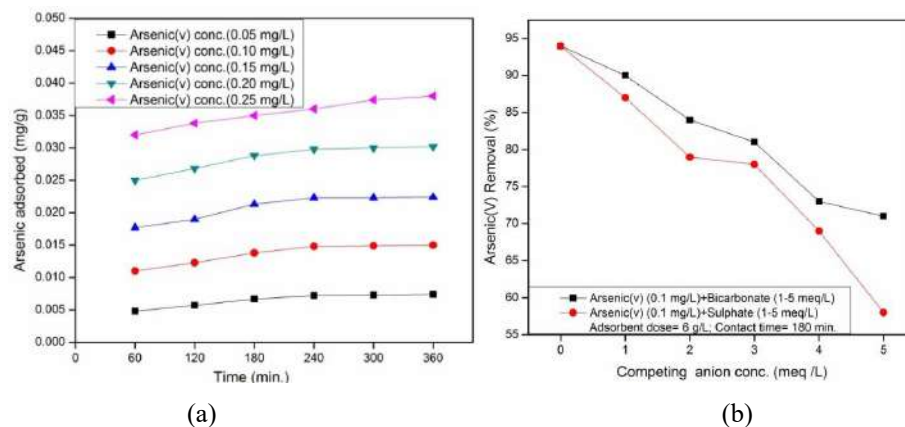


Fig. 4 (a): Effect of contact time on As(V) sorption. 4(b): Effect of competing anion on As(V) sorption.

Hydration energy with low value has more affinity towards adsorption in comparison to the ions which has high hydration energy (Gu et al. 2004, Song et al. 2012).

Column Experiments for As(V) Removal

The column study has also been done for enhancing the field applicability of HBO1 adsorbent in water treatment. A glass column (2cm diameter) was filled upto 12 cm depth with HBO1 powder mixed homogeneously with inert sand particles (1:4 ratio). As(V) solution was passed through the column with an influent concentration of 0.085 mg/L and 1.23 mL/min flow rate, which gave empty bed contact time (EBCT) as 30.65 minutes. Effluent samples were analysed for remaining As(V) concentration. The pH and breakthrough curve is shown in Fig. 5.

It is observed that the breakthrough of the column occurs around 500 minutes of duration after passing 615 mL of contaminated water, which gave a complete As(V) removal by consuming 13.1 µg/g of HBO1 adsorbent. The exhaustion point was found after 750 minutes after passing about 922 mL of contaminated water by consuming 19.6 µg/g adsorbent. Hence, fixed bed column study using HBO1 as adsorbent produces 615 mL of drinking water (As(V) ≤ 0.01mg/L) free from As(V) (0.085 mg/L) at inflow rate of 1.23 mL/min and pH 7.0 (±0.1), which indicates the applicability of HBO1 for arsenic removal from the aqueous solution. In a similar study, Fritsche (1993) conducted experiments using yellow bismuth hydroxide in column study for nitrate and other anions removal experiment and found 93 % of nitrate removal with 58.6 mg/L as influent nitrate concentration. Whereas in another study Singh et al. (2012) revealed the nitrate sorption through hydrous bismuth oxide (HBO2 and HBO3) in column study and reported the 5.31 mg/g and 6.2 mg/g of nitrate sorption capacity of adsorbent with 62 mg/L of nitrate as influent

using 5 g of wet precipitate of yellow hydrous bismuth oxide each.

Characterization

XRD analysis: Fig. 6 shows the XRD pattern of HBO1 which exhibits many peaks at 2 theta values of 24°, 26.2°, 29.57°, 30.24°, 32.72°, 47.1° and 57.2°. Crystalline nature of adsorbent was confirmed by the presence of sharp peaks (Ramli et al. 2007). Peaks corresponding to $2\theta = 29.57, 30.24$ and 32.72 are related with $\text{Bi}_{12}\text{O}_{17}\text{Cl}_2$ (File no-370702) as per the X-pert high score software (2009) which confirms the crystalline nature of HBO1. The observed composition of hydrous bismuth oxide ($\text{Bi}_{12}\text{O}_{17}\text{Cl}_2$) indicates the presence of chloride inside it and similar results were also observed by Srivastav et al. (2013).

SEM and EDS: The SEM image of HBO1 before and after As(V) adsorption was taken to know its surface characteristics with magnification: 50 K and 200 nm resolution (Fig. 7). The smooth surface and spherical nature of grains were found before adsorption but relatively high rough surface and angular grain were spotted after adsorption. The elemental analysis of the raw and exhausted adsorbent was also studied. The point of incidence of the spectrum and the resultant EDS spectrum for each test is attached and the elements found are shown in Fig. 7. Bismuth and chloride are the compositions of HBO1 before adsorption and but, after adsorption As(V) become an integral part of HBO1. This is probably due to the active chloride ion present in the matrix of adsorbent and with suitable condition its gets partially exchange with chloride and partially adsorbed in the rough surface of the adsorbent. Thus, appearance of As(V) in the exhausted adsorbent indicates that sorption of As(V) has possibly taken place on HBO1.

Kinetic studies: Kinetics studies have been conducted to evaluate the performance of a given adsorbent and mechanism

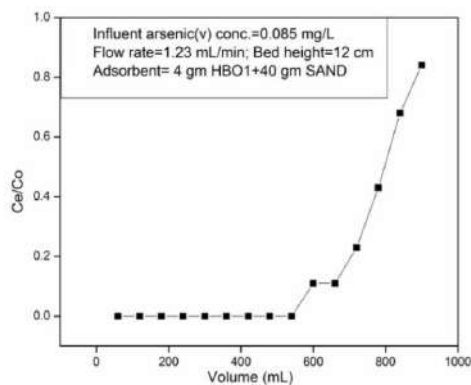


Fig. 5: As(V) sorption through column experiment.

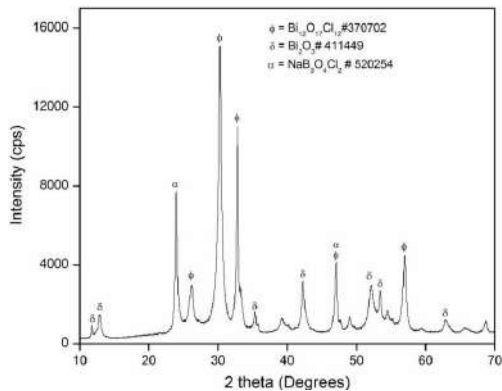


Fig. 6: XRD pattern of HBO1 powder.

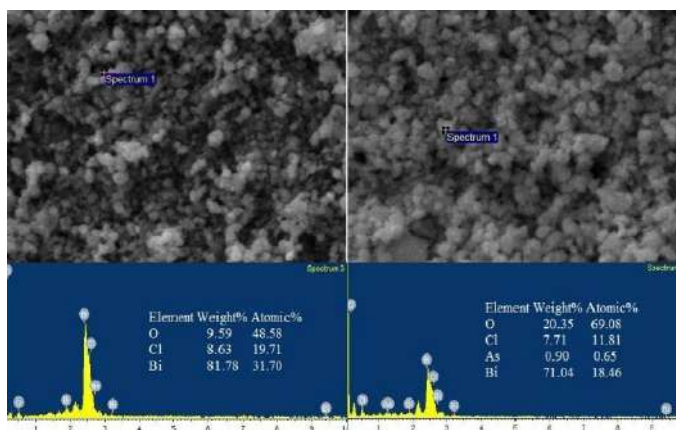


Fig. 7: SEM and EDS of HBO1 before and after adsorption.

of removal. In order to understand the sorption mechanism, three kinetic models have been applied with experimental results. Effect of five initial As(V) concentration (50, 100, 150, 200, 250 $\mu\text{g/L}$) and variation in contact time (60 minutes to 360 minutes) was observed. It was noticed that most of the arsenic removal took place within 180 min. and adsorption capacity increased from 4.8 to 36 $\mu\text{g/g}$. Pseudo-first-order, Pseudo-second-order and Weber-Morris kinetic models were applied to validate experimental data and derived kinetics parameters are given in Table 2.

Pseudo-first order: Lagergren (1898) presented a first-order rate equation to describe the kinetic process of liquid solid phase adsorption as mentioned in eq (2):

$$\log(q_e - qt) = \log q_e - \frac{K_1}{2.303t} \quad (2)$$

Where, q_e and q_t are adsorption capacity ($\mu\text{g/g}$) at equilibrium and at any time t ; K_1 = pseudo-first-order rate constant (time^{-1}). The linear interpolation of slope from the plots between $\log(q_e - q_t)$ versus t will give the adsorption rate constant (K_1). Fig. 8a presents the pseudo-first-order kinetic plot of As(V) sorption on HBO1 in aqueous solution. The plot of ' $\log(q_e - q_t)$ ' versus ' t ' was almost linear as it gave with rate constant ($K_1 \times 10^{-3}$) of 2.303, 4.606, 4.606, 4.606 and

2.303 min^{-1} . The value of K_1 showed the decreasing trend along with increasing initial As(V) concentration from 0.10 to 0.25 mg/L . A similar conclusion was drawn by Pirila et al. (2011) using hydrous titanium dioxide as adsorbent for arsenic removal. The rate constant during observations were found as 3.26×10^{-3} , 4.02×10^{-3} and 3.96×10^{-3} for arsenic sorption at 298K.

Pseudo-second order: The pseudo-second order adsorption kinetic model is given by Ho and McKay (1999) as given in eq. (3).

$$\frac{t}{qt} = \frac{1}{K_2 q_e^2} + \frac{t}{q_e} \quad (3)$$

Where, q_e and q_t are adsorption capacity ($\mu\text{g/g}$) at equilibrium and at any time t ; K_2 = pseudo-second-order rate constant ($\text{g}/\mu\text{g}/\text{min}$). The linear interpolation of the graph between t/q_t versus t will give the values of q_e (1/slope) and adsorption rate constant K_2 (slope²/intercept). From Fig. 8b, the linear plot was observed which indicates the validity of pseudo-second-order kinetic model for all five initial As(V) concentrations. The values of pseudo-second-order rate constant ($K_2 \times 10^{-3}$) were calculated as 1.813, 1.892, 1.647, 1.841 and 2.527 within the specified concentration range. The reaction rate was faster for 250 $\mu\text{g/L}$ initial As(V) concentration, whereas

Table 2: The kinetic model parameters for the sorption of As(V) on HBO1.

Initial As(V) conc. ($\mu\text{g/L}$)	Pseudo-first order			Pseudo-second order			Weber-Morris model	
	$K_1 \times 10^{-3}$ (min^{-1})	q_e ($\mu\text{g/g}$)	R^2	$K_2 \times 10^{-3}$ ($\text{g}/\mu\text{g}/\text{min}$)	q_e ($\mu\text{g/g}$)	R^2	k_i ($\mu\text{g}/\text{g}/\text{min}^{0.5}$)	R^2
50	2.303	2.647	0.678	1.813	8.621	0.993	0.281	0.919
100	4.606	3.908	0.825	1.892	16.394	0.997	0.359	0.928
150	4.606	4.886	0.712	1.647	24.393	0.988	0.458	0.894
200	4.606	4.753	0.714	1.841	32.251	0.999	0.459	0.897
250	2.303	3.404	0.708	2.524	38.462	0.999	0.346	0.914

a slower reaction rate was observed at intermediate initial As(V) concentration (50, 100, 150, 200 $\mu\text{g/L}$). The lower values of K_2 indicate fast adsorption process (Ayoob et al. 2008). The correlation coefficients of pseudo-second-order kinetics were having a high degree of correlation than the pseudo-first-order. Hence, the kinetic study indicates pseudo-second-order reaction in the sorption process of As(V) by HBO1.

Weber-Morris model: The linear form of the intraparticle diffusion model given by Weber–Morris (Weber Jr et al. 1963) is as follows in eq. (4):

$$q = k_i\sqrt{t} \quad \dots(4)$$

Where, q = Arsenic adsorbed ($\mu\text{g/g}$); k_i = Rate constant; t = contact time (min). The values of intraparticle diffusion rate constants k_i could be determined from the slopes of the plots between \sqrt{t} ($\sqrt{\text{min}}$) and q ($\mu\text{g/g}$). From Fig. 8c, the plots show poor linearity ($R^2 = 0.894, 0.897$) at 150 and 200 $\mu\text{g/L}$ arsenic concentrations and high linearity ($R^2 = 0.919, 0.928$ and 0.914) at 50, 100 and 250 $\mu\text{g/L}$ arsenic concentrations. The intraparticle diffusion rate constants k_i were found to be 0.281, 0.359, 0.458, 0.459 and 0.346 $\text{mg/g}/\text{min}^{0.5}$ for initial arsenic concentration of 50, 100, 150, 200 and 250 $\mu\text{g/L}$ respectively. A linear representation of data elucidates the diffusion of the solute particle with the available pore site of adsorbent (Sujana & Mohanty 2010). Further non zero

intercepts represent the slow and complex diffusion process, which is not governed by a single mechanism (Gupta & Bhattacharyya 2011).

Adsorption isotherm models: Adsorption isotherm models have been incorporated to calculate the maximum adsorption capacity of the adsorbent. At the equilibrium stage, there is an apparent distribution of a solute between the solid and liquid phases (Manna & Ghosh 2007). Langmuir and Freundlich models are the most frequently used quantitative equations to describe present experimental adsorption data. Langmuir isotherm is based on the principle that each site on the surface of adsorbent is equally capable for adsorbing one molecule of adsorbate in a single monolayer thickness, whereas Freundlich isotherm could be applicable for heterogeneous surfaces of adsorbent with multilayer sorption (Milmile et al. 2011).

Langmuir isotherm: The Langmuir isotherms were chosen to determine the maximum adsorption capacity corresponding to the complete monolayer coverage on the hydrous bismuth oxide (HBO1). As given in eq. (5):

$$\frac{1}{q_e} = \frac{1}{q_0 b C_e} + \frac{1}{q_0} \quad \dots(5)$$

Where, C_e is the solute concentration at equilibrium ($\mu\text{g/L}$); q_e is the equilibrium arsenic uptake ($\mu\text{g/g}$); q_0 and bare Langmuir constants related to maximum monolayer capacity ($\mu\text{g/g}$) and energy of adsorption ($\text{L}/\mu\text{g}$). Value of q_0

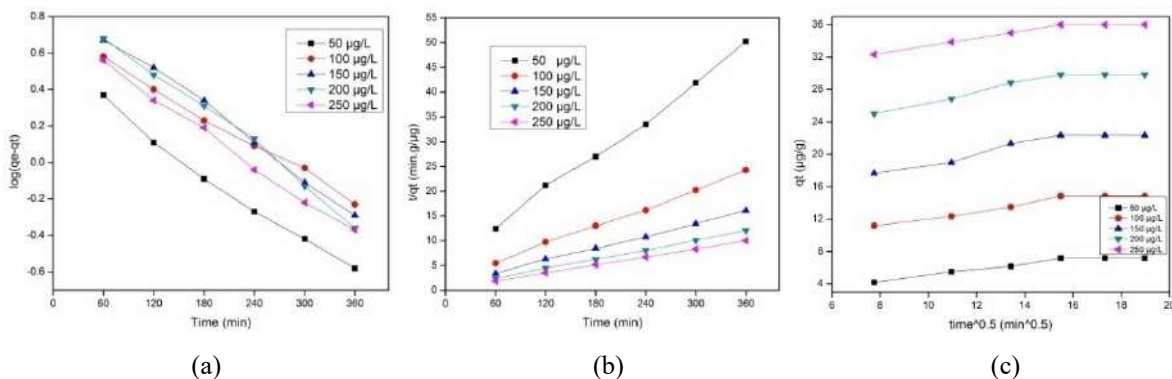


Fig. 8: Kinetic plot of As(V) on HBO1 (a) Pseudo-first order (b) Pseudo-second order (c) Weber–Morris kinetic.

Table 3: Isotherm parameters with thermodynamics for the sorption of Arsenic(v) on HBO1.

Temperature (K)	Langmuir parameters			Freundlich parameters			Dubinin–Radushkevich parameters			Thermodynamic parameters		
	q_0 ($\mu\text{g/g}$)	b ($\text{L}/\mu\text{g}$)	R^2	K_f	n	R^2	q_a ($\mu\text{g/g}$)	E (kJ/mole)	R^2	G° (kJ/mol)	H° (kJ/mol)	S° (J/mol)
298	83.33	0.011	0.96	1.14	0.97	0.94	4.073	5.42	0.96	-0.61	18.84	64.97
308	100	0.012	0.95	1.17	0.98	0.95	4.072	8.63	0.97	-0.95	-	-
318	125	0.019	0.97	1.24	0.99	0.96	4.067	6.20	0.96	-1.92	-	-

and b are calculated from the slope and intercept $1/C_e$ and $1/q_e$ (Fig. 9a) and is given in Table 3. q_0 was found to be 83.33, 100 and 125 $\mu\text{g/g}$ at 298K, 308K and 318K respectively. The Langmuir isotherm plot at different temperatures gives higher values of correlation coefficients (R^2). The highest value of ' q_0 ' was obtained as 125 $\mu\text{g/g}$ at the temperature of 318K (Table 4). A high value of q_0 at elevated temperature indicates the enhancement in arsenic sorption potential of HBO1 (Singh et al. 2015).

Freundlich isotherm: The expression of Freundlich equation is given below (eq. 6):

$$\log q_e = \log K_f + \frac{1}{n} \log C_e \quad \dots(6)$$

Where, q_e = Equilibrium arsenic uptake ($\mu\text{g/g}$); C_e = Solute concentration at equilibrium ($\mu\text{g/L}$); K_f and n are the Freundlich constants corresponding to adsorption capacity and adsorption intensity, respectively. The value of " n " could be correlated with the favourable and unfavourable condition of adsorption. Hence " n " represents the bonding between adsorbate and adsorbent. Beneficial or favourable adsorption could be read if the value of n (>0) lies in between 1 and 10 (Ho & McKay 2011).

Fig. 9b shows the linearized plot of Freundlich isotherm for As (V) adsorption on HBO1. Regression coefficients (R^2) was found higher (>0.95) at all temperature. Based on the value of " n " adsorption seems to be 'beneficial' at elevated temperature of 318 K. Freundlich parameter, K_f is found as 1.14, 1.16 and 1.24 at 298K, 308K and 318K (Table 3). Increased value of K_f at higher temperature indicates the favourable condition of adsorption (Sharma et al. 2009). The adsorption patterns of HBO1 can be described well by the Langmuir isotherm as it has high correlation coefficient values than Freundlich with a maximum adsorption capacity of 125 $\mu\text{g/g}$ at a temperature of 318K. The suitability of

Langmuir isotherm leads to the conclusion that the homogeneous nature of sorption site dominated over the surface of adsorbent and single layer arsenic sorption took place over the surface of HBO1.

Dubinin-Radushkevich (D-R) isotherm: Dubinin-Radushkevich isotherm has also been included in the present study to make a clear understanding between adsorption and ion exchange. The equation of D-R isotherm is given below in eq. (7):

$$\ln q_e = \ln q_a - K^\circ \varepsilon^2 \quad \dots(7)$$

Where q_e =Arsenic adsorbed at equilibrium ($\mu\text{g/g}$), q_a = Theoretical adsorption capacity, K° = Adsorption energy constant.

E = Polanyi potential is given as follows in eq. (8) (Islam et al. 2010):

$$\varepsilon = RT \ln \left(1 + \frac{1}{C_e} \right) \quad \dots(8)$$

Where, R is the universal gas constant (kJ/mol K); T is the temperature(K). The high values of R^2 at 298K, 308K and 318K temperatures show a good correlation of data with D-R isotherm. The values of $K^\circ(\text{mol}^2/\text{J}^2)$ were calculated from Fig.8c and found as 0.017, 0.0067 and 0.013 $\text{mol}^2\text{kJ}^{-2}$ respectively at 298K, 308K and 318K.

The adsorption energy (E) was calculated using the following relation given in eq (9) (Sharma et al. 2009):

$$E = 1/\sqrt{(2K^\circ)} \quad \dots(9)$$

Process of adsorption can be easily classified into chemical, physical and ion exchange based on the adsorption energy (E). Physical adsorption will prevail if adsorption energy is below 8 kJ/mol , if it is between 8-16 kJ/mol ion exchange will take place, while if it is over 16 kJ/mol then

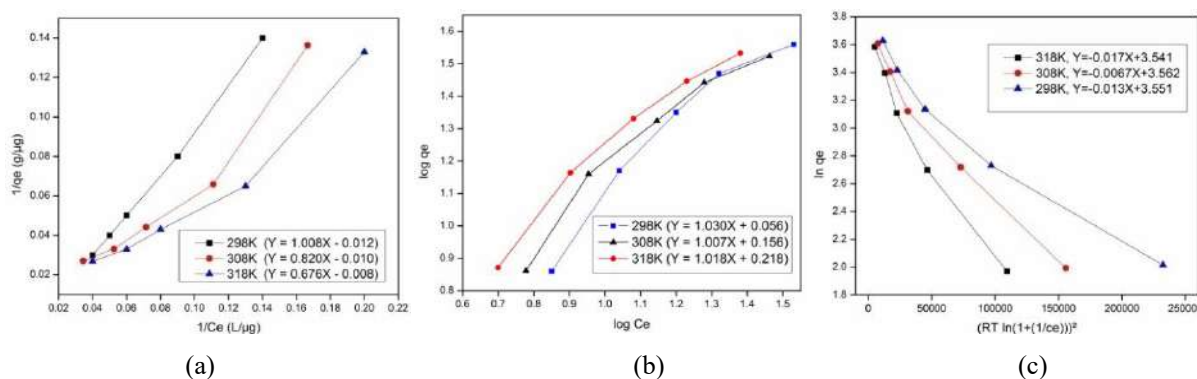


Fig. 9: Isotherm plot of As(V) sorption by HBO1 (a) Langmuir isotherm (b) Freundlich isotherm (c) DR isotherm.

Table 4: Arsenic(v) removal from water using hydrous metal oxides (HMOs)

Adsorbent	Optimum Temperature (°C)	Removal efficiency/potential (mg/g)	Optimum pH	Contact Time (h)	References
Granular titanium dioxide	25	41.4	7.3	2	Bang et al.(2005)
Manganese dioxide	-	53	4.3–3.9	2	Lenoble et al.(2004)
Hydrous stannic oxide	27	4.3	6.5–8.5	4	Manna and Ghosh (2007)
Hydrous ferric oxide	40	<100%	2-12	4	Jang and Dempsey (2008)
Cupric oxide	21-25	22.6	6-10	0.5	Martinson and Reddy (2009)
Magnetite (Fe ₃ O ₄)	20-30	0.485	8	1	Shipley et al.(2010)
Hydrous titanium dioxide	20-23	22.0–33.4	4-6	4	Pirila et al. (2011)
Hydrous zirconium oxide	25	3.6	7	4	Hang et al. (2011)
Iron oxide nano materials	25	671.1	6-9	1	Luther et al.(2012)
Hydrous cerium oxide	25	107	7	24	Li et al. (2012)
Zirconium oxide-coated marine	35	0.270	7	1.25	Khan et al. (2013)
Manganese oxide	25	71.2%	6	24	Hou et al. (2017)
Hydrous bismuth oxide	25	0.013-0.019	6.6-8.4	3	Present study

mechanism will be known as chemical adsorption (Inglezakis & Zorpas 2012). The values of E using Eq. (10) were found as 5.42, 8.63 and 6.20 kJ/mol respectively at the studied temperatures. Hence, the adsorption of arsenic on HBO1 is governed by physical adsorption process (Kanjalil et al. 2017). Srivastav et al. (2013) research supported the findings of adsorption energy highlighting the probability of physical adsorption.

Among all adsorption isotherm models, Langmuir isotherm as well as Freundlich fits well at all selected temperatures for arsenic sorption by HBO1. Based on the calculation of mean adsorption energy (E) from D–R isotherm, the mechanism of arsenic removal by HBO1 fall under the category of the physical adsorption process.

Many adsorbents have been tested for As(V) sorption from aqueous solution and listed in Table 4. The adsorption capacity of hydrous cerium oxide is reported as 107 mg/g (Li et al. 2012). While cupric oxide demonstrated the adsorption capacity of 22.6 mg/g (Martinson & Reddy 2009), hydrous titanium dioxide showed the capacity of 22.0–33.4 mg/g (Pirila et al. 2011). Iron oxide nanomaterial and zirconium oxide-coated marine came with an adsorption capacity of 671.1 mg/g (Luther et al. 2012) and 0.270 mg/g (Khan et al. 2013). In the present study, increasing value of arsenic sorption potentials was demonstrated by hydrous bismuth oxide (HBO1) with increasing temperature of 298 to 318 K and maximum of 19.6 mg/g adsorption capacity noted down at temperature of 318 K.

Thermodynamics Studies

Thermodynamic parameters like Gibbs free energy (G°),

enthalpy (H°) and entropy (S°) were determined for arsenic adsorption on HBO1 from eqs. (6) and (7) (Banerjee et al. 2014).

$$\ln M = \frac{\Delta S^{\circ}}{R} - \Delta H^{\circ}/RT \quad \dots(6)$$

$$\Delta G = -RT \ln M \quad \dots(7)$$

Where, R = Gas constant (8.314 J/mol K), T = Absolute temperature (Kelvin), M = Standard thermodynamic equilibrium constant (L/g).

Values of 'M' is obtained by plotting $\ln(q_e/C_e)$ versus q_e and extrapolating to zero q_e as the methods reported by Khan & Singh (1987). The intersection with the vertical axis gives the value of 'M'. Further, the value of ΔH° and ΔS° were calculated from the slope and intercept from the graph between $\ln M$ and $1/T$ (Liu and Liu 2008) as summarized in Table 4.

Spontaneous nature of the As(V) sorption by HBO1 is confirmed as the negative value of ΔG° was found at all temperatures. The more spontaneous behaviour of adsorption at higher temperature could be observed with a high value of ΔG° with increasing temperatures (Raji & Anirudhan 1998). The positive value of ΔH° suggests the endothermic nature of the sorption process (Tangkawanit et al. 2005). A positive value of ΔH° with magnitude 13.96 kJ/mol was also reported by Singh et al. (2015) during nitrate adsorption on hydrous bismuth oxide. No remarkable change in entropy (ΔS°) has been observed due to sorption of arsenic by HBO1. Similar results have been documented by Liu & Liu (2008) with a low value of entropy in sorption thermodynamics and further Chaudhry et al. (2017) verified with a value of 0.0144 kJ/mol/K as entropy change in his arsenic removal experiment using zirconium oxide-coated sand.

CONCLUSION

The present study elucidates hydrous bismuth oxide (HBO1) has augmented removal efficiency towards As(V) among arsenic species from aqueous solution. As(V) removal efficiency of 94 % and As(V) sorption potential of 13.1-19.6 mg/g has been found in batch and fixed-bed column study respectively. Elution of chloride can be better correlated with ion exchange phenomenon but adsorption energy calculation indicates that the process is governed by physical adsorption. Hence a mixed mechanism of ion exchange and physical adsorption can be concluded in As(V) sorption by HBO1. XRD analyses reveal the relevant peaks corresponds to $\text{Bi}_{12}\text{O}_{17}\text{Cl}_{12}$ (ID: 370702) indicating the presence of chloride inside it. Thus, results attribute that adsorbent shows a high efficiency of arsenic sorption and can be used as an efficient scavenger of arsenic from aqueous solution.

The affinity of hydrous bismuth oxide towards arsenic in addition to nitrate and fluoride (reported in the literature) makes it a unique adsorbent. Hence, hydrous bismuth oxide could be a better alternative for the simultaneous removal of all three major water toxins such as nitrate, fluoride and arsenic from aqueous solution. This aspect needs to be explored in future studies with close monitoring.

ACKNOWLEDGEMENTS

All the necessary facilities for this work have been provided by the Indian Institute of Technology (Banaras Hindu University), India. The author avails the opportunity to express sincere thanks to anonymous reviewers for their valuable comments and suggestion.

REFERENCES

- Andelković, I., Amaizah, N.R.R., Marković, S.B., Stanković, D., Marković, M., Kuzmanović, D. and Roglič, G. 2017. Investigation of mechanism and critical parameters for removal of arsenic from water using Zr-TiO₂ Composite. *Env. Tech.*, 38: 2233-2240.
- Ayoob, S., Gupta, A.K. and Bhat, V.T. 2008. A conceptual overview on sustainable technologies for defluoridation of drinking water and removal mechanisms. *Critical Rev. Environ. Sci. Tech.*, 38(6): 401-470.
- Banerjee, S., Sharma, G.C., Chattopadhyaya, M.C. and Sharma, Y.C. 2014. Kinetic and equilibrium modeling for the adsorptive removal of methylene blue from aqueous solutions on of activated fly ash (AFSH). *J. Environ. Chem. Eng.*, 2: 1870-1880.
- Bang, S., Patel, M., Lippincott, L. and Meng, X. 2005. Removal of arsenic from groundwater by granular titanium dioxide adsorbent. *Chemosphere*, 60: 389-397.
- Basu, T. and Ghosh, U.C. 2011. Influence of groundwater occurring ions on the kinetics of As (III) adsorption reaction with synthetic nanostructured Fe(III)-Cr(III) mixed oxide. *Desalination*, 266: 25-32.
- Basu, T., Gupta, K. and Ghosh, U.C. 2012. Performances of As(V) adsorption of calcined (250°C) synthetic iron(III)- aluminum(III) mixed oxide in the presence of some groundwater occurring ions. *Chem. Eng. J.*, 183: 303-314.
- Bhatnagar, A. and Sillanpaa, M. 2011. A review of emerging adsorbents for nitrate removal from water. *Chem. Eng. J.*, 168: 493-504.
- Chaudhry, S.A., Khan, T.A. and Ali, I. 2017. Zirconium oxide-coated sand based batch and column adsorptive removal of arsenic from water: Isotherm, kinetic and thermodynamic studies. *Egypt. J. Petrol.*, 26: 553-563.
- Clesceri, L.S., Greenberg, A.E. and Eaton, A.D. 2005. *Standard Methods for the Examination of Water Wastewater*, American Public Health Association, 20th ed., Washington, DC.
- Deng, M., Wu, X., Zhu, A., Zhang, Q. and Liu, Q. 2019. Well-dispersed TiO₂ nanoparticles anchored on Fe₃O₄ magnetic nanosheets for efficient arsenic removal. *J. Environ. Manage.*, 237: 63-74.
- Doušova, B., Machovic, V., Koloušek, D., Kovanda, F. and Dornicak, V. 2003. Sorption of As (V) species from aqueous systems. *Water Air Soil Pollution*, 149: 251-267.
- Fritsche, U. 1993. Removal of nitrate and other anions from water by yellow bismuth hydroxide. *J. Environ. Sci. Health (A) Tox. Hazard. Subst. Environ. Eng.*, 28: 1903-1913.
- Gu, B., Ku, Y.K. and Jardine, P.M. 2004. Sorption and binary exchange of nitrate, sulfate, and uranium on an anion exchange resin. *Environ. Sci. Technol.*, 38(11): 3184-3188.
- Gupta, K. and Ghosh, U.C. 2009. Arsenic removal using hydrous nanostructure iron (III)-titanium(IV) binary mixed oxide from aqueous solution. *J. Hazard. Mater.*, 161: 884-892.
- Gupta, S.S. and Bhattacharyya, K.G. 2011. Kinetics of adsorption of metal ions on inorganic materials: A review. *Adv. Colloid Interface. Sci.*, 162: 39-58.
- Hang, C., Li, Q., Gao, S. and Shang, J.K. 2011. As(III) and As(V) Adsorption by hydrous zirconium oxide nanoparticles synthesized by a hydrothermal process followed with heat treatment. *Ind. Eng. Chem. Res.*, 51: 353-361.
- Ho, Y.S. and McKay, G. 1999. Pseudo-second order model for sorption processes. *Process Biochem.*, 34: 451-465.
- Hou, J., Luo, J., Song, S., Li, Y. and Li, Q. 2017. The remarkable effect of the coexisting arsenite and arsenate species ratios on arsenic removal by manganese oxide. *Chem. Eng. J.*, 315: 159-166.
- Iesan, C.M., Capat, C., Ruta, F. and Udrea, I. 2008. Evaluation of a novel hybrid Inorganic/organic polymer type material in the arsenic removal process from drinking water. *Water Res.*, 42: 4327-4333.
- Inchaurrondo, N., Di Luca, C., Mori, F., Pintar, A., Zerjav, G., Valiente, M. and Palet, C. 2019. Synthesis and adsorption behavior of mesoporous alumina and Fe-doped alumina for the removal of dominant arsenic species in contaminated waters. *J. Environ. Chem. Eng.*, 7(1): 102901.
- Inglezakis, V.J. and Zorpas, A.A. 2012. Heat of adsorption, adsorption energy and activation energy in adsorption and ion exchange system. *Desalin. Water Treat.*, 39: 149-157.
- Islam, M., Mishra, P.C. and Patel, R.K. 2010. Physicochemical characterization of hydroxy-apatite and its application towards removal of nitrate from water. *J. Environ. Manage.*, 91: 1883-1891.
- Jang, J.H. and Dempsey, B.A. 2008. Co-adsorption of arsenic (III) and arsenic (V) onto hydrous ferric oxide: effects on abiotic oxidation of arsenic (III), extraction efficiency and model accuracy. *Environ. Sci. Technol.*, 42: 2893-2898.
- Kanjilal, T., Bhattacharjee, C. and Datta, S. 2017. Assessing treatment of lead (Pb II) from industrial wastewater on dried bulbs of water hyacinth: adsorption capacity, isotherm and kinetic study. *Int. J. Environ. Tech. Mgt.*, 20: 101-127.
- Khan, A.A. and Singh, R.P. 1987. Adsorption thermodynamics of carbofuran on Sn (IV) arsenosilicate in H⁺, Na⁺ and Ca²⁺ Forms. *Colloids and Surf.*, 24: 33-42.
- Khan, B.I., Solo-Gabriele, H.M., Dubey, B.K., Townsend, T.G. and Cai, Y. 2004. Arsenic speciation of solvent-extracted leachate from new and weathered CCA-treated wood. *Environ. Sci. Technol.*, 38(17): 4527-4534.

- Khan, T.A., Chaudhry, S.A. and Ali, I. 2013. Thermodynamic and kinetic studies of As(V) removal from water by zirconium oxide-coated marine sand. *Environ. Sci. Pollut. Res.*, 20: 5425-5440.
- Kong, S., Wang, Y., Zhan, H., Yuan, S., Yu, M. and Liu, M. 2014. Adsorption/oxidation of arsenic in groundwater by nanoscale Fe-Mn binary oxides loaded on zeolite. *Water Environ. Res.*, 86(2): 47-155.
- Lagergren, S. 1898. About the theory of so-called adsorption of soluble substances. *K. Sven. Vetensk. Akad. Handl.*, 24: 1-39.
- Lenoble, V., Chabrouillet, C., Al Shukry, R., Serpaud, B., Deluchat, V. and Bollinger, J.C. 2004. Dynamic arsenic removal on a MnO₂-loaded resin. *J. Colloid Interface Sci.*, 280: 62-67.
- Li, R., Li, Q., Gao, S. and Shang, J.K. 2012. Exceptional arsenic adsorption performance of hydrous cerium oxide nanoparticles: Part A. Adsorption capacity and Mechanism. *Chem. Eng. J.*, 185: 127-135.
- Li, Y., Liu, Z., Li, Q., Zhao, Z., Liu, Z. and Zeng, L. 2011. Removal of arsenic from Waelz zinc oxide using a mixed NaOH-Na₂S leach. *Hydrometallurgy*, 108: 165-170.
- Li, Z., Deng, S., Yu, G., Huang, J. and Lim, V.C. 2010. As(V) and As(III) removal from water by a Ce-Ti oxide adsorbent: Behavior and mechanism. *Chem. Eng. J.*, 161: 106-113.
- Liu, Y. and Liu, Y.J. 2008. Biosorption isotherms, kinetics and thermodynamics. *Sep. Purif. Technol.*, 61: 229-242.
- Luther, S., Borgfeld, N., Kim, J. and Parsons, J.G. 2012. Removal of arsenic from aqueous solution: A study of the effects of pH and interfering ions using iron oxide nanomaterials. *Microchem. J.*, 101: 30-36.
- Manna, B. and Ghosh, U.C. 2007. Adsorption of arsenic from aqueous solution on synthetic hydrous stannic oxide. *J. Hazard Mater.*, 144: 522-531.
- Martinson, C.A. and Reddy, K.J. 2009. Adsorption of arsenic(III) and arsenic(V) by cupric oxide nanoparticles. *J. Colloid Interface Sci.*, 336: 406-411.
- Milmlie, S.N., Pande, J.V., Karmakar, S., Bansiwala, A., Chakrabarti, T. and Biniwale, R.B. 2011. Equilibrium isotherm and kinetic modeling of the adsorption of nitrates by anion exchange Indion NSSR resin. *Desalination*, 276: 38-44.
- Mudhoo, A., Sharma, S.K., Garg, V.K. and Tseng, C.H. 2011. Arsenic: an overview of applications, health, and environmental concerns and removal processes. *Crit. Rev. Environ. Sci. Technol.*, 41: 435-519.
- Nath, B., Sahu, S.J., Jana, J., Goswami, A.M., Roy, S., Sarkar, M.J. and Chatterjee, D. 2008. Hydrochemistry of arsenic-enriched aquifer from rural west bengal, india: a study of the arsenic exposure and mitigation option. *Water Air Soil Pollution*, 190: 95-113.
- Ngai, T.K.K. 2002. Arsenic speciation and evaluation of an adsorption media in Rupandehi and Nawalparasi Districts of Nepal. Dissertation, Massachusetts Institute of Technology, USA.
- Ngai, T.K.K., Murcott, S., Shrestha, R.R., Dangol, B. and Maharjan, M. 2006. Development and dissemination of Kanchan arsenic filter in rural Nepal. *Water Sci. Technol: Water Supply*, 6(3): 137-146.
- PAN alyticalX[®] Pert High Score Plus Software: V 3.0, 2009.
- Park, J.Y., Byun, H.J., Choi, W.H. and Kang, W.H. 2008. Cement paste column for simultaneous removal of fluoride, phosphate, and nitrate in acidic wastewater. *Chemosphere*, 70: 1429-1437.
- Park, Y.J., Yang, J., Choi, H.J. and Lee, S.M. 2012. Removal of arsenic from aqueous solution using hybrid metal oxide. *Environ. Eng. Res.*, S1: S15-S19.
- Pirila, M., Martikainen, M., Ainassaari, K., Kuokkanen, T. and Keiski, R.L. 2011. Removal of aqueous As(III) and As(V) by hydrous titanium dioxide. *J. Colloid Interface Sci.* 353: 257-262.
- Puente-Urbina, A. and Montero-Campos, V. 2017. Porous materials modified with Fe₃O₄ nanoparticles for arsenic removal in drinking water. *Water Air Soil Pollution*, 228: 374.
- Raji, C. and Anirudhan, T.S. 1998. Batch Cr(VI) removal by polyacrylamide-grafted sawdust: Kinetics and thermodynamics. *Water Res.*, 32(12): 3772-3780.
- Ramli, I., Tze, C.M. and Hin, T.Y. 2007. Effect of sodium hydroxide concentration on the physic chemical characteristic of α -Bi₂O₃ nanocrystals. *J. Solid State Sci. Technol.*, 15: 30-42.
- Ranjan, M., Singh, P.K. and Srivastav, A.L. 2019. A review of bismuth-based sorptive materials for the removal of major contaminants from drinking water. *Environ. Sci. Pollut. Res. Int.*, <https://doi.org/10.1007/s11356-019-05359-9>.
- Ranjan, M., Singh, P.K., Srivastav, A.L. and Kumar, V. 2019. Adsorptive properties of cation added hydrous bismuth oxide on nitrate sorption. *J. Water Chem. Tech.*, 41(5): 283-291.
- Ranjan, M., Srivastav, A.L. and Shaktibala 2015. Effects of addition of cationic ligands in hydrous bismuth oxide on removal of fluoride from aqueous solutions. *Curr. Sci.*, 108: 1673-1682.
- Ren, Z., Zhang, G. and Paul, C.J. 2011. Adsorptive removal of arsenic from water by an iron-zirconium binary oxide adsorbent. *J. Coll. Int. Sci.*, 358: 230-237.
- Ruixia, L., Jinlong, G. and Hongxiao, T. 2002. Adsorption of fluoride, phosphate, and arsenate ions on a new type of ion exchange fiber. *J. Coll. Int. Sci.*, 248: 268-274.
- Sarkar, A. and Paul, B. 2016. The global menace of arsenic and its conventional remediation - A critical review. *Chemosphere*, 158: 37-49.
- Sharma, Y.C., Uma and Upadhyay, S.N. 2009. Removal of a cationic dye from wastewater by adsorption on activated carbon developed from coconut coir. *Energy Fuels*, 23: 2983-2988.
- Shipley, H.J., Yean, S., Kan, A.T. and Tomson, M.B. 2010. A sorption kinetics model for arsenic adsorption to magnetite nanoparticles. *Env. Sci. & Poll. Res.*, 17: 1053-1062.
- Singh, P.K. 1999. Nitrate removal from water by bismuth based media. PhD Dissertation, Indian Institute of Technology, Kanpur.
- Singh, P.K., Banerjee, S., Srivastava, A.L. and Sharma, Y.C. 2015. Kinetic and equilibrium modeling for removal of nitrate from aqueous solutions and drinking water by a potential adsorbent, hydrous bismuth oxide. *RSC Adv.*, 5: 35365-35376.
- Singh, P.K., Srivastav, A.L., Ghosh, D.K. and Chandra, Y.C. 2012. Preparation and properties of hydrous bismuth oxides for nitrate removal from aqueous solutions. *Desalin. Water Treat.*, 40: 144-152.
- Sinha, S., Amy, G., Yoon, Y. and Her, N. 2011. Arsenic removal from water using various adsorbents: magnetic ion exchange resins, hydrous ion oxide particles, granular ferric hydroxide, activated alumina, sulfur modified iron, and iron oxide-coated microsand. *Environ. Eng. Res.*, 16(3): 165-173.
- Song, H.O., Zhou, Y., Li, A.M. and Mueller, S. 2012. Selective removal of nitrate by using a novel macroporous acrylic anion exchange resin. *Chin. Chem. Lett.*, 23: 603-606.
- Srivastav, A. L. and Ranjan, M. (ed.) 2020. Inorganic water pollutants. Inorganic pollutants in water. Elsevier Publications. pp. 1-10.
- Srivastav, A.L., Singh, P.K. and Sharma, Y.C. 2015. Synthesis of a novel adsorbent, hydrous bismuth oxide (HBO2) for the removal of fluoride from aqueous solutions. *Desalin. Water Treat.*, 55: 604-614.
- Srivastav, A.L., Singh, P.K., Srivastava, V. and Sharma, Y.C. 2013. Application of a new adsorbent for fluoride removal from aqueous solutions. *J. Hazard Mat.*, 263: 342-352.
- Srivastav, A.L., Singh, P.K., Weng, C.H. and Sharma, Y.C. 2014. Novel adsorbent hydrous bismuth oxide for the removal of nitrate from aqueous solutions. *J. Hazard Toxic Radioact. Waste*, 04014028:1-8.
- Sujana, M.G. and Mohanty, S. 2010. Characterization and fluoride uptake studies of nano-scale iron oxide-hydroxide synthesized by microemulsion method. *Int. J. Eng. Sci. Technol.*, 2: 1-12.
- Swain, S.K., Mishra, S., Patnaik, T., Patel, R.K., Jha, U. and Dey, R.K. 2012. Fluoride removal performance of a new hybrid sorbent of Zr(IV)-ethylenediamine. *Chem. Eng. J.*, 184: 72-81.
- Tangkawanit, S., Rangriwatananon, K. and Dyer, A. 2005. Ion exchange of Cu²⁺, Ni²⁺, Pb²⁺ and Zn²⁺ in analcime(ANA) synthesized from Thai perlite. *Microporous and Mesoporous Mater.*, 79: 171-175.

- Ustun, G.E., Solmaz, S.K.A. and Birgul, A. 2007. Regeneration of industrial district wastewater using a combination of Fenton process and ion exchange-A case study. *Resour. Conserv. Recyc.*, 152: 425-440.
- Vaclavikova, M., Gallios, G.P., Hredzak, S. and Jakabsky, S. 2008. Removal of arsenic from water streams: An overview of available techniques. *Clean Technol. Environ.*, 10: 89-95.
- Wagle, D. and Shipley, H.J. 2016. Adsorption of arsenic (V) to titanium dioxide nanoparticles: effect of particle size, solid concentration, and other metals. *Environ. Eng. Sci.*, 33(5): 299-305.
- Weber Jr, W.J. and Morris, J.C. 1963. Kinetics of adsorption on carbon from solution. *J. Sanit. Eng. Div.*, 89: 31-59.
- Wu, K., Zhang, J., Chang, B., Liu, T., Zhang, F., Jin, P., Wang, W. and Wang, X. 2017. Removal of arsenic (III, V) by granular Mn-oxide-doped Al oxide adsorbent: Surface characterization and performance. *Env. Sci. & Poll. Res.*, 24: 18505-18519.
- Yao, Y., Gao, B., Inyang, M., Zimmerman, A.R., Cao, X., Pullammanappalli, I.P. and Yang, L. 2011. Removal of phosphate from aqueous solution by biochar derived from anaerobically digested sugar beet tailings. *J. Hazard Mater.*, 190: 501-507.
- Zhang, G., Ren, Z., Zhang, X. and Chen, J. 2013. Nanostructured iron(III)-copper(II) binary oxide: A novel adsorbent for enhanced arsenic removal from aqueous solutions. *Water Res.*, 47: 4022-4031.
- Zhang, W., Liu, C., Wang, L., Zheng, T, Ren, G., Li, J., Ma, J., Zhang, G., Song, H., Zhang, Z. and Li, Z. 2018. A novel nanostructured Fe-Ti-Mn composite oxide for highly efficient arsenic removal: Preparation and performance evaluation. *Colloids Surf. (A) Physicochem. Eng. Asp.*, <https://doi.org/10.1016/j.colsurfa.2018.10.077>.
- Zhou, Q., Teng, Y. and Liu, Y. 2017. A study on soil-environmental quality criteria and standards of arsenic. *Appl. Geochem.*, 77: 158-166.
- Zhu, N., Yan, T., Qiao, J. and Cao, H. 2016. Adsorption of arsenic, phosphorus and chromium by bismuth impregnated biochar: Adsorption mechanism and depleted adsorbent utilization. *Chemosphere*, 164: 32-40.



Carbon Emission Estimation of Prefabricated Buildings Based on Life Cycle Assessment Model

Wenfang Zhou

Department of Engineering Management, School of Urban Construction Engineering, Wenhua College, Wuhan 430074, China

†Corresponding author: Wenfang Zhou; whut_zwf@126.com

Nat. Env. & Poll. Tech.
Website: www.neptjournal.com

Received: 05-08-2020

Revised: 31-10-2020

Accepted: 02-12-2020

Key Words:

Prefabricated buildings
Carbon emission
Energy conservation
Emission reduction

ABSTRACT

As a typical secondary industry in China, the building industry promotes China's construction and development significantly. The urban construction scale is expanding continuously with the increase of the urbanization rate. However, resources needed for construction and influences of construction on the ecological environment are enormous, which further cause resource consumption and environmental destructions. Therefore, changing the traditional mode of construction and promoting the development of prefabricated buildings vigorously are conducive to realize the goal of environmental protection and resource conservation. In this study, a life cycle assessment model for prefabricated buildings was constructed based on the basic data of resource and energy consumption in the production stage, transportation stage, and field installation stage. The total carbon emission of a prefabricated building in Wuhan City was estimated, and specific energy conservation and emission reduction measures were proposed. Results show that prefabricated buildings have become a major manifestation of the industrialization of construction, represented by America, Germany, and Japan. In the case study, the total carbon emission of prefabricated components in the project is 3277.66 t, in which the carbon emissions in the production stage, transportation stage, and field installation stage account for 86.58%, 12.37%, and 1.05%, respectively. Based on the above research results, the further decrease in carbon emissions of prefabricated buildings by promoting the development of building energy efficiency and prefabricated buildings, accelerating R&D and innovation of prefabricated building technologies, and strengthening training to designers related with installation of prefabricated buildings is suggested. Research conclusions have important significance in various aspects, such as providing case-based references and guidance to the carbon emission reduction of prefabricated buildings and supply basic data to decrease carbon emission caused by the production of building materials, developing new environmentally friendly materials to relieve the impact of carbon emissions from the building industry on the environment, realizing energy conservation and emission in the field of construction, and promoting the sustainable development of prefabricated buildings.

INTRODUCTION

Human productivity has increased significantly after the industrial revolution. However, the blind pursuit of economic development has caused excessive consumption of earth resources and serious damage to the ecological environment. China's economy achieves rapid development. As an important department of material production, the building industry also has undergone rapid development. The construction and operation of the building industry are human activities that incur the maximum natural resource consumption. The rapid development of the building industry brings considerable resource and energy consumption and serious environmental pollution when it promotes national economic development and improves the quality of life of people. In addition to severe environmental and economic situations, the traditional building industry is also facing many social problems, such as low labour productivity and

lack of technological innovation. Moreover, enterprises have to pay for the continuously increasing labour cost, low recovery and high recovery cost of building materials, and considerable emissions of construction wastes because of the intensifying ageing of the population and the vanishing demographic dividends in China, thus restricting the sustainable development of the building industry in the social dimension significantly. Understanding how to decrease carbon emission in the construction and development of low-carbon buildings is needed during building industrial development in a low-carbon society.

Recently, the building industry in Hubei Province has developed rapidly. The total output value (100 million Yuan) of the building industry and floor spaces under construction (10,000 m²) in 2010-2019 were increasingly quickly (Fig. 1). The annual growth rates reached 32.31% and 29.72%, respectively. Such rapid development of the building

industry has brought considerable pressures over the environment. Hubei Province entered into the list of low-carbon pilot provinces in 2010. As the capital of Hubei Province, Wuhan City has also been making great efforts to lower energy consumption in the building industry to comply with the construction needs of low-carbon pilot cities. The “13th Five-year Plan” Outline for Building Industrial Development in Hubei Province stipulated explicitly that the energy-saving standard for new residential buildings is increased from 50% to 65%. Thus, prefabricated buildings will be a dominant trend in the building industry. Prefabricated buildings refer to buildings that are assembled at a construction site by several components that had been prefabricated or semi-prefabricated in factories. In this background, prefabricated buildings are highly appreciated for their high production efficiency, short construction period, small resource consumptions, and low environmental pollution. Moreover, many enterprises are promoting prefabricated buildings under the guidance of relevant policies and innovating assembly technologies concerning energy conservation and environmental protection, aiming to improve environmental-friendly performance of the buildings and promote sustainable development of the building industry. Prefabricated buildings are an important way to develop environmental-friendly buildings in China at present. Studying the environment-friendly performance of prefabricated buildings throughout the life cycle is conducive for the promotion of the development of China’s building industry toward green buildings and the relief of resource wastes and environmental pollution in the building industry.

EARLIER STUDIES

Energy consumption during the construction of buildings

is increasing yearly and is accompanied by serious environmental pollution. These are related to the large-scaled unreasonable use of concrete and steel and backward construction technologies. Improved energy-saving efficiency of buildings is one of the best methods for developing prefabricated buildings. Prefabricated buildings have been studied extensively in foreign developed countries because of the environment-friendly construction mode, the factorization of prefabricated component production, design standardization, the informatization of engineering management, and decoration integration. Concerning the carbon emission of prefabricated buildings and the realization of energy-saving and emission reductions, Gerwick pointed out at the annual conference of PCI (Precast/Prestressed Concrete Institute) in 1991 that the development of prefabricated concrete structures was a new opportunity for the building and industrial development in the United States and even worldwide and that the United States was one of the countries that studied prefabricated buildings early. Moreover, they proposed that prefabricated concrete buildings and steel buildings mainly focused on large and medium-sized cities (Gerwick 1991). Jaillon et al. believed that the building industry in Hong Kong depended on traditional field construction to a large extent and that the wet industry uses extensive applications of wood templates. They also discussed the sustainable development of prefabricated structures in high-rise buildings. Results have shown that, compared with traditional buildings, prefabricated buildings have significantly higher environmental, economic, and social benefits (Jaillon et al. 2008). Pons et al. analysed prefabricated buildings from the perspective of technology and sustainable development to determine how prefabricated buildings improve their quality

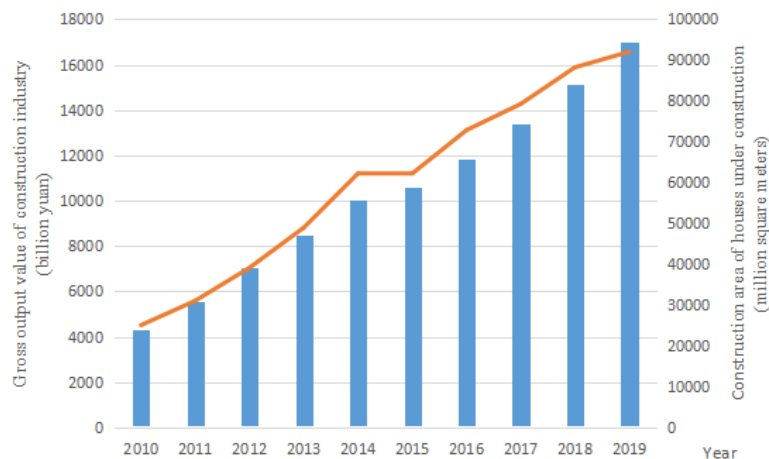


Fig. 1: Total output value (100 million Yuan) and floor spaces under construction (10,000 m²) of the building industry in Hubei Province in 2010-2019.

and decrease their influences on the environment. Carbon emission differences between industrialized technologies and the non-prefabricated technology were compared using the full life cycle assessment (LCA), which has proven that prefabricated buildings can decrease resource consumption and waste production (Pons et al. 2011). Aye et al. carried out quantitative analysis on the energy-saving effects of multiple modularized prefabricated steel and wood residential buildings and found that prefabricated steel structures could decrease as much as 78% of material consumption compared with traditional concrete structures (Aye et al. 2012). Mao et al. analysed the calculation boundaries and five emission sources during the construction of prefabricated buildings, constructed a quantitative model based on the process, and carried out a preliminary study on the differences of greenhouse gas emissions between a semi-prefabricated project and a conventional architectural project in China. They concluded that the greenhouse gas emission per square meter in the semi-prefabricated project was lower than that of the conventional architectural project (Mao et al. 2013). Based on the theory of full life cycle, Lu W. et al. carried out an empirical study on carbon emissions during the manufacturing and cross-border transportation of precast slabs, assessed the potential of precast slabs in decreasing wastes, and proposed specific measures to decrease carbon emissions (Lu et al. 2013). Bonamente et al. investigated carbon emission and energy footprints in the Italian prefabricated building department performed parametric estimation on greenhouse gas emission and energy consumptions in different stages of the life cycle of buildings and proposed measures to decrease carbon emissions of the building industry (Bonamente et al. 2014). Dong et al. compared carbon emissions of prefabricated construction and traditional cast-in-situ construction based on a private residential building in Hong Kong and established the LCA model. The results show that the carbon emission of this residential building was equal to 669 kg CO₂ per square meter and that the prefabricated concrete structure could decrease its carbon emission per cubic meter by 10% (Dong et al. 2015). Based on two typical residential buildings, Cao et al. combined the construction environmental performance assessment system based on LCA and building health impact assessment system to evaluate the energy consumptions of prefabricated construction technology and conventional construction technology. They concluded that prefabricated buildings had high energy utilization, and the total energy consumption decreased by 20.49% (Cao et al. 2015). Hong et al. believed that prefabricated structure was an effective strategy to increase the production efficiency of the building industry. Using a case study based on practical prefabricated buildings, He discussed energy use throughout the life cycle

of prefabricated components and effects of prefabricated components on total energy use. Results demonstrated that prefabricated buildings could control energy saving by decreasing waste production and improving quality, and it saved energy consumption by 4-14% in the whole life cycle (Hong et al. 2016). Hong et al. established a cost-benefit analysis framework and discussed the basic cost composition of a prefabricated construction project. According to research results, key attention should be paid to promote the development of prefabricated construction technologies and optimize the structural integrity of prefabricated components in the future to develop their economic benefits fully (Hong et al. 2018). Ling et al. evaluated the environmental impact of a temporary house with a renewable energy source system and constructed an LCA model for each stage. Moreover, the LCA model for a temporary residential building oriented to carbon emission reduction was proposed, which was conducive to promote the sustainable development of prefabricated temporal residential buildings (Ling et al. 2018). Hossain et al. evaluated the wood waste management system using the LCA model from the perspective of environmental protection and concluded that influences of chipboard and wood-cement composite, which were made of wood waste composite on the environment, were relieved significantly (Hossain et al. 2018). The above literature review shows that, in foreign developed countries, especially the USA, Germany, and Japan, the prefabricated construction technological system is well developed, and the energy-saving technologies are more mature. In particular, prefabricated buildings have become a major manifestation of building industrialization in economically developed countries. According to the literature review, prefabricated buildings can bring social progress in standardization, high efficiency, and sustainable development. However, prefabricated buildings still face various challenges against promotion in China because of a shortage of cost, technologies, and management. In this study, the carbon emissions of a prefabricated building in Wuhan City, Hubei Province, China in the production stage, transportation stage, and installation stage were estimated by the LCA model, and specific energy conservation and emission reduction measures were proposed.

MODELS

Life cycle assessment (LCA) is a research methodology that evaluates the influences of a product on the environment throughout its life cycle. LCA has been extensively applied in various fields, including engineering, material, and equipment. The LCA model is composed of the determination of objective and scope, list analysis, impact assessment, and result analysis.

OBJECTIVE AND SCOPE

The research objective is to compare carbon emissions of components of prefabricated buildings in different stages based on the carbon emission estimation of LCA theory and analyze carbon emission sources and major influencing factors in different stages of the life cycle. A prefabricated building involves various types of components in different sizes. For the convenience of comparison, the unit volume (1 m³) was chosen as the evaluation index of one functional unit, which could evaluate carbon emission relatively accurately.

List Analysis

List analysis is a process of data acquisition and reviewing, and it is the key and foundation of LCA. Based on classification statistics of data concerning material consumption, mechanical consumption, and component transportation in different life stages of prefabricated building, all data related with carbon emission factors of different materials and energy sources were collected into a list for further processing and computing. This list is called the list of life cycle.

Carbon Emission Calculation Model

Carbon emission mainly refers to emissions of greenhouse gases represented by CO₂ and accompanied by CH₄ and N₂O. The International Energy Agency unified emissions of various greenhouse gasses into CO₂ equivalent (CO₂-eq) for quantitative analysis on carbon emission. Carbon emission sources that may exist during construction, service and waste stages in life cycle prefabricated buildings are listed in Table 1.

Table 1: Carbon emission sources in the building industry.

Stages	Descriptions
Production and processing of prefabricated components	Carbon emissions from mining, production, and transportation of raw materials to the prefabricated component factory; carbon emissions from the consumed resources and instruments used in the production of prefabricated components; carbon emissions from resource consumption during transportation of prefabricated components; and carbon emissions from energy consumption for mechanical operation during the field assembly
Transportation of prefabricated components	Carbon emissions from resource consumption during transportation
Field installation	Carbon emissions from the energy consumption for the operation of construction equipment and machines during the installation of prefabricated components

According to Eq. (1), an LCA model of carbon emissions of a prefabricated building is the sum of CO₂-eq of greenhouse gases in different stages.

$$Q = Q_m + Q_t + Q_c \quad \dots(1)$$

Where Q_m , Q_t and Q_c are carbon emissions in the production and processing stage, transportation stage, and field installation stage of prefabricated components, respectively.

Impact Assessment and Result Interpretation

Impact assessment refers to the quantitative analysis and evaluation of environmental influences in different stages of a life cycle based on the list analysis data. Carbon emissions of different types of components in the life cycle and contributions of different components to carbon emissions in different life stages were analysed, aiming to determine key influencing factors and links of carbon emission. Impact assessment can provide basic data for the energy conservation and emission reduction of prefabricated buildings and offer a development direction for energy-saving buildings.

CASE STUDY

In this study, the carbon emission of a prefabricated building in Wuhan City throughout the life cycle was calculated. The selected prefabricated building for the case study covers a building area of approximately 67500 m² and involves complete types of prefabricated components with a prefabrication rate of 63%. Prefabricated components in the manufacturing factory were transported by heavy semitrailer tractors. These heavy semitrailer tractors have a carrying capacity of 30 t and are loaded with diesel. The diesel consumption is 45 L/100 km. The project site is 57 km from the manufacturing factory. The main types of prefabricated components for prefabricated buildings include balcony clapboards, precast shear walls, precast infilled wall (external wall), precast infilled wall (internal wall), superposed slabs, superposed beams, balconies, and stairs. In this study, a statistical analysis of the material composition, production techniques, and energy consumption of prefabricated components in main prefabricated component factories in Wuhan City was carried out. Prefabricated components adopt flow line production, and electricity consumption is the sole mechanical energy consumption. Data in different stages were brought into the model, and carbon emissions in different stages were calculated according to Eq. (1). Results are shown in Table 2.

Table 2 shows that the total carbon emission of prefabricated components in the selected project throughout the life cycle reaches 3277.66 t, in which carbon emissions in the production stage, transportation stage, and field

Table 2: Carbon emissions of prefabricated components in different stages.

Prefabricated components	Carbon emission in the production stage (T)	Carbon emission in the transportation stage (T)	Carbon emission in the field installation stage (T)
Precast shear wall	48.23	6.98	0.87
Precast shear wall	1567.27	182.33	17.23
External wall	347.92	76.81	4.45
Internal wall	179.35	40.91	2.98
Superposed slabs	367.34	63.12	4.29
Superposed beams	39.71	3.81	0.64
Balconies	198.29	20.16	2.16
Stairs	89.63	11.25	1.93
Total	2837.74	405.37	34.55

installation stage contribute 86.58%, 12.37%, and 1.05%, respectively. The production stage is the key stage to decrease the carbon emission of prefabricated components. According to a refined analysis of the production process, carbon emission in the production stage mainly comes from carbon emissions that are produced by used building materials, and concrete and rebar are major carbon emission sources. Therefore, the decrease in waste of concrete and rebar during practical production should be given attention. Given that cement is the major component of concrete, a recommendation is to replace cement with superplasticizer during concrete manufacturing, which can increase the strength of prefabricated components and decrease carbon emissions from the source as much as possible. Steel materials are essential in construction. The utilization of materials shall be increased, and material wastes shall be decreased reasonably. When decreasing the waste of aluminium materials, alternative materials with a relatively small carbon emission factor can be used as embedded parts, which can decrease carbon emission significantly. Carbon emission in the transportation stage is related to the workload of prefabricated components and transportation distance. A suggestion is to choose prefabricated component factories near the project to decrease carbon emission in the transportation stage. In the production stage, the precast shear wall contributes to the maximum carbon emissions, followed by superposed beams. Carbon emission is great given that rebar consumption is large. In the field installation stage, carbon emission per cubic meter is related to the complexity of component installation. When complexity claims are high, mechanical energy consumption at installation and carbon emissions increase. Given the whole project, carbon emissions of different prefabricated components are related to workloads directly.

ENERGY CONSERVATION AND EMISSION REDUCTION MEASURES

Promoting the Development of Building Energy-Saving Technologies and Prefabricated Buildings

The building design level shall be improved. The use functions of buildings and requirements on energy-saving, water-saving, land-saving, material-saving, and environmental protection shall be highlighted. Economical, reasonable, safe, and reliable architectural design products with applicable functions, advanced technologies, and environmental harmony shall be provided. The government-invested public welfare buildings and indemnificatory housing, such as office buildings, schools, hospitals, and cultural buildings, shall execute green building standards. Regions with proper conditions are encouraged to execute green building standards completely. Moreover, green buildings have to be developed vigorously. Green construction shall be promoted from materials and techniques, and the leading support of the technological system shall be strengthened. It is suggested to strengthen modernized standard construction in the building industry; establish a fast transformation mechanism between technological innovations and technological standard systems; encourage and support social institutions and enterprises to compile their own standards for prefabricated buildings; and set up engineering construction standard systems for prefabricated building design, part production, construction, quality inspection, acceptance check, and evaluation.

Accelerating Technological R&D and Innovation for Prefabricated Buildings

It is suggested to (1) set up a standard-based authentication mechanism to restrict projects and products to execute relevant standards strictly; (2) strengthen R & D supports of key technologies; (3) perfect the government-industry-university research cooperative innovation mechanism; attach high attention to optimize new technological R & D and application environment; summarize and promote advanced technological systems for different types of building products; (4) organize R&D of renewable energy sources, new wall materials, external wall insulation, and energy-efficient doors and windows; (5) accelerate the transformation of mature building energy-saving and green building technologies to standards; (6) accelerate the promotion of the evaluation and labelling system for green buildings and green building materials; (7) build a provincial evaluation and labelling management information platform for green buildings and green building materials; (8) make independent and integrated evaluations to green building materials, techniques,

technologies, and products; strengthen the integration of green construction technologies and materials; recommend overall evaluated green building product systems; and (9) implement bases of green building material industries and engineering application pilots in typical regions and projects.

Strengthen Training to Assembly-Related Designers

Training helps construction workers to deepen their understanding of the energy-saving design philosophy of prefabricated buildings and properties and the applications of thermal insulation materials. Specific training plans shall be formulated to field construction workers according to their job tasks to help them fully understand their jobs and importance, thus assuring the construction quality and further protecting the overall quality of the building. The systematic management of prefabricated component factories is needed, and relevant production standards and operation codes have to be published. Relevant departments shall make spot checks irregularly to implement conditions of manufacturing shop standards and norms, product quality, and production environment and perfect the supervision and leadership of sections at all levels. Prefabricated factories shall set up a quality inspection department to check the quality of raw materials and produce prefabricated components. Besides, factories shall set up a perfect management system for the component warehouse. Before the production, systematic training shall be provided to production workers, and an assessment system has to be formulated. Only workers who pass the assessment are allowed to participate in production activities.

CONCLUSIONS

The building industry consumes considerable natural resources and causes huge environmental pollution while promoting national economic development. As a CO₂ emission power, China is facing great pressure in emission reduction. Understanding how to decrease carbon emission in the construction and development of low-carbon buildings are needed during building industrial development in a low-carbon society. In this study, the total carbon emissions caused by resource and energy consumption in the production stage, the transportation stage, and the field installation stage of a prefabricated building in Wuhan City were estimated. Results show that prefabricated buildings have become a major manifestation of the industrialization of construction, represented by America, Germany, and Japan. In the case study, the total carbon emission of prefabricated components in the project is 3277.66 t, in which carbon emissions in the

production stage, transportation stage, and field installation stage account for 86.58%, 12.37%, and 1.05%, respectively. The above research results suggest the further decrease of carbon emissions of prefabricated buildings by promoting the development of energy-efficient and prefabricated buildings, acceleration of R & D, the innovation of prefabricated building technologies, and strengthening the training of designers regarding the installation of prefabricated buildings. Further studies on the comparison of carbon emissions between prefabricated buildings and traditional buildings, the effects of prefabricated buildings on environmental and economic sustainable development, and the establishment of green evaluation system of prefabricated buildings are needed.

REFERENCES

- Aye, L., Ngo, T., Crawford, R. H., Gammampila, R. and Mendis, P. 2012. Life cycle greenhouse gas emissions and energy analysis of prefabricated reusable building modules. *Energy and Buildings*, 47(47): 159-168.
- Bonamente, E., Merico, M. C., Rinaldi, S., Pignatta, G., Pisello, A. L., Cotana, F. and Nicolini, A. 2014. Environmental impact of industrial prefabricated buildings: carbon and energy footprint analysis based on an LCA approach. *Energy Procedia*, 61: 2841-2844.
- Cao, X., Li, X., Zhu, Y. and Zhang, Z. 2015. A comparative study of environmental performance between prefabricated and traditional residential buildings in China. *Journal of Cleaner Production*, 109(16): 131-143.
- Dong, Y. H., Jaillon, L., Chu, P. and Poon, C. S. 2015. Comparing carbon emissions of precast and cast-in-situ construction methods - A case study of high-rise private building. *Construction and Building Materials*, 99: 39-53.
- Gerwick, B. C. 1991. The global advance emerging opportunities at home and abroad. *PCI Journal*, 36(6): 32-37.
- Hossain, M. U. and Poon, C. S. 2018. Comparative LCA of wood waste management strategies generated from building construction activities. *Journal of Cleaner Production*, 177(10): 387-397.
- Hong, J., Shen, G. Q., Li, Z. and Zhang, B. 2017. Barriers to promoting prefabricated construction in China: A cost-benefit analysis. *Journal of Cleaner Production*, 172(1): 649-660.
- Hong, J. K., Shen, G. Q., Mao, C., Li, Z. D. and Li, K. J. 2016. Life-cycle energy analysis of prefabricated building components: An input-output-based hybrid model. *Journal of Cleaner Production*, 112: 2198-2207.
- Jaillon, L. and Poon, C. S. 2008. Sustainable construction aspects of using prefabrication in dense urban environment: A Hong Kong case study. *Construction Management & Economics*, 26(9): 953-966.
- Lu, W. and Yuan, H. 2013. Investigating waste reduction potential in the upstream processes of offshore prefabrication construction. *Renewable & Sustainable Energy Reviews*, 28(8): 804-811.
- Ling, D., Yu, W. and Hong, L. Z. 2018. Carbon reduction measures-based LCA of prefabricated temporary housing with renewable energy systems. *Sustainability*, 10(3): 718.
- Mao, C., Shen, Q. P., Shen, L. Y. and Tang, L. Y. 2013. Comparative study of greenhouse gas emissions between off-site prefabrication and conventional construction methods: Two case studies of residential projects. *Energy and Buildings*, 66(5): 165-176.
- Pons, O. and Wadel, G. 2011. Environmental impacts of prefabricated school buildings in Catalonia. *Habitat International*, 35(4): 553-563.



Fish Community Structure and Ecological Health Assessment of the Shuaishui River Basin, China

Y. X. Fang*, G. J. Liu*† and R. J. Liu**

*School of Public Affairs, University of Science and Technology of China, Hefei 230061, China

** CAS Key Laboratory of Crust-Mantle Materials and Environment, School of Earth and Space Sciences, University of Science and Technology of China, Hefei, Anhui 230026, China

†Corresponding author: G. J. Liu; 13956911439@163.com

Nat. Env. & Poll. Tech.
Website: www.neptjournal.com

Received: 26-02-2020

Revised: 20-03-2020

Accepted: 02-05-2020

Key Words:

Shuaishui river
Fish community
Ecological health
Ecological management

ABSTRACT

The Shuaishui River originates from the southern mountainous area of Anhui Province and is an important water source for local residents. The ecological environment of this basin has been seriously damaged because of the effects of human disturbance. In August 2016, a field study of five units of the Shuaishui River Basin was conducted to understand the fish community structure and assess the ecological health status. A total of 43 fish species were collected from the entire river basin, and they belonged to 4 Orders, 10 Families, and 31 Genera. The maximum number of species belonged to the family Cyprinidae, and the main trophic guild was omnivorous fish. Among the five units, species number was the highest in unit 2 (27 species) and the lowest in unit 3 (12 species). The dominant species in the five units were mainly typical mountain-stream fish, such as *Zacco platypus*, *Acrossocheilus fasciatus*, and *Vanmanenia stenosoma*. In some areas, *Varicorhinus barbatulus* or *Rhinogobius cliffordpopei* also showed great dominance because of the impacts of the local habitat conditions. Redundancy analysis showed that altitude, water velocity, stream order, and water surface width were the main factors that influenced the distribution and species composition of the fish. Eigenvalues of the first two axes were 0.183 and 0.082 and explained 40.9% and 18.3% of the species-environment relationship variables, respectively. The ecological health of the five units and the entire basin was assessed based on the arithmetic mean of three indicators, namely, number of classification units, Shannon-Wiener index, and Berger-Parker dominance index. The results indicated that the ecological health status was relatively poor in unit 3, general in units 1 and 5, and good in units of 2 and 4. The status of the entire basin was general. To the best of our knowledge, this is the first comprehensive assessment of the ecological health of the Shuaishui River Basin, and it has great significance for the ecological management and protection of this basin.

INTRODUCTION

China has the most amount of island waters worldwide (Wan 2016). However, most watersheds in China are experiencing various degrees of water pollution, decline in species diversity, ecosystem degradation, and other problems because of the rapid development of the economy, irrational use of water resources, and increased discharge of sewage. The ecological health of watershed ecosystems has become one of the most important factors that restrict sustainable development of the socio-economy (Department of Nature and Ecology Conservation, Ministry of Environmental Protection of China 2014). To effectively assess the ecological health of watershed ecosystems, physical, chemical, and biological methods have been used by some researchers in China (Wan 2016). Recently, the biological assessment methods have become one of the most commonly used methods because of their unique

advantages, and fish and macrozoobenthos are usually been selected as the main evaluation groups (Tang et al. 2002). Species diversity, population, and community characteristics of fish play important roles in indicating the ecological health of a watershed (Karr 1986). Besides, fish generally have a longer life history and wider movement range, which can reflect long-term and large-scale changes in the water environment (Karr 1981). The pressures caused by stress factors in the water environment can be reflected in the physiological, morphological, or behavioural characteristics of fish (Barbour et al. 1999). However, most watershed ecological health assessment studies in China were conducted in large rivers or plain rivers, and there are relatively few studies on mountain rivers. Fish communities are more sensitive and vulnerable to environmental changes in mountain rivers than in other rivers because of the complex geological and climatic conditions, and they are at a higher risk of endangerment and extinction (Wan 2016).

Therefore, it is important to assess the ecological health of watersheds of mountain rivers.

The Shuaishui River is located in Huangshan City, and it originates from the southern mountainous area of Anhui Province. It is the source of three important rivers in China, namely, Xin'an, Fuchun, and Qiantang Rivers, and it is an important water source for Huangshan City. The total length of the mainstream is 148.2 km, and the watershed area is about 1,522 km². On the basis of its topographical features, the whole river can be divided into three sections. The upper reaches, with deep water and rapid flow in the channel, can be found above Xikou Town; the middle reaches, from Xikou Town to Yuetan Village; and the lower reaches, with shallow water and slow velocity in the channel, below Yuetan Village. The Shuaishui River Basin belongs to the north subtropical monsoon climatic zone, with four distinct seasons and abundant rainfall. The annual average temperature is 16.2°C, and the annual average rainfall is 1613.7 mm. Recently, the ecological health of Shuaishui River has been seriously damaged because of disorderly sand mining, sluice and dam construction, and unreasonable land use. However, assessment of the ecological health of this watershed has not yet been reported.

In August 2016, a field study was conducted to understand the species diversity and community characteristics of fish resources and assess the ecological health of the Shuaishui River Basin. To facilitate ecological management, we first divided the Shuaishui River Basin into different units based on the watershed standard in China (Department of Nature

and Ecology Conservation, Ministry of Environmental Protection of China 2014) and then analysed each unit and the whole river basin. The main objectives of our study were to (1) understand the species diversity and community characteristics of fish in the Shuaishui River Basin and different units; (2) identify the main factors that affect the spatial distribution of fish in the Shuaishui River Basin; and (3) assess the ecological health of the different units and whole river basin by using the fish data. The results of this study are not only of great significance for the protection and restoration of fish resources but also provide a scientific basis for the ecological management of the Shuaishui River Basin.

MATERIALS AND METHODS

Field Sampling

In August 2016, fishes in the Shuaishui River Basin were surveyed. According to the river network complexity and field reachability, a total of 38 sampling points were set in the whole basin (Fig. 1). At each sampling point, the fish were collected using an electric fishing device by one person. The collection time was 30 min, and the sampling length was 100 m. The fishing area included different habitats, such as deep pools, shallow waters, and rapid waters that can be waded. The collected specimens were identified in the fresh state, and individual number and weight (accurate to 0.1 g) of different species were measured. Species that could not be identified in the field were fixed with 10% formaldehyde and brought back to the laboratory for identification.

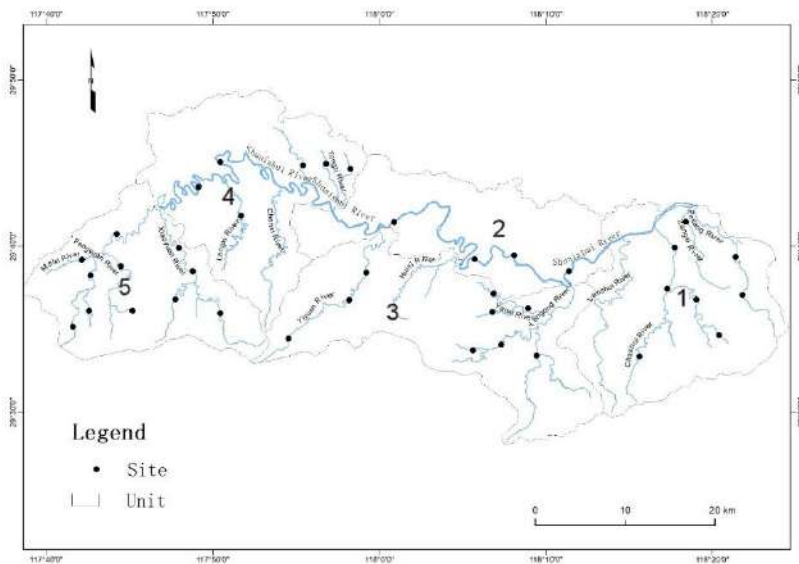


Fig. 1: Location of the sampling sites in different units in the Shuaishui River basin.

Measurement of Environmental Parameters

Local habitat parameters, physicochemical parameters, and stream levels were measured at each sampling point. The local habitat parameters were altitude, water surface width, channel width, water velocity, water temperature and substrate type, and physiochemical parameters were pH, salinity, dissolved oxygen and electrical conductivity. The altitude was measured using a handheld GPS (Garmin etrex type), water surface width and channel width were measured with a laser rangefinder (Trupulse 200), and water velocity was measured using a portable flow meter (Global FP211). The sediment type was determined with a visual scoring method and divided into six levels: 1 (<0.06 mm), 2 (0.06-1 mm), 3 (2-5 mm), 4 (15-63 mm), 5 (64-256 mm), and 6 (>256 mm) (Zhang et al. 2017). The water temperature was measured with a digital thermometer, and dissolved oxygen, electrical conductivity, and turbidity were measured using a portable dissolved oxygen meter (YSI 550A), electrical conductivity meter (YSI Pro 30), and turbidity meter (Rex WZS-185 type), respectively. The stream order was divided using a previously described method (Strahler 1957). The smallest tributary is called the first-order stream; the confluence of two streams with the same stream order causes an increase in the stream order. When a low-level stream flows into a high-level stream, its influence on stream order is ignored (Kuehne 1962).

Data Analysis

To facilitate the assessment and management of the watershed, the Shuaishui River Basin was divided into five different units based on the similarity of the natural conditions and administrative division (Department of Nature and Ecology Conservation, Ministry of Environmental Protection of China 2014). The five units are shown in Fig. 1. One-way analysis of variance (ANOVA) was used to test the differences in the environmental parameters. If a significant variance was detected, Tukey's honest significant difference multiple comparisons were conducted to further examine the differences between groups (Zhang et al. 2015). Based on different trophic guilds, all the collected fish were classified as herbivorous, carnivorous, and omnivorous fish; according to the different tolerances to pollution, all the fish were divided into three levels: sensitive, general, and tolerant. To determine the dominant fish species, the relative importance index (IRI%) was calculated:

$$IRI\% = \left\{ \frac{(W_i\% + N_i\%) \times F_i\%}{\sum_{i=1}^n (W_i\% + N_i\%) \times F_i\%} \right\} \times 100\%$$

Where, $W_i\%$ is the weight per cent of the i -th species in the catch, $N_i\%$ is the individual number per cent of the i -th species in the catch, and $F_i\%$ is the occurrence frequency of the i -th species.

The relationship between the fish and environmental parameters was analysed by the CANOCO software. The species matrix was constructed using the individual number data for fish. To satisfy the assumption of homogeneity and normal distribution, $\log(x+1)$ was used to transform the data. Then, detrended correspondence analysis was performed to evaluate the response model. Because the gradient value was less than 3, redundancy analysis (RDA) was performed to determine the relationships between the species and environmental parameters. To assess the ecological health, the following three indexes were used (Department of Nature and Ecology Conservation, Ministry of Environmental Protection of China 2014):

1. **Number of classification units (S):** The number of classification units of fish present at a sampling point.
2. **Shannon-Wiener index (H):** The formula is $H' = -\sum (P_i)(\log_2 P_i)$, where P_i is the individual proportion of the i -th species.
3. **Berger-Parker dominance index (D):** The formula is $D = N_{max}/N$, where N_{max} is the individual number of the most dominant species at a sampling point, and N is the total individual number at a sampling point.

The three indexes were standardized, and then the arithmetic mean values of the three indexes were calculated. The ecological health was assessed according to the following grades: excellent ($0.8 \leq N < 1$), good ($0.6 \leq N < 0.8$), general ($0.4 \leq N < 0.6$), relatively poor ($0.2 \leq N < 0.4$), and poor ($0 \leq N < 0.2$) (Department of Nature and Ecology Conservation, Ministry of Environmental Protection of China 2014).

RESULTS

Environmental Parameters

The environmental parameters of the five units in the Shuaishui River Basin are listed in Table 1. One-way ANOVA showed that, except for sediment types, water velocity, and pH, significant differences were observed among the environmental parameters ($P < 0.05$). Unit 2 had the lowest average altitude and the highest channel width, water surface width, and water temperature, whereas unit 5 had the highest average altitude and lowest channel width, water surface width, and water temperature. No significant differences were found among units 1, 3 and 4 (Table 1).

Table 1: Environmental parameters of the five units in the Shuaishui River Basin (mean \pm SD). The different superscript letters in the table indicate significant differences ($P < 0.05$).

	Unit 1	Unit 2	Unit 3	Unit 4	Unit 5
Altitude (m)	242.0 \pm 159.7 ^{ab}	161.8 \pm 20.0 ^a	214.8 \pm 58.6 ^{ab}	212.3 \pm 41.6 ^{ab}	337.5 \pm 86.8 ^b
Substrate type	4.5 \pm 0.4	3.7 \pm 0.9	4.7 \pm 0.7	4.3 \pm 0.8	4.2 \pm 0.6
Water velocity (cm/s)	15.3 \pm 7.1	19.0 \pm 15.7	12.4 \pm 7.5	19.2 \pm 9.0	22.1 \pm 11.4
Channel width (m)	23.6 \pm 22.5 ^a	115.6 \pm 42.2 ^b	24.9 \pm 10.4 ^a	36.0 \pm 39.8 ^a	23.4 \pm 9.3 ^a
Water surface width (m)	10.0 \pm 5.0 ^a	59.4 \pm 28.1 ^b	14.4 \pm 7.1 ^a	18.1 \pm 22.2 ^a	7.6 \pm 5.5 ^a
Water temperature ($^{\circ}$ C)	29.1 \pm 3.7 ^{ab}	32.7 \pm 1.7 ^b	27.7 \pm 2.3 ^a	28.4 \pm 4.0 ^{ab}	26.4 \pm 1.6 ^a
pH	8.40 \pm 0.41	8.31 \pm 0.44	8.09 \pm 0.42	8.17 \pm 0.38	8.44 \pm 0.65
Dissolved oxygen (mg/L)	11.86 \pm 0.81 ^a	10.03 \pm 1.23 ^b	10.98 \pm 0.92 ^{ab}	10.80 \pm 0.84 ^{ab}	11.14 \pm 1.14 ^{ab}
Conductivity (μ S/cm)	61.01 \pm 13.41 ^a	40.78 \pm 7.34 ^b	33.42 \pm 9.97 ^b	45.61 \pm 3.72 ^b	34.55 \pm 6.18 ^b
Salinity (ppt)	0.033 \pm 0.010 ^a	0.023 \pm 0.005 ^b	0.014 \pm 0.007 ^b	0.002 \pm 0.000 ^b	0.018 \pm 0.004 ^b

Species Composition

A total of 2579 individuals were collected from the entire Shuaishui River Basin, with a total weight of 9182.46 g. A total of 43 species were identified, and they belonged to 4 Orders, 10 Families and 31 Genera (Table 2). Cyprinidae was the dominant family (33 species) and accounted for 76.7% of the total species, followed by Siluriformes (five species) and Perciformes (four species), which accounted for 11.6% and 9.3% of the total species, respectively. Only one species that belonged to the order Synbranchiformes, *Monopterus alba*, was found, and it accounted for 2.3% of the total species. Among the five units, unit 2 had the largest species number (27 species), followed by unit 4 (26 species);

units 5 and 1 had 22 and 21 species, respectively; and unit 3 had only 12 species.

With respect to the three trophic guilds, the maximum number of species were omnivores (25 species), accounting for 58.1% of the total species; 7 and 11 species were herbivorous and carnivorous and accounted for 16.3% and 25.6% of the total species, respectively. With respect to the tolerance of pollution, *Acrossocheilus fasciatus*, *Rhynchocypris oxycephalus*, *Opsariichthys bidens*, *Botia superciliaris*, *Leptobotia taeniops*, *Vanmanenia stenosoma*, *Pseudobagrus ondon*, and *Liobagrus styani* were sensitive species; *Pseudorasbora parva*, *Monopterus alba*, *Cyprinus carpio*, *Misgurnus anguillicaudatus*, and *Carassius*

Table 2: Species composition in the five units of the Shuaishui River Basin (mean \pm SD).

Species	Code	Tolerance	Trophic guild	Unit 1	Unit 2	Unit 3	Unit 4	Unit 5
Cypriniformes								
Cyprinidae								
<i>Zacco platypus</i>	Zac-pla	General	O	+	+	+	+	+
<i>Acrossocheilus fasciatus</i>	Acr-fas	Sensitive	H	+	+	+	+	+
<i>Phoxinus oxycephalus</i>	Pho-oxy	Sensitive	O	+		+		+
<i>Carassius auratus</i>	Car-aur	Tolerant	O		+		+	
<i>Hemiculter leucisculus</i>	Hem-leu	General	O		+			
<i>Pseudorasbora parva</i>	Pse-par	Tolerant	O	+	+			
<i>Pseudorasbora elongata</i>	Pse-elo	General	O		+			
<i>Cyprinus carpio</i>	Cyp-car	Tolerant	O		+			
<i>Hemibarbus labeo</i>	Hem-lab	General	C		+			
<i>Opsariichthys bidens</i>	Ops-bid	Sensitive	C	+			+	+
<i>Microphysogobio fukiensis</i>	Mic-fuk	General	O		+		+	+
<i>Platysmacheilus exiguus</i>	Pla-exi	General	O					+
<i>Microphysogobio tafangensis</i>	Mic-taf	General	O					+

Table Cont...

Species	Code	Tolerance	Trophic guild	Unit 1	Unit 2	Unit 3	Unit 4	Unit 5
<i>Microphysogobio kiatingensis</i>	Mic-kia	General	O		+		+	+
<i>Squalidus intermedius</i>	Squ-int	General	O		+	+	+	+
<i>Squalidus wolterstorffi</i>	Squ-wol	General	O	+			+	
<i>Aphyocypris chinensis</i>	Aph-chi	General	O	+				
<i>Gnathopogon taeniellus</i>	Gna-tae	General	O				+	
<i>Rhodeus ocellatus</i>	Rho-oc	General	H				+	+
<i>Rhodeus fangi</i>	Rho-fan	General	H			+	+	
<i>Rhodeus sinensis</i>	Rho-sin	General	H	+	+	+	+	
<i>Acheilognathus sp.</i>	Ach-eil	General	H		+		+	
<i>Acheilognathus barbatulus</i>	Ach-bar	General	H		+			
<i>Acheilognathus gracilis</i>	Ach-gra	General	H		+			
<i>Sarcocheilichthys nigripinnis</i>	Sar-nig	General	O	+				
<i>Sarcocheilichthys parvus</i>	Sar-par	General	O	+	+		+	+
<i>Varicorhinus barbatulus</i>	Var-bar	General	O			+	+	+
Cobitidae								
<i>Cobitis sinensis</i>	Cob-sin	General	O	+	+	+	+	+
<i>Botia superciliaris</i>	Bot-sup	Sensitive	C		+			
<i>Misgurnus anguillicaudatus</i>	Mis-ang	Tolerant	O	+	+	+	+	+
<i>Leptobotia taeniops</i>	Lep-tae	Sensitive	C	+				+
Mastacembelidae								
<i>Mastacembelus aculeatus</i>	Mas-acu	General	C	+	+			
Homalopteridae								
<i>Vanmanenia stenosoma</i>	Van-ste	Sensitive	O	+	+	+	+	+
Perciformes								
Gobiidae								
<i>Rhinogobius cliffordpopei</i>	Rhi-cli	General	C	+	+	+	+	+
<i>Rhinogobius sp.</i>	Rhi-nog	General	C	+	+		+	+
<i>Rhinogobius giurinus</i>	Rhi-giu	General	C	+	+			
Serranidae								
<i>Siniperca undulata</i>	Sin-und	General	C		+		+	
Eleotridae								
<i>Odontobutis obscurus</i>	Odo-obs	General	C	+	+	+	+	+
Siluriformes								
Amblycipitidae								
Liobagrus styani	Lio-sty	Sensitive	C				+	
Bagridae								
<i>Pelteobagrus eupogon</i>	Pel-eup	General	O		+			
<i>Pseudobagrus pralli</i>	Pse-pra	Sensitive	O				+	+
<i>Pseudobagrus ondon</i>	Pse-ond	Sensitive	O	+			+	+
Synbranchiformes								
Synbranchidae								
<i>Monopterus alba</i>	Mon-alb	Tolerant	O	+			+	+

auratus were tolerant species; and the others were general species.

Dominant Species

In this study, species with IRI higher than 5% were regarded as the dominant species. The number of dominant species in the five units was 5, 7, 3, 5, and 4 species (Table 3). *Acrossocheilus fasciatus*, *Vanmanenia stenosoma*, *Zacco platypus* were the three main dominant species in the entire Shuaishui River Basin.

Main Influencing Factors

The RDA and Monte Carlo permutation tests indicated that the altitude, water velocity, stream order, and water surface width had significant effects on the spatial distribution of the

fish. Fig. 2 shows the two-dimensional RDA biplots for the species-environmental variables. The eigenvalues of the first two axes were 0.183 and 0.082 and contributed to 40.9% and 18.3% of the total variance, respectively. The water surface width mainly contributed to the first axis; water velocity, second axis; and altitude and stream order, both axes.

Ecological Health Assessment

The assessment results based on the arithmetic mean values of the three evaluation indexes are listed in Table 4. The mean values of the five units (from 1 to 5) are 0.48, 0.70, 0.29, 0.64, and 0.57, respectively. Based on the set level, unit 3 was relatively poor, units 1 and 5 were general, and units 2 and 4 were good. The mean value of the entire Shuaishui River Basin was 0.51, and the health status was general.

Table 3: Dominant species in the five units of the Shuaishui River Basin.

Dominant species	Weight (g)	Per cent weight (%)	Individual number	Per cent individual number (%)	IRI (%)
Unit 1					
<i>Zacco platypus</i>	198.5	11.2	51	10.4	11.90
<i>Acrossocheilus fasciatus</i>	630.2	35.5	132	27.0	41.29
<i>Phoxinus oxycephalus</i>	295.1	16.6	71	14.5	6.86
<i>Vanmanenia stenosoma</i>	213.4	12.0	75	15.3	15.06
<i>Rhinogobius cliffordpopei</i>	69.5	3.9	71	14.5	12.17
Unit 2					
<i>Zacco platypus</i>	25.5	7.0	8	5.5	8.70
<i>Acrossocheilus fasciatus</i>	33.6	9.2	4	2.8	8.32
<i>Sarcocheilichthys parvus</i>	76.1	20.9	33	22.8	30.32
<i>Botia superciliaris</i>	28.3	7.8	8	5.5	9.23
<i>Misgurnus anguillicaudatus</i>	33.7	9.3	7	4.8	6.52
<i>Vanmanenia stenosoma</i>	47.1	12.9	16	11.0	5.55
<i>Rhinogobius cliffordpopei</i>	18.5	5.1	22	15.2	14.06
Unit 3					
<i>Acrossocheilus fasciatus</i>	1481.5	45.4	233	38.1	62.51
<i>Varicorhinus barbatulus</i>	813.4	24.9	112	18.3	7.19
<i>Vanmanenia stenosoma</i>	669.2	20.5	180	29.5	24.93
Unit 4					
<i>Zacco platypus</i>	326	19.2	122	21.0	26.35
<i>Acrossocheilus fasciatus</i>	520.2	30.6	127	21.8	34.41
<i>Acheilognathus sp.</i>	154.9	9.1	106	18.2	10.76
<i>Misgurnus anguillicaudatus</i>	148.8	8.8	28	4.8	7.12
<i>Vanmanenia stenosoma</i>	159.9	9.4	66	11.3	10.90
Unit 5					
<i>Zacco platypus</i>	272.7	13.1	86	11.4	12.51
<i>Acrossocheilus fasciatus</i>	674.1	32.3	183	24.3	35.34
<i>Vanmanenia stenosoma</i>	514.5	24.7	190	25.3	31.14
<i>Rhinogobius sp.</i>	125.4	6.0	138	18.4	11.05

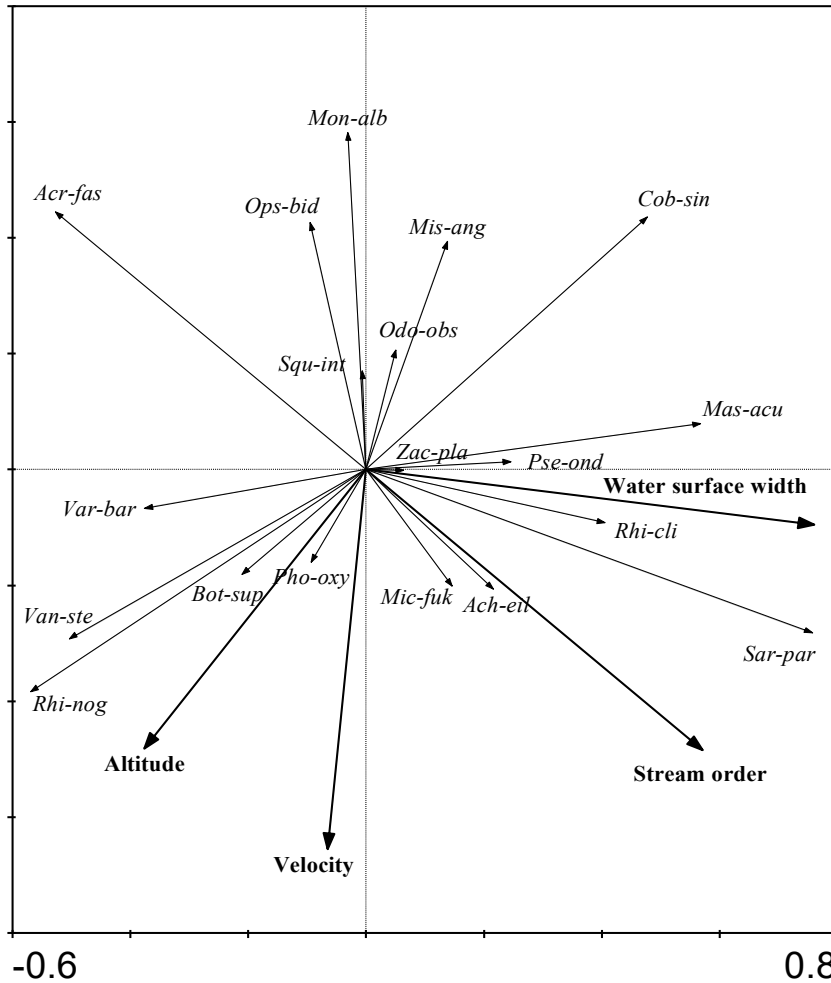


Fig. 2: Redundancy analysis for the correlation between fish distribution and environmental parameters (the abbreviations have been defined in Table 2).

Table 4: River health assessment of the five units of the Shuaishui River Basin.

	Number of classification unit (S)	Shannon-Wiener index (H)	Berger-Parker dominance index (D)	Arithmetic mean	Health status
Unit 1	0.44	0.34	0.66	0.48	General
Unit 2	0.75	0.48	0.87	0.70	Good
Unit 3	0.17	0.27	0.43	0.29	Relatively poor
Unit 4	0.64	0.51	0.76	0.64	Good
Unit 5	0.45	0.49	0.77	0.57	General

DISCUSSION

Species Composition and Spatial Distribution

Many studies have shown that artificial changes to the natural habitat of mountain rivers decrease the suitability of locally sensitive fish while increasing the suitability of

tolerant fish (Scott & Helfman 2001); usually, this causes the fish that originally inhabited the downstream regions to invade the upstream regions successfully (Rahel 2002). In this study, a total of 43 species of fish were collected from the Shuaishui River Basin, and the number of species is significantly lower than that in the adjacent Qingyi River Basin (57 species) in mountainous areas of Anhui

Province (Xiang 2011). This indicates that the ecological environment of the Shuaishui River Basin may have changed greatly. Some pollution-tolerant species that are usually distributed in stationary or slow-flowing waters (such as *Carassius auratus*, *Pseudorasbora parva*, *Rhodeus ocellatus*, *Misgurnus anguillicaudatus*, and *Monopterus alba*) were found upstream of the Shuaishui River Basin. A large number of small dams (mainly low-head dams) in the Shuaishui River Basin may be the main cause for this phenomenon. For agricultural irrigation and domestic water use, small dams were built everywhere in the Shuaishui River Basin, which changed local habitat parameters such as water velocity, water temperature, and sediment type and inevitably caused changes to the fish community structure and species diversity (Zhang et al. 2017).

In addition, an alien invasive species, *Lepomis auritus*, has been reported in other mountain rivers of Anhui Province (Wan et al. 2015). In the present study, no alien invasive fish were found, except for *Procambarus clarkii*, were found in the Shuaishui River Basin. *Procambarus clarkii*, a crayfish, belongs to the order Decapoda and family Cambaridae and it is native to northern Mexico and the southern United States. It is widely distributed in many countries worldwide because of its strong adaptability. The occurrence of this species in the Shuaishui River Basin also indicates that the ecological environment has undergone major changes. Some species that are endemic to China were found in this basin, namely, *Pseudorasbora elongata*, *Phoxinus oxycephalus*, *Microphysogobio tafangensis*, and *Microphysogobio kiatingensis*, but the population sizes were small.

Among the five units, species number was the lowest in unit 3 and the highest in unit 2. Differences in the natural environment and anthropogenic disturbances may be the main reasons for this phenomenon. The altitude of unit 2 is the lowest of the five units, and most sampling sites in this unit were located in fourth-order streams. According to Matthews (1986), species diversity usually increased with an increase in stream order because of increased spatial heterogeneity. The reason for the minimum species number in unit 3 may be mainly related to the relatively serious fishing activities in this region.

Main Influencing Factors and Health Assessment

In general, biotic, abiotic, and historical factors (such as species formation and extinction) have important filtering roles in local fish communities and affect the species composition, community structure, and spatial distribution of fish at different spatial scales (Dauwalter et al. 2008). Previous studies in China have shown that the fish community structure

in mountain rivers is mainly influenced by the local habitat environment and spatial river position. The local habitat environment includes altitude, water velocity, sediment type, conductivity, water temperature, and water depth, and spatial river position mainly includes stream order, link, and downstream link (Yan et al. 2011, Li et al. 2015). In this study, the RDA showed that the main parameters that affected the spatial distribution of fish were altitude, water velocity, water surface width, and stream order, which is consistent with the above-mentioned conclusions. Altitude has always been regarded as an important environmental factor because environmental factors such as water temperature and water velocity will change correspondingly with a decrease in altitude. The RDA sequence diagram showed that *Phoxinus oxycephalus* and *Vanmanenia stenosoma* are mainly distributed in water bodies with a high altitude and water velocity, whereas *Misgurnus anguillicaudatus*, *Monopterus alba*, *Mastacembelus aculeatus*, and *Odontobutis obscurus* are distributed in waters with a low altitude and water velocity. The stream order and water surface width also had significant effects on the fish community, and this may be mainly because the diversity and complexity of the habitat increased as the stream order and water surface width increased. The RDA sequence diagram showed that *Sarcocheilichthys parvus* and *Microphysogobio fukiensis* are mainly distributed in streams with a higher stream order and large water surface width, whereas *Acrossocheilus fasciatus* and *Opsariichthys bidens* are mainly distributed in streams with lower stream order.

The ecological health of the Shuaishui River, an important river in the mountainous area of Anhui Province, is related to the sustainable development of the regional economy. The ecological health assessment results showed that units 1 and 5 were general, units 2 and 4 were good, and unit 3 was relatively poor. This indicated that the health status of the different units in the Shuaishui River Basin varied greatly, and the main reason may be related to the different economic levels and anthropogenic disturbances. To protect and manage the Shuaishui River Basin, it is necessary to perform targeted management of the different units. We suggest (1) increased monitoring of the water environment and fish resources and control of the polluted waters; (2) improved fishery administration, implementation of a no-fishing system, and restoration of the natural habitat of fish in the Shuaishui River Basin; (3) enhancement of artificial fisheries to increase fishery resources and species diversity in the Shuaishui River Basin; and (4) evaluation of the impacts of dams on fish resources in this basin and establishment of scientific and rational dam-control strategies.

ACKNOWLEDGEMENTS

We thank Dr Wei Chen for helpful comments and suggestions. This work was supported by the National Natural Science Foundation of China (No. 41173032), Key Program for Science and Technology Development of Anhui Province (No. 1804b06020358).

REFERENCES

- Barbour, M.T.J., Gerritsen, B.D., Snyder, B.D. and Stribling, J.B. 1999. Rapid Bioassessment Protocols for Use in Streams and Wadeable Rivers: Periphyton, Benthic, Macroinvertebrates, and Fish. Second Edition. Environmental Protection Agency, Office of Wetlands, Oceans, and Watersheds, Washington, D. C.
- Dauwalter, D.C., Splinter, D.K., Fisher, W.L. and Richard, M. 2008. Biogeography, ecoregions, and geomorphology affect fish species composition in streams of eastern Oklahoma, USA. *Environmental Biology of Fishes*, 82(3): 237-249.
- Karr, J.R. 1981. Assessment of biotic integrity using fish communities. *Fisheries*, 6(6): 21-27.
- Karr, J.R., Fausch, K.D. and Angermeier, P.L. 1986. Assessing Biological Integrity in Running Waters. A Method and its Rationale. Illinois Natural History Survey, Champaign, Special Publication.
- Kuehne, R.A. 1962. A classification of streams, illustrated by fish distribution in an eastern Kentucky creek. *Ecology*, 74(4): 1659-1673.
- Li, Y., Yan, Y., Zhu, R., Zhou, K., Chu, L., Wan, A. and Wang, X. 2015. Spatial variations in fish assemblages within the headwater streams of the Wanhe watershed: A review network-based approach. *Journal of Fishery Sciences of China*, 21(5): 988-999.
- Matthews, W.J. 1986. Fish faunal "breaks" and stream order in the eastern and central United States. *Environmental Biology of Fishes*, 17(2): 81-92.
- Ministry of Environmental Protection, China 2014. Technical Guidelines for River Basin Ecological Health Assessment (Revised). pp. 1-62.
- Rahel, F.J. 2002. Homogenization of freshwater faunas. *Annual Review of Ecology and Systematics*, 33: 291-315.
- Scott, M.C. and Helfman, G.S. 2001. Native invasions, homogenization, and the mismeasure of integrity of fish assemblages. *Fisheries*, 26(11): 6-15.
- Strahler, A.N. 1957. Quantitative analysis of watershed geomorphology. *Transactions of American Geophysical Union*, 38(6): 913-920.
- Tang, T., Cai, Q. and Liu, J. 2002. River ecosystem health and its assessment. *Chinese Journal of Applied Ecology*, 13(9): 1191-1194.
- Wan, A. 2016. The health diagnosis of headwater stream based on fish cohort in Pihe River catchment. Nanjing: Doctoral Dissertation of Nanjing University.
- Wan, A., Zhang, X., Fang, Y., Zhong, M., Li, N. and An, S.Q. 2015. Being vigilant to spreading and breeding of the green sunfish in Ta-pieh mountain area. *Acta Hydrobiologica Sinica*, 39(4): 685.
- Xiang, X. 2011. The research of spatial and temporal patterns in fish assemblages during the Qingyi watershed. Wuhu: Master Dissertation of Anhui Normal University.
- Yan, Y.Z., Xiang, X.Y., Chu, L., Zhan, Y.J. and Fu, C.Z. 2011. Influences of local habitat and stream spatial position on fish assemblages in a dammed watershed, the Qingyi Stream, China. *Ecology of Freshwater Fish*, 20(2): 199-208.
- Zhang, X.K., Wang, H.L., Wan, A., Fang, Y.X., Liu, Z.G., Zheng, A.F., Chen, M.M. and Yu, D.P. 2017. Fishes in headwater streams of the Pihe River basin: spatial distribution pattern and its main influencing factors. *Journal of Lake Science*, 29(1): 176-185.



Heavy Metals in Soils and Vegetation from Wastewater Irrigated Croplands Near Ahmedabad, Gujarat: Risk to Human Health

Bibhabasu Mohanty^(**)†, Anirban Das^{*}, Reema Mandal^{*}, Upasana Banerji^{***}(****) and Sukanya Acharyya^{*}

^{*}Department of Sciences, Pandit Deendayal Petroleum University, Gandhinagar-382007, Gujarat, India

^{**}Department of Civil Engineering, SAL Institute of Technology and Engineering Research, Ahmedabad-380060, Gujarat, India

^{***}Physical Research Laboratory, Navrangpura, Ahmedabad-380009, Gujarat, India

^{****}National Center for Earth Science Studies, Thiruvananthapuram-695011, Kerala, India

†Corresponding author: Bibhabasu Mohanty; bibhabasu.mohanty@gmail.com

Nat. Env. & Poll. Tech.
Website: www.neptjournal.com

Received: 20-08-2020

Revised: 05-10-2020

Accepted: 16-10-2020

Key Words:

Hazard quotient

Heavy metals

Risk-assessment

Wastewater irrigation

ABSTRACT

Heavy metal accumulation in soils, and subsequently, in vegetation by long-term wastewater irrigation has a potentially detrimental effect on humans via their transfer along the food chain. In this reconnaissance study the effects of wastewater irrigation on the accumulation of heavy metals (Co, Cr, Cu, Mn, Ni, Pb and Zn) in soils and vegetables from croplands along some ~60 km stretches of Sabarmati River, near Ahmedabad city were assessed. Geochemical factors associated with metals in the soil-water environment seem to regulate more the metal transfer (soil-to-vegetable) than the physiological factors associated with the vegetable's types.

The risk associated with the dietary intake of metal contaminated vegetables was quantified by Hazard Quotient (HQ). HQ was found to be very less sensitive on to the dietary intake pattern (e.g., leafy versus non-leafy vegetables) of the consumers. In contrast to low risk associated with Co, Cu, Ni and Zn with very low HQ values, high risk was found for Pb (HQ of $\sim 6.1 \pm 0.6$) followed by both Mn and Cr (HQ of $\sim 1.0 \pm 0.1$). Based on the results on wastewater irrigation in the studied region, we suggest more efficient treatment of wastewater facilities and semi-decadal monitoring of heavy metal in vegetables grown under wastewater irrigated soils.

INTRODUCTION

Discharge of untreated or inefficiently treated municipal and industrial wastewater to waterways/soils resulting in degradation of water/soil quality is a major environmental concern in many (semi) urban areas of several countries. A decline in the availability of clean surface water or groundwater has led farmers to look for easily available alternate sources of irrigation waters in the form of domestic/municipal/ industrial wastewaters. In addition, higher crop productivity has tempted farmers to the use of wastewaters for irrigation as these waters are enriched with essential NPK-nutrients.

It is now well recognized that long-term wastewater irrigation by and large leads to increasing levels of metals (e.g., Cr, Cu, Pb, Ni, Zn, Hg, Co, Mn, etc.) in irrigated soils and vegetations, and has a potentially detrimental effect on humans via heavy metal transfer via the food chain (Chopra 2015, Milacic & Kralj 2003 Singh et al. 2004, Jassir et al. 2005, Sharma et al. 2006, Singh & Jaswant 2006, Akpor et al. 2014). A few of these heavy metals (e.g., Zn, Mn, Ni, Cu and Cr) though are required by humans in trace levels, but uptake

of heavy metals beyond their respective permissible limits into the human body leads to cardiovascular, nervous, kidney and bone diseases (WHO 1998, Jarup 2003). For example, Cd, As and Cr are carcinogenic, whereas, Hg and Pb are known to cause abnormal growth of children and reduction in haemoglobin synthesis (Ahmad 2016, Chopra 2015). As vegetables are important sources of carbohydrates, proteins, minerals and fibres and are one of the major components of the human diet, accumulation of higher levels of heavy metals in vegetables is a cause of concern to human health (Tripathi et al. 1997, Khillare et al. 2004, Wang et al. 2005, Demirezen & Aksoy 2006, Chary et al. 2008, Tiwari et al. 2011). In the above context, it is thus important to assess heavy metals in vegetable crops grown in wastewater irrigated croplands.

Previously, investigations have been carried out in this domain in several countries (Mapanda et al. 2005, Gebrekidan et al. 2013, Hu et al. 2014, Ahmad et al. 2016, Qureshi et al. 2016). For example, extensive studies have been carried out in Ethiopia wherein it was concluded that risk to human health associated with the heavy elements in vegetables was low but the long-term effect needs to be assessed further

(Woldetsadik et al. 2017, Gebreyohannes et al. 2018). In contrast, Mapanda et al. (2005) reported significantly high Cr, Cu, Cd, Zn, Pb and Ni in wastewater irrigated croplands in Zimbabwe. In China, Hu et al. (2014) on their study on greenhouse vegetation and its soils concluded that the leafy vegetables had relatively higher concentrations of heavy metals and higher transfer factor than root-type and fruit-type vegetables. In Dubai, prohibition exists for wastewater use in agriculture and it was found from experiments conducted using treated wastewater that heavy metals posed little threat to human health (Qureshi et al. 2016).

In India, urbanization has resulted in a high population density in the medium-to-large scale cities. This has led to increasing processing-demands on the municipal wastewater treatment plants and has resulted in the spreading of the wastewater irrigated lands surrounding the cities (Chary et al. 2008). The potential impact of wastewater irrigation in accumulation of heavy metals in the soils and subsequently in vegetables has resulted in a few studies from Indian cities (Gupta et al. 2010, Ghosh et al. 2012, Chopra et al. 2015, Saha et al. 2015). For example, the sewage water irrigated vegetables in Kolkata (3rd most populated Indian city) were found to have higher concentrations of Pb and Cd than their respective limits prescribed by FAO/WHO (Saha et al. 2015). One of the recent studies (Chopra et al. 2015) analysed the trend of trace metal accumulation in different parts of plants; e.g., Pb accumulated in the flower part, Cu and Zn in the leafy part whereas Ni, Cd and Cr in the root part. Gupta et al. (2010) linked a stress-like condition in two plant species (*Colocasia esculentum* and *Raphanus sativas*) to trace metal accumulation in their tissues which increased the sugar content and decrease in their chlorophyll and soluble protein contents. Higher accumulation levels of heavy elements were found in vegetation grown in wastewater irrigated soils compared to tube-well irrigated soils highlighting the risk in their consumption (Rattan et al. 2005, Tiwari et al. 2011). Sharma et al. (2009) pointed out that post-harvest processes of transport and storage can lead to higher heavy metals concentration in vegetables collected at the production site, i.e. irrigated field, compared to those from the market areas.

The case studies above are skewed to the northern and eastern regions of the country (Agrawal 2003, Sharma et al. 2006, 2008, 2009, Tiwari et al. 2011), and except for a few (Tiwari et al. 2011, Tripathi et al. 1997), case studies focusing on the western regions of India are sparse. The present study is focused on wastewater irrigation from Ahmedabad, a city which has a history of wastewater irrigation since the last few decades (Palrecha et al. 2012). There has not been, to the best of our knowledge, any article published from the region on wastewater irrigation. Therefore, this reconnaissance study

is an attempt to bridge the existing gap and was undertaken to assessing heavy metals in vegetable crops grown in wastewater irrigated croplands along some ~60 km stretch of Sabarmati River and their effects on a large population, from an important yet unexplored region in western India.

The specific goals of the present study are: (i) to get base-line data of the selected heavy metals (Co, Cr, Cu, Mn, Ni, Pb and Zn) above in a group of largely consumed vegetables such as brinjal, tomato, cabbage, cauliflower and spinach, collected from different locations where wastewater irrigation has the predominant role, (ii) quantitative assessment of the transfer of metals by using the index transfer factor from soils to the vegetables, and the factors controlling it, and (iii) finally a quantitative assessment of the health risk by using the index hazard quotient posed by the ingestion of metals via consumption of vegetables to the greater population of the Ahmedabad city.

MATERIALS AND METHODS

Study area: The study area is located around the disposal point of Vasna Sewage Treatment Plant (STP) of Ahmedabad city, which is located along the bank of the River Sabarmati. Ahmedabad city has a population of greater than six million and an urban area of 464 km². According to Ahmedabad Municipal Corporation (2011), the city has an existing wastewater treatment capacity of 1075 Million Litre per Day (MLD) compared to the actual requirement of 1186 MLD. According to an estimate by International Water Management Institute, New Delhi (2012), about 9450 hectares in and around the Ahmedabad region is irrigated by wastewater. This comprises nearly 45% of the net irrigated area of 21086 hectares.

Vasna STP (capacity 240 MLD) is located along the bank of Sabarmati River and processes domestic wastewater emanating from household and small business activities within the limits of Ahmedabad Municipal Corporation (AMC). The catchment area of the Sabarmati River is surrounded by two semi-industrial units, Narol and Vatva, which host many small to medium-sized industries (e.g., plastics, small-scale chemical factories, metal and alloy processing, electrochemical processing, dyes and paints, wood and paper mills, etc.). Mixing of industrial effluents into the environs of the area studied occurs by two pathways. Firstly, wastewaters from these industrial units are carried directly or indirectly through small channels or sub-channels into the Sabarmati River. Regulations by the state government's pollution control authority, Gujarat Pollution Control Board, require efficient treatment of all industrial effluents before they are discharged to the environs; however, the industrial units are not well known for adopting the best practices and

inefficiently treated industrial effluents are released often into the environs. Secondly, through drainage channels, the semi-treated/untreated industrial effluents from the industrial sites are carried into the sewer channels and finally into the Vasna STP. The latter of the two above processes is expected to have a lower impact on the environment due to wastewater treatment at the STP before their release to the Sabarmati River. Therefore, the croplands in the study area which are irrigated by wastewater from Sabarmati River channels derive their heavy metals from the domestic activities and a significant yet uncertain contribution from the industrial activities. Therefore, this process underscores the potential risk of pollutant transfer to the vegetation grown in croplands of the study area.

Sampling and Sample Processing

Samples used for this study included five types of different vegetables ($n = 38$), wastewater irrigated soils in which vegetation are grown ($n = 8$) and wastewater samples ($n = 3$). For the collection of soils and vegetation, eight different sampling locations were selected: Gyaspur, Visalpur, Kasindra, Saroda, Chandisar, Kaloli, Asmalli and Khada (Fig. 1). At two locations, two of the vegetable samples were not available for collection. Gyaspur is the point from where the wastes from Vasna STP are disposed to Sabarmati River; three samples were collected from this site. The sampling sites are located along the Sabarmati River up to a maximum distance of 60 km from the point of disposal (i.e., Vasna).

Samples were collected during October and November of the year 2015. In the study area, July, August and September generally account for most of the rains during the year and

very scanty rainfall occurs during the sampling months. In fact, during the two sampling-months, the total number of rainy days was zero. The impact of low rainfall during October and November leads to the very low flow of the Sabarmati River and hence underscores the contamination effect of river water by the wastewater.

Five different types of vegetation samples such as brinjal (*Solanum melongena*), tomato (*Solanum lycopersicum*), cabbage (*Brassica oleracea* var. *capitata*), cauliflower (*Brassica oleracea* var. *botrytis*) and spinach (*Spinacia oleracea*) were collected. These largely constitute the staple diet of the population in the study area and consumed mainly amongst the vegetables. The samples were washed with tap water profusely, followed by de-ionized water and uneatable portions were removed and then samples oven-dried at 80°C. Dried samples were crushed by using an agate mortar and pestle, homogenized and stored in plastic containers to avoid heavy metal contamination. For extraction of heavy elements, 0.3 g of samples was digested with 6 mL of HNO₃ at 175°C for 10 min at 30 bar pressure and 50°C at 30 bar pressure. After digestion, samples were diluted up to 30 mL with 2% HNO₃. The digested samples were stored for analysis of Co, Cr, Cu, Mn, Ni, Pb and Zn.

Eight soil samples were collected from the croplands where municipal wastewater drawn from the Sabarmati River is used for irrigation. Samples were collected by using a plastic scoop from a depth of 15 cm and were sieved with 1-mm sieve (100 mesh) to remove unwanted particles, and dried at 105°C for 24 hours. The samples were stored in airtight zip-lock pouches at room temperature. For heavy element analysis in soil samples, 0.3 g of sample was taken, mixed

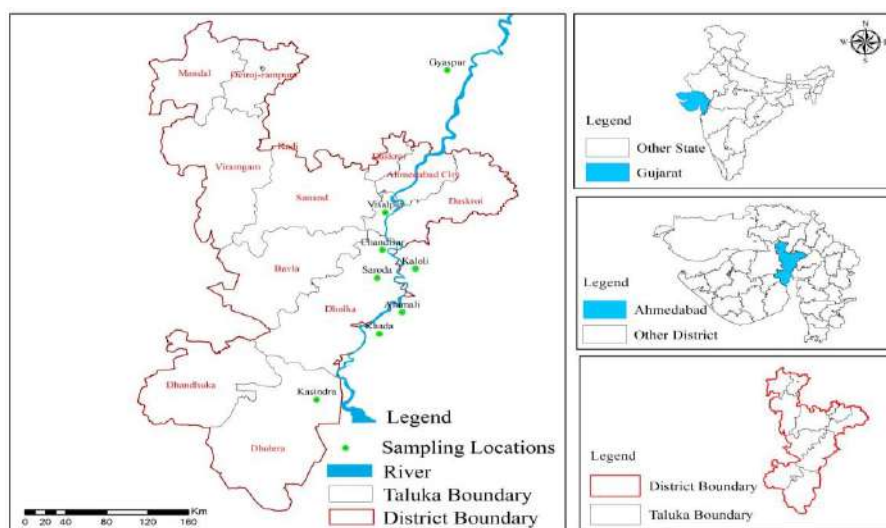


Fig. 1: Study area showing the sampling locations.

with 6 mL of HNO₃ and 1 mL of HF. The samples were then digested in Titan MPS Direct Temperature Control™ digester of Perkin Elmer.

Three wastewater samples (~500 mL) were collected in HDPE bottle from three different points of disposal. To avoid deterioration due to microbial activity, 2 mL of concentrated HNO₃ was added after filtration of the samples. Measurement of pH, electrical conductivity, total dissolved solids, and the temperature was carried out on site. For heavy metal analysis, the sample was diluted up to 300 µS of conductivity. Samples were acidified and stored at 4°C till further analysis.

During sampling and its processing care was taken to avoid contact of the samples with metals surfaces, to avoid any heavy metal contamination from any processes/sources in and around the working environment.

Analysis of Samples

The heavy metal concentration in digested samples was measured by inductively coupled plasma mass spectrometry (ICP-MS; PerkinElmer, Thermo-X series2) at Physical Research Laboratory, Ahmedabad. The digested samples were analysed for various heavy elements like Co, Cr, Cu, Mn, Ni, Pb, Zn by aspirating the sample in ICPMS, which was calibrated using Merck multi-elemental standards. The instrument reproducibility was determined by carrying out replicate the analysis for the elements analysed while the accuracy was observed using certified reference standards such as NOVA (Amin et al. 1972) and MAG (Govindaraju 1994). Analytical precisions of measurement for heavy elements were better than ±5% and accuracy within ±6% (Banerji et al. 2017).

The pH, electrical conductivity, total dissolved solids, and temperature of the sewage samples were measured by a multiple parameter kit. Soil pH was measured by a hand-held pH meter in the samples by mixing a known weight of soil with de-ionized water in the weight ratio of 1:2 and keeping it undisturbed for 10 minutes.

Statistical and Uncertainty Analyses

Student's *t*-test was used to compare averages with their corresponding *p*-values to bring out the statistical significance (or otherwise) of such comparisons. The statistical and mathematical tools of Microsoft Excel Software were used for such calculations. Principal Component Analysis (PCA) was performed by using Statistical Package for Social Services (SPSS) software, statistics version 23. Additionally, overall uncertainty in parameters such as transfer factors and hazard quotients was carried out by using error propagation technique assuming a certain % error on the individual parameters in their respective equations.

RESULTS AND DISCUSSION

Heavy Metals in Wastewater

The pH, TDS, temperature and heavy metal concentration in the three wastewater samples are reported in Table 1. These parameters provide information about the quality of one of the important point sources (i.e., sewage) that contaminate the water of the river. pH in the samples ranged from nearly neutral to moderately alkaline (7.1 to 8.4) while the temperature varied from 32.0°C to 32.7°C. A large variation, a factor of 6, was observed in the electrical conductivity (2117 to 12750 µS.cm⁻¹) and the total dissolved solids (1061 to 6360 ppm).

Concentrations of heavy metals (µg.mL⁻¹) in the disposed sewage water samples were found to vary in the following ranges (Table 2): Co (2.1-2.2), Cr (1.4-1.9), Cu (0.1-0.9), Mn (0.2-3), Ni (1-1.9), Pb (0.4-1.6) and Zn (5.1-19). These values are higher than their respective prescribed safe limits of heavy metals used for irrigation provided by Indian Standard, World Health Organization (WHO) and European Union Standards. For example, when compared to the Indian Standard values, the average Cr is found to be higher by a factor of ~3, whereas these factors are ~12 for Pb, ~2 for Cu, ~13 for Mn and ~2.5 for Zn. For Ni the Indian standard value is not reported; however, when compared

Table 1: Physico-chemical characteristics and heavy metal concentration (µg.mL⁻¹) in sewage samples.

Outlet No	pH	EC (µS/cm)	TDS (ppm)	Temp (°C)	Co	Cr	Cu	Mn	Ni	Pb	Zn
1	7.09	2117	1061	32.0	2.1	1.5	0.9	1	1.7	1.5	17.4
2	7.50	12750	6360	32.6	2.2	1.9	0.1	3	1.9	1.6	19
3	8.45	5950	2980	32.7	2.1	1.4	0.1	0.2	1	0.4	5.1
Guideline for safe limits of heavy metals in irrigated water (µg.mL ⁻¹)											
Indian Standard (2000)					-	0.05	0.05	0.10	-	0.10	5.0
WHO/FAO (2007)					-	0.10	0.20	0.20	0.20	5.0	2.0
European Standard (2006)					-	-	-	-	-	-	-

to the EU value, the average Ni was found to higher by a factor of ~6. Such comparison could not be made for Co as the permissible limits by the Indian, WHO and EU were not reported.

A comparison of the wastewater concentration data in the present study was made with those collected from a nearby city, Vadodara (Tiwari et al. 2011), though industrial wastewater was used for irrigation. It was observed that the average Cr, Pb and Ni in industrially treated wastewater are higher by factors of about 3.5-4 than in the sewage treated water, whereas for Mn it is ~7 and for Cu it is ~16. Such a higher concentration of heavy metals in industrially treated water is not unexpected considering the difference in nature of the samples in the two studies. In our study, the collected wastewater is treated wastewater from the STP which is linked to domestic activities and a few small scale industrial activities operating near the treatment plant, and by and largely unaffected by large scale industrial activities. In the case study of Tiwari et al. (2011), industrial wastewater in their study area was primarily derived from chemical, petrochemical, dyes and paints, and agrochemical industries. Tiwari et al. (2011) also found 1-2 orders of magnitude lower levels of heavy metals in groundwater compared to the industrial wastewater. From the discussion above, from a qualitative standpoint, the metal concentrations generally followed the trend: [Metal]_{Industrial Water} > [Metal]_{Sewage Water} >> [Metal]_{Ground Water}

Heavy Metals in Wastewater Irrigated Soils

For the collected soil samples, the pH varied from 6.5 to 7.8 (Table 2). The soil samples closest to and farthest from the

point-of-discharge, i.e. Gyaspur and Khada respectively, have alkaline pH of 7.8 and 7.4, respectively, while sample at Saroda (~20 km downstream) was acidic (pH=6.5). Rest of the samples have close to neutral pH, in the range of 7.0 ± 0.2 . The mobility of metals in soil zones is regulated by processes such as adsorption, precipitation and complexation, and soil pH is one of the parameters which affects these processes. Processes/factors regulating soil pH though complicated depends on the exchangeable cations in soils, the chemistry of the water that passes through the soil zones, presence of ligands and the soil carbonates.

Average concentrations ($\mu\text{g.g}^{-1}$) of metals in the eight soil samples follow the trend: Zn (421 ± 62) > Mn (336 ± 49) > Cu (201 ± 30) > Cr (71 ± 20) > Ni (51 ± 8) > Pb (42 ± 6) > Co (9 ± 1); the observed variability between the lowest and highest concentrations in all metals are within a factor of 2. Successive-pair *t*-tests show that the averages are statistically different with confidence limits of > 99% ($p < 0.01$).

A closer analysis of the soil data highlights a few important observations. All the metals exceed the range/upper limit of WHO/EU standard values. Good inter-correlations (r^2 ranges from 0.73-0.99) between almost all of the metal concentrations were observed which is suggestive of common processes/sources that contribute to these metals in the soils. Among the eight soil sample collection sites, the sample collected from Gyaspur had the maximum concentration of all analysed metals compared to other sites. Gyaspur is the area where the effluents from Vasna treatment plant get disposed off which leads to the maximum accumulation of these metals in the agricultural field compared to all other sites.

Table 2: pH and heavy metal concentration ($\mu\text{g.g}^{-1}$) in irrigated soil samples.

Location	pH	Co	Cr	Cu	Mn	Ni	Pb	Zn
Kasindra (S1)	6.82	9.5	55.7	216	367	55.9	43.6	465
Saroda (S2)	6.53	9.3	92.0	212.1	363	53.4	46.3	447
Chandisar (S3)	6.83	8.8	64.7	210.2	338	52.8	45.8	428
Kaloli (S4)	6.95	7.9	64.4	171.4	281	41.9	37.9	367
Asamali (S5)	7.20	7.8	52.2	161.1	280	42.4	34.6	341
Khada (S6)	7.40	8.3	62.3	185.3	311	46.3	35.1	385
Gyaspur (S7)	7.80	11.2	109.3	255.6	425	64.6	50.2	535
Visalpur (S8)	7.28	8.9	66.2	197.7	323	49.3	44.7	400
Guideline for safe limits of heavy metals in irrigated soil ($\mu\text{g.g}^{-1}$)								
Indian Standard (2000) ^a		-	-	135-270	-	75-150	250-500	300-600
WHO/FAO (2007) ^a		-	-	-	-	-	-	-
European Standard (2006) ^a		-	150	140	-	75	300	300
MACs for trace elements in agricultural soils ^b		20-50	50-200	60-150	-	20-60	20-300	1-300

^a Singh et al. (2010); ^b Kabata-Pendias & Mukherjee (2007)

There was a decrease in metal concentration as a function of distance from the Gyaspur site. When concentrations of individual metals were plotted as a function of distance, all other metals (except for Cr) show reasonably good correlation ($r^2 > 0.56$) with negative slopes and positive intercepts. The intercept of each plot provides an assessment of the concentration at the Gyaspur-site (0 km), and it is interesting to note that these values matched reasonably well with their respective measured values. The decrease of metal concentration in soils at the downstream sites can be attributed to natural variation or a linear decrease, or a combination of both. Natural variability as a cause for the

downstream decrease may still be likely for metals Pb, Cr and Co where the decrease is reasonably low; however, for the other metals, it is unlikely as the decrease in concentrations is large considering the distance from the origin-site. The most likely cause for a decrease of Ni, Cu, Mn and Zn is their particle reactivity when they are carried along the course of the river, which in turn, is reflected in the soils at respective sites.

Heavy Metals in Vegetables

Concentrations (dry wt. basis) of Co, Cr, Cu, Mn, Ni, Pb and Zn (Table 3) in edible parts of the vegetables varied

Table 3: Heavy metal concentrations ($\mu\text{g.g}^{-1}$; dry weight basis) in vegetable samples.

Plant species	Co	Cr	Cu	Mn	Ni	Pb	Zn
Brinjal: Visalpur	0.34	5.60	5.90	106.7	3.10	1.00	12.44
Saroda	0.12	5.80	8.80	15.10	2.80	0.70	12.74
Khada	0.12	5.80	8.50	15.62	2.80	0.70	13.40
Asmalli	0.13	6.40	9.10	15.81	3.00	0.60	14.57
Gyaspur	4.20	7.00	0.04	47.00	0.70	6.90	44.10
Kasindra	0.09	7.20	7.60	12.78	3.50	0.50	11.44
Chandisar	0.10	7.50	9.30	12.35	3.80	0.50	12.53
Kaloli	0.20	8.80	8.10	17.37	4.10	1.30	15.86
Tomato: Chandisar	0.35	6.70	6.20	13.57	3.50	3.70	10.05
Kaloli	0.121	9.00	9.90	15.00	4.20	0.80	19.13
Asmalli	0.23	5.90	7.10	16.27	2.90	1.70	12.27
Saroda	0.33	5.80	5.10	21.14	3.10	4.00	9.00
Visalpur	0.20	5.40	7.20	20.77	2.70	0.90	12.81
Kasindra	0.46	7.60	7.50	17.79	3.80	5.00	12.19
Khada	0.51	5.80	7.20	19.96	2.90	5.60	12.06
Gyaspur	2.20	6.70	0.04	25.00	1.20	4.20	21.50
Cabbage: Chandisar	0.323	7.8	3	60.14	4.2	1.6	10.6
Saroda	0.124	5.4	2.2	15.31	2.8	0.4	13.99
Visalpur	0.481	6	3.3	24.71	3.1	4.5	8.93
Kasindra	0.317	7.6	2.3	31.73	4	2.4	10.5
Khada	0.322	5.6	2.1	39.12	3.1	1.4	10.49
Gyaspur	2.2	5.3	2.0	18.0	2.8	0.4	4.4
Chandisar	0.323	7.8	3	60.14	4.2	1.6	10.6
Saroda	0.124	5.4	2.2	15.31	2.8	0.4	13.99
Cauliflower: Chandisar	0.227	7.1	3.4	19.06	3.8	1.3	16.4
Kaloli	0.146	6.2	3.7	13.08	3.3	1.3	14.64
Asmalli	0.165	5.6	2.3	18.12	2.9	1.1	16.04
Saroda	0.212	5.3	2.2	20.43	2.7	0.8	14.76
Visalpur	0.193	5.6	2.5	18.98	3.0	1.7	18.78
Kasindra	0.213	7.8	2.4	19.14	3.9	0.8	14.09
Khada	0.142	5.2	2.1	14.97	2.7	0.8	14.34

Plant species	Co	Cr	Cu	Mn	Ni	Pb	Zn
Gyaspur	2.2	6.2	0.07	13.0	0.8	0.4	9.5
Spinach: Chandisar	0.412	8.9	9.8	40.13	3.9	2.4	31.22
Kaloli	0.302	5.6	6.8	109.8	3.1	0.7	16.19
Asmalli	0.316	5.3	5.7	104	2.7	0.7	11.86
Saroda	0.126	5.8	8.7	15.59	2.8	0.6	13.93
Visalpur	0.246	5.4	6.5	86.4	2.3	1.1	16.71
Kasindra	0.381	9.5	8.9	41.51	4.1	2.4	32.57
Khada	0.276	5.6	7	88.12	2.5	1.1	19.5
Gyaspur	11.3	11.8	0.067	15.0	2.9	8.4	11.3
Guideline for safe limits of heavy metals in agricultural products ($\mu\text{g}\cdot\text{g}^{-1}$)							
Indian Standard (2000) ^a	-	30.0	-	1.5	2.5	50.0	
WHO/FAO (2007) ^a	-	40.0	-	-	5.0	60.0	
European Standard (2006) ^a	-	-	-	-	5.0		
Mean TE concentrations in food crop and Vegetables grown in various countries ^b	0.005-0.27	3-8	-	0.06-1.3	0.2-2.4	1.2-2.7	

^aSingh et al. (2010); ^bKabata-Pendias and Mukherjee (2007)

substantially among the different vegetables and different metals, indicating that the metal assimilation process is both plant and element-specific. Tiwari et al. (2011) pointed out that metal accumulation and its translocation into different parts of the plant is metal-specific and did not follow any particular pattern. In the following discussion, concentrations of elements in different vegetables, and a comparison with values reported from other studies are made.

Cobalt (Co): Co is required by *Rhizobium* that fixes the nitrogen. The range of Co reported for vegetation worldwide is 0.005-0.27 $\mu\text{g}\cdot\text{g}^{-1}$ and the range obtained from this study falls within 0.1-4.2 $\mu\text{g}\cdot\text{g}^{-1}$, excluding one sample with a value of 11.3 $\mu\text{g}\cdot\text{g}^{-1}$. It is interesting to note that the highest Co values observed in all vegetable categories belong to the Gyaspur site; the average Co value at the Gyaspur site is 4.4 $\mu\text{g}\cdot\text{g}^{-1}$ compared to values of 0.2-0.3 $\mu\text{g}\cdot\text{g}^{-1}$ for the remaining sites ($p < 0.01$). The maximum average concentration was observed for the (leafy) spinach (1.7 $\mu\text{g}\cdot\text{g}^{-1}$) which is ~2.5 times of the average obtained for brinjal, tomato, cabbage, and ~4 times that of the average value of cauliflower (spinach > brinjal > tomato > cabbage > cauliflower) ($p = 0.025$). Kabata-Pendias & Mukherjee (2007) reported that the leafy plants like lettuce, cabbage and spinach had a high Co concentration compared to grasses and cereals.

Chromium (Cr): Cr in all vegetables ranged from 5.2 to 11.8 $\mu\text{g}\cdot\text{g}^{-1}$ with an average of $6.6 \pm 1.5 \mu\text{g}\cdot\text{g}^{-1}$. All values in the present study are higher than the range (0.01-0.41 $\mu\text{g}\cdot\text{g}^{-1}$) found in vegetation all over the world (Kabata-Pendias & Mukherjee 2007). The average (plant) values are also higher than tolerable level (2 $\mu\text{g}\cdot\text{g}^{-1}$) and to the toxic levels (5 $\mu\text{g}\cdot\text{g}^{-1}$) for plants reported by Kabata-Pendias & Mukherjee (2007).

The spinach sample collected at Gyaspur have the highest Cr (11.8 $\mu\text{g}\cdot\text{g}^{-1}$) and cauliflower from Khada area have the lowest Cr (5.2 $\mu\text{g}\cdot\text{g}^{-1}$). Based on the average concentration in vegetable samples the following trend was obtained: spinach > brinjal > tomato > cabbage > cauliflower ($p = 0.001$); however, all average values are similar within their (1σ) variation.

Copper (Cu): Cu is one of the essential nutrients to plants due to its physiological effect on the growth of the plant; however, excess of it is detrimental to plants as it causes membrane damage and suppresses enzymatic activities (Alaoui-Sosse et al. 2004). Critical limit of Cu toxicity in plants is reported to be 20-30 $\mu\text{g}\cdot\text{g}^{-1}$. Compared to these values the WHO/FAO values are much lower, in the range of 0.2-5.0 $\mu\text{g}\cdot\text{g}^{-1}$, while the range that has been reported for various countries fall in 3-8 $\mu\text{g}\cdot\text{g}^{-1}$ (Kabata-Pendias & Mukherjee 2007).

In the analysed samples, Cu ranges from 0.04-9.9 $\mu\text{g}\cdot\text{g}^{-1}$ and amongst the vegetables the average values follows the order: brinjal > spinach > tomato > cabbage > cauliflower ($p = 0.009$). None of the samples exceeds the toxic limit; however, ~60% of the samples exceed the upper limit of the WHO/FAO range. Interestingly, Chary et al. (2008) reported much lower values of Cu (0.1-1.7 $\mu\text{g}\cdot\text{g}^{-1}$) in vegetation grown in sewage irrigated soils from Hyderabad. Due to the strong absorption of Cu^{2+} into an inorganic fraction and/or its complexation with organic matter, Cu is less mobile in soils. Cu bioavailability is reduced when the pH value exceeds 7.0 (Avci & Deveci 2013) and at higher pH hydrolysed species of Cu becomes important for its uptake by plants. Intriguingly, very low levels of Cu (0.04-2 $\mu\text{g}\cdot\text{g}^{-1}$) in vegetables were observed at the Gyaspur site which has relatively high soil

pH of 7.8. The average Cu at the eight sites (considering all vegetables) ranges from 0.4-7.1 $\mu\text{g.g}^{-1}$ and shows a moderate negative correlation ($r^2=0.51$) with pH, and corroborates with the above proposition of Avci & Deveci (2013).

Manganese (Mn): Mn is essential nutrient for the growth of plants that helps in the formation of the chloroplasts, nitrogen metabolism and synthesis of some enzymes. In the measured vegetable samples, Mn varies from ~12 (brinjal) to ~110 $\mu\text{g.g}^{-1}$ (spinach), and amongst the vegetables the average values follow the order: spinach > cabbage > brinjal > tomato > cauliflower ($p = 0.017$). The average Mn in spinach is 2-3 times higher compared the other vegetables suggesting leafy structure accumulate more of Mn compared to non-leafy ones.

Nickel (Ni): Ni is an important component of plant enzyme involved in N-fixation from urea/inorganic nitrogen and regulates normal growth of the plant tissues. Due to its role, Ni gets absorbed by many plant species in their tissues naturally and is found at relatively higher levels (Yusuf et al. 2011). Ni is also found in irrigation waters where sewage sludge and animal waste are mixed.

The Ni concentration in the samples varies from 0.7-4.2 $\mu\text{g.g}^{-1}$ and it compares to the range of 0.05-5.0 $\mu\text{g.g}^{-1}$ (Adriano 2001) and 0.06-1.3 $\mu\text{g.g}^{-1}$ for various countries reported by Kabata-Pendias & Mukherjee (2007). The average concentration in all but one vegetable samples centred on the value of ~3 $\mu\text{g.g}^{-1}$, and a slightly higher average value is observed for the cabbage samples (~3.3 $\mu\text{g.g}^{-1}$). These average values are very similar to those (2.0-4.7 $\mu\text{g.g}^{-1}$) reported in Turkish vegetation (Avci & Deveci 2013). About 90% of the samples exceed the Indian MAC limit of Ni (1.5 $\mu\text{g.g}^{-1}$); however, these average values are all higher by a factor of ~15 compared to the WHO/EU and WHO/FAO safe limits of 0.2 $\mu\text{g.g}^{-1}$.

It is also interesting to note that the average value at Gyaspur (1.7 $\mu\text{g.g}^{-1}$) is significantly lower than a somewhat similar value ($3.8 \pm 0.1 \mu\text{g.g}^{-1}$) observed at Kasindra, Chandisar and Kaloli. In the Indian context, similar observations and range of values were reported for leafy vegetables such as spinach, cabbage and amaranthus having more absorption affinity towards Ni (Singh et al. 2010, Sharma et al. 2006). For instance, Chary et al. (2008) reported average values of 3.1 $\mu\text{g.g}^{-1}$ for spinach and brinjal samples from wastewater irrigated areas near Hyderabad.

The mobility of Ni in soil plays an important role for bioavailability, due to moderate alkali condition the mobility of Ni increase in the soil. An increasing trend (with a weak correlation; $r^2= 0.54$) is observed between soil pH and average Ni in plants which possibly is an indication that soil pH influences the mobility of Ni from the soil-water system to

the plants amidst other parameters that also can regulate Ni in plants. The trend observed for Ni was cabbage > spinach > tomato > brinjal > cauliflower ($p = 0.001$).

Lead (Pb): Pb is a persistent toxicant to plants and is derived through atmospheric depositions and from soil uptake. Pb gets accumulated in the soil through various sources like industrial emission and discharges, burning of gasoline, and wastewater irrigation. Pb is not required in plants as a nutrient (similar to Cd), and possibly is reflected by generally low levels in uncontaminated soils (Kabata-Pendias & Mukherjee 2007), with less temporal and spatial variability (Rai & Tripathi 2008).

Pb in the samples varies from 0.4-8.4 $\mu\text{g.g}^{-1}$ with an average of ~2 $\mu\text{g.g}^{-1}$. These values compare with the range of Pb in plants in several countries (0.2-2.4 $\mu\text{g.g}^{-1}$; Kabata-Pendias & Mukherjee 2007) and ~30% of samples have Pb greater than or equal to the upper limit and all samples are in excess of the lower limit of the range. The average Pb values of all the plant types in this study (1.0-3.2 $\mu\text{g.g}^{-1}$) are higher than the FAO/WHO guidelines (0.5-1.0 $\mu\text{g.g}^{-1}$) and to the WHO/EU range of 0.1-0.3 $\mu\text{g.g}^{-1}$. On the basis of average values, the decreasing trend follows the order: tomato > spinach > cabbage > brinjal > cauliflower ($p = 0.006$). The samples from the Gyaspur site in particular exhibit high Pb levels with an average of 4.1 $\mu\text{g.g}^{-1}$ and the highest Pb (8.4 $\mu\text{g.g}^{-1}$) was measured in the spinach sample-facts that underscore the risks of growing vegetation near to the wastewater disposal point, and the retention of Pb by leafy vegetables as pointed out by Adriano (2001). The soil pH/alkaline nature of the soil is one of the major factors for limited bioavailability of Pb (Avci & Deveci 2013), a fact supported by a linear decrease of average Pb in all vegetables and the soil pH with a moderate correlation between them ($r^2 = 0.43$).

Zinc (Zn): Involvement in metabolic activities makes Zn an essential plant nutrient. Zn in the vegetables varies from 4 $\mu\text{g.g}^{-1}$ in cabbage to a maximum of 44 $\mu\text{g.g}^{-1}$ in brinjal, incidentally from the same site. The range observed in the study compares to the range of 1-27 $\mu\text{g.g}^{-1}$ observed for plants world-wide (Kabata-Pendias & Mukherjee 2007); 1.1-11.2 $\mu\text{g.g}^{-1}$ (Chary et al. 2008); 8-148 $\mu\text{g.g}^{-1}$ (Avci & Deveci 2013); 22-47 $\mu\text{g.g}^{-1}$ (Arora et al. 2008). Chary et al. (2008) have observed that ~40% of the Zn was associated in soluble and/or exchangeable phase(s) and was the most bio-available among other metals such as Cr, Cu, Ni, Co and Pb; however, that did not result in higher Zn in the vegetation compared to values reported in other studies. Chary et al. (2008) attributed high percentages of exchangeable/soluble Zn might be due to low soil pH (5.9-7.3). A somewhat contrasting observation was reported by Avci & Deveci (2013) who measured higher Zn in vegetables grown in soils

whose pH varied from 7.5 to 8.3. The concentration of metal in vegetable samples followed the trend of spinach > brinjal > cauliflower > tomato > cabbage ($p = 0.001$).

Principal Component Analysis (PCA) is applied to the vegetable samples to group heavy metals for source identification based on the % of the variance in the dataset. While performing PCA, varimax rotation method was used with Kaiser Normalization. Based on the Eigenvalues > 1, three components suggest 76.34% of the total variation. Principal Component-1 (PC1) accounts for 32.70% of variance, whereas PC2 for 25.9% and PC3 for 17.73%. Values greater than 0.7 in each component were considered. Factor 1 has higher positive loading for Cr, Pb, Co; Factor 2 has higher positive loading for Ni and Cu, and Factor 3 has for Mn and Zn. It is understood that heavy metals in vegetables are ultimately derived from the soil (soil-water system) hence it is important to identify the sources that contribute to the metals in the wastewaters. Effluents from small-scale metal and alloy processing, electrochemical processing, and dye and paint units hosted even (in domestic areas) within the limits of AMC and close to Vasna STP also act as a source of metals such as Fe, Pb, Cd, Cu, Zn and Cr found in the wastewaters of municipal wastewater treatment plant. Zn is contributed from different household items such as laundry detergents and cosmetics and can be derived from fertilizers. Cr and Ni mainly mix into the sewage through the usage of stainless steel cookware and through the process of cleaning them and to a large extent from metal and metal processing industries. Similarly, the sewer hook-ups and old pipelines act as the source of Pb and Cu. Different food grains, nuts, vegetables, and faeces are known to contribute a significant amount of Mn in the wastewater (Drozdoва 2019).

Transfer of Heavy Metals From Soil to Vegetables

Enrichment of heavy elements in plants is defined in terms of soil to plant transfer factor (TF; equation-1). It is defined as the ratio of concentrations (dry weight basis) of any metal in the plant (C_{plant}^M) to that in the irrigated soil (C_{soil}^M). In equation-2, all 'e-terms' refer to the error involved in their respective parameters.

$$TF_{plant}^M = \frac{C_{plant}^M}{C_{soil}^M} \quad \dots(1)$$

$$e_{TF_{plant}^M} = TF_{plant}^M \times \left[\left(\frac{e_{C_{plant}^M}}{C_{plant}^M} \right)^2 + \left(\frac{e_{C_{soil}^M}}{C_{soil}^M} \right)^2 \right]^{1/2} \quad \dots(2)$$

Where, the sub-/super-script M , $plant$ and $soil$ refer to metal, plant and soil, respectively.

Transfer factor is important to be studied as it provides

the first step in metal transfer to plants before it enters human via plants. According to (Mirecki et al. 2015) a TF value of >1 would indicate that elements are accumulated by the plants, ratio ~1 indicates less uptake, and ratio < 1 would indicate that plants would exclude metal from uptake. In the above equation-1, it is assumed that C_{plant}^M is derived exclusively from the soil (i.e. by root uptake); however, this assumption is not valid if there is any other source (e.g., atmospheric deposition) of a metal, or other post-harvest processes (e.g. transport, storage) increase the metal concentration. This latter apprehension assumes importance from the study of (Sharma et al. 2009) in which they reported higher concentrations in vegetables at the market sites compared to those at production sites. The ramification of the above finding, if true, though requires validation from other studies, is that urban consumers are even at higher risk than rural consumers provided the source of the vegetable remains the same.

In this study, the calculated values of TFs (Table 4) of heavy elements vary from <0.00 to 0.40, with an exceptionally higher value of 1.01 for a spinach sample collected from the Gyaspur site. Error propagation analyses showed that 5% measurement-uncertainty in each of concentration values translate to an overall uncertainty of 7.1% in calculated value of transfer factor. For the cases of metals, the following ranges, average and standard deviation in their TF values were observed: TF^{Cr} (0.05-0.14; 0.10 ± 0.02), TF^{Ni} (0.01-0.10; 0.06 ± 0.02), TF^{Cu} (< 0.00-0.06; 0.03 ± 0.02), TF^{Pb} (0.01-0.17; 0.04 ± 0.04), TF^{Mn} (0.03-0.39; 0.10 ± 0.10), TF^{Zn} (0.01-0.08; 0.04 ± 0.02) and TF^{Co} (0.01-1.01; 0.08 ± 0.17). Amongst the vegetables, the following ranges, average and standard deviation were observed: $TF_{brinjal}$ (<0.00-0.38; 0.06 ± 0.07), TF_{tomato} (< 0.00-0.38; 0.07 ± 0.03), $TF_{cabbage}$ (0.01-0.20; 0.05 ± 0.04), $TF_{cauliflower}$ (<0.00-0.20; 0.04 ± 0.03) and $TF_{spinach}$ (< 0.00-1.01; 0.09 ± 0.15).

TF values in this study are low compared to those reported in other Indian studies. For instance, for spinach reported values ranged from 0.5-0.91 (Tiwari et al. 2012 from Vadodara); 0.20-0.82 (Sharma et al. 2008 from Varanasi); 0.10-0.25 (Lokeshwari et al. 2006 from Bangalore) and to a very high set of values (9-32) reported by Rattan et al. (2005) in and around the capital city, Delhi. Our sets of values (<0.00-1.01) are somewhat similar to those observed by Chary et al. (2008) who reported in the range of 0.00-0.58. For cabbage, the reported values ranged from 0.50-0.65 (Tiwari et al. 2012); 0.26-1.36 (Sharma et al. 2008) and these compare to the values of 0.01-0.20 obtained in this study. For another commonly consumed vegetable, brinjal, the values (0.00-0.38) obtained in this study are higher than values 0.0-0.06 (Chary et al. 2008); however, are lower than

Table 4: Transfer factor of heavy metals in vegetable grown in wastewater irrigated soils.

Plant	TF	Co	Cr	Cu	Mn	Ni	Pb	Zn
Brinjal	Range	0.01-0.30	0.07-0.10	0.01-0.05	0.03-0.30	0.01-0.10	0.01-0.10	0.02- 0.80
	Mean	0.06	0.09	0.03	0.09	0.06	0.03	0.03
	SD	0.10	0.02	0.01	0.10	0.02	0.04	0.01
Tomato	Range	0.01-0.10	0.06-0.10	0.01-0.05	0.04-0.06	0.01-0.10	0.02-0.10	0.01-0.05
	Mean	0.05	0.09	0.03	0.05	0.06	0.07	0.03
	SD	0.02	0.02	0.01	0.01	0.02	0.04	0.01
Cabbage	Range	0.01-0.10	0.04-0.10	0.01-0.10	0.04-0.20	0.04-0.07	0.01-0.10	0.008-0.03
	Mean	0.06	0.07	0.01	0.08	0.05	0.04	0.02
	SD	0.02	0.03	0.003	0.05	0.01	0.03	0.008
Cauliflower	Range	0.01-0.10	0.05-0.10	0.001-0.01	0.03-0.06	0.01-0.07	0.01-0.03	0.01-0.05
	Mean	0.04	0.08	0.01	0.05	0.05 0.02	0.008	0.03
	SD	0.06	0.01	0.006	0.01		0.02	0.01
Spinach	Range	0.01-1.00	0.08-0.10	0.001-0.04	0.03-0.30	0.04-0.07	0.01-0.10	0.02-0.07
	Mean	0.15	0.10	0.03	0.20	0.06	0.04	0.04
	SD	0.30	0.01	0.01	0.10	0.01	0.05	0.01

the ranges of 0.60-0.79 (Tiwari et al. 2012) and 0.26-1.36 (Sharma et al. 2008).

An attempt was made to understand the high variability in the TF values. Variations in TFs are expected for both the cases, fixed plant-different metals and fixed metal-different plants. In the case of fixed plant-different metals, physiological aspects of metal uptake from soil by the plant remain somewhat similar and the variations are largely due to the differential (bio-) geochemical aspects related to the different metals in/around the prevailing soil-water system. Most important factors are pH of the soil-water system, organic ligands in the soils, abundances of organic/inorganic carbon in soils, bioavailable fraction of any metal, abundance of Fe-Mn oxides or (oxy-) hydroxides. In the case of fixed metal-different plants, variations in TFs are due to their physiological aspects of metal uptake. Since the factors controlling TF values for a fixed plant (& different metals case) are more than the case with fixed metal (& different plants) we anticipate more variations in the former case which has been found to hold good for our case study.

For the two cases, variability in TFs is assessed by the maximum to the minimum values. For fixed plant-different metals case, the following order was observed in the maximum-to-minimum values: spinach (3849) > brinjal (2282) > tomato (1255) > cauliflower (717) > cabbage (25). In contrast, when the metal is fixed and vegetables remain the variant the corresponding lowest value (maximum to minimum) was found for Cr (3) and the highest for Cu (369); and amongst metals, it follows the order: Cu (369) > Co (97) > Pb (21) > Mn (13) > Zn (10) Ni (9) > Cr (3).

One of the studies (Tiwari et al. 2011) which reported TF values in vegetables irrigated using tube-well water, as well

as wastewater, provides important insights into the factors controlling heavy element transfer to the edible portion of the plants. Transfer factor values were found to be higher for tube-well water irrigated ones compared to wastewater ones for metals (Cd, Cu, Fe, Mn, Ni and Zn). Exceptions were observed for Cr and Pb, as these two metals were found to be below the detection limit in the vegetable samples irrigated using tube-well water, resulting in a zero TF value. Despite lower metal concentration in tube-well water irrigated vegetables compared to wastewater ones, the reason for the higher values of TFs in the former is a disproportionately lower metal concentration in the tube-well irrigated soils compared to wastewater irrigated soils. Therefore, the sensitivity of the term C_{soil}^M is more than that of C_{plant}^M in determining the magnitude of TF. The important implication of the above analysis, if it can be extended to other field sites, is that the use of TF in any kind of *prima-facie* risk-assessment associated with consumption of vegetable can be misleading without knowing its origin, i.e. the soil in which it is grown.

Risk Assessment

In this study hazard quotient (HQ; equation 3) is used as the index for risk-assessment (Chien et al. 2002). An HQ_M value of >1 (for any metal) means that there is a potential risk associated with the metal due to its dietary intake-the higher is the value of HQ, the greater is the risk associated with it (Khaled & Muhammad 2016). Hazard quotient is preferred for risk assessment for the facts that it incorporates the reference dose (which is the prescribed upper limit of dose for any metal) in the calculation and, interpretation of HQ value for risk assessment becomes simpler. HQ values calculated in this study and many earlier ones will provide

lower bound estimates of the overall risk associated with any metal as other components (other than vegetables) of human consumption are not considered, and other routes of metal intake/ingestion to the body (inhalation and skin exposure) are not taken into account in the calculation.

$$HQ_M = \frac{C_M \times (1 - f_{\text{moisture}}) \times CR}{BW \times RFD_M} \times 10^{-3} \quad \dots(3)$$

$$e_{HQ_M} = H_{Q_M} \times \left[\left(\frac{e_{C_M}}{C_M} \right)^2 + \left(\frac{e_{f_{\text{moisture}}}}{f_{\text{moisture}}} \right)^2 + \left(\frac{e_{CR}}{CR} \right)^2 + \left(\frac{e_{BW}}{BW} \right)^2 + \left(\frac{e_{RFD_M}}{RFD_M} \right)^2 \right]^{1/2} \quad \dots(4)$$

Where, C_M is the (consumption weighted) average metal concentration on a dry weight basis (in $\mu\text{g}\cdot\text{g}^{-1}$); f_{moisture} = fraction of moisture content in vegetables (a reported value of 0.915 was used, also verified from our laboratory experiments); CR = consumption rate of (uncooked) vegetable (in $\text{g}\cdot\text{day}^{-1}$; value of 300 g was used); BW = average (kilogram) body weight (kg bw; 58 kg was used based on Indian standard value for an adult); RFD_M = reference dose for the metal in $\text{mg}\cdot(\text{kgbw})^{-1}\cdot\text{day}^{-1}$ (taken from values reported in Qu et al. 2012 and references therein). In equation-4, all 'e-terms' refer to the error of the parameters explained above.

In the equation above assigning a representative value of the metal concentration in vegetables ($\mu\text{g}\cdot\text{g}^{-1}$) is a sensitive parameter to the calculated value of HQ, and hence, a sensitivity analysis was made by choosing three different approaches: (i) nature of vegetables ($n = 38$) were not segregated by consumption pattern and daily vegetable consumption of 300 g (fresh) vegetable was used in the calculation, (ii) vegetables were segregated into leafy (spinach; $n = 8$) and non-leafy (others; $n = 30$), and consumption amounts of 100 and 200 g, respectively, were used, and (iii) furthermore, non-leafy was segregated into the four vegetables and therefore, the consumption amounts in

the third approach used are 50 g each for the four vegetables (cabbage, cauliflower, tomato and brinjal) and 100 g for the spinach. Therefore, it follows from the above discussion that the latter two approaches are by and large consumption weighted average metal concentrations.

Based on the three approaches, the following ranges were found for the HQ values (Table 5): Cr (0.970-0.984); Ni (0.067); Cu (0.056-0.059); Pb (6.149-6.239); Mn (1.007-1.166); Zn (0.022-0.023) and Co (0.018-0.021). HQ values calculated from these approaches show very consistent results indicating lesser sensitivity on how the average concentration is calculated, and would, therefore, be representative values. Error propagation analyses showed that 5% uncertainty in each of parameters (in equation-3) translates to an overall uncertainty of ~11% in the calculated value of HQ values. Results indicate that there is little risk associated with Zn, Co, Cu and Ni, even if other components (e.g., other food/drink components) would have been considered in the calculation. For instance, an increase in consumption amount by a factor of ~5 would increase HQ by the same factor (say, the maximum HQ value of Ni would increase from ~0.07 to a value ~ 0.35), yet well beyond the HQ limit of 1 for any risk to human health.

HQ_{Cr} values of $\sim 0.97 \pm 0.10$ are very close to the threshold value underscoring the risk associated with Cr from vegetables. Error propagation analysis leads to the upper limits of these values greater than 1. If other food components are included in the calculation there is the likelihood that HQ_{Cr} values would be greater than critical risk value of 1. Along with similar arguments, there is a risk associated with Mn with higher than one HQ_{Mn} values (1.01 ± 0.10). The most notable risk associated is with the case of Pb with the highest HQ values (6.15 ± 0.61) and the population of the Ahmedabad city are exposed severely to the risk of Pb due to ingestion via vegetable consumption. The continuous use of sewage for irrigation may increase the exposure dose to the human being, which may cause various health-related

Table 5: Hazardous quotient values.

Heavy Metals	R _d D Values ($\text{mg}\cdot\text{kg}^{-1}\cdot\text{day}^{-1}$)	Source	Approach-1	Approach-2	Approach-3
Co	0.02	Kamunda et al. ^c	0.018	0.021	0.021
Cr	0.003	IRIS ^a	0.970	0.984	0.984
Cu	0.04	Qu et al. ^b	0.056	0.059	0.059
Mn	0.014	Harmanescu et al. ^d	1.007	1.156	1.156
Ni	0.02	IRIS ^a	0.067	0.067	0.067
Pb	1.4×10^{-4}	Qu et al. ^b	6.149	6.255	6.239
Zn	0.3	IRIS ^a	0.022	0.023	0.023

^a Integrated Risk Information System, U.S. EPA; ^b Qu et al. (2012); ^c Kamunda et al. (2016); ^d Harmanescu et al. (2011)

threats and it should seriously be considered at the least for Pb, and Mn, and likely also for Cr.

CONCLUSIONS

Concentrations of heavy metals (Co, Cr, Cu, Mn, Ni, Pb and Zn) in wastewaters, in soils and, in vegetations grown in wastewater irrigated croplands near Ahmedabad city, India, were measured by high-precision ICP-MS. The basic objective is to assess the potential risk to human health to a significant fraction of ~six million population of the city. The study, perhaps the first reports, brings out the following observations and the conclusions:

1. Concentrations of heavy metals [e.g., Co (2.1-2.2), Cr (1.4-1.9), Cu (0.1-0.9), Mn (0.2-3), Ni (1-1.9), Pb (0.4-1.6) and Zn (5.1-19); all in $\mu\text{g ml}^{-1}$] in wastewaters exceed their respective MACs values for irrigation purpose set by Indian/WHO/European agencies.
2. Average concentrations ($\mu\text{g.g}^{-1}$) of metals in the eight soil samples follow the trend: Zn (421 ± 62) > Mn (336 ± 49) > Cu (201 ± 30) > Cr (71 ± 20) > Ni (51 ± 8) > Pb (42 ± 6) > Co (9 ± 1). The average are distinctly different with confidence limit >90% ($p < 0.01$). Good inter-correlations between the analysed metals are observed which is suggestive of common sources/process contributing to them, predominantly enriched by the wastewater irrigation. Except for Cr, all metals show a downstream decrease of concentrations.
3. Concentrations of metals in vegetables vary in the range [Co (0.10-11.3), Cr (5.2-11.8), Cu (0.04-9.9), Mn (12.3-110), Ni (0.7-4.2), Pb (0.4-8.4) and Zn (4.4-44); all in $\mu\text{g.g}^{-1}$; dry weight basis]. Variation of concentration though is plant-specific; bio-availability of metals is an important factor for metal assimilation in plants. The pH of the soil-water system seems to regulate bio-availability of (at least) Cu, Pb, Ni and Zn.
4. High variability was observed in the transfer factor values. Geochemical factors related to different metals in the soil-water system seem to regulate more the transfer factor than the physiological differences between various plant species.
5. Hazard quotient was calculated for assessing the risk associated with heavy metals via consumption of the vegetables. HQ values suggest that there is no risk associated with Co, Cu, Ni and Zn; however, there is a high risk associated with Pb and Mn, and likely also from Cr. Finally, more efficient treatment of wastewater treatment facilities and, frequent monitoring of heavy metals in soils and in vegetation from the area are suggested.

ACKNOWLEDGEMENTS

We thank Dr. Ravi Bhushan and Dr. A. K. Sudheer from Physical Research Laboratory for their suggestions during ICP-MS analyses.

REFERENCES

- Adriano, D.C. 2001. Trace Elements in Terrestrial Environments, seconded. Springer-Verlag, New York.
- Agrawal, M. 2003. Enhancing food chain integrity: quality assurance mechanisms for air pollution impacts on fruit and vegetable system. Final Technical Report II submitted to Department of International Development, UK, R 7530.
- Ahmad, K., Ashfaq, A., Khan, Z.I., Ashraf, M., Akram, N.A., Yasmin, S., Batool, A.I., Sher, M., Shad, H.A., Khan, A., Rehman, S.U., Ullah, M.F. and Noorka, I.R. 2016. Health risk assessment of heavy metals and metalloids via dietary intake of a potential vegetable (*Coriandrum sativum* L.) grown in contaminated water irrigated agricultural sites of Sargodha, Pakistan. *Human Ecol. Risk Assess.*, 22: 597-610.
- Akpor, O.B., Ohiobor, G.O. and Olaolu, T.D. 2014. Heavy metal pollutants in wastewater effluents: Sources, effects and remediation. *Advances in Bioscience and Bioengineering*, 2(4): 37-43.
- Alaoui-Sosse, B., Genet, P., Vinit-Dunand, F. and Toussaint, M.L. 2004. Effect of copper on growth in cucumber plants (*Cucumis sativus*) and its relationships with carbohydrate accumulation and changes in ion contents. *Plant Science*, 166: 1213-1218.
- Amin, B.S., Likhite, S.D., Radhakrishnamurty, C. and Somayajulu, B.L.K., 1972. Susceptibility stratigraphy and paleomagnetism of some deep Pacific Ocean cores. In: *Deep Sea Research and Oceanographic Abstracts*, 19(3): 249-252.
- Arora, M., Kiran, B., Rani, S., Rani, A., Kaur, B. and Mittal, N. 2008. Heavy metal accumulation in vegetables irrigated with water from different sources. *Food Chemistry*, 111: 811-815.
- Avci, H. and Deveci, T. 2013. Assessment of trace element concentrations in soil and plants from crop land irrigated with wastewater. *Ecotoxicology and Environmental Safety*, 98: 283-291.
- Banerji, U.S., Bhusan, R. and Jull, A.J.T. 2017. Mid-late Holocene monsoonal records from the partially active mudflat of Diu Island, Southern Saurashtra, Gujarat, Western India. *Quaternary International*, 443: 200-210.
- Chary, N.S., Kamala, C.T. and Raj, D.S.S. 2008. Assessing risk of heavy metals from consuming food grown on sewage irrigated soils and food chain transfer. *Ecotoxicology and Environmental Safety*, 69(3): 513-524.
- Chien, L.C., Hung, T.C., Choang, K.Y., Choang, K.Y., Yeh, C.Y., Meng, P.J., Shieh, M.J. and Han, B.C. 2002. Daily intake of TBT, Cu, Zn, Cd and As for fishermen in Taiwan. *Sci. Total Environ.*, 285: 177-85.
- Chopra, A.K. and Pathak, C. 2015. Accumulation of heavy metals in the vegetables grown in wastewater irrigated areas of Dehradun, India with reference to human health risk. *Environ. Monit. Assess.*, 187(7): 1-8.
- Cui, Y.J., Zhu, Y.G., Zhai, R.H., Chen, D.Y., Huang, Y.H., Qui, Y. and Liang, J.H. 2004. Transfer of metals from near a smelter in Nanning, China. *Environmental International*, 30: 785-791.
- Demirezen, D. and Aksoy, A. 2006. Heavy metal levels in vegetables in Turkey are within safe limits for Cu, Zn, Ni, and exceeded for Ca and Pb. *Journal of Food Quality*, 29: 252-256.
- Drozdzova, J., Raclavska, H., Raclavsky, K. and Skrobankova, H. 2019. Heavy metals in domestic wastewater with respect to urban population in Ostrava, Czech Republic. *Water and Environment Journal*, 33: 77-85.
- Gebrekidan, A., Weldegebrail, Y., Hadera, A. and Van Der Bruggen, B. 2013. Toxicological assessment of heavy metals accumulated in vegetables and fruits grown in Ginfel River near Sheba Tannery, Tigray, Northern Ethiopia. *Ecotoxicol. Environ. Saf.*, 95: 171-178.

- Gebreyohannes, T. and Asgedom, A.G. 2018. Toxicological assessment of Pb, Cd and Cr in lettuce and onion grown around Ellala River in Mekelle, Tigray, Ethiopia. *Ethiop. J. Sci. & Technol.*, 11(3): 287-313.
- Ghosh, A.K., Bhatt, M. and Agrawal, H. 2012. Effect of long term application of treated sewage water on heavy metal accumulation in vegetables grown in Northern India. *Environ. Monit. Assess.*, 184: 1025-36.
- Govindaraju, K. 1994. Compilation of working values and descriptions for 383 Geostandards. *Geostand. Newsl.* 18, 1-158.
- Gupta, S., Satpati, S., Nayek, S. and Garai, D. 2010. Effect of wastewater irrigation on vegetables in relation to bioaccumulation of heavy metals and biochemical changes. *Environ. Monit. Assess.*, 165: 169-77.
- Harmanescu, M., Alda, L.M., Bordean, D.M., Gogoasa, L. and Gergen, L. 2011. Heavy metals health risk assessment for population via consumption of vegetables grown in old mining area; a case study: Banat County, Romania. *Chemistry Central Journal*, 5: 64.
- Hu, W.Y., Chen, Y., Huang, B. and Niedermann, S. 2014. Health risk assessment of heavy metals in soils and vegetables from a typical greenhouse vegetable production system in China. *Hum. Ecol. Risk Assess.*, 20: 1264-1280.
- Jarup, L. 2003. Hazards of heavy metals contamination. *Br. Medical Bulletin*, 68: 167-182.
- Jassir, M.S., Shaker, A. and Khaliq, M.A. 2005. Deposition of heavy metals on green leafy vegetables sold on roadsides of Riyadh city, Saudi Arabia. *Bulletin Environmental Contaminant Toxicology*, 75: 1020-1027.
- Joint FAO/WHO Expert Committee on Food Additives 1999. Summary and conclusions. In: 53rd Meeting, Rome, June 1-10.
- Joint FAO/WHO Expert Committee on Food Additives 1999. Toxicological Evaluation of Certain Food Additives. ILSI Press International Life Sciences Institute, Washington, DC.
- Kabata-Pendias, A. and Mukherjee, A.B. 2007. Trace Elements from Soil to Human. Springer, NewYork.
- Kamunda, C., Mathuthu, M. and Madhuku, M. 2016. Health risk assessment of heavy metals in soils from Witwatersrand gold mining basin, South Africa. *International Journal of Environmental Research and Public Health*, 13: 663.
- Khaled, S.B. and Muhammad, A.A. 2016. Field accumulation risks of heavy metals in soil and vegetable crop irrigated with sewage water in western region of Saudi Arabia. *Saudi Journal of Biological Sciences*, 23: S32-S44.
- Khillare, P.S., Balachandran, S. and Meena, B.R. 2004. Spatial and temporal variation of heavy metals in atmospheric aerosols of Delhi. *Environmental Monitoring and Assessment*, 90: 1-21.
- Lokeshwari, H. and Chandrappa, G. T. 2006. Impact of heavy metal contamination of Bellandur Lake on soil and cultivated vegetation. *Current Science*, 5: 622-627.
- Mapanda, F., Mangwayana, E.N., Nyamangara, J. and Giller, K.E. 2005. The effect of long term irrigation using wastewater on heavy metal contents of soils under vegetables in Harare. *Zimbabwe Agric. Ecosyst. Environ.*, 107: 151-65.
- Milacic, R. and Kralj, B. 2003. Determination of Zn, Cu, Cd, Pb, Ni and Cr in some Slovenian foodstuffs. *European Food Research and Technology*, 217: 211-214.
- Mirecki, N., Agic, R., Sunic, L., Milenkovic, L. and Ilic, S.Z. 2015. Transfer factor as indicator of heavy metals content in plants. *Fresenius Environmental Bulletin*, 24: 4212-4219.
- Palrecha, A., Kapoor, D. and Malladi, T. 2012. Wastewater irrigation in Gujarat: An Exploratory Study IWMI- TATA Water Policy Programme.
- Qu, S.C., Ma, Z.W., Yang, J., Liu Y., Bi, J. and Huang L. 2012. Human exposure pathways of heavy metals in a lead-zinc mining area, Jiangsu Province, China. *PLoS ONE*, 7(11).
- Qureshi, A.S., Hussain, M.I., Ismail, S. and Khan, Q.M. 2016. Evaluating heavy metal accumulation and potential health risks in vegetables irrigated with treated wastewater. *Chemosphere*, 163: 54-61.
- Rai, P.K. and Tripathi, B.D. 2007. Heavy metals in industrial wastewater, soil and vegetables in Lohta village, India. *Toxicological & Environmental Chemistry*, 90: 247-257.
- Rattan, R. K., Datta, S. P., Chhonkar, P. K., Suribabu, K. and Singh, A. K. 2005. Long term impact of irrigation with sewage effluents on heavy metal contents in soils, crops and ground water—a case study. *Agriculture, Ecosystem and Environment*, 109: 310-322.
- Saha, S., Hazra, G.C., Saha, B. and Mandal, B. 2015. Assessment of heavy metals contamination in different crops grown in long term sewage irrigated areas of Kolkata, West Bengal, India. *Environ. Monit. Assess.*, 187: 4087-99.
- Sharma, R.K., Agrawal, M. and Marshall, F.M. 2006. Heavy metals contamination in vegetables grown in waste water irrigated areas of Varanasi, India. *Bulletin of Environmental Contamination and Toxicology*, 77: 311-318.
- Sharma, R.K., Agrawal, M. and Marshall, F.M. 2008. Heavy metals (Cu, Cd, Zn and Pb) contamination of vegetables in Urban India: A case study in Varanasi. *Environmental Pollution*, 154: 254-263.
- Sharma, R.K., Agrawal, M. and Marshall, F.M. 2009. Heavy metals in vegetables collected from production and market sites of a tropical urban area of India. *Food and Chemical Toxicology*, 47: 583-591.
- Singh, A., Sharma, R.K., Agrawal, M. and Marshall, F.M. 2010. Risk assessment of heavy metal toxicity through contaminated vegetables from waste water irrigated area of Varanasi, India. *Tropical Ecology*, 51(2S): 375-387.
- Singh, K.P., Mohon, D., Sinha, S. and Dalwani, R. 2004. Impact assessment of treated/untreated waste water toxicants discharge by sewage treatment plants on health, agricultural, and environmental quality in waste water disposal area. *Chemosphere*, 55: 227-255.
- Singh, V.K. and Jaswant, S. 2006. Toxicity of industrial wastewater of the aquatic plant *Lemna minor* L. *Journal of Environmental Biology*, 27: 385-390.
- Tiwari, K.K., Singh, N.K., Patel, M.P., Tiwari, M.R. and Rai, U.N. 2011. Metal contamination of soil and translocation in vegetables growing under industrial waste-water irrigated agricultural field of Vadodara, Gujarat, India. *Ecotoxicological and Environment Safety*, 74: 1670-1677.
- Tripathi, R.M., Ragnath, R. and Krishnamurthy, T.M. 1997. Dietary intake of heavy metals in Bombay City, India. *Science of Total Environment*, 208: 149-159.
- Wang, X., Sato, T., Xing, B. and Tao, S. 2005. Health risks of heavy metals to the general public in Tianjin, China via consumption of vegetables and fish. *Science of Total Environment*, 350: 28-37.
- WHO, 1998. Cadmium, *Environmental Health Criteria*, Vol. 134. World Health Organization, Geneva.
- Woldetsadik, D., Drechsel P., Keraita, B., Itanna, F. and Gebrekidan, H. 2017. Heavy metal accumulation and health risk assessment in wastewater-irrigated urban vegetable farming sites of Addis Ababa, Ethiopia. *International Journal of Food Contamination*, 4(9): 1-13.
- Yusuf, K., Fariduddin, Q., Hayat, S. and Ahmad, A. 2011. Nickel: An overview of uptake, essentiality and toxicity in plants. *Bulletin of Environmental Contamination and Toxicology*, 86(1): 1-17.



Analysis of Temporal Evolution Characteristics of Annual Precipitation in the Yellow River Delta

Xianqi Zhang*(**)(***), Yang Yang*† and Zhiwen Zheng*

*School of Water Conservancy, North China University of Water Resources and Electric Power, Zhengzhou 450046, China

**Collaborative Innovation Centre of Water Resources Efficient Utilization and Protection Engineering, Zhengzhou 450046, China

***Technology Research Centre of Water Conservancy and Marine Traffic Engineering, Henan Province, Zhengzhou 450046, China

†Corresponding author: Yang Yang, 1099672847@qq.com

Nat. Env. & Poll. Tech.
Website: www.neptjournal.com

Received: 31-01-2020

Revised: 22-02-2020

Accepted: 02-05-2020

Key Words:

Precipitation
Mutation
ITA
Wavelet analysis

ABSTRACT

Precipitation is an important component in the climate system and plays a key role in water resources protection, drought and flood prevention. Innovation Trend Analysis (ITA) method, R/S method, maximum entropy spectrum analysis and wavelet analysis were used to study the evolution characteristics of the Yellow River Delta annual precipitation from 1954 to 2014. The results suggest that the precipitation series changed significantly and showed an overall downward trend, and may show an upward trend in the future, which is relatively strong. There are three-time scales of annual precipitation variation: 20-32a, 8-18a, and 3-6a. The quasi-27 year was the main oscillation period of the average annual precipitation in the Yellow River Delta, the secondary major period was 13 years, and the small-scale oscillation period was 5 years. Precipitation changed suddenly in 1980 and 2003. In contrast, there was no significant mutation point in 2002-2014.

INTRODUCTION

Precipitation is the main climate change factor that affects the distribution and function of a wetland and is one of the leading factors for the rational development of water resources and regional freshwater supply. Freshwater has become the key factor restricting the development of the Yellow River Delta. Therefore, it is necessary to study the characteristics and law of precipitation evolution, which can provide a theoretical and scientific basis for the sustainable development of the Yellow River Delta. At present, the study of precipitation evolution has become a public topic for many scholars at home and abroad. Common trend analysis methods include moving average method (Pei & Guo 2001), Mann Kendall rank correlation method (Mann 1945), cumulative horizon method (Ran et al. 2010), quadratic smoothing method (Li et al. 2018), R/S analysis method (Liu et al. 2019). Liebmann & Marengo (2001) studied the relationship between seasonal rainfall characteristics and temperature changes in the Amazon. Galy-Lacaux et al. (2009) studied the long-term trend of precipitation chemical characteristics in rural areas of Banizoumbou. Sohoulane Djebou et al. (2014) and other scholars applied the entropy theory to study the relationship

and its evolution characteristics between precipitation time and precipitation in the southwestern United States. Zhang et al. (2020) studied the historical trend of temperature, precipitation and runoff in the North China plateau basin by Mann Kendall. Zuo et al. (2019) analysed the precipitation characteristics in Tongzhou district of Beijing from 1966 to 2016 with Morlet wavelet transform. Ding et al. (2014) studied the temporal and spatial evolution of precipitation in a typical small watershed in the humid region of South China. Yang & Sun (2013) used the R/S method to analyze the runoff time series period. The above traditional methods only analysed the variation of sequence from one side of trend or mutation, but not from the whole (including cycle, trend and mutation, etc.) to judge whether the sequence has a mutation. According to the previous research results, this study adopts a new trend research method- ITA (Wu & Qian 2017, Huang et al. 2018). The ITA method has no limitations and is suitable for series-related, non-normal distribution, or short record lengths. It can identify the trend of low, medium and high value simply and clearly. Hurst coefficient can represent the variation of hydrological series as a whole from the perspective of time. R/S analysis method is usually used to analyze the time-series features and long-term memory

process. The maximum entropy spectrum method overcomes the problems of data windowing and frequency resolution error. Wavelet analysis can carry out multi-scale refinement analysis of functions or signals. Therefore, this paper puts forward an analysis method to identify and test the variation and degree of variation of hydrological time series as a whole, which provides basic data support for agricultural production, water resource management and social and economic development of the Yellow River Delta.

MATERIALS AND METHODS

Method of Precipitation Trend Analysis

ITA method: ITA method (Wu et al. 2017, Huang & Qian 2018) is an innovative trend analysis method based on the linear comparison of the scattered points 1:1 (45°) on the cartesian coordinate system. It is divided into two equal parts according to the time series, and the sub-series are arranged in ascending order. The first sub-series is the X-axis, and the second sub-series is the Y-axis. If two subsequences are equal, indicating no trend, the points in the scatter plot fall on the 1:1 line. If these points fall above the 1:1 line, it indicates that the time series presents an increasing trend. On the contrary, there is a downward trend in the time series. At the same time, precipitation is divided into low, medium and high parts with 40% and 60% as the boundary according to the ascending sequence. ITA index D is used to characterize the trend, as shown in formula (1). When the range of value variation is small, but the influence of variation trend on production and life is too large to be ignored, the index value is not enough to clearly show the variation trend, then formula (2) can be referred to.

$$D = \frac{1}{n} \sum_{i=1}^n \frac{10 \times (y_i - x_i)}{\bar{x}} \quad \dots(1)$$

$$D = \frac{1}{n} \sum_{i=1}^n \frac{100 \times (y_i - x_i)}{\bar{x}} \quad \dots(2)$$

R/S analysis method: R/S analysis method was first proposed by Hurst (Hurst et al. 1965, Wallis & Matalas 1970, Rao & Bhattacharya 1999), a British hydrologist, and also known as the standard range analysis method. It was first used in hydrological research. In recent years, with the progress of science and technology, it has been widely used and developed in data analysis (Hjelmfelt et al. 1988, Tarboton et al. 1988, Zhang et al. 2005). Set time series $\{x(t)\}, t = 1, 2, \dots, n$. Where $\tau \geq 1$ and is an integer, when any value is taken:

Construct a mean number column:

$$x_t = \frac{1}{\tau} \sum_{i=1}^{\tau} x(t), \quad \tau=1, 2, \dots, n \quad \dots(3)$$

Cumulative dispersion:

$$x(t, \tau) = \sum_{k=1}^t [x(k) - x_{\tau}], \quad 1 \leq t \leq \tau \quad \dots(4)$$

Range sequence:

$$R(t) = \max x(t, \tau) - \min(t, n) \quad \dots(5)$$

Standard deviation:

$$s(t) = \sqrt{\frac{1}{\tau} \sum_{t=1}^{\tau} [x(t) - x_{\tau}]^2} \quad \dots(6)$$

For the ratio: $(\tau)/S(\tau) = R/S$, if $R/S \propto \tau^H$, if , it can be said that sequence has Hurst phenomenon. H is the Hurst function. Judging the persistence and anti-sustainability of time series trends (Teverovsky et al. 1999, Huang et al. 2002) according to definitions. If $0 \leq H \leq 0.5$, it means that the time series is an anti-persistent or ergodic time series with a stronger mutation or variability than the random sequence, and the general trend of precipitation change is contrary to the past in terms of precipitation index. If $H = 0.5$, it means that the time series is a random swimming series, the observations are completely independent and the precipitation indicators change randomly in terms of precipitation index. If $0.5 < H < 1$, indicating that the time series is persistent or trend-enhancing, the overall trend of the change in precipitation in the future is the same as in the past

Precipitation Cycle Test Method

Maximum entropy spectrum analysis: The Burg recursive algorithm (Bassingthwaite et al. 1994) is a commonly used maximum entropy spectrum analysis method. The algorithm is simple and the spectral resolution is relatively high. The specific steps are as follows:

Calculate the initial value

$$\varphi_i(0) = \frac{1}{N} \sum_{n=1}^N |x(n)|^2 \quad \dots(7)$$

$$e_0(n) = b_0(n) = x(n) \quad \dots(8)$$

Let $p = 1$, find the reflection coefficient

$$K_p = -\frac{2 \sum_{k=p}^{n-1} e_{p-1}(k) \cdot b_{p-1}(n)}{\sum_{n=p}^N [e_{p-1}(n)^2 + b_{p-1}^2]} \quad \dots(9)$$

$$a_{11} = K_1, \sigma_1^2 = (1 - |K_1|^2) \varphi_x(0)$$

Find $e_1(n), b_1(n)$ from K_1 and the following formul

$$e_p(n) = e_{p-1}(n) + K_p b_{p-1}(n-1) \quad \dots(10)$$

$$b_p(n) = b_{p-1}(n-1) + K_p e_{p-1}(n) \quad \dots(11)$$

Following the recursive relationship of Levinson of $a_{pk} = a_{p-1,k} + K_p a_{p-1,p-k}$ and $a_{pp} = K_p$, when $p = 2, a_{11}, a_{22}, \sigma_2^2$ are obtained.

Repeat the above process until equals the required AR model order. Find all the AR model parameters a_{pk} , and then use the following formula to find the power spectral density.

$$P_{Burg}(\omega) = \frac{\sigma_p^2}{|1 + \sum_{k=1}^p a_{pk} e^{-jw(k)}|} \quad \dots(12)$$

Morlet wavelet: Morlet wavelet analysis has been extensively studied in the periodic variation of precipitation (Adamowski & Chan 2011, Chen et al. 2019). Morlet wavelet analysis has a phase difference of $\pi/2$ between the real part and the imaginary part of the complex function. It can reveal the various change periods hidden in the time series, reflect the trend of the reaction system at different time scales and predict the future development trend of the system (Abry & Veitch 1998, Zhao et al. 2019). Wavelet function self-oscillation may cause errors caused by pseudo-oscillation of signals. The error can be eliminated by analysing the wavelet coefficient of variation, and the amplitude and phase change information of the signal in the time series can be obtained simultaneously. The basic principle of Morlet wavelet analysis is as follows.

The form of wavelet generating function is:

$$\psi(x) = \pi^{1/4} e^{icx} e^{\frac{x^2}{z}} \quad \dots(13)$$

Its subwavelet is:

$$\psi_{a,b}(x) = |a|^{-1/2} \psi\left(\frac{x-b}{a}\right) \quad \dots(14)$$

Where, the parameter a represents the scale of expansion and the parameter b represents the translation distance. In the Fourier analysis, T has the following relationship with parameter a :

$$T = \frac{4\pi a}{c + \sqrt{2+c^2}} \quad \dots(15)$$

The trend of time series and the information of time and position can be obtained by wavelet analysis. To obtain valuable information, the essence of the wavelet transform is to analyze one-dimensional signals in terms of time and frequency, to analyze the time-frequency structure of the climate system in detail. The wavelet coefficients obtained from the analysis are related to time and frequency, so the transformation results can be presented in a two-dimensional image.

When analysing the precipitation, the wavelet real part contour map can reflect the periodic changes of the precipitation series at different time scales and its distribution in the time domain, to judge the future trend of precipitation at different time scales. The contour curve is the real part value of the wavelet coefficient, and the real part value of the wavelet coefficient is positive, which represents abundant precipitation. Instead, it means less precipitation.

Precipitation mutation research method: Precipitation abrupt change refers to the sharp change of precipitation from one stable state to another stable state. The test and analysis of precipitation abrupt change is an important part of studying the long-term change characteristics of precipitation. When the statistical law of the data sample changes obviously at a certain moment, the moment point is called the change point. The discrimination of the variable point is generally considered from two different aspects: one is whether the numerical characteristics of the distribution change under the premise that the observed value distribution before and after the change point remains unchanged; The other is whether the distribution function of the observed value changes before and after the change point. The observed value originally obeys a certain distribution, but changes to another distribution after the change point. Mutation analysis by Mann-Kendall (M-K) method (Mann et al. 2015, Xiao et al. 2019): time series data (x_1, x_2, \dots, x_n) is n independent samples with the same distribution of random variables, where m_i represents the cumulative count of the i -th sample $x_i > x_j$ ($1 \leq j \leq i$) and defines a statistic C_k :

$$c_k = \sum_{i=1}^k m_i \quad \dots(16)$$

$$E(c_k) = k(k - 1)/4 \quad \dots(17)$$

$$\sigma(c_k) = k(k - 1)(2k + 5)/72 \quad \dots(18)$$

$$UF_K = (c_k - E(c_k))/\sqrt{\sigma(c_k)} \quad \dots(19)$$

Where $E(c_k)$, $\sigma(c_k)$ is the mean and variance of c_k , UF_K is the normalization of C_k . By reversed sequence data $(x_n, x_{n-1}, \dots, x_1)$ repeat the above process, make $|UB_k| = -UB_k$, $k = n, n - 1, \dots, UB_1 = 0$. If the UF and UB curves intersect within the confidence interval, they are the possible abrupt transition points.

CASE ANALYSIS

Data Sources

Taking the annual precipitation data of the Yellow River Delta from 1954 to 2018 as an example, this paper studies and analyzes the evolution characteristics of annual precipitation in the Yellow River Delta. The location of the study area is shown in Fig. 1. The data were obtained from the China meteorological data website (<http://data.cma.gov.cn/>) and the Statistical Yearbook of Shandong province. The sequence independence test was conducted by Von Neuman's Q statistics. The test results showed that under the confidence level $\alpha = 0.05$, the test statistics - Q was 1.724 and was not in the critical value. Therefore, the null hypothesis was accepted and the precipitation data from 1954 to 2014 were considered as independent samples.

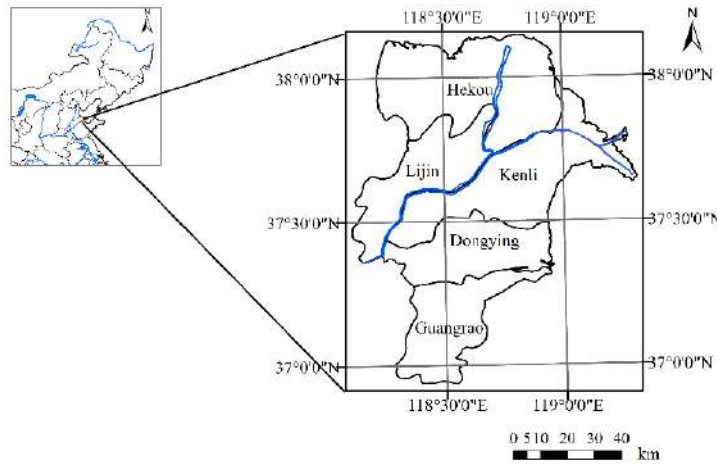


Fig. 1: The location map of the study area.

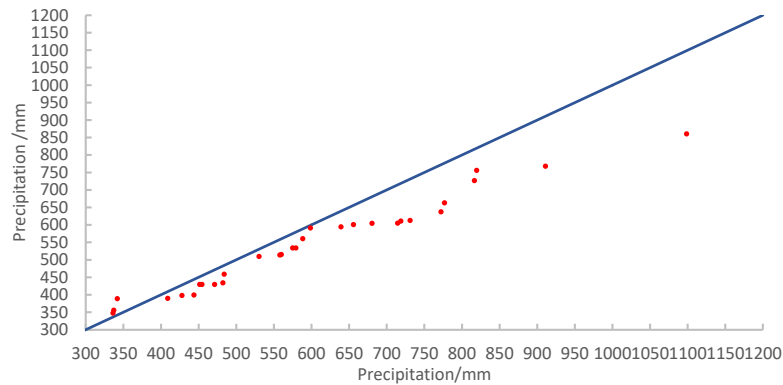


Fig. 2: Precipitation trend analysis.

Evolution Characteristic Analysis

Trend analysis: (1) ITA method was used to analyze the average annual precipitation for 61 consecutive years from 1954 to 2014, and the data of the first year was omitted. The first subsequence is 1955-1984, is the X-axis; The second subsequence is 1985-2014, which is the Y-axis. Draw the precipitation trend analysis diagram, and the analysis results are shown in Fig. 2.

ITA index D is calculated according to formula (2), as shown in Table 1.

As can be seen from Fig. 2, each point fell below the 1:1 line, showing a downward trend as a whole. When the precipitation is between 400mm-600mm, each point was close to the 1:1 line, with no obvious trend change. When the

Table 1: ITA index D.

Overall	Low	Medium	High
-9.48	-2.77	-5.87	-18.01

precipitation is between 650mm-800mm, the precipitation decreased significantly and gradually increased. However, at 800mm-850mm, the downward trend suddenly rebounded. When the precipitation reaches above 900mm, the downward trend became more obvious. At the same time, according to ITA index D in Table 1, the overall precipitation showed a downward trend, which gradually increased with the increase of precipitation.

(2) R/S analysis was performed on the annual average precipitation for 61 consecutive years from 1954 to 2014, and the R/S annual precipitation diagram was drawn. The results are shown in Fig. 3.

Periodic analysis: (1) In order to clarify the implied period of the precipitation time series, different time series lengths were selected to determine the consistency and stability of the implied period of different time series lengths. Therefore the three-time series of 40, 50 and 60 years were selected. The maximum entropy power spectrum was shown in Fig. 4.

(2) The Morlet continuous complex wavelet transform

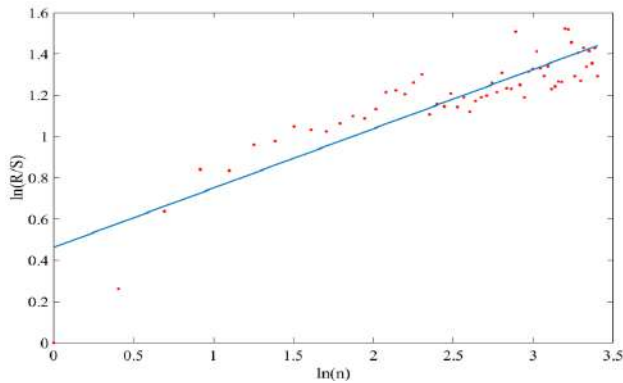


Fig. 3: R/S annual precipitation diagram.

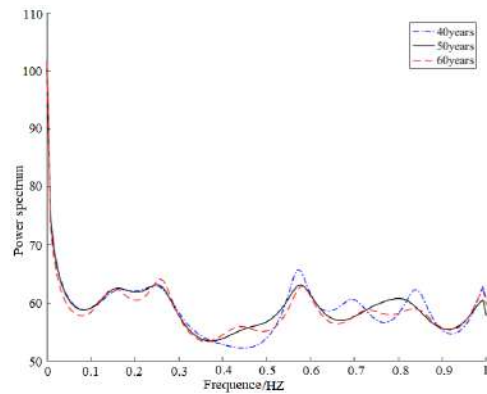


Fig. 4: MEM power spectrum of three precipitation sequences.

commonly used in the analysis of complex hydrological time series is selected to calculate the annual average precipitation of in the Yellow River, Shandong Province from 1954-2014. The wavelet coefficient transform diagram of precipitation and precipitation wavelet variance diagram are shown in Fig. 5 and Fig. 6 respectively.

Morlet continuous complex wavelet transform indicates that there were obvious interannual and chronological changes in precipitation, from top to bottom there were three-time scales of 20-32a, 8-18a, and 3-6a. The wavelet variance graph of precipitation suggests that there were three peaks of precipitation, corresponding to the time scale of 27, 13 and 5 years. Among them, the 27 year scale corresponds to the peak of wavelet variance and the period of oscillation are the strongest, which was the first main period of precipitation change, and plays a major role in the evolution of precipitation series. The second to third main periods of

precipitation change were 13 and 5 years in turn. The three periods play a decisive role in the change characteristics of precipitation in the whole time domain of the Yellow River Delta, but the 27 year period is the main one

Precipitation mutation test: The M-k method is used to analyze the annual average precipitation of the meteorological station in the Yellow River Delta from 1954 to 2014. The calculation results are shown in Fig. 7.

According to the M-K mutation test, UF is a standard normal distribution with a significance level of 0.05. From 1954 to 1980, the curve of UF and UB showed an upward trend. In the 1960s, the curve of UF exceeded the critical line of confidence level. It intersected in 1980 and 2003. Since 1987, the curve of UF was less than 0. From 2002 to 2014, there were many intersections between the curve of UF and UB.

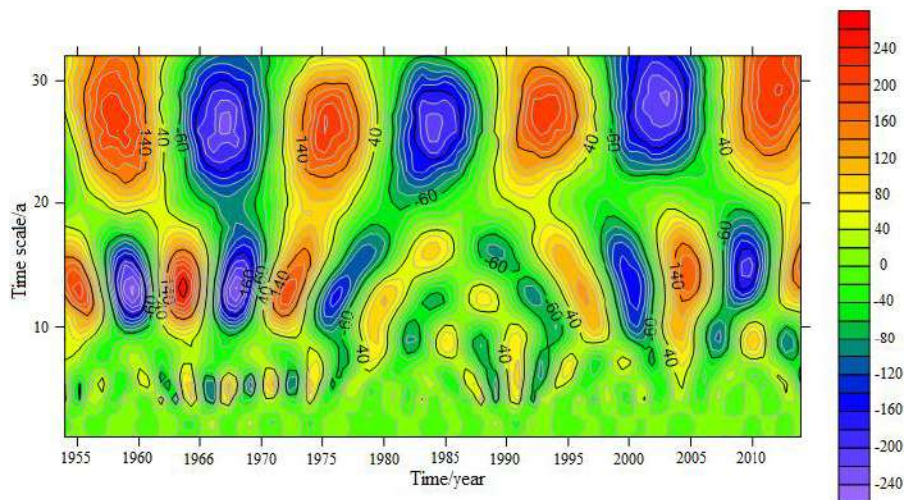


Fig. 5: Wavelet coefficient transform diagram of precipitation.

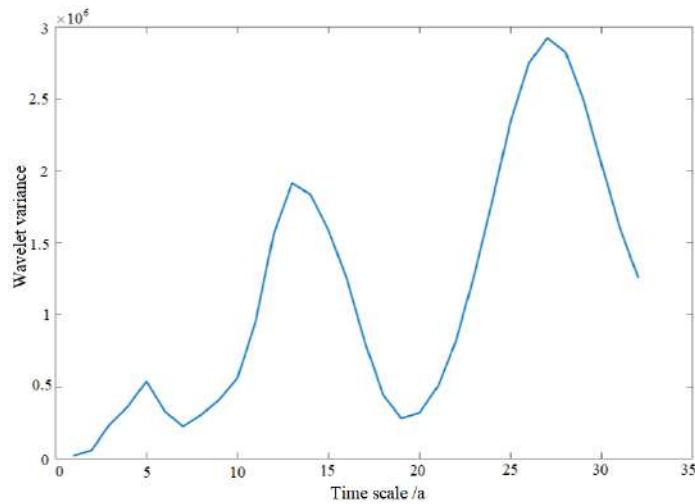


Fig. 6: Precipitation wavelet variance diagram.

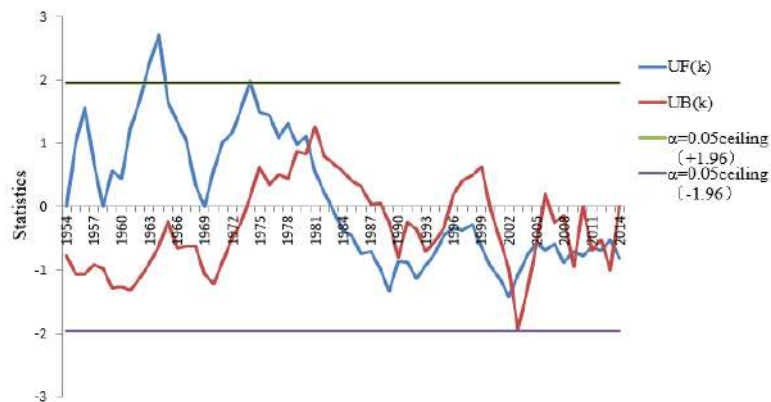


Fig. 7: M-K method mutation point test of annual average precipitation.

DISCUSSION

The precipitation trend analysis chart of 60 years is obtained by the ITA method. It indicates that the precipitation in the Yellow River Delta had a significant downward trend, and the downward trend increased gradually with the increase of precipitation. The results of R/S analysis suggest that the annual precipitation in this area showed a significant decreasing trend, which is consistent with the results of ITA analysis. In the future, the precipitation may show an increasing trend, and the trend is relatively strong.

The maximum entropy spectral analysis indicates that the optimal frequency value of the three sequence lengths was 0.24, the reciprocal was 4.167, and 5 years was chosen as the quasi period of the 61-year annual average precipitation sequence of the Yellow River Delta.

Morlet continuous complex wavelet transform indicates that there were three-time scales of precipitation: 20-32a, 8-18a, and 3-6a. From the scale of 20-32 years of analysis, the precipitation changes had a period of abundance - dry - abundance - dry - abundance - dry - abundance, with strong turbulence and globality. For this large-scale alternation of abundance and dry, the precipitation in Yellow River Delta showed a significant abrupt change characteristic. Specifically, before 1963, 1971-1980, 1988-1997, after 2007, the precipitation was abundant. 1963-1970, 1981-1987, 1998-2007, the precipitation was poor. By 2014, the contours have not been closed, indicating that the period after 2014 is in an abundant period. At this time, the periodic variation of precipitation was localized on the large time scale and the vibration was the strongest. From the 8-18 year scale analysis, the precipitation had 13 periods of abundance and

dry alternating. Specifically, before 1957, 1963-1965, 1971-1974, 1978-1985, 1995-1998, 2003-2006, after 2012, the precipitation was abundant. 1958-1962, 1966-1970, 1975-1977, 1986-1994, 1999-2002, 2007-2011, the precipitation was poor. For the change of precipitation on a smaller scale below 8 years, the shock centre in 1954-1990 is 4a. At this time, the change of the runoff period was the weakest on the small time scale. The results of Morlet continuous complex wavelet transform and R-S analysis are consistent with each other.

According to the M-K mutation test, UF is a standard normal distribution with a significance level of 0.05. Observing the UF and UB curves, the precipitation was larger during 1954-1980, showing an upward trend. During the 1960s, the UF curve exceeded the confidence level critical line and precipitation increased significantly. UF and UB curves intersected in 1980 and 2003. Influenced by the sudden change of sunspot and earth rotation period, the precipitation changed abruptly in 1980 and 2003. Since 1987, the UF curve has been less than 0, indicating a downward trend in precipitation. UF and UB curves have multiple intersections. Combined with trend analysis results, there was no significant mutation time in the annual precipitation in this region from 2002 to 2014. The reason may be that the annual natural precipitation is small. The annual natural precipitation change is more sensitive to the impact of heavy rainfall, and the relative variation of precipitation is large, resulting in poor precipitation variation and complex mutations. In addition, the impact of human activities is also an important reason for the complexity of precipitation mutations.

CONCLUSIONS

1. The analysis of ITA indicates that the precipitation in the Yellow River Delta had a significant downward trend in the past 61 years, and the downward trend gradually increased with the increase of precipitation. The R/S analysis suggests that the annual precipitation in the region had a significant downward trend in the past 61 years, which is consistent with the results of ITA analysis. However, the precipitation may show an upward trend in the future, and the trend is relatively strong.
2. The quasi-period of 61 annual precipitation in the Yellow River delta was about 5 years, which is consistent with the small scale oscillation period obtained by wavelet analysis based on maximum entropy spectral analysis and Burg recurrence theory.
3. According to the M-K mutation test, during 1954-1980, the precipitation showed an upward trend. In the 1960s,

the trend is obvious. In contrast, it showed a downward trend after 1987. In 1980 and 2003, the precipitation had a mutation. In 2002-2014, there was no significant mutation time point.

4. Although this paper comprehensively evaluates the evolution characteristics of precipitation, it doesn't consider the physical mechanism of precipitation change. There are some shortcomings, which need to be further optimized.

ACKNOWLEDGEMENTS

The authors wish to thank the National Natural Science Foundation of China (51609087, 51709114), National Key Research and Development Plan Project (2017YFC1501201), Key Scientific Research Project of Colleges and Universities in Henan Province (CN) (17A570004), Collaborative Innovation Centre of Water Resources Efficient Utilization and Protection Engineering, Henan Province.

REFERENCES

- Abry, P. and Veitch, D. 1998. Wavelet analysis of long-range-dependent traffic. *IEEE T. Inform. Theory*, 44(1): 2-15.
- Adamowski, J. and Chan, H. 2011. A wavelet neural network conjunction model for groundwater level forecasting. *Journal of Hydrology*, 407(1-4): 28-40.
- Bassingthwaight, J.B. and Raymond, G.M. 1994. Evaluating rescaled range analysis for time series. *Ann. Biomed. Eng.*, 22(4): 432-444.
- Ding, H.L., Xiao, W.G., Chen, X.H., Zhang, Y. and Chen, L.L. 2014. Analysis of precipitation change trend in Binjiang river basin. *Journal of China Hydrology*, 34(05): 67-74.
- Chen, S.C., Huang, B.S., Shi, F.X., Qiu, J. and Shen, D.X. 2019. Spatial and temporal variation and probability statistical characteristics of extreme precipitation in the Beijiing river basin from 1956 to 2016. *China Rural Water and Hydropower*.
- Galy-Lacaux, C., Laouali, D., Descroix, L., Gobron, N. and Lioussé, C. 2009. Long term precipitation chemistry and wet deposition in a remote dry savanna site in Africa (Niger). *ACP*, 9: 1579-1595.
- Hjelmfelt, A.T. 1988. Fractals and the river length catchment ratio. *JAWRA*, 24(2): 455-459.
- Huang, D., Liu, Z.B. and Jiang, Q.M. 2018. Application of non-parametric Mann-Kendall and innovative trend method analysis to groundwater quality parameters variation: a case study from aquifers in Xinsankuang Coal mine. *Journal of Water Resources and Water Engineering*, 29(3): 7-13.
- Huang, Y., Zhou, Z.F., Wang, J.G. and Wang, J.H. 2002. Application of R/S method to dynamic groundwater analysis. *Journal of Hohai University*, 30(1): 83-87.
- Hurst, H.E., Black, R.P. and Simaika, Y.M. (ed.) 1965. *Long-term Storage: An Experimental Study*. London: Constable.
- Li, G., Chen, Z.R., Tian, W., Zhao, J. and Li, Y. 2018. Novel grating signal subdivision method based on exponential smoothing algorithm. *Journal of Chongqing University of Technology (Natural Science)*, 32: 86-92+236.
- Liebmann, B. and Marengo, J. 2001. Interannual variability of the rainy season and rainfall in the Brazilian Amazon basin. *JCLI*, 14(22): 4308-4318.

- Liu, Y.H., Li, Y.B., Liang, X.Y. and Ran, C.H. 2019. Evaluation and change of water resources carrying capacity in China. *Resources and Environment in the Yangtze Basin*, 28(05): 80-91.
- Mann, H.B. 1945. Non-parametric test against trend. *J. Econometrica*, 13(3): 245-259.
- Mann, M.E., Bradley, R.S. and Hughes, M.K. 2015. Global-scale temperature patterns and climate forcing over the past six centuries. *Nature*, 392(6678): 779-787.
- Pei, Y.X. and Guo, M. 2001. The fundamental principle and application of sliding average method. *Journal of Gun Launch & Control*, 1: 21-23.
- Qiang, Z., Tong, J., Marco, G. and Stefan, B. 2005. Precipitation, temperature and runoff analysis from 1950 to 2002 in the Yangtze basin, China. *Hydrol. Sci. J.*, 50: 65-80.
- Ran, L., Wang, S. and Fan, X. 2010. Channel change at Toudaoguai station and its responses to the operation of upstream reservoirs in the upper Yellow River. *J. Geogr. Sci.*, 20(2): 231-247.
- Rao, A.R. and Bhattacharya, D. 1999. Hypothesis testing for long-term memory in hydrologic series. *J. Hydrol.*, 216(3): 183-196.
- Sohoulade Djebou, D.C. 2014. Analysis of watershed topography effects on summer precipitation variability in the southwestern United States. *J. Hydrol.*, 511(7): 838-849.
- Tarboton, D.G., Bras, R.L. and Rodriguez-Iturbe, I. 1988. The fractal nature of river networks. *Water Resour. Res.*, 24(8): 1317-1322.
- Teverovsky, V., Taqqu, M.S. and Willinger, W. 1999. A critical look at Lo's modified R/S statistic. *J. Stat. Plan. Infer.*, 80(1-2): 211-227.
- Wallis, J.R. and Matalas, N.C. 1970. Small sample properties of H and K-Estimations of the Hurst coefficient h. *Water Resour. Res.*, 6(6): 1583-1594.
- Wu, H. and Qian, H. 2017. Innovative trend analysis of annual and seasonal rainfall and extreme values in Shaanxi, China, since the 1950s. *Int. J. Climatol.*, 37(5), pp.2582-2592..
- Xiao, Y., Yuan, S.J., Zhang, B., He, X.T. and Yu, F. 2019. Spatial and temporal distribution of precipitation in Dadu river basin. *Yangtze River*, 50(S1): 60-67.
- Yang, L.X. and Sun, D.Y. 2013. The application of R/S to the periodic analysis of runoff time series. *Yellow River*, 35(9): 51-52.
- Zhang, A.L., Gao, R.Z., Wang, X.X., Liu, T.X. and Fang, L.J. 2020. Historical trends in air temperature, precipitation, and runoff of a plateau inland river watershed in North China. *Water*, 12(1): 74.
- Zhang, S.W., Wang, W.S., Ding, J. and Chang, F.X. 2005. Application of fractal theory to hydrology and water resources. *Advances in Water Science*, 16(1): 141-146.
- Zhao, H., Zhang, M.S. and Pan, R.Z. 2019. Prediction and analysis of future rainfall change in pilot project sponge city based on wavelet analysis. *Water & Wastewater Engineering*, 9: 29-35.
- Zuo, B.B., Xu, Z.X., Ren, M.F. and Li, P. 2019. Study on precipitation characteristics of Tongzhou district, Beijing from 1966 to 2016. *Journal of Beijing Normal University (Natural Science)*, 5: 556-563.



Modelling Sorption and Leaching Behaviour of Sulphate in Light Sierozem (Calcids) Columns with Rape Straw Biochar Amendments with Steady Flow

B. W. Zhao†, X. J. Nan, Y. Q. Li, H. Liu and K. X. Duan

School of Environmental and Municipal Engineering, Lanzhou Jiaotong University, No. 88, West Anning Rd., Lanzhou 730070, P. R. China

†Corresponding author: Baowei Zhao; zhbw2001@sina.com

Nat. Env. & Poll. Tech.
Website: www.neptjournal.com

Received: 07-02-2020

Revised: 22-02-2020

Accepted: 02-05-2020

Key Words:

Biochar
Sorption
Leaching
Light sierozem
Modelling

ABSTRACT

Biochar amendments could enhance retention of nutrients such as ammonium (NH_4^+), nitrate (NO_3^-), and phosphate (PO_4^{3-}) in soils. However, the situation for sulphate (SO_4^{2-}), which is an indispensable nutrient element for crop growth, is unclear. In this paper, the effects of biochar derived from rape (*Brassica campestris* L.) straw at 600°C on the sorption and leaching of SO_4^{2-} in light sierozem (Calcids) was studied in columns, where biochar amendment rate, column soil height, solution pH value and initial sulphate concentration were selected as factors. It is shown that the transport of sulphate was a significant non-equilibrium process and the sorption and leaching curves (SLCs) of sulphate were asymmetrical. The breakthrough time would be increased by increasing biochar amendment and soil column height, and by decreasing solution pH value and initial sulphate concentration. The SLCs of bromide trace were fitted to determine dispersion coefficient (D) using equilibrium convection dispersion equation (CDE_{eq}). The non-equilibrium (two-site) model ($\text{CDE}_{\text{non-eq}}$) with the results from CDE_{eq} was used to simulate the transport processes of sulphate in the soil column, with good fitness, using software CXTFIT 2.1 fitting. The results could supply an implication for biochar application in loess areas.

INTRODUCTION

Sulphur is an indispensable nutrient element for crop growth (Frossard et al. 2012). It is a protein and amino acid constituent element, acts as an enzymatic reactive centre and is an important medium for chlorophyll, sitosterone, glutathione and coenzyme syntheses. Although sulphur is not a structural element of plant cells, it plays an important role in plant growth regulation, detoxification, defence and resistance, and quality of plant (Frossard et al. 2012). Therefore, the migration and conversion of sulphur in soils have been paid more and more attention (Blum et al. 2013, Matusik 2014).

Biochar is the product derived from biomass pyrolysis under limited oxygen conditions. Biochar can be used as a soil amendment to improve soil quality and to increase crop production. The indirect nutrient value of biochar is its ability to retain nutrients in the soil and thus to reduce nutrient leaching losses, resulting in increased nutrient uptake by plants and crop production (Lehmann & Joseph 2009). Recently, many reports showed that when biochars were added into soils, the nutrient ions (NH_4^+ , NO_3^- and PO_4^{3-}) in soils were retained, the nitrogen and phosphorus leaching losses in soils were reduced, and plant uptake of

these nutrients was improved (Saarnio et al. 2013, Zheng et al. 2013, Soenne et al. 2014, Mandal et al. 2016, Zhang et al. 2016). However, to our knowledge, few reports on the effect of biochar on sulphur fate (e.g. sorption and leaching) in soil have appeared in the literature (Zhao et al. 2017).

The solute transport in porous media is a complex physical and chemical process (Marín-Benito et al. 2013, Jing et al. 2014). To date, a few soil column experiments have been conducted to investigate the retention and leaching of ammonium (NH_4^+), nitrate (NO_3^-), and phosphate (PO_4^{3-}) ions in the presence of biochars (Laird et al. 2010, Yao et al. 2012, Jing et al. 2014, Kanthle et al. 2016, Pratiwi et al. 2016, Xu et al. 2016, Feng et al. 2017, Lou et al. 2017, Joseph et al. 2018, Shi et al. 2020). However, no predicting or modelling for nutrient migration is found in these researches. The non-equilibrium convection dispersion equation ($\text{CDE}_{\text{non-eq}}$) is often used to describe the process of reactive solute transport in soil. $\text{CDE}_{\text{non-eq}}$ can be grouped into two categories, i.e. Two-region Model (TRM) and Two-site Model (TSM) (Huo et al. 2013, Srinivasan & Sarmah 2014). As stagnant water and slow reaction are concerned in these models, the sorption and leaching of solute can be described more accurately. However, up to date, there have been few applications of

these models to describe the nutrient migration in soils in the present of biochars.

Loess soils (e.g. light sierozem (Calcids)) have high porosity and permeability, low organic matter content and loosely packed particles. It seems that biochar should be added into loess soils to improve retention of nutrients (e.g. sulphur) and crop growth. Thus, in this paper, the column experiments were conducted to investigate the sorption and leaching of sulphate in light sierozem (Calcids) with the amendment of rape straw biochar. The main objectives of this experiment were to (i) evaluate the effects of biochar amendment rate, column soil height, solution pH value and initial sulphate concentration on the sorption and leaching of SO_4^{2-} ; and (ii) model the sorption and leaching processes of sulphate in light sierozem columns with CDE_{non-eq} using software CXTFIT 2.1 fitting.

MATERIALS AND METHODS

Chemicals and Materials

Analytical grade sodium sulphate and potassium bromide with spectral purity were purchased from Shanghai Chemical Co., China. Deionized water was used in all the experiments.

Rape (*Brassica campestris L.*) straw was collected from Baiyin, Gansu, China. The feedstock was washed with tap water, air-dried, ground using a grinder and passed through a 0.43 mm sieve. This < 0.43 mm fraction was placed in crucibles and heated in a muffle furnace at 600°C for 6 h to pyrolyze the biomass. The obtained samples were washed with 1 mol·L⁻¹ HCl 4 times, washed with deionized water several times and then dried in an oven at 80°C. The prepared biochar was labelled as BS600. The basic properties of the biochar are as follows: pH 5.36; BET specific area 157.5 m²·g⁻¹; element composition, C 80.51%, H 1.85%, N 1.17%, O 15.79% and S 0.68%; atomic ratios, (N + O)/C 0.21, H/C 0.02.

The soil to be tested was collected from a rural farm field of light sierozem in Yuzhong County, Lanzhou, China; stones and other debris were picked out, and the soil was left to dry naturally. Then, the soil was thoroughly mixed and passed through a 20-mesh sieve. The basic physicochemical properties of the soil are as follows: pH 7.97; organic matter content 14.12 g·kg⁻¹; cation exchange capacity (CEC) 5.65 cmol·kg⁻¹; efficient sulphur 36.7 mg·kg⁻¹.

Column Sorption and Leaching

The glass column was 2.5 cm in diameter. At the bottom of the column, there was a sheet of cotton and a quartz sand layer approximately 1.5 cm in height, which should prevent

the elution of soil fines. The column was packed with soil or the mixture of soil and BS600. After the column was filled, a quartz sand layer was placed upon it to obtain the uniform distribution of solution at the surface. The column was firstly saturated with water. Then, at a steady flow state ($v = 7.64 \text{ cm}\cdot\text{h}^{-1}$), Br^- (0.05 mol·L⁻¹) or SO_4^{2-} solution was input using a peristaltic pump until a constant concentration of solute in the effluent was obtained. Then, distilled water was pumped into the column to facilitate leaching. The effluent was collected at each 0.1 pore volume (PV) interval. The Br^- concentration in the effluent was analysed using the ion-selective electrode method, and SO_4^{2-} was analysed using barium chromate indirect atomic absorption spectrometry (AAS) (Ni et al. 2012). The BS600 amendment rate (0%, 5%, 10% and 15%), height of soil column (5, 10, 15 and 20 cm), solution pH value (3, 5, 7 and 9) and initial SO_4^{2-} concentration (50, 100, 150, and 200 mg·L⁻¹) were kept as 5%, 10 cm, 7 and 50 mg·L⁻¹, respectively, except that they were tested as influencing factors. The bulk density (ρ_b) of the packed columns was determined as 1.14, 0.93, 0.83 and 0.75 g·cm⁻³ with the BS600 amendment rate at 0%, 5%, 10% and 15%, respectively.

Solute Transport Modeling

The equilibrium convection dispersion equation (CDE_{eq}) (1) was used to describe the one-dimensional homogeneous transport of nonreactive solute Br^- in the soil without or with BS600 (Pang & Close 1999, Fan et al. 2011):

$$R \frac{\partial C}{\partial t} = D \frac{\partial^2 C}{\partial x^2} - v \frac{\partial C}{\partial x} \quad \dots(1)$$

Where, C is the solute concentration (mg·L⁻¹); t is time (h); x is the vertical distance (cm); D is the dispersion coefficient (cm²·h⁻¹), and v is the average pore water velocity (cm·h⁻¹). The following initial and boundary conditions are assumed for Br^- transport in a column (Shao et al. 1998, Pang & Close 1999, Inoue et al. 2000, Kamra et al. 2001, Fan et al. 2011):

$$C(x, 0) = 0 \quad \dots(2)$$

$$C(0, t) = C_0 \quad \dots(3)$$

$$\left[-D \frac{\partial C}{\partial x} + vC \right]_{x=0^+} = vC_0 \quad \dots(4)$$

Where, C_0 is the initial concentration of solute (mg·L⁻¹). Parameter D was calculated from the fitting of the sorption and leaching curve (SLC) for nonreactive solute Br^- using CXTFIT 2.1, where the value of the retardation coefficient (dimensionless) (R) was set to 1 because it is assumed that bromide ions have minimal sorption onto soil particles (Fan et al. 2011). The obtained D parameters were later used as input for modelling sulphate transport.

Two-site Model (TSM) and Two-region Model (TRM) can be put into the same dimensionless form when considering the description of linear sorption and steady flow (Huo et al. 2013, Srinivasan & Sarmah 2014). If dimensionless parameters are used, the CDE_{non-eq} for solute transport is described as:

$$\beta R \frac{\partial C_1}{\partial T} = \frac{1}{P} \frac{\partial^2 C_1}{\partial Z^2} - \frac{\partial C_1}{\partial Z} - \omega(C_1 - C_2) \quad \dots(5)$$

$$(1 - \beta)R \frac{\partial C_2}{\partial T} = \omega(C_1 - C_2) \quad \dots(6)$$

$$f = \frac{\beta R - 1}{R - 1} \quad \dots(7)$$

$$a = \frac{\omega V}{(1 - \beta)RL} \quad \dots(8)$$

Where the subscript 1 and 2 refer to equilibrium and non-equilibrium sorption sites; the retardation factor R can be calculated directly from solution breakthrough curves; β is the fraction factor (dimensionless); a is the first-order mass transfer coefficient governing the rate of solute exchange between both phases (h^{-1}); f is the fraction of exchange sites assumed to be at equilibrium for the TSM; ω is the dimensionless mass transfer coefficient; L is the length of the column (cm); and the dimensionless parameters T , Z and P (peclt number) are defined as $T = Vt/L$, $Z = x/L$ and $P = VL/D$, respectively. The degree of non-equilibrium can be directly evaluated with the β and ω values. When the β value equals to 1, there is no physical non-equilibrium process for non-reactive solute or all the sorption sites are instantaneously

occupied by a reactive solute (Pang & Close 1999). When the β value is less than 1, the sorption of reactive solute is rate-limited, where high ω value indicates the fast sorption/diffusion process occurs while low ω value indicates the slow sorption/diffusion process exists (Brusseau et al. 1989). In this paper, the results from CDE_{eq} and the non-equilibrium (two-site) model was used to simulate the transport processes of sulphate in the soil column.

RESULTS AND DISCUSSION

Br⁻ SLCs

Fig. 1 shows the sorption and leaching curves (SLCs) for transport ($v = 7.64 \text{ cm.h}^{-1}$; $L=10 \text{ cm}$, $C_0 = 0.05 \text{ mol.L}^{-1}$ and $\text{pH} = 7$) of the nonreactive bromide ions (Br^-) through columns with the BS600 addition rates of 0%, 5%, 10% and 15%, respectively. Although the addition rates of BS600 were different, the SLCs were symmetrical without tailing. However, with the increase in the amount of biochar added, the PV also increased from 1.3 to 1.5. In the present study no preferential flow of Br^- was observed in any of the columns, as the maximum breakthrough for the bromide trace was similar on all occasions, and no significant tailing was observed in the Br^- SLCs, which is an indication of a well saturated soil column.

The SLCs of the nonreactive solute Br^- were fitted with CDE_{eq} using CXTFIT 2.1, and the results are shown in Fig. 1 and listed in Table 1. All the modelled curves were well fitted the experimental data (Fig. 1), with no tailing

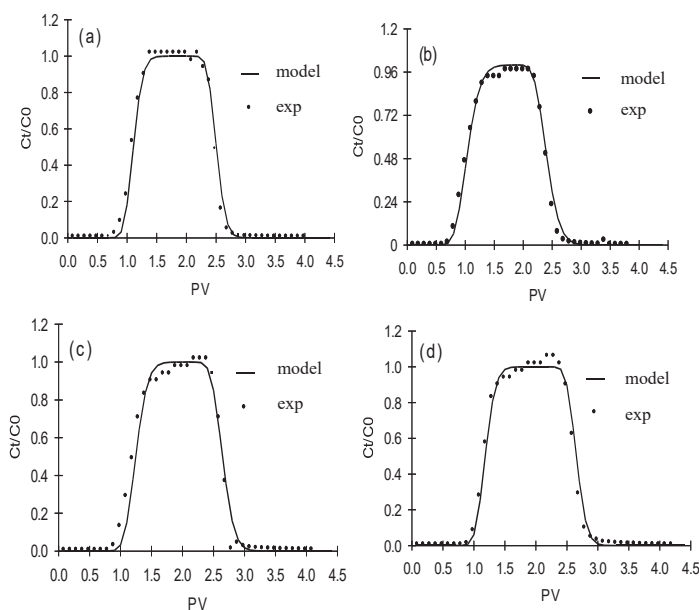


Fig. 1: Experimental and stimulated SLCs for Br^- transport in columns with 0% (a), 5% (b), 10% (c) and 15% (d) BS600 amendment.

Table 1: Fitted parameters using CDE_{eq} for SLCs of Br^-

BS600 addition (%)	D ($cm^2 \cdot h^{-1}$)	r^2	MSE
0	0.48	0.997	0.0005
5	1.11	0.995	0.0008
10	0.57	0.987	0.0025
15	0.47	0.997	0.0006

and asymmetry, indicating the absence of physical non-equilibrium conditions during the transport of Br^- through the soil columns. The values of the regression coefficient r^2 and mean square error (MSE) are larger than 0.987 and less than 0.0025 respectively, indicating that CDE_{eq} fits the transport of nonreactive solute Br^- well. Meanwhile, the values of D were obtained as 0.48, 1.11, 0.57 and $0.47 \text{ cm}^2 \cdot h^{-1}$, respectively.

Effect of Biochar Amendment Rate

Fig. 2 includes the experimental and stimulated SLCs corresponding to the SO_4^{2-} transport in soil columns ($v = 7.64 \text{ cm} \cdot h^{-1}$; $L = 10 \text{ cm}$, $C_o = 50 \text{ mg} \cdot L^{-1}$ and $pH = 7$) with 0, 5%, 10% and 15% BS600 addition. Four SLCs are asymmetrical and tailing, showing that BS600 is an important factor in SO_4^{2-} transport in the columns. The breakthrough times were 1.6, 1.7, 1.9 and 2.1 PV for the columns with 0, 5%, 10% and 15% BS600. The breakthrough time was delayed with the addition rate of BS600 increasing. These phenomena illustrate that the addition of high content of biochar could be beneficial to the retention of sulphate in the soil and reduction in the loss of sulphur. Besides, the breakthrough time in the

SO_4^{2-} SLC with no BS600 addition shifted significantly by 1.3 to 1.6 compared with that of Br^- with no BS600 addition (Fig. 1), which showed SO_4^{2-} is a reactive solute to the soil. Moreover, with the addition rate of BS600 increasing from 5% to 15%, PVs in the SO_4^{2-} SLCs shifted by 1.7 to 2.1. This indicates that biochar amendment changed further the sorption properties of soil and was indicative of the influence of the retardation. It can be deduced that the retardation is mainly due to the roles of sorption-related processes of sulphate onto soil or biochar-soil mixture. In our previous study (Zhao et al. 2017), sulphate sorption on BS600, soil and BS600-soil mixture was investigated by batch experiments. It was shown that sulphate was mainly sorbed onto BS600 through electrostatic interaction, whereas onto the soil via electrostatic interaction and formation of poorly soluble $CaSO_4$. Shi et al. (2020) designed the column leaching experiment over 30 days to evaluate the effects of a granular biochar-mineral urea composite on cumulative N release and of dissolved organic carbon (DOC). Significant loss decrease of NH_4^+ -N and DOC by >70% and by 8% was founded. Loss decrease of NH_4^+ -N could be due to NH_4^+ adsorption onto or by functional groups such as $-COO^-$ ($-COOH$), amino and $-O^-$ ($-OH$) on the biochar surfaces while that of DOC was attributed to the formation of organo-mineral micro-aggregates.

The SLCs of SO_4^{2-} in columns with the different BS600 addition rates were fitted with CDE_{non-eq} and the results are shown in Fig. 2 and listed in Table 2. CDE_{non-eq} could fit

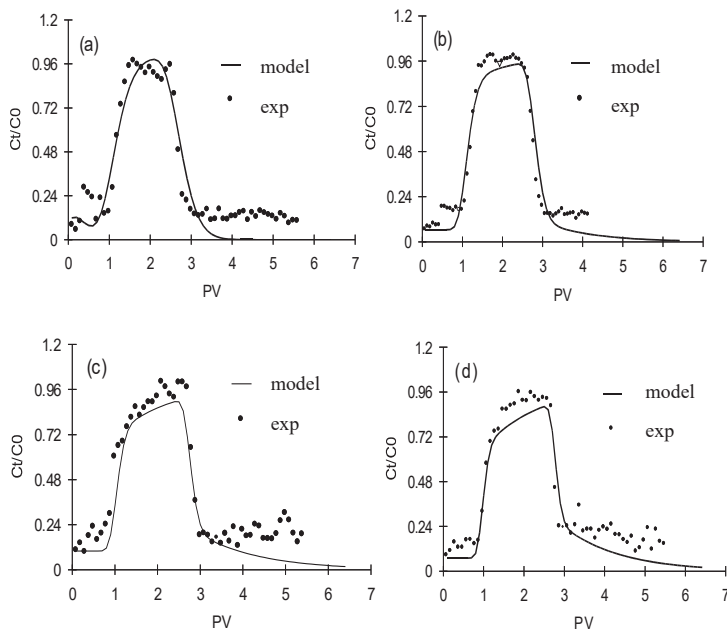


Fig. 2: Experimental and stimulated SLCs for SO_4^{2-} transport in columns with 0% (a), 5% (b), 10% (c) and 15% (d) BS600 amendment.

Table 2: Fitted parameters using CDE_{non-eq} for SLCs of SO₄²⁻ through different columns.

Column		<i>R</i>	<i>β</i>	<i>ω</i>	<i>r</i> ²	<i>MSE</i>
BS600 addition (%)	0	1.47	0.85	0.32	0.98	0.0019
	5	1.33	0.85	0.16	0.96	0.0061
	10	1.53	0.82	0.21	0.99	0.0019
	15	1.71	0.74	0.28	0.97	0.0033
Column soil height (cm)	5	1.13	0.89	0.14	0.88	0.0010
	10	1.33	0.85	0.16	0.96	0.0061
	15	1.48	0.72	0.35	0.88	0.0013
	20	1.50	0.69	0.45	0.93	0.0076
Solution pH value	3	2.03	0.57	0.43	0.97	0.0027
	5	1.69	0.65	0.40	0.95	0.0054
	7	1.72	0.65	0.31	0.96	0.0040
	9	1.59	0.63	0.40	0.95	0.0044
Initial SO ₄ ²⁻ concentration (mg.L ⁻¹)	50	1.46	0.69	0.14	0.96	0.0054
	100	1.42	0.78	0.15	0.98	0.0032
	150	1.33	0.92	0.19	0.96	0.0041
	200	1.46	0.79	0.15	0.96	0.0054

the transport of the reactive solute SO₄²⁻ well (*r*² 0.96 and *MSE* 0.0061). The resultant *β* values are 0.85, 0.85, 0.82 and 0.74, respectively, for the four column runs. These *β* values are much lower than 1, indicating a part of the sorption sites did not participate in the instantaneous adsorption, *i.e.* SO₄²⁻ adsorption was in the non-equilibrium state. In column tests, the transport, adsorption and desorption of solute are taking place in a dynamic system that is subject to the effects of hydrodynamic conditions. All the *R* values are larger than 1, which also indicated the sorption and leaching processes were non-equilibrium. Thus, the CDE_{non-eq} is more adequate for simulating SO₄²⁻ transport in the soil or the soil with BS600 amendment. In other words, non-equilibrium sorption should be taken into account in simulating SO₄²⁻ transport in the saturated loess.

Effect of Column Soil Height

Fig. 3 illustrates the experimental and stimulated SLCs corresponding to the sorption and leaching of SO₄²⁻ in soil columns (*v* = 7.64 cm.h⁻¹; *C*₀ = 50 mg.L⁻¹ and pH = 7) with 5, 10, 15 and 20 cm of column soil height and 5% BS600 content. The SLCs of SO₄²⁻ through columns were all asymmetrical, indicating the interaction of SO₄²⁻ with the soil to a greater extent with increasing column soil height. The phenomena in Fig. 3 (a) and (b) are not significant, but those in Fig. 3 (c) and (d) are significantly asymmetrical tailing. The breakthrough time of 1.6, 1.7, 1.9 and 2.0 PV for SO₄²⁻ in Fig. 3 (a), (b), (c) and (d) were observed, respectively. With the increase in column soil height, the contact between soil or soil with biochar and SO₄²⁻ increased. It seemed that the

time-dependent interactions occurred between SO₄²⁻ and the soil components (Brusseau et al. 1989). The previous study showed that dissolved nutrients (NO₃⁻ and PO₄³⁻) are first taken up into biochar pores along a concentration gradient and through capillary action, followed by surface sorption and retention processes which block biochar pores and result in deposition of a nutrient-rich organomineral (plaque) layer (Joseph et al. 2018).

The obtained parameters *R*, *β* and *ω* from the SLCs fitting by CXTFIT 2.1 using CDE_{non-eq} approach are listed in Table 2 (*r*² 0.88, *MES* 0.0076). All the retardation coefficient *R* values are larger than 1 and increased with column soil height increasing. The values of *β* and *ω* further indicates that the system was under non-equilibrium conditions at the selected flow rates. The values of *ω* change from 0.14 to 0.45 and the values of *β* is less than 1, indicating there is some fraction of immobile water or rate-limited sorption sites.

Effect of Initial Solution pH

Fig. 4 shows the experimental and stimulated SLCs that corresponding to the SO₄²⁻ transport (*v* = 7.64 cm.h⁻¹; L=10 cm, and *C*₀ = 50 mg.L⁻¹) in soil columns with 5% BS600 amendment rate and with different pH values of the initial solutions. The SLCs are asymmetrical and tailing. PV decreased from 2.0 to 1.6 when the initial pH values rose from 3 to 9. This could be attributed to the effects of pH values on the adsorption capacity of adsorbents. It has been reported that the sorbed amount of SO₄²⁻ on the soil, BS600, and BS600-soil decreased as the solution pH values increased from 2 to 12 (Zhao et al. 2017). The variation of sorbed

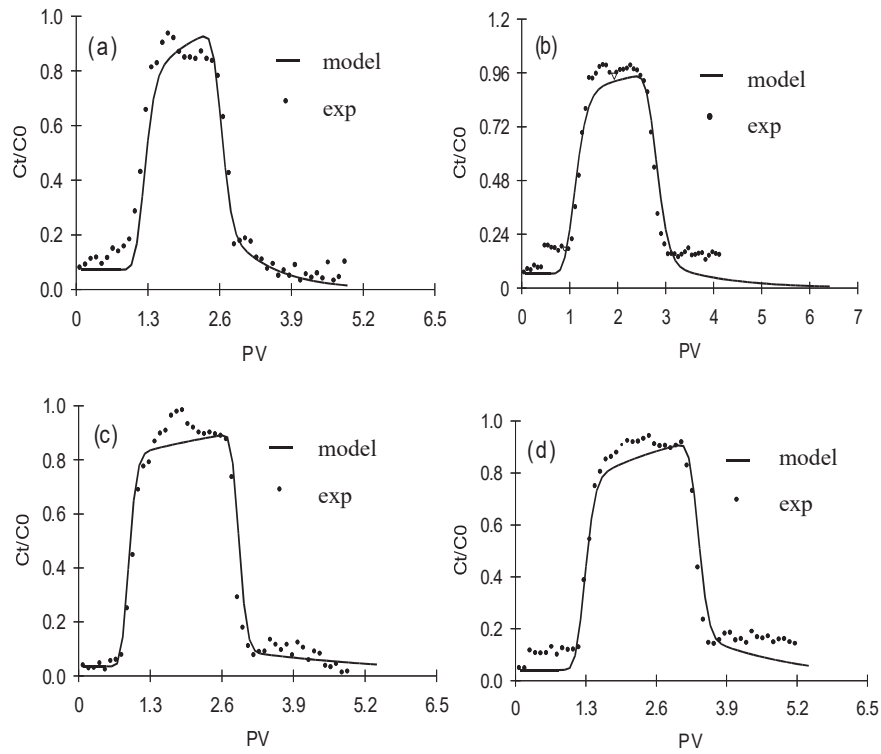


Fig. 3: Experimental and stimulated SLCs for SO_4^{2-} transport in columns in 5 (a), 10 (b), 15 (c) and 20 cm (d) height.

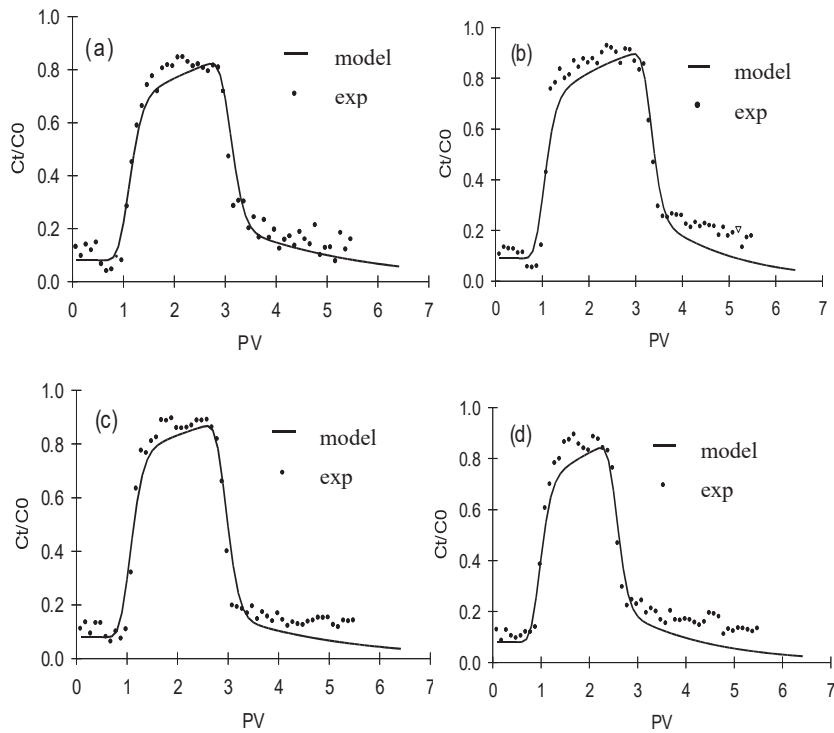


Fig. 4: Experimental and stimulated SLCs for SO_4^{2-} transport in columns with 3 (a), 5 (b), 7 (c) and 9 (d) of solution pH value.

amount of SO_4^{2-} with pH values might be due to changes in the electrostatic interactions between SO_4^{2-} and the charged sorbent surfaces. At higher pH values, the soil and biochar surfaces were more negatively charged, and therefore, the sorbed amount of SO_4^{2-} decreased. Moreover, OH^- competed with SO_4^{2-} onto the sorbent surface sites, which also led to a decrease in the sorbed amount of SO_4^{2-} (Zhao et al. 2017).

The fitted parameters for SO_4^{2-} SLCs using $\text{CDE}_{\text{non-eq}}$ models by CXTFIT 2.1 are also listed in Table 2. $\text{CDE}_{\text{non-eq}}$ could fit the transport of the reactive solute SO_4^{2-} well (r^2 0.95 and MSE 0.0054). When the initial solution pH values were 3, 5, 7 and 9, the values of R were 2.03, 1.69, 1.72 and 1.59, respectively, indicating the adsorption capacity of SO_4^{2-} decreased at large as the pH increased. Lou et al. also found that an increase in the retardation coefficient R causes an increase in the adsorption capacity (Lou et al. 2005). However, the values β and ω have no significant difference.

Effect of Initial SO_4^{2-} Concentration

Fig. 5 illustrates the experimental and stimulated SLCs corresponding to the sorption and leaching of SO_4^{2-} in soil columns ($\nu = 7.64 \text{ cm.h}^{-1}$; $L = 10 \text{ cm}$ and $\text{pH} = 7$) with 50, 100, 150 and 200 mg.L^{-1} of initial SO_4^{2-} concentrations and

5% BS600 amendment. The breakthrough times were 1.7, 1.6, 1.6 and 1.4 PV when initial concentrations were 50, 100, 150 and 200 mg.L^{-1} , respectively. This also shows that an increase in the initial concentrations of solutions led to less breakthrough time. It was shown in our previous study (Zhao et al. 2017), that the maximum sorption capacities of BS600, BS600-soil mixture and the soil for SO_4^{2-} were 19.57, 26.81, and 28.63 mg.g^{-1} , respectively. Higher concentration gradients of SO_4^{2-} in the systems would lead to a higher occupation rate of the reactive sorption sites (Takaya et al. 2016) and then less breakthrough time.

As seen in Table 2, $\text{CDE}_{\text{non-eq}}$ could fit the transport of the reactive solute SO_4^{2-} well (r^2 0.96, MES 0.0054). The change in initial concentrations of sulphate did not result in a significant change in R , β and ω values.

CONCLUSION

The sorption and leaching of sulphate through soil columns with or without BS600 amendment was a significant non-equilibrium process and the sorption and leaching curves (SLCs) of sulphate were asymmetrical and tailing. Increasing biochar amendment and column height would lead to a

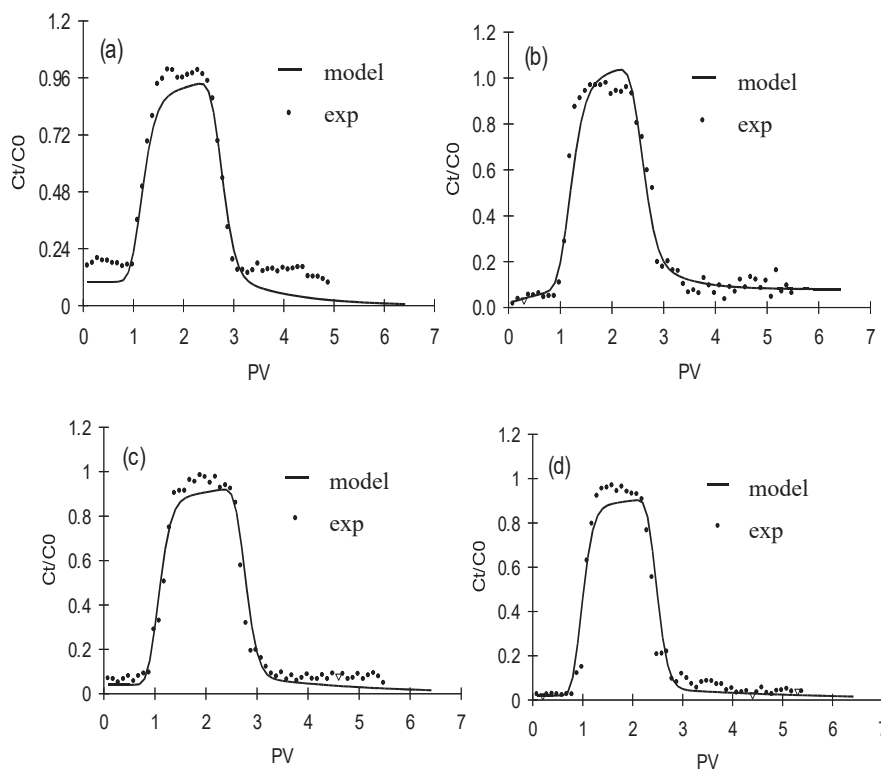


Fig. 5: Experimental and stimulated SLCs for SO_4^{2-} transport in columns with 50 (a), 100 (b), 150 (c) and 200 mg.L^{-1} (d) of initial SO_4^{2-} concentration.

delaying breakthrough time and much sulphate retention. Meanwhile, decreasing solution pH value and initial sulphate concentration also enhanced the retention effect. The non-equilibrium convection dispersion equation ($CDE_{\text{non-eq}}$) could be used to fit the sorption and leaching behaviour of sulphate well, using software CXTFIT 2.1 fitting.

ACKNOWLEDGEMENT

This work was financially supported by the National Natural Science Foundation of China (51766008, 21467013, 21167007).

REFERENCES

- Blum, S. C., Lehmann, J., Solomon, D., Caires, E. F., Reynaldo, L. and Alleoni, F. 2013. Sulphur forms in organic substrates affecting S mineralization in soil. *Geoderma*, 200: 156-164.
- Brusseau, M. L., Rao, P. S. C., Jessup, R. E. and Davidson, J. M. 1989. Flow interruption: A method for investigating sorption non-equilibrium. *J. Contam. Hydrol.*, 4: 223-240.
- Fan, Z. S., Casey, F. X. M., Hakk, H., Larsen, G. L. and Khan, E. 2011. Sorption, fate, and mobility of sulfonamides in soils. *Water Air Soil Pollut.*, 218: 49-61.
- Feng, Y., Lu, H., Liu, Y., Xue, L., Dionysiou, D. D., Yang, L. and Xing, B. 2017. Nano-cerium oxide functionalized biochar for phosphate retention: preparation, optimization and rice paddy application. *Chemosphere*, 185: 816-825.
- Frossard, E., Bünemann, E. K., Oberson, A. and Kertesz, M. A. 2012. Phosphorus and Sulphur in Soil. CRC Press, pp. 26.2-26.15.
- Huo, L., Qian, T., Hao, J. and Zhao, D. 2013. Sorption and retardation of strontium in saturated Chinese loess: experimental results and model analysis. *J. Environ. Radioactiv.*, 116: 19-27.
- Inoue, M., Simunek, J., Shiozawa, S. and Hopmans, J. W. 2000. Simultaneous estimation of soil hydraulic and solute transport parameters from transient infiltration experiments. *Adv. Water Resour.*, 23: 677-688.
- Jing, Y., Chen, X., Li, Q., Jin, Z., Huang, Q., Zhang, J., Chen, C. and Lu, S. 2014. Effects of biochar application on the vertical transport of NO_3^- -N in the red soil and its simulation. *Chinese J. App. Ecol.*, 25: 3161-3167.
- Joseph, S., Kammann, C. I., Shepherd, J. G., Conte, P., Schmidt, H.P., Hagemann, N., Rich, A. M., Marjo, C. E., Allen, J., Munroe, P., Mitchell, D. R. G., Donne, S., Spokas, K. and Graber, E. R. 2018. Microstructural and associated chemical changes during the composting of a high temperature biochar: Mechanisms for nitrate, phosphate and other nutrient retention and release. *Sci. Total Environ.*, 618: 1210-1223.
- Kamra, S. K., Lennartz, B., Genuchten, M. and Widmoser, P. 2001. Evaluating non-equilibrium solute transport in small soil columns. *J. Contam. Hydrol.*, 48: 189-212.
- Kanthle, A. K., Lenka, N. K., Lenka, S. and Tedia, K. 2016. Biochar impact on nitrate leaching as influenced by native soil organic carbon in an Inceptisol of central India. *Soil Tillage Res.*, 157: 65-72.
- Laird, D., Fleming, P., Wang, B., Horton, R. and Karlen, D. 2010. Biochar impact on nutrient leaching from a Midwestern agricultural soil. *Geoderma*, 158: 436-442.
- Lehmann, J. and Joseph, S. 2009. *Biochar for Environmental Management: Science and Technology*, Earthscan.
- Lou, Y., Zhang, Y. and Lin, X. 2005. Effect of forms of nitrogen fertilizer on the bioavailability of heavy metals in the soils amended with biosolids and their uptake by corn plant. *J. Zhejiang Univ.*, 31: 392-388.
- Lou, Z., Sun, Y., Bian, S., Baig, S. A., Hu, B. and Xu, X. 2017. Nutrient conservation during spent mushroom compost application using spent mushroom substrate derived biochar. *Chemosphere*, 169: 23-31.
- Mandal, S., Thangarajan, R., Bolan, N. S., Sarkar, B., Khan, N., Ok, Y. S. and Naidu, R. 2016. Biochar-induced concomitant decrease in ammonia volatilization and increase in nitrogen use efficiency by wheat. *Chemosphere*, 142: 120-127.
- Marín-Benito, J. M., Brown, C. D., Herrero-Hernández, E., Arienzo, M., Sánchez-Martín, M. J. and Rodríguez-Cruz, M. S. 2013. Use of raw or incubated organic wastes as amendments in reducing pesticide leaching through soil columns. *Sci. Total Environ.*, 463-464: 589-599.
- Matusik, J. 2014. Arsenate, orthophosphate, sulphate, and nitrate sorption equilibria and kinetics for halloysite and kaolinites with an induced positive charge. *Chem. Eng. J.*, 246: 244-253.
- Ni, Z., Tang, F., Qu, M. and Mo, R. 2012. Determination of effective sulphur in soil by indirect AAS. *Chinese J. Soil Sci.*, 43: 1136-1138.
- Pang, L. and Close, M. E. 1999. Non-equilibrium transport of Cd in alluvial gravels. *J. Contam. Hydrol.*, 36: 185-206.
- Pratiwi, E. P. A., Hillary, A. K., Fukuda, T. and Shinogi, Y. 2016. The effects of rice husk char on ammonium, nitrate and phosphate retention and leaching in loamy soil. *Geoderma*, 277: 61-68.
- Saarnio, S., Heimonen, K. and Kettunen, R. 2013. Biochar addition indirectly affects N_2O emissions via soil moisture and plant N uptake. *Soil Biol. Biochem.*, 58: 99-106.
- Shao, M., Horton, R. and Miller, R. K. 1998. An approximate solution to the convection-dispersion equation of solute transport in soil. *Soil Sci.*, 163: 339-345.
- Shi, W., Ju, Y., Bian, R., Li, L., Joseph, S., Mitchell, D. R. G., Munroe, P., Taherymoosavi, S. and Pan, G. 2020. Biochar bound urea boosts plant growth and reduces nitrogen leaching. *Sci. Total Environ.*, 701: 134424.
- Soenne, H., Hovi, J., Tammeorg, P. and Turtola, E. 2014. Effect of biochar on phosphorus sorption and clay soil aggregate stability. *Geoderma*, 219-220: 162-167.
- Srinivasan, P. and Sarmah, A. K. 2014. Assessing the sorption and leaching behaviour of three sulfonamides in pasture soils through batch and column studies. *Sci. Total Environ.*, 493: 535-543.
- Takaya, C. A., Fletcher, L. A., Singh, S., Anyikude, K. U. and Ross, A. B. Phosphate and ammonium sorption capacity of biochar and hydrochar from different wastes. *Chemosphere*, 145: 518-527.
- Xu, N., Tan, G., Wang, H. and Gai, X. 2016. Effect of biochar additions to soil on nitrogen leaching, microbial biomass and bacterial community structure. *Eur. J. Soil Biol.*, 74: 1-8.
- Yao, Y., Gao, B., Zhang, M., Inyang, M. and Zimmerman, A. R. 2012. Effect of biochar amendment on sorption and leaching of nitrate, ammonium, and phosphate in a sandy soil. *Chemosphere*, 89: 1467-1471.
- Zhang, H., Chen, C., Gray, E. M., Boyd, S. E., Yang, H. and Zhang, D. 2016. Roles of biochar in improving phosphorus availability in soils: A phosphate adsorbent and a source of available phosphorus. *Geoderma*, 276: 1-6.
- Zhao, B., Nan, X., Xu, H., Zhang, T. and Ma, F. 2017. Sulphate sorption on rape (*Brassica campestris* L.) straw biochar, loess soil and a biochar-soil mixture. *J. Environ. Manage.*, 201: 309-314.
- Zheng, H., Wang, Z., Deng, X., Herbert, S. and Xin, B. 2013. Impact of adding biochar on nitrogen retention and bioavailability in agricultural soil. *Geoderma*, 206: 32-39.



Water Resources and Management System of the Himalayan Region: Case Study of Mizoram, India

Brototi Biswas[†] and Abinada Azyu

Department of Geography & RM, Mizoram (Central) University, Aizawl, Mizoram, India

[†]Corresponding author: Brototi Biswas; brototibiswas@gmail.com

Nat. Env. & Poll. Tech.
Website: www.neptjournal.com

Received: 12-08-2020
Revised: 18-09-2020
Accepted: 15-10-2020

Key Words:

Water resources
Water management
Sustainability
Himalayas

ABSTRACT

The Himalayan region has been known as water abundant region in the form of innumerable natural water resources such as springs, streams, rivulets, etc. However, off late owing to climatic and anthropogenic reasons the entire region is soon turning into a water-deficit region leading to serious handicaps in undertaking the basic economic activities, affecting the diversity of livelihood and the drinking water sector. The problem becomes more acute in the dry season or non-monsoonal season. There seems to be a research void in the sustainable water resource planning of the Himalayan states. The present work is an attempt to study this research void through grass-root level analysis of the villages in Mizoram. Twelve villages of the Phullen RD block of Aizawl district, Mizoram were studied to understand the water supply and problems associated with water availability in the rural areas of Mizoram. In the villages of Mizoram, particularly the villages of the study area, Tuikhur or village spring source (VSS) and piped water supply constitute the main lifeline of water supply. Other sources of water include rainwater harvested and water taken from the stream or river. The springs which were once perennial have become seasonal owing to lack of spring shed management. Rainwater harvesting, barring inconsequential villages, is meagrely existent in this region of abundant rainfall with almost 130 days of rainfall. In the absence of proper water resource planning, there is a huge deficit of water every month with the average requirement of the study area being 2,49,148 gallons per month with a supply of just 2,14,248 gallons per month. However, water surplus was also observed in villages having a proper water management system in the form of rainwater harvesting and spring shed management.

INTRODUCTION

The Himalayan region, the source of innumerable water resources, is facing the problem of scarcity among plenty with an increased paucity of water owing to environmental and anthropogenic reasons. The countries in this region are facing newer and tougher challenges in meeting the basic requirement of water, food, and energy owing to rapid population rise and its associated phenomenon (Banerjee et al. 2015, Mukherji et al. 2015). With rising instances of human intervention in the natural environment, the various environmental cycles, particularly the hydrological cycle is getting affected (Biswas et al. 2019). To add to the woe, climate change, recent trends of rainfall vagaries, the geological structure of the aquifers, etc. have resulted in declining water availability in the many streams, springs, and rivers of this region (MoWR 2012, Gupta & Kulkarni 2018). Many such water resources of this region have lost their perennial characteristics. This has led to acute water shortages in almost all the cities and towns of the Himalayan region. The worst affected seems to be the rural regions where access to potable water is a constraint from both physical and

economical point of view. Reduction in water availability is a major constraint for crop production, hydropower generation, and maintaining food security across the world (Magadza 2000). Thus, it is imperative to assess the socio-economic vulnerability linked to water shortage and livelihood diversification (O'Brien et al. 2004, Huq et al. 2015, Kinouchi et al. 2019, Kuchimanchi et al. 2019, Ramprasad 2018). In a report to the NITI Ayog et al. (2018) stated that almost half of the perennial springs in the Himalayan region have lost their perennial nature and have become seasonal. Severe water shortage has been reported from various regions like Kathmandu in Nepal, Darjeeling, Mussoorie, and Shimla in India, Thimphu in Bhutan and Kabul in Afghanistan (Snyder 2014). The National Water Policy of India (NWP) was adopted in 1987 and subsequently revised in 2002 and 2012 (MoWR 2002, Kumar 2017). However the same failed to address the deteriorating water reserves and supply primarily for the hilly regions. The potential of the innumerable springs in the Himalayan states for quenching the thirst of the region has been widely acknowledged. At present, the GOI through NITI Ayog has been emphasizing rejuvenation and recharge of these springs to bring about water sustainability. Spring

shed management has been actively taken up by Sikkim through the initiative *Dhara Vikas* which is led by Rural Management and Development Department (RMDD) and other stakeholders utilizing the rainfall-runoff to recharge the spring sheds, thereby increasing the spring discharge and making them perennial. Such initiative through various NGOs is also seen in Uttarakhand where various springs have been rejuvenated and have regained their perennial status.

North-eastern India, especially the Himalayan state of Mizoram, comes under tropical monsoonal climate owing to which it receives ample rainfall. Further owing to its mountainous terrain, the region is blessed with numerous springs, streams, and rivers. Thus water was never a problem. However, in recent years, the acute shortage of water, particularly in the non-monsoonal season, is witnessed not only in the urban areas but also the rural areas with the drying up of a majority of water sources. Although schemes and initiatives like *Dhara Vikas* have already reached various Himalayan states of Himachal Pradesh, Nagaland, and Uttarakhand, the same is yet to be seen in Mizoram. There seems to be a research void in the socio-ecological situation of the region and an appraisal of the most important resource of humanity in this region of affluence. The present work is an attempt to study this research void through grass-root level analysis of the villages of Mizoram. 12 villages of the Phullen RD block of Aizawl district, Mizoram were studied

to understand the water supply and problems associated with water availability in the rural sector of Mizoram. The main objective of such study is to understand and identify the socio-ecological gaps, identify ways and means for better governance of water resources and encourage the policymakers for a conservational and sustainable development approach of water resources particularly in the rural regions of Mizoram where most of the inhabitants do not possess access to the potable water supply. Further, once the rural belt is made sustainable, the urban regions will also be benefitted.

STUDY AREA

The study was conducted for the entire Phullen RD block of Aizawl district, Mizoram enclosed within $23^{\circ}81'80''$ N and $24^{\circ}06'89''$ N and $93^{\circ}01'38''$ E and $93^{\circ}14'57''$ E as represented in Fig. 1. The block is constituted of 12 villages namely Daido, Khawlian, Lamherh, Luangpawh, Tlangnuam, Khawlek, Phuaibuang, Phullen, Suangpuilawh, Thanglai-lung, Vanbawng and Zawngin. All the 12 villages are part of this research work. Phullen block, having a total area of 515 km² is situated in the north-east part of Aizawl district where it shares state boundary with Manipur and district boundary with Champhai in the East. Phullen RD block is surrounded by Ngopa RD block in the east situated in Champhai district, Thingsultlhiah RD block of Aizawl district in the south, and

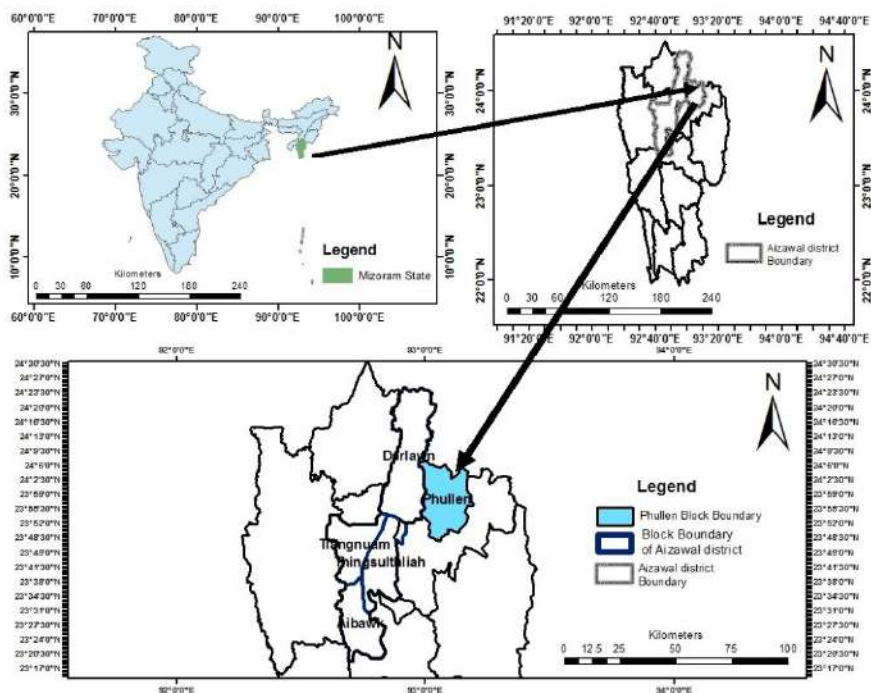


Fig. 1: Area of the study.

Darlawn RD block of Aizawl district in the west. The study area has a population of 13,303 according to the 2011 census. The elevation ranges between 269 MSL (Thanglailung) to 422 MSL (Phuaibuang). The literacy level of the study area is more than 90.73%. About 85% of the total population of the block is engaged in agriculture or related primary sector according to census 2011 data. Agriculture is primarily in the form of Jhum.

This mountain terrain, extending from north to south direction, is composed of predominantly sandstone and shale of the late tertiary period. The region has medium dense forest cover with the majority of the vegetation being of Bamboo variety which also serves as a resource for Mizoram. The climate is tropical monsoonal with a moderate climate throughout the year. Summer temperature ranges between 20°C to 29°C (March to May) while the winter temperature ranges between 7°C to 22°C (November to February). The region is under the influence of southwest monsoonal winds for the greater part of the year with an annual average rainfall ranging between 250 cm to 270 cm. Phullen block has two perennial rivers, Tuivawl and Tuivai. The rivers flow through the study area in a general south-north direction. Both the rivers are joined by several streams and rivulets both perennial and non-perennial. Every village has springs, locally termed as *Tuikhurs*, indicating that the region has good water potential.

MATERIALS AND METHODS

Qualitative and quantitative methodologies of a questionnaire survey and data analysis were carried out. Since the

objective involves water resources, it was done through field observation, Google earth, and other android based processes like Geotagging through a mobile device.

At the onset, the various sources of water supply for each of the villages of the study area were investigated, followed by a questionnaire survey of the number of households that depend on various types of water resources, daily seasonal consumption of water per household in each village, water availability from various sources per month and the material used for collecting and storing of water.

Secondly, based on the demand and supply of water from the various sources statistical analysis was done on the constraints of sustainable livelihood maintenance through SPSS software and MS Excel. The analysis has been represented through tables and graphs.

The respondents of the survey ranged from the villagers, Village council president, BDO office of Phullen block and PHED (Public Health Engineering Department) officials. The respondents were categorized according to age and sex. A total of 100 respondents from each village were surveyed which included 50 males and 50 females. 50% of the respondents belonged to the age group of 18 to 30, 25% belonged to the age group of 31-50 and the rest 25% belonged to age group 51-80. Most of the respondents had their own houses (85%) while a few had rented accommodation (15%) in the entire study area. The education level of the respondents has been given in Fig. 2 while the monthly income levels of the respondent households of each of the village are provided in Table 1.

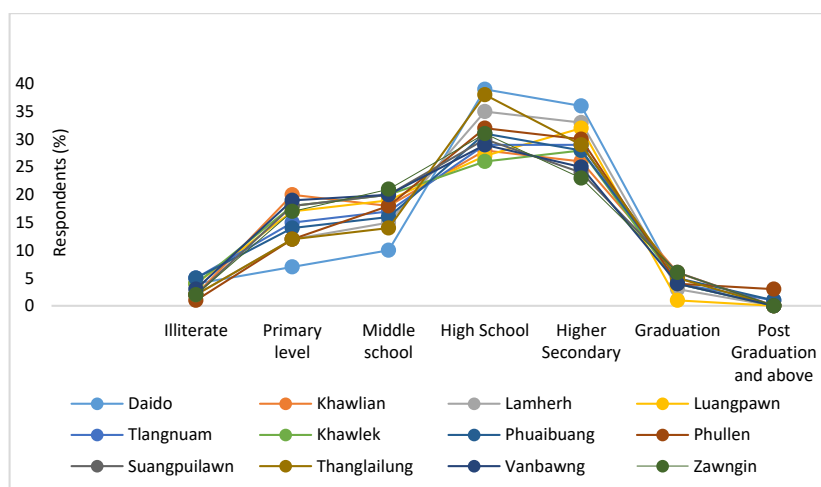


Fig. 2: Educational level of the respondents of the study area.

Table 1: Monthly income levels of respondent households in the study area.

Sr No.	Villages	Number of Households	Income categories in %			
			< Rs 8,000	Rs 8001-12,000	Rs 12,001-15,000	>Rs 15,000
1	Daido	95	23	42	31	4
2	Khawlian	420	22	44	32	2
3	Lamherh,	128	16	36	42	6
4	Luangpawm	99	14	37	39	10
5	Tlangnuam	98	11	34	44	11
6	Khawlek	151	21	38	39	2
7	Phuaibuang	430	13	41	38	8
8	Phullen	460	8	31	49	12
9	Suangpuilawn	450	14	43	37	6
10	Thanglailung	170	16	46	36	2
11	Vanbawng	243	9	46	41	4
12	Zawngin.	131	15	45	36	4

Source: Computed by authors based on field survey.

DISCUSSION

The study region which is part of Mizoram state has a bounty of water resources in the form of steams, rivulets, springs, and most importantly abundant rain for the greater part of the year. Ideally speaking thus, water should not be a problem in this region. However, climate change and anthropogenic activities along with lack of integrated watershed management have resulted in the water surplus regions of the Himalayan belt to water deficit region leading to serious handicap in undertaking the basic economic activities, affecting the diversity of livelihood and the drinking water sector (McPhillips 2017, Maplecroft 2011, Sharma et al. 2019, Kelly & Adger 2000, Shrestha et al. 2019, O'Brien et al. 2004). In general, the villages of the study area, as is elsewhere in Mizoram, is most affected during the

non-monsoonal season/dry season. Hence the study has been specially conducted keeping in view the water availability during the season of scarcity.

Various Sources of Water in the Study Area

In the villages of Mizoram, particularly the villages of the study area, *Tuikhur* or village spring source (VSS) and piped water supply constitute the main lifeline of water supply. The Piped water supply is managed by the PHED department. Other sources of water include rainwater harvested and water taken from the stream or river. Water taken from streams is mostly done by private operators depending on the demand for water by the villagers. These are the important sources of water in rural areas obtained by the villagers for their daily uses. The various water sources in the study area (Fig. 3) have been analysed briefly in the following section.



Fig 3: Sources of water supply in the study area (clockwise from top left; PHED, Tuikhur, Rainwater harvesting, private operators).

Tuikhur

Till today, one of the most important sources of water supply in the rural areas can be considered as *Tuikhur* or village spring source (VSS). The villagers, especially the poor family greatly depend on *Tuikhur* water for their daily needs. Almost every village has access to such water sources. It is a perennial water source, however in recent times with rainfall variability and various anthropogenic reasons many of these sources either dries up or has reduced water quantity during the dry season or non-monsoonal season of Mizoram (Table 2). It is mainly used for drinking, cooking, cleaning and washing purposes. But during the scarcity of water, the villagers are prohibited from using *Tuikhur* water for cleaning and washing.

Piped Water Supply

Piped water supply or water connection involves drawing of water from the streams and rivers by PHED. In most of the villages, the pumping system is used for collecting water from the streams and river. The pumping system is the method of lifting water from the river or stream through high a lift pump driven by the power in which water is transported to the storage reservoir. The location of the reservoir is put at a higher elevation within the village so that distribution can also be done easily through the gravity feed system. The construction charge is generally borne by the government or sometimes by the individual Village councils. Water is hauled from the local streams/tributaries, Kawrawng, Leisang, Ramrikawn, Mauhar, Kawrte, etc. The private household connection, at Rs 300/month, given by PHED receives

water for about an hour per week. The total amount of water obtained is about 2,000 litres per week. Certain villages also have public water distribution points supplied by PHED, where the total amount received is about 225-300 litres/month. The supply is highly irregular during the dry season.

Rainwater

Rainwater is harvested during the rainy season. Owing to climatic conditions the houses have sloping roofs with corrugated sheets, aiding in the collection of rainwater. The same is stored in barrels or large plastic containers. During the monsoonal season, the water is used mainly for washing purposes and watering individual kitchen gardens. Sometimes it is even used for drinking after filtering it. There is no definite data available for rainwater harvesting and water obtained from private operators. The total amount of rainwater that is stored by individual households is around 3000 litres/month. This is primarily stored for the dry months and lasts for about 2 months. The water obtained from private operators are need-based; as and when required. So far only Suangpuilawn village has utilized rainwater harvesting to a great extent.

Water From Stream

Water is pumped indiscriminately from streams or rivers during the dry season. The water is pumped into barrels or tanks of 2000 litres capacity and sold to the villagers by private operators. The price of water generally ranges from Rs 600 per 1500 litres to Rs 900 for 2000 litres.

Water Supply and Management System in the Study Area

As is observed from the preceding section, the study area does not have any fixed water supply system. It follows a 3 tier system of Public Health Engineering Department (PHED), Government of Mizoram; Village council level through the management system of *Tuikhur*; and private level through household rainwater harvesting and buying of water from private operators as and when the need arises. In certain villages like Suangpuilawn and Thanglailung community rainwater harvesting has been undertaken by the respective Village council on large scale for ensuring village level self-sufficiency. Water requirement, supply and management system differ quantitatively among each of the 12 villages owing to population size, water management system, the elevation of the village and monetary capacity of the residents.

Households and Water Consumption Pattern

The average amount of water available to the villages is around 2,14,248.6 gallons of water per month. This excludes

Table 2: Spring water source of the study area.

Sr No	Villages	Springs/ <i>Tuikhurs</i>	
		Total	Perennial
1	Daido	05	03
2	Khawlian	04	01
3	Lamherh,	04	03
4	Luangpawm	05	04
5	Tlangnuam	05	04
6	Khawlek	04	04
7	Phuaijuang	05	03
8	Phullen	07	03
9	Suangpuilawn	12	08
10	Thanglailung	04	02
11	Vanbawng	04	02
12	Zawngin.	05	04

Source: Computed by authors based on field survey.

the water obtained from private sources. Based on the total population of each village, the per head water availability was computed and is represented in Table 3. The per head water availability on an average stands at a meagre 21 lpcd or 5.63 gallons which is much lower than the minimum service delivery of 55 lpcd or 14.52 gallons as decided by Jal Jeevan Mission, under Ministry of Water Resources, India (<https://pib.gov.in>). The extreme scarcity particularly in the dry season forces the population to restrict consumption, stop agricultural practices and compels the women-folk to trudge daily in search of water from distant streams/springs and buy water from private sources at a high price.

Owing to scarcity, water is used in a very controlled manner in the dry season. The excess usage like watering of plants/kitchen garden is curtailed, recycling of available water is encouraged (reusing water used for washing vegetables/clothes) and a general restriction of water usage is practised as represented in Fig. 4. With decreased water

supply from various sources during the lean period, PHED water supply becomes the major source of water for the study area as represented in Fig 4. With the unavailability of a community-based rainwater harvesting system and household rainwater harvesting system owing to financial reasons, the stored rainwater does not last long. Thus the share of rainwater in meeting water demand of the study area is too meagre as observed in Fig. 4. Water obtained at a high price from private operators comes to a close second for almost all the villages barring Suangpuilawn. The village is self-reliant concerning to meeting its water demand. Almost 25% of the water need of Suangpuilawn is met through planned community based and household rainwater harvesting system. The village has 5 large water storage tanks of 3000 litres each for community rainwater harvesting (Fig 5). Eighty seven households out of 450 total households of the village, constituting about 19.33% of the total population, have individual household rainwater harvesting systems each having storage tanks of 2500 litres.

Table 3: Water availability for the study area.

Villages	Total population	Water availability (gallons/month)	Water availability (gallons/per head/month)
Daido	615	80942.57	4.39
Khawlian	2400	396972.6	5.51
Lamherh	618	124451.8	6.71
Luangpawm	478	96449.52	6.73
Tlangnuam	440	94204.05	7.14
Khawlek	769	135256.5	5.86
Phuaibuang	2500	365879.4	4.88
Phullen	2700	402810.8	4.97
Suangpuilawn	2400	403814.7	5.61
Thanglailung	980	150076.6	5.10
Vanbawng	1255	206741.7	5.49
Zawngin	740	113383	5.11

Source: Computed by authors based on field survey.

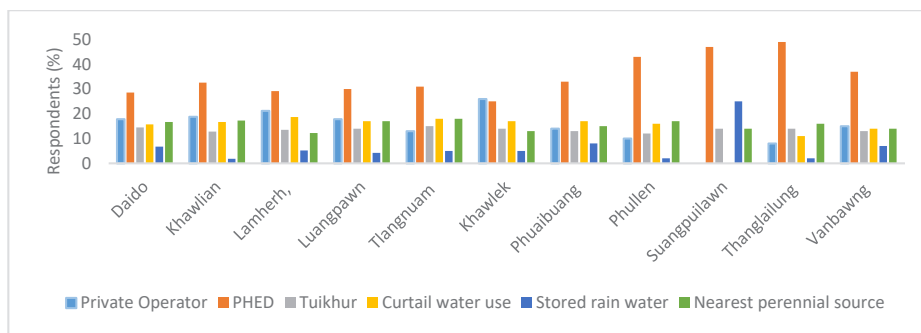


Fig. 4: Meeting water demand during the lean period for the study area.



Fig 5: Community rainwater harvesting tanks of Suangpuilawn village.

Demand-Supply Gap

The average requirement of the study area is 9,43,125 litres per month or 2,49,148 gallons per month with the highest requirement from Khawlian village (4,89,776.5 gallons per month) as visible from Fig. 6 and an average supply of just 2,14,248 gallons per month. However, the largest deficit is noticed in Phuaibuang village with a shortfall of 1,04,374.7 gallons per month of water. Suangpuilawn and Thanglailung are the only villages having NIL water deficit owing to wide-scale rainwater harvesting system and planned water management.

The total requirement of water for the entire study area is 29,89,777 gallons of water per month. The total water supply/

availability from Tuikhurs, PHED and rainwater harvesting (including water haulage from distant streams/springs) is 25,70,983.3 gallons of water per month as represented in Table 4. Thus there is a total deficit of 4,18,793.25 gallons of water per month. This is predominantly during the dry season. A huge part of this deficit thus has to be filled by the private operators at a hefty price.

To understand whether there is a significant difference between demand and supply of water among all the villages of the study area, a two-sample *t*-test was conducted. The statistical analysis yielded Pearson’s correlation value of 98% and p-value of 0.006, indicating a significant difference between the variables, demand and supply of water.

To statistically analyze the level of significance between the various available water sources among the various villages, ANOVA was conducted and the result is presented in Table 5. The p-value of 0.001 represents a significant difference between the various water sources and their availability among the villages.

Table 4: Water supply details of the study area.

Village	Tuikhurs	PHED	Rain water
	Supply in gallons/month		
Daido	48977.65	26417.29	5547.63
Khawlian	82897.45	302742.1	11333.02
Lamherh	56031.07	62080.63	6340.149
Luangpawm	63559.99	29587.36	3302.161
Tlangnuam	61974.96	19020.45	13208.64
Khawlek	80044.38	45701.91	9510.223
Phuaibuang	101442.4	204998.2	59438.9
Phullen	130448.6	267078.8	5283.457
Suangpuilawn	91958.58	254398.5	57457.6
Thanglailung	40576.95	104876.6	4623.025
Vanbawng	69900.14	126274.6	10566.91
Zawngin	59755.9	42531.83	11095.26

Source: Computed by authors based on field survey.

Issues and Challenges

The key challenge of the study area is the disparity between population and water availability per capita. *Tuikhurs* and rainwater harvesting systems are traditional systems while the PHED system is 30-35 years old. The topography of the region hampers water haulage which is being done by Gravity feed system and pumping system, thereby increasing the infrastructural cost. All the systems are quite old and are unable to cater to the population. Renovation of storage tanks, repair of pipelines, feeder lines, and rainwater harvesting systems are lacking in the study area. The region receives abundant rainfall from May to September (average 130 days/year) owing to its strategic location. One of the works of

Table 5: ANOVA test for various available water sources among the villages.

ANOVA						
Source of Variation	SS	df	MS	F	P-value	F-crit
Between Groups	99200000000	2	49600000000	8.547011	0.001	3.28
Within Groups	192000000000	33	5800000000			
Total	291000000000	35				

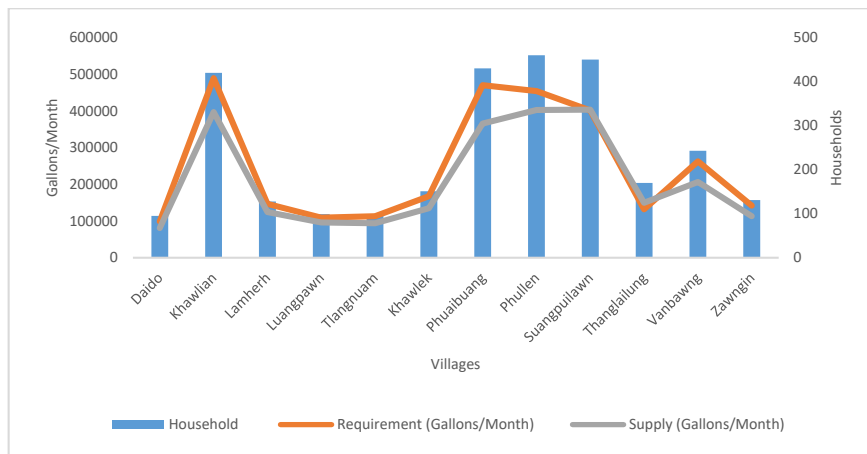


Fig 6: Demand and supply of water resource along with the number of households in each village.

PHED, Government of Mizoram is to undertake rainwater harvesting scheme, under various centrally (Government of India) sponsored schemes. Under this scheme, PHED must construct 7500 litres of storage tank for a family of 6 members for water availability of 10 lpcd for 120 days of the dry season. However, not a single such structure was found in any of the villages of the study area. In the absence of impounding of rainwater, which is to the extent of about 250-270 cm of annual average rainfall, the scope of catchment recharge of the dying and dried up springs/*Tuikhurs* and availability of water in dry season through individual/community rainwater harvesting is wasted and lost. Such anthropogenic callousness also induces environmental threats like soil erosion, run-off and increased instances of rainfall-induced landslides owing to slope instability triggered by enhanced run-off along the steep down slopes. Further, most of the villages do not have all-weather roads which hinder access to the surrounding rivers/streams (Tuivai river and Tuivawl river).

CONCLUSION

The study region is blessed with very heavy rainfall at an annual average of 250 cm to 270 cm. This is one of the highest in India. Owing to its mountainous terrain it has a plethora of water resources in the form of various streams, springs (locally called *Tuikhurs*) and a huge potential from rainwater harvesting system. *Tuikhur* forms the main lifeline

of the study area encompassing 12 villages of Phullen RD block of Aizawl district, Mizoram. However, during the dry seasons, almost 50% of *Tuikhurs* in each of the villages dry up owing to lack of spring shed management. Thus, the water resources of the study area face a huge demand-supply gap particularly in the dry season (winter season) and are unable to meet the basic per capita water requirement of 55 lpcd as decided by Jal Jeevan Mission, under Ministry of Water Resources, India. The per capita water availability on an average stands at a meagre 21 lpcd. The short-fall is met by buying water from private operators at a very hefty price. Further, lack of all-weather roads hinders accessibility to the surrounding rivers/streams. The dearth of proper planning is one of the reasons for this huge demand-supply gap which is proved by the self-dependency of Suangpuilawn village with regard to the water resource. Proper management of spring shed and rainwater harvesting system has made this village self-sufficient in water needs throughout the year. The only way forward for the study region is to utilize and plan its already existing resource-rainfall, in such a way as to enhance spring shed management cum recharge, impounding of rainfall by constructing various water ponds and proper rainwater harvesting system both at the community level and household level.

The present study provides a grassroots level diagnosis of the present situation of the villages of Aizawl district.

However, one can find the same picture throughout the villages of the state as well as the other Himalayan states. As such studies like this will provide the pre-requisite ground-level data for further integrated water resource planning.

Spring shed management through rainwater harvesting is not a new concept in India. In Sikkim, through Dhara Vikas, an atlas of 700 springs have been created along with the rejuvenation of springs. Such initiatives have also been taken in Uttarakhand.

Taking cognizance of the gravity of the situation in this region of bounty yet scarcity of water resource, various stakeholders both at the government level and NGOs along with the academic body must take part in ensuring the basic need of humanity through proper planning.

REFERENCES

- Banerjee, S., Mukherjee, A., Sattar, A. and Biswas, B. 2015. Change detection of annual temperature and rainfall in Kalimpong station under hill zone of West Bengal. *Indian Journal of Hill Farming*, 28(2): 81-84.
- Biswas, B., Jadhav, R. and Tikone, N. 2019. Rainfall distribution and trend analysis for upper Godavari basin, India, from 100 Years Record (1911-2010). *Journal of the Indian Society of Remote Sensing*, 47(10): 1781-1792. <https://doi.org/10.1007/s12524-019-01011-8>
- Gupta, A. and Kulkarni, H. 2018. Report of the NITI Aayog Working Group on Inventory and Revival of springs in Himalayas for Water Security as Part of Initiatives on Sustainable Development of Mountains of Indian Himalayan Region. Submitted to NITI Aayog, Government of India.
- Huq, N., Hugé, J., Boon, E. and Gain, A.K. 2015. Climate change impacts in agricultural communities in rural areas of coastal Bangladesh: a tale of many stories. *Sustainable*, 7: 8438-8460. <https://doi.org/10.3390/su7078437>.
- Kelly, P.M. and Adger, W.N. 2000. Theory and practice in assessing vulnerability to climate change and facilitating adaptation. *Clim. Change*, 47: 325-352.
- Kinouchi, T., Nakajima, T., Mendoza, J., Fuchs, P. and Asaoka, Y. 2019. Water security in high mountain cities of the Andes under a growing population and climate change: a case study of La Paz and El Alto, Bolivia. *Water Secur.*, 6: 100025.
- Kuchimanchi, B.R., Nazareth, D., Bendapudi, R., Awasthi, S. and D'Souza, M. 2019. Assessing differential vulnerability of communities in the agrarian context in two districts of Maharashtra, India. *Clim. Dev.*, 11(10): 918-929. <https://doi.org/10.1080/17565529.2019.1593815>.
- Kumar, D.N. 2017. Water management in India: The multiplicity of views and solutions. *International Journal of Water Resources Development*, 34(1): 1-15. doi: 10.1080/07900627.2017.1351333.
- Magadza, C.H.D. 2000. Climate change impacts and human settlements in Africa: Prospects for adaptation. *Environ. Monit. Assess.*, 61: 193-205.
- Maplecroft, 2011. *Climate Change Risk Atlas 2010, Vulnerable Nations and Safe Havens*.
- McPhillips, D. 2017. 10 Countries with the Worst Water Supply. *U. S. News and World Report*.
- MoWR 2012. *National Water Policy 2012*. Ministry of Water Resources, Government of India, Delhi. Available at: http://mowr.gov.in/sites/default/files/NWP2012Eng6495132651_1.pdf.
- MoWR 2002. *National Water Policy*. Ministry of Water Resources, Government of India, Delhi.
- Mukherji, A., Molden, D., Nepal, S., Rasul, G. and Wagnon, P. 2015. Himalayan waters at the crossroads: issues and challenges. *International Journal of Water Resources Development* 31(2): 151-160. doi:10.1080/07900627.2015.1040871.
- O'Brien, K., Leichenko, R., Kelkar, U., Venema, H., Aandahl, G., Tompkins, H., Javed, A., Bhadwal, S., Barg, S., Nygaard, L. and West, J. 2004. Mapping vulnerability to multiple stressors: climate change and globalization in India. *Glob. Environ. Chang.*, 14: 303-313. <https://doi.org/10.1016/j.gloenvcha.2004.01.001>.
- Ramprasad, V. 2018. Debt and vulnerability: indebtedness, institutions and smallholder agriculture in South India. *J. Peasant Stud.*, 0: 1-22. <https://doi.org/10.1080/03066150.2018.1460597>.
- Sharma, E., Molden, D., Rahman, A., Khatiwada, Y.R., Zhang, L., Singh, S.P., Yao, T. and Wester P. 2019. *The Hindu Kush Himalaya Assessment*. Springer Int. Publ. <https://doi.org/10.1007/978-3-319-92288-1>.
- Shrestha, R.P., Pasakhala, B. and Qasim, S. 2019. Assessing household vulnerability to climate variability in far-west Nepal. *Nature*, 12: 83-118.
- Snyder A. 2014. Shortage in the Mountains of Plenty: Water Supply in Mountain and Hill Cities Throughout the Hindu-Kush Himalayan Region, ICIMOD and The World Food Prize. Available at: https://www.worldfoodprize.org/documents/filelibrary/images/youth_programs/2014_interns/2014_br_research_papers/SnyderAbigail_LONGReport_56ED38F157B76.pdf.



Kinetics Studies on Toxic Hexavalent Chromium Removal from Aqueous Solutions by Magnetic Nano-Magnetite

Q. Wang*, L.P. Liang*†, F.F. Xi*, Q. Wu*, Y.Y. Xue*, L.B. Cheng*, Y.T. Zhang* and X. Meng**

*School of Civil Engineering, College of Life Science, College of Textile and Garment, Shaoxing University, Shaoxing, 312000, P. R.China

**Key Laboratory of Clean Dyeing and Finishing Technology of Zhejiang Province, Shaoxing University, Shaoxing, 312000, P. R.China

†Corresponding author: Liping Liang; liangliping0702@163.com

Nat. Env. & Poll. Tech.

Website: www.neptjournal.com

Received: 11-02-2020

Revised: 02-03-2020

Accepted: 02-05-2020

Key Words:

Magnetic nano-Fe₃O₄
Hexavalent chromium
Chemical kinetics
Magnetic separation

ABSTRACT

In this study, the chemical co-precipitation method was used to prepare magnetic nano-Fe₃O₄. In order to investigate the adsorption capacity of magnetic nano-Fe₃O₄ for Cr(VI) in aqueous solution, three aspects of solution pH, magnetic nano-Fe₃O₄ dosage and initial solution concentration were studied. The experimental results showed that Cr(VI) adsorption capacity by magnetic nano-Fe₃O₄ decreased with increasing pH and increased with the increasing initial concentration of Cr(VI) ions and magnetic nano-Fe₃O₄ dosage. In addition, the experimental data were fitted to the adsorption kinetics and three adsorption isotherms. It could be seen that the adsorption process of Cr(VI) by magnetic nano-Fe₃O₄ accorded with pseudo-second-order kinetics, which demonstrated that the adsorption process was controlled by chemical adsorption. And it was also found to be well represented by the Freundlich isotherm model. The maximum capacity obtained from the Langmuir model was 34.0136 mg/g, indicating that magnetic nano-Fe₃O₄ is an efficient adsorbent.

INTRODUCTION

Heavy metal chromium is widely used in industrial production such as electroplating, tanning, metal polishing, dye production and printing (Aroua et al. 2007). A large amount of chromium-containing wastewater is discharged into rivers without strict treatment and it is listed as the most toxic pollution in wastewater (Gu et al. 2013), which places a heavy burden on the environment and ecology. Chromium exists mainly in the form of Cr(III) and Cr(VI) in water, and the toxicity of Cr(VI) is much higher than Cr(III), which is 100 times that of Cr(III). In addition, Cr(VI) is easily released in water, so it can easily enter the body of animals and plants to cause damage. Therefore, reducing or immobilizing Cr(VI) to Cr(III) in sewage is a very important strategy for the treatment of heavy metal chromium pollution. According to the toxicity of chromium to the human body, the World Health Organization stipulates that the maximum concentration of Cr(VI) in drinking water is 50 µg/L, and the United States Environmental Protection Agency has stipulated that the total chromium content in national drinking water must not exceed 100 µg/L (Zhu et al. 2012).

At present, the treatment technologies for Cr(VI) pollution in sewage mainly include ion exchange method (Gode &

Pehlivan 2005, Pehlivan & Cetin 2009), adsorption method (Bhattacharya et al. 2008, Kobya 2004), electrochemical precipitation method (Golder et al. 2011, Golder et al. 2007), biological method (Barrera-Díaz et al. 2012) and reverse osmosis method (Yoon et al. 2009). Among them, the adsorption method has been widely studied and applied to actual sewage treatment for its advantages such as low cost, high efficiency, simple treatment process and no secondary pollution. The key to the adsorption method is the choice of adsorbent, commonly used adsorbents include activated carbon (Gupta et al. 2013), biomass adsorbents (Bilal et al. 2013), clay minerals (da Fonseca et al. 2006), and zeolites. These materials can effectively remove heavy ions from wastewater. In recent years, with the development of nanotechnology and nanomaterials, there are more and more types of nanomaterials that can be used to adsorb heavy metal ions. And the nanometre material itself has the characteristics of small particle size and huge specific surface area, which is conducive to the adsorption of heavy metals and has greatly promoted the treatment of heavy metal ions in sewage. A large number of studies have shown that graphene, carbon nanotubes and other nano-materials have a good adsorption effect on Cr(VI) (Luo et al. 2013, Salam 2017, Sharma et al. 2015, Sherlala et al. 2018, Zhu et al. 2012). However, after

the adsorption of nano-materials is completed, they still have good dispersibility in the water. It is difficult to enrich and recover nano-materials from the water bodies by traditional methods such as centrifugation and filtration, which will exacerbate environmental pollution (Lu et al. 2016).

Therefore, people have gradually favoured the application of magnetic nano-materials in water pollution control. The unique surface effect and magnetic response characteristics of magnetic nano-materials make it to have the advantages of efficient enrichment and simple desorption in the process of water pollution adsorption and removal, which can effectively avoid secondary pollution to the ecological environment. Ferric oxide is the main component of magnetite. It is rich in natural magnetite, widely distributed and inexpensive. The preparation of magnetic Fe_3O_4 with special properties has aroused great interest from scientific researchers. Research finds that Fe_3O_4 nanoparticles synthesized under different conditions have a regular structure (Fan & Yao 2007). Therefore, many researchers have prepared a series of Fe_3O_4 -based composite magnetic nano-materials and successfully applied them to the adsorption of heavy metal ions, dyes and other pollutants (Du et al. 2017, Hu et al. 2011, Shen et al. 2012).

In this study, pure magnetic nano- Fe_3O_4 was prepared by chemical precipitation method, and the adsorption capacity of pure magnetic nano- Fe_3O_4 for Cr(VI) was explored from the three aspects of pH, amount of adsorbent and initial concentration of Cr(VI).

MATERIALS AND METHODS

Materials

The reagents used in this experiment include ferric trichloride ($\text{FeCl}_3 \cdot 6\text{H}_2\text{O}$), ferrous dichloride ($\text{FeCl}_2 \cdot 4\text{H}_2\text{O}$), concentrated ammonia, potassium dichromate ($\text{K}_2\text{Cr}_2\text{O}_7$), diphenylcarbazide ($\text{C}_{13}\text{H}_{14}\text{N}_4\text{O}$), acetone, concentrated sulfuric acid and nitrogen were all of the analytical grade and used without further processing.

Synthesis of the Adsorbent

In this experiment, magnetic nano- Fe_3O_4 was prepared by a chemical co-precipitation method. Firstly, dissolved 8.115 g of ferrous chloride ($\text{FeCl}_2 \cdot 4\text{H}_2\text{O}$) and 3.98 g of ferric chloride ($\text{FeCl}_3 \cdot 6\text{H}_2\text{O}$) in 160 mL of distilled water. Secondly, transferred it into a 250 mL three-necked flask and placed in a thermostatic water bath at 80°C and continuously passed nitrogen through for 30 minutes at a stirring speed of 350 rpm to remove dissolved oxygen in the water. Finally, 40 mL of concentrated ammonia was slowly added dropwise, and the reaction was continued for 30 minutes. After the reaction was finished, the precipitate was filtered, washed



Fig. 1: The magnetic nano- Fe_3O_4 solution can easily be separated by a magnet.

repeatedly with distilled water and dried in an oven at 80°C to obtain magnetic nano- Fe_3O_4 particles. After the materials were completed, to verify whether the magnetic nano- Fe_3O_4 can be easily separated from the solution, the prepared materials were dispersed in an aqueous solution, and then the magnet was used to separate them. The result is shown in Fig. 1. It could be seen that magnetic nano- Fe_3O_4 can be easily separated by the magnet.

Batch Adsorption Experiment

Accurately weighed 0.2829 g of dried $\text{K}_2\text{Cr}_2\text{O}_7$ was dissolved in distilled water, then transferred into a 1 L volumetric flask to prepare the stock solution of 20 mg/L. It was later diluted to the corresponding concentrations in subsequent experiments. During the experiment, it was diluted to a certain ratio and heated in a constant temperature water bath at 25°C . At a speed of 350 rpm, a certain amount of magnetic nano- Fe_3O_4 was added for reaction, and a small amount was sucked out with a syringe at a specified time point. The solution was filtered through $0.45 \mu\text{m}$. After the filtrate was added with a developer, the wavelength was adjusted to 540 nm for absorbance measurement.

Experimental Data Analysis

Add 0, 0.10, 0.25, 0.50, 1.00, 2.00, 3.00, 4.00, and 5.00 mL chromium standard solutions to a series of 25 mL colorimetric tubes and dilute to the mark with water. The absorbance was then measured following the same pretreatment and measurement procedures as the water sample. Then, a standard curve of absorbance Cr(VI) concentration was plotted based on the measured absorbance of Cr(VI), and the equation was obtained as $y = 38.219x - 0.02738$, $R^2 = 0.9998$. Due to the high correlation coefficient ($R^2=0.9998$), it had been seen that there was a good linear relationship between concentration and absorbance, which indicated that the accuracy of hexavalent chromium concentration is higher. Then the amount of adsorption could be calculated by equation 1.

$$q_e = \frac{(C_0 - C_e)V}{W} \quad \dots(1)$$

Where, q_e is the equilibrium concentration of Cr(VI) (mg/L), C_0 and C_e are the initial and equilibrium concentration of Cr(VI) (mg/L), respectively. V is the volume of Cr(VI) solution (L) and W is the weight of magnetic nano- Fe_3O_4 (g).

RESULTS AND DISCUSSION

Effect of Initial pH on Adsorption of Cr(VI) by Magnetic Nano- Fe_3O_4

Under the condition of the initial concentration of Cr(VI) (10 mg/L) and the dosage of magnetic nano- Fe_3O_4 (1 g/L), the effect of the initial pH on the efficiency of removing Cr (VI) is shown in Fig. 2. As shown in the figure, the adsorption efficiency of Cr(VI) depended on the solution pH and increased with the decreasing pH. The pH change of the water environment will affect the stability of various forms to a certain extent. Cr(VI) ions mainly exist as HCr_2O_7^- at $\text{pH} < 1$, $\text{Cr}_2\text{O}_7^{2-}$ at $\text{pH} 1-6$, and CrO_4^{2-} at $\text{pH} > 7$ (Zang et al. 2007). As the pH value increases, the chromate anion will change from $\text{Cr}_2\text{O}_7^{2-}$ to CrO_4^{2-} , and the area occupied by the average single Cr(VI) adsorption increases, so the adsorption of Cr(VI) by the magnetic nano- Fe_3O_4 decreases significantly. In addition, the change of pH affects the surface charge of Fe_3O_4 ; as the pH decrease, H^+ increases in the solution and soon interact with $-\text{OH}$ on the surface of Fe_3O_4 resulting in the increasing of $-\text{FeOH}$ and $-\text{FeOH}^{2+}$, and then Fe_3O_4 with a positive charge on the surface in the solution is more likely to adsorb negatively charged $\text{Cr}_2\text{O}_7^{2-}$ ion (Wang et al. 2011). As the pH increases, the OH^- concentration in the solution also increases. On the contrary, the concentration of OH^- in the solution increases with pH increasing, leading to the

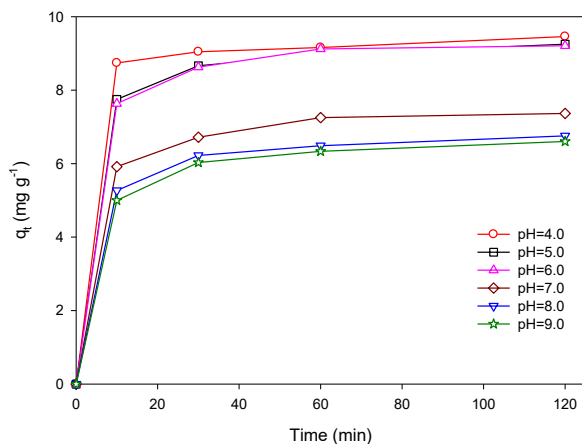


Fig. 2: Effect of pH on the kinetics of Cr(VI) removal by nano- Fe_3O_4 .

surface $-\text{FeO}^-$ iron concentration of magnetic nano- Fe_3O_4 increasing. At this time, the negatively charged CrO_4^{2-} and the negatively charged iron oxide in the solution will have electrostatic repulsion between the surfaces, which will reduce the adsorption capacity of Cr(VI) by magnetic nano- Fe_3O_4 .

Effect of Dosage of Magnetic Nano- Fe_3O_4 on Cr(VI) Removal Efficiency

Under the same conditions Cr(VI) concentration of 10 mg/L and pH 6, the effect of the addition amount of magnetic nano- Fe_3O_4 on the adsorption efficiency of Cr (VI) is shown in Fig. 3. It can be seen that with the increase of the dosage, the adsorption amount per unit amount of the adsorbent became smaller but the adsorption capacity of Cr(VI) does increase with the increase of the dosage. This may be due to the increase in the amount of adsorbent added to a certain extent, which will lead to a decrease in the specific surface area and efficiency of the adsorbent, resulting in a reduction in the number of active sites (Akçay et al. 2009).

Effect of Initial Concentration on the Removal Efficiency of Cr(VI) by Magnetic Nano- Fe_3O_4

The effect of the initial concentration on the removal efficiency and removal rate of Cr(VI) by magnetic nano- Fe_3O_4 under the condition of pH 6 and the dosage of magnetic nano- Fe_3O_4 (1 g/L) are shown in Fig. 4. It can be seen that the adsorption amount per unit amount of the adsorbent gradually increases with the increase of Cr(VI) concentration. When the concentration increased from 10 mg/L to 100 mg/L, the concentration of Cr(VI) adsorbed per unit amount of adsorbent increased from 9.19 mg/g to 28.5 mg/g. There are sufficient active sites in contact with Cr(VI) ions, which increases the adsorption efficiency.

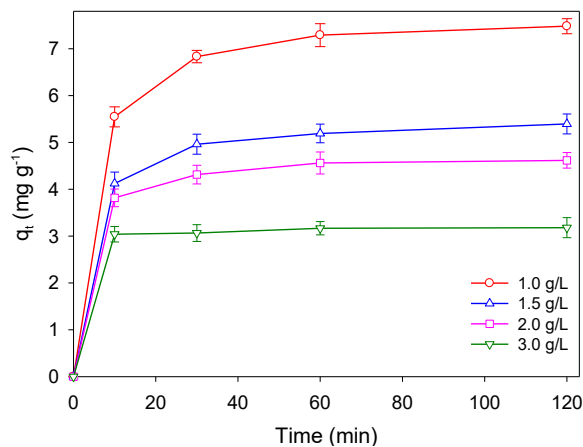


Fig. 3: Effect of magnetic nano- Fe_3O_4 dosage on the kinetics of Cr(VI) removal by magnetic nano- Fe_3O_4 .

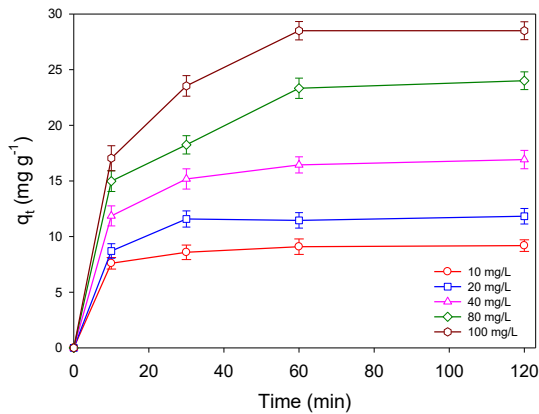


Fig. 4: Effect of initial Cr(VI) concentration on the kinetics of Cr(VI) removal by magnetic nano-Fe₃O₄.

Adsorption Isotherm

The adsorption isotherm refers to the relationship curve between the concentrations of solute molecules in the two phases when the adsorption process on the two-phase interface reaches equilibrium at a certain temperature. At a certain temperature, the relationship between the concentration of separated substances in the liquid and solid phases can be expressed by the adsorption equation. The relationship between the adsorbent and the adsorbate can be deduced from the graph. To understand the adsorption effect and maximum adsorption capacity of this adsorbent, it is necessary to establish an equilibrium curve and select the most suitable curve.

The Langmuir equation is one of the commonly used adsorption isotherm equations. It was proposed by the physical chemist Langmuir Itying in 1916 based on molecular motion theory and some assumptions. Langmuir adsorption isotherm can be expressed by equation 2.

$$\frac{q_e}{C_e} = \frac{C_e}{q_m} + \frac{1}{k_L q_m} \quad \dots(2)$$

Where, q_e is the adsorption amount of hexavalent chromium at equilibrium (mg/L), C_e is Cr(VI) concentration at equilibrium (mg/L), q_m is saturated adsorption capacity (mg/L), and k_L is the equilibrium constant of Langmuir adsorption isotherm.

Freundlich isotherm describes actual adsorption, which is an empirical formula. It is derived from the modification of the Langmuir idealization equation. Therefore, it is considered that adsorption is reversible and is not strictly monolayer adsorption. It can be expressed by equation 3.

$$\text{Ln}q_e = \text{Ln}K_F + \frac{1}{n} \text{Ln}C_e \quad \dots(3)$$

Where, q_e is the adsorption amount of Cr(VI) in equilibrium (mg/g), C_e is the concentration of Cr(VI) at equilibrium (mg/L), and K_F is Freundlich constant.

Tempkin considers the effects of some indirect adsorbate/sorbent interactions and indicates that due to these interactions, the heat of adsorption of all molecules in the layer decreases linearly with coverage. And Tempkin isotherms can be represented by equation 4.

$$q_e = \frac{RT}{b_T} \text{Ln}A_T + \left(\frac{RT}{b_T}\right) \text{Ln}C_e \quad \dots(4)$$

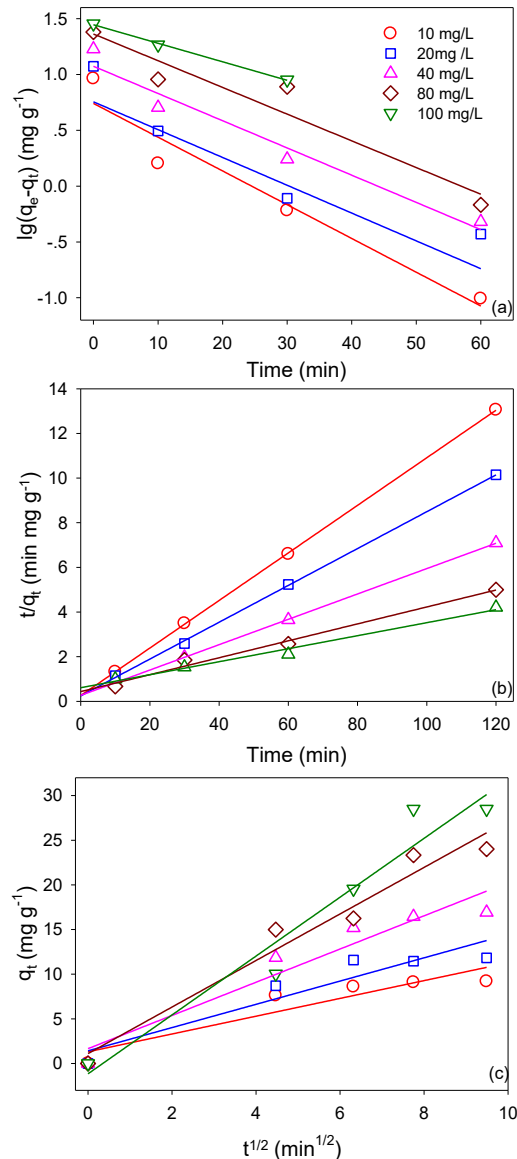


Fig. 5: Simulated results of pseudo-first-order kinetics (a), pseudo-second-order kinetics (b), and intraparticle diffusion (c) at different initial Cr(VI) concentrations.

Table 1: Langmuir, Freundlich and Temkin model constants and correlation coefficients for Cr(VI) removal by magnetic nano-Fe₃O₄ at 25°C.

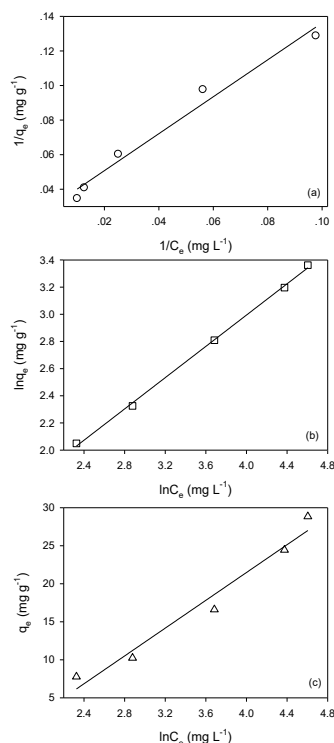
Temperature	Langmuir			Freundlich			Temkin		
	R ²	Q _m	b	R ²	K _F	n	R ²	A	B
25°C	0.9888	34.0136	0.0275	0.9994	1.9949	1.7367	0.9829	0.1919	9.1413

Table 2: Comparisons of rate constants and calculated q_e by the pseudo-first-order kinetics, pseudo-second-order kinetics and intraparticle diffusion models and experimental q_e values obtained at different initial Cr(VI) concentrations.

Cr(VI) (mg/L)	Experiment q _e (mg/g)	pseudo-first-order kinetics			pseudo-second-order kinetics			intraparticle diffusion	
		R ²	q _e	K ₁	R ²	q _e	K ₂	R ²	K _{id}
10	9.1920	0.9720	5.5068	0.6955	1.0000	9.3897	0.0441	0.9275	0.9960
20	11.8280	0.8324	5.6885	0.0573	0.9997	12.1212	0.0280	0.9405	1.3019
40	16.9240	0.9788	11.8522	0.0562	1.0000	17.6056	0.1210	0.9607	1.8589
80	24.0080	0.9618	23.0569	0.0550	0.9942	26.3852	0.0033	0.9792	2.6052
100	28.500	0.9989	27.9126	0.0382	0.9927	34.3642	0.0014	0.9721	3.2951

Where, q_e is the amount of solute adsorbed per unit weight of nano-Fe₃O₄ (mg/g), C_e is the equilibrium concentration of Cr(VI). And R, A, T and b are Temkin constants.

The dependence of adsorption on the concentration of Cr(VI) in equilibrium was studied, and the experimental data were fitted to the Langmuir model, Freundlich model and Temkin model, respectively. The fitting results are

Fig. 6: Simulated results of Langmuir (a), Freundlich (b), Temkin (c) isotherms for Cr(VI) removal by magnetic nano-Fe₃O₄ at 25°C.

shown in Fig. 5 and the linear correlation coefficient and the model constants are given in Table 1. As can be seen from Table 1, the linear correlation coefficients (R²) of the Langmuir model and Freundlich model were 0.9888 and 0.9994, respectively. Both of them have extremely higher than R² than Temkin model (0.9829). In comparison, the R² of the Freundlich model was higher than the R² of the Langmuir model. Therefore, the adsorption behaviour of Cr(VI) by magnetic nano-Fe₃O₄ was more suitable for the Freundlich model description. In the meanwhile, according to the Langmuir model, the maximum adsorption amount of Cr(VI) by magnetic nano-Fe₃O₄ was calculated to be 34.0136 mg/g, indicating that nano-Fe₃O₄ has higher adsorption performance.

Adsorption Kinetics

To investigate the adsorption process of Cr(VI) by magnetic nano-Fe₃O₄, the experimental data were fitted by pseudo-first-order kinetics, pseudo-second-order kinetic and the intraparticle diffusion model. The Kinetic formulas can be expressed by equations 5-7.

$$\ln(q_e - q_t) = \ln q_e - k_1 t \quad \dots(5)$$

$$\frac{t}{q_t} = \frac{1}{k_2 q_e^2} + \frac{t}{q_e} \quad \dots(6)$$

$$q_t = k_{id} t^{1/2} + C \quad \dots(7)$$

Where, q_e and q_t (mg/g) are the amounts of Cr(VI) at equilibrium and at any time t. While k₁ and k₂ are the rate constants of pseudo-first-order and pseudo-second-order adsorption. And k_{id} is the rate constant of the intraparticle diffusion model and C is truncation. The kinetic parameters were obtained by a linear regression method. The results are shown in Fig. 6 and Table 2, respectively. It could be found

that the linear correlation coefficient of the pseudo-second-order kinetics was much higher than the linear correlation coefficient of the pseudo-first-order kinetics and the intraparticle diffusion model, indicating that pseudo-second-order kinetics was more suitable for describing the adsorption behaviour of hexavalent chromium by magnetic nano-Fe₃O₄. This illustrated that the process was mainly controlled by chemisorption.

CONCLUSION

In this study, the adsorption properties of chromium ions by magnetic nano-Fe₃O₄ were studied at different pH, different dosage of magnetic nano-Fe₃O₄ and different Cr(VI) concentrations, respectively. In addition, the adsorption process of nano-Fe₃O₄ to Cr(VI) was explored by fitting the experimental data with the adsorption isotherm model and adsorption kinetics. The experimental results showed that the adsorption rate and the amount of adsorption gradually decreased when the solution pH increased, and increased with the increasing of the initial concentration of Cr(VI) and the dosage of magnetic nano-Fe₃O₄. Besides, the data fitting results showed that the adsorption of Cr(VI) by magnetic nano-Fe₃O₄ conformed to the Freundlich isotherm adsorption model and the maximum adsorption amount of Cr(VI) was 34.0136 mg/g, suggesting that magnetic nano-Fe₃O₄ was excellent adsorbent. Moreover, the adsorption process corresponded to pseudo-second-order kinetic, which was mainly controlled by chemisorption.

ACKNOWLEDGEMENTS

The authors gratefully acknowledge the financial support of the National Natural Science Foundation of China (Grant No. 41807468), Zhejiang Provincial Natural Science Foundation of China (Grant No. LY18E080018), Shaoxing Public Welfare Project (Grant No. 2017B70042), State Key Laboratory of Pollution Control and Resource Reuse Foundation (Grant No. PCRRF18021).

REFERENCES

Akçay, G., Kılınç, E., Akçay, M.J.C., Physicochemical, S.A. and Aspects, E. 2009. The equilibrium and kinetics studies of flurbiprofen adsorption onto tetrabutylammonium montmorillonite (TBAM). *Colloids Surface A.*, 335(1-3): 189-193.

Aroua, M.K., Zuki, F.M. and Sulaiman, N.M. 2007. Removal of chromium ions from aqueous solutions by polymer-enhanced ultrafiltration. *J. Hazard. Mater.*, 147(3): 752-758.

Barrera-Díaz, C.E., Lugo-Lugo, V. and Bilyeu, B. 2012. A review of chemical, electrochemical and biological methods for aqueous Cr(VI) reduction. *J. Hazard. Mater.*, 223: 1-12.

Bhattacharya, A., Naiya, T., Mandal, S. and Das, S. 2008. Adsorption, kinetics and equilibrium studies on removal of Cr(VI) from aqueous

solutions using different low-cost adsorbents. *Chem. Eng. J.*, 137(3): 529-541.

Bilal, M., Shah, J.A., Ashfaq, T., Gardazi, S.M.H., Tahir, A.A., Pervez, A., Haroon, H. and Mahmood, Q. 2013. Waste biomass adsorbents for copper removal from industrial wastewater—a review. *J. Hazard. Mater.*, 263: 322-333.

da Fonseca, M.G., de Oliveira, M.M. and Arakaki, L.N. 2006. Removal of cadmium, zinc, manganese and chromium cations from aqueous solution by a clay mineral. *J. Hazard. Mater.*, 137(1): 288-292.

Du, Z., Zhang, Y., Li, Z., Chen, H., Wang, Y., Wang, G., Zou, P., Chen, H. and Zhang, Y. 2017. Facile one-pot fabrication of nano-Fe₃O₄/carboxyl-functionalized baker's yeast composites and their application in methylene blue dye adsorption. *Appl. Surf. Sci.*, 392: 312-320.

Fan, X. and Yao, K. 2007. Structural and magnetic properties of Fe₃O₄ nanoparticles prepared by arc-discharge in water. *Sci. Bull.*, 52(20): 2866-2870.

Gode, F. and Pehlivan, E. 2005. Removal of Cr(VI) from aqueous solution by two Lewatit-anion exchange resins. *J. Hazard. Mater.*, 119(1-3): 175-182.

Golder, A.K., Chanda, A.K., Samanta, A.N. and Ray, S. 2011. Removal of hexavalent chromium by electrochemical reduction-precipitation: Investigation of process performance and reaction stoichiometry. *Sep. Purif. Technol.*, 76(3): 345-350.

Golder, A.K., Chanda, A.K., Samanta, A.N. and Ray, S. 2007. Removal of Cr(VI) from aqueous solution: electrocoagulation vs chemical coagulation. *Sep. Sci. Technol.*, 42(10): 2177-2193.

Gu, H., Rapole, S.B., Huang, Y., Cao, D., Luo, Z., Wei, S. and Guo, Z. 2013. Synergistic interactions between multi-walled carbon nanotubes and toxic hexavalent chromium. *J. Mater. Chem. A.*, 1(6): 2011-2021.

Gupta, V.K., Ali, I., Saleh, T.A., Siddiqui, M. and Agarwal, S. 2013. Chromium removal from water by activated carbon developed from waste rubber tires. *Environ. Sci. Pollut. Res.*, 20(3): 1261-1268.

Hu, X., Liu, B., Deng, Y., Chen, H., Luo, S., Sun, C., Yang, P. and Yang, S. 2011. Adsorption and heterogeneous Fenton degradation of 17 α -methyltestosterone on nano Fe₃O₄/MWCNTs in aqueous solution. *Appl. Catal., B.*, 107(3-4): 274-283.

Kobya, M. 2004. Removal of Cr(VI) from aqueous solutions by adsorption onto hazelnut shell activated carbon: kinetic and equilibrium studies. *Bioresour. Technol.*, 91(3): 317-321.

Lu, Z., Hao, Z., Wang, J. and Chen, L. 2016. Efficient removal of europium from aqueous solutions using attapulgite-iron oxide magnetic composites. *J. Ind. Eng. Chem.*, 34: 374-381.

Luo, C., Tian, Z., Yang, B., Zhang, L. and Yan, S. 2013. Manganese dioxide/iron oxide/acid oxidized multi-walled carbon nanotube magnetic nanocomposite for enhanced hexavalent chromium removal. *Chem. Eng. J.*, 234: 256-265.

Pehlivan, E. and Cetin, S. 2009. Sorption of Cr(VI) ions on two Lewatit-anion exchange resins and their quantitative determination using UV-visible spectrophotometer. *J. Hazard. Mater.*, 163(1): 448-453.

Salam, M.A. 2017. Preparation and characterization of chitin/magnetite/multiwalled carbon nanotubes magnetic nanocomposite for toxic hexavalent chromium removal from solution. *J. Mol. Liq.*, 233: 197-202.

Sharma, V.K., McDonald, T.J., Kim, H. and Garg, V.K. 2015. Magnetic graphene-carbon nanotube iron nanocomposites as adsorbents and antibacterial agents for water purification. *Adv. Colloid. Interfac.*, 225: 229-240.

Shen, H., Pan, S., Zhang, Y., Huang, X. and Gong, H. 2012. A new insight on the adsorption mechanism of amino-functionalized nano-Fe₃O₄ magnetic polymers in Cu (II), Cr(VI) co-existing water system. *Chem. Eng. J.*, 183: 180-191.

Sherlala, A., Raman, A., Bello, M. and Asghar, A. 2018. A review of the applications of organo-functionalized magnetic graphene oxide nanocomposites for heavy metal adsorption. *Chemosphere*, 193: 1004-1017.

- Wang, X.S., Zhu, L. and Lu, H.J. 2011. Surface chemical properties and adsorption of Cu (II) on nanoscale magnetite in aqueous solutions. *Desalination*, 276(1-3): 154-160.
- Yoon, J., Amy, G., Chung, J., Sohn, J. and Yoon, Y. 2009. Removal of toxic ions (chromate, arsenate, and perchlorate) using reverse osmosis, nanofiltration, and ultrafiltration membranes. *Chemosphere*, 77(2): 228-235.
- Zang, Y.B., Hou, W.G. and Wang, W.X. 2007. Adsorption-desorption of chromium(VI) on Mg-Al hydrotalcite-like compounds part I. Adsorption. *Acta. Chim. Sinica*, 65(9): 773-778.
- Zhu, J., Wei, S., Gu, H., Rapole, S.B., Wang, Q., Luo, Z., Haldolaarachchige, N., Young, D.P. and Guo, Z. 2012. One-pot synthesis of magnetic graphene nanocomposites decorated with core@ double-shell nanoparticles for fast chromium removal. *Environ. Sci. Technol.*, 46(2): 977-98



Genotoxic Effect of Iron Oxide Nanoparticles Treated Tannery Effluent on Zebrafish *Danio rerio*

D. Tamilmathi and M. R. Rajan†

Department of Biology, The Gandhigram Rural Institute (Deemed to be University) Gandhigram-624 302, Tamil Nadu, India

†Corresponding author: M.R. Rajan; mrrrajanbio@gmail.com

Nat. Env. & Poll. Tech.
Website: www.neptjournal.com

Received: 07-04-2020

Revised: 30-05-2020

Accepted: 03-06-2020

Key Words:

Genotoxicity
Iron oxide nanoparticles
Tannery effluent
Zebrafish

ABSTRACT

The present study deals with the genotoxic effect of iron oxide nanoparticles treated tannery effluent on zebrafish *Danio rerio*. The chemical co-precipitation method was used for the synthesis of iron oxide nanoparticles which were characterized by SEM, EDAX, XRD, FTIR and VSM. Physico-chemical characteristics of tannery effluent were also estimated. Iron oxide nanoparticles were used as nano-adsorbents in reducing the toxic substances present in tannery effluent. Behavioural studies and genotoxic effect on zebrafish exposed to different concentrations of iron oxide nanoparticles treated tannery effluent and control (raw tannery effluent) were carried out. Biochemical composition such as protein, carbohydrate and lipid were estimated in the muscles and gills of zebrafish on 14th day after exposure. SEM images of iron oxide nanoparticles were observed at 5 μm and 10 μm which were spherical. EDAX spectrum recorded on synthesized iron oxide nanoparticles was identified in 7 peaks. FT-IR spectrum of iron oxide nanoparticles was analysed in the range of 500-4000 cm^{-1} and spectral bands were observed. Physico-chemical parameters of treated tannery effluent were decreased as the different concentrations of iron oxide nanoparticles increased. 200, 225 and 250 ppm treated tannery effluent were selected for median lethal concentration. No mortality was found in both control and iron oxide nanoparticles treated tannery effluent. The number of micronuclei was increased with increasing concentration of iron oxide nanoparticles when compared to control. Biochemical characteristics such as protein, carbohydrate and lipid in muscle and gills of zebrafish were higher in T₂ (225ppm) than control and other concentrations. From this, it can be concluded that iron oxide nanoparticles can be used as nano-adsorbent in treating tannery effluent for effective removal of toxic substances.

INTRODUCTION

One of the most serious environmental problems is the existence of hazardous and toxic pollutants in industrial wastewater because most of these wastewaters end up into the environment. The main source of freshwater pollution can be attributed to the discharge of untreated waste, dumping of industrial effluent and run-off from agricultural fields. Nowadays, there is continuously increasing worldwide concern for the development of wastewater treatment technologies. Different treatment technologies are available for the removal of toxic substances. Adsorption is considered as one of the most effective, efficient and economical methods for the removal of pollutants from wastewater. Among the different treatment methods, the utilization of nanoparticles for the removal of pollutants from industrial effluents has arisen as an attractive research direction. This is because, compared to bulk materials, nanomaterials based adsorbents possess much larger surface area, which can provide a greater number of active sites for adsorption. Some kinds of nanomaterials such as carbon nanotubes, manganese

oxides, zinc oxide, titanium oxide and iron oxide have been used as nano-adsorbents in many studies and showed excellent adsorption capacity for various heavy metals including chromium. Multi-wall carbon nanotubes have high dispersion and adsorption ability to remove heavy metals in wastewater treatment. Among these nano-adsorbents, the use of iron oxide nanoparticles has been received much attention due to their unique properties and effective in adsorption of toxic substances and heavy metals in tannery effluent (Lkhagvadulam et al. 2017).

Embryonic and larval *Danio rerio* (zebrafish) is increasingly used as a toxicological model to conduct rapid *in vivo* tests and developmental toxicity assays; the zebrafish features high genetic homology to mammals, robust, phenotypes, and high-throughput genetic and chemical screening have made it a powerful tool to evaluate *in vivo* toxicity. Recent studies employing zebrafish as an experimental model, comparing it with other *in vivo* and *in vitro* models, presenting zebrafish as a potent vertebrate tool to evaluate drug toxicity and

efficacy to facilitate more extensive, easy and comprehensive knowledge of new generation drugs (Caballero & Candiracci 2018).

The application of genotoxicity biomarkers in organisms allows for the assessment of mutagenic hazards and the identification of the sources and fate of the contaminants. Micronucleus (MN) test is an index of accumulated genetic damage during the lifespan of the cells is one of the most suitable techniques to identify integrated response to the complex mixture of contaminants. The large majority of studies on the genotoxic effect of the polluted water environment have been carried out with the use of bivalves and fish. Haemocytes and gill cells are the target tissues most frequently considered for the MN determination in bivalves. The erythrocyte MN test in fishes was also widely and frequently applied for genotoxicity assessment of freshwater and marine environment in situ using native or caged animals following different periods of exposure (Bolognesi & Hayashi 2011). The study related to the genotoxic effect of iron oxide nanoparticles treated tannery effluent on zebrafish *Danio rerio* is very important and required, hence the present investigation was made.

MATERIALS AND METHODS

Materials

Ferrous chloride (FeCl_2), ferric chloride (FeCl_3) and sodium hydroxide were used for the synthesis of the iron oxide nanoparticles (Fe_3O_4) and purchased from Loba Chemicals, India. All the reagents used for the synthesis of Fe_3O_4 nanoparticles were of analytical grade and used without further purification. All the glassware were washed, rinsed with deionized water, dried and heat sterilized in a hot air oven.

Methods

Synthesis of Iron Oxide Nanoparticles

The co-precipitation method was used for the synthesis of iron oxide nanoparticles. The aqueous solution of FeCl_2 and FeCl_3 was prepared in 1:2 ratio and NaOH (0.1N) was added with constant stirring within 30 minutes, the solution gets brownish yellow colour. The pH of the solution was 1. The aqueous solution with a further constant stirring, within 30 minutes a visible colour change was observed. The yellow colour aqueous solution turned into greenish-black precipitate and the pH was adjusted to 12. After the precipitation, it was centrifuged at 500 rpm within 3 minutes and added with ethanol in trace volume to collect the iron oxide nanoparticles which were allowed to air dry/dissolve in distilled water for 8 h sonication (50Hz frequency Vibronics -230V).

Characterization of Iron Oxide Nanoparticles

- (a) **Scanning Electron Microscope (SEM):** SEM analysis is a powerful investigative tool which uses a focused beam of electrons to produce complex, high magnification images of a sample's surface topography. Morphology of the sample (Fe_3O_4 NPs) was investigated using a scanning electron microscope (SEM) (LEO 1455 VP).
- (b) **Energy Dispersive X-ray Spectroscopy (EDAX):** A minute drop of nanoparticles solution was cast on aluminium foil and subsequently dried in the air before transferring it to the microscope. An energy dispersive X-ray detection instrument (EDAX) (HORIBA 8121-H) was used to examine the elemental composition of the sample.
- (c) **X-ray Diffraction (XRD):** Structure and crystalline size of Fe_3O_4 nanoparticles were determined by using XRD diffractometer with nickel-filter $\text{CuK}\alpha$ radiations in the 20 range ($\lambda = 1.5418\text{\AA}$) from an X-ray tube run at 40kV and 30ma.
- (d) **Vibrating Sample Magnetometer (VSM):** The magnetic property of Fe_3O_4 nanoparticles was determined by vibrating sample magnetometer.

Collection and Acclimation of Fish

For toxicity studies, zebrafish fingerlings ($3.5\pm 1.5\text{g}$) were collected from Aqua garden, Madurai and transported to the laboratory in polythene bags filled with oxygenated water. Fish were acclimated in round plastic troughs for 15 days at $28\pm 2^\circ\text{C}$. During acclimation, fish were fed with trainee feed containing fish meal, groundnut oil cake, wheat flour and rice bran in the form of dry pellets.

Sample Collection (Tannery Effluent)

Tannery effluent samples were collected in plastic containers from the discharged stream of tannery effluent situated in the central part of Dindigul town.

Physico-Chemical Characteristics of Tannery Effluent

The physico-chemical parameters such as colour, odour, pH, electrical conductivity, total solids, total dissolved solids, total suspended solids, hardness, sodium, potassium, calcium, magnesium, sulphate, chloride, dissolved oxygen, dissolved carbon dioxide, BOD, COD and copper were estimated by standard methods (APHA 2012).

Role of Iron Oxide Nanoparticles on Physico-Chemical Parameters of Tannery Effluent

The role of iron oxide nanoparticles on the physico-chemical characteristics of tannery effluent was examined. Iron oxide nanoparticles were used as nano-adsorbents in treating tan-

nery effluent with different concentrations such as 50ppm, 100ppm, 150ppm, 200ppm and 250ppm of Fe_3O_4 NPs.

Acute Toxicity Tests (LC_{50} Determination)

Acute toxicity tests were conducted in this study following International Standard Guidelines (ASTM 1993). This study was conducted for 96 hours at room temperature. The raw tannery effluent was taken as a control. Different concentrations of iron oxide nanoparticles treated tannery effluent such as 200ppm, 225ppm and 250ppm were used for further studies. Ten fish were maintained in triplicates.

Genotoxicity (Micronucleus Assay)

Blood samples were taken from the fish in control and each concentration of iron oxide nanoparticles treated tannery effluent, smeared on clean glass slides and dried for 10 minutes for removal of water content, and fixed in ethanol for 10 minutes. Then, the slides were stained with Geisma stain (3%). The slides were evaluated under a light microscope and erythrocytes were counted for each sample (Suganya et al. 2018).

Collection of Organ Samples

The organs such as muscle and gills were dissected from the fish in control and different concentrations of iron oxide nanoparticles treated tannery effluent on 1st day, 7th day and 14th day and stored frozen for further investigation.

Biochemical Characteristics

Total protein was determined spectrophotometrically at 660nm based on Lowry's method (Lowry et al. 1951). Total carbohydrate was determined based on the Anthrone method (Carrol et al. 1956). Total lipid was estimated by the method of Barnes & Blackstock (1973).

RESULTS AND DISCUSSION

Fe_3O_4 nanoparticles were synthesized by chemical co-precipitation method. Iron oxide nanoparticles can be syn-

thesized through co-precipitation of Fe^{2+} and Fe^{3+} by the addition of a base. The size, shape and composition of iron oxide nanoparticles synthesized through chemical methods depend on the type of salt used, Fe^{2+} and Fe^{3+} ratio, pH and ionic strength (Ali et al. 2016). Complete precipitation of Fe_3O_4 should be expected between pH 9 and 14 (Gupta & Wells 2004). The precipitated magnetite is black in colour. Fe_3O_4 produced are usually coated with organic or inorganic molecules during the precipitation process (Kim et al. 2001).

The morphology of the iron oxide nanoparticles was studied by scanning electron microscopy. It revealed the spherical and rectangular shapes of synthesized nanoparticles. It showed a clear image of highly dense iron oxide nanoparticles and micron-scale size range about 9.48mm (scale bar at 10 μm) and 9.48mm (scale bar at 5 μm) (Fig.1). Keerthika et al. (2017) reported that the iron oxide nanoparticles having micron-scale size range about 10.91mm (scale bar 5 μm) and 10.86mm (scale bar 10 μm). Hariani et al. (2013) reported that the SEM image of synthesized iron oxide nanoparticles have a clear image ranges from 30nm to 100nm. Similar results on SEM analysis of iron oxide nanoparticles had also been reported by Lida et al. (2007).

The presence of carbon (C), oxygen (O) and iron (Fe) was revealed in synthesized nanoparticles by EDAX spectral analysis. EDAX spectrum recorded on the iron oxide nanoparticles is shown at three peaks located between 0.5KeV and 6.5KeV. The two peaks of Fe element were located on the spectrum at 0.8 KeV and 6.5 KeV and another peak of O element was located on the at 0.5 KeV (Fig. 2). Keerthika et al. (2017) reported the EDAX spectrum of iron oxide nanoparticles which showed three peaks located between 2 KeV and 10 KeV maxima related to the iron characterized lines K.

The FTIR spectrum of iron oxide nanoparticles was analysed in the range of 400-4000 cm^{-1} . Fourier Transform Infrared Spectroscopy revealed the functional groups of iron

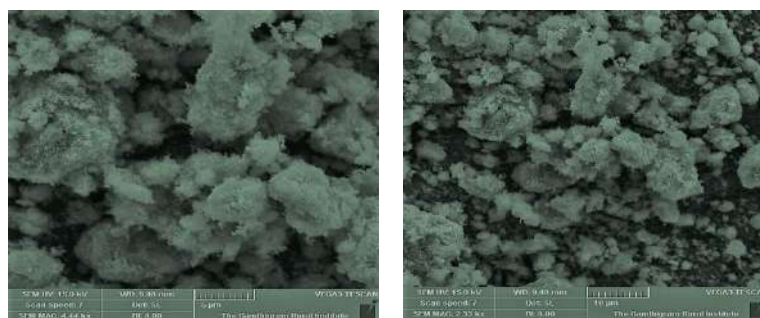


Fig. 1: SEM images of iron oxide nanoparticles.

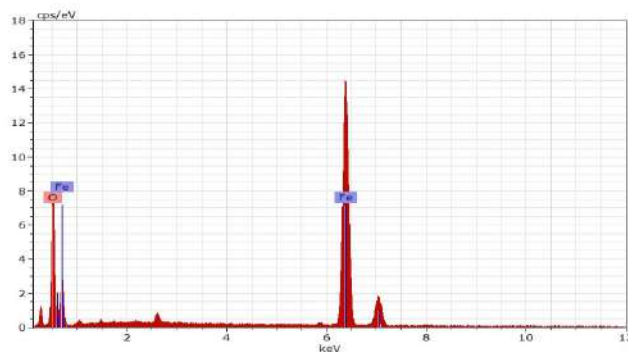


Fig. 2: EDAX image of iron oxide nanoparticles.

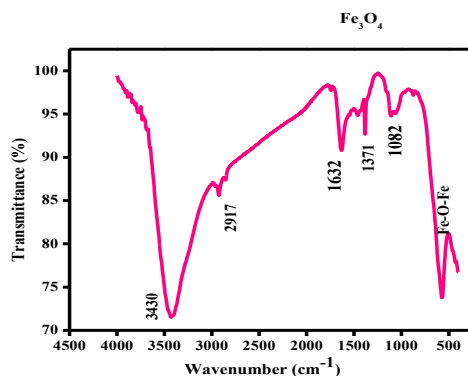


Fig. 3: FT-IR image of iron oxide nanoparticles.

oxide nanoparticles and viewed the functional groups of alcohol, phenol, alkanes, ketones, saturated aliphatic, alkyl halides and O-H, C-H, C-Br, C=O, C-I stretching of proteins (Fig. 3 and Table 1). Arokiyaraj et al. (2013) reported that the main functional groups of iron oxide nanoparticles are alcohol, phenols and primary amines. Similar results were obtained from the FT-IR spectrum of iron oxide nanoparticles confirmation peak at 511-535 cm⁻¹ (El-Kassas Hala et al. 2016).

The XRD diffraction peaks indexed with crystal planes are 19.5° (111), 30.02° (220), 35.22° (311), 54.08° (422), 64.55° (440) and 78.36° (444). The samples were scanned between angles 0° to 90° to obtain the equatorial reflection. Structure and crystalline size of nanoparticles were determined by XRD with JCPDS Card No.89-2355 and 89-3854. The average crystalline size of chemically synthesized iron oxide nanoparticles was 15.58 and 21.34 nm (Fig. 4). Suganya et al. (2016) reported that the synthesized iron oxide nanoparticles are crystal in nature and further confirmed by XRD and the nano-crystal average size is 10 to 16 nm. Wu et al. (2011) reported that XRD patterns of synthesized particles with the standard diffraction spectrum of the synthesized product are crystalline iron oxide. The

sharpness of XRD reflections indicates that the synthesized iron oxide is crystalline.

The magnetic properties of iron oxide nanoparticles were measured by Vibrating Sample Magnetometer (VSM) (Fig. 5). The synthesized iron oxide nanoparticles exhibit low saturation magnetization at 8.865 emu.g⁻¹ than the bulk Fe₃O₄. Similarly, Mahdavi et al. (2013) reported that all the nanoparticles exhibit superparamagnetic behaviour and have low saturation magnetization (Ms) values than the bulk Fe₃O₄ (92 emu.g⁻¹). The saturation magnetization (Ms) of the Fe₃O₄ magnetic nanoparticles increase from 58.60 to 78.00 emu.g⁻¹ with an increase of the nanoparticle sizes from 7.83 to 9.41 nm. The result was due to the surface order or disorder interaction of the magnetic spin moment.

The physico-chemical characteristics of raw tannery effluent are presented in Table 2. All the parameters were higher than treated tannery effluent. Unpleasant odour of tannery effluent was due to microbial growth (Muthukkauppan & Parthiban 2018). Very high EC is due to the higher concentration of acid-base and salt in water (Kataria et al. 1995). Also increase in BOD level is a reflection of microbial oxygen demand, leading to depletion of dissolved oxygen (Poole et al. 1977). Similarly, Rajan &

Table 1: FT-IR functional group representation of iron oxide nanoparticles.

Bands	Functional groups	Type of vibration	Intensity
3439.42	Alcohol, phenol	O-H stretch	Strong
2924.03	Alkanes	C-H stretch	Medium
1631.00	Ketones, saturated aliphatic	C=O stretch	Strong
1109.35	Alkane	C-OH stretch	Strong
1026.90	Alcohol group	C-F stretch	Strong
582.87	Alkyl halides	C-Br stretch	Medium
479.70	Alkyl halides	C-I stretch	Strong

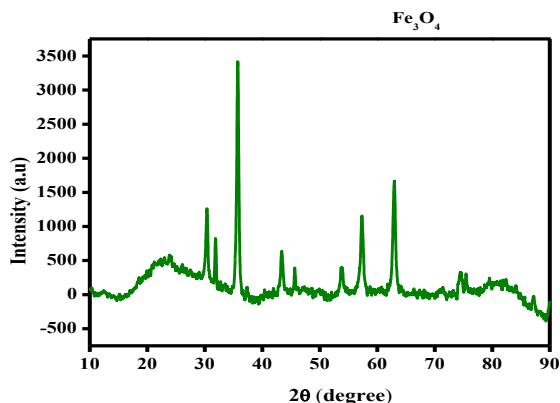


Fig. 4: XRD image of iron oxide nanoparticles.

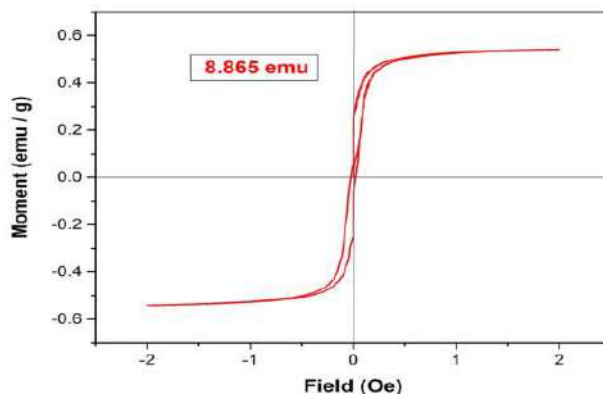


Fig. 5: VSM image of iron oxide nanoparticles.

Murali (2011) reported the physico-chemical characteristics of tannery effluent collected from a Common Tannery Effluent Treatment Plant located near Senkulam lake in Dindigul and treated with different leaves of plants for the removal of chloride. Lkhagvadulam et al. (2017) reported the use of maghemite nanoparticles for removal of Cr in tannery wastewater and maximum adsorption efficiency of total Cr was achieved 96.7% at an optimum condition and

also observed the best efficiency in removing major physico-chemical parameters (TCr, SS, COD, sulphide and turbidity) in tannery wastewater.

Different concentrations of iron oxide nanoparticles (50ppm, 100ppm, 150ppm, 200ppm and 250 ppm) were used as nano-adsorbents in treating tannery effluent to reduce the physico-chemical contaminants (Table 3). The maximum adsorption efficiency of iron oxide nanoparticles

Table 2: Physico-chemical characteristics of tannery effluent.

S. No.	Parameters	Units	Values
1.	Colour	-	Dark brown
2.	Odour	-	Unpleasant smell
3.	pH	-	8.55
4.	Electrical conductivity	Ms/cm	251.24
5.	Total solids	mg/L	17444.4
6.	Total dissolved solids	„	15190.4
7.	Total suspended solids	„	2254
8.	Total hardness	„	5844.8
9.	Sodium	„	2760
10.	Potassium	„	63.96
11.	Calcium	„	1840
12.	Magnesium	„	410.8
13.	Sulphate	„	62.12
14.	Chloride	„	4890.8
15.	Dissolved oxygen	„	3.39
16.	Dissolved carbon dioxide	„	25.2
17.	BOD*	„	1570
18.	COD**	„	21480
19.	Nitrogen	„	155
20.	Copper	„	0.016

*Biological Oxygen Demand, **Chemical Oxygen Demand.
All the values are an average of ten individual observations.

Table 3: Physico-chemical characteristics of Fe₃O₄ NPs treated tannery effluent.

S.No.	Parameters	Unit	Different concentration of iron oxide nanoparticles treated tannery effluent				
			50ppm	100ppm	150ppm	200ppm	250ppm
1.	Colour	-	Dark brown	Light brown	Light green	Light yellow	colourless
2.	Odour	-	-	-	-	-	-
3.	pH	-	8.30	8.22	7.92	7.54	7.11
4.	Electrical conductivity	Ms/cm	242.1	226.4	216.28	200,84	182.55
5.	Total solids	mg/L	3433	3233	2933	2850	2833
6.	Total dissolved solids	„	2912	2780	2655	2624	2100
7.	Total suspended solids	„	521	300	278	226	100
8.	Total hardness	„	5200	4400	3200	2800	2000
9.	Dissolved oxygen	„	4.04	6.464	6.48	6.52	6.56
10.	Dissolved carbon dioxide	„	18	16	14	10	6
11.	Chloride	„	3834	3550	3266	2840	2414
12.	Magnesium	„	290	282	266	250	243
13.	Sulphate	„	59	55.6	54.54	54.25	53
14.	BOD	„	1433	734	406	118.2	80.8
15.	COD	„	20000	12800	11200	9600	5600
16.	Nitrogen	„	124	109	90	72	55
17.	Sodium	ppm	2752	2715.4	2533	2032	1667
18.	Potassium	„	63.82	63.70	54.04	43.12	36.606
19.	calcium	„	908	400	342	301	297.8
20.	Copper	„	0.004	0.003	0.003	0.002	0.001

in treating tannery effluent was observed at low pH and high concentration of iron oxide nanoparticles (200 and 250 ppm). With the increase of adsorbent dose, the reduction of physico-chemical parameters of tannery effluent increase due to the increased available binding sites in the nano-composite for the complexation of metal ions (Saravanan et al. 2013). A faster initial removal rate was possible due to the availability of sufficient vacant adsorbing sites in the adsorbent (Sivakami et al. 2013).

No mortality was found in both control and different concentrations of iron oxide nanoparticles for LC₅₀ determination. The behavioural response gives a direct response of the animals to the pollutant. Observation of basic behavioural responses of zebrafish was made which showed jerking movement and breathing in water surface (Table 4). Suganthi et al. (2015) reported the behaviour patterns such as jerky movements, continuous opercular movement, and reduction in dorsal and anal fin movements in *O. mossambicus* treated with ZnO NPs. Sivakumar et al. (2014) evaluated the behavioural responses of *Danio rerio* exposed to raw tannery effluent which showed rapid swim with random movements and coughing due to inconvenience in breathing.

Micronucleus assay was done on 1st, 7th and 14th day (Table 5). Micronuclei in erythrocytes of zebrafish increases with increasing concentrations of iron oxide nanoparticles treated tannery effluent when compared to the control group. The number of micronuclei present in different concentrations of iron oxide nanoparticles treated tannery effluent differ significantly from the control group at (P < 0.001) on 1st day, (P < 0.01) on 7th and 14th day based

Table 4: Basic observation of zebrafish exposed to control and iron oxide nanoparticles treated tannery effluent.

S.No.	Activity	Observation
1	Circular swimming	Yes
2	Jerk movement	Yes
3	Bottom resting	No
4	Surface respiration	Yes
5	Aggressive movement	Yes
6	Excess of mucous secretion	No
7	Mortality observation	Yes
8	Behaviour observation	Yes
9	Breathing movement	Surface

Table 5: Micronucleus Assay.

Treatments	Micronuclei 0 th day	Micronuclei 7 th day	Micronuclei 14 th day
T ₀	3	13	18
T ₁	7**	15*	25*
T ₂	9**	18*	30*
T ₃	10**	20*	31*

Significantly different from the control group at **P < 0.001 and *P < 0.01 based on *t*-test.

on *t*-test. Similarly, Suganya et al. (2018) reported the increased amounts of micronuclei with increasing of the concentration of iron oxide nanoparticles when compared

to control group and less amount of micronuclei with a lower concentration of iron oxide nanoparticles. The micronucleus (MN) test in fish erythrocytes been has been successfully applied for the *in situ* detection of mutagenicity in a polluted environment and a significant increase in MN frequency in erythrocytes of fish collected in polluted marine or freshwater environments (Gustavino et al. 2001).

Biochemical characteristics such as protein, carbohydrate and lipid in zebrafish are higher in T₂ (225 ppm iron oxide nanoparticles treated tannery effluent) when compared to control (raw tannery effluent) and T₁ (200 ppm iron oxide nanoparticles treated tannery effluent) and T₂ (250 ppm iron oxide nanoparticles treated tannery effluent) (Figs. 6, 7 &

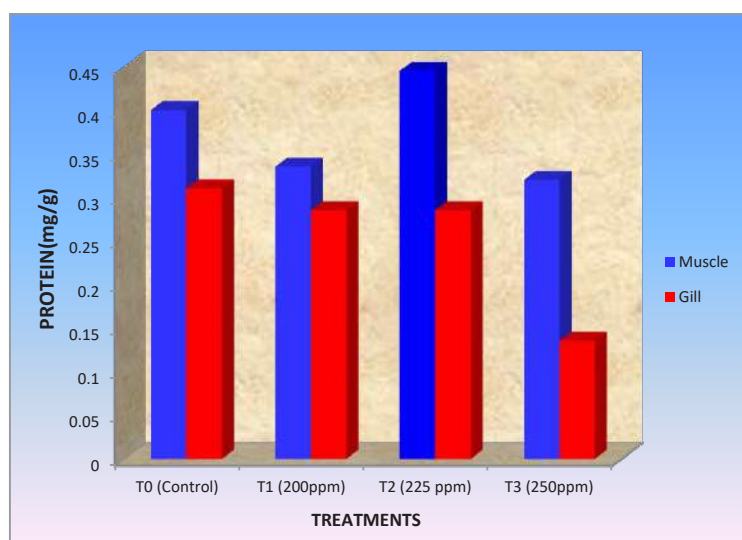


Fig. 6: Total protein level in muscle and gill of zebrafish on 14th day.

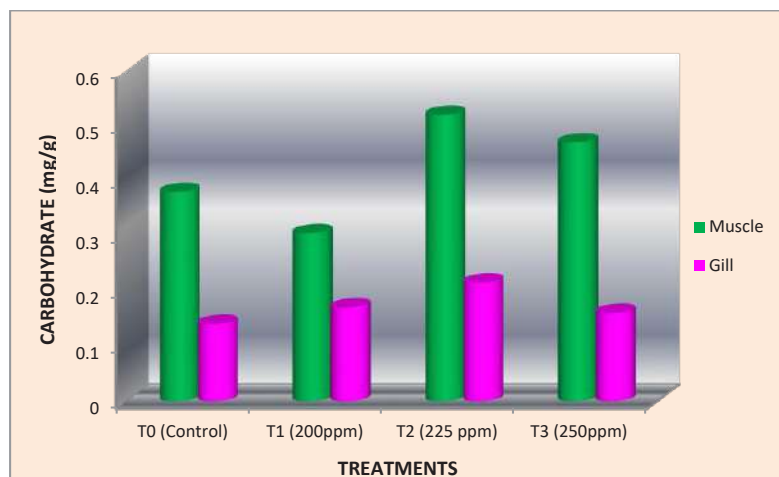


Fig. 7: Total carbohydrate level in muscle and gill in zebrafish on 14th day.

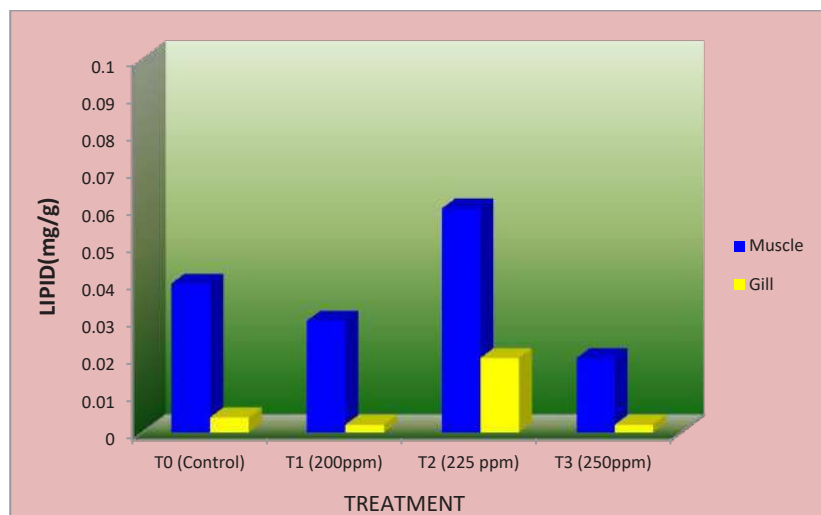


Fig. 8: Total lipid level in muscle and gill of zebrafish on 14th day.

8). The biochemical mechanisms in an organism play an important role during stress conditions due to the presence of toxicants in aquatic ecosystems. Thangam (2014) reported that pollutants in the aquatic media cause effects on fishes at a cellular or molecular level which results in significant changes in biochemical characteristics. Zhu et al. (2009) studied that the interaction of nanoparticles with chemical or biological systems may lead to biochemical disturbances or adaptive responses and these responses can be used to assess the health conditions of aquatic organisms. Keerthika et al. (2017) reported that the iron oxide nanoparticles altered the biochemical characteristics of *Labeo rohita*. Sivakumar et al. (2015) similarly reported that the biochemical parameters of muscle, gill and liver of zebrafish *Danio rerio* decrease significantly from control when exposed to raw tannery effluent. Palaniappan & Vijayasundaram (2008) reported that the arsenic intoxication induces significant alteration in the major biochemical composition of muscle proteins due to arsenic intoxication.

CONCLUSION

From this study, it is concluded that iron oxide nanoparticles can be used as nano-adsorbent in treating tannery effluent for effective removal of toxic substances.

ACKNOWLEDGMENT

The authors thank the Department of Biology, The Gandhigram Rural Institute (Deemed to be University) Gandhigram for offering facilities to carry out this study.

REFERENCES

- Ali, A., Zafer, H., Zia, M., Hag, I.U., Phull, A.R., Ali, J.S. and Hussain, A. 2016. Synthesis, characterization, applications and challenges of iron oxide nanoparticles. *Nanotechnol. Sci. Appl.*, 9: 49-67. doi: 10.2147/NSA.S99986.
- APHA, AWWA, WEF 2012. *Standard Methods for Examination of Water and Wastewater*. 22nd ed., American Public Health Association, Washington DC, USA.
- Arokiyaraj, S., Saravanan, M., Udaya Prakash, N.K., Valan Arasu, M., Vijayakumar, B. and Vincent, S. 2013. Enhanced antibacterial activity of iron oxide magnetic nanoparticles treated with *Argemone mexicana* L. leaf extract: An *in vitro* study. *Materials Research Bulletin*, 48: 3323-3327.
- ASTM 1993. *Standard practice for conducting acute tests with fishes, macroinvertebrates and amphibians*. Designation E 729-88. ASTM Standards on Aquatic Toxicology and Hazards Evaluation, pp. 102-121.
- Barnes, H. and Blackstock, J. 1973. Estimation of lipids in marine animals and tissues detailed investigation of the sulphophosphovanillin method for total lipids. *J. Exp. Mor. Bio. Ecol.*, 12: 103-118.
- Bolognesi, C. and Hayashi, M. 2011. Micronucleus assay in aquatic animals. *Mutagenesis*, 26(1): 205-213.
- Caballero, M.V. and Candiracci, M. 2018. Zebrafish as screening model for detecting toxicity and drugs efficacy. *JUMD Journal*, doi: org/10.20517/2572-8180.2017.15.
- Carrol, N.V., Longly, R.W. and Roe, J.H. 1956. Glycogen determination in liver and muscle by the use of anthrone reagent. *J. Biol. Chem.*, 220: 583-593.
- El-Kassas Hala, Y., Aly-Eldeen Mohamed, A. and Gharib Samiha, M. 2016. Green synthesis of iron oxide (Fe₃O₄) nanoparticles using two selected brown seaweeds: Characterization and application for lead bioremediation. *National Institute of Oceanography and Fisheries*, 35(8): 89-98.
- Gupta, A.K. and Wells, S. 2004. Surface modified superparamagnetic nanoparticles for drug delivery: Preparation, characterisation and cytotoxicity studies. *Institute of Electrical and Electronics Engineers Transactions on Nanobioscience*, 3(1): 66-73.

- Gustavino, B., Scornajenghi, K.A., Minissi, S. and Ciccotti, E. 2001. Micronuclei induced in erythrocytes of *Cyprinus carpio* (Teleostei, Pisces) by X-rays and colchicines. *Genetic Toxicology and Environmental Mutagenesis*, 494: 151-159.
- Hariani, P.L., Faizal, M., Ridwan, R., Marsi, M. and Setiabudidaya, D. 2013. Synthesis and properties of Fe₃O₄ nanoparticles by co-precipitation method to removal procion dye. *International Journal of Environmental Science and Development*, 4(3): 336-340.
- Kataria, H.O. and Jain, O.P. 1995. Physico-chemical analysis of river Ajnar. *Indian Journal of Environmental Protection*, 12(9): 6467.
- Keerthika, V., Ramesh, R. and Rajan, M.R. 2017. Toxicity assessment of iron oxide nanoparticles in *Labeo rohita*. *International Journal of Fisheries and Aquatic Studies*, 5(4): 01-06.
- Kim, D.K., Zhang, Y., Voit, W., Rao, K.W. and Muhammed, M. 2001. Synthesis and characterization of surfactant-coated superparamagnetic monodispersed iron oxide nanoparticles. *Journal of Magnetism and Magnetic Materials*, 225(1): 30-36.
- Lida, H., Takayanagi, K., Nakanishi, T. and Osaka, T. 2007. Synthesis of Fe₃O₄ nanoparticles with various sizes and magnetic properties by controlled hydrolysis. *Journal of Colloid and Interface Science*, 314(1): 274-280.
- Lkhagvadulam, B., Tsagaantsetseg, B., Tergel, D. and Chuluunkhuyag, S. 2017. Removal of chromium from a tannery wastewater by using a maghemite nanoparticles. *International Journal of Environmental Science and Development*, 8(10): 696-702.
- Lowry, O.H., Rosebrough, N.J., Lewis Farr, A. and Randall, R.J. 1951. Protein measurement with the Folin phenol reagent. *Journal of Biological Chemistry*, 193: 265-275.
- Mahdavi, M., Ahmad, M.B., Haron, M.J., Namvar, F., Nadi, B., Rahman, M.Z.A. and Amin, J. 2013. Synthesis, surface modification and characterization of biocompatible magnetic iron oxide nanoparticles for biomedical applications. *Molecules*, 18: 7533-7548.
- Murthy, B.N. and Ramarao, K.V. 1983. Ethology of fish *Tilapia mossambica* under lindane toxicity. *Geobios*, 10: 230-231.
- Muthukkauppan, M. and Parthiban, P. 2018. A study on the physicochemical characteristics of tannery effluent collected from Chennai. *International Research Journal of Engineering and Technology (IRJET)*, 5(3): 24-28.
- Palaniappan, P.L.R.M. and Vijayasundaram, V. 2008. Fourier transform infrared study of protein secondary structural changes in the muscle of *Labeo rohita* due to arsenic intoxication. *Food and Chemical Toxicology*, 46: 389-396.
- Poole, N.J., Wildish, D.J., Kristmanson, D.D. and Waldichuk, M. 1977. The effects of the pulp and paper industry on the aquatic environment. *Critical Reviews in Environmental Science and Technology*, 8(1-4): 153-195.
- Rajan, M.R. and Murali, S.R. 2011. Dechlorination of treated tannery effluent using leaves of plants. *Nature Environment and Pollution Technology*, 4: 573-578.
- Saravanan, D., Gomathi, T. and Sudha, P.N. 2013. Sorption studies on heavy metal removal using chitin/bentonite biocomposite. *International Journal of Biological Macromolecules*, 53: 67-71.
- Sivakami, M.S., Gomathi, T., Venkatesan, J., Jeong, H.S., Kim, S.K. and Sudha, P.N. 2013. Preparation and characterization of nanochitosan for treatment. *International Journal of Biological Macromolecules*, 57: 204-212.
- Sivakumar, P., Kanagappan, M. and Sam Manohar Das 2015. Flux of tissue substrates in *Danio rerio* exposed to raw tannery effluent. *International Journal of Engineering Research and General Science*, 3(6): 496-502.
- Sivakumar, P., Kanagappan, M. and Sam Manohar Das, S. 2014. Toxicity evaluation and behavioral responses of *Danio rerio* exposed to raw tannery effluent. *Journal of Entomology and Zoology Studies*, 2(6): 288-291.
- Suganthi, P., Murali, M., Sadiq Bukhari, A., Syed Mohamed, H.E., Basu, H. and Singhal, R.K. 2015. Behavioral and histological variations in *Oreochromis mossambicus* after exposure to ZnO nanoparticles. *International Journal of Applied Research*, 1(8): 524-531.
- Suganya, D., Rajan, M.R. and Ramesh, R. 2016. Green synthesis of iron oxide nanoparticles from leaf extract of *Passiflora foetida* and its antibacterial activity. *International Journal of Current Research*, 8(11): 08142-42085.
- Suganya, D., Ramakritinan, C. M. and Rajan, M.R. 2018. Adverse effects of genotoxicity, bioaccumulation and ionoregulatory modulation of two differently synthesized iron oxide nanoparticles on zebrafish (*Danio rerio*). *Journal of Inorganic and Organometallic Polymers and Materials*, 28(6): 2603-2611. doi:10.1007/s10904-018-0935-3.
- Thangam, Y. 2014. Effect of nitrite toxicity in carbohydrate metabolism to freshwater fish *Cirrhinus mrigala*. *IOSR Journal of Pharmacology and Biosciences*, 9(5): 03-11.
- Wu, S., Sun, A., Zhai, F., Wang, J., Xu, W., Zhang, Q. and Volinsky, A.A. 2011. Iron oxide magnetic nanoparticles synthesis from tailings by ultrasonic chemical co-precipitation. *Proceedings of Engineering*, 27: 632-637.
- Zhu, X., Zhu, L., Chen, Y. and Tian, S. 2009. Acute toxicities of six manufactured nanomaterial suspensions to *Daphnia magna*. *Journal of Nanoparticles Research*, 11: 67-75.



Comparative Study on Electrode Arrangement in Electrokinetic Remediation of Contaminated Soil

Yushan Wan[†], Juan Zhai and Anwei Wang

School of Environmental & Safety Engineering, Changzhou University, Jiangsu, China

[†]Corresponding author: Yushan Wan; wanyushan@cczu.edu.cn

Nat. Env. & Poll. Tech.
Website: www.neptjournal.com

Received: 08-03-2020
Revised: 14-04-2020
Accepted: 15-06-2020

Key Words:

Soil pollution
Electrokinetic remediation
Cadmium removal

ABSTRACT

To improve the efficiency of electrokinetic remediation of contaminated soil, by introducing single pollutant cadmium and setting up a self-made device test, electrokinetic remediation technology was applied to artificially simulated contaminated soil to explore the influence of three different two-dimensional electrode arrangements [triangle (2-e-1), rectangle (2-e-2) and hexagon (2-e-3)] on electrokinetic remediation of cadmium contaminated soil in this paper. The cathode of the test device was made of high purity (99.9%) graphite electrode, and the anode was made of stainless steel electrode. Under the condition that the voltage gradient, electrode material, electrolyte and electrification time of the three groups of tests were consistent, the current change, pH value, conductivity, total cadmium content and cadmium morphology of the three groups of tests were compared. The experimental results showed that the triangle (2-e-1) group, the current increased slowly during the process of power on, the pH value of soil was over acid, and the transformation rate of various forms of cadmium contained in the soil after the restoration was low. The current change rate of the rectangular (2-e-2) electrode arrangement was the highest, the soil environment was super alkaline, and the removal rate of cadmium was an average level. The hexagonal electrode arrangement (2-e-3) led a large current drop rate and a weakly alkaline pH environment, the removal efficiency of cadmium at sampling points (S1 and S2) near the anode was as high as 95.54%, and the comprehensive removal rate of cadmium at each sampling point reached 89.6%, moreover, the pollutant removal was uniform and efficient.

INTRODUCTION

Soil electrokinetic remediation is a technology that can remove heavy metals in the soil to a certain extent by applying a low DC power supply or voltage gradient to an electrode inserted into the ground (Bahemmat et al. 2016). The movement of heavy metals in soil has three mechanisms, namely electrophoresis, electroosmosis and electromigration. When the dissolved charged ions are transferred to the charged layer with opposite polarity through electric current artificially applied by the outside world, the ions migrate to the anode and the cathode and accumulate in the electrode area (Paramkusam et al. 2015, Ha et al. 2014), so that heavy metals in the soil are extracted and removed, which is the working principle of soil electrokinetic remediation technology. Due to the advantages of fewer chemical reagents requirement, no secondary pollution, less disturbance to soil and high remediation efficiency, this technology has become a research hotspot.

In the process of electrokinetic remediation of soil, the setting mode, electric field intensity, electrolyte composition, soil physicochemical properties of electrode materials have an impact on the remediation effect, and among these

factors, electrode materials and electrode arrangement have a greater impact on the remediation effect (Yang et al. 2014). In the process of electrodynamic repair, the single arrangement of electrodes will cause polarization, which will slow down the repair efficiency and increase energy consumption. In the aspect of electrode material selection, the electrolyte in the cathode chamber will gradually show strong alkaline state during the reaction process, while the liquid in the anode chamber gradually became strongly acidic. Therefore, to avoid the corrosion of the electrode and to take into account the conductivity and economic cost, the graphite electrode and stainless steel electrode are generally used in the laboratory. The morphological distribution of the heavy metal cadmium in the soil and the removal efficiency of cadmium under different electrode arrangements have been extensively analysed (Fang et al. 2015, Danmaliki et al. 2017, Wang et al. 2018). Turer & Genc (2005) used extraction method to evaluate the effect of two-dimensional electrode configuration on electric remediation and found that the removal rate of lead, zinc and copper in soil varied with the type of pollution. The total removal efficiency of lead, zinc and copper was 29% when using a circular electrode arrangement, which was lower than that with a flat electrode

arrangement. Kim et al. (2012) researched the electrokinetic remediation of rice soil contaminated by various metals using four one-dimensional electrode configurations. Zhai et al. (2018) studied the restoration of saline and alkaline land with a two-dimensional hexagonal arrangement of electrodes and found that the salt transport speed and removal efficiency were improved. Hu et al. (2014) compared the advantages and disadvantages of three electrode arrangements through the soil's final electroosmosis effect and found that when the electrodes were arranged in parallel dislocation, not only the displacement was the largest, but the current reduction rate was large, and the economic benefits were high (Hu et al. 2014).

In this experiment, the triangle (2-e-1), rectangle (2-e-2) and hexagon (2-e-3) arrangements of the electrode were used to conduct electrochemical remediation of contaminated soil. By comparatively analysing the pH value, conductivity, current change, total cadmium content and the morphological percentage of cadmium at each sampling point under different electrode arrangement mode, a more reasonable electrode arrangement mode was selected. This study provides a theoretical basis for the further application of electrokinetic remediation technology in soil.

MATERIALS AND METHODS

Experimental Material

The soil used in the experiment was collected from farmland near the Science and Education Town of Changzhou

University (31°41'7.94' N; 119°57'1.95' E). After removing leaves and gravel, the soil collected was air-dried and ground, and then subjected to sieving through a 2mm nylon sieve. Table 1 shows the physical and chemical properties of the tested clean soil.

CdCl₂ solution of a certain concentration was prepared using CdCl₂·2.5H₂O, and then the clean collected soil was added into CdCl₂ solution (the ratio of CdCl₂ solution to the soil was 1:1), followed by even stirring. The soil after culturing (natural culture at room temperature for 15 days) was naturally dried for nearly a week and then ground through a 2mm nylon sieve, resulting in the final contaminated soil sample.

Test Device

The electrokinetic remediation devices for contaminated soil are shown in Fig. 1-1, 1-2, 1-3, respectively. The devices are made of plexiglass and consist of electrode (cathode and anode) chamber, soil chamber and dc power supply. The device depth is 14cm, in the middle of which cathode chamber has a radius of 3cm. Electrodes are arranged in triangle, quadrangle and hexagon patterns. Cylindrical graphite (purity 99.9%) is used for the cathode, and stainless steel is used for the anode. The diameters of cathode and anode are both 1cm, and the distance between them is 14.5cm. The whole device also includes porous partition, non-woven filter cloth, peristaltic pump and copper wire, etc.

Table 1: Physical and chemical properties of the tested clean soil.

pH value	Conductivity ($\mu\text{S}\cdot\text{cm}^{-1}$)	Organic matter ($\text{g}\cdot\text{kg}^{-1}$)	Moisture content (%)	Cd content ($\text{mg}\cdot\text{kg}^{-1}$)
7.53	136	7.63	4.37	0.056

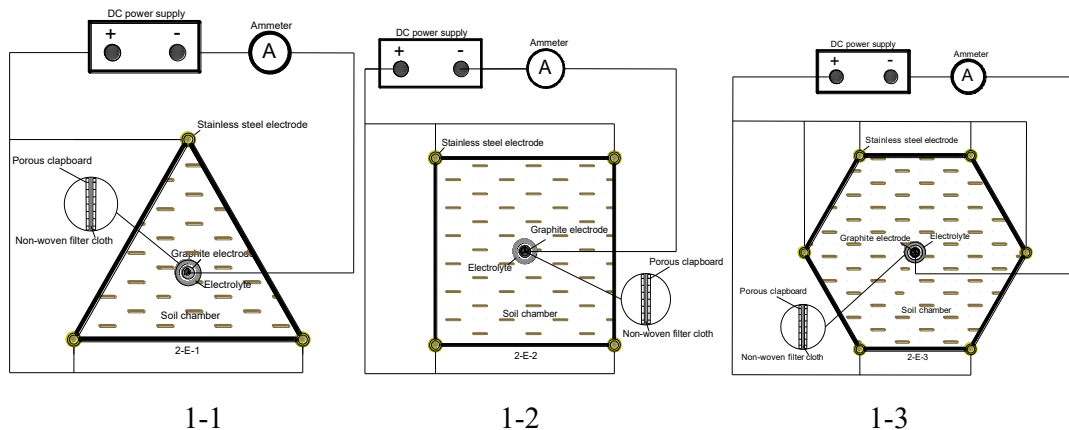


Fig. 1: Plane schematic diagram of electrode arrangement.

Test Design and Procedure

In the soil chamber of the device, 3kg of prepared cadmium contaminated soil was placed and compacted with appropriate pressure. In the cathode electrode chamber, the citric acid solution with a concentration of 0.1 mol.L^{-1} was added as the cathode electrolyte. A peristaltic pump was used for the circulation of electrolyte to prevent the increase of cathode pH, produce precipitation and inhibit the migration of heavy metals. After static equalization of soil for 24h, a constant voltage was applied for the test. To better explore the law of Cd migration and change and the optimal electrode arrangement, this experiment adopted the mode of stable and low current output. Since the cathode-anode distances in the three electrode arrangement are all equal to 14.5cm, so the control voltage gradients are all 2 v.cm^{-1} , and the power-on hours are all set to 120h. At the same time, equidistant samples were taken from the anode to the cathode in the soil chamber, and 5 sampling points were set, respectively, as shown in Fig. 2. The radius of each sampling point is 1cm, and the spacing of sampling points is 2.5cm.

Analytical Methods

The pH value and conductivity before and after soil remediation were determined by pH meter and conductivity meter.

Cadmium in the soil was dissolved by three kinds of acids (nitric acid -perchloric acid-hydrofluoric acid) digestion at high temperature, centrifuged by filter paper, and the precipitated particles in the soil were removed. The filtrate was determined by AAS (flame atomic absorption spectrophotometer). The precipitated particles in the soil were then removed by centrifugation with a filter paper, and the filtrate was then measured by AAS (flame atomic absorption spectrophotometer). Before and after soil remediation, all forms of cadmium in the soil were extracted using the Tessier five-step method, and the same standard curve was used in the test. After the soil samples before and after remediation were digested, the contents of the full amount of cadmium and different forms of cadmium were measured as the same batch (Cameselle 2015).

RESULTS AND DISCUSSION

At present, studies on electrokinetic remediation of contaminated soil are mostly concentrated on current change after remediation, soil conductivity, soil pH value, soil total Cd content and soil Cd morphological analysis. In this experiment, electrodes were arranged in a two-dimensional arrangement to form a uniform electric field to improve remediation efficiency. Meanwhile, to reflect the spatial

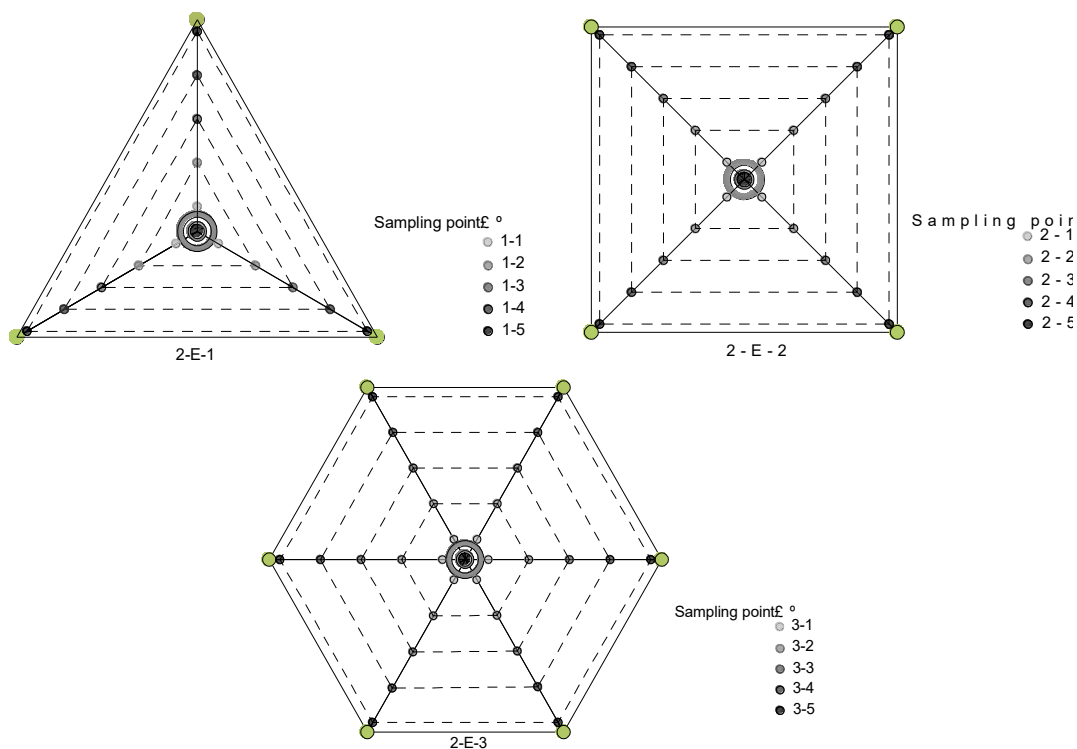


Fig. 2: Schematic diagram of sampling point distribution and electrode position.

distribution of the repair effect, samples were selected at different geometric positions after remediation. This paper focuses on the analysis of soil pH value, conductivity, total Cd content and morphology under the three electrode arrangements, and makes a more comprehensive comparison of the three electrode arrangements in combination with the law of current change.

Current Change During Electrokinetic Remediation

Under different electrode arrangements, the current changes were recorded every 2h, and the rule of current changes with reaction time is shown in Fig. 3. It was found that the current changes in the three groups of tests all rose to a peak in a short period and then fell to a steady-state. At the early stage of soil remediation, the current of the three groups of tests increased continuously and reached its peak at 30h. Due to the hydrolysis between the anode and the cathode, a large amount of H^+ generated by the anode and OH^- generated by the cathode migrate to each other. During the migration of H^+ to the cathode, the soil presents an acidification state, which promotes the dissociation of Cd^{2+} in the soil, increases the migration rate and the concentration of movable ions between soil micropores, so that the current can be gradually increased (Kim et al. 2012). The figure shows that the current increases faster in group 2-E-3 and 2-E-2 than in group 2-E-1. This indicates that more H^+ is generated by anodic ionization, which is conducive to increasing the migration rate of Cd ions and further enhancing the removal efficiency of Cd in the soil. With the increase of soil remediation time, the number of mobile ions between soil micropores and the amount of Cd^{2+} that can migrate in soil gradually reach a balance. At this point, the nature of the soil itself gradually stabilizes, and the current begins to decline and tends to balance. In addition, the soil can absorb part of Cd^{2+} , which meets OH^- near the cathode, resulting in the formation of precipitation.

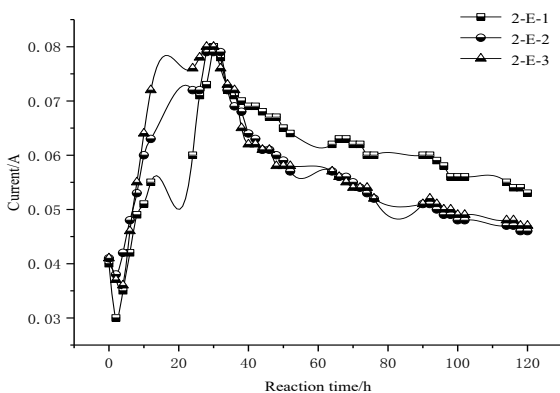


Fig. 3: Current varies with reaction time.

The precipitation may cause the reaction process to stop, which is not conducive to Cd migration.

pH Value at Each Sample Point Changed After Soil Remediation

Under different electrode arrangements, sampling points were taken from the anode to the cathode at an interval of 2.5cm. pH value at each point was measured after soil remediation, and the mean pH value was obtained based on multiple sets of parallel samples. The change of pH value at each sample point in the three test groups was obtained, as shown in Fig. 4. As can be seen from the figure, the pH value of the clean soil before remediation was 7.53; after 120h of electrokinetic remediation, the pH value of the soil increased with the increase of the distance from the anode. This is because, with the progress of electrolysis reaction in contaminated soil, a large amount of H^+ generated near the anode and OH^- generated near the cathode constantly migrate into the soil, resulting in a continuous decrease or increase of soil pH near the electrodes at both ends.

From the comparison test, it can be seen that the soil pH values at sample points S1, S2 and S3 in the 2-E-1 group are more acidic than those in the other two groups; while in the 2-E-2 group, the soil pH value at S5 is 9.12, which leads to an over alkaline soil environment. Studies have shown that super acidic and super alkaline environments will affect the rate and direction of soil electroosmosis, and reduce the Cd ion to react with OH^- generated by cathode to form precipitation, resulting in blocking of soil micropores, decrease of soil conductivity, and decreased removal efficiency of Cd in the soil (Xu et al. 2016, Amrate et al. 2005). When the pH value of the soil is 3-5, almost all cadmium in the soil can be extracted and removed. When the pH value is 6-7, the extraction efficiency of cadmium decreases to 70%; when the pH value is greater than 10, cadmium in the soil cannot

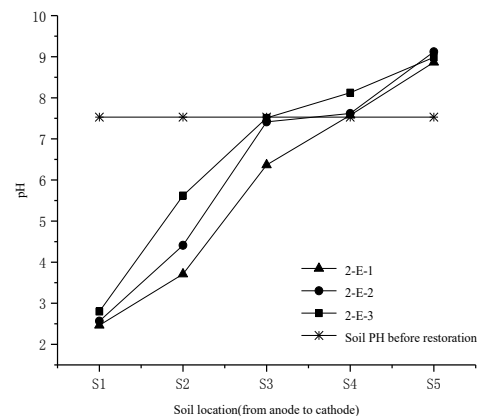


Fig. 4: pH value of soil at each sampling point after electric remediation.

be extracted and removed. In the 2-E-3 group test, the pH value at the sampling point S5 that is closest to the cathode was 8.98, and the pH value at S4 was 8.13. Compared with the pH value of 7.53 before soil remediation, the whole soil reaction chamber presented a weakly alkaline environment, which reduced the adsorption of soil on Cd, promoted the movement of Cd ions toward the cathode and improved the removal efficiency of Cd.

The Change of Conductivity at Each Sampling Point After Soil Remediation

Under different electrode arrangements, the conductivity at each sampling point varies with the distance from the anode, as shown in Fig. 5. The conductivity of the tested soil was $136 \text{ S}\cdot\text{cm}^{-1}$. It can be found from Fig. 5 that the highest conductivity was at the sampling point (S1) that is closest to the anode, which then began to decline rapidly with a large initial decline rate, and gradually tended to be stable. The conductivity at S5 that is closest to the cathode was the lowest in the whole curve distribution. The conductivity of the soil reflects the degree of difficulty in the movement of ions during electrolysis. In the process of electrokinetic remediation, the lower the soil conductivity is, the less the number of ions that can migrate in the electrolytic reaction is (Adikesavan & Rajasekar 2018). After the experimental, it can be measured that the electrical conductivity of the S1 sampling point is much higher than that of the initial soil. This is due to that in the electrolysis process, some anions and Cd ions are enriched near the anode; secondly, soil acidification near the anode can dissolve the precipitates in the soil, resulting in a continuous decrease of pH value. Different amounts of precipitates dissolved at different sampling points lead to different conductivity values. In the 2-E-3 test group, the conductivity was about twice that of the tested soil, indicating that the arrangement of hexagonal electrodes could increase the migration rate of Cd ions.

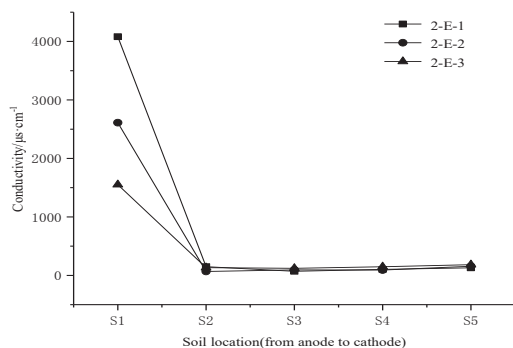


Fig. 5: Soil electrical conductivity at each sampling point after electric remediation.

Total Cadmium Content in Soil After Electrokinetic Remediation

As can be seen from Fig. 6, after the test, the total cadmium content at all sampling points was lower than that of the tested soil, and the cadmium content gradually increased from the anode to the cathode (S1-S5). Fig. 6 shows that the Cd^{2+} in the soil migrated from the anode to the cathode, and finally accumulated near the cathode, leading to a concentration change of Cd^{2+} . At the same time, a citric acid solution was used as the circulating electrolyte of the cathode during the electrokinetic remediation process to activate the soil before remediation. Citric acid is an organic acid complexing agent, which has excellent activation and complexation effect on cadmium ions in the tested soil (Bes & Mench 2008, Habibul et al. 2016). It can reduce the pH content in the soil, inhibit the adsorption of the soil, and makes the electrokinetic remediation have higher cadmium removal efficiency. The removal efficiency of cadmium at the sampling points near the anode (S1 and S2) was as high as 95.54%, and that at the sampling points away from the cathode and anode (S3 and S4) decreased to about 86.67%. The removal efficiency of cadmium in the area closest to the cathode decreased to 66%-72%. The average removal rate of cadmium of the 2-E-3 group was 89.74%, which was increased by 25.63% compared with that of the 2-E-1 group and 2-E-2 group. The removal rate of cadmium of 2-E-2 group was 12.27% higher than that of the 2-E-1 group. Therefore, it can be known the electrode arrangement mode in group 2-E-2 and 2-E-3 has a good effect in maintaining the stability of soil properties and removing the uniformity of pollutants.

Morphological Analysis of Cadmium in Soil After Electrokinetic Remediation

After soil remediation, pH value, conductivity and Cd content of the soil all changed. In this study, Tessier five-step method was adopted to conduct a morphological analysis

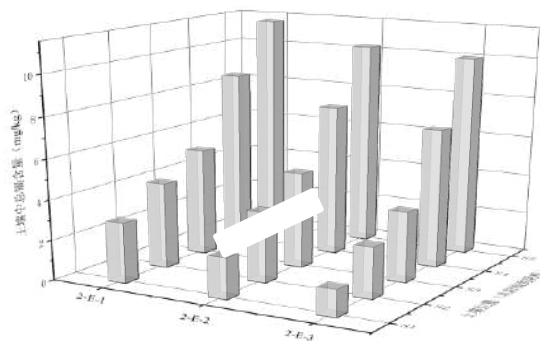


Fig. 6: Total cadmium content at each sampling point after electric repair.

of cadmium at all sampling points for the three test groups. The percentages of different forms of cadmium are shown in Fig. 7.

As shown in Fig.7, for three test groups of 2-E-1, 2-E-2, 2-E-3, the contents of exchangeable cadmium (EXC) showed an increasing trend, and the contents of Cd in the form of FeMnOx, Carb and OM all showed a decreasing trend with different decreasing rates, while the content of cadmium in residue state (RES) fluctuated slightly after soil electrokinetic remediation.

In the region (S1-S2) that is close to the cathode, the exchangeable cadmium content is high, and the increased amount after remediation is larger. This is because the soil pH value in the S1-S2 region is low after electrokinetic remediation, and the cadmium in the unstable state is easy

to be converted to exchangeable state. The exchangeable cadmium in S1 of the 2-E-1 group increased from 41.75% to 45.85%, and that in the 2-E-3 group increased by 4.55%. At the sampling point S2, the contents of cadmium for three groups increased by 5.60%, 8.42% and 8.44%, respectively. The contents of Cd in the form of Carb and FeMnOx at the sample point S3-S5 decreased relative to the initial value, and the reduction ratio decreased with the increase of the distance from the anode. This is because under the action of an electric field, partially charged Cd^{2+} reacts with the OH⁻ generated by the cathode to form precipitation during the migration process, resulting in a smaller current and a lower conversion rate of various forms of cadmium in the contaminated soil (Vengris et al. 2010, Gang et al. 2012). The electrode arrangement for group 2-E-2 and 2-E-3 can increase the electrical conductivity in the soil. In the reductive environment, the cadmium in the form of FeMnOx can be easily converted to the exchangeable cadmium, so the content in the soil is reduced. The content of organic cadmium in soil depends on the content of organic matter in the soil. Through comparing the three test groups, the decline rate of organic cadmium is small and relatively stable, and the organic cadmium region in the 2-E-3 group is evenly distributed, which is conducive to the release of Cd. With the increase of electrokinetic remediation time, the form of cadmium in the soil will gradually change from an unstable state to a stable state.

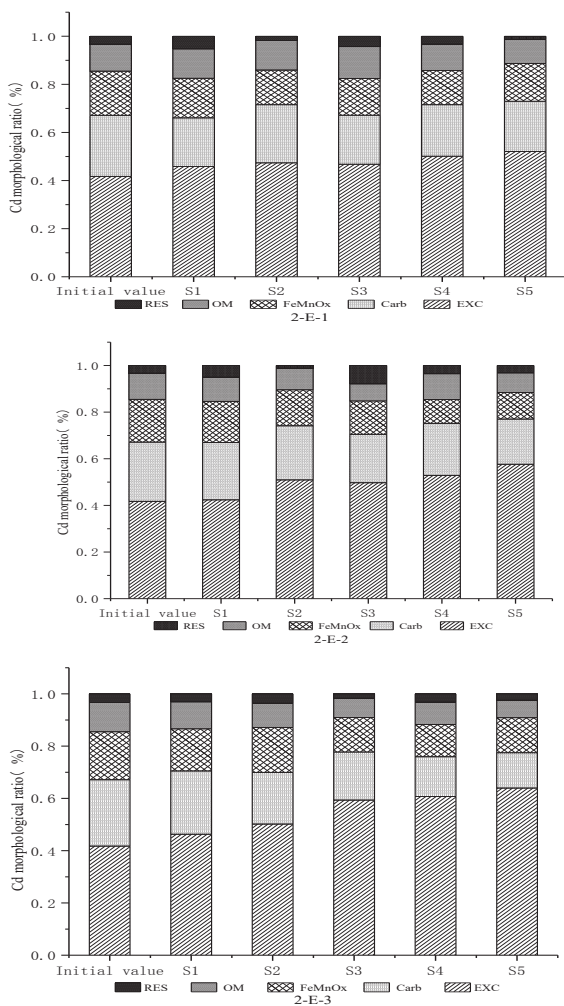


Fig. 7: Morphological distribution of cadmium at various sampling points in soil.

CONCLUSION

1. Through the comparison of three two-dimensional electrode arrangements, it was found that the hexagonal electrode arrangement (2-E-3) brought a large current drop rate, a weak alkaline environment. After electrokinetic remediation, the removal efficiency of cadmium at the sampling points (S1 and S2) near the anode was as high as 95.54%, and the removal rate of cadmium at each sampling point could be as high as 89.6%. Therefore, it is recommended to adopt a hexagonal arrangement of electrodes when removing Cd pollution in soil by electrokinetic remediation.
2. The Tessier five-step extraction method was adopted to divide the cadmium in soil into five forms after soil remediation. It was found that the cadmium in the form of FeMnOx and Carb was effectively removed. The content of exchangeable Cd near the cathode area was relatively high, and the content of cadmium in RES state was almost unchanged. Hexagonal electrode arrangement involved an even distribution of organic state (OM) cadmium, which is conducive to the release of Cd.

3. The practicality of two-dimensional hexagonal electrode arrangement was validated experimentally. With this electrode arrangement, the removal rate of pollutants uniformly is increased, so it has a good application prospect.

ACKNOWLEDGEMENT

This research was supported by the Postgraduate Research & Practice Innovation Program of Jiangsu Province, China.

REFERENCES

- Adikesavan, S. and Rajasekar, A. 2018. A statistical approach of zinc remediation using acidophilic bacterium via an integrated approach of bioleaching enhanced electrokinetic remediation (BEER) technology. *Chemosphere*, 207: 753-763.
- Amrate, S., Akretche, D.E., Innocent, C. and Seta, P. 2005. Removal of Pb from a calcareous soil during EDTA-enhanced electrokinetic extraction. *Science of the Total Environment*, 349: 56-66.
- Bahemmat, M., Farahbakhsh, M. and Kianirad, M. 2016. Humic substances-enhanced electroremediation of heavy metals contaminated soil. *Journal of Hazardous Materials*, 312: 307-318.
- Bes, C. and Mench, M. 2008. Remediation of copper-contaminated topsoils from a wood treatment facility using in situ stabilisation. *Environmental Pollution*, 156: 1128-1138.
- Cameselle, C. 2015. Enhancement of electro-osmotic flow during the electrokinetic treatment of a contaminated soil. *Electrochimica Acta*, 181: 31-38.
- Danmaliki, G.I., Saleh, T.A. and Shamsuddeen, A.A. 2017. Response surface methodology optimization of adsorptive desulfurization on nickel/activated carbon. *Chemical Engineering Journal*, 313: 993-1003.
- Fang, L., Fu, R.B. and Xu, Z. 2015. Optimization of electrode configuration in soil electrokinetic remediation. *Environmental Science*, 36: 678-680.
- Gang, L., Guo, S., Li S., Zhang, L. and Wang, S. 2012. Comparison of approaching and fixed anodes for avoiding the 'focusing' effect during electrokinetic remediation of chromium-contaminated soil. *Chemical Engineering Journal*, 203: 231-238.
- Ha, H., Olson, J.R., Bian L. and Rogerson, P.A. 2014. Analysis of heavy metal sources in soil using kriging interpolation on principal components. *Environmental Science & Technology*, 48: 4999-5007.
- Habibul, N., Hu, Y. and Sheng, G.P. 2016. Microbial fuel cell driving electrokinetic remediation of toxic metal contaminated soils. *Journal of Hazardous Materials*, 318: 9-14.
- Hu, P., Yang, B., Dong, C., Chen, L., Cao, X. and Zhao, J. 2014. Assessment of EDTA heap leaching of an agricultural soil highly contaminated with heavy metals. *Chemosphere*, 117: 532-537.
- Kim, D.H., Jo, S.U., Choi, J.H., Yang, J.S. and Baek, K. 2012. Hexagonal two dimensional electrokinetic systems for restoration of saline agricultural lands: A pilot study. *Chemical Engineering Journal*, 198: 110-121.
- Kim, W.S., Park, G.Y., Kim, D.H., Jung, H.B., Ko, S.H. and Baek, K. 2012. In situ field scale, electrokinetic remediation of multi-metals contaminated paddy soil: Influence of electrode configuration. *Electrochimica Acta*, 86: 89-95.
- Paramkusam, B.R., Srivastava, R.K. and Mohan, D. 2015. Electrokinetic removal of mixed heavy metals from a contaminated low permeable soil by surfactant and chelants. *Environmental Earth Sciences*, 73: 1191-1204.
- Turer, D. and Genc, A. 2005. Assessing effect of electrode configuration on the efficiency of electrokinetic remediation by sequential extraction analysis. *Journal of Hazardous Materials*, 119: 167-174.
- Vengris, T., Binkien, R. and Sveikauskait, A. 2010. Electrokinetic remediation of lead, zinc and cadmium contaminated soil. *Journal of Chemical Technology & Biotechnology*, 76: 1165-1170.
- Wang, G., Zhang, S., Zhong, Q., Xu, X., Li, T. and Jia, Y. 2018. Effect of soil washing with biodegradable chelators on the toxicity of residual metals and soil biological properties. *Science of the Total Environment*, 209: 776-782.
- Xu, Y., Xu, X., Hou, H., Zhang, J., Zhang, D. and Qian, G. 2016. Moisture content-affected electrokinetic remediation of Cr(VI)-contaminated clay by a hydrocalumite barrier. *Environmental Science & Pollution Research*, 23: 6517-6523.
- Yang, J.S., Kwon, M.J., Choi, J., Baek, K. and O'Loughlin, E.J. 2014. The transport behavior of As, Cu, Pb, and Zn during electrokinetic remediation of a contaminated soil using electrolyte conditioning. *Chemosphere*, 117: 79-86.
- Zhai, X., Li, Z., Huang, B., Luo, N., Huang, M. and Zhang, Q. 2018. Remediation of multiple heavy metal-contaminated soil through the combination of soil washing and in situ immobilization. *Science of the Total Environment*, 635: 92-99.



Electronic Waste Recycling Mode and Control Measures in China Based on PEST and SWOT

Linsheng Wang[†] and Wei Yang

College of Electronic Information Engineering, Henan Polytechnic Institute, Nanyang 473000, China

[†]Corresponding author: Linsheng Wang; wanglinsheng_317@163.com

Nat. Env. & Poll. Tech.
Website: www.neptjournal.com

Received: 28-09-2020

Revised: 18-11-2020

Accepted: 15-12-2020

Key Words:

E-waste
Recycling mode
Control measures
PEST
SWOT

ABSTRACT

The service life of electronic (e-) products is decreasing gradually due to the continuous improvement of manufacturing technologies and increasing prices and performance of these products, thereby accelerating the growth of e-waste. Only a small proportion of e-waste is disposed of according to standards in China. Due to a contradiction between high output and low disposal, environmental pollution and resource waste caused by e-waste intensify daily. To further analyze the e-waste recycling mode from a macroscopic level and thereby propose specific control measures, we first reviewed studies on e-waste recycling modes and control measures in foreign developed countries. Second, the e-waste recycling mode in China was analysed through political, economic, social and technological (PEST) and strengths, weaknesses, opportunities and threats (SWOT) models in combination with practical situations in China. Finally, e-waste control measures were proposed from various perspectives. Results show that the ambiguous definition of responsibilities for different e-waste disposal subjects in China has led to serious environmental pollution. This pollution, the extensive waste of natural resources, and frequent occurrence of social crises are three consequences of environmental pollution caused by e-waste in China. All four factors in the PEST model have laid the foundation to accelerate e-waste recycling in the country. Environmental pollution caused by e-waste can be relieved by perfecting relevant laws and regulations for e-waste recycling and disposal; establishing and perfecting the punitive system for e-waste recycling corporate responsibility; strengthening technological support, promotion, and education on e-waste recycling; and increasing the market supervision efforts and manufacturers' consciousness of responsibility. Research conclusions can provide important references to analyze e-waste status, achievements, challenges, and existing problems in disposal as well as their causes. These factors can also propose countermeasures and suggestions in e-waste disposal in accordance with practical situations in China based on insights into the experiences of foreign countries with a typical level of development.

INTRODUCTION

With the continuous development of information and manufacturing technologies, new electronic and electrical (e-) products that possess evident advantages in price, performance, and appearance are developed to replace the old ones. Moreover, the consumption concept and behaviour of the public change and the service life of e-products is shortened with the improvement of people's living standards, thereby accelerating the growth of e-waste. In China, only a small proportion of e-waste is disposed of in a standard manner. Environmental pollution and resource waste caused by e-waste have intensified daily because of the contradiction between high output and low disposal. Although China possesses a vast territory and rich mineral resources, per-capita resource availability in the country is much lower than the world average because of China's large population base. Thus, resource shortage has become a great challenge to sustainable economic development in China.

The contradiction between resource waste and resource shortage is increasingly prominent. During classification, melting, and extraction of e-waste, a large amount of toxic substances such as lead, mercury, and cadmium are released into air, land, and water, thereby causing secondary pollution. If e-waste is not decomposed properly, then radioactive and heavy metal elements in electronics may be leaked and may cause serious environmental pollution. Moreover, traditional landfill or combustion of e-waste without remaining value may also cause damage to the soil and other environments.

With improving economic levels, increasing material demands of consumers, and the accelerating rate of urbanization in China (Fig. 1), electronic products have become popular quickly and annual consumption of electronics is increasing significantly. Meanwhile, the quantity of obsolete electronics is also growing. E-waste consists of discarded mobile phones, computers, and e-accessories in household waste. With respect to disposal

in China, most types of e-waste recycled by non-professional enterprises are only cleaned, repaired, or assembled, and then resold to secondary markets or underdeveloped areas. Alternatively, precious metals in e-waste are extracted through low-technology and high-pollution methods, such as acid leaching and combustion. Both these disposal methods can bring serious damage to the environment. In recent years, China has achieved progress in e-waste recycling. However, faced with increasing problems in e-waste recycling, the country cannot accomplish e-waste recycling simply by depending on the government or restricting the activities of manufacturers. Thus, understanding the serious environmental pollution caused by e-waste and proposing an e-waste recycling mode that effectively conforms to the economic and social development status of China to address environmental pollution and ecological damage caused by e-waste.

PAST STUDIES

With the rapid economic development and continuous improvement of people's living standards, e-products have entered the consumption market quickly and e-waste has caused serious environmental pollution. Foreign developed countries have conducted many studies on e-waste recycling mode and control measures. Most of these studies have focused on theoretical aspects of extended responsibility of manufacturers, e-waste recycling and disposal system, and e-waste disposal costs and benefits, which have gained abundant research achievements. Major studies on e-waste recycling mode and control measures are introduced as

follows. Liu et al. investigated progress in policies for old household appliance recycling and disposal in China and found that capital flow and logistics in old household appliance management had unique features. Specifically, nearly 60% of household appliance waste was sold to individual recyclers and finally treated illegally, which brought serious environmental pollution (Liu et al. 2006). Allenby et al. conducted a comparative study on e-waste recycling management institutions and systems in Japan, Europe, Taiwan, Korea, and other countries and regions; they concluded that a relevant incentive system had to be established based on laws to solve e-waste recycling problems in the United States (Allenby et al. 2008). Lu et al. discussed China's e-waste recycling management system thoroughly, finding that legal e-waste recycling and disposal enterprises were unable to compete with ubiquitous illegal enterprises if they failed to lower recycling costs through all means (Lu et al. 2008). Cheung et al. investigated Guiyu County, China, a village witnessing intensive e-waste disposal. Recycling of printed circuit boards (PCBs) in Guiyu County might cause considerable risks to the environment and human health. According to research results, recycling lead and copper in PCBs could cause serious health risks to local workers and residents, especially children (Cheung et al. 2008). Ru et al. believed that the quantity of e-waste was increasing quickly in China; however, China had neither established a corresponding recycling and disposal system nor provided appropriate administrative supervision. The researchers also pointed out several challenges encountered in the implementation of new relevant laws and regulations and proposed feasible suggestions (Ru et al. 2010). Chen et

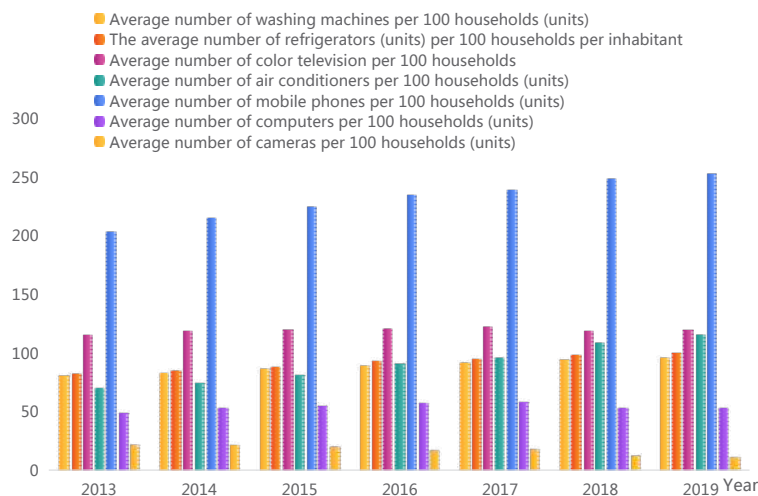


Fig. 1: Number of major electronic products owned per 100 households in China, 2013-2019.

al. investigated e-waste recycling and contents of brominated flame retardants (BFRs) in urban dust in South China, finding serious environmental degradation in the study area (Chen et al. 2010). Halluete et al. argued that strict laws and regulations can require manufacturers to recycle products at disposal and great secondary environmental pollution related to waste storage might occur unless the affected products had stable designs and inputs simultaneously. In particular, many e-products had harmful substances that might cause serious problems if left unrecycled (Halluete et al. 2012). Atasu et al. identified the stakeholders of e-waste recycling in Washington, which included e-recyclers, consumers, management organizations, local government and system renovation providers; the researchers stated the need to formulate comprehensive policies to control e-waste pollution (Atasu et al. 2013). Covaci et al. believed that large-scale e-waste has been produced worldwide due to the rapid development of the electronic industry; they investigated the existence of organo-phosphorous flame retardant and plasticizers (PFRs) in several wild insects collected from e-waste recycling areas in Guangdong Province, and found that e-waste recycling area might be an important local pollution source (Covaci et al. 2018). Tian et al. pointed out that China, the largest e-waste producer in the world, was facing a great challenge in how to control the negative effects of e-waste on the environment; they concluded that e-waste management was crucial to sustainable economic development in China. Moreover, the effects of contracts signed by the manufacturers on different retail modes were discussed (Tian et al. 2018). Chen et al. investigated several soil samples from Guiyu county, an e-waste recycling town in southeast China and concluded that e-waste recycling caused significantly serious soil damages (Chen et al. 2018). Mor et al. believed that the boom in the e-industry and acceleration of technological progress brought large number of waste electronic and electrical equipment. They investigated the production and various control means of e-waste in Chandigarh, India. According to the questionnaire survey results, only 30% of respondents were aware of e-waste and their environmental influences. The average annual output of e-waste per household in Chandigarh, India amounted to 17 kg and the annual output reached 4,100 t, causing severe environmental pollutions (Mor et al. 2019). Bernardes et al. discussed e-waste management based on the Australian recycling plan and found that waste computers were the sole type of equipment with sufficient internal values and could be recycled in China without any external subsidy; the researchers also analysed the importance of subsidies, rules and regulations, and supervision in e-waste recycling (Bernardes et al. 2019). Lang et al. evaluated emission reduction benefits and efficiency of e-waste

recycling in China by using the directional distance function of DEA. Results showed that the total emission reduction benefits of e-waste in 29 Chinese provinces amounted to 6.34 billion yuan, and considerable potential remains in emission reduction in e-waste recycling (Lang et al. 2019). Aboelmaged studied the decisive factors in young consumers' intention toward e-waste recycling in the emerging economic environment and found that recycling habits and perceived attitudes were important influencing factors in the e-waste recycling intention of young people (Aboelmaged 2020). According to Chinese and foreign studies on e-waste disposal, foreign theories, including legislation and establishment of theoretical models, are reliable and the extended responsibility system of manufacturers has been implemented to define e-waste disposal responsibilities. Such an extended responsibility system for manufacturers shows a stage of large-scale promotion. However, the responsibilities of e-waste disposal subjects have not been defined in China due to special national conditions. Moreover, attitudes and measures implemented by the government, enterprises, social organizations, and individuals in e-waste disposal have not been determined yet. Studies on the role of different subjects in e-waste disposal are also insufficient. As a result, the status of e-waste recycling in China was analysed through a combination of political, economic, social, and technological (PEST) factors and strengths, weaknesses, opportunities, and threats (SWOT), and specific e-waste control measures were proposed. Research conclusions can provide important references to establish and make high-efficiency operation of a perfect e-waste disposal system, thereby relieving environmental pollution and resource waste.

E-WASTE POLLUTION HAZARDS IN CHINA

Serious Environmental Pollution

E-waste has complex chemical compositions. It contains a large amount of toxic and harmful substances that can pollute soil, water, animals, and plants once they are leaked to the natural environment with the direct disposal of e-waste. Abundant heavy metals and toxic chemical substances enter into animals and plants through the soil and water, which further causes death or mutation of these organisms. Human beings may suffer dysgenesis, chronic diseases, and cancer due to long-term exposure to such environments, or from consuming polluted water, animal meat, and plant products. The environmental hazards of e-waste can be classified into long-term and latent ones. The degradation rate of high-technology artefacts formed by complex processing is low in nature because the artificial synthesis of many chemical substances is beyond the capability of natural degradation. The ecological environmental deterioration

caused by overflowing e-waste and long-term accumulation of toxins in the human body may generate multiplier effects. Furthermore, most e-waste is generated in large and medium-sized cities in China but are basically transferred to remote towns and villages with weak supervision in processing. Although this approach solves the problem of garbage siege, it can intensify the exposure to e-waste and aggravate the damage to the local environment, thereby causing greater difficulty and cost of e-waste control.

Extensive Waste of Natural Resource

At present, the e-waste disposal and processing techniques in China are underdeveloped, as manifested by the prevalence of unreasonable and non-scientific disposal techniques, small-scale processing, serious environmental pollution, and low-recovery efficiency of valuable heavy metals. Processing technologies and equipment of large enterprises are mainly imported from Western developed countries, which restricts their development due to limitations in capital and technology. China is a country with a relative resource shortage, and its long-term extensive economic development leads to relatively low utilization of resources and considerable resource waste. The resource constraint in China has intensified gradually and the contradiction with non-sustainable economic development has become increasingly prominent in recent years. Thus, promoting industrial transformation and updating and adjusting industrial structures is necessary. E-waste can be disposed of in two ways. One is through disassembly and reassembly, which involves great potential safety hazards. This type of disposal is generally performed illegally and accounts for an extremely small proportion of the total e-waste. The other is by extracting valuable resources by disassembling e-waste artificially with original tools, open burning, or direct acid leaching in open recycling areas, while the remaining parts are abandoned randomly in fields, rivers, and channels as garbage, or mixed with municipal waste. Both simple and extensive disposal methods have caused a great waste of natural resources.

Frequent Occurrence of Social Crises

Continuous renovation of e-products also causes social problems while enriching and facilitating human life. The memory function of e-products may cause information safety risks. For example, personal privacy information and even confidential information of enterprises and governments might be disclosed as a result of improper disposal of waste computer disks, memory cards of cameras, and mobile phones. On the one hand, the ecological environmental damage caused by e-waste pollution can influence the physical health and life quality of citizens to various extents, and infringe on people's right to live in a healthy environment.

On the other hand, e-waste pollution hazards have long-term potential characteristics. Thus, increasing the priority of e-waste disposal in the public policy agenda and formulating countermeasures and taking corresponding timely action is necessary. On the contrary, e-waste pollution is likely to cause a social crisis directly and bring immeasurable losses if it becomes a prominent public hazard.

ANALYSIS OF E-WASTE RECYCLING MODE BASED ON PEST AND SWOT

PEST Analysis

Political factors: China has to take the initiative in supporting the development of new recycling modes, including intelligent recycling and automatic recycling machines by exploring the "Internet + recycling" mode and path; insisting on green and sustainable development; pursuing the civilized development of production-oriented public welfare and good ecology; accelerating the construction of a resource-saving and environmentally friendly society, and forming a modernized construction pattern of harmonious development between humans and nature.

Economic factors: A recycling-based society is an economic mode that emphasizes the harmonious development between humans and nature. It is a development that not only can meet the contemporary demands of people but also causes no harm to the life of offspring. Social and economic resources on earth are limited. People have to focus on high-efficiency use and recycling of resources. Traditional development is achieved at the expense of resource consumption and resources can only be wasted after use. Recycling economic development is an update of resource recycling technology and equipment. It changes the traditional development mode of "resource-product-waste" and establishes a recycling economic development mode of "resource-product-waste-renewable resource".

Social factors: Citizens' environmental consciousness and awareness of social responsibility in e-waste recycling have been enhanced gradually. The environmental protection industry is highly recognized in public. These conditions have brought a good opportunity for the development of the "Internet + recycling" industry. The growing consciousness of environmental protection and understanding of e-waste pollution also promotes the comprehensive implementation of e-waste recycling modes.

Technological factors: At present, four major recycling modes for e-waste are used in China. First, the repair departments of manufacturers and waste recycling stations repair, renovate, and refit e-waste and then relaunch the products on the market for secondary consumers. Second,

disassembly workshops recycle e-waste and collect metal materials, especially precious and rare metals, through simple means for secondary marketing. Third, e-waste is sold to households in rural and poverty-stricken areas through donation or market circulation of used home appliances. Fourth, e-waste is landfilled with household waste directly. At present, e-waste output is considerable, but only a small proportion of it is recycled through standard channels. As the aforementioned four recycling modes have low technological and equipment levels and low utilization of high-quality renewable resources, e-waste causes great resource wastage and serious environmental pollution.

SWOT Analysis

Strengths: The development philosophy of the e-waste recycling industry conforms to the national development strategy. The government aims to develop a green economy as well as establish a green system and culture so that the public can benefit from green dividends. The market bidding mode based on consumer-to-business processes can help e-waste owners select the best buyer, connect the upstream and downstream of the industrial chain through timely locking, fast transaction, Internet, big data, and Internet of Things (IoT). In this manner, e-waste owners make decisions on disposal and resource value can be maximized. Based on big data analysis, idle logistics staff can be mined and matched effectively and the best transport channel can be recognized accurately the first time, thereby effectively optimizing the logistics path, decreasing the logistics marginal cost of merchants, and increasing the social employment rate. Massive information sharing is achieved and the problems of information asymmetry and few disposal channels faced by e-waste owners are solved through online registration and offline setting of fixed recycling stations. This approach increases circulation and values in the effective use of resources.

Weakness: In the early stage of “Internet + recycling,” the business model of the industry was hardly accepted by merchants. Moreover, e-waste owners might not believe in this model. Thus, promoting “Internet + recycling” and establishing cooperation with merchants is a great challenge. “Internet + recycling,” which uses big data, cloud computing, and IoT as the core technologies propose high requirements on the operation mode and technical personnel. It faces certain challenges in attracting talent and technological support. Information disclosure is an important problem. Many people prefer to keep their e-waste to themselves for fear of privacy exposure and even reject the “Internet + recycling” mode due to the lack of security in certain platforms.

Opportunity: The “Internet + recycling” approach is developing and penetrating into traditional industries. “Internet

+ recycling” has unique innovations and features compared with existing e-waste recycling platforms. It provides more convenient and intelligent services to both suppliers and customers and achieves a seamless connection between on-line and offline resources. With the rapid popularization of household appliances and digital products, product updates are accelerated and e-waste in daily life increases accordingly. In recent years, the low-carbon lifestyle has become increasingly popular and the educational background of people has improved, thereby strengthening citizen’s awareness of environmental protection to a certain extent. Big data and cloud computing technologies have developed rapidly and have been applied to daily life gradually. New technologies have awakened people’s curiosity and motivated them to continuously try them.

Threat: The development of a secondary recycling platform has entered a relatively stable stage. It owns a relatively mature operation mode and stable customer sources. However, most recycling platforms in China are new and inevitably affected by competitors. With the increasing attention to national policies and citizens’ awareness of environmental protection and resource recycling as well as the rapid development of the Internet industry, the industrial development of the e-waste recycling market has considerable potential. This development is accompanied by a strong influx of competitors.

E-WASTE CONTROL MEASURES

Perfecting Laws and Regulations on E-Waste Recycling and Disposal

E-waste control by law is a fundamental guarantee of effective e-waste recycling and an essential way to ensure waste resource recycling. Thus, establishing and perfecting relevant laws and regulations is an essential approach to manage e-waste recycling, standardize e-waste disposal, determine the responsibilities of all parties, constrain their behaviours, and finally ensure environmental protection, resource recycling, and sustainable development. The government of China at all levels has to face up to problems in e-waste recycling, analyze the causes of these problems thoroughly, establish and integrate waste recycling systems, and determine the overall framework of e-waste recycling.

Establishing and A Punitive System for E-Waste Recycling Corporate Responsibility

With regard to the legal, regulatory and management systems for e-waste recycling and disposal in Germany and other countries in the European Union, China aims to analyze their experiences carefully and establish relevant legal

systems according to practical situations. On the one hand, China's existing laws and regulations on e-waste recycling and disposal are mainly guidelines rather than normative documents, thereby resulting in inadequate deterrence and law enforcement as well as great difficulties in practical implementation. On the other hand, existing laws and regulations on the responsibilities of e-waste recycling are mainly in a scattered and coarse state. A suggested approach is to determine the responsibilities and duties of all parties according to legislation, determining economic incentives and punishment measures, enlisting e-waste recycling responsibilities in law-based management, and creating a good legal environment for all parties to participate in e-waste recycling positively. The problem of responsibility in e-waste recycling can be solved as long as a complete legal and regulatory system is established and perfected, thereby paving the way for follow-up responsibility practices in e-waste recycling.

Strengthening Technological Support and Promotion and Education for E-Waste Recycling

Technological support will be strengthened. E-waste recycling technologies will be evaluated in terms of environmental protection and economic efficiency. Accurate evaluations of e-waste collection, recycling, and disposal efficiencies, as well as the relevant costs or benefits, are used as the reference to improve recycling and disposal technologies. Meanwhile, the supporting information management system is established and an e-waste information platform is built to realize communication and sharing of information resources among various departments. As consumers play an important role in e-waste recycling, publicity and education are extremely important. Assisted by the Ministry of Education and the media, the government will educate the public about hazards brought by incorrect disposal of e-waste. The risks posed by e-waste to the environment and human health as well as the significance of e-waste recycling, teaching the public about e-waste recycling and harmless disposal, increasing the environmental protection consciousness of the entire society, and forming a good atmosphere for economic development. Special training on e-waste recycling will be conducted, disassembly and disposal enterprises are expected to increase the consciousness of enterprises in environmental protection through laws, and businesses will be guided toward continually improving their disposal technologies and environmental management levels.

Increasing Market Supervision Efforts and Manufacturers' Consciousness of Responsibility

Environmental protection departments in China at all levels will (1) strengthen mutual communication, increase

supervision and safety monitoring means, and enhance supervision over law enforcement in the e-waste recycling industry; (2) establish an examination and verification system for e-waste disposal enterprises, insist on eliminating and banning backward disposal facilities and abilities with serious pollution, suspend facilities with e-waste handling capacity that is much less than the declared capacity unless the desired handling capacity is reached; and (3) strengthen supervision and examination in regions with prominent e-waste environmental pollution, and impose a penalty on enterprises for falsification, environmental pollution, and violations against laws and regulations, as well as restrict the participation of these enterprises in relevant e-waste disposal activities for a certain period. Manufacturers are asked to assume corresponding responsibilities in e-waste recycling and establish internal management files for e-waste during the production process. E-product manufacturers are encouraged to set up a recycling and disposal system or authorize a qualified unit for disassembly if they cannot perform these tasks.

CONCLUSIONS

waste can bring serious damage to soil, water sources, air, and human health. With the massive growth of the e-industry and progress of e-technologies, a great deal of e-products are consumed every year. E-waste, such as battery and heavy metals, causes various environmental damage on non-standard recycling and disposal although the industry brings considerable profits to the state. In this study, research on e-waste recycling modes and control measures in foreign developed countries were first reviewed. Second, the e-waste recycling mode in China was analysed through the PEST and SWOT models by combining practical situations in the country. Third, e-waste control measures were proposed from various perspectives. Results show that environmental pollution caused by e-waste in China were manifested in three aspects, such as serious ecological environmental pollution, considerable natural resource waste, and frequent occurrence of social crises. The PEST and SWOT models conformed to the characteristics of macroscopic management in China. Both the PEST and SWOT analysis results showed that the e-waste recycling mode in China was equipped with a good policy space. Finally, specific e-waste control measures were proposed, including perfecting laws and regulations on recycling and disposal; establishing a punitive system for e-waste recycling corporate responsibility; strengthening technological support, promotion, and education related to e-waste recycling; and increasing the market supervision efforts and manufacturers' consciousness of responsibility. Further studies on intelligent e-waste control based on the cooperation game model among the government,

manufacturing enterprises, and third-party professional recycling enterprises; measurement of influencing factors in consumers' intention to recycle e-waste; as well as incentive policies for recycling enterprises, cloud computing, and big data can be conducted in the future.

ACKNOWLEDGMENT

This work was supported by the Young Core Teacher Training Plan of Henan Provincial Higher Vocational School (2019GZGG018) and the 2019 Young Core Teacher Training Plan of Henan Industrial Vocational and Technical College.

REFERENCES

- Aboelimged, M. 2021. E-waste recycling behaviour: An integration of recycling habits into the theory of planned behaviour. *Journal of Cleaner Production*, 278: 124182.
- Allenby, B., Williams, E., Kim, J., Kahhat, R., Ming, X. and Peng, Z. 2008. Exploring e-waste management systems in the United States. *Resources Conservation & Recycling*, 52(7): 955-964.
- Atasu, A., Gui, L., Özlem Ergun and Toktay, L.B. 2013. Implementing extended producer responsibility legislation: a multi-stakeholder case analysis. *Journal of Industrial Ecology*, 17(2): 262-276.
- Bernardes, A. M., Dias, P. and Huda, N. 2019. Ensuring best e-waste recycling practices in developed countries: An Australian example. *Journal of Cleaner Production*, 209(1): 846-854.
- Chen, S. J., Luo, X., Mai, B., Ma, Y. J., Tian, M. and Wang, J. 2010. Brominated flame retardants in house dust from e-waste recycling and urban areas in South China: Implications on human exposure. *Environment International*, 36(6): 535-541.
- Chen, X. W., Deng, W. J., Giesy, J. P., Li, N. and Zheng, H. L. 2018. PBDEs and Dechlorane Plus in the environment of Guiyu, Southeast China: A historical location for E-waste recycling (2004, 2014). *Chemosphere*, 199(May): 603-611.
- Cheung, K. C., Duzgoren-Aydin, N. S., Leung, A. O. W. and Wong, M. H. 2008. Heavy metals concentrations of surface dust from e-waste recycling and its human health implications in southeast China. *Environmental Science & Technology*, 42(7): 2674-80.
- Covaci, A., Tang, B., Poma, G., Cuykx, M., Luo, X. J. and Liu, Y. 2018. Occurrence of organophosphorus flame retardants and plasticizers in wild insects from a former e-waste recycling site in the Guangdong province, South China. *The Science of the Total Environment*, 650(1): 709-712.
- Hallite, J. A., Linton, J. D. B. E., Yeomans, J. S. C. and Yoogalingam, R. 2012. The challenge of hazardous waste management in a sustainable environment: Insights from electronic recovery laws. *Eco-Management and Auditing*, 12(1): 31-37.
- Lang, H., Qin, Y., Xu, M., Han, Y., Ye, W. and Zhang, S. 2019. Emission reduction benefits and efficiency of e-waste recycling in China. *Waste Management*, 102: 541-549.
- Liu, Matsui, Y. X. and Tanaka, M. 2006. Electrical and electronic waste management in China: Progress and the barriers to overcome. *Waste Management & Research Journal of the International Solid Wastes & Public Cleansing Association Iswa*, 24(1): 92-101.
- Lu, B., Xu, C. and Yang, J. 2008. WEEE flow and mitigating measures in China - Science Direct. *Waste Management*, 28(9): 1589-1597.
- Mor, S. and Ravindra, K. 2019. E-waste generation and management practices in Chandigarh, India and economic evaluation for sustainable recycling. *Journal of Cleaner Production*, 221(June 1): 286-294.
- Ru, Y. H., Veenstra, A., Wang, R.J., Wang, Y. and Wang, Y. C. 2010. Recent developments in waste electrical and electronics equipment legislation in China. *International Journal of Advanced Manufacturing Technology*, 47(5): 437-448.
- Tian, F., Xue, R. and Zhang, F. 2018. A system dynamics model to evaluate effects of retailer-led recycling based on dual chains competition: A case of e-waste in China. *Sustainability*, 10(10): 3391.



Survey of Environmental Baseline in the Nunukan Agriculture Area, Indonesia

Ramdiana Muis*†, Nani Angraini**, Fitri Ariani***, Sattar Yunus**** and Zulkifli*****

*Department of Urban and Regional Development, Universitas Muhammadiyah, Pare-Pare, 91131, Indonesia

**Department of Environmental Engineering, Universitas Bosowa. Makassar, 90231, Indonesia

***Department of Chemical Engineering, Universitas Bosowa. Makassar, 90231, Indonesia

****Department of Mechanical Engineering, Universitas Muslim Indonesia, Makassar, 90231, Indonesia

*****Department of Agriculture, Universitas Muslim Maros, Maros, 90511, Indonesia

†Corresponding author: Ramdiana Muis; ramdiana.uts@gmail.com

Nat. Env. & Poll. Tech.

Website: www.neptjournal.com

Received: 29-03-2020

Revised: 28-04-2020

Accepted: 21-06-2020

Key Words:

Environmental baseline

Water quality

Air quality

Soil quality

Agriculture area

Nunukan Regency

ABSTRACT

South Nunukan District has a complex ecosystem which has the river, terrestrial, coastal and oceanic ecosystems, and has been demarcated by the Government of The Nunukan Regency for agricultural purposes. This research was conducted to determine the preliminary environmental baseline of agricultural activities that have been and will take place in this region. Methods of measuring environmental quality were carried out by (1) measuring water quality by taking water samples at four locations and tested in a laboratory; and also measuring aquatic biota by taking samples in rivers and testing at a laboratory, (2) measuring air quality at three sample locations using an air quality meter, and noise using a sound level meter, (3) measuring soil quality by taking five samples at the study site and conducting soil quality testing in the laboratory. The result of this study concluded that this area is suitable to be used as an agriculture and plantation area by adding various engineering technologies and fertilizing. This is supported by the results of water, air, noise and soil quality tests from several samples showing the average within and below the permissible limit (WPL and BPL). For a small number of parameters that do not meet quality standards (APL), environmental engineering efforts need to be done.

INTRODUCTION

The progressive development of cities in the world including the Industrial Acceleration in the last two decades has brought many impacts on the environment, which are caused by pollution in water, soil and air that in turn can disturb human health (World Health Organization 2002, Sattar et al. 2012, Rashid et al. 2014).

Indonesia is an archipelagic country and Nunukan island is one of the islands located in the Kalimantan region. Based on the Spatial Plan of the Nunukan Regency 2013-2033, the South Nunukan District is intended for agriculture and plantation areas. To support these objectives, environmental conditions that are appropriate for their purpose are needed. South Nunukan District is geographically affected by river ecosystems (Tanjung Harapan River), terrestrial, coastal and oceanic ecosystems so that this region has complex conditions.

As an area designated for food storage, water is a vital part because it is a basic need for irrigation and other agricultural needs (Kumari et al. 2009). The rise of population, modern agriculture, and industrialization can put gigantic pressure

on freshwater bodies, causing a threat to mankind's healthy existence (Karne et al. 2009). To reduce the environmental damage caused by development, preliminary studies are needed to see the baseline environment, this is aimed at realizing sustainable development (Sari et al. 2014).

This study has been conducted to evaluate environmental parameters in water, air and soil. Furthermore, water quality has been measured in several areas such as a river, reservoir, surface water and groundwater around South Nunukan District. The assessment of water quality can support the function of the land. By using water variable, this study measures the physicochemical and biological characteristics of the water body and groundwater as study areas and compare them to The Indonesian Government Regulation Number: 82 of 2001, concerning Water Quality Management, Control and Diversity Index of Shannon-Wiener.

Also, measurements of air quality and noise were carried out around South Nunukan District where most of the cities in Indonesia have been reported for particulate air pollution and give an impact on the environment (Sattar et al. 2014, Saini et al. 2018, Sattar et al. 2019). Finally, soil quality was also analysed to determine soil fertility in the study area.

MATERIALS AND METHODS

Study Area Description

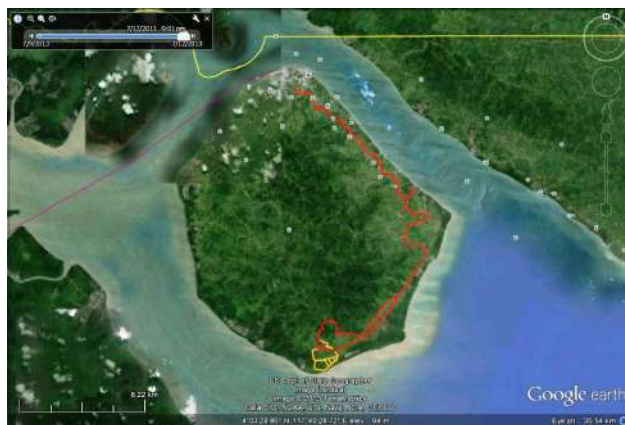
The population of South Nunukan District in 2018 was 26,827 occupying an area of 174.4 km². Population growth that occurred as a result of the development was almost evenly distributed in each district so that it attracted newcomers to live and settle in South Nunukan subdistrict. The opening of employment in the plantation sector, especially oil palm and the wood processing industry and the service sector was another reason why more people feel attracted to move and live here (BPS-Statistics of Nunukam Regency 2016).

The South Nunukan district is located around the catchment of the Tanjung Harapan River in Nunukan Island and situated on the edge of the southern coast (117°40'34.39" E, 3°58'25.36" N). This area was planned as an integrated agricultural production zone. This land is called transitional swampland or tidal swamp where the strength of tidal currents from the sea is slightly greater or equal to the strength of currents from the headwaters of the river. Fig. 1 shows the location of the island.

Sampling Methods

The sampling sites are shown in Fig. 1. The samples were collected at four areas including river, groundwater, surface water and reservoir water in the South Nunukan District in plastic bottles before rinsing them with the sample water. The water samples were then brought to the laboratory for physicochemical quality and biological parameters testing. The methods follow The Indonesian Government Regulation Number: 82 of 2001, concerning Water Quality Management and Control.

Biological measurement was done using the indicator of aquatic biota (Holt & Miller 2010). Plankton was sampled



(Source: Google Earth, 2020)

Fig. 1: The location map.

using a plankton net by filtering 100 litres of water. Then, it was stored in 10 mL plankton bottles and preserved with 4% formalin solution to be observed in the laboratory. The plankton was separated into phytoplankton and zooplankton groups, to determine the diversity of species and their abundance. Plankton's determination was made by using the key of plankton determination made by Shirota (1966).

For air quality measurements, samples were taken from 3 locations and the measurement was made at the site using an ambient gas sampler (Impinger Model: MD-51MP), while measurement of noise levels at locations using a sound level meter.

To determine the level of soil fertility in the study area, identification and analysis of the physical (sand, dust and clay) and chemical properties of the soil were carried out through soil analysis, i.e. pH, C, N, C/N, P₂O₅, Ca, Mg, K, Na, KTK and BK. The soil samples were taken from 5 locations and brought to the laboratory for analysis with reference to the guidelines of soil analysis (BPN-Institute of Soil Research 2003).

RESULTS AND DISCUSSION

Water Quality

The results of the study for all parameters are given in Table 1. Based on various physicochemical parameters, each water sample was classified into within permissible limits (WPL), below permissible limits (BPL) and above permissible limits (APL).

The Total Dissolved Solids (TDS) is defined as the total amount of the solid material dissolved in water containing salts, dangerous metals and other materials in water. The results of the analysis of TDS in Sample 4 (S4) are higher than those of Sample 1, Sample 2 and Sample 3. The order of TDS concentration found at the sampling site was S4 > S1 > S3 > S2, even the concentrations in S4 and S1 exceed the permissible limit (1000 mg/L). The results of these measurements indicate that the river water in the planned location of the activity has been polluted. The sulphates showed the highest concentration at S4 (489,881 mg/L) which exceeds the permissible limit (400 mg/L), while S1, S2 and S3 have still below the permissible limit. The dissolved oxygen (DO) exceeds the permissible limit (> 6 mg/L) at all the 4 sample locations, while the total phosphorus as P was only present at S1 which exceeds the permissible limit (0.2 mg/L) with a concentration value of 0.872 mg/L. The concentration of P at S1, S2 and S3 were not below the detection limit.

The measurement of water quality in Table 1 shows that the Dissolved Oxygen (DO), Cl, and sulphate parameters are high, but these values are considered to still meet the class

Table 1: The physicochemical, dissolved metal and microbiological parameters of 4 water samples in the South Nunukan District.

Physic Parameters	S1	S2	S3	S4	PL
Temperature	28	28	28	28	
TDS	1350 (-)	144	296	5628 (-)	1000
TSS	23.6	10.8	13.2	4	50
Dissolved Metal Parameters	S1	S2	S3	S4	
As	-	-	-	-	0.05
Co	-	-	-	-	0.2
Ba	-	-	-	-	1
Br	-	-	-	-	1
Se	-	-	-	-	0.01
Cd	< 0.0003	< 0.0003	< 0.0003	< 0.0003	0.01
Cr ⁶⁺	0	0	0	0	0.05
Cu	< 0.0001	< 0.0001	0,0066	0.0066	0.02
Fe	0.463 (-)	0.015	0.118	0.041	0.3
Pb	< 0.0074	< 0.0074	< 0.0074	< 0.0074	0.03
Mn	< 0.0001	< 0.0001	< 0.0001	< 0.0001	0.1
hg	-	-	-	-	0.001
Zn	< 0.0001	< 0.0001	< 0.0001	< 0.0001	0.05
Cl	547.836 (-)	15.762 (-)	15.762 (-)	102.24 (-)	600
CN	-	-	-	-	0.02
Fluoride	-	-	-	-	0.5
NO ₂ as N	0	0	0	0	0.06
Sulphate	51.079 (-)	19.693 (-)	74.644 (-)	489.881 (-)	400
Cl ₂	0	0	0	0	0.03
H ₂ S	0	0	0	0	0.002
Microbiological Parameters	S1	S2	S3	S4	
Coliform	93	23	32	14	1000
Chemical Parameters	S1	S2	S3	S4	
pH	7.29	6.94	7.02	7.09	6.0-9.0
BOD	1.044	0.959	0,98	0.928	<2
COD	5.493	5.049	5.16	4.882	<10
DO	6.972 (-)	7.049 (-)	6.962 (-)	7.418 (-)	>6
Total Phosphate as P	0.872 (-)	0	0	0	0.2
NH ₃ -N	0.097	0	0.436	0.989	10

*Where: (-)= Above permissible limits, - = Not Analysed; 0 = Not detected

*Where: S1-River Water, S2-Groundwater, S3-Surface Water, S4-Reservoir Water, PL-Permissible Limit

I water criteria based on Government Regulation Number 82 Year 2001, concerning Water Quality Management and Control Water Pollution.

The phosphate (P) is above the permissible limit at the S1 (river water) test location, this shows the occurrence of river pollution by agricultural fertilizers entering the river water through drainage and rainwater flow. This causes high growth of algae in river water (eutrophic condition) which

will cause the reduction of dissolved oxygen endangering the river water ecosystem. Table 2 gives the range of plankton diversity index which is 1.32, this value shows that the quality of river waters is in the moderate polluted category. The uniformity and dominance index show stable conditions and there is no type of plankton domination.

According to Wilhm (1975), based on the zoobenthos diversity index, water quality can be categorized as heavily

Table 2: The phytoplankton of Tanjung Harapan river samples in the South Nunukan District.

Phytoplankton	Result (ind/m ³)	Benthos	Result (ind/m ³)
<i>Asterionella</i> sp.	166	<i>Corbicula</i>	95
<i>Skeletonema</i> sp.	166	<i>Melanooides</i> sp.	31
<i>Chaetoceros</i> sp.	333	<i>Pilsbryconcha</i> sp.	31
Zooplankton			
<i>Moina</i> sp.	166		
Plankton		Makrozoobenthos	
Total Abundance	831 (ind/m ³)	Total Abundance	157 (ind/m ³)
Number of types	4 types	Number of types	3 types
Diversity Index	1.32	Diversity Index	0.94
Uniform Index	0.96	Uniform Index	0.85
Dominance Index	0.28	Dominance Index	0.56

*Where: (-) Above permissible limits

polluted ($0 < H' < 1$), moderate polluted ($1 < H' < 2$), lightly polluted ($2 < H' < 3$) and is very lightly polluted ($3 < H' < 4.5$). The range of H' values is part of an assessment of water quality with the physical chemistry of water. Lee et al. (1978) stated that the diversity index value (H') in heavily polluted waters, smaller than one ($H' < 1$), moderately polluted (1.0-1.5), lightly polluted (1.6-2.0), and not contaminated by a large H of two ($H > 2.0$). The category of water quality and pollution level based on Shannon-Weiner's macrozoobenthos diversity index are divided into four groups, as given in Table 3.

The macrozoobenthos community of the three river water stations has a density of a range of 157 individuals/m³, 3 types of macrozoobenthos which belong to 2 groups, including *Bilvalvia*, 2 types namely *Corbicula* sp. and *Pilsbryconcha* sp., Gastropod Class 1 types namely *Melanooides* sp.

The results of the diversity index analysis show that the waters of the river have been heavily polluted, the range of diversity index is < 1 , as well as the index of uniformity, the range of 0.85 indicates the individual distribution of each species in heavy and unstable conditions, while the level of dominance index tends to be high at 0.56 shows that some types dominate abundance or that each individual cannot

Table 3: Pollution rate classification (Lee 1978).

Shannon Index	Water Quality	Pollutant Category
<1	Slight	Heavy Pollution
>1-2	Light	Moderate Pollution
>2-3	Moderate	Light Pollution
>3-4.5	Good	Moderate Pollution/ Not Polluted
>4.5	Heavy	Not Polluted

utilize resources optimally. It seems that there are more abundant species than other types.

Air Quality

Based on the results of the measurement of air quality using the Indonesian Standard Number 41 of 1999, concerning the Quality Standards of the National Ambient, all parameters are below permissible limits (BPL) which indicates that air pollution does not occur, as given in Table 4.

Noise Quality

Based on the results of noise measurement using the Indonesia Minister of Environment Standard Number 48/MENLH/II/1996 concerning Noise Level Standards, no air pollution occurs (BPL) because there is no value above 70 dBA (Table 5).

Soil Quality

Laboratory analysis results in Table 6 show that in general soil conditions at the study site have moderate fertility with clay texture about 33-47% clay composition.

Soil fertility was relatively low, especially for the macro nitrogen element, but has a moderate phosphating content. Levels of organic soil C are very low at 1.64-2.69% of the ideal 5%, so fertilization with organic fertilizer is highly recommended before planting. The content of macroelements N 0.16-0.21% or very low to low, this requires the addition of urea fertilizer large enough to meet the needs of plant nitrogen.

Fig. 2 presents information about the general soil conditions in South Nunukan Subdistrict, Nunukan Regency which has a moderate fertility rate with a clay texture having 33-47% clay composition, 15-31% dust and the 4% sand. Soil fertility is relatively low, especially for the macro nitrogen element but it has a good phosphate content. The type of

Table 4: Air Quality in The South Nunukan District.

Parameter	S-1	S-2	S-3
Sulphur Dioxide (SO ₂)	20.879	26.098	24.326
Carbon Monoxide (CO)	39.502	25.393	19.220
Nitrogen Dioxide (NO ₂)	23.786	40.588	35.365

Where: S1-River Water, S2-Groundwater, S3-Surface Water, S4-Reservoir Water

Table 5: Noise measurement.

Parameter	S-1	S-2	S-3	PL
dBA	52.6	47.3	45.1	70

Where: S1-River Water, S2-Groundwater, S3-Surface Water, S4-Reservoir Water, PL: Permissible Limit

Table 6: The results of soil analysis samples.

Soil Parameter	S1	S2	S3	S4	S5
pH	4.2	3.8	5.5	4.9	4.5
C	2.21	1.89	2.14	2.69	1.64
N	0.17	0.16	0.18	0.21	0.16
C/N	13	12	12	13	10
P2O5	9.23	8.24	7.66	10.56	9.33
Ca	4.26	3.52	3.22	2.98	4.13
Mg	2.16	1.63	1.89	1.99	2.07
K	0.25	0.19	0.33	0.21	0.17
Na	0.39	0.24	0.22	0.26	0.27
KTK	23.07	24.32	24.36	21.85	21.66
KB	31	23	23	25	31
Texture					
a. Sand	41	35	29	34	49
b. Dust	15	32	24	31	15
c. Clay	44	33	47	35	36
Texture Class	Clay	Clay Stick	Clay	Clay Stick	Sand Clay



Source: Survey, 2015

Fig. 2: Land condition.

soil has less organic matter so that it can stabilize the soil structure and be resistant to erosion. The content of organic matter determines the sensitivity of the soil to erosion as the organic matter affects the structure of the soil. Soils that contain enough organic matter generally cause the soil structure to become stable so that it is resistant to soil erosion (Sarief 2001). Organic soil C levels are very low, i.e. 1.64-2.69% of the ideal 5%, so fertilization with organic fertilizer is highly recommended before planting rice to enable the soil in binding water be maximized. The content of macroelements N (0.16-0.21%) or very low to low level and this requires the addition of urea fertilizer large enough to meet the needs of plant nitrogen (Hanafiah 2010).

CONCLUSION

Based on the environmental baseline data of the South Nunukan District, it can be concluded that this area is suitable to be used as an agriculture and plantation area in accordance with The Nunukan Regional Spatial Plan (2013-2033) by adding various engineering technologies and fertilizing.

This is supported by the results of water, air, noise and soil quality tests from several samples showing the average below permissible limit (BPL). It was found that for some parameters, which did not meet the quality standards, some environmental engineering actions should be taken.

REFERENCES

- BPN-Institute of Soil Research 2003. Guidelines of Soil Analysis.
- BPS-Statistics of Nunukam Regency 2016. Nunukan Regency of Figure 2016.
- Karne, A.V. and Kulkarni, P.D. 2009. Studies on physico-chemical characteristics of freshwater bodies in Khatav Tahsil, Maharashtra. *Nature Environment and Pollution Technology*, 8(2): 247-251.
- Hanafiah, K.A. 2010. *Fundamentals of Soil Sciences*. Rajawali Press, Jakarta.
- Holt, E.A. and Miller, S.W. 2010. Bioindicators: Using organisms to measure environmental impacts. *Nature Education Knowledge*, 3(10): 8.
- Kumari, S.B., Priyatharshini, K., Julie, M.P. and Manimegalai, M. 2009. Study of well waters in the area around paper mill industry, Udumalpet, Tamilnadu. *Nature Environment and Pollution Technology*, 8(4): 845-847.
- Lee, C.D., Wang, S.B. and Kuo, C.L. 1978. Benthic macroinvertebrate and fish as biological indicators of water quality, with reference of community diversity index. *International Conference on Water Pollution Control in Development Countries*, Bangkok.
- Rashid, M., Sattar, Y., Ramli, M., Sabariah. and Puji, L. 2014. PM₁₀ black carbon and ionic species concentration of urban atmospheric in Makassar of South Sulawesi Province, Indonesia. *Atmospheric Pollution Research*, 5: 610-615. doi: 10.5094/APR.2014.070.
- Saini, M., Rusdi, N., Sattar, Y. and Ibrahim. 2018. The influence of throat length and vacuum pressure on air pollutant filtration using ejectors. *AIP Conference Proceedings*, doi.org/10.1063/1.5042939.
- Sari, T.G.F., Makmur, M. and Rozikin, M. 2014. Effectiveness of UKL-UPL Implementation in reducing environmental damage (study at the Malang Regency Environmental Agency and Communities around PT Tri Surya Plastik District Lawang). *Jurnal Administrasi Publik (JAP)*, 2(1): 161-168.
- Sarief, E.S. 2001. *Fertility and Fertilization of Agricultural Land*. Pustaka Buana, Bandung.
- Sattar, Y., Rashid, M., Ramli, M. and Sabariah, B. 2014. Black carbon and elemental concentration of ambient particulate matter in Makassar Indonesia. *IOP Conf. Series: Earth and Environmental Science*, 18. 012099. doi: 10.1088/1755-1315/18/1/012099.
- Sattar, Yunus. Mohd. Rashid., Ramli Mat., Sabariah Baharun and Hasfalina C. Man 2019. Characteristics of the PM₁₀ in the urban environment of Makassar, Indonesia. *Journal of Urban and Environmental Engineering*, 13(1): 198-201. doi: 10.4090/juee.2009.v13n1.198207.
- Sattar., M. Rashid., R. Mat. and L. Puji 2012. A preliminary survey of air quality in Makassar City South Sulawesi Indonesia. *Jurnal Teknologi (Sciences & Engineering)*, 57: 123-136.
- Shirota, A. 1996. *The plankton of South Vietnam*. Overseas Technology Coop. Agency Japan, pp. 416.
- WHO 2002. *The World Health Report 2002: Reducing Risks, Promoting Health Life*, World Health Organization, Geneva.
- Wilhm, J. F. 1975. Biological indicator of pollution. In: Whitton, B.A. (editor). *River Ecology*. Blackwell Scientific Publications. Oxford, London, pp. 370-402.



A Novel Approach for Disposing Agriculture Waste, Minimizing Air Pollution and Amending Soil Through Biochar Production and Application

M. P. Choudhary*†, H. D. Charan** and B. Acharya*

*Department of Civil Engineering, Rajasthan Technical University, Kota-324 010, India

**Bikaner Technical University, Bikaner-334 004, India

†Corresponding author: M. P. Choudhary; choudhary_mp@yahoo.co.in

Nat. Env. & Poll. Tech.

Website: www.neptjournal.com

Received: 29-03-2020

Revised: 26-05-2020

Accepted: 03-06-2020

Key Words:

Biochar
Crop residues
Soil properties
Greenhouse gas
Climate change

ABSTRACT

The burning of crop residues (traditionally called '*Parali*') has recently become a hot topic in India because it is presumed to be one of the reasons for abnormally high levels of air pollution in New Delhi, the capital city of India, after harvesting of Kharif crops during winter months. During the process of finding out a feasible solution for quick disposal of agricultural waste in a safer way, a novel method has been developed by the authors in which crop residue is converted into a useful product, biochar, which can be applied back to the fields for amendment of soil. It not only reduces the introduction of harmful gases into the environment but also improves the physical and chemical properties of the soil. This method is very simple and can be adopted by an individual farmer without much investment and technical skills. Many studies have been conducted on the factors involved in the production and use of biochar as a soil amendment; but in India, not much work has been carried out yet, as it is relatively a new concept in terms of using biomass for biochar production and application. Although biochar is not a new product, it has drawn the attention of researchers and other stakeholders in the near past because of its usefulness in improving the physical and chemical properties of the soil and at the same time reducing greenhouse gas emission, which is one of the biggest challenges for the modern world to protect the environment.

INTRODUCTION

It has been noticed that the capital city of India, New Delhi is facing a severe problem of air pollution for some years during the winter season when harvesting of *Kharif* crops takes place in Delhi and nearby states like Punjab, Haryana, Rajasthan, Uttar Pradesh and Madhya Pradesh.

The yearly outbreak of smog during the months of October-November in New Delhi is known to occur due to open burning of crop residues by the farmers of the nearby States. The severity of the problem can easily be understood with an example when New Delhi witnessed the worst category of air quality index in winter 2017. During this period, the concentration of fine particulate matter ($PM_{2.5}$) was observed at the highest level ever at $640 \mu\text{g}/\text{m}^3$ (ETB 2017) against the annual permissible limits of $40 \mu\text{g}/\text{m}^3$ prescribed by the national ambient air quality standards of India (NAAQS 2009). This situation has arisen recently because the Indian farmers have started making use of modern harvesters and crop cutters which cut only the useful upper part of the crops like rice and millet and bottom parts are left behind on the fields which are further set on fire by the farmers to prepare the fields for the next *Rabi* crops

in a shorter period and without any cost. Fig. 1 shows an agriculture field near Kota, Rajasthan in which crop residues are set to fire by the farmer. Although, the National Green Tribunal (NGT), New Delhi has imposed a ban on the open burning of crop residues in the country in 2015 (DTE 2015) still Indian farmers are not abiding by it in its strict sense. A large generation of agriculture waste further aggravates the situation. According to the Ministry of New and Renewable Energy (MNRE), Govt. of India, about 500 Million Tons (MT) of crop residue is generated every year out of which about 92 MT is directly burned in the fields (NPMCR 2014).

There are studies available in the literature highlighting factors involved in the production and use of biochar for soil amendment (Barus 2016, Carter et al. 2013, Ding et al. 2016, Gokila & Baskar 2015, Lydia & Rianne 2015, Parmar et al. 2014, Tammeorg et al. 2017); but in India, not much work has been carried out yet, as it is relatively a new concept in terms of using crop residues for the production of biochar and its application. Therefore, it was decided to carry out a study in which a novel and easy method of biochar production from crop residues is found out and the consequences of applying biochar as soil improvement are studied.



Fig.1: Crop residues set to fire in a field near Kota, Rajasthan.

MATERIALS AND METHODS

Biochar

Biochar is a carbon-rich product formed by a process called pyrolysis, in which the biomass is heated either in the absence of or with a limited amount of oxygen at a temperature above 250°C. An extensive range of feedstock biomasses had been employed for producing biochar like wastes of organic nature, agriculture, kitchen, residues of trees and forests, bio-energy crops and even sewage sludge also (Nartey & Zhao 2014). The properties of each biomass feedstock like ash and moisture content, calorific value, mass, density and particle size are different and hence the produced biochar also have different physical and chemical characteristics (Shareef & Zhao 2014).

The important characteristics of biochar are pH, ash, surface area, volatiles and water holding capacity, bulk density and pore-volume (Shareef & Zhao 2014). The exclusive property of biochar is its high porosity which increases the capacity of water and nutrient retention. Also, a large number of pores in biochar offer a favourable environment for soil bacteria by protecting them against drying and predation (Das et al. 2016).

Biochar had been motivated by the intriguing properties of ancient Terra Preta, originated from Amazon basin. It has been identified as a soil amendment and has very specific properties of adsorption and stability that make it unique among organic soil amendments (Lehmann 2007). Recently, biochar has gained more attention because the production of biochar and its presence/storage in soils has been recommended as a way of extenuating climate change by impounding carbon and at the same time providing energy and increased crop yields (Woolf et al. 2010). It has been reported that biochar remains in the soil for a very long time because the mass of the material opposes to the decomposition by microorganisms. During pyrolysis, the molecular biomass configuration is transformed into a stable type and

the atmospheric carbon gets combined with biomass and when plants are pyrolyzed, biochar is placed in soil (Shareef & Zhao 2014). Hence, biochar acts as a tool to sequester carbon in the soil.

Production of Biochar

Production of carbon-affluent product, biochar is carried out through a process known as pyrolysis, wherein heating of biomass or any other organic substance takes place either in the absence of or with a limited amount of oxygen at temperatures above 250°C (Lehmann 2007). The charcoal is also made with the same process but biochar is altogether taken as a different product than charcoal and other carbon products in that it is used as a soil amendment (Lehmann & Stephen 2015). In recent times, biochar has drawn more attention due to its scope and role in the alleviation of climate change and potential for soil amendment and sustainable cultivation (Lehmann et al. 2011).

Biochar can also be produced from waste materials including those that may otherwise produce even more harmful greenhouse gases (e.g., manure or green wastes) (Lehmann & Stephen 2015). So, it is beneficial to make use of waste materials in a useful manner and safe disposal at the same time. Biochar can be prepared from locally available weed biomass also, which will reduce the weed mass in the fields on one hand and on the other, it will enhance the growth of plants by improving the physical, chemical and biological characteristics of soil and hence contributing to increased crop yield (Das et al. 2016).

Production of biochar can be carried out either at an individual field by a farmer or in industrial setups (Lehmann & Stephen 2015, Woolf et al. 2010), making it significant for a large number of socio-economic conditions. Different types of pyrolysis techniques are available at a commercial level which yields varying amounts of biochar and associated bioenergy products like syngas and bio-oil (Woolf et al. 2010). The biomass can be pyrolyzed in a reactor through gasification or carbonization at different temperature and time depending on the final anticipated use of the end product (Ogbonnaya & Semple 2013). Biochar obtained at high temperatures (500°C) has been found suitable for direct use as a fuel because of high contents of carbon, retention time, pH and electrical conductivity whereas biochar obtained at low temperatures (300 to 350°C) are found appropriate for land application (Singh et al. 2015).

A Novel Method of Biochar Production

For Indian conditions, biochar can be produced by individual farmers in their fields in conventional kilns made by locally available material or at community kilns by using

the agricultural wastes and other by-products, so that the biochar produced can be utilized again for applying in the fields for the upcoming crops. A novel method of producing biochar has been developed by the authors wherein the agricultural waste is heated in a drum of capacity 220 litres. The experimental setup of the method is shown in Fig. 2 to Fig. 5.

The biochar produced as above at the field level from agricultural waste is crushed to small pieces, air-dried and

passed through a 4.75 mm size sieve to get the uniform size of biochar. The important characteristics of biochar like grain size distribution, pH, moisture content, specific gravity and electrical conductivity were determined in the laboratory as per the standard methods (IS: 2720, 2015) and results are presented in Table 1.

Soil Sample and Characteristics

The soil samples were collected from the agricultural fields



Fig. 2: Drums used for biochar production.



Fig. 3: Drum filled with crop residues.

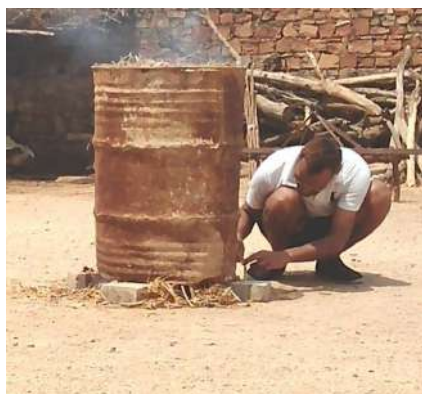


Fig. 4: Igniting the crop residues.



Fig. 5: Biochar produced in the drum is crushed to small pieces.

Table 1: Physico-chemical characteristics of Biochar.

Characteristic	Value
pH	9.8
Moisture (%)	8.1
Specific Gravity	1.62
Electrical Conductivity (mS/cm)	5.12
Grain Size Distribution (% Retained)	
2 mm-4.75 mm (Coarse)	23.6
0.425 mm-2 mm (Medium)	46.2
0.075 mm-0.425 mm (Fine)	30.2



Fig. 6: Collecting soil sample from a field.

of village Kosana in district Jodhpur, Rajasthan, India. The samples were prepared for tests as per the IS: 2720 (Part1)-1983 in the geotechnical engineering laboratory of the Department of Civil Engineering, Rajasthan Technical University, Kota, India. Fig. 6 shows the collection of the soil sample from field whereas Fig. 7 to Fig. 10 show arrangements for different laboratory tests.

First of all, the soil samples were oven-dried, pulverized and then sieved through 4.75 mm size sieve to decide about the soil classification. The sieve size analysis resulted into constituents of soil as 69% of sand, 16.2% of silt and 14.8% of clay and hence the soil sample was classified as SC (Clayey Sand) as per the Unified Soil Classification System (USCS). Table 2 represents a summary

of the main physical characteristics of soil and Fig. 11 shows the grain size distribution curve of the soil sample and biochar.

The Atterberg limits of the soil sample were found out. It was observed that liquid limit; plastic limit and shrinkage limit of the soil were 39%, 19% and 15% respectively.

Biochar as Soil Amendment

The application of biochar to the soil is anticipated as a new technique to set up a major, enduring sink for atmospheric carbon dioxide in global ecosystems. Along with decreasing emissions and escalating the confiscation of greenhouse gases, the biochar production and its use in soils bring direct payback through enhanced soil productiveness and



Fig. 7: Sieve set used for particle size analysis.



Fig. 8: Pycnometer used for finding specific gravity of soil.



Fig. 9: Soil samples prepared for finding Atterberg limits.



Fig. 10: Cone penetrometer used for finding the liquid limit.

Table 2: Characteristics of the soil sample.

Characteristic	Value
pH	8.2
Specific Gravity	2.58
Electrical Conductivity (mS/cm)	0.94
Grain Size Distribution (% Retained)	
2 mm-4.75 mm (Coarse Sand)	6.0
0.425 mm-2 mm (Medium Sand)	30.4
0.075 mm-0.425 mm (Fine Sand)	32.6
0.002 mm-0.075 mm (Silt)	16.2
< 0.002 mm (Clay)	14.8
Consistency Limits (%)	
Liquid Limit	39
Plastic Limit	19
Shrinkage Limit	15

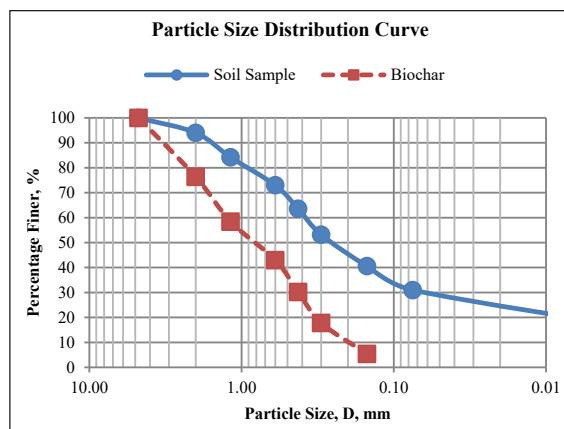


Fig. 11: Grain size distribution curve of the soil sample and Biochar.

amplified crop yield as well (Lehmann et al. 2006). Biochar has been acknowledged as a soil amendment and has very explicit properties of adsorption and stability that make it distinctive among organic soil amendments (Lehmann 2007).

Testimonials are available that biochar remains in the soil for a very long time because the mass of the material opposes to the decomposition by microorganisms. During pyrolysis, the molecular biomass configuration is transformed into a stable type and the atmospheric carbon gets combined with biomass and when plants are pyrolyzed, biochar is placed in soil (Shareef & Zhao 2017). Hence, biochar acts as a tool to confiscate carbon in the soil.

To study the effect of biochar on consistency behaviour of soil, tests were carried out to find out the liquid limit, plastic limit and shrinkage limit of the soil amended with different per cent by weight (% w/w) of biochar like 5%, 10%, 15%, 20% and 25%. For this purpose, the biochar was added in dry condition to the soil and the soil-biochar mix was thoroughly mixed. The tests of consistency limits were performed as per the standard methods (IS: 2720, 2015).

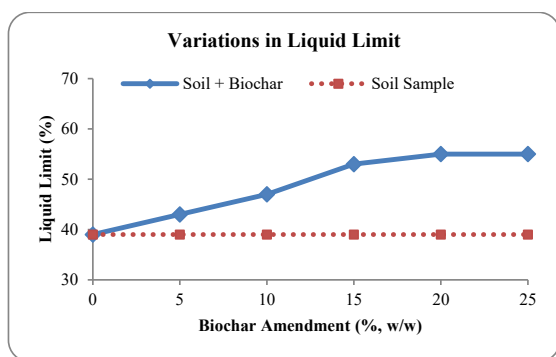


Fig. 12: Effect of Biochar amendment on the liquid limit of soil.

RESULTS AND DISCUSSION

The result of the biochar amendment on the liquid limit of the soil is shown in Fig. 12. It was found that liquid limit of the soil amended with biochar increased from 39% to 43%, 47%, 53%, 55% and remained constant at 55% on addition of biochar at 5%, 10%, 15% 20% and 25% (w/w) respectively. It can be inferred from the results that liquid limit of the soil increases with adding up of biochar into it up to a certain point because biochar has high porosity and surface area which increases the liquid limit of the soil-biochar composite.

Fig. 13 shows the effect of biochar amendment on the plastic limit of the soil. It was observed that plastic limit of the soil-biochar composite increased from 19% to 24% when 5% biochar (w/w) was added to the soil and thereafter it slowly increased for 10% and 15% and remained constant at 20% addition of biochar. Further, it was not possible to find the plastic limit of the soil-biochar composite at 25% (w/w) biochar amendment because the composite did not show any plastic behaviour. It crumbled at higher water contents. Hence, we can infer that the initial increase in plastic limit is

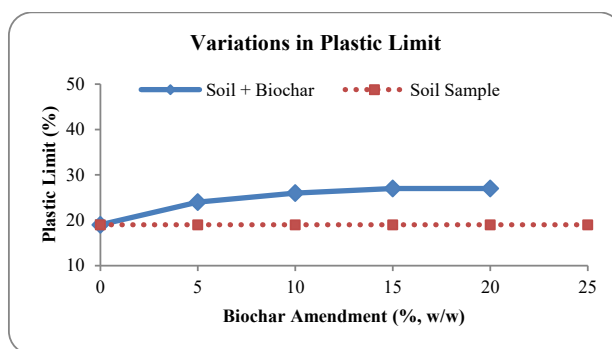


Fig. 13: Effect of Biochar amendment on the plastic limit of soil.

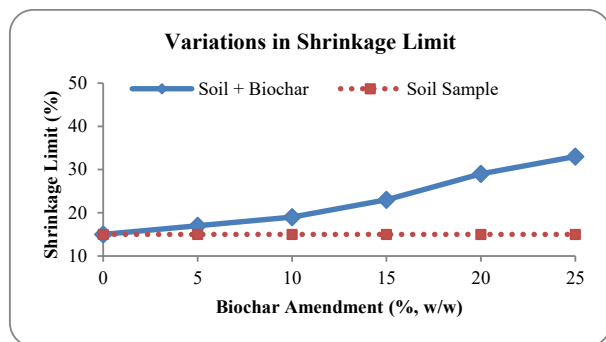


Fig. 14: Effect of Biochar amendment on shrinkage limit of the soil.

because of the water absorbing capacity of the soil-biochar composite up to a certain limit.

Fig. 14 shows the variations in shrinkage limit of the soil amended with biochar at different ratios. The initial increase in shrinkage limit up to 10% addition of biochar is slightly slow but thereafter it goes up sharply up to 25% (w/w). The increase can be seen from 15% in the soil sample to 17%, 19%, 23%, 29% and 33% respectively in the soil-biochar composite. The increase in shrinkage limit indicates that there is a higher void ratio in the biochar as compared to soil and hence soil amended with biochar requires more amount of water to change from solid-state to semi-solid state.

Thus, we can see that the consistency limits have increased upon adding up of biochar to the soil up to a certain per cent by weight and therefore, the physical properties of the soil are improved, which supports and verifies the hypothesis available in the literature that biochar can act as a soil amendment and in the Indian context, it has good potential due to large quantities of crop residues generated every year.

CONCLUSIONS

The present study reveals that biochar can easily be produced at an individual level in the fields after harvesting is over by utilizing the crop residues without much cost and time. The technique of producing biochar is very simple and needs no particular technical knowledge and skill. The study showed that the amendment of soil with biochar in different per cent by weight has sound effects on the consistency behaviour of the soil. The liquid limit, plastic limit and shrinkage limit of the soil amended with biochar increases up to a certain point. Hence, we can conclude that if the Indian farmers start producing and using biochar in their agricultural fields, the agricultural waste, which has otherwise no utility, has a very good potential of disposal and management by conversion into biochar, improving the soil properties when applied in fields and at the same time reducing the level of air pol-

lution and greenhouse gases, especially in New Delhi and the country as a whole. It can be termed as a single panacea for environmental protection in which agricultural waste is utilized, soil amendment is achieved and air pollution is controlled.

REFERENCES

- Barus, J. 2016. Utilization of crops residues as compost and biochar for improving soil physical properties and upland rice productivity. *J. Degraded Mining Lands Manage.*, 3(4): 631-637.
- Carter, S., Shackley, S., Sohi, S., Suy, T.B. and Haefele, S. 2013. The impact of biochar application on soil properties and plant growth of pot grown lettuce (*Lactuca sativa*) and cabbage (*Brassica chinensis*). *Agronomy*, 3: 404-418.
- Das, S.K., Avasthe, R.K. and Matber Singh. 2016. Carbon-negative biochar from weed biomass for agricultural research in India. *Curr. Sci.*, 110(11): 2045-2046.
- Ding, Y., Liu, Y., Liu, S., Li, Z., Tan, X., Huang, X., Zeng, G., Zhou, L. and Zheng, B. 2016. Biochar to improve soil fertility: A review. *Agron. Sustain. Dev.*, 36 :36. <https://doi.org/10.1007/s13593-016-0372-z>.
- DTE (Down To Earth) 2015. <https://www.downtoearth.org/in/news/air/paddy-burning-ngt-orders-fine-imposition-on-erring-farmers-51698>. Accessed 18 March 2020.
- ETB (Economics Times Bureau) 2017. Odd-even plan for five days in Delhi from Monday. <https://economictimes.indiatimes.com/news/politics-and-nation/odd-even-plan-for-five-days-in-delhi-from-monday/articleshow/61575418.cms>, Accessed 18 March 2020.
- Gokila, B. and Baskar, K. 2015. Influence of biochar as a soil amendment on yield and quality of maize in alfisols of Thoothukudi district of Tamilnadu, India. *Int. J. Plant, Animal Env. Sci.*, 5(1): 152-155.
- Indian Standards (IS): 2720 2015. Method of Tests for Soils, various parts published by Bureau of Indian Standards, New Delhi.
- Lehmann, J. 2007. Bio-energy in the black. *Frontiers Ecol. Env.*, 5: 381-387.
- Lehmann, J. and Stephen Joseph 2015. *Biochar for Environmental Management: Sci. Tech. Implementation*. 2nd edn. Routledge, London.
- Lehmann, J., Gaunt, J. and Rondon, M. 2006. Bio-char sequestration in terrestrial ecosystems— A review. *Mitigation Adaptation Strategies for Global Change*, 11: 403-427.
- Lehmann, J., Rillig Matthias, C., Janice Thies, Masiello Caroline, A., Hockaday William, C. and Crowley David 2011. Biochar effects on soil biota- A review. *Soil Biol. Biochem.*, 43(9): 1812-1836.
- Lehmann Johannes. 2007. A handful of carbon. *Nature*, 447: 143-144.
- Lydia Fryda and Rianne Visser 2015. Biochar for soil improvement: Evaluation of biochar from gasification and slow pyrolysis. *Agric.*, 5: 1076-1115.
- NAAQS (National Ambient Air Quality Standards) 2009. Central Pollution Control Board, India. <http://www.moef.nic.in/sites/default/files/notification/Recved%20national.pdf>, Accessed 18 March 2020.
- Nartey, D., Obemah and Zhao Baowei 2014. Biochar preparation, characterization, and adsorptive capacity and its effect on bioavailability of contaminants: An overview. *Advances in Materials Sci. Eng.*, <http://dx.doi.org/10.1155/2014/715398>.
- NPMCR (National Policy for Management of Crop Residues) 2014. Available online: http://agricoop.nic.in/sites/default/files/NPMCR_1.pdf, Accessed 18 March 2020.
- Ogbonnaya, Uchenna and Semple T. Kirk 2013. Impact of biochar on organic contaminants in soil: A tool for mitigating risk. *Agronomy*, 3: 349-375.
- Parmar, Aditya, Nema Prabhat, K. and Agarwal, Tripti 2014. Biochar production from agro-food industry residues: a sustainable approach for soil and environmental management. *Curr. Sci.*, 107(10): 1673-1682.

- Shareef, T. M. E. and Zhao, B. W. 2017. The fundamentals of biochar as a soil amendment tool and management in agriculture scope: an overview for farmers and gardeners. *J. Agric. Chem. Env.*, 6: 38-61.
- Singh, Anita, Biswas, A.K., Singh Rashmi, Lakaria Brij Lal and Dubey, A.K. 2015. Effect of pyrolysis temperature and retention time on mustard straw-derived biochar for soil amendment. *J. Basic. Appl. Sci. Res.*, 5(9): 31-37.
- Tammeorg, Priit, Bastos, Ana Catarina, Jeffery Simon, Rees Frédéric, Kern Jürgen and Graber Ellen, R. 2017. Biochars in soils: Towards the required level of scientific understanding. *Journal of Environmental Engineering and Landscape Management*, 25(2): 192-207.
- Wolf, Dominic, Amonette James, E., Street-Perrott, F., Alayne, Lehmann Johannes and Joseph Stephen 2010. Sustainable biochar to mitigate global climate change. *Nat. Commun.*, 1: 56.



A Study on Development of Pollution Index Models and Multivariate Statistical Analysis for Heavy Metals in the Soils of APIIC, Visakhapatnam

G. V. Satyanarayana*, T. Byragi Reddy**, R. S. S. Srikanth Vemuri*†, K. Suryanarayana Rao* and Manoj Kumar Karnena***

*Department of BS&H, Vignan's Institute of Engineering for Women, Visakhapatnam, India

**Department of Environmental Sciences, Andhra University, Visakhapatnam, India

***Department of Environmental Science, GITAM Institute of Science, GITAM (Deemed to be) University, Visakhapatnam, India

†Corresponding author: R. S. S. Srikanth Vemuri; vrsssrikanth@gmail.com

Nat. Env. & Poll. Tech.
Website: www.neptjournal.com

Received: 05-02-2020

Revised: 22-02-2020

Accepted: 15-04-2020

Key Words:

Heavy metals
Pollution index model
Soil pollution
Anthropogenic activities

ABSTRACT

Soil pollution is a worldwide problem caused by both natural and anthropogenic activities. This has resulted in health and physiological problems to both plants and animals. This study investigated heavy metals in soils within the immediate vicinity. Soils from Seven APIIC zones in Visakhapatnam were collected and analysed for physicochemical characteristics and heavy metals. The data obtained were subjected to the pollution index model and multivariate statistical analysis. The data obtained showed that the soils are rich in zinc, and heavy metals are above trace level with a minor positively skewed distribution. The analysis of pollution index, geoaccumulation index and ecological risk factors in soils in all the locations showed that they are mainly contaminated and polluted by Cd followed by Zn. The mean heavy metal concentrations around APIIC can be arranged in increasing order as $Cr < Co < Pb < Cu < Cd < Zn$. Element pairs such as Zn-Pb, Zn-Cu, Zn-Cd, Pb-Cu, Pb-Cd, Cu-Cr, Cd-Co and Cr-Co showed strong positive correlation coefficient "r" indicating their association in the study area. The observed concentrations of heavy metals revealed that soil contamination has been increasing and measures must be taken to ensure the adoption of more environment-friendly practices.

INTRODUCTION

Heavy metals are released into the environment by both natural and anthropogenic sources. The chemical weathering of minerals; and the anthropogenic sources that are associated with industrial, agricultural, mining, land disposal of waste, waste incineration, etc. are the major sources of these metals (Guerra et al. 2012). The soil contamination by heavy metals due to these activities are becoming a major concern throughout the world. Heavy metals contamination of topsoil has been a major concern for their toxicity, persistence and recalcitrant nature. Toxicity of these compounds has been reported extensively (Momodu & Anyakora 2010, Anyakora et al. 2013). They amass over the time in soils, which act as a sink from which these toxicants are discharged into the groundwater and plants and end up through the food chain causing different toxicological impacts. Impacts of raised concentrations of heavy metals to soil capacities, soil microbial composition and microbial development have for some time been accounted for under both field and laboratory conditions (Tyler et al. 1989). Health effects of elevated levels of Zn are severe vomiting, diarrhoea, bloody urine, liver and kidney failure and anaemia (Fosmire 1990), while excessive

Pb causes inhibition of haemoglobin synthesis, dysfunction of the kidneys, reproductive systems and cardiovascular system (Ferner 2001). Other effects of Pb are damage to the gastrointestinal system, mental retardation in children, infertility and abnormalities in pregnancy (Dara 2000). Excess Cd has been reported to bring about renal dysfunction, anaemia, hypertension, bone marrow disorder, cancer, kidney damage, bronchitis, liver and brain disorder (Dara 2000), while, high concentration of manganese could result in kidney failure, liver and pancreases malfunctioning (Underwood 1977). Human activities in urban areas largely contribute to the contamination of urban soils and this is a major health concern. Iwegbu et al. (2006) reported elevated concentration of Cd, Cr, Cu, Pb, Ni, Co and Zn in an automobile mechanic workshop soil while Dauda & Odoh (2012) in their study revealed the high degree of contamination of Pb, Cd and Zn in soil from fuel filling stations in Benue state. In addition, Ubwa et al. (2013) reported high levels of Cd, Zn, Ni, Cr and Pb from the soils around the Gboko area. The extent of human impact is now so pervasive and profound, that there is a need to investigate the levels of heavy metals in soils from different anthropogenically influenced sites. The objective of

this study is to determine the physicochemical characteristics and heavy metals in surface and sub-surface soils from the selected sites in Visakhapatnam.

MATERIALS AND METHODS

Study Area

Visakhapatnam is one of the major port cities on the east coast of India. After bifurcation of Andhra Pradesh state in 2014, this city became its business capital with an area of 550 km². Seven areas were randomly selected as sampling sites in APIIC zone and located using GPS positions (Table 1). The base map (Fig.1) was prepared from these sampling locations.

Sampling and Preparation

Soil samples were taken from depths of 0-15 cm. All the soil samples were stored in clean polythene bags and brought to the laboratory. The soil samples were air-dried, ground and passed through 2 mm sieve for physicochemical and heavy metal analysis.

Physico-Chemical Analysis of Soil Samples

The soil pH and conductivity were determined in 1 (soil):5 (water) suspension using HM digital meter-CO-100 and Equip-Tronics EQ-614 respectively. Soil texture and organic

carbon were determined by the hydrometer method (Jacob & Clark 2002) and Walkley-Black wet oxidation method (Nelson & Sommers 1982) respectively. A factor of 1.72 was multiplied with organic carbon content to determine Soil organic matter.

Heavy Metal Analysis

For heavy metal (Zn, Cr, Cu, Cd, Co and Pb) determination, one gram of soil was digested with 15 mL of aqua regia at 80°C till a transparent solution was obtained (Wen & Allen 1999). The digested samples were filtered and diluted with de-ionized water up to 50 mL and analysed for the metals, viz. zinc (Zn), chromium (Cr), copper (Cu), cadmium (Cd), cobalt (Co) and lead (Pb) by atomic absorption spectrophotometer (AAS).

Pollution Index Model

Contamination factor (C_f): Lacatusu (2000) standards were adopted in the current study for the interpretation of the contamination factor. The factors were used to ascertain the soil contamination levels by heavy metals. The C_f is the ratio of the concentration of heavy metals to the background value. These values are in the range of 1-6.

$$\text{Contamination factor (C}_f\text{)} = \frac{C_m}{C_b} \quad \dots(1)$$

Where, C_m is the concentration of metals and C_b is the background value.

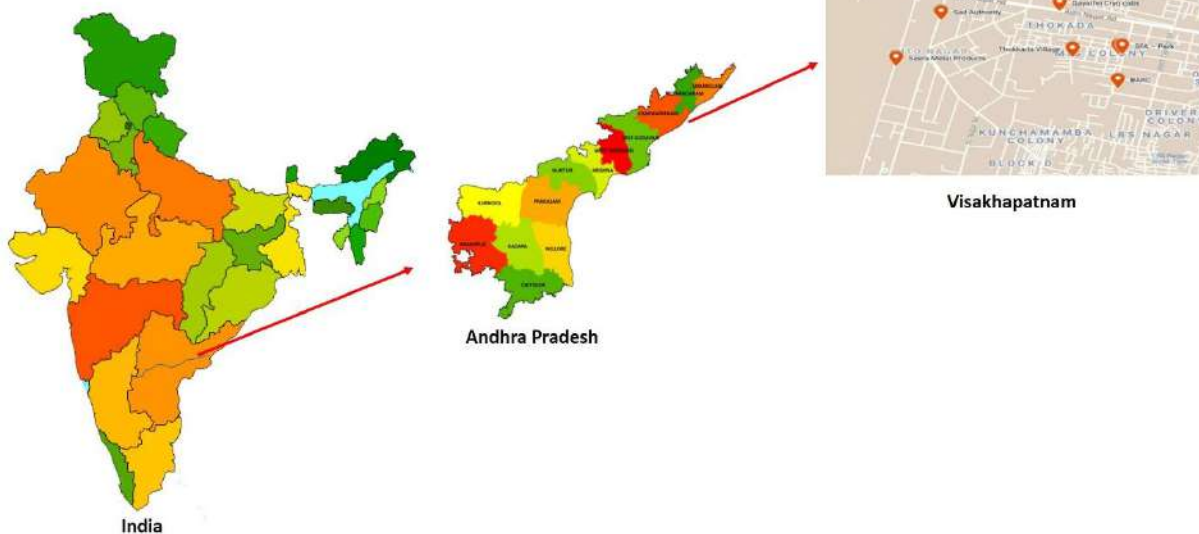


Fig. 1: Location map of the study area.

Table 1: Sampling sites and GPS positions.

S.no	Locations	Name	GPS positions	
1	Seera Metal Products	S1	N 17.695042	E 83.185539
2	Sail Authority	S2	N 17.698512	E 83.188167
3	Gayathri Cryo cabs	S3	N 17.699218	E 83.195095
4	BARC	S4	N 17.693370	E 83.198513
5	LIG – Park	S5	N 17.695945	E 83.198546
6	SFA – Park	S6	N 17.695955	E 83.198760
7	Thokkada Village	S7	N 17.695727	E 83.195859

The EGASPIN (2002) target values for heavy metals (Table 2) were taken as the background value for the analysis. The range for the significance of intervals of contamination is given in Table 3.

Pollution Index (PI): It is a measure of the degree of overall contamination in a particular location. Tomlinson et al. (1980) procedure was used for calculating the pollution index (PI) for each location as per Equation 2.

Table 2: Target values for heavy metals (mg/kg).

Metals	Target values (mg/kg)	Intervention values (mg/kg)
Iron (Fe)	38000	-
Zinc (Zn)	140	720
Lead (Pb)	85	530
Cobalt (Co)	20	240
Copper (Cu)	36	190
Chromium (Cr)	100	380
Nickel (Ni)	35	210
Manganese (Mn)	850	-
Arsenic (As)	1.0	10
Cadmium (cd)	0.8	17

Source: EGASPIN, 2002

Table 3: Significance of intervals of contamination factor/pollution index (C_f/PI).

C _f /PI	Significance
< 0.1	Very slight contamination
0.10 – 0.25	Slight contamination
0.26 – 0.5	Moderate contamination
0.51 – 0.75	Severe contamination
0.76 – 1.00	Very severe concentration
1.1 – 2.0	Slight pollution
2.1 – 4.0	Moderate pollution
4.1 – 8.0	Severe pollution
8.1 – 16.0	Very severe pollution
> 16.0	Excessive pollution

Source: Lacatusu (2000)

$$PI = (C_f1 \times C_f2 \times C_f3 \times \dots \times C_fn)^{1/n} \dots(2)$$

Where, n is the number of metals and C_f is the contamination factor. The PI is a potential tool that was used to access environmental pollution.

Geo- Accumulation index (I_{geo}): Muller (1979) formula was used in this study to calculate the index and the values for the various metals are given in Equation 3.

$$I_{geo} = \log_2 (C_n/1.5 B_n) \dots(3)$$

Where,

C_n = Contamination of the heavy metal in the soil.

B_n = Geochemical background of the element or world average of the element in shale.

Muller proposed seven classes (ranging from 0-6) of the geo-accumulation index to classify the levels of contamination of soils by the metals.

Class 0 = I_{geo} ≤ 0 (practically uncontaminated)

Class 1 = 0 ≤ I_{geo} ≤ 1 (uncontaminated to moderately contaminated)

Class 2 = 1 ≤ I_{geo} ≤ 2 (moderately contaminated)

Class 3 = 2 ≤ I_{geo} ≤ 3 (moderately to heavily contaminated)

Class 4 = 3 ≤ I_{geo} ≤ 4 (heavily contaminated)

Class 5 = 4 ≤ I_{geo} ≤ 5 (heavily to extremely contaminated)

Class 6 = 5 ≤ I_{geo} ≤ 6 (extremely contaminated)

The values that fall other than 6 of the above classes are considered to be in an open class. In that class, the value of the element is many-folds greater than the background value of the metal (Table 4).

The background value taken is considered from world average value in shale (mg/kg) of the metals determined in the study are Fe = 47200, Zn = 95, Pb = 20, Co = 19, Cu = 45, Cr = 90, Ni = 68, Mn = 850, As = 13 and Cd = 0.3 mg/kg.

Ecological risk factor (E_r): Hakanson (1980) suggested the ecological risk factor, which is a quantitative expression of potential ecological risk of the given contamination and

Table 4: Toxic response factor for calculation of ecological factor calculation.

Metals	Toxic response factor
Iron (Fe)	NA
Zinc (Zn)	1
Lead (Pb)	5
Cobalt (Co)	5
Copper (Cu)	5
Chromium (Cr)	2
Nickel (Ni)	5
Manganese (Mn)	1
Arsenic (As)	10
Cadmium (cd)	30

NA: Not available

is defined as the ratio of the toxic response factor to the contaminant as given in Equation 4.

$$E_r = T_r \times C_f \quad \dots(4)$$

Where, T_r is the toxic response factor for a given contaminant and C_f is the contamination factor. The risk factors are divided into 5 categories.

- $E_r < 40$ (low potential ecological risk)
- $40 \leq E_r < 80$ (moderate potential ecological risk)
- $80 \leq E_r < 160$ (considerable potential ecological risk)
- $160 \leq E_r < 320$ (high potential ecological risk)
- $E_r \geq 320$ (very high ecological risk)

The aim of the risk factor was originally a diagnostic tool for water pollution control, but currently, we utilized it for accessing the soil quality of a location that is contaminated with heavy metals.

Statistical Analysis

The analysis of physicochemical characteristics and heavy metal content of soil and plant samples was done in triplicates and the data are presented as mean \pm standard error.

Table 5: Physico-chemical properties of soils.

Sample	pH	Electrical conductance (mmhos)	Organic carbon %	Zn mg/kg	Pb mg/kg	Cu mg/kg	Cd mg/kg	Cr mg/kg	Co mg/kg
1	8.26	124	0.558	68.7	20.9	78.9	36.6	36.4	10.5
2	8.05	98.7	0.93	34.1	8.3	22.1	41.7	41.4	20.8
3	8.23	79	0.679	227.9	4.8	23.7	33.8	10.2	15.3
4	7.94	138	1.37	152.3	51.8	48.9	71.5	10.9	15.1
5	7.7	87	1.051	103.9	43.8	9.2	89	5.33	15.6
6	7.74	45	0.456	35.4	5.8	7.19	50.5	0.01	20.6
7	8.22	61.8	0.296	10.84	0.79	1.9	24.5	2.58	10.9

Statistical analysis was done with the help of Microsoft excel computer software programs.

RESULTS AND DISCUSSION

Soil Physicochemical Properties

The physicochemical properties of soils are given in Table 5. The studied soil is slightly (S5, S6) and moderately alkaline (S1, S2, S3, S4, S7). The pH of the soil is in a range of 7.7-8.26. Soil electrical conductivity, which is a major indicator of salinity of the soil, was found to be low (45-135 mS/cm).

The Soil Organic Matter (SOM) which is the storehouse of plant nutrients and mineral recycling (Rattan et al. 2005) was found to be low (0.296-1.37 %) which can be attributed to the sandy texture of the soil.

Heavy Metal Analysis

Table 5 represents the contents of heavy metals (Zn, Cr, Cu, Cd, Co and Pb) studied in the soils. The Zn, Cr, Cu and Co are required for plants for metabolic activities (Jolly et al. 2013). They ranged from 10.8 to 227.9, 0.01 to 41.4, 1.9 to 78.9 and 10.5 to 20.8 mg/kg respectively. Cd and Pb, which are known toxins and carcinogens (Rajaganapathy et al. 2011), ranged from 24.5 to 71.5 and 0.79 to 51.8 mg/kg. Although extensive use of agrochemicals is prevalent in Visakhapatnam posing a severe risk of heavy metal contamination of soil, the levels of heavy metals in studied soils were below the various maximum permissible limits (Table 6 & 7). This might be due to leaching of metals to lower soil layers, due to the sandy texture of soil and precipitation. The soil heavy metal contents observed in the present study were at similar levels to the heavy metals observed in soil by Dheri et al. (2007).

Pollution Index Model

Zn: PI/C_f values vary from 0.07 to 1.63 in different samples. Sample S7 shows very slight contamination whereas samples S3 and S4 show slight pollution and the remaining samples

Table 6: Contamination Factor/pollution Index for heavy metals for various stations.

Metal	Station 1	Station 2	Station 3	Station 4	Station 5	Station 6	Station 7
Zn	0.490714	0.243571	1.627857	1.087857	0.742143	0.252857	0.077429
Pb	0.245882	0.097647	0.056471	0.609412	0.515294	0.068235	0.009294
Cu	2.191667	0.613889	0.658333	1.358333	0.255556	0.199722	0.052778
Cd	45.75	52.125	42.25	89.375	111.25	63.125	30.625
Cr	0.364	0.414	0.102	0.109	0.0533	0.0001	0.0258
Co	0.525	1.04	0.765	0.755	0.78	1.03	0.545

Table 7: Geoaccumulation index at different stations.

Metal	Station 1	Station 2	Station 3	Station 4	Station 5	Station 6	Station 7
Zn	0.145114	0.072029	0.481389	0.3217	0.219466	0.074775	0.022897
Pb	0.209697	0.083277	0.04816	0.519727	0.43946	0.058193	0.007926
Cu	0.351836	0.09855	0.105684	0.218058	0.041025	0.032062	0.008473
Cd	24.48133	27.89267	22.60844	47.82556	59.53111	33.77889	16.38778
Cr	0.081159	0.092307	0.022742	0.024303	0.011884	2.23E-05	0.005752
Co	0.110895	0.219677	0.161589	0.159477	0.164758	0.217565	0.115119

show moderate contamination. Geoaccumulation index of Zn in all samples indicates that soil has moderate contamination. An ecological risk factor is very low in all samples.

Pb: PI values vary between 0.01 and 0.52. Severe contamination to soil happened by Pb in samples S4 and S5. Negligible distribution occurred in sample S7. According to geoaccumulation index, the soil is not exclusively contaminated by Pb in all samples. Ecological risk factor through Pb is low in all samples.

Cu: Contamination factor varies from 0.05 to 2.19. Moderate pollution is caused by Cu in sample S1, and slight pollution observed in sample S4. Soils in all the stations show moderate contamination by Cu. Low potential risk factor observed for all soils.

Cd: Excessive pollution is caused by Cd in all stations. The PI values vary from 30 to 89. These high values are due to welding operated small-scale engineering workshops located near the stations. Geoaccumulation index suggests that soils in all the locations are extremely contaminated by Cd. Ecological risk factor values exist in terms of thousands. It clearly shows that these soils are in very high ecological risk. These soils are not at all suitable for cultivation as well as a living.

Cr: Pollution index suggests that soils are contaminated from slight to the severe condition in observed locations. Geoaccumulation index also suggests that soils in all locations are uncontaminated by Cr. Ecological risk factor is negligible in case of Cr.

Co: Pollution index values vary from 0.5 to 1.04. Severe

contamination of soil was observed by cobalt in all locations, particularly in samples S2 and S6. Geoaccumulation index shows moderate contamination by Co to soils in all samples. Low potential toxic response factor was observed in all locations.

Statistical Analysis

The standard statistical analysis (mean, standard deviation, skewness, kurtosis) carried out to describe the physicochemical characteristics and heavy metals contents in the soil is presented in Tables 8 and 9.

Effect of pH: As per the US Department of Agriculture (USDA 1993), samples S5 and S6 are slightly alkaline and samples S1, S2, S3, S4 and S7 are moderately alkaline. Positive correlation was obtained for pH with EC ($r = 0.22$), Zn ($r = 0.11$), Cu ($r = 0.41$) and Cr ($r = 0.43$). Higher pH value indicates a low value of organic carbon (McIntosh & Allen 1993). This is clear when observing samples S1 and S4.

Effect of electrical conductance (EC): EC values vary between 45 mmhos and 138 mmhos. Higher value was observed in the sample S4 and lower value in sample S6. Higher EC values indicate the availability of various salts in the soil and also shows that leaching of soil leads to contamination of groundwater. The positive correlation was obtained with all parameters except Co ($r = -0.29$), which indicates that EC is interdependent on all parameters except cobalt.

Effect of organic carbon (OC): OC varies in the range of 0.291.37%. Sample S4 has a higher OC value of 1.37%, whereas sample S7 has a lower value of 0.29%. The data in

Table 8: Statistical analysis.

	pH	EC mmhos	OC %	Zn mg/kg	Pb mg/kg	Cu mg/kg	Cd mg/kg	Cr mg/kg	Co mg/kg
Minimum	7.7	45	0.296	10.84	0.79	1.9	24.5	0.01	10.5
Maximum	8.26	138	1.37	227.9	51.8	78.9	89	41.4	20.8
Median	8.05	87	0.679	68.7	8.3	22.1	41.7	10.2	15.3
Mean	8.02	90.5	0.763	90.45	19.46	27.41	49.66	15.26	15.54
Standard deviation	0.2344	32.87	0.374	77.37	20.44	27.53	22.89	16.67	4.092
Skewness	-0.4367	0.170	0.501	0.995	0.943	1.290	0.947	1.035	0.157
Kurtosis	-1.764	-0.87	-0.61	0.217	-0.98	1.056	-0.09	-0.82	-1.19
Standard error	0.2333	1.754	2.272	2.262	2.355	1.505	2.348	1.144	2.365
Standard error of mean	0.0886	12.42	0.142	29.25	7.738	10.40	8.652	6.299	1.547
Variance	0.0550	1081	0.140	5986	419.2	757.7	524.0	277.8	16.74
Coefficiency of variation	2.9233	36.33	49.07	85.54	105.2	100.4	46.10	109.2	26.33

Table 9: Correlation matrix for soil parameters.

Correlation	pH	EC mmhos	OC %	Zn mg/kg	Pb mg/kg	Cu mg/kg	Cd mg/kg	Cr mg/kg	Co mg/kg
pH	1.0000	0.2204	-0.3988	0.1120	-0.4636	0.4155	-0.8170	0.4289	-0.5961
EC mmhos	0.2204	1.0000	0.6862	0.3217	0.6769	0.8216	0.2798	0.5677	-0.2988
OC %	-0.3988	0.6862	1.0000	0.4546	0.8400	0.2392	0.7539	0.1484	0.2498
Zn mg/kg	0.1120	0.3217	0.4546	1.0000	0.3313	0.2268	0.2249	-0.1528	-0.0818
Pb mg/kg	-0.4636	0.3217	0.8400	0.3313	1.0000	0.3525	0.8623	-0.0609	-0.1148
Cu mg/kg	0.4155	0.8216	0.2392	0.2268	0.3525	1.0000	-0.0512	0.6130	-0.4159
Cd mg/kg	-0.8170	0.2798	0.7539	0.2249	0.8623	-0.0512	1.0000	-0.2549	0.2518
Cr mg/kg	0.4289	0.5677	0.1484	-0.1528	-0.0609	0.6130	-0.2549	1.0000	0.0370
Co mg/kg	-0.5961	-0.2988	0.2498	-0.0818	-0.1148	-0.4159	0.2518	0.0370	1.0000

Table 8 clearly indicate that organic carbon is strongly interdependent on Pb ($r = 0.84$) and Cd ($r = 0.75$) and moderately correlate with Zn ($r = 0.45$), Cu ($r = 0.24$) and Co ($r = 0.25$), whereas weakly interdependent on Cr ($r = 0.15$). A negative correlation was observed with pH ($r = -0.39$) which shows that organic carbon oppositely dependent on pH.

Analysis of Heavy Metals

Effect of Zn: Amount of Zn present in given samples varies between 10.84 mg/kg and 227.9 mg/kg. Sample S7 has lower value of 10.84 mg/kg and sample S3 a higher value of 227.9 mg/kg. The positive correlation obtained with all parameters except Cr and Co even though the correlation is weakly interdependent on pH, EC, OC, Pb, Cd and Cu

Effect of Pb: Amount of Pb present in given samples varies from 0.79 mg/kg to 51.8 mg/kg. In sample S7 have lowest value (0.79 mg/kg) whereas sample S4 contains the highest value of 51.8 mg/kg. A positive correlation was observed with EC, OC, Zn, Cu and Cd whereas a negative correlation with Cr and Co. Among EC, OC, Zn, Cu and Cd, OC is strongly

correlated with Pb ($r = 0.84$). In the study areas, due to the presence of automobile service centres fuel effluent wastage with Pb and organic carbon enters into the soil. In fuels, Pb and Cd are added as anti-knocking agents hence there is a strong correlation between Pb and organic carbon.

Effect of Cu: Amount of Cu present in given the samples varies from 1.90 mg/kg to 48.9 mg/kg. 1.90 mg/kg is the lowest value in sample S7, and 48.9 mg/kg be the highest value in sample S4. Positive correlations were observed with EC, OC, Zn, Pb and Cr, and weak negative correlation with Cd ($r = -0.05$) and a strong negative correlation with Co ($r = 0.41$).

Effect of Cd: Amount of Cd lies between 24.5 mg/kg and 71.5 mg/kg. Sample S4 gets a higher value (71.5 mg/kg), and sample S7 a lower value (24.5 mg/kg). The positive correlation was obtained with EC, OC, Zn, Pb and Co whereas a negative correlation with pH and Cr.

Effect of Cr: Chromium ranges from 0.01 mg/kg to 41.4 mg/kg. Sample S6 has a least value of 0.01 mg/kg,

and sample S2 the highest value. The positive correlation obtained with pH, EC, OC and Cu but a negative correlation with Zn, Pb and Cd whereas no correlation with Co.

Effect of Co: The values of cobalt in samples vary between 10.5 mg/kg and 20.8 mg/kg. Sample S1 has a lower value of 10.5 mg/kg, and sample S6 a higher value (20.6 mg/kg). A slight positive correlation was observed with OC and a partial negative correlation with all parameters except Cr and no correlation with Cr. Abundance of Co in the soil acts as an inhibitor for soil biological activity (Zaborowska et al. 2016).

CONCLUSION

It can be thus concluded from the present study that the studied soil samples were slightly-moderately alkaline with moderate SOM. The heavy metal content in the soil is above the trace levels despite intensive anthropogenic practices which can be due to the sandy texture of soil and leaching of metals to lower ground layers. From the analysis of PI, geoaccumulation index and ecological risk factors, soils in all the locations are mainly contaminated and polluted by Cd followed by Cu and Zn. The remaining metals moderately influence soil pollution. Major soil pollution control precautions should be taken in stations 4, 5 and 6. Station 7 observed moderate soil contamination of all metals. Multivariate statistical methods applied in this study proved useful in the characterization of heavy metals sources in soils form APIIC zone. Zinc showed excessively high concentrations in the study area. The increasing orders of heavy metals in soils are Cr, Co, Pb, Cu, Cd and Zn. Element pairs such as Zn-Pb, Zn-Cu, Zn-Cd, Pb-Cu, Pb-Cd, Cu-Cr, Cd-Co and Cr-Co showed strong positive correlation indicating their association in the study area. Therefore, measures must be taken to ensure the adoption of more environmentally friendly practices.

REFERENCES

- Anyakora, C., Ehianeta, T. and Umukoro, O. 2013. Heavy metal levels in soil samples from highly industrialized Lagos environment. *Afr. J. Environ. Sci. Technol.*, 7(9): 917-924.
- Dara, S. S. and Mishra, D. D. 2006. *A Textbook of Environmental Chemistry and Pollution Control*. S. Chand Publishing.
- Dauda, M. S. and Odoh, R. 2012. Heavy metals assessment of soil in the vicinity of fuel filling station in some selected local government areas of Benue State, Nigeria. *Der Chemica Sinica.*, 3(5): 1329-1336.
- USDA 1993. *Soil Survey Manual*. Soil Survey Division Staff, Washington DC.
- Dheri, G. S. Brar, M. S. and Malhi, S. S. 2007. Heavy metal concentration of sewage-contaminated water and its impact on underground water, soil and crop plants in alluvial soils of northwestern India. *Commun. Soil. Sci. Plan.*, 38 (9-10): 1353-1370.
- EGASPIN 2002. *Environmental Guidelines and Standards for the Petroleum Industry in Nigeria*.
- Ferner, D. J. 2001. Toxicity, heavy metals. *Med. J.*, 2(5): 1.
- Fosmire, G. J. 1990. Zinc toxicity. *Am. J. Clin. Nutr.*, 51(2): 225-227.
- Guerra, F. Trevizam, A. R. Muraoka, T. Marcante, N. C. and Canniatti-Brazaca, S. G. 2012. Heavy metals in vegetables and potential risk for human health. *Sci. Agric.*, 69(1): 54-60.
- Hakanson, L. 1980. An ecological risk index for aquatic pollution control. A sedimentological approach. *Water Research*, 14(8): 975-1001.
- Iwegbue, C. M. A., Bassey, F. I., Tesi, G. O., Nwajei, G. E. and Tsafe, A. I. 2013. Assessment of heavy metal contamination in soils around cassava processing mills in sub-urban areas of Delta State, Southern Nigeria. *NJBAS*, 21(2): 96-104.
- Jacob, H. and Clarke, G. 2002. *Methods of Soil Analysis, Part 4, Physical Method*. Soil Science Society of America, Inc, Madison, Wisconsin, USA, 1692 p.
- Jolly, Y. N., Islam, A. and Akbar, S. 2013. Transfer of metals from soil to vegetables and possible health risk assessment. *Springer Plus*, 2(1): 385-391.
- Lacatusu, R. 2000. Appraising levels of soil contamination and pollution with heavy metals. *European Soil Bureau*, 4: 93-402.
- McIntosh, P.D. and Allen, R.B. 1993. Soil pH declines and organic carbon increases under hawkweed (*Hieracium pilosella*). *New Zealand Journal of Ecology*, 17(1): 59-60.
- Momodu, M. A. and Anyakora, C. A. 2010. Heavy metal contamination of groundwater: The Surulere case study. *Res. J. Environ. Earth. Sci.*, 2(1): 39-43.
- Müller, G. 1979. Schwermetalle in den sediments des Rheins-Veränderungseitt 1971. *Umschan*, 79: 778-783.
- Nelson, D. W. and Sommers, L. E. 1982. *Methods of Soil Analysis. Part 2*. pp. 539-579.
- Rajaganapathy, V., Xavier, F., Sreekumar, D. and Mandal, P. K. 2011. Heavy metal contamination in soil, water and fodder and their presence in livestock and products: A review. *JEST*, 4(3): 234-249.
- Rattan, S. S. 2005. *Theory of Machines*. Tata McGraw Hill Publishing Company Limited. New Delhi.
- Tomlinson, D. L., Wilson, J. G., Harris, C. R. and Jeffrey D. W. 1980. Problems in the assessment of heavy-metal levels in the estuaries and the formation of pollution index. *Helgol. Mar. Res.*, 33, 566-575.
- Tyler, G., Pålsson, A. M. B., Bengtsson, G., Bååth, E. and Tranvik, L. 1989. Heavy-metal ecology of terrestrial plants, microorganisms and invertebrates. *Water. Air. Soil. Poll.*, 47(3-4): 189-215.
- Ubwa, S. T., Atooo, G. H., Offem, J. O., Abah, J. and Asemave, K. 2013. Effect of activities at the Gboko abattoir on some physical properties and heavy metals levels of surrounding soil. *IJC*, 5(1): 49.
- Underwood, E. J. 1977. Zinc in animal tissues and fluids. Trace elements in human and animal nutrition. In: *Trace Elements in Human and Animal Nutrition*, 4th Ed., pp. 196-242, Academic Press, New York
- Wen, X. and Allen, H. E. 1999. Mobilization of heavy metals from Le An River sediment. *Sci. Total. Environ.*, 227(2-3): 101-108.
- Zaborowska, M., Kucharski, J. and Wyszowska, J. 2016. Biological activity of soil contaminated with cobalt, tin, and molybdenum. *Environ. Monit. Asses.*, 188(7): 398.



Phytochemical Evaluation, FT-IR and GC-MS Analysis of Leaf Extracts of *Pergularia daemia*

M. Maheshwari[†] and P. Vijayarengan

Department of Botany, Annamalai University, Annamalai Nagar, Chidambaram, Tamil Nadu, India

[†]Corresponding author: M. Maheshwari; maheswarim1994m@gmail.com

Nat. Env. & Poll. Tech.
Website: www.neptjournal.com

Received: 03-04-2020

Revised: 23-04-2020

Accepted: 27-05-2020

Key Words:

Pergularia daemia
Phytochemical analysis
FT-IR analysis
GC-MS analysis

ABSTRACT

Pergularia daemia is traditionally used to treat various ailments like anthelmintic, antipyretic and expectorant and to treat infantile diarrhoea, malarial intermittent fever, asthma, mental disorder, toothache and cold. In the present study leaf extracts of *P. daemia* was subjected to qualitative phytochemicals, GC-MS and FT-IR analysis. The quantitative analysis of the leaves showed the presence of flavonoids, steroids, alkaloids, terpenoids, saponins, phenols, carbohydrates, amino acids, tannins and cardiac glycosides. The GC-MS study of methanol extract revealed 16 compounds. Some major compounds identified are 9-Octadecenoic Acid (E), Cis- Vaccenic Acid, N-Hexadecanoic Acid, 1- Dimethyl (Butyl), Silyl Oxy Butane along with other minor constituents. FT-IR analysis revealed the presence of 12 functional groups such as amines, alkanes, carbon dioxide and alkynes. The results suggested that *P. daemia* contains significant photo components and can be used as a source for many pharmacological studies and a curative for various ailments.

INTRODUCTION

All the natural products are a source of many traditional medicines and even some synthetic herbal medicines. In some parts of the world, herbal medicines are generally used to treat various diseases. In India, the medical systems using medicinal plants are Ayurveda, Siddha, Homeopathy, etc. to treat various ailments (Pushpangadan & Atal 1984). According to the World Health Organization (WHO), more than 80% of the world's population in poor and underdeveloped countries depends on traditional plant-based medicines for their primary healthcare needs (WHO 1993). The search for an alternative system of medicine having potential anti-inflammatory, antibiotic and other activities has gained importance considering the harmful side effects of modern synthetic medicines (Akharayi et al. 2012). India is very much rich with many species of plants having medicinal value. These plants are broadly used by the society as herbal medicines or as pharmaceutical preparation of modern medicine. Since herbal medicines are prepared from materials of plant origin, they are prone to contamination, deterioration and variation in composition.

Pergularia daemia Forsk is a perennial twinning plant belonging to the family Asclepiadaceae. This plant is widely distributed in the roadside of India and also in the tropical and subtropical regions. The entire plant possesses high medicinal value and traditionally used in treating various ailments for human beings. Some people used this plant to treat jaundice.

This plant is used as laxative, anthelmintic, antipyretic, expectorant and also in infantile diarrhoea. The extract of the leaves of *P. daemia* is applied to treat rheumatic swelling and also used in the preparation of purgative medicinal oil given for amenorrhoea, rheumatism and dysmenorrhoea. The bark of the root is also used as a purgative in rheumatic cases (Wealth of India 1966). The root of this plant is used to treat anaemia, mental disorders, leprosy, piles, uterine and menstrual disorders (Yoganasimhan 2000). The whole plant is employed for pulmonary afflictions, biliousness, asthma, piles, cough, leprosy and syphilis, and leaves are used in infantile diarrhoea, and as an expectorant, uterine tonic and emetic (Mohammed et al. 2004). Therefore, the present study aimed to document the phytochemicals using GC-MS and FT-IR in the leaf extract of *P. daemia* to explore its chemical resource.

MATERIALS AND METHODS

Collection of Plant Materials

Pergularia daemia leaves were collected from Mayiladuthurai, Tamil Nadu during March 2018.

Preparation of the Extracts

The collected leaves were washed thoroughly in tap water and rinsed with distilled water to remove dust particles. Then it was surface sterilized with 10% sodium hypochlorite solution

and rinsed with sterile distilled water. After that, it was shade-dried at room temperature for 15 days and then the leaves were packed in brown cover and kept in an oven at 60°C for an hour to make grinding easy. After an hour, the leaves were ground using an electrical blender. The powdered plant materials were then packed in a ziplock pouch. One hundred gram of powder was extracted with different organic solvents like hexane, acetone, ethyl acetate and methanol for 8 hours using the Soxhlet apparatus and solvent was evaporated under vacuum in a rotary evaporator (Heidolph, Germany) and the dried powder was stored at 4°C for further use.

Phytochemical Analysis

The different extracts of *P. daemia* were used for qualitative phytochemical analysis for alkaloids, flavonoids, terpenoids, steroids, phenols, saponins, cardiac glycosides, tannin, carbohydrates and amino acids (Trease & Evans 1989, Harborne 1973).

Test for flavonoids: To 2 mL of crude extract taken in a test tube, 3-4 drops of 1% sodium hydroxide solution was added. Development of intense yellow colour, which becomes colourless on the addition of dilute hydrochloric acid, indicates the presence of flavonoids.

Test for steroids: Two mL of extract was dissolved in 2 mL of chloroform and filtered. The filtrate was treated with 2 mL of concentrated sulphuric acid, shaken and allowed to stand. Development of a golden yellow colour indicates the presence of steroids.

Test for alkaloids: Two mL of extract was stirred with 2 mL of 2N hydrochloric acid and Mayer's reagent (1.36 g mercuric chloride and 5 g of potassium iodide) and 100 mL of distilled water was added to it. Development of yellow coloured precipitate indicates the presence of alkaloids.

Test for terpenoids: Two mL of extract was dissolved in 2 mL of distilled water and treated with a few drops of copper acetate solution. Development of green colour indicates the presence of terpenoids.

Test for saponins: Two mL of extract was diluted with distilled water and made up to 20 mL. This was shaken in a graduated cylinder for 20 minutes. Development of 1 cm thick layer of foam indicates the presence of saponins.

Test for phenols: Two mL of extract was treated with a few drops of ferric chloride solution. Development of green colour indicates the presence of phenols.

Test for carbohydrates: Two mL of extract was dissolved in 5 mL of distilled water and filtered. Filtrate was treated with a few drops of alcoholic α -naphthol solution in a test tube. Development of the violet ring at the junction indicates the presence of carbohydrates.

Test for amino acids: 2 mL of extract was treated with a few drops of concentrated nitric acid. The colour change from green to yellow shows the presence of amino acids.

Test for cardiac glycosides: Extract was hydrolysed with dilute HCl and then subjected to test for glycosides. 2 mL of the extract was treated with ferric chloride solution and immersed in a water bath for 5 minutes. The mixture was cooled and extracted with equal volumes of benzene. The layer of benzene was separated and treated with ammonia solution. The colour change from green to pink colour in the ammonia layer indicates the presence of cardiac glycosides.

Test for tannins: Two mL of crude extract in 1% gelatin solution containing sodium chloride was added. Development of white colour precipitate indicates the presence of tannins.

Fourier Transform Infra-Red Spectra

IR spectrum was recorded in a spectrophotometer (Thermo Scientific NICOLET-iS5). The active principle was mixed with KBr and pellet technique was adopted to record the spectra.

Gas Chromatography-Mass Spectrometry (GC-MS) analysis

The GC-MS analysis was carried out using Varian 3800 gas chromatography equipped with mass selective detector coupled to front injector type 1079. The chromatography was fitted with DB 5 MS capillary column (30 m \times 0.25 mm i.d., film thickness μ m). The injection temperature was set at 280°C, and the oven temperature was initially at 45°C then programmed to 300°C at the rate of 10°C/min and finally held at 200°C for 5 min. Helium was used as a carrier gas with a flow rate of 1.0 mL/min. One microliter of the sample (diluted with acetone 1:10) was injected in the split mode in the ratio of 1:100. The percentage of the composition of the compound was calculated by the GC peak areas. GC-Mass spectrometry (GC-MS) analysis of compounds was performed using Varian 3800 gas chromatography equipped with Varian 1200 L single quadrupole Mass spectrometer. GC conditions were the same as reported for GC analysis and the same column 1000 amu. The compounds were identified based on the comparison of their retention indices (RI), retention time (RT), mass spectra of WILEY, NIST library data of the GC-MS system and literature data (Adams 2009).

RESULTS

The preliminary phytochemical screening of the leaf extracts of *P. daemia* shows to contain flavonoids, steroids, alkaloids, terpenoids, saponins, phenols, carbohydrates, amino acids,

tannin and cardiac glycosides in all the extracts (Table 1). The methanol extracts yielded a very high number of secondary metabolites when compared to other extracts. The phytochemicals identified in different extracts were in the order methanol (7 compounds), acetone (5 compounds), ethyl acetate (4 compounds) and hexane (3 compounds). The principal functional groups present in the methanolic leaf extract of *P. daemia* were identified by FT-IR analysis and presented in Table 2. Absorbance and functional groups are interpreted as follows, 3385.04 cm^{-1} indicate N-H stretching, 2922.55, 2854.24 cm^{-1} indicate C-H stretching; 2318.57 cm^{-1} indicate the O=C=O stretching; 2242.64 cm^{-1} indicate C \equiv C stretching; 1711.78 cm^{-1} indicate C=O stretching; 1631.88 cm^{-1} indicate C=C stretching; 1453.19 cm^{-1} indicate C-H bending; 1370.51 cm^{-1} indicate O-H bending; 1241.95, 1168.56 cm^{-1} indicate C-O stretching and 1030.27 cm^{-1} indicate S=O stretching. Some major compounds were amine, alkane, carbon dioxide, alcohol

and alkyl aryl ether. The FT-IR spectrum of *P. daemia* is shown in Fig. 1.

The GC-MS analysis of methanol extracts of leaves of *P. daemia* was analysed and represented in Table 3. From the GC-MS study, a total of 16 major compounds were identified. Mass spectrum of the bioactive compounds with their retention time (RT) is shown in the (Fig. 2). Some major compounds were 9-octadecenoic acid (E), cis-vaccenic acid, n-hexadecanoic acid, 1-dimethyl (butyl), silyl oxy butane, etc. The name, molecular weight, molecular formula and chemical structure of the compounds were noted.

DISCUSSION

The medical system deeply depends upon medicinal plants and their products for the production of drugs. The world requires a new source of crude drugs because due to over-exploitation and climatic changes, the currently used source

Table 1: Preliminary phytochemical analysis of leaf extracts of *Pergularia daemia*.

Phytochemical compounds	Hexane	Acetone	Ethyl acetate	Methanol
Flavonoids	+	++	-	+++
Steroids	-	-	+	-
Alkaloids	+	+	-	+
Terpenoids	-	+	-	++
Saponins	-	-	-	+
Phenols	-	-	+	-
Carbohydrates	+	++	-	+++
Amino acids	-	+	-	-
Tannin	-	-	+	++
Cardiac Glycosides	-	-	+	+

(+++)= More strong, (++)= Strong, (+)=Positive (Present), (-)= Negative (Absent)

Table 2: FT-IR absorption and functional group of leaves of *Pergularia daemia*.

Sl.No.	Wave Number	Molecular motion	Functional group	Absorption intensity
1	3385.042	N-H Stretching	Amine	Strong
2	2922.553	C-H Stretching	Alkane	Medium
3	2854.249	C-H Stretching	Alkane	Medium
4	2318.570	O=C=O Stretching	Carbon Dioxide	Strong
5	2242.643	C \equiv C Stretching	Alkyne	Weak
6	1711.785	C=O Stretching	Carboxylic Acid	Strong
7	1631.884	C=C Stretching	Alkene	Medium
8	1453.198	C-H Bending	Alkane	Medium
9	1370.512	O-H Bending	Alcohol	Medium
10	1241.957	C-O Stretching	Alkyl Aryl Ether	Strong
11	1168.569	C-O Stretching	Ester	Strong
12	1030.271	S=O Stretching	Sulfoxide	Strong

Table 3: GC-MS analysis of methanolic leaf extract of *Pergularia daemia*.


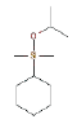
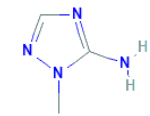

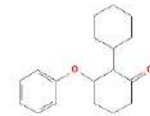
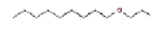
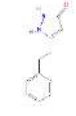
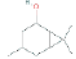

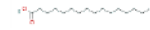



Peak No.	Rt	Chemical compound	Molecular formula	Molecular weight (g/mol)	Peak area %	Chemical structure
1	2.134	Tricyclon [4.2.1.1(2,5)] Decan-9-One Oxime	C ₁₀ H ₁₅ NO	165.23	3.53	
2	3.983	Cyclohexyldimethylisopropoxysilane	C ₁₁ H ₂₄ OSi	200.39	1.11	
3	4.470	1H-1,2,4-Triazol-5-Amine, 1-Methyl-	C ₃ H ₆ N ₄	98.11	3.99	
4	5.491	4-Pyridinemethanol, Hexahydro-. Alpha., Alpha.-Dimethyl-	C ₈ H ₁₇ NO	143.23	1.53	
5	5.595	[1,1'-Bicyclohexyl]-2-One	C ₁₂ H ₂₀ O	180.29	0.90	
6	6.077	N-Propyl Nonyl Ether	C ₁₂ H ₂₆ O	186.33	1.28	
7	9.812	5-Phenethyl-2H-Pyrazol-3-ol	C ₁₁ H ₁₂ N ₂ O	188.23	3.67	
8	9.916	5-Caranol, Trans, Trans-(+)-	C ₁₀ H ₁₈ O	154.24	1.23	
9	10.285	N-Hexadecenoic Acid	C ₁₆ H ₃₂ O ₂	256.42	3.18	
10	11.741	N-Hexadecanoic Acid	C ₁₆ H ₃₂ O ₂	256.42	16.90	
11	12.034	Hexadecanoic Acid, Ethyl Ester	C ₁₈ H ₃₆ O ₂	284.5	1.69	
12	13.065	9-Octadecenoic Acid, (E)-	C ₁₈ H ₃₄ O ₂	282.46	27.80	
13	13.433	Cis-Vaccenic Acid	C ₁₈ H ₃₄ O ₂	282.5	21.52	

Table Cont....

Peak No.	Rt	Chemical compound	Molecular formula	Molecular weight (g/mol)	Peak area %	Chemical structure
14	16.393	Quinoline, 1,2,3,4-Tetrahydro-1-((2-Phenylcyclopropyl) Sulfonyl)-, Trans-	C ₁₀ H ₁₉ No ₂ S	147.21	3.49	
15	17.660	1-Dimethyl(Butyl) Silyloxybutane	C ₁₀ H ₂₄ OSi	188.38	4.61	
16	17.792	Silane, Dimethyl(Dimethyl(3-Phenylpro-2-Enyloxy) Silyloxy) (3-Phenylpro-2-Enyloxy)-	C ₂₂ H ₃₀ O ₃ Si ₂	398.6	3.58	

Agilent Resolutions Pro

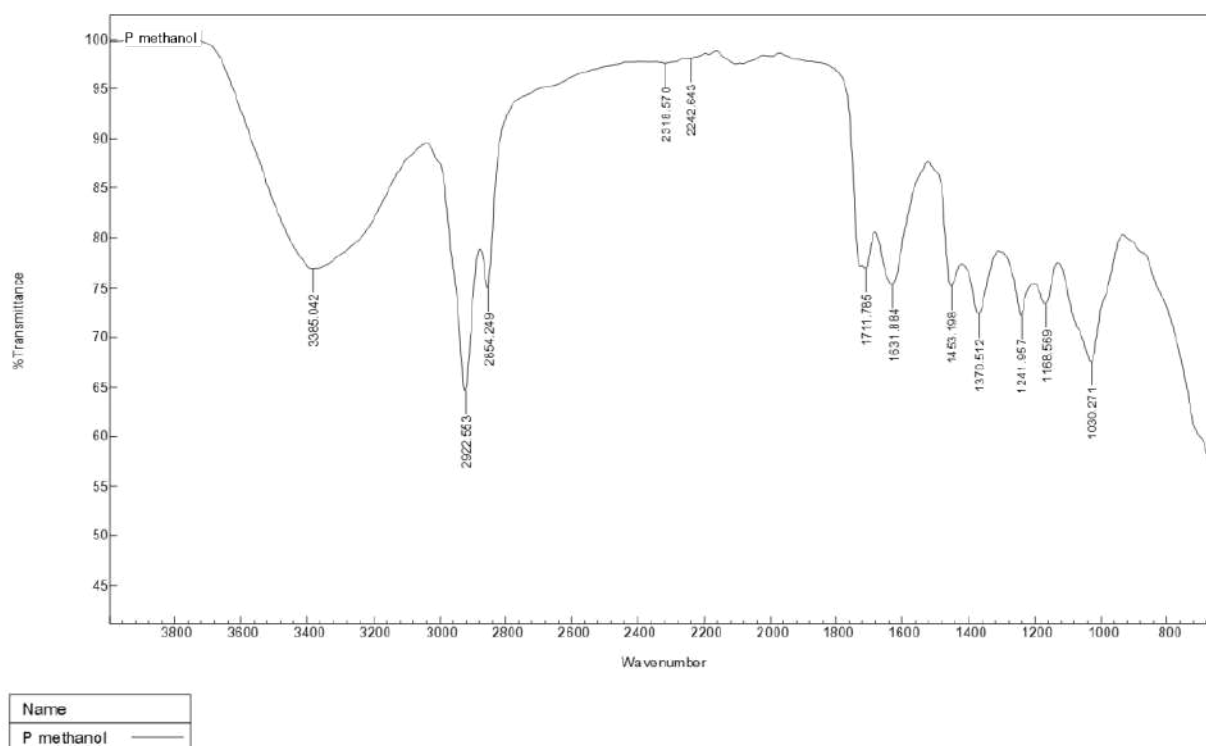


Fig. 1: FT-IR absorption and functional group of leaves of *Pergularia daemia*.

plants become threatened. Phytochemicals such as alkaloids have hypoglycaemic activities (Cherian & Augusti 1995a). The root of *P. daemia* has a high amount of tannins and plays a major role in the treatment of intestinal disorders like diarrhoea and dysentery (Akinpelu & Onakoya 2006). *P. daemia* contains alkaloids, tannins, flavonoids, cardiac glycoside and terpenes. Phytol is one among sixteen compounds of the present study. Phytol is important acyclic diterpene alcohol that is a precursor for vitamins E and K. Similarly, the

presence of phytol was observed in the leaves of *Lantana camara* (Mittal et al. 1962) and *Mimosa pudica* (Sridharan et al. 2011). The results of the present study by GC-MS confirmed the presence of bioactive compounds which may be responsible for their medicinal values and physiological activities (Ismaila et al. 2011). The ethanolic extracts of *P. daemia* possess significant hepatoprotective effect in carbon tetrachloride (CCl₄) model of intoxication in rats (Sureshkumar & Mishra 2006). Saponins, terpenoids, flavonoids

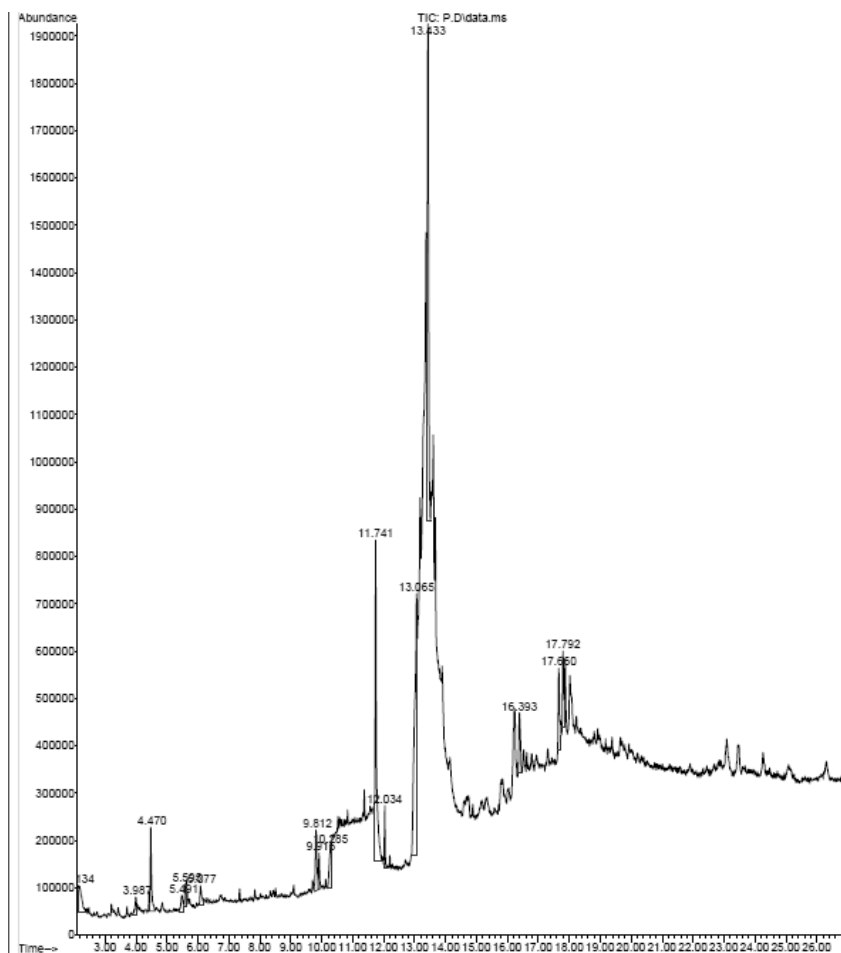


Fig. 2: GC-MS Analysis of Methanolic extract of leaves of *Percularia daemia*.

and alkaloids have anti-inflammatory properties whereas flavonoids, tannin and alkaloids show hypoglycaemic activities (Cherian & Augusti 1995b). Terpenoids are used to strengthen skin, increase the concentration of antioxidants in wounds and restore inflamed tissues by increasing blood supply. Alcohol extract of the leaves of *Kigelia pinnata* has earlier been reported for the presence of hexadecanoic acid compound (Grace et al. 2002) and it is also reported in *Melissa officinalis* (Kumar & Manimegalai 2008, Sharafzadeh et al. 2001). These reports are in accordance with the result of this study. Further investigation is needed to identify the pharmacological importance and phytochemistry of the leaves of *Percularia daemia*.

CONCLUSION

This study documents the phytochemical constituents of leaf extract of *P. daemia* through quantitative analysis, GC-

MS, and FTIR. GC-MS analysis revealed the presence of 16 compounds and FT-IR with 12 major functional groups. Further, this study suggests *P. daemia* can be considered as a potential candidate for extraction pharmacologically active compounds.

ACKNOWLEDGEMENT

We would like to thank the Instrumentation Centre of Ayya Nadar Janaki Ammal College (Autonomous) Sivakasi for their immense help to make GC-MS analysis of the extract and also thankful to Department of Chemistry, Annamalai University for FT-IR Spectral Analysis.

REFERENCES

- Adams, R.P. 2009. Identification of essential oil compounds by Gas Chromatography Mass Spectrometry, 4th Edn. Allured Publishing Corporation, Carol Stream, IL, USA.

- Akharayi, C., Bobeye, B. and Adetuyi, F.C. 2012. Antibacterial phytochemical and antioxidant activities of the leaf extracts of *Gliricidia sepium* and *Spathodeacm panulata*. W. Appl. Sci. J., 16(4): 523- 530.
- Akinpelu, A.D. and Onakoya, Z.T.M. 2006. Antimicrobial activities of medicinal plants used in folkore remedies in South Western. Afri. J. Biotech., 5: 1078-1081.
- Cherian, S. and Augusti, K. T. 1995a. Insulin sparing action of leucopelargonidin derivative isolated from *Ficus bengalesis* L. Indian J. Exp. Biology, 33: 608-611.
- Cherian, S. and Augusti, K. T. 1995b. Insulin sparing action of leucopelargonidin derivative isolated from *Ficus bengalesis* L. Indian J. Exp. Biology, 33: 608-611.
- Grace, O.M., Light, M.E., Lindsey, K.L., Moholland, D.A. and Staden, J.V. 2002. Antibacterial activity and isolation of antibacterial compounds from fruit of the traditional African medicinal plant, *Kigelia africana*. Afr. J. Bot., 68: 220-222.
- Harborne, J.B. 1973. Methods of plant analysis. In: Phytochemical Methods. Chapman and Hall London. 74-79.
- Ismaila, Y., Sudi, Denban, M., Ksgbiyal and Emmanuel, K. 2011. Nutritional and physiological screening of *Senna obtusifolia* indigenous to Mubi, Nigeria. Adv. App. Sci. Res., 2(3): 432-437.
- Kumar, S.M. and Manimegalai, S. 2008. Evaluation of larvicidal effect of *Lantana camara* L. against mosquito species *Aedes aegypti* and *Culex quinquefasciatus*. Adv. Biol. Res., 2: 39-43.
- Mittal, O.P., Tammz, C. and Reichstein, T. 1962. The glycosides of *Pergularia extensa*. Helv. Chim. Acta. Glycosides and Aglycons, CCXXVII., 45: 907.
- Mohammed, S., Kasera, P. K. and Shula, J. K. 2004. Unexploited plants of potential medicinal value from the Indian Thar desert. Natural Product Radiance, 3: 69-74.
- Pushpangadan, P. and Atal, C.K. 1984. Ethno-medico-botanical investigations in Kerala: Some primitive tribals of Western Ghats and their herbal medicine. Journal of Ethnopharmacology, 11: 59-77.
- Sharafzadeh, S., MortezaKhosh-Khui and Javidnia, K. 2011. Aroma profile of leaf and stem of lemon balm (*Melissa officinalis* L.) grown under greenhouse conditions. Adv. Environ. Biol., 5: 547-550.
- Sridharan, S., Meenaa, V., Kavitha, V. and Nayagam, A.A.J. 2011. GC-MS study and phytochemical profiling of *Mimosa pudica* L. J. Pharm. Res., 4: 741-742.
- Sureshkumar, S.V. and Mishra, S.H. 2006. Hepatoprotective effect of extracts from *Pergularia daemia* Forsk. J. Ethnopharmacol., 107: 164-168.
- Trease, G.E and Evans, W.C. 1989. Pharmacognosy, 2nd Edn. Braille Tiridel and Macmillan Publishers 242-245.
- Wealth of India 1966. Raw Materials: VII. N-Pe Publications and Information, Directorate, CSIR, New Delhi, India.
- WHO, IUCN, WWF 1993. Guidelines on the Conservation of Medicinal Plants. Switzerland: IUCN Gland. Essential Medicines and Health Products Information Portal. 2-8317-0136-8.
- Yoganarasimhan, S. N. 2000. Medicinal Plants of India. Vol.1. Bangalore: Interline Publishing Pvt. Ltd. 405.



Regression Analysis of Normalized Difference Vegetation Index (NDVI) to Compare Seasonal Patterns and 15 Year Trend of Vegetation from East to West of Nepal

I. Sharma†, P. Tongkumchum and A. Ueranantasun

Prince of Songkla University, Thailand

†Corresponding author: Ira Sharma; irasg123@gmail.com

Nat. Env. & Poll. Tech.
Website: www.neptjournal.com

Received: 26-11-2019

Revised: 02-01-2020

Accepted: 01-03-2020

Key Words:

Cubic spline function
Vegetation patterns
Linear regression model
NDVI

ABSTRACT

Understanding the changing patterns and trend of vegetation is essential for its socio-environmental values. Normalized difference vegetation index (NDVI), a satellite based data obtained from Moderate Resolutions Imaging Spectro-radiometer (MODIS) were analysed. The data have a characteristic resolution of 250×250 m² and a 16-day composite period. They were ordered separately for each sample plot from east, centre and west of Nepal, for 15 years period, 2000 to 2015. MODIS, Land Surface Temperature (LST) data were used to identify unreliable NDVI values and hence eliminated. Also, the unusually fluctuating NDVI values during the rainy season were removed. A cubic spline function (for seasonal patterns), linear regression model (for NDVI trend) and generalized estimating equations (GEE for comparison of the changing trends) were the models used. The results showed a patterned annual seasonal vegetation and significant trends during the 15 years. Seasonal growth showed a peak in rainy season and trough in the winter season, with slight temporal variation among the areas with a characteristic shift of seasonal greening (start of greening) and browning (end of greening) from east to west of Nepal. The NDVI trend was significantly rising in eastern and western suburban areas while the central urban city had a significant decline. The temporal shift of start and end of the season from east to west can be of value to agriculturalists.

INTRODUCTION

The global climate has been changing and so is the trend of vegetation throughout the world. On one hand, vegetation is one of the prone factors to climate change while on the other hand, the vegetation helps to curb the effects of climate change effects. Moreover, changes in vegetation constantly help to change the climate factors at local or regional level (Meng et al. 2019, Zhu et al. 2016). Both increasing (Li et al. 2011, Liu et al. 2019) or decreasing patterns of vegetation have been observed in Asia. Apart from being geo giants of Asia, China and India represent as 'greening leaders' (Dunne 2019). Nepal, a small landlocked country between China and India, owns agriculture and forest as a major national economic resource and essentially needs to be aware of the changing trends of vegetation in the country.

The climate-changing factors, for instance, temperature and rainfall are mostly correlated with vegetation (Liu 2017, Anbazhagan & Paramasivam 2016, Kaufmann et al 2003). The changes in terrestrial vegetation can modify regional and global climate at diurnal, seasonal and long term (Bounoua et al. 2000). The Australian Government Bureau

of Meteorology (BoM 2014) suggests that the ability to link events in the natural world to a cycle that predicts seasonal changes is essential in the successful development of any community. These natural barometers are not uniform across the land but instead use the reaction of plants and animals to gauge what is happening in the environment. The cropping intensity (yield, the timing of plantation and harvest etc.) response to climate can help the understanding of proper growth, development and net production, which is practically influenced by previous year's knowledge in most of the developing countries (Cooper et al. 1997). To understand the climate and seasonal effect to vegetation and crops, its start and end are required to appropriately fix the calendar of vegetation or other crops cycles. This start or end of crop seasons would change by time and space, the knowledge of which can eventually yield better.

The spatio-temporal characteristics of remote sensing data are considered to be the primary advantage in environmental studies. MODIS is a sensor, fitted aboard the Terra and Aqua satellites by the National Aeronautics and Space Administration (NASA). It monitors environmental changes due to vegetation, temperature, droughts and flood on Earth

(NASA 2015). The Normalized Difference Vegetation Index (NDVI) is a data product from MODIS which is much common (NASA 2015, Eckert et al. 2014, Suepa et al. 2016) and more reliable (Yin et al. 2012) than other data types and much useful for local (Zhang et al. 2013), regional (Piao et al. 2011) or global scale (Liu 2017) study purpose. NDVI is a type of vegetation index which is dependent on the spectral behaviour of vegetation that characteristically absorbs in the red and blue wavelengths, reflects in the green wavelength, strongly reflects in the near-infrared (NIR) wavelength. Based on this principle, the data for vegetation index is calculated by the given equation (Ozyabuz et al. 2015).

$$\text{NDVI} = (\text{NIR} - \text{RED}) / (\text{NIR} + \text{RED})$$

Various previous studies, showing positive and negative trends of vegetation change, have commonly applied linear regression model (Kaufmann et al. 2003, Karnieli et al. 2010, Zhang et al. 2013). Moreover, a lot of variation does exist among their works regarding the methods, data types and management (Eckert et al. 2014, Piao et al. 2011, Chandola et al. 2010, Mishra & Chaudhuri 2015). Nonetheless, the analysis of the bulk data in smaller temporal and spatial sections for understanding the characteristics of vegetation (such as phenology, the start of the season (greening) and end of the season (browning)) in a particular locality in detail is entirely lacking. Also, the knowledge of intra-annual pattern together with the annual trend of vegetation in Nepal is still rare. Therefore, this study aims to assess the seasonal pattern and the trend of vegetation in Nepal from 2000 to 2015.

MATERIALS AND METHODS

This study was carried out in three purposively selected districts of Nepal, Dhankuta (East), Kathmandu (Center) valley and Surkhet (West). All the three are from the same geographical area, the hilly region, so that the other influencing factors would be least in effect, east - Dhankuta (27.15°N, 87.35°E), centre - Kathmandu (27.59°N, 85.39°E) and west - Surkhet (28.62°N, 81.88°E) of Nepal (Fig. 1). Department of Forest Resource and Survey (DFRS 2015), Department of Hydrology and Meteorology (DHM 2015) and National Population and Housing Survey 2011 (NPHS 2012) of the government of Nepal have reported that Dhankuta is an eastern suburban area of 892 km² with a population density of 183/ km². It has an annual temperature ranging from 14.6°C (January) to 24.9°C (April), annual rainfall 1,121 mm and has an average altitude of 1,192 m. Kathmandu is an urban area located in the central region, with the area of 899 km² and the population density of 4,416/ km². Its annual temperature ranges from 6.6°C (January) to 16.6°C (May), annual rainfall 1,667 mm and has an average altitude of 1,337 m. Surkhet is a suburban area located in the western region,

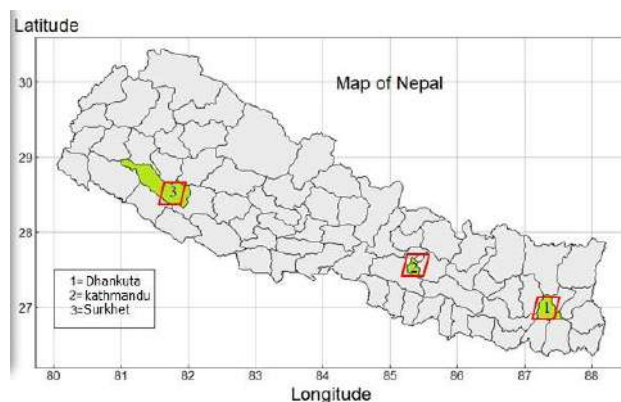


Fig. 1: Map of Nepal highlighting the three study areas.

with the area of 2,451 km² and the population density 143/ km². The annual temperature of this city ranges from 15.1°C (January) to 27.0°C (April), rainfall 1,392 mm (July) and has an average altitude of 875 m. The conventional seasons in the country were classified as summer, rainy and winter which falls from March to May, June to August and December to February respectively.

The NDVI data were downloaded from MODIS's website (ORNL DAAC 2015). Data were specified for a period from 2000, the starting point of MODIS service, to 2015. The NDVI data were observed in every 16-day interval period, there were around 23 observations every year, that made a total of 345 observations for 15 years. In each of the three selected areas, NDVI observation occurred in 6561 grids (81×81). The data for all three regions were retrieved by the same process.

The raw data of each NDVI grid were divided by 10000 to obtain the values ranging from -1 to +1. The negative values up to 0 correspond to water. The values from 0 to 0.1 mean soil, rocks or concrete, the snow land and barren land. Low positive values (0.2 to 0.4) represent shrubs and grassland. The value close to 1 (0.6 and above) means the forest (Weier & Herring 2000). A higher NDVI value represented the denser vegetation in the area.

The seasonal pattern of vegetation in an area does not vary much among its nearby grids unless the geography and climate features of the area is hugely changed. That is why, only the central position grid, out of 6561, is chosen for analysing the seasonal pattern of vegetation. However, even though the trend of NDVI (that means the change of vegetation by time) can vary in the shorter distance too, all the grids are not considered for analysis to avoid the special correlation of the data. Hence, 49 locations were systematically selected to represent the whole study site. Then, from each location, four surrounding grids were chosen for

analysis and that made 196 grids altogether. The process was repeated for all three sites one by one.

Data Management

First of all, NDVI was plotted with respect to observation day as shown in Fig. 2 (a, b and c). Here, n is the total number of observations and every dot on each vertical grid line represents one observation value on the same recording period. Therefore, every vertical line on the x-axis displays 15 dots of NDVI values corresponding to a particular day in each of the 15 years. This plot starts from Julian day 1 and ends on day 365. The data structure needs to be further managed before going into analysis due to big data gaps (big NDVI gap between consecutive 8 day's series is practically impossible in case of vegetation growth) and unreliable values (all data of a particular satellite for a particular site would be unusual when temperature data is deemed faulty). Those data are believed to reduce the value outcome of the result and hence eliminated before analysis. From Fig. 2, cross marked points are the sparse NDVI data and blue dots are indicated to be unreliable values, all are eliminated before analysis.

The Statistical Methods

First of all, the NDVI data for the central grid were analysed to identify the annual seasonal pattern by using a cubic spline function. The form of the function is,

$$S_t = \alpha + bt + \sum_{k=1}^p c_k (t - t_k)_+^3 \quad \dots(1)$$

Where, S_t is the spline function, α , b and c_k are the parameters in the model. k is the location of knot. t denotes time in Julian day, that is, specified day of the year. $t_1 < t_2 < \dots < t_p$ are specified knots and $(t - t_k)_+$ means that $(t - t_k)$ is positive for $(t > t_k)$ and zero otherwise.

The data were, then, seasonally adjusted to stabilize the mean of the data. The seasonal adjustment was computed by,

$$y = (x - S_t) - \text{mean}(x - S_t) + \bar{x} \quad \dots(2)$$

Here, y is the seasonally adjusted NDVI, x is NDVI after removal of unreliable and doubtful values, S_t is the fitted values from cubic spline function and \bar{x} is the mean of x . The seasonally adjusted NDVI data were further used for analysing the time series trend in 15 years period.

Thereafter, the NDVI trends of selected 196 grids (out of $n=6561$) were identified by fitting linear models to seasonally adjusted data separately for each of 196 sample grids. The form of the linear model is,

$$y = \alpha + \beta t + \varepsilon \quad \dots(3)$$

Here, y is the seasonally adjusted NDVI, α is intercept

and β is the coefficient of t that represents observation day and ε is the error term.

However, the linear trend in each grid had a slight spatial correlation with the nearby grids. To tackle this problem, the Generalised Estimation Equations (GEE) were finally applied in this study. GEE is an extension of a linear model that is specially designed for correlated data (Liang & Zeger 1986). Furthermore, from the fitted models explaining the NDVI changes for all 15 years, it was difficult to distinguish the details of trends within this period. Therefore, the data were divided into three periods of 5 years each (2000-2004, 2005-2009 and 2010-2015) before fitting the model. At last, 95% confidence intervals were calculated for each sub-period and finally plotted to show the NDVI changes in three subsections of 15 years' period in each of the three study regions, separately. The GEE (Dormann et al. 2007) equation is illustrated as follows,

$$E(Y) = \mu = g^{-1}(T\gamma) \quad \dots(5)$$

Here, Y is a vector of seasonally adjusted NDVI, $E(Y)$ or μ is an expected value of Y , g^{-1} is an inverse link function, T is a matrix of observation days and γ is a vector of regression coefficients.

All data analysis and graphical displays were carried out using R Statistical Programming version 3.2.1 (R Core Team 2015).

RESULTS

Seasonal Pattern from Cubic Spline Function

Based on trial and error, eight knots (blue plus sign at the bottom of Fig. 2 a, b and c) were fixed at the position of 15, 40, 70, 120, 150, 200, 230 and 350 days of the year, to fit cubic spline function. The plots of fitted values from cubic spline function for east, centre and west areas showed that r squared increased from, respectively, 11, 15 and 58, (before) to 86, 50 and 82 after the data management process.

The NDVI in the east region extended from 4-8.5 (Fig. 2 a), meaning, it consists of shrubs as well as the densely wooded forest. The central region showed a narrow variation, from 0.65 to 0.90, indicated that vegetation is dominantly the big trees. The western region was identified with a range from 0.4 to 0.8 meaning the area equally had both shrub and trees.

Besides, a lot of variations in vegetation response towards the seasonal effects were observed. The three seasons in Nepal are broadly classified as, summer: March, day 61 to May, day 150, rainy: June, day 151 to August, day 240 and winter: December, day 360 to February, day 60. When the data were plotted from day 1 to day 365, the NDVI in each selected region [Fig. 2 (a-c)] showed the growth pattern with a peak

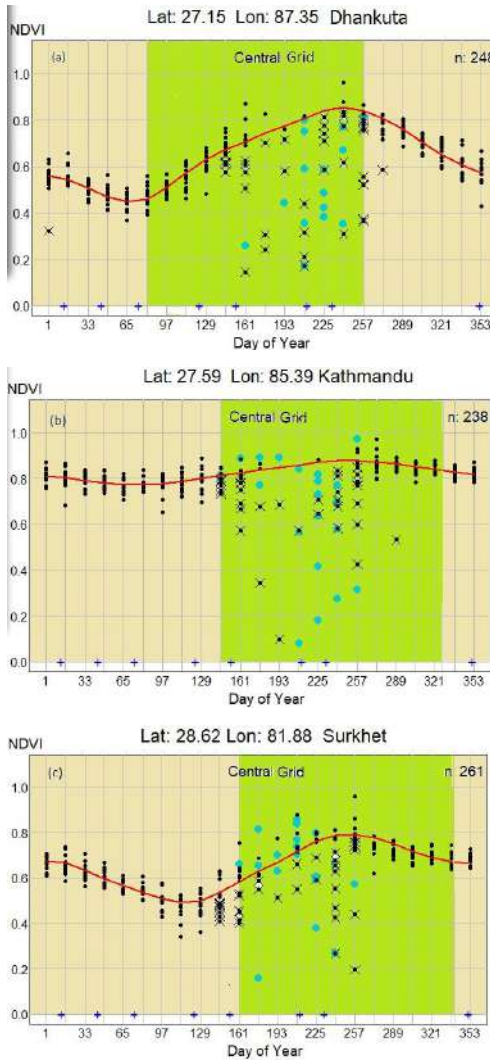


Fig. 2: Seasonal patterns of NDVI in (a) east, (b) centre and (c) west areas.

in the rainy season and gradually declined to trough in winter. The beginning of the season (greening) in east, centre and west took place in days 81, 97, 129 while the end of the season (browning) occurred on 257, 273, 273 days respectively. Here, both greening and browning are earlier in the east than the other areas. The result of seasonal patterns of vegetation in Kathmandu valley and Surkhet are similar with some difference in eastern Dhankuta. In former two areas, NDVI peaks in the rainy season and declines to trough in the winter season [Fig. 2(b) and 2(c)] where the greening is remarkably late by 60 to 70 days as compared to the eastern region. These graphs clear that start of the season (greening of vegetation) had a trend to move from east to the westward area and same was the case of browning.

Time Series Trends from Linear Model

The results from the linear regression models of 196 selected grids, were plotted separately for 15 years. In Fig. 3, only two grid plots were selected to represent increasing and decreasing trends from each of the three locations. The green horizontal line across the graph explains the NDVI trend for 15 years period the annual seasonal fluctuation cycle of NDVI, derived from the spline function was added back to the plot and shown in the red line. In Fig. 3 to Fig. 5, black dots are data points plotted year wise. The cross dots are the data eliminated at the time of cubic spline fit. The increasing or decreasing trend (Inc/dec) per decade and respective p-values from linear regression show how much vegetation has been changed from 2000 to 2015. Here, n represents the number of observations in each plot.

In the eastern region [Fig. 3 (a) and (b)], the total increasing trend was in 85.20% area and out of that 69.5% was found significant. The decreasing trend was in 14% with 47% being significant in the area. Hence, we can say that majority of vegetation was tending to rise in this area. The central region [Fig. 4 (a) and (b)] has a mixed form of result. The total rise was seen in 56.50% area and only 40.70% was significant. The decreasing trend was in 40.10% out of which 60.30% were significant. The result is almost balanced between increasing and decreasing trends. Therefore, the net gain or trend seemed to be balanced here. Finally, in the western

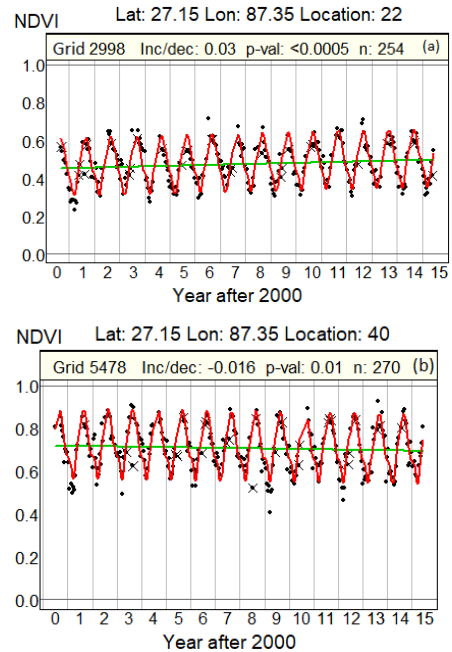


Fig. 3: Increasing (a) and decreasing (b) trend in the east, Dhankuta.

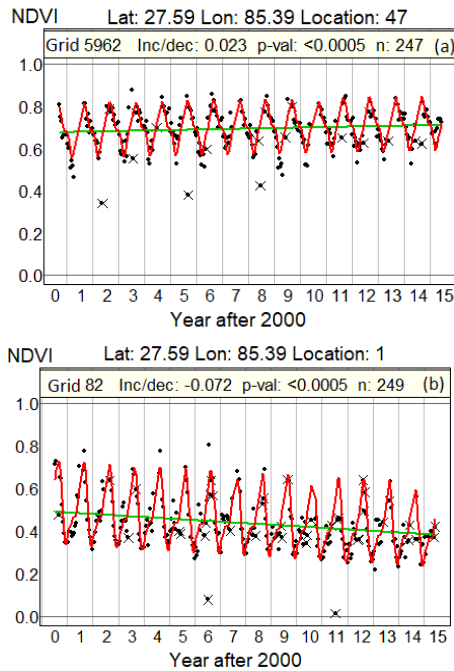


Fig. 4: Increasing (a) and decreasing (b) trends in central Kathmandu.

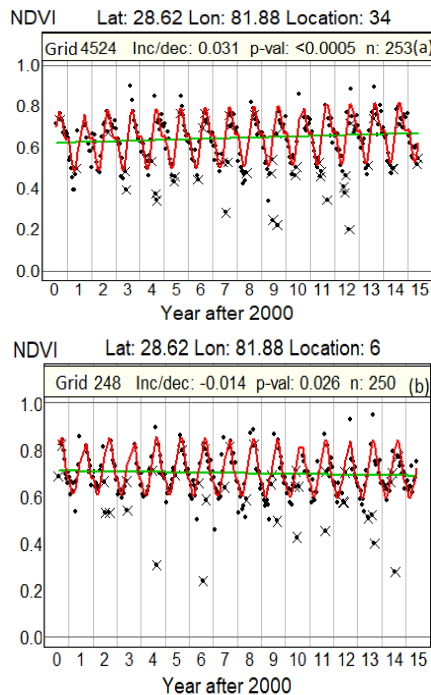


Fig. 5: Increasing (a) and decreasing (b) trends in Surkhet.

part [Fig. 5 (a) and (b)], the increase was seen in 81.63% of the area and 75% was significant. Also, out of the total decreasing trend, 80.76% was significant.

GEE and Confidence Interval Plot

All the 196 grids' data for 15 years, were stacked into one, separately for every area. The data were then divided into three time sections of five years each, they are, 2000-2004, 2005-2009 and 2010-2015. Finally, to take account of the autocorrelation of the data, GEE were fitted to each of five years of data in each site. A 95% CI plots were drawn from the mean of predicted values from the model to show vegetation trends in three time sections (Fig. 6). The red horizontal line is the level of no change of NDVI and the area above it indicates the increasing pattern and below it means the vegetation is decreasing state. The colourful vertical lines are CI plots of coefficients from the GEE model.

The results from CI plots are much interesting. The changes in vegetation at different time frames were compared among the groups using CI plots and the overall temporal change were compared among the three study areas.

East

The eastern area showed significant increasing trends of vegetation with the highest rate (0.022 per decade, p -value < 0.05) in the first period from 2000-2004 and the lowest rate (0.019 per decade, p -value < 0.05) in the latest phase, 2010-2015 (Fig. 6, green CI lines). Hence, the eastern area has an overall increasing trend but the rate of change is gradually declining. The recent trend showed that the mean increase in NDVI is 0.019 per decade.

Centre

The red CI lines (Fig. 6) all lying at or below 0 change line indicate that the net change is negative here. In the central area, the negative values of NDVI showed that vegetation is declining with a faster rate in the latest period (-0.006 per decade, p -value < 0.05).

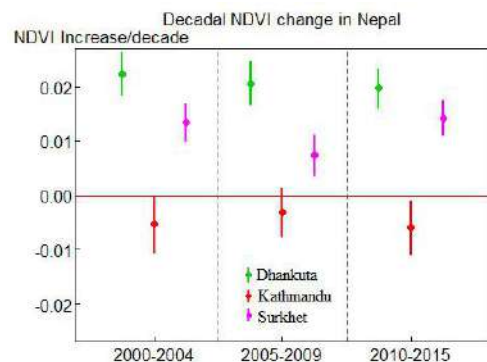


Fig. 6: Fifteen years trend of NDVI in the east (a), centre (b) and west (c) areas.

West

In the western area, the vegetation is significantly increasing in overall study period similar to in eastern area (Fig. 6, pink CI lines). However, this area showed a recent faster rate of increment as compared to the earlier periods. The recent five years showed that the mean increase rate is 0.014 per decade (p -value < 0.05).

DISCUSSION

The seasonal pattern of vegetation, in this study, showed that it grew the highest in the rainy season and gradually declined to the lowest in the winter season, probably due to defoliation and physiological dormancy. Minimum and maximum NDVI help us in identifying the intra-annual vegetation change (Liu 2017). This result is consistent with other studies in tropical or temperate vegetation (Suepa et al. 2016, Zang et al. 2016, Chen et al. 2014, Evrendilek & Gulbeyaz 2008, Yin et al. 2016). Also, it is scientifically proved that a relatively cooler air temperature reduces the plant physiology including its growth (Fitter & Hay 2002). The seasonal fluctuation of vegetation may occur due to several climatic factors like the temperature, rainfall, humidity and the seasons which this study does not explain. The east area is quicker to be affected by the seasonal change (both start of greening and browning). It might be due to its proximity of the area to the Bay of Bengal, where Nepal draws the monsoon from. That is why it receives earlier and more precipitation during rainy season resulting in a shift of seasonal changes from east to westward region. The phenological shift was studied (Suepa et al. 2016) in Southeast Asia but on the annual (temporal) basis. While in our study, the seasonal shift of vegetation pattern is intra-annual and spatial type. This result will particularly be helpful in the agricultural sector to understand the annual climate response of vegetation or crops, especially to understand the existing phenological characteristics of the area.

Actually, the vegetation trends have nothing to do with the monsoon and seasons. It reflects the direction of change over a period of time. This study identified that the annual vegetation trend is considerably rising in east and west areas of Nepal while the central Kathmandu showed a declining trend. The Global NDVI trend studied during 1982-2012 showed an increasing trend in many parts of the world including India and Southeast China (Liu et al. 2015). Nepal lies in between these two blocks and possibly have a similar increasing trend overall. But Kathmandu being a growing urban area and densely populated city, might have been affected by several local environmental factors to show a decline of vegetation and hence, detecting the local varia-

tion of vegetation change within a country is unique in this study.

The method of data management had contributed to obtaining much improved result from cubic spline to obtain the seasonal patterns and also the method can be applicable for analysing other noisy data. Here, the spline function along with linear regression and GEE models have been successfully used to analyse the seasonal pattern and the time series trends of NDVI.

However, this study is limited to local sites and study does not answer the overall factors contributing to these particular trends and patterns. This can be further worked out.

CONCLUSION

To sum up, this study shows the changes in NDVI in two ways. First, the seasonal pattern at a grid level, that clears the local level intra-annual change and second, the trend of vegetation in 15 years period. Moreover, a comparison of rates of changes within specified time segments can be made clear by CI plots. Eastern part of Nepal shows a wider range of vegetation with faster annual greening and browning than the rest of the two areas. The vegetation in Nepal has been increasing from 2000 to 2015 in sub-urban areas (Dhankuta and Surkhet) while it decreases in the urban region (Kathmandu). The study has academic implication in assessing the seasonal changes and time-series trends. It can also provide important information for urban planners, agriculturalists and the environmental experts. The study underpins the focus on analysing the potential reason behind this kind of NDVI changes in Nepal.

ACKNOWLEDGMENTS

This work had been supported by the Higher Education Research Promotion and Thailand's Education Hub of Higher Education Commission (grant number, TEH-AC 018/2015). We acknowledge the Department of Mathematics and Computer Science, Prince of Songkla University, for providing facilities for this study. We are grateful to Professor Don McNeil for his immense guidance during the study.

REFERENCES

- Anbazhagan, S. and Paramasivam, C.R. 2016. Statistical correlation between land surface temperature (LST) and vegetation index (NDVI) using multi-temporal Landsat TM data. *International Journal of Advanced Earth Science and Engineering*, 5(1): 333-346. DOI: 10.23953/cloud.ijaese.204.
- BoM 2014. Indigenous weather knowledge. Commonwealth of Australia, Bureau of Meteorology (ABN 92 637 533 532. URL: http://www.bom.gov.au/iwkw/climate_culture/Indig_seasons.shtml.

- Bounoua, L., Collatz, G. J., Los, S. O., Sellers, P. J., Dazlich, D. A., Tucker, C. J. 2000. Sensitivity of climate to changes in NDVI. *American Meteorological Society*, 13: 2277-2292.
- Chandola, V., Hui, D., Gu, L., Bhaduri, B. and Vatsavai, R. R. 2010. Using time series segmentation for deriving vegetation phenology indices from MODIS NDVI data. *IEEE International Conference on Data Mining Workshops*, pp. 202-208. DOI 10.1109/ICDMW.2010.143.
- Chen, B., Xu, G., Coops, N. C., Ciais, P., Innes, J., Wang, G., Myeni, R. B., Wang, Tongli., Krzyzanowski, J., Li, Q., Cao, L. and Liu, Y. 2014. Changes in vegetation photosynthetic activity trends across the Asia-Pacific region over the last three decades. *Remote Sensing of Environment*, 144: 28-41.
- Cooper, G., McGechan, M.B. and Vinten, A.J.A. 1997. The influence of a changed climate on soil workability and available workdays in Scotland. *J. Agric. Eng. Res.*, 68: 253-269.
- DFRS 2015. State of Nepal's Forest. Department of Forest Research and Survey, MFSC, Government of Nepal. Kathmandu. Retrieved from: www.dfrs.gov.np. Assessed on 20 January 2015.
- DHM 2015. Study of climate and climatic variables in Nepal. Ministry of Science, Technology and Environment. Department of Hydrology and Meteorology. Government of Nepal. Kathmandu. Retrieved from: www.dhm.gov.np. Accessed on 27 May 2017.
- Dormann, C.F., McPherson, J.M., Araujo, M.B., Bivand, R., Bolliger, J., Carl, G. and Davies, R.G. 2007. Methods to account for spatial autocorrelation in the analysis of species distributional data: A review. *Ecography*, 30: 609-628.
- Dunne, D. 2019. One-third of world's new vegetation in China and India, satellite data shows. *Eco business*, Singapore. <https://www.eco-business.com/news/one-third-of-worlds-new-vegetation-in-china-and-india-satellite-data-shows/>
- Eckert, S., Husler, F., Liniger, H. and Hodel, E. 2014. Trend analysis of MODIS NDVI time series for detecting land degradation and regeneration in Mongolia. *Journal of Arid Environments*, 113: 16-28.
- Evrendilek, F. and Gulbeyaz, O. 2008. Deriving Vegetation Dynamics of Natural Terrestrial Ecosystems from MODIS NDVI/EVI Data over Turkey. *Sensors*, 8: 5270-5302.
- Fitter, A. H. and Hay, R. K. M. 2002. *Environmental Physiology of Plants*, 3rd Edn. New York: Academic Press. ISBN 0-12-257766-3: 194-240.
- Karnieli, A., Agam, N., Pinker, R. T., Anderson, M., Imhoff, M. L., Gutman, G. G. and Panov, N. 2010. Use of NDVI and land surface temperature for drought assessment: Merits and limitations. *Journal of Climate*, 23: 618-633.
- Kaufmann, R. K., Zhou L., Myneni, R. B., Tucker, C. J., Slayback, D. and Shabanov, N. V. 2003. The effect of vegetation on surface temperature: a statistical analysis of NDVI and climate data. *Geophysical Research Letters*, 30(22): 1-4.
- Li, B., Yu, W. and Wang, J. 2011. An analysis of vegetation change trends and their causes in Inner Mongolia, China from 1982 to 2006. *Advances in Meteorology*. Article ID 367854. <http://dx.doi.org/10.1155/2011/367854>.
- Liang, K. and Zeger, S. L. 1986. Longitudinal data analysis using generalized linear models. *Biometrika*, 73: 13-22.
- Liu Y., Li, Y., Li, S. and Motesharrei, S. 2015. Spatial and temporal patterns of global NDVI trends: correlations with climate and human factors. *Remote Sensing*, 7(10): 13233-13250. DOI:10.3390/rs71013233.
- Liu, R.G. 2017. Compositing the minimum NDVI for MODIS data. *IEEE Transactions on Geoscience and Remote Sensing*, 55(3): 1396-1406.
- Liu, Y., Xue, Y., MacDonald, G., Cox, P. and Zhang, Z. 2019. Global vegetation variability and its response to elevated CO₂, global warming, and climate variability – a study using the offline SSiB4/TRIFFID model and satellite data. *Earth System Dynamics*, 10: 9-29. <https://doi.org/10.5194/esd-10-9-2019>.
- Meng, M., Huang, N., Wu, M., Pei, J., Wang, J. and Niu, Z. 2019. Vegetation change in response to climate factors and human activities on the Mongolian Plateau. *Peer J*. 7: e7735. doi: 10.7717/peerj.7735.
- Mishra, N. B. and Chaudhuri, G. 2015. Spatio-temporal analysis of trends in seasonal vegetation productivity across Uttarakhand, Indian Himalayas, 2000-2014. *Applied Geography*, 56: 29-41.
- NASA 2015. *Global Climate Change: Vital Signs of the Planet*. Available from: <http://climate.nasa.gov/effects> Accessed 31 December 2015.
- NPHS 2011. 2012. National Population and Housing Survey. Government of Nepal. Kathmandu.
- ORNL DAAC 2015. MODIS subset of NASA Earth Data. Available from http://daacmodis.ornl.gov/cgi-bin/MODIS/GLBVIZ_1_Glb/modis_subset_order_global_col5.pl Accessed 5 October 2015.
- Ozyabuz, M., Bilgili, C. and Salici, A. 2015. Determination of vegetation changes with NDVI method. *Journal of environmental protection and ecology*, 16(1): 264-273.
- Piao, S., Wang, X., Ciais, P., Zhu, B., Wang, T. and Liu, J. 2011. Changes in satellite-derived vegetation growth trend in temperate and boreal Eurasia from 1982 to 2006. *Global Change Biology*. 17: 3228-3239, DOI: 10.1111/j.1365-2486.2011.02419.
- R Core Team 2015. R: A language and environment for statistical computing. R Foundation for Statistical Computing, Vienna, Austria. URL <http://www.R-project.org/>.
- Suepa, T., Qi, J., Lawawirojwong, S. and Messina, J. 2016. Understanding spatio-temporal variation of vegetation phenology and rainfall seasonality in the monsoon Southeast Asia. *Environmental Research*, 147: 621-629.
- Weier, J. and Herring, D. 2000. *Measuring Vegetation (NDVI and EVI)*. NASA Earth Observatory. Available from: <http://earthobservatory.nasa.gov/Features/MeasuringVegetation/>. Accessed 20 December 2015.
- Yin, H., Udelhoven, T., Fensholt, R., Pflugmacher, D. and Hostert, P. 2012. How normalized difference vegetation index (NDVI) trends from advanced very high resolution radiometer (AVHRR) and système probatoire d'observation de la terre vegetation (SPOT VGT) time series differ in agricultural areas: an inner Mongolian case study. *Remote Sens.*, 4: 3364-3389. DOI:10.3390/rs4113364.
- Yin, G., Hu, Z. and Chen, X. 2016. Vegetation dynamics and its response to climate change in Central Asia. *Journal of Arid Land*, 8(3): 375-388.
- Zang, Y., Zhu, Z., Liu, Z., Zeng Z., Ciais, P., Huang, M. and Liu, Y. 2016. Seasonal and interannual changes in vegetation activity of tropical forests in Southeast Asia. *Agricultural and Forest Meteorology*, 224: 1-10.
- Zhang, Y., Gao, J., Liu, L., Wang, Z., Ding, M. and Yang, X. 2013. NDVI-based vegetation changes and their responses to climate change from 1982 to 2011: A case study in the Koshi River Basin in the Middle Himalayas. *Global and Planetary Change*, 108: 139-148.
- Zhu, Z., Piao, S., Myneni, R.B., Huang, M., Zeng, Z., Canadell, J.G. and Ciais, P. 2016. Greening of the earth and its drivers. *Nature Climatic Change*, 6: 791-795.



Plastic and Petroleum Hydrocarbon Degrading Potentials of Single and Mixed Bacterial Cultures Isolated from Garbage Areas of Darrang, Assam

R. S. Ahmed and M. D. Swargiary†

Department of Biosciences, Assam Don Bosco University, Tapesia Gardens, Sonapur-782 402, Assam, India

†Corresponding author: M.D. Swargiary; maitrayee.zoo@gmail.com

Nat. Env. & Poll. Tech.
Website: www.neptjournal.com

Received: 01-03-2020
Revised: 13-03-2020
Accepted: 27-05-2020

Key Words:

Bacterial isolates
Biodegradation
Plastics
Petroleum hydrocarbons

ABSTRACT

The ability of bacterial isolates viz., *Enterococcus cloacae* and mixed bacterial isolates, to degrade plastic was studied. The bacteria were isolated from waste effluent sites viz., industrial waste sites of Nilon's pickle factory, Dalgaoon and market waste sites of Balugaon vegetable market, Kharupetia, Assam. Plastic degradation was carried out at different time intervals within 15 and 30 days. It was observed that degradation increased with an increase in the time interval and hence effective observation was recovered after 30 days interval. Polythene bags showed maximum degradation by *Enterococcus cloacae* (85.25%). Plastic degradation was observed by Scanning Electron Microscope (SEM). In biodegradation of petroleum hydrocarbon, *Enterococcus cloacae*, *Pseudomonas putidia* and *Ralstonia pickettii* were found to degrade oil as well as they were able to grow in presence of petroleum hydrocarbons.

INTRODUCTION

Nowadays plastic pollution has become a threat to global ecology and pollution arises from both terrestrial and marine sources. Plastic pollution occurs mainly for two reasons, firstly due to the illegal or inappropriate dumping of domestic and industrial refuse and secondly due to the poorly contained static and transported waste (Webb et al. 2013). The main disadvantage of plastics is that they are resistant to biodegradation. Plastics and thermocols cause environmental pollution and have ecological damaging effects by getting accumulated in the environment as they are stable (Sharma et al. 2014). Biodegradation is a change in a material caused by the biological activity of microorganisms like bacteria, yeast, fungi and actinomycetes (Bhardwaj 2012, Sharma 2014). It has been documented that microbial biodegradation increases the rate of degradation of plastics without causing any harm to the environment (Yoon 2012).

Petroleum hydrocarbon contamination occurs due to accidents or leaks and accidental spills during the exploration, production, refining, transport, and storage of petroleum and petroleum products which drastically disturbs the marine life (Atlas 1981). Petroleum hydrocarbons generally spread to vast area which may span across hundreds of squares of miles (Mandri & Lin 2007). The degradation of petroleum hydrocarbons by microorganisms is a complex process which depends on nature and the amount of the hydrocarbons present (Swift et al. 1997). One of the important factors

which limit biodegradation of oil pollutants in the environment is their limited availability to microorganisms. Petroleum hydrocarbon compounds generally bind to the soil components which are difficult to be removed or degraded. Hydrocarbons are susceptible to microbial attack and individual microorganisms are capable of degrading only a limited number of crude oil and depend on the presence of metabolically diverse microbial communities. The bioremediation technologies applied to hydrocarbon-polluted environments highly depend on the biodegrading capabilities of native microbial populations or exogenous microorganisms used as inoculants. Oil biodegradation of subsurface does not require oxygen; it does require certain essential nutrients like nitrogen, phosphorus, potassium, etc. Microbes present in the soil and their catabolic activity play a vital role in degrading soil hydrocarbon contaminants like petroleum, crude oils, etc. Since the different microorganisms such as bacteria, fungi, protozoa, algae and actinomycetes present in the soil have varying capacity to degrade the petroleum hydrocarbons, the present study is aimed to study the degradation of plastics and petroleum hydrocarbon by Scanning Electron Microscope.

MATERIALS AND METHODS

Sample Collection

Plastic samples (polythene bags) were collected from the industrial garbage (waste disposable site dumped with a

polythene bag and plastic cup) from Nilon's pickle industrial area of Dalgaon, Darrang (Assam).

Surface Sterilization of Samples

The collected polythene bags were cut into 1×1 cm pieces and cleaned with tap water and surface sterilized with ethanol. It was then washed with distilled water, 0.1% mercuric chloride and again washed with distilled water (Begum et al. 2015).

Plastic Biodegradation Procedure

For biodegradation of plastic (polythene bags) minimal media (Alexander 1981, Atlas 1981, Ahmed et al. 2014, Akpe et al. 2015, Aneta et al. 2018), having a composition of 0.3g of NH_4NO_3 , 0.5g of K_2HPO_4 , 0.1g of NaCl, 0.02g of $\text{MgSO}_4 \cdot 7\text{H}_2\text{O}$ and 2g of agar was prepared. Then from the plates of pure culture bacterial colonies were picked up with the help of inoculating loop and streaked on minimal salt agar. Polythene bags of 1×1 cm were cut and placed on the minimal salt agar plates. The sterile polythene bags pieces were weighed and recorded before inoculating into the culture medium. The control was maintained with plastic (polythene bags) in the microbe-free medium. After 1 month incubation, the growth of microorganisms was observed on the polythene bags strips.

Determination of Dry Weight of Residual Polythene

To measure the biodegradation residual plastic, polythene bags were initially weighed. From the culture plate containing bacteria, after 1 month of incubation, and plastics were collected with a sterile loop, washed thoroughly with distilled water, shade dried and weighed again for final weight. It was calculated as follows (Usha et al. 2011):

$$\text{Weight loss \%} = \frac{(\text{Initial weight} - \text{Final Weight})}{\text{Initial weight}} \times 100 \quad \dots(1)$$

Screening of Polythene Biodegradation by Scanning Electron Microscope (SEM)

Three samples consisting of a mixed culture of bacterial strains that degrade plastic, the best plastic degrading strain, *Enterococcus cloacae* considered as the isolates of interest and control with only media was taken for further analysis through Scanning Electron Microscope (SEM). SEM analysis was carried out for obtaining more structural information about polythene strips. The samples were smeared on a small piece of adhesive carbon tape which was fixed on a brass stub and general hair dryer was used to dry the polythene samples. The samples were then subjected to gold coating using sputtering unit (Model: Q150RES) with 1×10^{-1} mB pressure and 2nm of resolution. The gold coated samples

were placed in SEM (Gemini) chamber and scattered electron images were recorded at different magnifications.

Biodegradation of Petroleum Hydrocarbons

Petroleum was collected from a petrol pump in Khanapara, (Meghalaya). 28g of nutrient agar (Hi media) was dissolved in 1000mL of distilled water and sterilized in an autoclave for 20 minutes at 121 psi. 100µL of overnight bacterial culture in nutrient broth (Hi media) was measured and poured in a sterile Petri plate, 100µL of petroleum hydrocarbon was then poured over the bacterial culture and in the same plate autoclaved and cooled nutrient agar was poured over both culture and oil. Immediately the plates were kept for incubation at 37°C for 3-4 days and bacterial growth was observed on the oil containing Petri plates.

RESULTS AND DISCUSSION

Biodegradation of polythene sheets was observed by using *Enterococcus cloacae* and a mixed population of bacterial isolates which were isolated from both the soil samples. After 30 days of incubation at 37°C, microbial growth (Fig. 1) was observed in polythene containing areas. Scanning Electron Microscope (SEM) analysis (Fig. 2 and Fig. 3) showed more degradation of polythene sheets, presence of roughness, degradation portions in *Enterococcus cloacae* cultured sheets when compared to the sheets which were cultured with mixed bacterial culture. eZAF Smart quadrant SEM results (Table 1 to Table 5) shows the amount of elements present on K shell and M shell as well as their weight percentage and atomic percentage. It was observed from the tables that the amount of elements in the control polythene sheet (Table 1) was less compared to the polythene sheets inoculated with *Enterococcus cloacae* (Table 2 and Table 3). The weight percentage and atomic percentage of elements present on the polythene sheet inoculated with mixed bacterial isolates (Table 4 and Table 5) were also found less as compared to the elements present on the polythene sheet taken as control (Table 1) and the polythene sheet inoculated with *Enterococcus cloacae* (Table 2 and Table 3).

In case of weight loss graph (Fig. 4) degradation was observed within 15 days in *Enterococcus cloacae* containing polythene sheet (59.02%) and in mixed culture containing sheet (51.22%). Thirty days time interval degradation studies (Fig. 4) showed that the plastic sheets were degraded by *Enterococcus cloacae* (85.25%) and mixed culture (73.18%) and there was weight loss whereas, in control sample without bacterial culture did not show any change in their weight and no roughness observed in SEM micrographs. However, in this study plastics took longer degradation by bacteria which needs further study because polythene sheet degradation

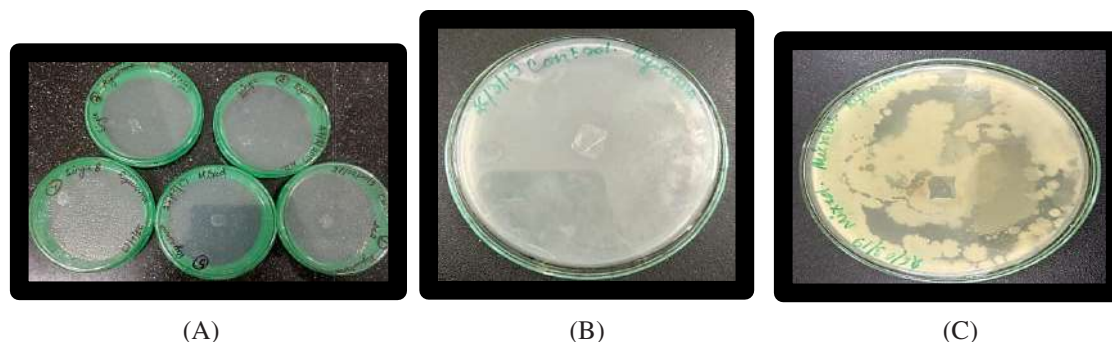


Fig. 1: (A) Day 1; Biodegradation of polythene sheets; (B) & (C) Day 30; Biodegradation of polythene sheets.

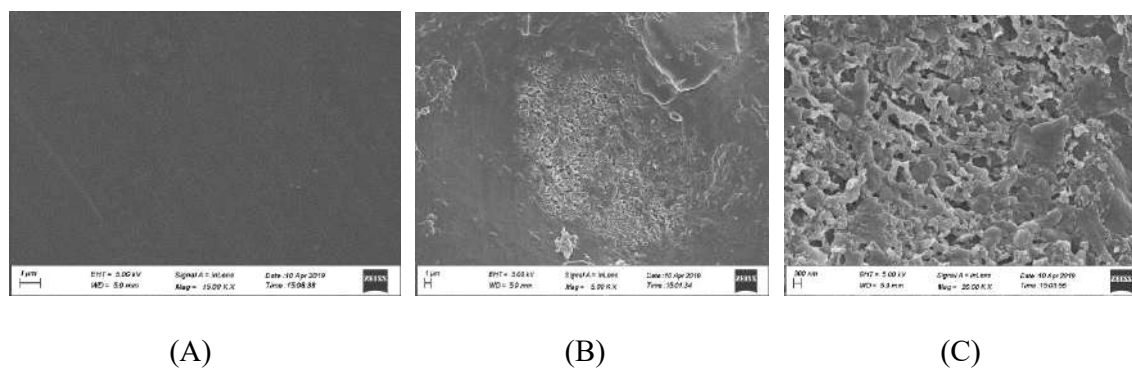


Fig. 2: SEM images of the polythene sheets after 30 days of the biodegradation at 28°C in the sterilized media inoculated with *Enterococcus cloacae*. (A) Control, (B) & (C) inoculated with *Enterococcus cloacae*.

Table 1: eZAF smart quant results selected area 1 (control polythene sheets).

Element	Weight %	Atomic %	Net Int.	Error %	Kratio	Z	A	F
C K	84.79	95.80	3931.82	4.60	0.6179	1.0471	0.6960	1.0000
O K	2.59	2.20	41.47	38.82	0.0044	0.9973	0.1694	1.0000
MgK	1.18	0.66	83.38	8.10	0.0084	0.9156	0.7741	1.0003
SiK	1.34	0.65	105.48	6.76	0.0112	0.8990	0.9277	1.0014
AuM	10.09	0.70	247.78	8.44	0.0767	0.5657	1.3449	0.9982

Table 2: eZAF smart quant results selected area 1 from polythene sheet 2 (incubated with *Enterococcus cloacae*).

Element	Weight %	Atomic %	Net Int.	Error %	Kratio	Z	A	F
C K	83.43	93.69	3683.25	4.53	0.6103	1.0430	0.7014	1.0000
O K	5.31	4.48	82.21	20.37	0.0091	0.9932	0.1733	1.0000
MgK	1.09	0.61	72.25	8.81	0.0077	0.9114	0.7706	1.0004
SiK	1.28	0.62	95.04	6.87	0.0107	0.8948	0.9276	1.0015
AuM	8.89	0.61	206.40	8.96	0.0673	0.5629	1.3483	0.9981

Table 3: eZAF smart quant results selected area 1 from polythene sheet 2 (incubated with *Enterococcus cloacae*).

Element	Weight %	Atomic %	Net Int.	Error %	Kratio	Z	A	F
C K	81.68	92.81	2780.06	4.68	0.5924	1.0476	0.6923	1.0000
O K	6.42	5.47	78.84	18.46	0.0113	0.9978	0.1761	1.0000
MgK	0.66	0.37	34.01	13.23	0.0046	0.9159	0.7632	1.0004
SiK	1.36	0.66	78.45	6.65	0.0113	0.8993	0.9256	1.0014
AuM	9.88	0.68	178.75	8.38	0.0750	0.5659	1.3439	0.9982

Table 4: eZAF smart quant results selected area 1 from polythene sheet 2 (incubated with mixed bacterial isolates).

Element	Weight %	Atomic %	Net Int.	Error %	Kratio	Z	A	F
C K	67.22	81.66	2460.77	6.04	0.4070	1.0660	0.5680	1.0000
O K	16.00	14.59	297.85	13.71	0.0331	1.0159	0.2037	1.0000
NaK	1.73	1.10	74.56	10.27	0.0093	0.9186	0.5852	1.0001
MgK	1.01	0.60	63.56	10.05	0.0067	0.9332	0.7190	1.0003
SiK	1.16	0.60	85.23	7.38	0.0096	0.9166	0.8957	1.0013
AuM	11.34	0.84	265.14	7.82	0.0865	0.5768	1.3181	1.0027
ClK	0.74	0.30	34.16	15.08	0.0059	0.8517	0.9389	0.9976

Table 5: eZAF smart quant results selected area 2 from polythene sheet 2 (incubated with mixed bacterial isolates).

Element	Weight %	Atomic %	Net Int.	Error %	Kratio	Z	A	F
C K	80.88	93.20	3437.52	4.76	0.5829	1.0540	0.6838	1.0000
O K	5.49	4.75	85.81	24.67	0.0098	1.0042	0.1773	1.0000
NaK	0.42	0.25	18.39	28.36	0.0024	0.9079	0.6178	1.0001
MgK	0.89	0.51	57.13	10.22	0.0062	0.9223	0.7584	1.0003
SiK	1.00	0.49	72.75	8.62	0.0084	0.9057	0.9197	1.0013
AuM	11.32	0.80	257.41	8.07	0.0861	0.5700	1.3368	0.9983

studies with plastic and thermocol by using microbes revealed that thermocol degrades faster as compared to plastics. This study conforms with studies of various workers (Begum et al. 2015, Dey et al. 2016), where polythene degradation by *Desulfotomaculum nigrificans* and *Pseudomonas alcaligenes* increased with incubation period and there was a dramatic increase in weight loss of polythene bags (Usha et al. 2011). Their studies also established that polythene bags and plastic cups incubated for 2, 4 and 6 months with the microbial culture of *Pseudomonas* sp., *Bacillus* sp., *Staphylococcus* sp., *Aspergillus nidulans*, *Aspergillus flavus*, *Streptomyces* sp. and *Pseudomonas* sp. degraded 37.09% of polythene and 28.42% of plastics in 6 months period. So, the results established in this study bear similarity as the elements which were present in the polythene sheets as depicted in Fig. 2 and Fig. 3 were also found to change after 30 days of incubation.

In presence of petroleum hydrocarbon and minimal required medium as depicted in Fig. 5, the growth of *Enterococcus cloacae* (isolated from soil sample 2), *Ralstonia pickettii* (isolated from soil sample 1) and *Pseudomonas putidia* (isolated from soil sample 1) was observed which indicates that the bacterial strains can consume oil and tolerate oil and grow in petroleum hydrocarbon containing media. The results in this study are thus in conformity with other workers (Horowitz et al. 1975, Latha & Kalaivani 2012, Marjadi & Dharaiya 2012, Vinothini et al. 2015), which established that *Bacillus subtilis* and *Pseudomonas aeruginosa* were able to degrade the oil. Earlier studies (Ahmed et al. 2014) showed that the biodegradation of crude oil is possible in contaminated water by local isolates of *Enterobacter cloacae* and observed that *E. cloacae* E1 degraded $70.00 \pm 0.40\%$ of the crude oil as well as (Dey

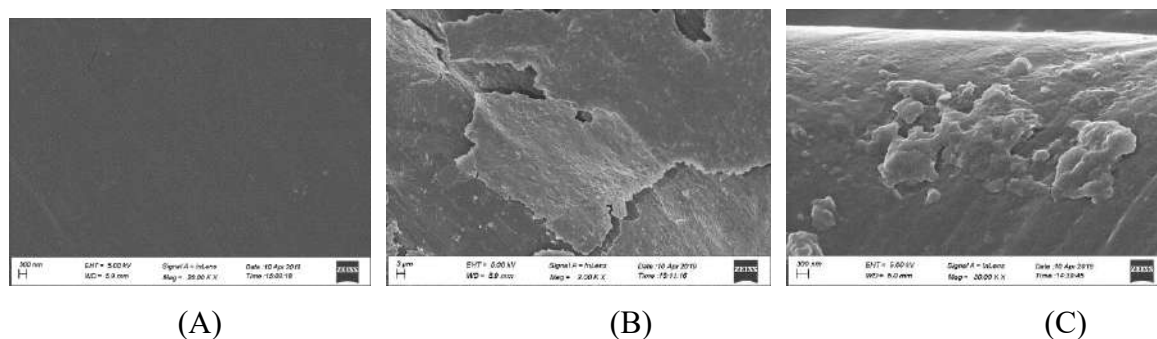


Fig. 3: SEM images of the polythene sheets after 30 days of the biodegradation at 28°C in the sterilized media inoculated with (B) & (C) mixed bacterial strains vs (A) control.

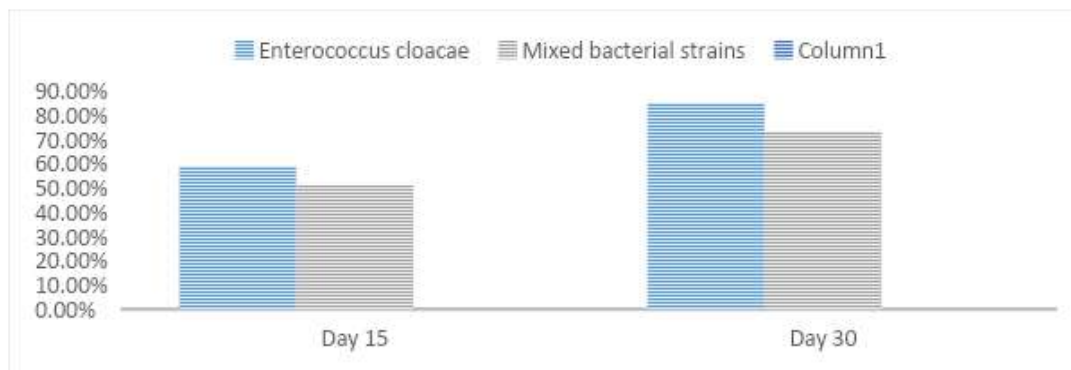


Fig. 4: Weight loss graph of bacterial degradation of polythene bag.

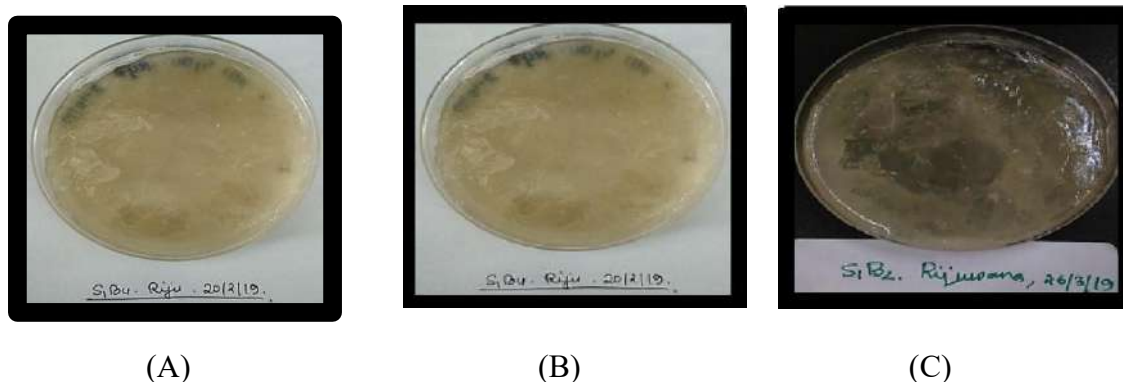


Fig. 5: Biodegradation of petroleum hydrocarbon. (A) The plate shows the growth of *Enterococcus cloacae*, (B) Plate shows the growth of bacterial strain *Ralstonia pickettii*, (C) Plate shows the growth of bacterial strain *Pseudomonas putida* in presence of petroleum hydrocarbon and minimal required medium.

et al. 2016) biodegradation of petroleum and crude oil by *Pseudomonas putida* and *Bacillus cereus*, which supports this study for biodegradation of petroleum hydrocarbon.

CONCLUSION

Garbage areas are mostly involved in environmental pollution and due to the presence of wastes like industrial, biological and household may contain many hazardous substances which can cause dangerous health issues in human. It also contains some non-degradable waste like plastics, polythene bags, petroleum hydrocarbons, etc. which play a major role in soil infertility. In this study bacteria viz., *Enterococcus cloacae*, *Pseudomonas putida* and *Ralstonia pickettii* were isolated from two garbage areas of Darrang, Assam during the period July 2018 to April 2019 and used for plastic and petroleum hydrocarbon degradation, and through Scanning Electron Microscope studies the polythene degradation was observed.

ACKNOWLEDGEMENT

Our sincere thanks to the Head, Department of Chemistry,

Gauhati University for the Scanning Electron Microscope facility.

REFERENCES

- Ahmed, A.W., Alzubaidi, F.S. and Hamza S.J. 2014. Biodegradation of crude oil in contaminated water by local isolates of *Enterobacter cloacae*. Iraqi Journal of Science, 55: 1025-1033.
- Akpe, R. A., Ekundayo, O. A., Aigere, P. S. and Ifeoma O. G. 2015. Bacterial degradation of petroleum hydrocarbons in crude oil polluted soil amended with cassava peels. American Journal of Research Communication, 3: 99-118.
- Alexander, M. 1981. Biodegradation of chemicals of environmental concern. Science, 211: 132-138.
- Aneta, K., Urbanek, R.W. and Miroczuk, A.M. 2018. Degradation of plastics and plastic-degrading bacteria in cold marine habitats. Applied Microbiology and Biotechnology, 102: 7669-7678.
- Atlas, R.M. 1981. Microbial degradation of petroleum hydrocarbons: an Environmental Perspective. Microbiological Reviews, 180-209.
- Begum, M. A., Varalakshmi, B. and Umamageswari, K. 2015. Biodegradation of polythene bag using bacteria isolated from soil. International Journal of Current Microbiology and Applied Sciences, 4: 674-680.
- Bhardwaj, H., Gupta, R. and Tiwari A. 2012. Microbial population associated with plastic degradation. Scientific Reports, 5: 272-274.
- Dey, S., Singh, A.K. and Singh, G. 2016. Biodegradation ability of bacteria

- on plastic and thermocol cups. *European Journal of Biomedical and Pharmaceutical Sciences*, 3: 10.
- Horowitz, A., Gutnick, D. and Rosenberg, E. 1975. Sequential growth of bacteria on crude oil. *Applied Microbiology*, 30(1): 10-19.
- Latha, R. and Kalaivani, R. 2012. Bacterial degradation of crude oil by gravimetric analysis. *Advances in Applied Science Research*, 3: 2789-2795.
- Mandri, T. and Lin, J. 2007. Isolation and characterization of engine oil degrading indigenous microorganisms in Kwazulu-Natal, South Africa. *African Journal of Biotechnology*, 6: 23-27.
- Marjadi, D. and Dharaiya, N. 2012. Bioprospecting and characterization of poly- β hydroxyalkanoate (PHAs) producing *Pseudomonas* spp. isolated from edible oil contaminated soil. *Research in Biotechnology*, 3: 1-8.
- Sharma, J., Gurung, T., Upadhyay, A., Nandy, K., Agnihotri, P. and Mitra, A.K. 2014. Isolation and characterization of plastic degrading bacteria from soil collected from the dumping grounds of an industrial area. *International Journal of Advanced and Innovative Research*, 3: 225-232.
- Swift, G., Domb, A. J., Kost, J. and Wiseman, D. M. 1997. Non-medical biodegradable polymers, environmentally degradable polymers. In: *Handbook of Biodegradable Polymers*, Amsterdam, Harwood Academic, pp. 473-511.
- Usha, R., Sangeetha, T. and Palaniswamy, M. 2011. Screening of polythene degrading microorganisms from garbage soil. *Libyan Agriculture Research Center Journal International*, 2: 200-204.
- Vinothini, C., Sudhakar, S. and Ravikumar, R. 2015. Biodegradation of petroleum and crude oil by *Pseudomonas putida* and *Bacillus cereus*. *Int. J. Curr. Microbiol. App. Sci.*, 4: 318-329.
- Webb, H.K., Arnott, J., Crawford, R.J. and Ivanova, E.P. 2013. Plastic degradation and its environmental implications with special reference to poly (ethylene terephthalate). *Polymers*, 5: 1-18.
- Yoon, M.G., Jeon, H.J. and Kim, M.N. 2012. Biodegradation of polyethylene by a soil bacterium and alkB cloned recombinant cell. *Journal of Bioremediation and Biodegradation*, 3(4): 1-8.



Kinetics of Adsorption of Reactive Red 120 Using Bentonite Modified by CTAB and Study the Effect of Salts

Hasan Fadhil Al Rubai †*, Ahmed Khudhair Hassan*, Muntadhar Salih Sultan** and Waleed Mohammed Abood***

*Ministry of Science and Technology, Environment and Water Directorate, Baghdad, Iraq

** Department of Chemistry, College of Science, University of Al-Mustansiriya, Baghdad, Iraq

***Ministry of industry, Industrial Research and Development Authority, Chemical Research Center, Baghdad, Iraq

†Corresponding author: Hasan Fadhil Al Rubai; hasanfalrubai66@gmail.com

Nat. Env. & Poll. Tech.
Website: www.neptjournal.com

Received: 07-12-2020

Revised: 24-02-2020

Accepted: 28-03-2020

Key Words:

Adsorption
Decolorization
Modified bentonite
Reactive red 120

ABSTRACT

Commercial bentonite was activated by aluminium hydroxide and then modified by cetyl trimethyl ammonium bromide (CTAB). The properties of modified bentonite were diagnosed using FTIR, X-ray diffraction and SEM. The adsorption of Reactive Red 120 (RR120) onto supported bentonite (B.A.CTAB) was investigated. The influence of various experimental parameters, such as temperature, initial concentration of dye, adsorbent dosages, initial pH and inorganic salts on RR120 removal was studied. The results showed that the optimum conditions for dye adsorption on modified bentonite are: temperature = 303K, pH = 3.5, contact time = 10 min, adsorbent dosage = 0.1 g and RR120 concentration 96 mg.L⁻¹, it achieved a removal efficiency of 91%. The pseudo-second-order version yields a higher fit to the experimental facts than the pseudo-first-order model. The consequences revealed that Langmuir version turned into extra appropriate to explain RR120 adsorption than the Freundlich model. Also, the thermodynamic function such as ΔG° , ΔH° and ΔS° was evaluated. The consequences of various inorganic anions (which included Cl⁻, SO₄²⁻, CO₃²⁻, and so forth.) on the removal activity of RR 120 adsorption on modified bentonite was examined.

INTRODUCTION

The rapid development in the field of industry with the increasing discharge of industrial wastewater has become a major problem in the pollution of the environment (Zhang & Qiu 2019). Azo dyes are commonly used in the textile industry. These dyes are highly poisonous and difficult to decompose and their presence in wastewater leads to high organic pollution content, deep colour and significant effluence on microorganisms (Qiu 2019). There are significant challenges to getting rid of this pollution to obtain high quality water. In recent years, many wastewater treatment technologies have evolved from textile industries including adsorption, advanced oxidation, electrochemical methods, coagulation, etc. (Suba & Rathika 2016); but prefer the method of adsorption because it is a low cost, easy to operate and highly efficient in dealing with various organic and inorganic pollutants (Fan et al. 2015). Many of the adsorbent materials are economically or easy to access and have been verified in many research studies such as ferric hydroxide (Konicki et al. 2015), blast furnace slag (Zhang et al. 2013), palygorskite (Giustetto & Wahyudi 2011), palm ash (Hameed et al. 2007), zeolite (Engin et al. 2008), and oxide tailings (Giri et al. 2011). Bentonite is

clay, in particular, constituted by way of the clay mineral montmorillonite (Lim et al. 2013). Montmorillonite surface is hydrophilic and has low affinity for no polar liquids (Orucoglu & Hacıyakupoglu 2015). The positive inorganic cation on the surface of bentonite can be replaced with organic matter that changes the properties of its surface from hydrophilic to hydrophobic bentonite to obtain a highly efficient rate of adsorption of organic pollutants such as dyes, phenols and other environmental contaminants (Yan et al. 2015). Cetyl trimethyl ammonium bromide (CTAB) is an organic material that can control the size and shape of alkaline particles and their properties and can reduce the surface tension of nanoparticles (Caglar et al. 2016). In this study, CTAB was chosen as a modified material for the bentonite surface to remove the dye solution. The factors influencing adsorption of a dye such as adsorbent dosage, solution pH, initial concentration of dye solution and temperature have been evaluated. Meanwhile, kinetics, adsorption isotherms, and thermodynamics were also investigated to explore the adsorption mechanism of RR120 onto B-A-CTAB. Also, the effects of various inorganic anions (such as Cl⁻, SO₄²⁻, CO₃²⁻, NO₃⁻, HPO₃⁻³) on the decolourization efficiency were studied.

MATERIALS AND METHODS

Materials

Reactive red 120 (RR 120) was obtained from Ciba uniqueness chemical compounds and used with none in addition purification. Cetrimonium bromide ($C_{19}H_{42}BrN$, CTAB) was obtained from Chuchardt (Germany). NaOH and H_2SO_4 have been used to modify the pH which changed into bought from Appli Chem (GmbH). $AlCl_3$, NaCl, Na_2SO_4 , Na_2CO_3 , $Na_2HPO_3 \cdot 5H_2O$ and $NaNO_3$ were obtained from Fluka. The raw bentonite was purchased from China. All solutions were prepared using distilled water.

Preparation of Modified Bentonites

At first, the raw bentonite was purified by dissolved 100 g of it in one litre of distilled water with stirring for 30 minutes. The solution was then left to settle for 20 minutes. After this process, the solid phase was separated by filtration, then washed with deionized water and dried in the oven at 303K. The bentonite was ground to obtain a powder and pure. In the second step, bentonites were activated by the aluminium hydroxide prepared by the following Eq. (1) (Yan et al. 2010).



$Al(OH)_3$ is added slowly to pure bentonite by a ratio (10 mmol Al/1.0 g bentonite) with a stirring at 303 K for 24 h. Finally, the modified bentonite by CTAB was prepared according to the references reported (Zhu et al. 2009). B-A-CTAB was organized with the aid of including a certain quantity of CTAB solution to a 0.02 aqueous suspension of 20 g of B-Al below moving. The suspension solution was heated for three hours at 313 K, accrued with the aid of filtration, washed, dried at 353 K to constant mass, activated for 1 h at 413 K, saved in a complete airtight plastic vial in a desiccator until addition use.

Batch Experiments

Adsorption of RR120 on modified bentonite turned into done in a batch gadget. A 50 mL RR120 solution (50-150 mg/L) within conical flasks. The aggregate was shaken using thermostatically achieve shaker right away. The shaker velocity worked at one hundred fifty rpm. The samples had been withdrawn (6 mL) at precise time periods (5, 10, 15, 20, 30, 45, 60 min), centrifuged for 10 min to detach the dye solution from the adsorbent, and evaluated for the colouration elimination efficiencies at $\lambda_{max} = 535$ nm using ultraviolet and visible spectroscopy (Japan; Optima Model SP – 3000; UV / VIS) geared up with a quartz cell of 1.0 cm path duration.

Techniques used to Determine the Properties of Adsorbents

The scanning electron microscope (SEM, Ties can Vega III Czech Republic) was used to study their surface morphology and Fourier transformed infrared spectrophotometer (IR Prestige – 21 Shimadzu) were performed in the range of 4000-500 cm^{-1} with KBr pellets. The X-ray diffraction (XRD) patterns of the sample were measured with Shimadzu Corporation Lab-X (XRD-6000) and recorded in the range of (3-80) deg with speed 5.0 deg min^{-1} and preset time 0.6 sec.

RESULTS AND DISCUSSION

Analysis and Calculation

Decolourization activity was expressed in all optimization study in terms of decolourization efficiency (%), and it was calculated as follows:

$$\text{Degradation efficiency \%} = [(C_0 - C_t) / C_0] \times 100\% \quad \dots(2)$$

In which C_0 ($mg \cdot L^{-1}$) is the initial concentration of dye and C_t ($mg \cdot L^{-1}$) is the concentration of dye of reaction time t (min).

$$q_t = (C_0 - C_t) V / W \quad \dots(3)$$

Where q_t ($mg \cdot g^{-1}$) is the quantity of RR120 dye adsorbed according to unit mass of adsorbent, $V(L)$ is the volume of solution, and $W(g)$ is the mass of the adsorbent.

Adsorption Kinetics

Two kinetic sorts the pseudo-first-order, and the pseudo-second-order have been used to suit into the experimental facts received from the colour removal steps. The Lagergren pseudo-first-order model is given by Eq. (4) (Fang et al. 2019):

$$\log(q_e - q_t) = \log q_e - k_1 t / 2.303 \quad \dots(4)$$

Where in q_t ($mg \cdot g^{-1}$) is the adsorption ability at time t , q_e ($mg \cdot g^{-1}$) is the adsorption potential at equilibrium, and k_1 (min^{-1}) represents the rate constant of the pseudo-first-order version. Eq. (5) is the pseudo-second-order (Wang & Wu 2006) defined as follows:

$$t/q_t = 1/k_2 q_e^2 + t/q_e \quad \dots(5)$$

Where k_2 ($L \cdot mg^{-1} \cdot min^{-1}$) is the rate constant of the pseudo-second-order model.

Adsorbent Characterization

FTIR spectroscopy is a touchy approach to probe the interaction kind configuration and topical environment of the surfactant cations within the interlamellar vicinity of bentonite (Luo et al. 2019). The comparative FTIR spectra of P-Bent, P-Bent-Al and P-Bent-Al-CTAB are shown in Fig. 1. The band at 3622 cm^{-1} assigned to stretching vibrations of structural OH groups (Tomic et al. 2015), whereas the bands at 3441 and 1639 cm^{-1} can be assigned to the O-H deformation

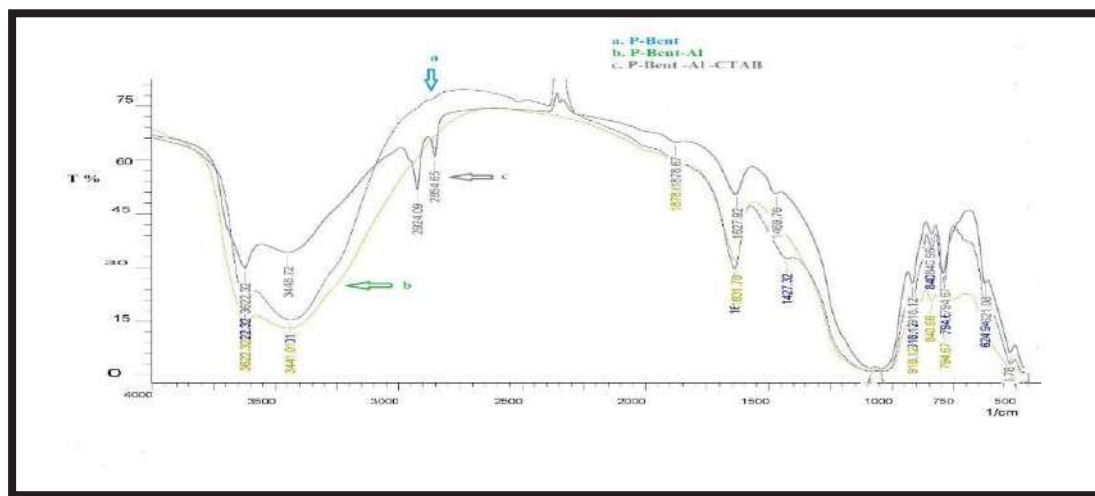


Fig. 1: FTIR spectra of a. P-Bent, b. P-Bent-Al and c. P-Bent-Al-CTAB.

of water (Ayodele & Hameed 2013). The Si-O stretching vibrations are shown at 1088 and 1042 cm^{-1} , respectively (Tomic et al. 2015). The band absorption at 918 cm^{-1} can be assigned to the deformation of Al-Al-OH in the octahedral layers (Ayodele & Hameed 2013). Coupled Al-O/Si-O appeared at (841,795,625) cm^{-1} and Al-O-Si deformations appeared at 521 cm^{-1} , indicating the existence of the essential

structure of bentonite (Tomic et al. 2015). In FTIR spectra of B-Al a considerable growth within the density of the bands at 3410 and 1636 cm^{-1} of sorbed water molecules, due to the creation of hydroxy-aluminium cations increasing large quantities of water and hydroxyl. However, a considerable reduction in the intensities of these two bands while CTAB cations had been introduced (Ayodele & Hameed 2013).

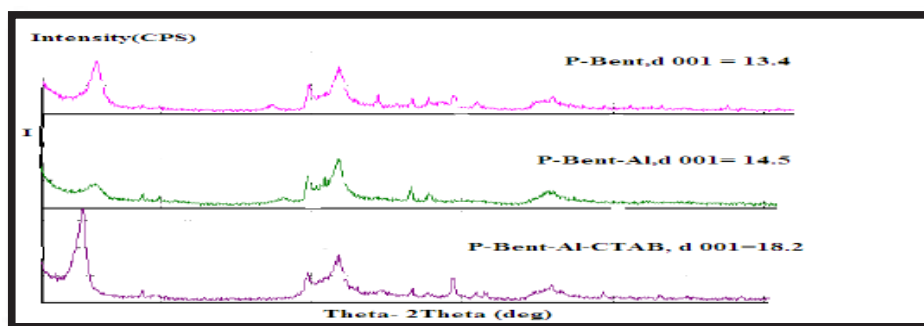


Fig. 2: XRD modality of behaviour the adsorbent.

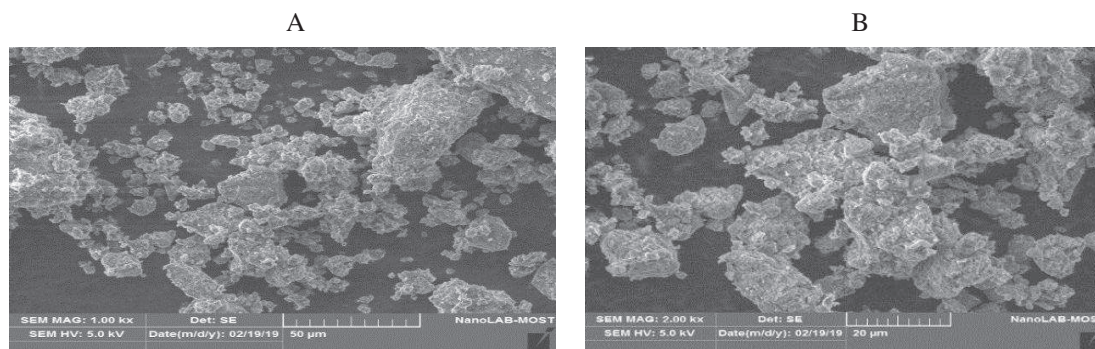


Fig. 3: SEM photos of the adsorbents. (A) Pure Bentonite, and (B) P-B-A-CTAB.

The bands at (2928 and 2855) cm^{-1} had been observed for B-A-CTAB. They could be indicated to the anti-symmetric and symmetric stretching vibration modes of $-\text{CH}_3$ and $-\text{CH}_2$ similarly, the bending vibration of $-\text{CH}_3$ was observed at 1470 cm^{-1} in organic intercalator. XRD assessment comes to be done which will pick out the mineralogical shape of the supported bentonite adsorbents and the XR-Diffraction styles are verified in Fig. 2. It may be visible that comparable diffraction peaks attributable to the complicated additives of adsorbents had been detected in those three samples. The principle crystalline phases determined in pure-Ben for SiO_2 , located at 2θ (Theta) of 6.61°, 19.6°, 21.69°, 26.59°, 36.71° and 62.04°, which have been consistent with that of the literature mentioned (Tiwari et al. 2011). The boom of basal wideness from 13.4 Å for pure-Bent to 18.2 Å for B-A-CTAB changed into due to the competing of Al and CTAB molecule into the interlayer distance area of pure-Bent that increased its interlayer spacing and later confirmed RR120 adsorption potential, which changed into, also assured via FTIR. SEM photographs of the adsorbents are given in Fig. 3. Even though it was no longer possible to precisely limit the particle size of the adsorbents, big aggregates of platelets component with small particles, especially among 20 and 50 micrometres in length and have been determined

for the pure bent. Under the modification, the average particle size reduces; small and properly unattached particles can be located, particularly for B-A-CTAB. This commentary advised that some disaggregation of bentonite particles happened for the duration of the modification.

Effect of Different Factors on the Decolorization Efficiency of RR120

Comparison of various adsorbents: An experiment was performed to compare three adsorbents on the dye solution. Fig. 4 shows the efficiency of colour removal over time. The decolourization efficiency is high for the Bent-Al-CTAB up to 93% in 30 minutes and is higher than pure bentonite and activated by aluminium. Bentonite pure isn't a powerful adsorbent for the organic compounds in water. These results show that the modified bentonites' ability to remove the colour of the dye solution has been strongly enhanced after surface modification, as surface properties have changed from hydrophilic to hydrophobic form (Xu et al. 2017). Modified bentonite was used in further studies.

Effluence of adsorbent dosage: Fig. 5 shows the effect of changing bentonite modified dose on the decolourization efficiency of dye solution. It was found the efficiency of removal of the colour increases with the increase of the dose

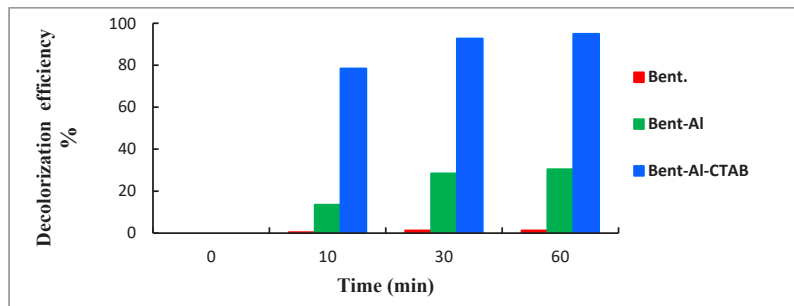


Fig. 4: Assessment of the three adsorbent on decolorization performance (adsorbent dosage: 0.1g, temperature: 303K, pH = 6.0, rpm =150 and RR120 concentration: 96 mg.L^{-1}).

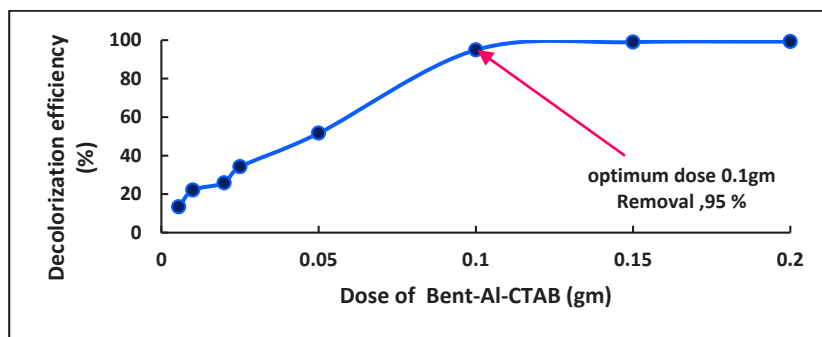


Fig. 5: Effect of adsorbent dosage on decolorization efficiency: (temperature 303K, pH = 6, rpm =150, contact time = 60 min and RR120 concentration: 96 mg.L^{-1}).

of bentonite modified, but it is not necessary to use a dose greater than 0.1 gm because the decolorization efficiency was not affected greatly. When the dose of B-A-CTAB is 0.1 g, the efficiency of colour removal reached 95%. Thus this amount of the modified bentonite has been used for the next experiments.

Effluence of pH: For the purpose to take a look at the effect of pH on the adsorption potential of B-AI-CTAB, acidic pH 3.5 and alkaline pH 9.0 and previously studied pH 6.0 were selected (Fig. 6). The efficiency of removal (91%, 80% and 47%) was obtained for pH (3.5, 6 and 9) respectively, at contact time 10 minutes. Low degradation efficiency with pH increase may be due to that the pH affected the surface charge of the adsorbent and the degree of ionization of adsorbate (Xu et al. 2017). At lower pH, the protonation of surface -OH groups to $-OH_2^+$ (Bouزيد et al. 2015), consequently the positive sites increased, thereby electrostatic attraction enhanced between the positively charged adsorption sites and negatively charged dyes. In alkaline condition, the protonation of surface -OH decreased and consequently, the positive sites decreased, and on the other hand, the abundance of OH^- ions competing with the anionic dye for adsorption sites, resulted in the reduction of exchangeable dye anionic on the adsorbent (Bouزيد et al. 2015).

Effect of primary dye concentration: Preliminary concentration of dyes is a good-sized parameter for sensible inspiration. Therefore, it is vital to have a look at the effect on the primary dye concentration, and the effects are shown Fig. 7. It indicates elevated colour elimination performance with decreased concentration of dye RR120. As the concentration of dye lowers from 150 mg.L^{-1} to 50 mg.L^{-1} , the decolorization performance of dye grows from 48% to 93% within 15 min of the adsorption process. The degradation performance of dye reduced as the preliminary concentration increased, this brings about the settlement with proposed whilst the positioned range of susceptible sites, the competitive adsorption might contact the adsorption and degradation of contaminants on the surface of particles, and further reduce the reaction velocity (Jafari et al. 2016).

Study of adsorption kinetics: Two kinetic models pseudo-first-order and pseudo-second-order have been used to fit the experimental data points obtained from the decolorization processes. An assessment of the consequences with the precise line is plotted in Figs. 8 and 9 and the kinetic parameters are summarized in Table 1. The (R^2) correlation coefficients of the pseudo-first-order version are lower than the ones of the pseudo-second-order model, and the calculated (q_e) adsorption potential at equilibrium appeared to be

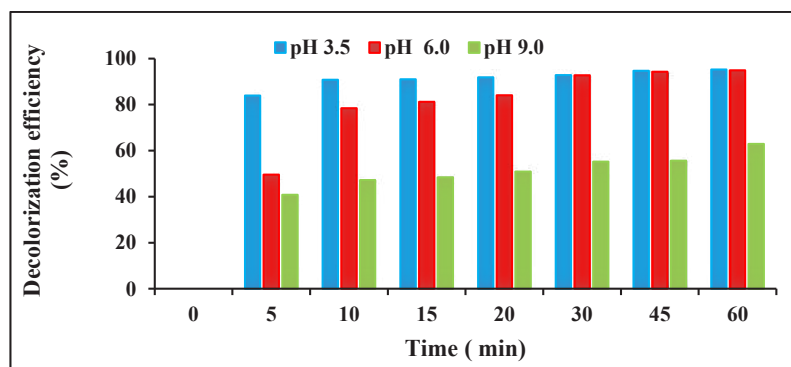


Fig. 6: Effect of initial pH on decolorization efficiency (303K, adsorbent dosage = 0.1g, rpm =150 and RR120 concentration: 96 mg.L^{-1}).

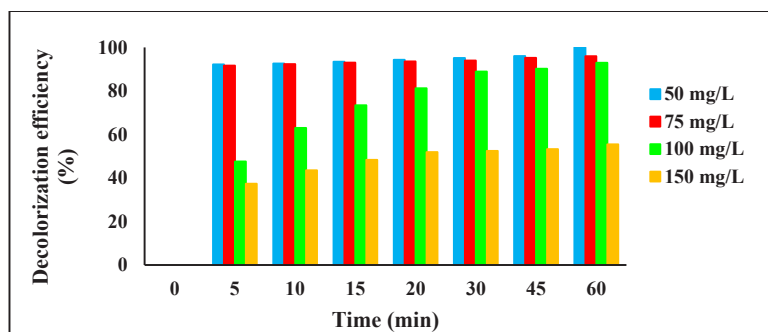


Fig. 7: Effect of variations in initial dye concentration on the decolorization efficiency (pH = 6.0, 303K, adsorbent dosage = 0.1g, rpm =150).

near the empirical values, indicating that pseudo 2nd order model version yields a higher match to the empirical data than the pseudo-first-order model. Comparable outcomes were pronounced for the adsorption of AGYG, AB93, ATBA and AB25 onto B-A-CTAB (Yan et al. 2015).

Effect of temperature and adsorption isotherms: The effect of temperature on the adsorption process is an important parameter and should be studied. As can be observed in Fig. 10, the removal rate for RR 120 was enhanced by increasing the temperature from 293K to 303K and the colour removal

from 60% and 81% respectively was achieved at 15 min of the adsorption process. This increase can be attributed to faster mass transfer in solution and increased collision frequencies between adsorbents and dye molecules. However, removal efficiency decreased as temperature increased further to 313 K and 323 K indicating that the RR120 adsorption on modified bentonite is exothermic by nature and these results are similar in previous reports (Yan et al. 2010).

The Langmuir and Freundlich isotherms were used and expressed by Eqs. (6) and (7) respectively.

Table 1: The kinetic parameters for Reactive red 120 on modified bentonite.

T (k)	C_o (mg.L ⁻¹)	$q_{e, exp}$ (mg.L ⁻¹)	Pseudo-first-order model		Pseudo-second-order model			
			q_{1e} (mg.g ⁻¹)	k_1 (min ⁻¹)	R^2	q_{2e} (mg.g ⁻¹)	k_2 (g.mg ⁻¹ .min ⁻¹)	R^2
303	50	25.30	1.99	0.0217	0.9858	25.38	0.0426	0.9994
	75	26.30	2.43	0.0596	0.9284	26.50	0.0601	0.9999
	100	46.96	29.78	0.0744	0.9520	51.81	0.0033	0.9990
	150	46.40	12.50	0.0380	0.8084	47.62	0.0074	0.9082
293	96	45.13	80.50	0.1239	0.8956	55.60	0.0017	0.9890
313	96	46.30	20.72	0.1078	0.7558	52.63	0.0040	0.9940
323	96	38.13	42.34	0.0857	0.9493	43.84	0.0030	0.9840

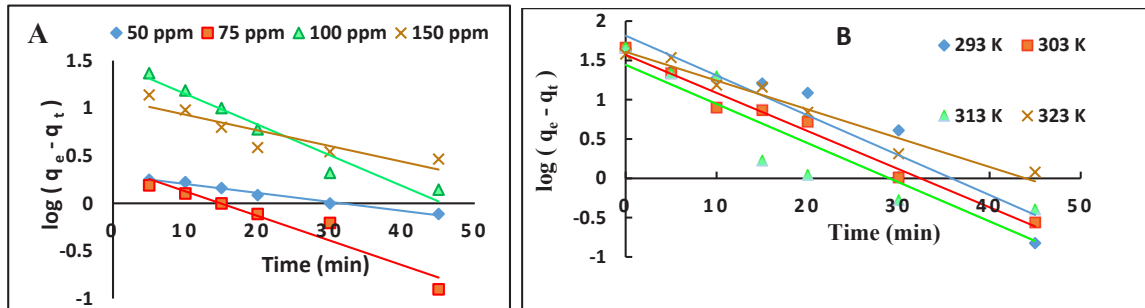


Fig. 8: The pseudo-first-order kinetics plots for the adsorption of RR120 onto Bent-AI-CTAB at (A) diverse RR120 preliminary concentrations and (B) various temperatures.

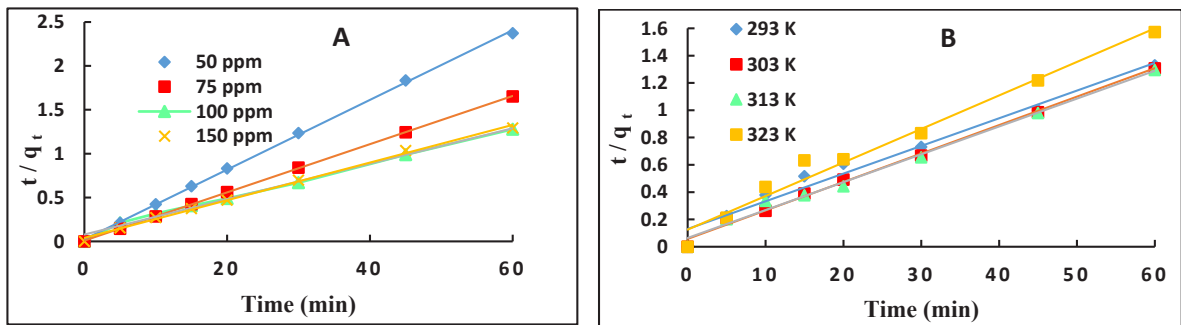


Fig. 9: The pseudo-second-order kinetics draws for the adsorption of RR120 onto B-A-CTAB at (A) many RR120 initial concentrations and (B) various temperatures.

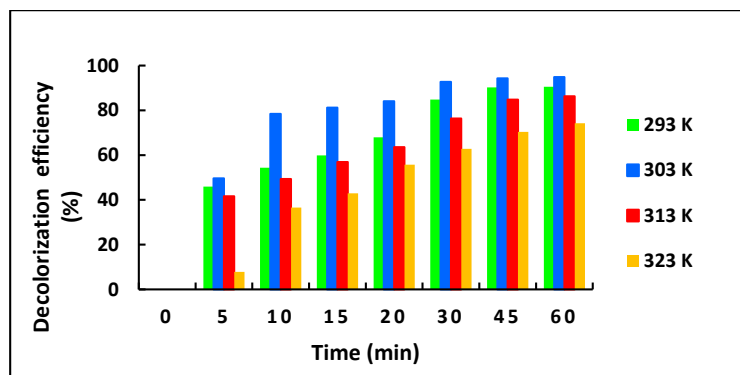


Fig. 10: Influence of variations in temperature on the decolorization efficiency (pH = 6.0, adsorbent dosage = 0.1g, rpm =150 and RR120 concentration = 96 mg.L⁻¹).

$$C_e / q_e = 1 / K_L q_m + C_e / q_m \quad \dots(6)$$

$$\ln q_e = \ln K_F + (1/n) \ln C_e \quad \dots(7)$$

Where, q_e (mg.g⁻¹) and q_m (mg.g⁻¹) are the equilibrium adsorption quantity at the adsorbate and the monolayer saturation adsorption quantity on the adsorbent, respectively. C_e (mg.L⁻¹) is the equilibrium concentration of adsorbate. K_L and K_F are the Langmuir and Freundlich isotherm constant, respectively. The suitable lines are plotted in Fig. 11 and the isotherm parameters are

summarized in Table 2. The correlation coefficients (R^2) of Langmuir isotherm had been better than that of Freundlich isotherms, and the monolayer saturation adsorption amount (q_m) changed closer to the calculated value ($q_{e,max}$), indicating that the Langmuir isotherm outfitted fine to the experimental information, and the monolayer coverage nature of the adsorbate on the surface of B-A-CTAB (Karaca et al. 2008).

Study thermodynamic of the adsorption process:

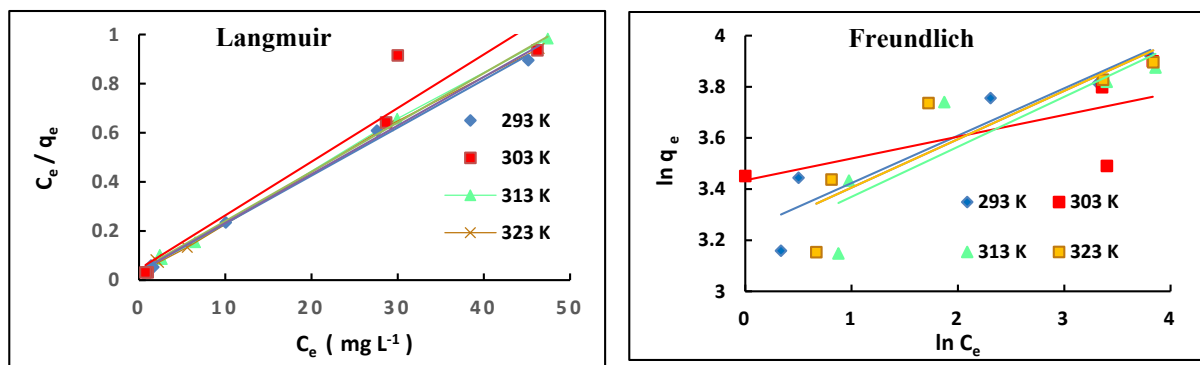


Fig. 11: Langmuir and Freundlich isotherms for Reactive red 120 adsorption on modified bentonite.

Table 2: The isotherm parameters for RR120 adsorption on modified bentonite.

Model	Parameters	T (K)			
		293	303	313	323
Langmuir	q_m (mg.g ⁻¹)	51.28	45.66	49.75	50.51
	K_L (L.mg ⁻¹)	0.0007	0.001	0.0008	0.0006
	R^2	0.9965	0.9231	0.9987	0.9986
Freundlich	n	5.397	11.737	5.115	5.291
	K_F	25.485	31.016	23.098	24.953
	R^2	0.8898	0.4613	0.7690	0.7890

Table 3: Thermodynamic functions for RR120 adsorption on modified bentonite.

T(K)	K_c	ΔG^0 (KJ mol ⁻¹)	ΔS^0 (J mol ⁻¹ K ⁻¹)	ΔH^0 (KJ mol ⁻¹)
303	126.47	-11.62	-93.78	-40.1
313	38.83	-10.68		
323	48.03	-9.74		

Thermodynamic functions such as free energy change (ΔG^0), enthalpy change (ΔH^0) and entropy change (ΔS^0) have been evaluated and can be calculated from Eq. (8)-(10), respectively:

$$\ln K_c = -\Delta H^0 / RT + \Delta S^0 / R \quad \dots(8)$$

$$K_c = C_{AE} / C_{SE} \quad \dots(9)$$

$$\Delta G^0 = \Delta H^0 - T \Delta S^0 \quad \dots(10)$$

Where, K_c is the equilibrium constant, R (8.314 J mol⁻¹ K⁻¹) and T (K) are ideal gas constants and thermodynamic temperature, respectively. C_{AE} is the quantity of dye (mg) adsorbed on the adsorbent per L of the solution at equilibrium. C_{SE} is the equilibrium concentration (mg.L⁻¹) of the dye solution. The thermodynamic parameters are summarized in Table 3. The negative ΔG^0 and ΔH^0 indicated the adsorption was spontaneous and exothermic, the rise of temperature was not conducive to the adsorption process, which was consistent with the experimental results. Whereas, negative ΔS^0 showed that the adsorption was entropy decrease process. Adsorption dye molecules become constrained by their association with surface atoms. In doing so, they lose some degrees of freedom compared to their pre-adsorption status. Consequently, it decreases in free energy and entropy decreases in enthalpy.

Effect of the salt: The effect of the salt on the elimination performance of RR 120 adsorption on modified bentonite

become tested through the usage of the extraordinary salts as NaCl, Na₂SO₄, Na₂CO₃, NaNO₃, and Na₂HPO₃.5H₂O (Fig. 12). The results show that the presence of NaCl and NaNO₃ enhances the decolorization efficiency. Whilst the presence of Na₂SO₄, Na₂CO₃ and Na₂HPO₃.5H₂O decrease the decolorization effectiveness because SO₄²⁻, CO₃²⁻ and HPO₃²⁻ ions compete with dye molecules and occupy the reactive places on modified bentonite surface (Sribenja & Saikrasun 2015).

CONCLUSIONS

The activated bentonite was modified by CTAB then confirmed by techniques FTIR, X-ray diffraction and SEM. The second-order kinetic model can well explain the dye degradation process using B-A-CTAB. The Langmuir isotherm had been better than that of Freundlich isotherms. The presence of NaNO₃ and NaCl enhances the decolorization efficiency while the ions SO₄²⁻, CO₃²⁻ and HPO₃²⁻ were inhibiting the process of dye removal.

REFERENCES

- Ayodele, O. B. and Hameed, B. H. 2013. Synthesis of copper pillared bentonite ferri oxalate catalyst for degradation of 4-nitrophenol in visible light assisted Fenton process. *J. Ind. Eng. Chem.*, 19: 966-974.
- Bouzd, S., Khenifi, A., Bennabou, K. A., Trujillano, R., Vicente, M. A. and Derriche, Z. 2015. Removal of Orange II by phosphonium-modified Algerian Bentonites. *Chem. Eng. Commun.*, 202: 520-533.
- Caglar, B., Topcu, C., Coldur, F., Sarp, G., Caglar, S., Tabak, A. and Sahin, E. 2016. Structural, thermal, morphological and surface charge properties of dodecyl trimethyl ammonium-smectite composites. *J. Mol. Struct.*, 1105: 70-79.
- Engin, A. B., Ozdemir, O., Turan, M. and Turan, A. Z. 2008. Color removal from textile dye bath effluents in a zeolite fixed bed reactor: determination of optimum process conditions using Taguchi method. *Hazard. Mater.*, 159: 348-353.
- Fan, Y., Liu, H. J., Zhang, Y. and Chen, Y. 2015. Adsorption of anionic MO or cationic MB from MO/MB mixture using polyacrylonitrile fiber hydrothermally treated with hyper-branched polyethylenimine. *J. Hazard. Mater.*, 283: 321-328.

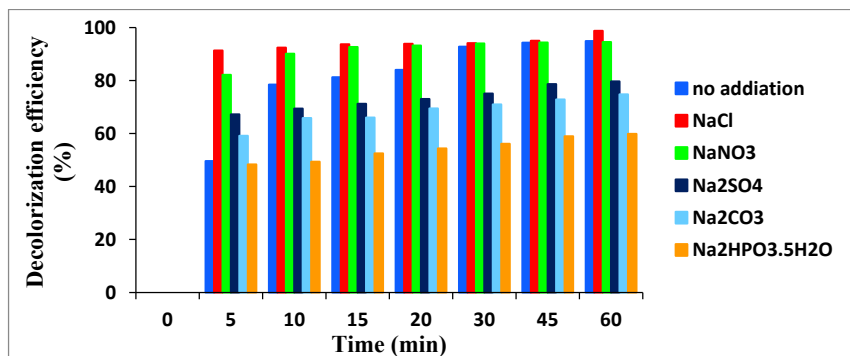


Fig. 12: Influence of addition of 0.01 inorganic salts on RR120 decolorization efficiency (pH = 6.0, adsorbent dosage = 0.1 g, rpm = 150 and RR120 concentration = 96 mg.L⁻¹).

- Fang, S., Yang, N., Qiu, M. and Huang, C. 2019. Degradation of dye C.I. Reactive red 15 in aqueous solution by kaolinite supported zero valent iron. *Nat. Environ. Pollut. Technol.*, 18(3): 963-968.
- Giri, S. K., Das, N. N. and Pradhan, G. C. 2011. Magnetite powder and kaolinite derived from waste iron ore tailings for environmental applications. *Powder Technol.*, 214: 513-518.
- Giustetto, R. and Wahyudi, O. 2011. Sorption of red dyes on palygorskite: synthesis and stability of red/purple Mayan nano composites. *Microporous Mesoporous Mater.*, 142: 221-235.
- Hameed, B. H., Ahmad, A. A. and Aziz, N. 2007. Isotherms, kinetics and thermodynamics of acid dye adsorption on activated palm ash. *Chem. Eng. J.*, 133: 195-203.
- Jafari, S., Tryba, B., Kusiak-Nejman, E., Kapica-Kozar, J., Morawski, A. W. and Sillanpaa, M. 2016. The role of adsorption in the photocatalytic decomposition of Orange II on carbon-modified TiO₂. *J. Mol. Liq.*, 220: 504-512.
- Karaca, S., Gurses, A., Acikyildiz, M. and Ejder, M. 2008. Adsorption of cationic dye from aqueous solutions by activated carbon. *Micropor. Mesopor. Mat.*, 115: 376-382.
- Konicki, W., Sibera, D., Mijowska, E., Lendzion-Bielun, Z. and Narkiewicz, U. 2013. Equilibrium and kinetic studies on acid dye Acid Red 88 adsorption by magnetic ZnFe₂O₄ spinel ferrite nanoparticles. *J. Colloid Interface Sci.*, 3: 152-160.
- Lim, S., Gomes, C. and AbKadir, M. 2013. Characterizing of bentonite with chemical, physical and electrical perspective for improvement of electrical grounding systems. *Int. J. Electrochem. Sci.*, 8: 11429-11447.
- Luo, J., Zhao, D., Wang, L., Asiri, A.M. and Alamar, K.A. 2019. Simultaneous removal of Cu (II) and 1- naphtha in wastewater by magnetic nanoparticle-grapheme oxide composites. *Nat. Environ. Pollut. Technol.*, 18(3): 777-787.
- Orucoglu, E. and Hacıyakupoglu, S. 2015. Bentonite modification with hexadecyl pyridinium and aluminum polyoxy cations and its effectiveness in Se(IV) removal. *J. Environ. Manage.*, 160: 30-38.
- Qiu, M. 2019. Degradation of azo dye acid orange 7 by zero valent activated with potassium persulphate. *Nat. Environ. Pollut. Technol.*, 18(1): 197-201.
- Sribenja, S. and Saikrasun, S. 2015. Adsorption behavior and kinetics of Lac dyeing on poly (ethylene mine) - treated bamboo fibers. *Fiber. Polym.*, 16: 2391-2400.
- Suba, V. and Rathika, G. 2016. Novel adsorbents for the removal of dyes and metals from aqueous solution- A review. *J. Adv. Phys.*, 5: 277-294.
- Tiwari, D., Laldanwngliana, C., Choi, C. H. and Lee, S. M. 2011. Manganese- modified natural sand in the remediation of aquatic environment contaminated with heavy metal toxic ions. *Chem. Eng. J.*, 171: 958-966.
- Tomic, Z. P., Asanin, D. P., Durovic-pejcev, R., Dordevic, A. and Makreski, P. 2015. Adsorption of acetochlor herbicide on inorganic-and organic-modified bentonite monitored by mid-infrared spectroscopy and batch adsorption. *Spectrosc. Lett.*, 48: 685-690.
- Wang, S. B. and Wu, H. W. 2006. Environmental-benign utilization of fly ash as low-cost adsorbents. *J. Hazard. Mater.*, 136: 482-501.
- Xu, D., Li, W., Wang, K., Bai, Y., Lin, Q. and Gao, M. 2017. Hydroxy aluminum and cetyl trimethyl ammonium bromide modified bentonite as adsorbent and its adsorption for Orange II. *J. Des. Water. Trea.*, 94: 244-253.
- Yan, L. G., Xu, Y. Y., Yu, H. Q., Xin, X. D., Wei, Q. and Du, B. 2010. Adsorption of phosphate from aqueous solution by hydroxyl-aluminum, hydroxy-iron and hydroxy-iron-aluminum pillared bentonites. *J. Hazard. Mater.*, 179: 244-250.
- Yan, L., Qin, L., Yu, H., Li, S., Shan, R. and Du, B. 2015. Adsorption of acid dyes from aqueous solution by CTMAB modified bentonite: Kinetic and isotherm modeling. *J. Mol. Liq.*, 211: 1074-1081.
- Zhang, J. and Qiu, M. 2019. Adsorption kinetics and isotherms of copper ion in aqueous solution by bentonite supported nano scale zero valent iron. *Nat. Environ. Pollut. Technol.*, 18(1): 269-274.
- Zhang, Y. J., Liu, L. C., Ni, L. L. and Wang, B. L. 2013. A facile and low-cost synthesis of granulated blast furnace slag-based cementations material coupled with Fe₂O₃ catalyst for treatment of dye wastewater. *Appl. Catal. B Environ.*, 138-139: 9-16.
- Zhu, R. L., Zhu, L. Z., Zhu, J. X., Ge, F. and Wang, T. 2009. Sorption of naphthalene and phosphate to the CTMAB-A113 intercalated bentonites. *J. Hazard. Mater.*, 168: 1590-1594.



Effect of Pyrolysis Temperature on Adsorption Characteristics of Biochar Derived from Corn Straw

Jing Dai, Ruolin Xu, Wangying Li, Yulin Li, Yang Yang, Yang Xiao, Huan Mao, Muqing Qiu, Hai Wang, Ningcan Yang and Li Han†

College of Life Science, Shaoxing University, Shaoxing, 312000, P.R. China

†Corresponding author: Li Han; 51778067@qq.com

Nat. Env. & Poll. Tech.
Website: www.neptjournal.com

Received: 30-12-2019

Revised: 19-01-2020

Accepted: 30-03-2020

Key Words:

Adsorption
Copper
Biochar
Corn straw
Pyrolysis

ABSTRACT

With the growth of population and the rapid development of industry, a large amount of wastewater containing heavy metals has been produced. How to treat wastewater containing heavy metals effectively is an important problem. In this study, biochar derived from corn straw is prepared at different carbonization temperatures by oxygen-limited carbonization, and finally, biochar derived from the corn straw at different temperatures is obtained. Then, the adsorption characteristics of ionic heavy metal copper in aqueous solution were studied by biochar prepared at different temperatures. Adsorption kinetics of copper in aqueous solution by biochar from corn straw is discussed in detail. Experimental results show that the adsorption capacity of Cu^{2+} ions in solution by biochar prepared at different temperatures is significantly different. The prepared biochar derived from corn straw is a fragmentary and porous structure. A lot of functional groups appear on the prepared biochar. The pseudo second order kinetic equation can better describe the entire adsorption of Cu^{2+} ions in solution by biochar prepared under different temperatures. The adsorption process of Cu^{2+} ions by biochar is controlled by liquid diffusion and intraparticle diffusion.

INTRODUCTION

With the growth of population and the rapid development of industry, a large amount of wastewater containing heavy metal pollution has been produced (Chiron et al. 2003, Jeon et al. 2003). These wastewater containing heavy metal can flow into water, soil and air through various means, which eventually are harmful to the environment (Arthur et al. 1993, Shukla 2000, Ömer et al. 2003). Once people drink sewage water or eat vegetables and food that have been irrigated by sewage, heavy metals in the water can enter the human body (Jung et al. 1998). These heavy metals will gradually accumulate in the human body, which eventually causes human pathological changes, abnormal fetal development, reproductive disorders, and physical fitness decline (Shen & Duvnjak 2005, Veli & Alyüz 2007). At present, the following two methods are mainly used to repair and control heavy metal pollution in water bodies. One approach is to reduce the migration and bioavailability of heavy metals in water. Another method is to completely remove heavy metals from the polluted water body (Bailey et al. 1999, Swami & Buddhi 2006, Sud et al. 2008, David et al. 2010).

Biochar is a highly aromatic refractory solid substance produced by slow pyrolysis and carbonization of biomass under complete or partial anoxic conditions (Chen et al. 2007). They are mainly mixtures of complex organic carbons,

such as acid and acid derivatives, phenol, cellulose, carbonyl, alkanes and olefin derivatives (Beck et al. 2011, Ahmad et al. 2014, Yasser et al. 2017). They have the characteristics of large specific surface area, good porosity and strong adsorption capacity (Ok et al. 2015). Therefore, biochar is widely used in agriculture and the environment. Biochar has good adsorption capacity for heavy metal pollutants and organic pollutants (Kaudal et al. 2016, Rehman et al. 2016). Researching on the adsorption mechanism of biochar on pollutants will be a benefit to understand the adsorption pathway of biochar, to better carry out the purification effect of biochar on pollutants (Ma et al. 1994).

Related studies have shown that different biomass feedstocks and biochars prepared at different pyrolysis temperatures have different properties, such as pore structure, surface functional groups and so on (Singh et al. 2012). Therefore, these characteristics determine the significant difference in the adsorption of heavy metals on biochar prepared under different conditions (Alkan & Dogan 2001, Altundogan et al. 2007).

In this study, biochar derived from corn straw is prepared at different carbonization temperatures by oxygen-limited carbonization, and finally, biochar derived from corn straw at different temperatures is obtained. Then, the adsorption characteristics of ionic heavy metal copper in aqueous

solution are studied by biochar prepared at different temperatures. Adsorption kinetics of copper in aqueous solution by biochar from corn straw is discussed in details. The above research results will provide a theoretical basis for the treatment of heavy metal pollution by biochar.

MATERIALS AND METHODS

Materials: Copper nitrate was purchased from Tianjin Tianli Chemical Reagent Co., Ltd. Corn straw came from a farm in the suburbs of Jinan City, Shandong Province.

Preparation of biochar: Biochar was prepared according to the following method. Weigh a certain amount of corn straw and wash it with deionized water three times. Dry in an oven at 80°C for 12 h. After being crushed, it is placed in a crucible. The lid was capped and transferred to a muffle furnace for pyrolysis at 300°C, 500°C and 700°C respectively for 6 h. After cooling to room temperature, the sample is taken out, ground and sieved through 100 meshes. The biochar derived from corn straw at 300°C, 500°C and 700°C respectively are obtained for adsorption experiments.

Adsorption experiments: 0.1 g of biochar powder was weighed into a 250 mL Erlenmeyer flask, and 100 mL of a copper nitrate solution containing a concentration of 20 mg/L was added. Then, the Erlenmeyer flask was placed in a constant temperature shaking box, and the adsorption experiment was carried out at the speed of 200 rpm at 25°C. The sample was determined with atomic absorption spectrophotometry.

Effect of contact time on the removal rate: Added 0.1 g of biochar powder into a 250 mL Erlenmeyer flask containing 100 mL of 10mg/L copper concentration, and placed in the incubator at 25°C and 200 rpm. The contact time was 5, 10, 20, 40, 60, 90, 120, 180, 240 and 360 min, respectively. The sample was taken from the supernatant, placed in a centrifuge tube and centrifuged at 8000 r/min for 5 min. Then, it was measured with atomic absorption spectrophotometry.

Analytical methods: The particle microstructure of biochar was determined by Scanning Electron Microscopy (JEOL 6500F, Japan). The functional groups on the surface of biochar were determined by Fourier Transform Infrared Spectroscopy (Varian Scimitar 2000). The wavenumber was ranged from 400 to 4000 cm⁻¹. The concentration of Cu²⁺ ion in solution was analysed by atomic absorption spectrophotometry.

The removal rate of Cu²⁺ ions was calculated as following:

$$Q = \frac{C_0 - C_t}{C_0} \times 100\% \quad \dots(1)$$

Where, C_0 and C_t (mg/L) are the initial and equilibrium concentrations of Cu²⁺ ions in solution respectively. Q (%) is the removal rate of Cu²⁺ ions.

The amount of adsorbed Cu²⁺ ion q_t (mg/g) at different time was calculated as following:

$$Q_t = \frac{(C_0 - C_t) \times V}{m} \quad \dots(2)$$

Where, C_0 and C_t (mg/L) are the initial and equilibrium liquid-phase concentrations of Cu²⁺ ion respectively. V (L) is the solution volume and m (g) is the mass of adsorbent used.

Adsorption kinetics of copper in aqueous solution by biochar: To study the adsorption kinetics of copper in aqueous solution by biochar, pseudo first order kinetic equation (Lagergren 1898), pseudo second order kinetic equation (Ho & McKay 1999), Elovich model (McLintock 1967) and Weber-Morris intraparticle diffusion model (Jeon et al. 2003) are adopted in this research. Their fitting equations are Eqns.3 to Eqns. 6, respectively.

$$\ln(Q_e - Q_t) = \ln Q_e - k_1 t \quad \dots(3)$$

Where, Q_t (mg/g) represents the amount of adsorption at time t . Q_e (mg/g) represents the amount of adsorption at the time of adsorption equilibrium. k_1 (min⁻¹) is the constant of pseudo first order kinetic equation.

$$\frac{t}{Q_t} = \frac{1}{k_2 Q_e^2} + \frac{1}{Q_e} t \quad \dots(4)$$

Where, Q_t (mg/g) represents the amount of adsorption at time t . Q_e (mg/g) represents the amount of adsorption at the time of adsorption equilibrium. k_2 (min⁻¹) is a constant of pseudo second order kinetic equation.

$$Q_t = \frac{1}{\beta} \ln \alpha \beta + \frac{1}{\beta} \ln t \quad \dots(5)$$

Where, Q_t (mg/g) represents the amount of adsorption at time t . α (g/mg/min) and β (g/mg) are constant of Elovich model. They represent the initial adsorption rate constant and the desorption constant, respectively.

$$Q_t = k_{ip} t^{1/2} + C \quad \dots(6)$$

Where, Q_t (mg/g) represents the amount of adsorption at time t . k_{ip} (mg/g/min^{-0.5}) and C is constant of Weber-Morris intraparticle diffusion model. C represents a biochar boundary layer.

RESULTS AND DISCUSSION

The characteristic of biochar: SEM images of biochar under a different carbonization temperature were determined by Scanning Electron Microscopy. The results are shown in Fig.1. It indicates that biochar derived from corn straw is a

fragmentary and porous structure. This structure is a benefit for adsorption of heavy metals by biochar. However, it also can be seen that this porous structure is destroyed as the carbonization temperature increases (Fig. 1c). This change will affect its adsorption capacity of heavy metals.

The functional groups on the surface of biochar under a different carbonization temperature are determined by Fourier Transform Infrared Spectroscopy (Varian Scimitar 2000). The wavenumber is ranged from 400 to 4000 cm^{-1} . The results are shown in Fig. 2.

Fig. 2 suggests that a lot of functional groups appear on the prepared biochar under different carbonization temperatures. The numbers and intensity of functional groups increase as the carbonization temperature increases at the first stage. When carbonization temperature reaches 700°C, the numbers and intensity of functional groups decrease. The carbonization temperature of 500°C is optimum temperature. For biochar under 500°C, there is a strong adsorption peak in the range of 3398 cm^{-1} , which may be referred to the stretching vibration of a hydroxyl radical group. It indicates that a large number of oxygen-containing functional groups appear on the surface of biochar, such as carboxyl groups, hydroxyl groups, carbonyl groups and so on. The peak at 2015 cm^{-1} may correspond to stretching vibration of a carboxyl group. The peak at 1608 cm^{-1} may correspond to

stretching vibration of the N-H group. The peaks at 1378 cm^{-1} and 1079 cm^{-1} may correspond to an aromatic group and C-O-C group respectively. The peaks at 620 cm^{-1} , 582 cm^{-1} and 428 cm^{-1} may correspond to C-H stretching functional group, -COO- bending vibration functional group and Si-O-Si functional group.

Adsorption capacity of Cu^{2+} ions by prepared biochar under different pyrolysis temperatures: 0.1 g of prepared biochar derived from corn straw under different pyrolysis temperatures is weighed into a 250 mL Erlenmeyer flask respectively, and 100 mL of a copper nitrate solution containing a concentration of 20 mg/L was added. Then, the Erlenmeyer flask was placed in a constant temperature shaking box, and the adsorption experiment was carried out at the speed of 200 rpm at 25°C. Samples were taken after 360 min for analysis. The adsorption rate of copper ions in solution by biochar under different temperatures is shown in Fig. 3.

It can be seen from the figure that when the pyrolysis temperature is between 300°C and 500°C, the adsorption capacity of copper ion in solution by biochar under different pyrolysis temperatures gradually increases as the pyrolysis temperature increases. It may be related to the adsorption mechanism of Cu^{2+} ions in solution by biochar under different pyrolysis temperature. With the increase of carbonization temperature, the adsorption mechanism of

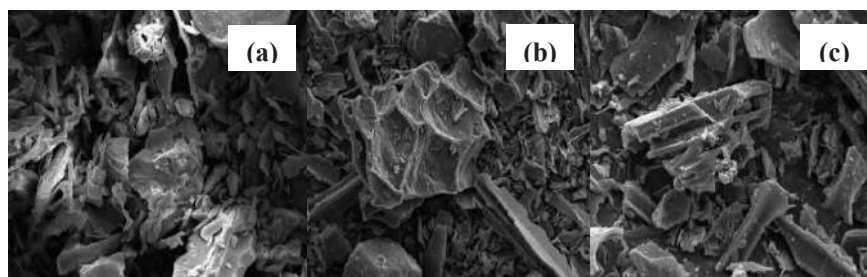


Fig. 1: SEM images of biochar [300°C (a), 500°C (b) and 700°C (c)].

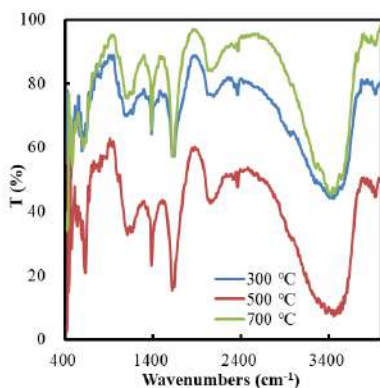


Fig. 2: FT-IR spectrum of biochars.

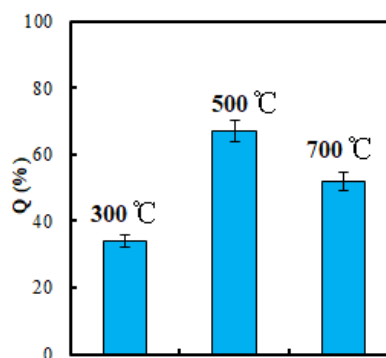


Fig. 3: Adsorption of Cu^{2+} ions by biochar under different pyrolysis temperatures.

Cu^{2+} ions in solution by biochar is from the distribution in the non-carbonized organic carbon component to the surface adsorption on the carbonized component. The types and density of surface functional groups of biochar prepared at different temperatures are different (Chen et al. 2008). For the biochar prepared at 700°C, the adsorption rate of Cu^{2+} ions in solution becomes low. It may be due to the effect of pore filling.

Effect of contact time on the removal rate: Effect of contact time on the removal rate of copper ions by biochar is shown in Fig. 4.

As shown in Fig. 4, it can be seen that the removal rate of copper ions by biochar increases quickly at the first stage of contact time. When contact time reaches 60 min, the removal rate of copper ions by biochar increases slowly. When contact time reaches 360 min, the removal rate of copper ions by biochar reaches equilibrium.

Adsorption kinetics of Cu^{2+} ion in aqueous solution by biochar: Pseudo first order kinetic equation: According to the adsorption data and Eqn. 3, curves fitting by pseudo first order kinetic equation for the adsorption of Cu^{2+} ions by biochar under different pyrolysis temperature are shown in Fig. 5. The parameters of kinetic adsorption by biochar under different pyrolysis temperatures are listed in Table 1.

It can be seen from Fig. 5 and Table 1 that pseudo first order kinetic can well fit the adsorption process in the initial stage of adsorption. However, in the following stage of adsorption, it gradually deviates from the fitted pseudo first order kinetic equation. Therefore, this equation does not describe the entire adsorption process well of Cu^{2+} ion by biochar under different pyrolysis temperatures. It can be concluded that the adsorption process of Cu^{2+} ion by biochar under different pyrolysis temperatures is affected by many influencing factors.

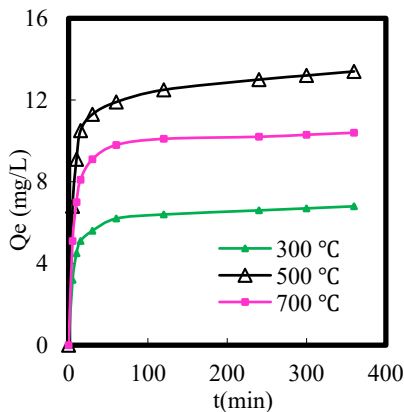


Fig. 4: Effect of contact time on the removal rate of copper ions by biochar.

Pseudo second order kinetic equation: According to the adsorption data and Eqn. 4, curves fitting by pseudo second order kinetic equation for the adsorption of Cu^{2+} ions by biochar under different pyrolysis temperatures are shown in Fig. 6 and Table 2.

It can be seen from Fig. 6 and Table 2 that the pseudo second order kinetic equation can better fit the entire stage of adsorption by biochar prepared under different temperatures. Comparing Table 1 and Table 2, it can be seen that the R^2 value of the pseudo first order kinetic equation is significantly higher than the R^2 value of the pseudo second order

Table 1: The parameters of pseudo first order kinetic adsorption by biochar under different pyrolysis temperatures.

Pyrolysis temperature (°C)	Q_e (mg/g)	k_1 (min ⁻¹)	R^2
300	14.256	0.0115	0.8539
500	26.459	0.0112	0.8625
700	22.784	0.0128	0.8122

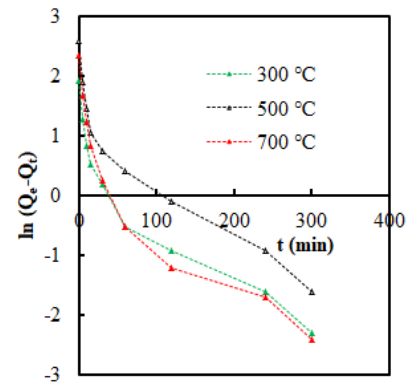


Fig. 5: Curves fitting by pseudo first order kinetic equation for the adsorption of Cu^{2+} ions by biochar under different pyrolysis temperatures.

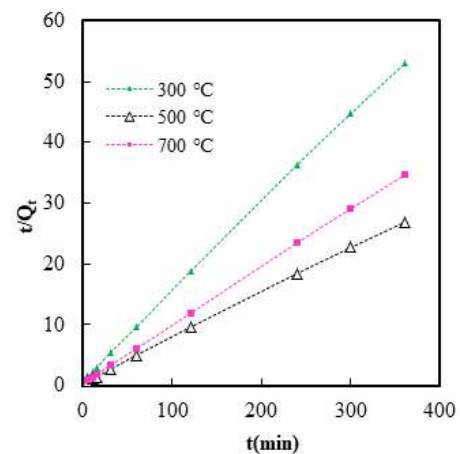


Fig. 6: Curves fitting by pseudo second order kinetic equation for the adsorption of Cu^{2+} ions by biochar under different pyrolysis temperatures.

Table 2: The parameters of pseudo second order kinetic adsorption by biochar under different pyrolysis temperatures.

Pyrolysis temperature (°C)	Q_e (mg/g)	k_2 (min^{-1})	R^2
300	14.912	0.00341	0.9998
500	27.681	0.00313	0.9997
700	23.124	0.00116	0.9998

kinetic equation. Therefore, the pseudo second order kinetic equation can better describe the whole process of adsorption by biochar prepared under different temperatures. The entire adsorption process includes a composite adsorption reaction of external liquid film diffusion, surface adsorption and intraparticle diffusion.

Elovich model: Elovich model is a description of the heterogeneous diffusion process that is controlled by the reaction rate and diffusion factor. The process includes the diffusion of the solute at the bulk or interface of the solution, activation and deactivation of the surface, and so on. Curves fitting by Elovich model for the adsorption of Cu^{2+} ions by biochar

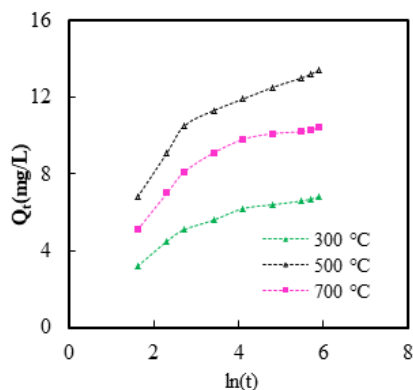


Fig. 7: Curves fitting by Elovich model for the adsorption of Cu^{2+} ions by biochar under different pyrolysis temperature.

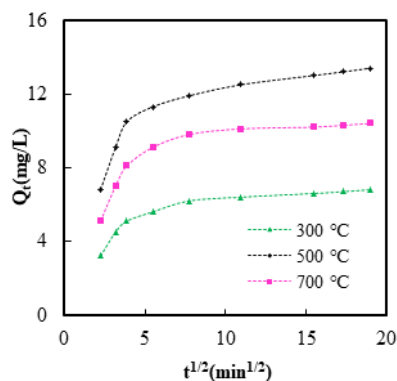


Fig. 8: Curves fitting by Weber-Morris intraparticle diffusion model for the adsorption of Cu^{2+} ions by biochar under different pyrolysis temperatures.

under different pyrolysis temperatures are shown in Fig. 7. It can be seen that the adsorption process of Cu^{2+} ions in solution by biochar prepared under different temperature deviates from the equation.

Weber-Morris intraparticle diffusion model: Curves fitting by Weber-Morris intraparticle diffusion model for the adsorption of Cu^{2+} ions by biochar under different pyrolysis temperature are shown in Fig. 8. It can be seen from the figure that the initial stage of the adsorption curve shows an upward trend and then gradually goes to a horizontal state. It may be the reason that when the heavy metal ions diffuse into the interior of the adsorbent, the diffusion resistance gradually increases and leads to a decrease in the diffusion speed. It can be seen from the model that the diffusion in the particle during the control phase of removal rate is not the only influencing factor, but is controlled by both liquid diffusion and intraparticle diffusion.

CONCLUSIONS

According to the above experiment, it can be concluded that the adsorption capacity of Cu^{2+} ions in solution by biochar prepared at different temperatures is significantly different. The carbonization temperature of 500°C is optimum temperature. A lot of functional groups appear on the prepared biochar. It will affect its adsorption capacity of heavy metals. The contact time and the initial copper concentration both affect the adsorption capacity of Cu^{2+} ions by biochar. The pseudo second order kinetic equation can better describe the entire adsorption of Cu^{2+} ions in solution by biochar prepared under different temperatures. The adsorption process of Cu^{2+} ions by biochar is controlled by liquid diffusion and intraparticle diffusion.

ACKNOWLEDGEMENTS

This work is supported by the Natural Science Foundation of Zhejiang Province, China (LGF19C030001 and LG-F20C030001). Authors are very grateful for their support.

REFERENCES

- Ahmad, M., Rajapaksha, A.U., Lim, J.E., Zhang, M., Bolan, N., Mohan, D., Vithanage, M., Lee, S.S. and Ok, Y.S. 2014. Biochar as a sorbent for contaminant management in soil and water: A review. *Chemosphere*, 99: 19-33.
- Alkan, M. and Dogan, M. 2001. Adsorption of Copper(II) onto perlite. *J. Colloid Interf. Sci.*, 243: 280-291.
- Altundogan, H.S., Arslan, N.E. and Tumen, F. 2007. Copper removal from aqueous solutions by sugar beet pulp treated by NaOH and citric acid. *J. Hazard. Mater.*, 149: 432-439.
- Arthur, W.R. and Gino, C.B.M. 1993. Adsorption of Cu, Pb, Zn, Co, Ni and Ag by goethite and hematite: a control on metal, mobilization from red beds into stratiform copper deposits. *Econ. Geol.*, 88: 1226-1236.

- Bailey, S.E., Olin, T.J., Bricka, R.M. and Adrian, D.D. 1999. A review of potentially low-cost sorbents for heavy metals. *Water Res.*, 33: 2469-2479.
- Beck, D.A., Johnson, G.R. and Spolek, G.A. 2011. Amending green roof soil with biochar to affect runoff water quantity and quality. *Environ. Pollut.*, 159: 2111-2118.
- Chen, J., Zhu, D. and Sun, C. 2007. Effect of heavy metals on the sorption of hydrophobic organic compounds to wood charcoal. *Environ. Sci. Technol.*, 41: 2536-2541.
- Chen, B., Zhou, D. and Zhu, L. 2008. Transitional adsorption and partition of nonpolar and polar aromatic contaminants by biochars of pine needles with different pyrolytic temperatures. *Environ. Sci. Tech.*, 42: 5137-5143.
- Chiron, N., Guilet, R. and Deydier, E. 2003. Adsorption of Cu(II) and Pb(II) onto a grafted silica: Isotherms and kinetic models. *Water Res.*, 37: 3079-3086.
- David, H., Paul, B., Karine, J., Cornu, J.Y. and Lebeau, T. 2010. Selection of low-cost materials for the sorption of copper and herbicides as single or mixed compounds in increasing complexity matrices. *J. Hazard. Mater.*, 182: 18-26.
- Ho, Y.S. and McKay, G. 1999. Pseudo second order model for sorption processes. *Process Biochemistry*, 34: 451-465.
- Jeon, B.H., Dempsey, B.A., Burgos, W.D. and Royer, R.A. 2003. Sorption kinetics of Fe(II), Zn(II), Co(II), Ni(II), Cd(II) and Fe(II)/Mn(II) onto hematite. *Water Res.*, 37: 4135-4142.
- Jung, J.H., Cho Y.H. and Pilsoo, H. 1998. Comparative study of Cu²⁺ adsorption of goethite, hematite and kaolinite: mechanistic modelling approach. *Bull. Korean Chem. Soc.*, 19: 324-327.
- Kaudal, B.B., Chen, D., Madhavan, D.B., Downie, A. and Weatherley, A. 2016. An examination of physical and chemical properties of urban biochar for use as growing media substrate. *Biomass Bioenergy*, 84: 49-58.
- Lagergren, S. 1898. About the theory of so-called adsorption of soluble substances. *Handlingar*, 24: 1-39.
- Ma, Q.Y., Traina, S.J., Logan, T.J. and Ryan, J.A. 1994. Effects of aqueous Al, Cd, Cu, Fe(II), Ni, and Zn on Pb immobilization by hydroxyapatite. *Environ. Sci. Technol.*, 28: 1219-1228.
- McLintock, I. 1967. The Elovich equation in chemisorption kinetics. *Nature*, 216: 1204-1205.
- Ok, Y.S., Chang, S.X., Gao, B. and Chung, H.J. 2015. SMART biochar technology shifting paradigm towards advanced materials and healthcare research. *Environ. Technol. Innov.*, 4: 206-209.
- Ömer, Y., Altunkaynak, Y. and Fuat, G. 2003. Removal of copper, nickel, cobalt and manganese from aqueous solution by kaolinite. *Water Res.*, 37: 948-952.
- Rehman, M.Z.U., Rizwan, M., Ali, S., Fatima, N., Yousaf, B., Naeem, A., Sabir, M., Ahmad, H.R. and Ok, Y.S. 2016. Contrasting effects of biochar, compost and farm manure on alleviation of nickel toxicity in maize (*Zea mays* L.) in relation to plant growth, photosynthesis and metal uptake. *Ecotoxicol. Environ. Saf.*, 133: 218-225.
- Shen, J. and Duvnjak, Z. 2005. Adsorption kinetics of cupric and cadmium ions on corn cob particles. *Process Biochem.*, 40: 3446-3454.
- Shukla, L.M. 2000. Sorption of zinc and cadmium on soil clays. *Agrochimica*, 44: 101-106.
- Singh, B.P., Cowie, A.L. and Smernik, R.J. 2012. Biochar carbon stability in a clayey soil as a function of feedstock and pyrolysis temperature. *Environ. Sci. Technol.*, 46: 11770-11778.
- Sud, D., Mahajan, G. and Kaur, M.P. 2008. Agricultural waste material as potential adsorbent for sequestering heavy metal ions from aqueous solutions- A review. *Bioresource Technol.*, 99: 6017-6027.
- Swami, D. and Buddhi, D. 2006. Removal of contaminants from industrial wastewater through various non-conventional technologies: a review. *Int. J. Environ. Pollut.*, 27: 324-346.
- Veli, S. and Alyüz, B. 2007. Adsorption of copper and zinc from aqueous solutions by using natural clay. *J. Hazard. Mater.*, 149: 226-233.
- Yasser M.A., Lee, S.E., Mohamed, B.M., Ahmed, N.T.V., Muhammad, F., Seop, K., Hyuck, S.K., Meththika, V., Adel, R.A., Usman, M., Al-Wabel, E.M., Eilhann, E.K. and Yong, S.O. 2017. Biochar, a potential hydroponic growth substrate, enhances the nutritional status and growth of leafy vegetables. *J. Clean. Prod.*, 156: 581-588.



Estimating Discharge of Nitrogen in Zero Water Exchange at I-Sharp Setiu, Terengganu, Malaysia, Based on System Dynamic Approach

Muhamad Safiih Lola* and Anton Abdulbasah Kamil**†

*School of Informatics and Applied Mathematics, Universiti Malaysia Terengganu, Kuala Terengganu, Malaysia

**Faculty of Economics, Administrative and Social Sciences, Istanbul Gelisim University, Istanbul, Turkey

†Corresponding author: Anton Abdulbasah Kamil; akamil@gelisim.edu.tr

Nat. Env. & Poll. Tech.
Website: www.neptjournal.com

Received: 10-01-2020

Revised: 21-01-2020

Accepted: 16-04-2020

Key Words:

Nitrogen

System dynamics approach

Sustainability

Zero water exchange

ABSTRACT

The present study was designed to display the integrated model of nitrogen discharge process (i.e. nitrites and nitrates; ammonia; chlorophyll and dissolved nitrogen, dissolved oxygen) which is part of the complete model of shrimp aquaculture of an Integrated Shrimp Aquaculture Park (i-Sharp) ecosystem in System Dynamic Model Aquaculture-System Policy (SD-AQEP). This study offers a comprehensive elaboration concerning the long-term process of nitrogen accumulation, as well as its effects on shrimp activities. Furthermore, the analysis of the model and the simulation results also show the conditions of nitrogen with several strategies for control and manipulation. For example, in situations where mixing of stock density is high and providing feed into ponds supplies is excessive, the nitrogen dynamic rapidly hits alarming levels. Aforementioned, the typical strategy in this setting such as stocking density and the best time to harvest could be established. Additionally, the model structure represents the discharge derived from the nitrogen process on varied settings of variables in aquaculture development. In conclusion, this model provides an experimental simulation platform that can be implemented by policy makers on long-term strategic management for developing or maintaining large-scale aquaculture development projects in the future.

INTRODUCTION

The marine shrimp aquaculture production has seen a rather rapid increment by 28.5 times from 3,057 tons in 1991 to 87,202 tons in 2010 (Chowdhury et al. 2013). This phenomenal hike, nonetheless, has sparked some disturbing environmental effects due to the aquaculture activities, where water is highly polluted from shrimp effluents. This is because of the shrimp cultured process releases significant amounts of organic matters, nutrients, phytoplankton, and suspended solids where the corresponding shrimp farm practices high quality feeds and promotes high volume of seawater intake (Boyd 1999). Thus, this unsustainable practice adopted by the shrimp industries especially in their methods of managing wastewater has spawn critics and concern previously (Naylor et al. 2000, Hidayah et al. 2016a, Hidayah et al. 2016b, Nobuyuki, et al. 2016, Hidayah et al. 2017).

In general, the ratio for water exchange (WE) daily is below 15%. This is a common practice for the aquaculture industry throughout the nation (Nik Hashim et al. 2013, Khairul et al. 2013, Akeem Babatunde et al. 2018). Herein, risks towards the environment and existing life forms in the water bodies are increased due to the accumulating discharge regurgitated from these aquaculture ponds.

In reality, a large-scale aquaculture project that focuses onto shrimp production setup in Terengganu, Peninsular Malaysia had been initiated by Blue Archipelago Berhad in 2009 known as Integrated Shrimp Aquaculture Park (i-Sharp) (Muhamad Safiih et al. 2016a). This particular project, which is located at Terengganu coastal area of Peninsular Malaysia, reflects a spawning area of a staggering 1,200 hectares (Muhamad Safiih et al. 2016b, Muhamad Safiih et al. 2017). Before the opening of i-Sharp, this project adopted the semi-biofloc system. Nonetheless, only some ponds were exposed to the fully biofloc system at the initial stage. As time progressed, the i-Sharp began focusing on a bio-secure recirculating system via biofloc technology. Some benefits of the biofloc system are that it uses low input seawater and the fact that the system re-circulates water (Zero Water Exchange, ZWE). By implementing the ZWE system, other colossal benefits are achievable, such as high efficiency, sustainable, competitive productivity, and lower feed conversion ratio where major possibilities of achieving to the sustainable management of aquaculture ponds are limited to the efficiency of biofloc system application (Nyan 2011). Besides, as for i-Sharp, water intake from natural sources is initially to fill in and to maintain the level of water in the aquaculture ponds. Such maintenance is undertaken mainly

to replace the volume of water reduced due to evaporation or filtration. However, only if the effluent can infiltrate natural waterways, such as a river, the remaining trace of cultured water and accumulated residue from the effluent could potentially affect the environment. Unfortunately, organisms like plants and aquatic life forms that exceed the capacity to withstand such changes are surely damaged and turn into environmental pollution. Nevertheless, these remaining sediments and essential wastes could be reprocessed to potentially benefit the agriculture industry (Tanentzap et al. 2015).

With that, nitrogen (N), is a key element associated with the aquatic environment as it functions as one of many variables useful for aquaculture management. Common input of N comes from the environment, but a study shows that N in aquaculture farm mainly results from the existing trace of nitrogen in feed used to enhance the growth of aquaculture productions (Thoman et al. 2001). However, as the feeds are digested, the extra non-digestible nitrogen element is excreted; thus, acting as fertilizer that helps in promoting the build-up of planktons and bacteria colonies (Moriarity 1997).

As such, the present study suggests a system dynamic model as the analytical tool in order to develop a conceptual framework useful in combining numerous nonlinear equations with complex feedback. The structural principle of a dynamic system is primarily dominated by the feedback loop structure that forms a central control for all the corresponding systems (Forrester 1968, Muhamad Safih et al. 2017, Muhamad Safih et al. 2019). Moreover, the positive feedback is set to keep all variables in an equilibrium state. This equilibrium state acts if any variable(s) in the negative feedback loop is moved from equilibrium to ensure that the system would return to its original state or at least towards a new equilibrium state. This system dynamic model approach analyses the sources of problem behaviour, as well as the feedback structure in the system. Therefore, the primary objective of this study is to build a system dynamic model to simulate the feed of N in intensive white shrimp (*Penaeus vannamei*) ponds during culture activities. In addition, the model developed by Burford & Lorenzen (2004) on Pacific tiger shrimp, *Penaeus monod* on cultured had been adopted in this study to describe the principal N transmigrations processes, as well as to identify several alternatives to improve yields.

MATERIALS AND METHODS

Model Description

The model for discharged nitrogen (N) represents the production system that reflects increased input of premium feeds and water supply that leads to stacking of nutrient discharged.

Hence, the cultured ponds generate effluents that are rich in chlorophyll-a, suspended solids, nutrients, and toxic waste; which are essential for agar bloom, thus resulting in high biochemical oxygen demand (Paez-Osuna 2001a, 2001b). This study also adopted the dynamic nitrogen model proposed by Burford & Lorenzen (2004), which had been carried out for intensive cultured of *P. monodon*, along with WE system. With that, the nitrogen dynamic model was applied to describe the complex and the dynamic behaviour of the N in the monitored ponds. Hence, this study adapted Burford's model to investigate the *P. vannamei* intensive culture that practised ZWE in i-Sharp. The basic model assumption does not require the presence of herbivore (non-plank tonic) in all ponds, where N input is exclusively from the feed, whereas the growth of shrimp and phytoplankton (or microorganisms) is not hindered due to lack of oxygen or phosphorus. Fig. 1 illustrates the transformation and removal of nitrogen in intensive shrimp pond. The arrows and the boxes represent for key nitrogen (N) components.

The variables embedded in the model are listed in the following: total ammonia, nitrates and nitrites, Chlorophyll-a (phytoplankton), N in algae biomass, dissolved N organic, and N in sediment. Besides, the demand for feed increased the input of N parallel to the growth of shrimp biomass. Additionally, it was noted that zooplankton, phytoplankton, and nitrifying and heterotrophic bacteria shared the available N excreted from shrimps in ponds (Burford et al. 2003). However, the accumulation of ammonia first caused a halt in feeding shrimp and then, giving impact on the population mortality (Chen et al. 1990). As for the *P. vannamei*, the post-larvae (PL) in ecdysis stage dies if the concentration of ammonia exceeds 10 mg.L^{-1} (Frias-Espericueta et al. 2000). Therefore, if a pond receives an increasing amount

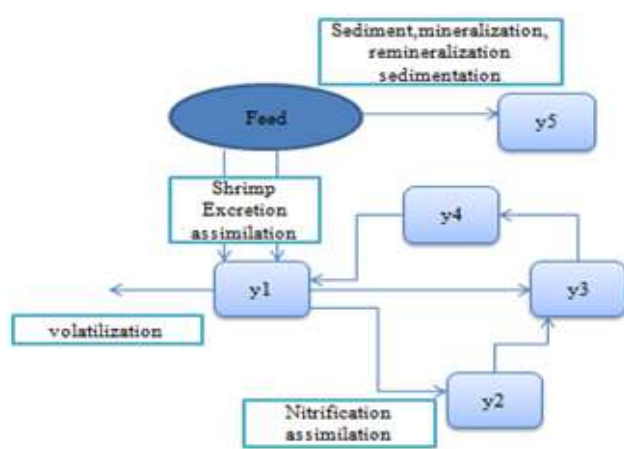


Fig. 1: Nitrogen transformations and removals in intensive white shrimp (*Litopenaeus vannamei*)

of feed, the density of phytoplankton would eventually limit its growth via self-shade. Burford & Lorenzen (2004) predict that the accumulation of ammonia after chlorophyll-a (phytoplankton) impedes its growth. In fact, some N is lost from the pond due to volatilization of ammonia, particularly due to high pH periods and heavy aeration.

The Causal Loop Diagram

The present dynamic model is comprised of causal loop diagrams to represent most of the feedback mechanisms, which is consist of reinforcing/positive feedback loop that is denoted by positive symbol '+' or counteract/negative feedback loop that is reflected by negative symbol '-', to depict a change that has taken place in the system variable (Muhamad Safih et al. 2019). As for this study, the feedback loop functions are a series of cause-and-effect correlated to each other, such that if a change in a given variable or system moves within the loop, it will come back to affect the same variable and other variables. Besides, if an original value or known as 'initials' increase in a variable; the feedback loop in this simulation would eventually result in an expending or increasing effect on the same variable, which is later identified as a 'reinforcing or positive' feedback loop by the system, while the vice versa situation exists if the decreasing effect on the very same variable happens and identified as negative (counteracting or a balancing loop) (Sterman 2002). The positive feedback loop can potentially stimulate volatile exponential growth or cause a collapse in the arrangement of the system associated with simulation behaviour.

Fig. 2 illustrates the causal loop for this study. The concentration of ammonia in the model of discharged nitrogen was fortified by two positive feedback loops that portrayed the processes of nitrates and ammonia. As a result, the negative feedback loops in the system were likely to stabilize the simulation and the asymptotically stable growth, where decaying patterns were observed from the system. Furthermore, the dissolved oxygen (DO) was controlled by two negative feedback loops that represented phytoplankton and shrimp farms. In an instance, increment in ammonia increases the level of nitrates.

The stock-flow diagram in Fig. 3 reflects the core of the discharge of nitrogen model, and it is also the process of quantization and materialization of the causal loop diagram by using Vensim software program (Mesgari et al. 2017). Moreover, based on the stock-flow diagram illustrated in Fig. 3, the related mathematical equation in the mathematical model of system dynamics can be developed.

Basic Model Formulation

This section discusses the formulations that are afflicted to

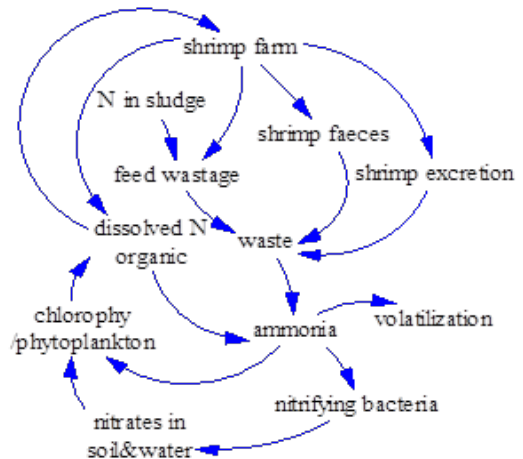


Fig. 2: The causal loop of the discharge of nitrogen model.

several significant model assumptions presented in this study. The mathematical formulations for the discharged nitrogen model in intensive shrimp ponds are derived from the study carried out by Burford & Lorenzen (2004). Such mathematical modelling incorporates a set of five conjoined differential equations that serve as the main nitrogen components.

Ammonia concentration (x_1)

$$\frac{dx_1}{dt} = qaN_0e^{-Mt}Wt^b + ry4(n+v)x_1 - \frac{(g \max light) \frac{x_1 + x_2}{(x_1 + x_2) + Ksn} Cx_3x_1}{x_1 + x_2} \quad \dots(1)$$

Nitrites and nitrates (x_2)

$$\frac{dx_2}{dt} = nx_1 - \frac{(g \max light) \left(\frac{x_1 + x_2}{(x_1 + x_2) + Ksn} \right) Cx_3x_1}{x_1 + x_2} \quad \dots(2)$$

Chlorophyll-a (x_3)

$$\frac{dx_3}{dt} = \left(\frac{(g \max light) \frac{x_1 + x_2}{(x_1 + x_2) + Ksn}}{x_1 + x_2} \right) x_3 - sx_3 \quad \dots(3)$$

Dissolved N organic (x_4)

$$\frac{dx_4}{dt} = scx_3 - rx_4 \quad \dots(4)$$

N in sediment (x_5)

$$\frac{dx_5}{dt} = (1-q)qaN_0e^{-Mt}Wt^b \quad \dots(5)$$

Where, x_1 = NH_3 concentrations (mg.L^{-1}), t = time (day); q = ratio of N waste released to the water as x_1 (enters the water as x_5), $qaN_0e^{-Mt}Wt^b$ is the total of N waste input per unit

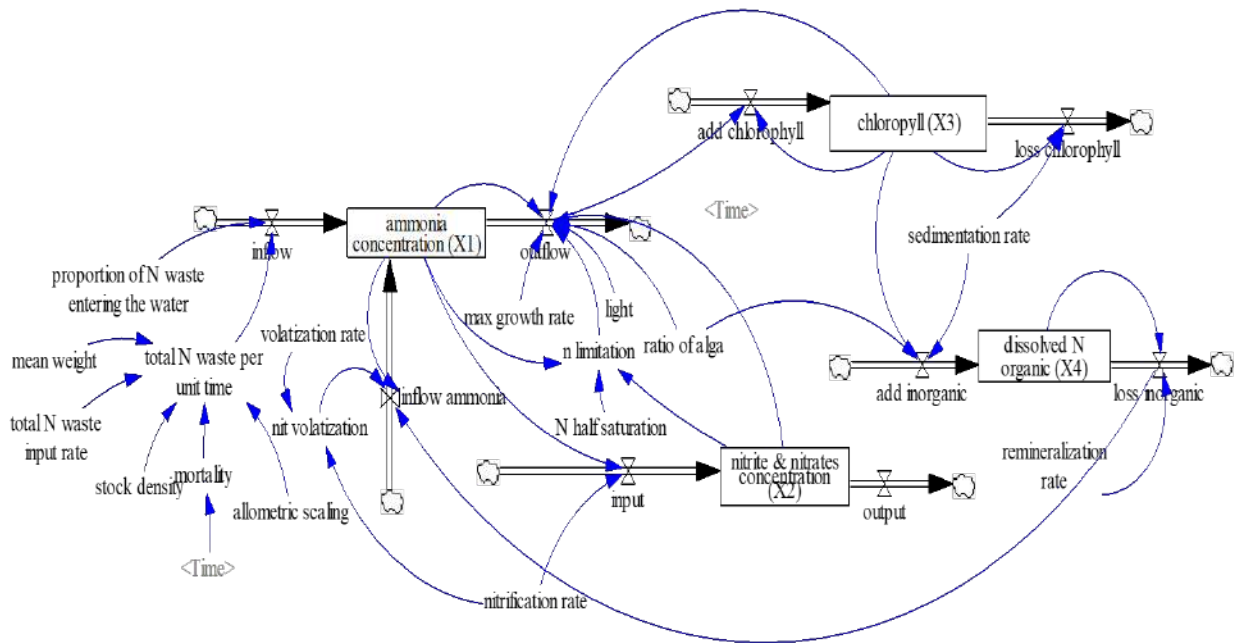


Fig. 3: The stock and flow of the discharge of nitrogen model.

time ($\text{mg}\cdot\text{g}^{-1}\cdot\text{day}$), r = re-mineralized rate of x_1 in sediment (day^{-1}), x_4 = weight of N (mg) in sediment L^{-1} of aqua-cultured water, n = nitrification rate (day^{-1}), v = volatilization rate (day^{-1}), x_2 = $\text{NO}_2 + \text{NO}_3$ concentration ($\text{mg}\cdot\text{L}^{-1}$), x_3 = chlorophyll-a concentration ($\text{mg}\cdot\text{L}^{-1}$) where the concentrations were obtained at a fixed “ cN/X_3 ratio of phytoplankton”, s = sedimentation rate of phytoplankton (day^{-1}), and x_5 = dissolved organic N ($\text{mg}\cdot\text{L}^{-1}$). Besides, the total N waste input, $a\text{N}_0e^{-\text{M}_t\text{W}_t^b}$, had been suggested to be proportional to the metabolism rate of vanamei population (Burford & Lorenzen 2004); where a is the total N waste x_1 and x_5 input rate ($\text{mg}\cdot\text{g}^{-1}\cdot\text{day}^{-1}$), and this parameter was ascertained as the value where N input over the cycle is equivalent to the total feed N that is dissimilated to vanamei tissue.

RESULTS AND DISCUSSION

The preliminary simulation suggests that the maximum weight of shrimp in the cultured pond had been stagnant at 1.63 g, with a stock density of 130 ppL and waste N input at 2.3. Moreover, the initial values for other variables are listed in Table 1.

Fig. 4 illustrates the simulation behaviour that was obtained during the base run. Since ammonia concentration functioned as a self-counterpoise mechanism controlled by two negative feedback loops, ammonia dissolved of nitrogen organic and chlorophyll eventually attained stability. This controlled the potential of self-increasing ammonia mechanisms using nitrates in water primarily due to the

nitrification process. As for the selected cultured, at the end of the simulation, the annual percentage of yield loss due to ammonia concentration had been recorded at 6%. Next, in the second experiment, the stock densities increased to 150ppL from its initial value; 130ppL. Therefore, increment in stock density decreased inorganic loss. In addition, the increased outflow of ammonia from the pond also helped to activate the first positive feedback loop. The results of these experiments are illustrated in Fig. 5, where it displays ammonia concentrations for both settings, inflow ammonia and outflow ammonia.

CONCLUSION

The dynamic discharge of nitrogen model offers a generic and comprehensive description concerning the long-term process of feed demand. As a result, the nitrogen input demonstrated an increase as the shrimp biomass grew. Through the integration of nitrates in water; nitrification and loss of inorganic elements into the discharged nitrogen resulted in a comprehensive and systemic model of nitrogen. The model analysis revealed two self-reinforcing, hence, the critical processes of discharge of nitrogen are indeed associated with the content of nitrates in water and nitrification. Furthermore, the ammonia discharges are in effect self-stabilizing. Nevertheless, the ammonia concentrations may play a critical role: if the stock density is high, the total feed waste hikes automatically in a rather rapid manner, and the applied nitrogen (N) is mostly stored in

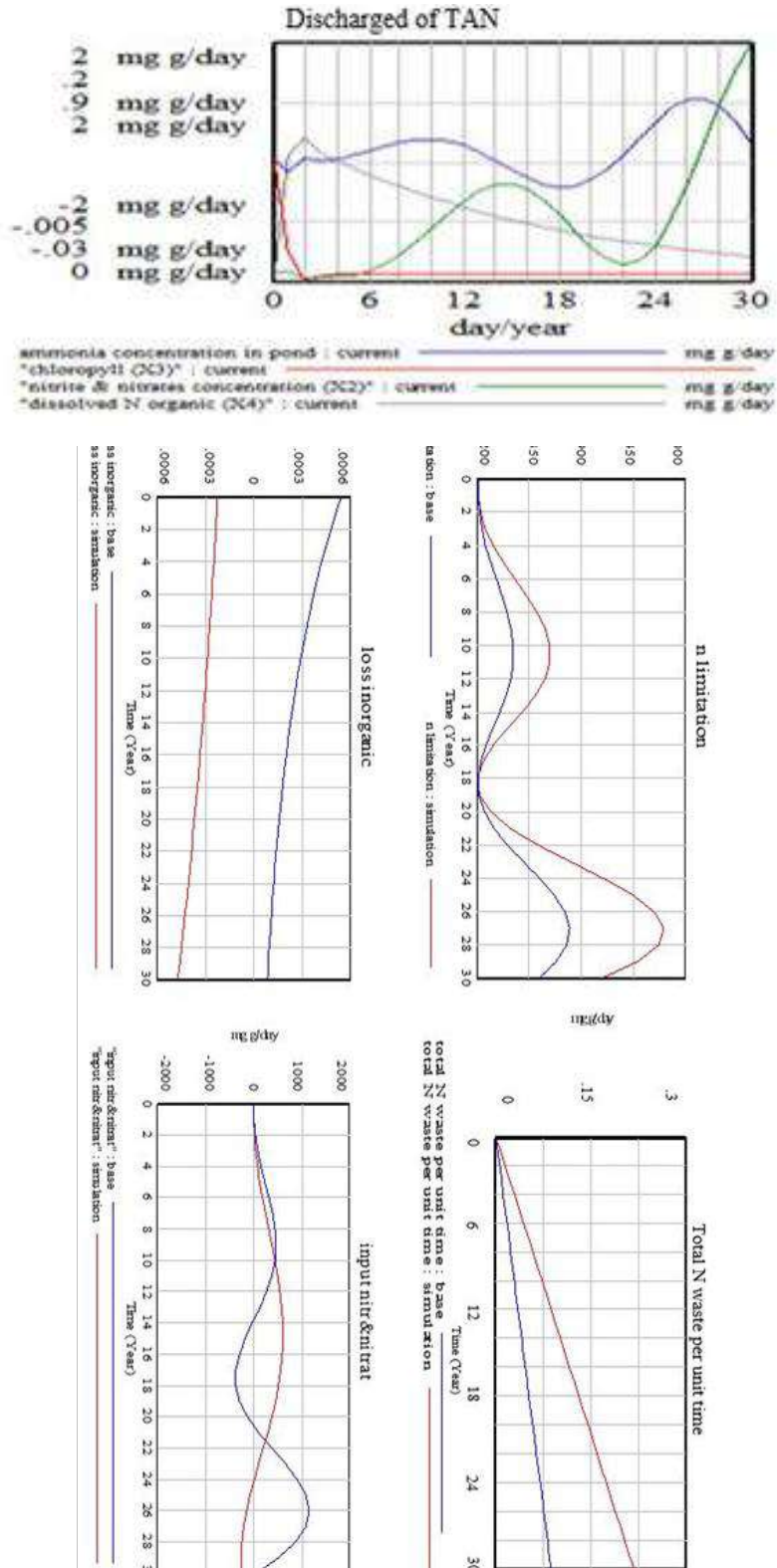


Fig. 4: The base run of the model.

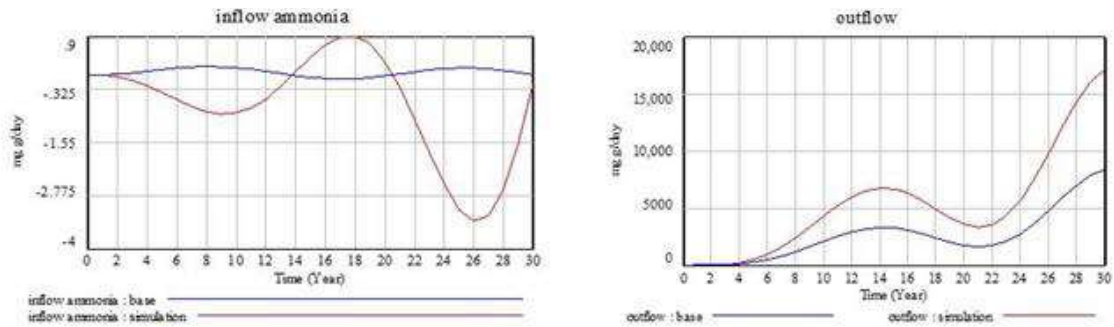


Fig. 5: Inflow ammonia and outflow ammonia simulation.

Table 1: Represent the other parameter value in ponds.

Parameter description	Symbol	Units	Value	Source
White shrimp population				
Shrimp growth coefficient	K	day ⁻¹	0.0086	Data obtained
Shrimp maximum weight	W	G	16.3	Data obtained
Shrimp stocking weight	W_0	G	6.0	Data obtained
Shrimp mortality	M	day ⁻¹	0.05	Data obtained
Stoking density	N_0	shrimp L ⁻¹	130	Data obtained
Nitrogen dynamics				
Waste N Input	A	mg.g ⁻¹ day ⁻¹	2.3	Burford & Lorenzen (2004)
Proportion of N entering as X_1	Q		0.9	Burford & Lorenzen (2004)
Allometric scaling of X_1 excretion	B		0.75	Burford& Williams (2001)
Pond depth	Z	M	1.2	Data obtained
N half-saturation	KSN	mg.L ⁻¹	0.008	Burford & Lorenzen (2004)
Sedimentation rate	s	day ⁻¹	0.8	Burford & Lorenzen (2004)
Nitrification rate	n	day ⁻¹	0.15	Burford & Lorenzen (2004)
Volatilization rate	v	day ⁻¹	0.05	Burford & Lorenzen (2004)
Sludge remineralization rate	r	day ⁻¹	0.06	Burford & Lorenzen (2004)
Phytoplankton parameters				
Maximum phytoplankton growth rate	$gmax$	day ⁻¹	1.9	Burford (1997)
Ratio surface/saturating light intensity	$I0/I sat$		2.4	Burford & Lorenzen (2004)
N/X_3 ratio of algae	c	m ⁻¹	13	Burford & Lorenzen (2004)
Extinction coefficient Non- X_3	$Kother$		2.5	Burford (1997)
Extinction coefficient X_3	$kX3$	m ⁻¹ mg ⁻¹	14	Burford (1997)

pond populations, particularly for shrimp and phytoplankton. More importantly, the typical feeding system was applied in this setting especially, to control the nitrogen level yields, which led to unprecedented exponentially growing ammonia levels, which also reflected the phytoplankton result for nutrients in the pond system. The model offers an experimental simulation laboratory, where numerous other scenarios and questions pertaining to the long-term discharge of nitrogen could be looked into and analysed. This particular model can also potentially be used by policy makers for long-term sustainability strategic management of

large scale aquaculture development projects. The proposed model can also be of interest among students and learners, in teaching and researching environmental sciences, as well as environmental management.

ACKNOWLEDGEMENTS

This study supported by Niche Research Grant Scheme (NRGS) for Setiu Wetland Development P1(R) (Second Phase) Vote No.: 53131/30, Ministry of Higher Education Malaysia. Acknowledgement for Terengganu Economic Development

Unit (UPEN), YDSM, Setiu District Welfare and Safety Committee (JKKK) and Setiu Overall Population for providing insights during interview and questionnaire sessions.

REFERENCES

- Akeem Babatunde, D., Ikhsan, N., Murni, K., Mohd Salleh, K. and Armaya'u Hamisu, B. 2018. African catfish aquaculture in Malaysia and Nigeria: Status, trends and prospects. *Fisheries and Aquaculture Journal*, 9(1): 1-5.
- Chowdhury, A.Z., Islam, M.N., Moniruzzaman, M., Gan, S.H. and Alam, M.K. 2013. Organochlorine insecticide residues are found in surface, irrigated water samples from several districts in Bangladesh. *Bull. Environ. Contam. Toxicol.*, 90(2): 149-154.
- Boyd, C.E. 1999. Aquaculture sustainability and environmental issues. *World Aquaculture*, 30(2): 10-13.
- Burford, M.A. and Lorenzen, K. 2004. Modeling nitrogen dynamics in intensive shrimp ponds: The role of sediment remineralization. *Aquaculture*, 229: 129-145.
- Burford, M.A., Costanzo, S., Denninson, W., Jackson, C.J., Jones, A.B., Mckinnon, A.D., Preston, N.P. and Trott, L.A. 2003. A synthesis of dominant ecological processes in intensive shrimp ponds and adjacent coastal environments in NE Australia. *Marine Pollution Bulletin*, 46(11):1456-1469.
- Chen, J.C., Liu, P.C. and Lei, S.C. 1990. Toxicity of ammonia and nitrite to *Penaeus monodon* adolescents. *Aquaculture*, 89: 127-137.
- Forrester, J.W. 1968. Industrial dynamics after the first decade. *Management Science*, 14(7): 398-415.
- Frias-Espicueta, M.G., Harfush-Melendez, M. and Paez-Osuna, F. 2000. Effects of ammonia on mortality and feeding of post larvae shrimp *Litopenaeus vannamei*. *Bulletin of Environmental Contamination and Toxicology*, 65: 98-113.
- Hidayah, M., Julia Hwei Zhong, M., Nor Azman, K., Suhaimi, S. and Mhd Ikhwanuddin, A. 2016a. Study on carbon sinks by classified biofloc phytoplankton from marine shrimp pond water. *Aquaculture, Aquarium, Conservation and Legislation*, 9(4): 845-853.
- Hidayah, M., Julia Hwei Zhong, M., NorAzman K. and Mhd Ikhwanuddin, A. 2016b. Biofloc application in closed hatchery culture system of pacific white shrimp, *Penaeus vannamei* in sustaining the good water quality management. *Journal of Fisheries and Aquatic Science*, 11(4): 278-286.
- Hidayah, M., Julia Hwei Zhong, M., Nor Azman, K., Suhaimi, S. and Mhd Ikhwanuddin, A. 2017. Identification of biofloc microscopic composition as the natural bioremediation in zero water exchange of Pacific white shrimp, *Penaeus vannamei*, culture in closed hatchery system. *Applied Water Science*, 7: 2437-2446.
- Khairul, A., Rahim, A., Yuzine, E. and Aziz, A. 2013. The influence of alien fish species on native fish community structure in Malaysian waters. *Kuroshio Science*, 7(1): 81-93.
- Mesgari, I., Jabalameli, M. S. and Barzinpour, F. 2017. System dynamics modeling for national agricultural system with policy recommendations: Application to Iran. *Pakistan Journal of Agricultural Sciences*, 54(2): 457-466.
- Muhamad Safiih, L., Siti Hanani, I., Mohd Noor Afiq, R. and Mhd Ikhwanuddin, A. 2016a. Forecasting towards planning and sustainable development based on a system dynamic approach: A case study of the Setiu District, State of Terengganu. *Open Journal of Statistics*, 6(5): 931-950.
- Muhamad Safiih, L., Mohd Noor Afiq, R., Mohd Naeim, A.R., Mhd Ikhwanuddin, A., Madzli, A. H., Syerrina, Z. and Marzuki, I. 2016b. A system dynamics model for analyzing the eco-aquaculture system with policy recommendations: Case study on Integrated Aquaculture Park (i-Sharp), Setiu Terengganu. AIP Conference Proceedings, AIP Publisher.
- Muhamad Safiih, L., Siti Hanani, I., Mohd Noor Afiq, R. and Mhd Ikhwanuddin, A. 2017. Sustainability of integrated aquaculture development project using system dynamic approach. *Journal of Sustainability Science and Management*, 12(2): 194-203.
- Muhamad Safiih, L., Mohd Noor Afiq, R., Mohd Fadli, H., Mohd Tajuddin, A., Kamil, A. A., Izham, M. Y., Yahaya, I. and Nur Zafirah, A.K. 2019. Sustainable development of Tasik Kenyir eco-tourism using system dynamics. In: Mohd Tajuddin, A., Aqilah, M., Mohamed, N.Z., and Muhamad Safiih, L. (eds.) *Greater Kenyir Landscapes*, p. 257-270. Cham, Switzerland: Springer Nature.
- Moriarty, D.J.W. 1997. The role of microorganisms in aquaculture ponds. *Aquaculture*, 151: 333-349.
- Naylor, R.L., Goldburg, R.J., Primavera, J.H., Kautsky, N., Bevrige, M.C.M., Clay, J., Folke, C., Lubchenco, J., Mooney, H. and Troell, M. 2000. Effect of aquaculture on world fish supplies. *Nature*, 405: 1017-1024.
- Nik Hashim, N. M., Azlina, A. A. and Nik Mohd, H. H. 2013. Technical efficiency in aquaculture industry using Data Envelopment Analysis (DEA) window: Evidences from Malaysia. *Journal of Sustainability Science and Management*, 8(2): 137-149.
- Nobuyuki Kawasaki, M.R.M., Kushairi, N. N., Fatimah, Y., Akio, I. and Ayato, K. 2016. Release of nitrogen and phosphorus from aquaculture farms to Selangor river, Malaysia *International Journal of Environmental Science and Development*, 7(2): 113-116.
- Nyan, T. 2011. Intensive shrimp culture water management: Biofloc technology and waste water treatment system. *Persidangan Tahunan MANCID ke 16 (16th MANCO)*. Penang.
- Paez-Osuna, F. 2001a. The environmental impact of shrimp aquaculture: causes, effects and mitigating alternatives. *Environmental Management*, 28: 131-140.
- Sterman, J.D. 2002. *System Dynamics: Systems thinking and modeling for a complex world*. Working Paper Series, Massachusetts Institute of Technology, Engineering Systems Divisions.
- Tanentzap, A.J., Lamb, A., Walker, S. and Farmer, A. 2015. Resolving conflicts between agriculture and the natural environment. *PLoS Biology*, 13(9): 1-13.
- Thoman, E.S., Ingall, E.D., Davis, D.A. and Arnold, C.R. 2001. A nitrogen budget for a closed, recirculating mariculture system. *Aquacultural Engineering*, 24: 195-211.



Effect of Chlorpyrifos 50% + Cypermethrin 5% EC on *Eisenia fetida* Exposed in Coco Peat and Sphagnum Peat

A. Rajini*† and K. Revathy**

*Department of Ecotoxicology, International Institute of Biotechnology and Toxicology, Padappai-601301, Kancheepuram, Tamil Nadu, India

**Meenakshi Academy of Higher Education and Research, K. K Nagar, Chennai-600 078, Tamil Nadu, India

†Corresponding author: A. Rajini; rajitox@gmail.com

Nat. Env. & Poll. Tech.
Website: www.neptjournal.com

Received: 27-01-2020

Revised: 17-02-2020

Accepted: 15-04-2020

Key Words:

Chlorpyrifos
Cypermethrin
Eisenia fetida
Sphagnum peat

ABSTRACT

Toxicity effect of Chlorpyrifos 50% + Cypermethrin 5% EC to terrestrial invertebrate *Eisenia fetida* in two different sphagnum peat substituted soil was assessed. Artificial soil substrate for earthworm toxicity test comprises of 70% sand, 20% clay and 10% sphagnum peat. In this study, coco peat was used as an alternative substitute for sphagnum peat. The LC₅₀ was 83.7 mg/kg for coco peat and 76.3 mg/kg for sphagnum peat soil. No significant difference was observed in mortality and biomass between the two soil substrates, but a significant difference was observed in the reproduction. Based on the observations, it is concluded that coco peat can also be used as an alternative to sphagnum peat in toxicity studies.

INTRODUCTION

Organophosphorus pesticide chlorpyrifos and pyrethroid cypermethrin are used extensively in individual or combination for agricultural and public health pest control. Pesticides reach the soil by leaching or from direct addition for controlling pests. The bioavailability of the pesticide may affect the exposed organisms leading to mortality or reduced population due to its effect on reproduction. Soil invertebrate earthworm is extensively used in the toxicity testing for assessing the damage caused to the soil due to the indiscriminate usage of pesticides. Chlorpyrifos has high application rate for termite treatments hence found in freshwater sediments. It exceeds Stockholm convention criteria for bioaccumulation. It is transported to long ranges and has been found consistently in arctic ice, snow, fog, air, seawater, lake sediments and fishes. It is also considered as an endocrine disrupter with anti-androgenic and estrogenic properties. Cypermethrin is a contact insecticide. Mali (2019) has stated that pyrethroid binds with soil components and thereby leaches into the groundwater as residues, which are harmful to the ecosystem. Pyrethroid molecule may bind to sex hormone and chronic exposure may result in disturbances in hormonal effects

In laboratories, pesticide risk to earthworm is assessed in artificial soil prepared based on guidelines and the

obtained data is used for regulatory risk assessment. For assessing the toxicity effect, artificial soil is prepared in the laboratory with sphagnum peat. Sphagnum peat in the artificial soil is an organic amendment as per OECD (1984), ISO (1993) and ISO (1998) guidelines. It consists of about 10% and other soil ingredients are 70% sand, 20% clay and 0- 1% calcium carbonate. Use of peat moss is decreasing due to its high cost and environmental considerations (Jung & Yang 2014). Jackie (2015) has reported that peat moss used in the United States comes from remote bogs in Canada and there is considerable controversy surrounding the mining of peat moss. As the mining is regulated, only about 0.02 % is available for harvest. International Peat Society points out that the mining process releases massive amounts of carbon into the atmosphere, and bogs continue to exhale carbon long after the mining concludes. Despite, manufacturers of peat moss claim that the bogs can be restored, the delicate community that inhabits the bog cannot be quickly re-established. Though peat moss is a renewable resource, it can take hundreds to thousands of years to form. Peat bogs purify fresh air and mitigate flood damage. Carbon dioxide is also preserved and trapped in the moss, 10% of all fixed carbon is stored in it but released into the air when mined.

Cocos nucifera is largely cultivated in Philippines, Indonesia, India and Sri Lanka and India has emerged as a premier

coconut producer with its annual production of about 12 billion (Jeyaseeli et al. 2010). Coco peat is a by-product of the coconut processing industry and it is available abundantly in tropical countries. Coco peat contains lignin, cellulose and hemicellulose (Yew & Wee 2014). Recycling of organic matter helps in the improvement of soil physical, chemical and biological properties (Kamalraj et al. 2017).

Very few studies have been conducted for replacement of sphagnum peat in artificial soil. Chlorpyrifos 50% + Cypermethrin 5% EC toxicity and its reproduction effect to earthworm *Eisenia fetida* were assessed with coco peat as an alternative substitute to sphagnum peat in the present study.

MATERIALS AND METHODS

Chlorpyrifos 50% and Cypermethrin 5% EC was purchased from commercial market. Earthworm, *Eisenia fetida* was obtained from the culture maintained at the Department of Ecotoxicology, IIBAT. Composted coco peat was procured from Varsha Enterprises, Bangalore and Sphagnum peat was imported from Gramoflor GmbH & Co, Germany as solid blocks. Peat procured was shade dried and pulverised by grinding machine and particle size of <2 mm was obtained using sieves. Kaolin clay was purchased from Romac India Ltd., Chennai and sand with a particle size of 50 to 200 microns was used.

Exposure of Earthworms in Artificial Soils

The artificial soils were prepared as per the guideline OECD (1984) for sphagnum and composted coco peat, separately. Artificial soil was prepared by mixing 70% sand, 20% clay and 10% peat. They were added in a laboratory homogeniser, homogenised for 20 minutes and stored in airtight containers at room temperature. Maximum water holding capacity was performed by the method specified in the guideline (OECD 2004) with slight modifications. About 175 mL of deionised water was used to moisten the soil for earthworm survival.

Glass beakers of 2 L capacity were filled with approximately 500 g of artificial soil. Earthworms were exposed to pesticide concentrations of 12.3, 22.1, 39.7, 71.4, 128.6, 231.5, 416.6 and 750 mg/kg of soil, a control group was also maintained. Pesticide concentrations were applied to the artificial soil and homogenised using a laboratory mixer and moistened with water. Earthworms of about 4-6 months old with a wet weight in the range of 260 to 450 mg/worm including gut contents with well-developed clitellum were acclimatised one day prior in the respective artificial soils. Shade dried and powdered cow manure was added on the top of the soil as food and feed consumption was observed visually and fresh feed was added once weekly. Four replications for each concentration and eight replications

for control were maintained with ten earthworms. The glass beakers were maintained in the test room with a temperature of $20 \pm 2^\circ\text{C}$ and light intensity range was kept at 400-800 lux. The earthworms were exposed for 28 days to the pesticide mixed soil. After 28 days, they were sorted from the soil and observed for mortality. The live earthworms were weighed and disposed of. After removal of the adult earthworms on day 28, five gram of cow manure was mixed into the artificial soil to feed the juveniles in the container. The soils were maintained in the same test conditions for an additional 28 days and for reproduction assessment the soil from the beakers was transferred to a tray and kept in a water bath at 50°C . The juveniles in each beaker were sorted and counted manually.

RESULTS

No mortality was observed in control and concentrations of 12.3, 22.1, 39.7 mg/kg in the soil containing coco peat and sphagnum peat, mortality was observed in the concentration of 71.4, 128.6, 231.5, 416.6 and 750 mg/kg soil in coco peat and sphagnum peat containing soil. In 39.7 and 71.4 mg/kg soil inability to burrow into the soil was observed in both artificial soils. No-observed effect concentrations related to mortality were found to be 39.7 mg/kg soil, for both the soils (Fisher's exact test). No observed effect concentration related to biomass was found to be 71.4 and 128.6 mg/kg for coco peat and sphagnum peat soils (Dunn's test). LC_{50} of Chlorpyrifos 50% + Cypermethrin 5% EC at 28 days after exposure was observed to be 83.7 mg/kg for coco peat soil and 76.3 mg/kg soil for Sphagnum peat soil and EC_{50} (Effective concentration based on reproduction) was 60.01 mg/kg coco peat soil and 45.48 mg/kg for sphagnum peat soil are summarised in Table 1.

The overall comparison at all the dose-response level on mortality between the soils was not significant (Two-factorial

Table 1: Comparison of mortality, biomass change and juveniles exposure to Chlorpyrifos 50% + Cypermethrin 5% EC in coco peat and sphagnum peat soils.

End points	Coco peat	Sphagnum peat
NOEC (mg/kg)	39.7	39.7
Mortality (%) [#]		
NOEC (mg/kg)	71.4	128.6
Biomass change (%) ^{##}		
NOEC (mg/kg)	22.1	<12.3
Reproduction (%) ^{##}		
LC_{50} (mg/kg) [§]	83.7	76.3
(Fiducial limits)	(76.2 - 92.1)	(68.9 - 84.2)
EC_{50} (mg/kg) [@]	60.01	45.48
(Fiducial limits)	(31.48 - 88.55)	(42.36 - 48.83)

NOEC-No-Observed Effect Concentration, Fisher's exact test[#], Dunn's for NOEC^{##}, 3 Probit Analysis[§], OECD Model 2 by MARQUARDT[@]

ANOVA, $p = 0.05$). The biomass of adult earthworms in the control group had an increase in both the controls of coco peat soil and sphagnum peat soil. Significant biomass change from control was observed in the concentration of 128.6 and 71.4 mg/kg soil in coco peat and sphagnum peat soils and are summarised in Table 2.

The overall dose-response biomass change for both the soils was not significant (Two-factorial ANOVA, $p = 0.05$). The mean number of juveniles observed in all the concen-

trations ranged from 0 to 60.25 and 0 to 76.0 in coco peat and sphagnum peat treated soils. The significant effect on reproduction was observed at 39.7 mg/kg soil for coco peat and 12.3 mg/kg soil sphagnum peat soil and are summarised in Table 3. Statistical analyses were performed using ECOSTAT software with SAS.

DISCUSSION

Pesticides have an impact on the physiology and behaviour

Table 2: Comparison of mortality and biomass change due to pesticide exposure in coco peat and sphagnum peat soils.

Concentration (mg/kg)	Mortality (%) [#]		Biomass change (%) ^{##}	
	COPS	SPPS	COPS	SPPS
Control	0.0	0.0	+47.95 (8.16)	+29.27 (13.72)
12.3	0.0 n.s.	0.0 n.s.	+49.43 n.s. (1.00)	+33.59 n.s. (4.96)
22.1	0.0 n.s.	0.0 n.s.	+54.69 n.s. (3.52)	+41.80 n.s. (5.69)
39.7	0.0 n.s.	0.0 n.s.	+46.92 n.s. (6.44)	+24.51 n.s. (13.71)
71.4	27.50* (15.0)	45.00* (12.91)	+38.51 n.s. (3.37)	+17.45 * (4.97)
128.6	95.00* (5.77)	95.00* (5.77)	-53.90* (53.58)	-54.05 * (53.57)
231.5	100*	100*	-100*	-100*
416.6	100*	100*	-100*	-100*
750	100*	100*	-100*	-100*
Statistical comparisons between soil ^{###}	P-value		0.7211 n.s.	
	0.0052*			

COPS - Coco peat soil; SPPS - Sphagnum peat soil; Mean of four replications; Figures in parentheses are Standard Deviation; n.s. = not significantly different; *= significantly different; Fisher's exact test ($\alpha = 0.05$)[#]; Dunns test ($\alpha = 0.05$)^{##}; Two-factorial ANOVA^{###}

Table 3: Comparison of reproduction effect of the pesticide in coco peat and sphagnum peat soils.

Concentration (mg/kg)	Juveniles (No.) [#]		Reduction over control (%)	
	COPS	SPPS	COPS	SPPS
Control	58.63 (6.16)	101.75 (11.06)	NA	NA
12.3	60.25 n.s. (4.79)	75.75* (12.45)	46.27	25.55
22.1	51.50 n.s. (5.80)	76.00* (6.38)	12.16	25.31
39.7	31.50* (3.11)	61.75* (5.56)	-2.76	39.31
71.4	8.50* (2.38)	6.50* (1.73)	85.50	93.61
128.6	0	0*	100	100
231.5	0	0*	100	100
416.6	0	0*	100	100
750	0	0*	100	100
Statistical comparisons between soil ^{###}	P value			
	<0.0001*		-	

Mean of four replications; Figures in parentheses are standard deviation; n.s. = not significantly different; *= significantly different; Trend test (Jonckheere-Terpstra) ($\alpha = 0.05$)[#]; Two-factorial ANOVA^{##}

of earthworms; the worms have developed mechanisms to detoxify themselves and spend a lot of energy for it, hence they do not reach the normal size. They are less successful at reproducing because they spend their energy on ridding themselves of the pesticides (Givaudan et al. 2014). Growth inhibition and reduction in biomass is an indicator of stress. Pesticide affects the energy dynamics and ultimately inhibit the growth and weight of the tested organisms. It has been reported that deltamethrin inhibited growth, and is correlated with the worm's strategy to reduce food intake to avoid the toxins (Mohamed et al. 2013). Avoidance of soils treated with cypermethrin was studied as a bioindicator in *Eisenia andrei* and earthworms were found in the untreated section of the soil (Sousa 2011). Zhou (2008) studied the effect of cypermethrin chronic exposure and observed that toxicity significantly increased to juveniles than adult earthworms and also growth and reproduction were severely affected. Wang et al. (2012) reported enzyme and cellulose activity of *Eisenia fetida* was inhibited by treatment with chlorpyrifos. Zhou et al. (2011) stated that pesticide mixture toxicity is not known since the toxicity data obtained are exclusively from individual pesticide; this may mislead the ecological risk of pesticides. Growth and reproduction of earthworms exposed to pesticides are useful bioindicators of soil pollution.

Peat is an organic material which plays a major role to determine toxicity level in earthworm toxicity testing. Fermented coir pith has been recommended as a composition of artificial soil and coir pith is a suitable alternative to Sphagnum peat moss for the composition of artificial soil modified for tropical regions (Abbiramy et al. 2012). De Silva et al. (2009) studied the suitability of coco peat, paddy husk and saw-dust as alternatives to sphagnum peat in the artificial soil for performing ecotoxicity studies and recommend the suitability of coco peat as an alternative to sphagnum peat. Water holding capacity of sphagnum peat was significantly higher than that of coco peat. Moisture content varied of coco and sphagnum peat was 30.07 to 32.66% and 32.81 to 37.76%, respectively. Total organic matter plays an important role to predict the biological response of earthworms and essential elements are higher in coco peat. Abbiramy et al. (2012) also observed similar physico-chemical characteristics in the two peat samples and it can be correlated with the obtained current results. Tiwari et al. (2019) indicated a potential risk of chlorpyrifos, cypermethrin individual pesticide and its combination. It had a synergistic cumulative impact in a dose-dependent manner during exposure to earthworms.

The present experimental results validate the use of coco peat as an alternative to sphagnum peat in the artificial soil prepared for toxicity studies.

CONCLUSION

From the results, it is concluded that the combination pesticide, Chlorpyrifos 50% + Cypermethrin 5% EC had a profound effect on the biomass and reproduction of the exposed earthworms in both the soils containing the coco and sphagnum peat and coco peat can be used as an alternative substitute of sphagnum peat.

ACKNOWLEDGEMENT

The author is thankful to IIBAT and Department of Ecotoxicology for providing the research facility.

REFERENCES

- Abbiramy, K.S., Ronald Ross, P., Thenmozhi, P., Muthulingam, M., Paramanandham, J. and Manoharan, V. 2012. The validation of modified tropical artificial soil by ecotoxicological studies on *Eisenia foetida*. International Journal of Development Research, 2(5): 1051-1056.
- De Silva, P.M.C.S. and Van Gestel, C.A.M. 2009. Development of an alternative artificial soil for earthworm toxicity testing in tropical countries. Appl. Soil Ecol., 43(2-3): 170-174. doi:10.1016/j.apsoil.2009.07.002.
- García, M., Scheffczyk, A., García, T. and Rombke, J. 2011. The effects of the insecticide lambda-Cyhalothrin on the earthworm *Eisenia fetida* under experimental conditions of tropical and temperate regions. Environ. Pollut., 159: 398-400.
- Givaudan, N., Wiegand, C., Le Bot, B., Renault, D., Pallois, F., Llopis, S. and Binet, F. 2014. Acclimation of earthworms to chemicals in anthropogenic landscapes, physiological mechanisms and soil ecological implications. Soil Biology and Biochemistry, 73: 49-58. doi: 10.1016/j.soilbio.01.032.
- ISO 1993. Soil quality-effects of pollutants on earthworms (*Eisenia fetida*), Part 1: Determination of acute toxicity using artificial soil substrate. ISO 11268-1. International Organization for Standardization, Geneva, Switzerland.
- ISO 1998. Soil quality-effects of pollutants on earthworms (*Eisenia fetida*), Part 2: Determination of effects on reproduction. ISO 11268-2. International Organization for Standardization, Geneva, Switzerland.
- Jackie, Carroll 2015. Peat Moss and Gardening - Information about Sphagnum Peat Moss <http://www.gardeningknowhow.com/garden-how-to/soil-fertilizer/peatmoss-information.html>.
- Jeyaseeli, D.M. and Raj, S.P. 2010. Chemical characteristics of coir pith as a function of its particle size to be used as soilless medium. Ecoscan, 4(2&3): 163-169.
- Jung, J.Y. and Yang, J.K. 2014. The suitability evaluation of lignocellulosic substrate as growing media substitute. African Journal of Biotechnology, 13(14): 1541-1549.
- Kamalaraj, R., Nandhivarman, M., Pynkhlainbor Thongni, Pradheeps, M. and Poyyamoli, G. 2017. Utilization of agrowastes for vermicomposting and its impact on growth and reproduction of selected earthworm species in Puducherry, India. Nature Environment and Pollution Technology.16(4): 1125-1133.
- Mali, G.V. 2019. Toxicological study of bifenthrin and its metabolites on earthworm (*Eisenia fetida*). Nature Environment and Pollution Technology, 18(4): 1387-1391.
- Mohamed, E. I. Badawy, Anter Kenawy and Ahmed, F. El-Aswad 2013. Toxicity assessment of buprofezin, lufenuron, and triflumuron to the earthworm *Aporectodea caliginosa*. International Journal of Zoology, 2013:174523. doi: 10.1155/2013/174523.

- OECD 1984. Guideline for Testing of Chemicals No. 207: Earthworm Acute Toxicity Test Organization for Economic Co-Operation and Development, Paris, France.
- OECD 2004. Guideline for Testing of Chemicals No. 222: Earthworm Reproduction Test (*Eisenia fetida/andrei*). Organization for Economic Co-Operation and Development, Paris, France.
- Sousa, A.P.A.D. and Andréa, M.M.D. 2011. Earthworm (*Eisenia andrei*) avoidance of soils treated with cypermethrin. *Sensors*, 11(12): 11056-11063.
- Tiwari, R.K., Singh, S. and Pandey, R.S. 2019. Assessment of acute toxicity and biochemical responses to chlorpyrifos, cypermethrin and their combination exposed earthworm, *Eudrilus eugeniae*. *Toxicology Reports*, 6: 288-297.
- Wang, J. H., Zhu, L.S., Liu, W., Wang, J. and Xie, H. 2012. Biochemical responses of earthworm (*Eisenia foetida*) to the pesticides chlorpyrifos and fenvalerate. *Toxicology Mechanisms and Methods*, 22(3): 236-241.
- Yew, B.S. and Wee F.H. 2014. Agricultural waste based-coco peat microwave absorber. *International Journal of Engineering Sciences & Emerging Technologies*, 7(2): 547-554.
- Zhou, S., Changqun, D., Xuehua, W., Michelle, W., Zefen, Y. and Hui, F. 2008. Assessing cypermethrin-contaminated soil with three different earthworm test methods. *Journal of Environmental Sciences*, 20: 1381-1385.
- Zhou, S., Duan, C., Michelle, W.H.G., Yang, F. and Wang, X. 2011. Individual and combined toxic effects of cypermethrin and chlorpyrifos on earthworm. *Journal of Environmental Sciences*, 23(4): 676-680.



Temperature-Sensitive Ionic Liquid-Based Dispersive Microextraction for Removal of Industrial Dyes in Water

Y. Wang[†], M.C. Wei, Q.C. Yu and M.T. Zhu

College of Life and Health Sciences, Anhui Science and Technology University, Fengyang 233100, P.R. China

[†]Corresponding author: Y. Wang; yanwang0129@126.com

Nat. Env. & Poll. Tech.
Website: www.neptjournal.com

Received: 19-01-2020

Revised: 18-02-2020

Accepted: 16-04-2020

Key Words:

Ionic liquid

Temperature-sensitive

Microextraction

Dye removal

ABSTRACT

In this study, a new and effective temperature-sensitive ionic liquid-based dispersive microextraction method was developed for dye removal from water. Through the temperature change, the ionic liquid (IL) could complete dispersion in the aqueous phase to fully contact with the dyes, and then it was recovered as particles enriching target substance by cooling. Parameters including chemical structure and amount of IL, dispersing solvent and its volume, extraction temperature, extraction time, pH adjustment and ionic strength were investigated and optimized in detail. Under the optimized conditions, the extraction recovery was 98.9% of methyl violet, 95.6% of Congo red, and 98.8% of methylene blue, respectively. The results showed that the major driving force for the extraction might be the hydrophobic interaction between the dye and IL. In short, the proposed technique is rapid, simple, relatively inexpensive and effective. This implies meaningful information for further research and application in the field of actual samples.

INTRODUCTION

Currently, food and textile industries often directly discharge significant raw coloured sewage due to pigments and dyes. Most of the dyes containing nondegradable aromatic structure have been considered to be one of the most problematic wastewaters (Liu et al. 2014). Those dyes have been reported to be genotoxic (Salem 2000). So, the development of an effective, viable, simple and rapid method for treatment and disposal of hazardous dyes is urgently needed. Various techniques including adsorption, biological process and photo-degradation have been generally used (Jiang et al. 2011, Sun et al. 2011, Zhu et al. 2011). However, these methods are commonly time-consuming, high solvent consumption, costly or ineffective.

To minimize the extraction process, several techniques have been developed. Among them, dispersive liquid-liquid microextraction (DLLME) has attracted wide interest in separation field due to its rapidity and simplicity (Zhao et al. 2012). In this technique, the dispersive solvent is injected immediately into the sample solution. Then a cloudy solution possessing droplets of extraction solvent is shaped, and the hydrophobic target analytes are transferred to the extraction phase, followed by centrifugation or filtration for recovery. The exposed large surface between sample analytes and extraction solvent can result in rapid mass transfer and high

extraction efficiency. Ionic liquids (ILs) are molten salts and exhibit unique physicochemical properties such as tunable viscosity and solubility, negligible vapour pressure, high thermal stability, and non-flammability (Rogers & Seddon 2003). They have been recently proposed as extraction solvents instead of traditional organic solvents in DLLME procedure (Abdolmohammad-Zadeh & Sadeghi 2010, Jha et al. 2018, Liu et al. 2009, Zhao et al. 2016a). Although abundant inspiring results have been realized, ILs still have some weaknesses in the DLLME procedure, including emulsification, relatively high viscosity and difficult recovery (Liu et al. 2014, Pena-Pereira et al. 2009). In recent years, temperature-sensitive ionic liquids, which can regulate their solubility in some solvents by changing the temperature, have got a great deal of attention. Temperature-sensitive ionic liquid-based dispersive liquid-liquid microextraction (TSIL-DLLME) is gradually becoming a new hot and promising technique (Padilla-Alonso et al. 2017, Sheikhan & Shirafkan 2016, Zhang & Shi 2010). In this process, the dispersion of IL can be achieved by heating, thus solubilizing IL in the sample solution to produce a homogeneous system. Then it was recovered as tiny particles enriching target solute by cooling. The special property makes it combine the advantages of both homogeneous and heterogeneous extractants.

Based on the above background, the present work aims to explore an effective way with solid hydrophobic IL (a kind of

temperature-sensitive ionic liquids) in the proposal of dyeing water. In this work, several *N*-butylbenzothiazolium ILs were prepared, and the development of a TSIL-DLLME procedure to extract three dyes (Methyl violet, MV; Methylene blue, MB; Congo red, CR) from water samples was proposed. All the variables, affecting the extraction process, were investigated and optimized in detail. The suggested method was proved to be available, rapid, simple and effective. The message acquired in this work provided an alternative approach for the removal of the dye in the practical application.

MATERIALS AND METHODS

Reagents and Materials

MV, CR and MB were purchased from Shanghai Macklin Biochemical Co., Ltd (China). 1-Bromobutane, 1-bromopentane, 1-bromohexane, 1-bromoheptane, and potassium hexafluorophosphate were of analytical grade and purchased from Aladdin Reagent Co. Ltd. (China). Benzothiazole was obtained from CS-Pharm Chemical Co. Ltd. (China). ILs, like *N*-butylbenzothiazolium hexafluorophosphate ($[C_4Bth][PF_6]$), *N*-pentylbenzothiazolium hexafluorophosphate ($[C_5Bth][PF_6]$), *N*-hexylbenzothiazolium hexafluorophosphate ($[C_6Bth][PF_6]$) and *N*-heptylbenzothiazolium hexafluorophosphate ($[C_7Bth][PF_6]$) were synthesized as described by a reference (Liu et al. 2014). All other chemicals were of analytical grade or higher.

Extraction Procedure

10.0 mL dye solution (40 mg/L) was poured into a 25 mL well-sealed colourimetric tube. 1 mL of dispersing solvent containing 100 mg $[C_nBth][PF_6]$ ($n = 4, 5, 6, 7$) was injected rapidly into the aqueous solution to form a cloudy solution. Then the mixture was heated at a controlled temperature to become a homogeneous system, and the analytes were extracted into the IL phase. Hereafter, the tube was cooled in an ice bath for 15 min to obtain a turbid solution. The

dispersed fine particles of the extraction phase were filtrated, and the concentration of the dye in the filtrate was subject to the quantitative analysis on a UV-vis spectrophotometer. All experiments were performed in triplicate.

The extraction recovery (ER , %) was defined as the percentage of the total dye amount extracted to the sedimented phase:

$$ER (\%) = (1 - \frac{C_f \times V_f}{C_0 \times V_0}) \times 100 \quad \dots(1)$$

Where, C_f and C_0 are the dye concentration (mg/L) in the filtrate phase and the sample solution, V_f and V_0 correspond to the volume of the filtrate solution and the sample solution, respectively.

RESULTS AND DISCUSSION

Selection of IL and Dispersive Solvent

An appropriate type of IL is essential for efficient extraction. In this work, four hydrophobic ILs were investigated, including $[C_4Bth][PF_6]$, $[C_5Bth][PF_6]$, $[C_6Bth][PF_6]$, and $[C_7Bth][PF_6]$. As can be observed, $[C_4Bth][PF_6]$ formed the best dispersion cloud during the cooling step. The phenomenon may be due to the relatively lower solubility of $[C_4Bth][PF_6]$ in the system. Furthermore, the dyes showed a better affinity for $[C_4Bth][PF_6]$. The results were shown in Fig. 1a. Considering these results, $[C_4Bth][PF_6]$ was chosen as the most appropriate extraction solvent for further experiments.

The dispersive solvent should effectively disperse the IL into the sample solution to increase the contact area. And the main point to be concerned in selecting dispersive solvent is its miscibility in both sample solution and IL. For this purpose, methanol, ethanol and acetonitrile were preliminarily screened and then tested as potential dispersive solvents. The results, as shown in Fig. 1b, demonstrated that acetonitrile exhibited the highest extraction efficiency for the three target dyes. Thus, acetonitrile was chosen as the disperser solvent for further study.

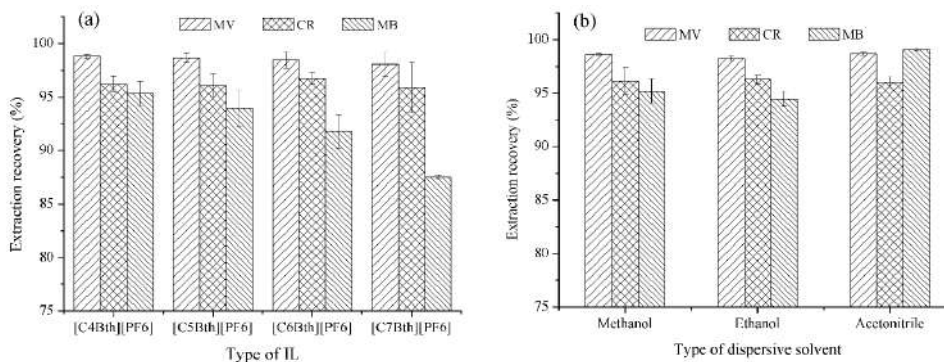


Fig. 1: Effects of various ILs and dispersive solvents on extraction recovery.

Effect of the Amount of IL

To establish the optimum amount of IL, the effect of the amount of $[C_4Bth][PF_6]$ was investigated in the range of 20–120 mg. This parameter was important as a very low amount of extraction solvent could complicate the recovery of the sedimented phase, while a very high amount needed much time to disperse the IL into the sample solution, which will affect the mass transfer. As can be observed in Fig.2, higher extraction recovery was obtained by increasing IL amount to 50 mg. Further increasing the IL amount showed no obvious change. The results indicated that 50 mg of IL was sufficient to extract dyes in the proposed system. Thus, 50 mg of IL was used for the following experiments.

Effect of Extraction Temperature

Temperature acts an important role for the complete dispersion of IL and mass transfer of dyes, which can increase the contact area between the dyes and IL (Zhang & Shi 2010). To evaluate the effect of extraction temperature on the recoveries of dyes, different temperature ranging from 40 to 90°C were tested. As shown in Fig. 3, the extraction recovery enhanced gradually with the increasing temperature and then remained stable. The rising temperature could improve the solubility and dispersion of IL into the sample solution. However, a higher temperature might lead to a certain amount of IL dissolving in the sample solution, in turn, affect the generation of the cloudy solution after cooling (Zhang et al. 2012). Besides, whether at 60°C or 70°C, there was no significant difference. Therefore, 60°C was selected as the further operating temperature.

Effect of Extraction Time

To study the effect of extraction time on the extraction recovery of dye into the IL phase, different extraction time ranging from 5 to 50 min were tested. As shown in Fig. 4, the maximum extraction recovery of dye into IL phase

was related to the extraction time of 10 min, and a longer time could not obtain higher extraction recovery. When the mixture of IL and the dispersive solvent was injected into the sample solution, it would take a short period of time for the dyes to transfer from aqueous phase to IL phase and to reach an equilibrium state. But the volatilization of acetonitrile might lead to the loss of dyes as the extraction time went longer. This behaviour was also observed by Liang et al. (2017), who summarized that with a longer time, the volatilization of organic solvent and consequent thermal effect of analytes could affect extraction efficiency. Thus, 10 min was selected as the optimum extraction time.

Effect of Dispersive Solvent Volume

The volume of acetonitrile affects the dispersion degree of $[C_4Bth][PF_6]$ in the aqueous phase, consequently influencing the formation of dispersion cloud, finally affecting the extraction efficiency. Therefore, the effect of the volume of acetonitrile was studied in the range of 0.5–1.5 mL. As shown in Fig.5, higher extraction recovery was obtained by increasing acetonitrile volume to 1.0 mL, and then it slightly decreased as the volume increasing. At low volume, the cloudy solution of IL could not form completely. On the contrary, the amount of the sedimented phase and extraction recovery of target dyes would decrease due to the increased solubility of IL in the sample solution. Hence, 1.0 mL of acetonitrile was chosen as the optimum disperser volume.

Effect of Sample pH

The pH of the sample solution is an essential factor in the extraction process. It could affect the existing form of the targets and the interaction mechanism between targets and IL. In this work, a broad pH range of 4.0–10.0 was evaluated and the results were presented in Fig.6. It was clear that the extraction recovery of MV and MB had not a remarkable change in the investigated pH range, while it was not the case in CR solution. The recovery of CR increased and reached a

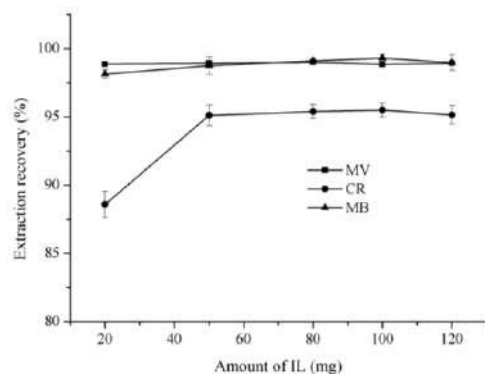


Fig. 2: Effect of amount of IL on extraction recovery.

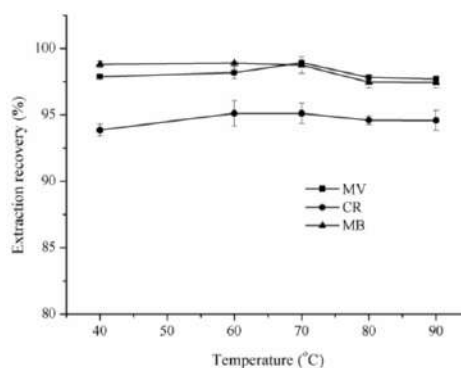


Fig. 3: Effect of extraction temperature on extraction recovery.

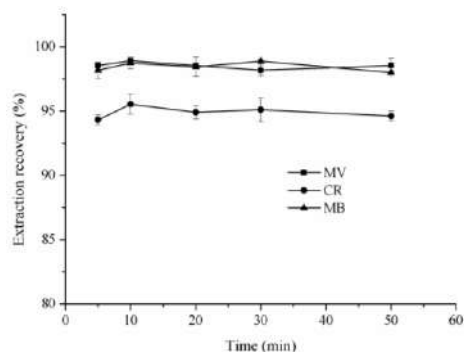


Fig. 4: Effect of extraction time on extraction recovery.

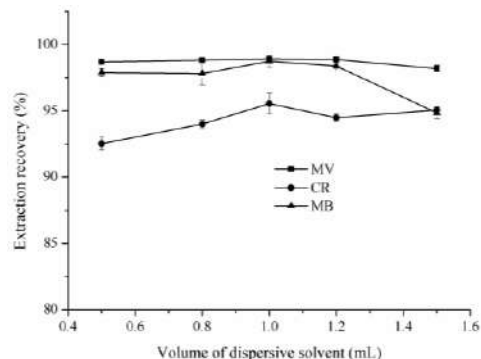


Fig. 5: Effect of dispersive solvent volume on extraction recovery.

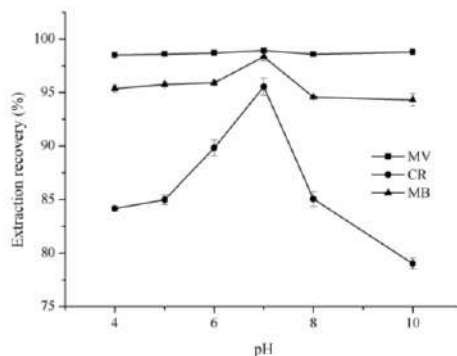


Fig. 6: Effect of sample pH on extraction recovery.

maximum value at a pH of 7.0, and thereafter decreased. The hydrophobic affinity of dye molecules to the IL phase may be driving force for extraction of dye into IL phase (Liu et al. 2014). Considering these results, the pH of 7.0 was chosen for the subsequent assay.

Effect of Ionic Strength

Under the previous optimum conditions, the effect of ionic strength was investigated by adding NaCl (0.2-1.0%, g/mL). Generally, the addition of salt could increase the extraction efficiency due to the possible salting-out effect. However, in the current study, the ionic strength did not have a remarkable effect on the extraction of dyes (data not shown in figure). This behaviour was also observed by Liang (Liang et al. 2017). Thus, this TSIL-DLLME procedure was performed without salt addition to the aqueous solution.

Analysis of Real Water Samples

To further evaluate the applicability and accuracy of the proposed method, drinking water and wastewater samples were analysed. To assess the matrix effect, water samples were spiked with target dyes at the concentration level of 10 mg/mL ($n = 3$). Theoretically, the recovery values will not exceed 100% in the recovery experiment. However, inherent errors such as operation error and system error are inevitable in practice. Thus, the recovery values were higher than 100%. It is a common phenomenon in method validation. In our study, the relative recovery values were in the range of 91.7-100.6%, with RSD of 1.5-4.1%. The results were summarized in Table 1. The results indicated that the suggested approach could be employed as an effective technique to extract these dyes from water.

Table 1: The relative recoveries and standard deviations of dyes in water samples.

Analyte	Added (mg/mL)	Relative recovery (%)		RSD (%)	
		drinking water	wastewater	drinking water	wastewater
MV	10.0	100.6	97.8	2.6	3.7
CR	10.0	93.0	91.7	1.8	4.1
MB	10.0	95.8	93.5	1.5	3.1

Table 2: Comparison of TSIL-DLLME with other procedures for the removal of dyes.

Target	Method	Extractant	Extractant volume or amount	Recovery (%)	Reference
Malachite green, Crystal Violet, Methylene blue	MSPE-DLLME	[Hpy]NTf ₂	70 µL	86.1-100.3	(Liang et al. 2017)
Malachite green, Crystal violet, Methylene blue	SPE	MCAX cartridges	–	75	(Xu et al. 2012)
Malachite green, Crystal violet	IL-DLLME	[C ₈ MIM]PF ₆	80 µL	91.7-97.2	(Zhang et al. 2012)
Malachite green, Gentian violet, Leucomalachite green, Leucogentian violet	MSPE	MWCNT@Fe ₃ O ₄	60 mg	87.0-92.8	(Zhao et al. 2016b)
Methyl violet, Congo red, Methylene blue	TSIL-DLLME	[C ₄ Bth][PF ₆]	50 mg	91.7-100.6%	Present method

Comparison of TSIL-DLLME Method with Previous Reported Procedures

The extraction efficiencies of MV, CR and MB were notably enhanced by the presented TSIL-DLLME method. As summarized in Table 2, the extraction solvent using in DLLME is [C₄Bth][PF₆], which involves some advantages such as temperature-sensitive phase-variable property, and reduction of exposure to toxic solvent. This method provided a relatively more sensitive and higher extraction recovery than previous reports. Meanwhile, the established method provided new insight into the extraction techniques of MV, CR and MB in water samples.

CONCLUSION

In this study, the TSIL-DLLME technique was successfully applied for the extraction of three dyes from water samples. The IL, [C₄Bth][PF₆], was possible to effectively extract target dyes by only changing solution temperature, and could be recovered by simple filtration. Under the optimized conditions, the extraction recovery was 98.9% of MV, 95.6% of CR, and 98.8% of MB, respectively. The main driving force for the extraction was hydrophobic interaction between the dye and IL. In real water samples, the suggested technique also showed satisfactory performance. Compared with the conventional methods, the proposed temperature-sensitive IL-based dispersive extraction technique is simple, rapid, relatively inexpensive and effective. The results display a good alternative to the current methods for the extraction of dyes from aqueous solution.

ACKNOWLEDGEMENTS

The work was supported by the Talent Introduction Special Foundation of Anhui Science and Technology University (SKYJ201601).

REFERENCES

- Abdolmohammad-Zadeh, H. and Sadeghi, G.H. 2010. Combination of ionic liquid-based dispersive liquid-liquid microextraction with stopped-flow spectrofluorometry for the preconcentration and determination of aluminium in natural waters, fruit juice and food samples. *Talanta*, 81(3): 778-785.
- Jha, R.R., Singh, C., Pant, A.B. and Patel, D.K. 2018. Ionic liquid based ultrasound assisted dispersive liquid-liquid micro-extraction for simultaneous determination of 15 neurotransmitters in rat brain, plasma and cell samples. *Anal. Chim. Acta.*, 1005: 43-53.
- Jiang, R., Zhu, H.Y., Guan, Y.J., Fu, Y.Q., Xiao, L., Yuan, Q.Q. and Jiang, S.T. 2011. Effective decolorization of azo dye utilizing SnO₂/CuO/polymer films under simulated solar light irradiation. *Chem. Eng. Technol.*, 34(2): 179-185.
- Liang, N., Hou, X., Huang, P., Jiang, C., Chen, L. and Zhao, L. 2017. Ionic liquid-based dispersive liquid-liquid microextraction combined with functionalized magnetic nanoparticle solid-phase extraction for determination of industrial dyes in water. *Sci. Rep.*, 7: 13844.
- Liu, J.B., Wang, L.T., Zhu, W.X., Jia, C.M., Deng, Q. and Yao, S. 2014. Temperature-assisted removal of triphenylmethane dyes from water with novel hydrophobic benzothiazolium ionic liquids. *Sep. Sci. Technol.*, 49(1): 146-153.
- Liu, Y., Zhao, E., Zhu, W., Gao, H. and Zhou, Z. 2009. Determination of four heterocyclic insecticides by ionic liquid dispersive liquid-liquid microextraction in water samples. *J. Chromatogr. A*, 1216(6): 885-891.
- Padilla-Alonso, D.J., Garza-Tapia, M., Chávez-Montes, A., González-Horta, A., Waksman de Torres, N.H. and Castro-Ríos, R. 2017. New temperature-assisted ionic liquid-based dispersive liquid-liquid microextraction method for the determination of glyphosate and aminomethylphosphonic acid in water samples. *J. Liq. Chromatogr. R. T.*, 40(3): 147-155.
- Pena-Pereira, F., Lavilla, I. and Bendicho, C. 2009. Miniaturized preconcentration methods based on liquid-liquid extraction and their application in inorganic ultratrace analysis and speciation: A review. *Spectrochim. Acta B*, 64(1): 1-15.
- Rogers, R.D. and Seddon, K.R. 2003. Ionic liquids-solvents of the future. *Science*, 302(5646): 792-793.
- Salem, I.A. 2000. Kinetics of the oxidative color removal and degradation of bromophenol blue with hydrogen peroxide catalyzed by copper (II) supported alumina and zirconia. *Appl. Catal. B-Environ.*, 28(3-4): 153-162.
- Sheikhian, L. and Shirafkan, M. 2016. Temperature-assisted ionic liquid-based dispersive liquid-liquid microextraction with following back-

- extraction for HPLCUV-Vis determination of 3-indole acetic acid in pea plants. *J. Iran. Chem. Soc.*, 13(5): 903-911.
- Sun, H., Wang, L., Qin, X. and Ge, X. 2011. Simultaneous determination of malachite green, enrofloxacin and ciprofloxacin in fish farming water and fish feed by liquid chromatography with solid-phase extraction. *Environ. Monit. Assess.*, 179(1-4): 421-429.
- Xu, Y.J., Tian, X.H., Zhang, X.Z., Gong, X.H., Liu, H.H., Zhang, H.J., Huang, H. and Zhang L.M. 2012. Simultaneous determination of malachite green, crystal violet, methylene blue and the metabolite residues in aquatic products by ultra-performance liquid chromatography with electrospray ionization tandem mass spectrometry. *J. Chromatogr. Sci.*, 50(7): 591-597.
- Zhang, H.F. and Shi, Y.P. 2010. Temperature-assisted ionic liquid dispersive liquid-liquid microextraction combined with high performance liquid chromatography for the determination of anthraquinones in Radix et Rhizoma Rhei samples. *Talanta*, 82(3): 1010-1016.
- Zhang, Z., Zhou, K., Bu, Y., Shan, Z. Liu, J., Wu, X., Yang, L. and Chen, Z. 2012. Determination of malachite green and crystal violet in environmental water using temperature-controlled ionic liquid dispersive liquid-liquid microextraction coupled with high performance liquid chromatography. *Anal. Methods*, 4(2): 429-433.
- Zhao, A., Wang, X., Ma, M., Wang, W., Sun, H., Yan, Z., Xu, Z. and Wang, H. 2012. Temperature-assisted ionic liquid dispersive liquid-liquid microextraction combined with high performance liquid chromatography for the determination of PCBs and PBDEs in water and urine samples. *Microchim. Acta*, 177(1-2): 229-236.
- Zhao, J., Wei, D. and Yang, Y. 2016a. Magnetic solid-phase extraction for determination of the total malachite green, gentian violet and leucomalachite green, leucogentian violet in aquaculture water by high-performance liquid chromatography with fluorescence detection. *J. Sep. Sci.*, 39(12): 2347-2355.
- Zhao, J., Zhu, Y., Jiao, Y., Ning, J. and Yang, Y. 2016b. Ionic-liquid-based dispersive liquid-liquid microextraction combined with magnetic solid-phase extraction for the determination of aflatoxins B1, B2, G1, and G2 in animal feeds by high-performance liquid chromatography with fluorescence detection. *J. Sep.Sci.*, 39(19): -3789 3797.
- Zhu, H.Y., Fu, Y.Q., Jiang, R., Jiang, J.H., Xiao, L., Zeng, G.M., Zhao, S.L. and Wang, Y. 2011. Adsorption removal of congo red onto magnetic cellulose/Fe₃O₄/activated carbon composite: Equilibrium, kinetic and thermodynamic studies. *Chem. Eng. J.*, 173(2): 494-502.



Development of Emissions Inventory and Pollution Classification for Energy-Intensive Heavy Metal Industries in A Densely Distributed Area

Jia Jia*, Jingjing Yang**†, Yawen Song***, Huimin Chen**** and Xi Zhang****

*School of Management Engineering, Zhengzhou University of Aeronautics, Zhengzhou 450046, China

**Information Management Department, Zhengzhou University of Aeronautics, Zhengzhou 450046, China

***School of Foreign Languages, Zhengzhou University of Aeronautics, Zhengzhou 450046, China

****Henan Tianlang Ecological Technology Co. Ltd., Zhengzhou 450046, China

†Corresponding author: Jingjing Yang; jasper@zua.edu.cn

Nat. Env. & Poll. Tech.
Website: www.neptjournal.com

Received: 02-03-2020

Revised: 05-06-2020

Accepted: 10-12-2020

Key Words:

Iron and steel industry
Air pollutants
Negative health impact
CAMx
Classification technology

ABSTRACT

The iron and steel industry puts considerable pressure on the regional environment of the Beijing-Tianjin-Hebei (BTH) area, and the PM_{2.5} pollution has caused serious harm to public health. To explore a detailed and high-resolution emission inventory of the iron and steel industry in the BTH region, a classification technology method with CAMx modelling system was developed and applied for classifying all the iron and steel enterprises in the BTH region. Besides, simulation scenarios were designed particularly for quantitatively assessing the effectiveness of the environmental protection measures. Results show that the pollutant emission of the iron and steel industry significantly contributes to the PM_{2.5}, SO₄²⁻, NO₃, and SOA concentrations in the atmospheric environment in sub-areas. Therefore, the enterprises in western and central sub-areas show high classification coefficients. Restricting pollutant emissions using the developed classification technology method is more effective in reducing the PM_{2.5} concentration of the BTH region compared with the proportional reduction method. Thus, the classification method should be primarily implemented for reducing the air pollutant emissions of the iron and steel industry in the BTH region.

INTRODUCTION

The iron and steel industry, which has rapidly grown along with the increasing demand derived from the rapid urbanization and various infrastructure construction activities, plays an important role in the development of China. However, the iron and steel industry has become one of the highest energy consumption and pollutant emission industries due to its rapid economic expansion (Tao et al. 2014). Enormous quantities of air pollutants were generated (Huang et al. 2014, Yang et al. 2017, Chen et al. 2014, Sina et al. 2019), resulting in significant regional environmental problems (Amodio et al. 2013). The Beijing-Tianjin-Hebei (BTH) region, wherein numerous iron and steel enterprises are gathered and the steel production capacity accounts for approximately one-third of China according to the report of the Ministry of Industry and Information Technology, has trapped itself in a dilemma known as the “Steel Overcapacity” (Li et al. 2017), which puts considerable pressure on the regional environment. Moreover, the iron and steel industry has been progressively recognized to have a strong impact on human health, thereby increasing mortality and morbidity rates due to respiratory diseases.

The iron and steel industry is identified as an energy and pollution-intensive manufacturing sector (Wang et al. 2016) and an important emission source of air pollutants (Li et al. 2016). Therefore, a systematic and reliable estimation of its emissions is essential for policymakers to address critical atmospheric environmental hazards. In most studies, the emission inventories of air pollutants treated the iron and steel industry as a whole in the industrial process emissions mainly due to data availability (Streets et al. 2003, Cheng et al. 2012, Zhou et al. 2014). High-resolution emission inventories of primary air pollutant emissions in the Pearl River Delta (PRD) region and the Yunnan and Hebei Provinces in China were built (Zheng et al. 2009, Tang et al. 2012, Zhao et al. 2012) based on the data from the statistical yearbooks. However, these studies revealed that the iron and steel industry was still treated as one of the large industrial point sources. Inventories of different industries were created to understand the operational process and pollutant emission characteristics effectively. Wu et al. (2015) estimated the direct emissions of air pollutants from the iron and steel industry. Wang et al. (Wang et al. 2016) built a comprehensive emission inventory for the iron and steel industry in China with multiple air pollutants. A comprehensive and

high-resolution atmospheric emission inventory of multiple air pollutants from the iron and steel industry in the BTH region, covering almost all the iron and steel plants and processes (coking, sintering, puddling, steelmaking and rolling), is developed in this study to examine the pollution characteristics and the negative effects on the atmospheric environment.

Identifying the most important pollution sources based on emission inventories is crucial for the development of effective emission control strategies. The comprehensive air quality model with extensions (CAMx) model, which could simulate the emission, dispersion, chemical reaction, and removal of pollutants by marching the Eulerian continuity equation forward in time for each chemical species, was developed (Pateraki et al. 2013, Bossioli et al. 2013). Guttikunda et al. (2014) applied the CAMx model to estimate the pollution contribution for individual coal-fired thermal power plants in India and advised that aggressive pollution control regulations are imperative for regional clean air. The CAMx model was also applied in the BTH region by Li et al. (2015) for comparing the pollution contribution between anthropogenic emissions and exploring the quantitative understanding of the source receptor relationships. The CAMx model was employed in this study to simulate the sensitivity of iron and steel enterprises to various pollutants, and the results were used for assessing and classifying the emission sources.

As an extension of previous efforts, this study provides a detailed and high-resolution emission inventory of the iron and steel industry in the BTH region and employs the CAMx

modelling system to simulate the sensitivity of enterprises to various pollutants. A classification technology method is developed based on the emission inventory and simulation results. This method is used for assessing the influence of pollution emission from sources on PM_{2.5} concentration and classifying the iron and steel enterprises in the BTH region. Multiple scenarios are also assumed and simulated to analyze the influence of reducing pollutant emissions of the iron and steel industry. The BTH region is probably the most important gathering centre of the iron and steel industries in China. Thus, this study provides a rare and valuable opportunity for examining the impact of pollutant emissions from iron and steel enterprises on air pollution. The results would also provide a scientific base for governments in China to make sound control policies and measures in the future, which aim to provide a clean air environment for people to reduce the negative impact of air pollution on human health.

MATERIALS AND METHODS

The emissions of air pollutants (SO₂, NO_x, CO and VOCs), PM_{2.5} (particles with an aerodynamic diameter of 2.5 μm), and total suspended particulate (TSP) from the iron and steel industry in the BTH region in 2015 are estimated in this study by applying a unit-based and bottom-up methodology with a refined activity database. Varied processes are sub-grouped and separately considered in this methodology in terms of different patterns of process facilities and pollution control measures. Fig. 1 shows the geographical locations of the iron and steel enterprises in the BTH region.

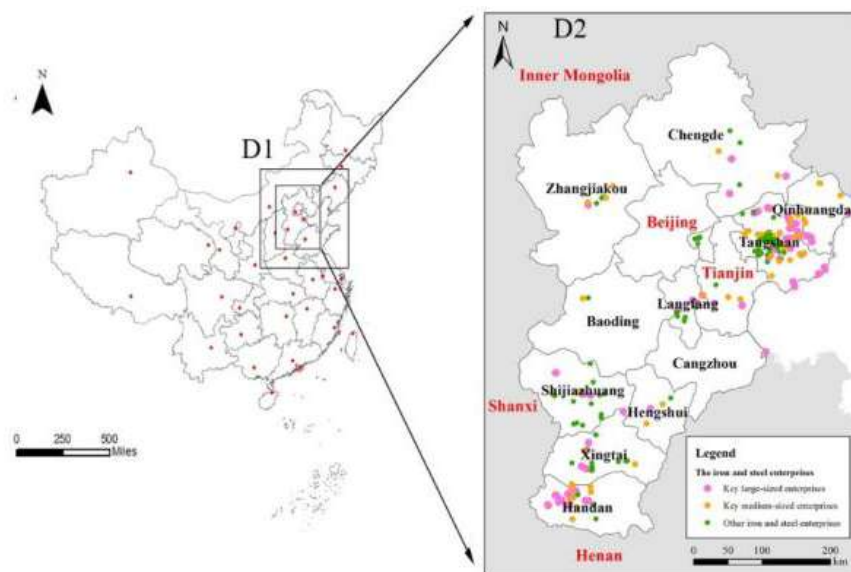


Fig. 1: Geographical locations of the iron and steel enterprises in the BTH region and the double nesting simulation domain of the CAMx model.



Fig. 2: Localization of the sampled iron and steel enterprises and the 14 sub-areas delineated as the pollution source inputs for the CAMx model.

Sampling Sites Description

In recent years, approximately 20 iron and steel enterprises in the BTH region and their air pollutant emission outlets were sampled and monitored by the members of the Key Laboratory of Beijing on Regional Air Pollution Control. The enterprises were selected based on the production process, pollution control facilities and geographical location. All the traditional iron and steel production processes were involved, and various kinds of pollution control facilities, including wet and semi-dry flue gas desulfurization facilities, bag filter facilities and electrostatic precipitator facilities, were also involved. Fig. 2 presents the localization of the sampled iron and steel enterprises.

The concentrations of SO_2 and NO_x were collected from the on-line monitoring device, which was widely popularized in the iron and steel enterprises in the BTH region. PM and VOC samples were respectively collected by filters and summa canisters by dilution sampling systems (Wang et al. 2016, Wei et al. 2014). The inductively coupled plasma mass spectrometry (ICP-MS, 7500a, Thermo), ion chromatography (IC, Metrohm 861 Advanced Compact IC), and thermal/optical carbon analyser (DRI Model 2001A, Desert Research Institute of United States) were used not only for determining the concentration of $\text{PM}_{2.5}$ and TSP from the well-stored samples collected from the air pollutant outlets under real conditions (Wang et al. 2015) but also for testing the concentration

of elements, water-soluble ions, and carbonaceous species, respectively. In addition, the VOC samples were measured by using gas chromatography-mass spectrometry (GC-MS, Model 7890A/5975C, Agilent Inc). Details of the sampling process, sample analysis, and quality control could be found in previous works published by the researchers of the Key Laboratory of Beijing on Regional Air Pollution Control (Wei et al. 2014, Li et al. 2014, Wei et al. 2016).

Emission Inventory and Uncertainty Analysis

The emission inventory of the iron and steel industry is calculated on the basis of the detailed activity data collected from investigation and source-specific emission factors (EF) to determine the emission characteristics of the gaseous pollutants and PM in iron and steel enterprises. This calculation is shown in Eq. (1).

$$E = EF \times AL \quad \dots(1)$$

Where E is the emission estimate for a source category, EF is the emission factor for the category, and AL is the collected activity data. Emission factors, rather than pollutants producing factors, are chosen for calculation in this study mainly because of the uneven and discrepant control measures and efficiencies in iron and steel enterprises in the BTH region. A bottom-up approach was used for developing the emission inventory for all iron and steel enterprises in the BTH region.

Previous works published by the researchers of the Key Laboratory of Beijing on Regional Air Pollution Control provide the emission inventories of other industries (e.g., power plants, chemical processing enterprises, and architectural material industry) and non-industrial sectors (e.g., pollutants from residential areas, dust from vehicles, roads, and construction sites) used in this study.

The iron and steel industry involves a series of interrelated processes. Considering the most recent study, the iron and steel industry inventory developed in this study includes the following main source categories. (1) Coking process, in which coals are carbonized to generate the coke. (2) Sintering process (including sintering and pelletizing sub-categories), in which raw materials comprising fine iron ores and flux materials are agglomerated by combustion to produce sinter products. This process involves two sub-categories: sintering and shaft furnace (pelletizing). (3) Puddling process, in which sinter and coke products are subsequently introduced in the blast furnace to generate pig iron. (4) Steelmaking process, in which molten iron is combined with scrap steels and fluxes and transported to furnaces to produce molten steel. This process includes the following sub-categories: basic oxygen furnace (BOF) and electric arc furnace (EAF). (5) Rolling process, in which molten steel is solidified to produce the final iron and

steel products. The sub-categories of this process include hot and cold rolling. (6) Unorganized, which particularly focuses on PM_{2.5} and TSP emissions for each process.

The resolution of activity data determines the preliminary resolution of emission inventory. A complete investigation of activity data was launched for all iron and steel enterprises of the BTH region to obtain detailed data for establishing a high-resolution emission inventory. Detailed statistic information was obtained with the assistance of provincial and municipal environmental protection bureaus and administration departments. The activity data contain the production of coke, sinter, pig iron, and crude and rolled steels, which were used for calculating the emission from each process of iron and steel enterprises, and the unorganized emission. Other data, including the removal efficiency of control facilities, operating expense, and economic cost, were also collected directly.

The emission factors in this study were acquired from three ways. (1) Sampling results, in which the emission factors were calculated on the basis of concentrations of gaseous pollutants and PM and the manufacture of products for each source category; (2) The Manual of Emission Coefficient; (3) existing studies, that is, the average emission factors of CO for varied process steps by referring to available research results and simultaneously considering comparable pollution control facilities (Streets et al. 2006). Essentially, the emission factors applied for developing the iron and steel inventory were acquired from the sampling results and existing studies (mainly for emission factors of CO). Meanwhile, the emission factors acquired from the Manual of Emission Coefficient and existing studies were also used for verification and comparison with the emission factors from sampling results. Table A1 lists the emission factors applied for calculating the emission inventory of the iron and steel industry in the BTH region and the comparison between emission factors from different ways.

Overall, the emission factors captured from the sampling results were slightly lower than those of previous studies. This finding is mainly attributed to the significant improvement of the pollution control technology in the iron and steel industry over the past few years and the increase in the popularization rate of pollutant control facilities. However, part of the NO_x emission factors in the sintering process and the PM emission factors in the steelmaking process showed adverse tendencies compared with others. This result is associated with the operation of only a few NO_x removal equipment (Wu et al. 2015) in the BTH region and the lower efficiency of the existing pollution control facilities than expected.

Modelling System

The CAMx model was employed in this study to simulate the impact of pollutant emissions of iron and steel enterprises

on the atmospheric environment, and the simulation results were used for assessing and classifying the emission sources. The Weather Research & Forecasting (WRF) model was used for simulating the meteorological background for air quality simulation. Particulate Source Appointment Technology (PSAT) was used in the simulating process as a source apportionment tool to estimate the contributions of respective emission sources (Wu et al. 2013), that is, adding reactive tracers into the CAMx model to apportion PM_{2.5} components from different sub-regions and source categories. Consequently, the source information of each selected species on each grid at each time step is delivered and developed (Li et al. 2015). The physical parameter schemes of the WRF and CAMx models for the air quantity simulation in this study were selected as follows: (a) two-way interactive grid nesting, (b) 12 vertical layers, and (c) gas-phase chemistry using the Carbon Bond-V mechanism, which includes 156 reactions formulations, and aerosol chemistry using the AER06 aerosol mechanism. Additional details of the CAMx model and PSAT algorithms can be found in the manual of the CAMx model.

A double nesting simulation domain was designed in this study for the integrated CAMx modelling system, as shown in Fig. 1. Domain 1 (D1) refers to the outside domain with a grid resolution of 27 km × 27 km. This domain covers the BTH region and surrounding provinces, including Shandong, Shanxi, most of Inner Mongolia, Liaoning, Shaanxi, Henan, Jiangsu, and parts of Jilin, Anhui, Hubei, with a total area of almost 1.8 million km². This design includes all possible external PM_{2.5} emission sources (which might affect the PM_{2.5} concentration in the BTH region) in the simulation emission inventory. Domain 2 (D2) refers to the inside domain with a grid size of 9 km × 9 km, covering mainly the BTH region. D2 presumably provides an effective PM_{2.5} simulation resolution.

In the air quality simulation, the simulation domain must be divided into a series of sub-areas to evaluate the pollutant transport between geographic boundaries of sub-areas labelled by the CAMx model. Fourteen sub-areas that delineated within the D2 domain represent the 14 pollution emission source inputs to the CAMx model, as indicated in Fig. 2. The 14 sub-areas are as follows: Beijing (BJ), Tianjin (TJ), Zhangjiakou (ZJK), Chengde (CD), Qinhuangdao (QHD), Tangshan (TS), Baoding (BD), Langfang (LF), Cangzhou (CZ), Shijiazhuang (SJZ), Hengshui (HS), Xingtai (XT), Handan (HD), and other regions (OT). The receptor points close to the state-controlled monitoring stations in each sub-area were selected to simulate the PM_{2.5} concentrations and emission contributions from the iron and steel industry and verify the CAMx model. In addition, the simulation results for each grid point in the D2 domain were

Table A1: Emission factors of pollutants applied for iron and steel industry in BTH region and the comparison with the manual and previous researches.

Source categories	Sub-categories	Scale	Emission factors/kg·ton ⁻¹					Comparison of emission factors/kg·ton ⁻¹					
			SO ₂	NO _x	PM _{2.5}	TSP	VOCs	CO	SO ₂	NO _x	PM _{2.5}	TSP	VOCs
<i>Coking</i>	Coking furnace	< 5 m	0.64	0.60	0.54	0.73	0.55	6.66 ^b	0.91 ^b	1.23 ^b	1.2-1.75 ^a	1.45 ^b	2.1-2.4 ¹
		> 5 m	0.58	0.44	0.41	0.59	0.41						
<i>Sintering</i>	Sintering head	<100 m ²	2.52	2.76	0.48	1.04	0.17	22.00 ^{b*}	2.80 ^{ac*}	0.61 ^{ac*}	0.54 ^{ac*}	1.59 ^{ac*}	0.22 ^{c*}
		100-200 m ²	2.22	1.51	0.20	0.43	0.14	22.00 ^{b*}	2.60 ^{ac*}	0.58 ^{ac*}	0.27 ^{ac*}	0.52 ^{ac*}	0.22 ^{c*}
		>200 m ²	0.80	0.77	0.11	0.27	0.13	22.00 ^{b*}	2.40 ^{ac*}	0.52 ^{ac*}	0.21 ^{ac*}	0.40 ^{ac*}	0.22 ^{c*}
	Sintering tail	<100 m ²	ND	ND	0.18	0.35	ND	-	-	-	-	-	-
		100-200 m ²	ND	ND	0.11	0.22	ND	-	-	-	-	-	-
		>200 m ²	ND	ND	0.09	0.20	ND	-	-	-	-	-	-
<i>Puddling</i>	Pelletizing	All	1.36	0.55	0.12	0.40	0.14	ND	2.00 ^{ac}	0.14 ^{ac}	0.13 ^{ac}	0.44 ^{ac}	ND
		<2000 m ³	0.11	0.16	0.85	1.76	0.04	23.7 ^{dg}	0.13 ^{ac}	0.17 ^c	0.11 ^{ch}	1.03 ^{ch}	ND
<i>Steelmaking</i>	BOF	>2000 m ³	0.09	0.14	0.29	0.60	0.04		0.11 ^{ac}	0.15 ^c	0.06 ^{ch}	0.16 ^{ch}	ND
		50-150 t	0.03	0.05	0.36	0.56	0.06	2.96 ^{dg}	ND	0.01 ^e	0.12 ^{ac}	0.27 ^{ac}	0.06 ^{df}
	EAF	>150 t	0.02	0.05	0.22	0.34	0.06		ND	0.01 ^e	0.14 ^{ac}	0.16 ^{ac}	0.06 ^{df}
		30-50 t	0.04	0.59	1.15	1.80	0.04	9.80 ^{dg}	0.01 ^{ch}	0.04 ^e	0.76 ^{ac}	0.85 ^{ac}	0.06 ^{df}
<i>Rolling</i>	Hot rolling	>50 t	0.03	0.54	0.52	0.81	0.04		0.01 ^{ch}	0.03 ^e	0.35 ^{ac}	0.39 ^{ac}	0.06 ^{df}
		All	0.09	0.08	0.02	0.04	0.12	ND	0.27 ^a	0.28 ^{ac}	0.03 ^{ac}	0.04 ^{ac}	0.02 ^{df}
	Cold rolling	All	0.13	0.08	0.01	0.02	0.06	ND	0.14 ^a	0.08 ^{ac}	0.01 ^{ac}	0.01 ^{ac}	0.06 ^{df}
<i>Unorganized</i>	Coking furnace	All	ND	ND	0.05	0.33	ND	ND	ND	ND	ND	ND	ND
	Sintering tower	All	ND	ND	0.14	0.56	ND	ND	ND	ND	0.07 ^{ac}	0.40 ^{ac}	ND
	Pelletizing	All	ND	ND	0.06	0.53	ND	ND	ND	ND	0.06 ^{ac}	0.52 ^{ac}	ND
	BF	All	ND	ND	0.53	1.83	ND	ND	ND	ND	ND	ND	ND
	BOF	All	ND	ND	0.14	0.56	ND	ND	ND	ND	ND	ND	ND
	EAF	All	ND	ND	0.33	1.26	ND	ND	ND	ND	ND	ND	ND
	Rolling	All	ND	ND	0.05	0.10	ND	ND	ND	0.07 ^{ac}	0.29 ^{ac}	ND	

^aThe Manual of Emission Coefficient, b (Zhao et al. 2008), c (Wu et al. 2015), d (Huang et al. 2011), e (Yang et al. 2013), f (Tsai et al. 2008), gh (Wang et al. 2015); ND: Not detected; * Both emission factors for the head of the sintering tower (sintering head) and the tail of sintering tower (sintering tail) were considered for calculating, which were not separated in the previous studies.

extracted, and their average values were used to investigate the influence of pollutant emissions from iron and steel enterprises on the atmospheric environment of the entire BTH region and calculate the sensitivity and classification coefficients for each enterprise.

Model Verification

The simulated $PM_{2.5}$ concentrations were compared in this study with the observed data to validate the model. The indicators for model verification include correlation coefficient (R), normalized mean bias (NMB), normalized mean error (NME), and the fraction (M_i/O_i) satisfying the condition $0.5 < M_i/O_i < 2$ (FAC), where M_i and O_i are the simulated and observed $PM_{2.5}$ concentrations at time i , respectively. The statistic approaches used in this study can be found in many previous literature works (Gao et al. 2015, Wang et al. 2014, Zhang et al. 2013). Fig. 3 presents the comparison results of the simulated and observed $PM_{2.5}$ mean daily concentrations in January, April, July, and October (respectively representing winter, spring, summer and autumn) of 2015 in typical sub-areas (BJ and SJZ were selected because of geographical location, TS and HD were selected because of the large number of iron and steel plant enterprises). The results indicate that high correlations between observed and simulated concentrations are obtained, with the simulation errors at an acceptable level. In particular, the values of R are larger than 0.65, with the NMB ranging from 14% to 26%, the NME ranges being 26%-49%, and the FAC ranges being 86%-126%.

The model validation errors come possibly from two sources: (1) uncertainties of the emission inventory; (2) errors from the WRF-CAMx modeling process itself. However, the comparison results generally indicate that an acceptable consistency between the simulated and observed concentrations has been achieved (Dong et al. 2013, Wang et al. 2010), and the WRF-CAMx modeling system can be utilized for simulation in this study.

Classification Technology Method

The developed classification technology method is not only used for classifying the enterprises through calculating the effects of pollutant emission from enterprises on the atmospheric environment but also applied for locating the priority control of atmospheric pollution sources for regional air quality management. The classification coefficients were calculated based on sensitivity and potential coefficients. CO was not analysed in this section due to its minimal influence on $PM_{2.5}$ concentrations (Streets et al. 2006). The detailed algorithms are presented below.

The sensitivity coefficient was selected to reflect the difference of air pollutant emissions from diverse sources on the atmospheric environment of the BTH region, which involve various influencing factors, such as spatial distance, meteorological condition, and topography condition.

$$SI_i = \sum_j \frac{SF_{i,j}}{S_j} = \sum_j \frac{C_{i,j} / Q_{i,j}}{S_j} \quad \dots(2)$$

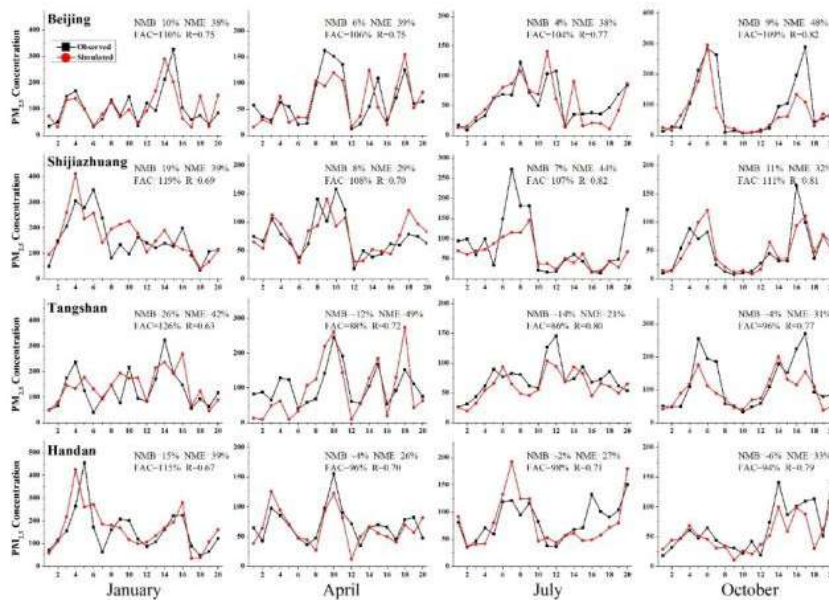


Fig. 3: Comparisons of the simulated and observed mean daily $PM_{2.5}$ concentrations in 2015 for typical sub-areas.

where SI_i represents the sensitivity coefficient for iron and steel enterprise i ; i represents emission sources, that is, the iron and steel enterprises in the BTH region; j represents gaseous pollutants, namely SO_2 , NO_x , $PM_{2.5}$, and VOCs; $SF_{i,j}$ represents the sensitivity coefficient of pollutant j from enterprise i and the unit contribution concentration of the emission of pollutant j from enterprise i on the receptor sites, which was calculated based on simulation results; $C_{i,j}$ represents the emission contribution concentration of pollutant j from enterprise i on the receptor sites; $Q_{i,j}$ represents the emission amount of pollutant j from enterprise i ; S_j is the national secondary standards of China for pollutants j .

Potential coefficients were selected to compare the control potential of air pollutant emissions of each enterprise.

$$PI_i = \sum_j \frac{P_{i,j}}{S_j} = \sum_j \frac{Q_{i,j} \times (R_{o,j} - R_{i,j})}{S_j} \quad \dots(3)$$

where PI_i represents the potential coefficient of iron and steel enterprise i ; $P_{i,j}$ represents the potential for emission control of pollutant j in enterprise i ; $R_{o,j}$ represents the removal efficiency of pollutant j by the most optimal control facilities; $R_{i,j}$ represents the removal efficiency of pollutant j by the actual control facilities in enterprise i . The potential coefficients of VOCs for each enterprise were assumed as the same due to the lack of statistical data on VOC control facilities.

A comprehensive indicator, which is called classification coefficient, was developed on the basis of calculation of sensitivity and potential coefficients to classify the enterprises.

$$CI_i = k_1 \times SI_i + k_2 \times PI_i \quad \dots(4)$$

where CI_i represents the classification coefficient for iron and steel enterprise i , k_1 and k_2 represent the weight coefficients of SI_i and PI_i , respectively, and the sum of k_1 and k_2 is equal to 1. The authors deemed that the weight coefficient of PI_i should be close to SI_i . Thus, k_1 and k_2 are assigned to 0.5 and 0.5, respectively. After normalization processing, the ranges of 0.80-1.00, 0.60-0.80, 0.40-0.60, 0.20-0.40, and 0.00-0.20 for classification coefficients respectively represent the first, second, third, fourth and fifth-level pollution, and these coefficients are arranged as the sequence from “most serious” to “least serious.”

RESULTS AND ANALYSIS

Emission Characteristics of Gaseous Pollutants and PM From Iron and Steel Enterprises

Fig. 4 shows the pollutant emission amount of the iron and steel enterprises and the contributions of different sub-categories in the sub-areas of the BTH region (BJ was not included due to the absence of iron and steel plant enterprises). Remarkable amounts of air pollutants emitted from iron and steel enterprises were also observed. The iron and steel industry is one of the most important sources of air pollutants in the BTH region, accounting for 23.7% of SO_2 , 10.6% of NO_x , 11.7% of TSP, 34.1% of CO and 7.5% of VOCs, which were emitted from iron and steel enterprises. Especially in TS, iron and steel enterprises contributed

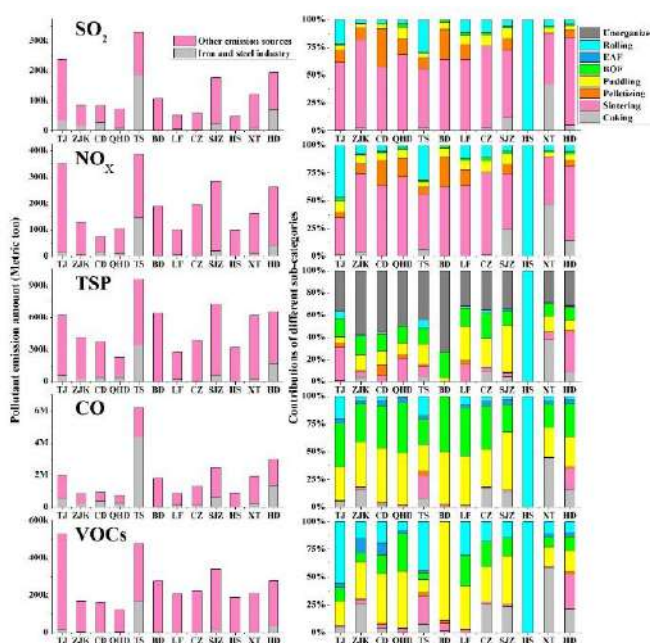


Fig. 4: Pollutant emission amount of iron and steel enterprises and contributions of different sub-categories in the BTH.

56.3%, 38.2%, 35.7%, 71.1%, and 35.4% of SO_2 , NO_x , TSP, CO, and VOCs, respectively, thereby illustrating that the iron and steel industry is the most important air pollution source in that area. In other sub-areas, such as HD, TJ, CD, and SJZ, a considerable amount of air pollutants were similarly emitted from the iron and steel enterprises. Thus, the iron and steel enterprises should be regarded as the main governance object to improve the quality of the atmospheric environment.

Among all the sub-categories, sintering was the most important contributor of SO_2 and NO_x in most sub-areas, which is consistent with the previous studies (Li et al. 2016). The vast contribution was mainly in connection with limited desulfurization and denitration efficiency in the BTH region, with XT and HS as two exceptions; the former largely emits SO_2 and NO_x in the coking process, and the latter only includes the rolling process. For TSP, unorganized particulate matters (summation of unorganized PM from each process) escaped from each manufacturing process of sub-categories with no pollution treatment measures and accounted for approximately 38.2% of TSP in a total of the BTH. This finding indicates considerable potential for TSP pollutant control in iron and steel enterprises, and the unorganized PM should be highlighted. Moreover, the contributions of sub-categories substantially varied between sub-areas. For example, TSP from sintering towers accounted for more than 25.0% in TJ and HD, whereas BOF and puddling provided additional contributions in BD and SJZ. CO pollutants were emitted in most sub-areas during the puddling and steelmaking processes in iron and steel enterprises, and the coking furnace was a contributor in XT, ZJK, and HD. Notably,

although the emission factors of CO for EAF were higher than those of BOF, the widespread application of BOF led to a high contribution rate of CO emission in the BTH region. The CO pollutant was not discussed below due to the lack of statistical data and its minimal impact on the $\text{PM}_{2.5}$ concentration. Considering the complexity of the rolling process, various procedures were involved in the process to produce and improve the number of steel productions, and most of the VOCs in HS, TJ, and TS were discharged during this process. The puddling process contributed most of the VOCs from the iron and steel industry in BD, QHD, LZ, SJZ, and CD, and the coking process contributed most in XT and CZ.

Impact of Pollutant Emission from Iron and Steel Enterprises on Atmospheric Environment

SO_2 , NO_x , VOCs, and TSP are emitted from various sources. Therefore, the concentrations of SO_4^{2-} , NO_3^- , SOA (second organic aerosol), and $\text{PM}_{2.5}$ in each sub-area were simulated from the iron and steel industry and other emission sources (such as other industrial, transportation, coal-burning, and dust sources). The unorganized $\text{PM}_{2.5}$ was distributed into coking, sintering, puddling, steelmaking, and rolling processes to compare the emission contribution from each process. Thus, the emission categories of the iron and steel industry were coking, sintering, puddling, steelmaking, and rolling. Fig. 5 shows the average emission contribution of $\text{PM}_{2.5}$, SO_4^{2-} , NO_3^- , and SOA in the sub-areas from each process of the iron and steel industry and other emission sources in 2015.

The iron and steel industry is one of the most important

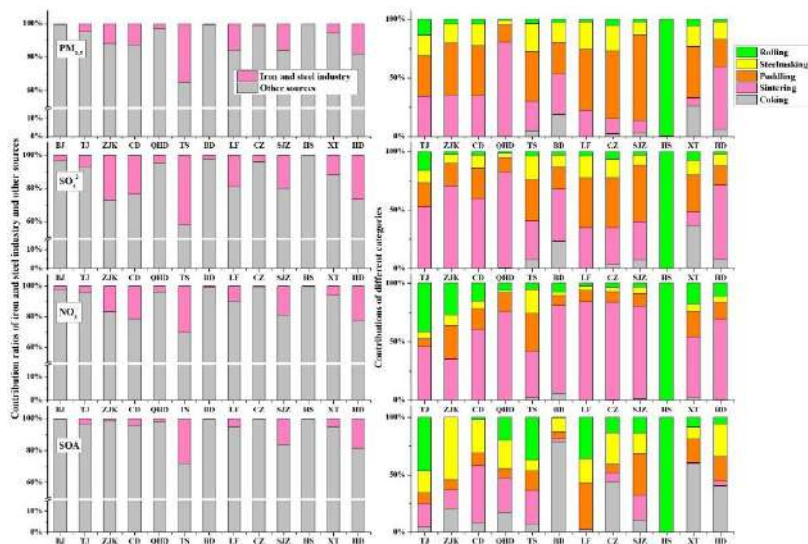


Fig. 5: Average emission contribution to $\text{PM}_{2.5}$, SO_4^{2-} , NO_3^- , and SOA in the sub-areas from each process of the iron and steel industry and other emission sources in 2015.

pollution sources in the BTH region, especially in TS and HD, which significantly contributed to $PM_{2.5}$, SO_4^{2-} , NO_3^- and SOA concentrations in the atmospheric environment in most of the sub-areas. The pollution contribution percentages of the iron and steel industry on $PM_{2.5}$, SO_4^{2-} , NO_3^- and SOA concentrations in TS were 31.0%, 42.3%, 30.2% and 28.1%, respectively. These concentrations were lower than the amount ratios of air pollutant emissions because most of the iron and steel enterprises were planted in suburbs, whereas the receptors of each sub-area were selected close to the state-controlled monitoring stations in urban areas. Overall, the atmospheric environment in most sub-areas of the BTH region was significantly influenced by the pollutant emissions of iron and steel enterprises.

As illustrated in Fig. 5, sintering and puddling contributed the majority of $PM_{2.5}$, SO_4^{2-} and NO_3^- emissions from the iron and steel industry in most sub-areas. For instance, sintering accounted for more than 50% of $PM_{2.5}$, SO_4^{2-} and NO_3^- emissions in HD and QHD, and nearly a half of $PM_{2.5}$ and SO_4^{2-} from the iron and steel industry were emitted from the puddling process in SJZ, CZ and LF. The puddling process contributed more $PM_{2.5}$ emissions than sintering in TS, which was inconsistent with the structure of pollutant emissions. This finding is mainly due to the substantially higher chimneys in the sintering process than those in other processes, which was conducive to the diffusion and attenuation of pollutants emitted from sintering towers. Notably, although puddling and steelmaking processes were not the most significant sources of SO_2 emission, their contributions for SO_4^{2-} concentration should also be regarded, and the desulfurization facilities should also be established for these processes. The simulation results of SOA were taken for a preliminary investigation to determine the contribution of different categories on SOA concentration. The VOC emission of the coking process in BD, XT, and HD contributed more than 40% of SOA concentration from the iron and steel industry in the atmospheric environment, while sintering provided additional contributions to CD. Puddling also remarkably contributed to LF, and the rolling process responded in TJ and TS. This complicated situation is not only limited by the applied modelling system but also influenced by the variant characteristics and species of VOCs emitted from each category of iron and steel enterprises.

Sensitivity Coefficients of Iron and Steel Enterprises

Fig. 6 shows the sensitivity coefficients of PPM (primary fine particulate matters, the components of $PM_{2.5}$ with no secondary reactions in the atmospheric environment, mainly including the primary organic compounds, elemental carbon, and crustal fine particles) (TSP-PPM), SO_4^{2-} (SO_2 - SO_4^{2-}), NO_3^- (NO_x - NO_3^-), and SOA (VOCs-SOA) for the iron

and steel enterprises in sub-areas. The maximum value of sensitivity coefficients of different processes was regarded in this study as the sensitivity coefficient of the enterprise, which was calculated on the basis of simulation results of the emission contribution of PPM, SO_4^{2-} , NO_3^- and SOA concentrations and the amount of TSP, SO_2 , NO_x and VOC pollutant emission from each enterprise in sub-areas. The sensitivity coefficients were applied to reflect the unit concentration of emission contribution from the enterprises on the atmospheric environment of the entire BTH region. A high sensitivity coefficient corresponds to a high concentration contribution of unit pollutant emission on the atmospheric environment.

Among the sub-areas, the sensitivity coefficients of iron and steel enterprises in BD, LF and SJZ were significantly larger than those of other sub-areas mainly due to geographical and meteorological factors. Considering the geography factor, these cities are located in the centre of the BTH region, resulting in the possible spread of their pollutants to the surrounding areas. Considering the meteorology factor, the regional meteorological condition in the BTH region was identified as stationary states in most circumstances (Li et al. 2015), which encouraged the diffusion of contaminants from the central sub-areas. Moreover, the special climate of the sea-land breeze (Wu et al. 2016) led to the large sensitivity coefficients of enterprises in TJ. Although TS and HD are the cities with numerous iron and steel enterprises, their sensitivity coefficients were relatively low. This finding was mainly caused by two reasons: on the one hand, the sensitivity coefficients were calculated for each enterprise rather than the summation of enterprises; on the other hand, the cities of TS and HD are located at the edge of the BTH region. By contrast, QHD had the smallest sensitivity coefficient compared with other sub-areas. Thus, QHD is a suitable destination for migrating the iron and steel enterprises from other sub-areas to realize the optimal disposition of the regional industry.

The comparison between sensitivity coefficients of different pollutants showed that the TSP emissions had a significantly higher contribution concentration of PPM than SO_2 , NO_x and VOCs on secondary components. This finding was mainly due to the direct contribution of fine particles in the TSP emissions to the atmospheric environment, while SO_4^{2-} , NO_3^- and SOA were formed through the complicated secondary chemical reactions. Besides, the sensitivity coefficients of SO_2 - SO_4^{2-} were slightly larger than that of NO_x - NO_3^- in most sub-areas. This result is consistent with the chemical generating mechanisms, in which the generation of NO_3^- from NO_x is complicated (Dong et al. 2013) and vulnerable to the neighbouring environment. The relatively low sensitivity coefficients of VOCs-SOA were mainly caused by the limitation of the CAMx model (Bossioli et al. 2013).

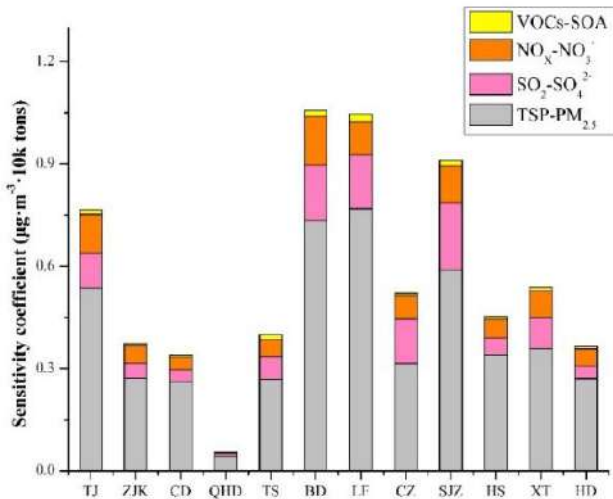


Fig. 6: Sensitivity coefficients of PPM, SO_4^{2-} , NO_3^- and SOA for iron and steel enterprises in the sub-areas of the BTH region.

Fig. 7 shows the wind rose schematic of partial sub-areas (BJ, TJ, TS, HD, ZJK, BD, LF, SJZ and XT) in the BTH region in 2015. As illustrated, the frequency of north-west wind for central sub-areas (such as BJ, BD, and LF) was quite low. This finding indicates that the emission of air pollutants in northern cities was rarely transported to the central and southern sub-areas, which might be the main reason for the relatively low sensitivity coefficients of the iron and steel enterprises in northern sub-areas (such as ZJK). The frequency of static wind (the speed of wind lower than 1 m/s) for central sub-areas was relatively high, and the static and stable climate promoted the steady spread of the air pollutants from central sub-areas to the surrounding areas, resulting in the high sensitivity coefficients of iron and steel enterprises in central sub-areas. Transporting the air pollutants of southern sub-areas (such as HD and XT), whose locations are relatively remote in the BTH region, to other sub-areas, was difficult.

Classification Result of Iron and Steel Enterprises

The classification coefficients of iron and steel enterprises in the BTH region were calculated on the basis of sensitivity and potential coefficients for each process of enterprises, and each kind of pollutant ($\text{PM}_{2.5}$, SO_2 , NO_x , and VOCs) was considered. The maximum value of the classification coefficients of different processes was regarded in this study as the classification coefficient of the enterprise due to the difference in the number of processes of each iron and steel enterprise. For example, some enterprises were equipped with the entire processes of coking, sintering, puddling, steelmaking, and rolling, while others were likely to comprise

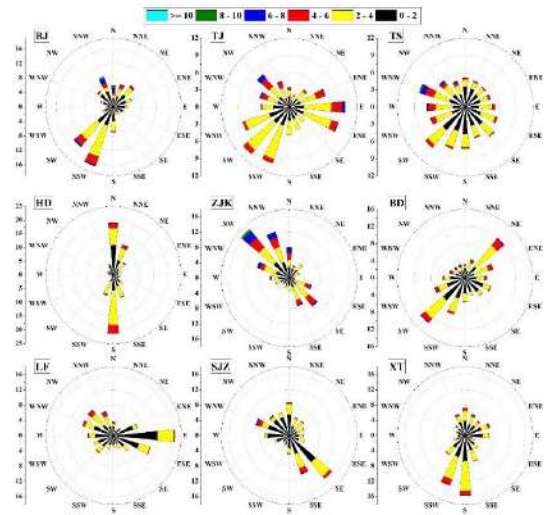


Fig. 7: Wind rose schematic of some sub-areas in the BTH region in 2015.

only one or two processes. The classification coefficients were calculated for each iron and steel enterprise. Therefore, the Kriging interpolation method built into the Geographic Information System was used as a spatial interpolation technique to analyze the distribution of classification results. Fig. 8 shows the classification results of each iron and steel enterprise in the BTH region.

The distributions of classification coefficients of iron and steel enterprises in the BTH region indicate that the

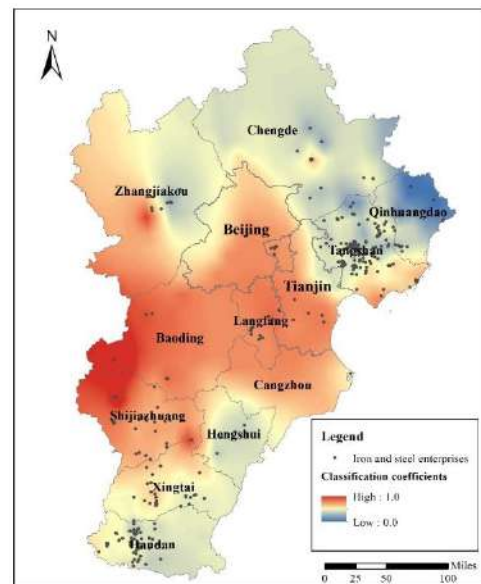


Fig. 8: Classification results of each iron and steel enterprise in the BTH region.

enterprises in western sub-areas, such as BD, SJZ and ZJK, had higher classification coefficients than those in eastern sub-areas, such as HS, TS, and QHD. On the one hand, the northwest wind was one of the dominant wind directions in the BTH region (Zhao et al. 2008). On the other hand, the western and eastern of the BTH region are dominated by plateau and plain, respectively. These findings prompted pollutant diffusion from west to east and prevented the diffusion from east to west. Moreover, the topographic features explain the difference between the classification coefficients of enterprises in sub-areas. In addition, the enterprises in central sub-regions had higher classification coefficients than those of other sub-areas considering the stationary atmospheric conditions, which frequently occurred in the BTH region and favoured pollutant diffusion from central sub-areas to surrounding areas.

As illustrated in Fig. 8, parts of the classification coefficients for enterprises in BD, SJZ and LF were higher than 0.80, which were classified as the first-level pollution known as “Most Serious.” These enterprises had the largest classification coefficients in the BTH region, which is consistent with their high emission sensitivity and control potential. Therefore, these enterprises should be preferentially considered when the iron and steel enterprises in the BTH region were demanded to close down for resolving the overcapacity and improving the quality of the atmospheric environment. Notably, the sensitivity coefficients of enterprises in ZJK were smaller than those of XT and CZ (Fig. 6), while their classification coefficients were nearly the same, even high for some enterprises in ZJK. This finding was mainly due to the high potential coefficients of the enterprises in ZJK, and these enterprises should also be highlighted. Among the sub-areas, the classification coefficients of enterprises in QHD were the smallest and classified as the fifth-level pollution, namely, “Least Serious.” This finding illustrates that their pollutants emission contributed fewer negative effects on the atmospheric environment in the BTH region than those of the enterprises in other sub-areas. Overall, the classification results suggested that the iron and steel enterprises in BD, LF, SJZ, and ZJK should be given the priority to control, while the enterprises in QHD should be taken into the least consideration to control the acquisition of improved air quality for the BTH region.

CONCLUSION

The iron and steel industry has a strong negative impact on human health. Therefore, a detailed and high-resolution emission inventory of the iron and steel industry in the BTH region was built with detailed activity information based on

the emission factors calculated for each sub-category of iron and steel enterprises.

The CAMx modelling system was implemented to investigate the influence of pollution emission from sources on PM_{2.5} concentration and simulate the emission sensitivity of enterprises to various pollutants. A classification technology method was then developed and applied to classify the iron and steel enterprises in the BTH region considering the sensitivity results and emissions control potential. Moreover, simulation scenarios were assumed and simulated to assess the influence of reducing the pollutant emissions of the iron and steel industry quantitatively.

As calculated in the inventory, the iron and steel industry is one of the most important pollutant sources in the BTH region, and the CAMx simulation results showed that the atmospheric environment in most sub-areas was significantly influenced by the pollutant emission of iron and steel enterprises. Therefore, the iron and steel enterprises in western and central sub-areas were classified to have higher classification coefficients than other sub-areas, providing a sequence of rectifying enterprises. The results obtained from this study can help make sound control policies and measures to reduce the negative impact of air pollution on human health.

ACKNOWLEDGMENT

This study was funded by the Science and Technology Planning Project of Henan Province in China (No. 192102310009).

REFERENCES

- Amodio, M., Andriani, E., De Gennaro, G., Di Gilio, A., Ielpo, P., Placentino, C.M. and Tutino, M. 2013. How a steel plant affects air quality of a nearby urban area: a study on metals and PAH concentrations. *Aerosol and Air Quality Research*, 13: 497-508.
- Bossoli, E., Tombrou, M., Helmis, C., Kurtenbach, R., Wiesen, P., Schäfer, K., Dandou, A. and Varotsos, K.V. 2013. Issues related to aircraft take-off plumes in a mesoscale photochemical model. *Science of the Total Environment*, 456: 69-81.
- Chen, Y. and Xie, S.D. 2014. Characteristics and formation mechanism of a heavy air pollution episode caused by biomass burning in Chengdu, Southwest China. *Science of the Total Environment*, 473: 507-517.
- Cheng, S., Zhou, Y., Li, J., Lang, J. and Wang, H. 2012. A new statistical modeling and optimization framework for establishing high-resolution PM10 emission inventory-I. Stepwise regression model development and application. *Atmospheric Environment*, 60: 613-622.
- Dong, X., Gao, Y., Fu, J.S., Li, J., Huang, K., Zhuang, G. and Zhou, Y. 2013. Probe into gaseous pollution and assessment of air quality benefit under sector dependent emission control strategies over megacities in Yangtze River Delta, China. *Atmospheric Environment*, 79: 841-852.
- Gao, Y., Zhang, M., Liu, Z., Wang, L., Wang, P., Xia, X., Tao, M. and Zhu, L. 2015. Modeling the feedback between aerosol and meteorological variables in the atmospheric boundary layer during a severe fog-haze event over the North China Plain. *Atmospheric Chemistry and Physics*, 15: 4279-4295.

- Guttikunda, S.K. and Jawahar, P. 2014. Atmospheric emissions and pollution from the coal-fired thermal power plants in India. *Atmospheric Environment*, 92: 449-460.
- Huang, C., Chen, C.H., Li, L., Cheng, Z., Wang, H.L., Huang, H.Y., Streets, D.G., Wang, Y.J., Zhang, G.F. and Chen, Y.R. 2011. Emission inventory of anthropogenic air pollutants and VOC species in the Yangtze River Delta region, China. *Atmospheric Chemistry & Physics*, 11: 4105-4120.
- Huang, R.J., Zhang, Y., Bozzetti, C., Ho, K.F., Cao, J.J., Han, Y., Daellenbach, K.R., Slowik, J.G., Platt, S.M., Canonaco, F. and Zotter, P. 2014. High secondary aerosol contribution to particulate pollution during haze events in China. *Nature*, 514: 218-222.
- Jia, J., Cheng, S., Liu, L., Lang, J., Wang, G., Chen, G. and Liu, X. 2017. An integrated WRF-CAMx modeling approach for impact analysis of implementing the emergency PM_{2.5} control measures during red alerts in Beijing in December 2015. *Aerosol & Air Quality Research*, 17: 2491-2508.
- Li, G., Cheng, S., Li, J., Wei, W., Wen, W. and Wang, G. 2014. Characterization of ambient ozone and its precursors around a coking plant. *Environmental Monitoring and Assessment*, 186: 3165-3179.
- Li, H., Wang, Q.G., Yang, M., Li, F., Wang, J., Sun, Y., Wang, C., Wu, H. and Qian, X. 2016. Chemical characterization and source apportionment of PM_{2.5} aerosols in a megacity of Southeast China. *Atmospheric Research*, 181: 288-299.
- Li, L., An, J.Y., Zhou, M., Yan, R.S., Huang, C., Lu, Q., Lin, L., Wang, Y.J., Tao, S.K., Qiao, L.P. and Zhu, S.H. 2015. Source apportionment of fine particles and its chemical components over the Yangtze River Delta, China during a heavy haze pollution episode. *Atmospheric Environment*, 123: 415-429.
- Li, W., Lu, C., Ding, Y. and Zhang, Y.W. 2017. The impacts of policy mix for resolving overcapacity in heavy chemical industry and operating national carbon emission trading market in China. *Applied Energy*, 204: 509-524.
- Li, X., Zhang, Q., Zhang, Y., Zheng, B., Wang, K., Chen, Y., Wallington, T.J., Han, W., Shen, W., Zhang, X. and He, K. 2015. Source contributions of urban PM_{2.5} in the Beijing-Tianjin-Hebei region: Changes between 2006 and 2013 and relative impacts of emissions and meteorology. *Atmospheric Environment*, 123: 229-239.
- Pateraki, S., Assimakopoulos, V.D., Maggos, T., Fameli, K.M., Kotroni, V. and Vasilakos, C. 2013. Particulate matter pollution over a Mediterranean urban area. *Science of the Total Environment*, 463: 508-524.
- Sina, A. and Kaur, D. 2019. Load frequency control of multi area interconnected power system using differential evolution algorithm. *Tehnicki Glasnik-Technical Journal*, 2013: 323-330.
- Streets, D.G., Bond, T.C., Carmichael, G.R., Fernandes, S.D., Fu, Q., He, D., Klimont, Z., Nelson, S.M., Tsai, N.Y., Wang, M.Q. and Woo, J.H. 2003. An inventory of gaseous and primary aerosol emissions in Asia in the year 2000. *Journal of Geophysical Research Atmospheres* 2003, 108, GTE 30-31.
- Tang, X., Zhang, Y., Yi, H., Ma, J. and Pu, L. 2012. Development a detailed inventory framework for estimating major pollutants emissions inventory for Yunnan Province, China. *Atmospheric Environment*, 57: 116-125.
- Tao, J., Gao, J., Zhang, L., Zhang, R., Che, H., Zhang, Z., Lin, Z., Jing, J., Cao, J. and Hsu, S.C. 2014. PM_{2.5} pollution in a megacity of southwest China: source apportionment and implication. *Atmospheric Chemistry and Physics*, 14: 8679-8699.
- Tsai, J.H., Lin, K.H., Chen, C.Y., Lai, N., Ma, S.Y. and Chiang, H.L. 2008. Volatile organic compound constituents from an integrated iron and steel facility. *Journal of Hazardous Materials*, 157: 569-578.
- Wang, G., Cheng, S., Lang, J., Yang, X., Wang, X., Chen, G., Liu, X. and Zhang, H. 2016. Characteristics of PM_{2.5} and assessing effects of emission-reduction measures in the heavy polluted city of Shijiazhuang, before, during, and after the Ceremonial Parade 2015. *Aerosol & Air Quality Research*, 17: 499-512.
- Wang, G., Cheng, S., Li, J., Lang, J., Wen, W., Yang, X. and Tian, L. 2015. Source apportionment and seasonal variation of PM_{2.5} carbonaceous aerosol in the Beijing-Tianjin-Hebei region of China. *Environmental Monitoring & Assessment*, 187: 143-155.
- Wang, K., Tian, H., Hua, S., Zhu, C., Gao, J., Xue, Y., Hao, J., Wang, Y. and Zhou, J. 2016. A comprehensive emission inventory of multiple air pollutants from iron and steel industry in China: Temporal trends and spatial variation characteristics. *Science of the Total Environment*, 559: 7-14.
- Wang, L., Wei, Z., Wei, W., Fu, J.S., Meng, C. and Ma, S. 2015. Source apportionment of PM_{2.5} in top polluted cities in Hebei, China using the CMAQ model. *Atmospheric Environment*, 122: 723-736.
- Wang, L.T., Wei, Z., Yang, J., Zhang, Y., Zhang, F.F., Su, J., Meng, C.C. and Zhang, Q. 2014. The 2013 severe haze over southern Hebei, China: model evaluation, source apportionment, and policy implications. *Atmospheric Chemistry and Physics*, 14: 3151-3173.
- Wang, S., Zhao, M., Xing, J., Wu, Y., Zhou, Y., Lei, Y., He, K., Fu, L. and Hao, J. 2010. Quantifying the Air Pollutants Emission Reduction during the 2008 Olympic Games in Beijing. *Environmental Science & Technology*, 44: 2490-2496.
- Wei, W., Cheng, S., Li, G., Wang, G. and Wang, H. 2014. Characteristics of ozone and ozone precursors (VOCs and NOx) around a petroleum refinery in Beijing, China. *Journal of Environmental Sciences*, 26: 332-342.
- Wei, W., Cheng, S., Li, G., Wang, G. and Wang, H. 2014. Characteristics of volatile organic compounds (VOCs) emitted from a petroleum refinery in Beijing, China. *Atmospheric Environment*, 89: 358-366.
- Wei, W., Lv, Z., Yang, G., Cheng, S., Li, Y. and Wang, L. 2016. VOCs emission rate estimate for complicated industrial area source using an inverse-dispersion calculation method: A case study on a petroleum refinery in Northern China. *Environmental Pollution*, 218: 681-688.
- Wu, D., Fung, J.C.H., Yao, T. and Lau, A.K.H. 2013. A study of control policy in the Pearl River Delta region by using the particulate matter source apportionment method. *Atmospheric Environment*, 76: 147-161.
- Wu, M., Luo, Y., Wu, D. and Fan, S. 2016. Observation on the characteristics of sea-land breezes and its influence to air quality over Pearl River Delta region during dry season. *China Environmental Science*, 36: 3263-3272.
- Wu, X., Zhao, L., Zhang, Y., Zheng, C., Gao, X. and Cen, K. 2015. Primary air pollutant emissions and future prediction of iron and steel industry in China. *Aerosol and Air Quality Research*, 15: 1422-1432.
- Yang, J., Ma, S., Gao, B., Li, X., Zhang, Y., Cai, J., Li, M., Huang, B. and Zheng, M. 2017. Single particle mass spectral signatures from vehicle exhaust particles and the source apportionment of on-line PM_{2.5} by single particle aerosol mass spectrometry. *Science of the Total Environment*, 593: 310-318.
- Yang, X., Zhang, L. and Jiang, D. 2013. Exhaust gas of iron & steel industry and emission characteristics of pm_{2.5} and pollution control measures. *Journal of Engineering Studies*, 5: 240-251.
- Zhang, Y. and Wu, S.Y. 2013. Fine scale modeling of agricultural air quality over the southeastern united states using two air quality models. Part II. Sensitivity studies and policy implications. *Aerosol and Air Quality Research*, 13: 1475-1491.
- Zhao, B. and Ma, J.Z. 2008. Development of an air pollutant emission inventory for Tianjin. *Acta Scientiae Circumstantiae*, 28: 368-375.
- Zhao, B., Wang, P., Ma, J.Z., Zhu, S., Pozzer, A. and Li, W.J.A.C. 2012. A high-resolution emission inventory of primary pollutants for the Huabei region, China. *Atmospheric Chemistry & Physics*, 11: 20331-20374.
- Zheng, J., Zhang, L., Che, W., Zheng, Z. and Yin, S. 2009. A highly resolved temporal and spatial air pollutant emission inventory for the Pearl River Delta region, China and its uncertainty assessment. *Atmospheric Environment*, 43: 5112-5122.
- Zhou, Y., Cheng, S., Chen, D., Lang, J., Zhao, B. and Wei, W. 2014. A new statistical approach for establishing high-resolution emission inventory of primary gaseous air pollutants. *Atmospheric Environment*, 94: 392-401.



Study and Physicochemical Characterization of the Diesel Particles Inducing Bronchopulmonary Obstructions and Inflammation

M. Bouzid^{†*}, A. Djadi^{**} and B. Bezzazi^{*}

^{*}Research Unit: Materials, Processes and Environment, University M'Hamed Bougara, Boumerdes, Algeria

^{**}Research Unit in Analysis and Technological Development in Environment, Center of Research in Physicochemical Analyzes, Bousmail, Algeria

[†]Corresponding author: M. Bouzid; technosante1@hotmail.fr

Nat. Env. & Poll. Tech.
Website: www.neptjournal.com

Received: 17-10-2019

Revised: 30-10-2019

Accepted: 16-01-2020

Key Words:

Diesel soot particles
Pulmonary obstruction
Micro-Visiography

ABSTRACT

Micro-Visiography reveals that diesel soot particles are soluble in the physiological pulmonary liquid. It also shows that these substances stick to bronchial capillary walls. Electronic microscopy reveals structures of non-homogeneous morphology with spherical, fibrous and platelet-like structures. Analysis of the surfaces of the aggregates by Energy-dispersive X-ray microanalysis (EDX) shows the composition of chemical charges. Besides, X-ray diffraction and thermogravimetric study show the existence of two phases: organic and crystalline, with a rubber elastomer aspect. Infrared and UV-Visible spectroscopic analysis confirmed the existence of reactive chemical groups.

INTRODUCTION

Air pollution poses intriguing questions (Li et al. 2016, Xu-Qin et al. 2016, Fanny et al. 2012, Zorana et al. 2011, Devries et al. 2016). Recently, important studies of the in-vitro behaviour of diesel particles in physiological fluids of the lungs have been reported. The visual graphic scan of a laboratory rabbits' lungs, exposed to small doses of diesel exhaust fumes, revealed an inflammation aspect induced by the presence of DEPs (Bouzid et al. 2017). The authors measured the electric charge of the particles and showed a close relationship with a new form of obstruction in the bronchial tree "suction cup effect". These mechanisms rise from electrostatic interactions with bronchi and bronchiole walls in the lung (Bouzid et al. 2017). Renewed interest in the inflammation aspect of the respiratory tract caused by the presence of DEPs has been described in the literature (Boland et al. 2001, Habert & Garnier 2015). These results are in perfect agreement with epidemiological studies. The incidence of allergic diseases is also associated with the presence of DEPs. Short-term exposure is sufficient to increase cardiorespiratory morbidity whereas chronic exposure may cause asthma, obstructive chronic bronchopneumopathy, lung cancer, and cancer of the bladder (Brewer et al. 2016, Hart et al. 2006, Traboulsi et al. 2017). The toxicity of diesel particles is linked to their capacity to cause oxidizing stress at the cellular level (Borgie et al. 2015, Aloui et al. 2016). The

metabolism of HAP by P450 cytochrome, epoxide hydrolase and dihydrodiol dehydrogenase (DHDH) produces DNA adducts which can lead to the development of various types of cancer (Aloui et al. 2016). Since 2012, exhaust fumes have been classified by the WHO as carcinogens (WHO 2013). To understand the mechanism of action of DEPs, the physico-chemistry element is essential. Stanmore et al. (2001) published a micrograph of diesel soot in which we can clearly distinguish the fractal form agglomerations. On the other hand, Yapp et al. (2013) presented a model of the formation of soot during combustion. Nanometric clusters were investigated by Transmission Electron Microscopy (TEM) (Fig. 1). This proposal is supported by theoretical studies. The soot particles are rich in carbon, NO_x, anhydrous sulphurous SO₂ and its derivatives, polycyclic aromatic hydrocarbons, oxygenated organic compounds (phenols, alcohols, aldehydes ketones). These products agglomerate around mineral carbon crystallites (Richter & Howar 2000).

The available literature is oriented towards modelling the partial behaviour in the lungs (de Vasconcelos et al. 2011), the formation of soot, analysis of reaction mechanisms, the chemical composition of the particle and its physicochemical properties (Abul & Shahidul 2013, Akridis & Rigopoulos 2016).

The objective of this work is a physicochemical analysis of diesel particles involved in broncho obstruction and

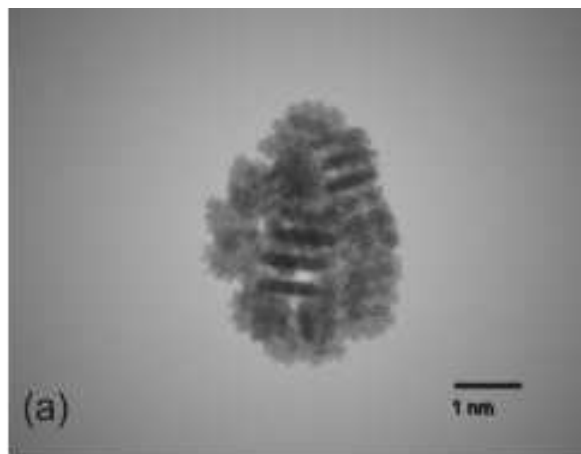
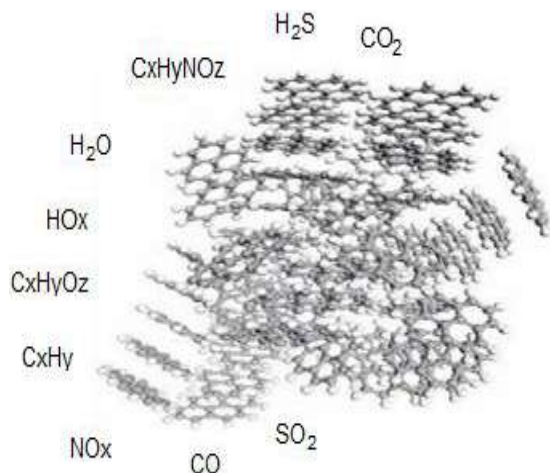


Fig. 1: Image of an aggregate of a diesel particle and model of HAP molecules involved in the formation of soot.

inflammation of laboratory rabbit lungs. This contribution identifies the solubility of the diesel particles in physiological pulmonary solutions by visiography. Microscopic and physicochemical studies can explain this behaviour.

MATERIALS AND METHODS

Diesel particles and pulmonary surfactant came from “Health Technology Algeria”, Ministry of Health.

Observation by Scanning Electron Microscope (SEM)

Several high-resolution pictures were taken of each sample in several zones and at different magnifications (400-20000 times). Selected parameters were pressure: 60 Pascal; beam of primary electrons: 5 and 10 Kv; electronic vessel (spot): between 3 and 3.5; secondary electron detector: (LFD); working distance: 7.9-9.9 mm; 400-200000 mm.

Analysis by Energy Dispersive X-ray Microanalysis (EDX)

Collection of spectra and elementary identification were performed by “global” mode which allowed for the identification of all the investigated elements.

The results of the microanalysis illustrate the presence of all the components sought for in form of spectrum provided with a summary table giving the mass and atomic percentages of each element.

PANalytical diffractometer: XPERT-PRO, copper anti-cathode ceramic radiation emitting tube, X-ray generator; power: 40 mA, 45 Kv. Software used for data acquisition: *Data Collector* from *PANalytical*; Data processing software: *High Score Plus* from *PANalytical*; Wavelength CuK α [Å]: 1.5418; Starting angle [$^{\circ}$ Th]: 2.0000; Final angle

[$^{\circ}$ Th]: 70.0000; Step size [$^{\circ}$ Th.]: 0.0170; Step time [S]: 91.7599.

Analysis by Infra-red Absorption Spectroscopy

The infra-red absorption spectrophotometry was carried out on pastilles made up of 1 mg of product dispersed in 300 mg of KBr using a Nicolet 5700 series equipment.

Analysis by Ultra Violet-Visible Absorption Spectroscopy

UV-Visible analysis was carried out using a standard spectrophotometer Lambda EZ210. Scanning varied between 190 and 1100 Nm of infinitely diluted solutions enables the determination of the absorption band of the products.

Thermogravimetric Analysis

To study the thermal properties, samples of approximately 2 mg were measured using a Seiko SC 5200 thermoanalyser (model 220 *TG/DTA*) at heating and flow rates of 10-50°C/min and 100 mL/min respectively.

RESULTS AND DISCUSSION

The behaviour of DEPs in physiological solution clearly shows the dissolution of the organic matter in form of a violet fog around the particles which dissipate (Fig. 2). Laser diffraction granulometry of the DEP powder reveals on average a specific surface of 1.85 m²/g and a diameter of 10 μ m (Devries et al. 2016, Bouzid et al. 2017).

SEM micrographs of the diesel soot particles sample at 50 μ m, considered as carbon gas (DEP), obtained by thermolysis are shown in Figs. 3 and 4. The morphology of the DEP deposit surface is non-homogeneous. We can observe spherical

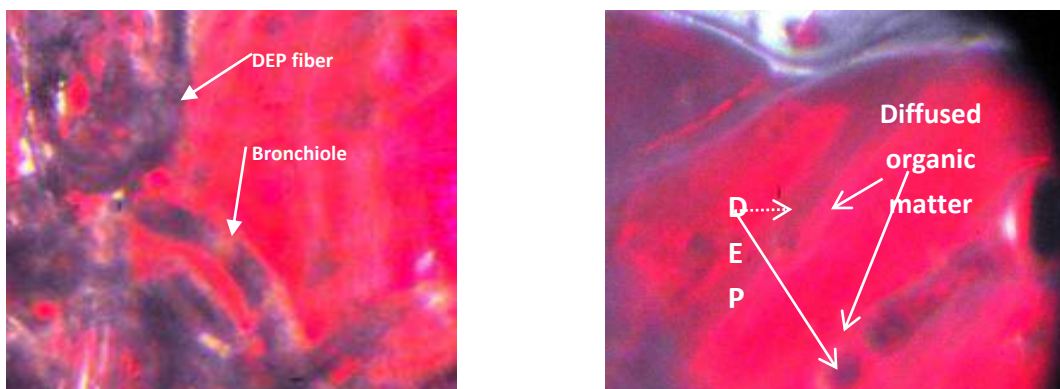


Fig. 2: Visio-scanography of DEP in physiological solution (optical filter 700 Nm).

carbon nanograins of variable diameters. The spheres meet to form randomly distributed wavelets. Furthermore, we can also see fibrous shapes of exhaust fumes in Fig. 4. Platelets forms appear on the two negatives.

The EDX spectrum (Fig. 5) of the surface of the diesel particle samples proves the presence of atomic elements on

their surface. Table 1 summarizes the mass and atomic percentages in each case.

As can be seen from Table 1, carbon and oxygen represent high percentages. The quantity of chloride and sodium is relatively important and is induced by marine footprint. In gasoline, sulphur is usually found in small quantities.

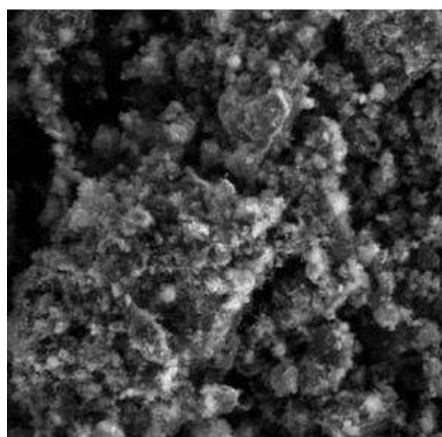


Fig. 3: SEM Spherical and platelet forms of DEP (30µm).

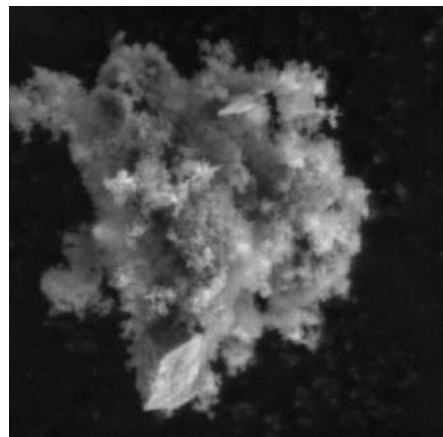


Fig. 4: SEM Fibrous Form of DEP (4µm).

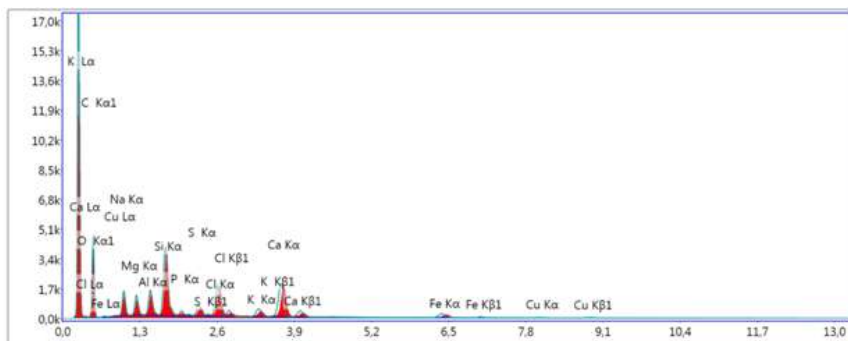


Fig. 5: Energy dispersive X-ray microanalysis of DEP.

Metals result from wear of machine parts. The remainder of the atoms probably accentuates air contamination.

The X-rays diffraction spectrum (Fig. 6) reflects the two phases which constitute the diesel particles, the amorphous phase made up of an organic part and a crystalline phase primarily made up of mineral and carbon crystallite (Akridis & Rigopoulos 2016).

Thermogravimetry confirms the XRD results. It quantifies the phases: organic matter 26.5% (evaporable matter) and crystalline inorganic matter 70% (Violi & Sarofim 2001). The organic substance (unburnt residues, HAP) makes up the mineral phases. This constitution explains the elastomer aspect which is expressed in the range (25-250°C) (Fig. 7).

Analysis by Infrared Spectroscopy

The Infrared spectrum (Fig. 8), shows signals on the 4000-1500 cm^{-1} region which contains longitudinal vibration bands of the main CH groups, O-H, C=O, N-H, ... Peak 3445 cm^{-1} corresponds to the '-OH' group whereas the peak 2922 cm^{-1} corresponds to the 'CH' group. We observed bands that are more or less broad because of the existence of a hydrogen bond. In the vicinity of 1550 cm^{-1} , it is probably the C = C that is expressed. Despite the complex structure of the soot particle, the infra-red remains readable and constitutes a reliable footprint.

Study by UV-Visible Spectroscopy

In solution, infinitely diluted in spectroscopic pentane, diesel

Table 1: Summary of mass and atomic percentages of each element.

Elements	Mass %	Atomic %	Total Intensity	Error %
C, K	63.29	74.54	4,572.00	7.59
O, K	20.78	18.37	1,230.28	10.18
Na, K	2.12	1.30	524.57	7.91
Mg, K	1.05	0.61	459.78	6.78
Al, K	1.17	0.61	617.34	5.02
Si, K	3.06	1.54	1,851.57	3.29
P, K	0.21	0.10	110.63	8.97
S, K	0.54	0.24	299.07	4.68
Cl, K	2.00	0.80	1,008.77	2.22
K, K	0.66	0.24	284.23	4.74
Ca, K	3.62	1.28	1,305.82	2.03
Fe, K	1.20	0.30	196.82	5.87
Cu, K	0.31	0.07	30.34	17.48

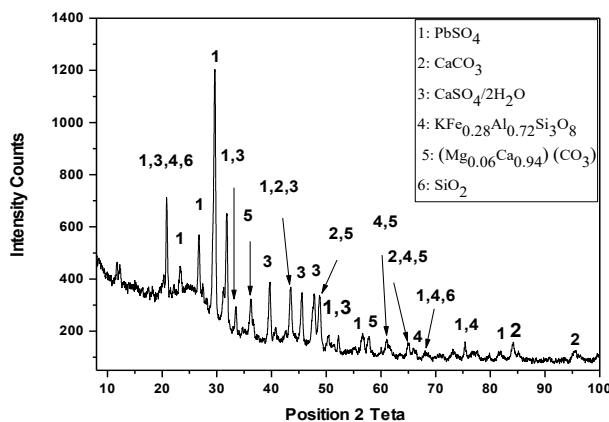


Fig. 6: X-ray diffraction spectrum of DEP.

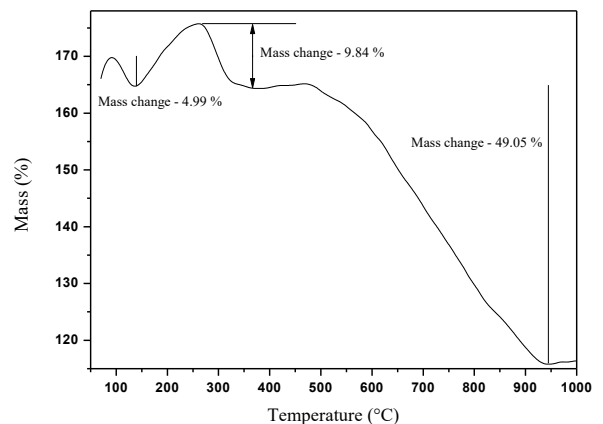


Fig. 7: Thermogravimetry of DEP.

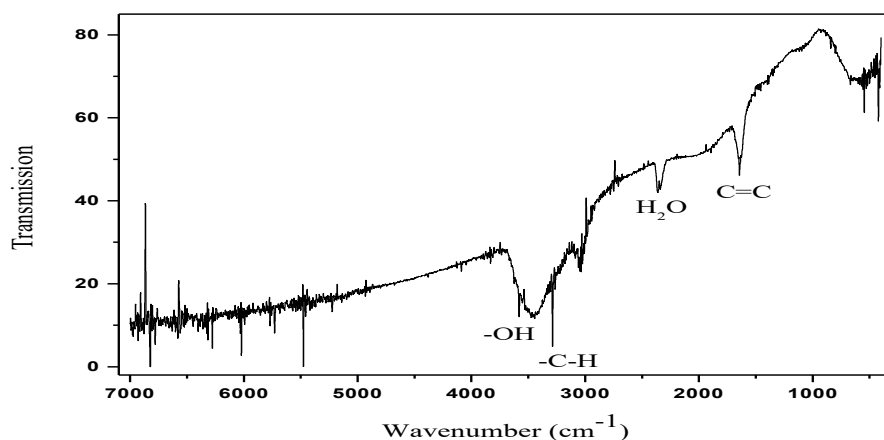


Fig. 8: Infra-red spectrum of DEP.

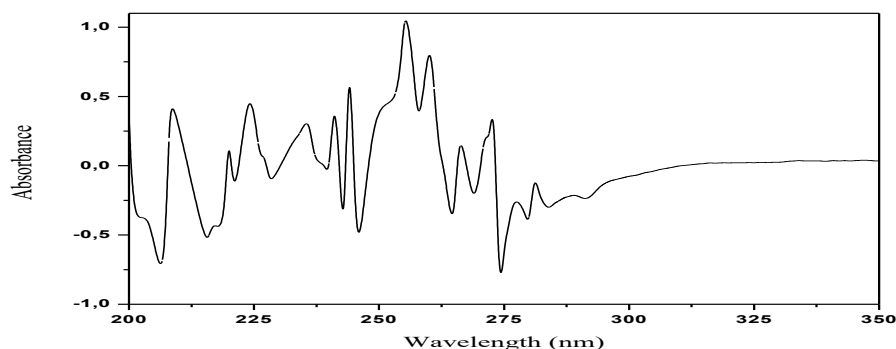


Fig. 9: UV-Visible spectrum of DEP in cyclohexane solution.

particles are partly dissolved. This type of solubility of many organic molecules gives a saw-teeth spectrum (Fig. 9).

CONCLUSION

The study by electronic microscopy highlights the aspects of exhaust diesel fumes. The gases consist of aggregates of spherical, platelet and fibrous forms. Associated EDX analysis, shows the presence of chemical elements in the fabric of soot. Micro-visiography of diesel soot in physiological solution reveals an instantaneous dissipation of organic substances in the physiological liquid. XRD indicates the presence of two phases: Amorphous, and crystalline in the same particle. Thermogravimetry highlights the elastomer aspect of the DEP particle. It confirms the existence of two phases and also, primarily quantifies organic and inorganic matter. Infrared and UV-Visible spectroscopy determines the reactive chemical functions present. Diesel particles have a complex composition. They penetrate the lung and are physically highly reactive due to the crystallites (effects of shearing). Besides, they are chemically highly reactive due to the reactivity of chemical charges of HAP and their derivatives.

REFERENCES

- Abul, H M. and Shahidul, I. 2013. Synthesis of carbon nanoparticles from kerosene and their characterization by SEM/EDX, XRD and FTIR. *American Journal of Nanoscience and Nanotechnology*, 1(2): 52-56.
- Akridis, P. and Rigopoulos, S. 2016. Modelling of soot formation in laminar diffusion flames using a comprehensive CFD-PBE model with detailed gas-phase chemistry. *Combustion Theory and Modelling*, 21(1): 35-48.
- Aloui, R., Magne, F., Devouassoux, G., Deverchere, J., Ritter, P., Bentaher, A. and Pacheco, Y. 2016. Effects of fine particulate matter from on bronchial epithelial cells. *Revue Des Maladies Respiratoires*, 33(9): 767-774.
- Boland, S., Baeza, A. and Francelyne Marano, S. 2001. Toxicité respiratoire des particules Diesel : les mécanismes cellulaires et moléculaires. *Médecine/Sciences*, 17: 596-603.
- Bouid, M., Djadi, A., Guetaf, H. and Bezzazi, B. 2017. Air pollution from diesel particles and chronic obstructive pulmonary disease - CT scan study. *European Scientific Journal*, 13(6): 504-512.
- Borgie, M., Ledoux, F., Verdin, A., Cazier, F., Greige, H., Shirali, P., Courcot, D. and Dagher, Z. 2015. Genotoxic and epigenotoxic effects of fine particulate matter from rural and urban sites in Lebanon on human bronchial epithelial cells. *Environmental Research*, 136: 352-362.
- Brewer, K., Egyed, M., Huang, L., Ling, B., Matz, C. and Rouleau, M. 2016. Human Health Risk Assessment for Diesel Exhaust. ISBN: 978-0-660-04556-6, Cat.: H129-60/2016F-PDF, Pub.: 150240.
- DeVries, R., Kriebel, D. and Sama, S. 2016. Low level air pollution and exacerbation of existing COPD: A case crossover analysis. *Environmental Health*, 15(1): 1-11.

- Yapp, E.K. and Kraft, M., 2013. Modelling soot formation: Model of particle formation. In: *Cleaner Combustion* Springer, London, pp. 389-407.
- Fanny, W.S., Ko, David and Hui, S.C. 2012. Air pollution and chronic obstructive pulmonary disease. *Respirology*, 17: 395-401.
- Habert, C. and Garnier, R. 2015. Health effects of diesel exhaust: A state of the art. *Revue des Maladies Respiratoires*, 32: 138-154.
- Hart, J.E., Laden, F., Schenker, M.B. and Garshick, E. 2006. Chronic obstructive pulmonary disease mortality in diesel-exposed railroad workers. *Environmental Health Perspectives*, 114(7): 1013-1017.
- Li, J.H., Sun, S.Z., Tang, R., Qiu, H., Huang, Q.Y., Mason, T.G. and Tian, L.W. 2016. Major air pollutants and risk of COPD exacerbations: a systematic review and meta-analysis. *International Journal of Chronic Obstructive Pulmonary Disease*, 11(1): 3079-3091.
- Richter, H. and Howar, J.B. 2000. Formation of polycyclic aromatic hydrocarbons and their growth to soot - A review of chemical reaction pathways. *Prog. Energy Combust. Sci.*, 26: 565-608.
- Stanmore, B.R., Brilhac, J.F. and Gilot, P. 2001. The oxidation of soot-experiments, mechanisms and models. *Carbone*, 39: 2247-2268.
- Traboulsi, H., Guerrina, N., Iu, M., Maysinger, D., Ariya, P. and Baglolle, C.J. 2017. Inhaled pollutants: The molecular scene behind respiratory and systemic diseases associated with ultrafine particulate matter. *Int. J. Mol. Sci.*, 18(243): 1-19.
- Vasconcelos, T.F. DE., Sapoval, B., Andrade, J. S., James J.R., Grotberg, B., Yingying, H.U. and Filoche, M. 2011. Particle capture into the lung made simple. *Journal of Applied Physiology*, 111: 1664-1673.
- Violi, A. and Sarofim, A.F. 2001. Quantum mechanical study of molecular weight growth process by combination of aromatic molecules. *Combustion and Flame*, 126: 1506-1515.
- WHO 2013. Review of evidence on health aspects of air pollution – REVIHAAP project. Technical report, World Health Organization.
- Xu-Qin, J., Xiao-Dong, M. and Di, F. 2016. Air pollution and chronic airway diseases: What should people know and do? *J. Thorac. Dis.*, 8(1): 31-40.
- Zorana, J., Andersen, M., Hvidberg, S., Jensen, S., Ketzel, M., Loft, S., Sørensen, M., Tjønneland, A., Overvad, K. and Raaschou-Nielsen, O. 2011. Chronic obstructive pulmonary disease and long-term exposure to traffic-related air pollution: A cohort study. *American Journal of Respiratory and Critical Care Medicine*, 183(4): 455-461.



Study on the Effects of Sewage Irrigation on Soil

Xiuli Li* and Xu Wu**(***)[†]

*School of Water Conservancy, North China University of Water Resources and Electric Power, Zhengzhou, 450045, China

**School of Water Conservancy and Hydroelectric Power, Hebei University of Engineering, Handan, 056038, China

***Hydrology and Water Resources Survey Bureau of Handan Hebei Province, Handan, 056001, China

[†]Corresponding author: Xu Wu; 466199307@qq.com

Nat. Env. & Poll. Tech.

Website: www.neptjournal.com

Received: 21-01-2020

Revised: 15-02-2020

Accepted: 16-04-2020

Key Words:

Sewage irrigation

Soil

Heavy metals

Potential ecological risk

Evaluation analysis

ABSTRACT

The long-term use of sewage to irrigate farmland will increase the content of heavy metals in the soil and cause soil pollution. Heavy metal pollution in soils will restrict the sustainable development of local agriculture and will have a negative impact on the ecological environment. In this paper, the irrigation areas using domestic sewage, mixed sewage and industrial sewage as an irrigation water source for many years have been selected as the research objects, and the content of the heavy metals lead (Pb), copper (Cu), zinc (Zn) and cadmium (Cd) in the soil with the depth of 0-20cm, 20-50cm and 50-80cm of three kinds of sewage irrigation areas are assessed using single factor pollution index method and Nemerow comprehensive index method, and the potential ecological risks of heavy metals in the soil are assessed using Hakanson ecological risk index method. The results show that the content of heavy metals Pb, Cu, Zn and Cd in different depths of the three sewage irrigation areas does not exceed the national standard limit, and the heavy metal pollution grade in the soil belongs to the safety grade, indicating that the content of heavy metals in the soil has not reached the alert level. The potential ecological risks of heavy metals in the soil show minor ecological risks judging from single indexes, while Cd shows that the ecological risks are at a strong level. Judging from the comprehensive potential ecological risk index, the potential ecological risks of the heavy metals in the study area is minor in graded, but the heavy metals in the soil of the mixed sewage irrigation area and the industrial sewage irrigation area have a moderate grade of potential ecological risks at the depth of 50-80 cm. Therefore, although the content of the heavy metals in the soil of the three kinds of sewage irrigation areas in the study area is safe, the potential ecological risk of Cd is quite high, which should be paid attention to.

INTRODUCTION

China is a large agricultural country, and irrigation water is essential for agricultural production, and the amount of irrigation water directly affects grain production. Because of the shortage of water resources and the aggravation of the situation of water pollution, competition for water between industry and agriculture is severe and the contradiction between supply and demand is prominent. However, with the development of economy, the water demand of industry is often met with by encroaching upon agricultural water consumption. Therefore, to ensure that farmland irrigation can be carried out normally, agriculture is forced to solve the problem of water demand through other ways. Sewage irrigation is one of the ways to solve the shortage of water in agriculture. The use of sewage irrigation not only improves the efficiency of water resources usage (Xin et al. 2011), relieves the pressure of water shortage in agriculture, but also can provide the nutrients needed for crop growth (Sheng et al. 2016). Rational use of sewage irrigation is an effective

way to realize the utilization of sewage resources and reduce the discharge of sewage. However, most of the sewage for irrigation is not treated or the degree of treatment is not up to the standard of farmland water, which will cause the heavy metals, organics, toxic and harmful substances in the sewage to enter into the soil along with the irrigation, and eventually cause soil pollution when accumulated to a certain extent (Chen et al. 2012, Liu et al. 2017). The quality of the soil is closely related to agricultural production, human health and ecological security, but the soil suffers from the pollution and destruction caused by human production activities and becomes the final acceptor of most pollutants (Burgess et al. 2015). Although the soil itself has a certain capacity of self-purification, when the concentration of the pollutants exceeds the carrying capacity of the soil, it will lead to the deterioration of the soil environment and adversely affect crops and agricultural products (Xu et al. 2018), thus endangering the health and safety of the humans. Using sewage for agricultural irrigation is a double-edged sword. How to use sewage irrigation reasonably and how to prevent and control

soil environmental pollution have become soil environmental problems that need to be solved urgently at present (Wang et al. 2003). Taking the soil of the studied irrigation areas using sewage irrigation as the research objects, and the heavy metal content in the soil as the research goal, this paper evaluates and studies the pollution indicators, which is of great significance to the timely understanding and study of the soil pollution situation and the sustainable and healthy development of agriculture in the study area.

MATERIALS AND METHODS

Sample point settings: The study area is located in the North China Plain, which is an important grain producing area and an industrial city in China. With the development of the industry in the study area, the impact on the environment is becoming more and more obvious. The main sources of water in the study area are domestic sewage, mixed sewage and industrial sewage, and the irrigation areas irrigated by different water sources are divided into domestic sewage irrigation area, mixed sewage irrigation area and industrial sewage irrigation area, and 5 sampling points have been set at appropriate positions in each irrigation area.

Sample collection and preservation: In the irrigation areas irrigated with different types of sewage, the soil samples were taken according to the depth of 0-20, 20-50 and 50-80 cm, 5 sampling points are set in each irrigation area respectively, and 5 soil samples of the same depth were mixed into one sample. The soils were naturally air-dried indoors, and the impurities were removed. They were later ground and screened with a 2 mm sieve and preserved for future use.

Determination of soil pH values: Soil pH was determined by a glass electrode pH meter.

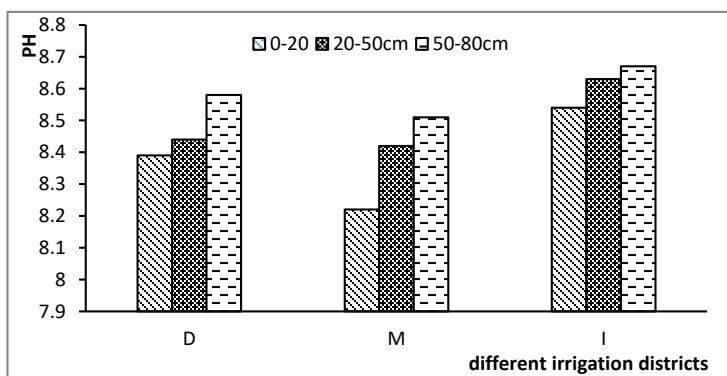
Determination of Pb, Cu, Zn and Cd in the soil: After the

digestion of soil samples the content of each heavy metal was determined by atomic absorption spectrophotometry.

RESULTS AND ANALYSIS

pH values of the soil: The pH value of the soil is one of the important indicators of soil fertility, and it also directly affects the transformation of the heavy metals in the soil (Wan et al. 2015). pH value also reflects the degree of acidity or alkalinity of the soil. According to the range of pH, the soil can be classified as strong acidity (pH value < 4.5), acidity (pH value 4.5-5.5), slight acidity (pH value 5.5-6.5), neutrality (pH value 6.5-7.5), slight alkalinity (pH value 7.5-8.5), alkalinity (pH value 8.5-9.0) and strong alkalinity (pH > 9.0). The different acidity or alkalinity of the soil has different effects on the growth of crops, and only when pH value is within the suitable range, can the soil benefit the growth and development the crops and can the absorption and utilization of various nutrients from the soil reach the highest level. The pH values of the soil depth of 0-20 cm, 20-50 cm and 50-80 cm in the irrigation areas of the three kinds of water quality were analyzed and presented in Fig. 1.

According to Fig. 1, it can be seen that (1) the pH values of the soil of the irrigation areas of different kinds of water quality all show an upward trend along with the increase of soil depth, but the pH values increase in each layer of the irrigation areas of different kinds of water quality are different. The pH value of the domestic sewage irrigation area increases by 0.60% from Layer 0-20cm to Layer 20-50cm and by 1.66% from 20-50cm to 50-80cm; the pH value of the mixed sewage irrigation area increases by 2.43% from Layer 0-20cm to Layer 20-50cm and by 1.07% from 20-50cm to 50-80cm, and. The pH value of the industrial sewage irrigation area increases by 1.05% from Layer 0-20cm to Layer 20-50cm and by 0.46% from 20-50cm to 50 -80cm; (2)



Note: D-domestic sewage irrigation area, M-mixed irrigation area, I-industrial sewage irrigation area

Fig. 1: pH value of soil at different depths in different irrigation areas.

according to the criteria of pH classification of soil acidity and alkalinity, it can be seen that the average pH value of the domestic sewage irrigation area is 8.47, the average pH value of the mixed sewage irrigation area is 8.38, therefore the soil of the irrigation areas of these two kinds of water quality is slight alkalinity, and the average pH value of the industrial sewage irrigation area is 8.61 which is alkalinity.

Heavy metal content in the soil: Based on the screening values of “Soil Environmental Quality Risk Control Standard for Soil Contamination of Agricultural Land” (GB15618-2018), the environmental quality evaluation on the soil of the irrigation areas using three kinds of sewage in the study area was carried out. Since the pH values in this study area are all greater than 7.5, when the soil pH >7.5, the standard values of the evaluation indicators of Pb, Cu, Zn and Cd in the soil are 170 mg/kg, 100 mg/kg, 300 mg/kg and 0.6 mg/kg, respectively.

The comprehensive assessment of the soil environmental pollution was carried out using the combination of single factor index method and Nemerow composite index method:

Single Factor Index Method

$$I = \frac{C_i}{C_0} \quad \dots(1)$$

In this formula, I is the single factor index of various evaluation indicators, C_i is the measured value(s) of various evaluation indicators, and C_0 is the standard value(s) of various evaluation indicators.

Nemerow Composite Index Method

$$PI = \sqrt{\frac{\bar{I}^2 + I_{max}^2}{2}} \quad \dots(2)$$

$$\bar{I} = \frac{1}{n} \sum_{i=1}^n I_i$$

In the formula: \bar{I} is the average value of the single factor indexes of the evaluation indicators; I_{max} is the maximum value of the single factor indexes of various evaluation indicators; PI is the comprehensive pollution index, and; n is the quantity of the indicators.

The evaluation criteria for the degrees of soil pollution using single factor index method and comprehensive index method are given in Table 1 (Liu et al. 2015).

The soil of different kinds of water quality is evaluated based on the measured values and standard values of various heavy metals and using single factor index and comprehensive index respectively, and the evaluation results are given in Table 2.

Table 1: Evaluation and grading criteria for heavy metal pollution in the soil.

Grade	Single Factor Pollution Index		Comprehensive Pollution Index	
	Pollution Index	Pollution Grade	Pollution Index	Pollution Grade
I	$I < 1$	Cleanness	$PI \leq 0.7$	Safety
II	$1 \leq I < 2$	Minor Pollution	$0.7 < PI \leq 1$	Alert
III	$2 \leq I < 3$	Mild Pollution	$1 < PI \leq 2$	Mild Pollution
IV	$3 \leq I < 5$	Moderate Pollution	$2 < PI \leq 3$	Moderate Pollution
V	$I \geq 5$	Severe Pollution	$PI > 3$	Severe Pollution

Table 2: Results of soil environmental quality evaluation.

Soil depth	Sampling point	I_i				\bar{I}	I_{max}	PI
		Pb	Cu	Zn	Cd			
0-20cm	D ₁	0.433	0.233	0.118	0.450	0.308	0.450	0.386
	M ₁	0.529	0.286	0.167	0.500	0.371	0.529	0.457
	I ₁	0.514	0.253	0.131	0.517	0.354	0.517	0.443
20-50 cm	D ₂	0.478	0.185	0.102	0.447	0.304	0.478	0.401
	M ₂	0.452	0.233	0.134	0.512	0.333	0.512	0.432
	I ₂	0.422	0.218	0.118	0.617	0.344	0.617	0.499
50-80 cm	D ₃	0.313	0.176	0.096	0.400	0.246	0.400	0.332
	M ₃	0.457	0.248	0.139	0.700	0.386	0.700	0.565
	I ₃	0.564	0.291	0.156	0.633	0.411	0.633	0.534

The degrees of soil pollution of different kinds of water quality were determined by comparing the results of soil environmental quality evaluation with the evaluation and grading criteria of heavy metal pollution in the soil.

It can be seen from Table 1 and Table 2 that: (1) all values of I_p , which are the single factor pollution index values of various heavy metal elements in the irrigation areas with different kinds of water quality at different soil depth are less than 1, indicating that the soil is clean and not contaminated by heavy metals; (2) the single factor pollution indexes of various heavy metal elements at different soil depths: the sequence of single factor pollution indexes of the soil at the depth of 20-50cm in the domestic sewage irrigation area at the 0-20cm layer of the mixed sewage irrigation area is $Pb > Cd > Cu > Zn$, and the sequence of the single factor pollution indexes of the soil at rest different depths is $Cd > Pb > Cu > Zn$; (3) the regular patterns of the variation of the heavy metal elements at different depths of the soil in different kinds of water quality are: the variation patterns of Pb, Cu and Zn in the mixed sewage irrigation area and in the industrial sewage irrigation area are both 0-20cm > 20-50cm < 50-80cm; the variation pattern of Cd is 0-20cm < 20-50cm > 50-80cm; the variation pattern of Cu, Zn and Cd in domestic sewage irrigation area is 0-20cm > 20-50cm > 50-80cm; and the variation pattern of Pb is 0-20cm < 20-50cm > 50-80cm; (4) the sequence of the comprehensive pollution indexes of the 0-20cm is: mixed sewage irrigation area > industrial sewage irrigation area > domestic sewage irrigation area, the sequence of the comprehensive pollution indexes of the 20-50cm is: industrial sewage irrigation area > mixed sewage irrigation area > domestic sewage irrigation area, and the sequence of the comprehensive pollution indexes of the 50-80cm is: mixed sewage irrigation area > industrial sewage irrigation area > domestic sewage irrigation area; and (5) the values of PI , which are the comprehensive pollution indexes of various heavy metals in irrigation areas with different kinds of water quality at different soil depth, are all less than 0.7, indicating that the soil pollution grade belongs to the safety level.

According to the evaluation results of the single factor index method and the comprehensive index method, none of the soils in the irrigation areas of different kinds of water quality in the study area is polluted by heavy metals, which accords with the national soil environmental quality requirements, therefore the soils can be used for the clean production of crops.

Potential ecological risk assessment of heavy metal content in the soil: Because the amount of the exposure to pollutants in the environment to various extents has an impact on human health, when the risks of the pollutants are being

assessed, multiple factors such as the pollutant content and toxicology are taken into overall consideration, therefore with the development of ecological risk assessment, models for the evaluation methods appear. The widely adopted method in assessing the ecological risks of heavy metals in the soil is the potential ecological risk index presented by Hakanson in 1980. This method closely correlates the effects of heavy metals on the ecology and the effects on the environment with the toxicological properties of the heavy metals while taking into consideration the content of heavy metals in the environment to quantitatively analyze the scale of potential risks of heavy metals in the soil, which is of great significance to the ecological risk assessment of heavy metals in the soil.

The calculation formula of the Hakanson potential ecological risk index is (He 2018):

$$P_i = C_i/B_i \quad \dots(3)$$

$$E_i = T_i/P_i \quad \dots(4)$$

$$RI = \sum_{i=1}^n E_i \quad \dots(5)$$

In the formula, C_i is the measured value of the content of heavy metal i in the soil; B_i is the calculated background value of heavy metal i in the soil; P_i is the pollution coefficient of heavy metal i in the soil; T_i is the toxicity coefficient of one single pollutant; E_i is potential ecological risk coefficient of heavy metal i in the soil; RI is potential ecological risk index of multiple heavy metals in the soil.

Hakanson potential ecological risk index method is adopted to specifically grade and assess the ecological risks of the heavy metals. The background values and toxicity coefficients of the heavy metals in the study area are given in Table 3, and the correlation between the potential ecological risk index and the pollution levels are presented in Table 4.

Based on the potential ecological risk index method, the E_i and RI of various heavy metals in the study area were calculated and given in Table 5.

Table 3: Background values and toxicity coefficients of the heavy metals.

Sampling point	Pb	Cu	Zn	Cd
T_i	5	5	1	30
B_i	21.5	21.8	78.4	0.094

Table 4: Correlation between the potential ecological risk index and pollution levels.

E_i	RI	Risk Grade
< 40	< 150	Minor
40 E_i < 80	150 RI < 300	Moderate
80 E_i < 160	300 RI < 600	Strong
160 E_i < 320	6000 RI	Very Strong
320 E_i		Extremely Strong

Table 5: Potential ecological risk index of the heavy metals in the soil E_i and RI .

Soil depth	Sampling point	E_i				RI
		Pb	Cu	Zn	Cd	
0-20cm	D ₁	17.13	5.34	0.45	86.17	109.09
	M ₁	20.93	6.55	0.64	95.74	123.87
	I ₁	20.33	5.80	0.50	98.94	125.57
20-50cm	D ₂	18.92	4.23	0.39	85.53	109.07
	M ₂	17.86	5.35	0.51	97.98	121.70
	I ₂	16.67	5.01	0.45	118.09	140.21
50-80cm	D ₃	12.38	4.04	0.37	76.60	93.39
	M ₃	18.08	5.69	0.53	134.04	158.35
	I ₃	22.30	6.66	0.60	121.28	150.83
Min		12.38	4.04	0.37	76.60	93.39
Max		22.30	6.66	0.64	134.04	158.35
Mean		18.29	5.41	0.49	101.60	125.79

According to Table 4 and Table 5, it can be seen that: (1) the values of E_i which are the ecological risk indexes of Pb, Cu and Zn in the soil at different depth and irrigated with different kinds of water quality, are all less than 40, and the ecological risk grade of the soil is minor. For Cd, except that the ecological risk coefficient of the domestic sewage irrigation area with the depth of 50-80cm is 76.6, which belongs to the moderate risk grade, the ecological risk coefficients of the rest of the soil in the irrigation areas with different kinds of water quality at different depth are within the range of $80 < E_i < 160$, and the ecological risk grades belong to the strong grades; (2) judging from the mean values of the soil at different depths, the ecological risk coefficient of Pb decreases with the increase of the soil depth; the variation pattern of the ecological risk coefficient of Cu and Zn is 0-20cm > 50-80cm > 20-50cm; and the variation pattern of ecological risk coefficient of Cd increases with the increase of the soil depth; (3) the sequence of the average ecological risk indexes of various heavy metal elements in a descending manner is Cd (101.60) > Pb (18.29) > Cu (5.41) > Zn (0.49). The ecological risk index of Cd is the highest in the soil of the study area, indicating that Cd in the soil has strong potential ecological risks, and the potential ecological risks of other heavy metal elements are quite low; (4) judging from the comprehensive ecological risk index, the ecological risk coefficients of the soil of 0-20cm and 20-50cm irrigated with different kinds of water quality are all less than 150, therefore the ecological risk grade is minor. The comprehensive ecological risk index of the soil of 50-80cm in the domestic sewage irrigation area is 93.39, which is less than 150, therefore the ecological risk grade is minor; the comprehensive ecological risk coefficients of the soil in the mixed sewage irrigation area and industrial

sewage irrigation area are 158.35 and 150.83 respectively, which are both higher than 150, therefore the ecological risk grade is moderate; (5) judging from the comprehensive risk indexes of different soil depths, the average values of the comprehensive ecological risk indexes of the soil in the irrigation areas with three different kinds of water quality with the depth of 0-20cm, 20-50cm and 50-80cm are, respectively, 119.51, 123.66 and 134.19, the overall average value of the comprehensive ecological risk indexes is 125.97, and the average values of all ecological risk indexes are all less than 150, therefore evaluated from the perspective of mean values, the comprehensive ecological risk grade of the study area is minor.

CONCLUSION

Sewage irrigation can alleviate the shortage of agricultural water, but the long-term use of sewage irrigation will cause the continuous accumulation of metals in the soil and lead to soil pollution. Heavy metal pollution in the soil will restrict the sustainable development of local agriculture and adversely affect the ecological environment and the quality of agricultural products, and then affect human health. This paper takes the irrigation areas which have been using sewage irrigation for many years as the research objects and evaluates the heavy metals in the soil in the study area to understand the pollution status and the potential ecological risks of heavy metals in the soil in the study area, as it is of great significance in ensuring the quality and safety of agricultural products and human health. The main conclusions are as follows: (1) judging from the pH values of the soil in the irrigation areas with different kinds of water quality at different depth in the study area, the soil in the study area is slightly alkaline

or alkaline. Risk control standards for the content of heavy metals in the soil are different as the acidity or alkalinity of the soil is different; (2) the status of heavy metal pollution in the soil is evaluated using single factor index method and Nemerow comprehensive index method. The contents of heavy metals Pb, Cu, Zn and Cd in the soil all belong to the safety grade, and the soil is not contaminated; (3) regarding the potential ecological risks in the soil, the heavy metals Pb, Cu and Zn show minor ecological risks judging from the single indexes, while Cd shows strong ecological risks; judging from the comprehensive index, the overall potential ecological risks of the heavy metals in the soil of the study area belong to the minor grade, but the potential ecological risks of the heavy metals in the mixed sewage irrigation area and in the industrial sewage irrigation area belong to moderate grade at the depth of 50-80 cm; (4) although the content of heavy metals in the soil does not exceed the standards, and still belongs to the safety grade, and judging from the comprehensive potential ecological risks, the potential ecological risks in the study area is not serious, the potential ecological risk grade of heavy metal Cd in the soil is quite high, and the comprehensive ecological risk grade of the soil in the mixed sewage irrigation area and the industrial sewage irrigation area at the depth of 50-80cm is moderate. Therefore, the potential ecological risks of Cd, 50-80cm in the soil of the mixed sewage irrigation area and the industrial sewage irrigation area in the study area should be paid great attention to.

REFERENCES

- Burges, A., Epelde, L. and Garbisu, C. 2015 Impact of repeated single-metal and multi-metal pollution events on soil quality. *Chemosphere*, 120: 8-15.
- Chen, T., Chang, Q.R., Liu, J., Liu, Z. and Liu, H.F. 2012. Pollution and potential environment risk assessment of soil heavy metals in sewage irrigation area. *Journal of Agro-Environment Science*, 31(11): 2152-2159.
- He, X. 2018. Ecological risk assessment and health risk assessment of soil heavy metals in Xi'an original irrigation area. Northwest University, 21-23.
- Liu, X.Y., Liang, Q., Gao, R.T., Zhang, H., Wang, L.J. and Zhou, S. X. 2015. Environmental risk assessment of soil heavy metal pollution of farmlands with long period of sewage irrigation. *Journal of Ecology and Rural Environment*, 31(4): 572-578.
- Liu, Y.P., Liu, H.Y., Wu, L., Xu, M., Cui, J.L., Gao, W.Y., Cheng, C. and Yu, X.H. 2017. Co-contamination of heavy metals and antibiotics in soils under husbandry wastewater irrigation in Guiyang City. *Acta Scientiae Circumstantiae*, 37(3): 1074-1082.
- Sheng, F., Wu, D. and Zhang, L.Y. 2016. Review on effect of reclaimed water irrigation on soil water movement in cropland. *Transactions of the Chinese Society of Agricultural Engineering*, 32(Supp. 2): 46-51.
- Wan, L., Zhang, M.Y., Lu, S. and Hu, K. 2015. Study progress on effect of polluted water irrigation on soil and problem analysis. *Ecology and Environmental Sciences*, 24(5): 906-910.
- Wang, G.L. and Lin, W.J. 2003. Contamination of soil from sewage irrigation and its remediation. *Journal of Agro-Environment Science*, 22(2): 163-166.
- Xin, S.Z., Li, H.F. and Su, D.C. 2011. Concentration characteristics and historical changes of heavy metals in irrigation sewage in China. *Journal of Agro-Environment Science*, 30(11): 2271-2278.
- Xu, J.M., Meng, J., Liu, X.M., Shi, J.C. and Tang, X.J. 2018. Control of heavy metal pollution in farmland of China in terms of food security. *Bulletin of Chinese Academy of Sciences*, 33(2): 153-159.



Effect of Temperature Downshifts on Performance and Microbial Community Structure on Pilot-Scale Sequencing Batch Biofilm Reactors Treating Hypersaline Wastewater

Shihu Liu*(**) Ziyuan Lin*, Jiong Zhou*, Yongsheng Zhang*, Jiale Wang* and Jian Zhou*†

*Key Laboratory of the Three Gorges Reservoir's Eco-Environments, Chongqing University, Chongqing, 400045, P.R. China

**Chongqing Drainage Co. Ltd, Chongqing, 400045, P. R. China

†Corresponding author: Jian Zhou; 15523829081@126.com

Nat. Env. & Poll. Tech.

Website: www.neptjournal.com

Received: 16-01-2020

Revised: 11-03-2020

Accepted: 16-04-2020

Key Words:

Pilot-scale SBBR;

Hypersaline wastewater;

PCR-DGGE;

Bacterial community

ABSTRACT

Low temperature and high salinity can strongly inhibit metabolic activities of the microbial population, resulting in low efficiency of biological wastewater treatment. Using 70 g.L^{-1} NaCl pickle mustard wastewater as influent, three pilot-scale sequencing batch biofilm reactors (SBBRs), subjected to temperature downshifts and fluctuation ranging from $30 \pm 4^\circ\text{C}$ to $10 \pm 4^\circ\text{C}$, were conducted over 200 days. Polymerase Chain Reaction-Denaturing Gradient Gel Electrophoresis (PCR-DGGE) was used to reveal the microbial community structure succession in reactors. Results showed that when the temperature was $10 \pm 4^\circ\text{C}$, the COD removal efficiencies of SBBRs (1, 2 and 3 kg COD $\text{m}^{-3} \text{d}^{-1}$ organic loading rate), were 91.6% ($\sigma = 0.11$), 87.84% ($\sigma = 0.12$) and 83.34% ($\sigma = 0.13$), respectively. Compared with the average removal efficiencies when the reactors operated at $30 \pm 4^\circ\text{C}$, the efficiency reductions of 1, 2 and 3 kg COD $\text{m}^{-3} \text{d}^{-1}$ reactors were 4.47%, 4.58% and 4.57%. As the temperature decreased, microbial population diversity did not change remarkably. However, the microbial structure changed significantly, bacteria which had strong adhesion and a wide growth temperature range were competitive. At low temperature, the predominant species were *Thalassolituus oleivorans*, *Halotalea alkalilenta* and *Kangiella koreensis*, which were all related to pollutant-degrading halophilic bacteria.

INTRODUCTION

Hypersaline wastewater is defined as a kind of wastewater containing more than 35 g.L^{-1} total dissolved solids, mainly generated by industries such as petroleum, printing and pesticide industry. Treatment of saline wastewater represents approximately 5% of the worldwide wastewater treatment requirements (Lefebvre et al. 2007). Generally, these types of wastewaters contain a high concentration of organic matter and toxic pollutants, discharge them to natural hydrologic cycle directly will do extensive damage to aquatic ecosystems (Lefebvre & Moletta 2006). Under these circumstances, investigating the processing technology becomes the key to solve the hypersaline wastewater pollution.

The existing treatment methods of saline wastewater principally include physical, chemical and biological technologies. Physicochemical methods (membrane filtration, electro-oxidation and ion exchange etc.) usually generate problems like high cost and complex management. Many researchers have focused on biological processes due to their high efficiency and low cost. At present, the

biological treatment is mainly conducted in the sequencing batch reactor (SBR), fixed-bed reactor, upflow anaerobic packed bed reactor, etc. However, high salinity will prevent common microorganisms from maintaining osmotic pressure balance, giving rise to bacterial plasmolysis, finally leading to the failure of bio-treatment. On the other hand, the high content of total dissolved organics in the saline wastewater will easily bring about sludge bulking, leading to increasing sludge volume index values and bad sludge settling property (Wang et al. 2015).

The discovery of halophilic bacteria provides a feasible solution for biological treatment of high salinity wastewater. Previous studies have shown that using halophilic bacteria to deal with brine wastewater is not only feasible but also can improve treatment performance in multiple kinds of bioreactors. The presence of a variety of heterotrophic halophilic bacteria can achieve efficient removal of organic matter in saline wastewater. However, how to effectively enrich halophile bacteria is a current issue of applying this technology. SBBR possesses both advantages of SBR and biofilm reactor, with high solids retention, the possibility of appropriate process control and strong resistance to

the loading fluctuation (Helness & Ødegaard 2001). By comparing the existing studies, the SBBR system required less time than SBR to start-up when operated at the same salinity.

All degradation and metabolic processes of microorganisms rely on enzyme-catalysed reactions, which can be markedly affected by temperature (Adams et al. 2010). Applying bio-technology to hypersaline wastewater treatment plant always struggles with seasonal changes. Especially when temperature plummets or winter comes, the low temperature can restrain the efficiency of the microbial enzyme systems, bringing about a deterioration of bio-treatment performance. However, the studies on the hypersaline wastewater treatment were primarily limited to the influence of several factors, like different reactor configuration, salinity and organic loading rate. Moreover, most studies about the effect of temperature on hypersaline wastewater bio-technologies focused on anaerobic biological treatments. Therefore, research of aerobic bio-technology removing COD in hypersaline wastewater at low temperature is important, especially using industrial wastewater instead of synthetic wastewater in pilot-scale water treatment.

This study was conducted to examine the performance of a set of pilot-scale SBBRs with different organic loading rates (OLR) treating 70 g.L^{-1} NaCl hypersaline wastewater. The effect of temperature downshifts on COD removal efficiency was investigated. PCR-DGGE was used to reveal the microbial community succession along with temperature decreasing. This study aims to demonstrate if the SBBR can deal with temperature shocks and oscillations when it is applied to treat hypersaline wastewater and to understand how microbial communities maintained their degradation ability at the low-temperature condition, providing useful information related to hypersaline wastewater treatment for future studies.

MATERIALS AND METHODS

Study site: The pilot-scale SBBRs used in the experiment were operated at the Fuling mustard factory. Fuling mustard factory is the pillar industry of the Three Gorges reservoir area in western China. Because a huge amount of sodium chloride was used during the production of the pickled mustard tuber, the factory produces hypersaline wastewater and needs to be pretreated before it is drained into a municipal sewage treatment system. The characteristics of the influent are presented in Table 1.

Description of pilot-scale SBBRs: The pilot-scale system (Fig. 1) consisted of three parallel SBBRs (S1, S2 and S3), each reactor with a total effective volume of 3.57 m^3 and dimensions of $3.0 \times 0.7 \times 1.7 \text{ m}^3$ (L×W×H). Poly-

Table 1: Characteristics of hypersaline pickled mustard tuber wastewater.

Parameter	Value (mean±SD)
Salinity (g.L^{-1} NaCl)	70 ± 6
NO_3^- -N (mg.L^{-1})	42 ± 3
COD (mg.L^{-1})	8243 ± 502
BOD_5 (mg.L^{-1})	4512 ± 612
pH	5.5 ± 0.5

urethane suspension spherical fillers were submerged in the reactor and their packing ratios were about 53%. Air was provided through microporous aerators equipped in the bottom of reactors to maintain the DO values between 5.7 - 6.3 mg.L^{-1} . The inflow was stored in a feed tank and supplied to the bioreactors by an influent pump. The variation of temperature controlled by a constant temperature room. SBBRs were run in a 24 h cycle, consisting of 0.25 h filling, 23.5 h aerobic reaction, and 0.25 h drawing.

Experimental procedure: The reactors were inoculated with dewatered activated sludge taken from a sewage wastewater treatment plant (WWTP) in Chongqing, China. In the first week, a visible thick biofilm was obtained by inoculation in salt-free condition and then began the formal operation. During operation, the OLR of the S1, S2 and S3 were controlled at 1.03 ± 0.07 , 2.03 ± 0.13 and $3.07 \pm 0.15 \text{ kg COD m}^{-3} \text{ d}^{-1}$ (they would be represented by an average value of 1, 2 and 3 $\text{kg COD m}^{-3} \text{ d}^{-1}$) by adjusting the volumetric exchange ratio (VER). The experimentation concluded three phases (phase I, II and III), each of which was characterized by different temperatures. During phase I, the water temperature was kept at $30 \pm 1^\circ\text{C}$. As the 70 g.L^{-1} NaCl influent was fed in, the salinity of the reactor gradually increased. While the salinities in the reactors were above 65 g.L^{-1} NaCl and the obtained COD removal efficiencies stably exceeded 60%, considered the reactors had been successfully started. Moved into the next phase after the reactors had been operated in stable condition at $30 \pm 1^\circ\text{C}$. In phase II, the temperature was adjusted to $20 \pm 2^\circ\text{C}$, operated SBBRs until the effluents were steady and entered

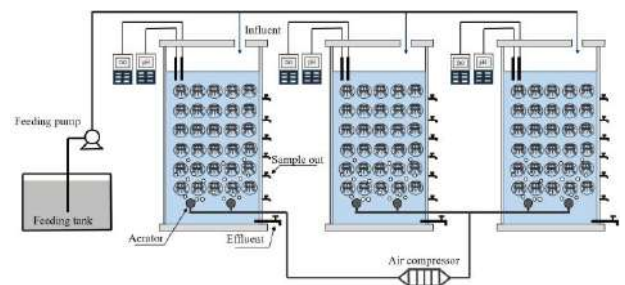


Fig.1: Schematic of the pilot SBBRs.

into phase III. In phase III, temperature was declined to $10 \pm 1^\circ\text{C}$, such a status further kept until the end of the experiment. During each stable period of phase I, II and III, the stability of SBBRs facing temperature oscillation was investigated. The temperature was controlled to fluctuate in the range of $30 \pm 4^\circ\text{C}$, $20 \pm 4^\circ\text{C}$ and $10 \pm 4^\circ\text{C}$ in phase I-III. Each stable effluent period lasted at least 30 days. Meanwhile, the COD of influent and effluent was measured every day.

Analytical methods: Temperature, dissolved oxygen (DO) and pH were measured by DO and pH meter (HACH, HQ30d, USA). COD and BOD_5 were analysed according to Standard Methods (APHA 2005).

DNA extraction: DNA of the inoculated sludge and biomass samples, which were collected from the stable effluent conditions of S3 during phase I, II and III, were extracted by using the method described by Miller et al. (1999). The extractions were checked by 0.8 % agarose gel electrophoresis and stored at -20°C for PCR amplification.

PCR amplification and DGGE: The highly variable V3 region of the bacterial 16S rRNA gene was amplified by a PCR universal primer pair 357F-GC (5'-GC-clamp-CCTACGGGAGGCAGCAG-3') and 518R (5'-ATTACCGCGGCTGCTGG-3') with a GC clamp (CGCCCGCCGCGCGCGGCGGGCGGGGCGG GGGCACGGGGGG) attached to the forward primer (Muyzer et al. 1993). The procedure of the amplification was as follows: 1 cycle of initial denaturation at 94°C for 5 min; then 30 cycles of denaturation at 94°C for 45 s, annealing at 60°C for 45 s, and extension at 72°C for 90 s. After that, 1 cycle of the final extension was set at 72°C for 10 min. PCR products were analysed by 2% agarose gel electrophoresis.

The expected sizes of the amplified fragments were 230 bp. The Dcode Universal Mutation Detection System (Bio-Rad, USA) was used to perform DGGE analysis. The PCR products were run on an 8% polyacrylamide gel with denaturing ranges from 37.5-55%. The temperature was set to 60°C simultaneously, DGGE at 200 V was run for 10 min, and then 80 V for 900 min. After electrophoresis, the gels were stained with ethidium bromide solution for 25 min before placing them under the Bio-Rad Versa Doc for observation and photographed. The images were processed with Bio-Rad Quantity One Software Version 4.6.2.

DNA sequencing and the phylogenetic tree: The desired bands in DGGE gels were cut off to study the effective strains. Each gel fragment was resolved in 50 μL sterile deionized water and kept overnight at 4°C . The DNA bands from the gel fragment were excised and PCR amplifications performed as above except using the primer without a GC clamp. The 16S rRNA gene fragment clones were sequenced

by the BGI Company (BGI, Shenzhen, China). The results were compared with the GenBank database using the Nucleotide Blast. A neighbour-joining algorithm-based phylogenetic tree was constructed using MEGA 5.0 software and bootstrap analyses for 1000 replicates were performed. The Dice-coefficients were analysed by Quantitation Software Version 4.6.2 software (Bio-Rad Laboratories, USA) to study the similarities in band patterns.

RESULTS AND DISCUSSION

Reactor performance: The COD removal efficiencies of the 1, 2 and 3 kg $\text{COD m}^{-3} \text{d}^{-1}$ SBBR (S1, S2 and S3) during the operation are shown in Fig. 2. During phase I, as the salinity increasing, COD removal efficiency in all the three reactors decreased. This adverse effect had lasted for 3-5 days before it started ameliorating. This phenomenon happened because the gradual increasing salinity caused plenty of microorganisms, which came from the inoculated sludge, could not adapt to high salinity and were eliminated (Chen et al. 2016). The salinities of S1, S2 and S3 all were increased to $67 \pm 2 \text{ g.L}^{-1}$ NaCl during the initial 17 days, and the removal

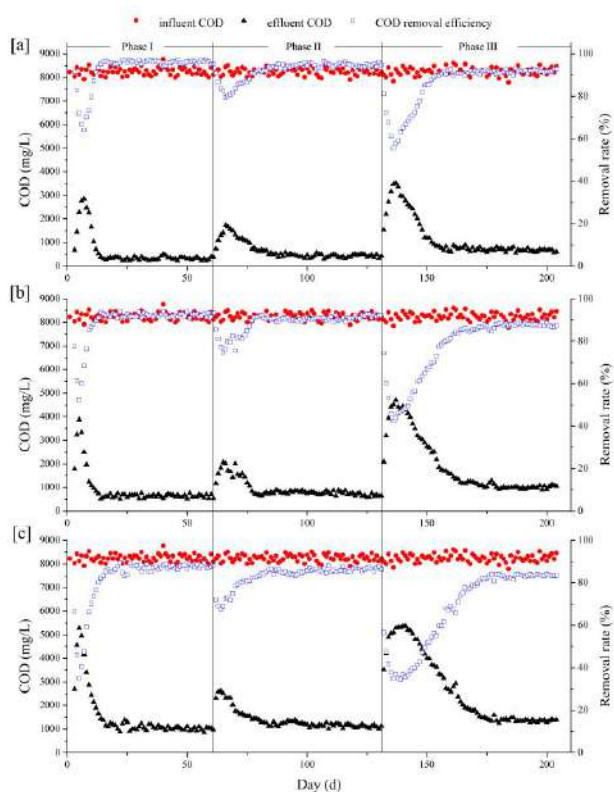


Fig. 2: The variations of COD concentrations in the influent and effluent of three SBBRs: 1 kg $\text{COD m}^{-3} \text{d}^{-1}$ SBBR reactor, [a]; 2 kg $\text{COD m}^{-3} \text{d}^{-1}$ SBBR reactor, [b]; 3 kg $\text{COD m}^{-3} \text{d}^{-1}$ SBBR reactor, [c].

rates of COD were steadily over 85%, which meant three reactors had successfully started up under 30°C. The rapid lifting of salinity often has a severe impact on the system's performance, leading to rapid deterioration and challenging restoration. In the study of Uygur & Kargi (2004), using SBR treating synthetic wastewater, the COD removal efficiency decreased from 96% to 32% as salt content increased from 0‰ to 6‰. The result of this study indicates that SBBR owns a better resistance to the increasing salinity and can start-up in a short time when it is applied to treat hypersaline wastewater.

Under $30 \pm 4^\circ\text{C}$ condition, the effluent COD of S1, S2 and S3 finally remained stable at $325 \pm 90 \text{ mg.L}^{-1}$, $625 \pm 100 \text{ mg.L}^{-1}$ and $1000 \pm 120 \text{ mg.L}^{-1}$. The corresponding average removal efficiencies approached to 96.07%, 92.42% and 87.91%, respectively. When the temperature dropped to $20 \pm 2^\circ\text{C}$, COD removal rates declined slightly at the beginning. After 15-21 days of acclimation, effluent COD of S1, S2 and S3 finally remained stable at $425 \pm 100 \text{ mg.L}^{-1}$, $775 \pm 80 \text{ mg.L}^{-1}$ and $1175 \pm 120 \text{ mg.L}^{-1}$. In phase II, the average removal efficiencies recovered to 94.85%, 90.62% and 85.78%, respectively. In phase III, as the temperature was further declined to $10 \pm 1^\circ\text{C}$, the COD removal efficiency decreased significantly. The domestication time S1, S2 and S3 used was much longer than they had spent during phase II. After 31, 47, 41 days, effluent COD of S1, S2 and S3 became steadily at $690 \pm 100 \text{ mg.L}^{-1}$, $1004 \pm 70 \text{ mg.L}^{-1}$ and $1375 \pm 100 \text{ mg.L}^{-1}$, and the average removal efficiencies were 91.6%, 87.84% and 83.34%, respectively.

The COD removal efficiency was higher in low OLR reactor. However, S3 still got a COD removal rate of more than 91% at 30°C. In this study, using SBBR to treat hypersaline industrial wastewater with high organic content

was feasible. During the temperature decreasing from 30°C to 10°C, more time was needed for reactors to regain stable performance when they adapted to 10°C conditions. It means low temperature gave a strong shock for SBBR. However, after S1, S2 and S3 had adapted to the declined temperature, a certain fluctuation of temperature did not bring about performance undulated. Although three SBBRs were subjected to low temperature, COD was effectively removed at 10°C with the average efficiency above 83%. The results were in line with the former studies, despite the fact that the COD removal efficiency was inhibited less seriously in this study than those reported at a similar level of temperature downshift. Li et al. (2012) observed that the COD removal efficiencies of a hybrid bioreactor at 25°C and 10°C were 94.78% and 66.27%, respectively. Jia et al. (2012) used an SBR to treat slaughterhouse wastewater, and the result showed that COD removal efficiencies were about 78%, 92% and 96% at 10°C, 20°C and 30°C. This research indicates that SBBR may own a better resistance to temperature decline and can successfully deal with temperature change.

Cycle profile: To understand more details about the process, 24 h cycle profiles of S1 (Fig. 3a), S2 (Fig. 3b) and S3 (Fig. 3c) were analysed at 10°C, 20°C and 30°C, respectively. The conversion rates of COD were distinctly higher in S3. Degradation rates were greatly affected by organic loading. With higher OLR, more nutrients were available for microorganism propagation and growth, leading to a larger population, and COD conversion happened faster.

In the same reactor, the COD degradation rates of 10°C, 20°C and 30°C were not significantly different from each other. Biofilm systems had stronger resistance to temperature changes compared to suspended sludge systems (Odegaard 2006). In the biofilm system, microorganisms were attached

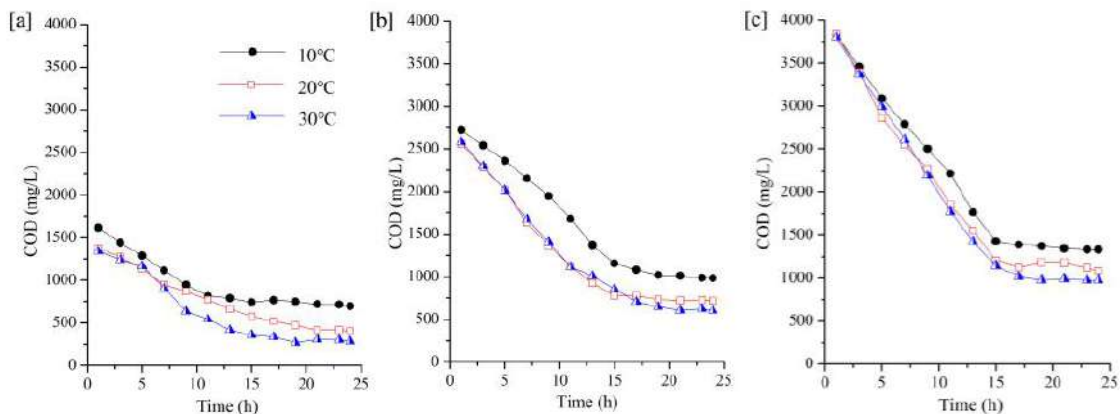


Fig. 3: The COD degradation cycle profile of three SBBRs: 1 kg COD m⁻³d⁻¹ SBBR reactor, [a]; 2 kg COD m⁻³d⁻¹ SBBR reactor, [b]; 3 kg COD m⁻³d⁻¹ SBBR reactor, [c].

growth, and more kinds of bacteria were reserved in the system, which was conducive to the growth of microorganisms which possessed the different temperature competitiveness. Combined with the DGGE analysis, when temperature downshifted to 10°C, species which could adapt to a wider range of temperature thrived and were responsible for COD removal. As a result, the system maintained a stable performance.

Bacterial community diversity: The diversities of the microbial community of samples were analysed by PCR-DGGE (Fig. 4). The banding patterns showed that microbial community structures of 3 kg COD m⁻³ d⁻¹ SBBR under different temperature (Lane 1, 2 and 3) changed significantly from inoculated sludge (Lane 0). That suggested majority of microorganisms in seed sludge could not survive in 70 g.L⁻¹ NaCl environment, few halophilic microorganisms from both seed sludge and mustard tuber wastewater gradually multiplied and became dominant populations (Chen et al. 2016).

The total number of bands of Lane 1, 2, 3 (30, 20 and 10°C) did not greatly vary from each other. However, microbial structure and population distribution changed significantly after S3 operated at low temperature. The Dice coefficients of lane 3 with Lane 1 and Lane 2 were 46.1% and 55.2%. The results indicate that the temperature has a notable effect on the microbial community structure. The same result was reported by Moura et al. (2009), revealing bacterial communities of an aerated lagoon could be grouped

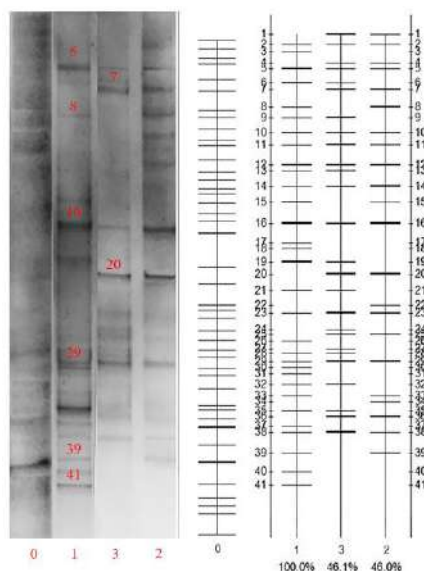


Fig. 4: The microbial communities of samples: inoculated sludge, Lane 0; S3 biofilm sample at 30°C, Lane 1; S3 biofilm sample at 20°C, Lane 2; S3 biofilm sample at 10°C, Lane 3. The left one was the DGGE patterns and the right one was the analysis result of the DGGE pattern by Quantitation Software Version 4.6.2.

into three clusters: fall/winter, spring and summer cluster by following the temperature change.

Bacterial community cluster analysis: After excising from the gel, 8 prominent bands were sequenced and successfully identified. The sequencing results are given in Table 2 and a phylogenetic tree was constructed (Fig. 5).

Compared to 30°C and 20°C samples (Lane 1 and Lane 2), the abundance of bacterial population represented by band 7, 20, 29 increased at 10°C (Lane 3). Band 7 and 20 only appeared at phase 2 and 3 (20°C and 10°C), were related to *Thalassolituus oleivorans*, *Halotalea alkalilenta*. *Thalassolituus oleivorans* is an aerobic heterotrophic, hydrocarbon-utilizing bacteria, motile using one to four polar flagella, growth occurs at 0.5-5.7% NaCl at 4-30°C, numerous isolates were obtained from the polar coastal area of Russia (Yakimov et al. 2004, Yakimov et al. 2007). Several studies used it to bio-remediate oil-polluted seawater (Hassanshahian et al. 2014a, Hassanshahian et al. 2014b). *Halotalea alkalilenta*, which is an aerobe heterotrophic bacteria tolerates up to 15% NaCl, motile by peritrichous flagella, and the temperature range for growth is 5-45°C (Ntougias et al. 2007). Band 29 was affiliated with *Kangiella koreensis* and occurred in S3 among all phases despite how the temperature had changed. *Kangiella koreensis* is a facultative anaerobic bacterium, can reduce nitrate to nitrogen gas under anaerobic conditions, non-motile. Growth occurs between 4-43°C and cannot grow without NaCl or in the presence of more than 13% NaCl (Yoon et al. 2012). Chun et al. (2012) had detected this strain in a full-scale seawater desalination process operated in a cartridge filter.

Band 5 and 16 were classified as *Marinimicrobium koreense* and *Zobellella taiwanensis*, respectively. They persistently existed during the whole cultivation process, but the bacterial population abundance decreased when the temperature dropped to 10°C. *Marinimicrobium koreense* is an aerobic chemoheterotroph bacterium, grows in the range 0-15% salinity (Lim et al. 2006). *Zobellella taiwanensis* is a facultative anaerobic bacterium which grows in 0-14% NaCl and can achieve anaerobic growth by undertaking either denitrification or fermentation (Lin & Shieh 2006). Both bacteria mentioned above grow at 10-45°C and frequently possess a single polar flagellum.

Band 8 and 39 were separately affiliated to *Simidiua agarivorans* and *Nitrincola lacisaponensis*, respectively, appeared only at 30°C and 20°C, entirely disappeared at 10°C. *Simidiua agarivorans* is a mesophilic halophilic bacterium, can grow in the range of 0.5-7% NaCl, 15-40°C. Nearly all cells are non-motile. It is capable of anaerobic growth by reducing nitrate to nitrite (Shieh et al. 2008). As a halotoler-

Table 2: Sequence analysis of bands excised from DGGE gels.

Band	Closest relative	Similarity (%)	Accession No.
5	<i>Marinimicrobium koreense</i>	100	NR_043222.1
7	<i>Thalassolituus oleivorans</i>	99	NR_028972.1
8	<i>Simiduia agarivorans</i>	100	NR_044318.1
16	<i>Zobellella taiwanensis</i>	94	NR_043630.1
20	<i>Halotalea alkalilenta</i>	100	NR_043806.1
29	<i>Kangiella koreensis</i>	98	NR_027574.1
39	<i>Nitrincola lacisaponensis</i>	100	NR_042984.1
41	<i>Nitratifactor salsuginis</i>	100	NR_041024.1

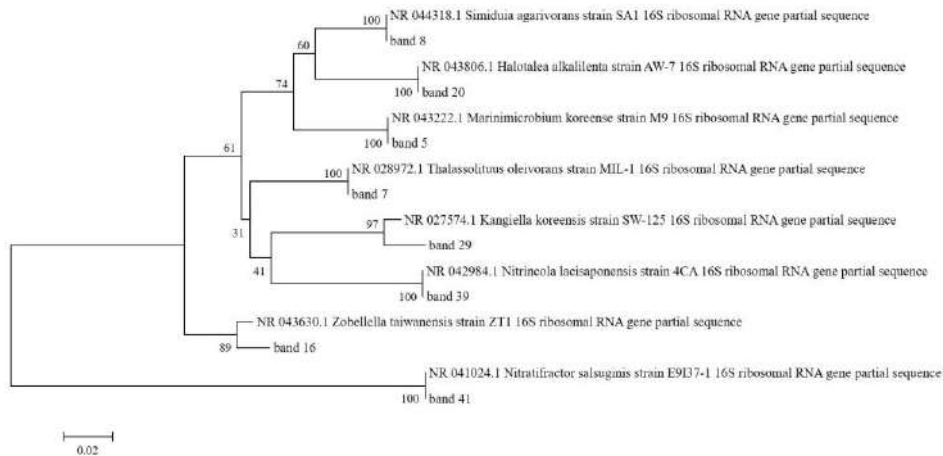


Fig. 5: Phylogenetic tree constructed by MEGA 5.0 software, and the sequences derived from DGGE patterns of the system.

ant and heterotrophic bacterium, *Nitrincola lacisaponensis* utilizes NO_2 and O_2 as electron acceptors. Cells can use single flagellum to move and can grow at 15-40°C. Band 41 was related to *Nitratifactor salsuginis*, vanished after the temperature dropped from 30°C. *Nitratifactor salsuginis* is a strictly chemoautotrophic denitrifying bacterium and grows at 28-40°C (Nakagawa et al. 2005).

Comparing the above results, bacteria which could adapt to a wide range of temperature gradually became dominant populations at 10°C. The presence of aerobic, anoxic and anaerobic microenvironments in biofilms provide living conditions for the facultative anaerobic bacterium. The study of Herald & Zottola (1988) showed that cells were shown to have single flagellum at 35 but several flagella at 10 °C which indicated when the temperature dropped, the bacteria with stronger adhesion were tended to be more competitive. In this research, under low temperature condition, the predominant strains tend to possess several flagella while bacteria with single flagella were decreasing. This phenomenon is consistent with the above conclusion.

The suitable temperature, salt tolerance range, and other characteristics of the identified bacteria were consistent with

the system parameters. It is considered that the microbial community dominated by halophilic bacteria had been successfully domesticated in SBBR, achieving a high organic matter removal efficiency at a different temperature. The declined temperature did not significantly reduce microbial diversity in the reactor, however, halophilic bacteria with a broad range of growth temperature gradually predominate because of the gradual succession.

CONCLUSION

In this study, pilot-scale SBBRs were quickly started up treating 70 g.L⁻¹ NaCl pickled mustard tuber wastewater. The effect of temperature downshifts on system treatment efficiencies and microbial population succession were investigated. Under 70 g.L⁻¹ NaCl condition, high COD removal efficiencies were obtained at 30°C, 20°C and 10°C in SBBRs with different OLR. The decrease in temperature caused a population succession. At 10°C, halophilic bacteria with better temperature resistance and stronger adhesion became dominant species, which were *Thalassolituus oleivorans*, *Halotalea alkalilenta*, *Kangiella koreensis*, *Marinimicrobium koreense* and *Zobellella taiwanensis*.

This study demonstrates that SBBR shows robustness to temperature downshifts and fluctuation when treating hypersaline industrial wastewater.

REFERENCES

- Adams, H.E., Crump, B.C. and Kling, G.W. 2010. Temperature controls on aquatic bacterial production and community dynamics in arctic lakes and streams. *Environ. Microbiol.*, 12(5): 1319-33.
- APHA 2005. Standard Methods for the Examination of Water and Wastewater, 21st Edn. American Public Health Association/American Water Works Association/Water Environment Federation, Washington DC.
- Chen, J., Yi, H., Wang, Y., Gong, B., Jian, Z. and Qing, X. 2016. Start-up and microbial communities of a simultaneous nitrogen removal system for high salinity and high nitrogen organic wastewater via heterotrophic nitrification. *Bioresource Technology*, 216: 196-202.
- Chun, Y., Ha, P.T., Powell, L., Lee, J., Kim, D., Choi, D., Lovitt, R.W., Kim, I.S., Mitra, S.S. and Chang, I.S. 2012. Exploring microbial communities and differences of cartridge filters (CFs) and reverse osmosis (RO) membranes for seawater desalination processes. *Desalination*, 298(29): 85-92.
- Hassanshahian, M., Emiazzi, G., Caruso, G. and Cappello, S. 2014a. Bioremediation (bioaugmentation/biostimulation) trials of oil polluted seawater: A mesocosm simulation study. *Marine Environmental Research*, 95(4): 28.
- Hassanshahian, M., Yakimov, M.M., Denaro, R., Genovese, M. and Cappello, S. 2014b. Using Real-time PCR to assess changes in the crude oil degrading microbial community in contaminated seawater mesocosms. *International Biodeterioration & Biodegradation*, 93(93): 241-248.
- Helness, H. and Ødegaard, H. 2001. Biological phosphorus and nitrogen removal in a sequencing batch moving bed biofilm reactor. *Water Science and Technology*, 43(1): 233.
- Herald, P.J. and Zottola, E.A. 1988. Attachment of *Listeria monocytogenes* to stainless steel surfaces at various temperatures and pH values. *Journal of Food Science*, 53(5): 1549-1562.
- Jia, Y., Gao, C., Zhang, L. and Jiang, G. 2012. Effects of pre-fermentation and influent temperature on the removal efficiency of COD, $\text{NH}_4^+\text{-N}$ and $\text{PO}_4^{3-}\text{-P}$ in slaughterhouse wastewater by Using SBR. *Energy Procedia*, 16(16): 1964-1971.
- Lefebvre, O. and Moletta, R. 2006. Treatment of organic pollution in industrial saline wastewater: a literature review. *Water. Res.*, 40(20): 3671-82.
- Lefebvre, O., Quentin, S., Torrijos, M., Godon, J.J., Delgenes, J.P. and Moletta, R. 2007. Impact of increasing NaCl concentrations on the performance and community composition of two anaerobic reactors. *Appl. Microbiol. Biotechnol.*, 75(1): 61-69.
- Li, T., Bo, L., Fan, Y., Zhang, S., Wu, Y. and Yang, L. 2012. Comparison of the removal of COD by a hybrid bioreactor at low and room temperature and the associated microbial characteristics. *Bioresource Technology*, 108(3): 28.
- Lim, J.M., Jeon, C.O., Lee, J.C., Song, S.M., Kim, K.Y. and Kim, C.J. 2006. *Marinimicrobium koreense* gen. nov., sp. nov. and *Marinimicrobium agarilyticum* sp. nov., novel moderately halotolerant bacteria isolated from tidal flat sediment in Korea. *International Journal of Systematic & Evolutionary Microbiology*, 56(Pt 3): 653.
- Lin, Y.T. and Shieh, W.Y. 2006. *Zobellella denitrificans* gen. nov., sp. nov. and *Zobellella taiwanensis* sp. nov., denitrifying bacteria capable of fermentative metabolism. *International Journal of Systematic & Evolutionary Microbiology*, 56(6): 1209-1215.
- Miller, D.N., Bryant, J.E., Madsen, E.L. and Ghiorse, W.C. 1999. Evaluation and optimization of DNA extraction and purification procedures for soil and sediment samples. *Applied & Environmental Microbiology*, 65(11): 4715.
- Moura, A., Tacão, M., Henriques, I., Dias, J., Ferreira, P. and Correia, A. 2009. Characterization of bacterial diversity in two aerated lagoons of a wastewater treatment plant using PCR-DGGE analysis. *Microbiological Research*, 164(5): 560-569.
- Muzyer, G., Waal, E.C.D. and Uitterlinden, A.G. 1993. Profiling of complex microbial populations by denaturing gradient gel electrophoresis analysis of polymerase chain reaction-amplified genes coding for 16S rRNA. *Applied & Environmental Microbiology*, 59(3): 695.
- Nakagawa, S., Takai, K., Inagaki, F., Horikoshi, K. and Sako, Y. 2005. *Nitratiruptor tergaricus* gen. nov., sp. nov. and *Nitratifractor salsuginis* gen. nov., sp. nov., nitrate-reducing chemolithoautotrophs of the epsilon-Proteobacteria isolated from a deep-sea hydrothermal system in the Mid-Okinawa Trough. *Int. J. Syst. Evol. Microbiol.*, 55(Pt 2): 925-933.
- Ntoungias, S., Zervakis, G.I. and Fasseas, C. 2007. *Halotalea alkalilenta* gen. nov., sp. nov., a novel osmotolerant and alkali tolerant bacterium from alkaline olive mill wastes, and emended description of the family Halomonadaceae Franzmann et al. 1989, emend. Dobson and Franzmann 1996. *International Journal of Systematic & Evolutionary Microbiology*, 57(Pt 9): 1975-1983.
- Odegaard, H. 2006. Innovations in wastewater treatment: the moving bed biofilm process. *Water Science & Technology*, 53(9): 17.
- Shieh, W.Y., Liu, T.Y., Lin, S.Y., Jean, W.D. and Chen, J.S. 2008. *Simidiuia agarivorans* gen. nov., sp. nov., a marine, agarolytic bacterium isolated from shallow coastal water from Keelung, Taiwan. *International Journal of Systematic & Evolutionary Microbiology*, 58(Pt 4): 895.
- Uygun, A. and Kargi, F. 2004. Biological nutrient removal from pre-treated landfill leachate in a sequencing batch reactor. *J. Environ. Manage.*, 71(1): 9-14.
- Wang, Z., Gao, M., She, Z., Wang, S., Jin, C., Zhao, Y., Yang, S. and Guo, L. 2015. Effects of salinity on performance, extracellular polymeric substances and microbial community of an aerobic granular sequencing batch reactor. *Separation and Purification Technology*, 144: 223-231.
- Yakimov, M.M., Giuliano, L., Denaro, R., Crisafi, E., Chernikova, T.N., Abraham, W.R., Luensdorf, H., Timmis, K.N. and Golyshin, P.N. 2004. *Thalassolituus oleivorans* gen. nov., sp. nov., a novel marine bacterium that obligately utilizes hydrocarbons. *International Journal of Systematic & Evolutionary Microbiology*, 54(1): 141-148.
- Yakimov, M.M., Timmis, K.N. and Golyshin, P.N. 2007. Obligate oil-degrading marine bacteria. *Current Opinions in Biotechnology*, 18(3): 257-266.
- Yoon, J.H., Kang, S.J., Lee, S.Y., Lee, J.S. and Oh, T.K. 2012. *Kangiella geojedonensis* sp. nov., isolated from seawater. *International Journal of Systematic & Evolutionary Microbiology*, 62(Pt 3): 511.



Novel Approaches Towards Sustainable Management of an Agricultural Residue - The Rice Husk

A. Geethakarathi†

Department of Civil Engineering, Kumaraguru College of Technology, Coimbatore-641 049, Tamilnadu, India

†Corresponding author: A. Geethakarathi; geethadivaakar2005@gmail.com

Nat. Env. & Poll. Tech.
Website: www.neptjournal.com

Received: 09-08-2020

Revised: 06-10-2020

Accepted: 16-10-2020

Key Words:

Adsorption
Biomaterials
Composting
Rice milling waste

ABSTRACT

Recent developments in the reuse of agricultural residues/resources have led to environmental sustainability and cleaner technology emphasizing the utilisation of natural resources. Novel approaches to sustainable and energy conservations inter-relates the scientific and practical applications employed in engineering solutions. The increasing importance of biomass had led to an acute need for mitigating global sustainable problems. In the third world economics, Rice Husk (RH) collected from rice milling industry is considered as one of the abundant and invaluable agro-based residues. A focus on industrial food production and its sustainability is due to the generation of huge quantity of RH. The improper handling and disposal management of RH has resulted in environmental and population health risk, due to its large space occupancy and leaching. The effective utilization and study of rice husk in various industrial applications such as construction industry, energy production, water purification and soil stabilization have shown acceptable results. This review discusses the current research works focussing on the suitability of RH and its ash over a wide field of applications. Silica being the dominant content in RH and Rice Husk Ash (RHA) has attracted interest among the researchers to develop it into high strength composite materials, porous nanomaterials, a precursor of renewable energy and soil stabilising biochars. Replacement of fine aggregates with RHA has improved the strength and durability of the concrete. The RHA is also developed into an adsorbent and coagulant in water purification. The binding between the ions present in impure water and highly reactive silica bond enhances the removal efficiencies of metal ions in water treatments. Very few researches are carried out using RH compared with the pyrolyzed RHA as an alternative. This paper highlights the various field of RH applications and suggests composting of RH with nitrogen-rich garden waste to obtain an enriched soil stabilizing product with high nutrient and organic value. This approach would restore RH in its the place of generation, thereby improving the economic value of the agricultural mass and sustainable way of living.

INTRODUCTION

The major sustainability challenge faced by the earth is environmental degradation caused by the deterioration of the biotic and abiotic resources. The huge quantity of waste generated from natural resources such as plants and biomass has led to a serious disposal problem along with the release of synthetic/man-made pollutants. The conventional practice in disposing of these wastes are either to burn or naturally convert into organic fertilizer under favourable conditions. The decomposition of organic matter leads to water pollution by releasing dreadful pathogens causing various diseases in the surrounding environment. Recent developments have shown several alternatives in broader field areas as low-cost materials in replacement with the conventional materials used. A few among those industries are the construction field, cement manufacturing, paint industry, ceramics, adhesives, water stabilizers, nanofibres, dietary fibres,

alcohol production, water purification, energy production, composting and landfill under controlled conditions.

One among the agricultural wastes is the Rice Husk (RH). This review paper discusses the wider applications of RH in various fields. Inefficient use of agricultural wastes on vegetative lands for soil amendment is limited. Studies have shown the negative nutrient balance leading to a decline in soil fertility in traditional farming (Tewodros et al. 2007). Replacement of nutrient and feed with organic amendments in an effective manner are viable options for soil fertility and crop production (Negassa et al. 2015, Dercon & Christiaensen 2011). The treatment methodology of RH as an alternate source is elaborated with their respective advantages and disadvantages. A suggestion is also given in using RH as a soil stabilizing agent by composting. The significance and utilization of compost derived from RH in increasing the soil organic content are also discussed.

Rice Husk (RH)

More than 50% of the world's population has rice grains (*Oryza sativa*) as their staple food. The RH generated from the milling industry form about 22% by weight of paddy and is used as an alternate fuel for paddy processing and producing energy through gasification (Patil & Sharanagouda 2017). India being the second-largest rice producer in the world produces about 20 million tonnes of RHA (Shwetha et al. 2014). The major rice producers across the globe are indicated in Table 1. The untreated RH comprises of 75% organic matter of that 25% of ash is generated. The chemical composition and analysis of RH is given in Table 2. The alternate usage of RH and RHA in a wide field of applications such as synthesis of highly porous carbon fibres, development as catalyst and chips and lightweight construction materials are briefly summarized in this review.

ALTERNATE USE OF RICE HUSK (RH)

Biochar Production

Recycling of crop residue is gaining back its intensification, due to awareness among the rural agricultural mass leading to the production of low-cost organic fertilizer. The production of biochar improves the soil fertility and increased nutrient contents of the soil, yielding effective plant growth. The presence of silica content enhances the bio-productivity in the biochar amended soil, thereby improving the silica mobilization to the plant growth. The silica beneficiates the plant by reducing metal toxicity, salt content and supports in increasing culm wall thickness and vascular bundle. Addition of biochar in agricultural land shows lower bulk density and improved water holding capacity by 77.92% (Lehmann et al. 2009). Studies analysed by Ghorbani & Amirahmadi (2018) on fertility management of soil, have shown influences of RH amended soil in pH, soil electrical conductance (EC), ion exchange, organic content and some macro element such as potassium and nitrogen.

Construction Industry

Agricultural biomass and residues such as husk and hulls of

Table 1: Countries with major rice production.

Country	Rice Production (in million tons)
China	205.21
India	104.80
Indonesia	71.29
Bangladesh	51.50
Vietnam	44.04

rice and groundnut, fibres of coir, kenaf and jute, straw and sawdust have been identified as most economically important replacements in constructional industries. The rice husk under the focus of study cannot be used as an alternative replacement material and is used only as RHA. 85-90% amorphous silica is obtained by the controlled burning of rice husk under an optimum derived temperature of 650°C to 850°C. The replacement of conventional aggregates with rice husk ash is used as a good binding ingredient in the cement industry and other construction industry (Nehdi et al. 2003).

The major factor influencing the grade of RHA is the burning condition of rice husk including the burning temperature. The RHA exist in two main forms such as crystalline and amorphous, which has a wide application in various industrial fields.

Unlike steel and ceramics industries using crystalline silica, amorphous silica is useful in construction and rubber industries (Mehta & Pitt 1976). Table 3 shows the preparation of RHA under various conditions with their strengths and workability. RHA in cement or concrete leads to the improvement in various properties due to its fibrous, crystalline and amorphous nature. Researchers have proved that a replacement of 70% of pozzolanic material by RHA yields higher durability and strength than conventional cement mortar. Though many ongoing research works are carried over due to the amorphous nature of silica, an increase in compressive strength observed in many studies was due to

Table 2: Chemical composition, proximate and ultimate analysis of rice husk.

Constituents	Rice Husk (by weight)
Silica (SiO ₂)	94.50
Oxide of manganese (MnO)	1.09
Oxide of iron (Fe ₂ O ₃)	0.54
Oxide of calcium (CaO)	0.48
Oxide of magnesium (MgO)	0.23
Alumina (Al ₂ O ₃)	0.21
Proximate Analysis	15
Fixed carbon (%)	
Volatile matter (%)	67
Ash (%)	18
Ultimate Analysis	40
Carbon (%)	
Hydrogen (%)	5
Nitrogen (%)	34.8
Oxygen (%)	0.8
Sulphur (%)	0.1

(Reference: Ghosh & Bhattacharjee 2013)

Table 3: Characterization of RHA in the construction industry.

S.No.	Constituents	Combustion time/ temperature	Analytical methods	28 days Compressive strength (Mpa)	References
1	10% RHA	400°C - 600°C	-	22	Godwin et al. (2013)
2	20% RHA + 10% Microsilica	6h/680°C	XRF	93.28	Zareei et al. (2017)
3	RHA	-	XRD, SEM	35.39	Kaur et al. (2018)
4	MgO + RHA	-	XRD FT-IR, OM, SEM	1.1	Qin et al. (2018)
5	20% RHA	1h-4h/550°C - 700°C	XRD, EDAX	168.6	Vigneshwari et al. (2018)

the increasing percentage of carbon present in RHA. The fineness nature of the RHA enhances the pozzolanic reaction and is effectively carried out in Reactive Powdered Concrete (RPC) production. The Silica Fume (SF), one of the major constituent present in the RPC makes the reaction rate faster. In India, researchers are also focusing on the suitability of RHA in replacing SFs (Raman et al. 2011, Van et al. 2014, Van Tuan et al. 2011).

Super-hydrophobic coatings and admixtures for construction materials are widely used in recent year due to their anti-corrosion, anti-icing and anti-fouling nature (Junaidi et al. 2016, Ramachandran et al. 2016, Tittarelli & Moriconi 2011). The replacement of nanoparticles in the super-hydrophobic coating is replaced with the RHA, which enhances the roughness by the hydrophobic coating on the concrete.

Energy Production

For millennia, the conventional energy source on the planet is the biomass. The burning of biomass such as hulls, corn and jute into fuel leads to a renewable energy source with high calorific value, thereby satisfying the energy consumption needs and demands. The RH contains 30 -50% of organic carbon with a high calorific value of 13,000 to 16,000 KJ/kg, whereas the power plant ranges between 9,500 KJ/kg to 27,000 KJ/kg. Table 4 gives the heating value of some of the predominantly used agricultural residues. Though the organic content and ash content is higher than coal, the fixed carbon content of RH is much lower than in coal. The lower fixed carbon content in RH and the wearing of components during Rice Husk processing is a major limitation of RH energy conversion. 198 kg of RH is utilized to generate 1 MWH by boiler with the emission of gases such as CO₂, CO, NO₂, SO₂ and total suspended particles (TSP). Due to the limitations, the rice husk fuel power plant is operated and appended with water pre-treatment and electricity generator units (Prasara & Gheewala 2017).

The bio-oil yielded by direct or indirect combustion minimizes the formation of biochar. The stored bio-oil and the other liquid derivatives such as carboxylic acids and other biomolecule compounds can be used in food and chemical

industries. It is also confirmed that the energy recovery from RH has a low release of CO₂ gas into the environment thus having a lesser impact than fossil fuels (Swaina et al. 2011).

Water Purification

Adsorption: Several biosorbents such as rice husk, corn, hemp, wheat straw, coffee and tea waste, fruit peel, seed hull and sawdust have been investigated for adsorbing the dyes and heavy metals present in water and wastewater. During the last decade, extensive research was explored and carried out in this area for removing organic and inorganic compounds such as chloro-phenols, other pharmaceutical and pesticide pollutants (Chuah et al. 2005, Gupta et al. 2006, Lata & Samadder 2014).

The pre-treatment of amorphous silica in developing it into highly reactive activated carbon with improved specific surface area is an important technique in the preparation of RH carbon. The effect of chemical treatment increased the surface properties of RHA and was reported by Alyosef et al. (2013), Salas et al. (2009). However, some limitations and setbacks were identified in the pre-treatment process observed from previous literature. The results for the work carried by Chen et al. (2018) showed non-interference of adsorption process due to the presence of potassium (K), calcium (Ca), magnesium (Mg) and manganese (Mn). About

Table 4: Calorific value of major agricultural residue/resource.

Agricultural residue	Heating or calorific value (MJ/kg)
Flax	17,800
Jute stick	17,800
Sugarcane bagasse	17,700
Corn stalks	16,800
Switchgrass	16,800
Hemp	16,500
Hay	16,200
Rice husk	16,000
Wheat straw	15,000
Rice straw	13,500

Table 5: Organic composition of rice husk.

Organic constituents	Composition in percentage
Hemicellulose	22.82 ± 1.50
Cellulose	33.32 ± 1.05
Lignin	20.32 ± 1.12
Ash	16.95 ± 1.90
Trace elements	3.25

70%-98% of these metal were further removed by leaching in suitable solvents such as water and acid. The adsorption capacity of 16.9 mg/g was observed on RH adsorbent in removing synthetic silk yarn. A positive value of H (160.97kJ/mol) showed endothermic adsorption (Sawasdee et al. 2017). Arsenic (As), one of the major groundwater contaminant had effective removal by column adsorption studies using RH adsorbent. Furthermore, intensive research in the development and applications of RH adsorbent is prevailing for the last three decades. Ahmaruzzaman & Vinod (2011) have reviewed the removal of pollutants on rice husk under favourable parametric conditions and their adsorption mechanisms.

Coagulant: A number of pure and complex form of silicon compounds like zeolite, silicon carbide, silicon chloride and nitride are extracted from 15% - 20% silica present in the RHA (Adylov et al. 2003, Matori et al. 2009). These extracted compounds are used in the purification of impurities with fine dispersion. These ligno-cellulosic derivative compounds contain active sites of tannins and lignin entrapping the heavy metal cations to form immobilized complexes or chelates through the ion exchange process. Table 5 represents the organic composition of RH.

Some of the agro and biomass wastes are by nature good in coagulation mechanism, which are derived from the various plant components such as seed, root, bark, leaves etc. These may be commercialized in future at a lower price for water purification technique. A cost-effective and environmentally friendly coagulant can be prepared and installed in a water purification system for removing suspended particles. Previous studies have shown effective removal efficiencies with proven results using plant-based coagulants.

A study was conducted to remove the turbid water using RHA derived from carbonization of RH. About 96% of turbidity was removed with high TDS (816 ppm) as observed by Adams et al. (2014) by using Rice hull ash as the coagulant. The coagulation mechanism and biological treatment process have shown higher removal of chemical oxygen demand (COD) of about 85% for various domestic and industrial effluents. Though effectiveness in the removal of organic matter was observed, excessive sludge generation, frequent pH variations, cost and skilled personnel were limiting these treatment techniques to be established at large scales (Mehta & Chavan 2009). Table 6 summarizes some of the recent treatment and process investigations in the removal of dyes, organic and inorganic constituents.

In India, a large part of the country has poor organic content in the soil. Sustainability and productivity are restored by appending the soil with the required and needed nutrients and conditioners. The efficiency of the plant growth and soil requirement is increased by the application of fertilizer produced from biomass and crop residues. The processed organic compost mixed soil strengthens the structure of the soil and void ratio, improves water holding

Table 6: Treatment methodology for water purification and removal efficiency.

Type of dye/metal ion	Purification technique	Modification/ Pre-treatment	Pollutant Removal Efficiency (%)	Reference
Strom water –Suspended Solids	Coagulation	RHA	93.34	Nnaji et al. (2017)
Basic Green 4	Adsorption	Con. Nitric acid pre-treatment	-	Guo et al. (2003)
Congo Red	Adsorption	Rice Husk	84	Han et al. (2008)
Phenols	Adsorption	ZnCl ₂ impregnation	80	Kalderis et al. (2008)
Acid Yellow 36	Adsorption	Steam activation	90	Malik (2003)
Methylene Blue	Adsorption	Rice husk	-	McKay (1986)
Cr (VI)	Electro-coagulation	Rice Husk	97	Ait Ouaiassa et al. (2013)
Zn(II)	Adsorption	Grounded	90	Roy et.al. (1993)
Cr(VI)	Adsorption	Acid impregnation/Carbonization	99	Srinivasan et al. (1988)
Pb	Adsorption	Tartaric acid impregnated	86	Wong et al. (2003)
Cu(II)	Column Adsorption	ZnCl ₂ impregnation	-	Yahaya et al. (2011)
As(V)	Column Adsorption	Rice Husk	90.7	Asif & Chen (2015)

Table 7: Rice husk composting and their physical and chemical properties.

Compost material	Compost period (days)	Physical Properties		Chemical Properties (%)						Plant yield (%)	Experimental Design	References
		pH	EC ds/m	OM %	N	P	K	C	C/N			
Rice Husk	90	7.66	1.16	9	0.55			21.14	38:1	7.77 (ton/da) (tomato)	Randomized plot	Zeynep & Coskun (2015)
RH + Enhydrobacter+ Aspergillus sp.	90	7.8	0.27	16	1.10	0.96	1.24	25.62	14:1	16 & 17 (black & red soil)	Pot Experiment	Thiyageshwari et al. (2017)
RH + Chicken bones	60	8.03	0.30	39	1.64	1.26	1.02	43.24	30:1	-	Complete Randomized plot & ANNOVA	Shareef et al. (2016)
RH	219	7.02	0.33	-	2.90	-	-	53.0	13:1	-	-	Leconte et al. (2009)

capacity and microbial activity. The compost-rich soil has high nutrients and can be used in natural and organic farming. The use of RH based compost processed through aerobic degradation increases the nutrient value of the unprocessed soil. The end products thus obtained can be used as a rich soil conditioner in small and large scale agro-farming for further substantial yield and productivity.

COMPOSTING

The sustainability of soil could be reached by adopting improved agricultural management and practices such as leguminous and cover crop plantation. This leads to the reduced application of fertilizers and pesticides, thereby enhancing carbon sequestration to restore the environment by preventing global warming. The improvement in soil quality and soil parameters are influenced by the organic and nutrient level of the soil (Cercioglu et al. 2014, Gulser & Candemir 2012). The biochemical and geological properties show good improvements in the addition of organic compost along with the soil. The abundance availability of rice husk is a major problem in the agricultural sector leading to environmental degradation. A suitable and sustainable approach in improving the agricultural land, thereby improving the soil and crop productivity is suggested in this study. By Applying 9% RHCA, Zeynep & Coskun (2015) could reach a tomato yield of 7.77 tons/da. Also, the usage of garbage compost resulted in an increased yield of about 43% in comparison with the application of chemical fertilizers. Researchers have reported that the addition of organic compost has improved the electric conductance of the soil (Candemir & Gulser 2011). Table 7 summarizes the application of various compost residues for plant growth and their effects on the physicochemical properties.

CONCLUSION AND FUTURE SCOPE

In most of the research work carried so far, RHA is utilised as the raw materials as an alternative source in various fields such as building construction, energy production, water purification etc. A very few attempts have been made in the disposal of RH as a natural component. One such way is the composting of RH yielding a higher C/N ratio to enrich the soil fertility. Studies have shown the higher organic matter in the end compost forms a strong stabilizing agent. The major elemental constituent of RH are K, Ca, Zn, Fe and Mn. Though the ionic leaching of the RH in natural dumping is studied, no specific effect in the degradation of contamination of the ground soil and water is discussed. Based on the review of various research papers, further study of this work will focus on the composting of the RH with a nitrogen-rich waste such as garden waste. The soil leaching studies during the composting are also to be studied.

REFERENCES

- Adams, F.V. and Mulaba-Bafubiandi, A.F. 2014. Application of rice hull ash for turbidity removal from water. *Physics and Chemistry of the Earth Parts A/B/C*, 72-75.
- Adylov, G., Faiziev, S.H., Paizullakhanon, M., Mukhsimov, S. and Nodirmatov, E. 2003. Silicon carbide materials obtained from rice husk. *Tech. Phys. Lett.*, 29(3): 221-223.
- Ahmaruzzaman, M. and Vinod, K. Gupta. 2011. Rice husk and its ash as low-cost adsorbents in water and wastewater treatment. *Ind. Eng. Chem. Res.*, 50: 13589-13613.
- Ait ouaissa, Y., Chabani, M., Amrane, A. and Bensmaili, A. 2013. Removal of Cr (VI) from model solutions by a combined electrocoagulation sorption process. *Chem. Engin. Tech.*, 36(1): 147-155.
- Alyosef, H.A., Eilert, A., Welscher, J., Ibrahim, S.S. and Denecke, R. 2013. Characterization of biogenic silica generated by thermo chemical treatment of rice husk. *Particulate Science and Technology*, 5: 524-532.
- Asif, Z. and Chen, Z. 2015. Removal of arsenic from drinking water using

- rice husk. *Appl. Water Sci.*, 7(3): 1449-1458.
- Candemir, F. and C. Gulser 2011. Effects of different agricultural wastes on some soil quality indexes in clay and loamy sand fields. *Communications in Soil Science and Plant Analysis*, 28-13 : (1)42.
- Cercioglu, M., Okur, B., Delibacak, S. and Ongun, A.R. 2014. Changes in physical conditions of a coarse textured soil by addition of organic wastes. *Eurasian Journal of Soil Science*, 3: 7-12.
- Chen, P., Gu, W., Fang, W., Ji, X. and Bie, R. 2017. Removal of metal impurities in rice husk and characterization of rice husk ash under simplified acid pretreatment process. *Environmental Progress & Sustainable Energy*, 36: 830-837.
- Chuah, T.G.A., Jumariah, I., Azni, S., Katayon, C.S.Y. and Thomas, C.S.Y. 2005. Rice husk as a potentially low-cost biosorbent for heavy metal and dye removal: An overview. *Desalination*, 175(3): 305-316.
- Dercon, S. and Christiaensen, I. 2011. Consumption risk, technology adoption, and poverty traps: evidence from Ethiopia. *J. Dev. Econ.*, 96: 159-173.
- Ghorbani, M. and Amirahmadi, E. 2018. Effect of rice husk biochar (RHB) on some of chemical properties of an acidic soil and the absorption of some nutrients. *J. Appl. Sci. Environ., Management*, 22(3): 313-317.
- Ghosh, R. and Bhattacharjee, S. 2013. A review study on precipitated silica and activated carbon from rice husk. *J. Chem. Eng. Process Technol.*, 4(4): 1-7.
- Godwin, A., Akeke, E., Maurice., Ephraim, I.Z.S., Akobo, O. and Joseph Ukpata 2013. Structural properties of rice husk ash concrete. *International Journal of Engineering*, 3(3): 57-62.
- Gulser, C. and Candemir, F. 2012. Changes in penetration resistance of a clay field with organic waste applications. *Eurasian Journal of Soil Science*, 1: 16-21.
- Guo, Y., Zhang, H., Tao, N., Liu, Y., Qi, J., Wang, Z. and Xu, H. 2003. Adsorption of malachite green and iodine on rice husk-based porous carbon. *Mater. Chem. Phys.*, 82: 107.
- Gupta, V. K., Mittal, A., Jain, R.M., Mathur, S. and Sikarwar 2006. Adsorption of safranin-t from wastewater using waste materials activated carbon and activated rice husks. *Journal of Colloid and Interface Science*, 303: 80-86.
- Han, R., Ding, D., Xu, Y., Zou, W., Wang, Y., Li, Y. and Zou, L. 2008. Use of rice husk for adsorption of congo red from aqueous solution in column mode. *Bioresour. Technol.*, 99: 2938.
- Junaidi, M.U.M., Ahmad, N.N.R., Leo, C.P. and Yee, H.M. 2016. Superhydrophobic coating synthesized from rice husk ash: anti-fouling evaluation. *Prog. Org. Coat.*, 99: 140-146.
- Kalderis, D., Koutoulakis, D., Paraskeva, P., Diamadopoulos, E., Otal, E., Olivares del valle, J. and Fer_nandez-pereira, C. 2008. Adsorption of polluting substances on activated carbons prepared from rice husk and sugarcane bagasse. *Chem. Eng. J.*, 144 (1): 42.
- Kaur, K., Singh, J. and Kaur, M. 2018. Compressive strength of rice husk ash based geopolymer: The effect of alkaline activator. *Construction and Building Materials*, 169: 188-192.
- Lata, S. and Samadder, R. 2014. Removal of heavy metals using rice husk: A review. *International Journal of Environmental Research and Development*, 4: 165-170.
- Lecante, M.C., Mazzarino, M.J., Satti, P., Iglesias, M.C. and Laos, F. 2009. Co-composting rice hulls and/or sawdust with poultry manure in ne Argentina. *Waste Management*, 29: 2446-2453.
- Lehmann, J., Czimczik, C., Laird, D. and Sohi, S. 2009. Stability of Biochar in the Soil. *Biochar for Environmental Management: Science and Technology*. London: Earthscan Publishing, pp. 183-205.
- Malik, P.K. 2003. Use of activated carbons prepared from sawdust and rice-husk for adsorption of acid dyes: a case study of acid yellow 36. *Dyes Pigments*, 56: 239.
- Matori, K.A., Haslinawati, M.M., Wahab, Z.A., Sidek, H.A.A., Ban, T.K. and Ghani, W.A.W.A.K. 2009. Producing amorphous white silica from rice husk. *J. Basic Appl.*, 1(3): 512.
- Mckay, G. 1986. Equilibrium studies for the adsorption of dyestuff from aqueous solutions by low-cost materials. *Water Air Soil Pollut.*, 29: 273.
- Mehta, P.K. and Pitt, N. 1976. Energy and industrial materials from crop residues. *Resource Recovery and Conservation*, 2: 23-38.
- Mehta, V. and Chavan, A. 2009. Physico-chemical treatment of tar-containing wastewater generated from biomass gasification plants. *World Academy of Science, Engineering and Technology*, 3(9): 9-29.
- Negassa, W., Gebrekidan, H. and Friesen, D.K. 2005. Integrated use of farmyard manure and np fertilizers for maize on farmers' fields. *J. Agric. Rural Dev. Tropics Subtropics*, 106(2): 131-141.
- Nehdi, M., Duquette, J. and Damatty el. 2003. Performance of rice husk ash produced using a new technology as a mineral admixture in concrete. *Cement Concr. Res.*, 33: 1203-1210.
- Nnaji, C.C., Mama, C.N., Ezekoye, D.A. and Iwuchukwu, I. 2017. Coagulation and clarification of wastewater using rice husk ash. *Desalination and Water Treatment*, 72: 266-273.
- Patil, N.B. and Sharanagouda, H. 2017. Rice husk and its applications: Review. *Int. J. Curr. Microbiol. App. Sci.*, 6(10): 1144-1156.
- Prasara, A. J. and Gheewala, S.H. 2017. Utilization of rice husk ash from power plants: A review. *Journal of Cleaner production*, 167: 1020-1028.
- Qin, L., Gao, X. and Chen, T. 2018. Recycling of raw rice husk to manufacture magnesium oxysulfate cement based lightweight building materials. *Journal of Cleaner Production*. 191: 220-232.
- Ramachandran, R., Kozhukhova, M., Sobolev, K. and Nosonovsky, M. 2016. Anti-icing superhydrophobic surfaces: controlling entropic molecular interactions to design novel icephobic concrete. *Entropy*, 18(4): 132-134.
- Raman, S.N., Ngo, T., Mendis, P. and Mahmud, P.N. 2011. High-strength rice husk ash concrete incorporating quarry dust as a partial substitute for sand. *Constr. Build. Mater.*, 25: 3123-3130.
- Roy, A.D., Greenlaw, P.N. and Shane, B.S. 1993. Adsorption of heavy metals by green algae and ground rice hulls. *J. Environ. Sci. Health., Part A*, 28: 37.
- Salas, S., Delvasto, R., Mejia de Gutierrez, D. and Lange 2009. Comparison of two processes for treating rice husk ash for use in high performance concrete. *Cement and Concrete Research*, 9: 773-778.
- Sawasdee, S., Jankerd, H. and Watcharabundit, P. 2017. Adsorption of dyes stuff in household-scale dyeing onto rice husk. *Energy Procedia.*, 138: 1159-1164.
- Shareef, R.S., Awang, Soh, Wahab, Z. and Rukunudin, I.H. 2016. Rapid composting of rice husks with chicken bones to produce compost rich with calcium and the effect of product compost in the increase of soil pH value. *Journal of Plant and Environmental Research*, 1(1): 24-30.
- Shwetha, M.K., Geethanjali, H.M. and Chowdary, K. 2014. A great opportunity in prospective management of rice husk. *International Journal of Commerce and Business Management*, 7(1): 176-180.
- Srinivasan, K., Balasubramanian, N. and Ramakrishnan, T.V. 1988. Studies on chromium removal by rice husk carbon. *Ind. J. Environ. Health*, 30: 376-387.
- Swaina, P.K., Dasa, L.M. and Naik, S.N. 2011. Biomass to liquid: a prospective challenge to research and development in 21st century. *Renew. Sustain. Energy Rev.*, 15: 4917-4933.
- Tewodros, F.D., Sjaastad, E. and Worku, T. 2007. Livelihood dependence on urban agriculture in addisababa, ethiopia. M.Sc. Dissertation. Norwegian University of Life Sciences.
- Thiyageshwari, S., Gayathri, P., Krishnamoorthy, R., Anandham, R. and Paul, D. 2018. Exploration of rice husk compost as an alternate organic

- manure to enhance the productivity of blackgram in Typic Haplustalf and Typic Rhodustalf. *International Journal of Environmental Research and Public Health*, 15(2): 358.
- Tittarelli, F. and Moriconi, G. 2011. Comparison between surface and bulk hydrophobic treatment against corrosion of galvanized reinforcing steel in concrete. *Cem. Concr. Res.*, 41: 609-614.
- Van Tuan, N., Ye, G., Van Breugel, K., Fraaij, A.L.A. and Bui, D.D. 2011b. The study of using rice husk ash to produce ultra high performance concrete. *Constr. Build. Mater.*, 25: 2030-2035.
- Van, V.T.A., Robler, C., Bui, D. and Ludwig, H.M. 2014. Rice husk ash as both pozzolanic admixture and internal curing agent in ultra-high performance concrete. *Cem. Concr. Compos.*, 53: 270-278.
- Vigneshwari, M., Arunachalam, K.A. and Angayarkanni 2018. Replacement of silica fume with thermally treated rice husk ash in reactive powder concrete. *Journal of Cleaner Production*, 188: 264-277.
- Wong, K. K., Lee, C.K., Low, K.S. and Haron, M.J. 2003. Removal of Cu and Pb by tartaric acid modified rice husk from aqueous solutions. *Chemosphere*, 50: 23.
- Yahaya, N.M.E.M., Abustan, I., Latiff, M.F.P.M., Bello, O.S. and Ahmad, M.A. 2011. Fixed-bed column study for Cu(II) removal from aqueous solutions using rice husk based activated carbon. *Int. J. Eng. Technol.*, 11(1): 248.
- Zareei, S.A., Ameri, F., Dorostkar, F. and Ahmadi, M. 2017. Rice husk ash as a partial replacement of cement in high strength concrete containing micro silica: evaluating durability and mechanical properties. *Case Studies in Construction Materials*, 7: 73- 81.
- Zeynep, D. and Gulser, C. 2015. Effects of rice husk compost application on soil quality parameters in greenhouse conditions. *Eurasian J. Soil Sci.*, 4(3): 185-190.



Pollution Assessment of Trace Elements in the Soil Planting Chinese Herbaceous Peony in Suzhou, China

L.H. Sun*† and S.B. Feng**

*School of Resources and Civil Engineering, Suzhou University, Anhui 234000, China

**Key Laboratory of Mine Water Resource Utilization of Anhui Higher Education Institute, Suzhou University, Anhui 234000, China

†Corresponding author: L.H. Sun; sunlinh@126.com

Nat. Env. & Poll. Tech.
Website: www.neptjournal.com

Received: 02-02-2020

Revised: 22-02-2020

Accepted: 02-05-2020

Key Words:

Pollution assessment
Trace elements
Farmland soil
Chinese herbaceous peony

ABSTRACT

Planting of the industrial crop is important for the rural revitalization in current China and the geological environment of soil is important for the development of the planting. In this study, twenty-eight surface soil samples in the farmland planting Chinese herbaceous peony in Suzhou have been collected and analysed for the concentrations of trace elements (As, Co, Cr, Cu, Ni, Pb and Zn along with Fe and Mn). The results indicate that iron is the most abundant element, followed by manganese, zinc, chromium, lead, nickel, copper, arsenic and cobalt. They have coefficients of variation ranged between 0.058 and 0.561, indicating that some of them might have multi-sources. The pollution indexes (including single pollution, geo-accumulation and the Nemerow composite indexes) indicate that the soil samples are no to slightly polluted. Multivariate statistical analyses (including correlation, cluster and factor analyses) have identified two sources (geogenic and agricultural related) responsible for the elemental concentrations in the soils.

INTRODUCTION

Rural revitalization strategy is one of the most important strategies in China (Lin 2020). It is an upgraded version of the new rural construction to avoid the decline of rural areas and agriculture in the process of urbanization (Ning 2019). Under this situation, the development of agriculture is becoming more and more important, because agriculture is not only the basic industry of China's national economy but also the cornerstone of the development of other industries.

As the most important aspect of agriculture, planting industry plays a decisive role in the development of modern agriculture, especially the characteristic planting industry, which refers to the special agricultural type with the characteristics of green and pollution-free, which makes full use of the unique advantageous agricultural resources in a certain region to develop and produce the planting products and processed products with high quality, high value and strong market competitiveness. And therefore, a large number of studies related to the spatial distribution, planting structure and market strategy et al. have been carried out (Liu & Gu 2011, Qiao & Wang 2012, Duan 2017).

Two factors are essential for the development of the characteristic planting industry, the product and the market. As to the product, the geological condition (including environment) is the most critical factor to determine whether

the characteristic crops can be planted. For example, the famous Chinese tea "Mount Huangshan Mao Feng" and famous pear "Dangshan pear" can only be produced in the city of Huangshan and Dangshan in the south and north Anhui province, China, respectively, that's because of the special geological environment (Fu et al. 2009, Wu et al. 2010). To be one of the most important aspects of the geological environment, the soil is the foundation of planting industry. It does not only determine what crops are suitable for planting, but also determine the quality of crops.

Suzhou is an important agriculture base located in the north Anhui province, China, and therefore, the soil environment is important for the development of agriculture in the area, and a large number of studies have been carried out, including the pollution assessment, source approximation and remediation et al. (Sun & Feng 2019, Sun 2020). In this study, a total of twenty-eight surface soil samples in the Chinese herbaceous peony plantation in Suzhou have been collected and the concentrations of nine kinds of elements have been measured, the goals of the study include: (1) getting the information about the pollution status and (2) identifying their sources. The study can provide scientific information for the planting of Chinese herbaceous peony because the root is the most important part to be used as a medicine, which is determined mostly by the quality of the soil.

MATERIALS AND METHODS

Study Area

Suzhou is the north gate of the Anhui province, China. It is located at the south of the Huang-Huai plain, with adjacent to Xuzhou of Jiangsu and Heze of Shandong in the north, Yongcheng of Henan in the west, Suqian of Jiangsu in the east (Fig. 1). The annual precipitation is 857 mm, with an average temperature of 14.4°C. Agriculture is the main industry of the area. Wheat, cotton, vegetable production and pig, cattle, sheep and fish farming are leading agricultural industries.

However, with the acceleration of agricultural and industrial modernization, the situation of agricultural environmental pollution in Suzhou is becoming more and more severe, especially the pollution of pesticides and fertilizers, manure of livestock and poultry, agricultural film and agricultural waste (Zhao 2013). Simultaneously, with the development of regional economy, some other kinds of pollutions have also influenced the geological environment, including the soil, water and air (Sun & Gui 2014, Sun & Feng 2019, Sun 2020).

Sampling and Analysis

Peony, one of the ten famous flowers of China, is also

known as the “Prime Minister of flowers” and the Mayflower God. It not only has a beautiful appearance but also has an extremely high edible and the medicinal value. Peony is the representative of modern characteristic planting industry in the area, which is mainly planted in the Haogou township in the northeast of Suzhou, which is 18 km to the urban area of Suzhou and 4 km to the East Railway Station of Suzhou, which is the main reason for its development of characteristic planting industry.

A total of twenty-eight surface soil samples in the farmland (< 10 cm depth) planting Chinese herbaceous peony have been collected in June 2019, and the detailed sample distributions are shown in Fig. 1. All of the soil samples have been first air-dried in room temperature, and then the debris (animals and plants) have been manually removed. After these procedures, all the samples were parched for 24h with 80°C in the dryer and then powdered to be smaller than 200 meshes (<0.075 mm). Finally, all the samples (powder) were compressed to be tablets under the pressure of 30 t.

The concentrations of nine elements (As, Co, Cr, Cu, Fe, Mn, Ni, Pb and Zn) were analysed by the X-ray fluorescence spectrometer (Innov-X Explorer 9000 SDD, USA) along with the National standard sediment sample of China

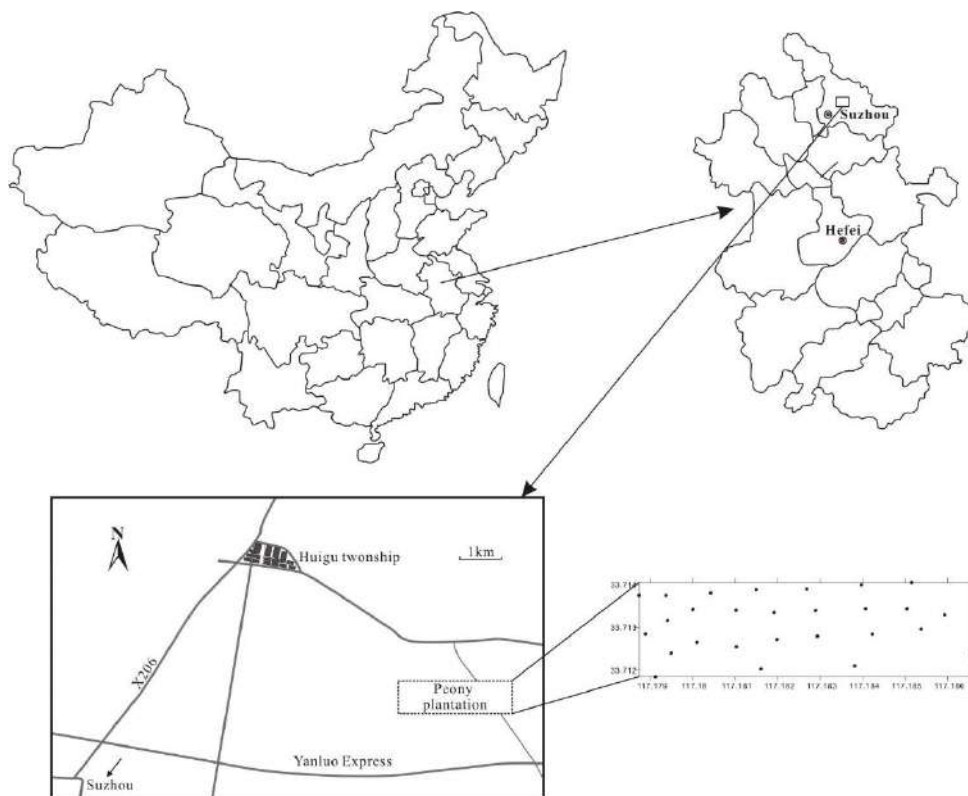


Fig. 1: Study area and sample locations.

(GSS-16) for calibration in the Key Laboratory of Mine Water Resource Utilization of Anhui Higher Education Institute, Suzhou University. Previous studies indicated that the portable XRF instrument gave excellent correlation with the laboratory-based reference AAS method (Radu and Diamond 2009). After the analyses, the concentrations of elements have been recalculated by $C_m = C_t \times (S_s/S_m)$. Where, C_m is the concentration of samples, C_t is the concentration of samples reported by the instrument, S_s and S_m are the standard and mean measured concentrations of the standard samples (GSS-16), respectively.

Data Treatment

All of the data were firstly processed for basic statistical analysis by the Mstat 12 software, and the minimum, maximum, mean, coefficient of variation and the p-value of the normal distribution test were obtained.

Then, a series of methods, including the single pollution index (P_i) (Liang et al. 2011), the geo-accumulation index (I_{geo}) (Praveena et al. 2008) and the Nemerow composite index (P_n) (Dai et al. 2008) were chosen for the quality evaluation of the samples.

Finally, some of the popularly used multivariate statistical methods in the environmental studies, including the correlation, cluster and factor analyses were applied in this study (through Mstat 12 software) for getting the qualitative information about the sources of elements.

RESULTS AND DISCUSSION

Elemental Concentrations

The analytical results of elemental concentrations are given in Table 1. It can be seen from the table that the elements in this study have the following decreasing order: Fe > Mn > Zn >

Cr > Pb > Ni > Cu > As > Co, and their mean concentrations are 36182, 707, 74.2, 67.3, 39.2, 33.5, 19.9, 12.9 and 12.7 mg/kg, respectively.

Previous studies revealed that the coefficient of variation (CV = standard deviation/mean) can be used for identifying the types of pollution distribution, high CV (> 0.90) and low CV (< 0.10) mean high and low extents of spatial variations, respectively, which indirectly suggest the high and low degrees of anthropogenic contributions, respectively (Sarkar 2011). In this study, the Co, Fe, Mn, Pb and Zn have low CVs (< 0.10), which means that the concentrations of these elements vary slightly from area to area indicating that they have relatively simple and homogeneous sources. Other elements have medium CVs (0.123-0.526), which indicate that they have moderate degrees of spatial variability indirectly suggesting the multi-source of them.

Moreover, the test of the normal distribution can also give information about the distribution of the elemental concentrations, because a normal distribution of the elemental concentration is always considered to represent a single source. In this study, most of the elements except for Mn and Ni have p-values > 0.05, indicating that they can pass the normal distribution test (p-value > 0.05), and suggesting that the elements except for Mn and Ni might have a single source.

Pollution Assessment

Single pollution index (P_i) has long been used for pollution assessment, which was defined by $P_i = C_m/C_s$. Where C_m and C_s are the concentration of sample and background, respectively. Previous studies revealed the pollution degrees can be classified to be three according to the threshold values of P_i : no pollution (<1), light pollution (1-2), moderate pollution (2-3) and significant (>3) (Liang et al. 2011).

Table 1: Descriptive statistics of elemental concentrations (mg/kg) in the soil samples.

Species	As	Co	Cr	Cu	Fe	Mn	Ni	Pb	Zn
N	28	28	28	28	28	28	28	28	28
Min	9.90	11.7	52.3	14.1	30888	587	7.40	33.9	62.4
Max	17.2	13.6	84.0	32.0	39278	815	79.1	43.6	88.1
Mean	12.9	12.7	67.3	19.9	36182	707	33.5	39.2	74.2
CV	0.138	0.034	0.123	0.215	0.058	0.098	0.526	0.064	0.080
p-value	> 0.15	> 0.15	> 0.15	0.146	> 0.15	< 0.01	< 0.01	> 0.15	> 0.15
Mean P_i	1.15	1.00	1.10	0.88	1.21	1.21	1.24	1.51	1.00
Highest P_i	1.53	1.07	1.38	1.42	1.32	1.40	2.94	1.68	1.19
Mean I_{geo}	-0.39	-0.59	-0.45	-0.80	-0.31	-0.31	-0.46	0	-0.59
Highest I_{geo}	0.03	-0.49	-0.12	-0.08	-0.19	-0.10	0.97	0.16	-0.34
Background	11.2	12.7	61	22.6	29800	583	26.9	26	74.2

In this study, the national soil environmental background values of China (A-layer, CEPA 1990) have been chosen to be the background, and the calculated results of P_i values are given in Table 1. As can be seen from the table, the soils samples have mean P_i values between 0.88 and 1.51, which indicates no (Cu) to light (other elements) pollution. However, as can be seen from the highest P_i values, four samples have P_i values of Ni higher than 2, which indicates moderate pollution.

Another index, the geo-accumulation index (I_{geo}) has also been applied for the pollution assessment. The calculation of I_{geo} is as $I_{geo} = \log_2[C_m/(1.5 \times C_s)]$. The classification of pollution degrees based on the I_{geo} values can be subdivided into five degrees: unpolluted (< 0), light (0-1), moderate (1-3), heavy (3-5) and serious (> 5) (Praveena et al. 2008). The mean I_{geo} values of the samples show “unpolluted” characters for all the elements ($I_{geo} < 0$), whereas some of the elements (As, Ni and Pb) have the highest I_{geo} values between 0 and 1, implying that they have light pollution for some of the locations.

Different with the P_i and the I_{geo} , another index, the Nemerow composite index (P_n) considers all the elements rather than the single ones, the calculation of the P_n is as $P_n = \text{SQRT}[(P_i m^2 + P_i x^2)/2]$. Where $P_i m$ and $P_i x$ are mean and maximum of P_i values of the elements, respectively. Based on the P_n values, the quality of soil can also be classified to be of five grades: safety (< 0.7), precaution (0.7-1.0), slightly polluted (1-2), moderately polluted (2-3) and seriously polluted (> 3) (Dai et al. 2008). In this study, the calculated P_n values for all the samples ranged from 1.20 to 2.31 (mean = 1.44), most of the samples (26) have $1.0 \leq P_n < 2.0$, which means that most of the soil samples in this study can be classified to be slightly polluted.

Sources of Elements

Because some of the elements with good correlation are always considered to have similar sources, the relationships

between elements can give information about their sources (Cobelo-garcía & Prego 2004). In this study, some of the elements show close positive relationships (correlation coefficients higher than the critical value $r_a = 0.374$, $\alpha = 0.05$, $n = 28$): e.g. As-Ni, Co-Fe, Co-Mn, Fe-Mn-Zn-Pb, Ni-Zn, Co-Cu, Co-Zn and Cu-Ni (Table 2). Such results suggest that their concentrations change simultaneously, and indicating that they might have been affected by similar factors, or have similar sources.

Cluster analysis has also long been used for environmental studies, especially the R-mode cluster analysis, has long been used for finding out the good relationships between elements, which might be an indication of the similar source of them (Chen et al. 1997, Chen et al. 2005). In this study, the hierarchical R-mode cluster analysis has been applied to the data, and the “Ward” linkage and the “Pearson” distance have been chosen for calculation, and the results are shown in Fig. 2 as a dendrogram. As can be seen from the figure, two main groups can be identified: As-Co-Cr-Cu-Ni (Group 1) and Fe-Mn-Zn-Pb (Group 2), which indicate that the elements in the similar group have similar sources.

Factor analysis is a commonly used statistical method to classify, simplify and identify the most important variables in data sets through dimensionality reduction. During environmental studies, factor analysis has long been used for tracing elemental sources (Lin et al. 2002). In this study, based on the criteria of the initial eigenvalue (> 1 , Kaiser criterion) (Maiz et al. 2000), two factors were obtained with total variance explanation of 64.7% (Table 3), the first one with strong positive loadings (> 0.75) of Fe, Mn and Zn and moderate positive loadings (0.50-0.75) of Co and Pb, has 41.6% of the total variance explanation. The second factor is characterized by strong positive loadings of Ni, and moderate positive loadings of As and Cu and it has 23.1% of the total variance explanation. Moreover, Cr has positive loading in factor 2. Such a result is similar to the results obtained by correlation and cluster analyses that two sources might be responsible for the elemental concentrations, Fe-Mn-Zn-

Table 2: Results of the correlation analysis.

	As	Co	Cr	Cu	Fe	Mn	Ni	Pb
Co	0.191							
Cr	0.193	-0.313						
Cu	0.081	0.430*	0.283					
Fe	-0.014	0.487**	-0.393	0.126				
Mn	-0.068	0.536**	-0.445	0.173	0.941**			
Ni	0.480*	0.342	0.026	0.459*	0.363	0.363		
Pb	-0.177	0.327	-0.408	-0.017	0.495**	0.615**	0.035	
Zn	-0.106	0.402*	-0.250	0.284	0.763**	0.783**	0.496**	0.520**

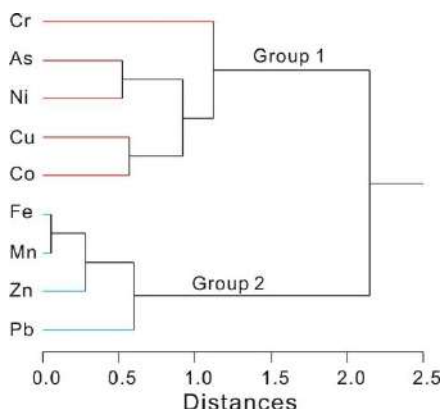


Fig. 2: Result of R-mode cluster analysis.

Pb and As-Cr-Cu-Ni are mainly contributed by the factor (source) 1 and 2, respectively. As to the Co, both sources are responsible.

Previous studies revealed that four sources are responsible for the heavy metals (including arsenic) in the farmland soil, including the natural/geogenic processes (weathering of soil parental materials), the dust fall (mainly related to the coal combustion and traffic), agriculture (related to the application of fertilizers and pesticides, and sewage irrigation) and mining activities (Huamain et al. 1999, Wang 2019). In consideration with the natural condition of the study area, two main sources can be considered to be responsible for the soil elements in this study: the geogenic source related to the formation of the soil (weathering) and the agricultural activities (application of fertilizers and pesticides). Although Suzhou is a coal producing area, the coal combustion and coal-related industry (coal chemical industry and coal electricity) are limited, and the sampling site is far away from the coal power plant and high density of traffic way, and therefore, the contribution of coal and traffic-related pollution to the soil in this study may be limited.

Based on this consideration, factor 1 can be explained to be the geogenic source, because the most abundant element Fe and Mn has the highest positive loadings in this factor relative to the factor 2. Although some other sources can affect the Fe concentration in the soil, it is hard to exceed the background value (29400 mg/kg) except for the existence of iron ore. Previous studies revealed that the application of superphosphate can increase the concentration of As in the soil (Wang et al. 2010), whereas the long-term use of pesticides can increase the Cu and Ni concentration in the soil (Wang 2019). Moreover, Cr can be released by the weathering of agricultural film. Therefore, the second factor can be explained to be the

Table 3: Results of factor analysis.

Factor	F1	F2
As	-0.180	0.644
Co	0.579	0.425
Cr	-0.609	0.405
Cu	0.112	0.722
Fe	0.890	0.159
Mn	0.943	0.135
Ni	0.297	0.803
Pb	0.742	-0.206
Zn	0.819	0.265
Eigen value	3.741	2.082
Variance explained	41.6%	23.1%

agricultural source because As, Cr, Cu and Ni have high positive loadings.

CONCLUSIONS

The following conclusions have been obtained:

- (1) The elemental concentrations are $Fe > Mn > Zn > Cr > Pb > Ni > Cu > As > Co$. They have low-medium coefficients of variation (0.058-0.526) and most of them have p-values of normal distribution test > 0.05 .
- (2) The single pollution, geo-accumulation and the Nemerow composite indexes suggest that the soils in this study are no-to-slightly polluted.
- (3) Statistical analyses indicate that the two sources are responsible for the soil elemental concentrations, the geogenic and agricultural.

ACKNOWLEDGEMENTS

This work was financially supported by the Natural Science Research Project of Universities in Anhui Province (KJ2020ZD64; KJ2020A0740) and the Scientific Foundation of Platform in Suzhou University (2016ykyf02).

REFERENCES

- CEPA (Chinese Environmental Protection Administration) 1990. Elemental Background Values of Soils in China. Environmental Science Press of China, Beijing.
- Chen, T.B., Wong, J.W.C., Zhou, H.Y. and Wong, M.H. 1997. Assessment of trace metal distribution and contamination in surface soils of Hong Kong. *Environmental Pollution*, 96(1): 61-68.
- Chen, T.B., Zheng, Y.M., Lei, M., Huang, Z.C., Wu, H.T., Chen, H., Fan, K.K., Yu, K., Wu, X. and Tian, Q.Z. 2005. Assessment of heavy metal pollution in surface soils of urban parks in Beijing, China. *Chemosphere*, 60(4): 542-551.
- Cobelo-García, A. and Prego, R. 2004. Influence of point sources on trace metal contamination and distribution in a semi-enclosed industrial

- embayment: the Ferrol Ria (NW Spain). *Estuarine, Coastal and Shelf Science*, 60(4): 695-703.
- Dai, J., Li, S., Zhang, Y., Wang, R. and Yu, Y. 2008. Distributions, sources and risk assessment of polycyclic aromatic hydrocarbons (PAHs) in topsoil at Ji'nan city, China. *Environmental Monitoring and Assessment*, 147(1-3): 317-326.
- Duan, Y.L. 2017. Development current situation and measures of plateau characteristic planting industry in Gannan Zhou. *Journal of Animal Science and Veterinary Medicine*, 36(1): 56-57+61.
- Fu, J.M., Shi, Z.G., Sun, L.H., Zhang, Y., Su, H.M. and Fang, G. 2009. Investigation and analysis on soil organic matter in Dangshan County of Anhui Province. *Journal of Anhui Agriculture Science*, 37(28): 13745-13746.
- Huamain, C., Chunrong, Z., Cong, T. U. and Yongguan, Z. 1999. Heavy metal pollution in soils in China: status and countermeasures. *Ambio*, 28(2): 130-134.
- Huang, Y., Li, T., Wu, C., He, Z., Japenga, J., Deng, M. and Yang, X. 2015. An integrated approach to assess heavy metal source apportionment in peri-urban agricultural soils. *Journal of Hazardous Materials*, 299: 540-549.
- Liang, J., Chen, C., Song, X., Han, Y. and Liang, Z. 2011. Assessment of heavy metal pollution in soil and plants from Dunhua sewage irrigation area. *International Journal of Electrochemical Science*, 6(11): 5314-5324.
- Lin, E.X. 2020. The effective way to break through the rural revitalization strategy. *Journal of Harbin University*, 41(1): 43-46.
- Lin, Y.P., Teng, T.P. and Chang, T.K. 2002. Multivariate analysis of soil heavy metal pollution and landscape pattern in Changhua county in Taiwan. *Landscape and Urban Planning*, 62(1): 19-35.
- Liu, F.Y. and Gu, C.Y. 2011. Current status, problems and development tactics of unique planting industry for Beijing Mentougou District. *Beijing Agriculture*, 6: 13-14+16.
- Maiz, I., Arambarri, I., Garcia, R. and Millan, E. 2000. Evaluation of heavy metal availability in polluted soils by two sequential extraction procedures using factor analysis. *Environmental pollution*, 110(1): 3-9.
- Ning, X. 2019. Pan-agriculture: agricultural transformation in the Rural Vitalization. *Journal of China Agricultural University (Social Sciences)*, 36(6): 5-12.
- Praveena, S.M., Ahmed, A., Radojevic, M., Abdullah, M.H. and Aris, A.Z. 2008. Heavy metals in mangrove surface sediment of Mengkabong lagoon, Sabah: multivariate and geo-accumulation index approaches. *International Journal of Environmental Research*, 2(2): 139-148.
- Qiao, J.J. and Wang, H.F. 2012. Spatial-temporal variation of village-level economy development based on characteristic planting in less developed regions-A case study of Shilipu Village in Henan Province. *Human Geography*, 2: 82-86
- Radu, T. and Diamond, D. 2009. Comparison of soil pollution concentrations determined using AAS and portable XRF techniques. *Journal of Hazardous Materials*, 171(1-3): 1168-1171.
- Sarkar, D., Datta, R. and Hannigan, R. 2011. *Concepts and Applications in Environmental Geochemistry (Vol. 5)*. Elsevier.
- Sun, L.H. 2020. Pollution assessment and source approximation of trace elements in the farmland soil near the trafficway. *Journal of Environmental Engineering and Landscape Management*, 28(1): 20-27.
- Sun, L.H. and Feng, S.B. 2019. Heavy metals in the surface soil around a coalmine: Pollution assessment and source identification. *Polish Journal of Environmental Studies*, 28(4): 2717-2724.
- Sun, L.H. and Gui, H.R. 2014. Source identification of heavy metals in river sediments by using factor analysis in combination with k-means cluster analysis. *Nature Environment and Pollution Technology*, 13(1): 73-77.
- Wang, G.L., Li, L.K., Hao, M.D. and Zhang, M. 2010. Effects of long-term fertilization on heavy-metal contents of soil and environmental quality evaluation. *Journal of Soil and Water Conservation*, 24(3): 60-63.
- Wang, N. 2019. Study and analysis of sources of heavy metal pollution in farmland soil. *China Metal Bulletin*, 1: 289-290.
- Wu, Y.D., Xiang, F. and Zhao, J.H. 2010. Approach to relationship between Huangshan tea quality and geological background of growing areas. *Resources Survey & Environment*, 31(1): 39-49.
- Zhao, Z.H. 2013. Reduction and control for agriculture pollution in Suzhou City of Anhui Province. *Environmental Protection and Technology*, 19(5): 47-48.



Contribution of Low-carbon Transport Policy to the Improvement of Urban Traffic Ecological Environment

Mingwei Li and Huijuan Zhao

College of Tourism, Xinyang Normal University, Xinyang, Henan, 464000, China

†Corresponding author: Mingwei Li; limingwei_happy@163.com

Nat. Env. & Poll. Tech.
Website: www.neptjournal.com

Received: 12-09-2020

Revised: 27-10-2020

Accepted: 07-12-2020

Key Words:

Low-carbon transport
Ecological environment
Urban traffic
Urbanization

ABSTRACT

With the acceleration of urbanization and motorization speed boost, the development of urban green traffic has become a focus of public concern and an important way to solve urban traffic problems, which has made the low-carbon transport policy been given more attention. However, since the urban traffic is affected by multiple factors, whether the application of low-carbon transport policy could obtain corresponding or higher output is uncertain. To clarify the effects of low-carbon transport to the improvement of urban traffic ecological environment, the main indicators that measure the contribution of low-carbon transport to urban traffic ecological environment were extracted from five aspects including people, cars, roads, transportation infrastructure and traffic environment. The Guangzhou city in China was taken as an example to select index data, the regression analysis was adopted by SPSS software. Results show that the contribution rate of the low-carbon transport policy to the improvement of urban transportation ecological environment is 4.42%. The conclusions obtained from this study are of great significance to improve the low-carbon travel policy and optimize the urban traffic ecological environment

INTRODUCTION

Transportation energy and emission reduction policy is a set of governmental regulation means to cope with global climate change and to alleviate the pressure of transportation energy consumption under the background of the low-carbon economy. Low-carbon transport first appeared in official documents in the UK in May 2007, the United Kingdom initially put forward the “Low-Carbon Transport Innovation Strategy”, and it also released “Low Carbon Transport: A Greener Future” in July 2009. Besides, in work arrangements to deal with climate change, China has made it clear that to speed up the construction of industrial construction and transportation systems characterized by low carbon emissions.

Currently, there is no clear and agreed definition for low-carbon transport. This study defines low-carbon transport in two aspects. Firstly, we focus on the characteristics of low-carbon. It is a kind of transportation development mode characterized by low energy consumption, low emission, and low pollution, which devotes itself to improve the energy efficiency and energy structure of transportation and slow down the carbon emission of transportation. The aim is to make the transportation system gradually get rid of the excessive dependence on fossil energy, realize the low-carbon transformation development. Secondly, focusing on transport demand satisfaction, low-carbon transport is a new

industrial form that cannot only meet the normal needs of economic and social development but also reduce the carbon intensity of transport volume. That is to say, low-carbon transport is a new industrial development mode with the lowest carbon intensity (or the highest carbon productivity) and the maximum utility achieved. Low-carbon transport is a development revolution. Its basic connotation is embodied in the characteristics of “three low” and “three high”. They are low consumption, low emission, low pollution, high energy efficiency, high efficiency, and high benefit. Besides, the transportation energy conservation and emission reduction policies are also for “three low, three high”. To standardize and guide the low-carbon transport development through government means.

By December 2019, China’s car ownership per capita has reached the global average (11 cars per 65 people, 0.17 cars per capita) from the current “70 cars per 1,000 people” (0.07 cars per capita). With the rapid increase of per capita car ownership, related issues such as vehicle energy conservation and emission reduction have become the focus of the government (Jiang et al. 2008). During the 13th Five-Year Plan period, the Chinese government launched the “urban public transport” demonstration project, which aims to ensure that the mode of public transport travel could be improved continuously with the strong support of local governments. It is expected that the share rate of public transport in cities

with rail transit will reach more than 60% by the end of the 13th Five-Year Plan period. Besides, an efficient public transport network will be formed to reduce the pressure and emissions of the urban transport operation, and continue to move closer to the direction of building low-carbon transport (Liu 2012, Li 2017). However, as one of the important means of transportation for urban development, private cars cannot be restricted by blindly developing public transport to ensure the normal development of the city. Therefore, based on the low-carbon transport policy, this study excavates its main factors in promoting the development of urban traffic ecological environment, clarifies its role in the whole process and promotes the development of urban traffic ecological environment are the current situation needs to solve.

This study evaluates the contribution value of low-carbon transport policy to the development of urban traffic ecological environment, which does not only help to clarify the relationship and the main indicators. It can also put forward strategies and suggestions for the development of urban traffic ecological environment according to the research results of the contribution rate and promote healthy and sustainable development strategies for urban traffic.

PAST WORK

In terms of the researches collected in this study, relative researches have been obtained on low carbon travel and transportation ecological environment. For example, developed countries in Europe and the United States have studied low-carbon transport for nearly 50 years. In this process, with the city scale, motor vehicle intelligence, and other factors, scholars have also put forward different research strategies in this field. Jess (1999) believed that zero emissions and less land cover are in line with the basic principles of urban low-carbon transport development. In addition, some scholars believe that transportation infrastructure and road planning have a greater impact on public transportation, and some cities in Europe and American are selected as the research objects to carry on the demonstration analysis. The results show there is not only a mutual interaction between travel time and price also affects the choice of travel mode and travel comfort, which will result in a low rate of ecological travel (Ryuichi 2009).

Scheiner (2010) used various mathematical models to evaluate the development of low-carbon transport in cities of different countries. The results show that the development of low-carbon transport has a certain impact on the traffic ecological environment. However, their findings are only qualitative results and there is no in-depth analysis of the specific impact from the quantitative point of view. Geenhuizen et al. (2003), Kahn (2006), Svensson et al. (2010) concluded that

low-carbon transport is the first choice for the development of ecological traffic. However, they put forward that it does not meet the requirements of traffic network development just based on the infrastructure construction, while the deep integration of sustainable transportation policy is imperative when developing the ecological traffic. Du et al. (2006), Jiang et al. (2008), Li et al. (2015) established different evaluation systems for the development of low-carbon transport from the perspective of sustainable development to discuss the relationship between sustainable development of urban traffic and ecological traffic. Yu et al. (2008) proposed that there is a competitive relationship between public transport and private transport by using operational research and econometric models to study the effects of low-carbon travel on the development of ecological traffic. It is considered that the effect of low-carbon transport on the traffic ecological environment is relatively perfect when the competitive relationship reaches a dynamic equilibrium state. Zeng et al. (2007) chose the Logit model to study the public transport problem, but more researches are to predict the development trend of public transport and the possible problems, while the impact of public transport on the development of ecological transport is less involved. Sun (2010) studied low-carbon transport based on the analysis of affecting factors and indicators by combining the mathematics and operational research methods research. Then the empirical analysis was carried out by collecting the data of the indicators and the countermeasures were put forward. According to the literature review, the relationship between low-carbon transport and transportation ecological environment has become the main attention of society and academia and has achieved certain results. However, the early discussions on the urban traffic-operating environment were limited to the problems faced by traffic development, such as traffic congestion, traffic safety, and so on. Afterwards, the related problems about the development of urban ecological traffic were studied with the increasingly serious traffic environment problems. Moreover, the existing results have separated the low-carbon travel and the ecological traffic, which cannot analyze the low-carbon travel and ecological traffic as related completely effectively. Therefore, the research on the interaction between the two needs to be strengthened, and the quantitative research from the perspective of contribution rate needs to be further deepened.

MATERIALS AND METHODS

Construction of the Index System

It can be seen that scholars have done some researches on the indicators of urban ecological traffic development and a partial index system has formed from the results of the

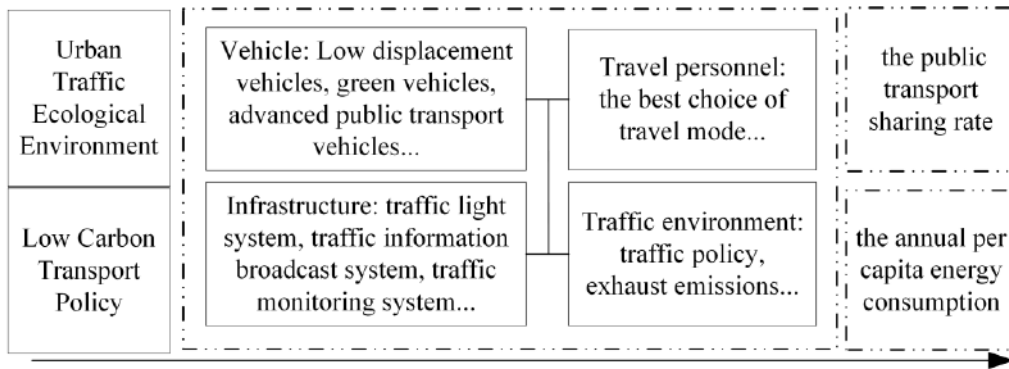


Fig. 1: Extraction path of the indexes.

literature analysis. Based on referring to the existing research results, considering the development of urban ecological traffic and the ecological environment requirements of low-carbon transport policies, we analysed and extracted indicators that can measure the ecological environment of urban traffic from five aspects. They are the travel personnel, vehicles, roads, transport infrastructure, and traffic operation environment. According to the index system, combined with the requirements and characteristics of low-carbon transport policies, the indicators were screened. Finally, it was considered that the public transport sharing rate and annual per capita energy consumption could be used to measure the ecological environment of transportation (Zhou et al. 2011). The specific index extraction path is shown in Fig. 1.

Index Interpretation

It was found that the index data cannot be directly collected, nor can the indicators be directly processed by the model when we processing the indexes. Instead, the influencing factors of each indicator should be extracted through certain procedures. The final influencing factors of the indicators should be determined through data collection, data processing and other operations on the influencing factors. Because the factors that affect the development of ecological traffic

are related to each other, there will be a phenomenon of cross-influencing factors when analysing the influencing factors of each index. Therefore, when extracting the influencing factors of the index, we should start from five aspects of travel personnel, vehicles, roads, and infrastructure and traffic environment reference to the extracting method of the ecological traffic development indicators.

Public transport sharing rate: The public transport-sharing rate refers to the proportion of public transportation (including conventional public transport, rapid public transport and rail transit, excluding taxis, buses, school buses) in the total travel volume of urban residents who choose public transport in their travel modes. This index is an important factor to promote the development of public transport and the rational structure of urban traffic. Besides, it is also one of the core indicators of urban ecological traffic evaluation. The Ministry of Construction and the Ministry of Public Security of China have stipulated in the “Green Traffic Model City Assessment Standard (2003)” that the public transport-sharing rate should not be less than 20% in large cities and 15% in medium cities. Furthermore, the International Association of Public Transport has put forward the standards for public transport sharing rate in the year 2001 (Pekka et al. 2002) as given in Table 1.

Table 1: International standard of the public transport sharing rate.

City	Public transport sharing rate (%)	City	Public transport sharing rate (%)	City	Public transport sharing rate (%)
Amsterdam	66.1	Copenhagen	51.1	Medellin	95
Barcelona	53.1	Glatz	53.6	Munich	59.4
Berlin	60.8	Helsinki	56	Paris	53.6
Berne	59.7	Hong Kong	83.8	Rio de Janeiro	85
Bogota	85	Lima	84	Salvador	86
Budapest	66.9	Lisbon	52	Vienna	64
Curitiba	71	Moscow	73.7	Warsaw	71.4

It found that travel personnel, vehicles, roads and traffic environment mainly affect the public transport-sharing rate according to the definition and evaluation criteria. In terms of the impact of travel personnel, the number of people who choose public transport determines the public transport-sharing rate to a certain extent immediately. The larger the proportion of public transport travel, the greater the sharing rate of public transport will be. However, to improve the number of people who choose public transport, it is necessary to provide enough public transport to meet the travel needs of travellers, which is a challenge to the local government. At the same time, there must be special roads and lanes for public transport to ensure safety, comfort and convenience. Only in this way can more people choose public transport to travel. In terms of traffic environmental impact, the impact on public transport sharing rate is mainly reflected in relevant policies, such as the low-carbon transport policy. For example, the restriction policy implemented by the traffic management department, the policy that external vehicles are not allowed entering the inner ring of the city for a limited period. Based on the above analysis, this study puts forward the calculation formula of public transport sharing rate.

$$f_1 = \frac{n_1}{N_1} \quad \dots(1)$$

In formula (1), f_1 represents the public transport sharing rate, n_1 represents the travel volume of public transport travel (unit: 10,000 person-times), and N_1 represents the total urban travel volume (unit: 10,000 person-times).

Annual per capita energy consumption: The transportation industry has always been regarded as one of the important fields of social carbon emissions and energy consumption. How to reduce the energy consumption and carbon

emissions of the transportation industry is being explored all over the world. In the past decade, China has made more breakthroughs and progress in the field of traffic energy conservation and emission reduction. For example, a large number of laws, plans, standards and norms related to energy conservation and emission reduction have been issued, providing important guidance for the development of energy conservation and emission reduction. A large number of energy conservation and emission reduction technologies and products have been popularized and applied, which effectively improves the production efficiency and service level of transportation, enhances the technical foundation and support capacity of transport energy conservation and emission reduction, and saves a lot of energy. Among them, the calculation formula of urban traffic energy consumption constraint is as follows.

$$C_{Energy} = \sum_{j=1}^n (e_j \times X_j) \text{ (MJ)}. \quad \dots(2)$$

Where, C_{Energy} is the urban energy consumption of urban energy transportation, e_j is the energy consumption factor of the j transportation mode, and X_j is the passenger turnover of the j transportation mode. Table 2 gives the values under different transportation modes.

According to the relevant research results and the above analysis, the calculation method of annual per capita travel energy consumption is as follows.

$$F_1 = \frac{m_1}{M_1} \quad \dots(3)$$

In formula (3), F_1 represents the annual per capita energy consumption, m_1 represents the total transportation energy consumption (unit: 10,000 tons of coal) and M_1 represents

Table 2: Energy consumption factors of different transportation modes.

Transportation modes	Private car	Bus	Taxi	Rail transit	Bicycle	On foot
e_j (MJ/per-km)	2.3	0.3	2.4	0.1	0	0

Table 3: The summary table of index influencing factors.

Index	Influencing factors
Public transport sharing rate	Public vehicle ownership per 10,000 Average daily passengers of public transport Per capita GDP Per capita road area Total urban travel: (total urban population multiply per capita daily travel times) Passenger volume of public transport Number of public transport vehicles
Annual per capita energy consumption	Total number of motor vehicles in the city Number of civil motor vehicles in the city Total fuel consumption for passenger transport Total social passenger volume Per capita GDP Per capita road mileage

the total urban travel (unit: 10,000 person-times).

According to formula (3), under the condition that the total amount of urban travel remains unchanged, the more fuel consumed by passenger vehicles, the worse the effect of ecological traffic development, and vice versa. Therefore, the index is mainly controlled by the total fuel consumption and population turnover, while the number of motor vehicles, road conditions and motor vehicle emissions affects the total fuel consumption and the population turnover is the total number of people turnover per unit time.

To sum up, the influencing factors of these two indicators are summarized as follows, as shown in Table 3.

Function expression of the index: Before analysing the functional relationship between the traffic ecological environment index and its influencing factors, the functional relationship of the index to measure the traffic ecological environment is first analysed. The functional relationship between ecological traffic and its indicators is as follows.

$$Y_G = F\{f_1(x_{11}, x_{12}), f_2(x_{21}, x_{22}, x_{23}), f_3(x_{31}, x_{32}, x_{33}), f_4(x_{41}, x_{42}, x_{43}), f_5(x_{51}, x_{52})\} \dots(4)$$

Where, Y_G represents the traffic ecological environment index, f_1, f_2, f_3, f_4, f_5 respectively represents the five aspects of the impact factors: travel personnel, vehicles, roads, infrastructure and traffic environment.

x_{11} represents the environmental awareness travel personnel, x_{12} represents the travel structure of travel personnel.

x_{21} represents the amount of vehicle ownership, x_{22} represents the vehicle emissions, x_{23} represents the vehicle institutions.

x_{31} represents the road network structure, x_{32} represents the per capita road area, x_{33} represents the public transport dedicated lane.

x_{41} represents the rationality of the traffic lights, x_{42} represents the rationality of the traffic signs, x_{43} represents the rationality of the public transport stations.

x_{51} represents the natural environment, x_{52} represents the relevant policies.

In analysing the functional relationship between each index and its influencing factors, the specific method is similar to the above. In this case, it is necessary to regard each index as a dependent variable and the corresponding influencing factor as an independent variable. The specific formula is as follows.

$$Y_{G1} = F_1(y_{11}, y_{12}, y_{13}, y_{14}) \dots(5)$$

Among them, Y_{G1} represents the index of the public transport-sharing rate, y_{11} represents the public vehicle ownership

per 10,000 people, y_{12} represents the average daily passenger number of public transport, y_{13} represents the per capita GDP, y_{14} represents the road area per capita.

$$Y_{G2} = F_2(y_{21}, y_{22}, y_{23}, y_{24}, y_{25}) \dots(6)$$

Where Y_{G2} represents the annual per capita energy consumption, y_{21} represents the total number of motor vehicles, y_{22} represents the number of other motor vehicles (vehicle ownership per capita), y_{23} represents the total energy consumption of passenger transport, y_{24} represents the total number of urban passenger transport, y_{25} represents the per capita GDP.

The quantitative function is reflected in the influencing process of the traffic ecological environment. When analysing the influence of a certain factor on the index, other factors must be assumed unchanged. Only in this way can be calculated the impact of a single factor on the analysis index accurately. Regression analysis can be used to find and reduce the correlation between the various influencing factors, to maintain the direct and independent effects of the influencing factors on ecological traffic.

Data Source

This study takes Guangzhou city in China as an example to collect data and analyze the contribution of the low-carbon transport policy to ecological traffic development. The reason for choosing Guangzhou is that: first, Guangzhou is in the critical period of the rapid development of urbanization and motorization. How to improve the traffic environment in Guangzhou has become a hot issue for the government and citizens. Second, the application of low-carbon transport policy in Guangzhou is in the leading position in China, and it has made certain achievements. With the rapid development of modernization, urbanization, and motorization, it has become an inevitable choice to solve the urban traffic problems in Guangzhou.

The data are collected from the year 2000 to 2015 of the *Guangzhou Economic and Social Development Statistics Bulletin*, the *Statistical Yearbook of Guangzhou*, and the *Guangzhou Transportation Yearbook*.

RESULTS ANALYSIS

Contribution of the Public Transport-Sharing Rate

The SPSS 22.0 software is used to analyze the data of influencing factors of public transport sharing rate. We chose the public vehicle ownership per 10,000 people, average daily passengers of public transport, the per capita GDP, per capita road area, total urban travel, passenger volume of public transport and umber of public transport vehicle as independent variables, and the public transport-sharing rate

Table 4: Models.

Model	R	R ²	Modified R ²	Error in standard estimates
1	0.961	0.924	0.915	0.013096
2	0.999	0.998	0.997	0.002475

as dependent variables. Then the multiple linear regression analysis was carried out (Table 4).

The regression equation is better according to the value of R, R² and modified R². For regression analysis, the input variables are the average daily passengers of public transport and the per capita GDP. Other variables are removed and the results are shown in Table 5.

By analysing the input variables, the final coefficient table is shown in Table 5, where the Sig = 0, which indicates that the obtained coefficients meet the regression requirements, then the following equation can be obtained.

$$Y_{G1} = 0.037 + 0.061y_{12} - 0.007y_{13} \quad \dots(7)$$

In calculating the contribution rate of Guangzhou's low-carbon transport policy to urban traffic ecological environment, the data from 2000-2014 are mainly collected. Because in 2014, the Guangzhou Energy Research Institute of the Chinese Academy of Sciences led the organization of Guangzhou Traffic Planning Research Institute, Guangzhou Institute of Architectural Sciences Co. Ltd., Guangzhou carbon emission rights exchange jointly launched the Guangzhou National low carbon pilot Project (Wang et al. 2018). That is, this study put forward that the low carbon transportation policy of Guangzhou has been implemented since 2014, so it is considered that the data before 2014 are not affected by the low carbon transportation policy. Therefore, taking the data from 2000 to 2014 as an example to do regression analysis, and the public transport-sharing rate in 2015 is estimated according to the regression equation.

Table 5: Coefficient.

Model		Non-standardized coefficient		Standardized coefficient	t	Sig.
		B	Standard error			
1	constant	0.071	0.027		2.646	0.027
	average daily passengers of public transport	0.048	0.005	0.961	10.448	0.000
2	constant	0.037	0.006		6.739	0.000
	average daily passengers of public transport	0.061	0.001	1.215	51.064	0.000
	per capita GDP	-0.007	0.000	-0.371	-15.617	0.000

Table 6: The model.

Model	R	R ₂	Modified R ²	Error in standard estimates
1	0.839	0.704	0.672	0.001210

While the public transport-sharing rate in 2015 can be known in the actual statistics yearbook of Guangzhou, then the actual value is subtracted from the predicted value, and the obtained value can be considered as the contribution of low-carbon transport policy. It should be noted that in calculating the contribution of low-carbon transport policies, the impact of other policy factors is not taken into account, but these policy factors are default to the impact of low-carbon transport policies. Finally, the contribution of low-carbon transport policy to the public transport-sharing rate is obtained as follows.

$$Y_{G1(2015 \text{ predicted value})} = 0.037 + 0.061y_{12} - 0.007y_{13} \\ = 0.037 + 0.061 * 6.927 - 0.007 * 9.957 = 0.392$$

$$Y_{G1(2015 \text{ actual value})} = 0.0387$$

The contribution value is that

$$E_1 = (Y_{G1(2015 \text{ predicted value})} - Y_{G1(2015 \text{ actual value})}) / Y_{G1(2015 \text{ actual value})} \\ = (0.392 - 0.387) / 0.387 \\ = 1.3\%$$

Contribution of the Annual Per Capita Energy Consumption

SPSS 22.0 software is used to analyze the data of influencing factors of public transport sharing rate. We chose the total number of motor vehicles in the city, the number of civil motor vehicles in the city, total fuel consumption for passenger transport, total social passenger volume, per capita GDP and per capita road mileage as dependent variables, and the annual per capita energy consumption as dependent variables. Then the multiple linear regression analysis was carried out (Table 6).

The regression equation is better according to the value of R, R² and modified R². For regression analysis, the input variable is the number of civil motor vehicles in the city.

Table 7: Coefficient.

Model		Non-standardized coefficient		Standardized coefficient	t	Sig.
		B	Standard error			
1	constant	0.034	0.004		7.230	0.000
	number of civil motor vehicles in the city	-0.086	0.019	-0.839	-4.631	0.001

Other variables are removed as shown in Table 7.

Then the following regression equation can be obtained.

$$Y_{G2} = 0.034 - 0.086y_{22} \quad \dots(8)$$

Finally, the contribution of low-carbon transport policy to the annual per capita energy consumption obtained as follows.

$$E_2 = (Y_{G2(2015 \text{ predicted value})} - Y_{G2(2015 \text{ actual value})}) / Y_{G2(2015 \text{ actual value})}$$

$$= (0.00949 - 0.009) / 0.009$$

$$= 5.4\%$$

The contribution value is that

$$E_2 = (Y_{G2(2015 \text{ predicted value})} - Y_{G2(2015 \text{ actual value})}) / Y_{G2(2015 \text{ actual value})}$$

$$= (0.00949 - 0.009) / 0.009$$

$$= 5.4\%$$

Wang et al. (2018) pointed out that the implementation strategy of urban traffic carbon emission reduction is focused on three aspects: avoidance, transfer and improvement. The avoidance strategy refers to avoiding unnecessary traffic demand from the source through reasonable urban spatial form and diversified land use. It mainly includes reducing travel times, shortening travel distance and so on, thus reducing traffic carbon emissions. The transfer strategy refers to the adjustment of traffic structure and the conversion of passengers who rely partly on private motorized transportation to green travel mode, including public transport, bicycle and walking traffic. The improvement strategy is aimed at the improvement of vehicle energy efficiency, which is essentially the research and application of low-carbon vehicles. The research results show that the transfer of urban public transport travel mode has the greatest emission reduction potential. Guangzhou is in the rapid construction stage of rail transit; the public transport service level will be greatly improved. Therefore, the main carbon reduction potential at this stage mainly comes from the mode transfer. While the carbon reduction effects of the traffic demand reduction strategy brought by urban planning are relatively lagging. According to statistics, the reduction in carbon emissions by public transport share in Guangzhou is accounted for 24 percent and the capita energy consumption occupied 76 percent. Therefore, when calculating the contribution of low-carbon policy to the development of

urban ecological traffic, this study calculates the contribution rate mainly adopts the following formula.

$$E = 0.24Y_{G1} + 0.76Y_{G2} = 0.24 * 1.3\% + 0.76 * 5.4\% = 4.42\%$$

That is, the contribution rate of low-carbon policy to the development of ecological traffic in Guangzhou is 4.42%.

CONCLUSIONS

The effects of low-carbon transport to the improvement of urban traffic ecological environment were explored in this study, the conclusions are as follows: the contribution rate of the low-carbon transport policy in Guangzhou of China to the improvement of urban transportation ecological environment is 4.42%. Low-carbon policy plays a great role in alleviating the improvement of urban traffic ecological environment. It can promote the priority development of public transport, optimize the travel structure and improve the green travel rate, slow down traffic congestion and reduce the driving time and distance of vehicles. Although low-carbon policies can improve the ecological environment of urban traffic, the urban traffic environment is becoming worse and worse with the increasing number of motor vehicles in major cities. While more practical actions should be carried out than the effects of low-carbon policy to improve the ecological level of urban traffic operation services.

ACKNOWLEDGMENT

This study was supported by the Humanity and Social Science Youth Foundation of the Ministry of Education of China (No. 19YJCZH082), the Science and Technology Project of Henan Province (No. 212400410259), and the Nanhu Scholars Program for Young Scholars of XYNU (No. 2017B).

REFERENCES

Du, S.P., Xiong, L. and Ding, W. D. 2006. Comprehensive evaluation of urban rail transit network planning based on green transportation principle. *Journal of Southwest Jiaotong University*, 41(3): 284-289.

Geenhuizen, M.V., Geerlings, H. and Priemus, H. 2003. Transport innovation: coping with the future. *Transportation Planning & Technology*, 26(6): 437-447.

Jesse, H. Ausubel. 1999. Reasons to worry about the human environment. *Technology in Society*, 13: 230-254.

Jiang, Y.H., He, X.Z. and Guo, X.C. 2008. Discussion on the evaluation

- index system of urban green traffic planning. *Journal of Hefei University of Technology (Nature Science)*, 31(9): 1399-1402.
- Kahn, M.E. 2006. The Environmental Impact of Suburbanization. *Journal of Policy Analysis and Management*, 19: 569-586.
- Li, M.W. 2017. Research on the Mode and Suggestion of "Internet+ Transportation" Fusion Development. *Journal of Xinyang Normal University (Philosophy and Social Sciences Edition)*, 37(1): 61-65.
- Liu, H.D. 2012. Public transportation share ratio forecasting based on box-cox dogit model. *Journal of transport information and safety*, 30(1): 47-51.
- Pekka, L.K. and Jukka, L. 2002. Profitability evaluation of intelligent transport system investments. *Journal of Transportation Engineering*, 128(3): 276-286.
- Ryuichi, K.A. 2009. Dynamic model system of household car ownership, trip generation, and modal split: model development and simulation experiment. *Transportation*, 36(6): 711-732.
- Scheiner, J. 2010. Social inequalities in travel behavior: trip distances in the context of residential self-selection and lifestyles. *Journal of Transport Geography*, 18(6): 679-690.
- Sun, X.Q. 2010. The coordinated development of urban traffic and integrated transport hub. *Science & Technology Information*, (11): 105-115.
- Svensson, M. and Johansson, M. V. 2010. Willingness to pay for private and public road safety in stated preference studies: Why the difference. *Accident Analysis & Prevention*, 42(4): 1205-1212.
- Wang, B. and Zhang, H.X. 2018. Development strategies of low carbon transportation in Guangzhou. *Urban Transport of China*, 16(4): 74-80.
- Yu, L.J. and Heydecker, B. 2008. Statistical distribution estimation method for traffic flow using probability weighted moments and maximum entropy principle. *Journal of Highway and Transportation Research and Development*, 2(25): 113-116.
- Zeng, X. and Wang, C.G. 2007. Improvement of logit model and its application in forecasting the distribution rations of passenger flows on Cheng-Yu intercity railroad. *Journal of Changsha Communications University*, 4(23): 50-53.
- Zhou, X.M. and Di, D. 2011. Urban passenger transportation terminal location based on bus-sharing ratio. *Journal of Tongji University (Natural Science)*, 39(9): 1313-1317.



The Toxic Effect of Fluoride and Arsenic on Behaviour and Morphology of Catfish (*Clarias batrachus*)

G. Sahu*† and V. Kumar**

*School of Life Sciences, Pt Ravishankar Shukla University, Raipur, 492010, India

**Department of Chemical Engineering, National Institute of Technology, Raipur, 492010, India

†Corresponding author: Gamini Sahu; gaminisahu@gmail.com

Nat. Env. & Poll. Tech.

Website: www.neptjournal.com

Received: 20-08-2020

Revised: 09-10-2020

Accepted: 15-10-2020

Key Words:

Clarias batrachus

Toxicity

Fluoride

Arsenic

ABSTRACT

In the present study, an attempt has been made to analyze the toxicity of fluoride and arsenic on morphology and behaviour of fish *Clarias batrachus*. Based on 96 hour LC₅₀ values at the 95% confidence limits of sodium fluoride (NaF) and arsenic trioxide (As₂O₃) obtained from the preliminary tests, various sub-lethal concentrations of NaF and As₂O₃ were selected for combined toxicity testing. During the experiment, fish were regularly observed for any changes in their external morphology and behaviour. Behavioural changes were observed in terms of air gulping, opercular movement, swimming activity, body position, general activity and food sensitivity. Control fish remained normal throughout the experiment period (96 hour) but erratic, exodus and speedy movements were found in all treated groups. The number of air gulps (per 15 min, 24-96 hour) significantly increased ($P < 0.001$) in the exposed Group I (20 mg.L⁻¹ As₂O₃) as compared to control. A significant increase ($P < 0.01$) in the number of opercular movements (per min for 24-96 hour) was recorded in treatment groups as compared to control. Apparent changes such as excessive mucous secretion, increased body discolouration, loosening of skin and complete loss of skin (head region and fins) were also observed. Skin loss was more intense in fish subjected to Group I.

INTRODUCTION

Although in the present global scenario, humans enjoy a longer and healthier life, nevertheless, rapid industrialization has initiated adverse health effects not only on workforces but also on the common masses (Yassi & Kjellstrom 1998). As a result, day after day, a large population in the world is under threat of exposure to a variety of toxic chemicals due to heavy contamination of its various ecological systems with various metals, non-metals and other organic and inorganic compounds. One of the biggest contributors to global water crisis (Bibi et al. 2015, Kumar et al. 2020), arsenic and fluoride are such chemicals that are prone to be toxicants and have various deleterious effects on organisms if taken beyond the permissible limit.

Fluorides are naturally released into the environment through the weathering and dissolution of minerals. Besides, various anthropogenic activities are also responsible for fluoride release into the atmosphere. In endemic areas, the most prominent effects in humans are dental, skeletal and non-skeletal fluorosis (Pujara & Pujara 2003). Arsenic is released into the environment naturally through volcanic action and low temperature volatilization. Industrial processes, such as mining, smelting of non-ferrous metals

and burning of fossil fuels contribute to anthropogenic arsenic contamination of air, water and soil (WHO 2001). Very high concentrations of arsenic have been detected in Mexico, Hungary, Chile, Argentina, USA, China, India, Bangladesh, Vietnam, Pakistan etc. (Patel et al. 2005, Jadhav et al. 2015). In India, arsenic occurrences in groundwater of Bengal Delta Plain (i.e. India and Bangladesh) are one of the largest environmental health disasters of the present century. Long term exposure to arsenic leads to adverse multisystem health effects.

Natural and industrial activities contribute to the entry of pollutants into aquatic ecosystems. Contaminated water induces significant changes in structural, physiological and biochemical processes of inhabiting fauna such as fishes (Sivakumar et al. 2014). Behavioural characteristics are sensitive indicators of toxic effects. Since behavioural states are correlated with brain neurotransmitter level and enzyme function, hence behavioural changes induced by toxicant may result in neurological dysfunction. The fluoride acts as an enzyme inhibitor, alters enzymatic activities, interrupting important metabolic processes (glycolysis, protein synthesis etc.) and affects nervous system during fluoride intoxication (Camargo 2003), resulting in negative changes in behaviour, reduced growth and decreased survival of the affected animal

(Alonso & Camargo 2009, Aguirre-Sierra et al. 2013). Lethal concentration causes serious acute intoxication in fish before death. Symptoms of fluorosis in fishes, such as increased fluoride level in the blood, lethargy, apathetic behaviour, anorexia, mucus secretion, violent swimming, equilibrium loss, skin darkening, mucus secretion, decreased respiratory rate and finally, death by complete muscular contraction or paralysis have been observed (Camargo 2003, Sahu et al. 2016). Alteration in behaviour pattern induced by sodium fluoride was observed in freshwater fish *Puntius sophore* (Narwaria & Saksena 2012) and marked changes in body position, habit, food sensitivity, swimming pattern and opercular movement were noted. In white-clawed Crayfish *Austropotamobius pallipes*, fluoride increased mortality, but escape response and feeding activity decreased with increasing water fluoride concentration and exposure time (Aguirre-Sierra et al. 2013).

Cholinesterase (ChE) is the most commonly observed indicator of neurological dysfunctions which is inhibited by many pollutants. Study of Tyler & Allan (2014), have shown reduced acetylcholinesterase (AChE) and choline acetyltransferase (ChAT) activity after arsenic exposure. In another study, female rats exposed to 20 mg kg⁻¹ body weight arsenic for 28 days showed a significant decrease in binding of 3HQNB to the muscarinic-cholinergic receptor of the hippocampus and frontal cortex. In this brain region, AChE activity reduced after arsenic exposure (Yadav et al. 2011). In freshwater climbing perch, *Anabas testudineus* (Bloch), exposure of sodium arsenite and mercuric chloride impaired behaviour characteristics, such as rapid opercular movement, erratic swimming, exodus trial and loss of equilibrium etc. (Akter et al. 2008). Bhavani & Karuppasamy (2014) reported the changes in behaviour parameters as an increase in opercular movement, erratic swimming, equilibrium loss, body dyspigmentation and mucus secretion all over the body of the Zebrafish (*Danio rerio*) exposed to arsenic trioxide for 96 hours. Aggression increased significantly with arsenic, while the operculum movement decreased nonsignificantly in mosquitofish, *Gambusia holbrooki*. Presence of algae further aggravates the arsenic effect rather than ameliorating (Magellan et al. 2014). Therefore, in the present study, an attempt has been made to analyze the toxicity of fluoride and arsenic on morphology and behaviour of catfish (*Clarias batrachus*).

MATERIALS AND METHODS

Live and healthy fishes (length: 20-25 cm, weight: 80-100 g) were procured from nearby fish hatcheries located in Raipur and Rajnandgaon districts of Chhattisgarh, India. The selected fishes were checked & ensured against injury, infection and disease. During 15 days of acclimatization

and experimentation period, fishes were fed with Taiyo fish food at *ad libitum*. Water was periodically changed every 24 hours to maintain a healthy environment for the fish during acclimation periods. Fishes were maintained at natural photoperiod at ambient temperature. Arsenic trioxide (reagent plus) was purchased from Sigma Aldrich Co., USA, while sodium fluoride (extra pure) was purchased from Hi-media Laboratory Pvt. Ltd., Mumbai for assessment of their toxicity towards model fish at the sub-lethal level.

Based on 96 hours LC₅₀ values and at the 95% confidence limits of sodium fluoride (NaF) and arsenic trioxide (As₂O₃), obtained from the preliminary tests, various sub-lethal concentrations viz., Group I (20 mg.L⁻¹ As), Group II (300 mg.L⁻¹ F), Group III (100 mg.L⁻¹ F+10 mg.L⁻¹ As) and Group IV (300 mg.L⁻¹ F+20 mg.L⁻¹ As) of sodium fluoride and arsenic trioxide were selected for individual and combined toxicity testing. The control group (Group V) was kept in an aquarium having tap water without the addition of sodium fluoride and arsenic trioxide. Each group stocked 05 fishes per aquarium with 40 L of water.

Behavioural Studies

During the experiment days, fish were regularly observed for any changes in their external morphology and behaviour. Observations were made on behavioural aspects, such as air gulping, operculum and swimming movements, general activity and equilibrium, and feeding activity. Opercular movements were noted for per minute and air gulps for 15 min. Morphological changes in fish, viz. skin colour and pigmentation in response to toxicants were also noted.

Statistical analysis was performed by statistical software. One way ANOVA was done in SPSS software (Trial version 16.0).

RESULTS AND DISCUSSION

Behavioural changes in terms of air gulping, opercular movement, swimming activity, body position, general activity and food sensitivity are depicted in Table 1 (A). The number of air gulps (per 15 min, 24-96 hour) significantly increased ($P < 0.001$) from 4.67 ± 0.88 in the control group to 23.67 ± 2.03 in the exposed Group I (20 mg.L⁻¹ As). Significant increase ($P < 0.01$) in the number of opercular movements (per min for 24-96 hour) was recorded in treatment groups as compared to control. The recorded values ranged from 11.67 ± 0.32 in the control group to 43.67 ± 2.03 in Group I (20 mg.L⁻¹ As) exposed group.

During 96 hour experiment period, treated fishes were very active and restless as compared to control fishes which appeared to be very quiet and relaxed and swam in a

Table 1(A): Behavioural response of *Clarias batrachus* in various concentrations of arsenic trioxide and sodium fluoride for a period up to 96 hours.

Parameters	Groups with different concentrations of fluoride and arsenic				
	Group I	Group II	Group III	Group IV	Group V
Air gulping (per 15 min)	14.33 ± 1.48 ^b	13.00 ± 1.15 ^a	7.67 ± 1.20 ^a	13.67 ± 1.45 ^a	4.67 ± 0.88 ^b
Opercular movement (per min)	43.67 ± 2.03 ^b	40.33 ± 1.53 ^a	37.67 ± 2.52 ^a	41.33 ± 1.73 ^a	31.67 ± 0.32 ^c
Swimming movement (24-96 h)	ES, Ex	ES	ES	ES, Ex	U
Body position (24-96 h)	H	H, SV	SV	H, SV	B
Equilibrium (24-96 h)	EL	EL	EL	EL	N
Food sensitivity (24-96 h)	VL	L	L	L	N

Mean ± SE (n = 3); (Group I- 20 mg.L⁻¹ As; Group II- 300 mg.L⁻¹ F; Group III- 10 mg.L⁻¹ As + 100 mg.L⁻¹ F; Group IV- 20 mg.L⁻¹ As + 300 mg.L⁻¹ F; Group V- Control). U uniform, ES erratic and speedy movements, Ex Exodus trials, H hanging mostly, N normal, EL equilibrium lost, VL very low, L low, B at the bottom, SV swimming vertically near the upper surface of the water.

horizontal pattern. Control fish remained normal throughout the experiment period (96 hour) but erratic and speedy movements were found in all treated groups. The test fishes at the concentration of Group I (20 mg.L⁻¹ As) and Group IV (20 mg.L⁻¹ As+300 mg.L⁻¹ F) showed exodus movements and sometimes they tried to hit the wall, jump above the water and move out of the tank. This shows the avoidance behaviour of fishes to the toxicants. Swimming activity of experimental fishes was found to be erratic and speedy. Fish move rapidly with gradual loss of equilibrium, while control fish normally swam horizontally and spent most of the time at the bottom. The fish exposed to arsenic were erratic, speedy with exodus movement, hanging vertically with mouth pointed towards the surface and have a slow response to food. A phenomenon known as *nudge and nip* has been observed; which involves following and biting other fish. This is a kind of aggressive response.

Morphological Manifestations

Morphological deformities due to arsenic trioxide and sodium fluoride are shown in Fig. 1(A), (B), (C), (D) and (E). Apparent changes were observed in the external morphology of the fish when exposed to arsenic trioxide and sodium fluoride, but control fish remained normal and healthy throughout the experimental period. Excessive mucous secretion, increased body discolouration, loosening of skin and complete loss of skin from the head region and fins were also observed. Skin loss was more intense in fish subjected to Group I (20 mg.L⁻¹ As). Also, haemorrhages in internal organs and skin including lower lip were seen in exposed fish. Some black spots were also seen in exposed fish.

Alterations in behaviour, such as loss of equilibrium, erratic swimming, hanging, restlessness, and decreased food consumption, increased rate of air gulping and rapid opercular movements observed in the present study depict beyond doubt, a stressful environment due to the presence of toxicants. Mucous formed in ample amounts, forms

a layer over the exposed surface of fish thus acting as a barrier to the entry of toxic substances. However, increased mucous secretion also reduces respiratory surface and area for gaseous exchange thereby leading to suffocation of fish which consequently, meets its oxygen demand by increasing air gulping. Arsenic trioxide is generally known to stimulate the peripheral nervous system as a result of increasing energy demand and oxygen utilization. In the same way, opercular movement of fish is increased following the exposure to arsenic and fluoride. Similar behaviour effects of other toxicants have been also seen in previous studies reported by various authors (Bhavani & Karuppasamy 2014, Kaur & Dua 2014, Aziz et al. 2015, Sangve 2020). Behavioural effects including erratic swimming, loss of equilibrium and low sensitivity to food, similar to reports by Sahu et al. (2017), Bhavani & Karuppasamy (2014), were also observed. Erratic swimming and loss of equilibrium observed in the present study may be due to impairment of the nervous system that is responsible for vital activities. In the present study, fish exhibited aggressive response, such as following and attacking other fish, besides, showing speedy movement, hyperactivity, hitting the wall and jumping out from the water, which signifies avoidance reaction in response to the toxicants. These activities may be due to the inactivation of acetylcholinesterase, an enzyme critical for the metabolism of acetylcholine. Arsenic and fluoride are reported to decrease the activity of acetylcholinesterase in rats (Tolins et al. 2014, Bharti & Srivashtava 2011). Free radical production is the potential mechanism of action of fluoride and arsenic-induced neurotoxicity (Shanmugam et al. 2018, Akter et al. 2017). Arsenic induces oxidative stress through overproduction of reactive oxygen species, which leads to improper brain development and associated behaviours (Sau et al. 2020, Flora et al. 2012). However, fluoride can inhibit the activity of free radical scavenging or antioxidant enzymes (Shanmugam et al. 2018).

Food consumption is the most sensitive end point because

(A) Group I (20 mg.L⁻¹ As)(B) Group II (300 mg.L⁻¹ F)(C) Group III (10 mg.L⁻¹ As + 100 mg.L⁻¹ F)(D) Group IV (20 mg.L⁻¹ As + 300 mg.L⁻¹ F)

(E) Group V (Control)

Fig. 1: Morphological deformities.

negative changes in behaviour increase the rate of mortality in affected fish and other animals (Anguirre-Sierra et al. 2013). Similar findings were reported by Yallappa & Nuzhat (2017), after exposing *Austropotamobius pallipes* to fluoride; their mean daily food consumption was decreased with increasing water fluoride concentration and exposing *Cyprinus carpio* to cadmium chloride and found that food consumption was affected and reduced over time. In some extent decrease in food uptake under toxicant stress environment is beneficial to lower the energy cost of digestion.

Morphological deformities were shown in the form of dullness in body colour, loosening of skin and complete loss of skin in head and fin. Similar observations were reported in previous studies on fish morphology (Devi & Mishra 2013, Anita et al. 2010). Aziz et al. (2015) reported darkening of skin and increased mucus secretion, gasping for breath,

inability to swim after 14 days of sodium fluoride exposure and finally death after long term exposure. Haemorrhage in internal organs and lower lip was observed in exposed fish. Similar damage was reported in *Channa punctatus* due to zinc and municipal wastewater toxicity and in *Labio rohita* and *Cirrhinus mrigala* exposed to tannery industry effluent and dyeing industry effluent respectively (Walia et al. 2013, Kaur et al. 2013). Morphological changes in fish were more intense in the arsenic treated group as compared to fluoride treated group, since heavy metals like arsenic, especially bind with keratin rich tissues (skin, hair and nails) and get deposited in skin tissues.

CONCLUSION

Behavioural and morphological alteration in *Clarias batrachus* under the influence of fluoride and arsenic can

be used as a sensitive biological marker to monitor aquatic contamination. From the present study, it becomes clear that arsenic and fluoride create a stressful environment by influencing the nervous system and by reducing the activity of some enzymes (AChE, ChAT). Even at very low concentration of arsenic trioxide seemed to be comparatively more effective in causing behavioural alteration and stress than sodium fluoride. From the result of the present investigation, we can say that the behavioural effect act as a 'first-line indicator' for evaluation of toxicity. Furthermore, research is needed in this field to better understand the mechanism of arsenic and fluoride combined toxicity.

REFERENCES

- Aguirre-Sierra, A., Bacchetti-De Gregoris, T., Berná, T., Salas, J.J., Aragón, C. and Esteve-Núñez, A. 2016. Microbial electrochemical systems outperform fixed-bed biofilters in cleaning up urban wastewater. *Enviro. Sci. Water Res. Technol.*, 2: 984-993.
- Aktar, S., Jahan, M., Alam, S., Mohanto, N.C., Arefin, A., Rahman, A., Haque, A., Himeno, S., Hossain, K. and Saud, Z.A. 2017. Individual and combined effects of arsenic and lead on behavioral and biochemical changes in mice. *Biol. Trace Elem. Res.*, 177: 288-296.
- Alonso, A. and Camargo, J.A. 2009. Long-term effects of ammonia on the behavioral activity of the aquatic snail *Potamopyrgus antipodarum* (Hydrobiidae, Mollusa). *Arch. Environ. Contam. Toxicol.*, 56: 796-802.
- Anita, T.S., Shobha, K. and Tilak, K.S. 2010. A study on acute toxicity, oxygen consumption and behavioural changes in the three major Carp, *Lebio rohita*, *Catla catla* (ham) *Cirrhinus mrigala* (ham.) exposed to fenvalerate. *Biores. Bull.*, 1: 33-40.
- Aziz, F., Azmat, R. and Jabeen, F. 2015. Fluoride Toxicity on behavioral and morphological variations in freshwater fish *Notopterus notopterus* (Pallas). *Int. J. Adv. Res.*, 3: 1223-1227.
- Bharti, V.K. and Srivastava, R.S. 2011. Effect of pineal proteins at different dose level on fluoride-induced changes in plasma biochemicals and blood antioxidants enzymes in rats. *Biol. Trace Elem. Res.*, 141: 1-3.
- Bhavani, K. and Karuppasamy, R. 2014. acute toxicity bioassay and behavioural changes on zebra fish, *Danio rerio* (Hamilton) under arsenic trioxide. *Int. J. Mod. Res Rev.*, 2: 40-46.
- Bibi, S., Farooqi, A., Hussain, K. and Haider, N. 2015. Evaluation of industrial based adsorbents for simultaneous removal of arsenic and fluoride from drinking water. *J. Cleaner Prod.*, 87: 882-896.
- Camargo, J.A. 2003. Fluoride toxicity to aquatic organisms: A review. *Chemosphere*, 50: 251-264.
- Devi, Y. and Mishra, A. 2013. Study of behavioural and morphological anomalies of fry fish of freshwater teleost, *Channa punctatus* under chlorpyrifos intoxication. *Int. J. Pharma. Bio. Sci.*, 4: 865-874.
- Flora, S.J.S., Mittal, M., Pachauri, V. and Dwivedi, N. 2012. A possible mechanism for combined arsenic and fluoride induced cellular and DNA damage in mice. *Metallomics*, 4: 78-90.
- Jadhav, S.V., Bringas, E., Yadav, G.D., Rathod, V.K., Ortiz, I. and Marathe, K.V. 2015. Arsenic and fluoride contaminated groundwaters: A review of current technologies for contaminants removal. *J. Environ. Manage.*, 162: 306-325.
- Kaur, R. and Dua, A. 2014. 96 h LC₅₀, behavioural alterations and histopathological effects due to wastewater toxicity in a freshwater fish *Channa punctatus*. *Environ. Sci. Pollut. Res.*, 22: 5100-5110.
- Kumar, V., Pandey, N., Dharmadhikari, S. and Ghosh, P. 2020. Degradation of mixed dye via heterogeneous Fenton process: Studies of calcination, toxicity evaluation, and kinetics. *Water Environ. Res.*, 92: 211-221.
- Magellan, K., Barral-Fraga, L., Rovira, M., Srean, P., Urrea, G., García-Berthou, E. and Guasch, H. 2014. Behavioural and physical effects of arsenic exposure in fish are aggravated by aquatic algae. *Aquatic toxicology*, 156: 116-124.
- Narwaria, Y.S. and Saksena, D.N. 2012. Acute toxicity bioassay and behavioural responses induced by sodium fluoride in freshwater fish *Puntius saphore* (Bloch). *Fluoride*, 45(1): 7-12.
- Patel, K.S., Shrivastava, K., Brandt, R., Jakubowski, N., Corns, W. and Hoffmann, P. 2005. Arsenic contamination in water, soil, sediment and rice of central India. *Environ. Geochem. Health.*, 27: 131-145.
- Pujara, N. and Pujara, P. 2003. Fluoride toxicity- A systematic review. *Int. J. Sci. and Res.*, 4: 2319-7064.
- Sahu G. and Poddar A. N. 2016. Effect of sodium fluoride on total protein and albumin globulin ratio of *Clarias batrachus* (Linn.) 1758. *J. Ravishankar Uni.*, 29 (2&3): 11-16.
- Sahu, S., Pervez, S. and Poddar, A. N. 2017. Combined toxicity and bioconcentration of fluoride and arsenic in African catfish *Clarias gariepinus* (Burchell, 1822). *Int. J. Environ. Agri. Biotechnol.*, 2: 967-976.
- Sangve, K.B. 2020. Behavioural study of freshwater fishes *Rasbora daniconius* and *Puntius saphore* exposed to sodium fluoride. *Int. Res. J. Sci. Eng.*, 8: 59-64.
- Sau, S., Sathua, K. B. and Flora, S.J.S. 2020. MiADMSA minimizes arsenic induced bone degeneration in Sprague Dawley rats. *Emerg. Contam.*, 6: 204-211.
- Shanmugam, T., Abdulla, S., Yakulasamy, V., Selvaraj, M. and Mathan, R. 2018. Mechanism underlying the neurotoxicity induced by sodium fluoride and its reversal by epigallocatechin gallate in the rat hippocampus: Involvement of NrF2/Keap-1 signaling pathway. *JoBAZ*, 79: 17.
- Sivakumar, P., Kanagappan, M., Manohar, S. and Das, S. 2014. Toxicity evaluation and behavioural responses of *Danio rerio* exposed to raw tannery effluent. *J. Eentomol. Zool. Stud.*, 2: 288-291.
- Tolins, M., Ruchirawat, M. and Landrigan, P. 2014. The developmental neurotoxicity of arsenic: Cognitive and behavioral consequences of early life exposure. *Ann. Global Health*, 80: 303-314.
- Tyler, C. R. and Allan, A. M. 2014. The effects of arsenic exposure on neurological and cognitive dysfunction in human and rodent studies: A review. *Curr. Environ. Health Rep.*, 2: 132-147.
- Walia, G.K., Handa, D., Kaur, H. and Kalotra, R. 2013. Behavioral and morphological changes in a freshwater fish, *Labeo rohita* exposed to tannery industry effluent. *Zool.*, 2: 514-516.
- WHO 2001. Environmental Health Criteria 224- Arsenic and Arsenic Compounds. International Programme on Chemical Safety, Geneva, Switzerland.
- Yadav, R.S., Chandravanshi, L.P., Shukla, R.K., Sankhwar, M.L., Ansari, R.W., Shukla, P.K., Pant, A.B., and Khanna, V.K. 2011. Neuroprotective efficacy of curcumin in arsenic induced cholinergic dysfunctions in rats. *Neurotoxicol.*, 32: 760-768.
- Yallappa, S. and Asiya Nuzhat, F.B. 2017. Toxic effect of biochemical and morphological changes on carp (*Cyprinus carpio*) exposed to cadmium chloride. *Int. J. Zool. Stud.*, 2: 222-228.
- Yassi, A. and Kjellstrom, T. 1998. Environmental health hazards. In: Stellman, J.M. (Ed.), *Encyclopedia of Occupational Health and Safety* 1, International Labour Organization, Geneva.



Stability Properties of Chromium in Cr(VI)-Contaminated Soil Stabilized by Calcium Polysulfide (CaS₅)

Yuan Yuan Li* and Ting Ting Zhang**(***)[†]

*Qingdao University of Technology, Qingdao, 266033, China

**Wisdri City Environment Protection Engineering Limited Company, Wuhan, 430205, China

***Wuchang Shouyi University, School of Urban Construction, Wuhan 430064, China

[†]Corresponding author: Ting Ting Zhang; ttz_dshb@163.com; ztt_cersm@163.com

Nat. Env. & Poll. Tech.
Website: www.neptjournal.com

Received: 06-02-2020

Revised: 22-02-2020

Accepted: 02-05-2020

Key Words:

Cr(VI)-contaminated soil
Stability properties
Speciation
Leachability
Calcium Polysulfide

ABSTRACT

Calcium polysulfide (CaS₅) is widely used in stabilizing Cr(VI)-contaminated soils. The stability properties of Cr(VI) and Cr are the most important indexes for evaluating the effectiveness of stabilized soil. This study investigated the effect of CaS₅ dosage and curing age on the stability properties of Cr(VI) and Cr in contaminated soils and the relationship between leachability and Cr speciation. Results show that increasing the CaS₅ dosage and curing age could improve the stability properties of Cr in stabilized soil. The leachability and Cr(VI) content in the stabilized soil significantly decreased along with increasing CaS₅ dosage and curing age. The changes in the leachability of the soil were attributed to the changes in the Cr speciation distribution and microstructure of the stabilized soil. The exchangeable fraction was mainly converted into an oxidizable fraction, and a dense structure (ettringite and elemental sulphur) was formed along with increasing CaS₅ dosage and curing age. The exchangeable and reducible fractions depended on Cr leachability, and the Cr in the synthetic precipitation leaching procedures predominantly resulted from the exchangeable and reducible fractions.

INTRODUCTION

As a common contaminant of soils in China (Zhang et al. 2018), chromium [Cr(VI)] is a toxic and carcinogenic material that has been categorized by the US Environmental Protection Agency (US EPA) as a class A human carcinogen (Kazakis et al. 2018). The chemical reduction can rapidly and effectively remove Cr(VI) and has been widely used to stabilize Cr(VI)-contaminated soils (Chrysochoou et al. 2010). Calcium polysulfide (CaS₅) is commonly used for the remediation of Cr(VI)-contaminated soil due to its cost-effectiveness. Reducing Cr(VI) by using CaS₅ can be formulated as (Zhang et al. 2018)



Although many studies have examined CaS₅-stabilized Cr(VI)-contaminated soils, most of these works have focused on Cr(VI) leachability and content (Wazne et al. 2007, Chrysochoou et al. 2010, Zhang et al. 2018). However, leaching tests, including toxicity characteristic leaching procedure (TCLP), synthetic precipitation leaching procedures (SPLP), and semi-dynamic leaching tests, can only provide a single leaching result at a specific period, and the leachability of Cr in stabilized soil is not a good predictor of the effectiveness of stabilized reductants

(Seaman et al. 1999, Tinjum et al. 2008). Previous studies show that the toxicity and mobility of heavy metals in soil are not only related to their content but are also greatly determined by the distribution of their speciation (Petrucci et al. 2011). Therefore, the speciation distribution of Cr(VI) is crucial in ensuring the environmental security of stabilized soil. In addition, the leachability content of Cr in stabilized soil remains constant regardless of the environment and service time. Many factors can also affect the stabilization process of Cr(VI)-contaminated soil, among which reductant dosage and curing age are the most important (Tinjum et al. 2008). However, very few studies have methodically investigated the effect of reductant dosage and curing age on the leachability and species distribution of Cr(VI) in contaminated soils stabilized by CaS₅.

Accordingly, this study explores the effect of CaS₅ dosage and curing age on the stability properties of Cr(VI) in CaS₅-stabilized soil. The relationship between the leachability and speciation distribution of the Cr(VI) in CaS₅-stabilized soil is also examined. The findings of this work provide novel insights that can aid in evaluating the environmental security of CaS₅-stabilized soil and in remediating Cr(VI)-contaminated soils by using CaS₅.

MATERIALS AND METHODS

Cr(VI)-Contaminated Soil

Given its representativeness and repeatability, Cr(VI)-contaminated soil was simulated by Chinese clay and $K_2Cr_2O_7$ in this study (Zhang et al. 2019). The Cr(VI) content of the soil was 1000 mg/kg, which is representative of Cr(VI)-contaminated soils in China (Zhang et al. 2009, Wang et al. 2014). The contaminated soil was mixed evenly and braised for 180 days under standard curing conditions (20°C, 95% humidity) to allow $K_2Cr_2O_7$ and the soil to react adequately and to obtain an ageing contaminated soil.

Stabilization of Cr(VI)-Contaminated Soil by CaS_5

The CaS_5 used in the study was Cascade®, a 29% CaS_5 solution obtained from Lian Yun Gang Industrial Technology Co. Ltd. without further purification. The experimental design is given in Table 1. The Cr(VI)-contaminated soil, CaS_5 and distilled water were homogenized in a mixer. The mixture was withdrawn from sealed plastic bottles after incubating for 3, 7, 15, 28, and 56 days at room temperature (20°C).

Test Methods

The Cr(VI) contents of the soil and filtrate were measured by following the US EPA methods 3060A and 7196A, respectively, whereas the leachability of Cr(VI) and Cr was measured by following the US EPA method 1312. The sequential extraction procedure followed the method recommended by Rauret et al. (1999). Agilent 7700 inductively coupled plasma mass spectrometry was used to determine the metal concentrations in the leachate.

Table 1: Experimental design for the study.

Test No.	CaS_5 /Cr(VI) molar ration	Curing age
1	0	7 d
2	1	7 d
3	2	7 d
4	3	7 d
5	5	7 d
6	3	0 d
7	3	3 d
8	3	7 d
9	3	28 d
10	3	56 d

RESULTS AND DISCUSSION

Leachability of Cr(VI) and Cr in Soil Before and After Stabilization

In view of the leaching environment to be encountered when the stabilized soils are reused, an SPLP test was conducted to simulate the scenario of leaching associated with acid rain. Fig. 1 shows the leaching characteristics of the stabilized soil under different conditions. Fig. 1(a) reveals that both Cr(VI) and Cr concentrations decrease along with an increasing CaS_5 /Cr(VI) molar ratio. For untreated soil, the Cr(VI) and Cr leaching concentrations were approximately 32.6 mg/L and 35.8 mg/L, respectively, which exceeded China's regulatory limits for hazardous wastes (China GB/T5085.3-2007). For CaS_5 stabilized contaminated soil, when the CaS_5 /Cr(VI) molar ratio increased from 1 to 5, the Cr(VI) and Cr leaching concentrations decreased from 8.2 mg/L and 17.6 mg/L to 0.14 mg/L and 4.08 mg/L, respectively.

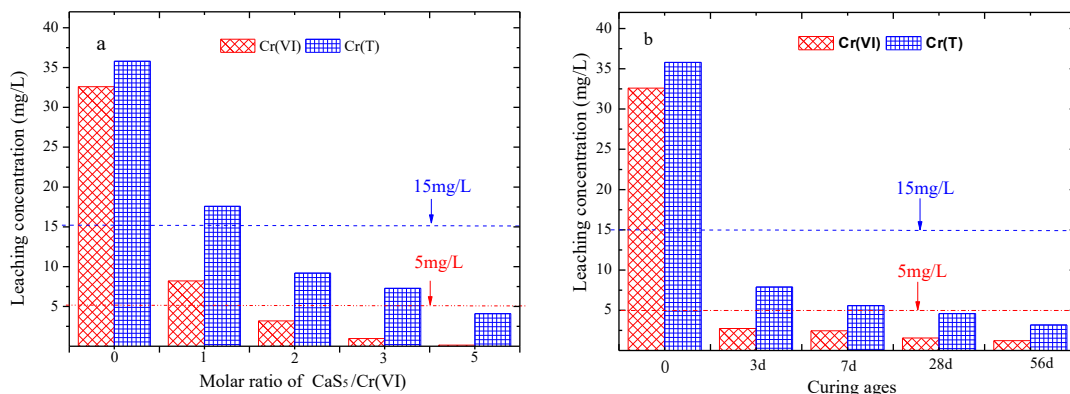


Fig. 1: Cr(VI) and Cr concentration of SPLP leachate under different conditions, (a) different CaS_5 and Cr(VI) molar ratio, (b) different curing ages.

In addition, when the CaS₅/Cr(VI) molar ratio exceeded 2, the Cr(VI) and Cr leaching concentrations complied with the regulatory limits of China and the US EPA (Moon 2008). The reduction in Cr(VI) concentration could be ascribed to the fact that Cr(VI) was reduced to Cr(III) and subsequently formed Cr(OH)₃ and ettringite precipitation or Cr(III) was bound to sulphides and adsorbed sulphur surface, thereby hindering Cr from migrating through the soil (Chrysochoou et al. 2010).

The variations in the Cr(VI) and Cr concentrations of the stabilized soil under different curing ages are shown in Fig. 1 (b). The leaching concentrations of Cr(VI) and Cr in the leachate decreased along with an extended curing age. When the CaS₅/Cr(VI) molar ratio was 3, the Cr(VI) and Cr concentrations complied with the regulatory limits of China and US EPA with a curing age of longer than 3 d. The decrease in Cr(VI) and Cr concentrations may be attributed to the ageing process, more and more Cr(VI) solubilization, reduction and the following Cr(OH)₃ and ettringite precipitation or adsorbed sulphur surface, making it harder for Cr to migrate through the soil, increasing the effectiveness of stabilized (Chrysochoou et al. 2010). As a result, the leaching concentrations of Cr(VI) and Cr decreased along with an extended curing age.

Cr(VI) Content in Soil Before and After CaS₅ Stabilization

Cr(VI) content is often measured to guarantee the environmental security of stabilized soils being reused as construction materials. The China Environmental Regulation recommends minimum Cr(VI) contents of 30 mg/kg and 5 mg/kg for industrial and civil reuse, respectively (China GB15618-2008). The Cr(VI) content in the soil before and after the stabilization of CaS₅ is shown in Fig 2. As shown in Fig. 2(a), the Cr(VI) content in soil decreased along with

an increasing CaS₅/Cr(VI) molar ratio, thereby suggesting that the CaS₅/Cr(VI) molar ratio significantly influences the effectiveness of the stabilized treatment. In addition, when the CaS₅/Cr(VI) molar ratio was 5, the Cr(VI) content of the contaminated soil was below the threshold specified by the China Environmental Regulation for industrial reuse (<30 mg/kg) (China GB15618-2008). Although the Cr(VI) and Cr leaching concentrations of the stabilized soil were negligible compared with those shown in Fig. 1, a considerable amount of Cr(VI) was still detected in the stabilized soil. Part residue Cr(VI) content of stabilized soil exceeded Environmental quality standards soil of China. The SPLP test underestimated the residue Cr(VI) content in the stabilized soil, and the leaching method could not reliably predict the remaining Cr(VI) content in the stabilized soil without performing an alkaline digestion test.

Fig. 2 (b) shows the variations in the Cr(VI) content in the soil as a function of curing age. As expected, the Cr(VI) content decreased along with an extended curing age, thereby suggesting that CaS₅ has good stability and long residence time in the soil. In addition, when the curing age was 3 d, the Cr(VI) content in the contaminated soil was below the threshold set by the China Environmental Regulation for industrial reuse (<30 mg/kg) yet satisfied the threshold for civil reuse (<5 mg/kg) when the curing age was extended to 56 d (China GB15618-2008) probably due to the fact that as the curing age increased from 3 d to 56 d, most of the reactions between Cr(VI) and CaS₅ were gradually completed, which could explain why the redox potential increased along with curing period.

Species Distribution of Cr(VI) in Soil Before and After Stabilization

The species distribution of Cr(VI) in the soil as a function of different CaS₅/Cr(VI) molar ratios and curing ages is shown

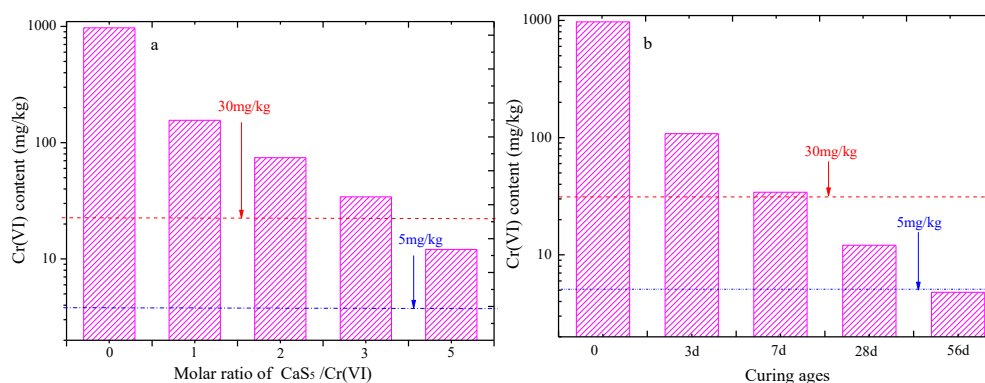


Fig. 2: Cr(VI) content in soil under different conditions, (a) different CaS₅/Cr(VI) molar ratio, (b) different curing ages.

in Fig. 3. Fig. 3(a) shows that for the untreated soil, Cr was mainly distributed in exchangeable (0.79 mg/g) and reducible fractions (0.13 mg/g), thereby indicating that Cr was highly mobile and toxic in the untreated contaminated soil. After CaS_5 was stabilized, the species distribution of Cr(VI) in the soil was significantly changed. Specifically, as the $\text{CaS}_5/\text{Cr(VI)}$ molar ratio and curing ages increased, the oxidizable content of Cr in the stabilized soil significantly increased. As shown in Fig. 3(a), the exchangeable fraction was mainly converted into an oxidizable fraction. Meanwhile, as the $\text{CaS}_5/\text{Cr(VI)}$ molar ratio of the stabilized soil increased from 0 to 5, the oxidizable content of Cr increased from 0.076 mg/g to 0.88 mg/g. In addition, a higher $\text{CaS}_5/\text{Cr(VI)}$ molar ratio benefitted the conversion of reducible fraction into an oxidizable fraction and decreased the reducible content of Cr from 0.15 mg/g to 0.021 mg/g. As shown in Fig. 3 (b), the oxidizable content of Cr increased from 0.076 mg/g to 0.68 mg/g, thereby demonstrating that the CaS_5 could significantly improve the chemical stability of Cr. $\text{CaS}_5/\text{Cr(VI)}$ molar ratio and curing age were identified as crucial factors that control the species distribution of Cr.

Species Distribution of Cr(VI) in Soil Before and After SPLP Extraction

The species distribution of Cr(VI) in the soil before and after SPLP extraction is shown in Fig. 4. After the SPLP extraction, the species distribution of Cr(VI) in the soil was significantly changed. The content of exchangeable and reducible fractions in all soils decreased, while the oxidizable and residual fractions were nearly unchanged. Fig. 4(a) shows that as the $\text{CaS}_5/\text{Cr(VI)}$ molar ratio of the stabilized soil increases from 0 to 5, the exchangeable content decreases from 0.79, 0.13, and 0.03 mg/g to 0.18, 0.06, and 0.010 mg/g, respectively, whereas the reducible content decreases from 0.13, 0.24, and 0.08 mg/g to 0.06, 0.16, and 0.02 mg/g, respectively. Meanwhile, Fig. 4 (b) shows that the exchangeable content decreases from 0.79, 0.13, and 0.02 mg/g to 0.18, 0.06, and 0.008 mg/g, respectively, whereas the reducible content decreases from 0.13, 0.24, and 0.14 mg/g to 0.06, 0.16, and 0.09 mg/g, respectively, as the curing age extends from 0 d to 56 d. These results clearly demonstrate that the exchangeable and reducible content of Cr depended on the Cr leachability in the SPLP test and on the safety of the stabilized soil.

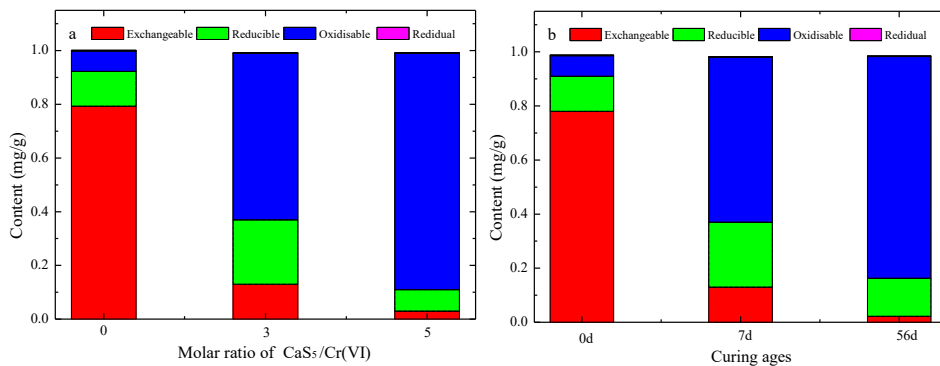


Fig. 3: Species distribution of Cr in soil under different conditions: (a) different $\text{CaS}_5/\text{Cr(VI)}$ molar ratio; (b) different curing ages.

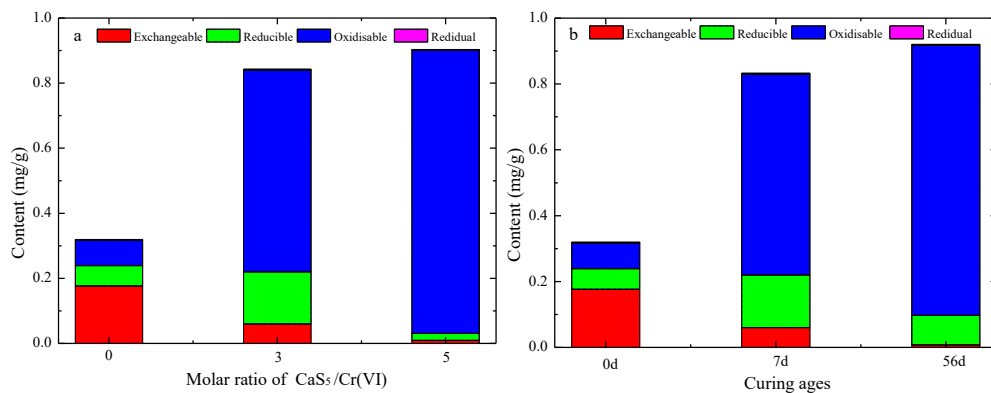
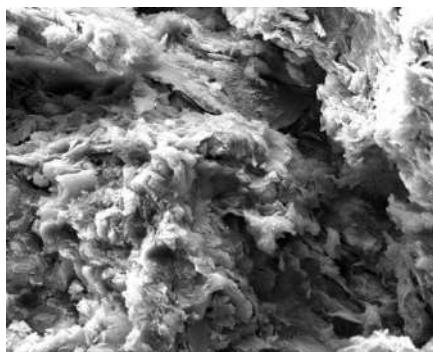


Fig. 4: Species distribution of Cr in soil after SPLP extraction (a) different $\text{CaS}_5/\text{Cr(VI)}$ molar ratio, (b) different curing ages.



(a) untreated contaminated soil.

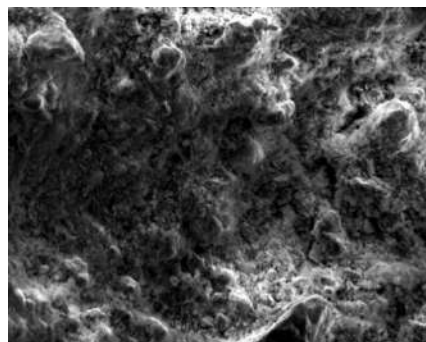
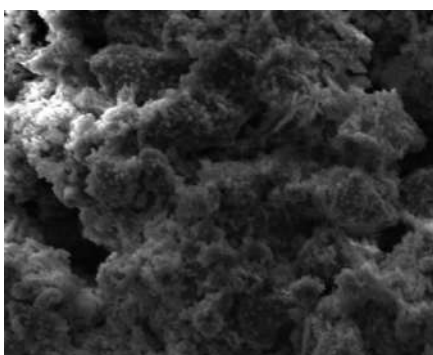
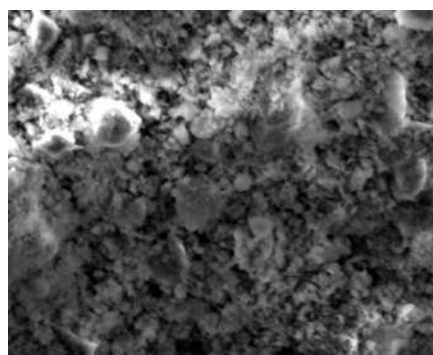
(b) $\text{CaS}_5/\text{Cr(VI)}$ molar ratio was 5 and Curing age was 7 d.(c) $\text{CaS}_5/\text{Cr(VI)}$ molar ratio was 3 and Curing age was 7 d.(d) $\text{CaS}_5/\text{Cr(VI)}$ molar ratio was 3 and Curing age was 56 d.

Fig. 5: SEM images of the stabilized soil under different conditions.

SEM Analysis

The typical SEM images of the stabilized soil under different conditions are shown in Fig. 5. The untreated contaminated soil (Fig. 5a) showed a large aggregate structure with a large void space between aggregations. When the $\text{CaS}_5/\text{Cr(VI)}$ molar ratio was 3 (Fig. 5 c), a low amount of ettringite and elemental sulphur was observed on the surface of the soil particles. By contrast, the SEM image of the soil with a $\text{CaS}_5/\text{Cr(VI)}$ molar ratio of 5 showed a large amount of ettringite and elemental sulphur covering the surface of soil particles and forming a dense structure in the stabilized soil (Fig. 5 b). When the curing age was extended from 7 d to 56 d (Fig. 5 c and d), the void volume was decreased, and the soil particles showed a dense structure, thereby suggesting that increasing the CaS_5 dosage and curing age would significantly change the microstructure of the soil and the stability properties of Cr. Zhou et al. (2017) and Chrysochoou et al. (2010) found that the Cr(III) uptake in ettringite hinders the release of Cr(III) from the soils during the leaching test.

Relationship Between Species Distribution and Leachability of Cr

The relationship between Cr species distribution and

leachability is given in Table 2. The content of exchangeable and reducible fractions in all soils was decreased, whereas the oxidizable and residual fractions were nearly unchanged. In other words, the Cr in the SPLP leachate predominantly resulted from the exchangeable and reducible fractions, and the Cr content depended on the Cr leachability recorded in the SPLP test and on the environmental security characteristics of the stabilized soil. As for CaS_5 -stabilized Cr(IV)-contaminated soils, the leachability content of Cr remained constant regardless of the environment and service time.

Table 2 shows that the Cr content in the SPLP leachate is approximately equal to the decrements in the exchangeable and reducible fractions of the soil after the SPLP extraction. These results indicate that the content of exchangeable and reducible fractions can be used to evaluate the potential leachability of Cr.

CONCLUSIONS

This study explores the speciation and leachability of Cr(IV)-contaminated soils stabilized by CaS_5 . A series of SPLPs, alkaline digestions, sequential extractions, and SEM tests were performed on Cr(VI)-contaminated soil. The effect of CaS_5 dosage and curing age on Cr(VI) speciation and

Table 2: Relationship between Cr species distribution and leachability of Cr in soil.

Soil types	Test indexes	Species distribution of Cr (mg/g)			
		Exchangeable	Reducible	Oxidizable	Residual
Untreated soil	Before SPLP extraction	0.793	0.13	0.076	0.0026
	After SPLP extraction	0.177	0.062	0.078	0.0023
	Variation	0.616	0.068	-0.002	0.0003
	Cr content in SPLP leachate	0.716	0.716	0.716	0.716
	Percentage	86.03%	9.50%	-0.27%	0.042%
CaS ₅ /Cr(VI) molar ratio was 3	Before SPLP extraction	0.13	0.24	0.62	0.00255
	After SPLP extraction	0.06	0.16	0.62	0.00255
	Variation	0.07	0.08	0	0
	Cr content in SPLP leachate	0.146	0.146	0.146	0.146
	Percentage	47.94%	54.79%	0	0
CaS ₅ /Cr(VI) molar ratio was 5	Before SPLP extraction	0.03	0.08	0.86	0.00253
	After SPLP extraction	0.0098	0.021	0.87	0.00253
	Variation	0.02	0.059	-0.01	0
	Cr content in SPLP leachate	0.082	0.082	0.082	0.082
	Percentage	24.40%	71.95%	-12.2%	0
Curing age was 7d	Before SPLP extraction	0.13	0.24	0.62	0.00255
	After SPLP extraction	0.06	0.16	0.62	0.00255
	Variation	0.07	0.08	0	0
	Cr content in SPLP leachate	0.146	0.146	0.146	0.146
	Percentage	47.94%	54.79%	0	0
Curing age was 56d	Before SPLP extraction	0.022	0.141	0.82	0.00256
	After SPLP extraction	0.0078	0.09	0.81	0.00256
	Variation	0.0142	0.051	0	0
	Cr content in SPLP leachate	0.064	0.064	0.064	0.064
	Percentage	22.19%	79.69%	0	0

leachability were evaluated, and the relationship between Cr(VI) leachability and speciation was investigated. The following conclusions can be drawn from the results:

1. Increasing the CaS₅ dosage and curing age can improve the stability of Cr in stabilized soil. The Cr(VI) leachability and content in stabilized soil significantly decreased along with increasing CaS₅ dosage and curing age. The leachability and Cr content of the stabilized soil was lower than the regulatory limits imposed by China and the US EPA when the CaS₅/Cr(VI) molar ratio was 3. Meanwhile, when the CaS₅/Cr(VI) molar ratio was 5, the Cr(VI) content in the soil met the environmental quality standards of China for industrial reuse (Cr(VI) < 30 mg/kg).
2. The change in the leachability of soil was attributed to the changes in Cr speciation distribution. According to the results of the sequential extraction test, the exchangeable fraction was mainly converted into oxidizable fraction

as the CaS₅ was stabilized. The exchangeable and reducible fractions depended on Cr leachability, and the Cr in the SPLP leachate predominantly resulted from these fractions. The content of exchangeable and reducible fractions can be used to evaluate the potential leachability of Cr.

3. Along with increasing CaS₅ dosage and curing age, the microstructure of the stabilized soil was changed along with the stability properties of the soil. The SEM images showed that the stabilized soil had a large amount of ettringite, and elemental sulphur covered the surface of the soil particles and formed a dense structure in the stabilized soil.

ACKNOWLEDGMENTS

This study was supported by the thirteenth 3551 talent program of China optical valley (long-term innovative of Ting Ting Zhang), National Natural Science Foundation of Shandong

province (ZR2020QE148), Natural Science Foundation of Qingdao University of Technology (2018TJZR002, 2019ZR007) and University research project of Shandong Province(J18KB059).

REFERENCES

- Chrysochoou, M., Ferreira, D.R. and Johnston, C.P. 2010. Calcium polysulfide treatment of Cr (VI)-contaminated soil. *Journal of Hazardous Materials*, 179(1-3): 650-657.
- Kazakis, N., Kantiranis, N. and Kalaitzidou, K. 2018. Environmentally available hexavalent chromium in soils and sediments impacted by dispersed fly ash in Sarigkiol basin (Northern Greece). *Environmental Pollution*, 235: 632-641.
- Moon, D.H., Wazne, M. and Jagupilla, S.C. 2008. Particle size and pH effects on remediation of chromite ore processing residue using calcium polysulfide (CaS₂). *Science of the Total Environment*, 399(1-3): 2-10.
- Petrucci, E., Montanaro, D. and Merli, C. 2011. Sequential extraction analysis provides decision-making tools for the use of contaminated sediments. *Chemistry and Ecology*, 27(S1): 107-118.
- Rauret, G., Lopez-Sanchez, J.F. and Sahuquillo, A. 1999. Improvement of the BCR three step sequential extraction procedure prior to the certification of new sediment and soil reference materials. *Journal of Environmental Monitoring*, 1(1): 57-61.
- Seaman, J.C., Bertsch, P.M. and Schwallie, L. 1999. In situ Cr (VI) reduction within coarse-textured, oxide-coated soil and aquifer systems using Fe (II) solutions. *Environmental Science & Technology*, 33(6): 938-944.
- Synthetic Precipitation Leaching Procedure, Method 1312. 1998. Environmental Protection Agency, Washington, D.C, U.S.
- Tinjum, J.M., Benson, C.H. and Edil, T.B. 2008. Treatment of Cr (VI) in COPR using ferrous sulfate-sulfuric acid or cationic polysulfides. *Journal of Geotechnical and Geoenvironmental Engineering*, 134(12): 1791-1803.
- Wazne, M., Jagupilla, S.C. and Moon, D.H. 2007. Assessment of calcium polysulfide for the remediation of hexavalent chromium in chromite ore processing residue (COPR). *Journal of Hazardous Materials*, 143(3): 620-628.
- Zhou, X., Zhou, M. and Wu, X. 2017. Reductive solidification/stabilization of chromate in municipal solid waste incineration fly ash by ascorbic acid and blast furnace slag. *Chemosphere*, 182: 76-84.
- Zhang, R., Zhang, N. and Fang, Z. 2018. In situ remediation of hexavalent chromium contaminated soil by CMC-stabilized nanoscale zero-valent iron composited with biochar. *Water Science and Technology*, 77(6): 1622-1631.
- Zhang, T.T., Xue, Q. and Wei, M.L. 2018. Leachability and stability of hexavalent chromium contaminated soil stabilized by ferrous sulfate and calcium polysulfide. *Applied Sciences*, 8(9): 1431.



Impact of Corporate Governance on Environmental Protection Investment of China's Listed Enterprises in High-polluting Industry

Kai Wang

Admissions and Employment Service Department, Xinyang Normal University, Xinyang, Henan, 464000, China

†Corresponding author: Kai Wang; wangkai19870@163.com

Nat. Env. & Poll. Tech.
Website: www.neptjournal.com

Received: 12-09-2020

Revised: 27-12-2020

Accepted: 09-01-2021

Key Words:

Listed Enterprises
High-polluting industry
Corporate governance
Panel data

ABSTRACT

With the rapid development of the economy, people's pursuit of the quality of life is getting higher. Thus, environmental pollution will be punished, and the high-polluting industry will face more problems in development. To explore the impact of corporate governance on environmental protection investment, 28 listed enterprises in high-polluting industry in China were selected as samples. Corporate governance was reflected from four aspects as explaining variables including shareholding structure, board composition, characteristics of the supervisory board and executive incentive. The relationship between corporate governance and high-polluting enterprises' environmental protection investment was analysed by using the data of China's listed enterprises in the high-polluting industry from 2015 to 2019. The results indicate that there is a positive correlation between legal person proportion and environmental protection investment of high-polluting enterprises, and a U-shaped relationship of the Herfindahl index. There is a significant positive correlation between board size and environmental protection investment of high-polluting enterprises, and the relationship is significantly negative of the size of the board of supervisors. The conclusions are helpful to improve the corporate governance of high-polluting enterprises, to enhancing environmental protection investment.

INTRODUCTION

It has become the consensus of all countries in the world to implement the strictest ecological environment protection system. The promulgation of various laws and policies reflected the state's attention to environmental protection and determination to control environmental pollution. The Ministry of Ecology and Environment of China has designated 16 industries, including thermal power, steel, cement, electrolytic aluminium, coal, metallurgy, chemical, petrochemical, building materials, paper making, brewing, pharmaceutical, fermentation, textile, leather and mining, as high-polluting enterprises. According to statistics, there were more than 500 high-polluting enterprises listed in China in these 16 industries. High-polluting enterprises discharged a large amount of waste gas, wastewater, waste residue and noise every year, causing research damage to the surrounding ecological environment. In recent years, on the one hand, the high-polluting industry's investment growth rate has declined and the debt burden has risen. On the other hand, Xi Jinping of Chinese President proposed, "Clearwater and green mountains are golden hills and silver mountains". The high-polluting industry is faced with greater pressure to transform. Therefore, under these circumstances, there is strong theoretical and practical significance not only to study the relationship between listed enterprises' governance and environmental protection investment in the

high-polluting industry but also to explore how to enhance environmental protection investment through standardizing corporate governance.

A new round of scientific and technological revolution and industrial change is emerging. Corporate governance and environmental protection investment are hot issues all the time. Environmental protection investment can not only improve the reputation of high-polluting enterprises but also respond to the national call to continuously optimize product structure and achieve technological upgrading. Good corporate governance can ensure high-polluting enterprises to increase environmental protection investment, but scholars have not studied different components of corporate governance affect environmental protection investment. It is necessary for high-polluting industry having an invincible position to reform and innovate in an open market environment. Thus, one of the effective ways is to standardize corporate governance.

PAST STUDIES AND RESEARCH HYPOTHESIS

Ownership Structure and Environmental Protection Investment

Relationship between equity nature and environmental protection investment: After the implementation of the reform of listed enterprises in the high-polluting industry,

equity gradually achieved the “full circulation”, state-owned non-tradable shares flow into the capital market (Wang et al. 2009). Corporate and institutional investors’ shareholding ratio increased gradually, but this did not necessarily lead to the reduction of state-owned shares. State-owned shares, “only one big share”, still existed in the short term. Agency problems and owner absence existed generally for listed companies in the high-polluting industry (Liu et al. 2011). State-owned shareholders chose improper incentives and regulations to managers easily lead to moral hazard problems, and it affected the environmental protection investment, for the reason that low environmental protection investment could help the enterprise gain more profit. Compared to state-owned shares, legal person shares had more “economic person” personality characteristics (Shleifer et al. 1986). The pursuit of them was the long-term and stable return on investment, using “voting by hand” to participate in the decision-making, to achieve the maximization of benefits. Legal person shares had obvious advantages in the supervision of managers. Tradable shares had strong flexibility and the holders were extremely dispersed, which had “take a ride” behaviour. Supervision to the operation and management of listed enterprises in the high-polluting industry was weak, and it was difficult to reach good corporate governance. Based on this, it puts forward the hypothesis:

Hypothesis 1a: there is a negative correlation between the proportion of state-owned shares and environmental protection investment of listed enterprises in the high-polluting industry.

Hypothesis 1b: there is a positive correlation between the proportion of corporate shares and environmental protection investment of listed enterprises in the high-polluting industry.

Hypothesis 1c: there is a positive correlation between the proportion of tradable shares and environmental protection investment of listed enterprises in the high-polluting industry.

Relationship between equity concentration and environmental protection investment: A relatively concentrated ownership structure could encourage shareholders to implement effective supervision, but the expansion of ownership concentration degree would possibly cause violations of the interests of small shareholders from the large shareholders. Listed enterprises in the high-polluting industry most were restructured from state-owned enterprises and as the controlling shareholder, the state was unable to perform the supervision responsibility, which made control eventually transferred to the hands of executives. It formed “insider control”. Based on this, it puts forward the hypothesis:

Hypothesis 2a: there is a positive correlation between the proportion of the first shareholder and environmental pro-

tection investment of listed enterprises in the high-polluting industry.

Hypothesis 2b: there is an inverted U relationship between Herfindahl index and environmental protection investment of listed enterprises in the high-polluting industry.

Relationship between equity balance degree and environmental protection investment: The theory of information asymmetry showed that large shareholders and small shareholders had different information, which caused the controlling shareholder to grab the interests of other shareholders. Equity balance of listed enterprises in the high-polluting industry could reduce these problems caused by information asymmetry (Azadegan et al. 2019). If the degree of equity balance was higher, then the restriction and supervision function between shareholders was stronger. However, if the equity balance degree was too high, it was easy to cause the decentralization of power. Decision-making efficiency might decrease. Based on this, it puts forward the hypothesis:

Hypothesis 3a: there is a U relationship between S index and environmental protection investment of listed enterprises in the high-polluting industry.

Hypothesis 3b: there is an inverted U relationship between Z index and environmental protection investment of listed enterprises in the high-polluting industry.

Board of Directors and Environmental Protection Investment

Relationship between board size and environmental protection investment: Directors of listed enterprises in the high-polluting industry would be operating efficiently under the board of directors of the scale effect, the big number of directors would easily cause members between communication and coordination disorder, leading to the low efficiency of the board of directors (Yermack 1996). The deterioration of the relationship between the board members is due to the competition for power and profit and the shirking of responsibility. It might lead to internal fierce struggle and consumption of resources (Lan et al. 2009). Besides, the larger number of board members easily led to “free rider” motivation. It was more likely to happen when ownership and company operating losses. Based on this, it puts forward the hypothesis:

Hypothesis 4: there is a negative correlation between board size and environmental protection investment of listed enterprises in the high-polluting industry.

Relationship between the proportion of independent directors and environmental protection investment: Independent directors usually did not have shares of listed enterprises in the high-polluting industry, which were not

directly influenced by the controlling shareholder of the company. The board of directors and executives are conducive a benefit for their independent judgment on the affairs of the company (Jensen et al. 1976). Independent directors were composed of experts in various fields, which could provide a reference for the scientific decision-making of the board of directors with various information and specialized knowledge. The proportion of independent directors on the board of directors was different, which had a great influence on the responsibilities of the board of directors (Qin 2018). Based on this, it puts forward the hypothesis:

Hypothesis 5: there is a positive correlation between the proportion of independent directors and the environmental protection investment of listed enterprises in the high-polluting industry.

Board of Supervisors and Environmental Protection Investment

As an internal supervision mechanism of listed enterprises in the high-polluting industry, the board of supervisors exercised supervision right on behalf of investors and was responsible for the general meeting of shareholders (Li et al. 2016). Its basic function was responsible for overseeing the company's all business activities and financial status. It could require that the board of directors and executives promptly corrected the ultra vires act in violation of the articles of association of the company, to reduce the probability of making mistakes and financial fraud. Based on this, it puts forward the hypothesis:

Hypothesis 6: there is a positive correlation between the scale of the board of supervisors and the environmental protection investment of listed enterprises in the high-polluting industry.

Executive Incentive and Environmental Protection Investment

Executives' shareholding ratio of listed enterprises in the high-polluting industry was very low. The long-term incentive effect was not obvious, mainly by salary. Based on the agency theory, when there was information asymmetry between executives and shareholders, the shareholders needed to sign a compensation performance contract with executives, to reduce the agency cost of executives caused by moral hazard and adverse selection (Wu et al. 2019). Then, they could achieve the maximization of their wealth. Based on this, it puts forward the hypothesis:

Hypothesis 7: there is a positive correlation between executive annual salary and environmental protection investment of listed enterprises in the high-polluting industry.

MATERIALS AND METHODS

Data Source

This study selected 28 listed enterprises in the high-polluting industry. Sample data was chosen from the CSMAR database, Wind database and annual reports from 2015 to 2019. The information comes from the Shanghai Stock Exchange, the Shenzhen Stock Exchange, and the official websites of enterprises. This study uses an Excel table to process the original data and SPSS19.0 software for processing and analysis.

Modelling

According to the above hypothesis, this study uses multiple linear regression models to examine the relationship between variables. The specific model is as follows:

$$y_{it} = c + \alpha \sum x_{it} + \beta \ln TA_{it} + \varepsilon_{it} \quad \dots(1)$$

Where, c is the intercept, α and β are the coefficients of explanatory variables. ε_{it} is the error term. y_{it} is shown as 0 or 1. It is judged from the information, which can be found in annual reports of the listed enterprises.

Variables

The proportion of state-owned shares, the proportion of corporate shares and proportion of tradable shares reflect equity nature. The proportion of the first largest shareholder and Herfindahl index reflect equity concentration. S index and Z index reflect equity balance degree. These variables all belong to the category of equity structure. Board size and the proportion of independent directors reflect board of directors. The scale of the board of supervisors reflects the board of supervisors. Executive annual salary reflects executive incentive. Corporate governance variables are given in Table 1.

RESULTS ANALYSIS

To eliminate heteroscedasticity, multivariate regression model uses respectively natural logarithm of the executive annual salary and total assets. This study selects variables that the relationships are significant and it uses a fixed effect and random effects panel regression method to analyze. The results are shown in model (1)-(2) in Table 2. Then it adds other variables regression and only presents the results by Hausman test such as the model (3)-(5). Finally, this study makes the global variable into the regression model and the results are shown in the model (6)-(7). The DW values of the model (1), (3)-(6) are 2.43, 2.46, 2.37, 2.43 and 2.40, which declare that multivariate regression model does not have a serial correlation. Thus, R^2 is greater than 0.56 and it has greatly improved. F value is all through the significant test.

Table 1: Corporate governance variable definition.

Variable properties	Variable names	Variable symbol	Variable interpretation	
Own- ership structure	Equity nature	Proportion of state-owned shares	GYG	State-owned shares/Total share capital
		Proportion of corporate shares	FRG	Legal person shares/Total share capital
		Proportion of Tradable shares	LTG	Negotiable shares /Total share capital
	Equity concentration	Proportion of the first largest shareholder	CR1	The first major shareholders holdings /Total share capital
		Herfindahl index	H10	Sum of squares of Share ratio of the top ten shareholders
	Equity balance degree	S index	S	The sum of Second shareholders to the tenth largest shareholder ratio
Z index		Z	The proportion of the first largest shareholder/Second share ratio of major shareholders	
Board of directors	Board size	DSS	Total number of board of directors	
	Proportion of independent directors	DDR	Number of independent directors/Total number of board of directors	
Board of supervisors	The scale of the board of supervisors	JSS	The total number of the board of supervisors	
Executive incentive	Executive annual salary	GGG	Average annual salary of the top three executives	

In model (1) and (3), the proportion of corporate shares is positively related to environmental protection investment at 1% significant level. The proportion of state-owned shares and proportion of tradable shares harm environmental protection investment, but the results are not significant, shown as model (3)-(6). In the model (1), (3)-(7), the proportion of the first largest shareholder has a significant negative impact on environmental protection investment, but the regression result does not support the expectation hypothesis. With the acceleration of the state-owned enterprises' reforming, state-owned shares of listed enterprises in the high-polluting industry gradually realize the market circulation. Nevertheless, in most cases, state-owned share as the largest shareholder remains unchanged. The problem of supervision absence resulting from the lack of major shareholders is serious, as well as insider control. However, large numbers of small shareholders are scattered in the circulation stocks, which results in a widely existing phenomenon of "getting a lift" and weakening of supervision to management. To maximize their interests, legal person shareholders with the characteristics of "economic man" will actively participate in corporate decision-making, supervise the management and promote corporate governance mechanism to work. Therefore, hypothesis 1b is proved and the others are not proved.

At 10% significant level, Herfindahl index is positively related to environmental protection investment, while its square term shows the opposite direction and the result is not significant. But, the results of single-variable regression

show that environmental protection investment decreases with the increase of Herfindahl index. When Herfindahl index is among 0~0.388, the environmental protection investment increases with Herfindahl index. When Herfindahl index is among 0.388~1, the environmental protection investment decreases. Therefore, hypothesis 2b is proved.

The failure of impacts of S and Z index on environmental protection investment reflects the weak force of ownership balance of listed enterprises in the high-polluting industry. Therefore, hypothesis 3b and 3a are both not proved.

In model (1), (3) and (4), board size is negatively related to the environmental protection investment significantly at the 10% level. The generally larger companies easily cause dysfunction, difficulties in communication and low efficiency of decision-making. In practice, the number of the board of directors has average more than 8 people in 23 listed enterprises in the high-polluting industry in 2019. Boards with big size cannot play a good role in supervisory and easily cause low efficiency of decision-making. The regression results are consistent with the theoretical expectations, so hypothesis 4 is proved.

In t model (5) and (6), the proportion of independent directors has a positive impact on environmental protection investment, which is consistent with theoretical expectations. The result is not significant. According to the theory of corporate governance, independent directors only receiving allowances, considered as external supervision of the company, can generate constraints on business activities and improve the financial situation of the enterprise; the

Table 2: Multivariable panel data regression results.

(Model)	Main variable regression		Added other explanation variables regression			All explanatory variables regression	
	(1)	(2)	(3)	(4)	(5)	(6)	(7)
Regression method	Fixed Effect	Random Effect	Fixed Effect	Fixed Effect	Fixed Effect	Fixed Effect	Random Effect
C	8.33***	0.75	8.63***	9.74***	9.12	8.61	-2.99
LnTA	-0.34***	-0.21***	-0.48***	-0.43***	-0.35***	-0.33***	-0.16***
GYG	-	-	-0.20	-0.90	-0.89	-1.00	2.27
FRG	1.89***	0.36	1.83***	1.11	1.14	1.12	2.69
LTG	-	-	-	-0.78	-0.70	-0.89	2.37
CR1	-10.32**	0.70	-11.17**	-11.23**	-10.42*	-11.81*	2.47
S	-0.74	1.32*	-0.54	-0.48	-0.33	2.13	1.37
S2	-	-	-	-	-	-237	1.58
H10	13.31*	0.68	13.76*	14.36*	14.31*	14.32*	-1.51
H102	-4.15	-0.33	-4.84	-5.67	-5.78	-621	1.04
Z	-	-	-	-	-	0.01	0.01
Z2	-	-	-	-	-	0.01	0.01
DSS	-0.11*	-0.09	-0.10*	-0.10*	-0.068	-0.07	-0.03
DDR	-	-	-	-	1.65	1.66	2.78**
JSS	-0.22***	0.10	-0.23***	-0.25***	-0.23***	-0.24***	0.04
LnGSS	0.12	0.18*	0.21	0.23	0.19	0.12	0.17*
R ²	0.57	0.12	0.57	0.57	0.65	0.58	0.15
F-statistic	3.42***	2.10*	3.76***	3.68***	3.51***	3.23***	1.51
DW value	2.43	1.65	2.46	2.37	2.43	2.40	1.89
Hausman	38.11***	-	38.44***	39.51***	40.32***	41.39**	-

Note: ***, **, * denote parameter estimates are significant at the level of 1%, 5%, 10%, models of (3)-(5) are tested by Hausman to determine which one is more suitable.

proportion of independent directors of listed enterprises in the high-polluting industry is 1/3 about the baseline. This is the main reason why the regression result is not significant. Therefore, hypothesis 5 is proved.

The influence of the board of supervisors on the environmental protection investment is significantly negative at the 1% level. A significant level of the board of supervisors on the negative impact of environmental protection investment has been improved after introducing other variables. Yang (2013) proposed to evaluate whether the board of supervisors had achieved the goal of effective supervision from the guarantee of ability and operation effectiveness. Board of supervisors should reach a certain scale to ensure the effectiveness of the operation. The member of supervisors of listed enterprises in the high-polluting industry all meet the specified requirements, but most of them also work for other companies or receive compensation from related entities, leading to the failure of the supervisory function. This not only wastes the enterprise's resources but also reduces the enterprise's operating efficiency. The regression results do not support the theory anticipated. So, hypothesis 6 is not proved.

The results show that the natural logarithm of executive annual salary on environmental protection investment is significantly positive at the 15% level. In the high-polluting industry, the annual salary of executives has a significant incentive effect on management. Moreover, the growth trend of the average annual salary of senior executives in the industry has proved the hypothesis well. So, hypothesis 7 is proved.

CONCLUSIONS

The impact of corporate governance on environmental protection investment of high-polluting enterprises is explored by using the data of 28 listed enterprises in high-polluting industry in China from 2015 to 2019. The conclusions are drawn as follows. (1) The proportion of corporate shares has a significant positive effect on the environmental protection investment, which means high-polluting enterprises may implement more actions that are conducive to environmental governance and environmental protection investment enhancement. (2) Herfindahl index and environmental protection investment have a significant

U-shaped relationship. More small and medium-sized shareholders may make good decisions for high-polluting enterprises, which can reduce environmental pollution and increase social identity. (3) A significant negative correlation is found between the board size and environmental protection investment. With the enlargement of the board size, the decision-making efficiency of the board of directors will drop, which will lead to environmental protection investment decline of listed enterprises in the high-polluting industry. (4) The scale of the board of supervisors and environmental protection investment show a significant negative correlation. With the enlargement of the board of supervisors' size, the environmental protection investment of listed enterprises in the high-polluting industry will be worse. Many supervisors may be unable to perform an effective supervisory function, leading to high-polluting enterprises carrying out environmentally harmful behaviours. (5) Executive annual salary has a significant positive effect on the environmental protection investment. Raising the annual salary of senior executives can help improve environmental protection investment of listed enterprises in the high-polluting industry. As a high polluter not only creates social environmental protection investment but also causes serious damage to the surrounding environment. High-polluting enterprises should attach great importance to environmental protection by strengthening corporate governance.

REFERENCES

- Azadegan, A., Golar, S., Kach, A. and Mousavi, N. 2018. Corporate environmental investments: a cross-national study on managerial decision making. *International Journal of Production Economics*, 5(199): 47-64.
- Jensen, M.C. and William, H.M. 1976. Theory of the firm: Managerial behavior, agency costs and ownership structure. *Journal of Financial Economics*, 3: 305-360.
- Lan, Y.J. and Xu, D.L. 2009. The empirical study of listed corporate board governance and value of China's commercial chain enterprises. *Comparative Economic and Social Systems*, 27(1): 171-175.
- Li, W.A. and Chen, H. 2016. The empirical study on the governance evaluation of the board of supervisors in China's listed enterprises. *Shanghai University of Finance and Economics*, 38(3): 78-84.
- Liu, Y.Y., Huang, Z., Xie, D.X. and He, X.F. 2011. The empirical study of Chinese listed companies ownership structure and environmental protection investment. *Economic and Management Research*, 37(2): 24-32.
- Qin, S.S. 2018. An empirical analysis of relationship between characteristics of the board of supervisors and enterprises' performance. *Journal of Capital University of Economics and Business*, 3: 51-55.
- Shleifer, A. and Vishny, R. 1986. Large shareholders and corporate control. *Journal of Political Economy*, 94: 461-488.
- Wang, X.H. and Xu, J. 2009. Ownership structure, capital structure and environmental protection investment of different growth opportunities - taking a distribution industry listed companies. *Business Economics and Management*, 7(3): 20-28.
- Wu, Y.H. and Wu, S.N. 2019. Executive compensation: incentives or self-interest: the evidence from China's listed enterprises. *Accounting Research*, 11: 40-48+96-97.
- Yang, D. 2013. Corporate governance and performance of enterprise - based on sociological analyses of Chinese experience. *Chinese Social Science*, 33(1): 72-94.
- Yermack, D. 1996. Higher market valuation of companies with a small board of directors. *Journal of Financial Economics*, 40(2): 185-211.



Development of Activated Carbon from Agricultural Waste: Sapota Peels

P. H. Patil*, V. R. Parate*, J. J. Jankar**†, A. S. Deshpande*** and B. N. Annapurve****

*Department of Food Technology, University Institute of Chemical Technology, North Maharashtra University (NMU), Jalgaon, Maharashtra, India

**MIT College of Food Technology, MIT ADT University, Pune, India

***Department of Technology, Shivaji University, Kolhapur, Maharashtra, India

****SDMVMS College of Food Technology, Aurangabad, Maharashtra, India

†Corresponding author: J. J. Jankar; jankjagruti@gmail.com

Nat. Env. & Poll. Tech.
Website: www.neptjournal.com

Received: 21-07-2020

Revised: 14-08-2020

Accepted: 15-10-2020

Key Words:

Sapota peels

Activated carbon

Lead removal

Wastewater purification

ABSTRACT

The present study aimed to develop the activated carbon from fruit waste like sapota peel and to optimize the condition of developed activated carbon for complete removal of lead ions from the desired concentration of a lead solution. The activated carbon was prepared from sapota peel by using sulphuric acid. The physicochemical characterization of the obtained activated carbon was done for various parameters along with analysis of crystal nature (XRD) and structural morphology (SEM). The optimum conditions for adsorption were studied by altering pH (2-10), agitation speed (50-250 revolution per minute), temperature (10-60°C), adsorbent dose (0.02-0.14 g) and contact time (30-240 minutes). The optimized conditions necessary for complete removal of lead ions by the prepared adsorbent were pH - 5.5, agitation speed - 200 revolutions per minute, temperature - 60°C, time - 3 hours and adsorbent dose - 0.12 g. This study can be further helpful in designing the process of wastewater treatment for the removal of toxic metals from water particularly lead by adsorption.

INTRODUCTION

The utilization of agricultural waste for the removal of heavy metals from the wastewater or the sewage has enticed much attention owing to its economic benefit and high removal efficiency which is attributed to different functional groups. Exposure of a person to heavy metals such as mercury and lead may cause the development of autoimmunity, in which his/her immune system attacks its own cells. This phenomenon results in joint disorders such as rheumatoid arthritis, and diseases of the kidneys, circulatory system, nervous system, and damaging of the foetal brain. Heavy metals, in higher doses, can cause irreversible brain damage (Barakat 2011). For the removal of heavy metals from the water, different techniques have been used for many years. Activated carbon method is one of them which is gaining more attention because of its advantageous nature. Pachaiyappan et al. (2012) have introduced activated carbon (AC) as a nongraphic, microcrystalline, tasteless and solid form of black carbonaceous material with a porous structure which has been considered as distinctive and multipurpose adsorbent owing to its extended surface area, microporous structure, high adsorption capacity, and a high degree of surface reactivity. Being a versatile material, activated carbon is exploited for the purification of water by removing the

perilous particles in water and exhaust gases used for the wastewater treatment as well. It is not only used for gas and water purification but also for sewage treatments and many other applications (Rajamani et al. 2018). AC can be acquired from the agricultural waste such as fruit waste and play an advantageous role by being effective, low-cost replacement for non-renewable coal-based granular activated carbons (GACs) provided that they have similar or better adsorption efficiency (Martin et al. 2003). Agricultural by-products available in large amount makes them a good source of raw material for activated carbon production (Malik et al. 2007). Different types of fruit wastes have been used for the production of activated carbon such as orange peels (Xie et al. 2014), watermelon peels (Gin et al. 2014), banana peels (Chafidz et al. 2018). The present investigation was focused on the production of activated carbon from sapota peels.

MATERIALS AND METHODS

Squander sapota peels have been used for the study. The Sapota peels were procured from the local fruit market, cleaned by washing, dried in a hot air oven at a temperature around 55°C and ground to powder form by using a grinder. The obtained powder was subjected to further analysis.

Analysis of Raw Material

Sapota peels were subjected for the analysis to determine various physicochemical characteristics by using standards delineated in Table 1.

Preparation of Metal Adsorbent

Activated carbon was prepared from the sapota peels by slightly modifying the method described by Demirbas et al. (2004). Peels were first dried and ground and the resulting powder was then activated by using sulphuric acid as shown in Fig. 1.

Characterization of the Prepared Adsorbent

The adsorbent was studied for different physicochemical characteristics such as bulk density and ash content as per procedures stipulated by CEFIC (European Chemical Industry Council). Bulk density was determined with the help of bulk density apparatus (DBK 5028-7). Adsorbent was also analysed for the moisture content and pH by Bureau of Indian Standards method IS 877, (1989). Adsorbent was analysed for its calorific value, which was determined by using Digital Bomb Calorimeter (Rajdhani Scientific, Model: RSB 6). The adsorbent was also tested for electrical conductivity by using conductivity meter of Systronic (Model 304) based

Table 1: Physicochemical characteristics of sapota peels.

Sr. No.	Parameters	Equipment/Instruments	Methods
1	Moisture	Electric hot air oven; Weighing balance	IS 996:1999
2	Fat	Soxhlet apparatus	IS 996:1999
3	Ash	Muffle furnace	IS 996:1999
4	Protein	Pelican KES 04 LVA	Kjeldahl method (Ranganna)
5	Crude Fibre	Pelican KES 04 LVA	IS 4706 , Part-2 (1978)
7	Lignocellulose content	Refluxing apparatus; water heater	Van Soest & Wine (1970)

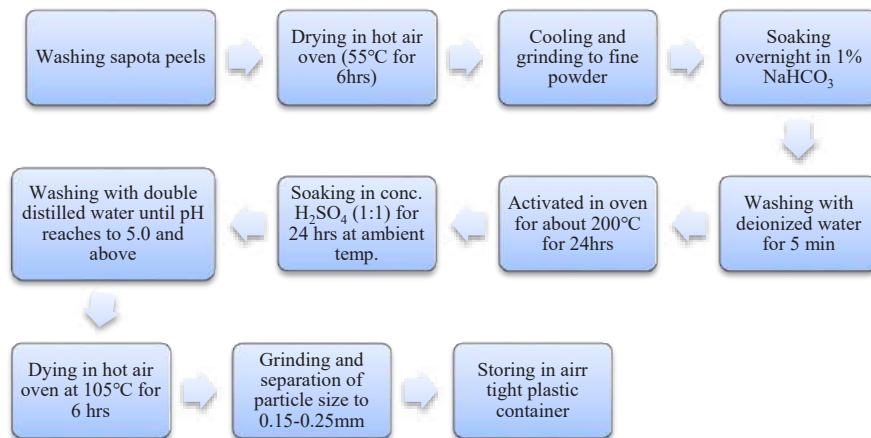


Fig. 1: Method of preparation of metal adsorbent from sapota peels.

on IS 14767, (2000) method. The yield of adsorbent was calculated by using the following equation (1):

$$\text{Yield \%} = \frac{\text{Weight of dried material before treatment}}{\text{Weight of dried material after treatment}} \times 100 \dots(1)$$

Study of Adsorbents in Removing Lead Ions Adsorption

Amount of carbon and structure of its lattice was determined by using X-ray diffraction determined by using XRD of BRUKER (Germany), Model: D8 ADVANCE with a scintillation detector. Morphological characteristics of sapota peel and adsorbent prepared from it were determined by using Scanning Electron Microscope (SEM) of HITACHI (Model: S-4800, TypeII) coupled with Energy Dispersive X-ray Spectroscopy (EDS) of BRUKER.

Optimization of Adsorption Condition

The effect of pH, agitation speed, temperature and adsorbent dose on adsorption capacity of prepared adsorbent from sapota peels was observed by keeping the other variables of adsorption such as the initial concentration of the lead solution (50 ppm), volume of lead solution (50 mL), particle size of adsorbent (0.15-0.25 mm) and contact time (4 h) constant. The effect of pH was studied by adjusting the pH of solutions at 2, 3, 4, 5, 6, 7, 8, 9, 10 using 0.1-0.5 M solution of NaOH

or HCl. The pH-adjusted solutions were stirred at 150 rpm at 30°C with 0.5 g adsorbent. The obtained optimum pH was then maintained in all the further study of adsorption. The effect of agitation on adsorption was examined by shaking the suspension of a lead solution containing 0.5 g of adsorbent at various speed (50, 100, 150, 200 and 250 rpm) in an incubation temperature of 30°C. The temperature effect on lead removal was observed by maintaining the temperature at 10, 20, 30, 40, 50 and 60°C keeping pH and agitation speed at an optimized level and adsorbent dose constant, i.e. at 0.5 g. The effect of adsorbent dose was studied by shaking lead solution with a various dose of adsorbent (0.1, 0.25, 0.5, 0.75, 1.0, 1.5, 2.0 and 2.25 g) keeping pH, agitation speed and temperature at optimum condition. % Removal was calculated by using the formula given below in equation (2).

$$\% \text{ Removal} = \frac{C_i - C_e}{C_i} \times 100 \quad \dots(2)$$

Where,

C_i is the initial concentration of metal ions and

C_e is the final concentration of metal ions in milligrams per litre.

The adsorption capacity was determined by using the following formula (3)

$$q_e = \frac{V (C_i - C_e)}{W} \quad \dots(3)$$

Where,

C_i is the initial concentration of lead ions in ppm.

C_e is the final concentration of lead ions in ppm.

V is the volume of solution in litre.

W is the weight of adsorbent in grams taken.

RESULTS AND DISCUSSION

Table 2 is showing the analysis results of sapota peel, which is a basic raw material, used in the current study.

Table 2: Results of dry raw material analysis.

Parameter	Result
Moisture %	16.16 ± 0.08
Fat %	5.19 ± 0.12
Total ash %	2.13 ± 0.16
Protein %	5.13 ± 0.06
Crude fibre %	68.02 ± 0.33
Cellulose %	39.56 ± 0.01
Lignin %	14.07 ± 0.31

All the values are means of triplicate determinations ± standard deviation (SD).

The chemical composition of the peels was found to contain 16.16 per cent (%) moisture, 2.13% ash, 5.19% fat, 5.13% protein, 68.02 % crude fibre, 39.56% cellulose and 14% lignin. As raw material found to contain a good amount of crude fibre, lignin, and cellulose content, it was considered for preparation of adsorbent in present work.

Characterization of Adsorbent

Physicochemical characteristics of prepared adsorbent (activated carbon) were analysed and results of the raw material analysis are represented in Table 2. The yield of carbon was found 68.02%, bulk density was 0.424 g/cm³ while specific conductance was 197.25 ms/M. The calorific value of prepared adsorbent carbon was 7557.23 Cal/g. Moisture content and ash content was 2.77% and 2.51% respectively. Fixed carbon content also showed good results of 71.23% (Table 3).

Crystal Nature Analysis

Crystal nature of adsorbent was analysed by XRD method. Fig. 2 showing XRD peak obtained for developed adsorbent, verifies that the produced material was carbon. The XRD result also confirmed that the obtained adsorbent was a mixture of 69.3% amorphous and 30.7% hexagonal-shaped crystalline crystals.

The SEM photographs of raw sapota peel and activated carbon prepared from sapota peel are shown in Figs. 3(a) and 3(b). It shows that the SEM photographs of raw sapota peel have no pores or very little caves, whereas the SEM photograph of developed carbon shows caves and pores type opening.

Optimization of Adsorption Study

pH optimization: Fig. 4 represents the effect of pH on adsorption. The solution pH is an important parameter that controls the adsorption process. The pH value affects the surface charge of the adsorbent, the degree of ionization and

Table 3: Physicochemical characteristics of the adsorbent.

Parameters	Results
Yield (%)	68.02
Bulk Density (g/cm ³)	0.424
Ash (%)	2.51 ± 0.11
Moisture (%)	2.77 ± 0.06
pH	6.03 ± 0.02
Conductivity (mS/m)	197.25
Calorific value (Cal/g)	7557.23 ± 0.02
Fixed carbon content (%)	71.23 ± 0.09

Values are mean (± SEM) of 3 determinations

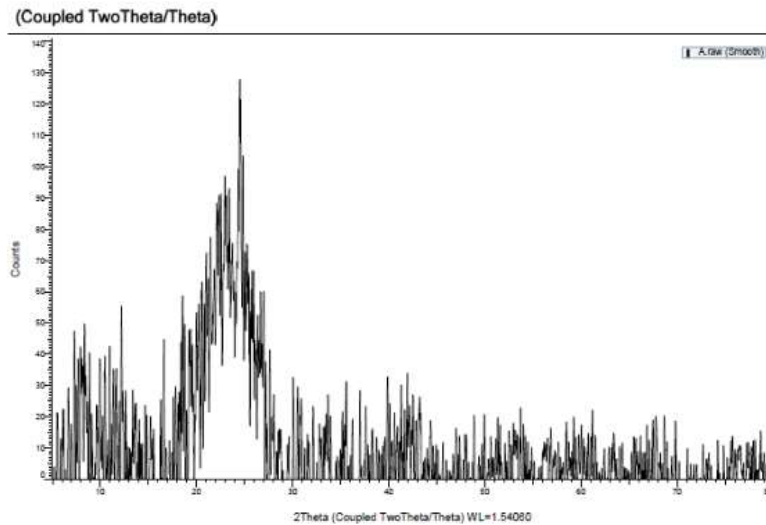


Fig. 2: X-ray diffraction (XRD) results of adsorbents.

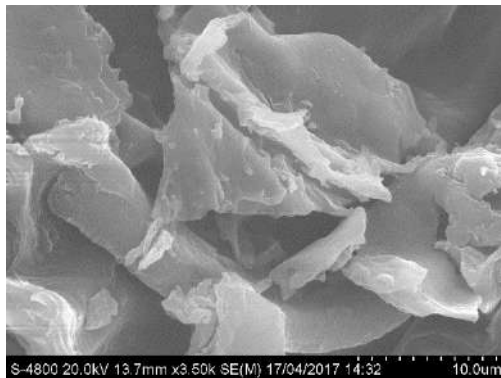


Fig. 3(a): Scanning electron microscope image of raw sapota peel.

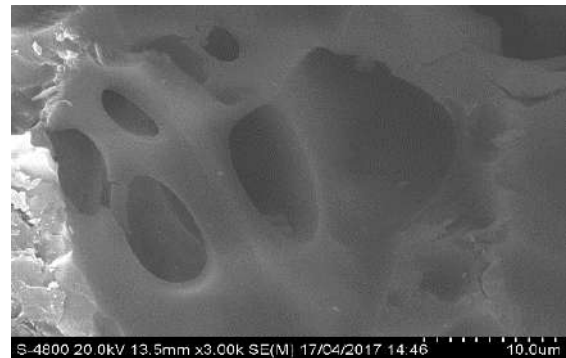


Fig. 3(b): Scanning electron microscope image of adsorbent after treatment.

speciation of the adsorbate during the adsorption process. The adsorption takes place by various mechanisms, and one of the import mechanisms is the electrostatic force of attraction between metal ion (possessing positive charge) and adsorbent surface (carrying negative charge). The pH of the aqueous solution is considered to be the most important parameter affecting the adsorption of the metal ion. From Fig. 3, it was observed as the pH increased the % removal of Pb also increased linearly. The adsorption was very low at pH 2 and 3 (36.96 and 49.08 % removal respectively) and then increased rapidly up to pH 6 (58.56% at pH 4, 72.74% at pH 5, 78.01% at pH 5.5, 96.32 at pH 6). At pH 6 and above the precipitation of Pb ion was observed due to formation of the metal complex as hydroxide. The % removal at pH 6 and above was high (96.32% at pH 6 and 97.16% at pH 7) because of both the combined effect of precipitation as well as of adsorption mechanism (Awwad & Salem 2012). Therefore to support the removal of Pb ion only by adsorption

and not by precipitation, the optimum pH for the adsorption was fixed at 5.5.

Agitation speed optimization: The effect of agitation speed on Pb adsorption is shown in Fig. 5. It was observed that % removal of Pb increased progressively as the agitation speed increased from 50 to 200 rpm. However, the adsorption was

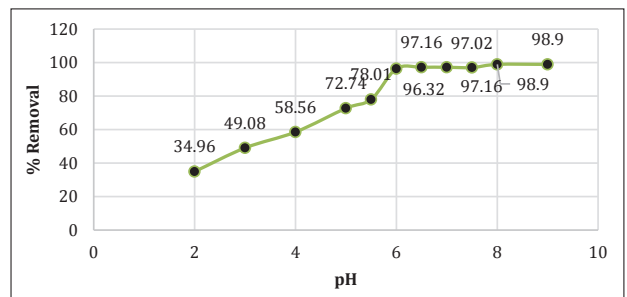


Fig. 4: Effect of pH on lead ions removal.

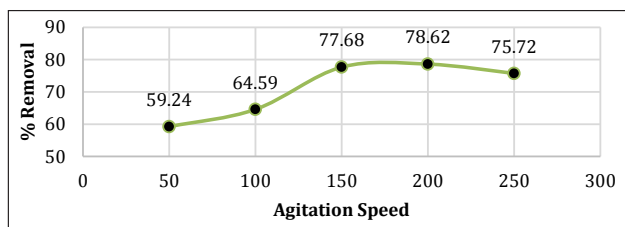


Fig. 5: Effect of agitation speed on lead ions removal.

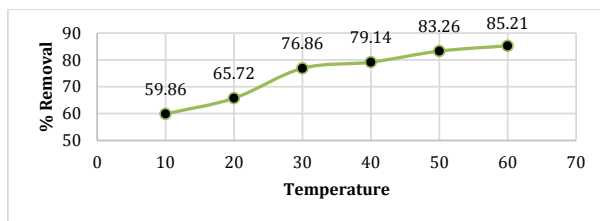


Fig. 6: Effect of temperature on lead ions removal.

found to be at 200 rpm (78.62 % removal) as compared to 150 rpm (77.68 % removal). As the shaking speed 200 rpm was sufficient to ensure the availability of all the binding sites of the adsorbent for the uptake of maximum Pb ion present in solution, the optimized agitation speed was therefore selected as 200 rpm.

Temperature optimization: The effect of temperature on lead ions removal given in Fig. 6, shows the % removal of lead ions. The removal of lead ions was observed to be increasing with an increase in temperature, i.e. from (10°C to 60°C). It means that the adsorption reaction was absorbing

heat to occur. The adsorption of lead ions was therefore considered endothermic. The 60°C temperature was therefore optimized for the said adsorption.

Contact time optimization: Fig. 7 shows the % removal for respective contact, i.e. from 0.5 hr to 4 hr. The adsorption was observed to be increasing with increasing contact time. Initially, the removal of Pb was high due to the availability of large surface area. As the adsorption commenced, with time there was exhaustion of adsorption sites with the adsorbent. Therefore, 3 hr time was optimized for the adsorption process.

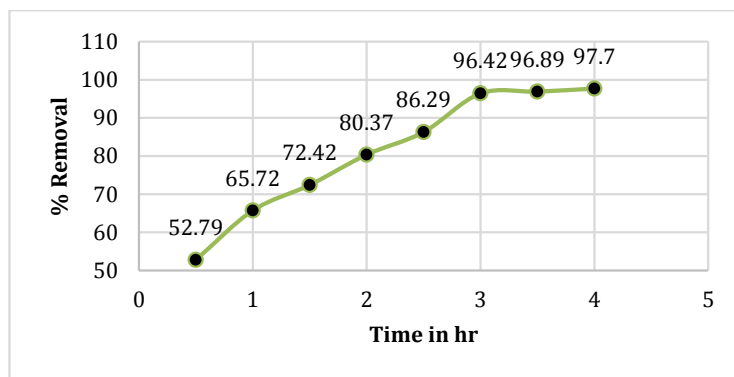


Fig. 7: Optimization of contact time for the removal of lead ions.

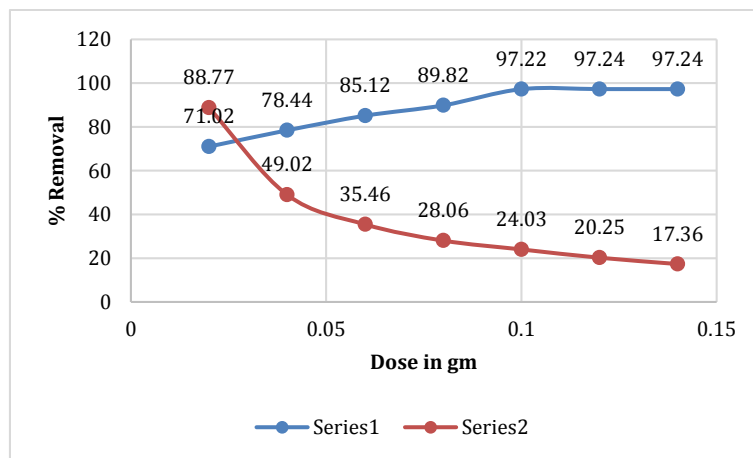


Fig. 8: Effect of dose of lead ions removal.

Adsorbent dose optimization: The effect of adsorbent dose on Pb adsorption is given in Fig. 8, showing % removal with respective adsorbent dose. % removal of Pb was found to be increasing with an increase in the dose of adsorbent, whereas the adsorption capacity found to be decreasing with increasing dose of the adsorbent. The % removal increased with increasing level of adsorbent due to the availability of large surface area which increased more numbers of adsorption sites. Therefore the adsorbent dose of 0.12 g is optimized for the said study of adsorption.

CONCLUSION

The effective metal adsorbent can be developed from Sapota peel by activating it with sulphuric acid. The optimized condition necessary for complete removal of lead ions by the prepared adsorbent was pH - 5.5, agitation speed - 200 revolutions per minute, temperature - 60°C, time - 3 hours and adsorbent dose - 0.12 g. This study can be further useful in designing the process of wastewater treatment for the removal of toxic metals from water particularly lead by adsorption.

REFERENCES

- Awwad, A.M. and Salem, N.M. 2012. Biosorption of copper(II) and lead(II) ions from aqueous solutions by modified loquat (*Eriobotrya japonica*) leaves (MLL). *Journal of Chemical Engineering and Materials Science*, 3(1): 7-17.
- Barakat, M.A. 2011. New trends in removing heavy metal from industrial wastewater. *Arabian Journal of Chemistry*, 4(4): 361-377.
- Chafidz, A., Astuti, W., Hartanto, D., Mutia, A. S. and Sari, P. R. 2018. Preparation of activated carbon from banana peel waste for reducing air pollutant from motorcycle muffler. *MATEC Web of Conferences*, 154: 01021.
- Demirbas, E., Kobya, M., Senturk, E. and Ozkan T. 2004. Adsorption kinetics for the removal of chromium (VI) from aqueous solutions on the activated carbons prepared from agricultural wastes. *Water SA*, 30(4): 533-540.
- Gin, W. A., Jimoh, A., Abdulkareem, A.S. and Giwa, A. 2014. Production of activated carbon from watermelon peel. *International Journal of Scientific & Engineering Research*, 5(2): 66-71.
- Hashem, S., Fayza, K., Foziah, F. and Mashaal, A. 2016. Comparative study on activated carbon prepared from various fruit peels. *International Journal of Innovative Research in Science, Engineering and Technology*, 5(3): 2750-2759.
- Malik, R., Ramteke, D.S. and Wate, S.R. 2007. Adsorption of malachite green on groundnut shell waste based powdered activated carbon. *Waste Manag.*, 27(9): 1129-1138.
- Martin, M.J., Artola, A., Balaguer, M.D. and Rigola, M. 2003. Activated carbons developed from surplus sewage sludge for the removal of dyes from dilute aqueous solutions. *Activated carbons developed from surplus sewage sludge for the removal of dyes from dilute aqueous solutions. Chemical Engineering Journal*, 94(3): 231-239.
- Pachaiyappan, S., Susan, V., Packiyam, R. and Seshadri, S. 2012. Production and characterization of activated carbon from banana empty fruit bunch and *Delonix regia* fruit pod. *Journal of Sustainable Energy & Environment*, 3: 125-132.
- Rajamani, R., Kumar, B., Sujith, A. and Karthick, E. 2018. Activated carbon production from waste biomass. *International Journal of Engineering and Technology (UAE)*, 7: 345-348.
- Xie, Z., Guan, W., Ji, F., Song, Z. and Zhao, Y. 2014. Production of biologically activated carbon from orange peel and landfill leachate subsequent treatment technology. *Journal of Chemistry*, 2014, Article ID 491912.



Numerical Simulation of Effect of Sand Thickness on Soil Evaporation

Wenju Zhao*†, Junhong Hu*, Zongli Li**, Ping Yu* and Changquan Zhou*

*College of Energy and Power Engineering, Lanzhou University of Technology, Lanzhou 730050, China

**General Institute for Water Resources and Hydropower Planning and Design, Ministry of Water Resources, Beijing, 100120, China

†Corresponding author: Wenju Zhao; wenjuzhao@126.com

Nat. Env. & Poll. Tech.
Website: www.neptjournal.com

Received: 27-01-2020

Revised: 22-02-2020

Accepted: 02-05-2020

Key Words:

Soil evaporation

Soil temperature

Sand mulching

Water and heat transport

ABSTRACT

Evaporation from the soil is an important component of evapotranspiration, and mulching greatly affects soil evaporation. We conducted numerical simulations to study the effect of the thickness of sand mulch on soil evaporation. We tested nine treatments: mulching with sand thicknesses of 1, 3, 5, 6, 8, 10, 15 and 20 cm plus an unmulched control (CK). Accumulated evaporation was significantly lower, and the resistance to evaporation was significantly higher, for the mulched treatments than CK. The volumetric soil water content (SWC) was significantly higher for the mulched treatments than CK, but SWC varied little for thicknesses >5 cm. Heating was slower and more uniform for the mulched treatments than for CK. With the increase of the thickness of sand, the temperature transmission was slowed down. The change of soil temperature was not obvious at thicknesses >15 cm. A thickness of 5 cm was the most effective for storing water and preserving heat. Our results provide a theoretical basis and technical guidance for the effective use and management of soil water in farmland in arid regions.

INTRODUCTION

Soil evaporation is the diffusion of soil water into the air in the form of vapour and is a special component of the hydrological cycle and also an important component of evapotranspiration (Morillas et al. 2013). Soil evaporation represents an important loss of soil water on farms in semi-arid regions, a key factor restricting agricultural planting (Mellouli et al. 2000, Danierhan et al. 2013, Lei et al. 2014). Mulching can effectively restrain the evaporation of farmland water, thus preserving soil water (Li 2003, Yuan et al. 2009). Mulching with sand is a common and effective practice with a long history for decreasing soil evaporation (Fairbourn et al. 1973, Nachtergaele et al. 1998, Zhao et al. 2017a). Studying soil evaporation under sand mulching is therefore important for the management of farmland water.

Many studies have reported that adding sand mulching to the soil surface can effectively restrict the evaporation of soil water. Yamanaka et al. (2004) found that resistance to the flow of water vapour increased exponentially with the thickness of a layer of gravel mulch on the soil surface. Gravel-sand mulches are more effective than bare soil in conserving soil water, and the water content increases with mulch thickness (Ma et al. 2011). Kaseke et al. (2012) reported that net and total evaporation were 2.03 and 3.42-fold higher from bare soil than from soil mulched with gravel. Gravel mulch substantially increases resistance to evaporation, and

mulched soils have much lower accumulated evaporation (Diaz et al. 2005, Qiu et al. 2014).

A numerical simulation is an efficient approach for studying changes to soil water and temperature during soil evaporation (Assouline et al. 2014, An et al. 2018, Balugani et al. 2018). The variables can be effectively controlled to ensure the accuracy of the test. Simulations can also address more complex problems than experimentation. VADOSE/W is finite-element software based on a soil-atmosphere model that mainly models infiltration, soil evaporation, temperature and water balance. It has been used with increasing popularity during the last decade for predicting the infiltration and evaporation of soil water (Weeks et al. 2006). Li et al. (2016) found that VADOSE/W could simulate the behaviour of the flow of water in unsaturated loessial soil, and Zhang et al. (2016) found that VADOSE/W could accurately simulate and predict unsaturated flow associated with capillary barrier covers. Zhao et al. (2017b) reported that VADOSE/W could reliably simulate soil evaporation under sand mulching and sand inclusion.

At present, sand mulching only depends on experience and lacks corresponding theoretical guidance in actual production. It is necessary to determine the effect of cover thickness on soil evaporation and temperature to optimize the thickness of the sand layer. The objectives of this study were to determine (i) the effect of sand thickness on soil-wa-

ter content (SWC) and soil temperature during evaporation, and (ii) the optimum mulch thickness. This study provides a theoretical reference for the rational use of land and the transfer of soil water and heat for agricultural production in sand-mulched fields.

NUMERICAL MODEL THEORY

Soil-Atmosphere Boundary Conditions

The key to numerical simulation is to determine reasonable boundary conditions for the model. We chose the flux boundary for the soil surface and the flow-boundary conditions for quantifying surface infiltration and actual evaporation. Wilson et al. (1994) considered atmospheric humidity, wind speed, solar radiation and other conditions at the soil surface and derived an equation for calculating soil-surface evaporation under the conditions of soil-atmosphere coupling:

$$AE = \frac{\Gamma Q_n + \eta E_a}{\Gamma + \eta A} \quad \dots(1)$$

Where, AE is actual vertical evaporative flux (mm/day), Γ is the slope of the curve for saturated vapour pressure versus temperature at mean air temperature (kPa/°C), Q_n is the total net radiation at the soil surface (mm/day), η is a psychrometric constant and $E_a = f(u)e_a(B-A)$, where $f(u) = 0.35(1+0.15 W_a)$, W_a is wind speed (km/h), e_a is the water-vapour pressure of the air above the soil surface (kPa), B is the inverse of atmospheric relative humidity and A is the inverse of the relative humidity at the soil surface.

Soil heat moves through the soil to the atmosphere, and atmospheric heat moves through the surface into the soil, so the temperature of the soil surface represents the temperature boundary condition and can be estimated (for conditions where no snowpack is present) as Wilson (1990):

$$T_s = T_a + \frac{1}{\eta f(u)}(Q_n - AE) \quad \dots(2)$$

Where, T_s is the temperature of the soil surface (°C) and T_a is the temperature of the air above the soil surface (°C).

General Flow Law

VADOSE/W is formulated on the basis that the flow of water, heat, vapour and gas through both saturated and unsaturated soil follows an appropriate form of a Darcy-type flow law:

$$q = ki \quad \dots(3)$$

Where, q is specific flux (m/s), k is conductivity (m/s) and i is a gradient of the potential.

Partial Differential Equations for Water and Heat Flow

The general governing differential equation for two-dimensional seepage can be expressed as:

$$\lambda_t \frac{\partial P}{\partial t} = \frac{1}{\rho} \frac{\partial}{\partial x} \left(D_v \frac{\partial P_v}{\partial x} \right) + \frac{1}{\rho} \frac{\partial}{\partial y} \left(D_v \frac{\partial P_v}{\partial y} \right) + \frac{\partial}{\partial x} \left(k_x \frac{\partial(P/\rho g + y)}{\partial x} \right) + \frac{\partial}{\partial y} \left(k_y \frac{\partial(P/\rho g + y)}{\partial y} \right) + Q \quad \dots(4)$$

Where, P is pressure (kPa), P_v is the vapour pressure of soil water (kPa), k_x is hydraulic conductivity in the x -direction (m/s), k_y is hydraulic conductivity in the y -direction (m/s), Q is the applied boundary flux (m/s), D_v is a coefficient for the diffusion of water vapour through soil (kg m/(kN·s)), y is the elevation head (m), ρ is the density of water (kg/m³), g is the gravitational acceleration (m/s²) and t is time (s).

For the transfer of heat:

$$\lambda_t \frac{\partial T}{\partial t} = L_v \frac{\partial}{\partial x} \left(D_v \frac{\partial P_v}{\partial x} \right) + L_v \frac{\partial}{\partial y} \left(D_v \frac{\partial P_v}{\partial y} \right) + \frac{\partial}{\partial x} \left(k_{tx} \frac{\partial T}{\partial x} \right) + \frac{\partial}{\partial y} \left(k_{ty} \frac{\partial T}{\partial y} \right) + Q_t + \rho c V_x \frac{\partial T}{\partial x} + \rho c V_y \frac{\partial T}{\partial y} \quad \dots(5)$$

Where, ρc is the volumetric specific heat (J/(m³·°C)), k_{tx} is thermal conductivity in the x -direction (W/(m·°C)), k_{ty} is thermal conductivity in the y -direction and is assumed equal to k_{tx} (W/(m·°C)), V_x is the Darcy water velocity in the x -direction (m/s), V_y is the Darcy water velocity in the y -direction (m/s), Q_t is the applied thermal-boundary flux (J/s) and L_v is the latent heat of vaporization (J/kg).

Coupling Heat and Mass Equations

Examination of the equations governing the transfer of heat and mass identified three unknown parameters: pressure (P), temperature (T) and vapour pressure (P_v). The third relationship between these parameters was necessary to solve the equations. This relationship can be described using the widely accepted thermodynamic relationship proposed by Edlefsen & Anderson (1943):

$$P_v = P_{vs} h_r = P_{vs} e^{\Psi g W_v / RT} \quad \dots(6)$$

Where, P_{vs} is the saturation vapour pressure (kPa) of soil water at temperature T , h_r is atmospheric relative humidity, Ψ is the total potential of the liquid-water phase expressed as an equivalent matric potential (m), W_v is the molecular weight of water (0.018 kg/mol), R is the universal gas constant (8.314 J/(mol·K)) and T is the temperature (K).

MODEL FORMULATION

Geometric Model

The experiment simulating evaporation used an indoor test

soil column with bare soil as the control group (CK) and columns with the soil surface mulched with sand 1.0, 3.0, 5.0, 6.0, 8.0, 10.0, 15.0 and 20.0 cm thick, simplified as a two-dimensional numerical model (Fig. 1). The diameter of the soil column was 10 cm, the height of the bare soil was 35.0 cm. The heights of the sand-mulched treatments were thus 36.0, 38.0, 40.0, 41.0, 43.0, 45.0, 50.0 and 55.0 cm. VADOSE/W was used to model the soil columns.

Model Parameters

Clay loam and sand were used in the experiments. The initial state of the soil column and the physical properties of the

soil and sand are presented in Table 1.

Simulated Experimental Conditions

The soil-atmosphere boundary was the upper boundary of the model, which can be used for the exchange of water and heat, and the lower boundary was impermeable. The recharge of groundwater was not included in the model. The relative humidity was 10% during soil-column evaporation, the wind speed was 0 m/s and potential evaporation was 10 mm/d. Each mulching treatment was also tested with two temperature treatments, an endothermic process (ENP) and an exothermic process (EXP), for studying the evaporation

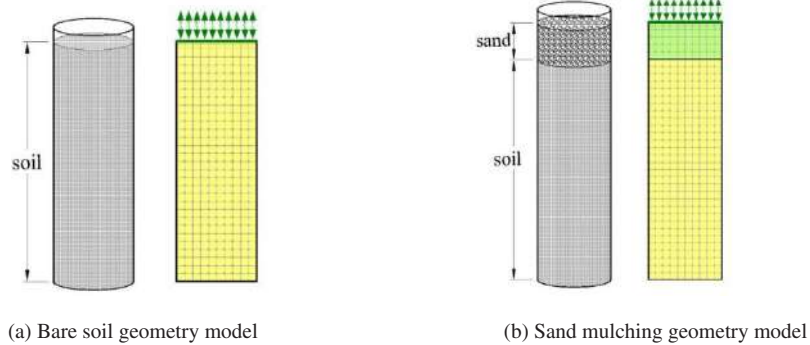


Fig. 1: Geometry model.

Table 1: Physical properties of the soil and sand in the experiment.

Soil texture	Particle size distribution (%)						Initial volume water content (m ³ /m ³)	Residual volume water content (m ³ /m ³)	Hydraulic conductivity (m/d)	Reference
	2.0~1.0 mm	1.0~0.5 mm	0.5~0.2 mm	0.2~0.02 mm	0.02~0.002 mm	<0.002 mm				
Clay loam	0.07	0.38	2.54	36.99	39.16	20.86	0.3636	0.028	0.040	Song et al. (2012)
Sand	10.17	16.58	73.25	—	—	—	0.1532	0.017	17.856	

Table 2: The endothermic and exothermic treatment number in the simulation experiment.

Endothermic number	Sand mulching (cm)	Internal temperature (°C)	Surface temperature (°C)	Exothermic number	Sand mulching (cm)	Internal temperature (°C)	Surface temperature (°C)
ENP ₀	CK	15	30	EXP ₀	CK	30	15
ENP ₁	1.0			EXP ₁	1.0		
ENP ₃	3.0			EXP ₃	3.0		
ENP ₅	5.0			EXP ₅	5.0		
ENP ₆	6.0			EXP ₆	6.0		
ENP ₈	8.0			EXP ₈	8.0		
ENP ₁₀	10.0			EXP ₁₀	10.0		
ENP ₁₅	15.0			EXP ₁₅	15.0		
ENP ₂₀	20.0			EXP ₂₀	20.0		

Notes: ENP_i and EXP_i (i = 0,1,3,5,6,8,10,15,20) represent the endothermic process and exothermic process of CK and the soil of sand thickness with 1,3,5,6,8,10,15,20 cm, respectively.

of sand-mulched soil at different temperatures. ENP had sand surface temperatures of 30°C and soil internal temperature of 15°C, and EXP had sand surface temperatures of 15°C and soil internal temperature of 30°C (Table 2).

RESULTS AND DISCUSSION

Effect of Sand Thickness on Cumulative Evaporation

The effect of sand thickness on cumulative evaporation for ENP and EXP are shown in Fig. 2. Cumulative evaporation for ENP and EXP was significantly higher in CK than the mulched treatments, regardless of sand thickness. This result was consistent with the findings of Wesemael et al. (1996), who also noted that sand mulching reduced evaporation. The reduction of cumulative evaporation decreased as sand thickness increased for all thickness treatments. The reduction was lowest for a thickness of 1 cm, but this thickness still considerably reduced evaporation compared to bare soil, because soil evaporation depends mainly on the capillary water movement (Xing et al. 2019). Mulching with sand can prevent capillary action in soil, so water can only diffuse as vapour, which greatly weakens the evaporation of soil water (Yamanaka et al. 2004).

Cumulative evaporation for CK and mulching with 1, 3, and 5 cm of sand were higher for ENP than EXP by 5.89, 2.1, 0.38 and 0.19 mm, respectively. Cumulative evaporation, however, was similar for ENP and EXP for sand thicknesses >5 cm. Cumulative evaporation decreased as sand thickness increased, consistent with the findings of Diaz et al. (2005), but did not vary significantly in our study for thicknesses >5 cm.

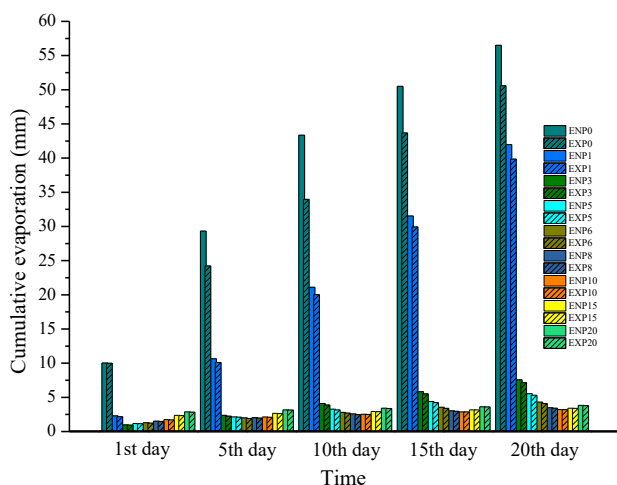


Fig. 2: Cumulative evaporation in ENP and EXP with different treatments.

Yamanaka et al. (2004) and Zhao et al. (2017b) also reported that resistance to evaporation did not increase with mulch thicknesses >5 cm. Wang et al. (2014), however, reported that evaporation was low when mulch thickness was >7 cm. The difference between these two conclusions may be due to different soil textures, particle-size distributions and study methods.

Effect of Sand Thickness on SWC

The effect of sand thickness on SWC for ENP and EXP is shown in Fig. 3. Mean SWC for ENP and EXP was lower in the surface layer (0-6 cm) than in other layers, especially for CK. Mean SWC for CK after evaporation was 0.13 m³/m³ lower in the 0-6 cm than the 18-36 cm layer, and mean SWC in the sand-mulched treatments was lower in the 0-6 cm than the other layers, but the difference was small. Mean SWC was similar among the layers for sand thicknesses >5 cm.

Mean SWC at the end of evaporation was 35.5% lower than initial SWC for CK and 16.5, 4.9 and 2.2% lower for sand thicknesses of 1, 5 and 15 cm, respectively. Mean SWC for each layer was higher for the sand-mulched treatments than CK and was lower for ENP than EXP, especially for CK. These results indicate that sand mulching resists the transfer of water during evaporation, and the thicker the sand, the more the resistance, consistent with the conclusions by Li (2003) and Wang et al. (2004).

Govers et al. (2010) and Modaihsh et al. (1985) also found that the degree of inhibition of evaporation and thus the reduction of water loss depended on the thickness of gravel mulch, with the most effective thicknesses of 5 cm (Govers et al. 2010) and 6 cm (Modaihsh et al. 1985), although Modaihsh et al. (1985) did not test a thickness of 5 cm.

Effect of Sand Thickness on Soil Temperature

The effect of sand thickness on soil temperature for ENP and EXP is shown in Fig. 4. Soil temperature for the treatments gradually increased with evaporation for ENP. Temperature after 15 days was highest for mulches 1 and 3 cm thick and then remained unchanged, while the other groups did not reach the highest temperature after evaporation. Heating was slower and more uniform for the mulched treatments than for CK. With the increase of the thickness of sand, the temperature transmission was slowed down. The change of soil temperature was not obvious at thicknesses >15 cm. Mean temperature after evaporation for ENP was higher for mulches 1, 3 and 5 cm thick than for CK. EXP and ENP were symmetrical, indicating that sand mulching preserved heat, consistent with the conclusions by Xie et al. (2010) and Lü et al. (2013).

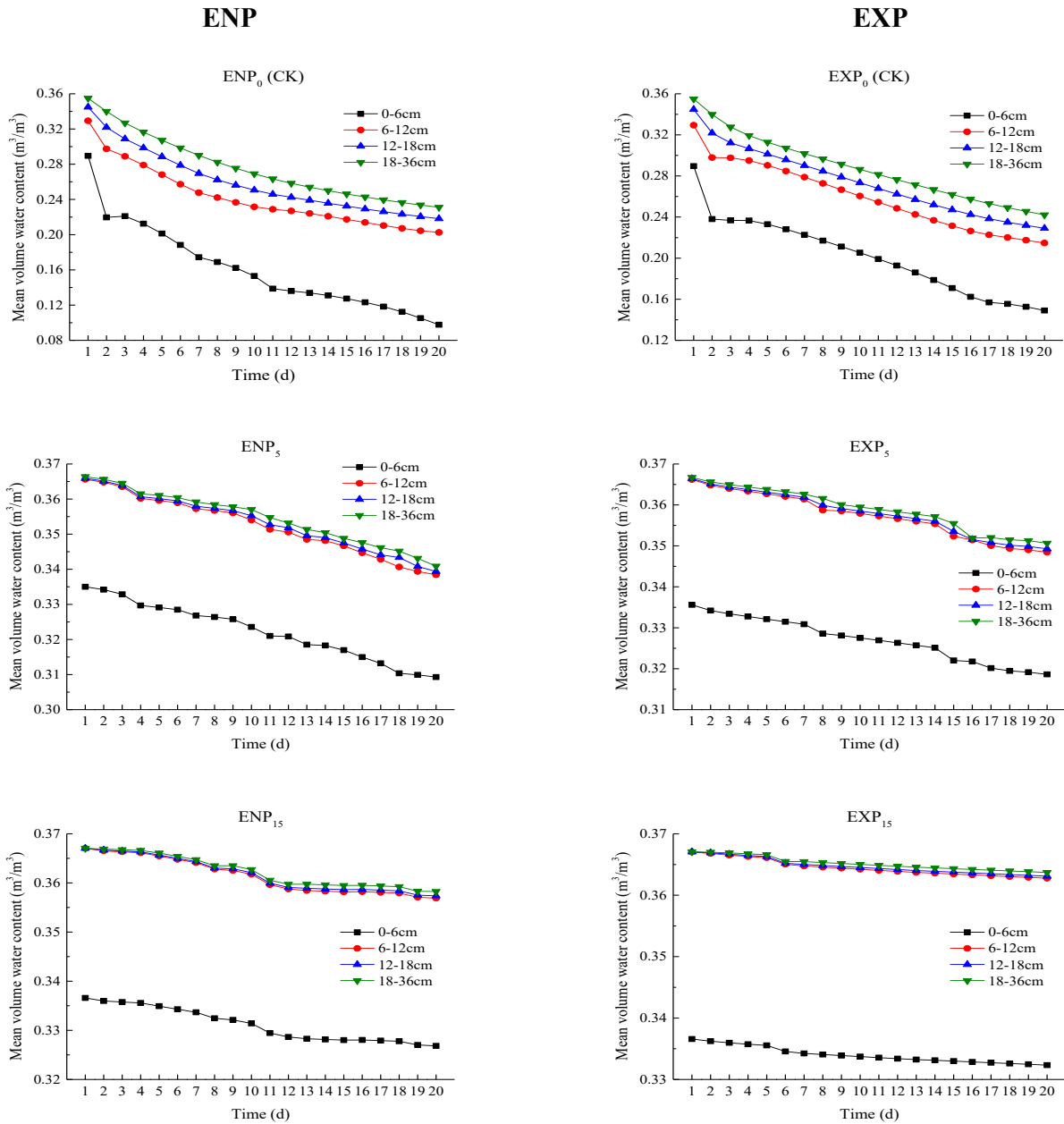


Fig. 3: Mean SWC of different layers in ENP and EXP.

Sand mulching could slow down the temperature transfer of ENP and EXP. Wang et al. (2014) also suggested that the thermal conduction effect of the mulch would lessen when the thickness of mulch is increased beyond a certain limit, which was 15 cm in our study.

CONCLUSION

Numerical simulation is to study the effects of sand thickness on cumulative evaporation, SWC and soil temperature

under endothermic and exothermic soil conditions during evaporation.

- (i) Sand mulching inhibited the movement of soil water during evaporation; the thicker the sand, the stronger the resistance. Cumulative evaporation was lower, and mean SWC was higher, for the mulched treatments than CK. Cumulative evaporation did not vary significantly for sand thicknesses >5 cm, and mean SWC for each layer varied little for ENP and EXP.

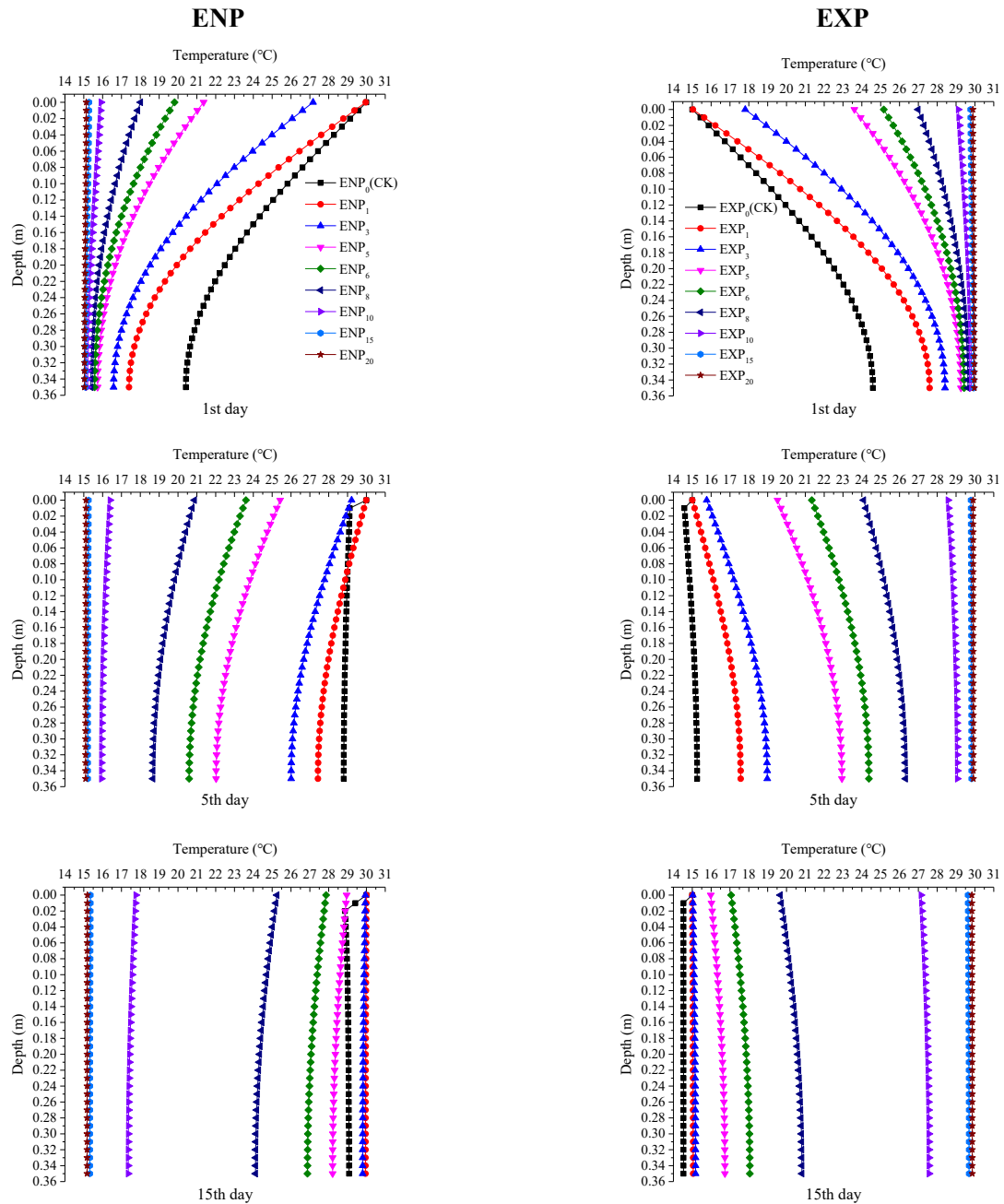


Fig. 4: The soil temperature of different times in ENP and EXP.

- (ii) Sand mulching could slow down the temperature transfer. The changes in soil temperature for both ENP and EXP were slower and more uniform with sand mulching than for CK. The change of soil temperature was not obvious at thicknesses >15 cm. A sand thickness of 5 cm could thus be more effective for storing water and preserving heat.

ACKNOWLEDGMENTS

The research was supported by National Natural Science Foundation of China (51869010), Guidance Program for Industrial Support of Colleges and Universities in Gansu Province (2019C-13), Longyuan Youth Innovation and Entrepreneurship Project and the Lanzhou University of Technology Hongliu first-class discipline funding.

REFERENCES

- An, N., Hemmati, S., Cui, Y. and Tang, C. 2018. Numerical investigation of water evaporation from Fontainebleau sand in an environmental chamber. *Engineering Geology*, 234: 55-64.
- Assouline, S., Narkis, K., Gherabli, R., Lefort, P. and Prat, M. 2014. Analysis of the impact of surface layer properties on evaporation from porous systems using column experiments and modified definition of characteristic length. *Water Resources Research*, 50: 3933-3955.
- Balugani, E., Lubczynski, M.W., van der, Tol.C. and Metselaar, K. 2018. Testing three approaches to estimate soil evaporation through a dry soil layer in a semi-arid area. *Journal of Hydrology*, 567: 405-419.
- Danierhan, S., Abudu, S. and Donghai, G. 2013. Coupled GSI-SVAT model with groundwater-surface water interaction in the riparian zone of Tarim River. *Journal of Hydrologic Engineering*, 18: 1211-1218.
- Diaz, F., Jimenez, C.C. and Tejedor, M. 2005. Influence of the thickness and grain size of tephra mulch on soil water evaporation. *Agricultural Water Management*, 74: 47-55.
- Edlefsen, N.E. and Anderson, A.B.C. 1943. Thermodynamics of soil moisture. *Hilgardia*, 15: 31-298.
- Fairbourn, M.L. 1973. Effect of gravel mulch on crop yields. *Agronomy Journal*, 65: 925-928.
- Govers, G., Vandaele, K., Desmet, P., Poesen, J. and Bunte, K. 2010. The role of tillage in soil redistribution on hillslopes. *European Journal of Soil Science*, 45: 469-478.
- Kaseke, K., Mills, A., Henschel, J., Seely, M.K., Esler, K. and Brown, R. 2012. The effects of desert pavements (gravel mulch) on soil microhydrology. *Pure and Applied Geophysics*, 169: 873-880.
- Lei, H. and Yang, D. 2014. Combining the crop coefficient of winter wheat and summer maize with a remotely sensed vegetation index for estimating evapotranspiration in the north China plain. *Journal of Hydrologic Engineering*, 19: 243-251.
- Li, X. 2003. Gravel-sand mulch for soil and water conservation in the semiarid loess region of northwest China. *Catena*, 52: 105-127.
- Li, P., Li, T. and Vanapalli, S.K. 2016. Influence of environmental factors on the wetting front depth: A case study in the Loess Plateau. *Engineering Geology*, 214: 1-10.
- Lü, H., Yu, Z., Horton, R., Zhu, Y., Zhang, J., Jia, Y. and Yang, C. 2013. Effect of gravel-sand mulch on soil water and temperature in the semiarid loess region of northwest China. *Journal of Hydrologic Engineering*, 18: 1484-1494.
- Ma, Y. and Li, X. 2011. Water accumulation in soil by gravel and sand mulches: influence of textural composition and thickness of mulch layers. *Journal of Arid Environments*, 75: 432-437.
- Mellouli, H.J., Van Wesemael, B., Poesen, J. and Hartmann, R. 2000. Evaporation losses from bare soils as influenced by cultivation techniques in semi-arid regions. *Agricultural Water Management*, 42: 355-369.
- Modaihsh, A.S., Horton, R. and Kikham, D. 1985. Soil water evaporation suppression by sand mulches. *Soil Science*, 139: 357-361.
- Morillas, L., Leuning, R., Villagarcía, L., Garcia, M., Serroano-Ortiz, P. and Domingo, F. 2013. Improving evapotranspiration estimates in Mediterranean drylands: The role of soil evaporation. *Water Resources Research*, 49: 6572-6586.
- Nachtergaele, J., Posen, J. and Van Wesemael, B. 1998. Application and efficiency of gravel mulches in southern Switzerland. *Soil & Tillage Research*, 46: 51-59.
- Qiu, Y., Xie, Z., Wang, Y., Ren, J. and Malhi, S.S. 2014. Influence of gravel mulch stratum thickness and gravel grain size on evaporation resistance. *Journal of Hydrology*, 519: 1908-1913.
- Song, R., Chu, G., Zhang, R., Bai, L. and Yang, J. 2012. Effects of sand mulching on soil infiltration, evaporation, and salt distribution. *Acta Pedologica Sinica*, 49: 282-288.
- Wang, Y., Xie, Z., Li, F. and Zhang, Z. 2004. The effect of supplemental irrigation on watermelon (*Citrullus lanatus*) production in gravel and sand mulched fields in the loess plateau of northwest China. *Agricultural Water Management*, 69: 29-41.
- Wang, Y., Xie, Z., Malhi, S., Vera, C. and Zhang, Y. 2014. Gravel-sand mulch thickness effects on soil temperature, evaporation, water use efficiency and yield of watermelon in semi-arid loess plateau, China. *Acta Ecologica Sinica*, 34: 261-265.
- Weeks, B. and Wilson, G.W. 2006. Prediction of evaporation from soil slopes. *Canadian Geotechnical Journal*, 43: 815-829.
- Wesemael, B.V., Poesen, J., Kosmas, C.S., Danalatos, N.G. and Nachtergaele, J. 1996. Evaporation from cultivated soils containing rock fragments. *Journal of Hydrology*, 182: 65-82.
- Wilson, G.W. 1990. Soil evaporative fluxes for geotechnical engineering problems. Ph.D. dissertation, University of Saskatchewan, Saskatchewan, Canada.
- Wilson, G.W., Fredlund, D.G. and Barbour, S.L. 1994. Coupled soil-atmosphere modeling for soil evaporation. *Canadian Geotechnical Journal*, 31: 151-161.
- Xie, Z., Wang, Y., Cheng, G., Malhi, S., Vera, C., Guo, Z. and Zhang, Y. 2010. Particle-size effects on soil temperature, evaporation, water use efficiency and watermelon yield in fields mulched with gravel and sand in semi-arid loess plateau of northwest China. *Agricultural Water Management*, 97: 917-923.
- Xing, X., Li, X. and Ma, X. 2019. Capillary rise and saliferous groundwater evaporation: effects of various solutes and concentrations. *Hydrology Research*, 50: 517-525.
- Yamanaka, T., Inoue, M. and Kaihotsu, I. 2004. Effects of gravel mulch on water vapour transfer above and below the soil surface. *Agricultural Water Management*, 67: 145-155.
- Yuan, C., Lei, T., Mao, L., Liu, H. and Wu, Y. 2009. Soil surface evaporation processes under mulches of different sized gravel. *Catena*, 78: 117-121.
- Zhang, W., Sun, C. and Qiu, Q. 2016. Characterizing of a capillary barrier evapotranspirative cover under high precipitation conditions. *Environmental Earth Sciences*, 75: 513. <https://doi.org/10.1007/s12665-015-5214-9>.
- Zhao, W., Cui, Z., Zhang, J. and Jin, J. 2017a. Temporal stability and variability of soil-water content in a gravel-mulched field in northwestern China. *Journal of Hydrology*, 552: 249-257.
- Zhao, W., Yu, P., Ma, X., Sheng, J. and Zhou, C. 2017b. Numerical simulation of soil evaporation with sand mulching and inclusion. *Water*, 9: 294. <https://doi.org/10.3390/w9040294>.



Effect of Heat Treatment Process on the Structure and Properties of Nano-TiO₂

R. Q. Gao†, Y. R. Huang, D. Liu and G. T. Li

School of Environmental and Municipal Engineering, North China University of Water Resources and Electric Power, Zhengzhou 450045, China

†Corresponding author: R. Q. Gao; 15838335721@163.com; gaoruqin@ncwu.edu.cn

Nat. Env. & Poll. Tech.
Website: www.neptjournal.com

Received: 11-02-2020

Revised: 02-03-2020

Accepted: 02-05-2020

Key Words:

Sol-gel method
Titanium dioxide
Sintering temperature
Crystal-type transformation
Photocatalysis

ABSTRACT

Nano-TiO₂ was prepared with butyl titanate as a precursor by sol-gel method. The samples were analysed by TG-DTA, X-ray diffraction, TEM and so on to assess the effects of different temperatures on the crystal structure, grain size, and microstructure of nano-TiO₂. Meanwhile, the catalytic effect of heat treatment temperature on the degradation performance of TiO₂ to methyl orange was investigated. The dynamic process of grain growth was preliminarily analysed by Eastman's particle growth theory. The result shows that TiO₂ particle size gradually increases with the heat treatment temperature. At 450 to 550°C, the grain is mainly anatase phase, a mixture of anatase and rutile phase was found at 650°C (mass ratio A:R = 9:1), and the degradation rate of nano-TiO₂ on methyl orange reaches 97.75%. When the calcination temperature exceeds 850°C, TiO₂ particles almost entirely are composed of rutile phase, and the photocatalytic activity decreases significantly. At 730°C, half of the crystalline TiO₂ is transformed from anatase to rutile form. The apparent activation energies of the anatase and rutile crystals of nano-TiO₂ are 18.15 kJ/mol and 42.56 kJ/mol, and the fastest grain growth occurs at 546°C and 1280°C respectively.

INTRODUCTION

Photocatalytic oxidation technology has the prominent characteristics of low energy consumption, strong oxidation ability, mild reaction conditions, and reduced secondary pollution when removing pollutants (Liu et al. 2013, Chekem et al. 2019, Varnagiris et al. 2019). It has the potential for broad application in sewage treatment and air purification (Reddy et al. 2017, Al-Mamuna et al. 2019, Srikanth et al. 2017), and the development of nano-TiO₂ has become an active area of scientific research (Zhang et al. 2014). The sol-gel method can be used to prepare nanometric catalysts with high purity, uniform particle size, and high chemical activity at low temperature, and the reaction conditions are easy to control and the preparation process is relatively simple (Hu et al. 2010, Hakki et al. 2019, Wei et al. 2018). Therefore, the sol-gel method has attracted more attention due to its significant advantages in film formation and doping modification; however, to prepare TiO₂ with high photocatalytic activity, powders with uniform grain size and a low degree of agglomeration are required. Among them, the heat treatment process is one of the important means to promote the transition from amorphous to the crystalline state and adjust the grain size (Liao et al. 2011, Tong et al. 2018, Sun et al. 2017). In this study, TiO₂ particles were synthesised by sol-gel method, and the effects of heat treatment on the crystal structure, particle size, and crystal morphology of TiO₂ particles were

analysed by XRD and TEM, and the reasons for TiO₂ phase transition during heat treatment were preliminarily analysed from the perspective of reaction kinetics, and the effect of heat treatment temperature on the photocatalytic performance of TiO₂ has also been discussed.

MATERIALS AND METHODS

Material: Butyl titanate (Tianjin Comeo Chemical Reagent Co., Ltd), anhydrous ethanol (Tianjin Fuyu Fine Chemical Co., Ltd), glacial acetic acid (Xilong Chemical Co., Ltd), concentrated nitric acid (Kaifeng Huatong Chemical Co., Ltd), polyethylene glycol-4000 (Tianjin Komio Chemical Reagent Co., Ltd), and methyl orange (Tianjin Gold Platinum Orchid Fine Chemicals Ltd) were of analytical purity.

Sample preparation and characterization: At room temperature, 10 mL of butyl titanate was fully mixed with 10 mL of anhydrous ethanol as Solution A. 4 mL of deionised water, 20 mL of glacial acetic acid, 2 mL of concentrated nitric acid, and 10 mL of anhydrous ethanol were fully mixed Solution B. Under vigorous stirring, Solution B was added (drop-wise) into Solution A, then 0.5 g polyethylene glycol-4000 was added (drop-wise), the hydrolysis temperature was maintained at 40°C, and then stirred for 2 h to ensure the sufficient chelation. The product was dried at a constant temperature 60°C for 24 h and ground into a fine powder. After calcination at different temperatures (450

to 850°C) for 2 h, TiO₂ powder can be obtained by cooling in the furnace to room temperature.

Using Al₂O₃ powder as reference material, the composite was subjected to TG-DTA thermal analysis by NETZSCH STA 499C integrated thermal analyser at a rate of 20°C/min in the air; we then used a JEOL 2100 transmission electron microscope (Shimadzu, Japan) to observe the microstructure of the composite. A Bruker D8-advance X-ray diffractometer (Germany) was used for phase analysis of the samples; and ASAP 2010 specific surface area and pore size analyser (Micromeritics Co., USA) was employed to determine the specific surface area and total pore volume.

Photocatalytic activity test: The prepared 100 mg TiO₂ (calcined sample at different temperatures and P_{25}) was added to the 200 mL methyl orange solution with a mass concentration of 10 mg/L. After magnetic stirring in the dark for 30 min, the adsorption and desorption of methyl orange on the surface of TiO₂ particles reached equilibrium. The specimen was then irradiated with UV light for 2 h (the main wavelength is 254 nm, the distance between the light source and the liquid surface is 80 mm), taking 10 mL every 0.5 h. After centrifugation, the supernatant was taken and the absorbance measured at the maximum absorption wavelength of methyl orange at 464 nm to allow calculation of the rate of degradation rate η :

$$\eta = \frac{A_0 - A}{A_0} \times 100\% \quad \dots(1)$$

Where, A_0 and A are the absorbances of the reaction solution before and after a certain illumination time.

RESULTS AND DISCUSSION

DTA-TG Analysis of the Sample

Fig.1 shows the TG-DTA curve of TiO₂ after drying at 105°C. It can be seen from the DTA curve that there is an endothermic peak between about 50°C and 100°C, and the mass loss on the TG curve is about 5%. This peak represents the process of water absorption and drainage within the material. There is an exothermic peak between 300°C and 400°C, and the mass loss on the TG curve is about 12%. This peak is caused by the exotherm caused by the combustion of organic matter in TiO₂ prepared by the sol-gel method. It has been reported in the literature that the powders prepared from titanium alcohols exhibit a strong exothermic peak at 400 to 500°C, which is the result of the transformation from amorphous TiO₂ to anatase-type TiO₂; however, the TiO₂ prepared with butyl titanate in this study only shows a weak similar exothermic peak on the DTA curve. There is a mass loss of 3% on the TG curve between 750°C and 950°C (while

the exothermic peak on the DTA curve is not obvious), as attributed to the phase transition of anatase TiO₂ to rutile TiO₂, indicating that the crystalline transition (anatase-rutile phase) is a slow, gradual process.

XRD Analysis

Fig. 2 illustrates the X-ray diffraction patterns of nano-TiO₂ prepared at different temperatures. It can be seen from the figure that the samples treated at 450°C and 550°C have diffraction peaks near $2\theta = 25.3^\circ, 37.7^\circ, 48.0^\circ, 53.8^\circ, 55.1^\circ,$ and 62.8° , corresponding to the (101), (004), (200), (105), (211) and (204) planes of anatase phase, respectively, indicating that the product is mainly composed of anatase phase; the diffraction peaks are wider than normal, indicating that the particles are small, and the grain development is irregular. Quite sharp diffraction peaks and weak rutile phases appear at 650°C (Daniyal et al. 2019, Zarhri et al. 2020). The characteristic diffraction peaks of the samples treated at 850°C and 950°C were $2\theta = 27.4^\circ, 36.0^\circ, 41.3^\circ, 54.3^\circ,$ and 69.1° corresponding to the (110), (101), (111), (211), and (301) planes of the rutile TiO₂, respectively, indicating that the products are mainly rutile. The phase change temperature of XRD is the heat treatment temperature when half of the

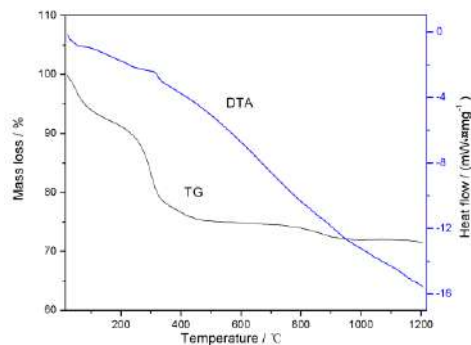


Fig. 1: TG-DTA patterns of TiO₂

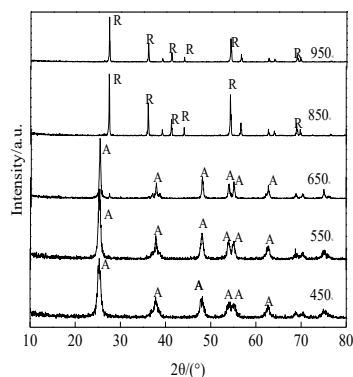


Fig. 2: XRD patterns of TiO₂ at different sintering temperatures.

anatase changes to rutile. As can be seen from Fig. 2, the phase change temperature is about 730°C.

For this TiO₂ the average particle size was estimated using the X-ray width method and the Scherrer formula. The mass percentage X_A of anatase phase in the samples was calculated thus (Zhang et al. 2017, Li et al. 2018): $X_A = I_A / (I_A + 1.265I_R) \times 100\%$, where, I_A is the diffraction intensity of the strongest characteristic peak of the anatase phase on the crystal plane (101), and I_R is the diffraction intensity of the strongest characteristic peak of the rutile phase on the crystal plane (110).

Table 1 gives the anatase and TiO₂ contents at different heat treatment temperatures and the respective grain sizes: with the increase of the heat treatment temperature, in nano-TiO₂, the anatase phase gradually changes to rutile phase. In the temperature range from 450 to 650°C, due to the random grain orientation, there are more grain boundary defects and greater activity, structural relaxation was first produced in the grain boundary during the heating process, and the atomic rearrangement occurred, thus making the structure tend to become more orderly thus reducing the free energy of the grain boundary. Therefore, the apparent grain growth is slow within this temperature range; however, when the temperature rises to 650°C, the structural relaxation process ends, the grain boundary migration

process begins, and the grain size increases rapidly after entering the phase of grain growth and merger of large grains with small grains.

TEM Analysis of Samples

Fig. 3 shows the micro-morphology of nano-TiO₂ at different calcining temperatures. The sample size at 450°C is small (about 10 nm) and the particle boundaries are fuzzy, indicating that TiO₂ has not yet formed complete grains at this calcination temperature, and most of the particles are in an amorphous state. The sample particles at 650°C are intact, the boundary is clear, and the particle size is about 20 nm. The sample particle size at 950°C is coarse (at about 80 nm), the boundary is clear, and the shape is not very regular. The test results are consistent with the analytical results of TiO₂ grain size at different heat treatment temperatures.

BET Analysis of Samples

Table 2 provides the specific surface area and pore structure of the samples at different heat treatment temperatures. As seen from Table 2, the specific surface area and pore volume of the samples prepared at different calcination temperatures decreases with increasing calcination temperature because the increased calcination temperature leads to the gradual growth and refinement of TiO₂ grains and the gradual

Table 1: Crystallite size and anatase content of samples at different heat treatment temperatures.

Sintering temperature/°C	450	550	650	850	950
Mass content/%	95.42	96.86	89.81	0.61	0.16
Diameter/nm	10.21	14.3	21.8	63.58	78.6

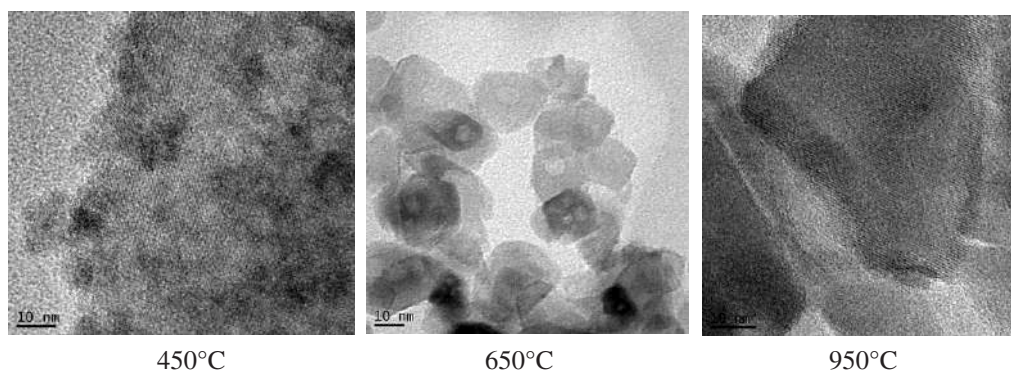


Fig. 3: TEM images of samples at different sintering temperatures.

Table 2: BET surface area and pore structure of samples at different heat treatment temperatures.

Sintering temperature/°C	450	550	650	850	950
$S_{BET}/(m^2 g^{-1})$	223.5	167.8	83.1	35.7	3.4
$V_{pore}/(cm^3 g^{-1})$	0.21	0.18	0.16	0.09	0.03

increase in grain size. When treated at 450°C, nano-TiO₂ had its maximum specific surface area and pore volume and, at thereat, the nano-TiO₂ had not yet formed crystals, remaining in an amorphous state with small particles and uniform pores. In the heat-treatment temperature range from 550°C to 850°C, the specific surface area and pore volume of TiO₂ samples gradually decreased with the increase of temperature after roasting. This is because the increase in heat treatment temperature resulted in obvious growth of TiO₂ grains. At the same time, because the small pores were subjected to greater pressure than the large pores during heat treatment, the pores formed by the accumulation of the original TiO₂ particles collapsed or disappeared, gradually forming larger holes. When the temperature reached 950°C, TiO₂ particles grew to 78.6 nm, the small particles merged to form larger particles, and the pore structure decreased in volume, so the specific surface area of the sample reached 3.4 m² g⁻¹ with a pore volume of 0.03 cm³·g⁻¹.

Phase Change Kinetic Analysis

According to Eastman particle growth theory:

$$D_t^2 - D_0^2 = kt^n \exp(-E/RT) \quad \dots(2)$$

Where, D_t is the particle size of the grain at time t (nm); D_0 is the grain size at the initial time (nm); k is constant; n is the reaction index; E represents the apparent activation energy (J/mol); R is the ideal gas constant, and T is the reaction temperature (K); because the grain size of the initial stage of the preparation is very small, $D_0 \approx 0$, and t^n can also be treated as a constant when the heat treatment time is fixed. Let $K = kt^n$, then formula (2) can be transformed into:

$$D_t^2 = kt^n \exp(-E/RT) = K \exp(-E/RT) \quad \dots(3)$$

$$2 \ln D_t = -E/RT + \ln K \quad \dots(4)$$

For (3) formula dD_t/dT

$$dD_t/dT = K^{1/2} \exp(-E/2RT) \frac{E}{2RT^2} \quad \dots(5)$$

Find the maximum value ($d^2D_t/dT^2 = 0$) for equation (5), and we obtain the temperature at which the fastest grain growth occurred T_{fast}

$$\frac{E}{4R} = T_{fast} \quad \dots(6)$$

Plotting $2 \ln D$ v. $1/T$ gives the straight line shown in Fig. 4, $2 \ln D$ and $1/T$ do not obey a single linear relationship

because the TiO₂ crystal type changes from anatase to rutile at around 730°C, and Section AB of the curve is dominated by the anatase phase, while Section BC is dominated by the rutile phase. The lines of best-fit are $y = -4.3669x + 10.7697$ ($R^2 = 0.9252$), and $y = -10.2403x + 17.2735$ ($R^2 = 0.9667$), respectively. From this, the apparent activation energies E_a and E_r of anatase and rutile grain growth can be calculated (Table 3). The apparent activation energy of rutile TiO₂ grain growth is larger than that of anatase-type growth. On the one hand, due to the early-stage growth, the TiO₂ particle size is small, lattice defects are large, the particle growth is almost spontaneous, and the energy required is very small. Increased heat treatment temperature, fewer lattice defects (lattice development tends to be complete), and TiO₂ grain growth difficulties, all cause the activation energy to increase; on the other hand, as the heat treatment temperature increases further, more of the smaller anatase TiO₂ grains are transformed into rutile phase grains, and some fully-grown grains even undergo a phase transition. Fewer small grains are available for the continuous growth of anatase grains in the samples, so the activation energy of grain growth is greatly increased (Amora et al. 2019, Jithin et al. 2017).

Effect of Heat Treatment Temperature on Photocatalytic Performance of Samples

Fig. 5 demonstrates the heat treatment temperature and its effect on photocatalytic activity: when the heat treatment temperature is between 450 and 650°C, a pairing effect occurs. When the heat treatment temperature is higher than 650°C, the photocatalytic activity of nano-TiO₂ decreases significantly. When the heat treatment temperature reaches 950°C, the removal rate of TiO₂ to the methyl orange aqueous solution is almost zero. This is because, when the calcination temperature is low, the degree of crystallisation degree of anatase is low and the particle size of TiO₂ is small, and the shorter the time required for the photogenic carrier to diffuse from the grain to the surface, the better the photogenic charge separation, and the lower the recombination probability of the electron and hole. On the other hand, the particle size of nano-TiO₂ is smaller, the proportion of surface atoms increases and the light absorption efficiency is higher. In addition, due to the large specific surface area of the nanoparticles and the large contact area upon which the reaction can occur, it is also beneficial to the adsorption of the reactants, which leads to its high photocatalytic activity (Cheng et al. 2016,

Table 3: Apparent activation energies, temperature of fastest grain growth, and crystalline phase transformation of samples.

Samples	$T_{trans}/^{\circ}C$		$T_{fast}/^{\circ}C$		$E_a/kJ. mol^{-1}$	$E_r/kJ. mol^{-1}$
	XRD	DYN	T_a	T_r		
TiO ₂	730		546	1280	18.15	42.57

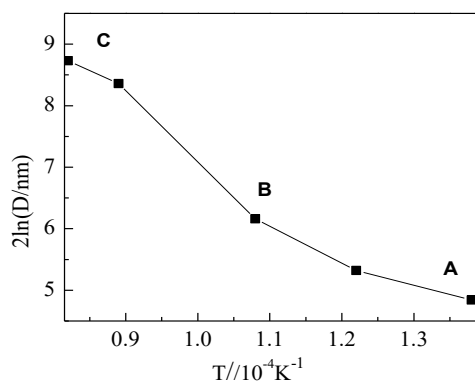


Fig. 4: Relationship between $2\ln D$ and $1/T$.

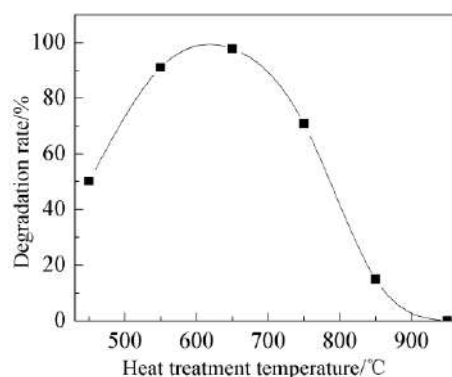


Fig. 5: The influence of sintering temperature on catalytic activity.

Sofiane & Bilel 2016). When calcined at 650°C, the anatase crystal type developed completely, while anatase-type TiO₂ was mixed with a small amount of rutile-type TiO₂, and the removal of methyl orange by photocatalytic degradation reached 97.75% (the photocatalytic activity of the sample prepared in this study, under the same conditions, had a P₂₅ value for methyl orange removal of up to 98.63%).

XRD analysis shows that P₂₅ also contained two crystal types (with 650°C calcined TiO₂ being similar therewith). This kind of mixed crystal TiO₂ is not a simple combination of anatase and rutile, but a thin rutile crystal layer grows on the surface of anatase crystal, forming the so-called “mixed crystal effect”, which not only does not hinder the absorption of light by the “nucleus”, but also because of the rutile TiO₂ having a narrow bandgap ($E_g = 3.0$ eV), it is easily excited by lower-energy light (which has a longer wavelength and is closer to ultraviolet light), owing to the difference in the rutile and anatase band gaps, the hole migrates from the valence band of anatase to the surface rutile valence band, and the photogenerated electron migrates from the rutile conduction band of the surface to the anatase phase, which effectively promotes the separation of photogenerated electron-hole separation in anatase and rutile crystals and reduces the recombination of electron-hole pairs, thus improving the photocatalytic activity of the catalyst (Kuang et al. 2020, Arbuj et al. 2010, Yu et al. 2003).

As the temperature continues to rise, the amount of rutile phase continues to increase, TiO₂ particles grow rapidly, and the specific surface area decreases. Furthermore, rutile-anatase high-temperature transition occurs, treatment factors caused by the difference in the surface state of the material arise, surface-active group reduction occurs (on the anatase-type TiO₂ surface with catalytically active groups OH⁻ and Ti³⁺), the TiO₂ surface undergoes a dehydrogenation reaction and the surface hydroxyl groups are lost, whereas hydroxyl groups can capture the photogenerated holes to form

highly-oxidised hydroxyl radicals ($\cdot\text{OH}$). In addition, rutile TiO₂ has poor adsorption capacity for O₂, a lower specific surface area, and photogenic electrons and holes are easily compounded. Moreover, the rutile type material has a low ability to adsorb oxygen, and photo-generated electrons are difficult to remove therefrom, which significantly reduces its photocatalytic performance (Xiao et al. 2010).

CONCLUSIONS

TiO₂ was prepared by sol-gel method, and the effects of heat treatment temperature on TiO₂ crystal structure, particle size, and photocatalytic performance were investigated. In addition, the phase transition of grains was analysed from the perspective of reaction kinetics. The results show that, with increasing calcination temperature, TiO₂ crystallisation was gradually completed, the grains gradually grew in size, and at 450 to 550°C, a thermally stable region was reached, the energy was mainly used for atomic rearrangement, reducing both the number and size of grain boundary defects and reducing the grain boundary free energy, so the particle size increase was small; beyond 650°C, the energy was used for grain boundary migration, and the grains grew rapidly: some grains in the sample were transformed from an anatase phase to a rutile phase. The rate of degradation of methyl orange solution reached a maximum when calcined at 650°C for 2 h. At this time, TiO₂ contained mixed anatase and rutile phases; this indicated that the mixed crystal effect of TiO₂ can effectively inhibit photogenic electron-hole recombination and that the sample has a better photocatalytic performance than single anatase-TiO₂.

ACKNOWLEDGEMENTS

This work was financially supported by the Natural Science Foundation of China (Grant No. 50708037), the National Science Fund for Excellent Young Scholars of China (Grant No. 51522402), and the Fund for Science and

Technology Research Projects of Henan Province (Grant No. 182102311080).

REFERENCES

- Al-Mamuna, M. R., Kaderb, S., Islam, M. S. and Khan, M. Z. H. 2019. Photocatalytic activity improvement and application of UV-TiO₂ photocatalysis in textile wastewater treatment: A review. *J. Environ. Chem. Eng.*, 7(5): 1-17.
- Amora, C. O., Elghnija, K., Virilan, C. T., Pui, A. and Elaloui, E. 2019. Effect of dysprosium ion (Dy³⁺) doping on morphological, crystal growth and optical properties of TiO₂ particles and thin films. *Physica B: Condens. Matter*, 560: 67-74.
- Arbuj, S. S., Hawaldar, R. R., Mulik, U. R., Wani, B. N., Amalnerkar, D. P. and Waghmode, S. B. 2010. Preparation, Characterization and photocatalytic activity of TiO₂ towards methylene blue degradation. *Mater. Sci. Eng.: B*, 168(1/2/3): 90-94.
- Chekem, C. T., Goetz, T., Richardson, Y., Richardson, Y., Plantarda, G. and Blinc, J. 2019. Modelling of adsorption/photodegradation phenomena on AC-TiO₂ composite catalysts for water treatment detoxification. *Catal. Today*, 328(15): 183-188.
- Cheng, P. F., Wang, Y. L., Xu, L. P., Sun, P., Su, Z. S., Jin, F. M., Liu, F. M., Sun, Y. F. and Lu, G. Y. 2016. High specific surface area urchin-like hierarchical ZnO-TiO₂ architectures: Hydrothermal synthesis and photocatalytic properties. *Mater. Lett.*, 175: 52-55.
- Daniyal, M., Akhtar, S. and Azam, A. 2019. Effect of nano-TiO₂ on the properties of cementitious composites under different exposure environments. *J. Mater. Res. Technol.*, 8(6): 6158-6172.
- Hakki, H. K., Allahyari, S., Rahemi, N. and Tabihi, M. 2019. Surface properties, adherence, and photocatalytic activity of sol-gel dip-coated TiO₂-ZnO films on glass plates. *Comptes Rendus Chimie*, 22(5): 392-405.
- Hu, Y. L., Liu, H. F. and Guo, X. P. 2010. Effect of water consumption on preparation of nitrogen-doped nanometer titanium dioxide by sol-gel method. *J. Silic.*, 38(1): 97-104.
- Jithin, M., Saravanakumar, K., Ganesan, V., Reddy, V.R., Razad, P. M., Patidar, M. M., Jeyadheepan, K., Marimuthu, G., Sreelakshmi, V. R. and Mahalakshmi, K. 2017. Growth, mechanism and properties of TiO₂ nanorods embedded nanopillar: Evidence of lattice orientation effect. *Superlattices and Microstruct.*, 109:145-153.
- Kuang, J. Y., Xing, Z. P., Yin, J. W., Li, Z. Z., Tan, S. Y., Li, M., Jiang, J. J., Zhu, Q. and Zhou, W. 2020. Ti³⁺ self-doped rutile/anatase/TiO₂(B) mixed-crystal tri-phase heterojunctions as effective visible-light-driven photocatalysts. *Arab. J. Chem.*, 13: 2568-2578.
- Li, Y., Ding, M. J. and Li, R. 2018. Hydrothermal preparation of clay-based TiO₂ and photocatalytic property thereof. *Inorganic Chem. Ind.*, 50(12): 75-82.
- Liao, Y. L., Que, W. X., Tang, Z. H., Wang, W. J. and Zhao, W. H. 2011. Effects of heat treatment scheme on the photocatalytic activity of TiO₂ nanotube powders derived by a facile electrochemical process. *J. Alloys and Compd.*, 509: 1054-1059.
- Liu, Z.C., Zheng J. T. and Zhao, D. F. 2013. Metal ion doping modified nano-TiO₂ band structure and photocatalytic properties. *Silic. J.*, 41(3): 402-408.
- Reddy, P. L., Kavitha, B., Reddy, P. A. K. and Kim, K. H. 2017. TiO₂-based photocatalytic disinfection of microbes in aqueous media: A review. *Environ. Res.*, 154: 296-303.
- Sofianea, S. and Bilel, M. D. 2016. Effect of specific surface area on photoelectrochemical properties of TiO₂ nanotubes, nanosheets and nanowires coated with TiC thin films. *J. Photochem. Photobiology A: Chem.*, 324: 126-133.
- Srikanth, B., Goutham, R., Narayan, R. B., Ramprasad, A., Gopinath, K.P. and Sankaranarayanan, A.R. 2017. Recent advancements in supporting materials for immobilised photocatalytic applications in waste water treatment. *J. Environ. Manage.*, 200: 60-78.
- Sun, M. L., Qian, H. Y. and Chen, J. 2017. Preparation and photocatalytic performance of TiO₂ thin films. *Bull. Chin. Ceram. Soc.*, 36(8): 2595-2599.
- Tong, Z., Wang, J. Y. and Fan, L. 2018. Effect of heat treatment on TiO₂ thin film and its photocatalytic performance. *J. Synth. Crystals*, 47(9): 1764-1769.
- Varnagir, S., Medvids, A., Lelis, M., Milcusa, D. and Antuzevics, A. 2019. Black carbon-doped TiO₂ films: Synthesis, characterization and photocatalysis. *J. Photochem. Photobiology A: Chem.*, 382(1): 1-9.
- Wei, X., Cai, H. D., Feng, Q. G., Liu, Z., Ma, D. C., Chen, K. and Huang, Y. 2018. Synthesis of co-existing phases Sn-TiO₂ aerogel by ultrasonic-assisted sol-gel method without calcination. *Mater. Lett.*, 228(1): 379-383.
- Xiao, N., Li, Z., Liu, J. W. and Gao, Y. 2010. Effects of calcination temperature on the morphology, structure and photocatalytic activity of titanate nanotube thin films. *Thin Solid Films*, 519(1): 541-548.
- Yu, J. G., Yu, H. G., Cheng, B., Zhao, X. J., Yu, J. C. and Ho, W. K. 2003. The effect of calcination temperature on the surface microstructure and photocatalytic activity of TiO₂ thin films prepared by liquid phase deposition. *J. Phys. Chem. B*, 107(50): 13871-13879.
- Zarhri, Z. K., Cardoso, M. A. A., Ziat, Y. N., Maryama, H., Omar, E. R., Julio, C. C. A. and David, A. A. 2020. Synthesis, structural and crystal size effect on the optical properties of sprayed TiO₂ thin films: Experiment and DFT TB-MBJ. *J. Alloys Compd.*, 819: 1-6.
- Zhang, Y. L., Yang, J. and Yu, X. J. 2017. Preparation, characterization, and adsorption-photocatalytic activity of nano TiO₂ embedded in diatomite synthesis. *Rare Met.*, 991-987 (12)36.
- Zhang, Y. L., Zhao, C. and Wu, C. 2014. Zn²⁺ preparation and properties of doped titanium dioxide composite films. *Journal of IOL*, 43(1): 19-24.



Studies on Engineering and Microstructure Properties of Chromium(VI)-Contaminated Soil

Yuan Yuan Li* and Ting Ting Zhang**(***)[†]

*Qingdao University of Technology, Qingdao, 266033, China

**Wisdri City Environment Protection Engineering Limited Company, Wuhan, 430205, China

***Wuchang Shouyi University, School of Urban Construction, Wuhan 430064, China

[†]Corresponding author: Ting Ting Zhang; ttz_dshb@163.com; ztt_cersm@163.com

Nat. Env. & Poll. Tech.

Website: www.neptjournal.com

Received: 02-02-2020

Revised: 25-02-2020

Accepted: 02-05-2020

Key Words:

Cr(VI)-contaminated soil
Physicochemical properties
Engineering properties
Microstructure

ABSTRACT

Hexavalent chromium [Cr(VI)]-contaminated soils have introduced a serious problem in China. Cr(VI) is hazardous to both the environment and public health and may degrade the engineering properties of soils. Accordingly, the effects of Cr(VI) on the physicochemical, mechanical, and microstructure properties of Chinese clay were investigated in this study. Results show that Cr(VI) had a considerable negative effect on the physicochemical, mechanical, and microstructure properties of soil. Specifically, Cr(VI) changed the physicochemical properties and degraded the mechanical properties of soil, led to the aggregation of soil particles, and created a large void space. Cr(VI) also changed the mineral composition of the soil and converted clay minerals into calcite. The changes in the microstructure and mineral composition of the soil were the primary reasons for the differences in the engineering properties of Cr(VI)-contaminated soil.

INTRODUCTION

The heavy metal contamination of soil in China has become severe due to the improper waste disposal practices and accidental chemical spills in the country (Wei et al. 2015). Heavy metals are hazardous to the environment and public health and may degrade the mechanical properties of soils, thereby placing engineering safety at risk (Du et al. 2013). Many studies have shown that the engineering properties of contaminated soils are closely related to the type and content of heavy metals. Zhang et al. (2014) studied the permeability behaviour of copper-contaminated clay and set a 0.5 g/L threshold for the influence of copper concentration on permeability. They found that the hydraulic conductivity and void ratio of contaminated clay decrease when the copper concentration is lower than 0.5 g/L. Li et al. (2015) showed that Pb(NO₃)₂ solutions can increase the maximum dry density and cohesion of typical clay in China yet reduce its optimum moisture content and swelling. This trend becomes more obvious at higher Pb(NO₃)₂ concentrations. Liu et al. (2016) showed that Zn(NO₃)₂ solutions decrease the void ratio and compression index of kaolin. However, when the Zn(NO₃)₂ solutions exceed 0.02 mol/L, the void ratio of kaolin is nearly unchanged. Chen et al. (2014) studied the strength properties and development of zinc- and cadmium-contaminated soil and found that zinc and cadmium degrade the strength of

the soil and that the strength of cadmium-contaminated soil is significantly lower than that of zinc-contaminated soil.

Previous studies show that the engineering properties of contaminated soils are closely related to the type and content of heavy metals. Many of these studies have focused on the engineering properties of soil contaminated with low-valence heavy metals, such as lead (Pb), zinc (Zn), copper (Cu), and cadmium (Cd), yet no peer-reviewed study has examined the engineering properties and microstructure development of soil contaminated with high-valence heavy metals, such as chromium (Cr), and no consensus has been reached regarding the effect of these high-valence heavy metals on the engineering properties and microstructure of soil. Systematical analyses on this subject are also lacking.

Hexavalent chromium [Cr(VI)] has become a source of environmental concern in China and has been classified by Chinese officials as the first major heavy metal that needs to be managed and controlled (Zhang et al. 2018). Accordingly, a series of tests, including pH, specific gravity, particle size distribution, compaction, strength, permeability, and shear strength tests, were conducted in this paper to study the effect of different content of Cr() on the engineering and microstructure properties of Chinese clay. The changes in the structure of Cr(VI)-contaminated soil were interpreted by performing nitrogen adsorption (BET), scanning electron

microscope (SEM) observations, and detailed mineralogical (XRD) tests. The findings of this work can facilitate the remediation and reuse of Cr(VI)-contaminated soil.

MATERIALS AND METHODS

Cr(VI)-Contaminated Soil

Given its representativeness and repeatability, Cr(VI)-contaminated soil simulated by Chinese clay and $K_2Cr_2O_7$ was used in this study (Zhang et al. 2019). Soil samples with a Cr(VI) content of 0, 500, 1000, 5000, and 10000 mg/kg were used to represent the universal concentration for Cr(VI)-contaminated soil in China (Zhang et al. 2009, Wang et al. 2014). The contaminated soil was mixed evenly and braised for 180 days under standard curing conditions (20°C, 95% humidity) to allow $K_2Cr_2O_7$ and the soil to react adequately and to obtain an ageing contaminated soil.

Methods

The Cr(VI)-contaminated soil was subjected to pH, specific gravity, compaction, strength, permeability, and shear strength tests following the relevant Chinese standards (GB/T50123,1999). For each test, the samples were prepared in triplicate and were denoted by C=0, 500, 1000, 5000, and 10000 mg/kg, where C represents their Cr(VI) content.

The changes in the crystalline phases of the Cr(VI)-contaminated soil was determined by using a D8 Advance X-ray diffractometer, whereas the changes in the surface area and pore size were determined by using a surface area analyser (Nova 1000e series, USA). Microscopic observations were obtained by SEM.

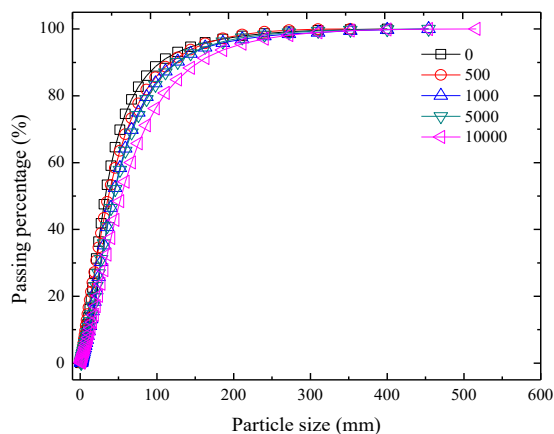


Fig. 2: Effect of chromium content on the grain-size distribution of the soil.

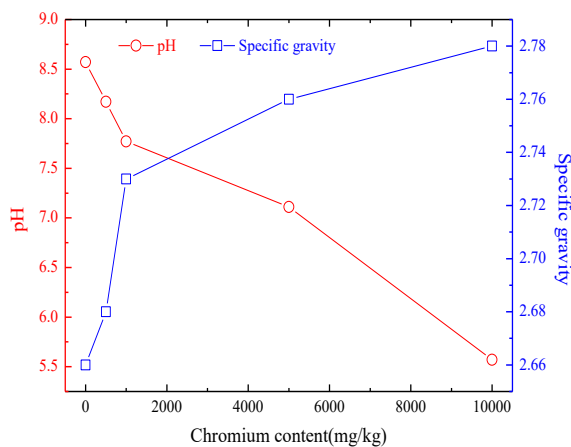


Fig. 1: Effect of chromium content on the pH and specific gravity of soil.

RESULTS AND ANALYSIS

pH and Specific Gravity

The effect of Cr(VI) content on the pH and specific gravity of the soil is shown in Fig. 1. An increase in Cr(VI) content from 0 mg/kg to 10000 mg/kg increased the specific gravity of the soil from 2.66 to 2.78 and reduced its pH from 8.57 to 5.51. The increase in soil specific gravity was attributed to the reaction of Cr(VI) with the clay mineral of soil via ion exchange and complex reaction, which embedded the Cr(VI) onto the soil particle surface and released low-density organic matter (Wu et al. 2014). Meanwhile, the reduction in pH could be attributed to the release of H^+ during the ion exchange between the soil particle and Cr(VI) (Miranda-Trevino et al. 2003).

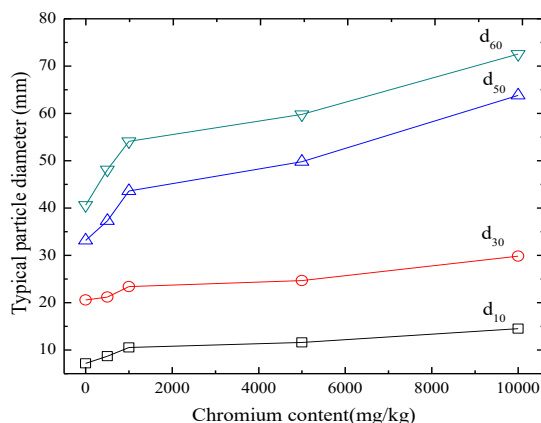


Fig. 3: Effect of chromium content on the typical particle diameter of soil.

Particle Size

The variations in the grain-size distribution and typical particle diameter of soil with different Cr(VI) contents are shown in Figs. 2 and 3. The soil particle size increased along with Cr(VI) content, which subsequently shifted the particle size distribution curve rightward and increased the typical soil particle diameter. The d_{10} , d_{30} , d_{50} , and d_{60} of the soil increased from 7.18, 20.58, 33.21, and 40.63 mm to 14.53, 29.84, 63.84, and 72.53 mm, respectively. The changes in the soil particle size could be attributed to the aggregation of soil permeated with Cr(VI) due to reduced DDL thickness of the soil particles (Morvan et al.1994).

Compaction

The effect of Cr(VI) content on the maximum dry density and optimum moisture content of the soil is shown in Fig. 4. The experimental data indicated that Cr(VI) could increase the maximum dry density of soil and decrease its optimum moisture content. The maximum dry density increased from 1.68 g/cm³ to 1.73 g/cm³, whereas the optimum moisture content decreased from 23.63% to 21.13%. Cr(VI) also resulted in the aggregation of soil particles, thereby increasing the maximum dry density. The decrease in soil particle size could also be attributed to the reduced DDL thickness of the soil particle, water holding capacity, and optimum water content (Li et al. 2015).

Unconfined Compression Strength

The effect of Cr(VI) content on the soil stress-strain curves is shown in Fig. 5. Generally, the shapes of these stress-strain curves considerably differed between low and high Cr(VI) content conditions. To illustrate, when the Cr(VI) content was less than 500 mg/kg, the contaminated soils exhibited brittleness as manifested in the rapid reduction in their post-peak stress along with an increasing strain. Similar behaviour

has been reported in natural soils (Horpibulsk 2011). When the Cr(VI) content exceeded 500 mg/kg, the contaminated soil behaved similarly to a ductile material with a gradual decrease in its post-peak stress along with a decreasing strain. Fig. 6 shows the variations in unconfined compression strength (q_u) and failure strain (ϵ_f) along with Cr(VI) content. The q_u of the soil decreased from 0.44 MPa to 0.21 MPa, whereas its ϵ_f decreased from 2.84% to 8.35%. q_u slightly changed when the Cr(VI) content was less than 500 mg/kg yet considerably decreased when the Cr(VI) content exceeded 500 mg/kg. The lowest q_u and highest ϵ_f were obtained when the Cr(VI) content increased to 10000 mg/kg. Fig. 6 shows that the Cr(VI) content is a crucial factor that controls the strength of Cr(VI)-contaminated soils. Therefore, at a specific curing time, a linear function indicated by Eqs. (1) and (2) was used to describe the relationship between the strength properties (q_u and ϵ_f) and Cr(VI) content of the soil.

$$q_{uc} = -2.12C + q_0 \quad \dots(1)$$

$$\epsilon_{fc} = 5.47C + \epsilon_0 \quad \dots(2)$$

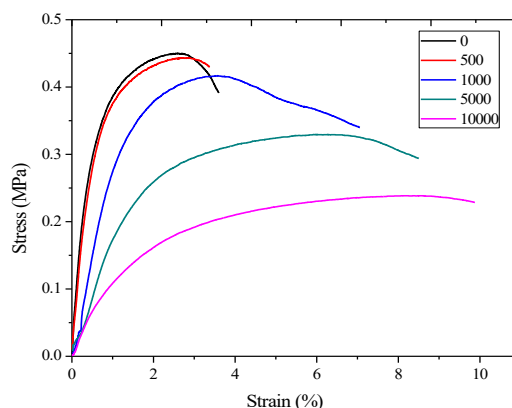


Fig. 5: Effect of chromium content on the stress-strain curves of soil.

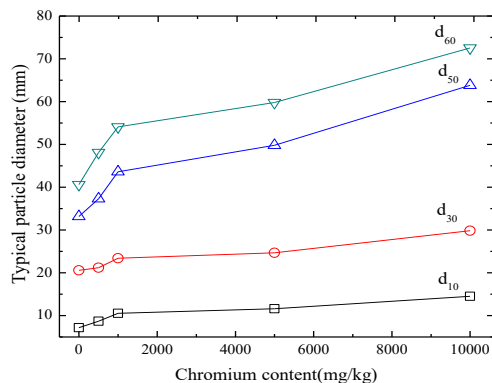


Fig. 4: Effect of chromium content on the maximum dry density and optimum moisture content of the soil.

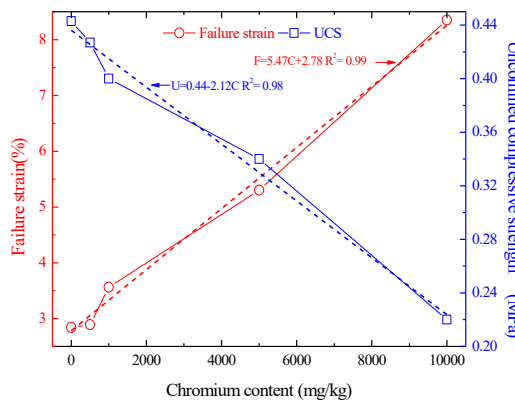


Fig. 6: Effect of chromium content on the unconfined compression strength and failure strain of soil.

Where C is the soil Cr(VI) content, ϵ_{fc} is the failure strain of the soil with Cr(VI) content, ϵ_0 is the failure strain of the Cr(VI)-free soils and is set to 2.78% in this paper, q_0 is the unconfined compressive strength of the Cr(VI)-free soil soils and is set to 0.44 MPa in this paper, and q_{uc} is the unconfined compressive strength of the soils with Cr(VI) content.

The changes in the strength properties of the soil could also be attributed to the Cr(VI) brought about by the aggregation of soil particles, which lowered the cementing strength between the soil particles and reduced the stability of the soil (Zha et al. 2014). Chen et al. (2014) found that the q_u of soil contaminated with 10000 mg/kg and 50000 mg/kg Pb was 15% and 50% lower than that of natural soil, respectively. Therefore, Cr(VI) considerably degraded the mechanical properties of the soil with respect to Pb.

Permeability

Fig. 7 shows the hydraulic conductivity of soil with different Cr(VI) contents. As the Cr(VI) content increased from 0 mg/kg to 10000 mg/kg, the hydraulic conductivity of the samples changed from 2.1×10^{-8} cm/s to 1.5×10^{-7} cm/s, which could be attributed to the reduced DDL thickness resulting from the aggregation of soil particles and shrinkage of soil clusters. Shrinkage can result in cracking and greatly increase hydraulic conductivity (Jo et al. 2005).

Shear Strength

The effect of Cr(VI) content on the shear strength of the soil is shown in Fig. 8 and Table 1. The shear strength and cohesion of the soil decreased along with an increasing Cr(VI) content and decreasing angle of internal friction. Cr(VI) can decrease the shear strength of soil mainly due to its degrading effects on cohesion. The aggregation of soil particles reduced the amount of soil contact points, thereby allowing the soil particles to move freely and decreasing both

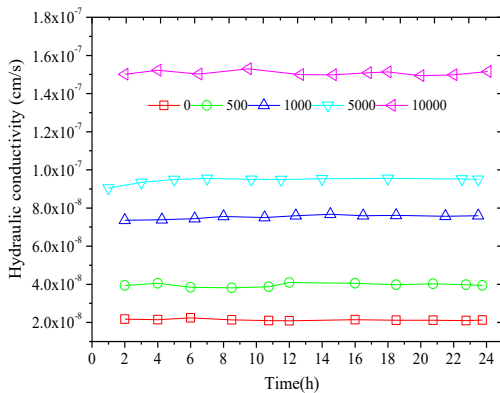


Fig. 7: Effect of chromium content on the hydraulic conductivity of the soil.

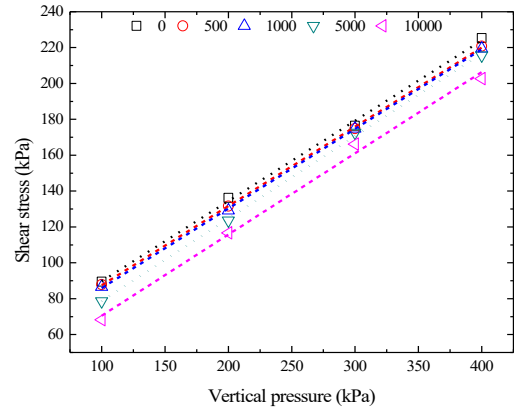


Fig. 8: Effect of chromium content on the shear strength of the soil.

Table 1: Effect of chromium content on the cohesion and angle of internal friction of soil.

Chromium content (mg/kg)	Cohesion (kPa)	Angle of internal friction
0	45.92	23.12°
500	43.91	23.35°
1000	41.48	23.55°
5000	35.63	23.82°
10000	25.19	24.76°

shear strength and internal friction. Cho et al. (2007) reported that the internal friction angle of soil is closely related to the shape of soil particles and that friction angle increases along with the irregularity of soil particles. By changing the soil grain size distribution and increasing the irregularity of soil particles, Cr(VI) increased the friction angle.

Nitrogen Adsorption

The effect of Cr(VI) content on the surface area and mean pore size of the soil is shown in Fig. 9. Cr(VI) increased the

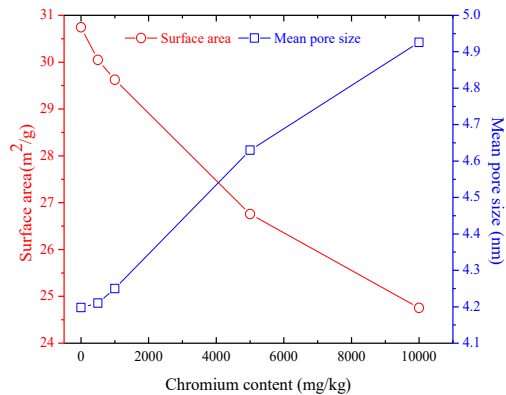


Fig. 9: Effect of chromium content on surface area and mean pore size of soil.

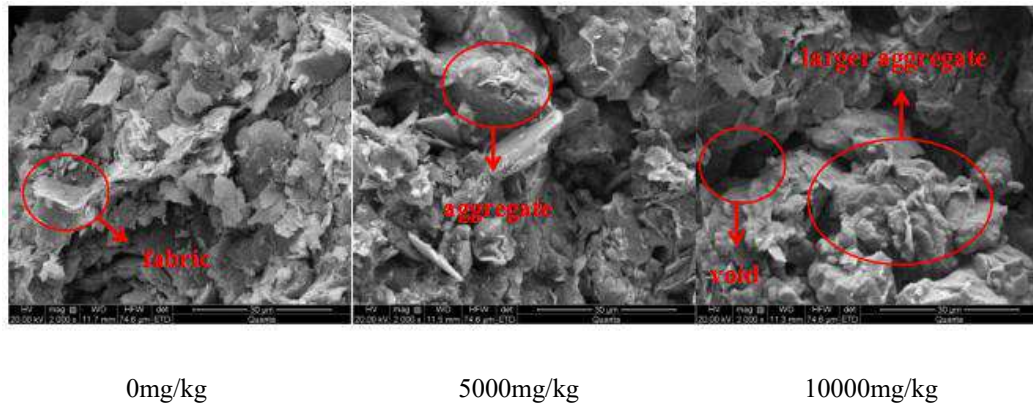


Fig. 10: Effect of chromium content on SEM pictures of soil.

mean pore size of the soil from 4.2 nm to 5.9 nm and reduced the surface area from 30.7 m²/g to 24.8 m²/g by aggregating the soil particles and shrinking the soil clusters. Therefore, a change in soil porosity could increase the void ratio, which in turn could increase the soil permeation rate.

SEM Observations Analysis

Fig. 10 shows the SEM images of soil samples with different Cr(VI) contents. The Cr(VI)-free soil generally had small particles with compact fabric forms. These particles mainly demonstrated a plane-to-plane contact and had many small pores. The soil with a Cr(VI) content of 5000 mg/kg had an aggregate structure and large particles with point-to-surface or edge-to-surface contact form. Meanwhile, the soil with a Cr(VI) content of 10000 mg/kg had a large aggregation formation and particles with point-to-surface or edge-to-surface contact forms separated by large void space. These SEM images highlight the variations in the particle size and permeability test results of different soil samples and altogether suggest that Cr(VI) could lead to the aggregation of soil particles, changes in the internal structure of the soil, and differences in mechanical behaviours.

XRD Patterns Analysis

Fig. 11 shows the XRD patterns of soil samples with different Cr(VI) contents. The major phases in the Cr(VI)-free soil were quartz, albite, illite, and montmorillonite, while the soil with 10000 mg/kg Cr(VI) only had calcite, thereby suggesting that Cr(VI) could also trigger clay mineral disintegrations. Li et al. (2015) and Ouhadi et al. (2006) suggested that heavy metals can convert clay minerals (kaolinite+illite+montmorillonite) into calcite and illite due to the ion exchange reactions among sodium, calcium magnesium, aluminium, and chromium ions. Meanwhile,

Shear et al. (1993) found that the mechanical properties of soil are greatly influenced by the clay mineral content in the soil. The reduction in clay content was in line with the results of the unconfined compression strength and shear tests.

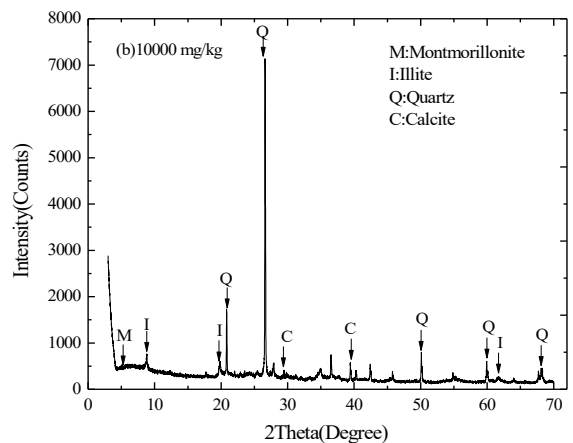
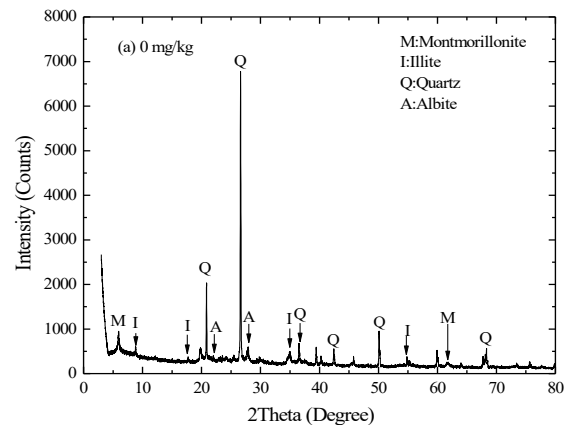


Fig. 11: XRD patterns of soil with different Cr(VI) content.

CONCLUSIONS

This study explores the effect of Cr(VI) on the engineering and microstructure properties of Chinese clay. The following conclusions can be drawn from the results:

1. Cr(VI) changes the physicochemical properties of soil. Specifically, Cr(VI) decreases the pH and optimum moisture content of the soil, and an increasing Cr(VI) content can increase the specific gravity, particle size, and maximum dry density of the soil.
2. Cr(VI) degrades the mechanical properties of soil. Specifically, an increasing Cr(VI) content corresponds to reductions in unconfined compression strength and shear strength, higher hydraulic conductivity, lower soil cohesion, and increased angle of internal friction.
3. Cr(VI) changes the microstructure and engineering properties of soil. According to the BET test results, an increase in Cr(VI) corresponds to an increase in the mean pore size of the soil. The SEM images show that the Cr(VI)-contaminated soil has an aggregate structure with a large void space, whereas the XRD images show that Cr(VI) changes the mineral composition of the soil and converts clay minerals (kaolinite+illite+montmorillonite) into calcite.

ACKNOWLEDGMENTS

This study was supported by the thirteenth 3551 talent program of China optical valley (long-term innovative of Ting Ting Zhang), National Natural Science Foundation of Shandong province (ZR2020QE148), Natural Science Foundation of Qingdao University of Technology (2018TJZR002, 2019ZR007) and University research project of Shandong Province (J18KB059).

REFERENCES

- Cheng, F. and Wang, X. 2014. Effects of mass ratio of heavy metal on geotechnical properties of contaminated soil. *Mining and Metallurgical Engineering*, 34(5): 14-18.
- Cho, G.C., Dodds, J. and Santamarina, J.C. 2007. Closure to particle shape effects on packing density, stiffness, and strength: natural and crushed sands. *Journal of Geotechnical and Geoenvironmental Engineering*, 133(11): 1474-1474.
- Du, Y.J., Jiang, N.J. and Liu, S.Y. 2013. Engineering properties and microstructural characteristics of cement-stabilized zinc-contaminated kaolin. *Canadian Geotechnical Journal*, 51(3): 289-302.
- Horpibulsk, S., Rachan, R., Suddeepong, A. and Chinkulkijniwat, A. 2011. Strength development in cement admixed Bangkok clay: laboratory and field investigations. *Soils and Foundations*, 51(2): 239-251.
- Jo, H.Y., Benson, C.H., Shackelford, C.D., Lee, J.M. and Edil, T.B. 2005. Long-term hydraulic conductivity of a geosynthetic clay liner permeated with inorganic salt solutions. *Journal of Geotechnical and Geoenvironmental Engineering*, 131(4): 405-417.
- Li, J., Xue, Q. and Wang, P. 2015. Effect of lead (II) on the mechanical behavior and microstructure development of a Chinese clay. *Applied Clay Science*, 105: 192-199.
- Liu, Z.B., Fang, W., Chen, Z. L. and YU, C. 2016. Experimental study of influence of zinc ions on one-dimensional compressibility of bentonite. *Rock and Soil Mechanics*, 8: 2211-2217, 2013.
- Miranda-Trevino, J.C. and Coles, C.A. 2003. Kaolinite properties, structure and influence of metal retention on pH. *Applied Clay Science*, 23(1-4): 133-139.
- Morvan, M., Espinat, D., Lambard, J. and Zemb, T. 1994. Ultrasmall-angle X-ray scattering of smectite clay suspensions. *Colloids and Surfaces A: Physicochemical and Engineering Aspects*, 82(2): 193-203.
- Ouhadi, V.R. and Goodarzi, A.R. 2006. Assessment of the stability of a dispersive soil treated by alum. *Engineering Geology*, 85(1-2): 91-101.
- Shear, D.L., Olsen, H.W. and Nelson, K.R. 1992. Effects of desiccation on the hydraulic conductivity versus void ratio relationship for a natural clay. *Transportation Research Record* 1369, pp. 130-135.
- Standard for Soil Test Method, 50123. 1999. Ministry of Housing and Urban-Rural Development of the People's Republic of China, Beijing, China.
- Turer, D. 2007. Effect of heavy metal and alkali contamination on the swelling properties of kaolinite. *Environmental Geology*, 52(3): 421.
- Wei, M.L., Du, Y.J., Reddy, K.R. and Wu, H.L. 2015. Effects of freeze-thaw on characteristics of new KMP binder stabilized Zn- and Pb-contaminated soils. *Environmental Science and Pollution Research*, 22(24): 19473-19484.
- Wang, Y., Fang, Z., Liang, B. and Tsang, E.P. 2014. Remediation of hexavalent chromium contaminated soil by stabilized nanoscale zero-valent iron prepared from steel pickling waste liquor. *Chemical Engineering Journal*, 247: 283-290.
- Wu, H. and Hu, L. 2014. Microfabric change of electro-osmotic stabilized bentonite. *Applied Clay Science*, 101: 503-509.
- Zha, F.S., Liu, J.J. and Xia, L. 2014. Engineering properties of heavy metal contaminated soil. *Chinese Journal of Underground Space and Engineering*, 10(2): 1982-1985.
- Zhang, D., Kong, H., Wu, D., He, S., Hu, Z. and Hu, X. 2009. Remediation of chromite ore processing residue by pyrolysis process with sewage sludge. *Bioresource Technology*, 100(11): 2874-2877.
- Zhang, T.T., Xue, Q. and Li, J.S. 2019. Effect of ferrous sulfate dosage and soil particle size on leachability and species distribution of chromium in hexavalent chromium contaminated soil stabilized by ferrous sulfate. *Environmental Progress & Sustainable Energy*, 38(2): 500-507.
- Zhang, T.T., Xue, Q. and Wei, M.L. 2018. Leachability and stability of hexavalent chromium contaminated soil stabilized by ferrous sulfate and calcium polysulfide. *Applied Sciences*, 8(9): 1431.
- Zhang, Z.H., Li, H.Y. and Shi, Y. M. 2014. Experimental study on permeability properties and micro-structure of clay contaminated by Cu²⁺. *China Civil Engineering Journal*, 47(12): 122-129.



Fenton Oxidation Kinetics of Azo Dye Acid Light Yellow 2G Wastewater by Online Spectrophotometry

Aifang Gao*(**)[†], Yiyun An*, Liuliu Ma*, Yingying Lian* and Aiguo Li*

*School of Water Resources and Environment, Hebei GEO University, Shijiazhuang 050031, China

**Hebei Province Collaborative Innovation Center for Sustainable Utilization of Water Resources and Optimization of Industrial Structure, Hebei Province Key Laboratory of Sustained Utilization and Development of Water Resources, Shijiazhuang 050031, China

[†]Corresponding author: llhx2006@126.com

Nat. Env. & Poll. Tech.
Website: www.neptjournal.com

Received: 03-02-2020

Revised: 28-02-2020

Accepted: 02-05-2020

Key Words:

Online spectrophotometry

Fenton oxidation

Acid Light Yellow 2G

Reaction kinetics

ABSTRACT

The online spectrophotometric technique was adopted to monitor the degradation of simulated Acid Light Yellow 2G (ALY 2G) solution with the Fenton oxidation process, and the kinetic process was also discussed. The effects of the initial concentration of H_2O_2 and Fe_2SO_4 , pH value, and initial dye concentration on the degradation process were studied. The results showed that the ALY 2G can be degraded by Fenton oxidation, and the colour removal rate of Acid Light Yellow 2G was 94.66% after 300 s when the concentration of simulated wastewater was 20 mg/L, the dosage of Fe^{2+} was 0.1 mmol/L, the dosage of H_2O_2 was 0.6 mmol/L, and the pH was 3. The degradation process was divided into two stages: the first stage, the degradation rate is very fast; in the second stage, with the extension of reaction time, the increase of decolourization rate decreases. The first stage of the reaction accords with the first-order kinetics, and the reaction rate constant K_{ap} is 0.04824 s^{-1} . The intrinsic reaction rate constant of ALY 2G and hydroxyl in aqueous solution in the Fenton oxidation method is $0.55 \times 10^9 \text{ M}^{-1}\text{s}^{-1}$.

INTRODUCTION

Textile and dyeing industries are one of the most important chemical industries. However, many printing and dyeing plants produce large amounts of high chroma wastewater during the production process (Xu et al. 2015b). Many aromatic agents, metals and chlorides contained in wastewater are toxic to aquatic organisms, human beings and even affect biosphere (Laszlo & Erzsebet 2008). Every year, 12% of synthetic dyes are run off during the production process, resulting in dye-containing wastewater with high chroma and chemical oxygen demand (COD), low biochemical oxygen demand, oxidation resistance and difficult biodegradation (Xu et al. 2016). Therefore, the most critical problem in the dyeing industry is how to treat visible pollutants contained in dye wastewater (Lee et al. 2006) to meet the industry emission standards.

Advanced oxidation processes (AOPs) have great potential for degrading organic pollutants in industrial wastewater. This oxidation mechanism produces strong oxidants, such as hydroxyl radicals (Cheng et al. 2016), which have high activity and are non-selective for decomposing organic pollutants into CO_2 , H_2O , and inorganic salts in the water environment (Inmaculada et al. 2015). Fenton oxidation ($\text{Fe}^{2+}/\text{H}_2\text{O}_2/\text{H}^+$)

has received the intensive attention in wastewater treatment due to its superior degradation efficiency, rapid reaction speed and moderate investment (Azizi et al. 2015). Under weak acidic conditions, Fe^{2+} is oxidized by H_2O_2 to form Fe^{3+} , hydroxyl ($\cdot\text{OH}$) and OH^- (Xu et al. 2015a), which produces highly reactive $\cdot\text{OH}$ to destroy the molecular structure of organic dyes, thus achieves the decolourization effect of dye wastewater. The spectrophotometer can record the mass concentration change of the dye (Gao et al. 2019a, Gao et al. 2019b, Sibel et al. 2012, Xu et al. 2018) and monitor the instantaneous state of the dye decolourization during the Fenton oxidation process. Therefore, the experimental results are real-time and reliable with a very minor error.

In the present study, azo dye Acid Light Yellow 2G was selected as the target pollutant. We studied the effect of initial Fe^{2+} , initial H_2O_2 concentration, initial pH value of the solution and different dye concentrations on the degradation of ALY 2G by the Fenton method. The decolourization kinetics performance of Fenton oxidation was studied based on the experimental data. The kinetic model of azo dye degradation with Fenton's reagent was established. In this study, the online spectrophotometric system was used to monitor the degradation of Acid Light Yellow 2G. The kinetic analysis

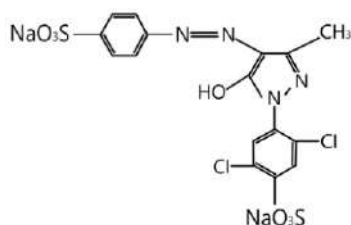


Fig. 1: Molecular structure of Acid Light Yellow 2G.

result was expected to provide basic experimental data for a deeper understanding of the Fenton oxidation process of wastewater containing ALY 2G dye.

MATERIALS AND METHODS

Chemical Reagents

The structure of Acid Light Yellow 2G is shown in Fig. 1. ALY 2G was purchased from Shijiazhuang Dyestuffs Company (China) and the ALY 2G solution was prepared by dissolving a requisite quantity of dye in ultrapure water. Ferrous sulphate ($\text{FeSO}_4 \cdot 7\text{H}_2\text{O}$) and hydrogen peroxide (H_2O_2) were purchased from Tianjin Damao Chemical Reagent Company, and sulfuric acid (H_2SO_4) from Modern Chemical Reagent Company. They were of reagent analytical grade.

Apparatus Set-up

The online spectrophotometric system is shown in Fig. 2. Reaction section (degradation device) includes a digital magnetic stirrer apparatus (Shanghai Instrument Company, China), and a 500 mL beaker. Optical measuring part contains UV-Vis spectrometer (UNICO 2802, Shanghai, China), cycle peristaltic pump and cuvette (1 mL). The recording unit is a computer with the monitoring frequency of 12 min^{-1} during the oxidation process.

Experimental Procedure

Fenton oxidation process was performed in a 500 mL vessel. With the role of a peristaltic pump, the simulated

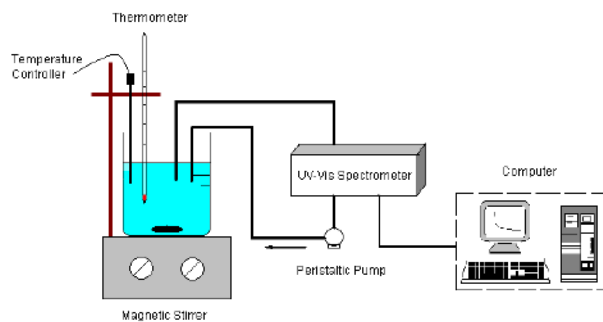


Fig. 2: Online spectrophotometric system.

dye wastewater was pumped into the cuvette of UV-Vis spectrophotometer. Absorbance at maximal absorption peak of dye was obtained by the spectrophotometer. The effects of FeSO_4 dosage, H_2O_2 dosage, initial pH, and initial dye concentration on the degradation of Acid Light Yellow 2G were studied by single-factor experiments.

Feasibility Analysis of Online Spectrophotometric Technique

Online spectrophotometry method was applied to analyze the decolourization of ALY 2G dye in the Fenton process. The UV-Vis spectra of ALY 2G, H_2SO_4 , Fe^{2+} , and Fe^{3+} are presented in Fig. 3. Azo dye ALY 2G has a maximum adsorption peak of 402 nm, which does not vary with the addition of H_2SO_4 , Fe^{2+} and Fe^{3+} . Therefore, during the experiment, online spectrophotometry can be used to monitor ALY 2G wavelength at 402 nm. The standard equations and standard curves for dye concentration (C) and absorbance (A) are given in Fig. 4. The relationship of the absorbance (A) at 402 nm against concentration (C) of ALY 2G is $A = 0.0309C + 0.0015$ ($R^2 = 0.9998$).

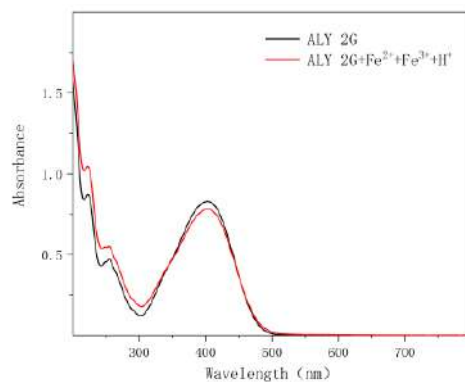


Fig. 3: Comparison of dye UV-Vis spectra between dye and dye ($+\text{H}_2\text{SO}_4+\text{Fe}^{2+}+\text{Fe}^{3+}$).

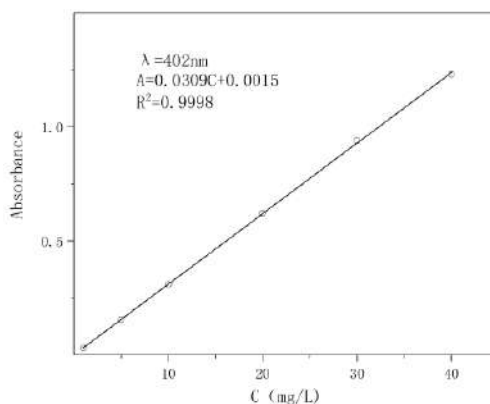


Fig. 4: Standard curve.

RESULTS AND DISCUSSION

Single Factor Experiment

The effects of initial FeSO_4 dosage, initial H_2O_2 dosage, pH value, and initial dye concentration on chroma removal have been discussed. When the reaction time reaches 300 s, the decolourization rate of the dye was calculated. The colour removal rate (R) is defined as given in Eqs. 1. C_0 and C represent the initial and the instant concentrations of the dye with reaction time, respectively.

$$R = \frac{C_0 - C}{C_0} \times 100\% \quad \dots(1)$$

The effect of FeSO_4 dosage: The effect of different dosages of Fe^{2+} on the dye decolourization rate is shown in Fig. 5. Under the dye concentration of 20 mg/L, H_2O_2 dosage of 0.6 mmol/L and pH of 3 conditions, Fe^{2+} concentration ranged from 0.04 to 0.4 mmol/L (temperature kept at 25°C). It can be observed from Fig. 5 that different concentrations of Fe^{2+} have a great effect on colour removal. When the Fe^{2+} concentration is 0.04-0.1 mmol/L, the colour removal rate becomes higher and higher as Fe^{2+} concentration increases. The colour removal rate was 93.46% when Fe^{2+} concentration was 0.1 mmol/L. In addition, the colour removal rate of ALY 2G increased sharply in the first 30 s stage with the increase of Fe^{2+} concentration. After 30 seconds, the colour removal rate of ALY 2G dye did not increase, but the decolourization rate decreased slightly when the concentration ranges of dye changed from 0.2 to 0.4 mmol/L. This experimental result makes us known that excessive Fe^{2+} concentration is not beneficial to decolourization of ALY 2G among Fenton oxidation process. This reason is that because the excess ferrous ion competes with the dye molecules for the hydroxyl radical $\cdot\text{OH}$ ($\text{Fe}^{2+} + \cdot\text{OH} \rightarrow \text{Fe}^{3+} + \text{OH}^-$) (Xu et al. 2015b). Therefore, choosing an appropriate amount of Fe^{2+} can improve the degradation effect of the ALY 2G dye. We have chosen the initial Fe^{2+} concentration of 0.1 mmol/L

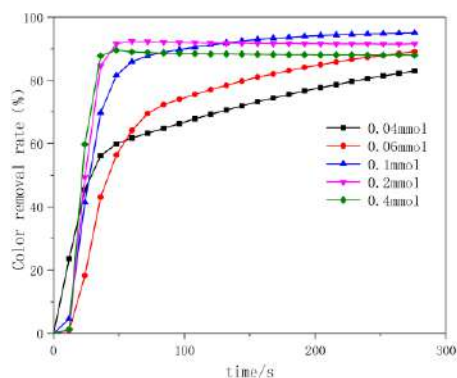
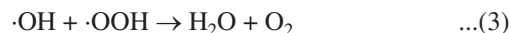
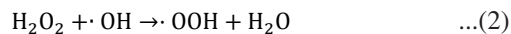


Fig. 5: Influence of initial Fe^{2+} concentration on dye removal.

as an optimum dosage for efficient decolourization to ALY 2G aqueous solutions.

The effect of initial H_2O_2 dosage: H_2O_2 is one of the very important factors affecting the degradation efficiency of dyes. The hydroxyl group can decompose the molecular structure of azo dyes, and then bleach ALY 2G dye wastewater. The hydroxyl group derives from H_2O_2 . Fig. 6 displays the effect of the decolourization rate R of ALY 2G on various H_2O_2 concentrations. We can see from Fig. 6 that experimental monitoring in 300s, the decolourization trends of ALY 2G under 0.6, 3 and 6 mmol/L concentrations are very similar. The decolourization rate was 84.53% (lowest value) when H_2O_2 concentration was 0.18 mmol/L. When the H_2O_2 concentration was increased to 0.6 mmol/L, the dye decolourization rate reached 93.38%. However, when the H_2O_2 concentration was 12 mmol/L, the decolourization rate was relatively low (90.52%). The reason is that excess H_2O_2 will consume $\cdot\text{OH}$ and compete with ALY 2G dye for hydroxyl radical $\cdot\text{OH}$ (Eqs. 2-3). This process results in the production of the hydroperoxyl radical ($\cdot\text{OOH}$ as a scavenger of hydroxyl radical) and then decreases the colour removal rate of dye (Sehested et al. 2003, Xu et al. 2016). In brief, we choose 0.6 mmol/L as an optimum H_2O_2 concentration of the decolourization of ALY 2G in the Fenton oxidation process.



The effect of solution pH: The pH of the solution plays an important role in dye degradation for the Fenton process. The influence of pH value on the decomposition of ALY 2G is illustrated in Fig. 7. The change trends of decolourization rate with various pH value are consistent. The decolourization rate increases from 57.12% to 94.66% as the pH value increases from 1.5 to 3. However, when the pH value further increases to 4, the decolourization rate decreases to be 89.39%. At the lower pH value (<3) the $\cdot\text{OH}$ is consumed by the excessive hydrogen ion ($\cdot\text{OH} + \text{H}^+ + \text{e}^- \rightarrow \text{H}_2\text{O}$), and

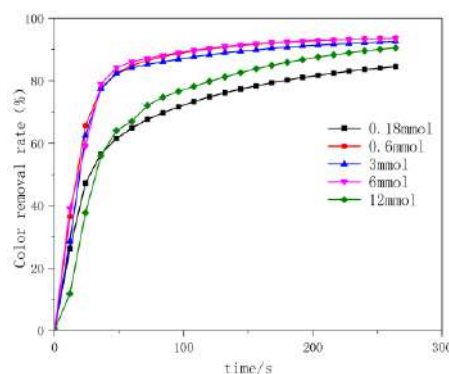


Fig. 6: Influence of initial H_2O_2 concentration on dye removal.

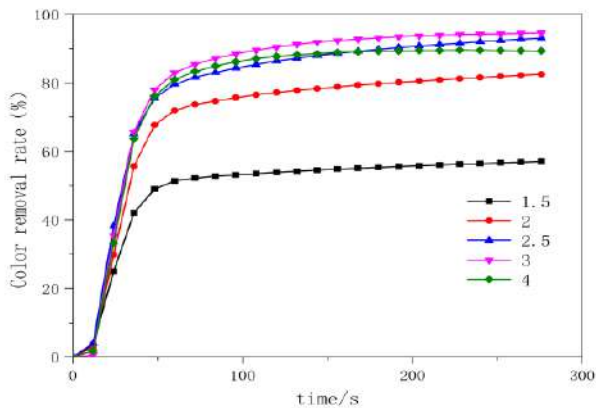


Fig. 7: Influence of initial pH on dye removal.

thus the decolourization rate is relatively small. When the solution ($\text{pH} > 3$), with the formation of the iron hydroxide complex, the hydrogen peroxide is decomposed and the ferrous ion catalyst is invalidated, which ultimately leads to a reduction in the oxidation ability of Fenton (Gao et al. 2014). Therefore, the pH value of 3 is considered to be the optimum value for the decolourization of azo dye ALY 2G in Fenton oxidation.

The effect of initial ALY 2G concentration: Fig. 8 shows the trend of the colour removal rate with various dye concentrations (conditions: $[\text{Fe}^{2+}] = 0.1 \text{ mmol/L}$, $[\text{H}_2\text{O}_2] = 0.6 \text{ mmol/L}$, and $\text{pH} = 3$). Although the initial concentrations of the dye ALY 2G were different (from 10 to 40 mg/L), the chroma removal rate of dye can all reach more than 90% and the difference of all removal rates is very small after 300s. Moreover, it can be seen that the reaction rate gradually decreases as increasing dye concentration between 50s and 150s. The reason for this is that as the initial concentration of the Acid Light Yellow 2G dye solution increases, the number of dye molecules in the solution increases, whereas the amount of $\cdot\text{OH}$ in the solution does not increase, which leads to a decrease in the reaction rate.

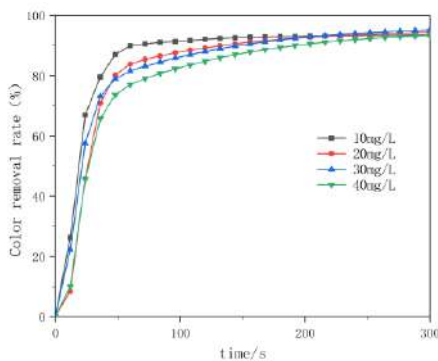


Fig. 8: Influence of initial dye concentration on dye removal.

Reaction Kinetic Fitting Analysis

Kinetic process analysis is helpful to understand the Fenton oxidation process. Acid Light Yellow 2G was decolourized successfully in the experimental process, and the first stage of decolourization was analysed by first-order kinetics (Gao et al. 2019b). The first-order kinetics calculation formula (Eqs. 4-5) is as follow:

$$\frac{dC}{dt} = K_{ap}t \quad \dots(4)$$

$$\ln \frac{C_0}{C_t} = K_{ap}t \quad \dots(5)$$

Where, t is the reaction time; C is the instant dye concentration; C_0 represents the initial dye concentration.

Figs. 9-12 show the changes of $\ln(C_0/C_t)$ with time under different initial Fe^{2+} concentrations, different H_2O_2 concentrations, different pH, and different dye concentrations, respectively. The linear fitting results of the relationship curve between $\ln(C_0/C_t)$ and time (t) are given in Table 1. The kinetic parameters are also listed in Table 1. The values of the kinetic parameters (the correlation coefficients R^2) are all above 0.94. It can be seen that the oxidation

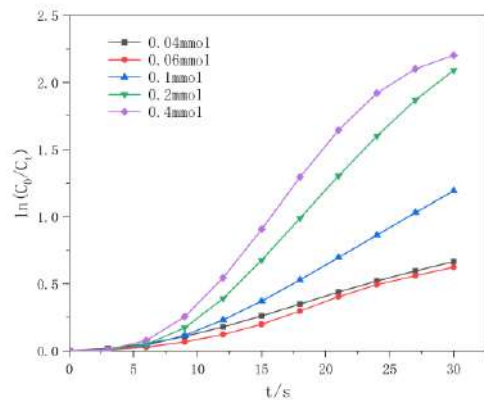


Fig. 9: First-order kinetics of reactions in different Fe^{2+} concentrations.

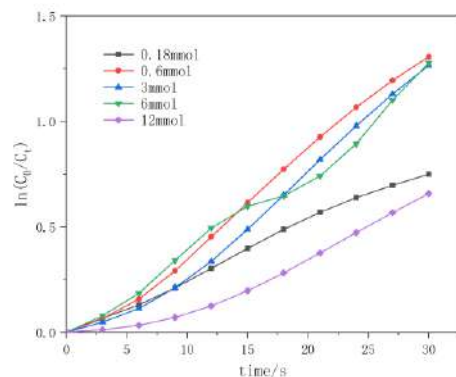


Fig. 10: First-order kinetics of reactions in different H_2O_2 concentrations.

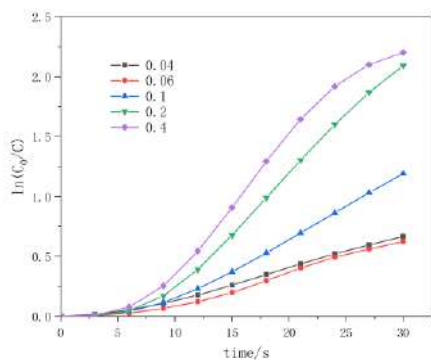


Fig. 11: First-order kinetics of reactions in different pH.

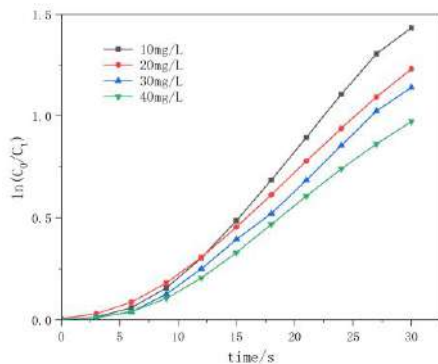


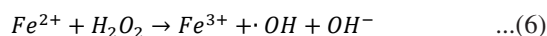
Fig. 12: First-order kinetics of reactions in different dye concentrations.

process of Acid Light Yellow 2G by Fenton method accords with first-order kinetics.

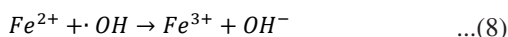
First-order kinetics fitting is performed for the fast reaction stage. The fast stage of the Fenton oxidation process abides by first-order kinetics. Under the optimal reaction condition in Fenton oxidation, the correlation coefficient is 0.98 and the reaction rate K_{ap} is 0.04824 s^{-1} .

Kinetics Study

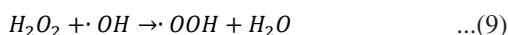
The Fenton oxidation method uses a catalyst Fe^{2+} and H_2O_2 to undergo a redox reaction to form a highly active $\cdot\text{OH}$ which can decompose the molecular structure of organic dyes. The reaction mechanism can be expressed by (Eqs. 6-14) (D represents dye molecules) (Gao et al. 2014, Gao et al. 2019b, Kuši et al. 2006, Sibel et al. 2012, Sehested et al. 2003).



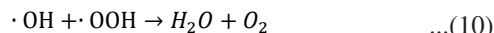
$$k_1 = 76 \text{ M}^{-1}\text{s}^{-1}$$



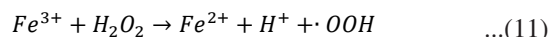
$$k_3 = 3.2 \times 10^8$$



$$k_4 = 4.5 \times 10^7$$



$$k_5 = 6.6 \times 10^{11}$$



$$k_6 = 0.02 \text{ M}^{-1}\text{s}^{-1}$$

The reaction rate of dye can be defined as:

$$-\frac{d[\text{D}]}{dt} = k_2[\cdot\text{OH}][\text{D}] \quad \dots(12)$$

According to the steady-state assumption, $[\cdot\text{OH}]$ can be obtained as follow:

$$\begin{aligned} \frac{d[\cdot\text{OH}]}{dt} &= k_1[\text{Fe}^{2+}][\text{H}_2\text{O}_2] - k_2[\cdot\text{OH}][\text{D}] - k_3[\text{Fe}^{2+}][\cdot\text{OH}] \\ &\quad - k_4[\text{H}_2\text{O}_2][\cdot\text{OH}] - k_5[\cdot\text{OH}][\cdot\text{OOH}] = 0 \end{aligned} \quad \dots(13)$$

$$-\frac{d[\cdot\text{OOH}]}{dt} = k_4[\text{H}_2\text{O}_2][\cdot\text{OH}] - k_5[\cdot\text{OOH}][\cdot\text{OH}] = 0 \quad \dots(14)$$

According to Eq. (14), we obtain:

$$k_5[\cdot\text{OH}][\cdot\text{OOH}] = k_4[\text{H}_2\text{O}_2][\cdot\text{OH}] \quad \dots(15)$$

According to Eqs. (13) and (15), we obtain:

$$\begin{aligned} \frac{d[\cdot\text{OH}]}{dt} &= k_1[\text{Fe}^{2+}][\text{H}_2\text{O}_2] - k_2[\cdot\text{OH}][\text{D}] - k_3[\text{Fe}^{2+}][\cdot\text{OH}] \\ &\quad - 2k_4[\text{H}_2\text{O}_2][\cdot\text{OH}] = 0 \end{aligned} \quad \dots(16)$$

$$[\cdot\text{OH}] = \frac{k_1[\text{Fe}^{2+}][\text{H}_2\text{O}_2]}{k_2[\text{D}] + k_3[\text{Fe}^{2+}] + 2k_4[\text{H}_2\text{O}_2]} \quad \dots(17)$$

Combined Eqs. (12) with (17), we obtained:

$$-\frac{d[\text{D}]}{dt} = \frac{k_1k_2[\text{Fe}^{2+}][\text{H}_2\text{O}_2][\text{D}]}{k_2[\text{D}] + k_3[\text{Fe}^{2+}] + 2k_4[\text{H}_2\text{O}_2]} \quad \dots(18)$$

Thus, Eq. (18) deduces to

$$\frac{[\text{H}_2\text{O}_2][\text{D}]}{-\frac{d[\text{D}]}{dt}} = \frac{[\text{D}]}{k_1[\text{Fe}^{2+}]} + \frac{k_3}{k_1k_2} + \frac{2k_4[\text{H}_2\text{O}_2]}{k_2k_1[\text{Fe}^{2+}]} \quad \dots(19)$$

By fitting the first-order kinetics to the oxidation reaction process in the last stage, the results show that the correlation coefficients are all above 0.95. It can be seen that the fast stage meets the first-order kinetics, so that:

$$-\frac{d[\text{D}]}{dt} = K_{ap}[\text{D}] \quad \dots(20)$$

Combined Eqs. (19) with (20), we obtained:

$$\frac{[\text{H}_2\text{O}_2]}{K_{ap}} = k[\text{D}]_0 + B \quad \dots(21)$$

$$B = \frac{k_3}{k_2k_1} + \frac{2k_4[\text{H}_2\text{O}_2]_0}{k_2k_1[\text{Fe}^{2+}]_0} \quad \dots(22)$$

The experimental results are shown in Fig. 13. $[\text{H}_2\text{O}_2]/K_{ap}$ has a good linear relationship with the dye concentration (R^2

Table 1: Degradation kinetics data.

FeSO ₄ (mmol/L)	H ₂ O ₂ (mmol/L)	pH	Dye concentration (mg/L)	First-order kinetics	
				K _{ap}	R ²
0.04	3	3	20	0.0239	0.98182
0.06	3	3	20	0.02298	0.95885
0.1	3	3	20	0.04236	0.95748
0.2	3	3	20	0.07708	0.95702
0.4	3	3	20	0.08617	0.96601
0.1	0.18	3	20	0.02634	0.99524
0.1	0.6	3	20	0.04658	0.99384
0.1	3	3	20	0.0448	0.98128
0.1	6	3	20	0.04107	0.98546
0.1	12	3	20	0.023	0.95326
0.1	0.6	1.5	20	0.02147	0.99136
0.1	0.6	2	20	0.03481	0.99652
0.1	0.6	2.5	20	0.0447	0.99558
0.1	0.6	3	20	0.04824	0.98836
0.1	0.6	4	20	0.04468	0.99148
0.1	0.6	3	10	0.05251	0.96378
0.1	0.6	3	20	0.03869	0.94459
0.1	0.6	3	30	0.04116	0.96418
0.1	0.6	3	40	0.03526	0.96477

= 0.97133). According to intercept B, the intrinsic reaction rate constant of the dye concentration and ·OH in the aqueous solution is obtained ($k_2 = 0.55 \times 10^9 M^{-1} S^{-1}$).

CONCLUSION

In this study, the degradation of the azo dye Acid Light Yellow 2G by Fenton method and its influence factors (initial dye concentration, initial solution Fe²⁺ concentration, initial H₂O₂ concentration, and initial pH value) were studied. The following conclusions can be made.

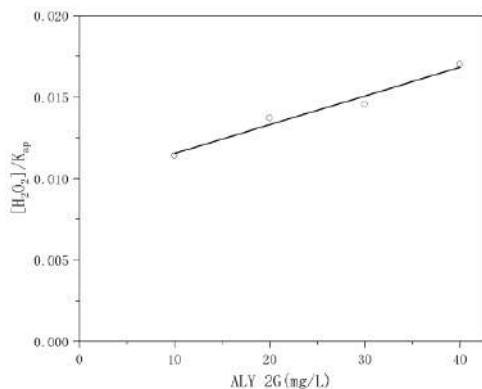


Fig. 13: Relationship between $[H_2O_2]/K_{ap}$ and $[D]_0$.

1. The online spectrophotometric method was used to monitor the absorbance of dye Acid Light Yellow 2G with Fenton oxidation. This technique is accurate, feasible and fast. The Fenton oxidation process can be divided into two stages: a rapid degradation stage ($t < 30s$) and a slow degradation phase ($t > 30s$).
2. The best experimental conditions for degradation of dyes are that FeSO₄ is 0.1 mmol/L, H₂O₂ is 0.6 mmol/L, initial pH is 3, and when the dye concentration is 20 mg/L, the colour removal rate is 94.66%. Fenton oxidation process conforms to first-order reaction kinetics in the first stage. According to the formula $K_{ap} = \ln(C_0/C_t)$, the first-order rate constant is the linear fitting slope. The reaction rate constant K_{ap} is $0.04824 s^{-1}$ under the best experimental conditions.
3. During the Fenton oxidation process, the intrinsic reaction rate constant of the ALY 2G dye and ·OH in aqueous solution was ($k_2 = 0.55 \times 10^9 M^{-1} S^{-1}$).

ACKNOWLEDGEMENTS

The work is partly supported by the Scientific Pre-Research Fund of Hebei GEO University in 2015(YK201501), the Young Talent Plan of Hebei Province 2016, and the Excellent Youth Foundation of Hebei Province Department of Education of China (Grant No. Y2011110)

REFERENCES

- Azizi, A., Moghaddam, M. R. A., Maknoon, R. and Kowsari, E. 2015. Comparison of three combined sequencing batch reactor followed by enhanced Fenton process for an azo dye degradation: Biodecolorization kinetics study. *Journal of Hazardous Materials*, 299: 343-350.
- Cheng, M., Zeng, G. M., Huang, D., Lai, C., Xu, P., Zhang, C. and Liu, Y. 2016. Hydroxyl radicals based advanced oxidation processes (AOPs) for remediation of soils contaminated with organic compounds: a review. *Chemical Engineering Journal*, 284: 582-598.
- Gao, A. F., Wang, W. P., Li, A. G. and Jiao, Z. 2014. Kinetics of reactive dark blue B-2GLN with Fenton oxidation process. *Chinese Journal of Environmental Engineering*, 8(6): 2407-2412.
- Gao, A. F., Li, A. G., Gao, Z. J., Peng, Z. X. and Wang, W. P. 2019a. Study of decolorization kinetics of reactive red B-2BF in Fenton oxidation process. *Fresenius Environmental Bulletin*, 28(9): 6435-6443.
- Gao, A. F., Li, A. G. and Wang, W. P. 2019b. Degradation kinetics of Reactive Dark Blue B-2GLN with Fenton oxidation process. *Desalination and Water Treatment*, 141: 301-309.
- Inmaculada, O., Anuska, M.C., Juan, M. L. and Santiago, E. 2015. Advanced technologies for water treatment and reuse. *Aiche Journal*, 61(10): 3146-3158.
- Kuši, H., Koprivanac, N., Boži, A. L. and Selanec, I. 2006. Photo-assisted Fenton type processes for the degradation of phenol: A kinetic study. *Journal of Hazardous Materials*, 136(3): 632-644.
- Laszlo, W. and Erzsebet, T. 2008. Irradiation treatment of azo dye containing wastewater: An overview. *Radiation Physics and Chemistry*, 77(3): 225-244.
- Lee, J. W., Choi, S. P., Thiruvenkatachari, R., Shim, W. G. and Moon, H. 2006. Submerged microfiltration membrane coupled with alum coagulation/powdered activated carbon adsorption for complete decolorization of reactive dyes. *Water Research*, 40(3): 435-444.
- Sibel, T., Tülin, G. and Osman, D. 2012. On-line spectrophotometric method for the determination of optimum operation parameters on the decolorization of Acid Red 66 and Direct Blue 71 from aqueous solution by Fenton process. *Chemical Engineering Journal*, 181: 431-442.
- Sehested, K., Bjergbakke, E. and Rasmussen, O. L. 2003. Reactions of H_2O_2 in the pulse-irradiated $Fe(II)-O_2$ system. *The Journal of Chemical Physics*, 51(8): 3159-3166.
- Xu, H., Li, M., Wu, F. M. and Zhang, J. 2015a. Optimization of Fenton oxidation process for treatment of hexoxeon industrial wastewater using response surface methodology. *Desalination and Water Treatment*, 55: 77-85.
- Xu, H., Yu, T. L., Wang, J. X. and Li, M. 2015b. Online monitoring of Fenton-mediated Reactive Red 6B oxidation kinetics. *Environmental Progress & Sustainable Energy*, 34: 1019-1027.
- Xu, H., Yu, T. L., Guo, X. X. and Wang, J. X. 2016. Fe^{3+}/H_2O_2 Fenton degradation of wastewater containing dye under UV irradiation. *Desalination and Water Treatment*, 57: 18028-18037.
- Xu, H., Zhang, D. D., Yu, T. L., Wu, F. M. and Li, H. 2018. Studying Fenton oxidation kinetics of mixed dyes wastewater and salt effect by online spectrophotometry. *Desalination and Water Treatment*, 102: 340-348.



Relationship Between NDVI and the Microbial Content of Soil in Detecting Fertility Level at Semarang Regency, Jawa Tengah, Indonesia

Ananto Aji*†, Sigit Bayhu Iryanthony**, Wahid Akhsin Budi Nur Sidiq* and Edy Trihatmoko*

*Department of Geography, Faculty of Social Science, Semarang State University, Semarang, Indonesia

**Center of Excellence for Science and Technology (PUD), Center for Coastal Rehabilitation and Disaster Mitigation Studies (CoREM), Universitas Diponegoro, Semarang, Indonesia

†Corresponding author: Ananto Aji; ajiananto@mail.unnes.ac.id

Nat. Env. & Poll. Tech.
Website: www.neptjournal.com

Received: 28-02-2020

Revised: 26-03-2020

Accepted: 02-05-2020

Key Words:

NDVI
Microbial content
Fertility level
Soil

ABSTRACT

Global warming is the most significant environmental issue that causes the utmost concern for researchers and scientists. Furthermore, impacts recorded include the potential for drought and the reduction of soil ability to support biomass production, subsequently posing a significant threat to agriculture. Moreover, vegetation density is known to support microorganism activities actively, and its analysis requires remote sensing techniques, involving normalized differential vegetation index (NDVI) and soil adjustment vegetation index (SAVI), associated with microbial content in the soil. Besides, the level recorded is assumed to have a strong correlation with soil fertility, which is a prerequisite for the development of vegetation cover. Hence, most of the research was conducted in fertile lands situated in the Ungaran, Merbabu, and Telomoyo volcanic areas. The results show the absence of a positive correlation between soil fertility and the number of microorganism's present, although the association with vegetation cover is relatively low.

INTRODUCTION

Land use is always changing and increasing (Lal & Kumar 2017, Rizk & Rashed 2015), both for settlements and industry, which triggers a reduction in the rate of vegetation cover (Islam et al. 2018). Furthermore, the increase of deforestation practices poses various threats (both long and short term), which consequently becomes global issues (Nanzad et al. 2019, Islam et al. 2018, Gillespie et al. 2018). The other effects of deforestation practices lead to the potential occurrence of drought (Rudiarto 2018), flooding (Dewi 2016), rising temperatures, and declining soil fertility in the future (Nugraha 2017).

The reduction in soil fertility as a global issue (Chauhan et al. 2017), characterized by a decrease in biomass resulting from leaf litter (Ning et al. 2019). This further triggers difficulty in improving plant growth, as it affects critical soil. Besides, the effect is profoundly felt in Java Island, due to the increase in surface temperature and its extreme differences between day and night.

Detecting land use through remote sensing methods has already developed (Myint et al. 2011, Coulter et al. 2016, Town et al. 2018), and the ability of geographic information system (GIS) is very efficient in calculating the extent of objects on the earth surface (Rizk & Rashed 2015, Rimal et

al. 2018, Lu & Wu 2019). Also, the capacity to detect objects and plant health is enhanced based on satellite imagery data (Arrogante-funes et al. 2018), as their visual analysis is often accurately calculated by pixel area (Bhaskaran et al. 2010). Meanwhile, the study requires the comparison of field data with information obtained from satellite imagery.

GIS can perform calculations on a regional scale, and broader (Iryanthony et al. 2019), and the results obtained are usually a combination of the classification. Besides, the vegetation index method is used to detect the level of plant density, and also to calculate the level of soil fertility in the presence of vegetation cover. Hence, GIS is efficient as software for calculating the area, which is generated from Landsat satellite data (Town et al. 2018, Iryanthony et al. 2019).

NDVI (normalized differential vegetation index) is an index used to identify the level of vegetation density from satellite (Filgueiras et al. 2019). Furthermore, it plays an essential role in determining the extent of thickness on a broad scale (Yangchengsi et al. 2019), by utilizing the red band that is sensitive to leaves, and the near-infrared (NIR) band known to be sensitive to leaf chlorophyll (Nanzad et al. 2019, Seo et al. 2019). Furthermore, most studies use NDVI for the detection of plant health, although some apply it for density. Conversely, the SAVI (soil adjustment vegetation index) method has also been used as a soil fertility detector (Huete 1988).

NDVI is very sensitive to areas without vegetation cover, thus necessitating SAVI in soil detection (Ren et al. 2018). However, its products are responsive to variations in soil colour, moisture, and saturation effects of high-density areas, depending on the regional character. Therefore, it demands efforts towards its improvement (Huete 1988), attained by developing an index, which reduces the dominance of red and NIR bands, through the vegetation canopy. Furthermore, the index is a transformation technique used to minimize the effect of brightness from these spectral wavelengths.

Soil organisms are found near the roots of plants (0-40 cm), especially during weathering, and most of them belong to a critical group of plants (flora) and animals (fauna). Besides, the microorganisms are difficult to be seen with the bare eye. Also, those organisms have thus been widely developed in the area of agriculture. Previous studies were closely related to soil fertility and plant growth, including phosphate solvent microbes (MPP). Furthermore, the types of microbes used include microbial symbiosis with *Azolla* plants, fastening with the N_2 atmosphere on both free-living and symbiotic species, mycorrhizal, and cellulose microbes.

Meanwhile, some forms of microorganisms have been developed for the improvement of lands polluted. Within the soil, bacteria have been identified as the most abundant group, which, together with others, play an essential role in the decomposition of organic matter, synthesis of acid or certain organic compounds, and N mineralization.

This study, therefore, aims to determine the ability and correlation of NDVI and SAVI results in detecting soil fertility at the upland areas of Semarang Regency. This detection was conducted through the analysis of microbial content as an indicator, and the types of microbes evaluated include bacteria, actinomycetes, fungi, microalgae, protozoa, nematodes, and worms. Besides, they were cumulatively measured in terms of total microbes (CFU/gram).

MATERIALS AND METHODS

Study Area

The study was conducted in all districts of Semarang Regency. For additional information, Semarang Regency has an altitude between 300-2500 m. This location is a stretch of Ungaran and Telomoyo Volcano, as well as a portion of Merbabu Volcano. Topographically, the regency is very diverse that possesses protected forests on each volcano, and some areas are always green. Also, the central part consists of the Rawa Pening Lake area, which comprises mostly of organic soil, composed of organic material. Therefore, the slope mainly entails vegetable and protected forest land, while Ungaran and Merbabu Volcano were adopted in other uses such as tea plantation. Furthermore, a small portion of coffee plants was also identified, although it is not a leading commodity in the region. The research area is shown in Fig. 1.

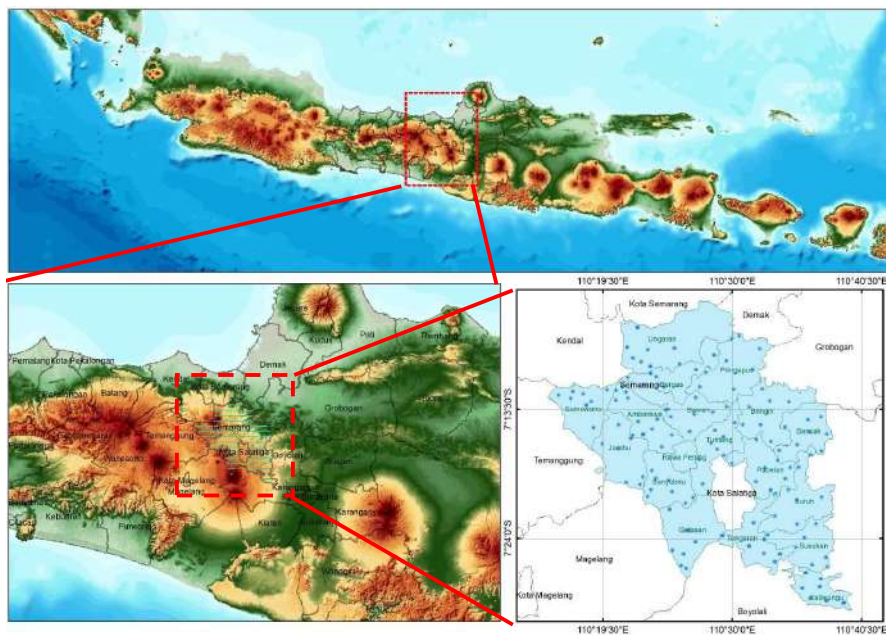


Fig. 1: Location and distribution of research samples in Semarang Regency symbolized by small dots.

Microbial Test

Microbial content tests were conducted on the soil samples obtained from the location (Fig. 1) for subsequent laboratory analysis. Meanwhile, the number of microbes was identified as the total population in the soil. The identification was measured by using a colony counter. Generally, the usual amount is about 107 CFU/g of soil or 107 colony-forming unit of microbes in 1 g of soil, and the degradation is said to have occurred at the value of <102 CFU/g of soil, both for dry land and wetlands. Besides, the measurement was performed using the plating technique, as stipulated in Government Regulation Number 150 of 2000, concerned with the Control of Soil Damage for Biomass Production. Therefore, the number recorded is a strong determinant of fertility, through the recognition of abundant microbes.

Soil samples were taken with guidance from the land damage map (Fig. 5A) obtained from the Ministry of Environment and Forestry, and the microbial content was used as one of the parameters for determining the richness of biomass. Furthermore, all microbial samples were obtained from areas with high critical levels, and the parameter for criticality was divided into five levels of damage. This study, therefore, produces a sample distribution data that is proportional in terms of damage level and random vegetation, to produce heterogeneously distributed values. Moreover, up to 130 samples spread throughout the Semarang Regency were collected, representing the 19 sub-districts (details are seen in Figs. 1 and 5).

Satellite Imagery Data

Landsat 8 OLI was utilized with a spatial resolution of 30 m, and cloud cover <10%. This satellite imagery was taken in the dry season to obtain minimal or cloud-free weather conditions. Furthermore, the obtained satellite imagery is the best representation of growth and vegetation variables, with the visible red band 4 (630-680 nm) and the NIR band 5 (845-885 nm) also widely utilized (Trihatmoko 2020). Besides, each is used to construct the NDVI and SAVI models, while the satellite imagery data was obtained from USGS.

The research also utilized Sentinel 2A as open access data, which is similar to Landsat imagery for its characteristics and metadata. Therefore, all data used were sourced from ESA and USGS, while image processing involved the use of a Semi-Automatic Classification Tool (SCP) extension in QGIS 3.4 vector software. Besides, some devices were combined extensions, and are thus adopted for processing, through SCP. It is possible to directly download Satellite imagery data through software, as they allow outputs in both radiometric and atmospheric correction process.

IDW model

The IDW (inverse distance weighted) method is a GIS model interpolation technique that is used to connect multiple data points values (Wong 2017), and also being linked to interpolation. Besides, the ability to numerically display information tends to enhance the ease of analysing the distribution (Lima et al. 2003). This model demands that the data is also linked, which subsequently creates contours (Mei & Tian 2016), and the IDW is known to possess excellent flexibility, in several applications (Buchori et al. 2017). These unique capabilities make the interpolation method appear more natural in the connection of one point to another. The equation as follows:

$$P_i = \frac{\sum_{j=1}^G P_j / D_{ij}^n}{\sum_{j=1}^G 1 / D_{ij}^n} \quad \dots(1)$$

P_i is the height value at the location i; P_j is the height value at the sampled location j; D_{ij} is the distance from i to j; G is the number of sampled areas, and n is the inverse-distance weighting power.

IV (INDEX OF VEGETASI)

Vegetation index in remote sensing plays a vital role in detecting the presence and cover of vegetation. Thus, NDVI derived from satellites serve as an essential index in the study of climate change, right from the early 1980s (Gholamnia et al. 2019). This technique is well-known to play a crucial role in land cover detection (Yangchengsi et al. 2019). The equation as follows:

$$NDVI = \frac{(Band\ 5 - band\ 4)}{(Band\ 5 + band\ 4)} \quad \dots(2)$$

This modelling combines NDVI with SAVI with soil conditions, as the latter is beneficial concerning the field parameters used, and the microbial content. Furthermore, the microorganism load is used as an indication for the level of fertility, marked by a high positive NDVI vegetation cover, and a good SAVI value. Hence, it is expected that there is a linear relationship between each IV and surface vegetation conditions, using the equation as follows:

$$SAVI = \left[\frac{(Band\ 5 - band\ 4)}{(Band\ 5 + band\ 4 + L)} \right] \times 1 + L \quad \dots(3)$$

The NIR band fills band 5 in the Landsat 8 OLI, and band 4 is red. Meanwhile, the NIR in the 2MSI sentinel image resides in band 6, and the red was in band 4.

RESULTS AND DISCUSSION

NDVI describes the greenness level of a plant. This index is a mathematical combination of the red and NIR band, which has been used for a long time as an indicator to identify and

characterize the condition of vegetation. Furthermore, the calculations are based on the principle stipulating that green plants grow more effectively by absorbing radiation in the visible light spectrum region (PAR or Photosynthetically Active Radiation), and also because they strongly reflect radiation from the NIR region. Besides, the concept of spectral patterns tends to use only the red band image on the mathematical algorithm. These spectral reflections are specifically ratios reproduced from the incoming radiation on each band. Hence they assume values between 0.0 and 1.0. By design, NDVI varies between -1.0 and +1.0., known to be functional, although not linear, and also equivalent to a simple infrared/red ratio (NIR/VIS). However, it possesses the advantage of being generally limited to the possible linearity of functional relationship with the nature of the vegetation (for example, it is characterized by the presence of biomass). Furthermore, simple ratios (different from NDVI) are always positive, with the tendency of possessing practical advantages. However, they also possess an unlimited mathematical range (0 to infinity), which is a comparable practical disadvantage.

The description range of NDVI values is -1 to 1, where the negatives (values close to -1) tend to correspond with water. Furthermore, values that approach zero (-0.1 to 0.1) generally relate to barren areas of rock, sand, or snow. At the same time, the positive and low records represent shrubs and grasslands (about 0.2 to 0.4), and higher values indicate tropical and moderate rainforests (values close to 1). Moreover, details on positive values <0 = non-living things, including roads, buildings, soil or dead plants, $0 - 0.33$ = unhealthy plants, $0.33 - 0.66$ = healthy plants, > 0.66 = very healthy plants.

NDVI results from the Sentinel 2A and Landsat 8 OLI satellite imagery in 2019, recorded in the dry season, showed a more accurate distribution of areas with dense vegetation. Besides, the weather condition during the time allowed all mostly forested regions to remain denser in contrast with other less vegetated plains. Unlike the rainy season, most areas tend to look green, since Indonesia enters the agricultural growth period. Therefore, being a protected area as a national park, Semarang Regency is observed to possess a higher thickness value.

The location of Ungaran, Bergas, and Sumowono are on the slopes of Ungaran Volcano, which contains some forests protected under the supervision of the Ministry of Environment and Forestry. These include Jambu, with the steep morphological condition that is impossible for settlements. Thus, most of the area is a stretch of vegetation in Telomoyo Volcano. Furthermore, Getasan is the slope area of Merbabu Volcano, included in the administration of Semarang and some of Boyolali Regency area.

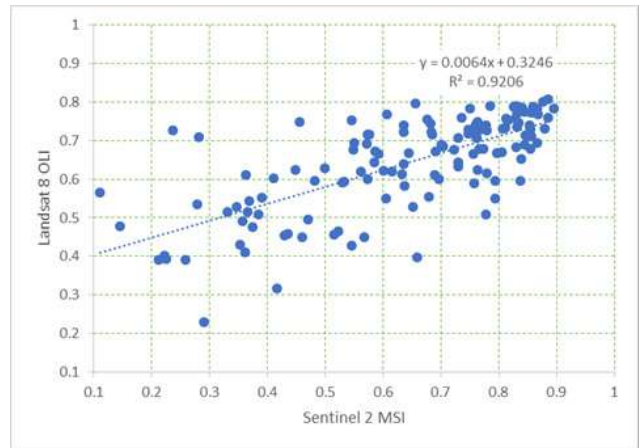


Fig. 2: Regression values of NDVI Sentinel and Landsat imagery.

The vegetation density evaluation capacity of Landsat and Sentinel data was similar, although the latter possesses a higher resolution (10 m). Moreover, Landsat is highly necessary while discussing long-term multi-temporal analysis. Besides, NDVI OLI data regression results showed a data distribution by the determination coefficient (R^2) at about 0.92 (Fig. 2). This value means that the data distribution of the two variables is mostly inline, and it means that they have a reasonable correlation of up to 92%. This correlation result was consistent with the theory of Zhang et al. (2018), where the association in atmospheric regression reached $R^2=0.90$. This result, therefore, shows close consistency and similarity between the value of Landsat and Sentinel (Fig. 3).

SAVI was used to correct NDVI for the effect of soil brightness in areas where the vegetative cover was low (Fig. 4). Therefore, the SAVI derived from Landsat Surface Reflectance was calculated as the ratio between R and NIR values, using a soil brightness correction factor (L) defined as 0.5 to accommodate most cover types. Besides, SAVI is similar to NDVI, although its user preference is in areas of low vegetative cover ($<40\%$). However, the reflectance attained on instances where large amounts of surface earth were exposed tends to affect NDVI values (which changes up to 20%). Also, "L" is the correction factor that ranges from 0 for very high to 1 for shallow vegetation cover, and a value of 0.5 is usually used for medium. Meanwhile, SAVI tends to possess a similar equation as NDVI when "L" is equal to zero. However, the adjustment factor was identified through trial and error, and when the vegetation index was identical for both dark and light soils.

The survey-based on the location of soil damage shows different distributions from the density of vegetation on NDVI (Fig. 5). Thus, a high value was concentrated in the Tengaran, Susukan, and Kaliwungu areas, as well as on the

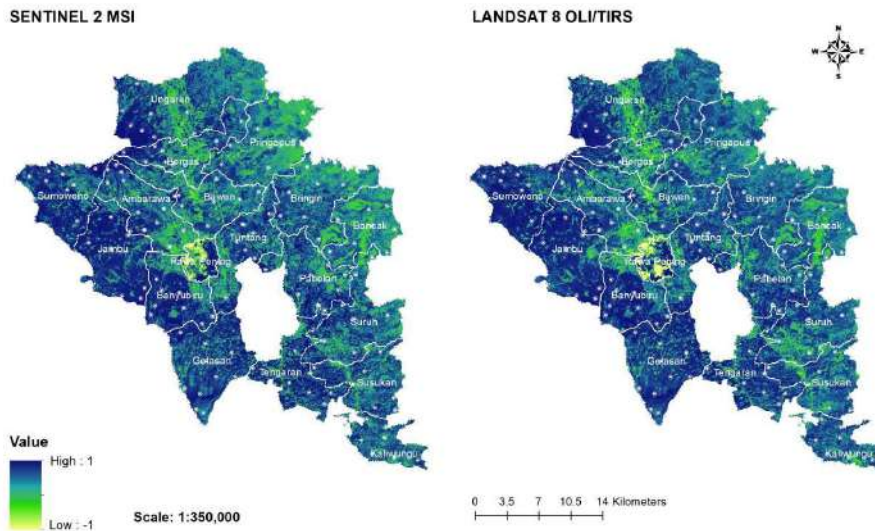


Fig. 3: NDVI results from satellite images of Sentinel 2A and Landsat 8 in 2019, recording in the dry season.

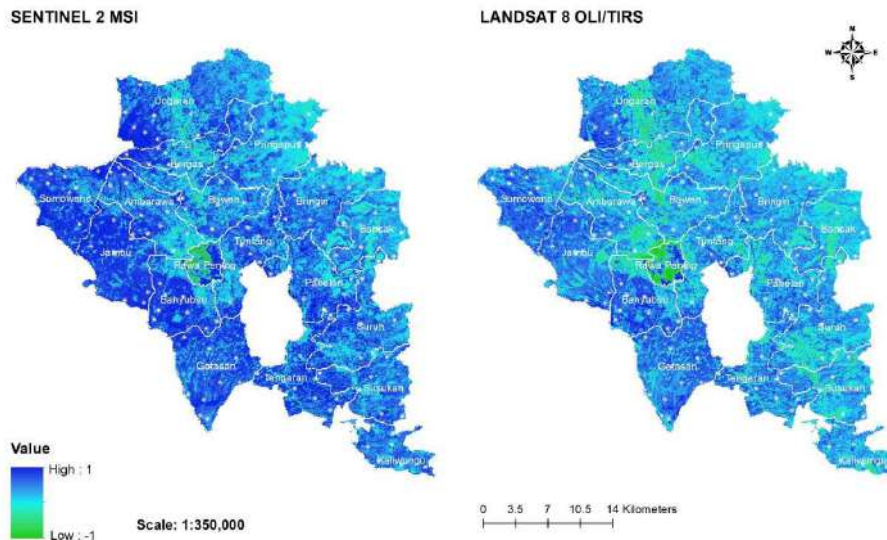


Fig. 4: The utilizing of SAVI of Sentinel 2A and Landsat 8 OLI in Semarang Regency.

Merbabu Volcano slope. This was mostly characterized by covers of paddy fields, and region with an adequate water source, with the possibility of harvest reaching three times in a year.

Testing the relationship between the number of microbes in the soil with the satellite imagery, with NDVI and SAVI values, showed a weak correlation. Thus, there was a limitation in its ability to identify objects at the surface. Meanwhile, the association between the NDVI Landsat 8 OLI and the number of microbes present in the soil was 0.09. This condition was similar to the relationship between SAVI Landsat 8 OLI and microbe quantity (0.03), although

the outcome was better than the Sentinel value, which was only 0.01. Furthermore, the correlation is shown in Fig. 6.

The ability of satellite imagery to identify soil fertility was shallow, as an insignificant relationship was established with the numbers of microbes. This identification capacity is a research gap in the development of soil fertility detection methods using satellite imagery data. Furthermore, weaknesses were observed in the use of SAVI and NDVI as parameters in the identification of soil surface vegetation objects. Also, another flaw in the satellite imagery-based analysis encompassed the difficulty in the ability of the imagery to penetrate the soil in areas with dense vegetation

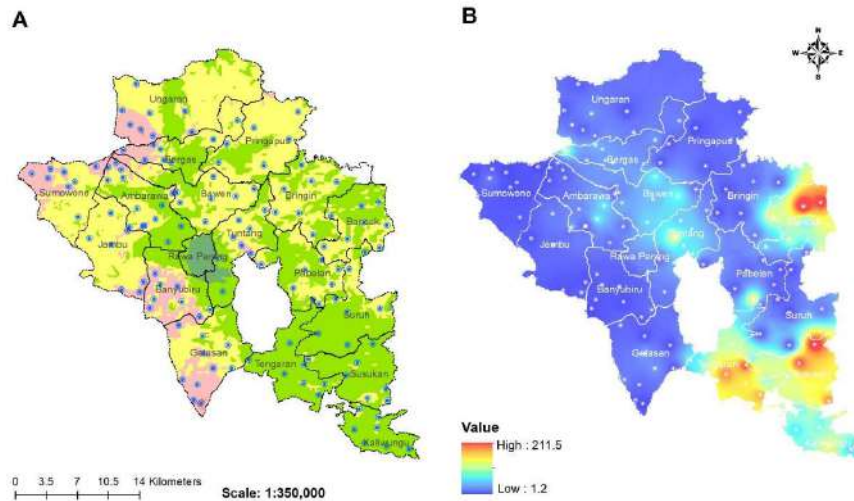


Fig. 5: Point sampling distribution based on land degradation maps issued by the Ministry of Environment and Forestry. B. IDW Interpolation of the amount of microbial content in the soil.

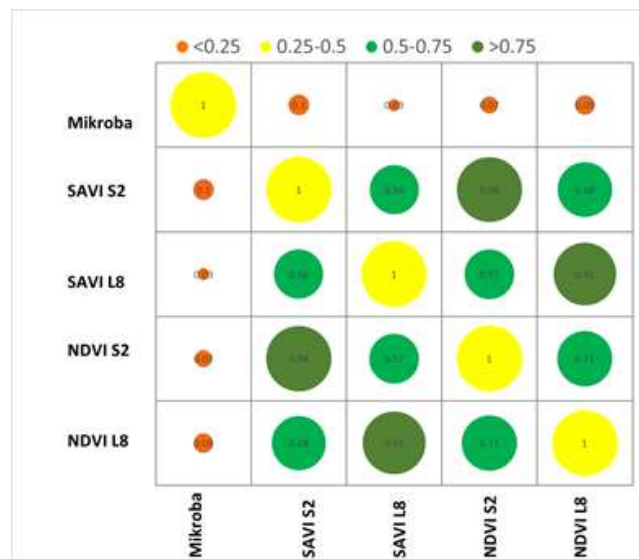


Fig. 6: Correlation matrix of the results of microbial surveys, SAVI Sentinel and Landsat, along with NDVI Sentinel and Landsat.

cover. Hence, there was still an insignificant relationship between the density recorded and the number of microbes. Furthermore, there are potentials to develop further methods for detecting soil fertility using satellite imagery.

CONCLUSION

There was a high similarity in the NDVI data obtained using Landsat 8 OLI and Sentinel 2A, due to the presence of sensors that move at almost the same wavelength. Moreover, Landsat satellite imagery tends to possess the same potential for resource observation with an equal number of sensors.

At the same time, Sentinel has a resolution of 10 meters, in contrast with Landsat of 15 meters, with pan-sharpening band 8. Furthermore, between NDVI and SAVI, both satellites produced very similar results because the outline possesses the same function in earth observation. Therefore, the relationship between vegetation index and the number of microbes in the identification of soil fertility was observed to be relatively weak. Thus, the next step requires the testing of several indexes that possess closer relationships with the number of microbes, with the aid of satellite imagery, to identify fertility levels more accurately.

ACKNOWLEDGEMENT

The authors are grateful to the Semarang Regency Environmental Agency for providing data on the distribution of land degradation maps and other assistance provided in supporting this research.

REFERENCES

- Arrogante-funes, P., Novillo, C.J. and Romero-calcerrada, R. 2018. Monitoring NDVI inter-annual behavior in mountain areas of Mainland Spain (2001-2016). *Sustainability*, 10(12): 4363. DOI: 10.3390/su10124363.
- Bhaskaran, S., Paramananda, S. and Ramnarayan, M. 2010. Per-pixel and object-oriented classification methods for mapping urban features using Ikonos satellite data. *Applied Geography*, 30(4): 650-665. <https://doi.org/10.1016/j.apgeog.2010.01.009>.
- Buchori, I., Sugiri, A., Mussadun, M., Wadley, D., Liu, Y., Pramitasari, A. and Pamungkas I.T.D. 2017. International Journal of Disaster Risk Reduction A predictive model to assess spatial planning in addressing hydro- meteorological hazards : A case study of Semarang City , Indonesia. *International Journal of Disaster Risk Reduction*, 0-1. DOI: 10.1016/j.ijdr.2017.11.003.
- Chauhan, P.S., Mishra, S.K., Misra, S., Dixit, V.K., Pandey, S., Khare, P., Khan, M.H., Dwivedi, S. and Lehri, A. 2017. Evaluation of fertility indicators associated with arsenic-contaminated paddy fields soil. *International Journal of Environmental Science and Technology*, 15: 2447-2458. <https://doi.org/10.1007/s13762-017-1583-9>.
- Coulter, L.L., Stow, D.A., Tsai, Y., Ibanez, N., Shih, H., Kerr, A. and Mensah, F. 2016. Remote Sensing of Environment Classification and assessment of land cover and land use change in southern Ghana using dense stacks of Landsat 7 ETM + imagery. *Remote Sensing of Environment*, 184: 396-409. DOI: 10.1016/j.rse.2016.07.016.
- Dewi, R.S., Bijker, W., Stein, A. and Marfai, M. A. 2016. Fuzzy classification for shoreline change monitoring in a part of the Northern coastal area of Java, Indonesia. *Remote Sensing*, 8(3): 190. DOI: 10.3390/rs8030190.
- Filgueiras, R., Mantovani, E. C. and Altho, D. 2019. Crop NDVI monitoring based on sentinel 1. *Remote Sensing*, 11(12): 1441. <https://doi.org/10.3390/rs11121441>.
- Gholamnia, M., Khandan, R., Bonafoni, S. and Sadeghi, A., 2019. Spatiotemporal analysis of MODIS NDVI in the semi-arid region of Kurdistan (Iran). *Remote Sensing*, 11(14): 1723.
- Gillespie, T. W., Ostermann-kelm, S., Dong, C., Willis, K. S., Okin, G. S. and Macdonald, G. M. 2018. Monitoring changes of NDVI in protected areas of southern California. *Ecological Indicators*, 88: 485-494. DOI: 10.1016/j.ecolind.2018.01.031.
- Huete, A.R. 1988. A soil-adjusted vegetation index (SAVI). *Remote Sensing of Environment*, 25(3): 295-309. [https://doi.org/10.1016/0034-4257\(88\)90106-X](https://doi.org/10.1016/0034-4257(88)90106-X).
- Iryanthony, S.B., Helmi, M. and Macklin, P.A. 2019. Utilizing Landsat satellite data (1990-2018) to detect water inundation for the management of human settlements in coastal zones, 12. Master Thesis. Universitas Diponegoro, Semarang.
- Islam, K., Rahman, F. and Jashimuddin, M. 2018. Modeling land use change using cellular automata and artificial neural network : The case of Chunati Wildlife Sanctuary, Bangladesh. *Ecological Indicators*, 88: 439-453. DOI: 10.1016/j.ecolind.2018.01.047.
- Lal, K., Kumar, D. and Kumar, A. 2017. Spatio-temporal landscape modeling of urban growth patterns in Dhanbad urban agglomeration, India using geoinformatics techniques. *Egyptian Journal of Remote Sensing and Space Science*, 20(1): 91-102. <https://doi.org/10.1016/j.ejrs.2017.01.003>.
- Lima, A., De Vivo, B., Cicchella, D., Cortini, M. and Albanese, S. 2003. Multifractal IDW interpolation and fractal filtering method in environmental studies: An application on regional stream sediments of (Italy), Campania region. *Applied Geochemistry*, 18(12): 1853-1865. DOI: 10.1016/S0883-2927(03)00083-0.
- Lu, Y. and Wu, P. 2019. Detection and prediction of land use/land cover change using spatiotemporal data fusion and the Cellular Automata-Markov model. *Environ. Monit. Assess.*, 191: 68. <https://doi.org/10.1007/s10661-019-7200-2>.
- Mei, G. and Tian, H. 2016. Impact of data layouts on the efficiency of GPU -accelerated IDW interpolation. *SpringerPlus*. <https://doi.org/10.1186/s40064-016-1731-6>.
- Myint, S. W., Gober, P., Brazel, A., Grossman-Clarke, S. and Weng, Q. 2011. Per-pixel vs. object-based classification of urban land cover extraction using high spatial resolution imagery. *Remote Sensing of Environment*, 115(5): 1145-1161. <https://doi.org/10.1016/j.rse.2010.12.017>.
- Nanzad, L., Zhang, J., Tuvdendorj, B., Nabil, M., Zhang, S. and Bai, Y. 2019. NDVI anomaly for drought monitoring and its correlation with climate factors over Mongolia from 2000 to 2016. *Journal of Arid Environments*, 164: 69-77. <https://doi.org/10.1016/j.jaridenv.2019.01.019>.
- Ning, J., Sheng, M., Yi, X., Wang, Y. and Hou, Z. 2019. Rapid evaluation of soil fertility in tea plantation based on near-infrared spectroscopy. *Spectroscopy Letters*, 51(9): 463-471. <https://doi.org/10.1080/00387010.2018.1475398>.
- Nugraha, A.L., Hani'Ah and Pratiwi, R.D. 2017. Assessment of multi hazards in Semarang City. *AIP Conference Proceedings*, 1857: 1-9. <https://doi.org/10.1063/1.4987112>.
- Ren, H., Zhou, G. and Zhang, F. 2018. Remote sensing of environment using negative soil adjustment factor in soil-adjusted vegetation index (SAVI) for aboveground living biomass estimation in arid grasslands. *Remote Sensing of Environment*, 209(79): 439-445.
- Rimal, B., Lifu, Z., Hamidreza, K., Barry, N.H., Sushila, R. and Peng, Z. 2018. Land use/land cover dynamics and modeling of urban land expansion by the integration of cellular automata and markov chain. *International Journal of Geo-Information*, 7(4):154. <https://doi.org/10.3390/ijgi7040154>.
- Rizk, I. and Rashed, M. 2015. Monitoring urban growth and land use change detection with GIS and remote sensing techniques in Daqahlia governorate Egypt. *International Journal of Sustainable Built Environment*, 4(1): 117-124. <https://doi.org/10.1016/j.ijsbe.2015.02.005>.
- Rudiarto, I., Handayani, W. and Setyono, J.S. 2018. A regional perspective on urbanization and climate-related disasters in the northern coastal region of central Java, Indonesia. *Land*, 7(1): 34. DOI: 10.3390/land7010034.
- Seo, B., Lee, J., Lee, K., Hong, S. and Kang, S. 2019. Field crops research improving remotely-sensed crop monitoring by NDVI-based crop phenology estimators for corn and soybeans in Iowa and Illinois, USA. *Field Crops Research*, 238(October 2017): 113-128.
- Town, D. T., Gondar, S., Halefom, A., Teshome, A., Sisay, E. and Ahmad, I. 2018. Dynamics of land use and land cover change using remote sensing and GIS: a case study of Islamabad Pakistan. *SpringerPlus* 5, 812 (2016): 165-174. <https://doi.org/10.1186/s40064-016-2414-z>.
- Trihatmoko, E. 2020. Coastal Dynamic in Northern Central Java by Geomorphological Approach. Doctoral Thesis. Universitas Gadjah Mada, Yogyakarta.
- Wong, D. W. S. 2017. Interpolation : inverse-distance weighting. *International Encyclopedia of Geography: People, the Earth, Environment and Technology*. <https://doi.org/10.1002/9781118786352.wbieg0066>.
- Wu, M., Yang, C., Song, X., Hoffmann, W. C., Huang, W., Niu, Z., Wang, C. and Yu, B. 2018. Monitoring cotton root rot by synthetic Sentinel-2

- NDVI time series using improved spatial and temporal data fusion. *Nature*, 2016: 1-12.
- Yangchengsi, Z., Long, G., Yiyun, C., Tiezhu, S., Mei, L., QingLan, J., Zhang, H. and Shanqin, W. 2019. Prediction of soil organic carbon based on Landsat 8 monthly NDVI data for the Jiangnan Plain. *Remote Sensing*, 11(14): 1683. DOI: 10.3390/rs11141683.
- Zhang, H.K., Roy, D. P., Yan, L., Li, Z., Huang, H., Vermote, E., Skakun, S. and Roger, J. 2018. Remote sensing of environment characterization of sentinel-2a and Landsat-8 top of atmosphere, surface, and nadir brdf adjusted reflectance and NDVI differences. *Remote Sensing of Environment*, 215: 482-494. <https://doi.org/10.1016/j.rse.2018.04.031>.



Adsorption of U(VI) in Solution by Biochar and FeS Nanoparticles

Xitong Zheng, Long Fu, Hao Deng, Keyuan Huang, Tianqi Liu, Yulin Deng, Jiaming Luo, Miao Xiang, Anjie Wang, Muqing Qiu, Li Han and Hai Wang[†]

School of Life Science, Shaoxing University, Huancheng West Road 508, Shaoxing, 312000, P. R. China

[†]Corresponding author: Hai Wang; wanghai@usx.edu.cn

Nat. Env. & Poll. Tech.
Website: www.neptjournal.com

Received: 15-06-2020
Revised: 06-10-2020
Accepted: 09-10-2020

Key Words:

Adsorption
U(VI)
Biochar
FeS

ABSTRACT

Uranium (U) is a common radionuclide in soil and groundwater. Uranium contamination often results from uranium mining and processing, nuclear energy power plants, nuclear weapon tests and nuclear accidents. Due to its toxicity and bioaccumulation, it was necessary to treat it effectively. Biochar and FeS nanoparticles were prepared for the treatment of U(VI) in solution. The characteristics of biochar and FeS nanoparticles were determined by Scanning Electron Microscopy, Energy Dispersive Spectrum and Fourier Transform Infrared Spectroscopy and BET adsorption method. The results showed that a large number of functional groups were present on the surface of biochar and FeS nanoparticles. The influencing factors, such as contact time, pH of the solution, initial concentration U(VI) and solution temperature, had an important influence on the adsorption capacity of U(VI) by biochar and FeS nanoparticles.

INTRODUCTION

The development of new energy has become a requirement for sustainable economic development and national defence construction. As a green energy source, nuclear energy has attracted extensive attention from countries around the world (Liu et al. 2010, Vogel et al. 2010). Among them, uranium as the main nuclear fuel needs to increase its development and smelting efforts. However, a large amount of uranium wastewater will be generated during the development, smelting and use of uranium. The direct discharge of uranium wastewater will cause water and soil pollution causing serious harm to the environment and humans (Lovering et al. 2016, Veliscek-Carolan 2016). Therefore, the treatment of uranium wastewater is urgent. The treatment of uranium wastewater usually adopts coagulation-filtration method, evaporation-concentration method, ion exchange method, biological method, adsorption method, etc. (Li et al. 2012). The coagulation-filtration method is a simple process and low cost. However, the concentration of uranium in the effluent of the wastewater treated by this method is relatively high and needs further treatment. The evaporative concentration method is simple, effective and has a high removal rate and high cost. The ion exchange method has good removal rate and low concentration of uranium in the effluent. However, the treatment cost is high, and it is easy to bring secondary pollution. The biological method has a high removal rate, but its practical application is difficult. Adsorption method is a

simple and efficient wastewater treatment method. In recent years, it has been widely used in the treatment of wastewater containing uranium (Feng et al. 2016, Sun et al. 2016, Li et al. 2019, Ma et al. 2019).

At present, the commonly used adsorbents are montmorillonite, kaolin, chitosan, graphene, nano-zero iron, biochar, etc. (Li et al. 2012, Decker et al. 2017, Qiu & Huang 2017). Biochar has become the main application and research adsorbent for pollutant removal in the water environment due to its wide source, economical and environmental protection (Jin et al. 2018). FeS nanoparticles are effective fixatives for the removal of heavy metals with low solubility of metal sulphide (Liu et al. 2008). FeS is a natural sulphide mineral and an excellent fixative for heavy metals for its unique molecular structure, compositions, and surface chemical properties (Maxim et al. 2007, Milad et al. 2018). Heavy metals can be immobilized by FeS through adsorption, ion exchange, and/or chemical precipitation of highly insoluble metal sulphides (Feng et al. 2008). Numerous studies have reported on the remediation of heavy metal contaminated water prepared in the laboratory by FeS (Hua & Deng 2008, Hyun et al. 2012, Lyu et al. 2017).

In this study, biochar and FeS nanoparticles were prepared. The characteristic of biochar and FeS nanoparticles are discussed. Adsorption experiments are carried out. The effect of the operational parameters (such as contact time, initial concentration of U(VI), pH in solution and temperature) on

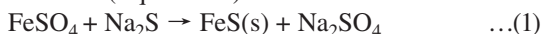
adsorption capacity by biochar and FeS nanoparticles were evaluated in details.

MATERIALS AND METHODS

Materials

Peanut shell was obtained from a farm in the city of Jinan, Shandong province, P.R. China. It was washed three times with water, then dried at 105°C for 24 h, and then milled into powder of 2 mm as the feedstock biomass for biochar production. Ten grams of peanut shell powder was pyrolyzed in a porcelain crucible under the oxygen-limited conditions at 450°C for 2 h in a muffle furnace. The biochar from peanut shell was obtained.

FeS nanoparticles were prepared through co-precipitation of $\text{Na}_2\text{S}\cdot 9\text{H}_2\text{O}$ and $\text{FeSO}_4\cdot 7\text{H}_2\text{O}$ in the aqueous phase under anoxic conditions (Equation 1).



All chemicals used in this study were of analytical grade. Sodium sulphide nonahydrate, iron sulphate heptahydrate, NaOH, H_2SO_4 , uranium nitrate hexahydrate ($\text{UO}_2\text{NO}_3\cdot 6\text{H}_2\text{O}$) were obtained from Fengchuan Chemical Technology Co. Ltd. (Tianjin, China).

Adsorption Experiments

Adsorption experiments were carried out on a shaker at 200 rpm under a constant temperature condition. Typically, an amount of the adsorbent was added into 100 mL U(VI) of initial concentration in a 250 mL Erlenmeyer flask. Flask was sealed by a bottle cap and placed in the shaker at 200 rpm and constant temperature. The anaerobic deionized water was used in adsorption experiments. The pH in the solution was adjusted by 0.1 mol/L HCl or NaOH solution. The entire adsorption process reached equilibrium and the supernatant was collected after filtration. The residual sample was centrifuged at 4000 rpm for 5 min. All the experiments

were carried out in duplicate and the data were analysed by the mean and standard deviation.

Analytical Methods

The U(VI) concentration in the supernatant was analysed by UV-vis spectrophotometry. The characteristics of biochar and FeS nanoparticles were determined by Scanning Electron Microscopy (SEM), Energy Dispersive Spectrum (EDS) and Fourier Transform Infrared Spectroscopy (FT-IR), respectively. The specific surface area, pore size and pore volume of biochar and FeS nanoparticles were determined by the BET adsorption method. The amount of adsorption was calculated using the following formula:

$$q_e = \frac{(C_0 - C_e)V}{m} \quad \dots(2)$$

Where, q_e (mg/g) is the amount of adsorption per unit mass of adsorbent at the end of adsorption. C_0 (mg/L) and C_e (mg/L) are the initial concentration of the adsorbate in the solution and the concentration at the equilibrium of adsorption. V (mL) is the volume of solution and m (g) is the dosage of the modified biochar.

RESULTS AND DISCUSSION

Characterization of Biochar and FeS Nanoparticles

SEM images of biochar and FeS nanoparticles were determined by SEM. As shown in Fig. 1A, the morphology of biochar was smooth and a few small fragments were present. While the surface of FeS was compact and aporate (Fig. 1B). The shape was cotton wool. The surface area of biochar ($52.17 \text{ m}^2/\text{g}$) was greater than that of FeS nanoparticles ($18.25 \text{ m}^2/\text{g}$). Some related researches have proved that surface area had an important role in the adsorption capacity.

From Fig. 2A, it could be concluded that biochar included a large number of elements, such as C, O, Si, Mg, K and Ca. Among them, elements of C and O for biochar

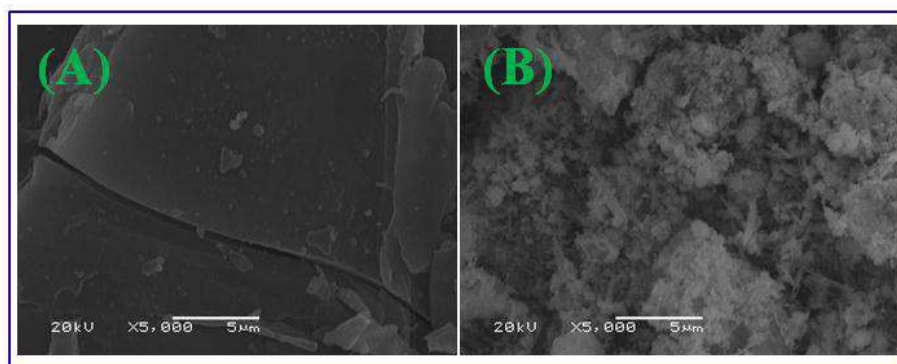


Fig. 1: SEM images of biochar (A) and FeS nanoparticles (B).

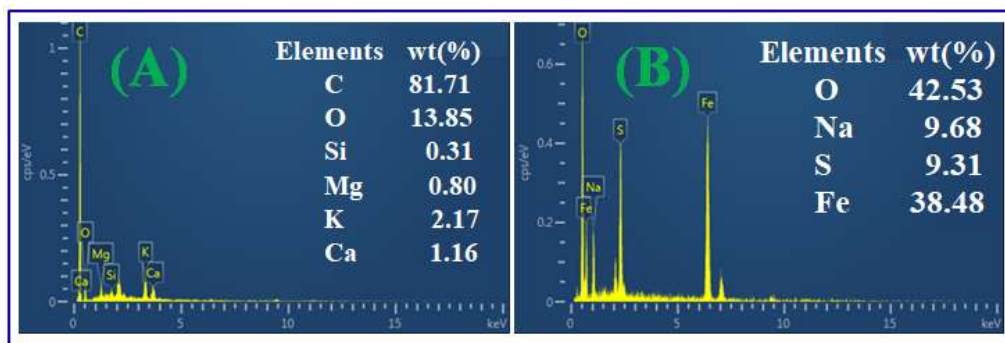


Fig. 2: EDS spectrum of biochar (A) and FeS nanoparticles (B).

were the main elements. Their weights were 81.71% and 13.85%, respectively. The weights of Si, Mg, K and Ca were 0.31%, 0.80%, 2.17% and 1.16%, respectively. For FeS nanoparticles (Fig. 2B), elements of O, Na, S and Fe were observed. Their weights were 42.53%, 9.68%, 9.31% and 38.48%, respectively. The elements of O and Fe were the main elements.

Fig. 3 displayed the characteristic stretching frequencies of biochar and FeS nanoparticles. Six peaks were observed for biochar at 3363, 2021, 1608, 1379, 1061 and 571 cm^{-1} , respectively. They were attributed to the vibrations of -OH, C-C, C=C, O=C-O, C-O and Si-O functional groups. These functional groups benefited for the adsorption of U(VI). For biochar, possible removal mechanisms consisted of electrostatic attraction and surface complexation (Ahmad et al. 2014). For FeS nanoparticles, four peaks were appeared at 3373, 1601, 1375 and 1074 cm^{-1} , respectively. They were attributed to -OH, O=C-O and C-O functional groups.

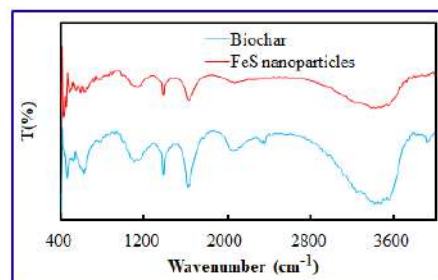


Fig. 3: FT-IR spectrum of biochar and FeS nanoparticles.

Adsorption Experiments

Adsorption experiments were carried out on a shaker at 200 rpm under a constant temperature condition. The effect of operation parameters (such as pH, contact time, initial concentration U(VI) and temperature) on adsorption capacity by biochar and FeS nanoparticles were tested. The experimental results are shown in Fig. 4.

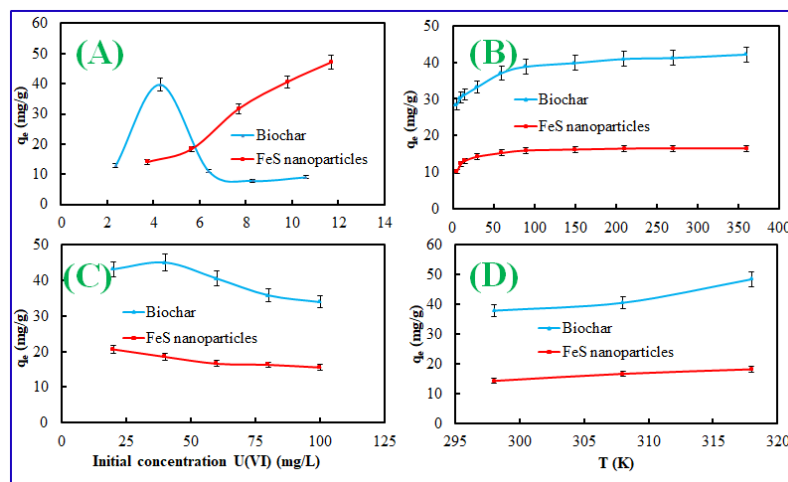


Fig. 4: Effect of operation parameters on adsorption capacity by biochar and FeS nanoparticles (A: pH, B: contact time, C: initial concentration of U(VI), D: temperature).

Effect of pH: pH in solution could affect the stability, surface potential and reactivity of biochar and FeS nanoparticles. Therefore, it was important to evaluate the effect of pH. Experimental conditions were as following: Initial concentration U(VI) was 60 mg/L, contact time was 360 min, dosage of biochar or FeS nanoparticle was 0.1 g, and temperature was 308 K. The initial pH in solution ranged from 2.0 to 12.0. Fig. 4A displayed the effect of initial pH in solution on the adsorption capacity of U(VI) by biochar and FeS nanoparticles. It suggested that the initial pH in solution influenced the adsorption capacity of U(VI) by biochar and FeS nanoparticles. It might be the reason that formation of U(VI) in solution varied with initial pH value in the solution. At alkaline pH, the dominant U(VI) species shifted from positively charged $(\text{UO}_2)_3(\text{OH})_5^+$ and $(\text{UO}_2)_4(\text{OH})_7^+$ to negatively charged $(\text{UO}_2)_3(\text{OH})_7^-$, $\text{UO}_2(\text{OH})_3^-$ and $\text{UO}_2(\text{OH})_4^{2-}$ (Zhu et al. 2019). Therefore, the initial pH in solution was an important operation parameter for adsorption of U(VI) by biochar and FeS nanoparticles.

Effect of contact time: Experimental conditions were: initial concentration of U(VI) was 60 mg/L, pH was 4.5, the dosage of biochar or FeS nanoparticle was 0.1 g and temperature was 308 K. The contact time was 5, 10, 15, 30, 60, 90, 150, 210, 270 and 360 min, respectively. Fig. 4B described the effect of contact time on the adsorption capacity of U(VI) ions in solution by biochar and FeS nanoparticles. As shown in Fig. 4B, the adsorption capacity of U(VI) increased quickly at the first stage. Then adsorption capacity of U(VI) increased slowly as the contact time increased. The adsorption capacity of U(VI) increased very less when the adsorption process reached adsorption equilibrium. For biochar and FeS nanoparticles, the adsorption equilibrium of contact time was 360 min. At the first stage, U(VI) could be very rapidly adsorbed by biochar or FeS nanoparticles because of many adsorption sites. As the initial concentration of U(VI) increased, adsorption sites were utilized fully and the adsorption process reached saturation gradually.

Effect of initial concentration U(VI): Experimental conditions were: contact time was 360 min, pH was 4.5, the dosage of biochar or FeS nanoparticle was 0.1 g and the temperature was 308 K. The initial concentration U(VI) was 20, 40, 60, 80 and 100 mg/L, respectively. The effect of initial concentration U(VI) on adsorption capacity of U(VI) by biochar and FeS nanoparticles is shown in Fig. 4C. It suggested that adsorption capacity decreased as the initial concentration U(VI) increased. When the initial concentration U(VI) was 100 mg/L, the adsorption capacity for biochar and FeS nanoparticles reached 34.12 and 15.52 mg/g, respectively. The adsorption capacity of biochar was better than that of FeS nanoparticles.

Effect of temperature: Experimental conditions were: initial concentration U(VI) was 60 mg/L, pH was 4.5, the dosage of biochar or FeS nanoparticle was 0.1 g and the contact time was 360 min. The temperature was 298, 308 and 318 K, respectively. It was found that the removal efficiency of U(VI) ion in aqueous solution increased with increasing solution temperature from 293 K to 313 K. It also indicated that the adsorption process is endothermic. The enhancement in the adsorption capacity might be due to the chemical interaction between adsorbates and adsorbent, creation of some new adsorption sites or the increased rate of intraparticle diffusion of adsorbate molecules into the pores of biochar or FeS nanoparticles at higher temperatures (Cho et al. 2011, Nethaji et al. 2013).

CONCLUSIONS

The biochar from the peanut shell and FeS nanoparticles was prepared. The characteristics of biochar and FeS nanoparticles were determined by SEM, EDS, FT-IR and BET adsorption method. The adsorption capacity and influencing factors of U(VI) in aqueous solution by the biochar and FeS nanoparticles were studied in detail by the adsorption experiments. The experimental results showed that the influencing factors, such as contact time, pH in solution, initial concentration U(VI) and solution temperature, had an important influence on the adsorption capacity of U(VI) by biochar and FeS nanoparticles.

ACKNOWLEDGMENTS

The research was supported by Natural Science Foundation of Zhejiang Province, China (LGF19C030001 and LG-F20C030001), Basic Public Welfare Research Project of Zhejiang Province (LGN20C150003) and the Key Research Program of Shaoxing University (2019LG1003).

REFERENCES

- Ahmad, M., Rajapaksha, A.U., Lim, J.E., Zhang, M., Bolan, N., Mohan, D., Vithanage, M., Lee, S.S. and Ok, Y.S. 2014. Biochar as a sorbent for contaminant management in soil and water: a review. *Chemosphere*, 99: 19-33.
- Cho, D.W., Chon, C.M., Kim, Y.J., Jeon, B.H., Schwartz, F.W., Lee, E.S. and Song H. 2011. Adsorption of nitrate and Cr (VI) by cationic polymer-modified granular activated carbon. *Chem. Eng. J.*, 175: 298-305.
- Decker, J.D., Folens, K., Clercq, J.D., Meledina, M., Tendeloo, G.V., Laing, G.D. and Voort, P.V.D. 2017. Ship-in-a-bottle CMPO in MIL-101(Cr) for selective uranium recovery from aqueous streams through adsorption. *J. Hazard. Mater.*, 335: 1-9.
- Feng, J., Zhu, B.W. and Lim, T.T. 2008. Reduction of chlorinated methanes with nano-scale Fe particles: effects of amphiphiles on the dechlorination reaction and two-parameter regression for kinetic prediction. *Chemosphere*, 73: 1817-1823.

- Feng, M.L., Sarma, D., Qi, X.H., Du, K.Z., Huang, X.Y. and Kanatzidis, M.G. 2016. Efficient removal and recovery of uranium by a layered organic-inorganic hybrid thiostannate. *J. Am. Chem. Soc.*, 138: 12578-12585.
- Hua, B. and Deng, B. 2008. Reductive immobilization of uranium(VI) by amorphous iron sulfide. *Environ. Sci. Technol.*, 42: 8703-8708.
- Hyun, S.P., Davis, J.A., Sun, K. and Hayes, K.F. 2012. Uranium (VI) reduction by iron(II) monosulfide mackinawite. *Environ. Sci. Technol.*, 46: 3369-3376.
- Jin, J., Li, S.W., Peng, X.Q., Liu, W., Zhang, C.L., Yang, Y., Han, L.F., Du, Z.W., Sun, K. and Wang, X.K. 2018. HNO₃ modified biochars for uranium(VI) removal from aqueous solution. *Biores. Technol.*, 256: 247-253.
- Liu, J., Valsaraj, K.T., Devai, I. and DeLaune, R. 2008. Immobilization of aqueous Hg(II) by mackinawite (FeS). *J. Hazard. Mater.*, 157: 432-440.
- Liu, M.X., Dong, F.Q., Yan, X.Y., Zeng, W.M., Hou, L.Y. and Pang, X.F. 2010. Biosorption of uranium by *Saccharomyces cerevisiae* and surface interaction under culture conditions. *Biores. Technol.*, 101: 8573-8580.
- Li, Z.D., Zhang, H.Q., Xiong, X.H. and Luo, F. 2019. U(VI) adsorption onto covalent organic frameworks-TpPa-1. *J. Solid State Chem.*, 277: 484-492.
- Li, Z.J., Chen, F., Yuan L.L., Zhao, Y.L., Chai, Z.F. and Shi, W.Q. 2012. Uranium(VI) adsorption on graphene oxide nanosheets from aqueous solution. *Chem. Eng. J.*, 210: 539-546.
- Lovering, J.R., Yip, A. and Nordhaus, T. 2016. Historical construction costs of global nuclear power reactors. *Energy Policy*, 91: 371-382.
- Lyu, H.D., Tang, J.C., Huang, Y., Gai, L.S., Zeng, E.Y., Liber, K. and Gong, Y.Y. 2017. Removal of hexavalent chromium from aqueous solutions by a novel biochar supported nanoscale iron sulfide composite. *Chem. Eng. J.*, 322: 516-524.
- Ma, F.Q., Nian, J.R., Bi, C.L., Yang, M., Zhang, C.H., Liu, L.J., Dong, H.X., Zhu, M.X. and Dong, B. 2019. Preparation of carboxylated graphene oxide for enhanced adsorption of U(VI). *J. Solid State Chem.*, 277: 9-16.
- Maxim, I.B., Edward, J.O., Eric E.R., Jeremy, B.F. and Kenneth, M.K. 2007. Adsorption of Fe(II) and U(VI) to carboxyl-functionalized microspheres: The influence of speciation on uranyl reduction studied by titration and XAFS. *Geochim. Cosmochim. Ac.*, 71: 1898-1912.
- Milad, M., Reza, T., Abolghasem, F. and Joel, T.M. 2018. Fe(III), Cu(II) and U(VI) binuclear complexes with a new isothiosemicarbazone ligand: Syntheses, characterization, crystal structures, thermal behavior and theoretical investigations. *Inorg. Chim. Acta*, 4821: 643-653.
- Nethaji, S., Sivasamy, S. A. and Mandal, A.B. 2013. Preparation and characterization of corn cob activated carbon coated with nano-sized magnetite particles for the removal of Cr(VI). *Biores. Technol.*, 134: 94-100.
- Qiu, M.Q. and Huang, P. 2017. Kinetic and thermodynamic studies on the adsorption of zinc ions from aqueous solution by the blast furnace slag. *Nature Environ. Poll. Technol.*, 16: 639-642.
- Sun, Y.B., Zhang, R., Ding, C.C., Wang, X.X., Cheng, W.C., Chen, C.L. and Wang, X.K. 2016. Adsorption of U(VI) on sericite in the presence of *Bacillus subtilis*: A combined batch, EXAFS and modeling techniques. *Geochim. Cosmochim. Ac.*, 180: 51-65.
- Veliscek-Carolan, J. 2016. Separation of actinides from spent nuclear fuel: A review. *J. Hazard. Mater.*, 318: 266-281.
- Vogel, M., Günher, A., Rossberg, A., Li, B., Bernhard, G. and Raff, J. 2010. Biosorption of U(VI) by the green algae *Chlorella vulgaris* in dependence of pH value and cell activity. *Sci. Total Environ.*, 409: 384-395.
- Zhu, W., Lei, J., Li, Y., Dai, L., Chen, T., Bai, X., Zhou, J., Wang, L. and Duan, T. 2019. Procedural growth of fungal hyphae/Fe₃O₄/graphene oxide as ordered-structure composites for water purification. *Chem. Eng. J.*, 355: 777-783.



Study on Hazards of Chemical Fibre Wastewater and Evaluation of Uncertainty in Environmental Monitoring

Yanchun Hao

Department of Quality Control, Jilin Railway Technology College, Jilin 132200, China

†Corresponding author: Yanchun Hao; haoyanchun1973@163.com

Nat. Env. & Poll. Tech.
Website: www.neptjournal.com

Received: 06-10-2020
Revised: 31-12-2020
Accepted: 21-01-2021

Key Words:

Wastewater
Chemical fibre hazards
Monitoring factor
Measurement uncertainty

ABSTRACT

China has a typical labour-intensive chemical fibre industry characterized by high energy consumption, severe pollution tendencies, and low resource utilization rate. The chemical fibre industry seriously harms the environment due to its small production scale, single product variety, low resource utilization efficiency, and weak technology strength. Investigating wastewater generated by chemical fibre production and improving the measurement uncertainty of monitoring factors are significant to chemical fibre wastewater treatment and environmental protection. A review of related literature on wastewater pollution in the chemical industry is conducted to summarize the types of wastewater hazards in the chemical fibre production process. An environmental monitoring uncertainty model is used to measure the wastewater monitoring uncertainty of a chemical fibre enterprise in Jilin City, Jilin Province in China. Findings show that the hazardous types of chemical fibre wastewater include polluting the surrounding environment, endangering human health, and destroying existing biodiversity. The monitoring quality reliability of the extended uncertainty model for the pH value, chemical oxygen demand, ammonia-nitrogen, and total phosphorous used in this case is superior to the direct chemical numerical detection quality. The monitoring uncertainty of chemical fibre wastewater can be further improved by perfecting the chemical fibre production process and the wastewater treatment process. Its environmental hazards can also be relieved by improving the environmental monitoring industry of wastewater and strengthening the R&D of related virtual instruments. This study can serve as a reference for enhancing the environmental monitoring quality of chemical fibre wastewater, compensating for the environmental monitoring errors, realizing the energy conservation and emission reduction of the chemical fibre industry.

INTRODUCTION

The manufacturing of chemical fibre is an industry occupied in all kinds of processes, such as preparation of chemical fibre stock solution, polymerization, spinning, and after-process treatment. The application of chemical fibres, the main raw materials in the textile industry, has been transformed from the garment field into industrial fields, such as automobile, building, indoor and outdoor building materials, and labour protection. The overall chemical fibre output in Mainland China presented a rising trend from 2014 to 2020, reaching the peak output of approximately 61,680,000 tons in 2020. As water resources are used in the chemical fibre production process in quantity, sewage and wastewater are discharged on a large scale. Chemical fibre wastewater refers to all kinds of wastewater generated in the chemical fibre production process. It includes polyethene terephthalate (PET), purified terephthalic acid (PTA), and cotton pump black liquor. Others may also contain viscose, strong acid, strong base, aldehydes, cyanide, and benzenes. All of which can easily generate toxic actions on microorganisms.

China is the largest producing and exporting country of textile products in the world. It also has the most complete global textile industrial chain. In the face of downturn pressure in the adjustment phase, the Chinese chemical fibre industry maintains a slow-growth trend. This output growth is supported by positive national measures facilitating high-quality development and accompanied by the aggravated environmental protection pressure. On November 10, 2020, the Ministry of Ecological Environment of China released Self-Monitoring Technology Guidelines for Pollution Sources-Chemical Fibres Manufacturing Industry. This guideline presents the general requirements for self-monitoring of pollutant discharging units in the chemical fibre manufacturing industry and the basic contents and procedures for the monitoring scheme, information records, and reports. The pollutant discharging units in the chemical fibre manufacturing industry should conduct individual monitoring of water and air pollutants, discharged noise, and impact on surrounding environmental quality in the production and operation phase. The monitoring facilities should also be set and maintained, and monitoring data

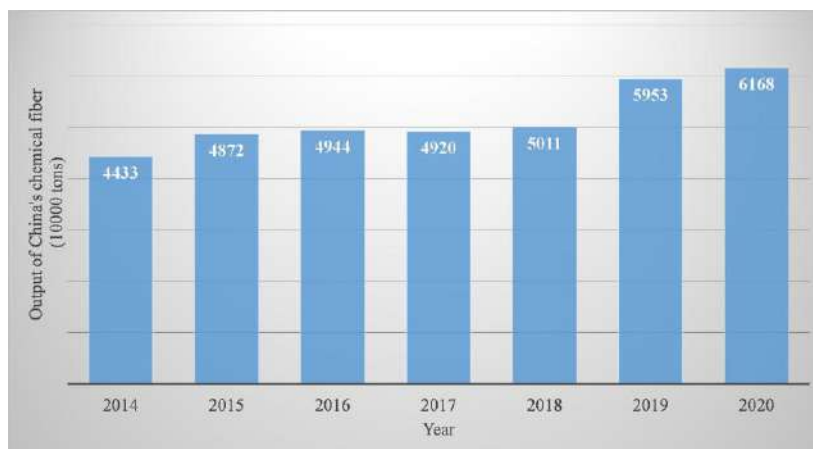


Fig. 1: The output of chemical fibre in China during 2014-2020.

should be recorded and saved for reference. Finally, the measurement uncertainty should be investigated to verify the monitoring system and the quality of monitoring data. These methods can help chemical fibre wastewater treatment and environmental protection.

OVERVIEW OF THE STUDY AREA

The wastewater treatment technology has originated from municipal sewage treatment and has been continuously developing for over 100 years. It is the result brought by the industrial revolution and urbanization. The serious pollution triggered by the chemical fibre manufacturing industry in China is in urgent need of solutions. Various chemical fibre manufacturing plants are dispersedly distributed in the country's vast territory, so the difficulty in wastewater treatment is large. Concerning the hazards of wastewater discharged by chemical enterprises and the uncertainty problem of the monitoring equipment, Orhon et al. (1994) evaluated the pollution degrees generated by household and industrial sources in Istanbul metropolitan area. They compared the pollutant load in Marmara Sea with the pollutants discharged by Istanbul metropolitan area. Aleksandra et al. (2009) deemed that the waste materials of pump mills were harmful to the surrounding environment. They analysed the environmental research results regarding the impact of surface water in pump mills. They also evaluated the production process factors following the wastewater concentration and distribution in water circulation. Escher et al. (2011) believed that industrial wastewater discharge contained many hazardous chemical substances, which entered the water environment through urban runoffs and agricultural production. The extensive distribution of organic micropollutants in the water

channel imposed harm to aquatic organisms and formed further pressure on residential drinking water. In Pakistan, Nasir et al. (2012) found that the industrial sector was damaging surface water and underground water qualities. The wastewater caused surface water and underground water pollution and endangered biodiversity, human health, and other ecosystems. Verma et al. (2012) deemed that the textile industry was one of the industries with the highest chemical intensity worldwide. Many complicated chemical pollutants would be generated in different textile processing links through wastewater. If directly discharged into the environment, they would trigger various undesirable changes and impact the current ecological status. Lambert et al. (2015) stated that most chemical plants would generate wastewater during the production process and the environmental hazards of wastewater were always the focus of attention. The potential safety hazards in the wastewater treatment would also lead to major risks. Shirkhanloo et al. (2015) investigated the heavy metal pollution in water, soil, and vegetables on a farm nearby the southern oil refinery in Teheran, Iran. The results showed that heavy metal content was high in industrial wastewater, which resulted in severe environmental pollution. Tayeb et al. (2015) showed that most municipal wastewaters were discharged into the sea without treatment in Algeria. They probed the influences of industrial production on dissolved oxygen (DO), chemical oxygen demand (COD), biochemical oxygen demand (BOD), and pH value in Oran Bay of Algeria. The results showed that the concentration of petroleum and grease released into the biological network in industrial production generated a large ecological impact. Wei et al. (2019) evaluated the environmental impact of industrial upgrading in Guangdong Province since 2008 using the panel data of prefecture-level cities. The results showed that the industrial upgrading in Pearl River Delta

led to minor water body pollution because the transfer of water-polluting industries was forbidden. As for the research on the environmental monitoring uncertainty, Batley (1999) investigated environmental monitoring programs. They found that the final analysis could be implemented only when the data quality was comprehensively guaranteed. Thus, the quality of environmental monitoring data was extremely significant. Rocke et al. (2003) deemed that the analytical chemical measurement in environmental monitoring relied upon the evaluation of measuring errors, and the measurement uncertainty should be quantified. They proposed a double-component error model to realize such goals. Conti et al. (2005) described a more detailed uncertainty theory to discuss the problems related to instrumental analysis and uncertainty correction. Nezhikhovskii (2009) introduced various aspects of measurement uncertainty in an analytical laboratory in Russia. They compared the differences in Russia from other countries in the estimation and application of measurement uncertainty. Boon et al. (2010) thought that the measurement method used to characterize environmental pollution was uncertain, which was generated by the field sampling and chemical analysis.

Based on the above literature, the development of the chemical fibre manufacturing industry plays an irreplaceable role in the socio-economic growth of various countries. However, the environmental disruption it causes cannot be underestimated, and treatment and discharge of polluted water sources require adequate attention. Especially in China, a developing country, the national policies focusing on the environmental monitoring field have been frequently formulated. In turn, the overall environmental monitoring industry has a steady growth, which somehow mitigates the environmental pollution. Overall, the monitoring data of related industries and enterprises cannot accurately reflect the current environmental status or provide a reliable basis for environmental governance work. In this study, the hazards caused by the wastewater discharge of chemical fibre manufacturing enterprises are analysed. A case analysis is conducted using the wastewater data of a chemical fibre manufacturing enterprise in Jilin Province. The uncertainty measurement is carried out for the automatic water quality monitoring instrument after the chemical fibre wastewater treatment. The sources of uncertainty components are analysed, the standard uncertainty is evaluated, and the uncertainty component with the greatest influence on the measurement result is determined and well-controlled. This study can serve as a reference for further monitoring of the main factors in chemical fibre wastewater. The findings can help guarantee the accuracy and precision of water quality monitoring results.

HAZARDS OF CHEMICAL FIBRE WASTEWATER

Polluting the Surrounding Environment

Chemical fibre wastewater contains many different pollutants, including phenols, organophosphorus, chlorine and different inorganic pollutants, organic and inorganic mixtures, solids, jellies and an oil slick. If their contents are not effectively reduced to below the national standard in the chemical fibre manufacturing process, they will result in irreversible and persistent environmental impact. Given their insufficient environmental awareness with ineffective monitoring measures, some chemical fibre manufacturing enterprises directly discharge the wastewater generated in the industrial production process into rivers, leading to water pollution in the surrounding area.

Endangering Human Health

The chemical fibre wastewater pollution will directly affect human health. If the polluted water body is accidentally consumed through drinking water or food chains, the toxic substances will make the human body suffer from acute, chronic toxicity to different degrees. Other water bodies may also contain the corresponding chemical substances with carcinogenesis, which can endanger human health. The toxic organic matter in wastewater cannot be easily degraded. Once they are mixed with different bodies of water, they will exert an extremely destructive environmental impact. This situation can lead to cancer and influence human health through aquatic organisms.

Destroying Biodiversity

The chemical fibre wastewater pollution can destroy the living space of organisms. Given that organic acids, alcohols, and epoxides are generated during the chemical fibre production, they will further experience oxidative decomposition reaction in water after being discharged. They will consume most of the dissolved oxygen in the water. In turn, they greatly affect the survival of aquatic animals and plants. The discharge of chemical fibre wastewater may also lead to a rise in the water temperature, unstable pH value, or excessive nutrient substances. All of which will threaten the growth of aquatic organisms. $\text{NH}_3\text{-N}$ in wastewater will cause the eutrophication of water bodies, as it consumes more dissolved oxygen. It will destroy the aquatic environment and impede the safe growth of fish and other water organisms.

MODEL PROFILE

Measurement uncertainty refers to a parameter related to the

measurement result and is used to characterize the dispersity reasonably assigned to the measured values. It is mathematically expressed by standard deviation or multiple of standard deviation. The half-breadth of the confidence interval of a given probability can also be used. The measurement uncertainty reflects the experience accumulation and measurement quality and level for one type of factor. In the environmental monitoring measurement, the uncertainty is introduced to evaluate the measurement quality. A mathematical model can qualitatively and qualitatively analyze the source and components of uncertainty. Thus, it can appropriately express the measurement result through the combination and extension of uncertainty.

The focus of the uncertainty measurement of chemical fibre wastewater monitoring is the content of one element or chemical compound in the solution. The standard measurement methods mainly include titrimetry, colourimetry, and spectrophotometry. The measurement process mostly involves standard liquid preparation, mass measurement, and volume measurement. They mainly follow the principle of indirect measurement, where the measurement result is obtained by combining the instrument-measured value with a standard curve. In this study, a universal mathematical model is used to investigate the measurement uncertainty problem (Peng et al. 2009).

$$C(x) = \frac{f(Y) \times V}{M} \times \frac{P}{R} \times K \quad \dots(1)$$

Where $c(x)$ is the content of one element in the measured solution. $f(Y)$ denotes a concentration function, namely, the functional relationship between sample concentration and instrument response value. v represents the volume of the measured solution. M is the mass of the measured sample. P is precision, expressing the precision influence generated in the operation process with a balance and measuring tool. R is recovery, reflecting the loss of the measured solution or polluted factor. K is the dilution ratio.

The fitting curve equations of standard liquid used by the measurement methods of pH, suspended solids, COD, $\text{NH}_3\text{-N}$, and total phosphorous (TP) in chemical fibre wastewater are simple linear regression equations. The combined measurement uncertainty is u_c , as expressed in Formula (2).

$$\frac{u_c^2}{C} = \left[\frac{u_{f(Y)}}{f(Y)} \right]^2 + \left[\frac{u_V}{V} \right]^2 + \left[\frac{u_M}{M} \right]^2 + \left[\frac{u_P}{P} \right]^2 + \left[\frac{u_R}{R} \right]^2 \quad \dots(2)$$

where u_c is the combined measurement uncertainty and $u_{f(Y)}$ is the uncertainty of concentration function after the curve fitting. u_V , u_M , u_P and u_R are the uncertainties in the volume measurement, mass measurement, precision measurement, and recovery measurement, respectively. Following Formula (2), the relative measurement uncertainty u_{crel} is extended and expressed, as seen in Formula (3).

$$u_{crel} = \sqrt{u_{f(Y)rel}^2 + u_{Vrel}^2 + u_{Mrel}^2 + u_{Prel}^2 + u_{Rrel}^2} \quad \dots(3)$$

Where u_{crel} is the combined relative measurement uncertainty. $U_{f(Y)rel}$ is the relative uncertainty of the concentration function after the curve fitting. u_{Vrel} , u_{Mrel} , u_{Prel} and u_{Rrel} are the relative uncertainties in the volume measurement, mass measurement, precision measurement, and recovery measurement, respectively.

CASE ANALYSIS

Acquisition of Environmental Monitoring Data

A chemical fibre enterprise in Jilin City, Jilin Province, was taken as the research subject. Monitoring points were arranged at its spinning wastewater collection tank, esterification wastewater collection tank, and wastewater discharge outlet to monitor the pH value, COD, $\text{NH}_3\text{-N}$, and TP from December 3 and 4, 2020 (for two consecutive days, four times per day). The monitoring results at the chemical wastewater discharge outlet are shown in Table 1.

Table 1 gives the discharge concentrations of COD, $\text{NH}_3\text{-N}$, TP, and the pH value during the monitoring period. These monitoring results were from the general wastewater discharge outlet of the studied enterprise. They all conformed to the standard discharge limits specified in Table 1 of the *Emission Standard of Pollutants for Petroleum Chemistry Industry* (GB31571-2015).

Uncertainty Evaluation of Monitoring Results

The monitoring was already completed in terms of work, and the monitoring results were qualified. However, this mean value method failed to evaluate the indications of

Table 1: Monitoring results at chemical fibre wastewater discharge outlet.

Monitoring item	1st time	2nd time	3rd time	4th time	5th time	6th time	7th time	8th time	Mean value and range	Standard present value
pH value	8.10	8.15	8.08	8.25	7.95	7.99	7.86	7.97	7.86–8.25	6–9
COD	33	30	30	32	31	34	33	36	32	70
$\text{NH}_3\text{-N}$	2.10	1.84	1.77	1.76	1.11	1.09	0.88	0.90	1.43	8.0
TP	0.28	0.26	0.26	0.26	0.52	0.54	0.56	0.50	0.40	1

the measurement results. It did not analyze the whole measurement process or provide quality evaluation and improvement suggestions for the enterprise or monitoring unit. Thus, analysis methods were also used. The main detecting instruments are shown in Table 2.

According to Formulas (1) and (2) of the universal model, the monitoring methods and detecting instruments of the above four monitoring quantities were combined to carry out the uncertainty source analysis and uncertainty calculation of each component. The calculation results of combined uncertainty are shown in Table 3.

The extended uncertainty is calculated using Formula (3), as given in Table 4.

The pH value of the aqueous solution is measured using the selected methods and instruments. Uncertainties caused by pH meter, repetition of measurement results, and standard buffer solution used by calibration instrument influence

the uncertainty measurement. With the development of instrument technology, the temperature and humidity in environmental factors can be included in the instrumental factors. Human factors and instrument variability are embodied in the repetition of measurement results. The main uncertainty sources are listed for the following measurements. For COD: standard potassium dichromate solution, calibration of standard ammonium ferrous sulphate solution, volume difference of ferrous ammonium sulphate consumed by the titration blank and water sample, measurement of the water sample, the molar mass of oxygen, and repetition of sample measurement. For $\text{NH}_3\text{-N}$: dilution of standard $\text{NH}_3\text{-N}$ solution, sampling, curve fitting, and measurement repetition. For TP: preparation of the standard stock phosphorus solution, dilution of stock solution to a working solution, standard curve fitting, and repetition of sample measurement. In general, the uncertainty triggered by the repetition of sample measures is too large, which is

Table 2: Analysis methods and detecting instruments used for five monitoring quantities of chemical fibre wastewater.

S/N	Monitoring type	Item name	Basis for the analysis method	Main detecting instrument
1	Wastewater	pH value	Water Quality-Determination of pH value-Glass Electrode Method (GB6920-1986)	pH meter
2		COD	Water Quality-Determination of pH value-Dichromate Method (HJ828-2017)	Standard COD digester
3		$\text{NH}_3\text{-N}$	Water Quality-Determination of pH value-Nessler's Reagent Spectrophotometry (HJ535-2009)	Ultraviolet and visible spectrophotometer
4		TP	Water Quality-Determination of pH value-Ammonium Molybdate Spectrophotometric Method (GB/T 11893-1989)	Ultraviolet and visible spectrophotometer

Table 3: Measurement uncertainties.

Monitoring item		Component uncertainty					Relative combined uncertainty (%)
		Uncertainty of concentration function	Uncertainty in volume measurement	Uncertainty in mass measurement	Uncertainty in precision measurement	Uncertainty in recovery measurement	
pH value	Standard (mol/L)	3.18×10^{-9}	—	—	2.62×10^{-9}	—	4.19
	Relative	0.0230	—	—	0.0350	—	
COD	Standard (mg/L)	—	0.0314	0.018	2.07	—	6.39
	Relative	1.77×10^{-3}	2.18×10^{-3}	9.00×10^{-4}	6.38×10^{-2}	4.42×10^{-4}	
$\text{NH}_3\text{-N}$	Standard (mg/L)	3.24×10^{-4}	3.13×10^{-2}	—	1.43	—	33.8
	Relative	5.22×10^{-3}	6.26×10^{-3}	—	0.338	5.34×10^{-3}	
TP	Relative	1.79×10^{-3}	5.20×10^{-3}	—	0.359	1.42×10^{-3}	35.9

Table 4: Extended uncertainty.

Monitoring item	Extended relative uncertainty ($k = 2$; %)	Extended uncertainty	Representation of measurement result ($k = 2$)
pH value	8.38	$(8.36\text{--}9.88) \times 10^{-9}$ mol/L	8.04 ± 0.04
COD	12.78	2.07 mg/L	(32 ± 2.07) mg/L
$\text{NH}_3\text{-N}$	67.6	0.97 mg/L	(1.43 ± 0.97) mg/L
TP	71.8	0.29 mg/L	(0.40 ± 0.29) mg/L

mainly ascribed to a long measurement period and different matter contents in samples.

POLICY SUGGESTIONS

Perfecting the Chemical Fibre Production Process

The production procedures of the chemical fibre manufacturing industry are complicated. The wastewater quality components are also varied. Thus, the most effective technical measures should be taken to conduct wastewater treatment and transform toxic substances into harmless components for recycling. In this way, the waste discharge in chemical fibre production can be reduced, and the environmental protection effect of chemical fibre manufacturing can be improved. The management of chemical fibre wastewater treatment process and technology should be strengthened to reduce the discharge of chemical fibre wastewater and mitigate environmental pollution. The quality of water treatment should also be improved to facilitate the progress of petrochemical fibre manufacturing. The most suitable wastewater treatment process and technical measures should be selected and used. For example, the physiochemical method can be used to treat chemical fibre wastewater. It removes oil droplets, suspended matters, and bacteria through de-oiling, air flotation, adsorption, and membrane separation. In turn, the wastewater quality can reach the related quality standards and be used as circulating water or boiler water in chemical fibre production. Ultimately, the discharge of chemical fibre wastewater can be reduced.

Improving the Wastewater Treatment Process

The differences between chemical fibre products and treatment methods are prominently manifested by the quantity difference of pollutant types. Therefore, the promotion and application should be reinforced in the chemical fibre manufacturing process. With continuous social progress, the chemical fibre wastewater treatment measures should be constantly studied, innovated, strengthened, and improved. In this way, the economic benefit of chemical fibre production can be elevated to the maximum extent, and the wastewater discharge cost and the water quality standard can be improved. For instance, the advanced oxidation technology can be used to decompose organic matters that can be hardly degraded by macromolecules through the chain reaction of free radicals under high-temperature, high-pressure, and catalytic conditions. When the membrane separation technology is used to separate the components after the chemical fibre wastewater treatment, the obtained by-product can generate profit. The treatment standards of chemical fibre wastewater have been continuously improved. Product safety and environmental protection are boosted

with the direct implementation of oil-water separation, improvement of chemical fibre wastewater treatment quality, application of various membrane materials, and development of new nanofilm separation technologies.

Strengthening the Development of the Environmental Monitoring Industry of Wastewater

The government should strengthen the policy inclination to the environmental monitoring field in the chemical industry. They can establish a national network focusing on air environmental monitoring, water quality monitoring, and pollution source monitoring. They should support the market for monitoring equipment to maintain the overall growth of the environmental monitoring industry. The enterprises dedicated to environmental pollution control should be encouraged to propose technological innovations for environmental monitoring. These innovations should emphasize remote and intelligent sewage pollution source analysis, transregional transmission, scientific decision-making, and precision regulation. The current technologies, such as miniaturized technology of environmental analytical instruments, online analysis technology of comprehensive water toxicity, and volatile organic compound online monitoring technology, should also be strengthened.

Enhancing the Virtual Instrument R&D for Environmental Monitoring

Virtual instruments have low cost, a wide range of applications, and strong repeatability. Thus, they are easier to use and more suitable for special environments, such as field operation, than traditional instruments. They can save materials and improve working efficiency if used to simulate the measured data. Accordingly, the extensive application of virtual instruments in environmental monitoring should be strengthened. The uncertainties of their components and their overall uncertainties should be determined and evaluated. For some components exceeding the related errors, they should be reasonably debugged and verified to ensure the smooth test and the accuracy of the environmental monitoring results.

CONCLUSIONS

The chemical fibre industry is the subject of China's consumer goods industry and is critical to national economic growth. It is a typical representative labour-intensive industry with high energy consumption and high pollution. The environmental monitoring of pollutants generated in the chemical fibre production should be strengthened, and the monitoring quality should be improved. These actions are significant to relieve the pressure triggered by economic growth to resource supply and facilitate efficient utilization

and recycling of resources. In this study, the hazard types of wastewater generated in the chemical fibre production were determined. The wastewater monitoring uncertainties of a chemical fibre industry in Jilin City, Jilin Province were measured using an environmental monitoring uncertainty model. The literature describes the chemical fibre industry as a labour-intensive industry with high energy consumption, which leads to severe environmental pollution. This claim is supported by the following findings in the current study: The main hazard types of chemical fibre wastewater are “polluting the surrounding environment, endangering human health, and destroying biodiversity”. The monitoring quality reliability of the extended uncertainty model for the pH value, COD, NH₃-N, and TP used in this case is superior to the direct chemical numerical detection quality. Thus, perfecting the chemical fibre production process, improving the wastewater treatment process, strengthening the development of the environmental monitoring industry of wastewater, and enhancing the virtual instrument R&D for environmental monitoring are proposed. In the future, an in-depth study can be implemented from the following aspects: a comprehensive evaluation of environmental monitoring indices for the chemical fibre industry, optimization of environmental monitoring uncertainty model, technical index standard of environmental monitoring instruments, exploration of energy conservation, and emission reduction paths for the chemical fibre industry.

ACKNOWLEDGEMENTS

This paper is sponsored by Scientific Promotion Project of Jilin Railway Technology College (No. KTTD2018003).

REFERENCES

Aleksandra Lewkiewicz-Małysa and Elzbieta Konopka 2009. Evaluation of waters environment hazard by pulp-mill liquors. *Polish Journal of Chemical Technology*, 10(4): 15-19.

- Batley, G. E. 1999. Quality assurance in environmental monitoring. *Marine Pollution Bulletin*, 39(1-12): 23-31.
- Boon, K.A., Taylor, P. D. and Ramsey, M. H. 2010. Estimating and optimising analytical and sampling uncertainty in environmental investigations: Application and evaluation. *Geostandards and Geoanalytical Research*, 31(3): 237-249.
- Conti, M.E., Muse, J.O. and Mecozzi, M. 2005. Uncertainty in environmental analysis: Theory and laboratory studies. *International Journal of Risk Assessment and Management*, 5(2): 311-335.
- Escher, B. and Leusch, F. 2011. Bioanalytical tools for safe water supplies: using cellular response to show toxicity effect. *Water*, 21: 31-33.
- Lambert, P. G. and Woodward, J. L. 2015. Learning from events: major process safety incidents from wastewater in process chemical plants, or take care of your wastewater or it will take care of you. *Process Safety Progress*, 30(1): 45-51.
- Peng, L.M., Zhi, H., Liang, Y. and Zhong, D.L. 2009. Mathematical model for general use in evaluation of uncertainty of some commonly used analytical methods. *Physical Testing and Chemical Analysis (Part B: Chemical Analysis)*, 45(5): 558-45.
- Nasir, A., Arslan, C., Khan, M. A., Nazir, N., Awan, U. K., Ali, M. A. and Waqas, U. 2012. Industrial wastewater management in district Gujranwala of Pakistan-current status and future suggestions. *Pakistan Journal of Agricultural Sciences*, 49(1): 79-85.
- Nezhikhovskii, G. R. 2009. Measurement uncertainty in quantitative chemical analysis: problems of the transition period. *Inorganic Materials*, 45(14): 1643-1647.
- Orhon, D., Uslu, O., Meriç S., Salihoglu, I. and Filibeli, A. 1994. Wastewater management for Istanbul: basis for treatment and disposal. *Environmental Pollution*, 84(2): 167-78.
- Rocke, D. M., Durbin, B., Wilson, M. and Kahn, H.D. 2003. Modeling uncertainty in the measurement of low-level analytes in environmental analysis. *Ecotoxicology and Environmental Safety*, 56(1): 78-92.
- Shirkhanloo, H., Mirzahosseini, S.A.H., Shirkhanloo, N., Moussavi-Najarkola, S.A. and Farahani, H. 2015. The evaluation and determination of heavy metals pollution in edible vegetables, water and soil in the south of Tehran province by gis. *Archives of Environmental Protection*, 41(2): 64-74.
- Tayeb, A., Chellali, M. R., Hamou, A. and Debbah, S. 2015. Impact of urban and industrial effluents on the coastal marine environment in Oran, Algeria. *Marine Pollution Bulletin*, 98(1-2): 281-288.
- Verma, A. K., Dash, R. R. and Bhunia, P. 2012. A review on chemical coagulation/flocculation technologies for removal of colour from textile wastewaters. *Journal of Environmental Management*, 93(1): 154-168.
- Wei, D., Liu, Y. and Zhang, N. 2019. Does industry upgrade transfer pollution: evidence from a natural experiment of Guangdong province in China. *Journal of Cleaner Production*, 229(20): 902-910.

... Continued from inner front cover

- The text of the manuscript should run into **Abstract, Introduction, Materials & Methods, Results, Discussion, Acknowledgement** (if any) and **References** or other suitable headings in case of reviews and theoretically oriented papers. However, short communication can be submitted in running with **Abstract and References**. The references should be in full with the title of the paper.
- The figures should preferably be made on a computer with high resolution and should be capable of withstanding a reasonable reduction with the legends provided separately outside the figures. Photographs may be black and white or colour.
- Tables should be typed separately bearing a short title, preferably in vertical form. They should be of a size, which could easily be accommodated in the page of the Journal.
- References in the text should be cited by the authors' surname and year. In case of more than one reference of the same author in the same year, add suffix a,b,c,.... to the year. For example: (Thomas 1969, Mass 1973a, 1973b, Madony et al. 1990, Abasi & Soni 1991).

List of References

The references cited in the text should be arranged alphabetically by authors' surname in the following manner: (Note: The titles of the papers should be in running 'sentence case', while the titles of the books, reports, theses, journals, etc. should be in 'title case' with all words starting with CAPITAL letter.)

- Dutta, A. and Chaudhury, M. 1991. Removal of arsenic from groundwater by lime softening with powdered coal additive. *J. Water Supply Res. Techno. Aqua.*, 40(1) : 25-29.
- Hammer, D.A. (ed.) 1989. *Constructed Wetlands for Wastewater Treatment-Municipal, Industrial and Agricultural*. Lewis Publishers Inc., pp. 831.
- Haynes, R. J. 1986. Surface mining and wetland reclamation. In: Harper, J. and Plass, B. (eds.) *New Horizons for Mined Land Reclamation*. Proceedings of a National Meeting of the American Society for Surface Reclamation, Princeton, W.V.

Submission of Papers

- The paper can be submitted by e-mail as an attachment in a single WORD file at **contact@neptjournal.com**
- The paper can also be submitted online in a single WORD file through the journal's website: **www.neptjournal.com**

Attention

1. Any change in the authors' affiliation may please be notified at the earliest.
2. Please make all the correspondence by e-mail, and authors should always quote the manuscript number.

Note: In order to speed up the publication, authors are requested to send the publication charges as soon as they get the 'initial acceptance' letter, and also correct the galley proof immediately after receipt. The galley proof must be checked with utmost care, as publishers owe no responsibility for mistakes. The papers will be put on priority for publication only after receiving the processing and publication charges.

Nature Environment and Pollution Technology

(Abbreviation: Nat. Env. Poll. Tech.)

(An International Quarterly Scientific Journal)

Published by



Technoscience Publications

A-504, Bliss Avenue, Opp. SKP Campus
Balewadi, Pune-411 045, Maharashtra, India

In association with

Technoscience Knowledge Communications

Mira Road, Mumbai, India

For further details of the Journal please visit the website. All the papers published on a particular subject/topic or by any particular author in the journal can be searched and accessed by typing a keyword or name of the author in the 'Search' option on the Home page of the website. All the papers containing that keyword or author will be shown on the home page from where they can be directly downloaded.

www.neptjournal.com

©Technoscience Publications: The consent is hereby given that the copies of the articles published in this Journal can be made only for purely personal or internal use. The consent does not include copying for general distribution or sale of reprints.

Published for Proprietor, Printer and Publisher: Mrs. T. P. Goel, B-34, Dev Nagar, Tonk Road, Jaipur, Rajasthan, India; Editors: Dr. P. K. Goel and Prof. K. P. Sharma